





(NASA-CP-2416-Vol-1) VORTEX FLOW  
AERODYNAMICS, VOLUME 1 (NASA) 404 p  
HC A18/MF A01

CSCL 01A

N86-27190  
THRU  
N86-27208  
Unclas

G3/02 43173 1140

# Vortex Flow Aerodynamics

## *Volume I*

*Edited by*  
James F. Campbell  
*Langley Research Center*  
*Hampton, Virginia*

Russell F. Osborn  
*Air Force Wright Aeronautical Laboratories*  
*Wright-Patterson Air Force Base, Ohio*

Jerome T. Foughner, Jr.  
*Langley Research Center*  
*Hampton, Virginia*

Proceedings of a conference sponsored by the  
NASA Langley Research Center, Hampton, Virginia,  
and the Air Force Wright Aeronautical Laboratories,  
Flight Dynamics Laboratory, Wright-Patterson  
Air Force Base, Ohio, and held at  
Langley Research Center  
October 8-10, 1985

**NASA**  
National Aeronautics  
and Space Administration  
Scientific and Technical  
Information Branch

## PREFACE

The objectives of the joint NASA/Air Force Vortex Flow Aerodynamics conference held at NASA Langley Research Center October 8-10, 1985, were to discuss fluid mechanics and aerodynamics of leading-edge vortex flows and vortex flaps. Papers were presented by researchers from the U.S. Air Force, NASA, industry, and universities.

The conference was organized in seven sessions as follows:

- Overview
- Vortex Theory 1
- Vortex Experiment
- Vortex Flap Analysis and Design
- Vortex Theory 2
- Vortex Flap Configuration Aerodynamics
- Vortex Flap Applications

The proceedings are published in three volumes as follows because of the range of classifications:

- Volume I, Unclassified (NASA CP-2416)
- Volume II, Unclassified, ITAR restricted (NASA CP-2417)
- Volume III, Confidential (NASA CP-2418)

Appreciation is expressed to the Langley/Wright Aeronautical Laboratories committee, which developed the structure of the conference and selected and reviewed papers, to the session chairmen and speakers, who contributed to the technical quality of the conference, and to the many individuals who contributed to the administrative and logistic success of the conference. The assistance of the Research Information and Applications Division of the NASA Langley Research Center in publishing these proceedings is also gratefully acknowledged. A list of attendees is included at the end of this document.

James F. Campbell  
Russell F. Osborn  
Jerome T. Foughner, Jr.

**PRECEDING PAGE BLANK NOT FILMED**

## CONFERENCE ORGANIZATION

### Welcome

R. V. Harris, Jr. (Langley)

### Session 1 - Overview

Chairman: P. J. Bobbitt (Langley)

### Session 2 - Vortex Theory 1

Chairman: P. J. Bobbitt (Langley)

### Session 3 - Vortex Experiment

Chairman: L. L. Presley (Ames)

### Session 4 - Vortex Flap Analysis and Design Studies

Chairman: L. R. Miranda (Lockheed, California)

### Session 5 - Vortex Theory 2

Chairman: B. Dillner (Boeing)

### Session 6 - Vortex Flap Configuration Aerodynamics

Chairman: M. Buck (Air Force Wright Aeronautical Laboratories)

### Session 7 - Vortex Flap Applications

Chairman: C. W. Smith (General Dynamics)

## CONTENTS

### Volume I

|   |     |
|---|-----|
| PREFACE .....   | 111 |
| 1. VORTEX LIFT RESEARCH: EARLY CONTRIBUTIONS AND<br>SOME CURRENT CHALLENGES .....                 | 1   |
| Edward C. Polhamus  |     |
| 2. LEADING-EDGE VORTEX RESEARCH: SOME NONPLANAR<br>CONCEPTS AND CURRENT CHALLENGES .....          | 31  |
| James F. Campbell and Russell F. Osborn   |     |
| 3. EXTENSIONS OF THE CONCEPT OF SUCTION ANALOGY TO<br>PREDICTION OF VORTEX LIFT EFFECT .....      | 65  |
| C. Edward Lan   |     |
| 4. RECENT EXTENSIONS TO THE FREE-VORTEX-SHEET THEORY<br>FOR EXPANDED CONVERGENCE CAPABILITY ..... | 85  |
| James M. Luckring, Keith D. Hoffler,<br>and Arthur C. Grantz                                      |     |
| 5. A DIRECT AND INVERSE BOUNDARY LAYER METHOD FOR<br>SUBSONIC FLOW OVER DELTA WINGS .....         | 115 |
| Shawn H. Woodson and Fred R. DeJarnette   |     |
| 6. AN EXPERIMENTAL INVESTIGATION OF VORTEX<br>BREAKDOWN ON A DELTA WING .....                     | 135 |
| F. M. Payne and R. C. Nelson  |     |
| 7. LASER VELOCIMETRY IN HIGHLY THREE-DIMENSIONAL<br>AND VORTICAL FLOWS .....                      | 163 |
| Charles J. Novak, Charles R. Huie,<br>and Kenneth C. Cornelius                                    |     |
| 8. IN-FLIGHT AND WIND TUNNEL LEADING-EDGE VORTEX<br>STUDY ON THE F-106B AIRPLANE .....            | 187 |
| John E. Lamar   |     |
| 9. BASIC STUDIES ON DELTA WING FLOW MODIFICATIONS<br>BY MEANS OF APEX FENCES .....                | 203 |
| Keith D. Hoffler, Dhanvada M. Rao,<br>and Mark C. Frassinelli                                     |     |
| 10. TOWARDS AN ADVANCED VORTEX FLAP SYSTEM - THE<br>"CAVITY" FLAP .....                           | 219 |
| Dhanvada M. Rao   |     |
| 11. VORTEX FLOW HYSTERESIS .....  | 231 |
| Atlee M. Cunningham, Jr.  |     |

|     |   |     |
|-----|---|-----|
| 12. | VISCOUS VORTICAL FLOW CALCULATIONS<br>OVER DELTA WINGS .....  | 249 |
|     | G. Blom, J. C. Wai, and H. Yoshihara  |     |
| 13. | AN EULER AERODYNAMIC METHOD FOR LEADING-EDGE<br>VORTEX FLOW SIMULATION .....  | 263 |
|     | Pradeep Raj and Lyle N. Long  |     |
| 14. | EULER ANALYSIS OF AN ELLIPTIC MISSILE BODY<br>AT ANGLES OF ATTACK .....   | 283 |
|     | James R. Sirbaugh   |     |
| 15. | COMPUTATION OF LEADING-EDGE VORTEX FLOWS .....  | 305 |
|     | Richard W. Newsome and James L. Thomas  |     |
| 16. | STEADY SUPERSONIC NAVIER-STOKES SOLUTIONS<br>OF A 75° DELTA WING .....  | 331 |
|     | Thomas A. Buter and Donald P. Rizzetta  |     |
| 17. | AN OVERVIEW OF THE FUNDAMENTAL AERODYNAMICS BRANCH'S<br>RESEARCH ACTIVITIES IN WING LEADING-EDGE<br>VORTEX FLOWS AT SUPERSONIC SPEEDS ..... | 349 |
|     | David S. Miller, Richard M. Wood,<br>and Peter F. Covell  |     |
| 18. | WATER TUNNEL RESULTS OF LEADING-EDGE VORTEX<br>FLAP TESTS ON A DELTA WING VEHICLE .....   | 379 |
|     | John H. Del Frate   |     |

#### Volume II\*

|   |   |
|---|---|
| PREFACE .....   | 111   |
| 1. ADVANCED FIGHTER TESTED FOR LOW-SPEED<br>AERODYNAMICS WITH VORTEX FLAPS .....  | 1   |
|   | Gregory M. Gatlin                           |
| 2. CRITICAL EVALUATION OF A VORTEX FLAP DESIGN<br>CONCEPT USING A 74° DELTA CONFIGURATION .....                         | 17  |
|   | Neal T. Frink                               |
| 3. THE LATERAL-DIRECTIONAL CHARACTERISTICS OF A<br>74-DEGREE DELTA WING EMPLOYING GOTHIC<br>PLANFORM VORTEX FLAPS ..... | 39  |
|   | Arthur C. Grantz                            |
| 4. AERODYNAMIC ASSESSMENT OF VORTEX FLAPS ON TWO FIGHTER<br>AIRCRAFT CONFIGURATIONS AT TRANSONIC SPEEDS .....           | 69  |
|   | John R. Klein, Julio Chu, and Neal T. Frink |

---

\*Volume II is published as NASA CP-2417.



|     |  |     |
|-----|--|-----|
| 5.  | SUBSONIC ANALYSIS AND DESIGN OF VORTEX FLAPS .....   | 97  |
|     | C. Edward Lan and C. C. Hsing  |     |
| 6.  | ATTACHED FLOW NUMERICAL METHODS FOR THE AERODYNAMIC<br>DESIGN AND ANALYSIS OF VORTEX FLAPS .....   | 111 |
|     | Harry W. Carlson and Christine M. Darden   |     |
| 7.  | PERFORMANCE ANALYSIS AND SUPERSONIC DESIGN<br>OF WING LEADING-EDGE VORTEX FLAPS FOR<br>THE CONVULIR F-106B .....                               | 123 |
|     | Lawrence B. Huebner and John E. Lamar  |     |
| 8.  | EXPERIMENTAL INVESTIGATION AT LOW- AND HIGH-SUBSONIC<br>SPEEDS OF A MODERATELY SWEEPED FIGHTER WING WITH<br>DEFLECTED LEADING-EDGE FLAPS ..... | 141 |
|     | Gary E. Erickson and Lawrence W. Rogers  |     |
| 9.  | EXPERIMENTAL STUDY OF VORTEX FLAPS ON A DELTA WING SWEEP<br>SERIES AT HIGH ANGLE OF ATTACK .....   | 169 |
|     | Thomas D. Johnson, Jr. and Jarrett K. Huffman  |     |
| 10. | AN INVESTIGATION OF THE SUBSONIC MANEUVER CHARACTERISTICS<br>OF TWO SUPERSONIC FIGHTER WING CONCEPTS .....                                     | 185 |
|     | Bryan A. Campbell and Gregory D. Riebe   |     |
| 11. | INVESTIGATION OF VORTEX FLAPS ON THE F-106B<br>AIRPLANE CONFIGURATION IN THE 30- BY 60-FOOT<br>WIND TUNNEL .....                               | 201 |
|     | Long P. Yip  |     |
| 12. | AERODYNAMIC TESTING AND ANALYSIS OF VORTEX FLAP<br>CONFIGURATIONS FOR THE 5-PERCENT SCALE F-106B .....   | 227 |
|     | James B. Hallissy, Neal T. Frink, and<br>Jarrett K. Huffman  |     |
| 13. | DESIGN AND WIND TUNNEL EVALUATION OF VORTEX<br>FLAPS FOR THE F-16XL .....  | 249 |
|     | Dennis B. Finley and W. Elliott Schoonover, Jr.  |     |
| 14. | DESIGN AND WIND TUNNEL EVALUATION OF VORTEX<br>FLAPS FOR THE USAF AFTI/F-111 .....   | 277 |
|     | W. Elliott Schoonover, Jr. and Frank R. Smith  |     |

#### Volume III\*

|   |     |
|---|-----|
| PREFACE .....   | 111 |
| 1. REFINEMENTS OF A VORTEX FLAP DESIGN METHOD<br>WITH SYSTEMATIC APPLICATIONS (U) ..... | 1   |
| Neal T. Frink   |     |

---

\*Volume III is published as NASA CP-2418.

VORTEX LIFT RESEARCH:  
EARLY CONTRIBUTIONS AND SOME CURRENT CHALLENGES

Edward C. Polhamus  
NASA Langley Research Center  
Hampton, Virginia

SUMMARY

This paper briefly reviews the trend towards slender-wing aircraft for supersonic cruise and the early chronology of research directed towards their vortex-lift characteristics. An overview of the development of vortex-lift theoretical methods is presented, and some current computational and experimental challenges related to the viscous flow aspects of this vortex flow are discussed.

INTRODUCTION

Beginning with the first successful controlled flights of powered aircraft, there has been a continuing quest for ever-increasing speed, with supersonic flight emerging as one of the early goals. The advantage of jet propulsion was recognized early, and by the late 1930's jet engines were in operation in several countries. High-speed wing design lagged somewhat behind, but by the mid 1940's it was generally accepted that supersonic flight could best be accomplished by the now well-known highly swept wing, often referred to as a "slender" wing. It was also found that these wings tended to exhibit a new type of flow in which a highly stable vortex was formed along the leading edge, producing large increases in lift referred to as vortex lift. As this vortex flow phenomenon became better understood, it was added to the designers' options and is the subject of this conference.

The purpose of this overview paper is to briefly summarize the early chronology of the development of slender-wing aerodynamic technology, with emphasis on vortex lift research at Langley, and to discuss some current computational and experimental challenges.

TOWARDS SLENDER-WING AIRCRAFT

I joined the Langley staff in July of 1944, shortly after Allied pilots had first encountered the German swept wing Me 262 jet fighter shown in figure 1. Since prototype jet aircraft had been built and flown previously by the Germans, British, and Americans, the most surprising feature of the Me 262 was its sweptback wing which contributed to a speed advantage through a delay of the onset of compressibility drag - a benefit of sweep not understood in the Allied nations at the time. Although the  $18^\circ$  of sweepback was the fortuitous result of a design change, in 1940, to fix a center-of-gravity problem, German researchers had, that same year, demonstrated in the wind tunnel that Busemann's 1935 supersonic swept wing theory (ref. 1) also applied to subsonic compressibility effects (ref. 2) and immediately began the design of more highly swept wings for the Me 262. Thus, the Me 262 program represents the



genesis of the trend towards slender-wing supersonic aircraft as illustrated in figure 2. The Me 262 had first flown in 1942, and advanced versions incorporating wings with sweep angles as high as  $50^\circ$  were studied (ref. 3). A  $40^\circ$  sweep version, shown in figure 2, had been tested in a German wind tunnel in 1941 and reached the prototype stage in early 1945 but was accidentally destroyed on the runway before its first flight (ref. 4).

Highly swept delta wings were also being studied in Germany but none reached the powered prototype stage, and the conclusion of the war brought an end to the studies.

The benefit of sweep with regard to high-speed flight remained a mystery outside of Germany until January 1945 when R. T. Jones of the Langley Research Center completed a theoretical study in which he demonstrated, independent of Busemann's work, that wing pressure distributions are determined solely by the "component of motion in a direction normal to the leading edge." He further pointed out that for efficient supersonic flight, the wing should be swept behind the Mach cone with the sweep angle being such that the normal component of velocity is below the airfoil's critical speed (ref. 5).

Jones' theoretical work and the subsequent acquisition of German swept wing data stimulated extensive swept wing research programs at Langley and Ames and aircraft development programs within the Air Force and industry. Two of the early U. S. aircraft utilizing the concept are shown on the right of figure 2. In 1947 the north American XP-86, which utilized some of the  $40^\circ$  swept wing data from the Me 262 program, made its first flight and became the first of a long line of swept wing jets optimized for high subsonic cruise and capable of supersonic dash (ref. 6). The Convair XF-92A, which first flew in 1948, represents the beginning of the evolution of the slender wings desirable for efficient supersonic cruise of interest to this paper (ref. 7).

While the slender wing combined with the jet engine made supersonic flight practical, its high-speed benefits did not come without a sacrifice in subsonic capabilities. It was, of course, recognized early that the slender, low-aspect ratio planforms required for efficient supersonic flight provided extremely poor subsonic performance due to their high level of induced drag. Their lift gradient was low, and it was found that the effectiveness of conventional high-lift flow control devices was poor. It was obvious that new design approaches were needed.

For those aircraft missions requiring very high levels of both subsonic and supersonic performance, the most obvious solution was the application of adjustable planform geometry in the form of variable sweep. The first wind tunnel study of symmetrical variable sweep appears to be that carried out in Langley's 300-MPH, 7- by 10-ft High-Speed Tunnel beginning in 1946. Further analytical research and experiments in the 7- by 10-ft High-Speed Tunnel in 1958 provided the variable sweep concept that led to the F-111, F-14, and B-1 aircraft (see refs. 8 and 9 for reviews).

#### THE DISCOVERY OF VORTEX LIFT

Another important event related to the application of slender-wing benefits to supersonic aircraft also took place in 1946 when researchers at Langley discovered a flow phenomenon that was to play an important role in the design of fixed planform slender-wing aircraft not requiring the high degree of multimission capability

offered by variable sweep. This phenomenon was the leading-edge vortex flow which is the subject of this conference.

The sequence of events leading to this discovery began in 1945 when American aerodynamists surveying German aeronautical developments decided that the Lippisch highly swept delta wing DM-1 test glider, shown on the left in figure 3, should be shipped to Langley for tests in the Full-Scale Tunnel. The Germans had planned to use the DM-1 for flight studies of the low-speed characteristics of a proposed supersonic aircraft (refs. 10 and 11). While the American team recognized that the wing was too thick for efficient supersonic flight, they felt that it offered an early opportunity to study the low-speed characteristics of highly swept delta wings under full-scale conditions and arrangements were initiated by a letter dated November 17, 1945 (United States Air Force in Europe to Commanding General, Army Air Forces, Washington, D.C., 1945).

The glider arrived at Langley early in 1946 and is shown in the Full-Scale Tunnel on the right of figure 3. It will be noted that several changes had been made, and the sharp leading edge shown in the photograph was the result of Langley research to improve the high lift characteristics. The Langley study, reported by Wilson and Lovell (ref. 12), discovered that the maximum lift of the original round leading-edge configuration was considerably lower than that obtained on similar wings previously tested at low Reynolds numbers in Germany and at Langley. A small model was quickly built and its flow characteristics studied. It was found that at low Reynolds numbers, laminar separation occurred at the leading edge, and a strong vortex developed which produced large lift increments. It was then reasoned that a sharp leading edge would produce a similar flow even at high Reynolds numbers, and the DM-1 was modified as shown. The results shown in figure 4 produced large vortex lift increments which offered a solution to the slender-wing high angle-of-attack lift capability problem. Their research provided the first insight on the effects of leading-edge radius and Reynolds number on vortex lift. A "cross-flow separation" model of the vortex flow was also proposed in their paper. Although this research remained under a security classification for four years, it did provide a stimulus for additional research at Langley and Ames and interest within the Air Force and the aircraft industry. Much of the international interest in vortex flow was generated somewhat later through its independent discovery by French researchers during studies carried out in 1951 and 1952, closely followed by related research in Great Britain (refs. 13 and 14).

#### THE CONTROLLED SEPARATION CONCEPT

Two of the primary characteristics of slender wings are illustrated in figure 5. One of the primary driving forces in the designers' selection of a slender wing for supersonic cruise is the reduction in lift-dependent drag shown on the left for a Mach number of 2.5. As pointed out by both Busemann (ref. 1) and Jones (ref. 5), sweeping the leading edge behind the Mach cone provides a subsonic type flow with upwash manifesting itself as a leading-edge thrust effect, as long as the flow remains attached, which more than offsets the adverse effect of aspect ratio reduction. However, as shown on the right, attached flow theory predicted the subsonic lift capability to be very low for a slender wing. The wing shown has a sweep of  $75^\circ$  selected for a cruise point of about  $M=2.5$ . If, however, the flow separates at the leading edge, vortex flow develops, and large vortex-lift increments are attained. This lift, associated with the large mass of air accelerated downward

by the nonplanar vortex sheets, greatly relieves the lift deficiency of slender wings with attached flow. With a sharp leading edge, the separation occurs simultaneously along the edge and, thereby, eliminates the spanwise stall progression which produces various stability and control problems. In addition, vortex-induced reattachment delays trailing-edge separation. Competing with these advantages, of course, is the increased drag resulting from the loss of leading-edge thrust.

The above slender-wing characteristics led to a new aircraft design concept which departed from the time honored "attached flow" wing design for certain flight conditions. Basically, this concept consisted of designing the wing for attached flow at supersonic cruise conditions using concepts such as conical camber with pressure components providing the leading-edge thrust effect but allowing the flow to separate at the leading edge and generate vortex lift to provide the low-speed lift required. This simplified the wing design by reducing the need for leading- and trailing-edge high-lift flow-control devices—devices which are relatively ineffective on highly swept wings and increase the complexity and weight.

The U. S. supersonic delta-wing aircraft designed in the mid 1950's to the early 1960's utilized this approach to various degrees as illustrated in figure 6 with a photograph of the B-70 in the landing mode. The photograph, taken around 1965, illustrates the strong leading-edge vortices generated by the thin,  $65.5^\circ$  delta wing and made visible by natural condensation. However, during this period, NASA's basic and applied research on leading-edge vortex flows lagged considerably behind that of Great Britain and France where researchers were enthusiastic over what many of them described as the "new aerodynamics." In 1962, an agreement was signed between the British and French to develop a supersonic commercial transport, and they soon agreed on the now well-known slender ogee-delta wing planform with the design based on the "controlled flow separation" concept. They improved the application of the design concept by detailed tailoring of the wing warp and planform to improve the performance of both the attached flow and vortex flow modes as well as the transition mode.

The result of this extensive development program was the remarkable "Concorde" supersonic commercial transport which is still the only supersonic transport in regular passenger service, although the Soviets are undoubtedly amassing considerable experience in their TU-144 flight programs. For details of the "Concorde" development, the reader is referred to references 14 and 15.

#### RENEWED LANGLEY INTEREST

Langley research related to vortex lift began to accelerate in the mid 1960's. Contributing to this acceleration was the interest generated by the extensive research in France and Great Britain in support of the Concorde, growing interest in supersonic cruise aircraft and lightweight highly maneuverable fighter aircraft, and the development at Langley of a three-dimensional theoretical approach that provided an improved understanding of leading-edge vortex flows for arbitrary planforms.

#### Vortex-Lift Theory Development

The three-dimensional theory referred to above is the leading-edge suction analogy developed at Langley in 1966 (ref. 16). Prior to this development, the



theoretical approaches were generally confined to slender-wing conical flow approximations in order to simplify the nonlinear system of equations resulting from the fact that neither the strength or shape of the free vortex sheet is known.

A chronology of some of the advances that have been made in the development of theoretical methods for predicting the aerodynamics of sharp-edged slender wings having leading-edge vortex flow is presented in figure 7. The total lift developed on a  $76^\circ$  delta wing as a function of angle of attack is used to illustrate the advances that have been made, and both experimental measurements and attached flow calculations are included for comparison purposes. Shown are three of the conical flow theories and two of the nonconical, or three-dimensional, theories.

The first mathematical model of the vortex flow was proposed and investigated by Legendre at ONERA in France in 1952 (ref. 17). Using a slender-body approach, he represented the leading-edge vortex sheets by two isolated vortices and solved for their position and strength by applying a Kutta condition at the leading edge and requiring that the vortices sustain no force. While this approach did produce a nonlinear vortex lift, the simplifying assumptions resulted in a greatly overpredicted lift force.

Improvements in Legendre's approach followed, and in 1955 Brown and Michael of the Langley Research Center replaced the no-force condition on the vortex by one on the vortex and a feeding sheet, taken together, which provided some improvement in the vortex lift prediction (ref. 18).

By the mid 1960's, many conical flow theories had been developed drawing on slender-wing concepts, the most notable of which was that of Smith of the RAE in England which, although still overpredicting the lift, provided an excellent representation of the spiral-shaped vortex sheet (ref. 19). These theories provided much insight into the vortex flow phenomena and contributed to early design concepts. However, their applicability to wings of practical interest was limited by their exclusion of effects such as, for example, the trailing-edge Kutta condition at subsonic speeds and the proximity of the Mach cone at supersonic speeds.

The difficulties in accounting for these three-dimensional effects were greatly relieved by the development of the "leading-edge suction analogy" in 1966 at the Langley Research Center (ref. 16). This analogy equates the normal force produced by the separation induced vortex flow to the attached flow leading-edge suction force. This allows three-dimensional linearized flow theory to be used for this nonlinear flow phenomenon thereby greatly reducing theoretical complexity as well as numerical run time and cost. An indication of its ability to overcome the limitations of slender-wing conical flow theories is illustrated in figure 7 for the low-speed case. Excellent agreement was also obtained for both lift and drag for a wide range of delta wings up to angles of attack where vortex breakdown or vortex asymmetry occur.

It was soon found that the suction analogy offered a broad range of prediction capability and the possibility of design-by-analysis capability. The method, therefore, was used to develop a coordinated theoretical-experimental vortex flow research program by a small group of Langley researchers, which will be described in the following section. However, before leaving the theory chronology, it should be pointed out that the researchers recognized the eventual need to provide a method that models the complete flow field and establishes surface pressure details.

Therefore, they contracted with the Boeing Company in 1973 to develop a higher order

panel method to model the leading-edge vortex flow. A schematic of the resulting theoretical model, known as the "free vortex sheet" (FVS) method, is shown on the right of figure 7 and will be described later.

Also supported was the development of some free vortex filament approaches in the university community to determine if they might provide a simpler method that would satisfy the design and analysis needs. However, the experience gained from these and other studies indicated that the filament formulations have failed to provide consistent and accurate load distributions, they exhibit undesirable numerical modeling sensitivity, and they are unduly complicated for the estimation of overall force/moment properties. A similar conclusion has been drawn by Hoeijmakers in reference 20, and no further reference to these methods will be made in this paper.

### The Langley Research Program

The suction analogy provided a vortex flow analysis tool that included three-dimensional effects and offered the designer the possibility of at least some limited design capability. With this new theoretical tool and their renewed vortex flow interest, the Langley researchers initiated a coordinated theoretical and experimental vortex flow research program. Although the bulk of their experimental research was performed at subsonic speeds in the 7- by 10-foot high-speed tunnel, they extended their studies to transonic, supersonic, and hypersonic speeds by scheduling time in other Langley facilities.

The purpose of this section is to briefly review the early years of this program which covered both performance- and stability-related vortex flow characteristics. For a more complete review of the program, the reader is referred to the summary papers by Lamar and Luckring (ref. 21) and by Lamar and Campbell (ref. 22).

Performance Characteristics - The initial application of the suction analogy illustrated in figure 7 was for incompressible flow, and it was found to provide excellent predictions of the lift and drag of sharp-edged delta wings over a large range of sweep angles and angles of attack (see refs. 16 and 23).

Since the analogy could be applied using the attached flow leading-edge suction from any accurate, attached flow theory, it was extended into the high subsonic and supersonic ranges early in the program (ref. 24). An example of this application is shown in figure 8 for a  $76^\circ$  delta wing at an angle of attack of  $18^\circ$ . The analogy was applied in the subsonic range using the Prandtl-Glauert transformation and in the supersonic range using linearized supersonic theory. The resulting vortex lift increments  $C_{L_V}$  are shown on the left compared with experiment, and agreement is excellent over the entire Mach range. The experimental values were obtained by subtracting attached flow theory values from the total measured lift. The results illustrate the ability of the analogy to predict the reduction in vortex lift encountered at supersonic speeds as the Mach cone approaches the leading edge. The latter is associated with the forward movement of the stagnation line which reduces the vortex strength until the sonic leading-edge case is reached and the leading-edge separation vortex vanishes—a phenomenon not accounted for by slender-wing theory.

The impact of the vortex flow on the lift-dependent drag parameter,  $\Delta C_D / C_L^2$ , as a function of  $C_L$ , is illustrated on the right of figure 8 for a Mach number of 2.0. It is seen that the suction analogy and experimental results are in



good agreement and illustrate that the drag increase associated with the loss of leading-edge thrust due to leading-edge separation diminishes rather rapidly with increasing lift coefficient. This phenomenon is, of course, a result of the reduced angle of attack required for a given lift coefficient when vortex flow is present.

This initial supersonic study made it clear, as in the subsonic case, that the incremental drag reductions available through camber and twist for the subsonic-edge case are considerably less than predicted by methods which ignore the vortex-lift effect on the zero suction case (see ref. 24).

The above research was extended soon after by Fox and Lamar (ref. 25) who performed a theoretical and experimental study on a very slender wing which was within the Mach cone well into the hypersonic speed range.

Regarding landing and takeoff performance characteristics, Fox (ref. 26) applied the analogy to the prediction of ground effects and validated his theory with an experimental study.

Basic research on the use of spanwise blowing to augment the vortex-lift capability of moderately swept wings was performed by Campbell who reviewed this and other jet-powered vortex augmentation schemes in reference 22.

Stability Characteristics - Slender-wing aircraft differ from their non-slender counterparts in such characteristics as the high angles of attack they encounter and their low inertia in roll, for example. These, when combined with the non-linear vortex flow characteristics made it important to develop a knowledge of the stability characteristics.

Examples of two of the stability-related studies carried out early in the program are illustrated in figure 9. On the left is an example from the theoretical and experimental study performed by Boyden (ref. 27) in which he investigated both the steady-state and oscillatory roll damping of slender wings. He developed a method of extending the analogy to the steady-state roll case and, as shown, his theory accurately predicted the large vortex induced damping.

The overall longitudinal load distribution, which is related to the longitudinal stability and pitch damping, is shown on the right of figure 9. Snyder and Lamar (ref. 28) have shown that although the analogy does not provide detailed surface pressures it does provide an accurate prediction of the longitudinal distribution of lift which can be translated into pitching moment and pitch damping. Their results illustrated the strong trailing-edge effects which limit the usefulness of conical flow theories.

Other stability-related studies include the lateral stability research performed by Davenport and Huffman (refs. 29 and 30) which covered the subsonic, transonic, and supersonic speed regimes and the investigation of vortex asymmetry by Fox and Lamar (ref. 25).

Some Extensions of the Analogy - By the early 1970's, the suction analogy had been found to provide accurate predictions of the vortex flow characteristics of slender sharp-edge delta wings for a wide variety of aerodynamic performance and stability parameters and was being routinely applied throughout much of the aeronautical community. The Langley research program was then extended to include arbitrary planforms and round leading edges as illustrated in figure 10. In addition to the

theoretical developments, an extensive parametric wind tunnel study was performed to evaluate the resulting methods.

The general approach for the arbitrary planform extensions is illustrated on the left of figure 10 for the cropped delta configuration. Briefly, the method developed accounts for the additional vortex lift over the aft portion of the wing by the two additional vortex lift terms. The first,  $\Delta C_{L_v}$ , accounts for the downstream persistence of the leading-edge vortex (but no additional feeding), while the second,  $C_{L_{vse}}$ , is a result of the additional feeding of vorticity predicted from the attached flow edge singularity distribution along the side edge. The initial research in this area, performed by Lamar, and the extensions by Luckring cover the wide variety of planforms listed on the figure and the details of this research have been reviewed by Lamar and Luckring in reference 21.

Let us now turn from the sharp-edge cases to those with round edges where the separation is no longer fixed at the leading edge and the amount of leading-edge suction lost is a function of the location of the separation line. In the early studies, as illustrated on the right of figure 10, some variations in the measured vortex normal force,  $C_{N_v}$ , and in the remaining (or residual) leading-edge suction,  $C_{S_r}$ , were observed that led to the belief that there may be a "conservation of suction." Leading to that belief was the fact that available data on slender delta wings of various leading-edge shapes indicated that the sum of the vortex induced normal force and the remaining (or residual) portion of the leading-edge suction was equal to the theoretical attached flow leading-edge suction,  $C_{S_{th}}$ . The original Langley study, performed in 1974, was published by Kulfan (ref. 31), with permission, who used it to develop a prediction method. The research was continued by Henderson (ref. 32), who found the concept to hold for a variety of configurations. More recently, this concept has been used to develop a vortex flow prediction method for both subsonic and supersonic flow by Carlson and Mack (ref. 33).

#### AIRCRAFT CONFIGURATION RESEARCH

During the latter part of the 1960's as Air Force interest in a new lightweight highly maneuverable fighter was growing, Langley researchers expanded their aerodynamic research in several related areas. One area was the application of vortex lift to provide a lightweight approach to the high lift capability required for transonic maneuvering as well as takeoff and landing performance. Some of the conceptual configuration types studied in the vortex lift program are illustrated in figure 11. The two general wing types are characterized as "classical slender wings" and "hybrid wings."

The configurations utilizing classical slender wings are represented here by the conventional slender delta tailless type and the close-coupled canard delta. The "hybrid" wings combine attached flows and vortex flows in various combinations to provide additional degrees of multi-design-point capability. Two subclasses of hybrid wing concepts are illustrated, one which used vortex-lift strakes and is biased towards transonic maneuvering and the other a slender cranked wing biased towards supersonic cruise. For this paper, the review of the research program will

be limited primarily to the vortex strake concept. A more complete review of the overall program can be found in reference 9.

### Vortex-Lift Strakes

Two events contributed to the development of Langley's vortex-lift strake research. As a result of their canard-wing research and their basic research related to the vortex lift of slender wings, it began to appear to the Langley researchers that the favorable effect of the canard trailing vortex (resulting from the energizing effect its sidewash produced on the wing upper surface boundary layer near stall) might be extended to higher angles of attack by the highly stable leading-edge vortex flow of a slender lifting surface (see ref. 34). During the same general time period, the Northrop Company noted a favorable impact on the maximum lift of the F-5A due to a small flap actuator fairing that extended the wing-root leading edge. This spurred interest in the influence of inboard vortex flow and eventually led to the development of the YF-17.

As a result of the Langley and Northrop vortex interaction studies, plans began to be formulated by mid 1971 for an expansion of the Langley program to investigate the hybrid-wing approach with the slender lifting surfaces which became known at Langley as "vortex-lift maneuver strakes." The initial phase of the program reported by E. J. Ray et al. (ref. 35), which was performed in the Langley 7- by 10-Foot High-Speed Tunnel during the early fall of 1971, utilized the double balance technique to isolate the strake and wing loads and appears to be the first tests to clearly illustrate the magnitude of the favorable effect the strake vortex flow induces on the main wing panel flow at maneuvering conditions. Figure 12 illustrates the large overall lift increase produced by the strake at maneuvering conditions. Also shown is the direct lift carried by the strake-forebody and the incremental lift changes on the main wing panel. The total lift results illustrated the nonlinear character of the lift produced by the strakes which produces high levels of maneuver lift with essentially no increase in high-speed low-altitude gust response. The division of the lift produced by the addition of the strake illustrated the large lift increment produced on the main wing as the highly stable vortex from the strake reorganizes the flow and delays the stall on the outer panel.

This study also demonstrated the large drag reductions in the high lift range. Recognizing that the degree of flow control on the main wing would be a function of the wing design, tests were also made with segmented leading-edge flaps deflected to simulate a high-lift design condition. As was expected, the tests indicated that as the wing design is improved to delay separation on the main wing panel, the beneficial effects of the strake are delayed to increasingly higher angles of attack.

From these studies, it appeared that the vortex-lift strakes combined with variable wing camber in the form of programmed leading-edge flaps could provide a low structural weight approach for the high maneuverability levels desired by the Air Force.

### The Lightweight Fighters

In the fall of 1971, representatives of the Fort Worth Division of General Dynamics visited Langley to discuss a problem related to their lightweight fighter design study (ref. 36). The design incorporated a lifting fuselage in the form of a



wide, flattened, and expanding fuselage forebody that blended into the wing. The uncontrolled separation from the fuselage forebody for this design was creating stability and performance problems at maneuvering conditions. The Langley researchers suggested that the edge of the wide "lifting" forebody be sharpened to fix the separation line. In addition to controlling the forebody separation, this would increase the strength and stability of the vortex shed from the forebody, thereby increasing the vortex lift as well as stabilizing the high angle of attack flow field over the aircraft. After their own studies of the suggestion, General Dynamics included the vortex-lift strake in their design which became the well-known and highly maneuverable F-16.

By the mid 1970's, considerable interest in a supersonic cruise fighter aircraft had developed within the Air Force. Referred to as a "supercruiser," this fighter concept placed major emphasis on efficient supersonic cruise performance while maintaining respectable subsonic performance and maneuverability. As mentioned earlier, the strong emphasis on supersonic cruise tends to dictate a wing at the opposite end of the hybrid wing scale relative to the highly maneuverable transonic fighters just described. In this case it is now the main wing panel that is made slender to improve supersonic cruise performance as well as utilize the vortex lift. The cranked outer panel provides improved subsonic and transonic performance. An extensive research program was carried out, and the reader is referred to reference 9 and its cited references for details of the program. The concept eventually was applied in the F-16XL "derivative" aircraft, resulting in an excellent combination of reduced supersonic wave drag, controlled separation in the form of vortex lift, and low structural weight while maintaining the wing span desired for subsonic performance.

Photographs of these two hybrid-wing aircraft in flight are shown in figure 13.

#### FREE-VORTEX-SHEET THEORY

The vortex lift design application just discussed was aided considerably by the suction analogy. However, a considerable amount of wind tunnel testing was required and, as in the case of attached flows, there is a continuing need for refinements in the theoretical modeling of the real flow to keep pace with aircraft design requirements.

The need for a theoretical model of the complete, three-dimensional flow field was recognized early in the Langley research program and, as interest in vortex flows accelerated, the Boeing/LRC free-vortex-sheet method was developed. The Langley researchers worked closely with Boeing to define the applicational needs and evaluate the method during development. The initial development work and some early applications were described in a joint paper by Gloss and Johnson (ref. 37).

#### The Basic Formulation

A schematic of the free-vortex-sheet model (FVS) is shown in the left of figure 14. The vortex sheets are modeled with biquadratically varying doublet panels representing: (1) the free sheet shed from the separation line, (2) the fed sheet which is a simplified model of the vortex core region, (3) a higher order near wake, and (4) a far (or trailing) wake. Neither the shape of these three-dimensional

sheets nor strength of the doublet distribution is known a priori resulting in a nonlinear problem requiring iteration schemes. What is essentially the current state of the free-vortex-sheet theory is described by Johnson et al. (ref. 38).

In addition to working closely with Boeing during the development, Langley researchers have made comprehensive validation and application studies, some of which have been reviewed by Luckring, Schoonover, and Frink, in reference 39. They describe their investigation of convergence techniques for both the wing flow and the near-wake flow as a means of reducing computational cost and present several examples of practical applications. Based on these and other studies, it appears that the basic version of the theory has provided the most accurate and versatile inviscid approach available for establishing the complete three-dimensional flow field and surface pressure distributions for arbitrary configurations throughout the subsonic flow regime. A review of the convergence capabilities of the free-vortex-sheet theory and a survey of its applications are covered in this conference by Luckring et al. (ref. 40).

#### Some Recent Extensions

In addition, the free-vortex-sheet theory appears to offer an excellent inviscid flow model to which various viscous effects can be added, and two of these type extensions are illustrated by the cross-sectional cuts presented on the right of figure 14.

The first deals with the stability of the primary vortex and its influence on vortex breakdown, a phenomenon that is often the primary factor in limiting the maximum lift attainable. To include the vortex breakdown in the basic theory Luckring (refs. 41 and 42) has coupled Navier-Stokes inner and outer core regions with the inviscid free sheet and investigated various vortex instability criteria. His resulting theoretical model appears to accurately include the important effect of the pressure gradient associated with the trailing-edge Kutta condition on the vortex breakdown.

The second viscous flow addition to the free-vortex-sheet theory, shown in figure 14, is the inclusion of the secondary separation which occurs when the boundary layer on the upper surface, which is swept towards the leading edge by the primary vortex flow, separates under the influence of the adverse spanwise pressure gradient outboard of the primary vortex. The resulting flow can include secondary and tertiary vortices and produces important redistributions of the surface pressures. Two approaches to the inclusion of the secondary separation in the theory are described in detail in other papers presented during this conference (refs. 43 and 44) and, therefore, will not be discussed in this paper.

Euler and Navier-Stokes solutions of the leading-edge vortex flow phenomenon, while not as yet being as generally applied to design and analysis projects as are the suction analogy and free-vortex-sheet theory, appear to offer extended capabilities for the future. Research on these methods is included in this conference (refs. 45 and 46) and will not be reviewed here.

## SOME CURRENT CHALLENGES

Since reviews of the progress in the development and application free-vortex-sheet theory will be presented in other papers in this conference, I have elected to use the theory to highlight a few computational and experimental challenges and to encourage a coordinated development of the various vortex flow theories and a close cooperation between theoreticians and experimentalists. The challenges discussed here will be confined to a few incompressible flow examples. However, some compressible flow challenges will be discussed in the overview paper by Campbell and Osborn (ref. 47) and many other undoubtedly surfaced during this conference.

### Predicted Flow Regimes

Figure 15 illustrates the free-vortex sheet theory prediction of three vortex flow regimes encountered on sharp-edged delta wings. The boundaries of the regimes are presented as a function of leading-edge sweep angle and angle of attack. One boundary is associated with the vortex stability as predicted by Luckring's addition of the viscous core regions to the free-vortex-sheet theory and is defined by the critical swirl condition (see sketch) of tangential velocity equal to axial velocity at the trailing edge. Above this boundary, the vortex would be expected to be unstable. It is interesting that the data of Wentz and Kohlman (ref. 48), defining vortex breakdown at the trailing edge, appears to substantiate the theory. Also shown is the experimental buffet onset condition established by Boyden and Johnson (ref. 49). A computational challenge in this flow regime might be the application of the theory to develop wing design criteria related to the delay of vortex breakdown to provide extended lift capability.

The other boundary shown in figure 15 is derived from the completely inviscid version of the free-vortex-sheet theory and establishes the angle of attack above which the vortex interactions, or crowding, cause the core paths to begin to diverge from each other laterally as illustrated in the sketch. Results are shown (for two wing thickness ratios) at the 40% longitudinal station and are typical of other stations. It will be noted that the experimental angle of attack corresponding to the onset of vortex asymmetry reported by Fox and Lamar (ref. 25) for a sharp-edge delta wing of aspect ratio 0.25 lies in the diverging core regime. Secondary separation effects would be expected to influence the boundary and represent a challenge related to the use of the free-vortex-sheet theory in studying certain aspects of the development of vortex asymmetry. It must be recognized, however, that there are, in all probability, other viscous-related effects that limit the core divergence and influence the criteria for stable asymmetric vortex flow.

### Overall Vortex Lift Effects

The influence of the above flow regimes on the overall lift characteristics as predicted by the free-vortex-sheet theory is illustrated in figure 16 for two slender sharp-edged delta wings having leading-edge sweep angles of  $70^\circ$  and  $80^\circ$ . The free-vortex-sheet solutions are shown by the solid lines, and the dashed lines represent solutions by the suction analogy. Experimental data (ref. 48) are shown by the symbols. The lift calculated by the suction analogy is believed to provide the "upper bound" of lift for conditions where no losses associated with vortex crowding



or vortex breakdown are encountered. The shaded region between the two theories represents the angle-of-attack range where the two theories depart. It is believed that this comparison illustrates the vortex crowding effect, discussed above, which hinders flow reattachment and results in incomplete recovery of suction as vortex normal force. The angle of attack corresponding to the diverging core boundary calculated by the free-vortex-sheet theory is shown by the solid arrow for both wings and appears to reasonably define the onset of incomplete suction recovery.

For the  $70^\circ$ -delta wing, the suction analogy and the free-vortex-sheet theory are in excellent agreement up to about an angle of attack of  $40^\circ$  and both agree with experiment until vortex breakdown is encountered. However, for the  $80^\circ$ -delta wing, the free-vortex-sheet solutions begin to show lift losses in the vicinity of  $20^\circ$ .

Also shown (by the half-solid arrows) are the calculated values of the angle of attack at which the critical swirl condition is predicted, and it is seen to be in reasonable agreement with the maximum lift coefficient which has been shown experimentally (ref. 48) to correspond closely to the vortex breakdown condition.

With regard to the maximum lift, the free-vortex sheet theory results shown for the  $80^\circ$  delta indicate that little increase would be expected by eliminating vortex breakdown. However for the  $70^\circ$  delta, which is currently of more practical interest for aircraft, the free-vortex sheet solutions indicate that large increases in maximum lift might be attainable by delaying vortex breakdown. As mentioned in the previous section, this offers a challenge to use the theory to establish wing warp and planform shaping that are more conducive to vortex stability. However, additional effects such as possible shocks or vacuum limits at the higher lifts must, of course, be considered.

With the comparisons of the suction analogy and the free-vortex sheet solutions offering a means of demonstrating the magnitude of various "real flow" effects, it is highly recommended that Euler and Navier-Stokes' studies of vortex lift be coordinated with the free-vortex-sheet studies as well as with those experimental studies which are designed to provide detailed knowledge of the "real flow."

### Secondary Separation

It has been reasonably well established that the overall lift of thin, sharp-edge, slender delta wings, of interest here, is relatively insensitive to Reynolds number. For this class of wings, where the primary separation is fixed at the sharp leading edge for any non-zero angle of attack regardless of the state of the boundary layer approaching the sharp edge, this is not totally unexpected. However, flow details associated with the state of the boundary layer on the wing upper surface can cause rather large variations in the local pressure distributions through their effects on the location of secondary separation lines. These well-known secondary separations occur when the flow under the primary vortex is swept toward the wing leading edge, by the action of the vortex, and encounters the adverse spanwise pressure gradient near the leading edge. This results in a secondary vortex having vorticity of the opposite sign. In general, the effects induced by the secondary separation have been envisioned using the vortical effects of the secondary vortex. However, an alternate modeling approach has been used, with reasonable success, by Blom et al., and Wai et al. (refs. 44 and 50) who assumed that "the secondary vortices are so embedded in the boundary layer that their displacement effects dominate over their vortical effects." Regardless of the various modeling details,

the experimental secondary-separation effects described below will be referred to as a "secondary vortex."

The secondary-separation characteristics are, of course, highly dependent upon the local state of the boundary layer and, therefore, on the Reynolds number and longitudinal station. This is illustrated in figure 17 using experimental, transition free, data from reference 51 for a  $76^\circ$  sharp-edge delta wing at an angle of attack of  $25^\circ$ . On the left is presented the spanwise variation of the upper surface pressure distribution at the mid longitudinal station for Reynolds numbers, based on root chord, of  $1.6 \times 10^6$  and  $6.4 \times 10^6$ . Also shown is the inviscid pressure distribution predicted by the free-vortex-sheet theory (FVS) including the effects of wing thickness but assuming no secondary vortex. The low Reynolds number data represent a laminar secondary separation condition and the well-known large reduction in suction pressures in the region of the primary vortex, accompanied by large increases in suction pressures in the region of the secondary vortex, is clearly evident. The higher Reynolds number data illustrate the turbulent separation case in which the secondary vortex is reduced in strength and its formation delayed to a more outboard position. The pressure distribution now approaches the theory more closely in the region of the primary vortex but still shows important effects near the leading edge which is particularly important for cambered wings or vortex flaps.

The right-hand portion of figure 17 illustrates the strong non-conical effects on the pressure distributions along mid semispan ray,  $y/s = 0.5$ , for both the inviscid theory and the experimental results. The most complete data were obtained at a Reynolds number of  $3.2 \times 10^6$  and clearly illustrate the transition from a laminar secondary separation to a turbulent separation in the region of  $x/c_0 = 0.35$ . Although the data for the other Reynolds numbers are incomplete, they appear consistent with the expectation that transition would occur downstream for the lower Reynolds number and upstream for the higher Reynolds number. Regarding the inviscid theory results from the free-vortex-sheet method, it appears that the theory may provide a reasonably accurate prediction of the pressures in this region of the wing as long as the turbulent secondary separation has its origin near the wing apex. It is of interest, however, that while the experimental results approach the theory at the high Reynolds number they do not do so in a monotonical fashion as will be discussed below.

To more clearly indicate the variation of the peak suction pressure coefficients under the primary vortex with Reynolds number, data taken from reference 51 have been analyzed in a somewhat different fashion and presented in figure 18 as a function of Reynolds number for both the  $x/c_0 = .25$  and  $x/c_0 = .50$  longitudinal stations. Also shown are the peak suction values measured under the secondary vortex.

Looking first at the  $x/c_0 = .25$  station, the experimental data indicate a rapid increase in peak suction level under the primary vortex with increasing Reynolds number as the cross flow under the vortex becomes turbulent and reduces the impact of the secondary separation. To provide a possible high Reynolds number asymptote for this suction peak, the value obtained from the inviscid free-vortex-sheet theory is also shown. Although it appears that the data may be approaching the inviscid theory monotonically, evidence to be discussed subsequently, relative to the  $x/c_0 = .50$  station, indicates a more complicated situation.

Also shown in the left of figure 18 is the variation of the experimental peak suction pressure under the secondary vortex. In this case when turbulent secondary separation occurs, there is a rapid decrease in the peak suction pressure magnitude.



Turning to the  $x/c_o = .50$  case on the right of figure 18, it is seen that, as discussed earlier, the transition to a turbulent secondary separation and the accompanying rapid increase in the suction pressure under the primary vortex occur at a lower value of Reynolds number than for the upstream station. However, it is important to note that as Reynolds number increases further, instead of approaching the inviscid theory monotonically, there is a decrease in the magnitude of the peak suction pressure coefficient under the primary vortex. Accompanying this variation is an increase in the magnitude of the peak suction pressure coefficient under the secondary vortex. The reason for this somewhat unexpected variation with Reynolds number is not completely apparent and more complete data extended to higher Reynolds numbers would be of great value. The fact that the decrease in the peak suction pressure coefficient under the primary vortex at the  $x/c_o = .50$  station occurs in the same Reynolds number range as the increase at the  $x/c = .25$  station may be an indication that as the transition to turbulent secondary separation moves forward, the resulting effects induced downstream may cause changes in the primary vortex strength such that no station asymptotes the inviscid theory value until transition occurs very near the wing apex. This would appear to be somewhat consistent with the observed insensitivity of the total lift to Reynolds number and possibly consistent with the apparent "conservation of suction" related to the suction analogy.

The above observations imply an important challenge in the development and evaluation of advanced theoretical methods as well as a challenge to extend the pressure data to higher Reynolds numbers.

#### A New Aerodynamic Facility

During 1984, the Langley Research Center placed in operation a new, high Reynolds number, transonic wind tunnel. This tunnel, the National Transonic Facility (NTF), applies the cryogenic, pressurized, wind tunnel principle to provide the very high Reynolds numbers required to match the full-scale viscous effects encountered with modern air vehicles. The cryogenic technology development and the construction and operation of the pilot facilities were performed by Langley researchers and technicians (see refs. 52 and 53), and the basic design of the NTF was carried out in a Project Office staffed by Langley personnel (see ref. 54). The performance envelope of the NTF (ref. 55) is shown in figure 19, and the degree to which the NTF extends the Reynolds number capability beyond the composite envelope of all other operational tunnels in the free world is readily apparent. This capability is of considerable importance to vortex lift research since strong viscous effects can occur at design conditions as well as off-design conditions.

As seen by the sketches in figure 19, the vortex lift research currently planned for the NTF includes the classical slender delta wing and the two classes of hybrid wings discussed earlier.

The  $65^\circ$  delta wing model incorporates an interchangeable leading edge to allow the study of leading-edge radius which, of course, has a strong effect on leading-edge separation characteristics, including the Reynolds number dependency. The model contains a large number of surface pressure orifices and is expected to provide considerable insight regarding the secondary separation characteristics in the full-scale Reynolds number range as well as evidence related to the question of the existence of a "conservation of suction" phenomenon. The unique capabilities of the NTF will also be utilized to study possible effects of condensation in the core on vortex bursting.

The vortex lift strake configuration utilizes the double-balance system to isolate overall loads and component interactions as well as wing and fuselage pressures. Although not as highly instrumented for detailed vortex flow research, the slender, cranked, wing configuration should offer valuable overall force and moment information with regard to vortex flow.

Additional details of the NTF models and research program can be found in references 56 and 57, and it is highly recommended that researchers involved in the development and evaluation of advanced vortex flow theoretical methods consider this program in the selection of configurations to be modeled theoretically.

#### CONCLUDING REMARKS

By way of conclusion, I would like to emphasize that, by design or not, vortex flow can be encountered on slender-wing aircraft at many points within their operational envelope. Since this flow influences both the aerodynamic and structural design, it is important that continued improvements in design and analysis theories be developed to meet the increasingly stringent design requirements. Towards this end, it appears highly desirable that a strong interaction be developed between those developing theoretical methods such as, for example, the free-vortex-sheet, Euler, and Navier-Stokes. Since viscous effects such as secondary separation can strongly influence the design of cambered leading edges and vortex flaps, for example, it is essential that both laminar and high Reynolds number turbulent secondary separation capabilities be included in the theories. In relation to the influence of viscous effects, it is important that the experimental capabilities of the National Transonic Facility be utilized and that a close coordination between the basic and applied theoreticians and the experimentalists be developed.

#### REFERENCES

1. Busemann, A.: Aerodynamischer Auftrieb bei Überschallgeschwindigkeit, Luftfahrtforschung, Bd 12, Nr 6, October 3, 1935, pp. 210-220.
2. Ludwig, H.: Sweptback Wings at High Velocities (Preliminary Results), Goodyear Aircraft Corp., Translation Report No. R-30-18, Part 7, August 1970.
3. Redemann, Hans: Messerschmitt Me 262. Teil 4: Nachtjager. Flug Review, Oct. 1970.
4. Survey of Messerschmitt Factory and Functions, Oberammergau, Germany. Air Technical Intelligence Review No. F-IR-6-RE, Aug. 1946.
5. Jones, Robert T.: Wing Planforms for High Speed Flight. NACA Rep. 863, June 27, 1945.
6. Blair, Morgan, M.: Evolution of the F-86. Paper presented at the AIAA Evolution of Aircraft Wing Design Symposium, Dayton, Ohio, March 18-19, 1980.
7. Hallion, Richard P.: Convair's Delta Alpha. Air Enthusiast Quarterly/Two, pp. 177-185, 1976.

8. Polhamus, Edward C.; and Toll, Thomas A.: Research Related to Variable Sweep Aircraft Development. NASA Technical Memorandum 83121, May 1981.
9. Polhamus, Edward C.: Applying Slender Wing Benefits to Military Aircraft. J. Aircraft, Vol. 21, No. 8, August 1984.
10. Rodgers, James J.: Design of German DM-1. Aviation, December 1946, pp. 78-79.
11. Brief Review of German Aerodynamic Studies. Air Technical Intelligence Review No. F-IR-1-RE, 6 May, 1946, pp. 75-77.
12. Wilson, H. A.; and Lovell, J. C.: Full-Scale Investigation of the Maximum Lift Flow Characteristics of an Airplane Having Approximately Triangular Planform. NACA RM L6K20, Nov. 1946.
13. Legendre, R.: Rolling Up of Vortex Sheets From the Edges of Lifting Surfaces. Recherche Aerospatiale, 1981-3.
14. Maltby, R. L.: The Development of the Slender Delta Concept. Aircraft Engineering, March 1968.
15. Poisson-Quinton, Philippe: First Generation Supersonic Transports. ONERA T.P. No. 1976-113.
16. Polhamus, E. C.: A Concept of the Vortex Lift of Sharp-Edge Delta Wings Based on a Leading-Edge-Suction Analogy. NASA TN D-3767, 1966.
17. Legendre, R.: Écoulement au voisinage de la pointe avant d'une aile a forte fleche aux incidences moyennes. Rech. Aero. 35, 1953.
18. Brown, C. E.; and Michael, W. H.: On Slender Delta Wings with Leading-Edge Separation. Journal of Aeronautical Sciences, Vol. 21, Oct. 1954, pp. 690-694.
19. Smith, J. H. B.: Improved Calculations of Leading-Edge Separation from Slender Delta Wings. R.A.E. - T.R. No. 66070, March 1966.
20. Hoeijmakers, H. W. M., and Bennekens, B.: "A Computational Model for the Calculation of the Flow About Wings With Leading-Edge Vortex Separation," High Angle of Attack Aerodynamics, AGARD CP-247, January 1979.
21. Lamar, J. E.; and Luckring, J. M.: Recent Theoretical Developments and Experimental Studies Pertinent to Vortex Flow Aerodynamics - With a View Towards Design. High Angle of Attack Aerodynamics, AGARD CP-247, Paper No. 24, Jan. 1979.
22. Lamar, John E.; and Campbell, James F.: Recent Studies at NASA Langley of Vortical Flows Interacting with Neighboring Surfaces. AGARD Symposium on Vortical Type Flows in Three Dimensions, Paper No. 10, April 1983.
23. Polhamus, Edward C.: Application of the Leading-Edge-Suction Analogy of Vortex Lift to the Drag Due to Lift of Sharp-Edge Delta Wings. NASA TN D-4739, 1968.



24. Polhamus, Edward C.: Prediction of Vortex-Lift Characteristics Based on a Leading-Edge Suction Analogy. AIAA Paper No. 69-1133, Oct. 1969.
25. Fox, Charles H., Jr.; and Lamar, John E.: Theoretical and Experimental Longitudinal Aerodynamic Characteristics of an Aspect Ratio 0.25 Sharp-Edge Delta Wing at Subsonic, Supersonic, and Hypersonic Speeds. NASA TN D-7651, August 1974.
26. Fox, Charles H., Jr.: Prediction of Lift and Drag for Slender Sharp-Edge Delta Wings in Ground Proximity. NASA TN D-4891, 1969.
27. Boyden, Richmond P.: Effects of Leading-Edge Vortex Flow on the Roll Damping of Slender Wings. AIAA Paper 70-540, 1970.
28. Snyder, Melvin H., Jr.; and Lamar, John E.: Application of the Leading-Edge-Suction Analogy to Prediction of Longitudinal Load Distribution and Pitching Moments for Sharp-Edge Delta Wings. NASA TN D-6994, 1971.
29. Davenport, Edwin E.; and Huffman, Jarrett K.: Experimental and Analytical Investigation of Subsonic Longitudinal and Lateral Aerodynamic Characteristics of Slender Sharp-Edge 74° Swept Wings. NASA TN D-6344, 1971.
30. Davenport, Edwin E.: Aerodynamic Characteristics of Three Slender Sharp-Edge 74° Swept Wings at Subsonic, Transonic, and Supersonic Mach Numbers. NASA TN D-7631, 1974.
31. Kulfan, R. M.: Wing Airfoil Shape Effects on the Development of Leading-Edge Vortices. AIAA Paper No. 79-1675, 1979.
32. Henderson, W. P.: Effects of Wing Leading-Edge Radius and Reynolds Number on Longitudinal Aerodynamic Characteristics of Highly Swept Wing-Body Configurations at Subsonic Speeds. NASA TN D-8361, Dec. 1976.
33. Carlson, H. W.; and Mack, R. J.: Studies of Leading-Edge Thrust Phenomena. AIAA Paper No. 80-0325, 1980.
34. McKinney, Linwood W.; and Dollyhigh, Samuel M.: Some Trim Drag Considerations for Maneuvering Aircraft. AIAA Paper 70-932, July 1970.
35. Ray, Edward J.; McKinney, Linwood W.; and Carmichael, Julian G.: Maneuver and Buffet Characteristics of Fighter Aircraft. Presented at the AGARD Specialists' Meeting on Fluid Dynamics of Aircraft Stalling. Lisbon, Portugal, April 1972.
36. Buckner, J. K.; Hill, W. P.; and Benepe, David: Aerodynamic Design Evolution of the YF-16. AIAA Paper No. 74-935, 1974.
37. Gloss, B. B.; and Johnson, F. T.: Development of an Aerodynamic Theory Capable of Predicting Surface Loads on Slender Wings With Vortex Flow. Proceedings of the SCAR Conference. NASA CP-001, 1976, pp. 55-67.
38. Johnson, F. T.; Lu, P.; Tinoco, E. N.; and Epton, M. A.: An Improved Panel Method for the Solution of Three-Dimensional Leading-Edge Vortex Flows. Volume I. - Theory Document. NASA CR-3278, July 1980.

39. Luckring, J. M.; Schoonover, W. E., Jr.; and Frink, N. T.: Recent Advances in Applying Free Vortex Sheet Theory for the Estimation of Vortex Flow Aerodynamics. AIAA Paper No. 82-0095, 1982.
40. Luckring, J. M.; K. D. Hoffer; and Grantz, A. C.: Recent Extensions to the Free-Vortex-Sheet Theory for Expanded Convergence Capability. Vortex Flow Aerodynamics - Volume I, NASA CP-2416, paper no. 4, 1986.
41. Luckring, James M.: A Theory for the Core of a Three-Dimensional Leading-Edge Vortex. AIAA Paper No. 85-0108, 1985.
42. Luckring, James Michael: A Method for Computing the Core Flow in Three-Dimensional Leading-Edge Vortices. PhD dissertation, Department of Mechanical and Aerospace Engineering. North Carolina State University, Raleigh, North Carolina, May 1985.
43. Woodson, S. H.; and DeJarnette, F. R.: A Direct and Inverse Boundary Layer Method for Subsonic Flow Over Delta Wings. Vortex Flow Aerodynamics - Volume I, NASA CP-2416, paper no. 5, 1986.
44. Blom, G.; Wai, J. C.; and Yoshihara, H.: Viscous Vortical Flow Calculations Over Delta Wings. Vortex Flow Aerodynamics - Volume I, NASA CP-2416, paper no. 12, 1986.
45. Newsome, R. W.; and Thomas, J. L.: Computation of Leading-Edge Vortex Flows. Vortex Flow Aerodynamics - Volume I, NASA CP-2416, paper no. 15, 1986.
46. Raj, P.; and Long, L. N.: An Euler Aerodynamic Method for Leading-Edge Vortex Flow Simulation. Vortex Flow Aerodynamics - Volume I, NASA CP-2416, paper no. 13, 1986.
47. Campbell, J. F.; and Osborn, R. F.: Leading-Edge Vortex Research: Some Nonplanar Concepts and Current Challenges. Vortex Flow Aerodynamics - Volume I, NASA CP-2416, paper no 2, 1986.
48. Wentz, W. H.; and Kohlman, D. L.: Vortex Breakdown on Slender Sharp-Edged Wings. AIAA Journal of Aircraft, Vol. 8, No. 3, March, 1971.
49. Boyden, Richmond P.; and Johnson, William G., Jr.: Preliminary Results of Buffet Tests in a Cryogenic Wind Tunnel. NASA TM 81923, July 1981.
50. Wai, J. C.; Baillie, J. C.; and Yoshihara, H.: Computation of Turbulent Separated Flows Over Wings. 3rd Symposium on "Numerical and Physical Aspects of Aerodynamic Flows," Long Beach, CA, 20-24 Jan. 1985.
51. Lemaire, D. A.: Some Observations of the Low-Speed Flow Over a Sharp-Edged Delta Wing of Unit Aspect Ratio. Dept. of Supply. AERO Report 126. Melbourne, 1965.
52. Goodyer, M. J.; and Kilgore, R. A.: The High Reynolds Number Cryogenic Wind Tunnel. AIAA Paper 72-995, September 1972.

53. Ray, E. J.; Kilgore, R. A.; and Adcock, J. B.: Test Results From the Langley High Reynolds Number Cryogenic Transonic Tunnel. AIAA Preprint 74-631, July 1974.
54. Howell, Robert R.; and McKinney, Linwood W.: The U. S. 2.5 Meter Cryogenic High Reynolds Number Tunnel. NASA CP-2009, 1977, pp. 27-51.
55. Igoe, W. B.: Characteristics of the U. S. National Transonic Facility. Paper No. 17, AGARD Lecture Series No. 111, 1980.
56. Gloss, Blair B.: Initial Research Program for the National Transonic Facility. AIAA Paper No. 84-0585, March 1984.
57. Campbell, James F.: The National Transonic Facility - A Research Perspective. AIAA Paper No. 84-2150, Aug. 1984.

ORIGINAL PAGE IS  
OF POOR QUALITY



Figure 1. The Messerschmidt ME 262 - the first swept-wing jet aircraft.

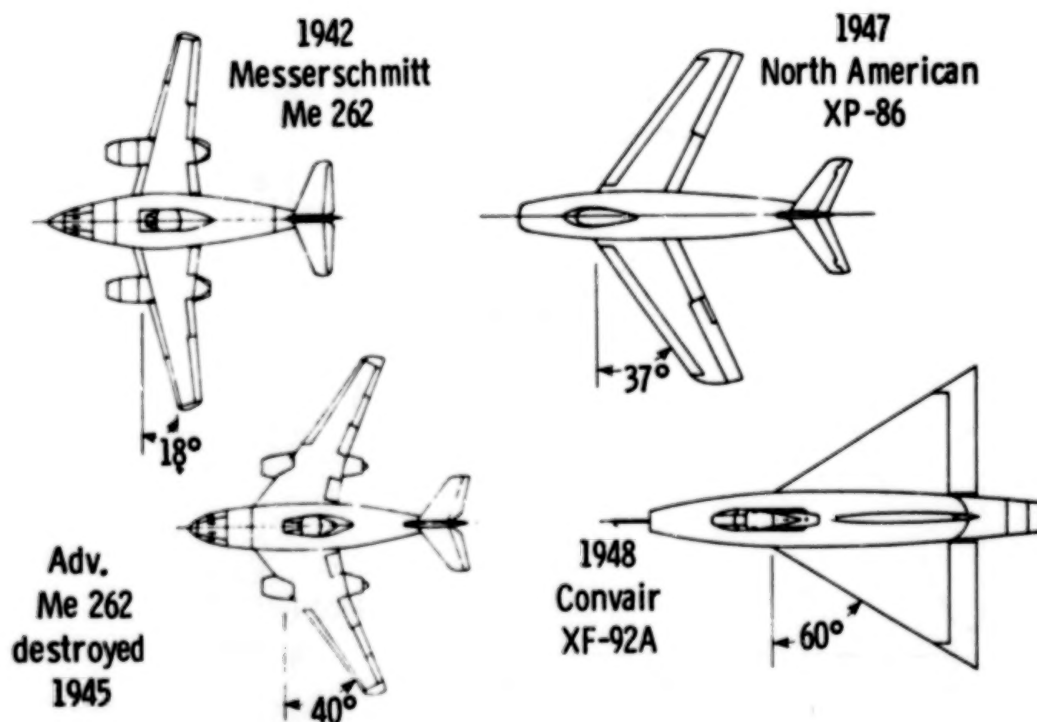


Figure 2. The trend towards slender-wing aircraft.

ORIGINAL PAGE IS  
OF POOR QUALITY

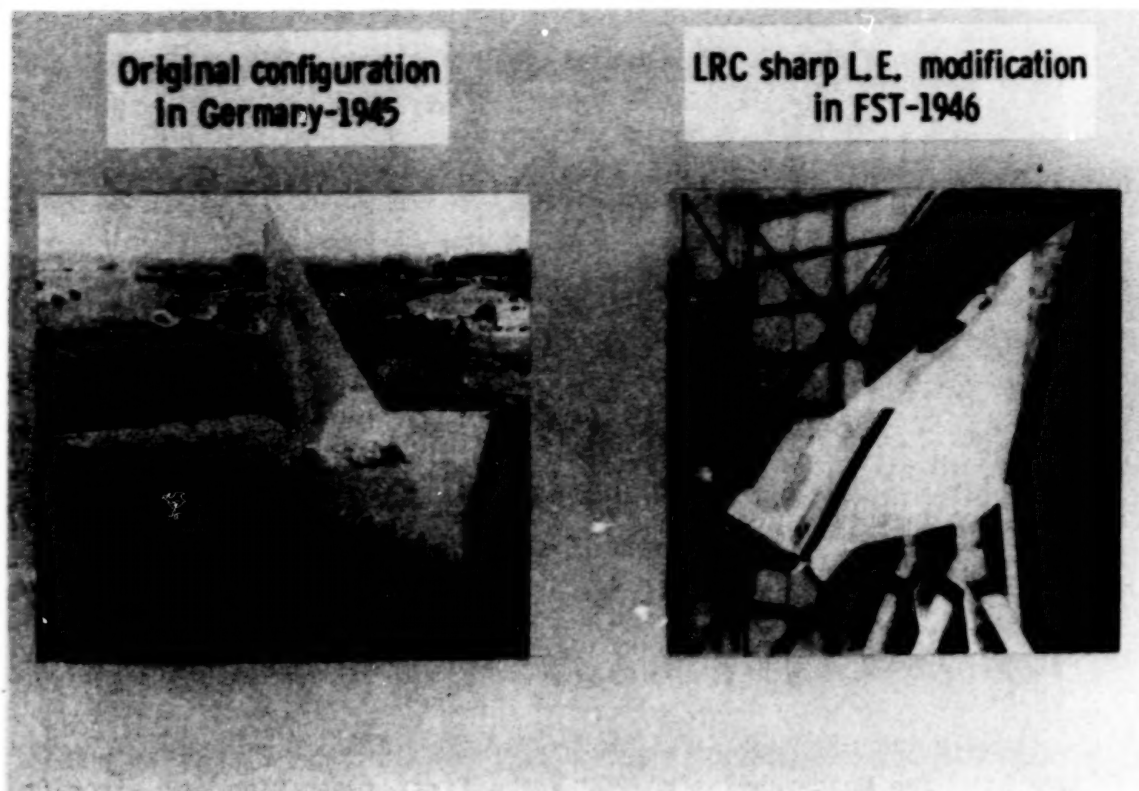


Figure 3. The Lippisch DM-1 test glider.

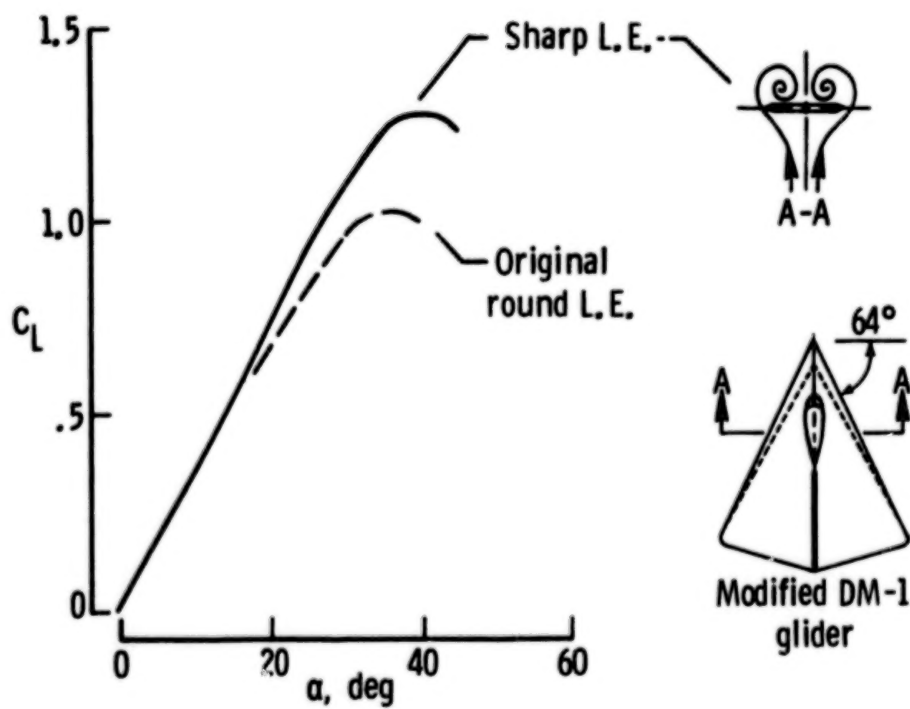


Figure 4. The first study of the leading-edge vortex occurred at Langley in 1946.



ORIGINAL PAGE IS  
OF POOR QUALITY

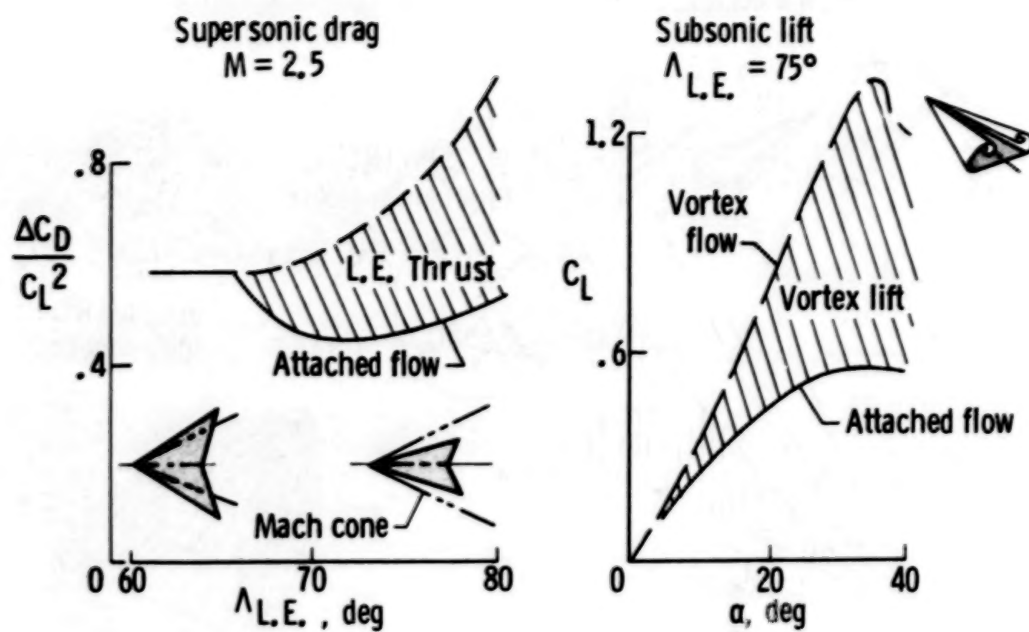


Figure 5. Some slender wing aerodynamic characteristics.



Figure 6. Illustration of the leading-edge vortices on the B-70.

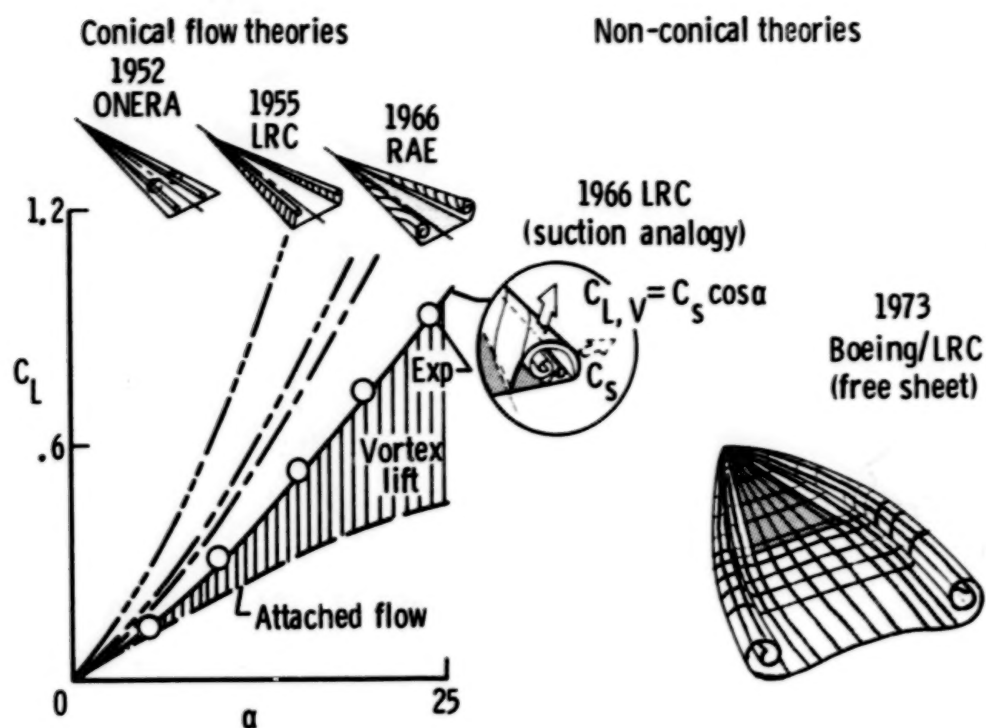


Figure 7. Chronology of vortex-lift theory development.

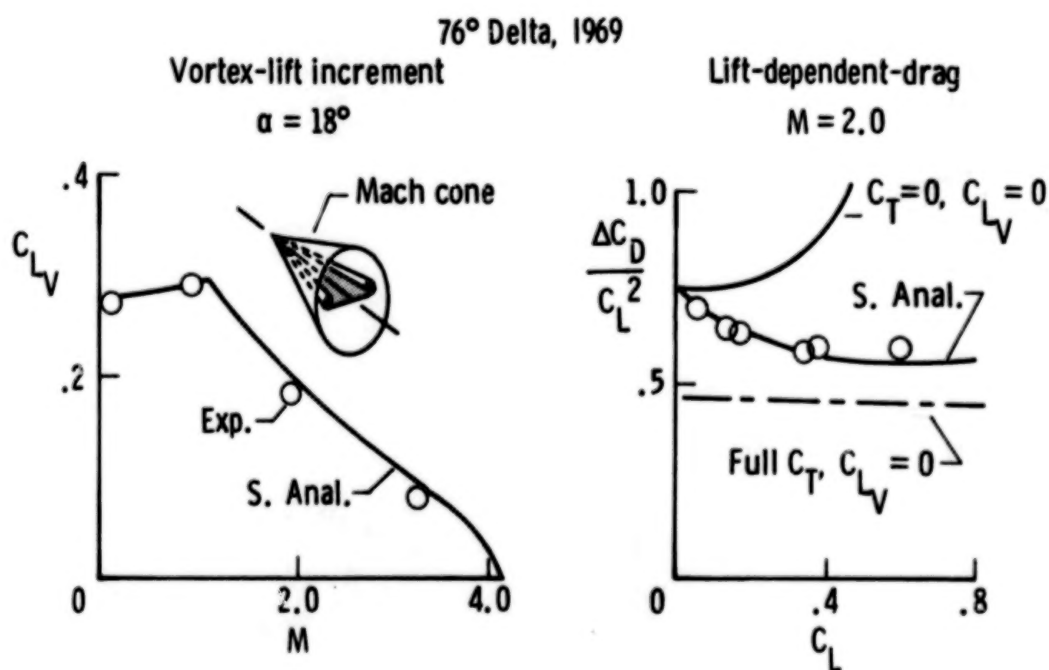


Figure 8. Prediction of some compressibility effects by the suction analogy.

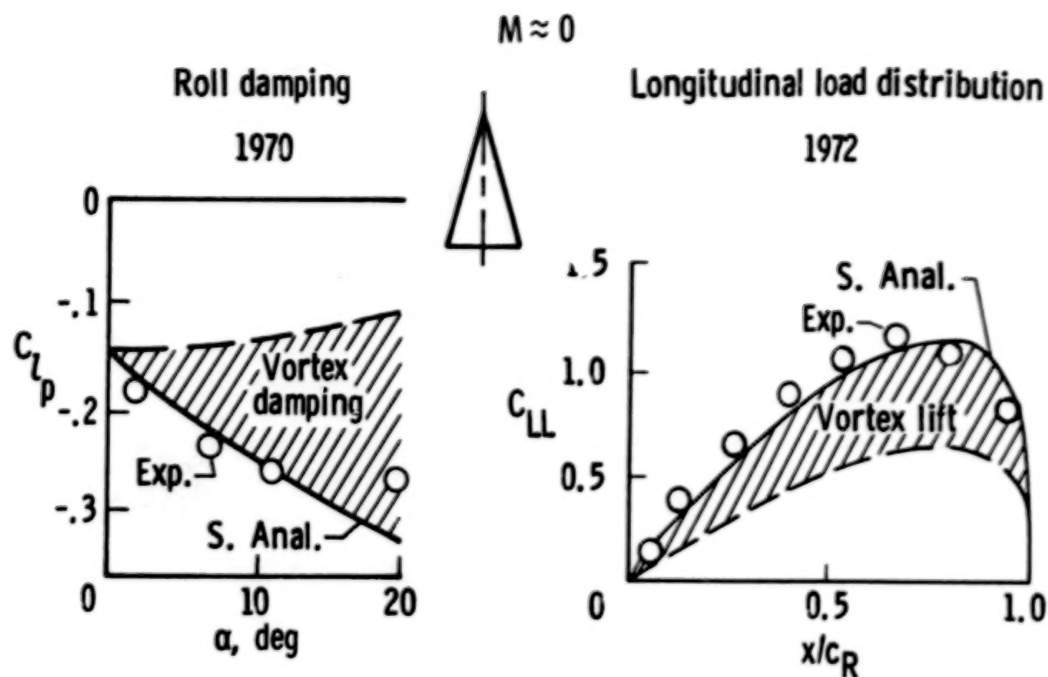


Figure 9. Prediction of some stability related parameters by the suction analogy.

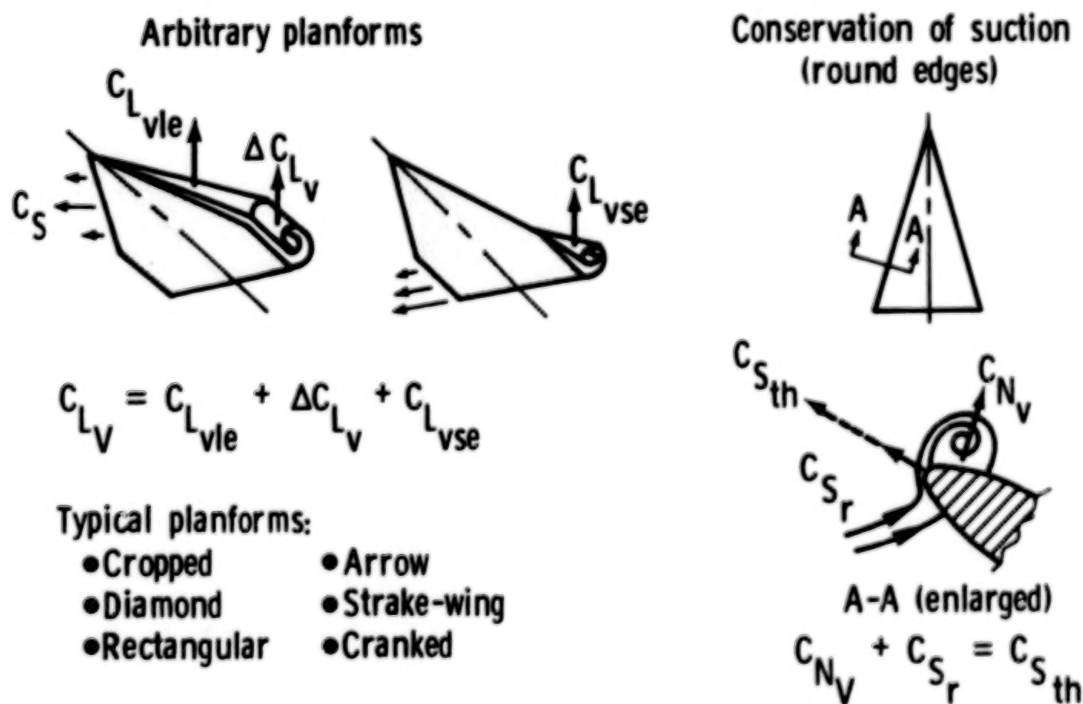


Figure 10. Some extensions of the suction analogy made in 1974.



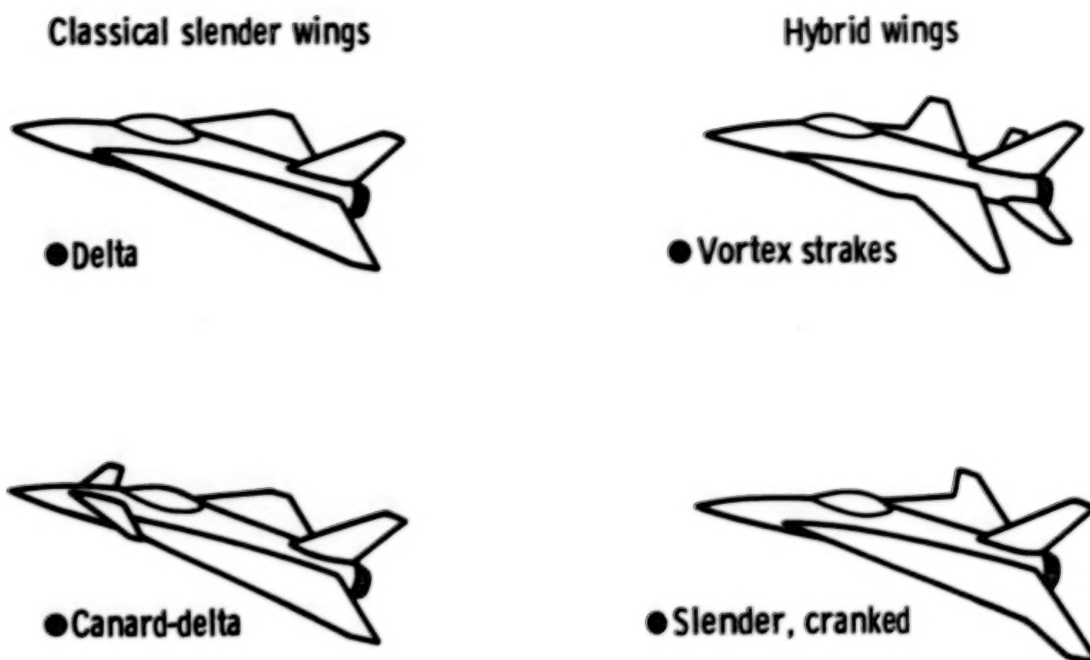


Figure 11. Some design applications of vortex lift.

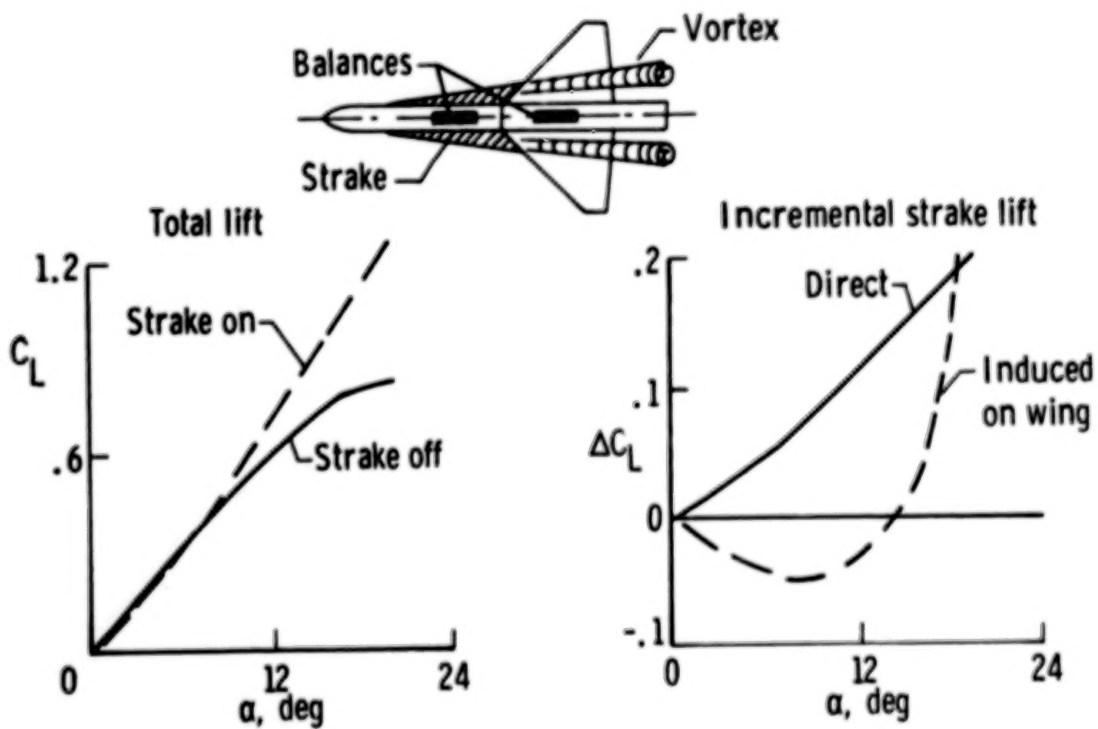


Figure 12. Effects of vortex-strakes on lift.



Figure 13. Examples of hybrid-wing aircraft.

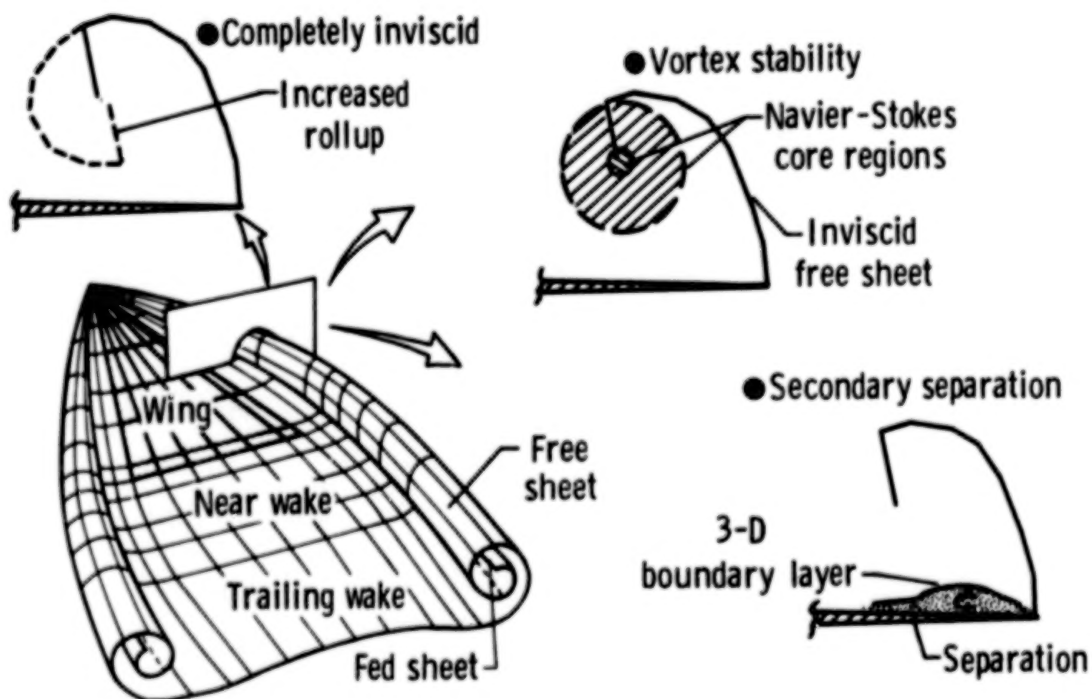


Figure 14. Some extensions of the free-vortex-sheet theory.

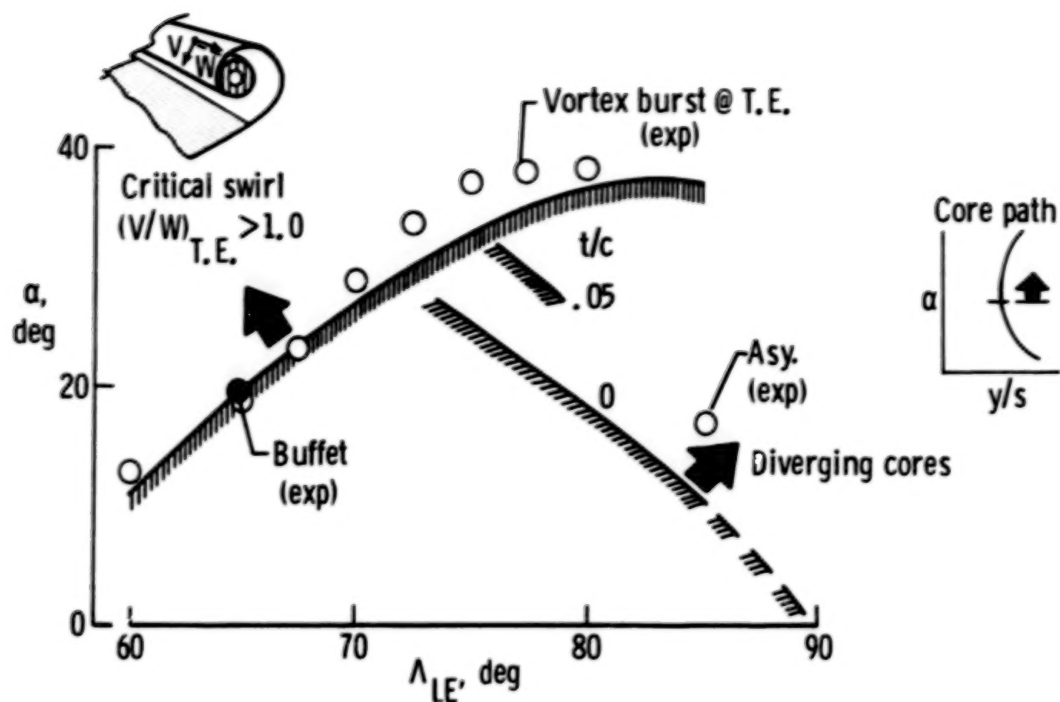


Figure 15. Prediction of vortex flow regimes by the free-vortex-sheet theory.

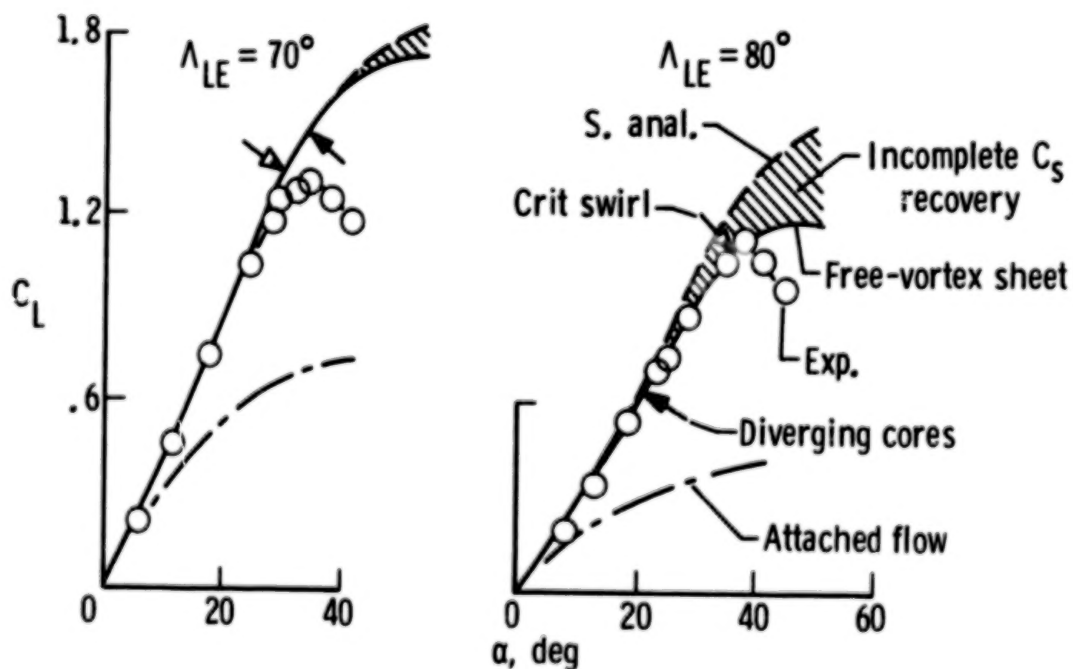


Figure 16. Influence of flow regimes on vortex lift of sharp-edge delta wings.



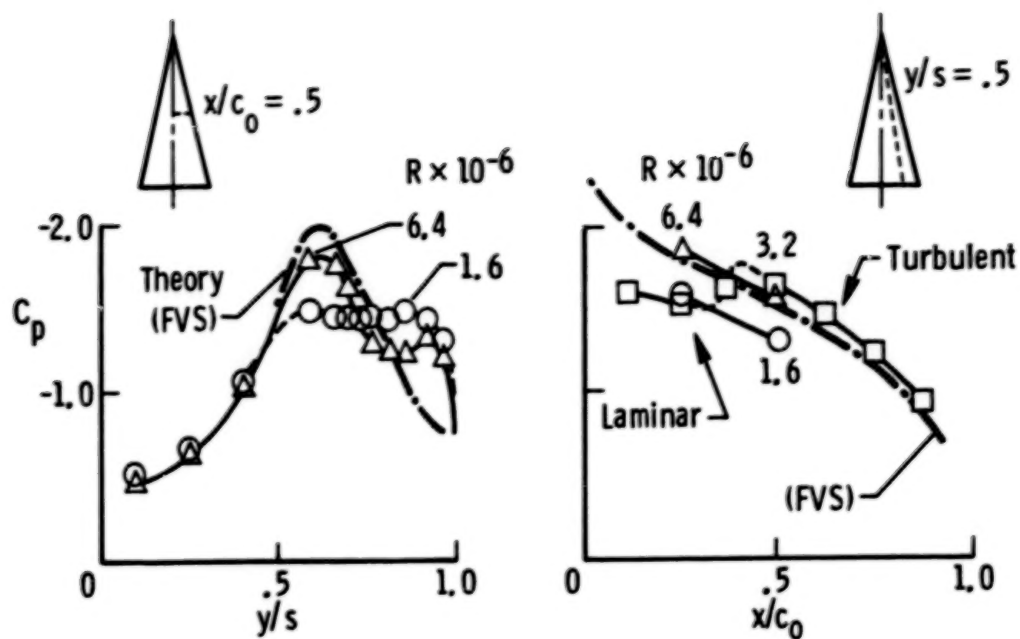


Figure 17. Effects of secondary separation on upper surface pressures.  $76^\circ$  delta at  $\alpha = 25^\circ$ .

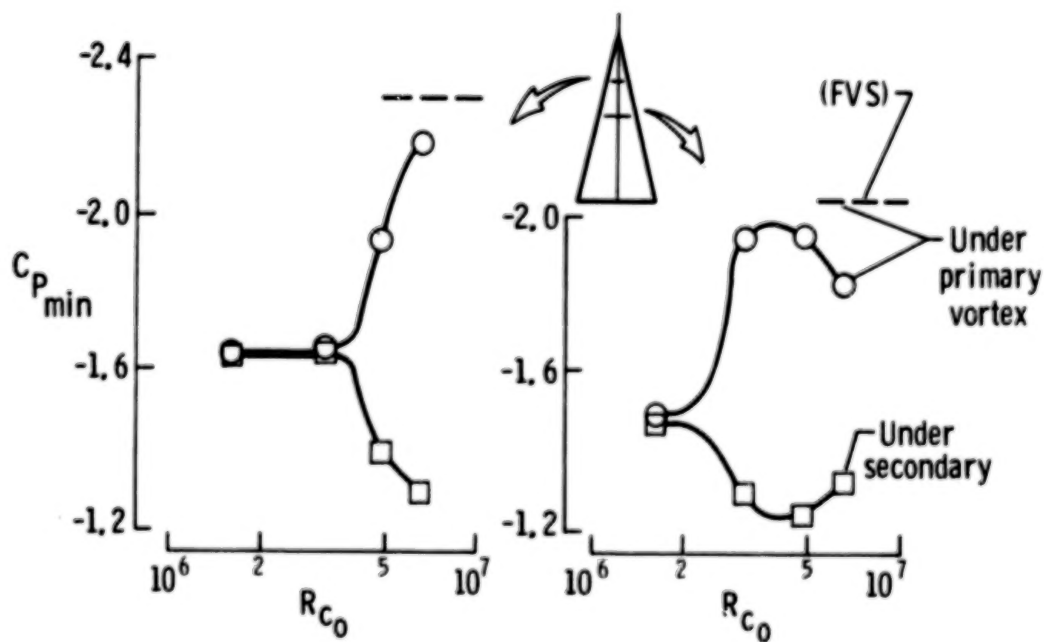


Figure 18. Effects of Reynolds number on upper surface minimum pressures.  $76^\circ$  delta at  $\alpha = 25^\circ$ .

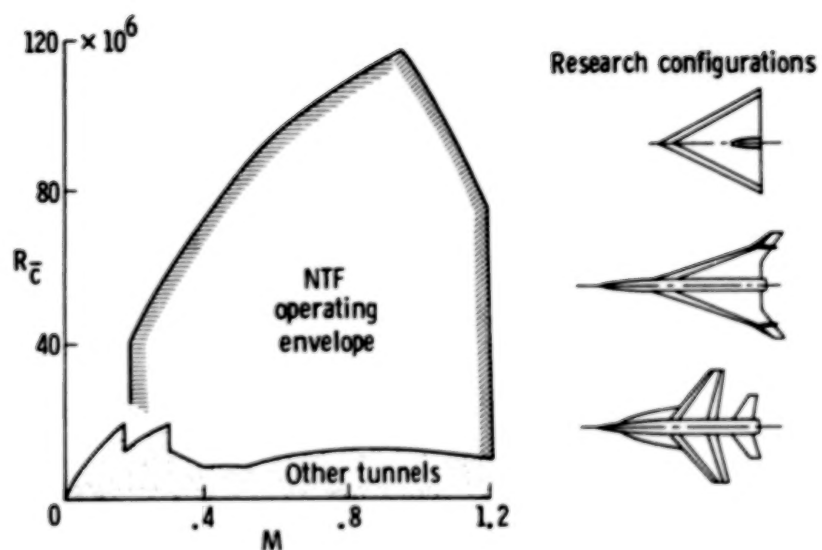


Figure 19. Reynolds number studies of vortex flow in the National Transonic Facility.

LEADING-EDGE VORTEX RESEARCH: SOME NONPLANAR CONCEPTS  
AND CURRENT CHALLENGES

James F. Campbell  
NASA Langley Research Center  
Hampton, Virginia

Russell F. Osborn  
Air Force Wright Aeronautical Laboratories  
Wright-Patterson Air Force Base, Ohio

SUMMARY

This paper provides some background information for the Vortex Flow Aerodynamics Conference and shows that current slender wing airplanes do not use variable leading-edge geometry to improve transonic drag polar. Highlights of some of the initial studies combining wing camber, or flaps, with vortex flow are presented. Current vortex flap studies were reviewed to show that there is a large subsonic data base and that transonic and supersonic generic studies have begun. There is a need for validated flow field solvers to calculate vortex/shock interactions at transonic and supersonic speeds. Many important research opportunities exist for fundamental vortex flow investigations and for designing advanced fighter concepts.

INTRODUCTION

In recent years, NASA and the AFWAL have become more concerned about the impact of separation-induced vortex flows on the design and off-design performance of military aircraft (refs. 1 and 2). The Advanced Tactical Fighter, as discussed recently by Piccirillo (ref. 3), is being considered to provide a significant increase in supersonic cruise efficiency over current fighters, while maintaining an equivalent transonic maneuver capability. This type of design is very challenging since optimum supersonic designs tend toward slender highly swept wings with low aspect ratio, while transonic designs have higher aspect ratios to help improve cruise and maneuver performance.

Much research has been conducted to try to bridge the gap between transonic and supersonic mission requirements by utilizing variable camber concepts such as leading-edge flaps and slats. Designed with attached flow, these leading-edge devices have been successfully employed on a variety of airplanes with low-to-moderate leading-edge sweep angles. However, application to slender, higher swept wings is limited by the onset of separated flows. An alternate design approach is to let the flow separate from the leading edge and use the vortex-induced suction pressures acting on a drooped leading edge to recover some of the leading-edge suction lost due to leading-edge separation. The current Vortex Flow Aerodynamics Conference brings together specialists to address wing leading-edge vortex flows and vortex flaps in particular.



The present paper is one of two background papers for the conference, and complements the information presented by Polhamus (ref. 4). The present paper reviews some of the current military aircraft which use variable leading-edge geometry to improve drag polar, and highlights some of the initial studies combining wing camber, or flaps, with vortex flow. The status of current vortex flap research will be presented, along with appropriate vortex theories which will be discussed during the conference. Some technical challenges will be discussed to highlight additional vortex flow research areas of interest. An extensive reference list is also included.

# SYMBOLS

|               |  |
|---------------|--|
| A             | aspect ratio of the wing   |
| $C_D$         | drag coefficient   |
| $C_L$         | lift coefficient   |
| $C_p$         | local pressure coefficient   |
| $\bar{c}$     | reference chord  |
| $c_r$         | root chord   |
| FVS           | Free Vortex Sheet  |
| LE            | leading edge   |
| L/D           | lift-to-drag ratio   |
| M             | Mach number  |
| $M_N$         | Mach number normal to the leading edge   |
| p             | nondimensional camber height for conically cambered wings in terms of local semispan |
| R             | Reynolds number  |
| $R_{\bar{c}}$ | Reynolds number based on mean aerodynamic chord                                      |
| s             | local semispan   |
| S             | reference area   |
| VLM           | Vortex Lattice Method  |
| VLM-SA        | Vortex Lattice Method coupled with the suction analogy                               |
| x/c           | fractional distance along a local chord  |
| 2y/b          | fractional distance along the semispan   |

|                      |   |
|----------------------|---|
| $y/s_{\delta_n = 0}$ | local lateral distance, nondimensionalized by semispan with flap undeflected          |
| $z/s_{\delta_n = 0}$ | local vertical distance, nondimensionalized by semispan with flap undeflected         |
| $\alpha$             | angle of attack   |
| $\alpha_N$           | angle of attack normal to wing leading edge   |
| $\delta_n$           | leading-edge flap deflection angle, positive down, measured normal to the hingeline   |
| $\delta_{TE}$        | trailing-edge flap deflection angle, positive down, measured normal to the freestream |
| $\Delta C_D$         | drag due to lift in figures 3 and 6, vortex flap increment in figure 18               |
| $\Lambda_{LE}$       | leading-edge sweep angle defined in figure 1  |

## AIRCRAFT GEOMETRY AND DRAG DUE TO LIFT

### Aircraft Geometry

In order to understand the importance of sweep and variable camber in the design of advanced aircraft, it is of interest to examine current airplane configurations for geometric trends.

There are many ways to represent airplane geometric variables. We have shown aspect ratio as a function of leading-edge sweep angle in figure 1, where  $\Lambda_{LE}$  is defined in the sketch. In order to be able to plot an airplane whose wing has more than one sweep angle, such as a double-delta or ogee planform, an effective sweep angle is defined by a line drawn from the apex of the reference planform to the leading edge of the tip chord. The data for the configurations were extracted from information in references 5 to 8, and are listed in Table I along with the symbol definition.

The data fall into two groups, one for fixed sweep and one for variable sweep, and show the obvious decrease in aspect-ratio with increase in sweep angle. The question which concerns us is which airplanes have variable leading-edge geometry and use that capability to improve drag polar. The solid symbols represent those aircraft. All variable leading-edge geometry is incorporated on wings with sweep angle less than  $50^\circ$ , with the exception of the Mirage 2000 and 4000 aircraft which have a sweep angle of  $60^\circ$ . A photograph of the Mirage 2000 with its variable leading-edge flaps deployed is presented in figure 2 (taken from ref. 9).

All of these variable flap configurations were designed to utilize attached flow for subsonic or transonic maneuver requirements. It is not known for what flow field the Mirage 2000 and 4000 flaps are designed. One of the problems with increasing the wing sweep angle is that it gets more difficult to keep the flow from separating. Simple sweep theory suggests that the  $C_L$  where the wing first

experiences flow separation is lower for the higher swept wing. This is due to the higher upwash at the leading-edge and larger section lift coefficients. Drooping the leading edge to keep the flow attached is effective at low lifts, but this shifts the pressure peak to the flap hingeline and ultimately results in hingeline separation.

For most of the fighter airplanes which have no variable leading-edge devices, wind tunnel studies of leading-edge flaps were conducted during the developmental stages of their projects. These data were then used to decide whether the aerodynamic benefits outweighed the penalties for incorporating them in the system. The benefits have not been large enough to pay for themselves, and the data are subsequently filed away, unpublished, because they were not "successful" and because the program is a proprietary one. This has been the case for the Viggen and F-16XL airplanes. The reason why variable flap-systems did not work is because separated flows dominate these slender wing configurations. In particular, the reattachment line for the leading-edge separation-induced vortex progresses quickly over the flap and onto the wing upper surface. Once this occurs, the vortex-induced suction pressures increase lift, but the flap becomes less effective for reducing drag. This has been a very difficult flow field for which to design drag-efficient shapes.

#### Subsonic Drag Due To Lift

The problem of achieving efficient drag polars is addressed in figure 3, which presents subsonic drag-due-to-lift data as a function of aspect ratio for a number of airplane models. The untrimmed data are plotted at a constant  $C_L$  of 0.5 and were obtained from references 10 to 20 for  $M = .6$  to  $.8$ . The solid symbols represent composite drag polars obtained from leading-and trailing-edge flap deflections. As would be expected, the results show that the aircraft with the higher aspect ratios have lower  $C_D$ , and, since flow control devices are used, these drag levels approach the full suction values. Decreasing aspect ratio results in higher drag for several reasons. There is a potential flow increase due to lower aspect ratio, the higher swept slender wings are less efficient in achieving high suction levels than the non-slender wing, and the low-aspect ratio wings do not use variable leading-edge flaps to achieve an optimum polar. The higher swept configurations have a fixed camber. Note that there were no data available for the Mirage 2000 or 4000.

Drag values are presented for a series of planar delta wings to give a reference condition. The data (ref. 13) correlate with the vortex lift estimates with zero suction (ref. 16). The F-16XL drag value departed from the data trend established by the Viggen, Mig-21, and F-106 aircraft. One reason for the higher maneuver drag for these slender wings is that they have a fixed camber shape that must function over a wide range of subsonic to supersonic cruise and transonic maneuver requirements. The high sweep angle at maneuver lifts results in a leading-edge vortex flow, and, hence, vortex lift. The loss of leading-edge suction leads to higher drag. These data suggest that there is a new design space available where variable leading-edge devices have seldom been used. As noted by Polhamus (ref. 4), there are many advantages of vortex flows which are designed into current fighters, such as the F-16, F-18, and the F-16XL. Note too that LE suction is not the only measure of fighter capability. Other factors, such as wing loading, instantaneous turn capability, agility, range, weapons carriage, etc., are some of the important measures. Also recall that the data are for a constant  $C_L$  and are untrimmed. Data trimmed at a constant load factor would provide a more definitive analysis.



The question is how do you make variable camber devices effective on higher swept configurations. There are two basic approaches to this problem. The classical approach is to keep the flow attached at the leading edge by drooping the leading edge into the upwash to lessen the leading-edge pressure peak. The reader is referred to references 21 and 22 for some early studies on delta wings. In the limit, the drooped leading edge matches the upwash which gives attached flow. The flow gradients are so strong at the hingeline, however, that the flow separates and forms a vortex aft of the hingeline and over the wing; this vortex gives a little increase in lift and a very large increase in drag. An alternate approach to this is to encourage the leading-edge flow to separate and use the resulting vortex flow to induce suction pressures on the forward-facing surface. Here also, the wing leading-edge is drooped into the upwash field, but you want the stagnation line to remain on the lower surface to insure upwash, and, hence, a vortex, all down the leading edge. For the remainder of the paper, we will be discussing some of the vortex flow research that began by looking at combining camber with the vortex flow, discuss how it evolved to the vortex flap concept, review the status of current vortex flap studies, discuss progress in vortex flow theories, and mention some challenges for additional vortex research.

### COMBINING WING CAMBER OR FLAPS WITH VORTEX FLOW

The purpose of this section is to provide a historical perspective of research that has been conducted to evaluate the effects of combining wing camber or flaps with leading-edge vortex flow. In particular, we will highlight some of the research that has been conducted during the past 10 years which helped give rise to the current NASA/AFWAL Vortex Flow Aerodynamics Conference. Combining the effects of wing camber or leading-edge flaps with the leading-edge vortex is a relatively new research area. The reader is referred to references 23 to 27 for some excellent state-of-the-art review papers which have been published over the past 8 years and contain a considerable number of references.

#### Some Initial Studies

Wentz's Experiment.- In 1972, Wentz (ref. 28) investigated the effects of leading-edge camber on the low-speed aerodynamics of slender delta wings. Apex and conical cambers were tested along with constant chord leading-edge flaps, which approximated the apex camber leading edge. An example of pressure data is shown in figure 4 for the conical camber configuration at  $\alpha = 10.3^\circ$ . The vortex reattachment line, indicated by the arrow, was obtained from tuft data. Recent analysis of the drag polar data for this conical camber configuration showed a suction level of about 40 percent at a  $C_L$  of 0.31 ( $\alpha = 10.3^\circ$ ), and about 28 percent at a  $C_L = 0.5$ .

Vortex Theories for Nonplanar Wings.- During the 1970's three theories were developed to calculate the vortex flow aerodynamics of cambered slender wings: conical flow, the Vortex Lattice Method-Suction Analogy, and the Free Vortex Sheet. These are shown in figure 5, taken from a 1978 paper by Lamar (ref. 29), and represent different levels of capability. The conical flow technique of Barsby (ref. 30) modeled the separated flow vortex sheet, but does not satisfy the trailing-edge Kutta condition. The Vortex Lattice Method - Suction Analogy (VLM-SA) was a modified version of the original suction analogy where Lamar accounted for a vortex lift vector for cambered and twisted wings. The Free Vortex Sheet (FVS) method, originally developed by the Boeing Company in 1974, does account for the trailing-



edge Kutta condition (ref. 31), and gives completely three-dimensional flow field calculations.

An important factor in the evolution of these theories from initial development was the critical correlation and validation studies. One example is the study by Kuhlman (ref. 32) who correlated pressure distributions obtained with the FVS code with Wentz's experiments for a conically cambered delta (ref. 28). Another example is Manro's investigation (ref. 33) to correlate FVS pressure distributions with experiment on an arrow wing having twist and camber.

The capability of these theories to estimate the effects of camber height on drag factor is shown in figure 6, taken from Lamar and Luckring (ref. 23). All of the theories predict a reduction in drag with an increase in camber height. However, because of its restricted assumptions, the conical flow method estimates lower drag than the FVS or VLM-SA techniques. For the range of camber heights shown here, the FVS and VLM-SA estimates are essentially the same. With this earlier version of the FVS, it was difficult to obtain converged solutions where the vortex was small and confined to a camber surface. Kuhlman (ref. 32) explored this difficulty for combinations of angle of attack and leading-edge droop, while Tinoco (ref. 34) performed one of the first studies using the FVS to design slender wing camber shapes to reduce drag.

Pre-Scamp Maneuver Design.— The first vortex design with the VLM-SA was produced by Lamar et al. (ref. 35) on the Pre-Scamp configuration shown in figure 7. This was part of a cooperative effort with General Dynamics to evaluate various transonic and supersonic (ref. 36) wing designs on a stretched F-16 fuselage. The tests were conducted in the NASA Langley Research Center 7- by 10-Foot High-Speed Tunnel (7x10 HST), in April 1978. The wing, which was designed for a maneuver  $C_L$  of 0.5, achieved the design flow field with the reattachment line occurring at the camber crest down the length of the wing and with attached flow downstream over most of the remainder of the wing. This resulted in a suction of 77 percent at the design point.

In addition to the fixed camber design, a planar wing was tested with leading- and trailing-edge flaps. The results are illustrated in figure 8, taken from reference 37, which shows  $L/D$  with Mach number for a cruise and maneuver condition. These data suggest that a combination of simple leading-edge and trailing-edge flaps could approximate the drag benefit due to the vortex flow at transonic maneuver, and that the same flaps at supersonic speeds (only the leading edge was deflected in these data, and at lower deflection angles) approach the  $L/D$  levels obtained for a fixed cruise camber. Polhamus described the NASA/GD co-op program in reference 27, where he presented another version of these data.

F-16 data (ref. 14) are shown to illustrate the effect of sweep, aspect ratio, and deflected flaps in going from a moderately swept transonic fighter to a slender supersonic-cruise-type fighter. The F-16 uses a combination of deflected flaps to optimize drag polar throughout its flight envelope. As noted in figure 8, the combination of increased sweep, or lower aspect ratio, and fixed camber for the slender wing reduces subsonic cruise and maneuver  $L/D$  and increases supersonic cruise efficiency. Using leading- and trailing-edge flaps on the slender wing lessens these subsonic reductions.

## The Vortex Flap Concept

Early Wind Tunnel Studies Explore Flap Hypothesis.- After the Pre-Scamp data were available in April 1978, Rao began a series of experiments in the Langley 7x10 HST to explore the vortex flap concept. Simple generic models, such as a 74° delta (ref. 38) and a highly swept arrow wing (ref. 39), were used to build the data base and evaluate parametric sensitivities. The sketches in figure 9 were taken from reference 40 and illustrate the vortex on the basic wing with no control and the flow due to the vortex flap, where the vortex is on the flap with reattachment of the flow at the hingeline and attached flow over the remainder of the wing. Two types of flaps were suggested, one that has a simple inboard hinge, and the other a folding type that deploys out from the lower surface. An alternate approach for controlling the leading-edge vortex for highly swept wings was proposed by Runyan (ref. 41), who investigated the effect of a leading-edge tab counterdeflected from the main portion of the flap.

The vortex flap flow field was verified experimentally by Rao (ref. 39) using smoke flow, as observed in figure 10, for a segmented flap arrangement on an arrow wing. Pressure measurements by Schoonover and Ohlson (ref. 42) demonstrated the shift in the suction pressures onto the flap compared to the pressures on the basic supersonic camber configuration (fig. 11). Deflecting the flaps reduces lift at a given angle of attack; therefore, a flapped configuration must increase angle of attack to get back to the same lift. This is apparent in the sketch at  $C_L = 0.5$ , where  $\alpha = 10.6^\circ$  for the basic configuration, and  $\alpha = 12.9^\circ$  with the flap. Vortex-induced pressures on the flap resulted in significant reductions in drag.

A considerable amount of data has been obtained for vortex flaps applied to many different research models. The majority of studies have been performed in low-speed and subsonic wind tunnels and have investigated a variety of flap arrangements. For example, research has been conducted on leading-edge devices (refs. 43, 44, and 45), the tabbed vortex flap (refs. 46 and 47), the upper surface flap (ref. 48), segmented flaps (ref. 49), apex flaps (ref. 50), trailing-edge flap effects (ref. 51), planform studies (refs. 52, 53, and 54), and lateral-directional research (refs. 55 and 56).

Vortex Analysis and Design.- There has been a steady evolution in the capabilities of vortex theories to model more complicated flow and geometry situations. This is true of the suction analogy as well as the FVS code. Both Carlson (ref. 57) and Lan (ref. 58) have extended the capabilities of the suction analogy. Lan, for example, derived an improved formulation for the rotated suction vector location for subsonic and supersonic flow. Instead of assuming the vector to be normal to the camber slope at the leading edge, it is moved to a rearward location, where it acts perpendicular to the camber line to account for the size and growth of the vortex. This analysis method, along with that of Carlson, led to the development of design techniques by Chang and Lan (ref. 59) and by Carlson (ref. 60).

The FVS code continued to be developed and refined by Langley, Boeing, and Northrop researchers to predict the vortex flow aerodynamics for a variety of flow conditions and configuration geometries. The reader is referred to references 24 and 61 for several status reports on verification and application efforts with the code. In 1982, Luckring (ref. 62) demonstrated that convergence could be improved by using a converged solution at a higher angle of attack as the starting solution for the next lower angle of attack. Additionally, vortex flap solutions were

obtained by using a vortex sheet transfer technique, where the converged sheet geometry from one flap deflection was used as the starting geometry for the next flap deflection. This improved formulation was used by Frink (ref. 63) to obtain estimates of vortex-flow flap hinge moments, and by Erickson (ref. 64) to obtain solutions for vortex-flapped wings having reduced sweep angle. An example of Erickson's results is presented in figure 12 for a  $65^\circ$  delta wing with a conical flap. The results are for  $M = 0.6$  and  $\alpha = 15^\circ$ . The converged sheet geometry is for a flap deflection of  $30^\circ$ , while the upper surface pressure distributions and vortex core positions are for flap deflections from  $0^\circ$  to  $40^\circ$ . Manro (ref. 65) conducted a related study which was to utilize the FVS code to predict the aeroelastic loads for an arrow wing.

A critical feature of the vortex flap flow field is the location of the reattachment line with respect to the flap hingeline. Frink (ref. 66) has developed a design procedure which achieves this type of flow, as is sketched in figure 13. The design technique came about as an attempt to add rationale to shape the flap to accommodate the vortex growth.

#### STATUS FOR VORTEX FLOW AERODYNAMICS CONFERENCE

The current Vortex Flow Aerodynamics Conference provides state-of-the-art papers on advances in vortex flow theories, as well as on vortex flap research over the past few years. This section of the paper gives a brief review of progress in vortex flap research, provides some needs for additional work, and presents highlights of research activities under way in vortex theories.

#### Vortex Flap Studies

Subsonic.— A large subsonic data base has been established for the vortex flap concept. As noted in figure 14, this includes pressure and load distributions, hinge moments, performance, longitudinal and lateral stability and control, and flow field diagnostics. Flap geometric variations include flap planform, hinge-line sweep, flap deflections, and flap and wing aerodynamic sections. The types of flaps, shown in figure 15, have increased to include upper surface, lower surface, and apex types. Most of the results presented at the conference are for the lower surface folding or hinged types of flaps. Hoffler presents results of studies on apex fences (ref. 67), while Rao discusses a new type of lower surface flap called a cavity vortex flap (ref. 68).

As suggested in figure 16, the flap concept is maturing at subsonic speeds because of the number of application studies which combine experiment with theoretical analysis and design methods. The sketches in figure 17 are an updated version of Schoonover's (ref. 69) and illustrate the variety of configurations for which flaps have been applied. Papers are presented at the conference on subsonic studies of both generic (refs. 70 to 74) and aircraft (refs. 17 and 18, and 75 to 77) types of models.

An example of data for aircraft models (from ref. 69) is shown in figure 18 to illustrate the effect of vortex flaps on subsonic drag reduction for the F-106, F-16XL, and the AFTI/F-111 configurations. Design studies for these three configurations are published at the conference and extend Frink's vortex-flap design procedure for simple delta wings (ref. 78), to wings with twist and camber, such as the F-106 delta wing (ref. 17), the F-16XL cranked wing (ref. 18), and the AFTI/



F-111 swept-wing panel (ref. 77). The parameter  $\Delta C_D$  is defined as the difference between the baseline drag with no flap and the configuration drag after the flap is added. The drag reduction increases with increased lift to about 200 to 250 drag counts near the design point. NASA Langley is considering a subsonic flight experiment on an F-106 airplane to verify the vortex-flap flow field and design procedure. An initial study of the vortex flow field over the F-106 is described by Lamar in reference 79.

Transonic/Supersonic.— Considerably fewer studies have been conducted at transonic and supersonic speeds than at subsonic speeds (see fig. 19). Some transonic data are provided by Klein (ref. 80) on a generic fighter model which had three highly swept wing planforms, for which a number of vortex flaps were designed. Hallissy (ref. 17) and Finley (ref. 18) present transonic results obtained on aircraft models of the F-106 and F-16XL, respectively.

Research at supersonic speeds has begun using generic models to study leading-edge vortex flows and their impact on supersonic aerodynamic performance. For example, Miller and Wood (ref. 81) investigated the leeside flow fields over planar delta wings, and classified the test data by the flow conditions normal to the wing leading edge. This is presented in figure 20. Recent supersonic studies (refs. 82 and 83) have examined delta wing aerodynamics in terms of upper and lower surface contributions and have assessed available prediction methods for estimating leading-edge vortex aerodynamics for planar and cambered delta wings. These evaluations suggest that additional codes are needed to analyze the vortex/shock interaction and the flap hingeline separation phenomena. These supersonic efforts are summarized by Miller in reference 84.

#### Leading-Edge Vortex Theories

Suction Analogy for Analysis and Design.— Considerable use has been made of the leading-edge suction analogy for providing preliminary analysis and design. In 1983, Lamar and Campbell (ref. 26) reviewed the extensions to the suction analogy that had been made to estimate strake-wing configurations, cambered wings, round leading edges, and a vortex breakdown criteria for estimating longitudinal and lateral-directional aerodynamics. Current extensions of the suction analogy principles are presented by Lan (ref. 85) which include the vortex action point, rounded leading edges, body vortex lift, and nonlinear wave drag for supersonic speeds (see fig. 21). In addition, the suction analogy has been incorporated into a number of design procedures. Frink (ref. 78) discusses the use of the analogy to design area efficient vortex flaps, while Lan (ref. 86) describes an optimization technique to design vortex flaps on wings for maximum L/D. Carlson (ref. 87) uses attainable thrust considerations to analyze and design wing flap systems. Huebner (ref. 88) describes an alternate procedure to Lan's (ref. 86) where a new optimizer is coupled with Lan's analysis to define vortex flaps at supersonic speeds.

Free Vortex Sheet Method.— The free-vortex-sheet method continues to provide the bulk of the subsonic flow-field calculations and integrated force and moment results to correlate with the various suction analogy and Euler codes. As noted in figure 21, Luckring (ref. 89) presents an updated version of the FVS formulation which has greatly improved convergence properties for a broad range of geometries, including vortex flaps. One of the recent innovations for the FVS was Luckring's work to develop a viscous core formulation to estimate vortex breakdown (ref. 90). Frink (ref. 72) obtains calculations for vortex flap pressure distributions and hinge moments for a 74° delta wing and shows the necessity for accounting for the



secondary vortex in theoretical models. Additional application results are presented by Grantz (ref. 73) and Erickson (ref. 91).

Euler Codes.- Euler codes began appearing in the literature in 1982 and have been developing rapidly. The results shown in figure 21 were obtained by Raj (ref. 92) for a  $71^\circ$  swept arrow wing at  $M = 0.85$  and  $\alpha = 15.8^\circ$ . The crossflow velocity field is shown for one location. The advantage of the Euler code is that it has the capability to compute very complicated flows such as the vortex/shock interactions. It is desirable to perform further subsonic validation studies between the Euler code vortex flows and wing surface pressures and the FVS code in order to take advantage of the large number of FVS solutions available. Recently, Kandil (ref. 93) used an integral equation approach to calculate a vortex/shock interaction on a delta wing.

Sirbaugh (ref. 94) presents a correlation study of Euler analysis for an elliptic missile body, while Raj (ref. 95) presents results of correlations with two cropped delta wings and an arrow wing. Newsome (ref. 96) provides a critical comparison between Euler and Navier-Stokes equations for the simulation of leading-edge vortex flows at supersonic speeds.

Three-Dimensional Boundary Layer Methods.- Three-dimensional boundary layer research is very important in order to get some viscous "smarts" into inviscid methods, such as the Free Vortex Sheet and Euler codes. Currently, separation lines must be specified for these codes. Recently, Wai (ref. 97) and DeJarnette (ref. 98) developed three-dimensional boundary layer techniques to estimate the boundary layer and secondary separation line on slender wings with vortex flows. The sketch in figure 22 is from reference 98. Woodson (ref. 99) and Blom (ref. 100) report on their respective techniques. Boundary layer techniques should be developed to estimate separation lines on slender wings with round leading edges, at leading-edge flap and trailing-edge flap hinge lines, and the secondary vortex separation line. This is a more critical problem at subsonic and transonic speeds where the Navier-Stokes solvers are not appropriate yet.

Navier-Stokes Solvers.- Navier-Stokes solutions are usually obtained for supersonic conditions so the solution domain is limited compared to the subsonic. An example of the flow detail is shown in figure 22 for a  $75^\circ$  delta wing at  $M = 1.95$  and  $\alpha = 10^\circ$ . These results were obtained by Rizzetta (ref. 101) and demonstrate the upper surface flow pattern, including the primary vortex reattachment line and the secondary separation line. Supersonic studies reported at the conference include Newsome (ref. 96), Buter (ref. 102), and Blom (ref. 100). Studies need to be extended down to subsonic and transonic speeds. One approach would be to use a converged FVS solution for  $M = 0.9$  as the starting solution to focus the grid and reduce run time.

#### SOME CHALLENGES FOR ADDITIONAL VORTEX RESEARCH

There are a number of opportunities to study flow field problems for slender wing configurations. These are listed here to provide some food for thought. Some of the research challenges are illustrated by flow situations on some current airplanes.

1. Combine attached flow and vortex flow fields in wing design.

2. Investigate vortex flow and shock wave interactions. An example is shown in figure 23 taken from reference 103 of an F-4 airplane at  $M = 0.95$  and an angle of attack of  $8^\circ$ . Where the vortex has started on the outboard panel, there is no evidence of the shock in the surface oil flow. Inboard the attached flow proceeds to the trailing-edge shock. The separated vortex results in an oblique flow which lowers the local normal Mach number to subsonic. Theoretical models are needed to exploit this favorable flow interaction.
3. Continue to develop 3-D boundary layer techniques to estimate separation lines at round leading edges, leading-edge flap and trailing-edge flap hingelines, and secondary vortex flows.
4. Conduct critical studies of  $M$  and  $R_n$  scaling of vortex development. An example of this is shown in figure 24 for the F-111 TACT airplane at  $M = 0.6$  and  $\alpha = 6^\circ$ . These flight data were obtained by Schoonover (ref. 104) and illustrate a vortex-induced pressure distribution at  $R_{\zeta} = 20 \times 10^6$ ; increase in  $R_{\zeta}$  to  $40 \times 10^6$  results in an attached flow pressure distribution.
5. Validate vortex theories for simple and mixed flow fields (panel, Euler, and Navier-Stokes techniques).
6. Provide additional vortex flap applications at transonic and supersonic speeds.
7. Investigate multiple vortex interactions. An example is shown in figure 25 for the B-1 airplane at  $M = 0.98$  and  $\alpha = 7^\circ$ . The flight vehicle experienced wing oscillations while in a windup turn (ref. 105). A wind tunnel model confirmed these oscillations and that they were due to two corotating vortices on the wing panel.
8. Study vortex interactions with inlet and exhaust flow fields.
9. Evaluate canard and strake effects on vortex flap design.
10. Expand theory and experimental data base for vortex breakdown. An example is shown in figure 25 for an F-18 water tunnel model (ref. 106). The vertical tails operate in the very turbulent flow field downstream of the vortex burst, which has led to tail oscillations and premature tail fatigue.

#### CONCLUDING REMARKS

This paper provides some background information for the Vortex Flow Aerodynamics Conference and resulted in the following observations:

Current slender wing airplanes do not use variable leading-edge geometries to improve drag polar for transonic maneuver conditions.

A large subsonic data base for the vortex flap concept has been generated; transonic and supersonic generic studies have started.

There is a need for validated flow field solvers for calculating vortex/shock interactions at transonic and supersonic speeds.

Many important research opportunities exist to theoretically and experimentally investigate fundamental vortex flows and apply that knowledge to analyze and design advanced fighter concepts.

#### REFERENCES

1. Design Conference Proceedings-Technology for Supersonic Cruise Military Aircraft, AFFDL-TR-77-85, Vol. 1, Colorado Springs, Colorado, Feb. 17-20, 1976.
2. Tactical Aircraft Research and Technology Conference, Oct. 21-23, 1980, NASA Langley, Hampton, Virginia. NASA CP-2162.
3. Piccirillo, A. C.: The Advanced Tactical Fighter--Design Goals and Technical Challenges. Aerospace America, November 1984, pp. 74-79.
4. Polhamus, E. C.: Vortex Lift Research: Early Contributions and Some Current Challenges. Vortex Flow Aerodynamics - Volume I, NASA CP-2416, paper no. 1, 1986.
5. Jane's All The World's Aircraft. Edited by J. W. R. Taylor, 1974 to 1984. Jane's Publishing Company, LTD.
6. The Encyclopedia of World Air Power. Consultant Editor, W. Gunston. Published by the Hamlyn Publishing Group LTD. London, England, 1980
7. DeLuca, J.; Arena, A.; Myers, W.; and Stevens, C.: F-14 Maneuver Slat Optimization Program: Final Report. Report A51-335-R-73-2. Grumman Aerospace Corp., December 1973.
8. Ropelewski, R. R.: "Aviation Week Pilot Report - Mirage 2000 Fighter Combines Acceleration, Low Speed Stability." Aviation Week & Space Technology. June 24, 1985, pp. 38-49.
9. Aviation Week & Space Technology, March 18, 1985, Vol. 122, No. 11, pp. 21.
10. Mantz, K.: Data Report of a 0.08 Scale Northrop YF-17 Force/Pressure Model Transonic Wind Tunnel Drag and Pressure Tests in the AEDC 16 Foot Wind Tunnel. Northrup, Hawthorne, CA, NOR 75-18, March 1975.
11. Northrop Corp.: Second F-5G Transonic Test. NAL-272, July 1980.
12. Niedling, L. F.: The F-15 Wing Development Program Presented at AIAA Symposium on "The Evolution of Aircraft Wing Design," Dayton, Ohio, March 18-19, 1980, AIAA-80-3044.
13. Wentz, W. H.; and Kohlman, D. L.: Wind-Tunnel Investigation of Vortex Breakdown on Slender Sharp-Edged Wings. NASA CR-98737, 1968.



14. Webb, J. B., et al.: F-16 Aerodynamic Design Data Report CDRL Sequence No. A027, General Dynamics Fort Worth, No. 16PR177, Contract F33657-75-C-0310, Revised Nov. 1976.
15. Ray, E. J.; and Hollingsworth, E. G.: Subsonic Characteristics of a Twin-Jet Swept-Wing Fighter Model With Maneuvering Devices. NASA TN D-6921, Jan. 1973.
16. Polhamus, E. C.: Application of the Leading-Edge Suction Analogy of Vortex Lift to the Drag-Due-To-Lift of Sharp-Edge Delta Wings. NASA TN D-4739, August 1968.
17. Hallissy, J. M.; Frink, N. T.; and Huffman, J. K.: Aerodynamic Testing and Analysis of Vortex Flap Configurations for the 5-Percent Scale F-106B. Vortex Flow Aerodynamics - Volume II, NASA CP-2417, paper no. 12, 1986.
18. Finley, D. B.; and Schoonover, W. E.: Design and Wind Tunnel Evaluation of Vortex Flaps For the F-16XL. Vortex Flow Aerodynamics - Volume II, NASA CP-2417, paper no. 13, 1986.
19. Roed, A.: Development of the SAAB-Scania Viggen. Canadian Aeronautics and Space Journal. June 1972, pp. 167-175.
20. Spearman, M. L.; and Corlett, W. A.: Stability and Control Characteristics at Mach Numbers From 0.60 to 2.50 of a Delta-Wing Fighter Airplane Model Having an Aft Horizontal Tail. NASA TM X-1752, 1969.
21. Whittle, E. F.; and Lovell, J. C.: Full-Scale Investigation of an Equilateral Triangular Wing Having 10-Percent-Thick Biconvex Airfoil Sections. NACA RM L8G05, 1948.
22. Riebe, J. M.; and Fikes, J. E.: Preliminary Investigation of the Effect of Camber on a 60° Delta Wing With Round and Beveled Leading Edges. NACA RM L9F10, August 1949.
23. Lamar, J. E.; and Luckring, J. M.: Recent Theoretical Developments and Experimental Studies Pertinent to Vortex Flow Aerodynamics--With a View Towards Design. AGARD CP-247, Paper No. 24, October 1978.
24. Bobbitt, P. J.: Modern Fluid Dynamics of Subsonic and Transonic Flight. AIAA 80-0861, May 1980.
25. Rao, D. M.: Vortical Flow Management for Improved Configuration Aerodynamics --Recent Experiences. AGARD CP-342, Paper No. 30, April 1983.
26. Lamar, J. E.; and Campbell, J. F.: Recent Studies at NASA-Langley of Vortical Flows Interacting With Neighboring Surfaces. AGARD CP-342, Paper No. 10, April 1983.
27. Polhamus, E. C.: Applying Slender Wing Benefits to Military Aircraft. Journal of Aircraft, Vol. 21, No. 8, August 1984, pp 545 - 559.



28. Wentz, W. H.: Effects of Leading-Edge Camber on Low-Speed Characteristics of Slender Delta Wings. NASA CR-2002, 1972.
29. Lamar, J. E.: Subsonic Vortex-Flow Design Study for Slender Wings. Journal of Aircraft, Vol. 15, No. 9, pp. 611 - 619, September 1978.
30. Barsby, J. E.: Flow Past Conically Cambered Slender Delta Wings With Leading-Edge Separation. Aeronautical Research Council Reports and Memoranda No. 3748, 1974.
31. Brune, G. W.; Weber, J. A.; Johnson, F. T.; Lu P.; and Rubbert, P. E.: A Three-Dimensional Solution of Flows Over Wings With Leading-Edge Vortex Separation. NASA CR-132709, Sept. 1975.
32. Kuhlman, J. M.: Analytical Studies of Separated Flow on Highly Swept Wings. NASA CR-3022, November 1978.
33. Manro, M. E.; Bobbitt, P. J.; and Kulfan, R. M.: The Prediction of Pressure Distributions on an Arrow-Wing Configuration Including the Effect of Camber, Twist, and a Wing Fin. NASA CP-2108, Nov. 1979.
34. Tinoco, E. N.; and Yoshihara, H.: Subcritical Drag Minimization for Highly-Swept Wings With Leading-Edge Vortices. AGARD CP-247, Paper No. 26, October 1978.
35. Lamar, J. E.; Schemensky, R. T.; and Reddy, C. S.: Development of a Vortex Lift Design Procedure and Application to a Slender-Maneuver-Wing Configuration. Journal of Aircraft, Vol. 18, No. 4, pp. 259-266, April 1981.
36. Miller, D. S.; and Schemensky, R. T.: Design Study Results of a Supersonic Cruise Fighter Wing. AIAA-79-0062, Jan. 1979.
37. Lamar, J. E.; and Campbell, J. F.: Vortex Flaps--Advanced Control Devices for Supercruise Fighters. Aerospace America. pp. 95-99, January 1984.
38. Rao, D. M.: Leading Edge Vortex-Flap Experiments on a 74 Deg. Delta Wing. NASA CR-159161, November 1979.
39. Rao, D. M.: Exploratory Subsonic Investigation of Vortex-Flap Concept on Arrow Wing Configuration. NASA CP 2108, pp. 117-129, November 1979.
40. Rao, D. M.: Leading-Edge 'Vortex Flaps' for Enhanced Subsonic Aerodynamics of Slender Wings. ICAS-80-13.5. October 12-17, 1980.
41. Runyan, L. J.; Middleton, W. D.; and Paulson, J. A.: Wind Tunnel Test Results of a New Leading-Edge Flap Design For Highly Swept Wings. NASA CP-2108. pp. 131-147, November 1979.
42. Schoonover, W. E.; and Ohlson, W. E.: Wind-Tunnel Investigation of Vortex Flaps on a Highly Swept Interceptor. ICAS-82-6.7.3, August 1982.
43. Rao, D. M.; and Johnson, T. D.: Investigation of Delta Wing Leading-Edge Devices. J. of Aircraft. Vol. 18, No. 3, March 1981, pp. 161-167.

44. Johnson, T. J.; and Rao, D. M.: Experimental Study of Delta Wing Leading-Edge Devices for Drag Reduction at High Lift. NASA CR-165846, February 1982.
45. Tingas, S. A.; and Rao, D. M.: Subsonic Balance and Pressure Investigation of a 60-degree Delta Wing With Leading-Edge Devices. NASA CR-165923, May 1982.
46. Yip, L. P.; and Murri, D. G.: Effects of Vortex Flaps on the Low-Speed Aerodynamic Characteristics of an Arrow Wing. NASA TP-1914, November 1981.
47. Hoffler, K. D.; and Rao, D. M.: An Investigation of the Tabbed Vortex Flap. J. of Aircraft. Vol. 22, No. 6, June 1985, pp. 490-497.
48. Rao, D. M.: Upper Vortex Flap - A Versatile Surface for Highly Swept Wings. ICAS Paper No. 82-6.7.1, August 1982.
49. Rao, D. M.: Segmented Vortex Flaps. AIAA 83-0424, January 1983.
50. Rao, D. M.; and Buter, T. A.: Experimental and Computational Studies of an Apex Flap Concept on a 74-Deg. Delta Wing. AIAA 83-1815, July 1983.
51. Grantz, A. G.; and Marchman, J. F.: Trailing-Edge Flap Influence on Leading-Edge Flap Aerodynamics. J. of Aircraft, Vol. 20, No. 2, February 1983, pp. 165-169.
52. Hom, K. W.; Morris, O. A.; and Hahne, D. E.: Low-Speed Investigation of the Maneuver Capability of Supersonic Fighter Wings. AIAA 83-0426, January 1983.
53. Erickson, G. E.; and McCann, M. K.: Experimental and Analytical Investigation of the Subsonic Aerodynamics of Slender Wings With Leading-Edge Vortex Flaps. AIAA 83-2113, August 1983.
54. Erickson, G. E.: Vortex/Linear Lift Augmentation. AFWAL TR-6 -3017. June 1985.
55. Grantz, A. C.: The Lateral-Directional Characteristics of a 74-Degree Delta Wing Employing Gothic Planform Vortex Flaps. NASA CR-3848, November 1984.
56. Carey, K. M.; and Erickson, G. E.: Vortex Flap Technology: A Stability and Control Assessment. NASA CR-172439, November 1984.
57. Carlson, H. W.; and Mack, R. J.: Estimation of Wing Nonlinear Aerodynamic Characteristics at Supersonic Speeds. NASA TP-1718, November 1980.
58. Lan, C. E.; and Chang, J. F.: Calculation of Vortex Lift Effect for Cambered Wings by the Suction Analogy. NASA CR-3449, July 1981.
59. Chang, J. F.; and Lan, C. E.: Design of Wings With Vortex Separated Flow. NASA CR-172198, September 1983.
60. Carlson, H. W.; and Walkley, K. B.: An Aerodynamic Analysis Computer Program and Design Notes For Low Speed Wing Flap Systems. NASA CR-3675, March 1983.

61. Campbell, J. F.: Vortex Flow Aerodynamics--An Emerging Design Capability. Background Article for Astronautics and Aeronautics Cover, pp. 54-58, May 1981.
62. Luckring, J. M.; Schoonover, W. E.; and Frink, N. T.: Recent Advances in Applying Free Vortex Sheet Theory for the Estimation of Vortex Flow Aerodynamics. AIAA-82-0095, Jan. 1982.
63. Frink, N. T.: Analytical Study of Vortex Flaps on Highly Swept Delta Wings. ICAS Paper No. 82-6.7.2, August 1982.
64. Erickson, G. E.: Application of Free Vortex Sheet Theory to Slender Wings With Leading-Edge Vortex Flaps. AIAA 83-1813, July 1983.
65. Manro, M. E.: Aeroelastic Loads Prediction for an Arrow Wing. Task III.- Evaluation of the Boeing Three-Dimensional Leading-Edge Vortex Code. NASA CR-3642, January 1983.
66. Frink, N. T.: Concept for Designing Vortex Flap Geometries. NASA TP-2233, December 1983.
67. Hoffler, K. D.; Rao, D. M.; and Frassenelli, M. C.: Basic Studies on Delta Wing Flow Modifications by Means of Apex Fences. Vortex Flow Aerodynamics - Volume I. NASA CP-2416, paper no. 9, 1986.
68. Rao, D. M.: Towards An Advanced Vortex Flap System - The "Cavity" Flap. Vortex Flow Aerodynamics - Volume I, NASA CP-2416, paper no. 10, 1986.
69. Schoonover, W. E.; Frink, N. T.; Hallissy, J. B.; and Yip, L. P.: Subsonic/Transonic Development of Vortex Flaps For Fighter Aircraft. Presented at the Symposium on Aerodynamics, NASA Langley, April 23-25, 1985.
70. Johnson, T. D; and Huffman, J. K.: Experimental Study of Vortex Flaps on a Delta Wing Sweep Series at High Angle of Attack. Vortex Flow Aerodynamics - Volume II, NASA CP-2417, paper no. 9, 1986.
71. Campbell, B. A.; and Riebe, G. D.: An Investigation of the Subsonic Maneuver Characteristics of Two Supersonic Fighter Wing Concepts. Vortex Flow Aerodynamics - Volume II, NASA CP-2417, paper no. 10, 1986.
72. Frink, N. T.: Critical Evaluation of a Vortex Flap Design Concept Using a 74° Delta Configuration. Vortex Flow Aerodynamics - Volume II, NASA CP-2417, paper no. 2, 1986.
73. Grantz, A. C.: The Lateral-Directional Characteristics of a 74-Degree Wing Employing Gothic Planform Vortex Flaps. Vortex Flow Aerodynamics - Volume II, NASA CP-2417, paper no. 3, 1986.
74. Gatlin, G. M.: Advanced Fighter Tested for Low-Speed Aerodynamics with Vortex Flaps. Vortex Flow Aerodynamics - Volume II, NASA CP-2417, paper no. 1, 1986.

75. DelFrate J. H.: Water Tunnel Results of Leading-Edge Vortex Flap Tests on a Delta Wing Vehicle. Vortex Flow Aerodynamics - Volume I, NASA CP-2416, paper no. 18, 1986.
76. Yip, L. P.: Investigation of Vortex Flaps on the F-106B Airplane Configuration in the Langley 30- By 60-Foot Wind Tunnel. Vortex Flow Aerodynamics - Volume II, NASA CP-2417, paper no. 11, 1986.
77. Schoonover, W. E.; and Smith, F. R.: Design and Wind Tunnel Evaluation of Vortex Flaps for the USAF AFTI/F-111. Vortex Flow Aerodynamics - Volume II, NASA CP-2417, paper no. 14, 1986.
78. Frink, N. T.: Refinements of a Vortex Flap Design Method with Schematic Applications (U). Vortex Flow Aerodynamics - Volume III, NASA CP-2418, paper no. 1, 1986.
79. Lamar, J. E.: In-Flight and Wind Tunnel Leading-Edge Vortex Study on the F-106B Airplane. Vortex Flow Aerodynamics - Volume I, NASA CP-2416, paper no. 8, 1986.
80. Klein, J. R.; Chu, J.; and Frink, N. T.: Aerodynamic Assessment of Vortex Flaps on Two Fighter Aircraft Configurations at Transonic Speeds. Vortex Flow Aerodynamics - Volume II, NASA CP-2417, paper no. 4, 1986.
81. Miller, R. M.; and Wood, D. S.: Leaside Flows Over Delta Wings at Supersonic Speeds. J. of Aircraft. Vol. 21, No. 9, September 1984, pp. 680-686.
82. Wood, R. M.; and Miller, D. S.: Fundamental Aerodynamic Characteristics of Delta Wings With Leading-Edge Vortex Flows. J. of Aircraft, Vol. 22, No. 6, June 1985, pp. 479-485.
83. Wood, R. M.; and Miller, D. S.: Assessment of Preliminary Prediction Techniques for Wing Leading-Edge Vortex Flows at Supersonic Speeds. J. of Aircraft, Vol. 22, No. 6, June 1985, pp. 473-475.
84. Miller, D. S.; Wood, R. M.; and Covell, P. F.: An Overview of the Fundamental Aerodynamics Branch's Research Activities in Wing Leading-Edge Vortex Flows at Supersonic Speeds. Vortex Flow Aerodynamics - Volume I, NASA CP-2416, paper no. 17, 1986.
85. Lan, C. E.: Extensions of the Concept of Suction Analogy to Prediction of Vortex Lift Effect. Vortex Flow Aerodynamics - Volume I, NASA CP-2416, paper no. 3, 1986.
86. Lan, C. E.; and Hsing, C. C.: Subsonic Analysis and Design of Vortex Flaps. Vortex Flow Aerodynamics - Volume II, NASA CP-2417, paper no. 5, 1986.
87. Carlson, H. W.; and Darden, C. M.: Attached Flow Numerical Methods for the Aerodynamic Design and Analysis of Vortex Flaps. Vortex Flow Aerodynamics Volume II, NASA CP-2417, paper no. 6, 1986.



88. Huebner, L. D.; and Lamar, J. E.: Performance Analysis and Supersonic Design of Wing Leading-Edge Vortex Flaps for the Convair F-106B. Vortex Flow Aerodynamics - Volume II, NASA CP-2417, paper no. 7, 1986.
89. Luckring, J. M.; Hoffler, K. D.; and Grantz, A. C.: Recent Extensions to the Free-Vortex-Sheet Theory for Expanded Convergence Capability. Vortex Flow Aerodynamics - Volume I, NASA CP-2416, paper no. 4, 1986.
90. Luckring, J. M.: A Theory for the Core of a Three-Dimensional Leading-Edge Vortex. AIAA Paper No. 85-0108, January 1985.
91. Erickson, G. E.; and Rogers, L. W.: Experimental Investigation at Low- and High-Subsonic Speeds of a Moderately Swept Fighter Wing with Deflected Leading-Edge Flaps. Vortex Flow Aerodynamics - Volume II, NASA CP-2417, paper no. 8, 1986.
92. Raj, P.: Computational Simulation of Free Vortex Flows Using an Euler Code. ICAS-84-1.3.1, September 1984.
93. Kandil, O. A.; and Yates, E. C.: Computation of Transonic Vortex Flows Past Delta Wings - Integral Equation Approach. AIAA 85-1582, July 1985.
94. Sirbaugh, J. R.: Euler Analysis of an Elliptic Missile Body at Angles of Attack. Vortex Flow Aerodynamics - Volume I, NASA CP-2416, paper no. 14, 1986.
95. Raj, P.; and Long, L. N.: An Euler Aerodynamic Method for Leading-Edge Vortex Flow Simulation. Vortex Flow Aerodynamics - Volume I, NASA CP-2416, paper no. 13, 1986.
96. Newsome, R. W.; and Thomas, J. L.: Computations of Leading-Edge Vortex Flows. Vortex Flow Aerodynamics - Volume I, NASA CP-2416, paper no. 15, 1986.
97. Wai, J. C.; Baillie, J. C.; and Yoshihara, H.: Computation of Turbulent Separated Flows Over Wings. Third Symposium on Numerical and Physical Aspects of Aerodynamic Flows. Long Beach, CA, January 20-24, 1985.
98. DeJarnette, F. R.; and Woodson, S. H.: Numerical and Experimental Determination of Secondary Separation on Delta Wings in Subsonic Flow. J. of Aircraft, Vol. 22, No. 7, July 1985, pp. 602-608.
99. Woodson, S. H.; and DeJarnette, F. R.: A Direct and Inverse Boundary Layer Method for Subsonic Flow Over Delta Wings. Vortex Flow Aerodynamics - Volume I, NASA CP-2416, paper no. 5, 1986.
100. Blom, G.; Wai, J. C.; and Yoshihara, H.: Viscous Vortical Flow Calculations Over Delta Wings. Vortex Flow Aerodynamics - Volume I, NASA CP-2416, paper no. 12, 1986.
101. Rizzetta, D. P.; and Shang, J. S.: Numerical Simulation of Leading-Edge Vortex Flows. AIAA 84-1544, June 1984.

102. Buter, T. A.; and Rizzetta, D. P.: Steady Supersonic Navier-Stokes Solutions of a 75° Delta Wing. Vortex Flow Aerodynamics - Volume I, NASA CP-2416, paper no. 16, 1986.
103. Gross, G. G.: Investigation of Scaling Effects in Transonic Wind Tunnel Testing. AFFDL-TR-72-60, June 1972.
104. Polhamus, E. C.; and Gloss, B. B.: Configuration Aerodynamics - High Reynolds Number Research --- 1980. NASA CP-2183, December 1980, pp. 217-234.
105. Dobbs, S. K.; Miller, G. D.; and Stephenson, J. R.: Self Induced Oscillation Wind Tunnel Test of a Variable Sweep Wing. AIAA 85-0739-CP, April 1985.
106. Erickson, G. E.: Vortex Flow Correlation. AFWAL-TR-80-3143. January 1981, pp. 166.

TABLE I.- SYMBOL DEFINITION OF DATA PLOTTED IN FIGURE 1  
(OBTAINED FROM REFERENCES 5-8)

(a) Fixed Sweep

| Symbol | Airplane             | $\Delta LE, \text{deg}$ | A    | Variable LE Geometry Used to Improve Drag Polar |
|--------|----------------------|-------------------------|------|---|
| △      | F-15A                | 46                      | 3.0  | No  |
| ◇      | F-16A                | 40                      | 3.2  | Yes   |
| ◇      | F-4E                 | 51                      | 2.8  | Yes   |
| ◇      | Viggen               | 55*                     | 2.5  | No  |
| △      | F-106                | 60                      | 2.1  | No  |
| △      | F-16XL               | 66.5*                   | 1.62 | No  |
| △      | MIG 21               | 57                      | 2.2  | No  |
| ◇      | KFIR                 | 61                      | 1.86 | No  |
| □      | Mirage 2000 and 4000 | 60                      | 2.0  | Yes   |
| ◇      | Mirage III           | 61                      | 1.94 | No  |
| ▽      | Mirage F-1           | 47.5                    | 2.8  | Yes   |
| ▽      | Sepecat              | 44                      | 3.1  | Yes   |
| ▽      | Jaguar GR-1          |                         |      |   |
| △      | F-5E                 | 32                      | 3.82 | Yes   |
| △      | F-20 <sup>1</sup>    | 32                      | 3.82 | Yes   |
| △      | F-18A                | 26                      | 3.52 | Yes   |
| ◇      | A-4F                 | 41                      | 2.91 | Yes   |
| ◇      | A-6E                 | 29                      | 5.31 | Yes   |
| ◇      | A-7D                 | 40*                     | 4.0  | Yes   |
| ◇      | MIG 25               | 39*                     | 3.5  | No  |
| ◇      | SR-71                | 60                      | 1.72 | No  |
| ▽      | Super Etendard       | 48                      | 3.2  | Yes   |
| ◇      | SU-15                | 49*                     | 3.1  | No  |
| ○      | B-70                 | 65.6                    | 1.74 | Undelected tip                                  |
|        |                      | 70.8*                   | 1.14 | Deflected tip                                   |
| ○      | Concord              | 67.5*                   | 1.93 | No  |

(b) Variable Sweep

|   |           |           |           |   |
|---|-----------|-----------|-----------|---|
| ○ | F-111F    | 16 → 72   | 7.6 → 1.6 | Yes (low $\Delta LE$ )                    |
| ○ | B-1B      | 15 → 67.5 | 9.6 → 3.1 | Yes (low $\Delta LE$ )                    |
| ◇ | MIG 23/27 | 16 → 72   | 7.3 → 2.4 | Yes (?)                                   |
| ○ | F-14A     | 20 → 68   | 7.3 → 2.6 | Yes ( $20^\circ < \Delta LE < 50^\circ$ ) |

\*Effective LE sweep angle (defined in figure 1)

<sup>1</sup>Preproduction airplane

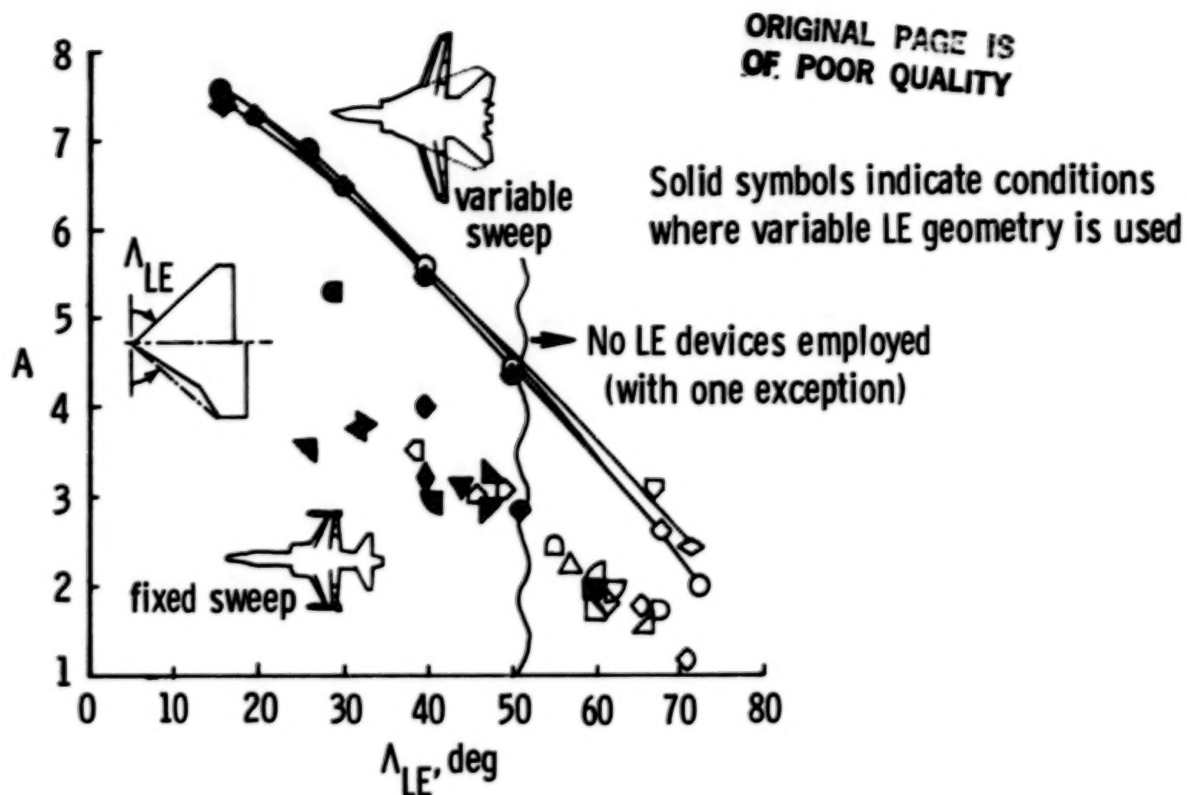


Figure 1.- Aircraft that use variable leading-edge geometry to improve maneuver drag polar. (See Table I for symbol definition.)

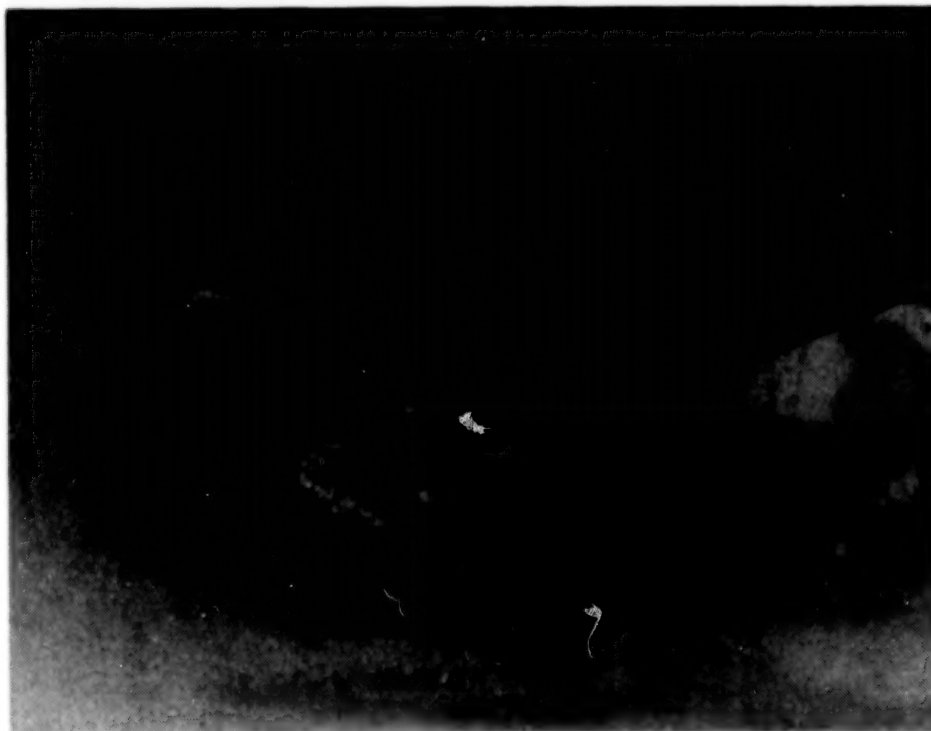


Figure 2.- Photograph of Dassault-Breguet Mirage 2000 with variable leading-edge flaps. (From ref. 9.)



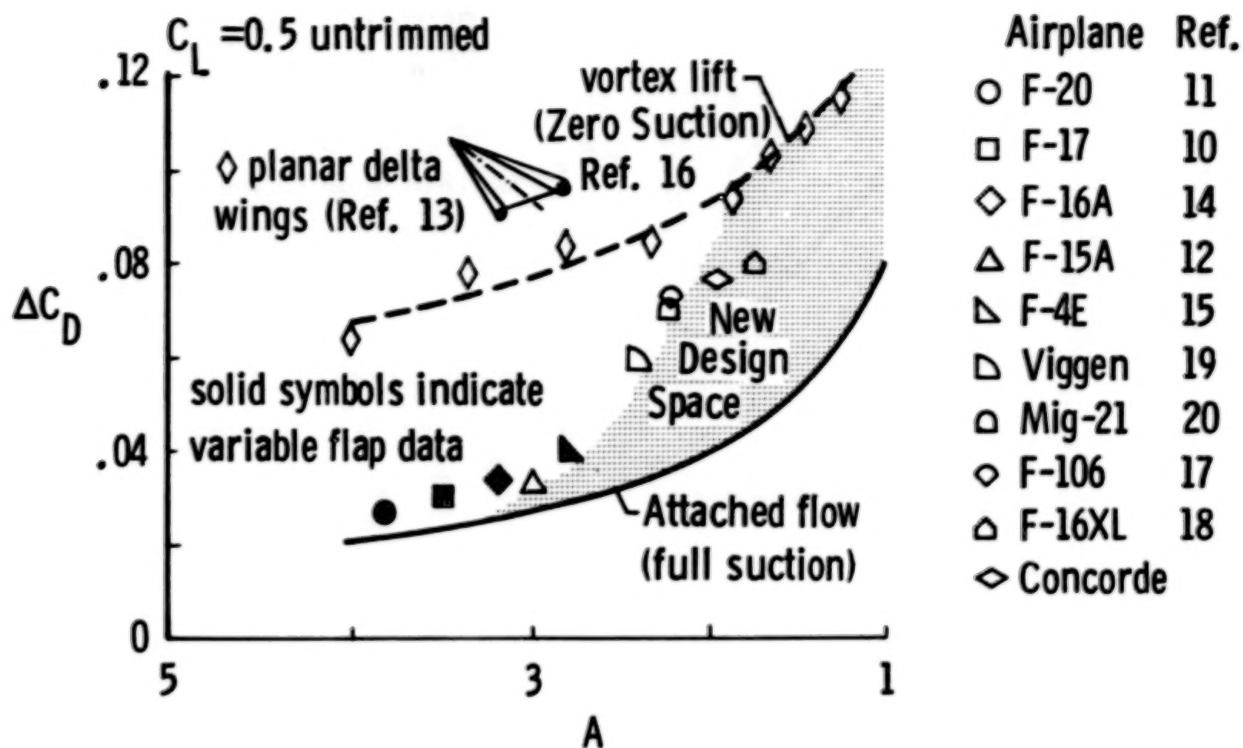


Figure 3.- Subsonic drag due to lift as a function of airplane model aspect ratio.

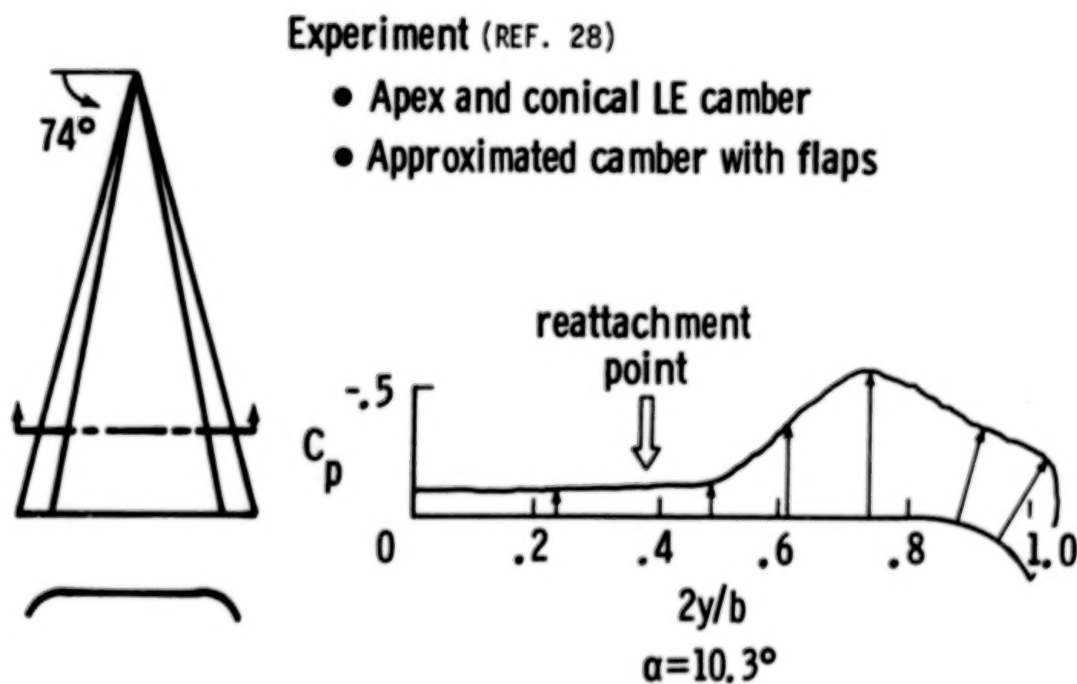


Figure 4.- Experimental investigation combining leading-edge camber on 74° delta wing with vortex flow. (From ref. 28.)

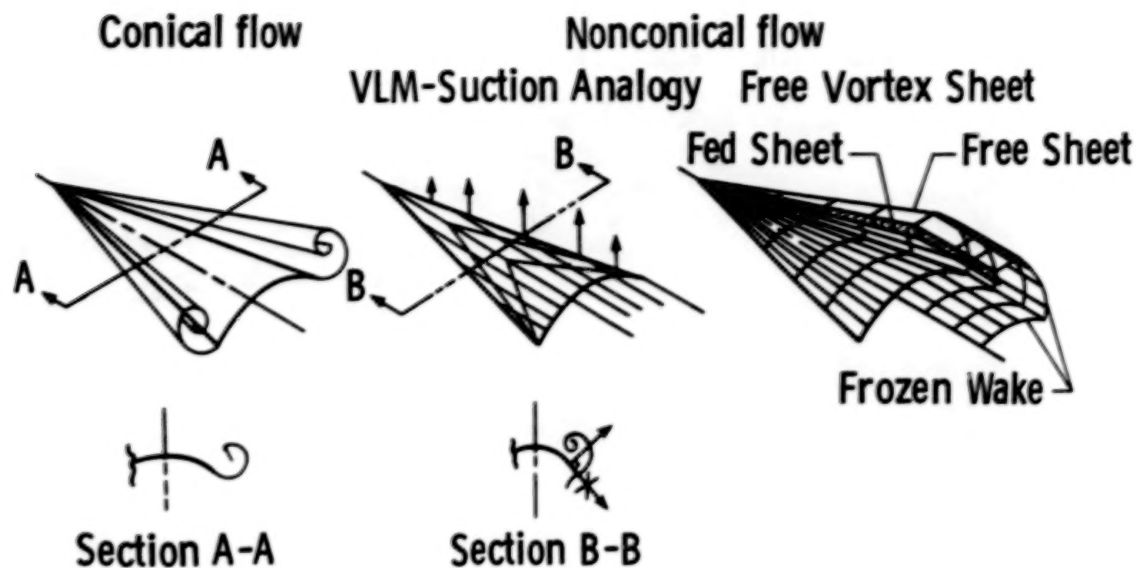


Figure 5.- Status of vortex theories for nonplanar wings in 1978.  
(From ref. 29.)

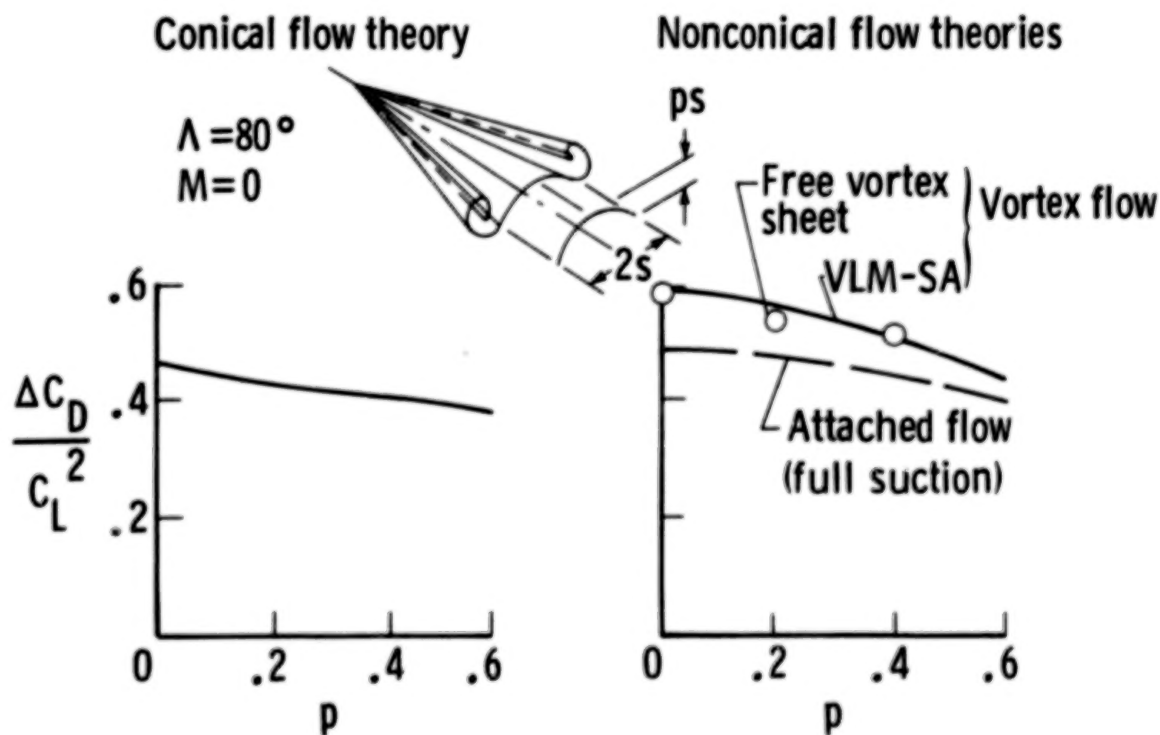
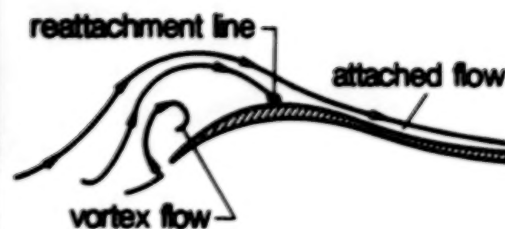


Figure 6.- Theoretical effect of camber height on drag factor.  
(From ref. 23.)

### Pre-Scamp Design



April 1978 (Langley 7x10 HST)

- Vortex design with vortex on dropped LE, reattachment at camber crest; attached flow downstream
- Achieved 77% suction at  $C_L = .5$ ,  $M = .85$

Figure 7.- Transonic maneuver vortex design for the Pre-Scamp configuration. (From ref. 35.)

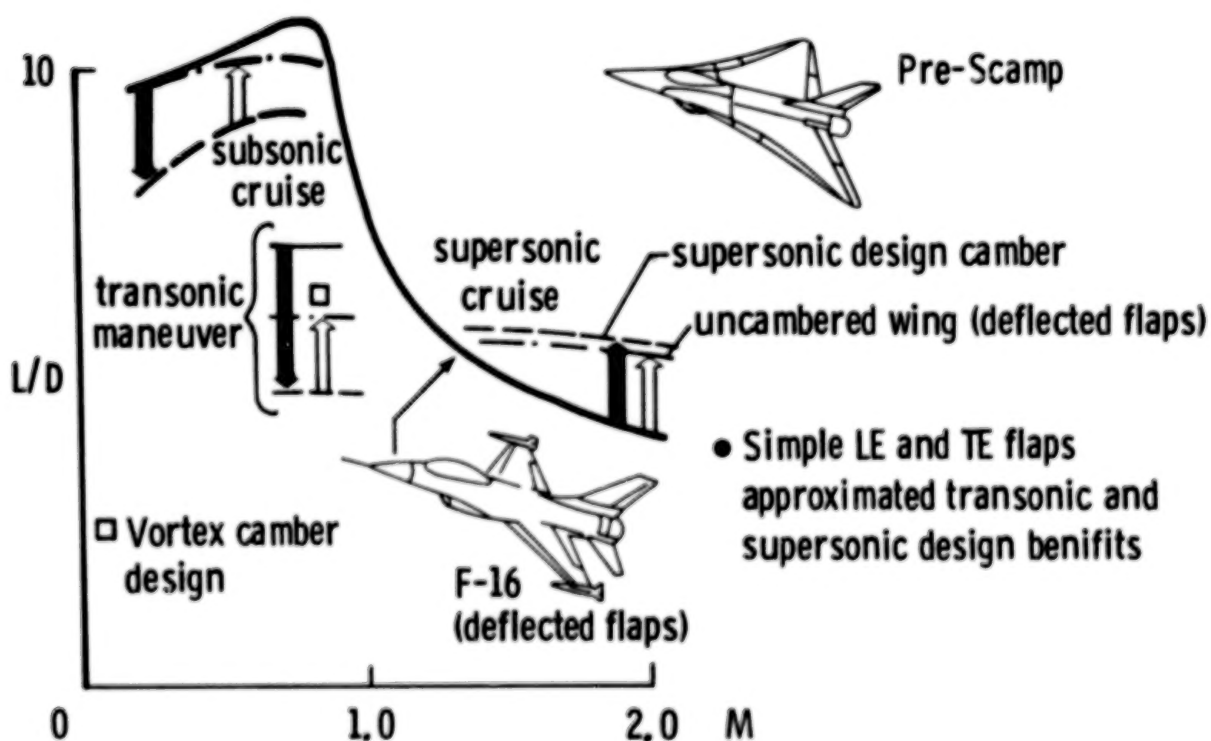


Figure 8.- Effect of sweep and articulated flaps on cruise and maneuver performance. (From ref. 37.)

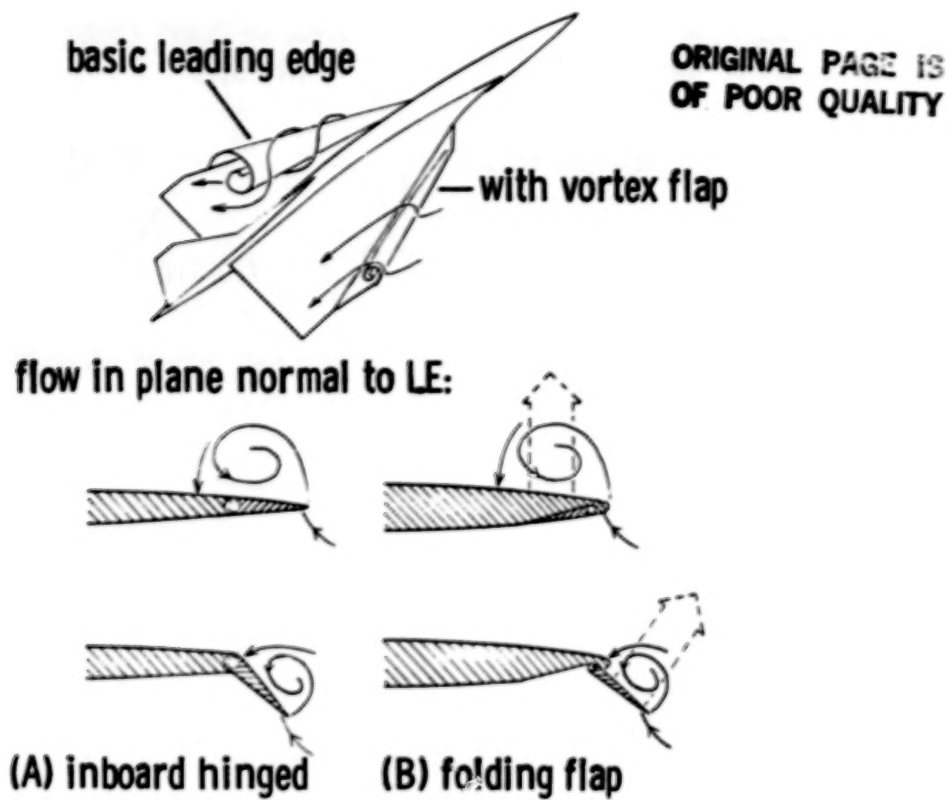


Figure 9.- The vortex flap concept. (From ref. 40.)

Smoke Visualization of Vortex on  
Segmented Flap (REF. 39)

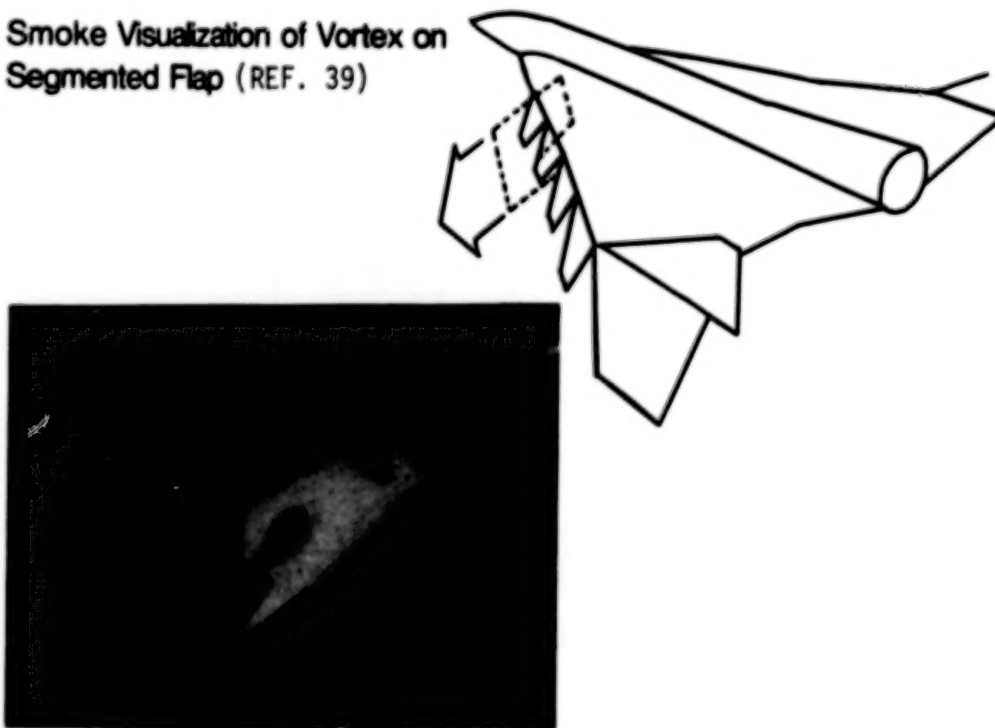


Figure 10.- Studies explore vortex flap hypothesis. (From ref. 39.)



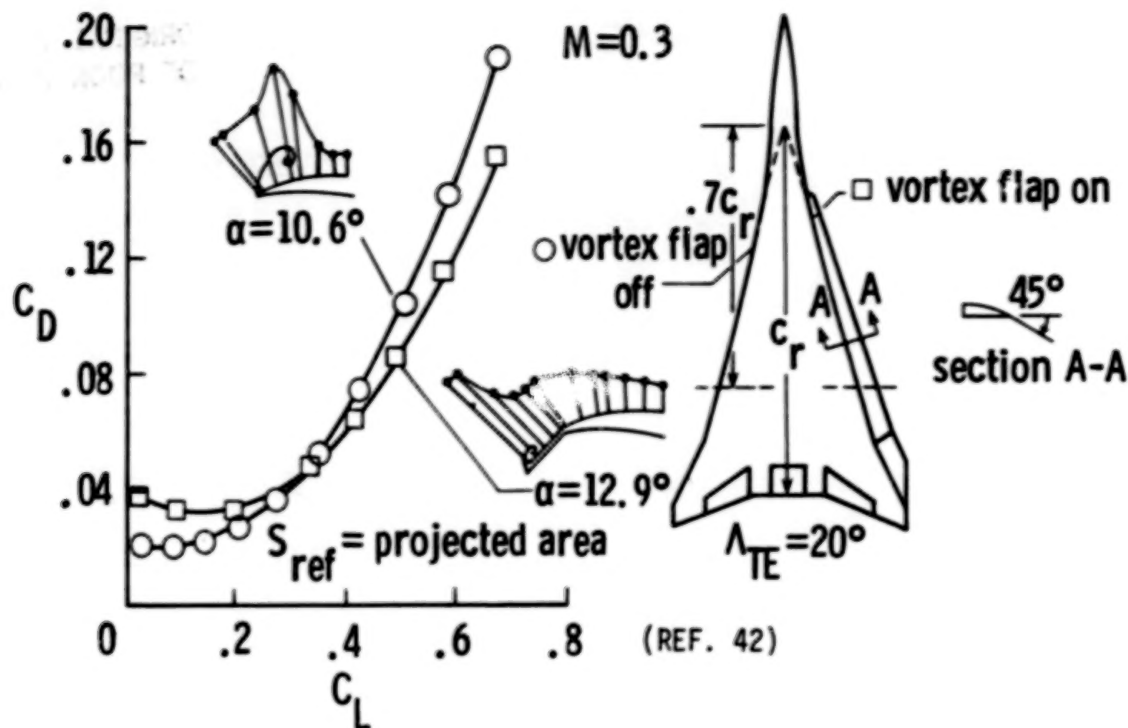


Figure 11.7 Drag polar for vortex flap applied to an NASA/Boeing fighter model. (From ref. 42.)

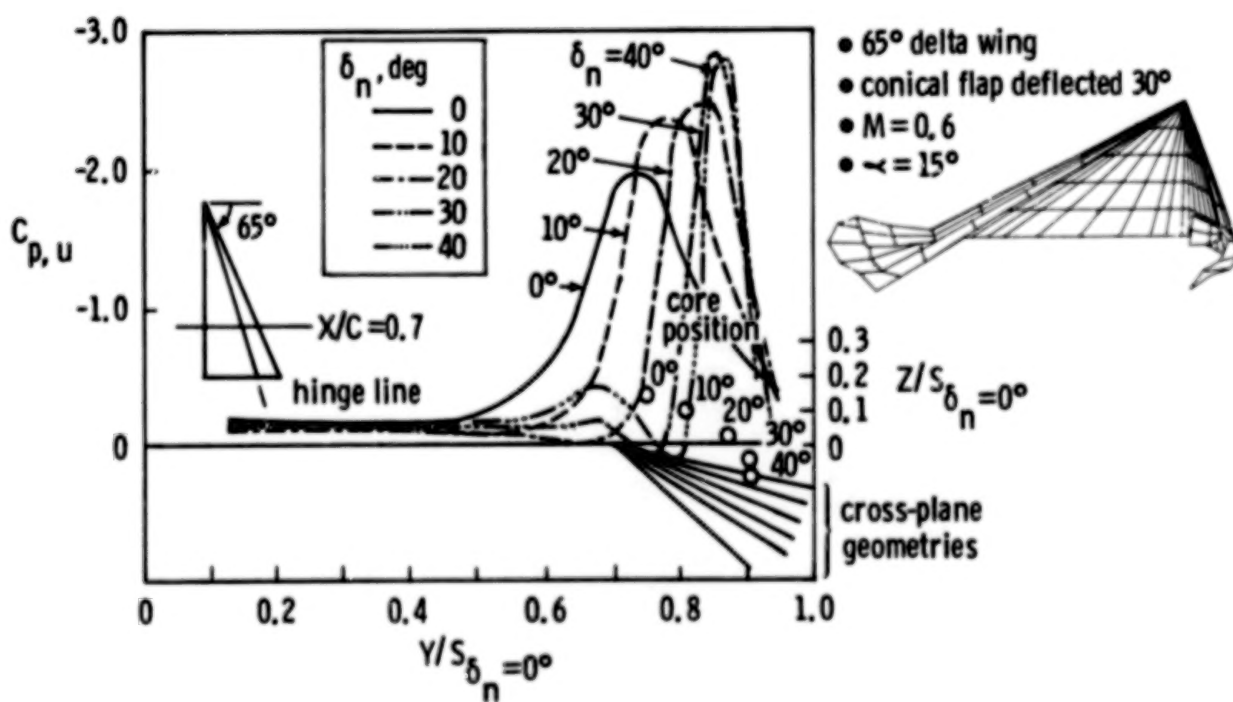


Figure 12.- Free Vortex Sheet analysis study of vortex flap pressure distributions. (From ref. 64.)

Concerns about:

- 1) flap size
- 2) vortex growth

lead to design logic:

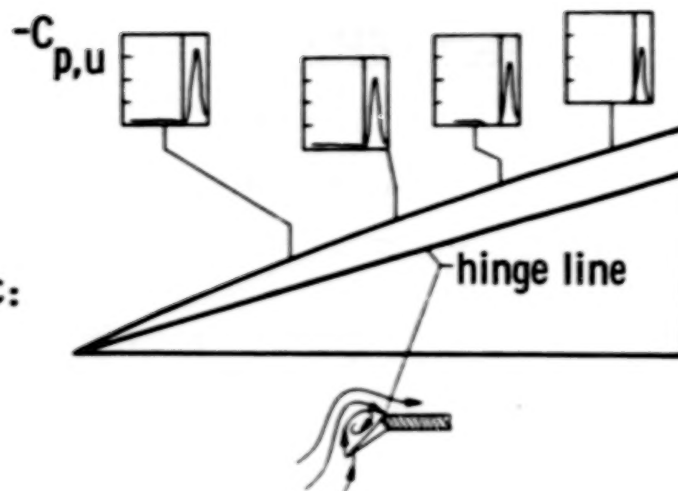


Figure 13.- Vortex flap design procedure. (From ref. 66.)

- Large Subsonic Data base
  - pressures
  - hingemoments
  - performance
  - stability and control
  - flow field diagnostics
- Basic Flap
  - flap planform, hinge line sweep
  - flap deflection
  - flap and wing aero section
- Alternate Flaps

Figure 14.- Status of current vortex flap studies at subsonic speeds. (From ref. 69.)

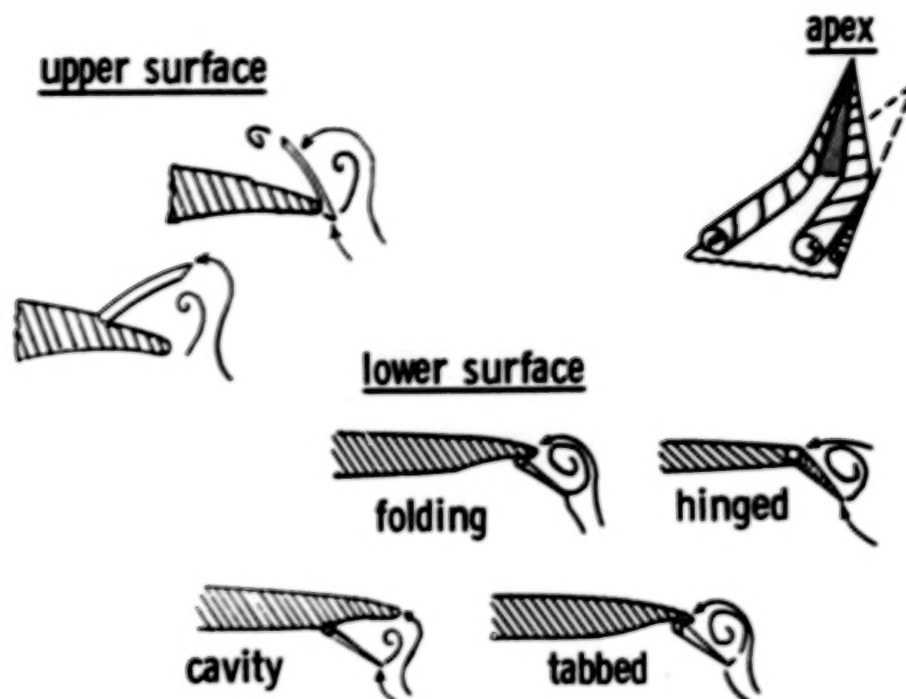


Figure 15.- Types of vortex flaps. (Adapted from ref. 37.)

- Concept is maturing subsonic
  - Experiments in concert with analysis and design theories
  - Applications to generic and aircraft models
  - Flight experiment being considered on F-106

Figure 16.- Summary of subsonic vortex flap studies.

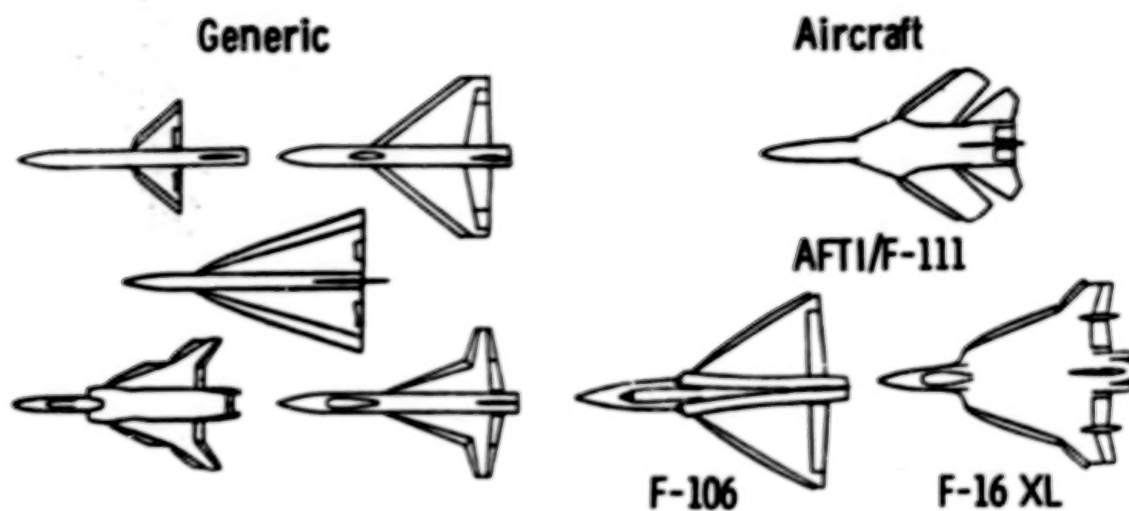


Figure 17.- Current configurations to which vortex flaps have been applied.  
(Updated from ref. 69.)

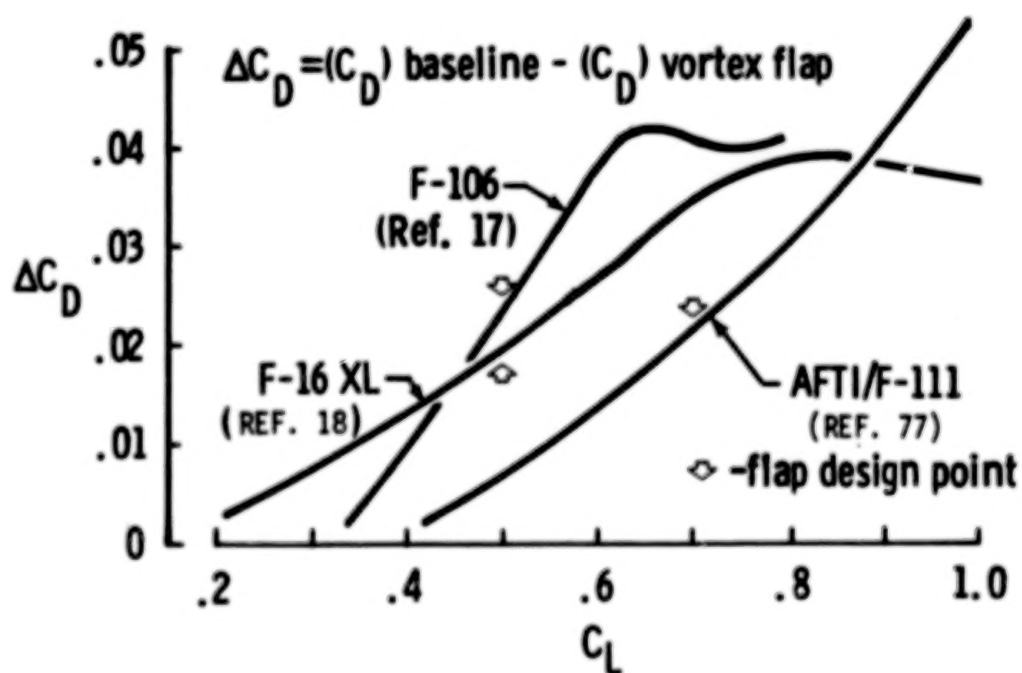


Figure 18.- Effect of vortex flaps on subsonic drag reduction;  $M = 0.6$ . (From ref. 69.)



- Generic studies have started
- Preliminary analysis tools are being validated
- Need additional codes to analyze vortex / shock interactions

Figure 19.- Status of current vortex flap studies at transonic and supersonic speeds.

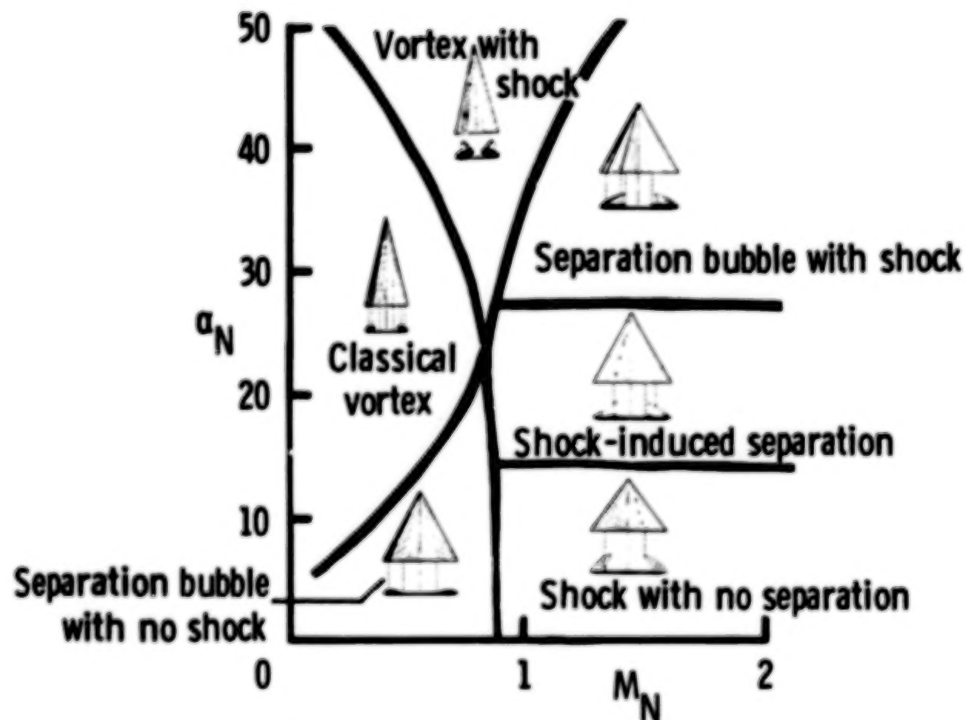
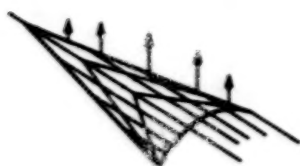


Figure 20.- Leeward flow over planar delta wings at supersonic speeds. (From ref. 81.)

### Suction Analogy



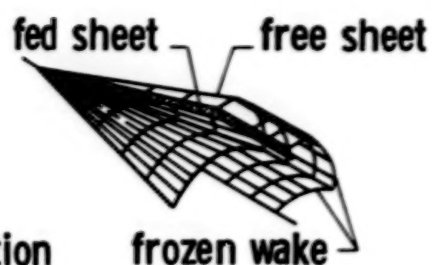
- Extensions of suction analogy principles

- Lan (Ref. 85)

- Use for design

- Lan (Ref. 85)
- Frink (Ref. 78)
- Carlson (Ref. 87)
- Huebner (Ref. 88)

### Free Vortex Sheet



- Expanded Capability

- Luckring (Ref. 89)

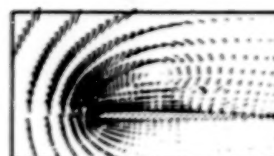
- Applications

- Frink, (Ref. 72)
- Grantz, (Ref. 73)
- Erickson (Ref. 91)

### Euler

$$M = 0.85, \alpha = 15.8^\circ$$

Raj (Ref. 92)

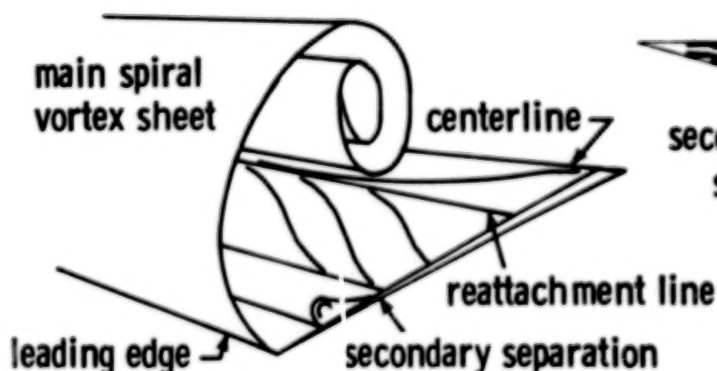


- Code development

- Sirbaugh (Ref. 94)
- Raj (Ref. 95)
- Newsome (Ref. 96)

Figure 21.- Progress in inviscid leading-edge vortex theories.

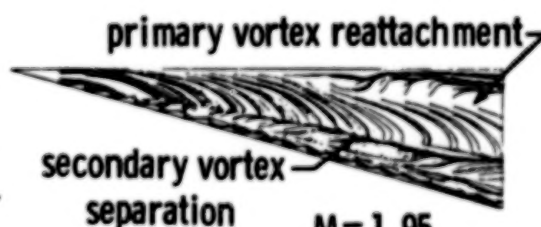
### 3-D Boundary Layer



- Subsonic secondary separation

- Woodson (Ref. 99)
- Blom (Ref. 100)

### Navier Stokes



$$M = 1.95$$

Rizzetta (Ref. 101)

- Supersonic studies

- Newsome (Ref. 96)
- Buter (Ref. 102)
- Blom (Ref. 100)

Figure 22.- Progress in viscous leading-edge vortex theories.

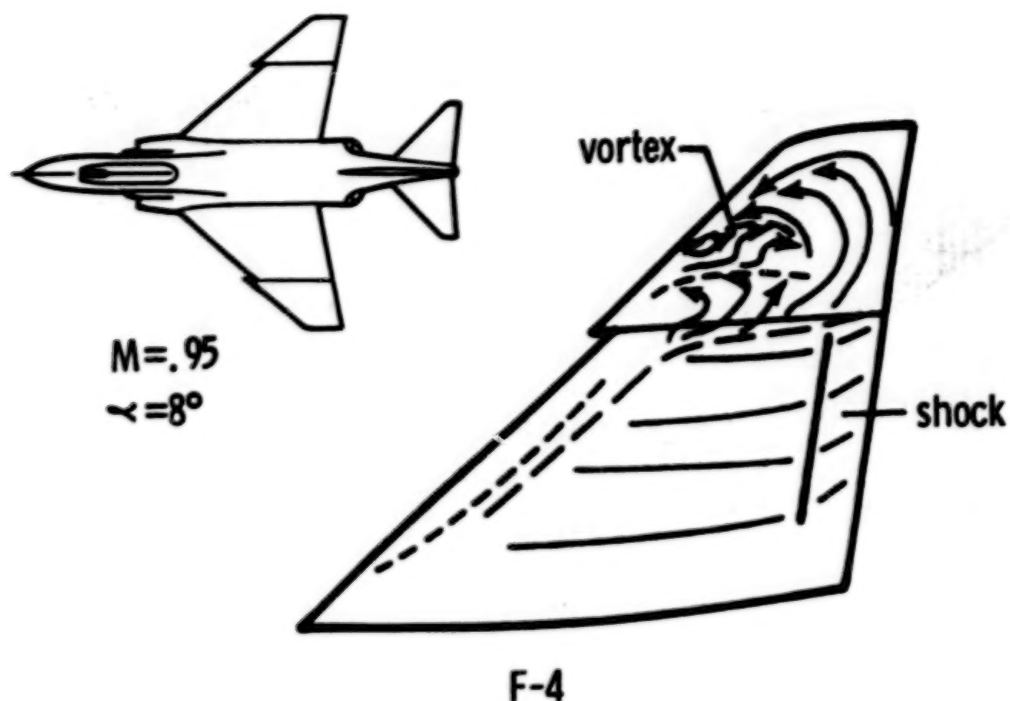


Figure 23.- An opportunity for research of vortex/shock interaction. (From ref. 103.)

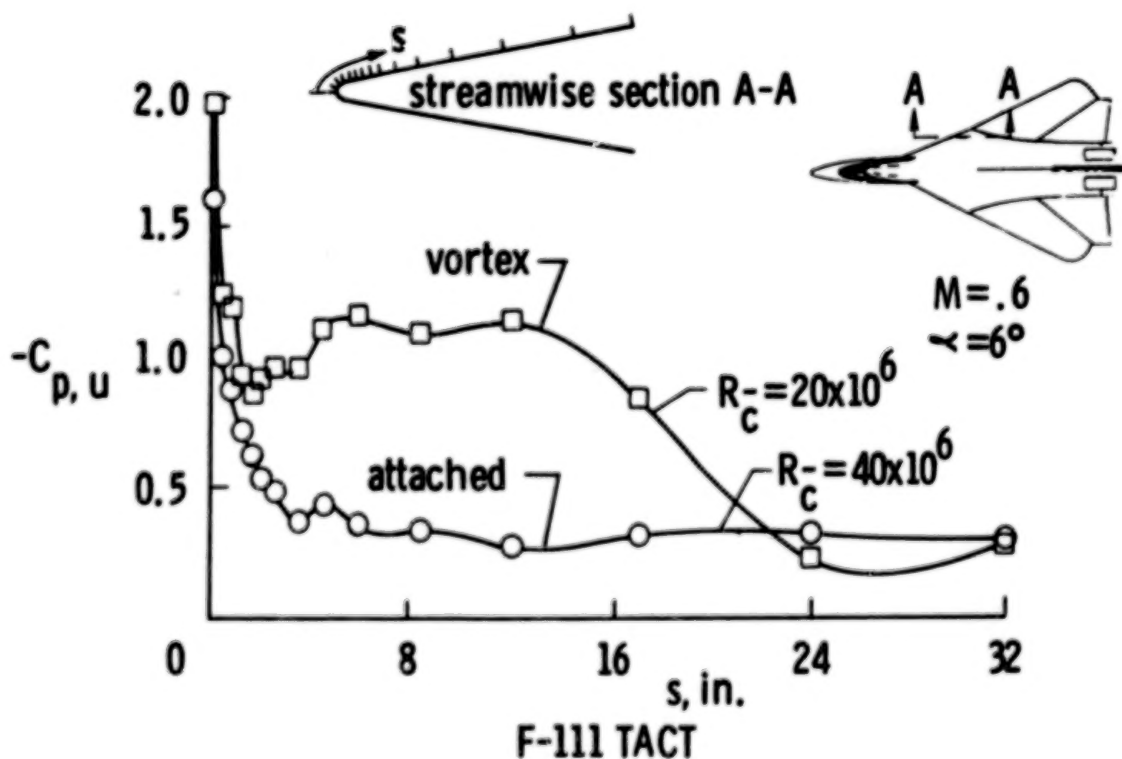
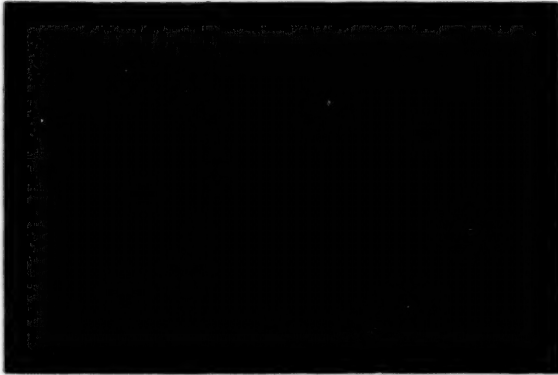


Figure 24.- An opportunity for research of the vortex development on a round leading edge. (From ref. 104.)

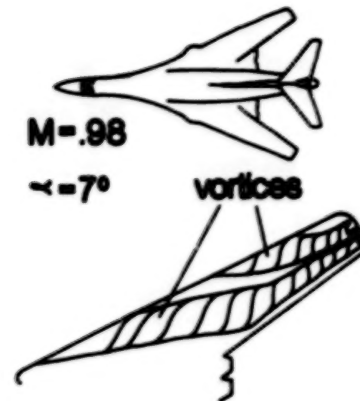
ORIGINAL PAGE IS  
OF POOR QUALITY

### Vortex Burst



F-18

### Multiple Vortex Interactions



B-1

Figure 25.- Opportunities for research of vortex burst (from ref. 106) and multiple vortex interactions (from ref. 105).



## EXTENSIONS OF THE CONCEPT OF SUCTION ANALOGY

## TO PREDICTION OF VORTEX LIFT EFFECT\*

C. Edward Lan  
Department of Aerospace Engineering  
University of Kansas  
Lawrence, Kansas

## SUMMARY

Flow field data for a double delta wing at low speed were used to determine the location of a vortex action point. The result was found to be consistent with what was determined for a delta wing. In supersonic flow, the action point location was determined empirically. For a wing with rounded leading edges, an assumption for initial vortex separation was shown to be equivalent to initial leading-edge bubble separation for airfoils. A theoretical formulation by the section analogy to determine the delayed vortex separation on a cambered wing with rounded leading edges was presented. The method of suction analogy was further shown to be applicable to predicting the body vortex lift.

## INTRODUCTION

Since Polhamus introduced the method of suction analogy for plane delta wings with sharp edges in subsonic and supersonic flows (refs. 1 and 2), various extensions of the method have been proposed and used successfully. For wings with nonzero tip chord, Lamar introduced the effect of side-edge vortex lift (ref. 3). When a vortex generated at the leading edge passes over some downstream planform area, additional lift is induced because of the vortex suction effect. This additional lift was incorporated into the method of suction analogy by Lamar as the augmented vortex lift (ref. 4). The latter may be positive as is the case for a cropped delta wing and a strake-wing configuration. Augmented vortex lift is negative for an arrow wing because of the lack of downstream area to receive the vortex action or to allow the reattachment of the vortex flow. For a noncambered wing, the vortex force was assumed to be acting at the leading edge and normal to the planform. However, for a positive-cambered wing, this assumption would produce too much thrust as compared with data. To allow for the determination of where the vortex force is acting, the concept of vortex action point was introduced (ref. 5). If the leading edge is rounded, the generation of vortex lift will be delayed. Kulfan presented a method to account for this effect for plane wings (refs. 6 and 7). Another method for the effect of rounded leading edges was developed by Carlson by using available experimental data (ref. 8).

The method of suction analogy has also been employed to calculate the roll damping of slender wings (ref. 9). The extension of it to calculating all lateral-directional characteristics of slender wings was made in reference 10. In reference 10, the effect of vortex breakdown was also incorporated by using a

---

\*This work was supported by NASA Grant NSG 1629.

numerical scheme to extend the available data for delta wings. Finally, an unsteady lifting-surface theory was used in developing the method of unsteady suction analogy (ref. 11). The latter can be used for predicting dynamic stability derivatives of slender wings.

In this paper, the concept of vortex action point is reconsidered for subsonic and supersonic flows. In addition, Kulfan's concept for plane wings with rounded leading edges is correlated with viscous flow calculations for airfoils. The extension of the method for cambered wings is described next. Finally, it is shown that the method of suction analogy can be applied to predict the vortex lift of slender bodies.

#### SYMBOLS

|            |  |
|------------|--|
| $c$        | local chord  |
| $C$        | sectional leading-edge singularity parameter = $\lim_{x \rightarrow x_{le}} \gamma(x)(x - x_{le})^{1/2}$ |
| $C_D$      | drag coefficient   |
| $C_{d_w}$  | sectional wave drag coefficient  |
| $C_l$      | sectional lift coefficient   |
| $C_L$      | lift coefficient   |
| $C_m$      | pitching moment coefficient  |
| $C_N$      | body normal force coefficient based on maximum cross-sectional area                                      |
| $C_{n,v}$  | sectional normal force coefficient due to body vortex lift   |
| $C_{N,vA}$ | total augmented vortex normal force coefficient on a body  |
| $C_p$      | pressure coefficient   |
| $c_s$      | sectional leading-edge suction coefficient   |
| $C_{sf}$   | sectional side-force coefficient of a body   |
| $C_{sf,N}$ | total suction force coefficient produced by a body nose section  |
| $c_t$      | sectional leading-edge thrust coefficient  |
| $f$        | ratio of vortex-induced vertical velocity to the free stream (eq. (2))                                   |
| $h$        | vortex action point location on a body defined in eqs. (15) and (16)                                     |
| $l_N$      | body nose length   |
| $M$        | Mach number  |

|            |   |
|------------|---|
| $r$        | vortex action point location measured from the leading edge (eq. (4)), or body radius |
| $r_o$      | leading-edge radius   |
| $V$        | velocity  |
| $x_s$      | body axial station at which the vortex separation starts                              |
| $\alpha$   | angle of attack   |
| $\alpha_1$ | sectional angle of zero lift  |
| $\alpha_s$ | angle of attack of initial vortex separation  |
| $\beta$    | sideslip angle or wave angle  |
| $\beta_s$  | oblique shock angle   |
| $\gamma$   | ratio of specific heats or bounded vortex density                                     |
| $\Lambda$  | sweep angle   |
| $\rho$     | density   |
| $\theta$   | angular coordinate of a body (fig. 8)   |
| $\theta_A$ | angular location of the augmented vortex action point on a body (eq. 21)              |
| $\theta_c$ | angular location of the body vortex action point (eq. (15) and fig. 10)               |

Subscripts:

|          |               |
|----------|---------------|
| $l$      | lower surface |
| $l_e$    | leading edge  |
| $u$      | upper surface |
| $\infty$ | free stream   |

### CONCEPT OF VORTEX ACTION POINT

In developing the concept of vortex action point, flow field data in cross-flow planes are needed, see figure 1(a). It is assumed that the velocity distribution around the vortex in the longitudinal plane parallel to the free stream is the same as that in the cross-flow plane (fig. 1(b)). If a control surface ( $\sigma$ ) is taken through the vortex center as shown in figure 1(c), the vortex force should be equal to the vertical component of the force due to the momentum transfer through the control surface  $\sigma$ . Since the vortex force acting on the wing is equal to  $c_{q,c}$  by the suction analogy, it follows that the force acting on the

control volume is

$$\begin{aligned}
 -c_s c \frac{1}{2} \rho V_\infty^2 &= \int_{\sigma} \rho \vec{V} \cdot d\vec{\tau} \\
 &= \int (\rho V_{z_{in}} - \rho V_{z_{out}}) \vec{V} \cdot d\vec{\tau}
 \end{aligned} \tag{1}$$

To find an average  $\vec{V}$ , let

$$|\vec{V}| = V_z = f V_\infty \tag{2}$$

where  $f$  is a constant. It follows that for a unit span,

$$\begin{aligned}
 \int (\rho V_{z_{in}} - \rho V_{z_{out}}) \vec{V} \cdot d\vec{\tau} &= -f V_\infty \left[ \int \rho V_{z_{in}} dr + \int \rho V_{z_{out}} dr \right] \\
 &= -f V_\infty 2\rho (f V_\infty) r
 \end{aligned} \tag{3}$$

where the integrals have been replaced with the average values. From equations (1) and (3), it is found that

$$r = \frac{1}{4f^2} c_s c \tag{4}$$

In reference 5,  $f$  was taken to be 0.5 so that  $r = c_s c$ . To show that this choice of  $f$  is reasonable in subsonic flow, the flow field data in reference 12 for a double delta wing at station (1) are rearranged in figure 2. By numerically integrating the velocity distribution to evaluate the integrals in equation (3), an average velocity with  $f = 0.53$  can be found. At station (2), the two leading-edge vortices have started to merge, so that the flow field data are not appropriate for the present purpose.

In supersonic flow, Squire et al. demonstrated by a vapor screen method that the vortex region became much flatter than that in subsonic flow (ref. 13), as shown in figure 3. Unfortunately, flow field velocity data are not available in reference 13 and, in fact, have not been found so far for other wing planforms. Therefore, an empirical method to determine an appropriate  $f$  value was used. By assuming different values for  $1/4f^2$  and comparing the calculated  $C_L$  and  $C_D$  values with data for different planforms with leading-edge flaps, it was found that a value of 8.0 for  $1/4f^2$  produced the best results. In other words,  $f = 1/4\sqrt{2}$ . Therefore, unless additional data prove otherwise, the following relation for the vortex action point will be used in supersonic flow:

$$r = 8(c_s c) \tag{5}$$



Some calculated results are compared with data in figures 4 and 5 (refs. 14 and 15). It is seen that the theory predicts the results quite well. Note that the effect of rounded leading edges accounted for in figures 4 and 5 will be discussed in the next section. The wave drag correction in figures 4 and 5 is to add the nonlinear effect to the predicted linear values based on the predicted sectional lift coefficients and the exact two-dimensional theory for a flat plate in supersonic flow. The wave drag correction is described in the Appendix.

#### VORTEX LIFT ON CAMBERED WINGS WITH ROUNDED LEADING EDGES

Kulfan assumes that on a slender wing the leading-edge vortex separation starts at an angle of attack at which the leading-edge drag equals the leading-edge thrust (refs. 6 and 7). To examine this assumption, experimental pressure data (ref. 16) and theoretical results from the Lockheed-Georgia airfoil code (ref. 17) were used. The airfoil negative pressure coefficient is integrated to give the leading-edge suction ( $c_{s_{le}}$ ), and the positive pressure coefficient is integrated to produce the leading-edge drag ( $c_{d_{le}}$ ). The integration is over the forward portion of the airfoil from the maximum thickness location if no separation bubble occurs. Otherwise, the integration is performed only over the region forward of the separation bubble. The results indicate that at the angle of attack ( $\alpha_s$ ) at which the separation bubble first occurs, the leading-edge thrust is about equal to the leading-edge drag (ref. 18). For symmetrical airfoils, this is illustrated in figure 6. For cambered airfoils, some calculated results are presented in figure 7. As shown, the leading-edge suction at  $\alpha_s$  tends to be greater than the leading-edge drag. This is due to the pressure thrust generated on the forward camber. To remove this camber thrust in performing the pressure integration, the slope of the upper airfoil surface is reduced by the local camber slope and that of the lower surface is increased by it. The results indicated in figure 7 by rectangular symbols (□) show that Kulfan's concept is still applicable for cambered airfoils if the camber thrust is removed from the calculated suction. In the thin airfoil or wing theory, this is always true because the calculated leading-edge thrust is concentrated at the leading edge and does not contain the camber thrust.

Having established that Kulfan's concept on the starting of a leading-edge vortex separation is related to the occurrence of leading-edge laminar separation, the next question is how this concept can be used in calculating the vortex lift on a cambered wing with rounded leading edges. The first task is to determine  $\alpha_s$ . For a cambered wing, the sectional leading-edge suction coefficient can be written as

$$c_s = K(\sin \alpha + \alpha_1)^2 \quad (6)$$

where  $K$  is a function of geometry and Mach number, and  $\alpha_1$  is the sectional angle of zero lift. In practice,  $\alpha_1$  can be found as follows. Let  $c_s'$  be the sectional leading-edge suction coefficient for the same wing without camber. Then

$$c_s' = K \sin^2 \alpha \quad (7)$$

From equations (6) and (7),  $\alpha_1$  can be found to be

$$\alpha_1 = [(c_s/c_s')^{1/2} - 1] \sin \alpha \quad (8)$$

For a wing, the sectional leading-edge thrust coefficient (ref. 19) can be shown to be

$$c_t = (\pi/2) C^2 (1 - M_\infty^2 \cos^2 \lambda_{le})^{1/2} / \cos \lambda_{le} \quad (9)$$

where  $C$  is the leading-edge singularity parameter and can be written as

$$C = K'(\sin \alpha + \alpha_1) \quad (10)$$

similar to equation (6). If  $C_1$  is  $C$  at  $\alpha_s$ , then

$$C_1 = C(\sin \alpha_s + \alpha_1) / (\sin \alpha + \alpha_1) \quad (11)$$

The expression for the leading-edge drag can be found in reference 20. By equating the leading-edge drag to the leading-edge thrust at  $\alpha_s$ , it is obtained that

$$\pi \frac{r_0}{c} \frac{\cos \lambda_{le}}{(1 - M_\infty^2 \cos^2 \lambda_{le})^{1/2}} = \frac{\pi}{2} C^2 \frac{(\sin \alpha_s + \alpha_1)^2}{(\sin \alpha + \alpha_1)^2} (1 - M_\infty^2 \cos^2 \lambda_{le})^{1/2} / \cos \lambda_{le}$$

from which  $\alpha_s$  can be obtained:

$$\alpha_s = \sin^{-1} \left( \pm \frac{\sin \alpha + \alpha_1}{C} \left( 2 \frac{r_0}{c} \right)^{1/2} \cos \lambda_{le} / (1 - M_\infty^2 \cos^2 \lambda_{le})^{1/2} - \alpha_1 \right) \quad (12)$$

where  $r_0$  is the leading-edge radius.

With  $\alpha_s$  calculated, the remaining sectional thrust coefficient at  $\alpha > \alpha_s$  is then given by equation (9) with  $C$  replaced by  $C_2$ , where

$$C_2 = C[\sin(\alpha - \alpha_s) + \alpha_1] / (\sin \alpha + \alpha_1) \quad (13)$$

Note that  $c_t$  must be converted to the sectional suction coefficient ( $c_s$ ) before the latter is assumed to become the vortex lift through the method of suction analogy. The relation between  $c_t$  and  $c_s$  for a cambered wing was derived in reference 5.

The above consideration has been applied to wings in both subsonic and supersonic flows with good success. In the supersonic flow, the wing must have a subsonic leading edge to produce the vortex lift. Some correlation with data was shown earlier in figures 4 and 5.

#### BODY VORTEX LIFT

If the aspect ratio of a slender thick wing is reduced, eventually it becomes a slender body. If the method of suction analogy is applicable to the former, it should also be applicable to the latter. Based on this understanding, the following method for calculating body vortex lift was developed. The method is based on the following assumptions and procedures.

- (a) The attached-flow solution is obtained with the axial distribution of G. N. Ward's vortex multiplets (ref. 21). The boundary condition is satisfied on the body surface.
- (b) At any axial station, vortex separation starts at a circumferential location where  $C_p$  is minimum and negative. This assumption has been shown to be reasonable (ref. 22). At low angles of attack,  $C_p$  may be positive everywhere near the nose. In this case, no vortex separation is assumed to occur. In reference 22, the axial station ( $x_s$ ) at which the vortex separation starts must be assumed or given by experimental data. Examples of calculated pressure distribution with and without vortex separation are illustrated in figure 8.
- (c) At any axial station, the side-force component of the negative  $C_p$  in the region assumed to have vortex separation is integrated to produce a sectional side-force coefficient (see fig. 9).

$$c_{sf} = \frac{1}{r(x)} \int_{\theta_{\min p}}^{\theta} r(x) C_p \sin \theta d\theta \quad (14)$$

The side force obtained is assumed to be the suction force produced by the separated vortex. This suction force is assumed to be acting at  $\theta_c$  (fig. 10) where

$$\theta_c = \theta_{\min p} - \Delta\theta \quad (15)$$

$$\Delta\theta = h c_{sf} \quad (16)$$

Equations (15)-(16) imply that the vortex action point is located at a distance from  $\theta_{\min p}$  being proportional to the suction force:

$$\Delta s = r \Delta \theta = h r c_{sf} \quad (17)$$

Based on equation (4),  $h$  should be

$$h = 1/4f^2 \quad (18)$$

To determine an appropriate value for  $f$ , data in reference 23 as presented in figure 11 are used. Applying the same method as used in figure 2,  $f$  is determined to be 0.70. For simplicity,  $f$  will be taken to be  $1/(2)^{1/2}$  in subsonic flow. In supersonic flow, no data were available for correlation so that an empirical value will be used. In summary, the following values for  $h$  will be used in the present method:

$$\begin{aligned} h &= 0.5 & , M_\infty < 1.0 \\ &= 3.0 & , M_\infty > 1.0 \end{aligned} \quad (19)$$

With  $\theta_c$  calculated from equation (15), the sectional normal force coefficient due to the vortex suction is given by

$$c_{n,v} = c_{sf} \cos \theta_c \quad (20)$$

- (d) Similar to a wing, the augmented body vortex lift exists whenever the planview of a body is not of the delta type. The concept used in calculating the augmented vortex lift for a wing (ref. 4) is also applicable for a body. Thus, if  $C_{sf,N}$  is the total suction force coefficient from the nose portion, then the augmented normal force coefficient ( $C_{N,vA}$ ) is given by

$$C_{N,vA} = \tilde{c} C_{sf,N} \cos \theta_A / l_N \quad (21)$$

where  $\tilde{c}$  is the length over which the nose vortex passes and  $l_N$  is the nose length. The term  $\theta_A$  is the location of augmented vortex action point and is assumed to be equal to  $\theta_c$  at the body shoulder.

Calculated results for an ogive cylinder at  $M_\infty = 0.3$  are compared with data in figure 12. The effect of Reynolds number is seen to increase the loading. In references 22 (ref. 24), different axial locations of



initial separation were assumed for different Reynolds numbers. The present results are seen to agree well with the data of higher Reynolds number. This is expected because an inviscid theory, such as the present one, is to simulate the flow field of infinite Reynolds number.

In figure 13 (ref. 25), results for a circular-arc-cylinder body at  $M_\infty = 1.6$  are presented. It is seen that the calculated results agree well with data up to  $\alpha = 32$  deg. Above  $\alpha = 32$  deg at  $M_\infty = 1.6$  or  $\alpha > 15$  deg at  $M_\infty = 2.3$  (not shown), the normal force is always underpredicted. This is probably because at high  $M_\infty$  and/or high angles of attack, the present linear theory cannot predict accurately the upper surface expansion and strong shock effect on the lower surface.

#### CONCLUDING REMARKS

The method of suction analogy, originally developed for a plane wing, was shown to be applicable to cambered wings by using the concept of vortex action point. For a wing with rounded leading edges, the method is still applicable if the delay in initial vortex separation is accounted for. The latter can be calculated by Kulfan's method. Kulfan's method was shown to be related to the leading-edge laminar separation. Extension of the suction analogy to predicting the body vortex lift has also been presented.

#### REFERENCES

1. Polhamus, E. C.: A Concept of the Vortex Lift of Sharp-Edge Delta Wings Based on a Leading-Edge-Suction Analogy. NASA TN D-3767, December 1966.
2. Polhamus, E. C.: Predictions of Vortex-Lift Characteristics by a Leading-Edge Suction Analogy. Journal of Aircraft, Vol. 8, April 1971, pp. 193-199.
3. Lamar, J. E.: Extension of Leading-Edge-Suction Analogy to Wings With Separated Flow Around the Side Edges at Subsonic Speeds. NASA TR R-428, October 1974.
4. Lamar, J. E.: Recent Studies of Subsonic Vortex Lift Including Parameters Affecting Stable Leading-Edge Vortex Flow. Journal of Aircraft, Vol. 24, December 1977, pp. 1205-1211.
5. Lan, C. E., and Chang, J. F.: Calculation of Vortex Lift for Cambered Wings by the Suction Analogy. NASA CR-3449, July 1981.
6. Kulfan, R. M.: Wing Airfoil Shape Effects on the Development of Leading-Edge Vortices. AIAA Paper No. 79-1675, 1979.
7. Kulfan, R. M.: Wing Geometry Effects on Leading Edge Vortices. AIAA Paper No. 79-1872, 1979.

8. Carlson, H. W., and Mack, R. J.: Studies of Leading-Edge Thrust Phenomena. *Journal of Aircraft*, Vol. 17, December 1980, pp. 890-897.
9. Boyden, R. P.: Effects of Leading-Edge Vortex Flow on the Roll Damping of Slender Wings. *Journal of Aircraft*, Vol. 8, July 1971, pp. 543-547.
10. Lan, C. E., and Hsu, C. H.: Effects of Vortex Breakdown on Longitudinal and Lateral-Directional Aerodynamics of Slender Wings by the Suction Analogy. AIAA Paper No. 82-1385, 1982.
11. Lan, C. E.: The Unsteady Suction Analogy and Applications. *AIAA Journal*, Vol. 20, December 1982, pp. 1647-1656.
12. Brennenstuhl, U., and Hummel, D.: Vortex Formation Over Double-Delta Wings. ICAS Paper No. 82-6.6.3, 1982.
13. Squire, L. C.; Jones, J. G.; and Stanbrook, A.: An Experimental Investigation of the Characteristics of Some Plane and Cambered 65° Delta Wings at Mach Numbers from 0.7 to 2.0. British ARC R&M No. 3305, July 1961.
14. Igglesden, M. S.: Wind Tunnel Measurements of the Lift-Dependent Drag of Thin Conically Cambered Slender Delta Wings at Mach Numbers 1.4 and 1.8. Royal Aircraft Establishment of Great Britain, Technical Note No. Aero. 2677, April 1960.
15. Menees, G. P.: Lift, Drag, and Pitching Moment of an Aspect-Ratio-2 Triangular Wing with Leading-Edge Flaps Designed to Simulate Conical Camber. NASA Memo 10-5-58A, December 1958.
16. McCullough, G. B., and Gault, D. E.: Examples of Three Representative Types of Airfoil-Section Stall at Low Speed. NACA TN 2502, September 1951.
17. Stevens, W. A.; Goradia, S. H.; and Braden, J. A.: Mathematical Model for Two-Dimensional Multi-Component Airfoils in Viscous Flow. NASA CR-1843, July 1971.
18. Su, I., and Lan, C. E.: Effect of Round Airfoil Nose on Leading-Edge Suction in Viscous Flow. Technical Report CRINC-FRL-426-3, The University of Kansas Center for Research, Inc., September 1984.
19. Lan, C. E.: A Quasi-Vortex-Lattice Method in Thin Wing Theory. *Journal of Aircraft*, Vol. 11, September 1974, pp. 518-527.
20. Robinson, A., and Laurmann, J. A.: *Wing Theory*. Cambridge University Press, 1956.
21. Ward, G. N.: *Linearized Theory of Steady High-Speed Flow*. Cambridge University Press, 1955.
22. Almosnino, D., and Rom, J.: Calculation of Symmetric Vortex Separation Affecting Subsonic Bodies at High Incidence. *AIAA Journal*, Vol. 21, March 1983, pp. 398-406.

23. Yanta, W. J.; Wardlaw, A. G., Jr.; and Sternklar, D.: Vortex Asymmetry Development on a Tangent Ogive. NSWC TR-82-394, Naval Surface Weapons Center, Silver Springs, Md., October 1982.
24. Tinling, B. E., and Allen, C. Q.: An Investigation of the Normal Force and Vortex Wake Characteristics of an Ogive-Cylinder Body at Subsonic Speeds. NASA TN D-1297, 1962.
25. Landrum, E. J., and Babb, C. D.: Wind-Tunnel Force and Flow-Visualization Data at Mach Numbers from 1.6 to 4.63 for a Series of Bodies of Revolution at Angles of Attack from  $-4^\circ$  to  $60^\circ$ . NASA TM 78813, March 1979.
26. Lighthill, M. J.: Higher Approximations in General Theory of High Speed Aerodynamics. Ed. by W. R. Sears, Princeton University Press, 1954.
27. Liepmann, H. W., and Roshko, A.: Elements of Gasdynamics. John Wiley & Sons, N.Y., 1957.

# APPENDIX

## CORRECTION FOR NONLINEAR WAVE DRAG

The correction for nonlinear wave drag is based on the difference in predicted results for a two-dimensional flat plate by the linear and exact theories. The linear theory shows that the drag coefficient is given by

$$c_{d_w} = 4\cos\alpha \sin^2\alpha / (M_\infty^2 - 1)^{1/2} \quad (A.1)$$

where the  $\alpha$ -terms are not linearized, so that the linearization is with respect to the compressibility effect only. For a three-dimensional wing,  $\alpha$  in equation (A.1) is the one associated with the predicted sectional lift coefficient ( $c_l$ ) as follows:

$$\alpha = \sin^{-1} [c_l (M_\infty^2 - 1)^{1/2}] / 4 \quad (A.2)$$

The exact theory for a flat plate in supersonic flow shows that the upper surface pressure is given by the Prandtl-Meyer solution (ref. 26, p. 383):

$$C_{P_u} = \frac{2}{\gamma M_\infty^2} \left[ \left( \frac{\sin^2 \beta}{\gamma - \cos 2\beta} \right)^{\gamma/(\gamma-1)} / \left( \frac{\sin^2 \beta_\infty}{\gamma - \cos 2\beta_\infty} \right)^{\gamma/(\gamma-1)} - 1 \right] \quad (A.3)$$

where  $\beta_\infty = \sin^{-1}(1/M_\infty)$  and  $\beta$  is found from

$$-\alpha + \beta - \left( \frac{\gamma+1}{\gamma-1} \right)^{1/2} \tan^{-1} \left[ \left( \frac{\gamma+1}{\gamma-1} \right)^{1/2} \tan \beta \right] = \beta_\infty - \left( \frac{\gamma+1}{\gamma-1} \right)^{1/2} \tan^{-1} \left[ \left( \frac{\gamma+1}{\gamma-1} \right)^{1/2} \tan \beta_\infty \right] \quad (A.4)$$

The lower surface pressure is given by the oblique shock solution (ref. 27, p. 86-88):

$$C_{P_l} = 2\sin\beta_s \sin\alpha / \cos(\beta_s - \alpha) \quad (A.5)$$

where  $\beta_s$  is obtained from

$$\tan\alpha = \cot\beta_s \frac{2M_\infty^2 \sin^2 \beta_s - 2}{(\gamma+1)M_\infty^2 - 2M_\infty^2 \sin^2 \beta_s + 2} \quad (A.6)$$

From equations (A.3) and (A.5), the pressure differential and the wave drag become



$$\Delta C_P = C_{P_l} - C_{P_u} \quad (A.7)$$

$$c_{d_w} = \Delta C_P \sin \alpha \quad (A.8)$$

The difference between the values given by equations (A.8) and (A.1) represents the correction to be added to the predicted sectional drag coefficient by the linear lifting surface theory.

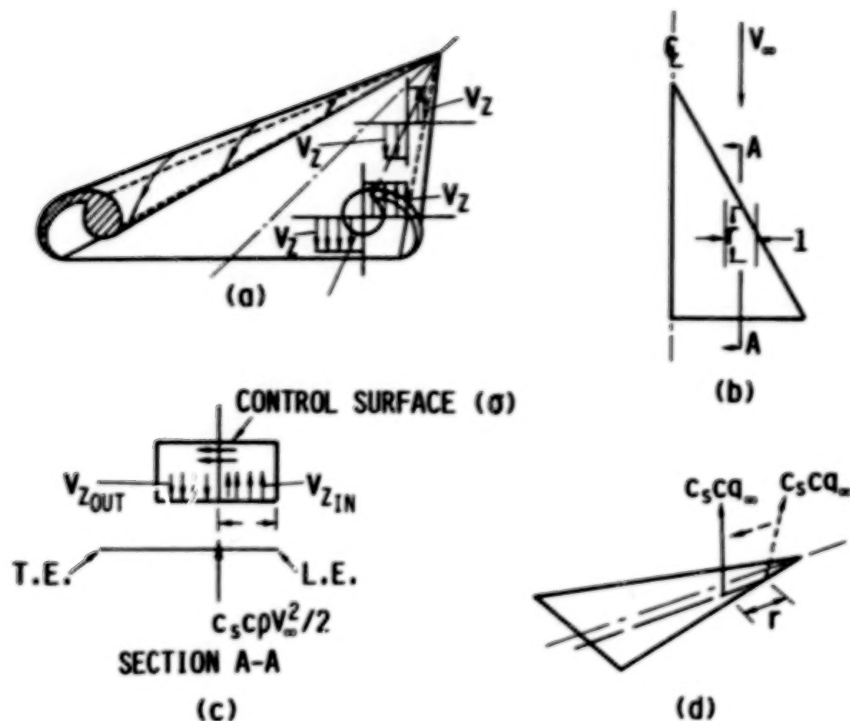


Figure 1. Geometry and flow field for defining vortex action point.

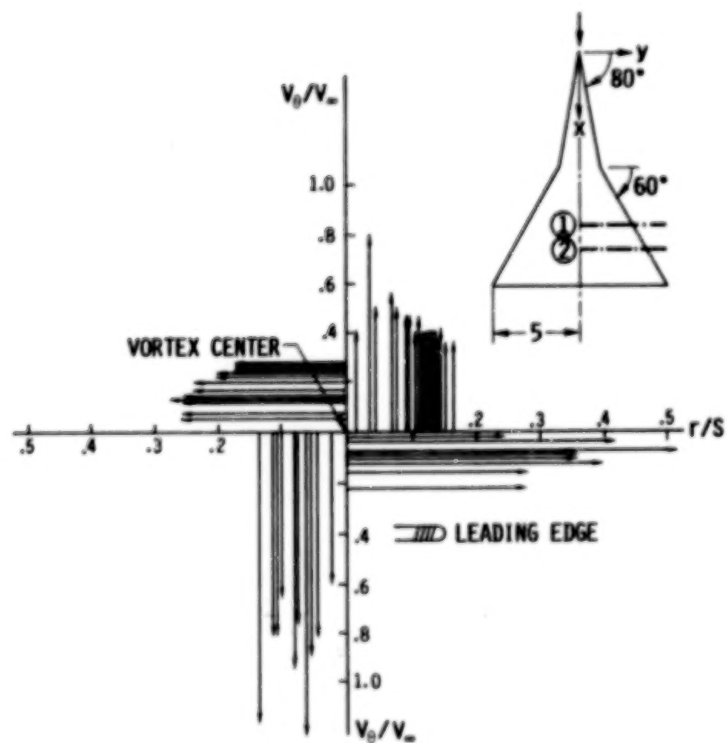


Figure 2. Flow field data at station 1 on a double delta wing at  $M_\infty = 0$ . Data from ref. 12.

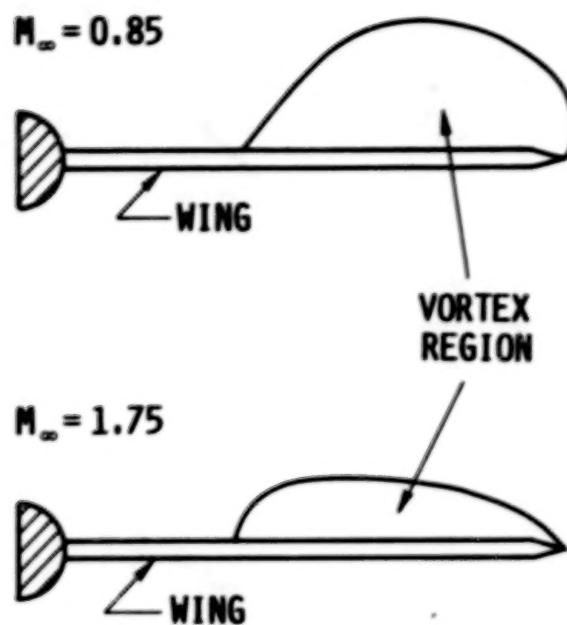


Figure 3. Vortex flow regions on a 65-deg plane wing at subsonic and supersonic speeds.  $\alpha = 8.1$  deg and  $R_e = 1.5 \times 10^6$ .

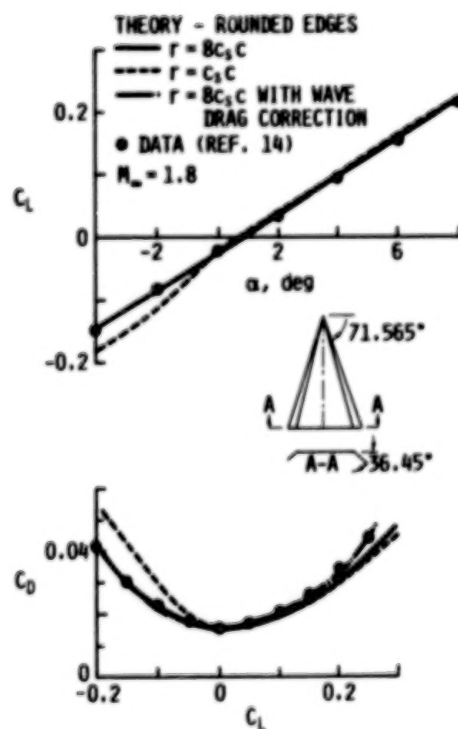


Figure 4. Longitudinal characteristics of a delta wing of aspect ratio 4/3 at  $M_\infty = 1.8$ .

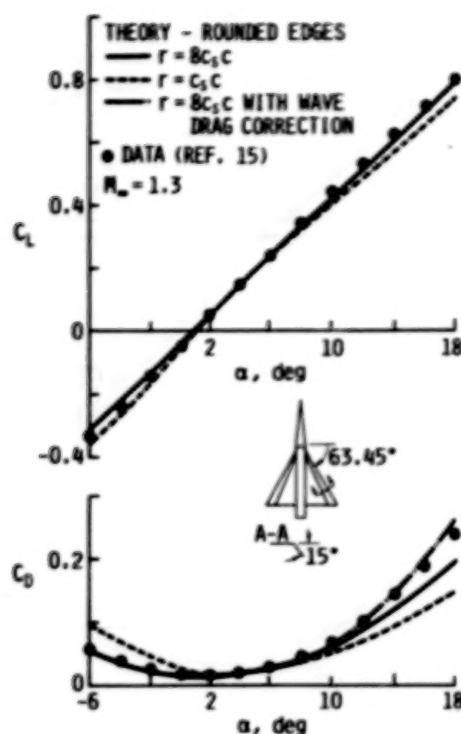


Figure 5. Longitudinal characteristics of a wing-body configuration of aspect ratio 2.0 at  $M_\infty = 1.3$ .

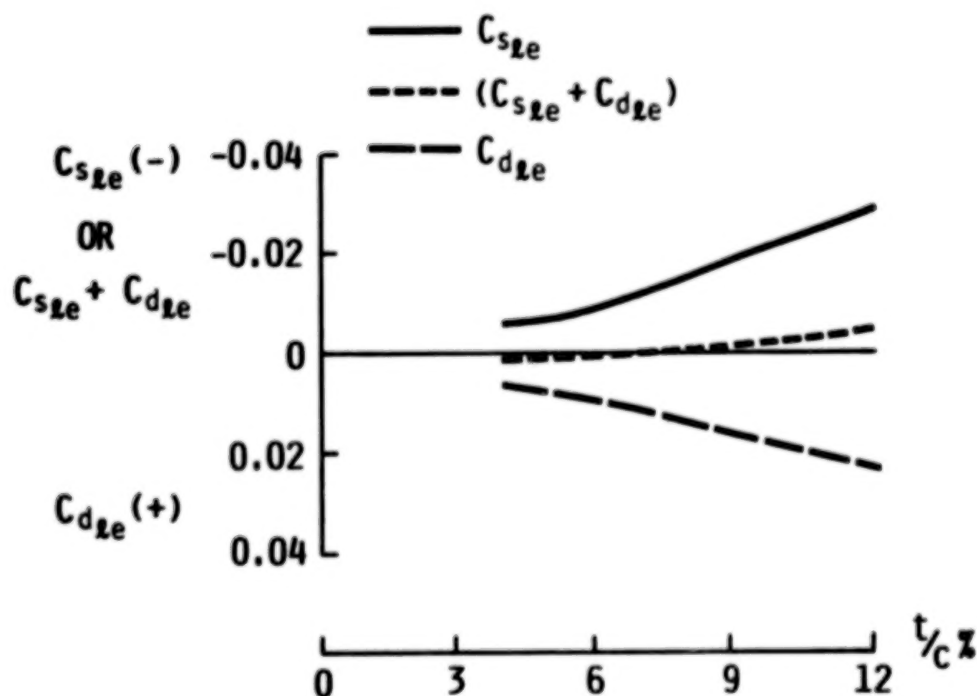


Figure 6. Thickness effect on leading-edge suction at angles of attack at which separation bubble first occurs on symmetrical six-series NASA airfoils.  $M_\infty = 0.17$ ,  $R_e = 5.8 \times 10^6$ .



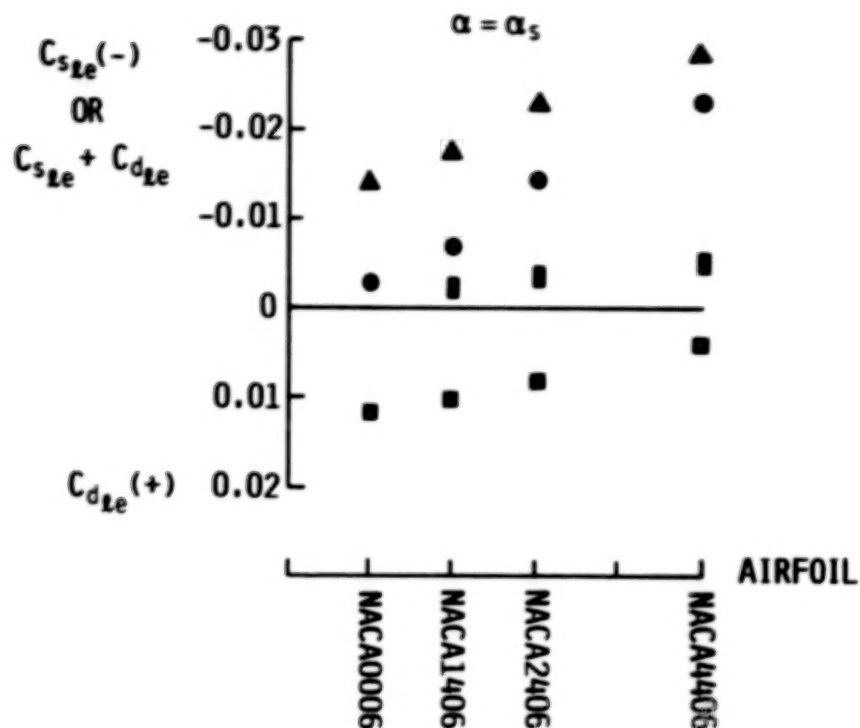


Figure 7. Camber effect on leading-edge suction at angles of attack at which separation bubble first occurs.  $M_\infty = 0.17$ ,  $R_e = 5.8 \times 10^6$ .

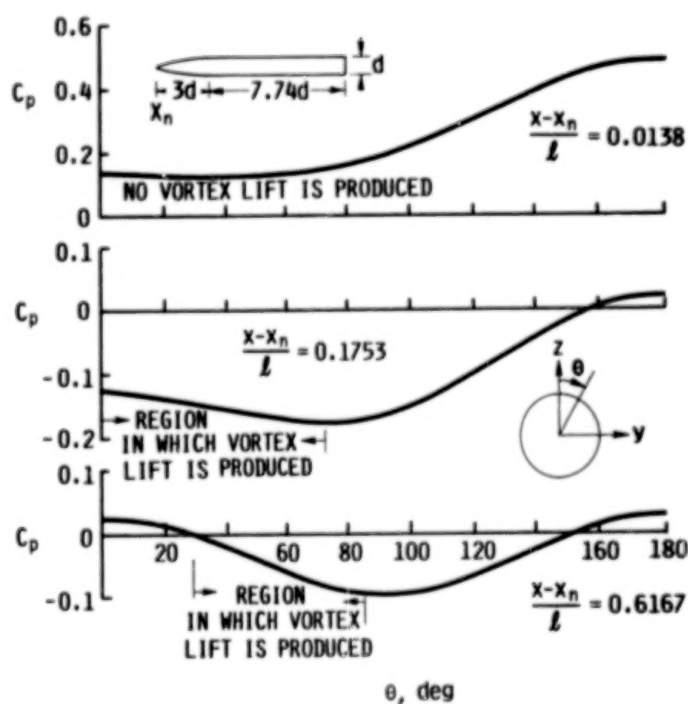


Figure 8. Calculated pressure distribution on an ogive cylinder at  $\alpha = 10$  degrees and  $M_\infty = 0.3$ .

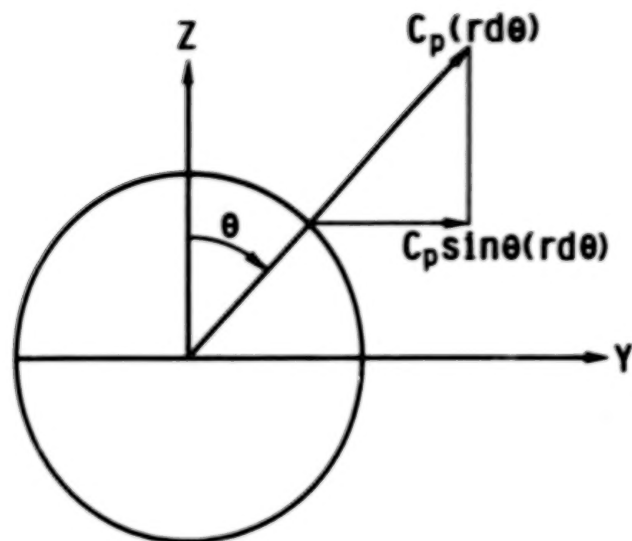


Figure 9. Calculation of positive side force.

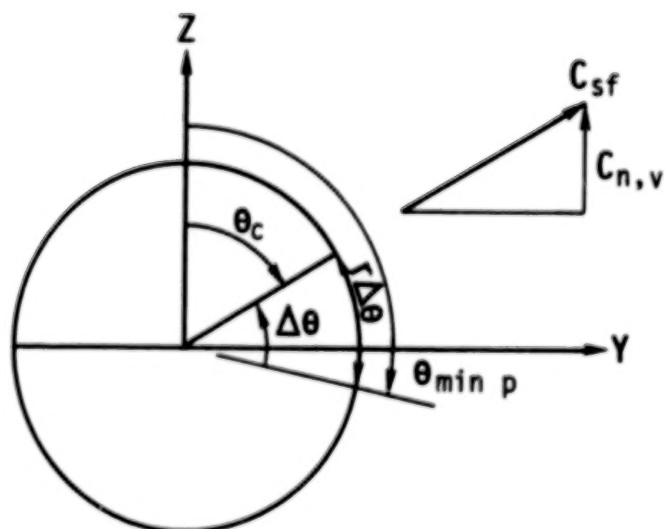


Figure 10. Vortex action point and vortex normal force on a body.

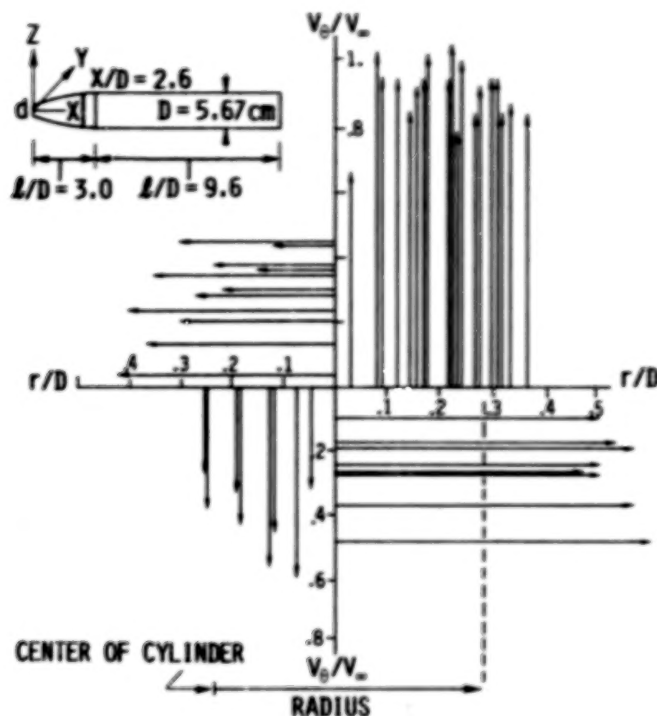


Figure 11. Flow field data from ref. 23 on a tangent ogive body at  $x/D = 2.6$ ,  $\alpha = 45^\circ$  and  $Re = 1.5 \times 10^5$ .

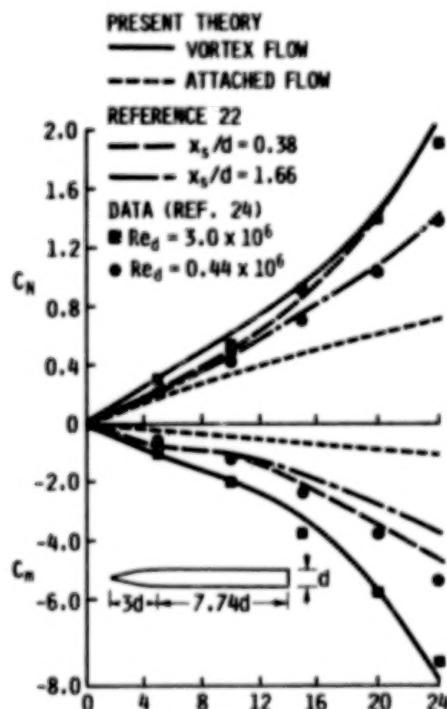


Figure 12. Normal force and pitching moment coefficients for an ogive-cylinder body at  $M_\infty = 0.3$ . Moment center at body nose. Reference area = base area and reference length =  $d$ .

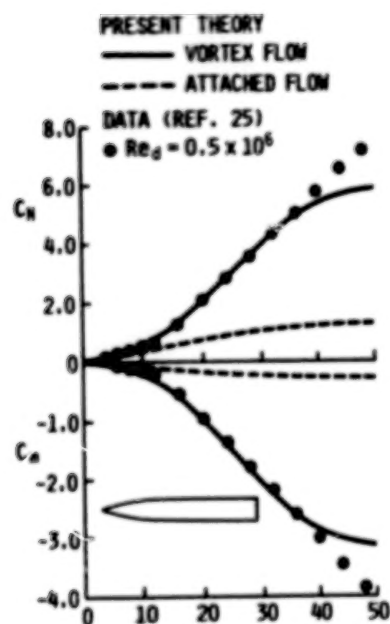


Figure 13. Normal force and pitching moment coefficients for a circular-arc-cylincer body at  $M_\infty = 1.6$ . Moment center at body nose. Reference area = base area and reference length = body length.



RECENT EXTENSIONS TO THE FREE-VORTEX-SHEET THEORY  
FOR EXPANDED CONVERGENCE CAPABILITY

James M. Luckring  
NASA Langley Research Center  
Hampton, Virginia

Keith D. Hoffler  
Vigyan Research Associates, Inc.  
Hampton, Virginia

Arthur C. Grantz  
Northrop Corporation  
Hawthorne, California

## SUMMARY

A new version of the free-vortex-sheet formulation is presented which has greatly improved convergence characteristics for a broad range of geometries. The enhanced convergence properties were achieved largely with extended modeling capabilities of the leading-edge vortex and the near-field trailing wake. Results from the new code, designated FVS-1, are presented for a variety of configurations and flow conditions with emphasis on vortex flap applications.

## INTRODUCTION

The design constraints for high-speed aircraft with efficient supersonic performance capability often result in highly swept wings which are conducive to separation-induced leading-edge vortex flows at moderate-to-high angles of attack. Although this type of separation can cause increased drag through the loss of leading-edge thrust, the vortex-lift characteristics resulting from this highly stable flow can be used to improve takeoff and landing capabilities, provide maneuver lift increments at subsonic and transonic speeds, and, most recently, reduce drag at moderate to high lift coefficients through the use of simple "vortex flaps." As for attached flow, however, the full exploitation of this vortex flow will require improved theoretical analysis and design techniques capable of providing reasonable estimates of the three-dimensional surface pressure distributions at a practical expenditure of human and computer resources.

However, the computation of these vortex flow effects has proven to be a challenging task. It is only during the last 10 years or so that methods have begun to emerge with the stated capability, even for simple three-dimensional geometries with sharp leading edges at subsonic speeds. Among these methods, the free-vortex-sheet theory has provided the best estimates of the inviscid surface pressure distributions for a rather broad class of generic wing shapes. The major drawback of this method has proven to be the difficulty often encountered in achieving converged results.

A new version of the free-vortex-sheet formulation, designated FVS-1, is presented in this paper which has greatly improved convergence properties for a broad range of geometries including vortex flaps. The convergence difficulties were approached from a fluid-mechanical viewpoint as opposed to that of numerical analysis. As a consequence, the basic numerical method for iteratively solving the nonlinear vortex flow problem required little change. The enhanced convergence properties were achieved largely with extended modeling capabilities of the leading-edge vortex and the near-field trailing wakes. Using this approach, considerable insight was gained into the underlying fluid mechanics of vortex modeling as related to convergence considerations. Results are presented which demonstrate the expanded convergence capabilities with emphasis on the salient features modeled as well as the aerodynamic consequences of these modeling techniques.

#### SYMBOLS

|                |   |
|----------------|---|
| AR             | aspect ratio  |
| b              | wing span   |
| $C_B$          | static root bending moment coefficient, static root bending moment/<br>( $q_\infty S_{ref} b$ ) |
| $C_D$          | drag coefficient, drag/( $q_\infty S_{ref}$ )   |
| $C_{D,0}$      | experimental value of drag coefficient at $C_L = 0$   |
| $\Delta C_D$   | drag-due-to-lift coefficient, $C_D - C_{D,0}$   |
| $C_L$          | lift coefficient, lift/( $q_\infty S_{ref}$ )   |
| $C_m$          | pitching moment coefficient, pitching moment/( $q_\infty S_{ref} \bar{c}$ )                     |
| $C_N$          | normal force coefficient, normal force/( $q_\infty S_{ref}$ )                                   |
| $C_p$          | static pressure coefficient, $(p - p_\infty)/q_\infty$  |
| $\Delta C_p$   | $C_{p,u} - C_{p,l}$   |
| c              | streamwise chord  |
| $\bar{c}$      | reference chord   |
| $c_r$          | root chord  |
| $c_t$          | tip chord   |
| E              | $\log(\Sigma r^2)$  |
| It             | iteration number  |
| $\lambda_{nw}$ | longitudinal extent of near wake in fraction of vortex-core diameter at<br>trailing edge        |

|                  |  |
|------------------|--|
| M                | Mach number  |
| N <sub>up</sub>  | number of update iterations  |
| $\hat{n}$        | unit normal vector   |
| p                | static pressure; also maximum camber height in fraction local semispan               |
| q <sub>∞</sub>   | freestream reference dynamic pressure, $(1/2) \rho_{\infty} U_{\infty}^2$            |
| r                | individual panel residual error  |
| S <sub>ref</sub> | reference area   |
| s                | local semispan   |
| t                | thickness  |
| U <sub>∞</sub>   | freestream reference velocity  |
| (u,v,w)          | perturbation velocity components   |
| (x,y,z)          | body-axis Cartesian coordinates  |
| $\alpha$         | angle of attack, degrees   |
| $\alpha_{50}$    | angle of attack for smooth onflow  |
| $\Delta\alpha$   | $\alpha - \alpha_{50}$   |
| $\beta$          | angle of sideslip, degrees; also, Prandtl-Glauert factor, $(1 - M_{\infty}^2)^{1/2}$ |
| $\delta$         | deflection angle, degrees, positive downward   |
| $\delta_f$       | vortex flap deflection angle normal to hingeline, degrees, positive downward         |
| $\Delta\delta_f$ | increment in $\delta_f$  |
| $\delta_t$       | side-edge rake angle, degrees, positive inboard                                      |
| $\Lambda$        | sweep angle, degrees   |
| $\lambda$        | taper ratio, $c_t/c_r$   |
| $\rho_{\infty}$  | freestream reference density   |
| $\Sigma$         | summation  |
| $\xi$            | vorticity vector   |
| $\cdot$          | vector dot product   |
| $  $             | vector magnitude   |

## Subscripts

|          |   |
|----------|---|
| f        | flap  |
| hl       | hingeline   |
| l        | lower surface   |
| le       | leading edge  |
| te       | trailing edge   |
| u        | upper surface   |
| 1        | first order in perturbation quantities; also, inboard   |
| 2        | second order in perturbation quantities; also, outboard |
| $\infty$ | freestream reference conditions                         |

## Abbreviations

|     |                   |
|-----|-------------------|
| Arg | argument          |
| FVS | free vortex sheet |

## CONVERGED FVS PARAMETER SPACE

A study was initially conducted to document the converged parameter space of the free-vortex-sheet method as demonstrated in the open literature. The results are detailed in Table 1 and partially summarized in figure 1. In Table 1, the results are organized by planform type, first for flat wings and then for cambered wings; within one class of planform and camber they are listed alphabetically by first author. It should be noted that most entries correspond to a range of solutions obtained for a systematic variation of some salient parameter such as angle of attack, Mach number, sweep angle, flap deflection angle, etc. Although a number of significant aspects of this solution space could be called out (not to mention details of the solutions themselves), the main point to be observed is the extent of geometric variation and freestream conditions over which the method has been successfully applied.

Some general features of free-vortex-sheet solutions are highlighted in figure 2. By virtue of explicitly modeling the leading-edge vortex, a variety of "real flow" effects are included in the FVS solutions which, to date, have not been calculable by simpler methods. The chief feature of these solutions is an accurate estimation of the three-dimensional, inviscid pressure field. By way of integration this also results in accurate force and moment estimates. In addition, high angle-of-attack vortex lift loss effects due to longitudinal vortex curvature near the trailing edge as well as vortex crowding are implicitly represented. Additional discussion of these effects has been given by Polhamus (1983, 1985).

Although not covered in this paper, the FVS method has recently been extended to account for two primary effects of viscosity and distributed vorticity, vortex breakdown and secondary vortex separation. (The method is still limited to flows



with a known primary separation line such as occurs with a sharp leading edge.) By imbedding a parabolized Navier-Stokes representation of an axisymmetric vortex core, Luckring (1985) showed that the condition of incipient vortex breakdown at the trailing edge of delta, arrow, and diamond wings could be predicted with a critical helix angle concept. Wai et al. (1985) demonstrated the first estimations of secondary vortex separation with the FVS method by modeling the upper surface boundary layer flow and interacting the viscous flow effects with the outer inviscid flow. Although continuing development of the vortex core and secondary vortex effects will be required, the initial findings of these studies are quite promising. The current status of secondary separation modeling by boundary layer techniques will be addressed in this conference by Blom et al. (1985) as well as by Woodson and DeJarnette (1985).

## METHOD EXTENSIONS

From the experience gained in utilizing the free-vortex-sheet method, four aspects of the formulation were chosen for modification. The first three aspects regard flow modeling considerations; they are the near-wake model, the restart capability, and the manipulation of the starting vortex sheet geometry. The fourth aspect regards the quasi-Newton scheme employed to solve the nonlinear system of governing equations.

### Near-Wake Considerations

The primary attributes of the near-wake flow field are summarized in figure 3 for the conditions of planar and nonplanar vorticity. In either case, the trailing-edge Kutta condition results in a near-wake flow which is tangent to the wing at the trailing edge. For planar vorticity the linear form of the pressure coefficient is appropriate and, when taken in conjunction with the no-load wake boundary condition, results in a wake flow where the magnitude of the vorticity vector is free, but its argument is fixed at the streamwise direction.

As is true for slender-body theory, nonplanar vorticity necessitates the inclusion of nonlinear terms in the equation for the pressure coefficient. Although these terms are second order in form, their contribution is of first order, particularly with regard to the sidewash ( $v$ ). Employing this more exact form of the pressure coefficient in conjunction with the no-load wake boundary condition yields a more realistic wake flow where both the magnitude and the argument of the vorticity vector are now free quantities. These effects allow the wake vorticity to skew laterally and significantly affect the satisfaction of the trailing-edge Kutta condition as was shown by Luckring et al. (1982), for leading-edge vortex flows. However, it must be emphasized that the driving mechanism of this wake effect is the presence of nonplanar vorticity, only one example of which is the leading-edge vortex problem. Other examples of conditions where these effects would also be important include wings with significantly nonplanar geometries such as wings with winglets or vortex flaps, regardless of whether the flow is attached or separated.

An example of the nonplanar effect is presented in figure 4 in the form of vorticity contours. Although both calculations utilized the higher order near wake, the attached flow case of figure 4a resulted in the wake vorticity orienting itself largely in the streamwise direction since the vorticity of this flow is planar. Here, it is evident that the conventional approximations made for the simple trailing wake are adequate for this flow. In the nonplanar vortex-flow case of



figure 4b the lateral skewing of the wake vorticity is significant; modeling this flow with a simple trailing wake would constitute a poor approximation. It is of interest to note the coalescence of vorticity downstream in the near wake. This is indicative of the wake vortex which occurs on slender wings with leading-edge separation; it is shed along the trailing edge and has the opposite sense of the leading-edge vortex.

From a convergence viewpoint, it is desirable to make the near wake as short as possible while maintaining the beneficial effects of this model. A long near wake would not only require more panels (increasing computational expense) but also require increasingly complicated wake flow effects to be represented, hampering convergence. Fortunately, the results of a near-wake length study (figure 5) show very little effect of the length of near wake modeled on the converged force and moment properties of a delta wing. In this figure, the near-wake length is presented in fractions of the vortex core diameter at the wing trailing edge. Also shown are the suction analogy estimates of the normal force coefficient for two angles of attack. Apparently the salient feature of the higher order near wake is to allow the wing vorticity to pass onto the wake with the proper orientation. As has been shown in other studies, details of the wake rollup have little effect on the wing flow itself. Additional calculations (not shown) indicated little sensitivity of the solution to near-wake paneling variations at a fixed near-wake length.

A comparison of the convergence histories for a wing with no near wake and a wing with a short near wake is shown in figure 6. Both solutions required eight iterations to drive the residual error below a tolerance of  $10^{-6}$ , and the overall character of the convergence was unchanged by adding the short near wake. It is noteworthy that the consequences of modeling nonplanar vorticity effects with the near wake have a larger effect on the solution than does driving the residual error down 10 orders of magnitude from unacceptable to fully acceptable levels.

The results of figure 6 also indicate that the overall force and moment coefficients are converged at a residual error level on the order of  $10^{-3}$ , as opposed to the default tolerance of  $10^{-6}$ . In figure 7, the effect of the residual error level on the spanwise pressure distributions very near the trailing edge (where convergence is generally slowest) also indicate that  $10^{-3}$  is acceptable for practical applications. Examination of the other calculations of this paper further supports this conclusion.

Computed force and moment properties for the unit-aspect-ratio delta wing of Hummel (1979) are compared with experimental values in figure 8. The wing was represented by mean plane doublet networks to account for the asymmetric beveling and thickness effects were not modeled. The calculations (with a short near wake) show excellent agreement with the experiment including camber effects which, for the most part, are due to the trailing-edge bevel (a trailing-edge-flap type of effect). Solutions were obtained down to relatively low angles of attack (in magnitude) and lift coefficients; at  $\pm 5$  degrees the computed vortex-lift increment was approximately  $\pm 0.03$  from the computed attached flow value. (The attached flow solutions are for zero leading-edge suction.)

Spanwise pressure distributions for  $20^\circ$  angle of attack correlate reasonably well with the experimental results (figure 9). Differences on the upper surface in peak suction magnitude and in the outboard values are largely due to secondary separation, a viscous flow effect. At the aft station shown, thickness effects also affect the quality of the correlation. This is the station of maximum thickness,

and the thin wing calculations reflect the singular nature of the modeled flow at this station.

### Partial Restart

A quasi-Newton method is used to solve the nonlinear equations for the free-vortex-sheet formulation. As with any Newton method, the starting solution must be "sufficiently close" to the converged answer if that answer is to be achieved. The basic FVS code has a full restart capability which is useful for changes in the far-field boundary conditions. Here the complete solution (singularities and vortex geometry) from a prior calculation is used as a starting solution for a new calculation of the same wing geometry (and paneling) at different freestream conditions. This capability has proven to be very useful and cost effective for computations over a range of freestream conditions such as angle of attack, Mach number, etc., and was used for the results of the Hummel delta wing just discussed. For cases where no prior information is available, the default approach was to base the initial vortex-sheet geometry on the conical-flow solution of Smith (1966) and to calculate the initial singularity distribution from a subset of the full governing equations.

The restart capability of this method has been extended to include a "partial restart" which is useful for changes in the near-field boundary conditions such as would arise for a change in wing geometry, paneling, etc. The partial restart allows for the transfer of an arbitrary vortex sheet geometry from some prior calculation to the current configuration of interest and solves for the initial singularity distribution by satisfying a subset of the full governing equations. This technique has been exploited for many of the vortex-flap solutions summarized in Table 1, primarily for achieving solutions over a range of vortex-flap deflection angles. However, it was found that the utility of the partial restart diminished as the differences in boundary conditions between an available and the desired solution increased. For this reason, additional vortex-sheet manipulation capability was implemented.

### Vortex Sheet Manipulation

For many practical applications the geometric properties of the leading-edge vortex can be dominated by some salient geometric characteristic of the wing. One example is the vortex flap application where the resultant vortex geometries are similar in a coordinate system normal to the flap surface. Therefore, a simple vortex manipulation capability was implemented which allows the initial vortex geometry to be arbitrarily rotated and/or scaled about the wing leading edge. This idea is illustrated in figure 10, where the vortex sheet from an available three-dimensional solution for a planar delta wing is first transferred (via the partial restart) to a wing with a deflected vortex flap, and is then rotated by the flap deflection angle. In practice, it is often advantageous to also slightly scale the resultant initial vortex geometry as well. The effects of this approach on convergence are shown in figure 11a. Use of the simple transfer, rotation, and scaling readily yielded a converged solution for a large increment in flap deflection; for small increments in flap deflection either the transfer alone or in conjunction with manipulation readily yielded the converged solution. Without these techniques converged results had not been achieved.

An example of the scaling effects is illustrated in figure 11b. The converged solution for a delta wing was transferred to the gothic wing and then scaled to



approximate the nonconical effects due to the gothic wing planform. Once again the calculation readily converged; using conical flow information for the starting solution, the prior version of the code would not yield a converged result.

The partial restart and vortex manipulation can be used to obtain solutions for more complex geometries and flow conditions. Shown in figure 12 is an example for a wing-body configuration with a gothic planform vortex flap deflected at a large angle. By organizing the calculations roughly as shown one can obtain intermediate solutions which are useful for interpreting the complete configuration solution as well as for determining incremental effects of geometric variations. In figure 13 an example is shown for a similar wing geometry but at sideslip conditions. Drawing upon simple-sweep concepts, symmetric calculations were first performed which, by the partial restart, provided good starting solutions for the complete configuration.

The approach taken for this case can also be cost effective since the gross solution features are established with the two symmetric calculations which nominally require one-half the computer resources of a full-span calculation for the same paneling and number of iterations. The symmetric precursor calculations could have been performed at reduced panelings, further affecting cost reduction. This feature has been exploited for various problems by initiating a solution with a coarse paneling and then, using the partial restart, obtaining solutions for finer panelings, much as is done with mesh sequencing in finite-difference formulations.

#### Modified Quasi-Newton Scheme

With the default quasi-Newton scheme of the free-vortex-sheet method the Jacobian matrix is fully formulated at the starting solution and then only every third iteration thereafter. For the intermediate iterations the values of the Jacobian are obtained with an approximate update procedure due to Broyden (1973). By this approach, there is no need to fully reevaluate the partial derivatives comprising the elements of the Jacobian for each iteration. So long as the method converges, this technique can reduce the cost of obtaining the solution. As with any approximation technique, however, the update method will work best in conditions where the elements being approximated vary linearly and, in actuality, undergo little change.

In general, the elements of the Jacobian will undergo greater change early in the iteration process, where residual error levels are high, than they will later in the calculation as the solution becomes established. Strictly reformulating the Jacobian matrix every three iterations can therefore result not only in unnecessary numerical difficulties early in a calculation (due to inherent approximations affiliated with the update procedure) but also in unnecessary numerical expense late in a calculation (due to Jacobian reformulation when an update would be just as good). Therefore, the Jacobian reformulation frequency was adjusted to be a function of the residual error level. The following approximate schedule was determined from numerical experimentation for the number of iterations employing the update procedure as a function of residual error level:

| error range     | $N_{up}$ |
|-----------------|----------|
| $E > 0.5$       | 1        |
| $0.5 > E > 0.1$ | 2        |
| $0.1 > E$       | 5        |

Several cases of this study were reanalyzed with the above Jacobian update schedule. Although no cases have been found which required this technique to obtain convergence, calculations with the adjusted Jacobian update schedule evidenced smoother convergence properties than did the baseline calculations. The cost of the modified calculation was comparable to the baseline calculation primarily because the increased Jacobian reformulation frequency at high residual error levels is traded off against the reduced frequency at low levels of error.

#### A DIRECT APPROACH FOR CAMBERED WINGS

The techniques described in this report can also be used directly to obtain solutions for cases where no prior information is available for use with the partial restart. An example is shown in figure 14 for wings with large camber at freestream conditions where the leading-edge vortex is small and acting on the forward-facing camber surface. The approach, to be subsequently described, will be first applied to the circular-arc conical-camber wings of Barsby (1974) and then to a vortex flap configuration.

Attached flow calculations were first performed with the free-vortex-sheet code to determine the smooth-onflow angle of attack. For these conical wings, this condition occurred along the entire leading edge within an angle of attack of about  $1^\circ$ . The modeling included the short near wake and the calculations incorporated the scheduled Jacobian update procedure. Because the angle of attack differs slightly from the smooth-onflow angle, the leading-edge vortex will be small and governed primarily by properties near the leading edge. To approximate these effects, the initial vortex geometry was based upon the conical flow solution of Smith (1966) for the incremental angle of attack beyond smooth onflow and was rotated by the transverse wing slope at the leading edge.

Calculations were performed for a unit-aspect-ratio wing, first with a nondimensional camber height of 0.4 for freestream conditions  $5^\circ$  above smooth onflow. The calculation readily converged, and some properties of the three-dimensional solution are shown in figure 15a at the wing trailing edge. The simple starting procedure just described provided a reasonable estimate of the converged vortex geometry. For comparison purposes, the flat-plate conical-flow solution is also shown. This solution emphasizes the significant effects camber has on the vortex solution and also indicates probable convergence difficulties if the flat-plate solution were to be used as a starting solution for the cambered wing.

A more extreme case is shown in figure 15b. From the previous calculation ( $p = 0.4$ ) it was apparent that the described starting procedure resulted in an oversized vortex, so the starting vortex geometry for the current calculation ( $p = 0.6$ ) was further scaled down by 50 percent. The calculation readily converged and resulted in an extremely small vortex. As a consequence, this solution exhibited nearly 90-percent suction, based upon the (usual) attached-flow/zero-suction and flat-plate-optimum drag levels.

As a final application, this direct approach was applied to a vortex flap geometry. The resultant convergence histories (figure 16) show the dramatic effects of the new formulation. It should be noted that convergence is displayed at a residual error level of  $10^{-6}$ ; as was shown earlier the solution is sufficiently established at a residual level of  $10^{-3}$  for practical purposes.

## CONCLUDING REMARKS

A variety of extensions have been implemented to the free-vortex-sheet formulation for the purpose of improving the convergence characteristics of the method. By extending the modeling capability of the code significant improvements in the convergence characteristics were realized without changing the basic numerical scheme. Some results of this study are summarized below.

Only a short near wake is required to capture the significant effects of nonplanar vorticity. The convergence of a calculation with a short near wake is nearly as fast as the convergence of a calculation with no near wake at all. With either wake representation, the solution properties evidenced little variation beyond a residual error level of  $10^{-3}$ .

A "partial restart" was added to the formulation. This allows for the use of an arbitrary vortex from a prior calculation as a starting solution. In addition, simple vortex manipulation features such as rotation and scaling proved to be very effective in enhancing convergence.

With the extensions described in this report, the utility of the FVS formulation has been extended to conditions where the vortex is small. This allows for three-dimensional calculations to be easily performed at low angles of attack and on configurations with highly deflected leading edges.

## REFERENCES

- Barsby, J. E. (1974): Flow Past Conically-Cambered Slender Delta Wings with Leading-Edge Separation. ARC R&M No. 3748, September.
- Blom, G.; Wai, J. C.; and Yoshihara, H. (1985): Viscous Vortical Flow Calculations over Delta Wings. Vortex Flow Aerodynamics - Volume I, NASA CP-2416, paper no. 12, 1986.
- Broyden, C. G. (1973): Quasi-Newton or Modification Methods. Numerical Solution of Systems of Nonlinear Algebraic Equations, edited by G. D. Bryne and C. A. Hall, Academic Press, New York.
- Brune, G. W.; Weber, J. A.; Johnson, F. T.; Lu, P.; and Rubbert, P. E. (1975): A Three-Dimensional Solution of Flows Over Wings with Leading-Edge Vortex Separation. Part I -- Engineering Document. NASA CR-132709, September.
- Brune, G. W.; and Rubbert, P. E. (1977): Boundary Value Problem of Configurations with Compressible Free Vortex Flow. AIAA Journal, pp. 1521-1523, October.
- Buter, T. A.; Rao, D. M.; and Schoonover, W. E., Jr. (1985): Experimental and Computational Investigation of an Apex Flap Concept on a 74 Degree Delta Wing. NASA CR-166080, December.
- Erickson, G. E. (1983): Application of Free Vortex Sheet Theory to Slender Wings with Leading-Edge Vortex Flaps. AIAA Paper No. 83-1813, July.
- Erickson, Gary E. (1985): Vortex/Linear Lift Augmentation. Volume VI--Free Vortex Sheet Computation Study. AFWAL TR-85-3017, June.



Frink, N. T. (1982): Analytical Study of Vortex Flaps on Highly Swept Delta Wings. Proceedings of the 13th Congress of ICAS, Paper No. 82-6.7.2, August.

Frink, N. T. (1986): Critical Evaluation of a Vortex Flap Design Concept Using a 74° Delta Configuration. Vortex Flow Aerodynamics - Volume II, NASA CP-2417, paper no. 2.

Gloss, B. B., and Johnson, F. T. (1976): Development of an Aerodynamic Theory Capable of Predicting Surface Loads on Slender Wings with Vortex Flow. NASA CP-001, pp. 55-67.

Harrison, W. F. (1982): M.A.W. Advanced Leading Edge Devices. Boeing Report No. D180-27024-1, March.

Harrison, W. F. (1982b): Effects of M.A.W. Camber on Vortex Flap Performance. Boeing Report No. D180-27050-1, April.

Hoffler, K. D. (1985): Investigation of the "Vortex Tab." NASA CR-172586, May.

Hummel, D. (1979): On the Vortex Formation Over a Slender Wing at Large Angles of Incidence. AGARD CP-247, Paper No. 15, January.

Johnson, F. T., Lu, P., Brune, G. W., Weber, J. A., and Rubbert, P. E. (1976): An Improved Method for the Prediction of Completely Three-Dimensional Aerodynamic Load Distributions of Configurations with Leading Edge Vortex Separation. AIAA Paper No. 76-417, July.

Johnson, F. T.; Lu, P.; Tinoco, E. N.; and Epton, M. A. (1980): An Improved Panel Method for the Solution of Three-Dimensional Leading-Edge Vortex Flows. Volume I-Theory Document. NASA CR-3278, July.

Kuhlman, J. M. (1978): Analytical Studies of Separated Vortex Flow on Highly Swept Wings. NASA CR-3022, November.

Lamar, J. E. (1978): Subsonic Vortex-Flow Design Study for Slender Wings. AIAA Paper No. 78-154, January.

Lamar, J. E.; and Luckring, J. M. (1979): Recent Theoretical Developments and Experimental Studies Pertinent to Vortex Flow Aerodynamics--With a View Towards Design. AGARD CP-247, Paper No. 24, January.

Luckring, J. M.; Schoonover, W. E., Jr.; and Frink, N. T. (1982): Recent Advances in Applying Free Vortex Sheet Theory for the Estimation of Vortex Flow Aerodynamics. AIAA Paper No. 82-0095.

Luckring, J. M. (1985): A Theory for the Core of a Three-Dimensional Leading Edge Vortex. AIAA Paper No. 85-0108, January.

Luckring, J. M.; Hoffler, K. D.; and Grantz, A. C. (1986): Recent Extensions to the Free-Vortex-Sheet Theory for Expanded Convergence Capability. Vortex Flow Aerodynamics - Volume I, NASA CP-2416, paper no. 4.

Manro, M. E. (1983): Aeroelastic Loads Prediction for an Arrow Wing--Task III -- Evaluation of the Boeing Three-Dimensional Leading-Edge Vortex Code. NASA CR-3642, April.

Polhamus, E. C. (1983): Applications of Slender Wing Benefits to Military Aircraft. AIAA Paper No. 83-2566, October.

Polhamus, E. C. (1985): Vortex Lift Research: Early Contributions and Current Challenges. Vortex Flow Aerodynamics - Volume I, NASA CP-2416, paper no. 1, 1986.

Reddy, C. S. (1979): Theoretical Study of Aerodynamic Characteristics of Wings Having Vortex Flow. NASA CR-159184, November.

Reddy, C. S. (1981): Investigation of Aerodynamic Characteristics of Wings Having Vortex Flow Using Different Numerical Codes. NASA CR-165706, April.

Reddy, C. S. (1981b): Effect of Sweep Angles on Aerodynamic Performance of Double Arrow Wing -- An Analytical Study. Journal of Aircraft, Vol. 18, No. 8, pp. 702-703, August.

Reddy, C. S. (1981c): Effect of Leading-Edge Vortex Flaps on Aerodynamic Performance of Delta Wings. Journal of Aircraft, Vol. 18, No. 9, pp. 796-798, September.

Smith, J. H. B. (1966): Improved Calculations of Leading-Edge Separation from Slender Delta Wings. RAE TR No. 66070, March.

Tinoco, E. N., and Yoshihara, H. (1979): Subcritical Drag Minimization for Highly Swept Wings with Leading Edge Vortices. AGARD CP-247, Paper No. 26, January.

Wai, J. C.; Baille, J.; and Yoshihara, H. (1985): Computation of Turbulent Separated Flows. Third Symposium on Numerical and Physical Aspects of Aerodynamic Flows, January.

Woodson, S. H.; and DeJarnette, F. R. (1985): A Direct and Inverse Boundary Layer Method for Subsonic Flow Over Delta Wings. Vortex Flow Aerodynamics - Volume I, NASA CP-2416, paper no. 5, 1986.

TABLE 1.- CONVERGED FVS PARAMETER SPACE, PUBLISHED RESULTS

(a) delta wings, uncambered

| Reference                      | Planform<br>Class | $\lambda_1$ | $\lambda_2$ | $\lambda_{te}$ | AR     | $\lambda$ | Camber<br>Class | $\delta_1$ | $\delta_{h1}$ | $\delta_2$ | Thickness<br>Wing | Fuel | Vortex<br>Span | Flow<br>$\alpha$ | $\beta$ | M       |
|--------------------------------|-------------------|-------------|-------------|----------------|--------|-----------|-----------------|------------|---------------|------------|-------------------|------|----------------|------------------|---------|---------|
| Brune,<br>et al.<br>(1975)     | Delta             | 70          | -           | 0              | 1.46   | 0         | Flat            | -          | -             | -          | Thin              | -    | Full           | 9-19             | 0       | 0       |
|                                |                   | 76          | -           | -              | 1.00   | -         | -               | -          | -             | -          | -                 | -    | -              | 10-20            | -       | -       |
| Brune,<br>et al.<br>(1977)     | Delta             | 74          | -           | 0              | 1.15   | 0         | Flat            | -          | -             | -          | Thin              | -    | Full           | 5-20             | 0       | 0.8     |
| Buter,<br>et al.<br>(1985)     | Delta             | 74          | -           | 0              | 1.15   | 0         | Flat            | -          | -             | -          | Thin              | -    | Full           | 10               | 0       | 0       |
| Erickson<br>(1983)             | Delta             | 55          | -           | 0              | 2.80   | 0         | Flat            | -          | -             | -          | Thin              | -    | Full           | 15               | 0       | 0.4     |
|                                |                   | 65          | -           | -              | 1.87   | -         | -               | -          | -             | -          | -                 | -    | Part           | -                | -       | -       |
|                                |                   | 75          | -           | -              | 1.07   | -         | -               | -          | -             | -          | -                 | -    | Full           | -                | -       | -       |
| Gloss,<br>et al.<br>(1976)     | Delta             | 63.4        | -           | 0              | 2.00   | 0         | Flat            | -          | -             | -          | Thin              | -    | Full           | 20               | 0       | 0       |
|                                |                   | 70          | -           | -              | 1.46   | -         | -               | -          | -             | -          | -                 | -    | -              | 14               | -       | -       |
| Hoffler<br>(1985)              | Delta             | 65          | -           | 0              | 1.87   | 0         | Flat            | -          | -             | -          | Thin              | -    | Full           | 16               | 0       | 0       |
| Johnson,<br>et al.<br>(1976)   | Delta             | 70          | -           | 0              | 1.46   | 0         | Flat            | -          | -             | -          | Thin              | -    | Full           | 14               | 0       | 0       |
|                                |                   | 74          | -           | -              | 1.15   | -         | -               | -          | -             | -          | -                 | -    | -              | 5-25             | -       | 0.6     |
| Johnson,<br>et al.<br>(1980)   | Delta             | 63.4        | -           | 0              | 2.00   | 0         | Flat            | -          | -             | -          | Thin              | -    | Full           | 20               | 0       | 0       |
|                                |                   | 70          | -           | -              | 1.46   | -         | -               | -          | -             | -          | -                 | -    | -              | 14               | -       | -       |
|                                |                   | 74          | -           | -              | 1.15   | -         | -               | -          | -             | -          | -                 | -    | -              | 15-30            | -       | -       |
|                                |                   | 76          | -           | -              | 1.00   | -         | -               | -          | -             | -          | -                 | -    | -              | 20               | -       | -       |
|                                |                   | 80          | -           | -              | 0.71   | -         | -               | -          | -             | -          | -                 | -    | -              | 15               | 5       | -       |
|                                |                   | 86.4        | -           | -              | 0.25   | -         | -               | -          | -             | -          | -                 | -    | -              | 2-25             | 0       | -       |
|                                |                   | 63-86       | -           | -              | 2-0.25 | -         | -               | -          | -             | -          | -                 | -    | -              | 20               | -       | -       |
| Kuhlman<br>(1978)              | Delta             | 63-86       | -           | 0              | 2-0.25 | 0         | Flat            | -          | -             | -          | Thin              | -    | Full           | 15               | 0       | 0       |
|                                |                   | 63-80       | -           | -              | 2-0.71 | -         | -               | -          | -             | -          | -                 | -    | -              | 20               | -       | -       |
|                                |                   | 82.7        | -           | -              | 0.52   | -         | -               | -          | -             | -          | -                 | -    | -              | 10-40            | -       | 0.8     |
|                                |                   | -           | -           | -              | -      | -         | -               | -          | -             | -          | -                 | -    | -              | 10.3             | -       | 0.7     |
|                                |                   | -           | -           | -              | -      | -         | -               | -          | -             | -          | -                 | -    | -              | 30               | -       | -       |
|                                |                   | -           | -           | -              | -      | -         | -               | -          | -             | -          | -                 | -    | -              | 20.8             | -       | 0.5-0.8 |
| Lamar<br>(1978)                | Delta             | 74          | -           | 0              | 1.15   | 0         | Flat            | -          | -             | -          | Thin              | -    | Full           | 15-25            | 0       | 0       |
|                                |                   | 80          | -           | -              | 0.71   | -         | -               | -          | -             | -          | -                 | -    | -              | 10-25            | -       | -       |
| Lamar,<br>et al.<br>(1979)     | Delta             | 74          | -           | 0              | 1.15   | 0         | Flat            | -          | -             | -          | Thin              | -    | Full           | 20               | 10      | 0.2     |
| Luckring,<br>et al.<br>(1982)  | Delta             | 63          | -           | 0              | 2.04   | 0         | Flat            | -          | -             | -          | Thin              | -    | Full           | 20               | 0       | 0.3     |
|                                |                   | 74          | -           | -              | 1.15   | -         | -               | -          | -             | -          | -                 | -    | -              | 10-25            | 0.5     | 0.2     |
|                                |                   | -           | -           | -              | -      | -         | -               | -          | -             | -          | -                 | -    | -              | 20               | 0.15    | -       |
|                                |                   | 82.7        | -           | -              | 0.52   | -         | -               | -          | -             | -          | -                 | -    | -              | 10               | 0       | 0.99    |
|                                |                   | -           | -           | -              | -      | -         | -               | -          | -             | -          | -                 | -    | -              | 20.8             | 0       | 0-0.99  |
| Luckring,<br>et al.<br>(1985b) | Delta             | 65          | -           | 0              | 1.87   | 0         | Flat            | -          | -             | -          | Thin              | -    | Full           | 15               | 0       | 0       |
| Polhamus<br>(1983)             | Delta             | 70          | -           | 0              | 1.46   | 0         | Flat            | -          | -             | -          | Thin              | -    | Full           | 10-30            | 0       | 0       |
|                                |                   | 80          | -           | -              | 0.71   | -         | -               | -          | -             | -          | -                 | -    | -              | 5-30             | -       | -       |
| Polhamus<br>(1985)             | Delta             | 70          | -           | 0              | 1.46   | 0         | Flat            | -          | -             | -          | Thin              | -    | Full           | 10-30            | 0       | 0       |
|                                |                   | 76          | -           | -              | 1.00   | -         | -               | -          | -             | -          | Thick             | -    | -              | 25               | -       | -       |
|                                |                   | 80          | -           | -              | 0.71   | -         | -               | -          | -             | -          | Thin              | -    | -              | 5-30             | -       | -       |
| Raddy<br>(1979)                | Delta             | 70          | -           | 0              | 1.46   | 0         | Flat            | -          | -             | -          | Thin              | -    | Full           | 10-30            | 0       | 0       |
|                                |                   | 76          | -           | -              | 1.00   | -         | -               | -          | -             | -          | -                 | -    | -              | 5-30             | -       | -       |
| Raddy<br>(1981)                | Delta             | 70          | -           | 0              | 1.46   | 0         | Flat            | -          | -             | -          | Thin              | -    | Full           | 15-40            | 0       | 0       |

TABLE 1.- CONTINUED

(b) arrow and diamond wings, uncambered

| Reference                     | Planform<br>Class | $A_1$ | $A_2$ | $A_{te}$ | AR   | $\lambda$ | Camber<br>Class | $b_1$ | $A_{b1}$ | $b_2$ | Thickness<br>Wing | Fuel | Vortex<br>Span | Flow<br>$\alpha$ | $\beta$ | M    |
|-------------------------------|-------------------|-------|-------|----------|------|-----------|-----------------|-------|----------|-------|-------------------|------|----------------|------------------|---------|------|
| Brune,<br>et al.<br>(1975)    | Arrow             | 71.2  | -     | 43.6     | 2.02 | 0         | Flat            | -     | -        | -     | Thin              | -    | Full           | 15.8             | 0       | 0    |
| Brune,<br>et al.<br>(1977)    | Arrow             | 74    | -     | 37       | 1.47 | 0         | Flat            | -     | -        | -     | Thin              | -    | Full           | 5-23             | 0       | 0.6  |
| Johnson,<br>et al.<br>(1976)  | Arrow             | 71.2  | -     | 43       | 2.00 | 0         | Flat            | -     | -        | -     | Thin              | -    | Full           | 11.9             | 0       | 0.4  |
|                               |                   | 74    | -     | 37       | 1.47 | -         |                 | -     | -        | -     |                   |      |                | 5-23             | -       | 0.6  |
| Johnson,<br>et al.<br>(1980)  | Arrow             | 71.2  | -     | 43       | 2.00 | 0         | Flat            | -     | -        | -     | Thin              | -    | Full           | 11.9             | 0       | 0.4  |
| Kuhlman<br>(1978)             | Arrow             | 70    | -     | 36.9     | 2.00 | 0         | Flat            | -     | -        | -     | Thin              | -    | Full           | 10-30            | 0       | 0    |
| Luckring,<br>et al.<br>(1982) | Arrow +           | 67    | -     | 55       | 2.50 | 0         | Flat            | -     | -        | -     | Thin              | -    | Full           | 7-14             | 0       | 0.76 |
| Polhamus<br>(1983)            | Arrow             | 70    | -     | 36.9     | 2.00 | 0         | Flat            | -     | -        | -     | Thin              | -    | Full           | 5-50             | 0       | 0    |
| Reddy<br>(1979)               | Arrow             | 70    | -     | 36.9     | 2.00 | 0         | Flat            | -     | -        | -     | Thin              | -    | Full           | 15-40            | 0       | 0    |
|                               |                   | -     | -     | 28.8     | 1.82 | -         |                 | -     | -        | -     |                   |      |                | -                | -       | -    |
|                               |                   | -     | -     | 15.4     | 1.62 | -         |                 | -     | -        | -     |                   |      |                | -                | -       | -    |
| Kuhlman<br>(1978)             | Diamond           | 70    | -     | -51.3    | 1.00 | 0         | Flat            | -     | -        | -     | Thin              | -    | Full           | 10-30            | 0       | 0    |
| Reddy<br>(1979)               | Diamond           | 70    | -     | -15.4    | 1.32 | 0         | Flat            | -     | -        | -     | Thin              | -    | Full           | 15-40            | 0       | 0    |
|                               |                   | -     | -     | -28.8    | 1.21 | -         |                 | -     | -        | -     |                   |      |                | -                | -       | -    |
|                               |                   | -     | -     | -39.5    | 1.12 | -         |                 | -     | -        | -     |                   |      |                | -                | -       | -    |
|                               |                   | -     | -     | -47.7    | 1.04 | -         |                 | -     | -        | -     |                   |      |                | -                | -       | -    |
| Reddy<br>(1981)               | Diamond           | 70    | -     | -51.3    | 1.00 | -         | Flat            | -     | -        | -     | Thin              | -    | Full           | 25-40            | 0       | 0    |
|                               |                   | -     | -     | -        | -    | -         |                 | -     | -        | -     |                   |      |                | -                | -       | -    |

+ B-1 Planform



TABLE 1.- CONTINUED

## (c) cropped wings, uncambered

| Reference                     | Planform<br>Class  | $A_1$ | $A_2$ | $A_{te}$ | AR   | $\lambda$ | Camber<br>Class | $\delta_1$ | $\delta_{h1}$ | $\delta_2$ | Thickness<br>Wing | Fuel  | Vortex<br>Span | Flow<br>$\alpha$ | $\beta$ | M   |
|-------------------------------|--------------------|-------|-------|----------|------|-----------|-----------------|------------|---------------|------------|-------------------|-------|----------------|------------------|---------|-----|
| Erickson<br>(1983)            | Cropped<br>Delta   | 65    | -     | 0        | 2.80 | 0.25      | Flat            | -          | -             | -          | Thin              | -     | Full           | 15               | 0       | 0.6 |
| Erickson<br>(1983)            | Cropped<br>Delta   | 55    | -     | 0        | 1.80 | 0.2       | Flat            | -          | -             | -          | Thin              | -     | Full           | 15               | 0       | 0.4 |
| Lockring,<br>et al.<br>(1982) | Cropped<br>Delta   | 63    | -     | 0        | 0.87 | 0.4       | Flat            | -          | -             | -          | Thin              | -     | Full           | 20               | 0       | 0.3 |
| Reddy<br>(1981)               | Cropped<br>Delta   | 63    | -     | 0        | 0.87 | 0.4       | Flat            | -          | -             | -          | Thin              | -     | Full           | 15-25            | 0       | 0.2 |
|                               |                    | 80    | -     | -        | 0.27 | 0.45      | -               | -          | -             | -          | -                 | -     | -              | 15-25            | -       | 0   |
| Henro<br>(1983)               | Cropped<br>Arrow   | 71.2  | -     | 43       | 1.65 | 0.1       | Flat            | -          | -             | -          | Thin              | -     | Full           | 16               | 0       | 0.4 |
|                               |                    | -     | -     | -        | -    | -         | -               | -          | -             | -          | Thick             | -     | -              | -                | -       | -   |
|                               |                    | -     | -     | -        | -    | -         | -               | -          | -             | -          | -                 | Thick | -              | -                | -       | -   |
|                               |                    | -     | -     | -        | -    | -         | -               | -          | -             | -          | -                 | -     | Part           | 8                | -       | -   |
|                               |                    | -     | -     | -        | -    | -         | -               | -          | -             | -          | Thin              | -     | -              | 6                | -       | -   |
| Reddy<br>(1981)               | Cropped<br>Arrow   | 63    | -     | 40       | 1.07 | 0.4       | Flat            | -          | -             | -          | Thin              | -     | Full           | 15-25            | 0       | 0.2 |
| Reddy<br>(1981)               | Cropped<br>Diamond | 63    | -     | -40      | 0.74 | 0.4       | Flat            | -          | -             | -          | Thin              | -     | Full           | 15-25            | 0       | 0.2 |

## (d) cranked wings, uncambered

| Reference          | Planform<br>Class | $A_1$ | $A_2$ | $A_{te}$ | AR      | $\lambda$ | Camber<br>Class | $\delta_1$ | $\delta_{h1}$ | $\delta_2$ | Thickness<br>Wing | Fuel | Vortex<br>Span | Flow<br>$\alpha$ | $\beta$ | M |
|--------------------|-------------------|-------|-------|----------|---------|-----------|-----------------|------------|---------------|------------|-------------------|------|----------------|------------------|---------|---|
| Erickson<br>(1983) | Cranked<br>Delta  | 72    | 62    | 0        | 1.68    | 0         | Flat            | -          | -             | -          | Thin              | -    | Full           | 15               | 0       | 0 |
| Kuhlman<br>(1978)  | Cranked<br>Delta  | 80    | 65    | 0        | 1.60    | 0         | Flat            | -          | -             | -          | Thin              | -    | Full           | 5-30             | 0       | 0 |
| Reddy<br>(1981)    | Cranked<br>Delta  | 80    | 65    | 0        | 1.60    | 0         | Flat            | -          | -             | -          | Thin              | -    | Full           | 15-30            | 0       | 0 |
|                    |                   | -     | -     | -        | 0.95    | 0.2       | -               | -          | -             | -          | -                 | -    | -              | -                | -       | - |
| Reddy<br>(1981)    | Cranked<br>Arrow  | 80    | 65    | 30       | 2.08    | 0         | Flat            | -          | -             | -          | Thin              | -    | Full           | 15-25            | 0       | 0 |
|                    |                   | -     | -     | -        | 1.10    | 0.23      | -               | -          | -             | -          | -                 | -    | -              | 15-30            | -       | - |
| Reddy<br>(1981b)   | Cranked<br>Arrow  | 70-80 | 65    | 30       | 2.6-2.1 | 0         | Flat            | -          | -             | -          | Thin              | -    | Full           | 20               | 0       | 0 |
|                    |                   | 80    | 60-70 | -        | 2.6-1.6 | -         | -               | -          | -             | -          | -                 | -    | -              | -                | -       | - |

TABLE 1.- CONTINUED

## (e) miscellaneous wings, uncambered

| Reference              | Planform Class  | A <sub>1</sub> | A <sub>2</sub> | A <sub>3</sub> | AR      | λ   | Camber Class | b <sub>1</sub> | b <sub>2</sub> | b <sub>3</sub> | Thickness Wing | Fuel       | Vortex Span | Flow α      | β | W   |
|------------------------|-----------------|----------------|----------------|----------------|---------|-----|--------------|----------------|----------------|----------------|----------------|------------|-------------|-------------|---|-----|
| Brune, et al. (1973)   | Gothic Arrow    | 50             | 87             | 56.3           | 1.60    | 0   | Flat         | -              | -              | -              | Thin           | -          | Full        | 14.3        | 0 | 0   |
| Erickson (1983)        | Gothic          | 62.5           | 76.6           | 0              | 1.35    | 0   | Flat         | -              | -              | -              | Thin           | -          | Full        | 15          | 0 | 0   |
| Frink (1985)           | Gothic          | 60             | 74             | 0              | 1.36    | 0   | Flat         | -              | -              | -              | Thin           | Thin Thick | Part Full   | 10-16<br>14 | 0 | 0   |
| Johnson, et al. (1980) | Rectangle       | 0              | -              | 0              | 0.2-1.2 | 1   | Flat         | -              | -              | -              | Thin           | -          | Full        | 20          | 0 | 0.2 |
| Reddy (1981)           | Naked Side Edge | 63             | -3-13          | 0              | 1.07    | 0.4 | Flat         | -              | -              | -              | Thin           | -          | Full        | 23          | 0 | 0   |

## (f) all planforms, conventional camber

| Reference                | Planform Class  | A <sub>1</sub> | A <sub>2</sub> | A <sub>3</sub> | AR   | λ   | Conventional Camber Class     | b <sub>1</sub> | b <sub>2</sub> | b <sub>3</sub> | Thickness Wing | Fuel | Vortex Span | Flow α | β | W    |
|--------------------------|-----------------|----------------|----------------|----------------|------|-----|-------------------------------|----------------|----------------|----------------|----------------|------|-------------|--------|---|------|
| Buter, et al. (1985)     | Delta           | 74             | -              | 0              | 1.15 | 0   | Apex Flap                     | 0-40<br>20     | -              | -              | Thin           | -    | Full Inbd   | 10     | 0 | 0    |
| Luckring, et al. (1985b) | Delta           | 76             | -              | 0              | 1.00 | 0   | T.E. Flap                     | -6             | -              | -              | Thin           | -    | Full        | -10-50 | 0 | 0    |
| Reddy (1981)             | Delta           | 75             | -              | 0              | 1.07 | 0   | Smooth Onflow, -<br>Cld = 0.3 | -              | -              | -              | Thin           | -    | Full        | 2-30   | 0 | 0    |
| Johnson, et al. (1980)   | Arrow           | 71.2           | -              | 43             | 1.65 | 0   | T.E. Flap                     | 8.3            | -              | -              | Thin           | -    | Full        | 11.9   | 0 | 0.4  |
| Manro (1983)             | Cropped Arrow   | 71.2           | -              | 43             | 1.65 | 0.1 | Twist<br>Twist/Camber         | -              | -              | -              | Thin           | -    | Full        | 16     | 0 | 0.4  |
| Harrison (1982b)         | Cranked Arrow + | 70             | 58             | 48             | 2.24 | 0   | L. E. Droup                   | 0-15           | 58             | -              | Thin           | -    | Part        | 20-25  | 0 | 0.65 |

+ AFTI/F-111 Planform and Camber

TABLE 1.- CONTINUED

(g) all planforms, conical camber

| Reference                | Planform Class | A <sub>1</sub> | A <sub>2</sub> | A <sub>te</sub> | AR   | $\lambda$ | Conical Camber Class | $\delta_1$ | A <sub>h1</sub> | b <sub>z</sub> | Thickness Wing | Fuel | Vortex Span | Flow $\alpha$ | $\beta$ | M |
|--------------------------|----------------|----------------|----------------|-----------------|------|-----------|----------------------|------------|-----------------|----------------|----------------|------|-------------|---------------|---------|---|
| Johnson, et al. (1980)   | Delta          | 74             | -              | 0               | 1.15 | 0         | Wentz                | -          | -               | -              | Thin           | -    | Full        | 10-31         | 0       | 0 |
| Kuhlman (1978)           | Delta          | 74             | -              | 0               | 1.15 | 0         | Wentz                | -          | -               | -              | Thin           | -    | Full        | 10-31         | 0       | 0 |
| Lamar (1978)             | Delta          | 74             | -              | 0               | 1.15 | 0         | Wentz                | -          | -               | -              | Thin           | -    | Full        | 15-25         | 0       | 0 |
|                          |                | 80             | -              | -               | 0.71 | -         | Barsby, p=0.2        | -          | -               | -              | -              | -    | -           | 10-25         | -       | - |
|                          |                | -              | -              | -               | -    | -         | Barsby, p=0.4        | -          | -               | -              | -              | -    | -           | 15-25         | -       | - |
| Luckring, et al. (1985b) | Delta          | 76             | -              | 0               | 1.00 | 0         | Barsby, p=0.4        | -          | -               | -              | Thin           | -    | Full        | 14            | 0       | 0 |
|                          |                | -              | -              | -               | -    | -         | Barsby, p=0.6        | -          | -               | -              | -              | -    | -           | 20            | -       | - |
| Reddy (1979)             | Delta          | 76             | -              | 0               | 1.00 | 0         | Nangia Wing E        | -          | -               | -              | Thin           | -    | Full        | 10-30         | 0       | 0 |
|                          |                | -              | -              | -               | -    | -         | Squire Wing 1        | -          | -               | -              | -              | -    | -           | 10-40         | -       | - |
|                          |                | -              | -              | -               | -    | -         | Squire Wing 2        | -          | -               | -              | -              | -    | -           | 15-40         | -       | - |
|                          |                | -              | -              | -               | -    | -         | Squire Wing 3        | -          | -               | -              | -              | -    | -           | -             | -       | - |
|                          |                | -              | -              | -               | -    | -         | Squire Wing 4        | -          | -               | -              | -              | -    | -           | -             | -       | - |
|                          |                | -              | -              | -               | -    | -         | Squire Wing 5        | -          | -               | -              | -              | -    | -           | 30-40         | -       | - |
| Reddy (1981)             | Delta          | 76             | -              | 0               | 1.00 | 0         | Nangia Wing B        | -          | -               | -              | Thin           | -    | Full        | 24,30         | 0       | 0 |
|                          |                | -              | -              | -               | -    | -         | Squire Wing 4        | -          | -               | -              | -              | -    | -           | 15-40         | -       | - |
|                          |                | -              | -              | -               | -    | -         | Squire Wing 5        | -          | -               | -              | -              | -    | -           | 20,30         | -       | - |
|                          |                | -              | -              | -               | -    | -         | Squire Wing 6        | -          | -               | -              | -              | -    | -           | 20,30         | -       | - |
| Tinoco, et al. (1979)    | Delta          | 74             | -              | 0               | 1.15 | 0         | Linear Twist         | 10         | -               | -              | Thin           | -    | Full        | 16-30         | 0       | 0 |
|                          |                | -              | -              | -               | -    | -         | -                    | 20         | -               | -              | -              | -    | -           | 17-30         | -       | - |
|                          |                | -              | -              | -               | -    | -         | Wentz/Tabbed         | -          | -               | -              | -              | -    | -           | 15-30         | -       | - |

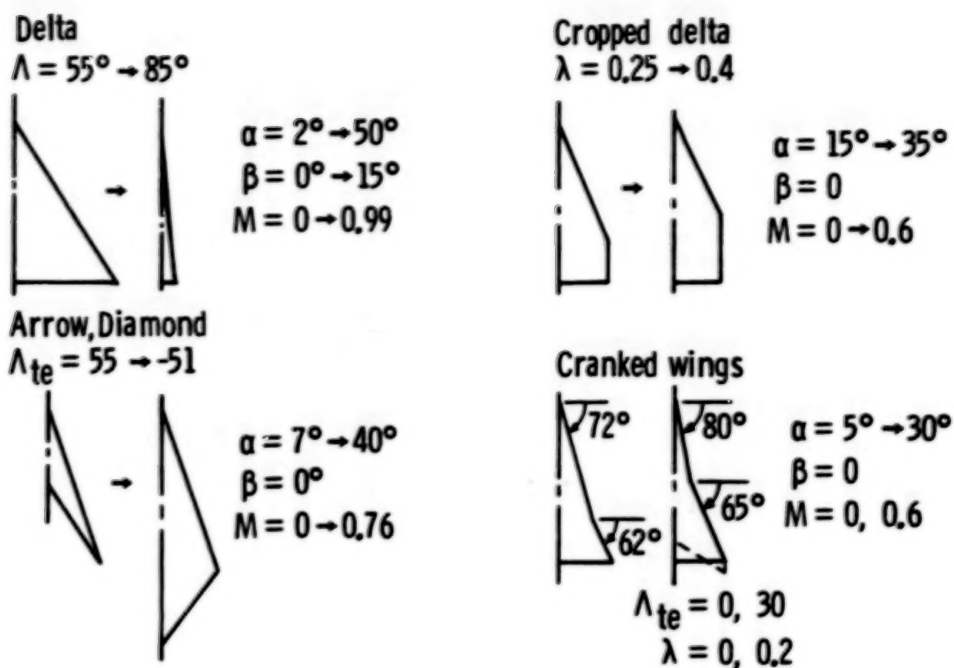
TABLE 1.- CONCLUDED

(h) all planforms, vortex-flap camber

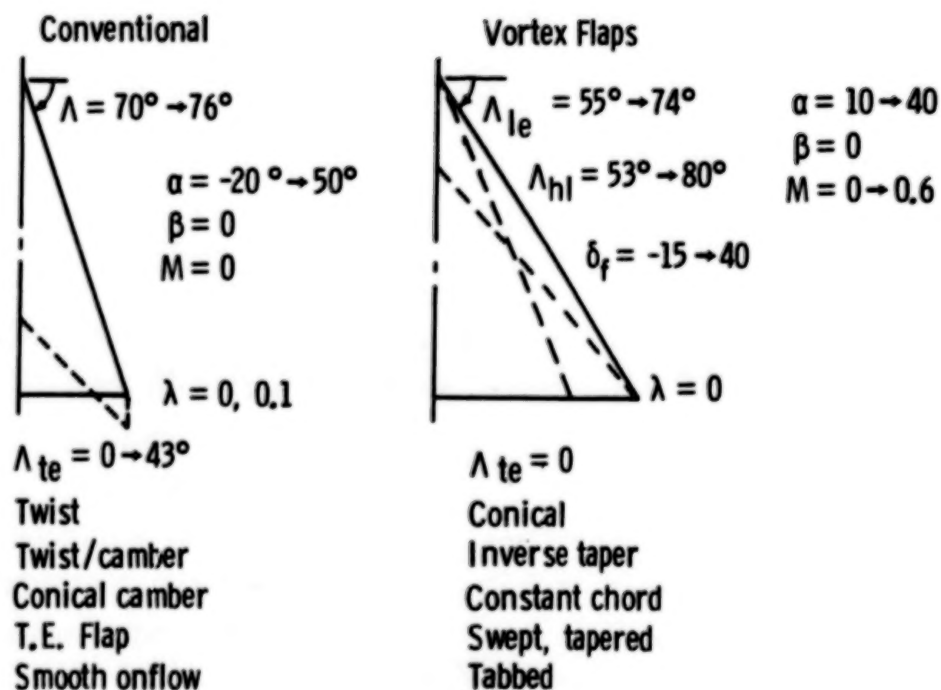
| Reference               | Planform Class  | A <sub>1</sub> | A <sub>2</sub> | A <sub>te</sub> | AR   | $\lambda$ | Vortex Flap Camber Class | $\delta_1$ | A <sub>h1</sub> | $\delta_2$ | Thickness Wing | Fuel  | Vortex Span | Flow # | $\beta$ | M    |
|-------------------------|-----------------|----------------|----------------|-----------------|------|-----------|--------------------------|------------|-----------------|------------|----------------|-------|-------------|--------|---------|------|
| Erickson (1983)         | Delta           | 65             | -              | 0               | 1.87 | 0         | Conical                  | -15-40     | 74              | -          | Thin           | -     | Full        | 15     | 0       | 0.6  |
|                         |                 | -              | -              | -               | -    | -         | -                        | 15         | -               | -          | -              | -     | -           | 11     | -       | -    |
|                         |                 | -              | -              | -               | -    | -         | -                        | 20         | -               | -          | -              | -     | -           | 15-20  | -       | -    |
|                         |                 | -              | -              | -               | -    | -         | -                        | 30         | -               | -          | -              | -     | -           | 15     | -       | 0    |
|                         | Cranked Delta   | 72             | 62             | -               | 1.68 | -         | Inverse Taper            | 15         | -               | -          | -              | -     | Part        | -      | -       | 0.6  |
|                         |                 |                |                |                 |      |           |                          | 15         | 77/70           | -          | -              | -     | Full        | 10,15  | -       | 0.6  |
| Erickson (1983)         | Delta           | 55             | -              | 0               | 2.80 | 0         | Tapered Chord            | 0-30       | 53              | 0-10       | Thin           | -     | Full        | 10-30  | 0-20    | 0.4  |
| Frink (1982)            | Delta           | 74             | -              | 0               | 1.15 | 0         | Constant Chord           | 10         | 74              | -          | Thin           | -     | Full        | 14     | 0       | 0    |
|                         |                 | -              | -              | -               | -    | -         | -                        | -          | -               | -          | -              | -     | Part        | -      | -       | -    |
|                         |                 | -              | -              | -               | -    | -         | Conical                  | 0-20       | -               | -          | -              | -     | -           | -      | -       | 0.3  |
|                         |                 |                |                |                 |      |           |                          | 20         | 79              | -          | -              | -     | Full        | 11-20  | -       | -    |
| Frink (1985)            | Gothic          | 60             | 74             | 0               | 1.36 | 0         | Gothic                   | 30         | 74              | -          | Thin           | Thin  | Part        | 11-19  | 0       | 0    |
|                         |                 | -              | -              | -               | -    | -         | -                        | 40         | -               | -          | -              | -     | -           | 15-21  | -       | -    |
|                         |                 | -              | -              | -               | -    | -         | -                        | 30         | -               | -          | -              | Thick | Full        | 14,15  | -       | -    |
| Harrison (1982)         | Cranked Arrow + | 70             | 58             | 48              | 2.24 | 0         | Tapered Flap A           | 15-45      | 58              | -          | Thin           | -     | Part        | 15-25  | 0       | 0.65 |
|                         |                 | -              | -              | -               | -    | -         | Tapered Flap B           | 25-35      | -               | -          | -              | -     | -           | -      | -       | -    |
|                         |                 | -              | -              | -               | -    | -         | Tapered Flap C           | 30         | -               | -          | -              | -     | -           | -      | -       | -    |
|                         |                 | -              | -              | -               | -    | -         | Tapered Flap D           | 30         | -               | -          | -              | -     | -           | -      | -       | -    |
|                         |                 | -              | -              | -               | -    | -         | Tapered Flap E           | 30         | -               | -          | -              | -     | -           | -      | -       | -    |
|                         |                 | -              | -              | -               | -    | -         | Twisted Flap B           | 35/25      | -               | -          | -              | -     | -           | 20,25  | -       | -    |
|                         |                 | -              | -              | -               | -    | -         | -                        | 25/35      | -               | -          | -              | -     | -           | -      | -       | -    |
|                         |                 | -              | -              | -               | -    | -         | -                        | 40/30      | -               | -          | -              | -     | -           | -      | -       | -    |
|                         |                 | -              | -              | -               | -    | -         | -                        | 45/30      | -               | -          | -              | -     | -           | -      | -       | -    |
|                         |                 | -              | -              | -               | -    | -         | -                        | 35/45      | -               | -          | -              | -     | -           | -      | -       | -    |
|                         |                 | -              | -              | -               | -    | -         | -                        | 45/35      | -               | -          | -              | -     | -           | 20     | -       | -    |
|                         |                 | -              | -              | -               | -    | -         | Apex 2, Flap A           | 30         | -               | -          | -              | -     | -           | 20-25  | -       | -    |
|                         |                 | -              | -              | -               | -    | -         | Apex 3, Flap A           | -          | -               | -          | -              | -     | -           | -      | -       | -    |
|                         |                 | -              | 65             | 55              | 1.64 | -         | Tapered Flap A           | -          | -               | -          | -              | -     | -           | 20,25  | -       | -    |
|                         |                 | -              | 58             | 48              | 2.24 | -         | Tapered Flap B           | -          | -               | -          | -              | -     | -           | -      | -       | -    |
|                         |                 |                |                |                 |      |           |                          | 0-30       | -               | -          | -              | -     | -           | 25     | -       | -    |
| Harrison (1982b)        | Cranked Arrow + | 70             | 58             | 48              | 2.24 | 0         | Flap D, L. E. Droop      | 35         | 58              | 0-23       | Thin           | -     | Part        | 20-25  | 0       | 0.65 |
| Hoffler (1985)          | Delta           | 65             | -              | 0               | 1.87 | 0         | Conical/Tabbed           | 0-30       | 74              | 0-30       | Thin           | -     | Full        | 16     | 0       | 0.1  |
| Luckring, et al. (1982) | Delta           | 72             | -              | 0               | 1.30 | 0         | Conical                  | 13         | 78              | -          | Thin           | -     | Full        | 14     | 0       | 0.2  |
|                         |                 | 74             | -              | -               | 1.15 | -         | -                        | 0-25       | 79              | -          | -              | -     | -           | -      | -       | 0    |
|                         |                 | -              | -              | -               | -    | -         | -                        | 20         | 76-80           | -          | -              | -     | -           | -      | -       | -    |
|                         |                 | -              | -              | -               | -    | -         | -                        | 79         | -               | -          | -              | -     | -           | 11-20  | -       | -    |
|                         |                 |                |                |                 |      |           | Constant Chord           | -          | 74              | -          | -              | -     | -           | 14     | -       | 0.3  |
| Reddy (1981c)           | Delta           | 74             | -              | 0               | 1.15 | 0         | Constant Chord           | -30        | 74              | -          | Thin           | -     | Full        | 15-20  | 0       | 0    |
|                         |                 | -              | -              | -               | -    | -         | Tapered Chord            | 24         | 71.4            | -          | -              | -     | -           | 15-35  | -       | -    |
|                         |                 | -              | -              | -               | -    | -         | -                        | -60-35     | -               | -          | -              | -     | -           | 20.6   | -       | -    |

+ APTI/F-111 Planform and Camber



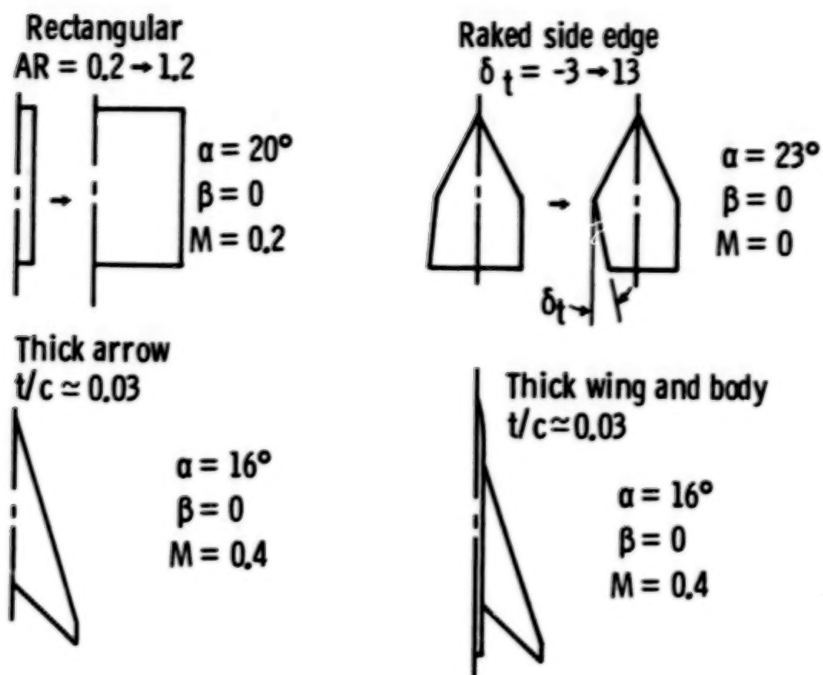


(a) flat wings



(b) cambered wings

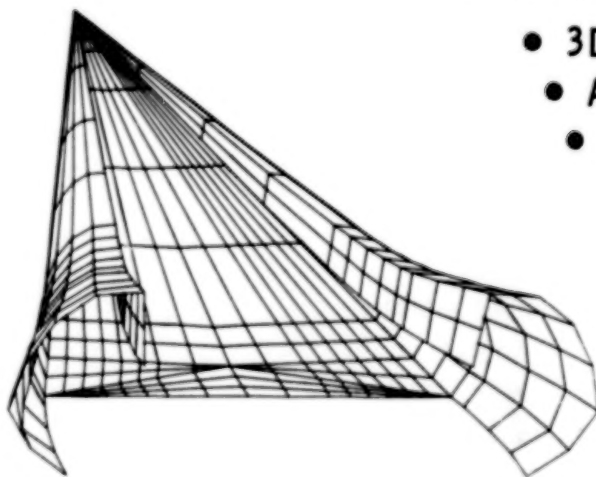
Figure 1.- Converged FVS parameter space. Published results.



(c) other wings

Figure 1.- Concluded.

### Vortex modeling $\rightarrow$ Real flow effects



- 3D pressure field
- Accurate forces and moments
- High  $-\alpha$  vortex lift loss
  - Vortex curvature
  - Vortex crowding
- Viscous flow extensions
  - Vortex breakdown
  - Secondary separation

Figure 2.- General solution features.

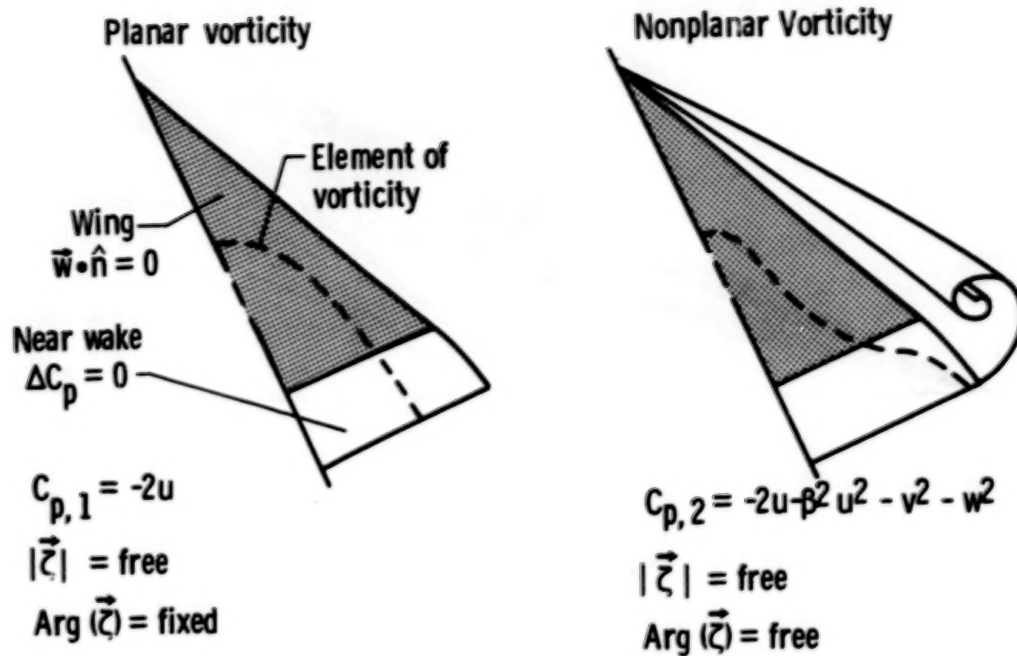
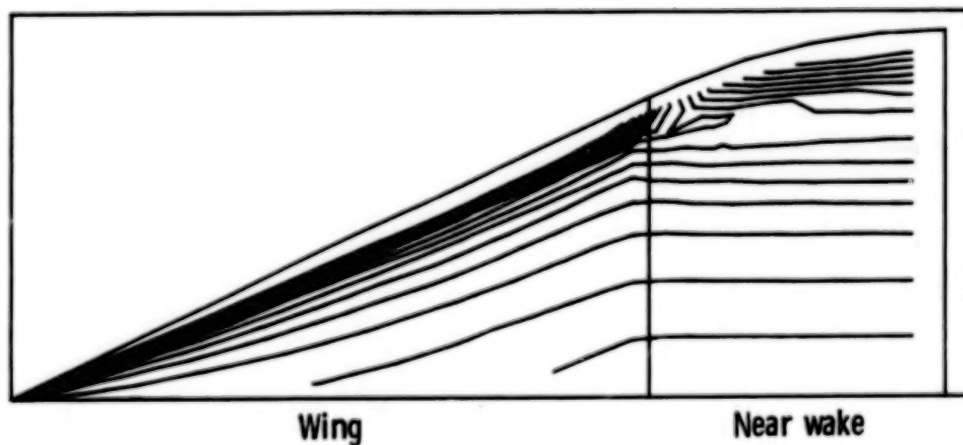
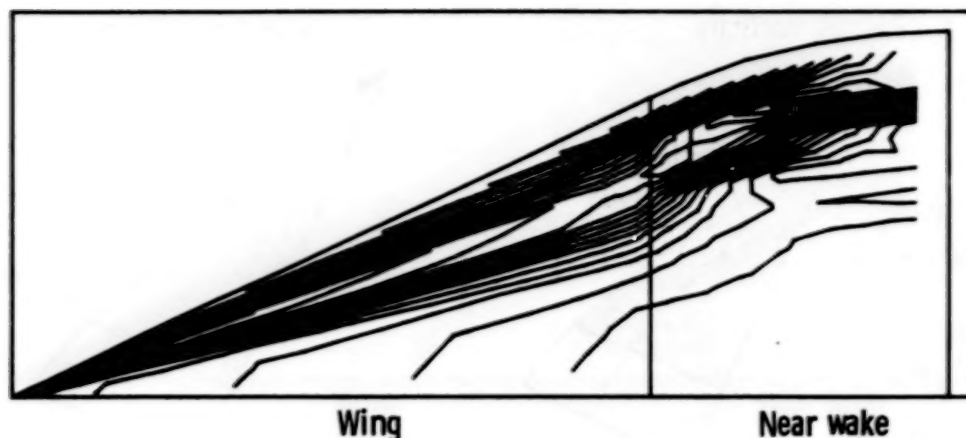


Figure 3.- Near-field wake attributes.



(a) attached flow

Figure 4.- Vorticity contours.  $\Lambda = 65^\circ$ ,  $\alpha = 15^\circ$ ,  $M = 0$ , increment = 0.1.



(b) vortex flow

Figure 4.- Concluded.

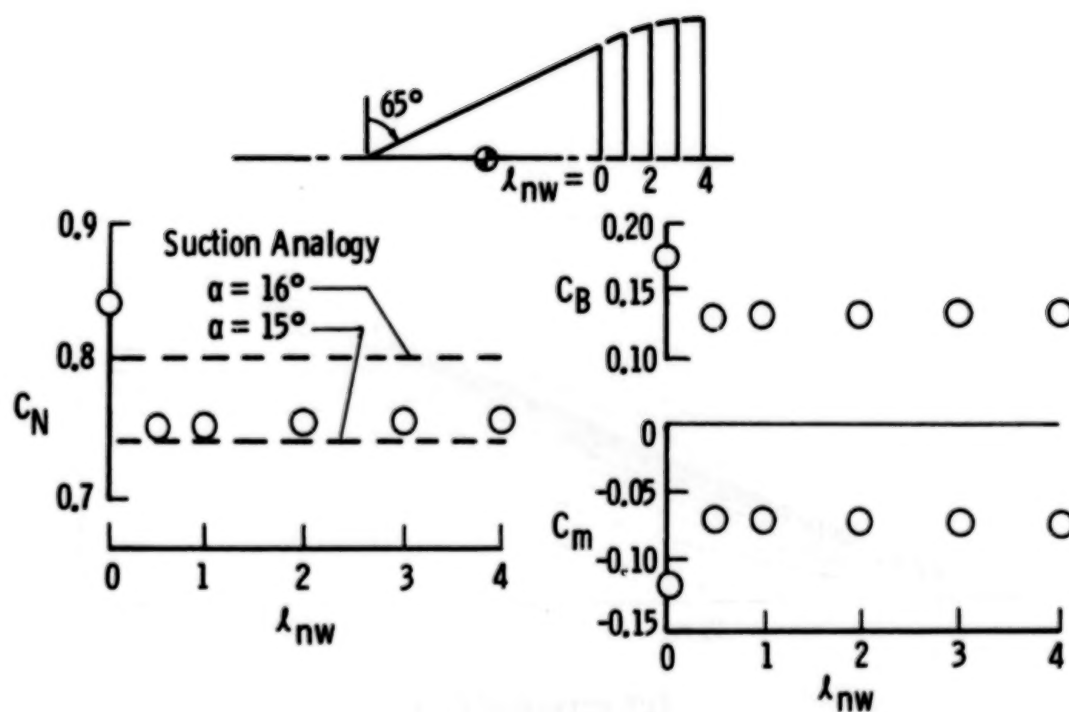


Figure 5.- Near-field wake length effects.  $\alpha = 15^\circ, M = 0$ .



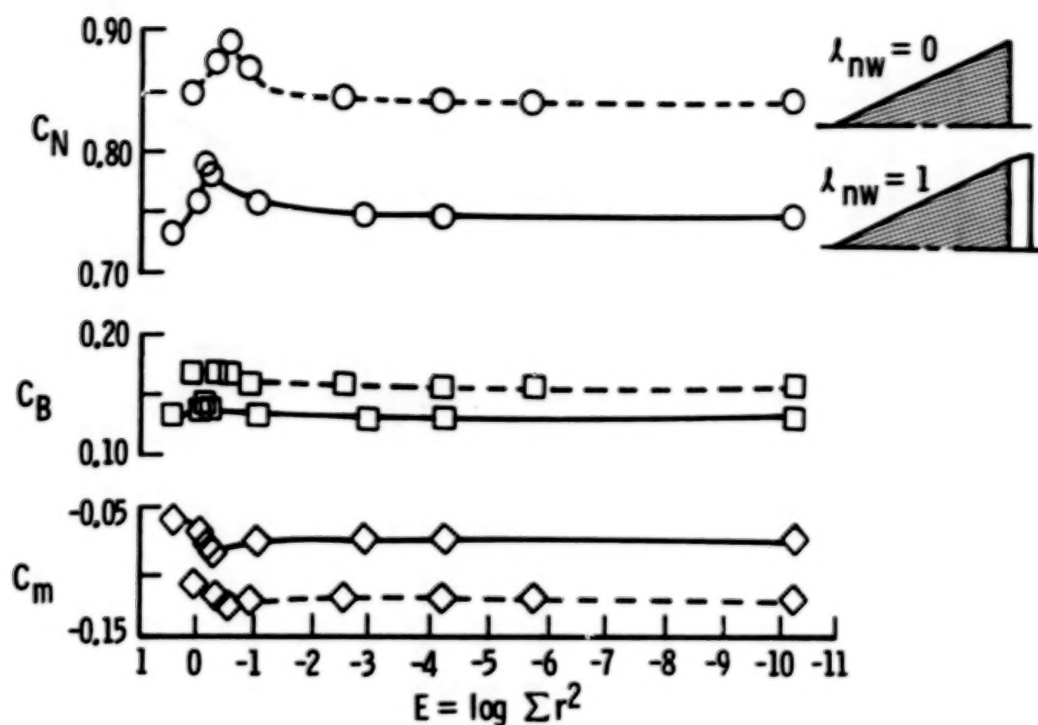


Figure 6.- Convergence histories.

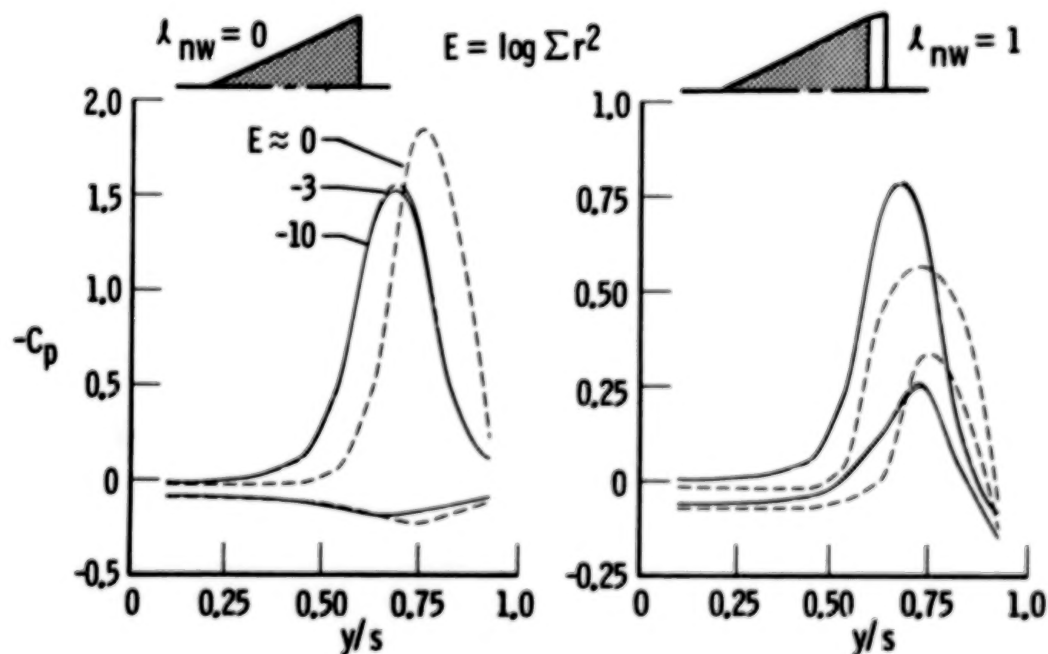


Figure 7.- Convergence effects on spanwise pressures.  $x/c_r = 0.975$ ,  $\Lambda = 65^\circ$ ,  $\alpha = 15^\circ$ ,  $M = 0$ .

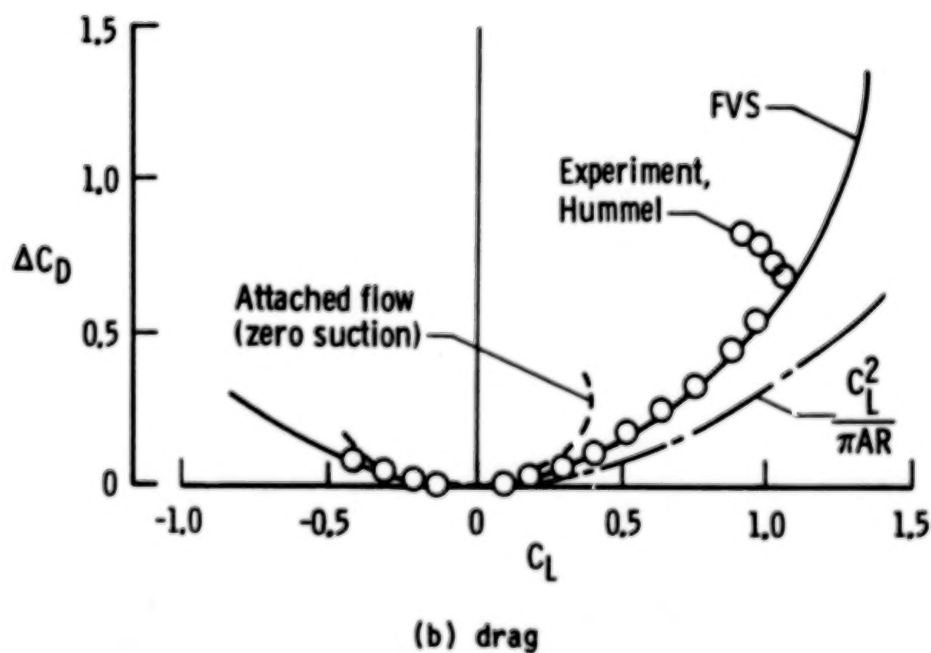
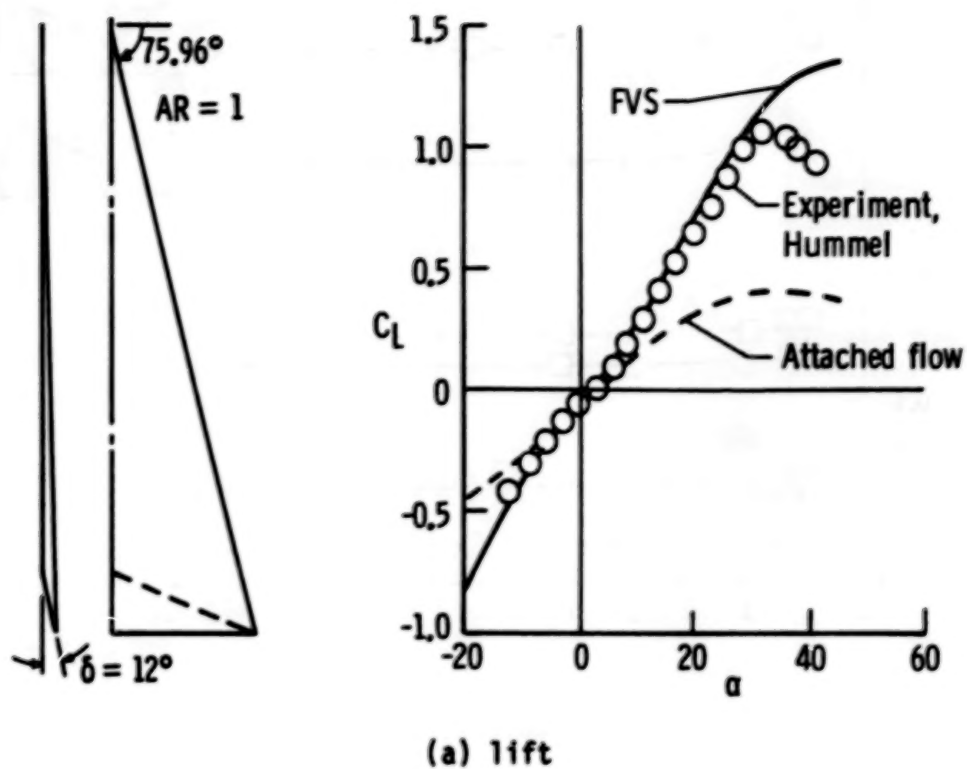
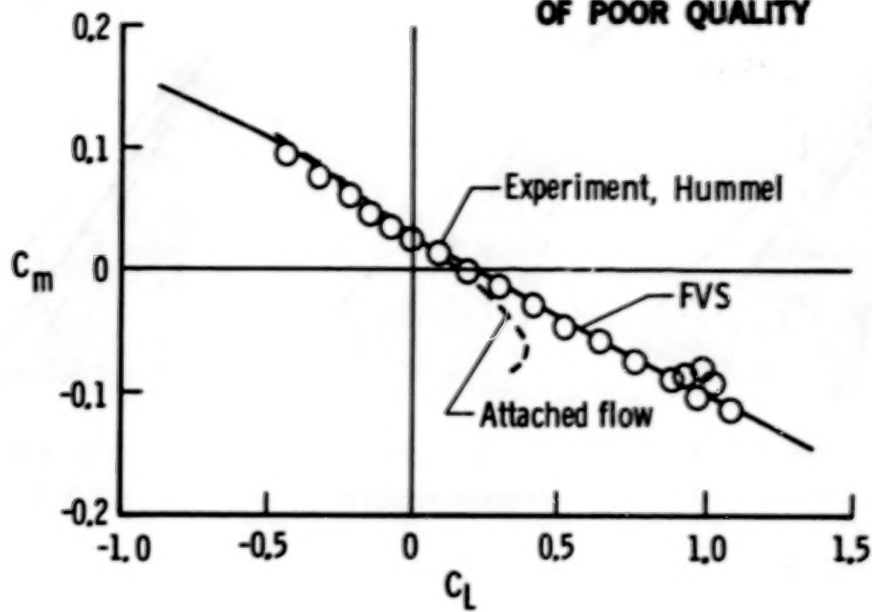


Figure 8.- Force and moment correlation for Hummel delta wing.

ORIGINAL PAGE IS  
OF POOR QUALITY



(c) pitching moment

Figure 8.- Concluded.

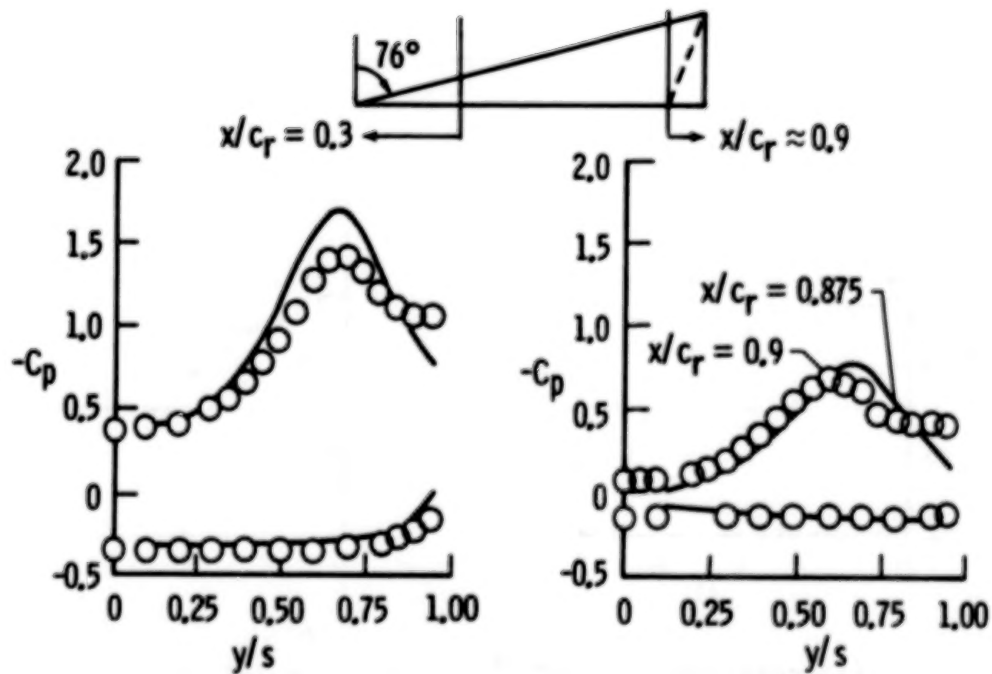


Figure 9.- Spanwise pressure correlation for Hummel delta wing.

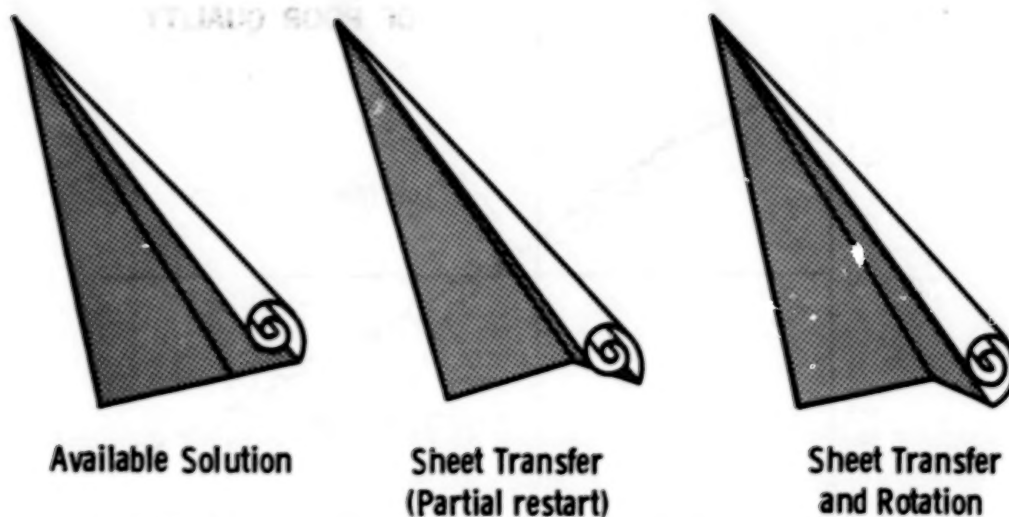
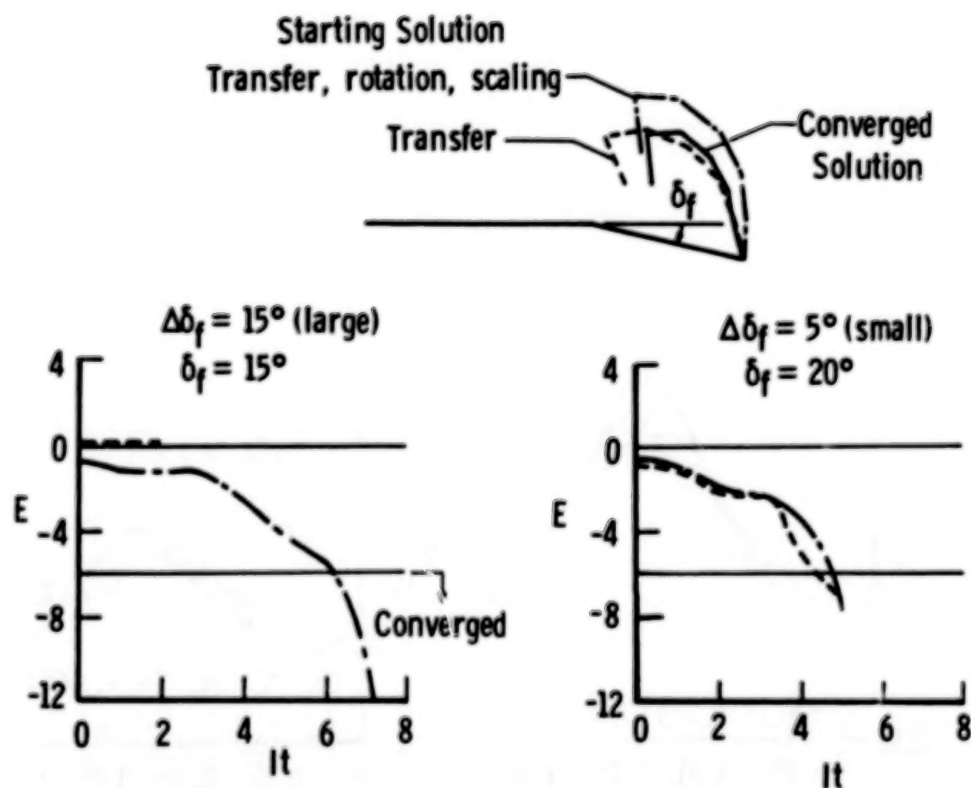
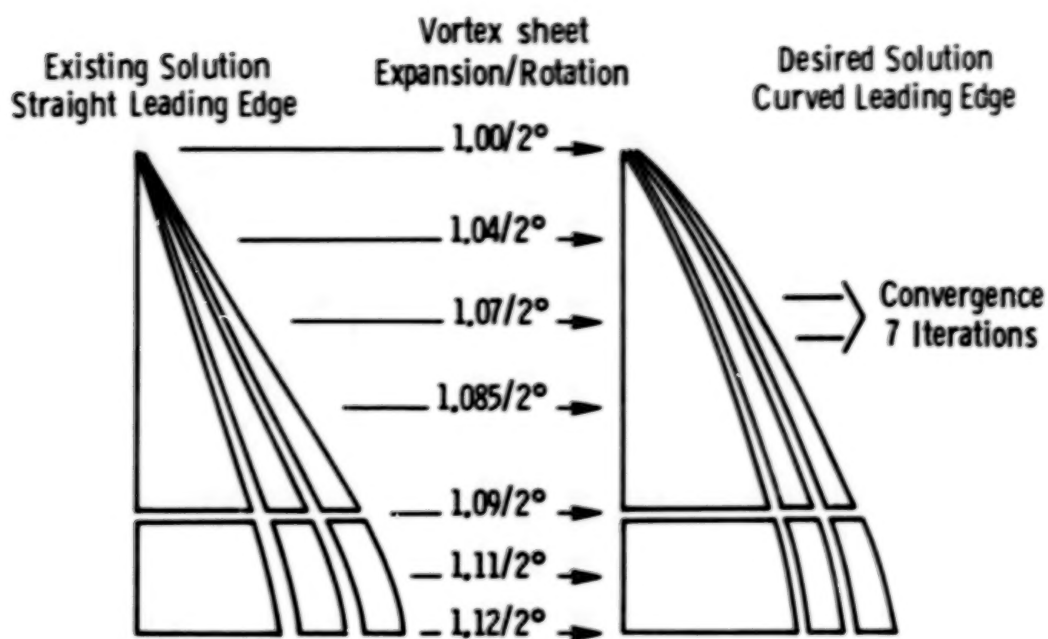


Figure 10.- Sheet rotation concept with partial restart.



(a) rotation;  $\Lambda = 65^\circ$ ,  $\Lambda_{h1} = 74^\circ$ ,  $\alpha = 16^\circ$ ,  $M = 0$

Figure 11.- Effect of vortex sheet manipulation.



(b) scaling;  $\Lambda = 74^\circ$ ,  $\alpha = 21^\circ$ ,  $M = 0$

Figure 11. Concluded.

Desired FVS solution :  
74° delta w/fuselage  
 $\delta_{le} = 40^\circ$   $\alpha = 21^\circ$

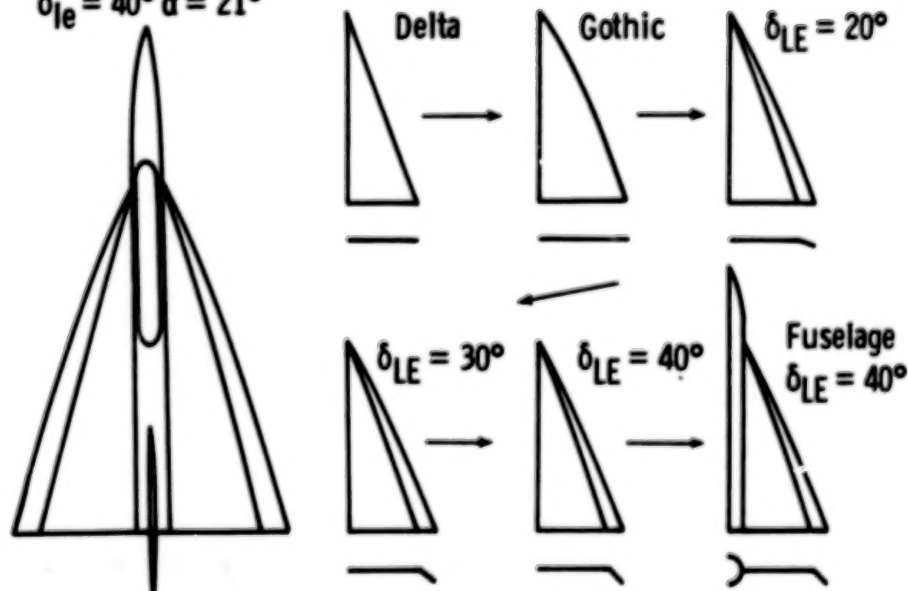


Figure 12.- Application of expanded restart to complex geometries.



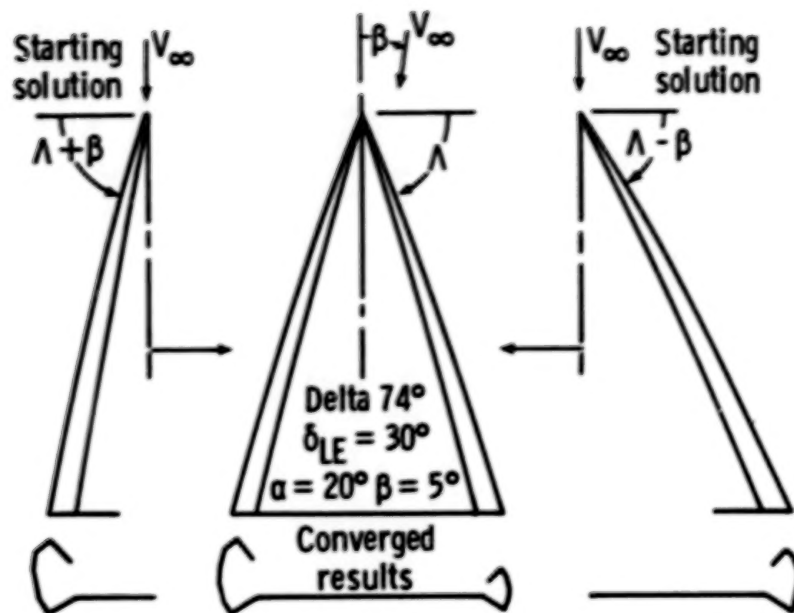
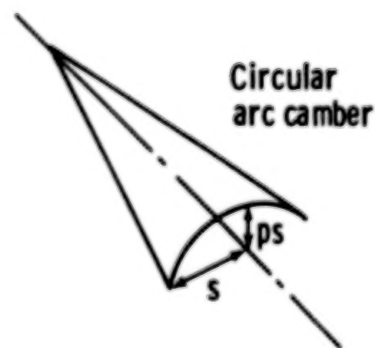


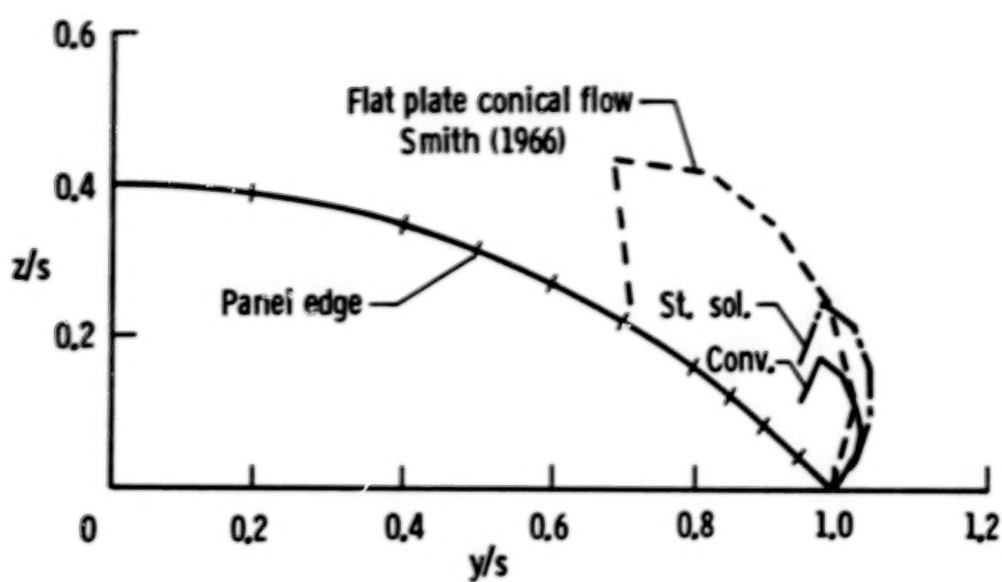
Figure 13.- Multiple vortex sheet partial restart.

- Attached flow analysis
  - $\alpha_{s0} = \alpha$  for smooth onflow
- Seek solution for small  $\Delta\alpha$ 
  - $\Delta\alpha = \alpha - \alpha_{s0}$
- Short near wake
- Vortex starting solution
  - size by conical flow at  $\Delta\alpha$
  - rotate by loading edge deflection

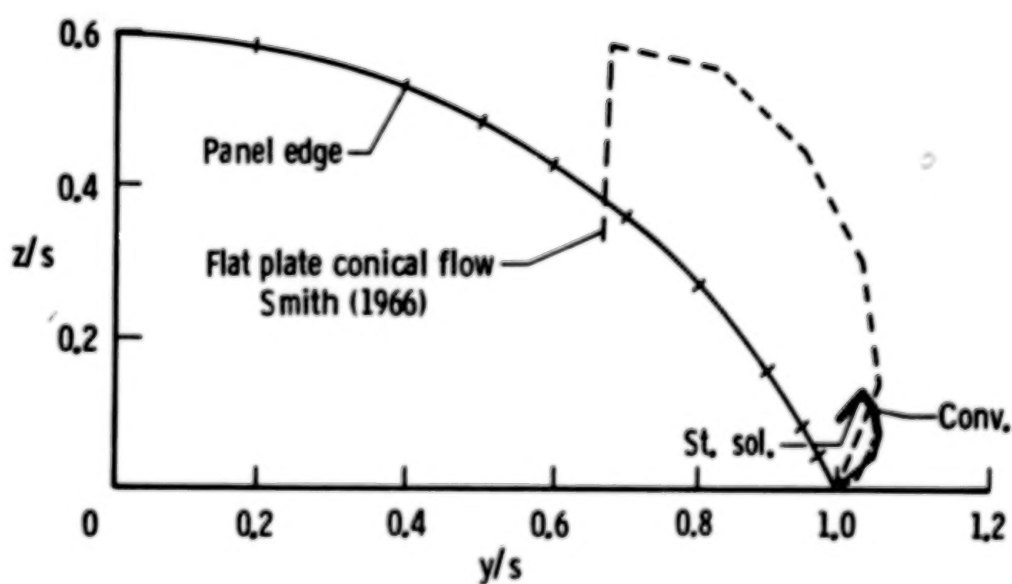


Barsby (1974)

Figure 14.- A direct approach for large camber.



(a)  $p = 0.4$ ,  $\alpha \approx 14^\circ$ ,  $\alpha_{50} \approx 9^\circ$



(b)  $p = 0.6$ ,  $\alpha = 20^\circ$ ,  $\alpha_{50} \approx 14^\circ$

Figure 15.- Converged results at trailing edge. AR = 1.

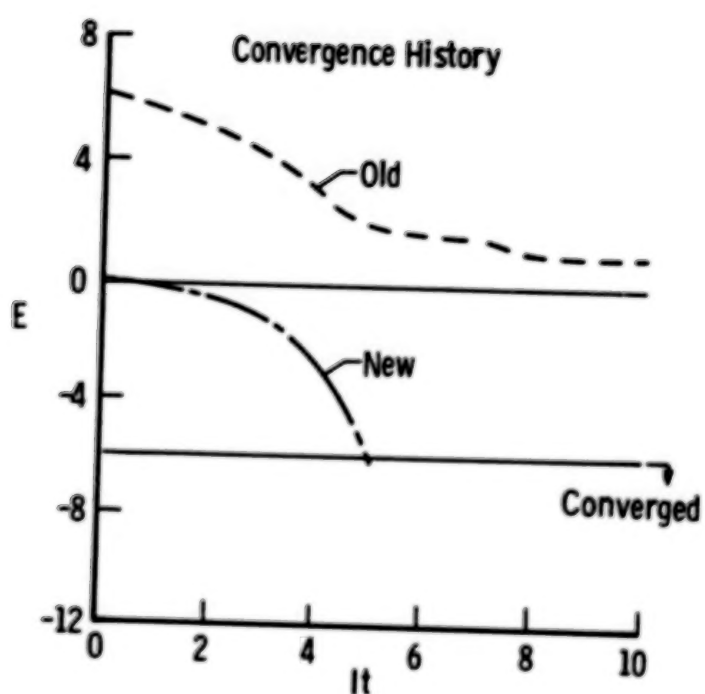


Figure 16.- Application for vortex flap.  $\alpha = 16^\circ$ .

A DIRECT AND INVERSE BOUNDARY LAYER  
METHOD FOR SUBSONIC FLOW OVER DELTA WINGS\*

Shawn H. Woodson and Fred R. DeJarnette  
North Carolina State University  
Raleigh, North Carolina

SUMMARY

A new inverse boundary layer method is developed and applied to incompressible flows with laminar separation and reattachment. Test cases for two-dimensional flows are computed and the results are compared with those of other inverse methods. One advantage of the present method is that the calculation of the inviscid velocities may be determined at each marching step without having to iterate.

The inverse method was incorporated with the direct method to calculate the incompressible, conical flow over a slender delta wing at incidence. The location of the secondary separation line on the leeward surface of the wing is determined and compared with experiment for a unit aspect ratio wing at 20.5 deg incidence. The viscous flow in the separated region was calculated using prescribed skin-friction coefficients.

INTRODUCTION

The flow field over slender, highly swept delta wings at moderate incidence is dominated by the presence of large counter-rotating, leading-edge vortices as shown in fig. 1. As the flow moves spanwise towards the leading edge, the adverse pressure gradient caused by the leading-edge vortices causes the boundary layer to separate along a secondary separation line, indicated in fig. 2.

A direct boundary layer method (one in which the external pressure is prescribed from an inviscid calculation or experiment) may be used to determine the location of the secondary separation line (ref. 1). However, in order to continue the solution from the secondary separation line to the leading-edge using boundary layer theory, an inverse method (one in which the wall shear or displacement thickness is specified) must be employed.

Inverse methods have been used by numerous authors since the early work of Catherall and Mangler (ref. 2). Catherall and Mangler used a prescribed displacement thickness distribution to drive a boundary layer method in which the external pressure was determined as part of the solution. In this manner, they were able to obtain a regular solution at separation. However, their numerical scheme developed instabilities in the reversed flow region and the integration was continued only by reducing the convergence criteria at each marching step. This problem of reversed-flow velocity profiles led directly to the FLARE approximation of Reyhner and Flugge-Lotz (ref. 3). In the FLARE approximation the streamwise

\* Research supported by NASA Langley Cooperative agreement NCCI-22.

convection of momentum is set equal to zero in the reversed flow region and the calculations proceed with the usual forward marching procedure.

For two-dimensional flows, Klineberg and Steger (ref. 4), Carter (ref. 5) and Cebeci et al. (ref. 6) have developed globally iterative schemes for flows with separation and reattachment. In those methods either the wall shear or displacement thickness is specified and the pressure is obtained iteratively using successive-under-relaxation schemes. Semi-inverse methods have been developed for interacting an inverse boundary layer method with an inviscid solution by Le Balleur (ref. 7), Carter (ref. 8), Kwon and Pletcher (ref. 9) and Veldman (ref. 10) among others. In these methods, the inviscid calculation proceeds in the direct manner with the viscous calculation performed in the inverse mode. Thus, an edge velocity is determined in both calculations which must be the same after convergence.

In three-dimensional flow calculations, several possible combinations of the viscous parameters could be used to drive an inverse method (e.g., CFX, CFY or DTX, DTY). However, Edwards and Carter (ref. 11) have shown that specifying the three-dimensional displacement surface and the component of vorticity normal to the surface leads to an elliptic set of equations and departure solutions for forward marching schemes.

In this paper, a new inverse boundary layer method is developed for separated flows. The method is non-iterative based on a predictor-corrector linearization of the discretized governing equations. For two-dimensional flows, the new method is used to compute the test case of Klineberg and Steger (ref. 4) for a specified wall shear and that of Carter (ref. 5) for the displacement thickness prescribed. The method is also applied to the incompressible, conical, laminar boundary layer flow on the leeward surface of a slender delta wing at incidence. The inviscid solution for the delta wing is determined using the Free Vortex Sheet (FVS) code which was originally developed at Boeing (ref. 12) and significantly enhanced by Luckring and others (refs. 13, 14) at NASA Langley. The viscous solution for the delta wing is determined in the direct mode until the secondary separation line is encountered ( $CFY < 0$ ), then the calculations are continued in the inverse mode to the leading edge by specifying the skin-friction coefficients to be constant and equal to their values at separation ( $CFX > 0$ ,  $CFY < 0$ ). The calculations are performed on a unit aspect ratio wing at 20.5 deg incidence which corresponds to the experiment of Hummel (ref. 15).

## ANALYSIS

### Governing Equations

For steady, incompressible flows, the three-dimensional laminar boundary layer equations in non-dimensional Cartesian coordinates are:

$$\frac{\partial u}{\partial x} + \frac{\partial v}{\partial y} + \frac{\partial w}{\partial z} = 0 \quad (1)$$

$$u \frac{\partial u}{\partial x} + v \frac{\partial u}{\partial y} + w \frac{\partial u}{\partial z} = u_e \frac{\partial u_e}{\partial x} + v_e \frac{\partial u_e}{\partial y} + \frac{\partial^2 u}{\partial z^2} \quad (2)$$



$$u \frac{\partial v}{\partial x} + v \frac{\partial v}{\partial y} + w \frac{\partial v}{\partial z} = u_e \frac{\partial v_e}{\partial x} + v_e \frac{\partial v_e}{\partial y} + \frac{\partial^2 v}{\partial z^2} \quad (3)$$

The velocity components  $u$ ,  $v$ , and  $w$  are in the  $x$ ,  $y$ , and  $z$ -directions, respectively, where  $x$  is in the streamwise direction,  $y$  is spanwise and  $z$  is normal to the  $x$ - $y$  plane. The Reynolds number has been removed from eqs. (1)-(3) by defining  $x = \bar{x}/\bar{L}$ ,  $y = \bar{y}/\bar{L}$ ,  $z = \sqrt{\text{Re}} \bar{z}/\bar{L}$ ,  $u = \bar{u}/\bar{U}_0$ ,  $v = \bar{v}/\bar{U}_0$  and  $w = \sqrt{\text{Re}} \bar{w}/\bar{U}_0$ . The super-script bars indicate dimensional quantities and  $\text{Re} = \bar{U}_0 \bar{L}/\bar{\nu}$ . The complete derivation of eqs. (1)-(3) is provided in reference 16. The boundary conditions on eqs. (1)-(3) are:

$$\text{at } z = 0 : u = v = w = 0$$

$$\text{and as } z \rightarrow \infty : u \rightarrow u_e, \quad v \rightarrow v_e \quad (4)$$

### Two-dimensional Flow

For two-dimensional flow,  $v = 0$  and eqs. (1) and (3) are transformed by defining,

$$X = x \quad \eta = \left( \frac{u_e}{x} \right)^{1/2} z \quad (5)$$

along with a stream function,  $\psi$ , where

$$u = \frac{\partial \psi}{\partial z} \quad \text{and} \quad w = - \frac{\partial \psi}{\partial x} \quad (6)$$

Define a parameter  $f$ , such that

$$\psi = (U_e X)^{1/2} f \quad (7)$$

Using eqs. (5) and (7) in eq. (6) yields,

$$\frac{u}{u_e} = \frac{\partial f}{\partial \eta} = F(\eta) \quad (8)$$

With eqs. (5)-(8), eq. (2) may be written as,

$$\frac{\partial^2 F}{\partial \eta^2} + \frac{\partial F}{\partial \eta} \left[ X \frac{\partial f}{\partial X} + \left( \frac{m+1}{2} \right) f \right] + m(1-f^2) = XF \frac{\partial F}{\partial X} \quad (9)$$

$$\text{where } m = \frac{X}{u_e} \frac{du_e}{dX} \quad (10)$$

The boundary conditions for eq. (9) are

$$\eta = 0 : f = F = 0, \quad \eta = \eta_e : F = 1.0 \quad (11)$$

### Conical Flow Over Delta Wings

For the delta wing a body-oriented coordinate system is defined through the transformation,

$$X = x, \quad Y = (y/x) \tan \Lambda, \quad Z = z/x \quad (12)$$

where  $\Lambda$  is the sweep angle of the delta wing. Define transformed velocity components by,

$$U = u, \quad V = v \tan \Lambda - uY, \quad W = w - uZ \quad (13)$$

Using eqs. (12) and (13) in eq. (1) it becomes,

$$\frac{\partial}{\partial X} (X^2 U) + \frac{\partial}{\partial Y} (XV) + \frac{\partial}{\partial Z} (XW) = 0 \quad (14)$$

Next define two stream functions,  $\psi$  and  $\phi$  as

$$X^2 U = \frac{\partial \psi}{\partial Z}, \quad XV = \frac{\partial \phi}{\partial Z}, \quad XW = -\frac{\partial \psi}{\partial X} - \frac{\partial \phi}{\partial Y} \quad (15)$$

and a boundary layer variable,  $\eta$ , by

$$\eta = (U_e X)^{1/2} Z \quad (16)$$

Introduce two functions  $f(X, Y, \eta)$  and  $g(X, Y, \eta)$  where,

$$\psi = (U_e X)^{1/2} X f, \quad \phi = \left(\frac{X}{U_e}\right)^{1/2} v_e g \quad (17)$$

For conical inviscid flow, fluid properties do not vary along rays; therefore, for any flow parameter,  $H$ ,  $\partial H / \partial X = 0$ . Then using eqs. (12), (16) and (17) in eq. (15), the following are obtained:

$$\frac{U}{U_e} = \frac{\partial f}{\partial \eta} = F(Y, \eta) \quad (18a)$$

$$\frac{V}{V_e} = \frac{\partial g}{\partial \eta} = G(Y, \eta) \quad (18b)$$

Equation (18) may be written as the vector equation,

$$\frac{\partial h}{\partial \eta} = H \quad (19)$$

$$\text{where } h = \begin{bmatrix} f \\ g \end{bmatrix} \quad \text{and} \quad H = \begin{bmatrix} F \\ G \end{bmatrix} \quad (20)$$

With eqs. (12)-(20), eqs. (2) and (3) may be combined and written as,

$$\frac{\partial^2 H}{\partial \eta^2} + \sigma \frac{\partial H}{\partial \eta} + \frac{V_e}{U_e} \left( \frac{\partial g}{\partial Y} \frac{\partial H}{\partial \eta} - G \frac{\partial H}{\partial Y} \right) = \Gamma \quad (21)$$

$$\text{where } \sigma = 1.5f + \beta g \quad (22)$$

$$\text{and } \Gamma = \begin{bmatrix} \beta_u(FG-1) \\ (FG-1) + \beta_v(G^2-1) \end{bmatrix} \quad (23)$$

The boundary conditions for eqs. (19) and (21) are:

$$\eta = 0 : \quad h = H = \begin{bmatrix} 0 \\ 0 \end{bmatrix}, \quad \eta = \eta_e : \quad H = \begin{bmatrix} 1 \\ 1 \end{bmatrix} \quad (24)$$

Equations (19) and (21) may be solved in the direct mode, using prescribed inviscid velocities, to calculate viscous properties such as skin-friction coefficients and integral thicknesses. However, in the inverse mode, the inviscid velocities are unknown functions and must therefore be eliminated from the left-hand side of eq. (21). This is accomplished through the additional transformation,

$$Y^* = \int_0^Y \left( \frac{U_e}{V_e} \right) dY \quad (25)$$

Using eq. (25) in eq. (21), the latter becomes,

$$\frac{\partial^2 H}{\partial \eta^2} + \sigma \frac{\partial H}{\partial \eta} + \frac{\partial g}{\partial Y^*} \frac{\partial H}{\partial \eta} - G \frac{\partial H}{\partial Y^*} = r \quad (26)$$

$$\text{where now, } \beta_u = \frac{1}{U_e} \frac{dU_e}{dY^*}, \quad \beta_v = \frac{1}{V_e} \frac{dV_e}{dY^*} \quad (27)$$

#### Numerical Procedure

The governing equations are differenced using the half-implicit finite-difference scheme of Matsuno (ref. 17). The scheme is second-order accurate and unconditionally stable, and was demonstrated by Woodson and DeJarnette (ref. 18) to yield accurate numerical results when compared to the exact solution of the three-dimensional boundary layer equations for parabolic flow over a moving flat plate.

For fully three-dimensional problems the scheme has the advantage that the crossflow derivative formulas are formed independent of the direction of the crossflow. Further, the scheme is non-iterative based on a predictor-corrector linearization, a convenient feature for inverse boundary layer methods. For any flow parameter,  $H$ , the notation  $H_{j,k} = H(Y_j^*, \eta_k)$  is used where,

$$\begin{aligned} Y_{j+1}^* &= Y_j^* + \Delta Y^*, & j &= 1, 2, \dots, JMAX \\ \eta_{k+1} &= \eta_k + \Delta \eta, & k &= 1, 2, \dots, KMAX \end{aligned} \quad (28)$$

Central difference operators are defined by:

$$\Delta_\eta H_{j,k} = (H_{j,k+1} - H_{j,k-1}) / \Delta \eta \quad (29)$$

$$\Delta Y^* H_{j+1/2,k} = (H_{j+1,k} - H_{j,k}) / \Delta Y^* \quad (30)$$

$$\delta_\eta H_{j,k-1/2} = (H_{j,k} - H_{j,k-1}) / \Delta \eta \quad (31)$$

$$\delta_\eta^2 H_{j,k} = (H_{j,k+1} - 2H_{j,k} + H_{j,k-1}) / \Delta \eta^2 \quad (32)$$

and a backward difference operator for the predictor stage by,

$$\nabla Y^* H_{j+1/2,k} = 2(H_{j+1/2,k} - H_{j,k}) / \Delta Y^* \quad (33)$$

With the operators defined above, eqs. (19) and (26) become at the predictor stage, respectively,

$$\delta_\eta h_{j+1/2,k-1/2} = (H_{j+1/2,k} + H_{j+1/2,k-1}) / 2 \quad (34)$$

$$\delta_\eta^2 H_{j+1/2,k} + \sigma_{j,k} \Delta_\eta H_{j,k} + \nabla Y^* g_{j+1/2,k} \Delta_\eta H_{j,k} - G_{j,k} \nabla Y^* H_{j+1/2,k} = \Gamma_{j,k} \quad (35)$$

at the corrector stage they are,

$$\delta_\eta h_{j+1,k-1/2} = (H_{j+1,k} + H_{j+1,k-1}) / 2 \quad (36)$$

$$\delta_\eta^2 (H_{j+1,k} + H_{j,k}) / 2 + \sigma_{j+1/2,k} \Delta_\eta H_{j+1/2,k} \quad (37)$$

$$+ \Delta Y^* g_{j+1/2,k} \Delta_\eta H_{j+1/2,k} - G_{j+1/2,k} \Delta Y^* H_{j+1/2,k} = \Gamma_{j+1/2,k}$$

Equations (34)-(37) may be written in the block tridiagonal matrix form,

$$h_k = h_{k-1} + \frac{\Delta \eta}{2} (H_k + H_{k-1}) \quad (38a)$$

$$- H_{k-1} + B_k H_k - H_{k+1} + a_k h_k = D_k \quad (38b)$$

where  $a_k$  and  $B_k$  are  $2 \times 2$  coefficient matrices and  $D_k$  is a vector. Equations (38) are linear tridiagonal matrix equations and may be solved using a block form of the Davis modified tridiagonal algorithm (ref. 19).



# Inverse Method

The term  $D_k$  in eq. (38b) contains terms with both  $\beta_u$  and  $\beta_v$  as coefficients. However, in the inverse mode these parameters are unknowns which must be determined from the solution. Taking advantage of the fact that eq. (38) is linear, one may write,

$$D_k = D_k^{(0)} + \beta_u D_k^{(1)} + \beta_v D_k^{(2)} \quad (39a)$$

$$H_k = H_k^{(0)} + \beta_u H_k^{(1)} + \beta_v H_k^{(2)} \quad (39b)$$

$$\text{and } h_k = h_k^{(0)} + \beta_u h_k^{(1)} + \beta_v h_k^{(2)} \quad (39c)$$

where the unknowns  $\beta_u$  and  $\beta_v$  are given by eq. (27). The boundary conditions associated with eq. (39) are:

$$\text{at } \eta = 0 : h_1^{(1)} = H_1^{(1)} = 0, \quad i = 0, 1, 2 \quad (40)$$

$$\text{and at } \eta = \eta_e : H_{KMAX}^{(0)} = 1, \quad H_{KMAX}^{(1)} = 0, \quad i = 1, 2$$

Carrying out the operations of eqs. (29)-(33), one may equate like powers of  $\beta_u$  and  $\beta_v$  to obtain

$$h_k^{(1)} = h_{k-1}^{(1)} + \frac{\Delta\eta}{2} (H_k^{(1)} - H_{k-1}^{(1)}), \quad i = 0, 1, 2 \quad (41a)$$

$$- H_{k-1}^{(1)} + B_k H_k^{(1)} - H_{k+1}^{(1)} + a_k h_k^{(1)} = D_k^{(1)}, \quad i = 0, 1, 2 \quad (41b)$$

This system of equations may be solved to obtain  $h_k^{(1)}$  and  $H_k^{(1)}$  for  $i = 0, 1, 2$ . The parameters  $U_e$  and  $V_e$  are then determined from either the specified wall shear stresses or integral thicknesses. A streamwise integral thickness is defined by,

$$\bar{\delta}_X^* = \int_0^\infty \left(1 - \frac{U}{U_e}\right) dz \quad (42)$$

Using eqs. (16) and (18a) in eq. (42) and integrating gives,

$$DTX = \frac{\bar{\delta}_X^*}{\bar{x}} \sqrt{Re_X} = \eta_e - f(\eta_e) \quad (43a)$$

In a similar manner,

$$DTY = \frac{\bar{\delta}_{Y^*}^*}{\bar{x}} \sqrt{Re_X} = \eta_e - g(\eta_e) \quad (43b)$$

With eq. (39c), eq. (43) may be written as,

$$DTX = \eta_e - f_{KMAX}^{(0)} - \beta_u f_{KMAX}^{(1)} - \beta_v f_{KMAX}^{(2)} \quad (44a)$$

$$DTY = \eta_e - g_{KMAX}^{(0)} - \beta_u g_{KMAX}^{(1)} - \beta_v g_{KMAX}^{(2)} \quad (44b)$$

Equations (44a) and (44b) are solved to obtain  $\beta_u$  and  $\beta_v$ . Now, returning to eq. (27) and taking second-order differences about the point  $j+1/2$ ,

$$\beta_u (U_{e_{j+1}} + U_{e_j}) = \frac{2}{\Delta Y^*} (U_{e_{j+1}} - U_{e_j})$$

Then it follows that

$$U_{e_{j+1}} = U_{e_j} \left( 1 + \frac{2}{\beta_u \Delta Y^*} \right) / \left( 1 - \frac{2}{\beta_u \Delta Y^*} \right) \quad (45a)$$

$$V_{e_{j+1}} = V_{e_j} \left( 1 + \frac{2}{\beta_v \Delta Y^*} \right) / \left( 1 - \frac{2}{\beta_v \Delta Y^*} \right) \quad (45b)$$

Next, consider if the wall shear were perscribed. The surface skin-friction coefficients are defined by

$$C_{fX} = \bar{v} \left( \frac{\partial \bar{U}}{\partial z} \right)_w / \frac{1}{2} \bar{U}_e^2, \quad C_{fY^*} = \bar{v} \left( \frac{\partial \bar{V}}{\partial z} \right)_w / \frac{1}{2} \bar{U}_e \bar{V}_e \quad (46)$$

Using eq. (5) in eq. (46) one obtains,

$$CFX = C_X \sqrt{Re_X} = 2 \left( \frac{\partial F}{\partial \eta} \right)_w \quad (47a)$$

$$CFY = C_{fY^*} \sqrt{Re_x} = 2 \left( \frac{\partial G}{\partial \eta} \right)_w \quad (47b)$$

Using second-order accurate difference expressions for the derivatives in eq. (47) yields,

$$CFX = \frac{18F_2 - 9F_3 + 2F_4}{3\Delta\eta} \quad (48a)$$

$$CFY = \frac{18G_2 - 9G_3 + 2G_4}{3\Delta\eta} \quad (48b)$$

Substituting eq. (39b) into eq. (48) gives two equations for the two unknowns,  $\beta_u$  and  $\beta_v$ . An advantage of the present method over some earlier methods (refs. 4-6) is that the solution for  $\beta_u$  and  $\beta_v$  is obtained without column iteration, as opposed to using an under-relaxation scheme. For regions of reversed flow the FLARE approximation is made at the predictor stage,

$$G \frac{\partial H}{\partial Y^*} = 0 \quad (49a)$$

while at the corrector stage,

$$G \frac{\partial H}{\partial Y^*} = G_{j+1/2,k} \left( \frac{H_{j+1/2,k} - H_{j,k}}{\Delta Y^*/2} \right) \quad (49b)$$

Equation (49) insures diagonal dominance of the Davis modified algorithm in the reversed flow region. Note that eq. (49) reduces the accuracy of the finite-difference method to first order. Carter (ref. 5) added an artificial "time-like" term to the  $B_k$  term in eq. (38b) to ensure unconditional diagonal dominance in his solution algorithm. For the cases computed thus far, no instabilities were encountered in the reversed flow region when evaluating the convective derivatives according to eq. (49).

## RESULTS AND DISCUSSION

### Two-dimensional Flow

Calculations using the inverse boundary layer method are first discussed for flow over a circular cylinder. The inviscid solution for flow over a circular cylinder is given from potential theory by,

$$u_e = 2 \sin \theta \quad (50)$$

where  $\theta$  is the angle measured with respect to the  $x$  axis which defines the cylinder ( $0 < \theta < \pi$ ). The boundary layer was computed in the direct mode until separation was encountered at  $\theta = 104.5$  deg and then the calculations were continued in the inverse mode by specifying the skin-friction coefficient to be constant and equal to its value one marching step beyond separation ( $CFX = 0$  or slightly negative). Let  $f$  in eq. (8) and  $F$  in eq. (9) be written as,

$$f_k = f_k^{(0)} + mf_k^{(1)} \quad (51a)$$

$$F_k = F_k^{(0)} + mF_k^{(1)} \quad (51b)$$

with corresponding boundary conditions,

$$\text{at } \eta = 0 : f_1^{(1)} = F_1^{(1)} = 0, \quad i = 0, 1 \quad (52)$$

$$\text{and at } \eta = \eta_e : F_{KMAX}^{(0)} = 1, \quad F_{KMAX}^{(1)} = 0$$

After substituting eq. (51) into eq. (9), two separate equations result; one for the variables with superscript (0) and another for superscript (1). After solving these two equations, the value of  $m$  can be calculated by substituting eq. (51) into eq. (48a). The values of  $m$  can then be used to numerically calculate  $u_e$  at each marching station. The resulting edge velocity is shown in fig. 3. The edge velocity from the inverse calculation departs tangentially from the potential flow curve at the separation point and  $\theta = \pi$  is no longer a stagnation point. The inverse method could be used to calculate the edge velocity over the entire cylinder provided the wall shear or displacement thickness distribution is known.

Klineberg and Steger (ref. 4) constructed a test case for a flow with separation and reattachment by prescribing the skin-friction distribution as,

$$CFX = \frac{.664}{12} (X-2)(X-6) = \tau_1, \quad X < 2, \quad X > 6 \quad (53)$$

$$CFX = \tau_1 [1 + \hat{a}(X-2)(X-6)], \quad 2 < X < 6$$

where  $\hat{a}$  is a given parameter. The resulting pressure gradient parameter,  $m$ , for  $\hat{a} = 0.225$  was calculated and is compared to that which was determined by Klineberg and Steger in fig. 4. Klineberg and Steger required between 400 to 800 iterations using a point successive-under-relaxation scheme for the calculation of  $m$  while the present results were obtained with one downstream pass. The corresponding displacement thickness and edge velocity for this case are given in fig. 5, and velocity profiles at three marching stations are shown in fig. 6. It was found that for

attached flow the profile for  $F_k^{(1)}$  was primarily positive, while for separated flow the majority of the  $F_k^{(1)}$  profiles were negative.

A second test case is that of Carter (ref. 5) in which the displacement thickness is prescribed according to the relation,

$$DTX = a_1 + a_2(X-X_0) + a_3(X-X_0)^2 + a_4(X-X_0)^3, \quad X < X_0$$

$$DTX = \hat{a}_1 + \hat{a}_2(X-X_1) + \hat{a}_3(X-X_1)^2 + \hat{a}_4(X-X_1)^3, \quad X_1 < X < X_2$$
(54)

where  $X_0 = 1.065$ ,  $X_1 = 1.35$ ,  $X_2 = 1.884$  and the values of the  $a$ 's are determined such that at  $X = X_0$  the value and slope of the displacement thickness match the Blasius flat plate distribution, and at  $X = X_1$ , DTX reaches a maximum value. The case identified by Carter as Case B has a maximum displacement thickness of 8.6 and its distribution is presented in fig. 7a along with the resulting skin-friction distribution in fig. 7b. The calculated value of  $m$  for this case is compared with Carter's results in fig. 8a. Carter also developed an "approximate forward marching" technique in addition to his globally iterative method, which employs the FLARE approximation. Both of his methods, however, used an under-relaxation scheme for the calculation of  $m$ . For the grid indicated in fig. 8, Carter's globally iterative scheme converged in 130 iterations and his forward marching procedure required an average of 41 column iterations at each marching step. The present method required only one downstream pass. The edge velocity is presented in fig. 8b.

This test case has a more extensive separated flow region than the Klineberg and Steger case with the approach to separation and reattachment much steeper. Note that  $m$  reaches a relative minimum just prior to separation and reattachment which satisfies Meksyn's criterion (ref. 20) for a regular solution. Velocity profiles at two  $x$ -locations are given in fig. 9. At the point  $X = 1.393$ , nearly half of the profile is in the reversed flow region, however, the magnitude of the reversed flow velocity is small compared to the edge value. For this test case, the maximum negative value of  $u$  is about one-tenth of  $u_e$ .

#### Conical Flow Over Delta Wings

The inviscid solution for the Hummel delta wing at 20.5 deg incidence was determined using the Free Vortex Sheet (FVS) theory (refs. 12-14). The FVS code solves the linearized Prandtl-Glauert equation for potential flow. It represents the wing, wake, and rolled-up vortex sheets by continuous quadratic doublet sheet distributions and the vortex core by a line distribution of vortices. Detailed pressure distributions as well as overall forces and moments are predicted by the FVS code; however, no effort is made to model the secondary vortices in the inviscid calculation.

The viscous calculations were begun in the direct mode beginning at the reattachment line (which was found to be located along the wing centerline for this case) and marched spanwise until the secondary separation line was encountered.



The secondary separation line is assumed to be the line along which  $CFY$  first goes through zero. The solution was then continued in the inverse mode by specifying the skin-friction coefficients to be constant and equal to their values at separation ( $CFY < 0$  but  $CFX > 0$ ). The spanwise distribution of the skin-friction coefficients is presented in fig. 10a with corresponding integral thicknesses in 10b. The secondary separation line was calculated to be along  $Y = 0.70$ . Hummel (ref. 15) observed from oil flow studies a secondary separation line along  $Y = 0.67$ . A discrepancy between the calculated and observed secondary separation line was expected, since the inviscid solution ignores completely the influence of the secondary vortices. Reference 1 showed that the secondary separation line could be calculated accurately with the direct boundary layer method when experimental pressure data were used. The momentum integral thicknesses and shape factors are shown in fig. 11. Both shape factors increase sharply in the vicinity of the secondary separation line with the spanwise shape factor remaining nearly constant afterwards while the streamwise shape factor decreases continually toward the leading edge. Velocity profiles at three spanwise stations are presented in fig. 12. Both profiles indicate the spanwise thickening of the boundary layer and the G profiles beyond the secondary separation line show a small region of reversed flow near the surface. The inviscid velocities determined from the FVS code and those calculated with the inverse method are presented in fig. 13. As expected, the gradients in the inviscid velocities calculated from the inverse boundary layer method are much less steep than those of the inviscid solution calculated neglecting the boundary layer.

Research is in progress to interact the boundary layer solution with the inviscid solution. Reference 21 used a three-dimensional integral turbulent boundary layer method to solve the flow field over a delta wing at incidence. The viscous and inviscid solutions were coupled and the resulting pressure distribution showed some improvement over the inviscid results near secondary separation.

#### CONCLUDING REMARKS

A three-dimensional, direct boundary layer method was extended to the inverse mode for separated flows. It is a predictor-corrector finite-difference method in which the FLARE approximation is made to the streamwise momentum term in the predictor stage but a finite-difference quotient is used for the corrector stage. This method allows the inviscid velocity to be calculated without iterations by marching into the separated flow region using prescribed skin-friction coefficients or integral thicknesses.

Two-dimensional test cases for laminar separation with prescribed skin friction or displacement thickness were found to compare well with other methods. Solutions were also obtained using the direct and inverse modes for conical inviscid flow over a delta wing at incidence. The direct mode was used to the secondary separation line and then the inverse mode continued the solution into the separated flow region with both skin-friction coefficients maintained at their values at secondary separation. Further studies are needed for the inverse mode in fully three-dimensional flows and interacting the boundary layer solution with the inviscid solution.

# SYMBOLS

|                        |  |
|------------------------|--|
| $a_k, b_k$             | coefficient matrices in eq. (38)   |
| $C_{f_X}, C_{f_{Y^*}}$ | skin-friction coefficients defined by eq. (46)   |
| $CFX, CFY$             | $C_{f_X} \sqrt{Re_x}, C_{f_{Y^*}} \sqrt{Re_x}$   |
| $D_k$                  | vector in eq. (38)   |
| $DTX, DTY$             | $\frac{\bar{\delta}_X^*}{\bar{x}} \sqrt{Re_x}, \frac{\bar{\delta}_{Y^*}^*}{\bar{x}} \sqrt{Re_x}$         |
| $f, g$                 | functions defined by eq. (17)  |
| $F, G$                 | velocity ratios given by eq. (18)  |
| $H, h$                 | vectors defined by eq. (20)  |
| $HX, HY$               | $MTX/DTX, MTY/DTY$   |
| $JMAX$                 | number of mesh points in spanwise direction  |
| $KMAX$                 | number of mesh points across the boundary layer  |
| $\bar{L}$              | reference length, m  |
| $m$                    | parameter defined by eq. (10)  |
| $MTX, MTY$             | momentum integral thicknesses  |
| $Re$                   | freestream Reynolds number, $\bar{U}_0 \bar{L} / \nu$  |
| $Re_x$                 | local Reynolds number, $(U_e X) Re$  |
| $u, v, w$              | non-dimensional velocity components in x, y, and z directions, respectively                              |
| $U, V, W$              | transformed velocity components given by eq. (13)  |
| $\bar{U}_0$            | freestream velocity, m/s   |
| $x, y, z$              | non-dimensional Cartesian coordinates streamwise, spanwise, and normal to the wing surface, respectively |
| $X, Y, Z$              | transformed coordinates given by eq. (12)  |
| $Y^*$                  | transformed spanwise coordinate given by eq. (25)  |

|                    |   |
|--------------------|---|
| $\hat{\alpha}$     | parameter in eq. (53)                                   |
| $\beta_u$          | $\frac{v_e}{U_e^2} \frac{dU_e}{dY}$                     |
| $\beta_v$          | $\frac{1}{U_e} \frac{dV_e}{dY}$                         |
| $\beta$            | $\beta_v - .5\beta_u$                                   |
| $\Gamma$           | parameter defined by eq. (23)                           |
| $\delta$           | central difference operators given by eqs. (31), (32)   |
| $\bar{\delta}_x^*$ | $\int_0^\infty (1 - \frac{\bar{U}}{U_e}) d\bar{z}$      |
| $\bar{\delta}_y^*$ | $\int_0^\infty (1 - \frac{\bar{V}}{V_e}) d\bar{z}$      |
| $\Delta$           | central difference operators defined by eqs. (29), (30) |
| $\nabla$           | backward difference operator defined by eq. (33)        |
| $\eta$             | transformed normal coordinate defined by eqs. (5), (16) |
| $\theta$           | angle of rotation for circular cylinder                 |
| $\Lambda$          | sweep angle of the delta wing                           |
| $\bar{\nu}$        | kinematic viscosity coefficient, $m^2/s$                |
| $\sigma$           | parameter defined by eq. (22)                           |
| $\psi, \phi$       | stream functions given by eqs. (7), (15)                |

#### Subscripts

|     |  |
|-----|--|
| e   | edge value                             |
| j,k | mesh point locations given by eq. (28) |
| v   | viscous calculation                    |
| w   | wall                                   |

Barred parameters are dimensional quantities.

## REFERENCES

1. DeJarnette, F. R. and Woodson, S. H.: "Numerical and Experimental Determination of Secondary Separation on Delta Wings in Subsonic Flow," AIAA J. Aircraft, Vol. 22, No. 7, July 1985, pp. 602-608.
2. Catherall, D. and Mangler, K. W.: "The Integration of the Two-Dimensional Laminar Boundary-Layer Equations Past the Point of Vanishing Skin Friction," J. Fluid Mech., Vol. 26, Pt. 1, Sept. 1966, pp. 163-182.
3. Reyhner, T. A. and Flugge-Lotz, I.: "The Interaction of a Shock Wave with a Laminar Boundary Layer," Int. J. Non-Linear Mech., Vol. 3, No. 2, June 1968, pp. 173-199.
4. Klineberg, J. M. and Steger, J. L.: "On Laminar Boundary Layer Separation," AIAA Paper No. 74-94, Feb. 1974.
5. Carter, J. E.: "Inverse Solutions for Laminar Boundary-Layer Flows with Separation and Reattachment," NASA TR R-447, Nov. 1975.
6. Cebeci, T., Keller, H. B., and Williams, P. G.: "Separating Boundary-Layer Flow Calculations," J. of Comp. Physics, Vol. 31, 1979, pp. 363-378.
7. Le Balleur, J. C.: "Couplage visqueux-non visqueux: méthode numérique et applications aux écoulements bidimensionnels transsoniques et supersoniques," La Recherche Aérospatiale, Vol. 183, 1978, pp. 65-76.
8. Carter, J. E.: "A New Boundary-Layer Interaction Technique for Separated Flows," NASA TM 78690, June 1978.
9. Kwon, O. K. and Fletcher, R. H.: "Prediction of Incompressible Separated Boundary Layers Including Viscous-Inviscid Interaction," J. Fluids Eng., Vol. 101, Dec. 1979, pp. 466-472.
10. Veldman, A. E. P.: "New Quasi-Simultaneous Method to Calculate Interacting Boundary Layers," AIAA J., Vol. 19, No. 1, Jan. 1981, pp. 79-85.
11. Edwards, D. E. and Carter, J. E.: "Analysis of Three-Dimensional Separated Flow with the Boundary Layer Equations," AIAA Paper No. 85-1499, July 1985.
12. Johnson, F. T., Lu, P., Tinoco, E. N., and Epton, M. A.: "An Improved Panel Method for the Solution of Three-Dimensional Leading-Edge Vortex Flows, Volume I - Theory Document," NASA CR 3278, July 1980.
13. Luckring, J. M., Schoonover, W. E., and Frink, N. T.: "Recent Advances in Applying Free Vortex Sheet Theory for the Estimation of Vortex Flow Aerodynamics," AIAA Paper No. 82-0095, Jan. 1982.
14. Luckring, J. M., Hoffler, K. D., and Grantz, A. C.: "Recent Extensions to the Free-Vortex-Sheet Theory for Expanded Convergence Capability," Vortex Flow Aerodynamics - Volume I, NASA CP-2416, paper no. 4, 1986.

15. Hummel, D.: "Zur Umstromung scharfkantiger schlanker Deltaflugel bei grossen Anstellwinkeln," Zeitschrift fur Flugwissenschaften, Vol. 15, Oct. 1967, pp. 376-385.
16. Schlichting, H.: Boundary Layer Theory, McGraw-Hill Book Company, New York, NY, 1968.
17. Matsuno, L.: "A Vector-Orientated Finite-Difference Scheme for Calculating Three-Dimensional Compressible Laminar and Turbulent Boundary Layers on Practical Wing Configurations," AIAA Paper No. 81-1020, 1981.
18. Woodson, S. H. and DeJarnette, F. R.: "A Three-Dimensional Boundary Layer Method for Flow over Delta Wings with Leading-Edge Separation," SAE Paper No. 851818 presented at the 1985 SAE Aerospace Technology Conference and Exposition, Long Beach, CA, Oct. 14-17, 1985.
19. Blottner, F. G.: "Introduction to Computational Techniques for Boundary Layers," Sandia Laboratories Report SAND - 79-0893, Albuquerque, New Mexico, 1979.
20. Meksyn, D.: New Methods in Laminar Boundary-Layer Theory, Pergamon Press, Inc., 1961.
21. Wai, J. C., Baillie, J. C., and Yoshihara, H: "Computation of Turbulent Separated Flows Over Wings," Third Symposium on Numerical and Physical Aspects of Aerodynamic Flows, Long Beach, CA, Jan. 21-24, 1985.

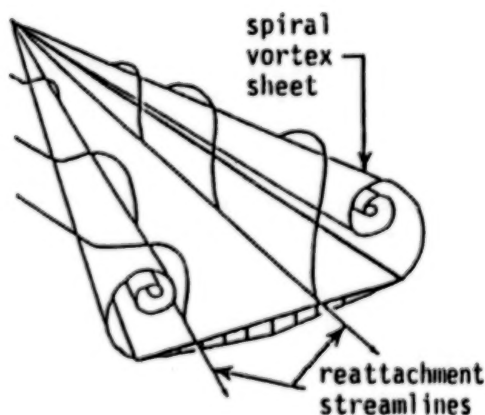


Fig. 1. Leading-edge vortex flow.

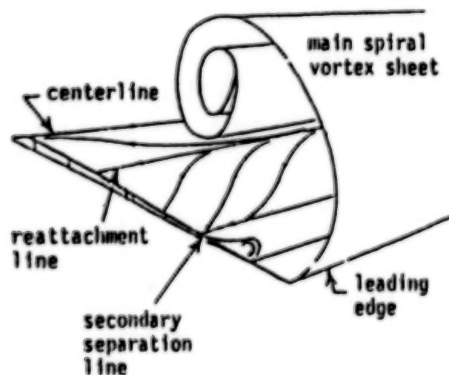


Fig. 2. Upper surface flow geometry.



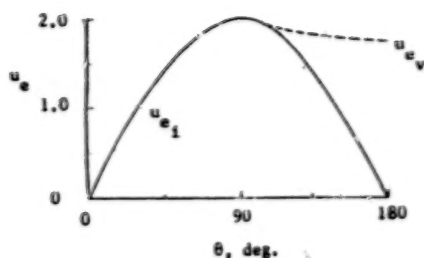


Fig. 3. Inviscid velocity over a circular cylinder.

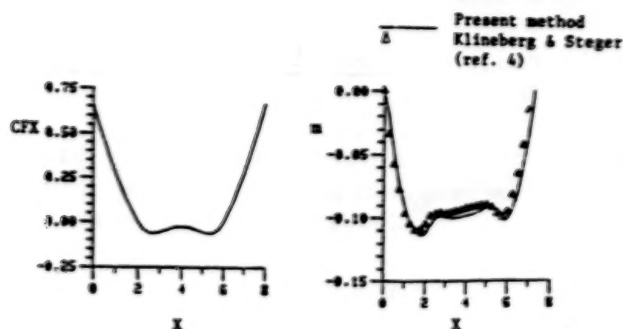


Fig. 4. Skin-friction coefficient and pressure gradient parameter.

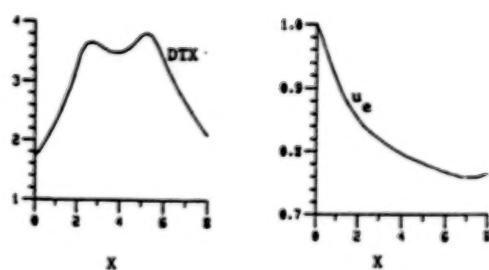


Fig. 5. Displacement thickness and edge velocity.

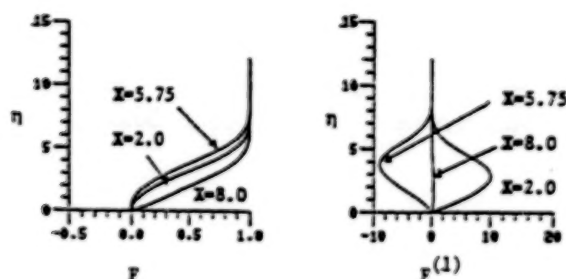


Fig. 6. Velocity profiles for Klineberg and Steger test case.

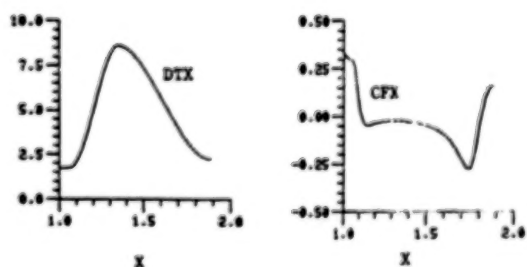


Fig. 7. Displacement thickness and skin-friction coefficient.

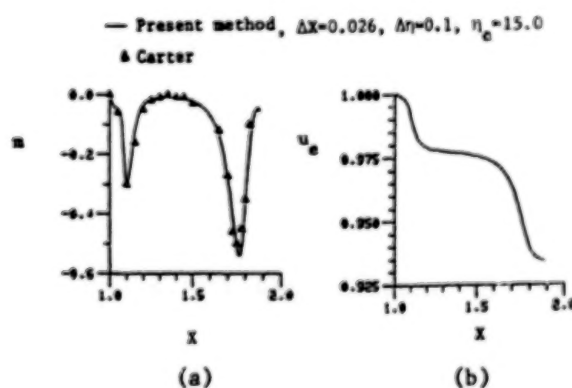


Fig. 8. Pressure gradient parameter and edge velocity.

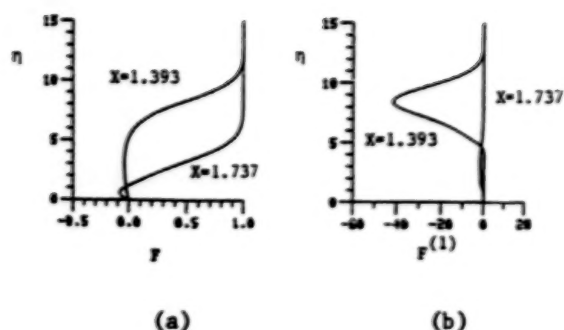


Fig. 9. Velocity profiles for Carter test case.

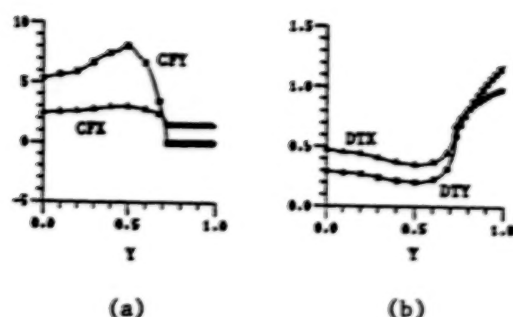


Fig. 10. Skin-friction coefficients and integral thicknesses.

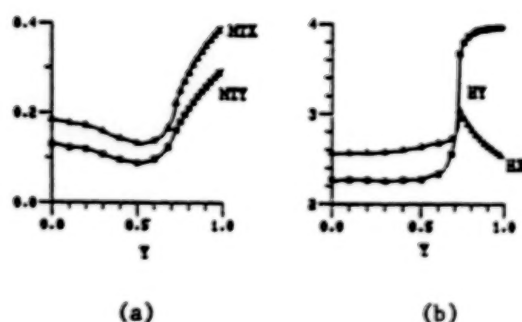


Fig. 11. Momentum integral thicknesses and shape factors.

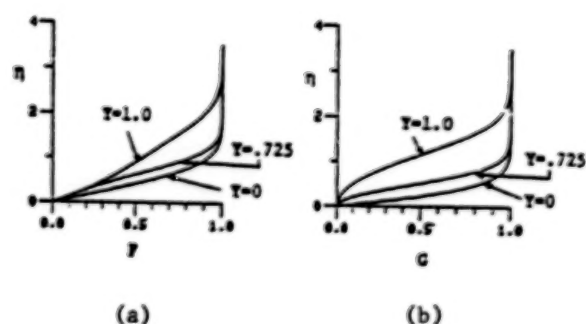


Fig. 12. Velocity profiles for the delta wing.

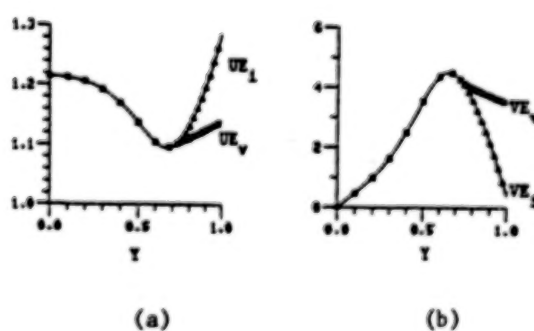


Fig. 13. Inviscid velocity components.

## AN EXPERIMENTAL INVESTIGATION OF VORTEX

## BREAKDOWN ON A DELTA WING\*

F. M. Payne and R. C. Nelson  
University of Notre Dame  
Notre Dame, Indiana

## Abstract

An experimental investigation of vortex breakdown on delta wings at high angles is presented. Thin delta wings having sweep angles of 70, 75, 80 and 85 degrees are being studied. Smoke flow visualization and the laser light sheet technique are being used to obtain cross-sectional views of the leading-edge vortices as they break down. At low tunnel speeds (as low as 3 m/s) details of the flow, which are usually imperceptible or blurred at higher speeds, can be clearly seen. A combination of lateral and longitudinal cross-sectional views provides information on the three-dimensional nature of the vortex structure before, during and after breakdown. Whereas details of the flow are identified in still photographs, the dynamic characteristics of the breakdown process have been recorded using high-speed movies. Velocity measurements have been obtained using a laser Doppler anemometer with the 70 degree delta wing at 30 degrees angle of attack. The measurements show that when breakdown occurs the core flow transforms from a jet-like flow to a wake-like flow.

## Introduction

The flow structure on the upper side of a delta wing at angle of attack is extremely complex. At moderate angles of attack the leeward flow field is dominated by highly organized vortical flows emanating from the wing leading edge. The vorticity shed from the leading edge rolls up into a pair of primary vortices which can create secondary vortices as illustrated in Figure 1.

One of the most interesting phenomena associated with leading edge vortices is their breakdown. The breakdown or bursting, as it is commonly called, refers to a sudden and rather dramatic structural change which usually results in the turbulent dissipation of the vortex. Vortex bursting is characterized by a sudden deceleration of the axial flow in the vortex core, the formation of a small recirculatory flow region, a decrease in the circumferential velocity and an increase in the size of the vortex.

---

\*This research is being supported by NASA Ames Research Center under NASA Grant NAG-2-258 and the University of Notre Dame. The authors wish to express their appreciation to Dr. Lewis B. Schiff of NASA Ames Research Center for his comments and suggestions during the course of this study. The authors also wish to express their gratitude to Dr. Terry Ng of the Department of Aerospace and Mechanical Engineering of the University of Notre Dame for providing laser Doppler anemometry measurements included in this paper as well as his comments on the interpretation of the flow visualization data.

The breakdown of leading-edge vortices has been under study since the late 1950's when research and design work on delta wing aircraft were initiated. Interest in the phenomenon has intensified in recent years as concepts for highly maneuverable aircraft have been developed. These high-performance aircraft are expected to operate routinely at angles of attack at which vortex breakdown is known to occur.

Several distinct types of vortex breakdowns have been identified in vortex tube experiments (Ref. 1); however, the two most common forms of breakdown on wings are the bubble and spiral types. The bubble or "axisymmetric" mode of vortex breakdown is characterized by a stagnation point on the swirl axis, followed by an oval-shaped recirculation bubble. The bubble is nearly symmetric over most of its length, but the rear is open and asymmetric (Figure 2).

The spiral mode of breakdown is characterized by a rapid deceleration of the core flow followed by an abrupt kink at which point the core flow takes the form of a spiral which persists for one or two turns before breaking up into large scale turbulence (Figure 3a). For leading-edge vortices the sense of the spiral winding has been observed to be opposite to the direction of rotation of the upstream vortex; however, the sense of rotation of the winding is in the same direction as the rotation of the upstream vortex (Figure 3b).

In vortex tube experiments in which the vortex swirl speed can be controlled and varied independently of Reynolds number (Ref. 1), the spiral type has been found to occur at low values of swirl for a given Reynolds number. As the swirl speed is increased the spiral form can be seen to transform into the bubble form at a certain critical value of swirl.

While the bubble type breakdown has been observed on delta wings in low Reynolds number water tunnel studies (Ref. 2), it is the spiral type which is more commonly observed in wind tunnel studies.

A wind tunnel smoke flow visualization study is described herein. Four delta wings with sweep angles of 70, 75, 80 and 85 degrees were tested at angles of attack from 10 to 40 degrees. The freestream velocity was 3 m/s. A low freestream velocity was chosen because details of the flow can be seen which are imperceptible at higher speeds.

Velocity profiles are presented for the leading-edge vortex on a 70 degree delta wing at 30 degrees angle of attack and a freestream velocity of 9.1 m/s. The axial and swirl velocity components were obtained in separate test runs using a single component laser. Since a frequency shifting unit was not available at the time of the test only the absolute value of the velocity was measured.

#### Experimental Equipment

All experiments reported on in this paper were conducted in the University of Notre Dame's low turbulence, subsonic smoke wind tunnel. The tunnel is of the indraft variety and is shown in Figure 4. Twelve anti-turbulence screens are located in front of a 24:1 area contraction cone. The combination of anti-turbulence screens and the large inlet contraction provides a uniform velocity profile with a turbulence intensity of less than 0.1% in the tunnel test section.



The test section is 1820mm long with a 610 x 610mm square cross section. The test section was designed with large plate glass windows in the top and both sides of the section to provide adequate viewing area for the visualization studies. Following the test section, the flow is expanded in a diffuser. The tunnel is powered by an eight-bladed fan and an 11kw AC induction motor located at the end of the diffuser section.

For visualization, smoke was generated by the flash vaporization of deodorized kerosene which was allowed to drip onto electrically heated plates. The smoke was pushed through the generator and into the smoke rake by a small squirrel cage blower. Figure 5 is a sketch of the smoke generator. The smoke rake consists of a heat exchanger, filter bag and smoke tubes. For this study, the smoke was introduced via a single tube as illustrated in Figure 6.

Four thin plexiglass delta wing models were used in this study. The models each had a root chord of 406mm and were 6.4mm thick with sweep angles of 70, 75, 80, and 85 degrees. The leading edge was beveled with a 25 degree angle. The models were sting mounted to a support system that provided very little interference to the flow.

To illuminate the smoke entrained into the leading-edge vortex system a laser light source was used. During the course of this study two different lasers were used. A Lexel Model 95, 8 watt argon ion laser and a Spectra Physics model 164, 4 watt argon ion laser were used in conjunction with a splitter lens having either a 20 degree or 60 degree spreading angle. The lens created a thin light sheet which passed through the test section. The laser light sheet was aligned either normal to the model surface or parallel to the vortices.

Both still and high-speed motion picture photography were used to record the visual data. A Nikon FM2, 35mm SLR camera and Kodak Tri-X 400 ASA black and white print film were used for the still photographs. For the high-speed movies a Milliken DBM-5, 16mm motion picture camera was used. Film frame rates of 500 frames per second (shutter speed 1/1300 sec) were used with Eastman 4-X Negative film.

Several preliminary experiments using a single component laser anemometer have been conducted using the 70 degree swept delta wing. The laser anemometer system consisted of a 4 watt argon ion laser (an output level of about 1 watt was obtained when operated with the 514.5nm line), a 50mm beam splitter and a 500mm focal length lens as the transmitting optics, and a receiving optics in an off-axis, forward scattering configuration. Kerosene smoke was used as the scattering particles. The signal was processed by a counter and the data were recorded by a data acquisition system based on a PDP 11/23 minicomputer.

## Experimental Results

### Flow Visualization Results

Smoke flow visualization and the laser sheet technique were used to study the structure of leading-edge vortices as they break down. Figure 7 is a sketch of the experimental setup. At low freestream velocities (as low as 3 m/s), details of the flow can be clearly seen which are usually imperceptible at higher speeds. A combination of lateral and longitudinal laser cross-sectional views provides



information on the three-dimensional nature of the vortex structure before, during and after breakdown. Close-up high-speed motion picture photography provides details of the dynamic characteristics of the breakdown process. An attempt is made to classify the observed breakdown modes using these methods.

Four thin sharp-edged delta wings with sweep angles of 70, 75, 80 and 85 degrees were photographed at angles of attack of 10, 20, 30 and 40 degrees. Vortex breakdown was observed to occur above all four wings at 40 degrees angle of attack. Since vortex breakdown is the phenomenon of primary interest here, only the results at 40 degrees angle of attack for each wing will be presented.

Early in the investigation it was discovered that operating at relatively low speeds resulted in better resolution of flow features due to a reduced level of turbulence in the test section and a higher density of smoke. For this reason a freestream velocity of 3 m/s was chosen for all flow visualization tests. This resulted in a Reynolds number based on root chord of approximately 85,000.

One notable consequence of operating at very low speeds was the tendency of the position of the breakdown to wander on the more highly swept wings. For the lowest sweep wing (70 deg), the breakdown locations of the vortices were approximately symmetric and steady except for a high-frequency longitudinal oscillation about some mean position. The magnitude of this oscillation was relatively small (about 1 cm). On the more highly swept wings the locations of the breakdowns became increasingly asymmetric and unsteady in their mean location. On the 85 degree sweep wing the breakdown location of both vortices was observed to wander forward and aft on the model apparently at random. However, if the tunnel speed was increased (to say 15 m/s) the unsteadiness in mean position disappeared although the breakdown positions still tended to be asymmetric. No measurable asymmetry could be identified in the model geometry; however, the accuracy in measurement of yaw angle was approximately 1/2 degree which could account for the asymmetric breakdown if the model was misaligned by that amount. In wind tunnel tests of highly swept delta wings (75-85 deg) at a Reynolds number of  $1 \times 10^6$ , Wentz (Ref. 3) observed that the breakdown location was quite sensitive to yaw. A misalignment of as little as 0.1 degrees was sufficient to cause asymmetric breakdown. The location of breakdown at 15 m/s for the four wings tested is presented in Figure 8.

In summary, the wandering of the mean location of breakdown on the 80 and 85 degree wings occurred only at low speeds but the asymmetry in mean breakdown location for those wings occurred at both low (3 m/s) and relatively high (15 m/s) speeds. The low-magnitude, high-frequency oscillation of the breakdown location occurred for all wings at all speeds tested.

Figure 9a depicts the geometry of the 70 degree wing. Figure 9b is a photograph of this model at 40 degrees angle of attack. A tube of smoke introduced upstream of the contraction cone impinges on the apex of the delta wing and is entrained into the vortices. A 1000 watt flood lamp placed outside the test section is illuminating the vortices through the glass side wall of the test section. Both vortices are breaking down about 1/3 of the way down the model from the apex.

Figure 9c is a multiple exposure photograph of the 70 degree delta wing using the laser sheet technique. Vortex cross sections are illuminated by passing the

laser beam through a cylindrical lens which splits it into a thin sheet or plane of light. The light sheet then cuts across the test section. In this case the sheet is perpendicular to the model. The light sheet is expanding at a half angle of approximately 10 degrees.

Note the absence of smoke in the core region of the vortices in the two most forward cross sections of Figure 9c. This lack of smoke can probably be attributed to one or more of the following factors. (1) The smoke is introduced only at the apex of the model, therefore, much of the fluid in the core region is entrained from areas which contain no smoke to begin with. (2) Velocities in the core can reach three to five times the freestream value which reduces the density of smoke entrained into the core. (3) High rotational velocities in the core tend to "spin" smoke particles out.

The first reason may be the most significant because the diameter of the region which is void of smoke was observed to vary depending on where the smoke filament impinged on the model. If the filament impinged on the lower surface below the apex, the void region was seen to increase in diameter. Despite the fact that the void may not correspond to the true diameter of the core, for the sake of simplicity, it will be referred to as the core in the remainder of this paper.

In the forward cross sections of Figure 9c, the presence of a core indicates that the vortex has not yet broken down. In the third and following cross sections, which are downstream of the breakdown points, no core regions are evident and the vortices appear turbulent and diffuse.

Figure 9d is a photograph of the 70 degree wing at the same conditions as previously stated except that the laser sheet has been rotated 90 degrees to illuminate a longitudinal cross section of the vortices. The dark core region maintains an approximately constant diameter until suddenly expanding just before breaking down. Downstream of the breakdown the vortices are rather featureless.

Figures 10, 11 and 12 present similar views of the 75, 80 and 85 degree wings respectively. Note that the breakdown occurs farther aft as the sweep angle is increased. Also note the fine details visible in the photographs of the 85 degree delta wing. The high sweep angle results in lower swirl velocities and therefore less diffusion of the smoke.

In Figure 12b the spiral nature of the vortices is visually emphasized by the appearance of striations in the smoke. The striations become visible when the flow is accelerated around the leading edge and the smoke mixes with entrained flow in the vortex. In this photograph the vortex on the right is breaking down at approximately the mid-chord position while the left vortex does not break down until somewhere in the wake. The combination of high sweep and low freestream velocity usually resulted in asymmetric vortex breakdown as previously discussed. Which vortex would breakdown first could not be predicted and was observed to change back and forth at irregular intervals. This was probably the result of small changes in the freestream conditions due to gusts or changes in the direction of the wind at the tunnel exit.

In Figure 12c it is possible to actually see the roll-up of the shear layer which forms the primary vortices and the development of secondary vortical-like



structures in the shear layer. The growth of these secondary structures is similar to the evolution of the classic Kelvin-Helmholtz instability. Gad-el-Hak and Blackwelder (Ref. 4) similarly observed the development of secondary vortical-like structures in a towing tank experiment with a 60 degree delta wing. In their experiments, which were conducted at a Reynolds number of 13,000 and also employed the laser sheet technique, dye injected near the leading edge was observed to roll-up into regions of strong concentration separated by a very thin braid of dye. These concentrated regions in the shear layer were assumed to be discrete vortices. The fact that these structures have been identified in both tow tank experiments using dye injection and wind tunnel experiments using smoke suggests that the observed structures are indeed associated with the flow and are not merely a consequence of the visualization method.

In Figure 12d it is the right vortex which is breaking down. Details in the recirculation zone or "bubble" region are clearly visible. Note that the vortices curve slightly away from the wing ("out" of the photograph) and since the laser sheet is planar, the laser cross section cuts at an angle through the vortices. This is why the core region is only visible for a portion of the entire cross section. The direction of the spiral on the right side of the lower vortex indicates the laser sheet is cutting across the underside of the vortex at that point.

An extremely useful tool in the analysis of complicated flows is the motion picture camera. In order to obtain a better understanding of the breakdown structure, a Milliken high-speed movie camera was used to photograph the phenomenon at 500 frames per second. The effective shutter speed for a single frame was 1/1300 of a second. In Figures 13-16, single frames from the 16mm movies have been isolated and enlarged. The photographs are longitudinal and lateral laser sheet cross sections of vortex breakdown on the 85 degree delta wing. Accompanying the photographs are sketches depicting the salient features observed in the movie frames.

One of the goals of this study is to identify the type or types of breakdowns which occur on sharp-edged delta wings at these Reynolds numbers; however, a certain amount of caution must be exercised when interpreting flow visualization results. What is not seen may be just as important as what is seen. The still photographs described above, together with the high-speed motion pictures, can be interpreted in various ways. The particular ambiguity which makes a definite identification of the breakdown process difficult in this case is that the smoke in these photographs is entrained into the outer region of the vortex and not into the core and it is the behavior of the core which is of primary interest. The core behavior must be inferred by observing a region void of smoke. With this difficulty in mind two possible breakdown forms will be described.

The first type of breakdown process resembles the bubble form described in vortex tube experiments found in the literature. In Figure 13 the core flow seems to expand around an oval shaped recirculation zone. At the exit of this recirculation zone the core flow appears to shed in the form of vortex rings which are then convected downstream. The cross section of these doughnut shaped vortex rings appears as a pair of holes in the smoke. Figure 14 shows a lateral cross section of the recirculation zone which is surrounded by a ring of core flow.

The breakdown process described was occasionally observed to change into what might be interpreted as a spiral mode. When this occurred the mean location of the breakdown moved downstream and took the form depicted in Figure 15. The large recirculation zone has disappeared and the core flow now appears to corkscrew downstream. In this case the holes in the flow are assumed to be cross sections of the spiraling core flow. This type of result was also obtained in wind tunnel tests at ONERA using the laser sheet technique (Ref. 5). In that study "holes" appearing in the wake of a breakdown were also observed and interpreted to be cross sections of the spiraling vortex core. Figure 16 shows a lateral cross section which appears to show a rotating core. After a short time this spiral mode would transform back into the "bubble" form and move upstream.

Further experiments are planned to verify one or both of the above descriptions of breakdown modes. In particular an attempt will be made to introduce smoke into the vortex core from a port in the surface of the model.

#### LDA Measurements

A laser anemometer was used to measure the axial and normal components of velocity through the vortex core of the 70 degree delta wing at 30 degrees angle of attack.

An example of these preliminary measurements is shown in Figure 17. This figure shows the change in axial velocity distribution before and after vortex breakdown. Breakdown of the vortex occurred between stations  $x/c = 0.47$  and  $x/c = 0.54$ . The axial velocity upstream of the vortex breakdown point is over three times the freestream velocity in the vortex core. However, the wake survey made just downstream of the breakdown shows a region of velocity deficit with respect to the surrounding flow.

The time required for a traverse of the vortex depended on the number of samples acquired at each point, the number of scattering particles in the flow, movement of the instrument to the next point, and the total number of points in the traverse. Thus, the LDA results represent a time average of the flow characteristics and do not entirely reflect the complicated nature of the breakdown region. Nevertheless, valuable insight is gained from the average velocity profiles.

Figure 18 shows the change in swirl velocity at various positions along the wing. Again we see a dramatic change in swirl velocity after breakdown has occurred.

#### Conclusions

Smoke flow visualization and the laser sheet technique have been shown to be effective tools in the study of vortical flow fields. The position of leading-edge vortices and the location of their breakdown at high angles of attack can be determined. Details of the breakdown process have been studied using still and high-speed motion picture photography.

The following observations were made concerning vortex breakdown on delta wings at low Reynolds number:

(1) At a given angle of attack, as the sweep angle is increased, the location of breakdown moves aft.

(2) For a given set of conditions the breakdown location oscillated at high frequency about a mean position and for highly swept wings (sweep = 80, 85 deg) at low speeds the mean position would migrate considerably forward and aft on the models.

(3) High-speed motion pictures revealed what appears to be two types of breakdown on the 85 degree wing, a bubble mode and a spiral mode. The two modes were seen to transform from one to the other apparently at random with the bubble form seeming to prefer a more upstream location relative to the spiral mode. The existence of more than one mode of breakdown as well as their behavior with respect to preferred location is consistent with observations of vortex breakdown in tubes reported in the literature.

(4) Velocity profiles obtained with a laser anemometer showed the development of a jet-like core flow which reached three times the freestream velocity before breaking down. After the breakdown the velocity profiles became wake-like in nature.

#### References

1. Faler, J. H. and Liebovich, S., "Disrupted States of Vortex Flow and Vortex Breakdown," Phys. Fluids 20, 1977, 1385-1400.
2. Lambourne, N. C. and Bryer, D. W., Aeronaut. Res. Council., "The Bursting of Leading Edge Vortices; Some Observations and Discussion of the Phenomenon," R & M No. 3282, 1961, 32 pp.
3. Wentz, W. H. and Kohlman, D. L., "Vortex Breakdown on Slender Sharp-Edged Wings," Journal of Aircraft, Vol. 8, No. 3, March 1971.
4. Gad-el-Hak, M. and Blackwelder, R. F., "The Discrete Vortices from a Delta Wing," AIAA Journal, Volume 23, No. 6, June 1985.
5. Werle, H., "Flow Visualization Techniques For the Study of High Incidence Aerodynamics," AGARD LSP-121, March 1982, Paper 3-1 to 3-24.



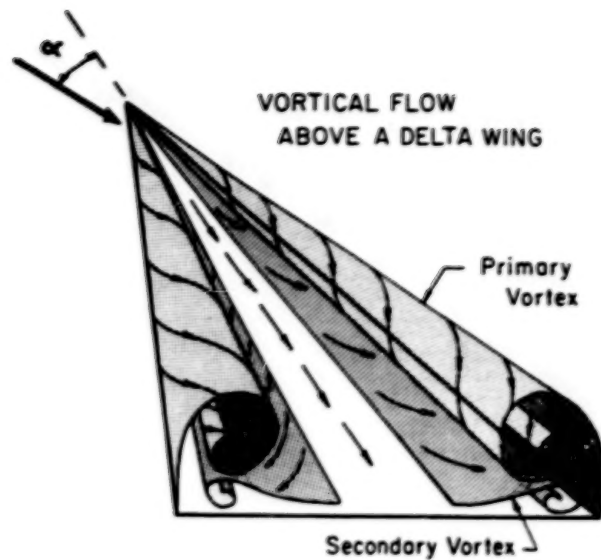


Figure 1. Flow over a delta wing.

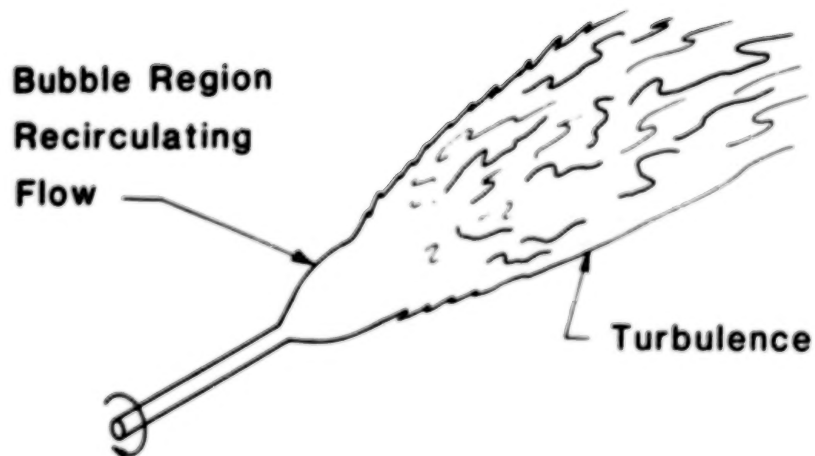
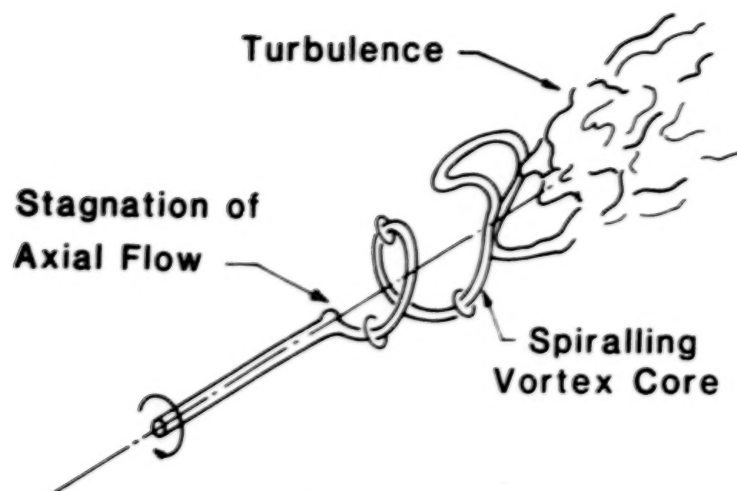
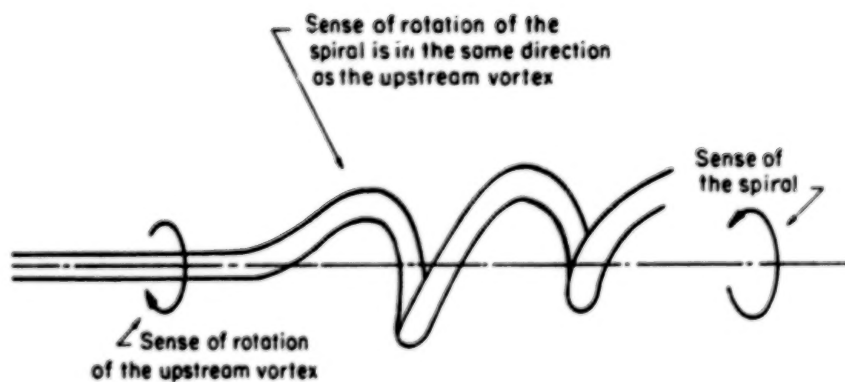


Figure 2. Bubble-type breakdown.



a. Spiral-type breakdown.



b. Sense of rotation of the spiral.

Figure 3. Spiral-type breakdown and sense of rotation of spiral.

ORIGINAL PAGE IS  
OF POOR QUALITY

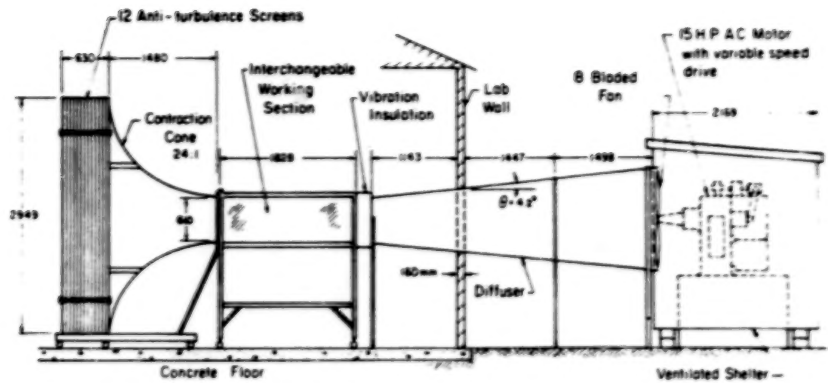


Figure 4. Schematic of wind tunnel.

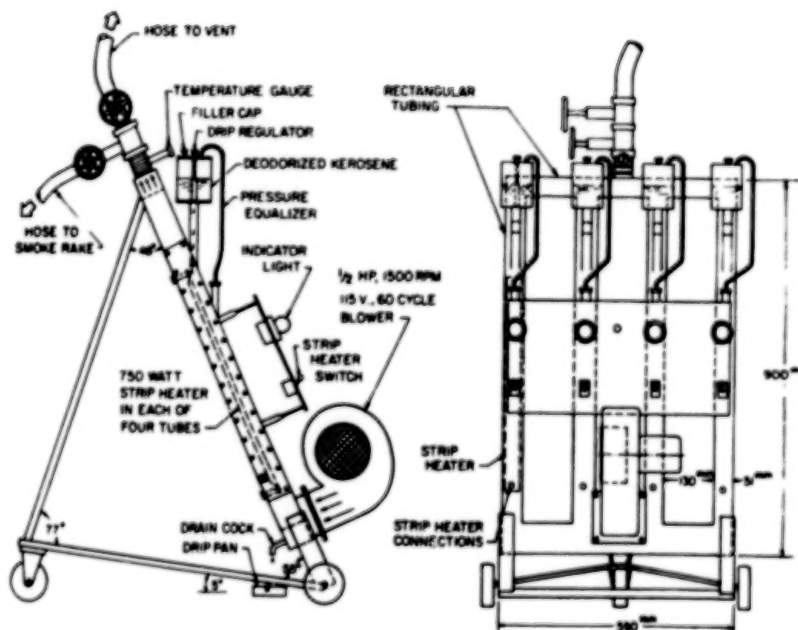


Figure 5. Schematic of smoke generator.

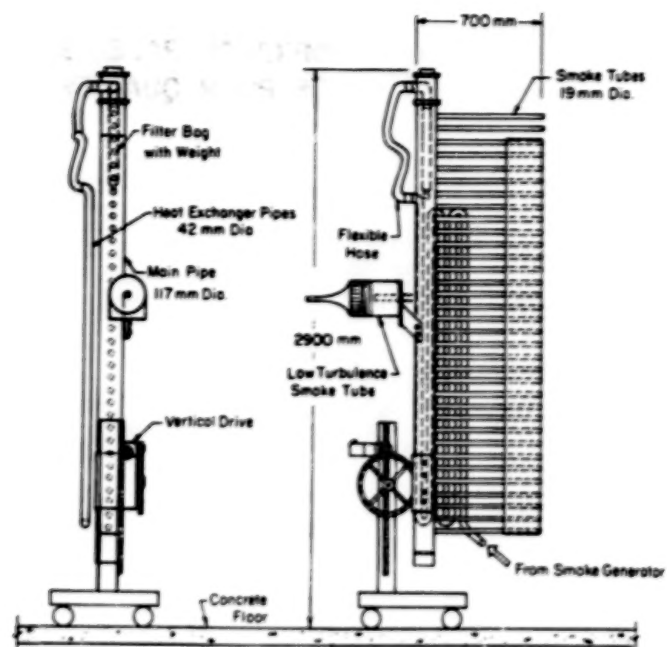


Figure 6. Schematic of smoke rake.

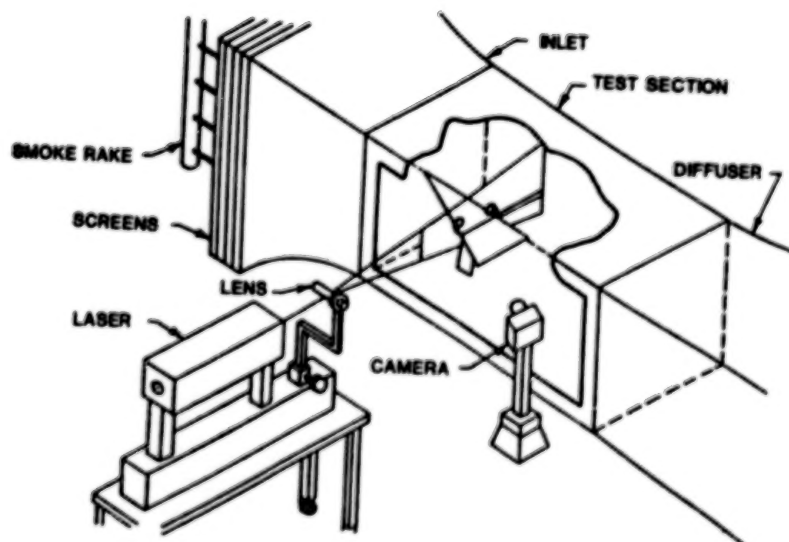


Figure 7. Schematic of experimental setup.

# LOCATION OF VORTEX BREAKDOWN $Re = 425,000$

- $-\Lambda = 70^\circ$
  - $-\Lambda = 75^\circ$
  - △  $-\Lambda = 80^\circ$
  - ◇  $-\Lambda = 85^\circ$
- Left Vortex  
 ---- Right Vortex

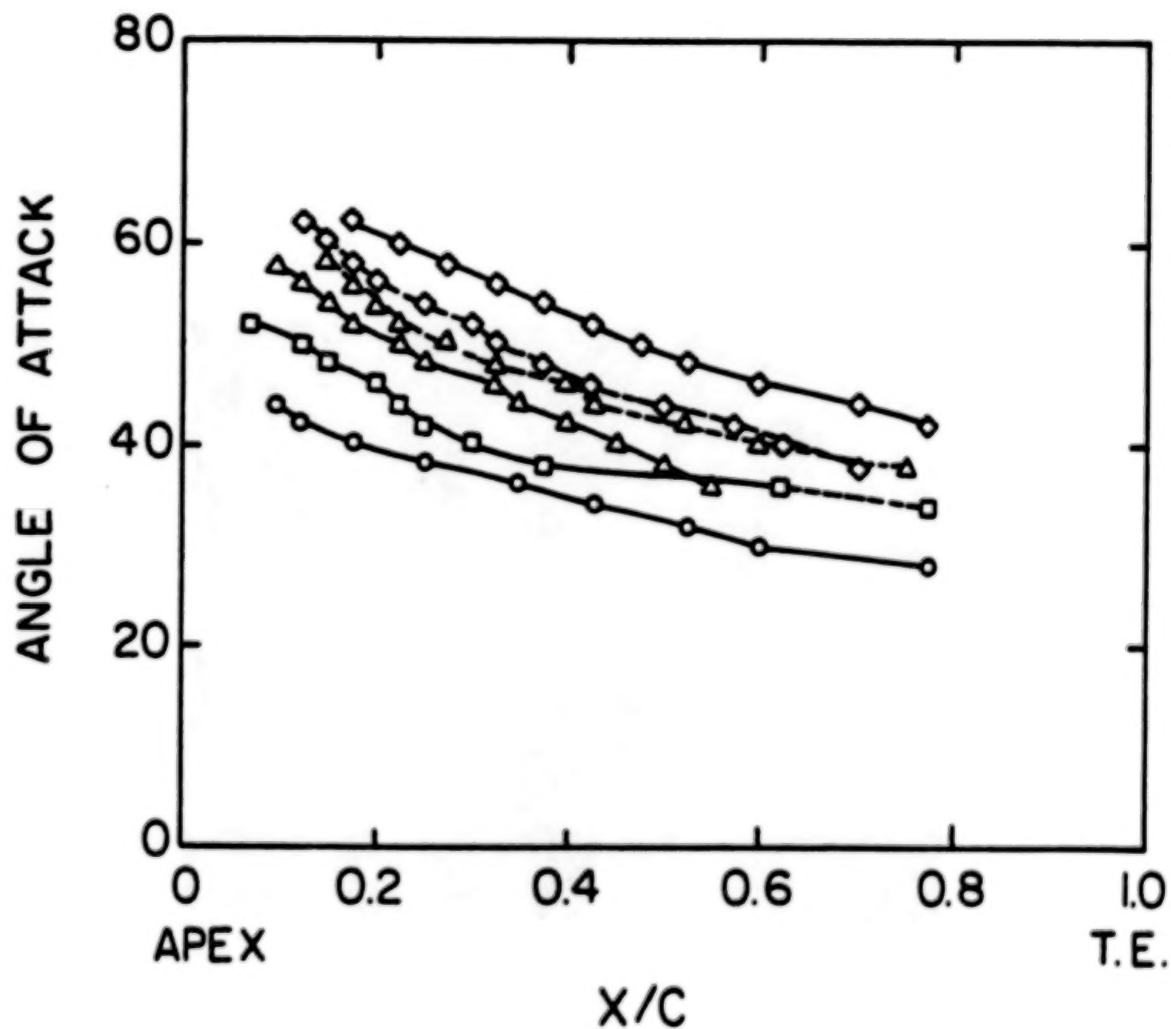
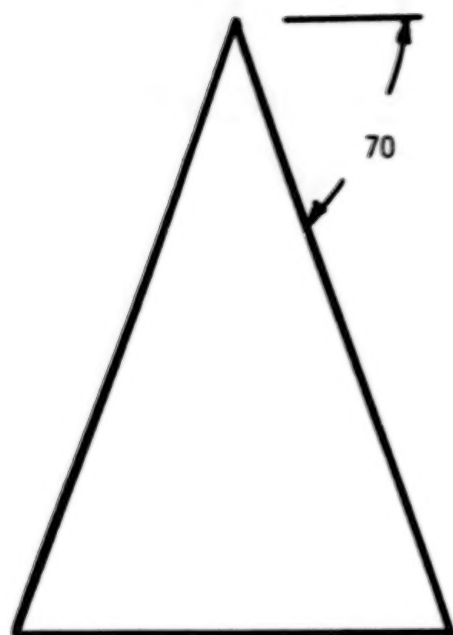



Figure 8. Location of vortex breakdown.





**Planview of Model**

  $LE = 70 \text{ degrees}$

$c = 406 \text{ mm}$

$AR = 1.46$

$t/c = 0.016$

**Beveled leading edge -25 degrees**

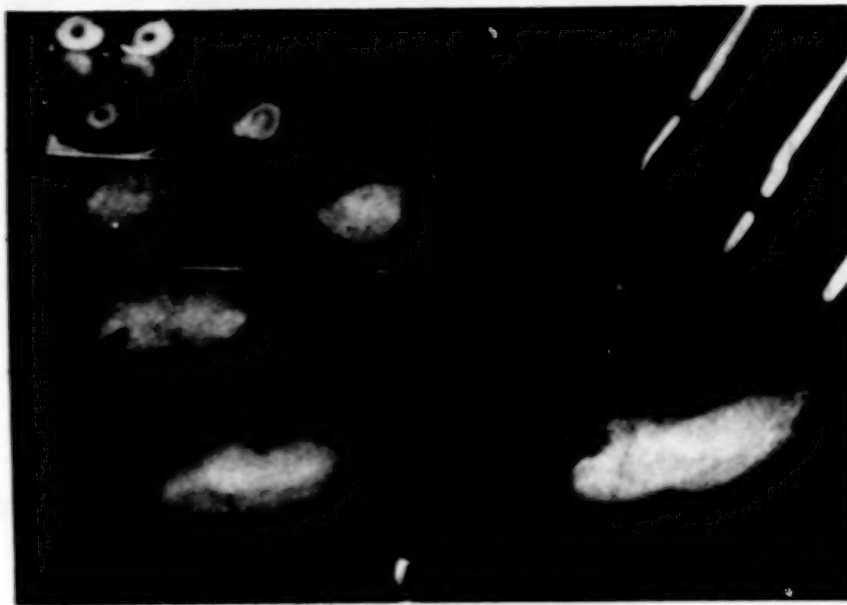
a. Geometry of 70-degree swept delta wing.



b. Smoke flow visualization with flood lamp illumination. Sweep = 70 deg,  $\alpha = 40 \text{ deg}$ ,  $V_\infty = 3 \text{ m/s}$ .

Figure 9. 70-degree swept delta wing.

ORIGINAL PAGE IS  
OF POOR QUALITY

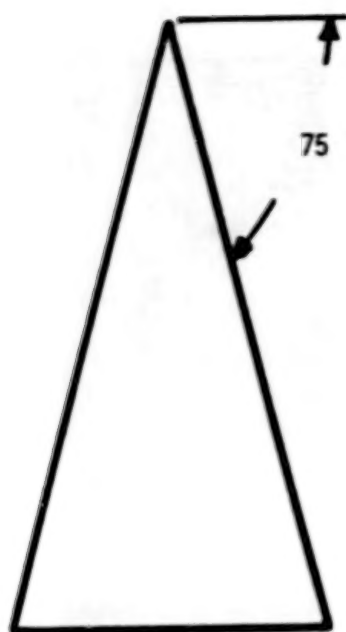


c. Lateral laser sheet cross sections.  
Sweep = 70 deg, Alpha = 40 deg,  $V_{\infty} = 3$  m/s.



d. Longitudinal laser sheet cross section.  
Sweep = 70 deg, Alpha = 40 deg,  $V_{\infty} = 3$  m/s.

Figure 9. Concluded.



**Planview of Model**

$\angle_{LE} = 75 \text{ degrees}$

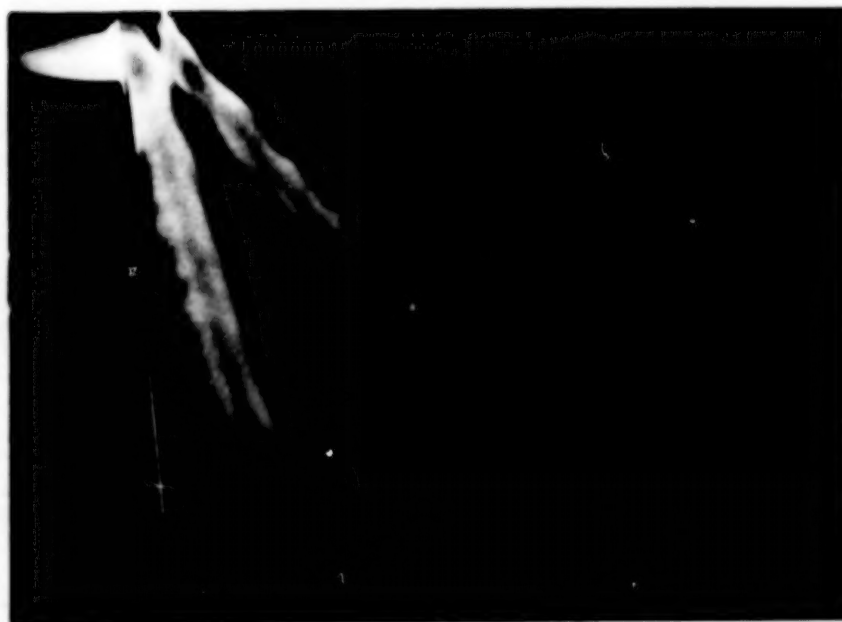
$c = 406 \text{ mm}$

$AR = 1.07$

$t/c = 0.016$

**Beveled leading edge -25 degrees**

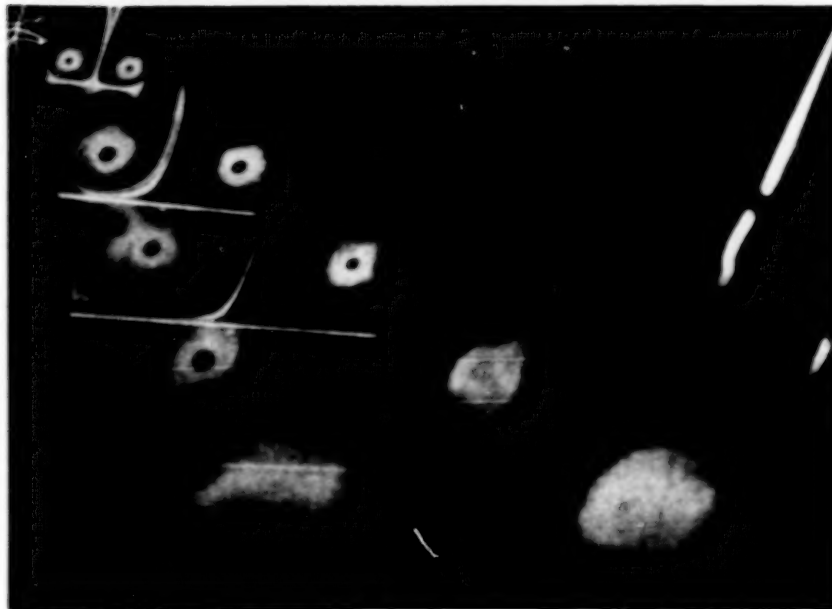
a. Geometry of 75-degree swept delta wing.



b. Smoke flow visualization with flood lamp illumination. Sweep = 75 deg,  $\alpha = 40 \text{ deg}$ ,  $V_{\infty} = 3 \text{ m/s}$ .

Figure 10. 75-degree swept delta wing.

ORIGINAL PAGE IS  
OF POOR QUALITY



c. Lateral laser sheet cross sections.  
Sweep = 75 deg, Alpha = 40 deg,  $V_{\infty} = 3$  m/s.



d. Longitudinal laser sheet cross section.  
Sweep = 75 deg, Alpha = 40 deg,  $V_{\infty} = 3$  m/s.

Figure 10. Concluded.



Planview of Model

$\angle_{LE} = 80 \text{ degrees}$

$c = 406 \text{ mm}$

$AR = 0.7$

$t/c = 0.016$

Beveled leading edge -25 degrees

a. Geometry of 80-degree swept delta wing.

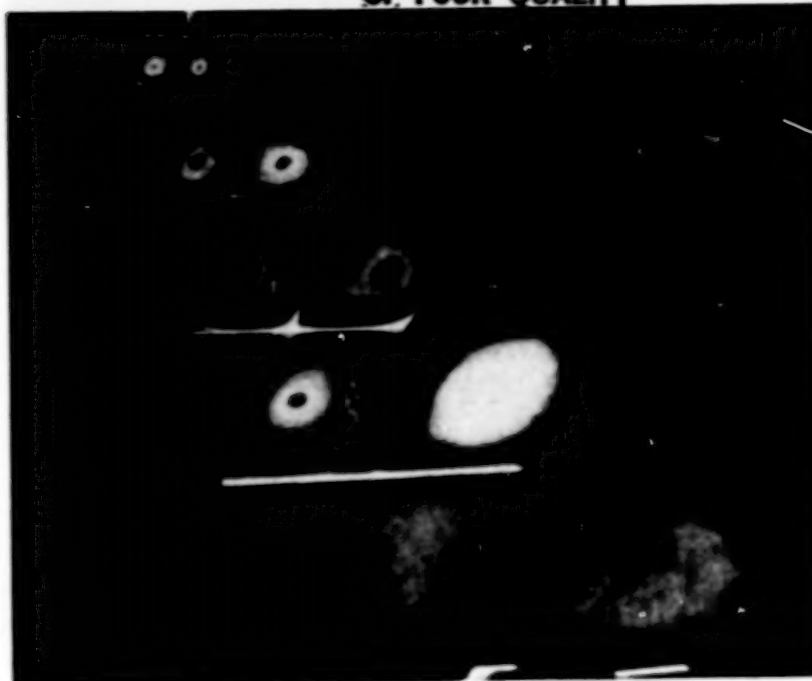


b. Smoke flow visualization with flood lamp illumination. Sweep = 80 deg,  $\alpha = 40 \text{ deg}$ ,  $V_{\infty} = 3 \text{ m/s}$ .

Figure 11. 80-degree swept delta wing.



ORIGINAL PAGE IS  
OF POOR QUALITY



c. Lateral laser sheet cross sections.  
Sweep = 80 deg, Alpha = 40 deg,  $V_{\infty} = 3$  m/s.




d. Longitudinal laser sheet cross section.  
Sweep = 80 deg, Alpha = 40 deg,  $V_{\infty} = 3$  m/s.

Figure 11. Concluded.



**Planview of Model**

 **LE = 85 degrees**

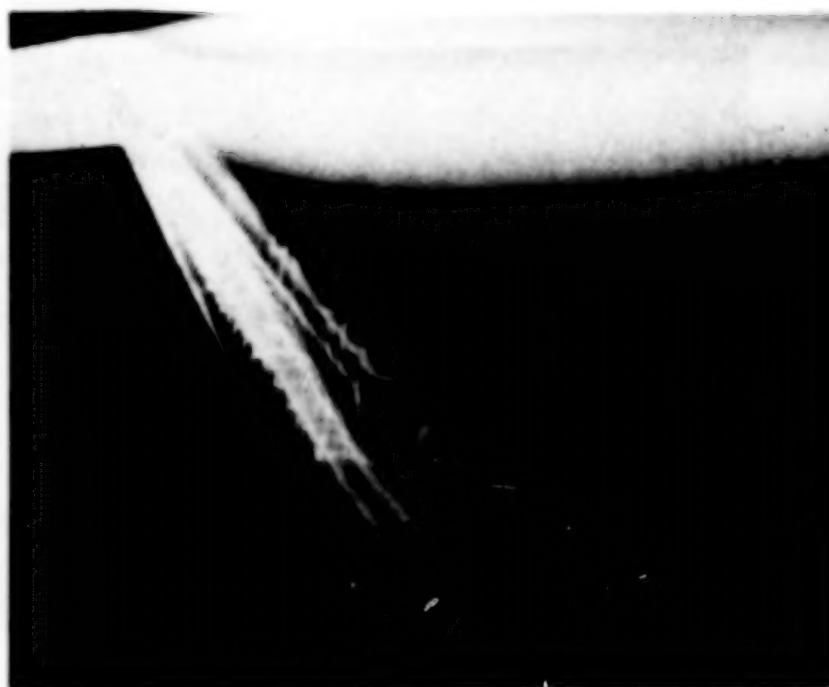
**c = 406mm**

**AR = 0.35**

**t/c = 0.016**

**Beveled leading edge -25 degrees**

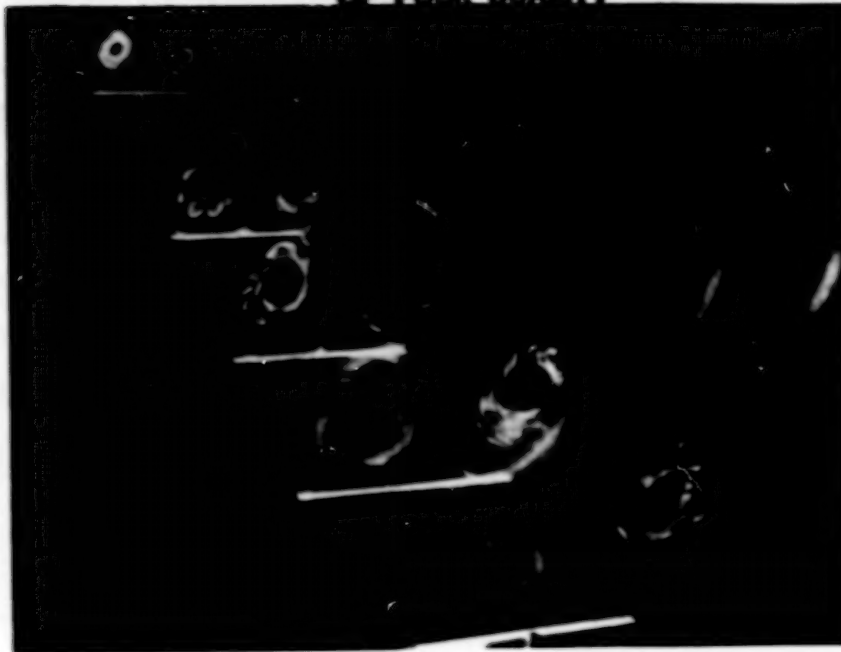
a. Geometry of 85-degree swept delta wing.



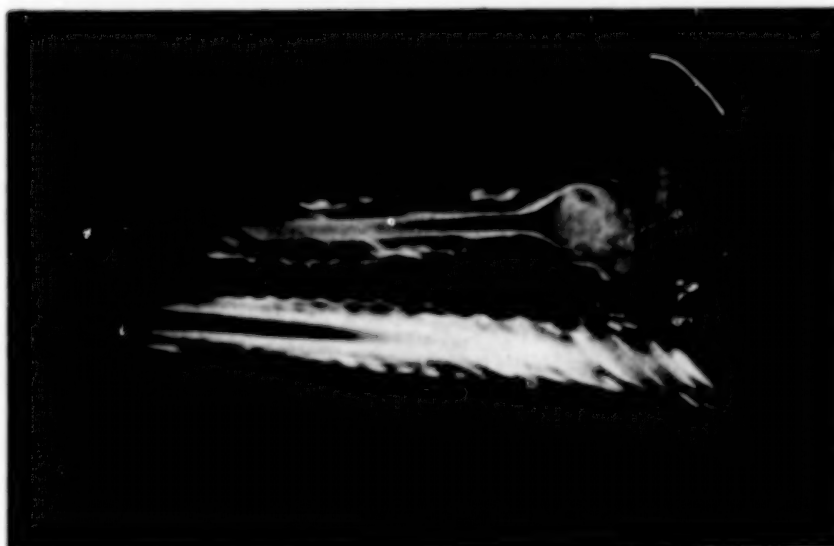
b. Smoke flow visualization with flood lamp illumination. Sweep = 80 deg, Alpha = 40 deg,  $V_{\infty} = 3$  m/s.

Figure 12. 85-degree swept delta wing.

ORIGINAL PAGE IS  
OF POOR QUALITY



c. Lateral laser sheet cross sections.  
Sweep = 85 deg, Alpha = 40 deg,  $V_{\infty} = 3$  m/s.



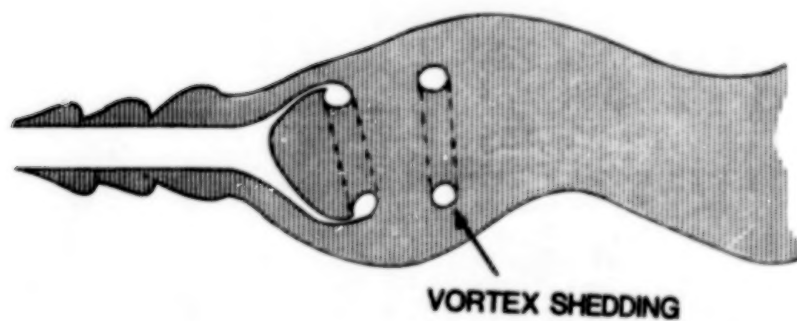
d. Longitudinal laser sheet cross section.  
Sweep = 85 deg, Alpha = 40 deg,  $V_{\infty} = 3$  m/s.

Figure 12. Concluded.



a. Enlargement from 16-mm movie frame. Bubble-type breakdown. Longitudinal cross section.

#### BUBBLE TYPE BREAKDOWN



b. Schematic representation of bubble-type breakdown. Longitudinal cross section.

Figure 13. Longitudinal view of bubble-type breakdown.

ORIGINAL PAGE IS  
OF POOR QUALITY



a. Enlargement from 16-mm movie frame.  
Bubble-type breakdown. Lateral cross  
section.

**BUBBLE TYPE VORTEX  
BREAKDOWN**

**SHEAR LAYER ROLL UP**



b. Schematic representation of bubble-  
type breakdown. Lateral cross section.

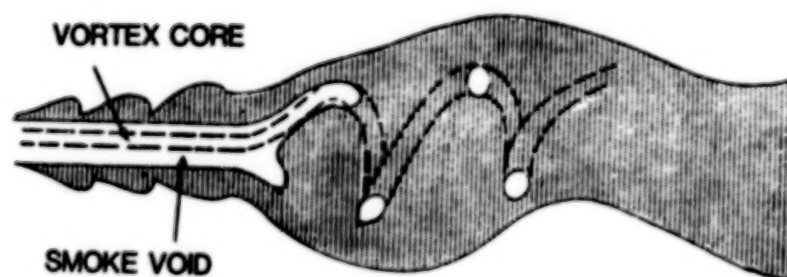
Figure 14. Lateral view of bubble-type breakdown.





a. Enlargement from 16-mm movie frame.  
Spiral-type breakdown. Longitudinal  
cross section.

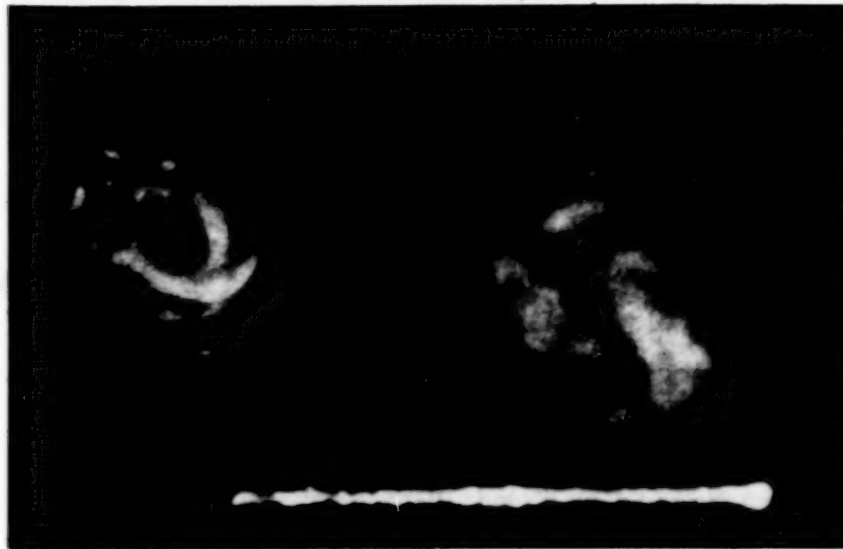
#### SPIRAL TYPE VORTEX BREAKDOWN



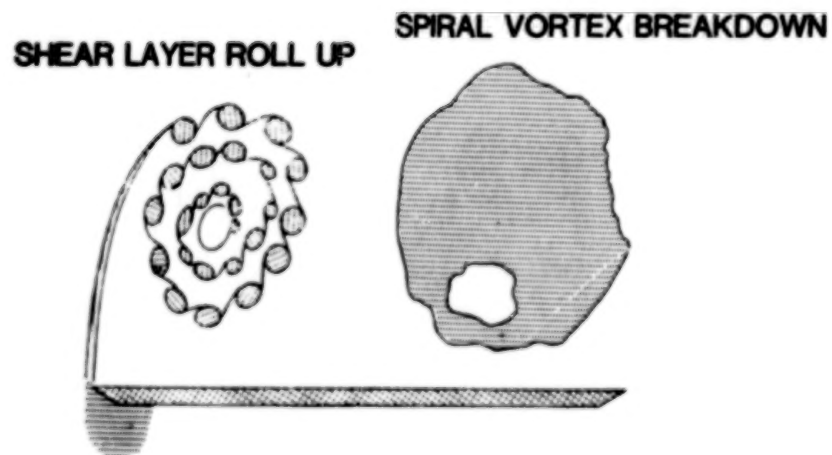
b. Schematic representation of spiral-  
type breakdown. Longitudinal cross  
section.

Figure 15. Longitudinal view of spiral-type breakdown.

ORIGINAL PAGE IS  
OF POOR QUALITY



a. Enlargement from 16-mm movie frame.  
Spiral-type breakdown. Lateral cross  
section.



b. Schematic representation of spiral-  
type breakdown. Lateral cross section.

Figure 16. Lateral view of spiral-type breakdown.

## DELTA WING L. E. VORTEX - AXIAL VELOCITY

Sweep Angle = 70 deg.

Angle of Attack = 30 deg.

$U$  = Freestream Velocity = 9.1 m/sec.

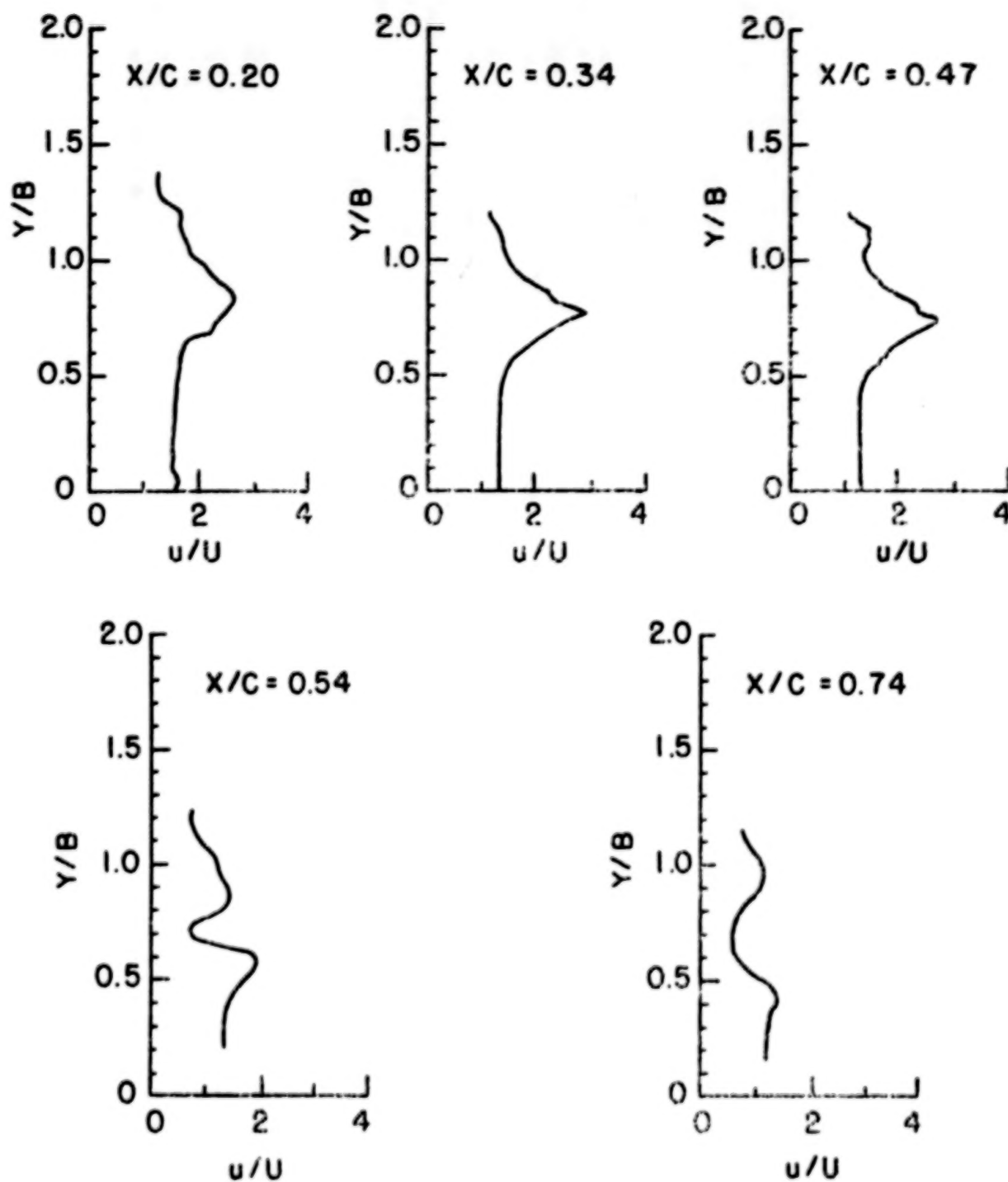


Figure 17. LDA measurements: axial velocity profiles.

## DELTA WING L.E. VORTEX - SWIRL VELOCITY

Sweep Angle = 70 deg.

Angle of Attack = 30 deg.

$U$  = Freestream Velocity = 9.1 m/sec.

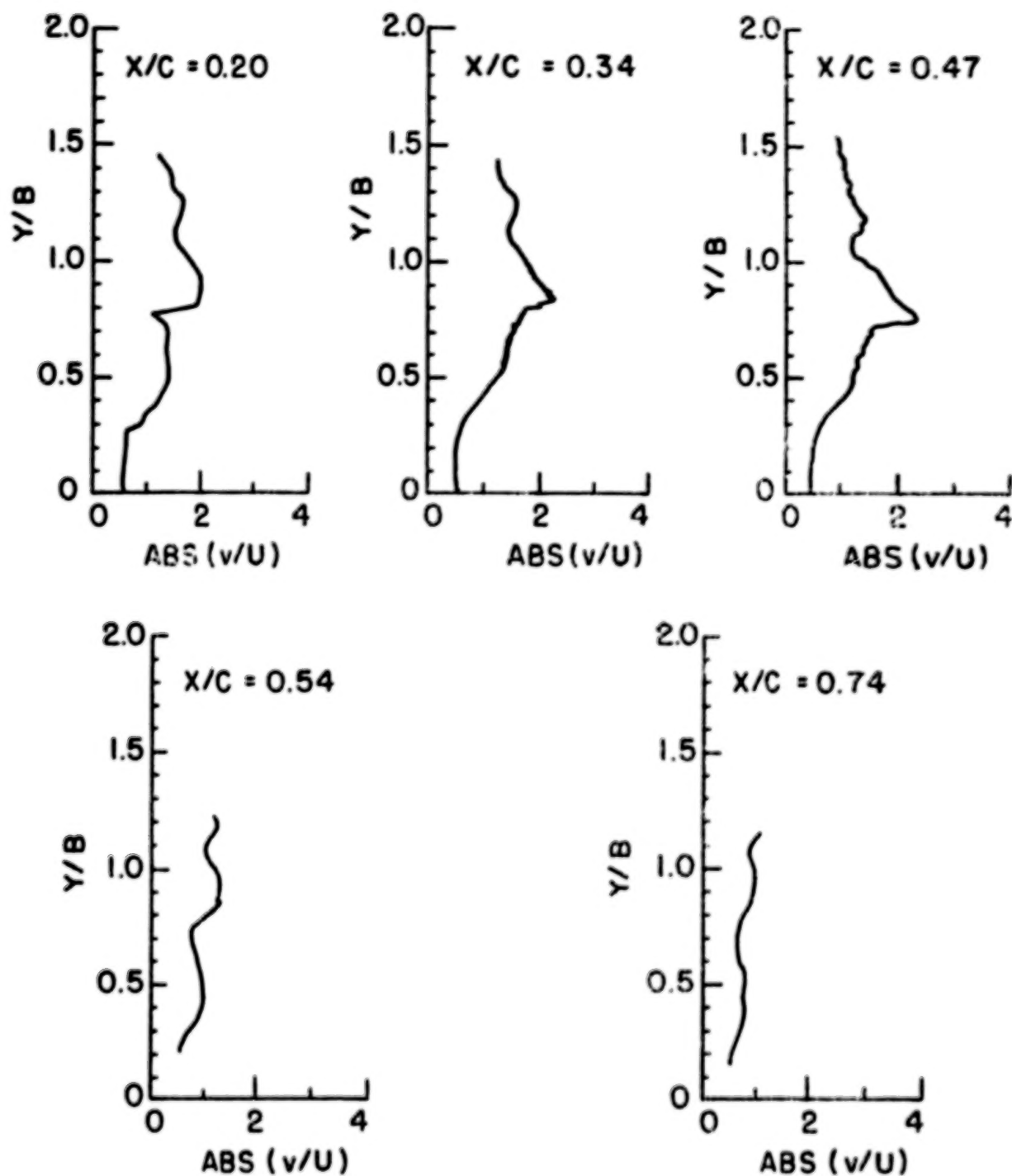


Figure 18. LDA measurements: swirl velocity profiles.

## LASER VELOCIMETRY IN HIGHLY THREE-DIMENSIONAL AND VORTICAL FLOWS

Charles J. Novak, Charles R. Huie, and Kenneth C. Cornelius  
Lockheed-Georgia Co.  
Marietta, Georgia

## SUMMARY

The need for experimentally determined 3-D velocity information is crucial to the understanding of highly 3-dimensional and vortical flow fields. In addition to gaining an understanding of the physics of flow fields, a correlation of velocity data is needed for advanced computational modelling. A double pass method for acquiring 3-D flow field information using a 2-D laser velocimeter (LV) is described. The design and implementation of a 3-D LV with expanded capabilities to acquire real-time 3-D flow field information are also described. Finally, the use of such an instrument in a wind tunnel study of a generic fighter configuration is described. The results of the wind tunnel study highlight the complexities of 3-D flow fields, particularly when the vortex behavior is examined over a range of angles of attack.

## INTRODUCTION

Since its conception by Yeh and Cummins (ref. 1) of Columbia University in 1964, the laser velocimeter (LV) has proved itself to be a most useful non-intrusive flow field velocity measuring instrument. Early versions of the instrument were limited to single direction velocity measurements and soon evolved to 2-D with reverse flow measurement capability. Yanta, in a recent paper (ref. 2), has described the LV's usefulness in the field of wind tunnel testing. Lockheed-Georgia Co. started LV research in 1968 and has had a continuing role in instrumentation development since then. Examples of the type of flow field measurements that have been acquired to date are shown in figures 1 and 2. These 2-D flow field vector plots have been the result of substantial efforts in LV research and application and have led to a better understanding of the physics of unpowered and powered flow fields.

Recent efforts in the analysis of three-dimensional (3-D) flow fields by the technique of computational fluid dynamics (CFD) have driven the need to develop fully 3-D measurement capabilities. The goal of Lockheed's research has been the development of a 3-D instrument for measurements in highly three-dimensional and vortical flow fields.

## INTERIM TECHNIQUE

During the period of 3-D LV development, the need for 3-D flow field information became so great that a double-pass, or as to be labeled further, a 2 x 2-D method of 3-D velocity measurement was developed. This method is comparatively low cost based on instrumentation requirements; however, an attendant two-fold increase in test time may make it unsuitable for many wind tunnel tests.



78158-887

The use of the 2 x 2-D method is relatively straightforward and involves the use of a 2-D LV. Two sets of measurements are made with pre-determined fringe orientations with respect to the wind tunnel coordinate system. Orientation of the first and second measurement fringe geometries (second set of measurements made later in time with respect to the first set) along with tunnel coordinates is shown in figure 3. These two sets of measurements result in 2-D velocity information in the plane  $H_1 - R_1$  and  $H_2 - R_2$ . Note that in this figure the vertical fringes are parallel in both measurement orientations ( $R_1 = R_2$ ). The desired end result, the on-axis velocity component,  $W$ , in the  $z$  direction, is found by subsequent post-processing of the two data sets.

#### Method Description

Data reduction is done off-line and is based on a formulation similar to that of 3-D hot wire anemometry. This formulation is the heart of the method and is left general for the sake of completeness. First, consider direction cosines with respect to the tunnel coordinate system and the instantaneous fringe velocities; that is,  $a_1, a_2, b_1, b_2, c_1, c_2$ , and  $H_1, R_1$ . Conversely the same may be done with respect to the second set of measurements so that  $a_3, a_4, b_3, b_4, c_3, c_4$  are used as direction cosines for the two perpendicular fringe velocities  $H_2, R_2$ . Finally, based on the determined direction cosines, each measured velocity component ( $H_1 - R_2$ ) may be expressed as a combination of the tunnel velocities and direction cosines. This results in:

$$a_1 U + b_1 V + c_1 W = H_1 \quad (1a)$$

$$a_2 U + b_2 V + c_2 W = R_1 \quad (1b)$$

$$a_3 U + b_3 V + c_3 W = H_2 \quad (1c)$$

$$a_4 U + b_4 V + c_4 W = R_2 \quad (1d)$$

yielding an overspecified set of equations which may be solved for the instantaneous tunnel velocities  $U, V$ , and  $W$  using an appropriate least-squares optimization of simultaneously solved equations.

Now, it is convenient to differentiate between mean and instantaneous velocities. This is done by assuming a mean velocity  $\bar{U}$ , and the departure from that mean as the velocity  $u'$ . Using that premise, equation 1a becomes:

$$a_1 (\bar{U} + u') + b_1 (\bar{V} + v') + c_1 (\bar{W} + w') = (\bar{H}_1 + h_1') \quad (2)$$

The same may be performed for  $R_1, H_2$ , and  $R_2$ , but is not shown here for brevity's sake. Further, if equation 2 is squared and then time averaged the end result is:

$$a_1^2 \bar{u}^2 + b_1^2 \bar{v}^2 + c_1^2 \bar{w}^2 + a_1 b_1 \overline{uv} + a_1 c_1 \overline{uw} + b_1 c_1 \overline{vw} = \bar{h}_1^2 \quad (3)$$

Once again similar expressions may be derived for  $\bar{r}_1, \bar{h}_2$ , and  $\bar{r}_2$ . Note that equation 3 contains the six principal Reynolds stresses as unknowns. Compiling these results yields 4 equations and 3 unknowns in the mean velocities and 4 equations and 6 unknowns in the time-averaged fluctuating or turbulence quantities. Clearly the experimentalist faces a dilemma in solving for the turbulence quantities in the flow field. He may either choose to use only mean velocities or use appropriate fringe orientations such that terms drop out. However, if 2-D instrumentation capabilities are examined and utilized fully, the measurement of  $H_1, R_1$  and  $H_2, R_2$

may be made such that the fluctuating cross products  $\overline{h_1 r_1}$  and  $\overline{h_2 r_2}$  are formed. This requirement of coincidence is needed to close the set of equations containing the six Reynolds stresses. Then, proceeding as before the expression for  $\overline{h_1 r_1}$  becomes:

$$\begin{aligned} \overline{h_1 r_1} = & a_1 a_2 \overline{u^2} + b_1 b_2 \overline{v^2} + c_1 c_2 \overline{w^2} + (a_1 b_2 + a_2 b_1) \overline{uv} + (a_1 c_2 + a_2 c_1) \overline{uw} \\ & + (b_1 c_2 + b_2 c_1) \overline{vw} \end{aligned} \quad (4)$$

Similarly, an expression for  $\overline{h_2 r_2}$  may be written. These two equations are then combined with the four previously derived equations, yielding 6 linear equations and 6 unknowns, all of which may be solved easily using a matrix inversion routine. The end result of this scheme is full 3-D flow field information to the first statistical moment.

## 2 x 2-D Method Usage

Usage of the method should be based upon data requirements and with these needs defined, fringe-tunnel geometries must be chosen with some discretion. If those details are ignored, matrix singularities may occur making the desired quantities unresolvable. Therefore, a prior knowledge of matrix behavior is desirable since some quantities, such as  $\overline{uw}$  and  $\overline{w^2}$ , may require pitch and roll in addition to yawing of the fringe systems with respect to the tunnel coordinates.

Errors in the method not only reflect uncertainties in the LV electronics but also in fringe angles and repositioning. As noted in figure 3, the redundancy in the V component ( $R_1 = R_2$ ) is not without purpose. Specifically, data quality is enhanced dramatically if profile matching is done with either  $\overline{V}$  or  $\overline{v^2}$ . Each of the corresponding sets of measurements is interpolated for any spatial offsets and their differences in position are averaged. Further, uncertainties also arise from inaccuracies in determining fringe angles with respect to the tunnel coordinate system. Reduction of these uncertainties is discussed fully by Orloff and Snyder (ref. 3) and the same principles were employed in the present work. Also as in their work, adoption of a rotating calibration device aided in reducing errors considerably during implementation of the 2 x 2-D method.

## Wind Tunnel Tests Using 2 x 2-D Method

The usefulness of this technique is illustrated in two experiments where 3-D LV information was provided through the 2 x 2-D methodology. The first experiment was designed to provide correlation data for 3-D boundary layer code development using advanced turbulence modelling. The wind tunnel model used was a low-aspect-ratio, highly swept fighter type wing on which upper and lower surface velocity measurements were made. Shown in figure 4 are the boundary layer profiles for both the chordwise and spanwise velocity components at 60% span on the lower surface. Shown in figure 5 is a contour map, in the survey region on the lower surface, of the dimensionless turbulence anisotropy parameter T. For isotropic flow, the value of T, as constructed from mean flow gradients and  $\overline{uv}$  and  $\overline{vw}$  shear stresses, tends to 0.5. Physically, it reflects the relative rate at which the chordwise and spanwise velocity gradients develop. Values of T tending towards zero represent turbulence that is predominantly strained in W or the spanwise direction and for values greater than one, straining is dominant in the chordwise direction.

A second experiment specifically designed to aid development of a coupled 3-D boundary layer and Euler code was successfully carried out using the 2 x 2-D method. In this experiment the wind tunnel model consisted of an aft-fuselage, representative of that for a modern transport aircraft. LV velocity surveys were conducted in both the open separation region and the near wake. Figure 6a shows the mean crossflow velocity profiles at a particular cross section station on the model and depicts the experimental line of crossflow reversal. Further, the presence of the trailing vortex can be seen in the streamwise velocity contours, as can be the fuselage and wing wakes, figure 6b.

The merits of the 2 x 2-D method are demonstrated in the types of data that become available with its employment in wind tunnel testing. However, due to inaccuracies and the time requirements involved with its use, a fully 3-D instrument would eclipse its usefulness in a typical production basis.

### 3-D LV DEVELOPMENT

#### Instrument Definition

At the conceptual stage of the 3-D LV development program substantial groundwork was laid with electronics/signal requirements. Previous 2-D experience showed that a simple one channel expansion to the current design would provide excellent signal handling capabilities. Therefore, the electronics used was based upon the single cycle validation circuitry and dual counter approach used previously on the 2-D instrument. From a design standpoint, important electronics/signal processing constraints were firmly established in the prior use of the 2-D burst-type detector electronics. This was the foundation for the 3-D LV development.

Velocity range and resolution are probably the most important of all constraints; however, optical system geometry, which defines accessibility to the flow field, is also a consideration from the practical standpoint. In addition to mean velocity measurement, turbulence intensities and other higher statistical moments about the mean are also needed. Additionally, in the realm of unsteady aerodynamics, temporal data may be required, either as conditionally sampled data or as spectral information about the flow field in question. Lastly, the 3-D instrument must be usable on a production testing basis. This includes stable alignment and substantial data rates that are comparable with existing 2-D instrumentation.

#### Optical System Choices

For wind tunnel testing purposes the logical choice for a light source is the Argon-Ion laser. This laser commonly used for wind tunnel testing has principal emission lines at wavelengths of 488.0 nm (blue) and 514.5 nm (green), each of which contains approximately 30% of the total power output. Additional emission lines located at 476.5 nm (deep blue) and 496.5 nm (blue-green) contain 10% each of the total power. Thus, the developer is given the choice of 4 emission lines to utilize, typically only two (488.0 and 514.5 nm.) or three (488.0, 514.5 and 476.5 nm.) of which are used for three-component velocity measurements. Regardless of wavelength, the on-axis velocity component must be measured with a separate set of fringes or indirectly through a non-orthogonal technique.

In addition to wavelength selection and fringe orthogonality or non-orthogonality, a choice between frequency domain or velocity domain processing of the Doppler signal may be of particular advantage for W component extraction. The



choices to be considered are presented in figure 7 and are based upon known techniques in arriving at the much sought after third component. Relative merits of each configuration must be weighed with respect to the type of use the instrument will see, and an indepth study of each is warranted.

### Optical Selection and Design

The construction of the existing wind tunnels at the Lockheed-Georgia Company and the lack of windows in the floors and ceilings make orthogonal fringe orientation impracticable. Further, previous experience has shown that a 3-D orthogonal system would almost always have a set of laser beams oriented perpendicular to the model's surface. This would represent serious glare problems and would render the system unusable in near-wall measurements. For these reasons the orthogonal fringe systems were removed from the selection process. As seen in figure 7, the remaining choices are from the non-orthogonal fringe category and are comprised of either a two or a three-color optical configuration. However, prior to optical and electronics fabrication a comparison of the operational aspects of each of these two types of optical configurations, as shown in figure 8, was performed.

Velocity range and resolution may be easily understood if the concept of effective fringes is introduced. As a means of understanding effective fringes, consider two non-orthogonal fringe systems propagating at 40 MHz and 60 MHz respectively and separated by an angle  $2k$ . This wavefront geometry is shown in figure 9 and may either be formed by a single wavelength or by two wavelengths such as the two and three-color systems would produce. Analyzing the expected photomultiplier tube (PMT) signals it can be seen that they will contain both a frequency component from the carrier (40 and 60 MHz) and one from the velocity of the media itself. This is seen clearly if the conventional expression for velocity is applied for each separate fringe system such that:

$$H_1 = \frac{\lambda}{2 \sin \theta/2} (f_{\text{media}} - f_{\text{shift}})_1 \quad f_{\text{shift}} = 40 \text{ MHz} \quad (5)$$

$$H_2 = \frac{\lambda}{2 \sin \theta/2} (f_{\text{media}} - f_{\text{shift}})_2 \quad f_{\text{shift}} = 60 \text{ MHz} \quad (6)$$

where  $\lambda$  and  $\theta$  are the respective wavelength and beam angles that contribute to the formation of the fringes. Note that the first term in equations 5 and 6 corresponds to the fringe spacing. From the 2 x 2-D method presented earlier it can be shown that the transverse, or on-axis velocity component,  $W$ , based only on yaw with respect to the tunnel coordinate system, is simply:

$$W = \frac{H_1 - H_2}{2 \sin k} \quad (7)$$

and  $k$  is the half angle between the fringe systems. Substituting equations 5 and 6 into equation 7 yields

$$W = \frac{\lambda}{4 \sin k \sin (\theta/2)} (\Delta f_{\text{media}} - \Delta f_{\text{shift}}) \Delta f_{\text{shift}} = 20 \text{ Mhz} \quad (8)$$

Note that this result, equation 8, bears resemblance to the original fringe spacing equations 5 and 6. Therefore, it is possible to think of the first term in equation 8 as the effective fringe spacing in the transverse direction and the second term as the associated frequency corresponding to the fringe crossing in units of inverse time. This concept of effective fringes (also shown graphically in figure 9 as the dashed lines perpendicular to the on-axis direction) is the backbone of the 3-D LV in non-orthogonal fringe systems and is made use of in velocity range and resolution comparisons.

Using this concept of effective fringes, a comparison of frequency and velocity domain processing (sometimes called pre- and post-processing) can be made. Frequency domain processing is carried out by heterodyning the two PMT signals containing the W component such that the U component is essentially removed from the signal leaving only that corresponding to W. From a practical standpoint this may be achieved by employing double balanced diode mixers. These mixers, also used to heterodyne the Bragg cell shift to a manageable range, operate on the basis that the local oscillator (LO) side is maintained at a constant amplitude of +7dBm. The reference (RF) side power level may be varied from -20dBm, where typical Doppler signals lie, all the way up to 0dBm. Noise levels increase when these input specifications are not met. So when using the circuits in actual testing, significant amplification is needed on the LO input side, as is seen in figure 10, to raise the signal to design specification levels. This represents the major drawback to frequency domain processing in the non-orthogonal fringe systems. Not apparent from figures 9 and 10 is an operational benefit that ensures against the likelihood of two particles in separate regions of the measurement volume being seen and processed as one particle. The heterodyning of the two signals, such that a W signal is formed, also eliminates the possibility of this situation occurring unless they enter and leave the fringe systems at the same point in time.

In comparison with frequency domain processing, velocity domain processing of signals eliminates the need for additional filters, amplifiers and mixers in the system. Instead of using effective fringes, the individual velocities from the non-orthogonal fringes are computed in a traditional 2-D manner and later combined discretely sample by sample (three-channel coincidence required during acquisition). Typically, higher uncertainties are present at this level of processing since uncertainties are additive, and unlike in frequency domain processing, amplitude restrictions do not exist. This may in turn help the signal-to-noise ratio (SNR) of the instrument in low SNR regions in the flow field.

#### Velocity Range and Resolution Determined

As an aid in comparing the two- and three-color 3-D LV optics configurations, an analytical model was developed to determine velocity range and resolution for a given set of input parameters. These included laser beam diameter, counter resolution and bandwidth, beam angles and fringe angles. Outputs of the model were effective fringe spacing, velocity range and resolution as well as frequency bandwidth. Using this model for initial comparisons yielded information that led to the selection of the most suitable optics configuration for highly three-dimensional and vortical flow fields.



Examples of the output of this model are shown in figures 11 and 12. Figure 11 is a plot of separation angle versus effective fringe spacing for several beam pair angles. With the existing 2-D beam pair angles ( $\theta$ ) at approximately 3.8 degrees and fringe spacings of 20  $\mu\text{m}$ , it is seen that substantial separation angles are needed to give effective fringe spacings of 20  $\mu\text{m}$  to 30  $\mu\text{m}$ . Once an effective fringe spacing is determined from figure 11 the user can proceed to figure 12 where velocity range and resolution are determined. To determine velocity range, the minimum beam diameter ( $D_E$  (mm)) is examined at the operating bandwidth of the electronics and the upper velocity limit is noted at this intersection on the horizontal velocity axis. Similarly, resolution is obtained for a given bandwidth and effective fringe spacing ( $D_f$  ( $\mu\text{m}$ )) by noting the intersection of the two curves on the horizontal axis. In addition to range and resolution, the bandwidth for a particular velocity range is also available through the use of figure 12. This is done simply by noting the angle of the focused laser beam pairs ( $\theta$ ) that applies and using that curve to determine the value of frequency bandwidth for a given velocity.

Using these charts to compare 3-D LV optics packages it was possible to determine performance prior to fabrication. Based on range and resolution requirements, typical of what is needed for vortical flows, the frequency bandwidth for the two-color system was found to overlap from one channel to another. To avoid this, the resolution became unacceptable, since the effective fringe spacing had to be made larger to increase the velocity range. Further complicating the matter, the wide fringe spacing also decreases the number of fringes in the measurement volume making alignment sensitive and valid data signals unavailable. Contrasting the two-color performance, the three-color system separates channels by wavelength (color) and not by bandwidth separation, hence, velocity crosstalk is non-existent for this optics package. For that reason the three-color system is more suitable since its upper velocity limits are dictated by the counter input bandwidth rather than the frequency crosstalk bandwidth. Thus, because velocity range and resolution are decoupled in the three-color system, resolution needs not be sacrificed for range when operating in flow fields where the transverse component may vary from zero to more than that of the freestream.

In addition to velocity measurement capabilities, a rather particular advantage of the three-color system in frequency domain processing was discovered during preliminary studies. Shown in figure 13 are block diagrams of the necessary electronics needed to frequency separate and mix signals such that the signal contributing to the  $W$  effective fringes may be processed. Note that one less signal split is needed in the three-color pre-processor. From an operational standpoint this gain of 2 in signal strength offsets the lower power levels of the third emission line (476.5 nm) from the Argon-Ion laser.

Based on the comparisons of both performance and operational capabilities, the three-color 3-D LV optics configuration was chosen since its merits far outweighed those of its two-color counterpart. While a two-color optics package was built its use is limited to low-speed flows and flows where the transverse component is small.

### THREE-COLOR 3-D LV DESCRIPTION

System fabrication and interfacing consisted of updating an existing 2-D system to 3-D capability. To accomplish this an additional set of receiving and transmitting optics was constructed based on the design used previously in 2-D LV studies. The optics, electronics and positioner are shown in figure 14. Previous experience has shown that rotating regions in the flow field may be particle

deficient. Hence, two 18 watt Argon-Ion lasers, one operating at 476.5 nm and the other multi-line, were used to boost signal-to-noise ratios in sparsely seeded regions in the flow field. The current configuration shown in figure 14 has complete flexibility in that both receiving and transmitting optics may be oriented arbitrarily with respect to the model and the wind tunnel. Similar to the setup of Yanta (ref. 4) is the large included angle between the non-orthogonal fringes. For the testing to be detailed later, the angle was set at 33 degrees, corresponding to a resolution of 0.3 m/sec and an upper velocity limit near 300 m/sec. This flexibility in optical design is advantageous since it reduces the number of regions in which the laser beams are obscured by either the model or the tunnel structure. Receiving optics are purposely separated to take advantage of the Mie scattering qualities that exist. In addition to optical wavelength separation between the 488.0 nm. and 476.5 nm channels, further insurance against optical filter bleed was provided by frequency separation with the use of Bragg cells operating at different frequencies.

Bench tests were conducted prior to production use of the instrument to insure system repeatability and accuracy. Resolution was verified experimentally through the use of a rotating calibration wheel as described earlier for the 2 x 2-D method. These tests were performed for two different fringe angles and compared with theory. As predicted, resolution in W behaved as the inverse sine of the angle  $2k$  between the non-orthogonal fringes. The results of the bench tests at  $W=0.0$  m/sec are as follows:

| $2k$     | $\Delta W$ Experiment | $\Delta W$ Theory    |
|----------|-----------------------|----------------------|
| 17.5 deg | .769 m/sec (2.5 fps)  | .738 m/sec (2.4 fps) |
| 30.0 deg | .462 m/sec (1.5 fps)  | .338 m/sec (1.1 fps) |

In addition to use during checkout, the rotating calibration device proved to be invaluable for routine alignment on a day to day basis in determining both fringe spacings and angles. With the operational limits established and verified the instrument was readied for production type testing.

### 3-D LV SURVEYS OF A GENERIC FIGHTER CONFIGURATION

Testing to date with the instrument has been limited because of its recent placement in service. However, this year's testing has included 3-D velocity surveys of a generic fighter configuration for the purpose of both CFD model development and the understanding of the flow field physics. Shown in figure 15 is the model geometry used for both numerically controlled model fabrication as well as for the CFD grid generation. The tip verticals were removed to facilitate LV testing. The geometry consists of a leading-edge strake sweep of 77 degrees followed by a wingsweep of 56 degrees. Testing was carried out in the Lockheed-Georgia Low Turbulence Wind Tunnel (.05% freestream turbulence) at a freestream velocity of 46 m/sec (150 fps). The corresponding Reynolds number based on centerline chord was 1.25 million. Shown in figure 16 are the model, tunnel and 3-D LV optics. Surveys were made of mean velocity in the Y-Z plane of the model at various X locations and several angles of attack and contained approximately 200 points each.

Data rate in the freestream region of the flow field was approximately 500 valid samples per second, whereas near the vortex core, the rate dropped to nearly 20 samples per second. Using laser sheet lighting for flow visualization purposes, seed

particles near the vortex core were observed to centrifuge outwards radially. To avoid these flow tracking problems, the mineral oil used for flow field seeding was size discriminated prior to injection into the wind tunnel. Based on the results of Dring and Suo (ref. 5), the Stokes flow model showed that a 1 micron diameter particle subjected to a radial acceleration of 150,000 meters per second squared (500 fps at a 1 in radius) resulted in a Stokes number of approximately 0.01. The tracking error associated with this situation is estimated at 3% in angular deviation. This analysis, as depicted in figure 17, warranted the use of a particle impactor to maintain seed size distribution centerlines below 1 micron in diameter.

Results of the 3-D LV surveys are shown in figures 18a-18f. These crossflow velocity vector plots show the chordwise development of the leading edge vortex at an angle of attack of 10 degrees. An examination of figures 18a and 18b shows only a single center or vorticity, apparently because the circumferential pressure gradient causes a coalescence of separate vortices from the strake and the wing leading edge. Contrasting these results, surveys taken at 18 degrees angle of attack showed vortex breakdown near the mid-chord location. Axial velocities, as shown in figure 19, change dramatically at vortex breakdown. The high peak in this velocity at 25% chord is entirely absent at 50% chord. Note that for the 13 degree angle of attack case, reversed axial velocities are seen near the center of the vortex. This can be directly attributed to a breakdown of the organized vortical flow. Lastly, as a result of the various surveys, the vortex core location can be tracked as a function of chord, span and height above the wing reference plane. Vortex breakdown and path are shown in figure 20 for both the 10 degree and 18 degree angle-of-attack cases.

#### RECOMMENDATIONS AND CONCLUSIONS

The 2 x 2-D LV method described was demonstrated to be a very powerful tool in making 3-D flow field measurement. The 3-D data were shown to be obtainable using a conventional 2-D instrument; however, due to its inaccuracies, it is recommended that its use should be carefully applied to particular situations that require turbulence information in addition to mean velocities. In the design study of two fully three-dimensional LV's, the three-color system was shown to be superior overall in both range and resolution. For these reasons, the system was fabricated for use in production testing of highly three-dimensional and vortical flows. Measurements over a generic fighter flow field justify the use of two large Argon-ion lasers. Based on this experience, it is recommended that higher powered lasers (0.5-1.0 watts/beam) be used to offset the diminished signal-to-noise ratios that are found at or near the core of a vortex.

#### REFERENCES

1. Yeh, Y. and Cummins, H. Z., "Localized Fluid Flow Measurements with a He-Ne Laser Spectrometer," Applied Physics Letter, Vol. 4, 1964, p. 176.
2. Yanta, W. J. "The Use of the Laser Doppler Velocimeter in Aerodynamic Facilities," AIAA 11th Aerodynamic Testing Conference, AIAA Paper 80-0435, March 18-20, 1980.
3. Orloff, K. L. and Snyder, P. K., "Reduction of Flow-Measurement Uncertainties in Laser Velocimeters with Nonorthogonal Channels," AIAA 21st Aerospace Sciences Meeting, AIAA Paper 83-0051, January 10-13, 1983, Reno, NV.

4. Yanta, W. J., "A Three-Dimensional Laser Doppler Velocimeter (LDV) for use in Wind Tunnels," ICIASF '79 Record, September 1979, Monterey, California.
5. Dring, R. P. and Suo, M., "Particle Trajectories in Swirling Flows," J. Energy, Vol. 2, No. 4, July-August 1978.



## GAW-1W/LV Mean Velocity Profiles

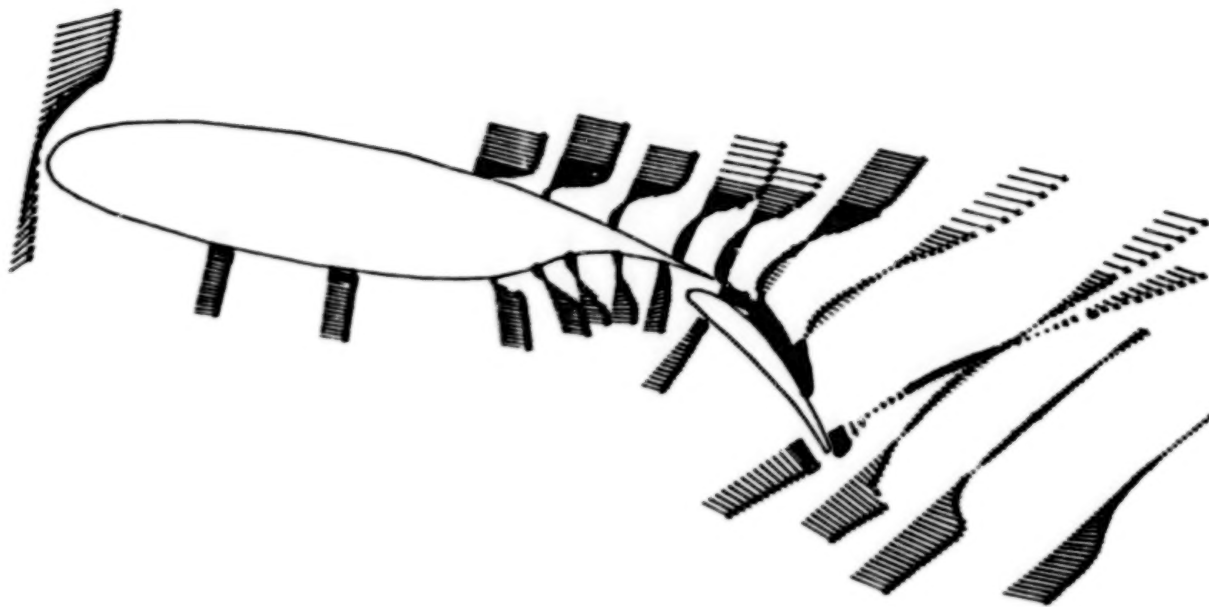


Figure 1

## CCW/LV Mean Velocity Vectors

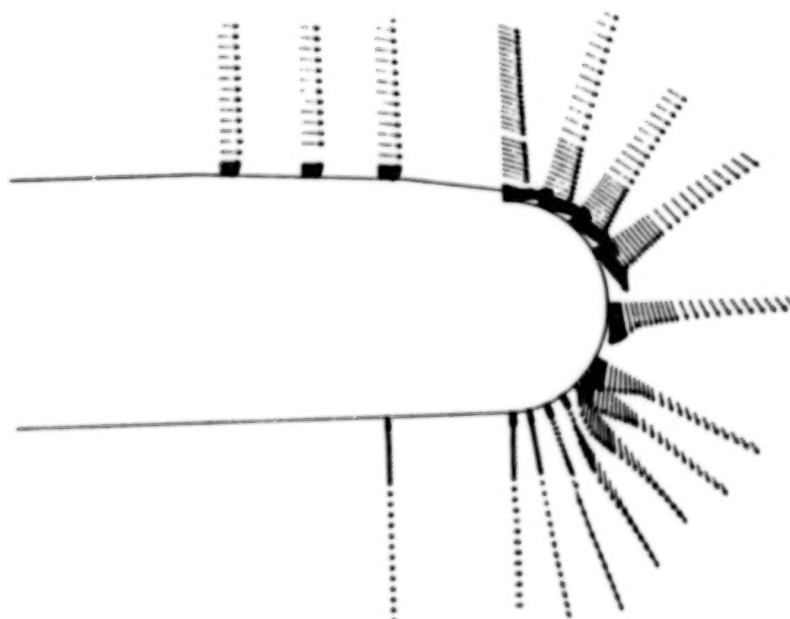


Figure 2



## LV Fringe and Wind Tunnel Coordinate System

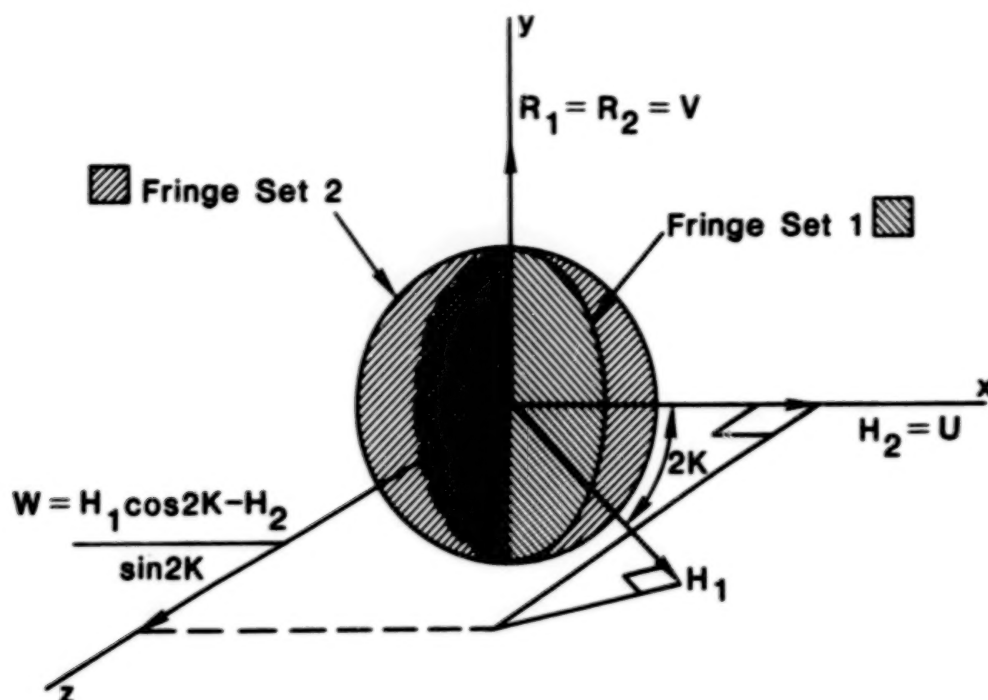


Figure 3

## 3-D Boundary Layer Measurements

### Using 2x2D Method

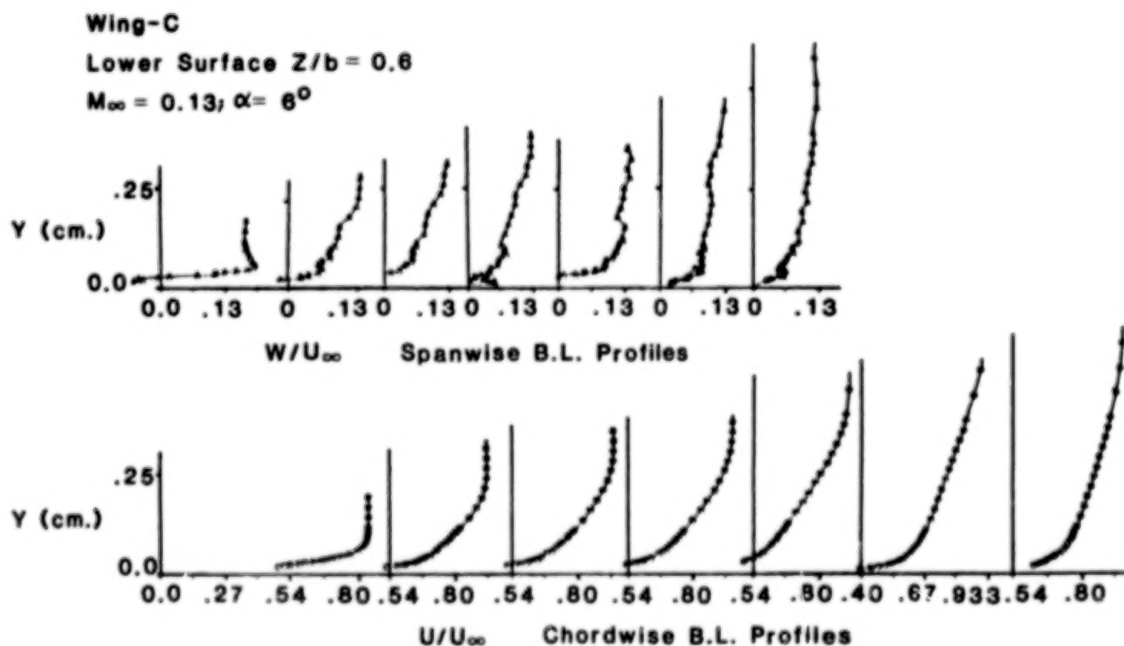


Figure 4

## Turbulence Anisotropy Measurements Using 2X2D Method

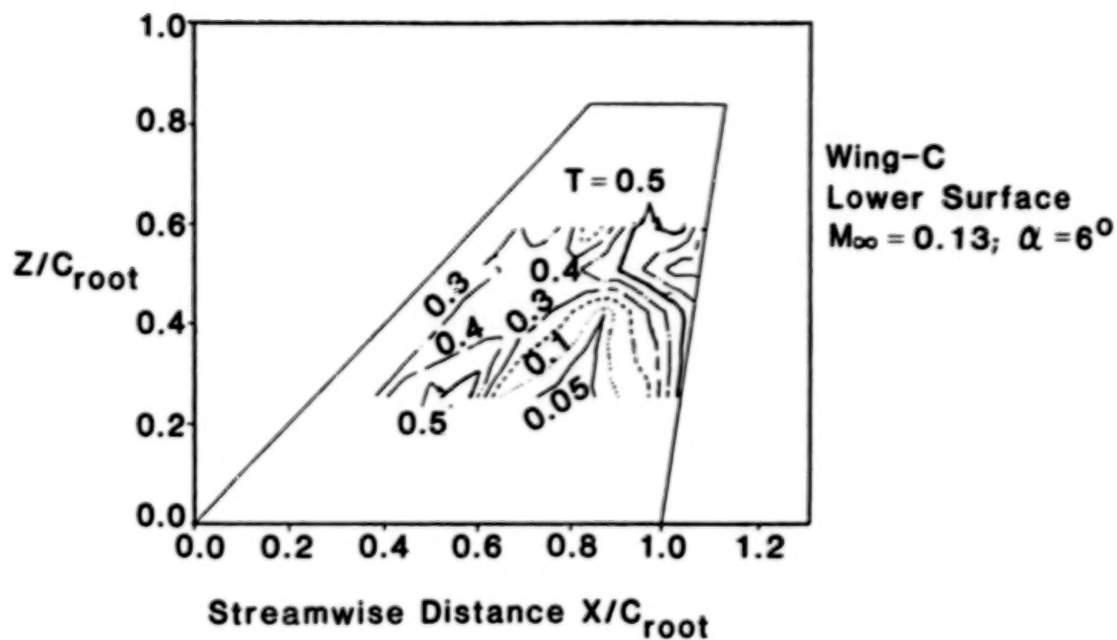


Figure 5

## Aft-Fuselage Measurements Using 2x2D Method

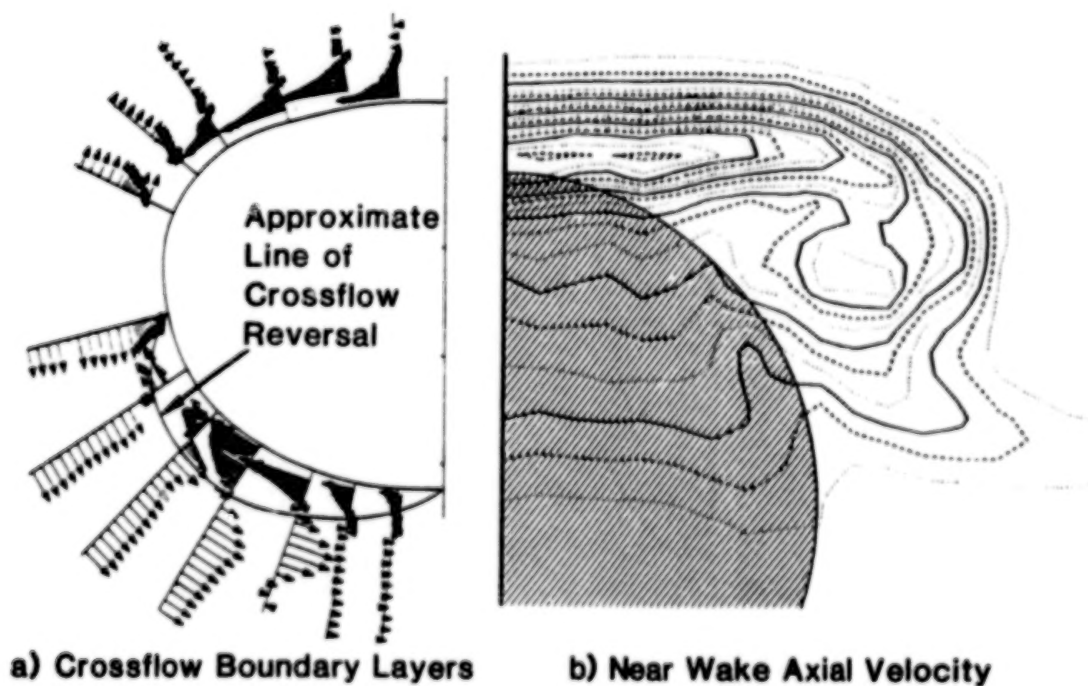


Figure 6

## 3-D LV Optical Configurations

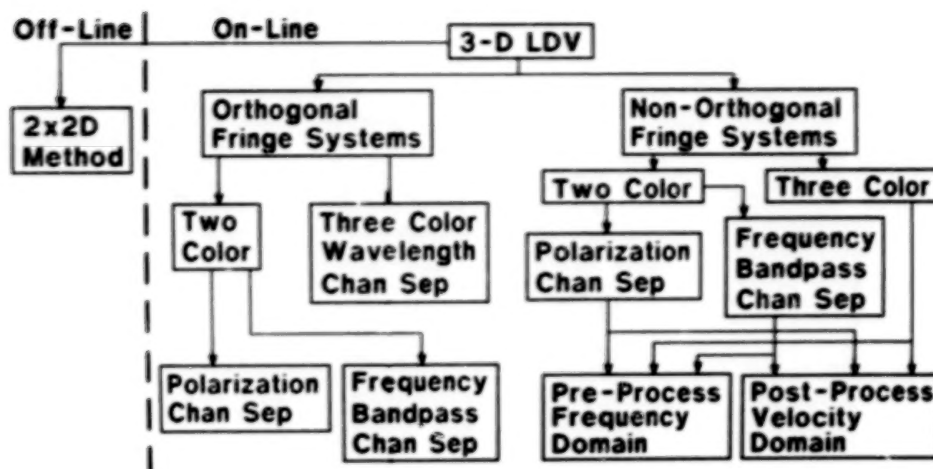


Figure 7

## 3-D LV Optical Beam Traces

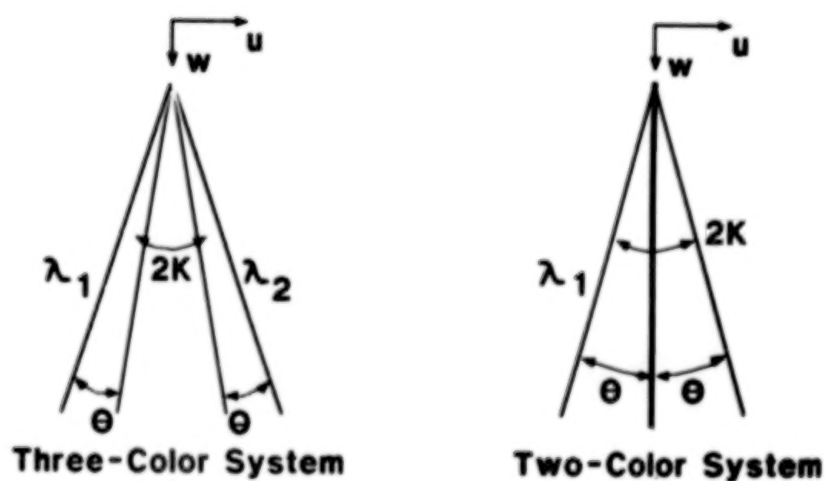


Figure 8

## Formation of Effective Fringes

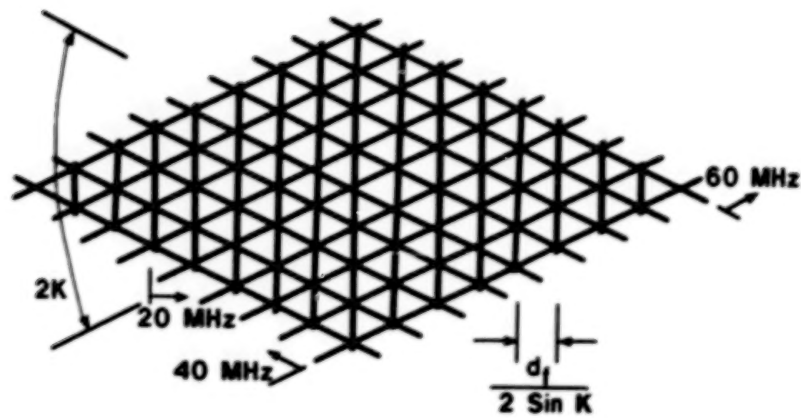


Figure 9

## Double Balanced RF Mixer

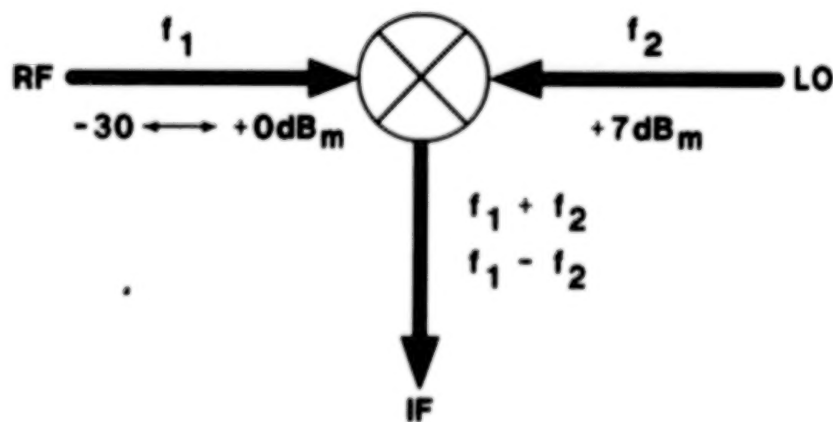


Figure 10

## Effective Fringe Spacing vs. Separation Angle

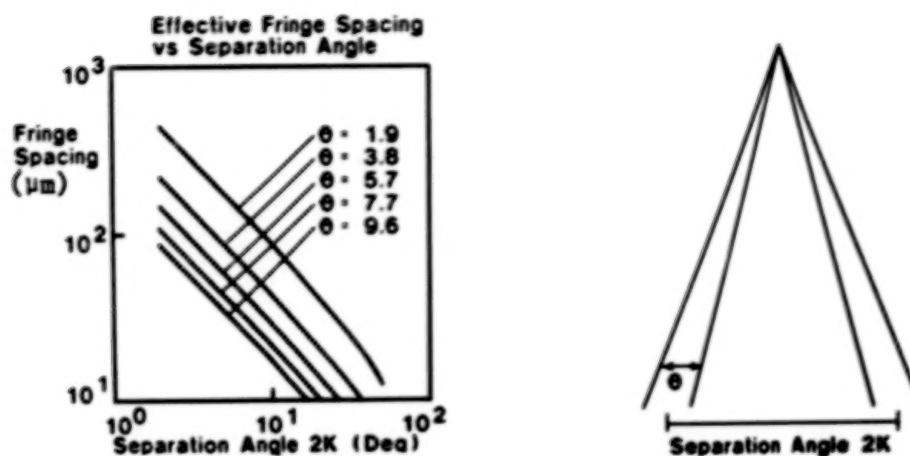


Figure 11

## Velocity Range and Resolution Chart for 3-D LV Design

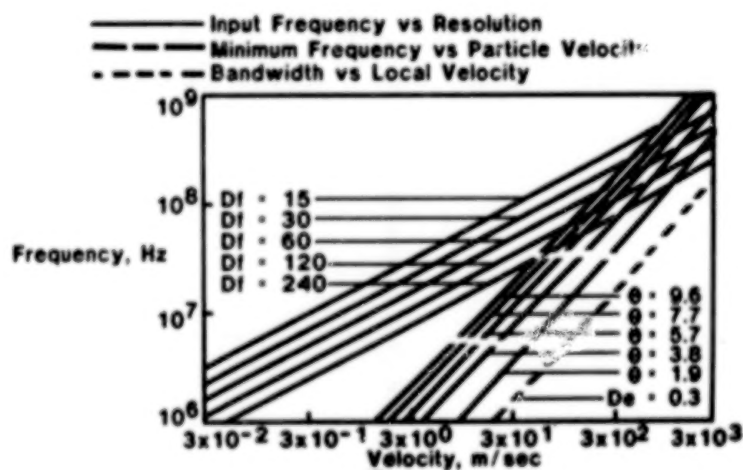


Figure 12



### 3-D LV Frequency Domain Processing Circuits

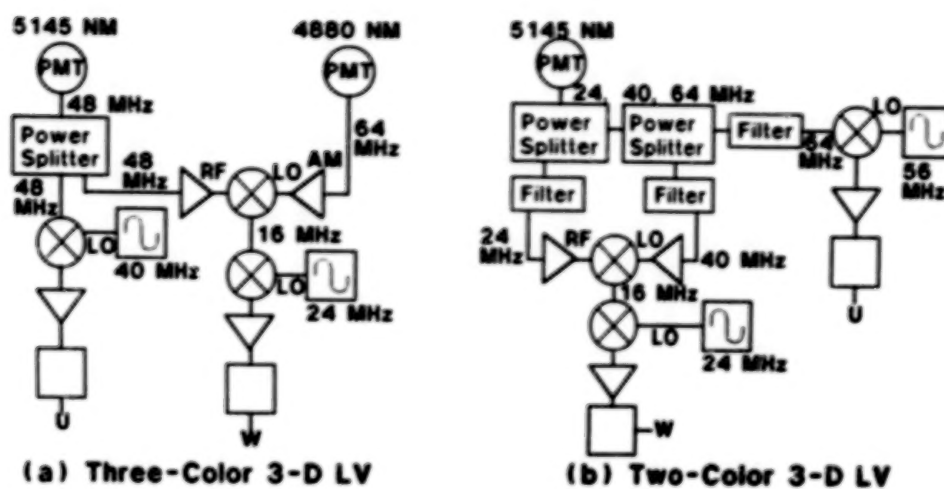


Figure 13

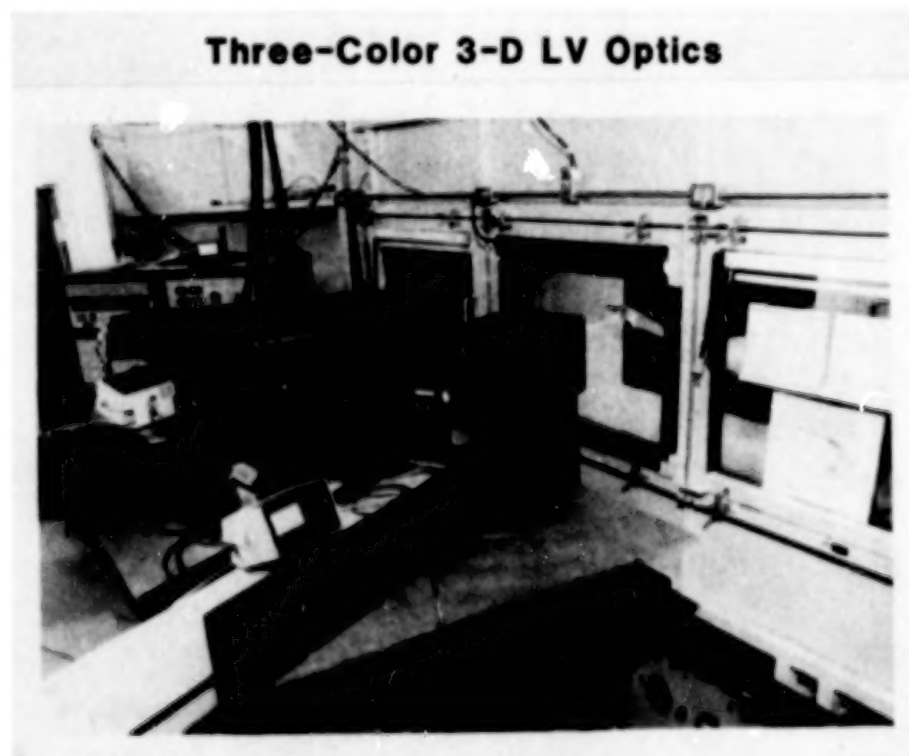
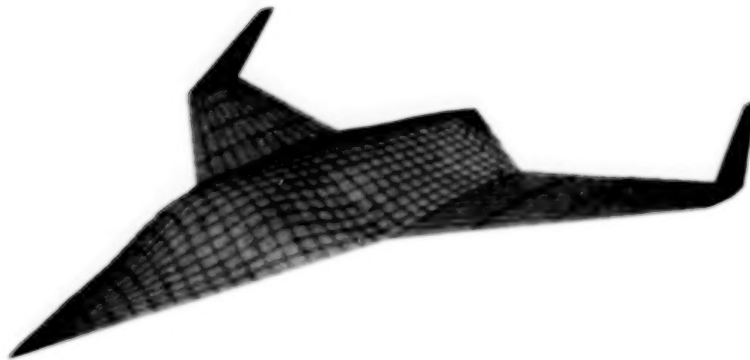


Figure 14

## **Generic Fighter Configuration**



**Figure 15**

## **Wind Tunnel Test Setup**

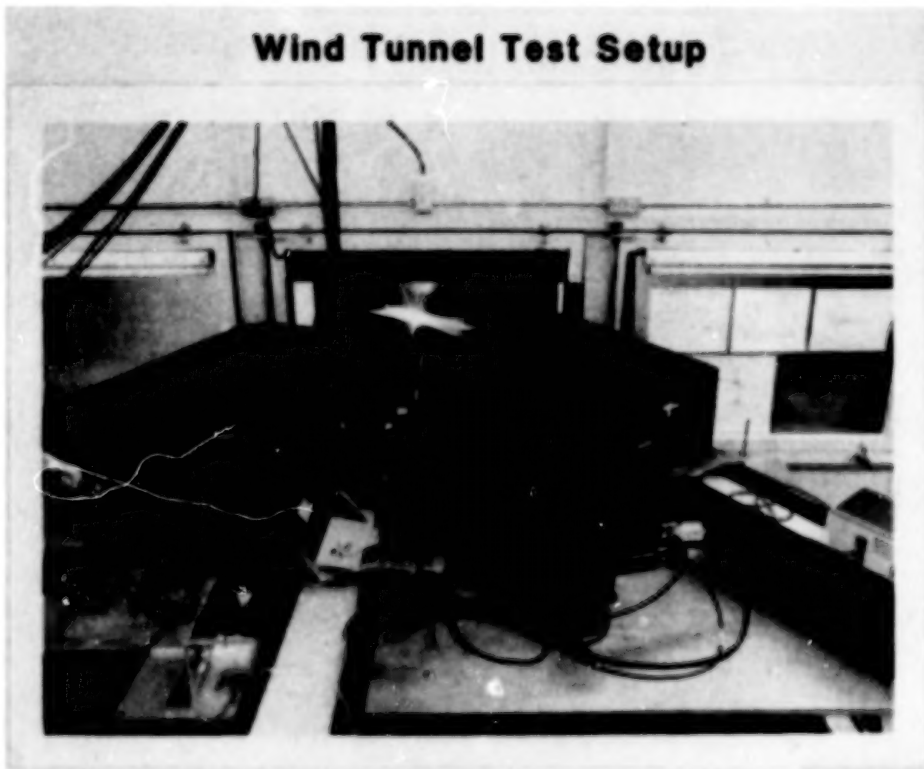


**Figure 16**

## Seed Particle Behavior in a Vortical Flow

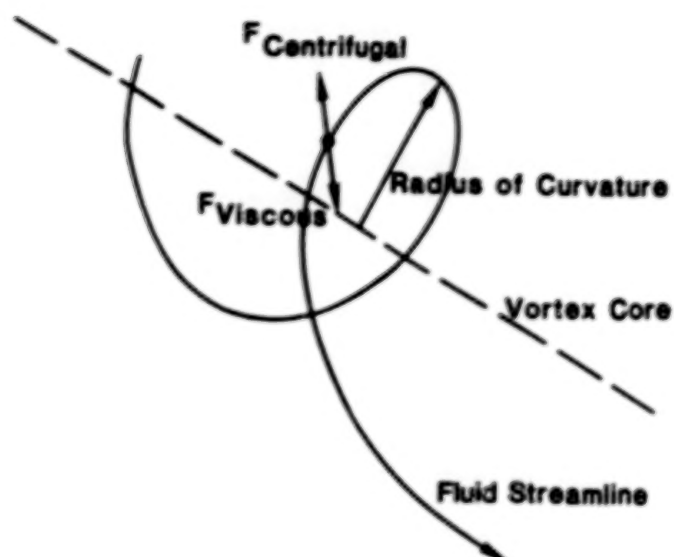
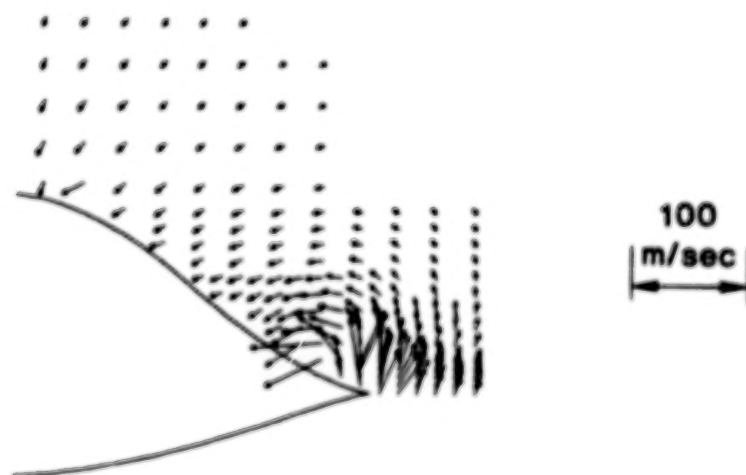


Figure 17

## Mean Crossflow Velocity Vectors

$$\alpha = 10^\circ \quad x/c = 0.000$$



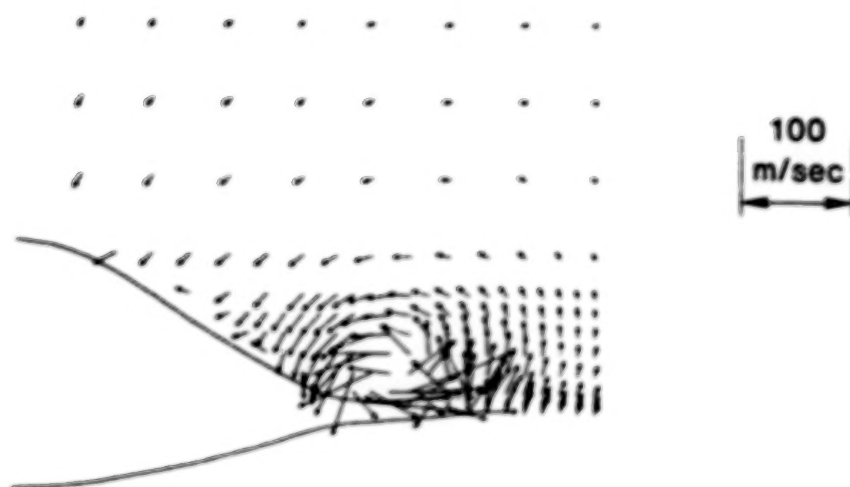
(a)

Figure 18

# Mean Crossflow Velocity Vectors

$\alpha = 10^\circ$

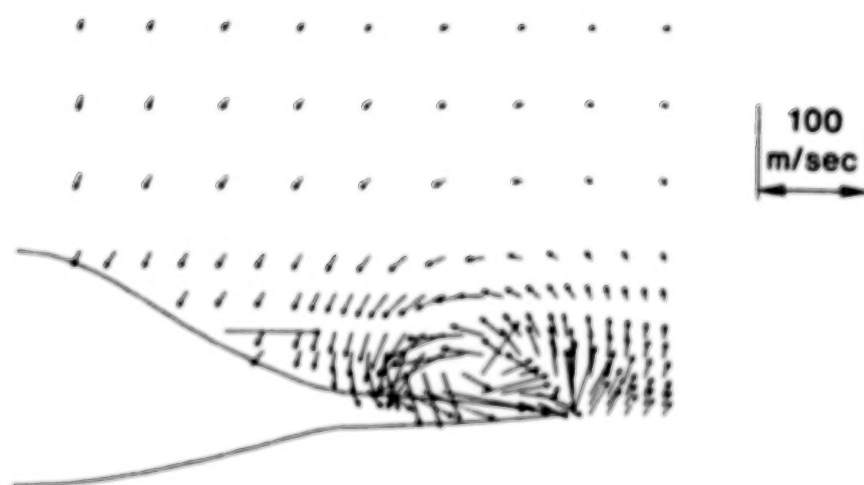
$x/c = 0.125$



(b)

$\alpha = 10^\circ$

$x/c = 0.250$



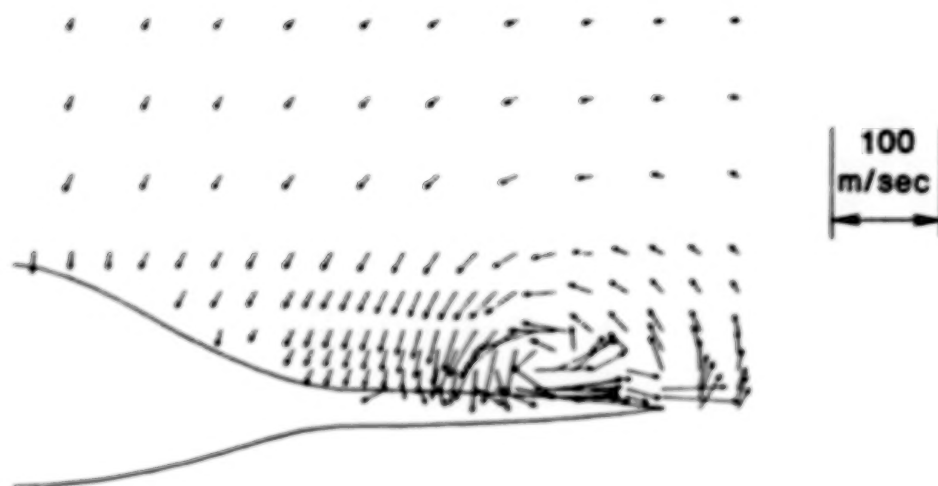
(c)

Figure 18 (Continued)

# Mean Crossflow Velocity Vectors

$\alpha = 10^\circ$

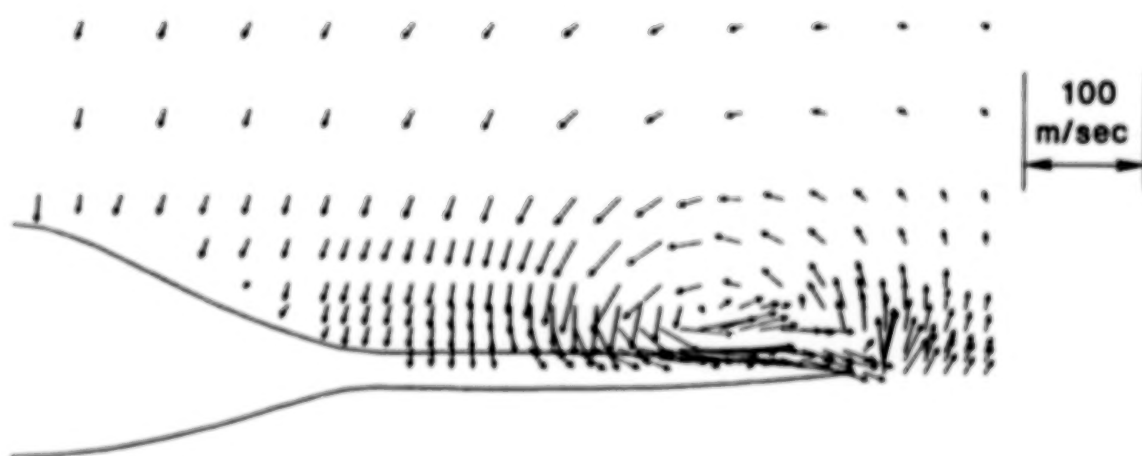
$x/c = 0.500$



(d)

$\alpha = 10^\circ$

$x/c = 0.750$



(e)

Figure 18 (Continued)

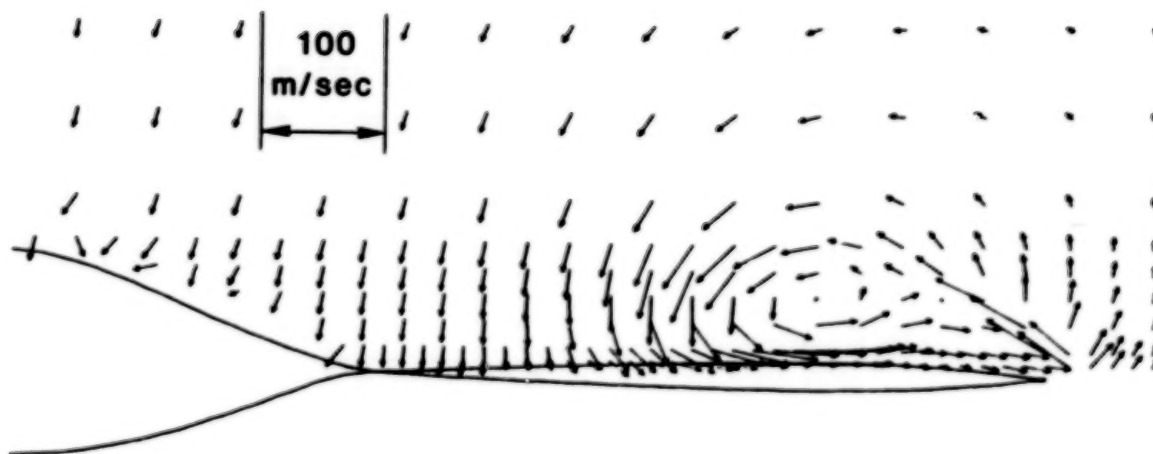




# Mean Crossflow Velocity Vectors

$\alpha = 10^\circ$

$x/c = 1.000$



(f)

Figure 18 (Concluded)

## Vortex Track

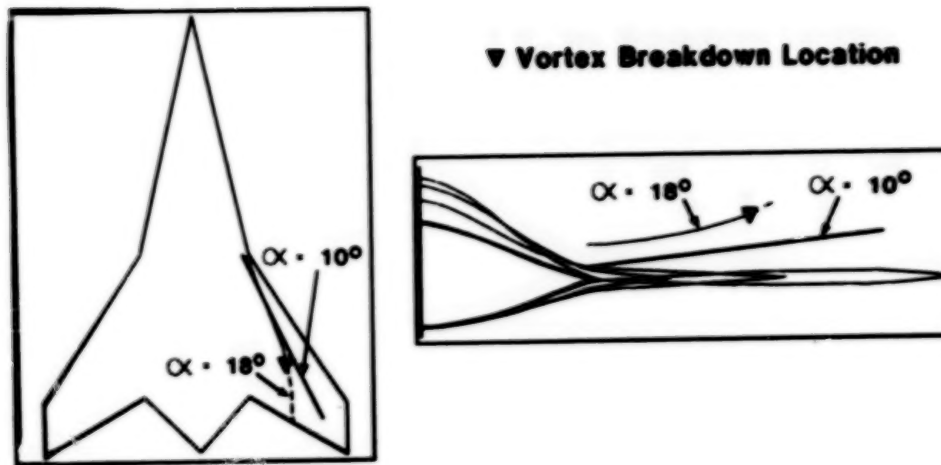


Figure 19

## Mean Axial Velocity

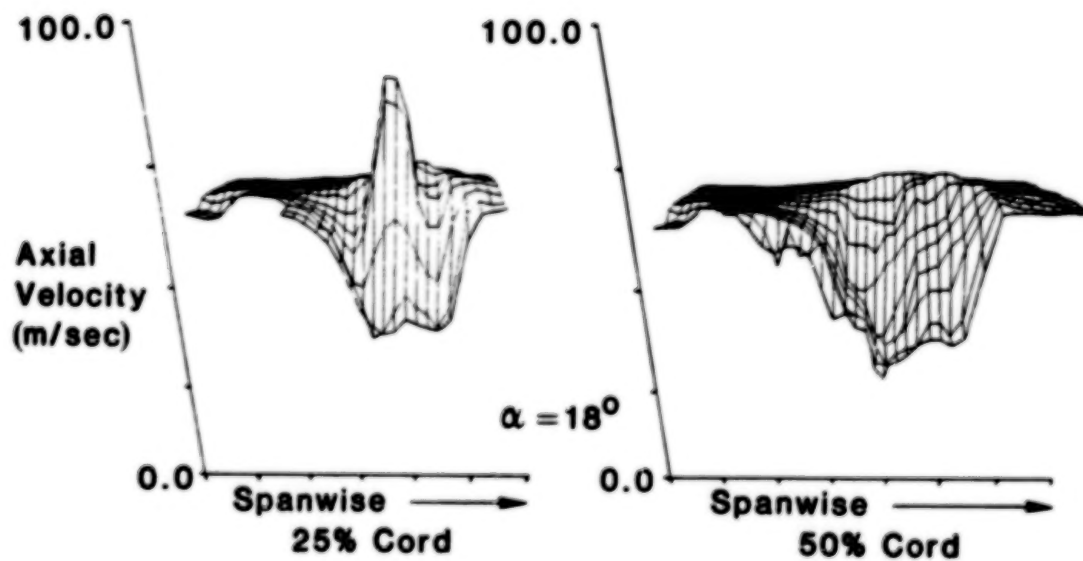


Figure 20

## IN-FLIGHT AND WIND TUNNEL LEADING-EDGE VORTEX STUDY ON THE F-106B AIRPLANE

John E. Lamar  
NASA Langley Research Center  
Hampton, Virginia

## SUMMARY

The vapor-screen technique has been successfully applied to an F-106B fighter aircraft during subsonic and transonic maneuvers. This system has allowed the viewing of multiple vortex systems on the wing upper surface at angles of attack less than  $19^\circ$ . In addition, similarities as well as differences were determined to exist between the vortex systems for a full-scale semispan model and the flight vehicle at  $20^\circ$  incidence. Furthermore, variations in Reynolds number and Mach number have been identified as to how they affect vortex system details at flight conditions.

## INTRODUCTION

The visualization of vortex systems which originate from aerodynamic surfaces is a common occurrence in wind tunnels, where techniques like tuft grids, schlieren, smoke wands, and vapor screens have been used (see refs. 1-6). Some of these seed the working fluid with smoke or sufficient water vapor (ref. 6) in order to highlight the core by either smoke entrainment or water condensation. This may occur along much of the length of the vortex, thereby yielding a visible record of the core path as can be seen in figure 1 for a wind tunnel model with upward deflected vortex flaps. Flight examples are not as readily available, but figure 2 shows the strake flow of an F-16 during a low-altitude maneuver. Both examples are the result of naturally occurring condensed water vapor (light areas) forming around and outlining the dark core regions.

In-flight use of smoke has been documented, in references 7 and 8, on delta wings to observe the leading-edge vortex breakdown progression (HP 115) and the outer panel flow (AVRO 707B) with increasing angle of attack, respectively. However, in order to obtain vortex system details, one needs to use a flight version of the vapor screen technique. Since the hardware to implement this was not available\* when interest was expressed in observing the Reynolds number effects on the vortex system for the F-106B, the equipment had to be developed.\*\* An illustration of what the vortex system looks like with such an implementation is shown schematically for the F-106B by the flight project logo in figure 3.

After the equipment was developed to seed the flow with vaporized propylene glycol in order that the observations be weather independent, illuminate the details with a light sheet, and record the events with a television system, applications were made

\*Reference 9 reports the Soviet use of a ruby laser sheet and atmospheric water vapor to observe the vortex system at subsonic speeds above an ogee wing up to high incidence.

\*\*Reference 10 used limited surface tufts near the middle of an F-106B wing during a flight test program and determined a reattachment line associated with a vortex system.

to both flight (see fig. 4) and wind tunnel vehicles. The particular information sought was to quantify the effect that the Reynolds number may have on the details of the leading-edge vortex system of full-scale vehicles at high angles of attack and subsonic speeds, including a 5-G transonic maneuver. This paper documents these results and offers a selected comparison of system details on a full-scale semispan F-106B model.

#### SYMBOLS

|          |  |
|----------|--|
| G        | acceleration due to gravity, ft/sec <sup>2</sup>                                   |
| K        | thousand   |
| LE       | leading edge   |
| $l$      | inboard distance to vortex core from leading edge, inches                          |
| M        | Mach number  |
| m        | inboard distance to inner edge of vortex system envelope from leading edge, inches |
| $R_n$    | Reynolds number  |
| TE       | trailing edge  |
| z        | vertical distance to vortex core above upper surface, inches                       |
| $\alpha$ | angle of attack, degree  |

#### TEST SETUP

The wind tunnel tests were performed on a half-airplane model of the F-106B mounted in the Langley Research Center 30- by 60-Foot Wind Tunnel. This model was made by cutting an airplane in half and mounting it wingtip upward from a reflection plane. It should be pointed out that the full-scale model differed primarily from the flight vehicle only in the leading-edge region. The former had all the camber, essentially conical, ahead of the local 90-percent semispan; whereas, the latter had its conic-like camber ahead of the 80-percent local semispan. They are called Case XIV and Case XXIX cambers, respectively, by the manufacturer.

The tests in the 30- by 60-Foot Wind Tunnel were for the purpose of establishing starting values for the flight project in the areas of seeding flow rate and probe position, light-sheet width and orientation, and TV camera parameters. One great uncertainty remained after the wind tunnel test, and it was whether sufficient seeding material could be produced to make the vortex system visible at flight speeds.

The range of test parameters for the wind tunnel and flight is given in figure 5. This range includes the vapor screen variables such as seeding flow rate and probe position, and light-sheet width and location, as well as the two different types of maneuvers flown. The wind tunnel conditions are standard ones with the dynamic pressure not exceeding 10 lb/ft<sup>2</sup>.

For both the 1-G constant altitude and the 5-G transonic maneuvers, six probe positions were tried in order to find the one that worked best overall. Five of these were underneath the leading edge and one was on top. These positions were numbered sequentially, and number 6 was found to be preferable. Its approximate location underneath the leading edge is shown on figure 6, along with the relative locations of the camera and light sheet.



The right side of this figure shows the view displayed on the monitor. Since the camera is looking down and aft onto the left wing panel, the wing trailing edge is at the top of the screen, the leading edge intersects the right side, and the fuselage cuts across the left corner. The light sheet is seen to lie in the middle of the screen and does not extend to the wing leading edge because of camber.

There were two light sheet locations used in the wind tunnel, one perpendicular to the fuselage centerline and the other perpendicular to the wing leading edge, as can be seen in figure 7. For the flight experiment, it was the intent to have the light also perpendicular to the leading edge. However, space constraints associated with attaching the light source to the fuselage limited the sheet to only reaching  $11^\circ$  ahead of perpendicular to the centerline as opposed to the  $30^\circ$  desired for this  $60^\circ$  swept wing. Hence, the light sheet location used in flight is closer to the more aft one used in the wind tunnel.

The slit width in the light sheet generator was varied from 0.003" to 0.041" for both wind tunnel and flight with most testing done at 0.041". In addition, most of the seeding was done with the pump operating at approximately 3 gallons per hour. For both of these systems, the intent was to use the smallest amount possible which would still seed and illuminate the vortex system sufficiently.

## RESULTS AND DISCUSSION

It should be remembered that the primary data taken, other than test conditions, during both the flight and wind tunnel tests are video-tape visual records of the vortex systems. Using these records, photographs of portions of particular flights were made from a monitor in order that a comparative study may be done and the pertinent test effects may be identified. (The photographs presented are from an orientation delineated on the right-hand side of figure 6.)

From flight, there are basically two kinds of effects to be presented corresponding to the two types of flights flown. The first type is one in which the altitude is held essentially constant, and the Mach number is adjusted to keep the aircraft at 1-G flight over an angle-of-attack range up to  $23^\circ$ . For each of these constant altitude flights, which ranged from 35,000 feet to 15,000 feet in 5,000-foot increments, the Mach number did not vary appreciably from 0.4; however, the Reynolds number increased by  $6 \times 10^6$  as the altitude decreased. The other type was for a transonic maneuver at 5-G and  $M \sim 0.8$ , accomplished during a spiral descent, at a fixed angle of attack,  $19^\circ$ , in which the Reynolds number varied significantly.

### Effect of Reynolds Number

The effect of Reynolds number can be seen in figures 8 to 13, using comparative photographs at angles of attack from  $17^\circ$  to  $23^\circ$ . These 1-G flights show that at  $17^\circ$ , leading-edge separation is well established at  $R_n = 26 \times 10^6$ , which corresponds to the highest altitude, but has not even begun at  $R_n = 32 \times 10^6$ . Between these extremes, progressively smaller amounts of leading-edge separation are noted with increasing Reynolds number. Much the same occurs at  $18^\circ$ , but at  $19^\circ$  there is a first indication of leading-edge separation at the highest Reynolds number. The delay in separation onset associated with increasing Reynolds number is not new for round-edged wings with camber, but that it would be observed in flight is remarkable.

It is also noteworthy to point out evidences of other vortical action inboard of the leading edge at  $\alpha = 19^\circ$  and  $R_n = 32 \times 10^6$ . The innermost may be associated with the juncture flow; however, the mid-semispan vortex may well be coming from the upper surface shear layer tearing and forming another system of the same rotational sense as at the leading edge. This may occur when the leading-edge vortex is not yet strong enough to dominate the entire outer panel flow. Figure 11 has been prepared to show the postulated positions of the various vortical systems at the 20,000-foot altitude. When this system is viewed from above, it has an appearance which resembles the discrete vortices in the feeding sheet, arranged roughly parallel to the leading edge, around the primary vortex found in water tunnel tests and reported in reference 11. One important difference is that, in flight, each vortex extends to the upper surface.

Figure 12 shows that, at  $20^\circ$ , only a single vortex system exists outboard and, as it gets bigger with decreasing Reynolds number, the innermost one grows smaller. The same is true at  $23^\circ$ , as seen in figure 13.

It is apparent from this series of comparative photographs that the leading-edge vortex is Reynolds number dependent. To help establish the quantitative dependence, figure 14 has been prepared in which the vortex system envelopes and "cores" have been determined for two different values of Reynolds number. They are displayed against the aft part of the left wing panel and are for values of angle of attack from  $18^\circ$  to  $23^\circ$ . The "cores" are not determined from finding the "black hole," since none was seen for these flights, but are established by an examination of where the smoke was the brightest and its rotation centered. The brightest smoke was chosen since it represented an increased density/reflectivity which one would expect to surround the very core itself. By superimposing the results shown in figure 14 onto a similarly recorded target board marked off in 6-inch squares, quantifiable information was established for the inner extent of the envelope and core location; this information is presented in figure 15.

From this figure it can be seen that, in general, the inner extent of the vortex system envelope and of the core locations is more inboard at the lower Reynolds number. Also, at the lower value, the envelope and core tend to be more monotonic in their growth with angle of attack. It is interesting to note that at  $20^\circ$  the results seem to coalesce, after which the measurements corresponding to the higher Reynolds number have a slower inboard growth. The core elevation seems insensitive to Reynolds number.

Figure 16 compares these results, taken from the Case XXIX flight wing, with those from the 30- by 60-Foot Wind Tunnel test of the Case XIV wing. Though the vortex flow was much unsteadier in the wind tunnel, as its lateral position oscillated between outboard and inboard, an interpolated aggregate position, shown by the filled diamond, does compare surprisingly well with the flight data. The interpolation is required since the light sheet locations used in the wind tunnel lie on either side of the flight position. Note that the height of the wind tunnel core is above the flight ones. No other conclusions can be drawn, since there was not enough time in the wind tunnel with the right probe position to get sufficient data.

#### Effect of Mach Number

Figure 17 provides details of the vortex systems for both 1-G and 5-G flights, which occurred at roughly 0.4 and 0.8 Mach number, respectively. These photographs were taken with two different light sheet widths, and the 5-G maneuvers were done both to

the left and right to rule out any centrifugal force effects on the results. Basically, with either light sheet width, the vortex appears similar under these test conditions. However, for the thinner light sheet and 5-G maneuver, one is able to see a core along with what appears to be a shear layer feeding into it.

To identify the effect of Mach number, the envelope and core are compared in figure 18 for these two different maneuvers. It is readily apparent that the doubling of Reynolds number has not delayed the leading-edge vortex formation to a higher angle of attack. This is in contrast to the effect of increasing Reynolds number discussed previously (see fig. 10). The more inboard extent of the envelope and of the core is therefore attributed to the Mach number doubling. This was an unexpected effect.

#### CONCLUDING REMARKS

In this paper, two basic topics have been covered: vapor screen technology implementation for manned flight vehicles, in particular, the F-106B, and the vortex system features revealed by using this technology in flight and in the wind tunnel. Regarding the first topic, it has been demonstrated that the vapor screen technique can be applied successfully to large-scale vehicles both in the wind tunnel and in flight under a variety of test conditions. These include the transonic maneuver, which future fighter aircraft will continue to need to perform.

Concerning the results obtained using this technique, significant differences have been noted in the size of the leading-edge vortex system and its core location at subsonic speeds with only relatively small changes in flight Reynolds number. The prime effect seems to be the well-known delay of separation on round-edged wings associated with increased Reynolds number. At 20° angle of attack, where flight and wind tunnel vortex system details could be directly compared, there was close overall agreement even with differences in wing camber and with the flight Reynolds number being greater by a factor of 2. This occurred in spite of the vortex system being more stable in flight than in the wind tunnel. In addition, during the transonic maneuver, the Mach number effect can overcome the trend of increasing Reynolds number to reduce the vortex system by producing a larger, more inboard, and well-defined vortex system relative to the constant altitude 1-G flight.

#### REFERENCES

1. Settles, G. S.: Flow Visualization Techniques for Practical Aerodynamic Testing. Presented at the Supersonic Tunnel Association Meeting, Williamsburg, Virginia, October 1983.
2. Peake, D. J.; and Tobak, M.: On Issues Concerning Flow Separation and Vortical Flows in Three Dimensions. Aerodynamics of Vortical Type Flows in Three Dimensions, AGARD CP-342, Paper No. 1, 1983.
3. Werlé, H.: Visualization des Ecoulements Tourbillonnaires Tridimensionnels. Aerodynamics of Vortical Type Flows in Three Dimensions, AGARD CP-342, Paper No. 8, 1983.
4. Wentz, W. H., Jr.; and Kohlman, D. L.: Wind-Tunnel Investigation of Vortex Breakdown on Slender Sharp-Edged Wings. NASA CR-98737, 1968.



5. Snow, W. L.; and Morris, O. A.: Investigation of Light Source and Scattering Medium Related to Vapor-Screen Flow Visualization in a Supersonic Wind Tunnel. NASA TM-86290, December 1984.
6. Jorgensen, L. H.: Prediction of Static Aerodynamic Characteristics for Slender Bodies Alone and with Lifting Surfaces to Very High Angles of Attack. NASA TR R-474, September 1977.
7. Fennell, L. J.: Vortex Breakdown - Some Observations in Flight on the HP 115 Aircraft. R&M No. 3805, British A. R. C., 1977.
8. Perry, D. H.; Port, W. G. A.; and Morrall, J. C.: Low Speed Flight Tests on a Tailless Delta Wing Aircraft (AVRO 707B). C.P. No. 1107, British A. R. C., 1970.
9. Burdin, I. Yu.; Zhirnov, A. V.; Kulesh, V. P.; Orlov, A. A.; Pesetskiy, V. A.; and Fonov, S. D.: Use of Laser Methods for the Study of Detached Flows in a Wind Tunnel and in Flight. Translated from "Scientific Notes of TsAGI-Central Institute of Aerohydrodynamics," USSR, 1981, pp. 1-19.
10. Chamberlin, R.: Flight Investigation of 24° Boattail Nozzle Drag at Varying Subsonic Flight Conditions. NASA TM X-2626, November 1972.
11. Gad-el-Hak, M.; and Blackwelder, R. F.: The Discrete Vortices from a Delta Wing. AIAA Journal, Vol. 23, No. 6, June 1985, pp. 961 and 962.

#### BIBLIOGRAPHY

Other useful papers dealing with in-flight flow visualization are listed below for completeness.

1. Roberts, S. C.; and Smith, M. R.: Flow-Visualization Techniques Used in Full-Scale Flight Tests. TRECOM Technical Report 64-39, U. S. Army Transportation Research Command, Ft. Eustis, VA., July 1964.
2. Curry, R.; Meyer, R. R., Jr.; and O'Connor, M.: The Use of Oil for In-Flight Flow Visualization. NASA TM-84915, August 1983.

ORIGINAL PAGE IS  
OF POOR QUALITY

Subsonic

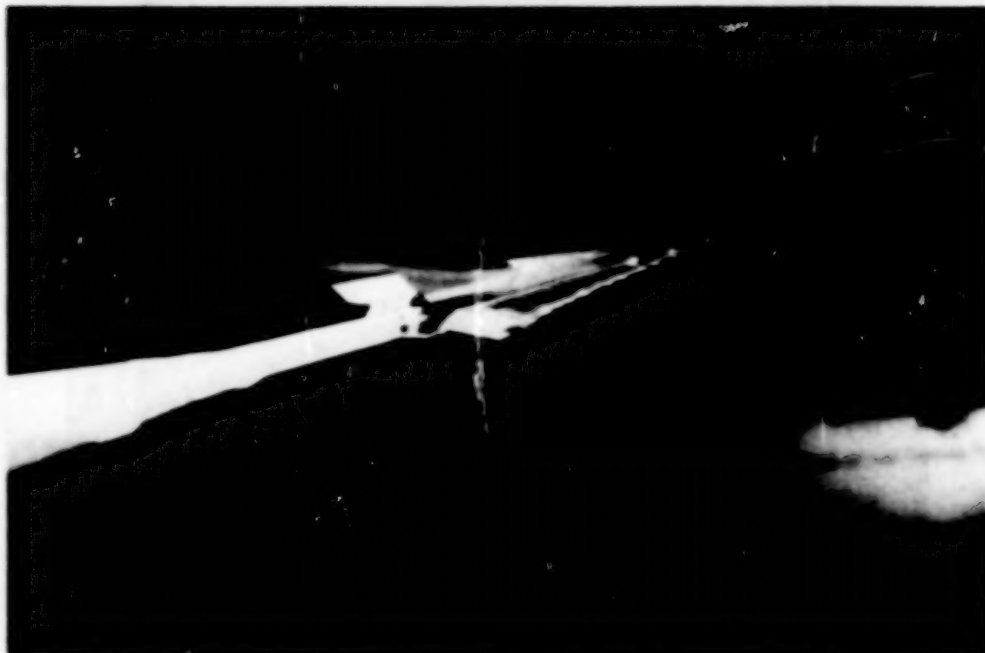


Figure 1. Leading-edge vortex core visualization on  $74^\circ$  delta with upward deflected vortex flap.



Figure 2. Strake vortex core visualization on F-16 during low-speed maneuver.



ORIGINAL PAGE IS  
OF POOR QUALITY



Figure 3. Flight project logo.

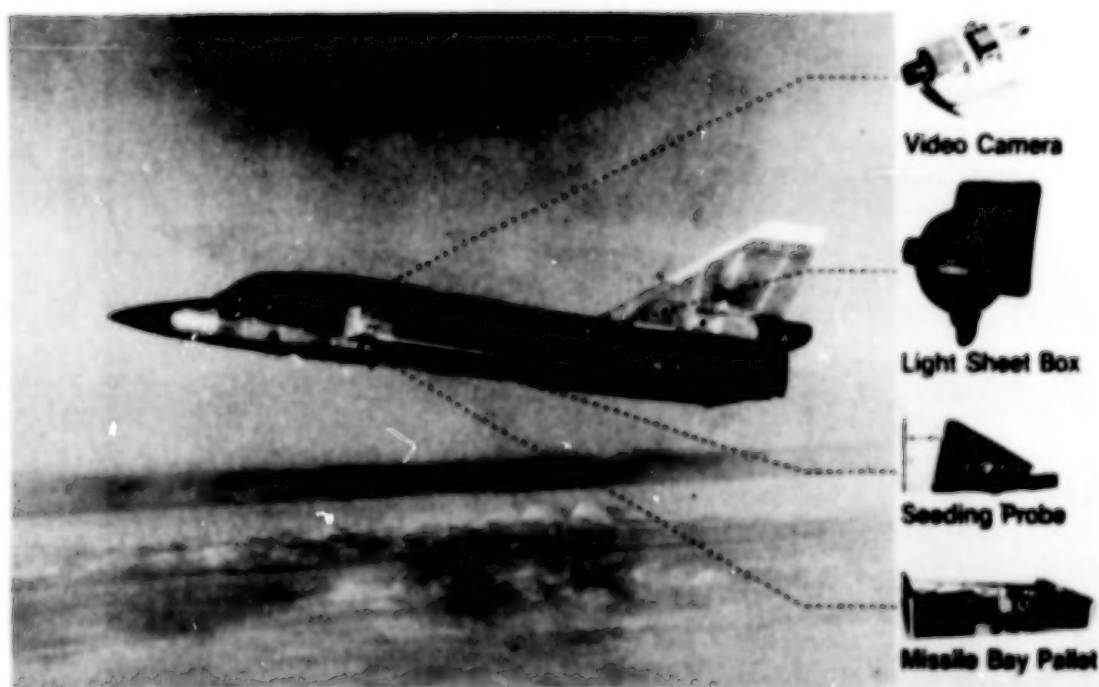


Figure 4. F-106 flow visualization elements.

● Vapor screen variables

- Seeding flow rate - (1.5 → 3.6 gal/hr) 3.0 gal/hr
- Probe position - 6 tried in flight, # 6 preferred  
- many tried in wind tunnel, one preferred
- Light slit/ sheet width - (.041", .012", .003") .041"
- Light sheet location - one in flight  
- two in wind tunnel

● Flight conditions

- Constant altitude 1-G decelerations - (35K, 30K, 25K, 20K, 15K, ft)  
 $M \sim .4$ ,  $\alpha \leq 23^\circ$
- Spiral descent  $\sim 5G$ , 40K, ft → 20K, ft (right and left)  
 $M \sim .8$ ,  $\alpha \sim 19^\circ$

● Wind tunnel conditions

- Mach number  $\leq .10$
- Angle of attack,  $12^\circ \rightarrow 20^\circ$
- Elevon deflection,  $15^\circ$  down →  $27^\circ$  up

Figure 5. Test parameters.

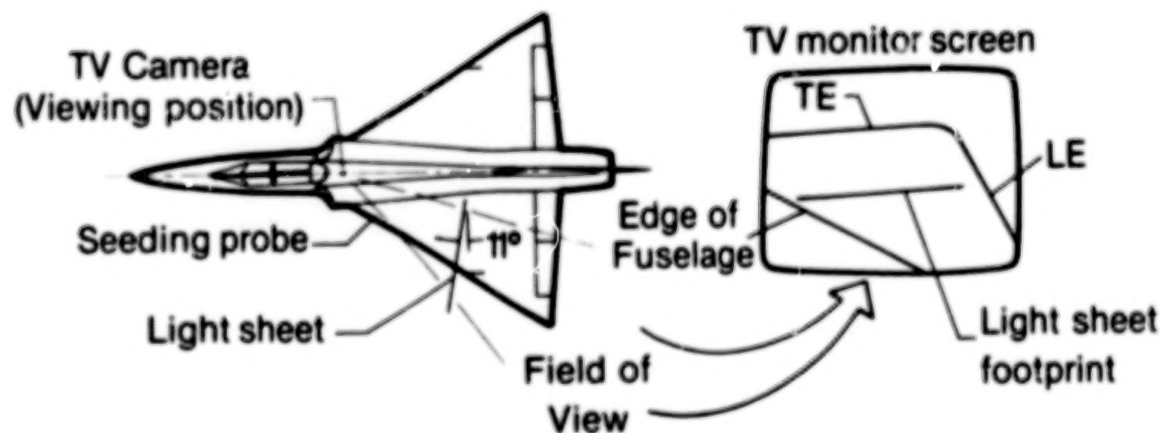


Figure 6. In-flight leading-edge vortex flow visualization on F-106B.

ORIGINAL PAGE IS  
OF POOR QUALITY

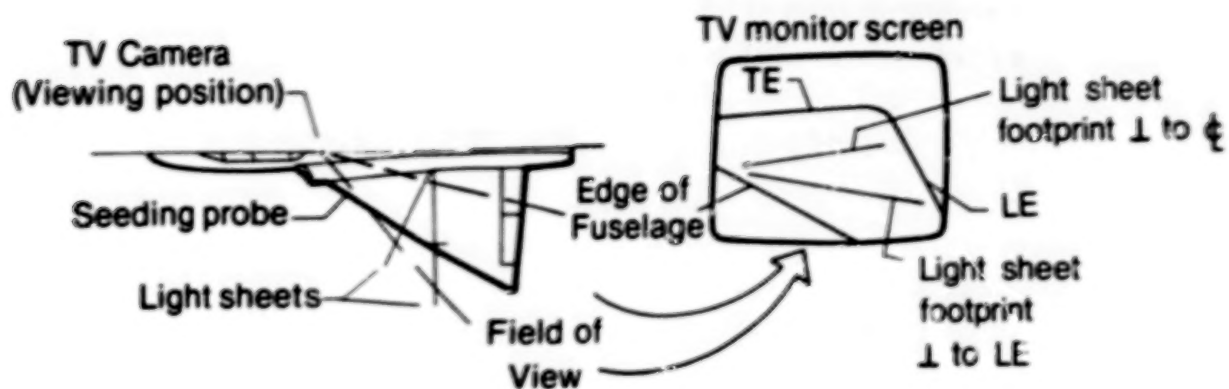


Figure 7 - Wind tunnel (30- by 60-ft) leading-edge vortex flow visualization on F-106B.

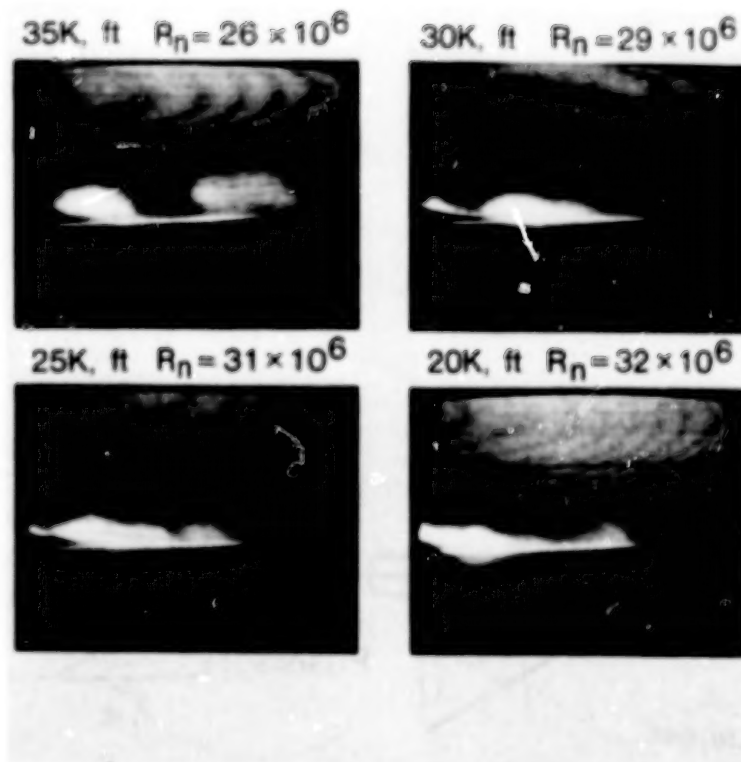


Figure 8. Effect of Reynolds number on vortex system,  $\sim 1G$ , probe #6, slit width = .041 in.,  $\alpha \sim 17^\circ$ .

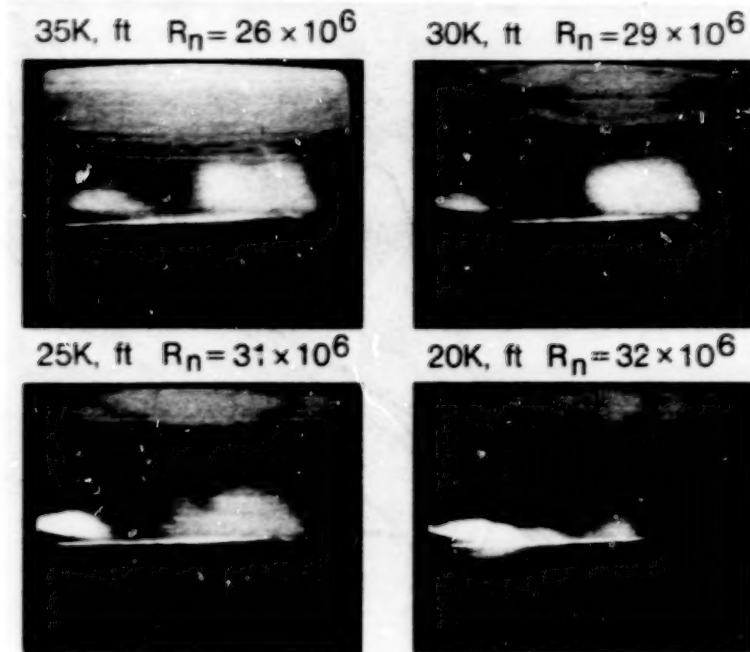


Figure 9. Effect of Reynolds number on vortex system,  $\sim 1G$ , probe #6, slit width = .041 in.,  $\alpha \sim 18^\circ$ .

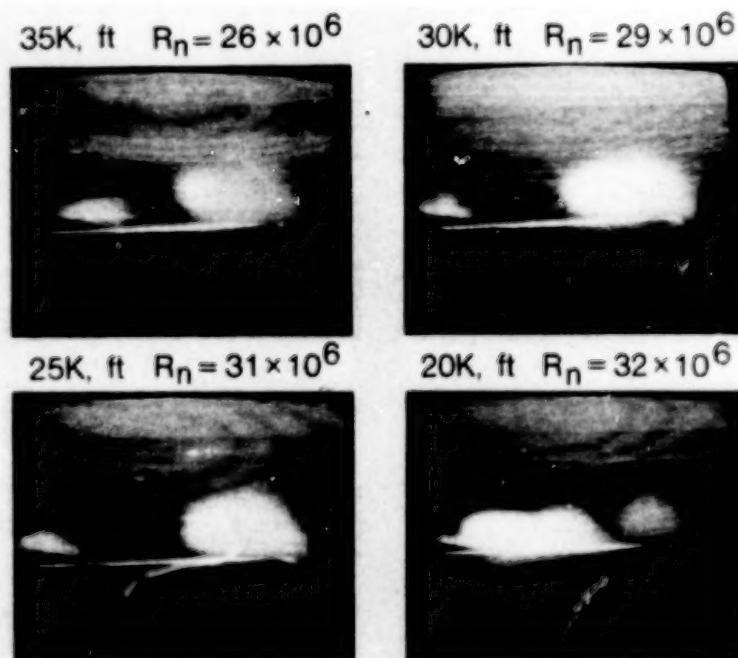


Figure 10. Effect of Reynolds number on vortex system,  $\sim 1G$ , probe #6, slit width = .041 in.,  $\alpha \sim 19^\circ$ .

ORIGINAL PAGE IS  
OF POOR QUALITY

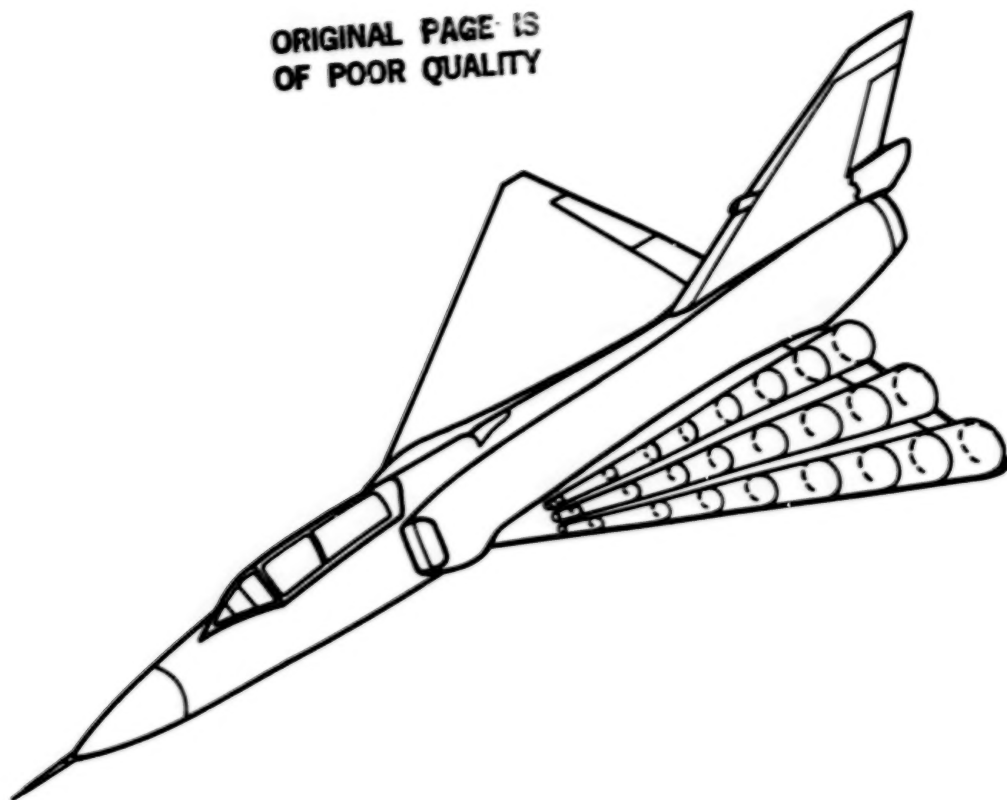


Figure 11. Multiple vortex systems on round-edged cambered delta,  
 $\alpha < 19^\circ$ , 1G.

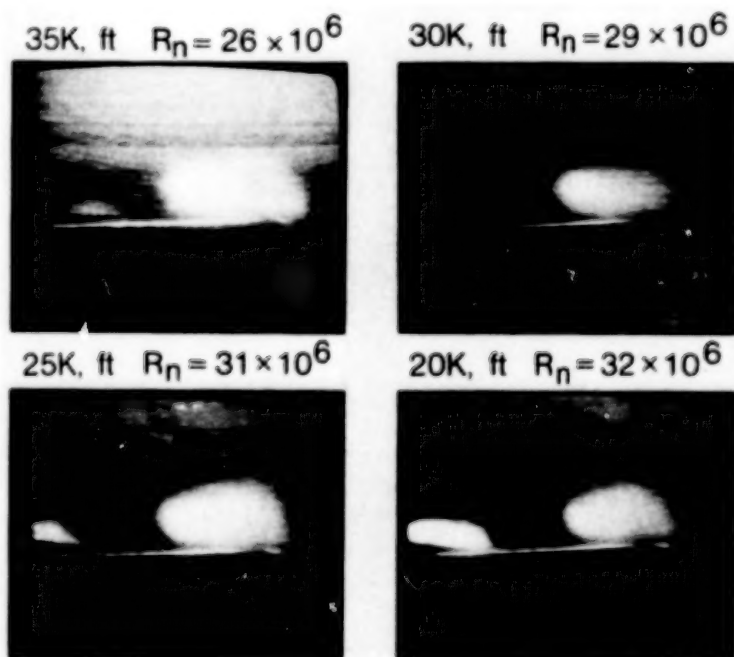


Figure 12. Effect of Reynolds number on vortex system,  $\sim 1G$ , probe #6,  
slit width = .041 in.,  $\alpha \sim 20^\circ$ .



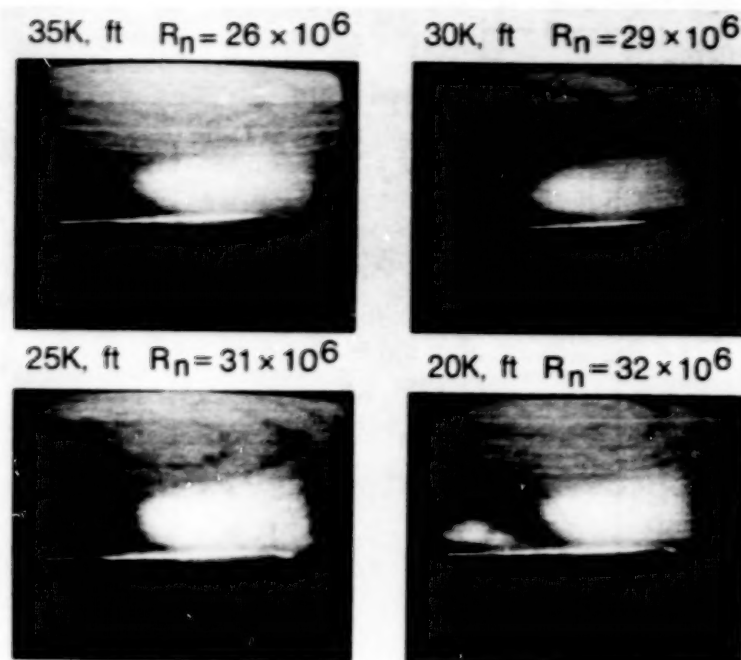


Figure 13. Effect of Reynolds number on vortex system, ~ 1G, probe #6, slit width = .041 in.,  $\alpha \sim 23^\circ$ .

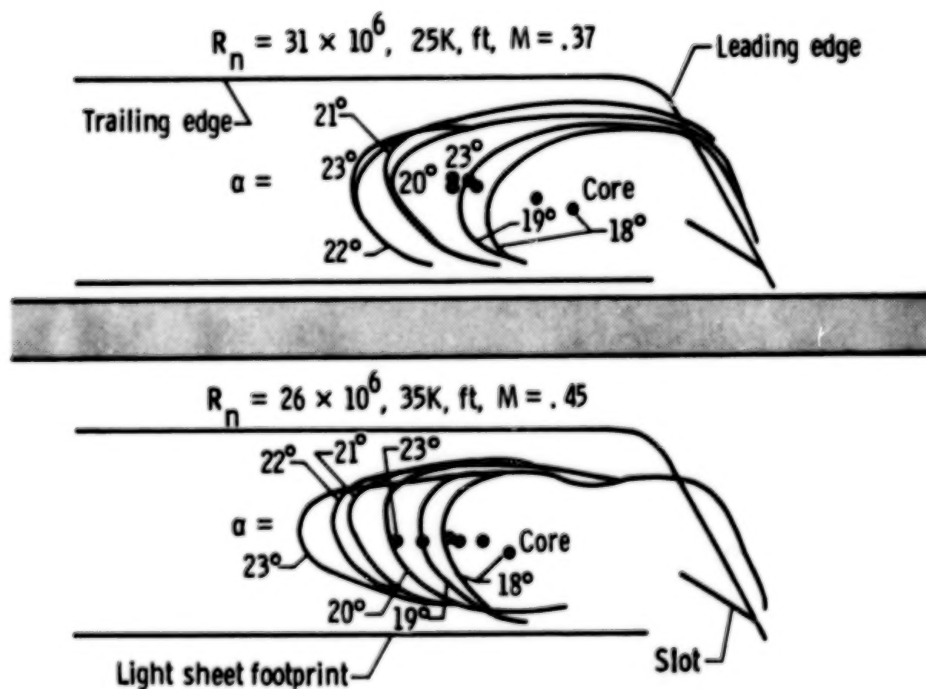


Figure 14. Effect of Reynolds number on vortex system, 1G, probe #6.

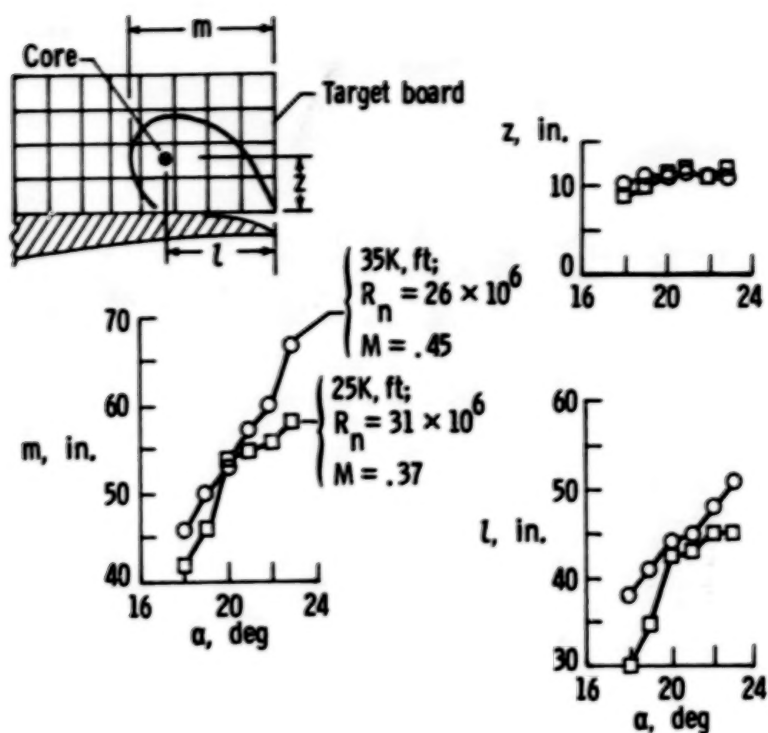


Figure 15. Measured vortex system details at two Reynolds numbers, 1G, probe #6.

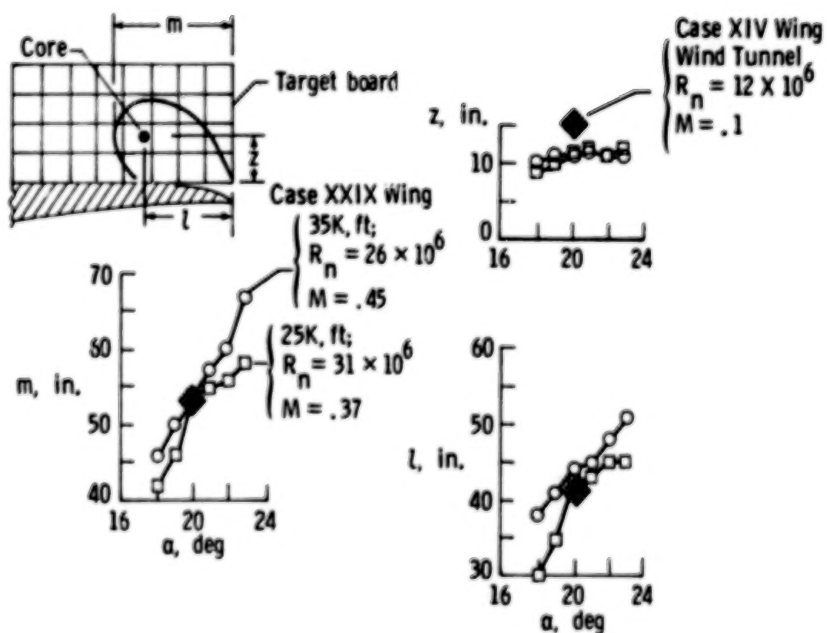


Figure 16. Measured vortex system details at three Reynolds numbers, 1G, probe #6.

ORIGINAL PAGE IS  
OF POOR QUALITY

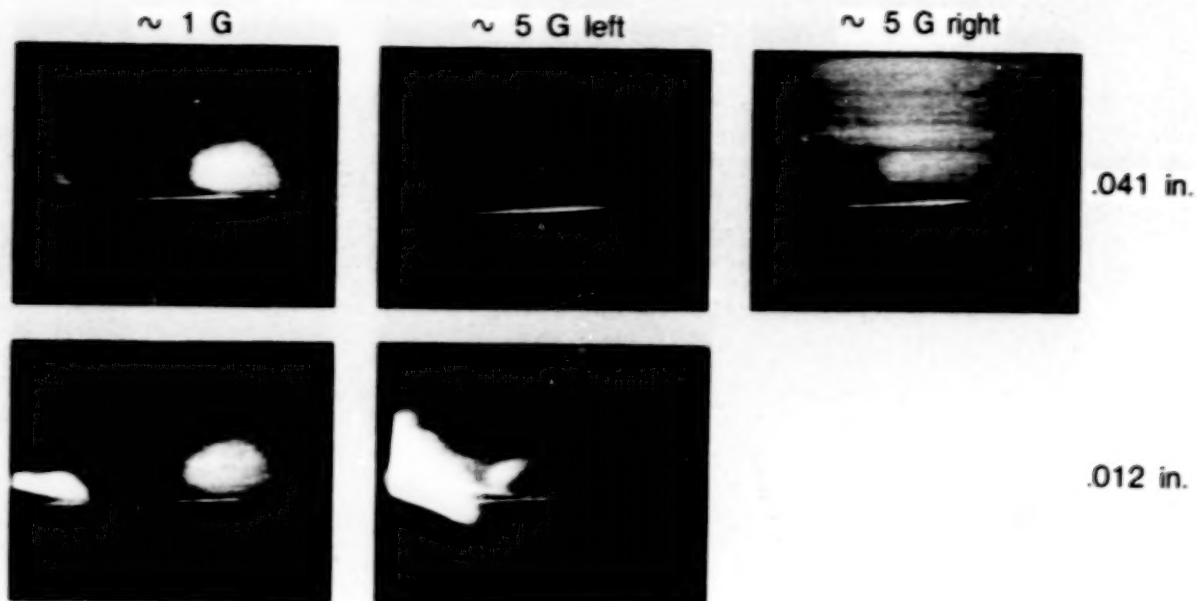


Figure 17. Vortex system details at two maneuvers and slit widths,  
 $\alpha \sim 19^\circ$ ,  $\sim 25K$  ft, probe #6.

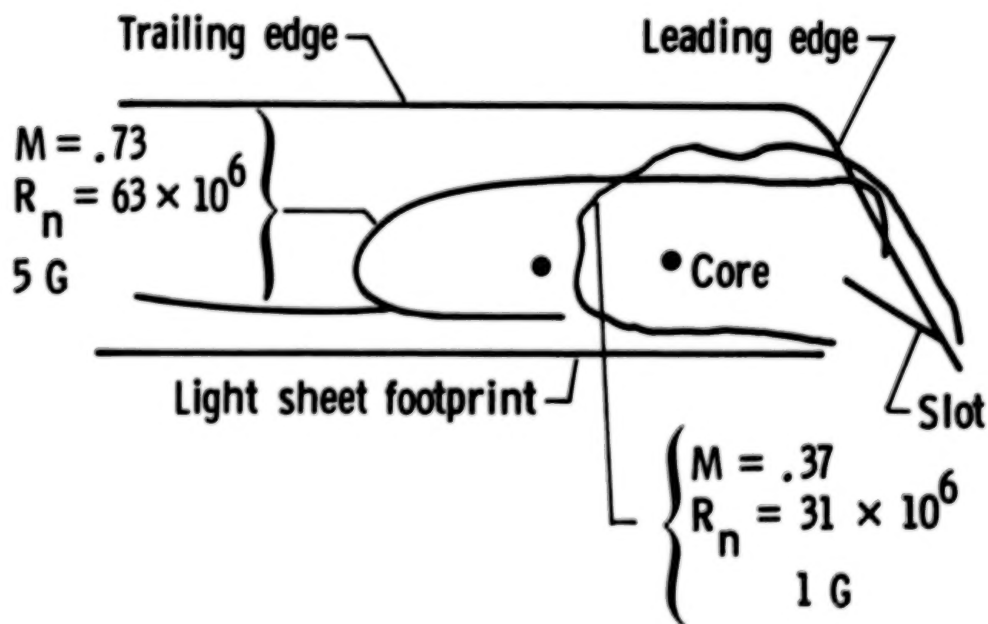


Figure 18. Effect of Mach number and load factor on vortex system,  
 $\alpha = 19^\circ$ ,  $25K$  ft.

## BASIC STUDIES ON DELTA WING FLOW MODIFICATIONS

### BY MEANS OF APEX FENCES

Keith D. Hoffler and Dhanvada M. Rao  
Vigyan Research Associates, Inc.  
Hampton, Virginia

Mark C. Frassinelli  
Air Force Wright Aeronautical Labs  
Wright-Patterson Air Force Base, Ohio

### SUMMARY

The effectiveness of 'apex fences' on a 60-deg delta wing at low speeds has been experimentally investigated. Resembling highly swept spoilers in appearance, the fences are designed to fold out of the wing apex region upper surface near the leading edges, where they generate a powerful vortex pair. The intense suction of the fence vortices augments lift in the apex region, the resulting positive pitching moment being utilized to trim trailing-edge flaps for lift augmentation during approach and landing at relatively low angles of attack. The fences reduce the apex lift at high angles of attack, leading to a desirable nose-down moment.

The above projected functions of the apex fence device were validated and quantified through low-speed tunnel tests, comprising upper surface pressure surveys on a semi-span model and balance measurements on a geometrically similar full-span wing/body configuration. Fence parameters such as area, shape, hinge position and deflection angle were investigated. Typical results are presented indicating the apex fence potential in controlling the longitudinal characteristics of a tail-less delta.

### SYMBOLS

|                  |   |
|------------------|---|
| AVERAGE CPU      | - Span-averaged CPU at local station                                    |
| CL               | - Lift coefficient, based on total wing area                            |
| CM               | - Pitching moment, based on total wing area and mean aerodynamic chord  |
| CPU              | - Upper surface pressure coefficient                                    |
| $C_R$            | - Root chord (inches)   |
| L/D              | - Lift-to-drag ratio  |
| X                | - Chordwise distance measured from apex (inches)                        |
| Y-LOC            | - Spanwise distance from root nondimensionalized by the local semi-span |
| $\alpha$ (ALPHA) | - Angle of attack (degrees)   |

- $\Delta CL\%$  -  $(CL, \text{fence on} - CL, \text{fence off}) / (CL, \text{fence off}) \times 100$
- $\delta_{TE, \text{ELEVATOR}}$  - Trailing-edge flap deflection, inboard only (degrees)
- $\delta_F$  - Fence deflection (degrees)

## INTRODUCTION

The aerodynamics of pitch control and longitudinal trim of highly swept fighter configurations have received considerable attention in recent years. Close-coupled canards are currently popular because of their ability to generate powerful pitching moments and low trim drag. However, the canard downwash reduces wing efficiency, and at high angles of attack canards tend to lose pitch-down capability. The adverse interaction between canard and wing vortices in sideslip also leads to non-linearities and roll instability at high alpha (ref. 1). Unloading the canard above a critical angle of attack is made difficult by the strong upwash induced locally by the forebody and wing.

A different approach towards pitch control of highly swept wings, viz., to modulate vortex lift in the apex region, was explored in the apex flap concept (ref. 2). The appeal of this concept was the ability to undeflect the apex, for cruise flight conditions, and deflect downward for recovery from high alpha. Tests showed however that like the canard the up-deflected apex flap also generated strong downwash over the wing, and suffered a severe lift loss in the neighborhood of the transverse hinge-line. The wing-alone model tested in reference 2 also could not represent the fuselage interference which is likely to degrade apex flap effectiveness. These considerations led the second author to propose an alternate method of apex lift control, viz., the apex fence.

Resembling highly swept spoilers, the apex fences are hinged to the wing upper surface along the leading edges (fig. 1). When folded out vertically at low angles of attack, the fences generate an intense vortex pair whose suction augments lift in the apex region, resulting in a nose-up moment. Conversely, at high angles of attack the fence vortices are greatly weakened and also raised higher above the apex; the combined effect is to reduce apex lift in comparison with the basic wing, thus generating a desirable nose-down moment. The apex fences will not be subject to fuselage interference and they also avoid the adverse transverse corner of the apex flap hinge. A noteworthy advantage of apex fences is that they can be shaped and oriented for most efficient vortex-generation capability quite independently of the wing planform.

Exploratory small-scale wind tunnel investigations of the apex fence concept applied to a 74 and 65 deg delta wing have been reported in reference 3. Upper surface pressure surveys supplemented with oil flow and helium bubble visualization confirmed the existence of strong and stable vortices produced by apex fences. These promising early results encouraged a more comprehensive study of the concept applied to a 60-deg delta wing, this sweep angle being more in keeping with the current fighter design studies. This investigation was undertaken primarily to validate and quantify the hypothesized aerodynamics effects of apex fences in controlling the longitudinal characteristics of a tail-less delta through the angle-of-attack range.



## MODELS AND TEST DETAILS

### Pressure Model

Major dimensions of the generic semi-span 60 deg delta wing body model are shown in figure 2. This model incorporated four spanwise rows of pressure taps, the first row being well inside the apex region occupied by the fence. The model was mounted on a boundary layer bypass plate seven inches above the tunnel floor. Six fence shapes were tested on this model, only two shapes being presented herein (fig. 3). The test was conducted in the North Carolina State University Merrill Subsonic Wind Tunnel at a mean-aerodynamic-chord Reynold's number of 0.67 million, and angles of attack ranging from zero to 30 deg.

### Force Model

Major dimensions of the force model are shown in figure 4. This model was geometrically similar to the pressure model and was fitted with four trailing-edge flaps. Only the inboard flap segments were deflected during the present tests. A total of eleven fence shapes were investigated, some at different mounting positions on the wing and some in asymmetric arrangement. Eight of the fences, all in symmetric configuration and mounted along the leading edge, are discussed herein. The fence shapes and their respective areas are presented in the figures with the results. Unless otherwise noted the fence deflection is 90 deg (i.e., perpendicular to the wing plane). The test was conducted in the Air Force Institute of Technology 5-Foot subsonic wind tunnel at a mean-aerodynamic-chord Reynolds number of 1.11 million. The sting was mounted in two alternate positions, giving a low (-6 to 30 deg) and a high (20 to 45 deg) angle-of-attack range.

## RESULTS AND DISCUSSION

### Pressure Results

Typical spanwise distributions resulting from vertical apex fences placed at the leading edge of the delta wing will be examined at a constant angle of attack of 10 deg (representative of the 'low-alpha' range). The Gothic (18.7 percent area) fence (fig. 5) results in broadening of the vortex suction footprint at the first two pressure stations (A and B), and a significant increase of the span-averaged local -CPU above the basic wing value with the load center shifted inboard. At the downstream stations (C and D) the spanwise distribution is similarly altered but the average -CPU is somewhat reduced. The Delta (11.7 percent area) fence (fig. 6) produces more accentuated suction peaks while the vortex footprints in this case are not as broad as with the Gothic fence. Nevertheless, the resulting -CPU average is practically equal with both fence configurations. At the aft station, the pressure fields due to the Gothic and Delta fences are almost identical.

The longitudinal variation of -CPU AVERAGE presented in figure 7 clearly shows the augmented apex suction due to both fences at  $\alpha = 10$  deg. Just the opposite effect is evident at  $\alpha = 30$  deg (representing the high-alpha case), when the apex suction is reduced below the basic wing value. Accordingly, a nose-up moment increment at low alpha and a nose-down effect at high alpha are to be expected due

to fence deployment, as postulated. This trend was encountered in varying degrees with all the fence configurations tested.

### Oil-Flow Study

Typical oil-flow photographs of the basic wing and the wing with the delta fence on at  $\text{ALPHA} = 9.5$  deg on the force model are presented in Figure 8. In this comparison, the oil streaks in the apex region are longer and more highly curved in a spanwise direction, indicating a significantly stronger vortex with the fence on. An inboard shift of the fence vortex is evident downstream and a separate leading-edge vortex appears, as observed in the foregoing pressure results.

### Balance Results

The Gothic and Delta fences studied on the semi-span pressure model were initially tested on the balance model. The lift and pitching moment characteristics are compared with the basic model in figure 9. The lift increment due to fences in the low-alpha range is evident, as is the nose-up pitching moment anticipated from the foregoing pressure results. Between the two fence shapes compared, the Gothic generates higher pitching moment increments; however, since this fence was also nearly 60 percent larger in area than the Delta, it was decided to study the area effect in some detail on these two fence shapes.

The original Gothic fence area was reduced serially in two steps: the height was reduced at constant length, and then the length was shortened. The result of height reduction (fig. 10) shows virtually no change in lift characteristics and a relatively small reduction in moment; length reduction results in a visible drop in lift and a more pronounced reduction in the pitching moment.

The Delta fence was cut in length in two successive steps. The results (fig. 11) show a roughly proportional drop in lift as well as pitching moment in the low-alpha range, the moment increments narrowing towards higher angles of attack.

To obtain a broader picture of the effect of fence area, the lift increments with various fence configurations at a constant angle of attack of 12 deg, with and without trailing-edge flap deflection for trim, are compared with the basic model (or fence-off case) in figure 12. Included in this comparison is a Double-Gothic fence shape, in which the rear half was tapered down to zero width. Most of the fences increased the untrimmed lift, with the exception of the smallest fences in each shape family which showed a lift loss at this angle of attack. However, all fences irrespective of size and shape produced marked increases in the trimmed lift due to down-deflected trailing-edge flaps (as indicated by the blackened portion of the bars). Generally, reduction of fence area also reduced the trimmed lift increment.

In an attempt to separate out the fence shape and area effects on the trimmed lift capability, the incremental lift at  $\text{ALPHA} 12$  deg is plotted versus fence area ratio for the three shape families in figure 13. An almost linear increase of trimmed lift coefficient with fence area is evident, an outstanding exception being the large Double-Gothic fence. Note that the smaller Double-Gothic fence was not geometrically similar, having a convex aft taper in contrast to a concave taper of the larger Double Gothic. While the present data are quite inadequate to draw conclusions regarding the Double-Gothic fence, their potential as an area-efficient fence shape is worthy of further investigation.

As already mentioned, the vortex load on the apex fences produces a drag component. While drag increment in combination with lift augmentation is a desired feature during approach and landing, it is of interest to examine the aerodynamic efficiency of apex fences as a trimming device. This may be done by comparing the  $L/D$  at a constant lift coefficient with and without the fences (see Table 1). The corresponding trailing-edge flap deflections for trim and angle of attack are also given. Because the basic delta wing requires an up-deflected trailing-edge flap to trim with a positive static margin, the angle of attack must be increased to obtain the same lift coefficient. In contrast, fence deployment allows a down deflection of trailing-edge flap for trim and therefore the angle of attack can be reduced for the same approach speed. For example, the Gothic fence provided a nearly 6 deg reduction in angle of attack from  $\text{ALPHA} = 18$  deg of the basic delta. The consequent wing drag reduction compensates for the fence drag to a large extent, as indicated by the relatively small decrease in  $L/D$ .

The foregoing results pertained to vertically deployed apex fence, i.e.  $\delta_f = 90$  deg; in practice, the hinged fences may be actuated to a smaller or a larger angle. The effect of varying fence deflection on either side of 90 deg is presented in figure 14 for the case of the large Double-Gothic fence. The results indicate that the fence angle controls the pitching moment in an almost linear fashion.

In some tests the high-alpha range was explored to observe the apex fence effect on pitching moment. A typical result is shown in figure 15 using Gothic fences, where a reversal of the longitudinal moment is evident at high angles of attack. Thus the apex fence can be viewed as a natural alpha-limiting device.

### CONCLUSIONS

Exploratory low-speed wind tunnel investigations were conducted to evaluate the effects of apex fences on a 60 deg delta wing/body configuration. An initial test program surveyed upper surface pressures on a semi-span model including the apex region between the fences, followed by balance measurements on a geometrically similar full-span model with trailing-edge flaps. The scope of the investigation covered varying fence shape, area and deflection angles.

The apex fences produced opposite effects over the wing apex region in the low-alpha and high-alpha regimes. At low angles of attack fence vortices augmented the suction level over the apex, whereas at high angles of attack the apex suction was reduced from the basic wing case. Balance data showed corresponding lift increase together with a nose-up pitching moment at low alpha, and lift loss with a nose-down moment at high alpha.

In combination with down-deflected trailing-edge flaps, fences in the low alpha range produced marked increases in the trimmed lift capability of the configuration. The trimmed lift increment was essentially proportional to fence/wing area ratio in case of Gothic and Delta fences. An exception was the Double-Gothic fence of 8.8 percent area, which indicated an area efficiency almost twice as high as the others.

Varying fence deflection angle (on either side of the nominal 90 deg position) was found to control the pitching moment in an almost-linear fashion, showing the apex fence to be a promising pitch control and trimming device. The effectiveness of asymmetric fence deployment in lateral and directional control is currently being evaluated.



## REFERENCES

1. Wedekind, G.: Tail Versus Canard Configuration, An Aerodynamic Comparison with Regard to the Suitability for Future Tactical Combat Aircraft. ICAS Proc. 1982, pp. 247-254.
2. Rao, D. M. and Buter, T. A.: Experimental and Computational Studies of a Delta Wing Apex Flap. AIAA Paper No. 83-1815, July 1983.
3. Wahls, R. A., Vess, R. J. and Moskovitz, C. A.: An Experimental Investigation of Apex Fence Flaps on Delta Wings. AIAA Paper No. 85-4055, October 1985.

## ACKNOWLEDGMENTS

This research was supported by the Air Force Flight Dynamics Laboratory, Wright-Patterson AFB, under contract No. FY1456-85-00032. Considerable assistance was received from Lt. Mike Stuart and Capt. Chris Smith, graduate students of the Air Force Institute of Technology (AFIT), which is greatly appreciated. The authors also extend their gratitude to AFIT for the use of a model, the 5-ft Tunnel Facility and associated personnel.

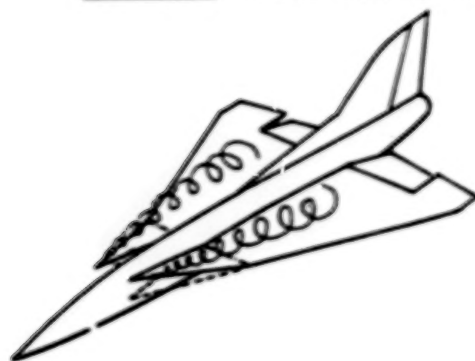
Table 1

TRIMMED  $C_L = 0.82$

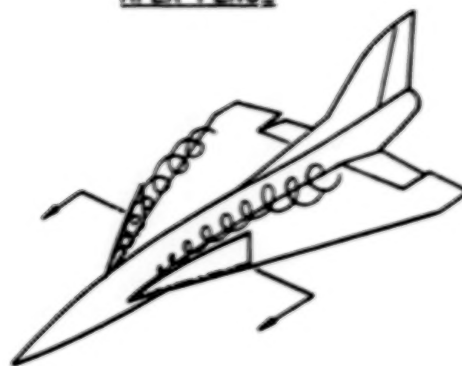
| <u>FENCE TYPE</u> | <u>AREA RATIO<br/>FENCE / WING</u> | <u><math>\delta_{TE, ELEVATOR}</math></u> | <u>L/D</u> | <u>ALPHA</u> |
|-------------------|------------------------------------|---|------------|--------------|
| FENCE OFF         | ----                               | -2.1°                                     | 2.92       | 17.9°        |
| GOTHIC FENCE      | 18.7 %                             | 26.8°                                     | 2.21       | 12.0°        |
| DELTA FENCE       | 11.7 %                             | 14.7°                                     | 2.64       | 14.0°        |



APEX FLAP (RAO, BUTER, 1983)



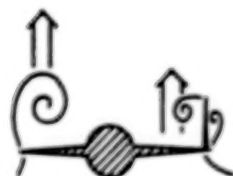
APEX FENCE



HYPOTHESIZED  
VORTEX PATTERNS  
IN APEX REGION:  
WITH LEFT FENCE DOWN,  
RIGHT FENCE UP



INCREASED LIFT  
AT LOW ALPHA



REDUCED LIFT  
AT HIGH ALPHA

Fig. 1. Apex fence concept.

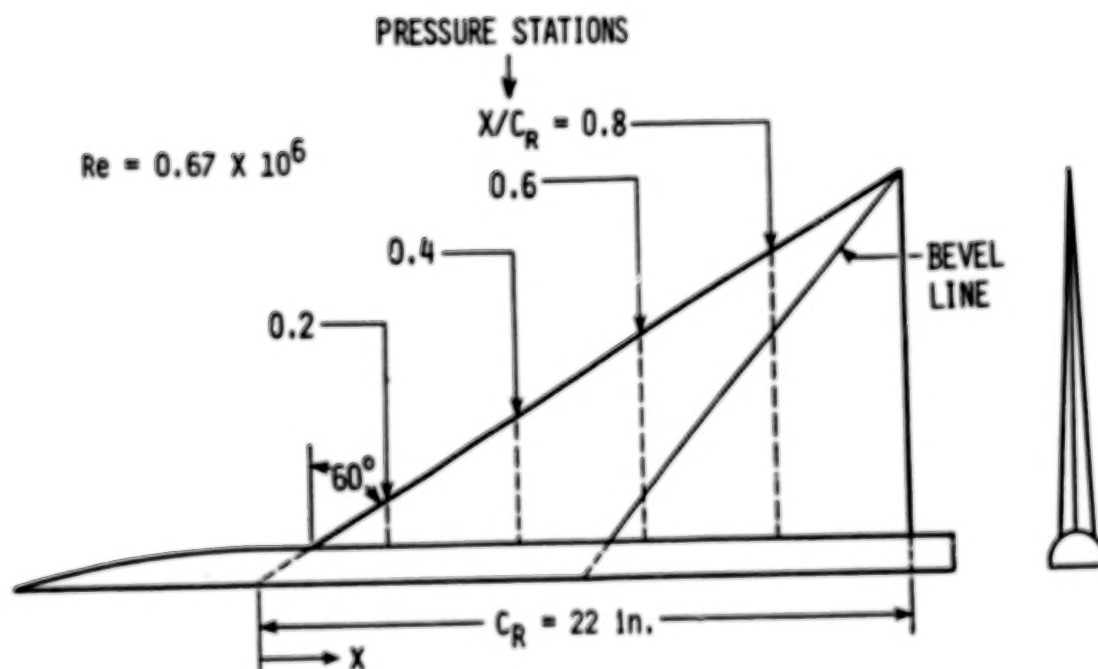


Fig. 2. 60-deg delta semi-span pressure model.

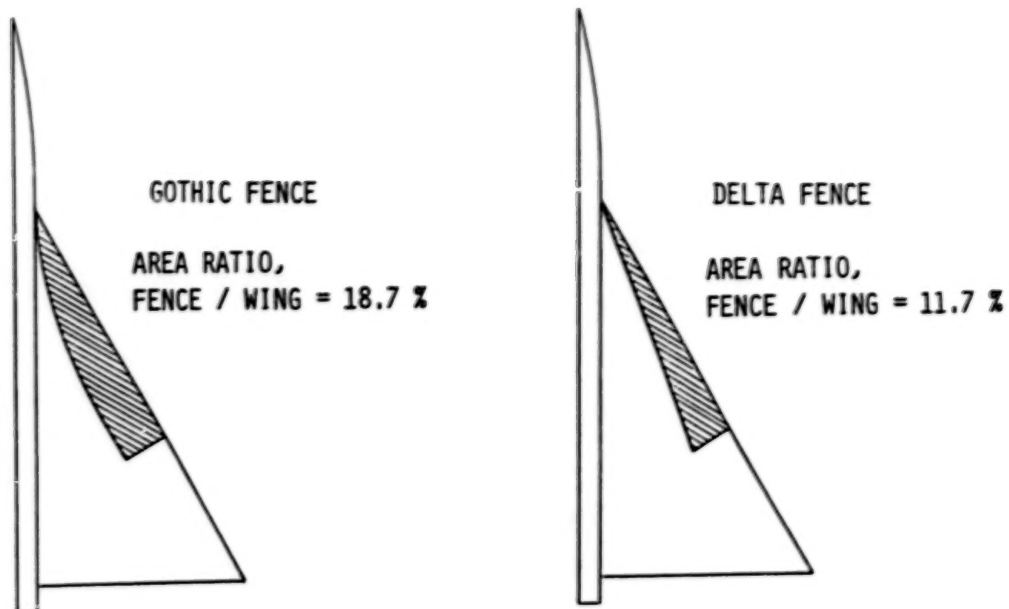


Fig. 3. Typical fence shapes tested on semi-span delta model.

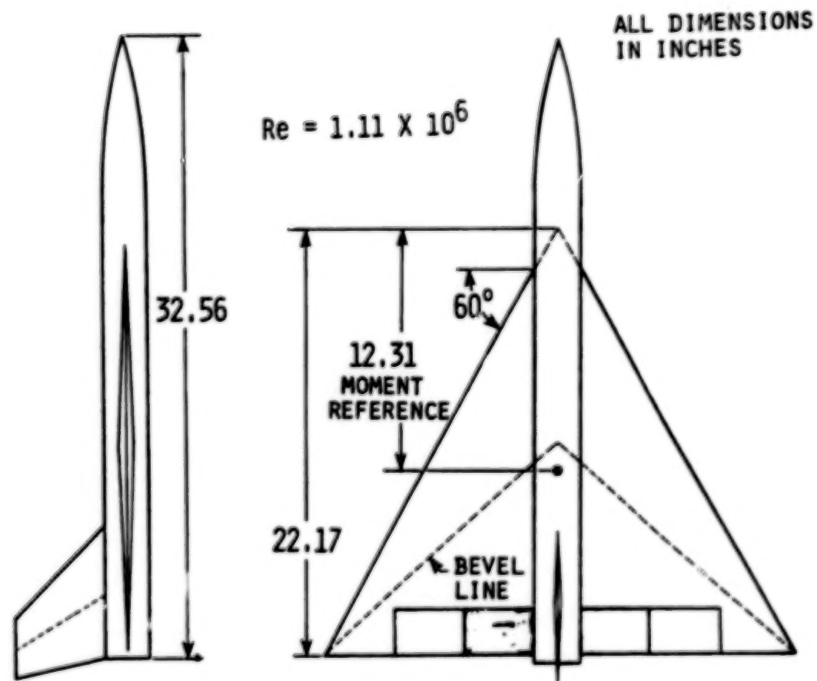


Fig. 4. 60-deg delta full-span force model.

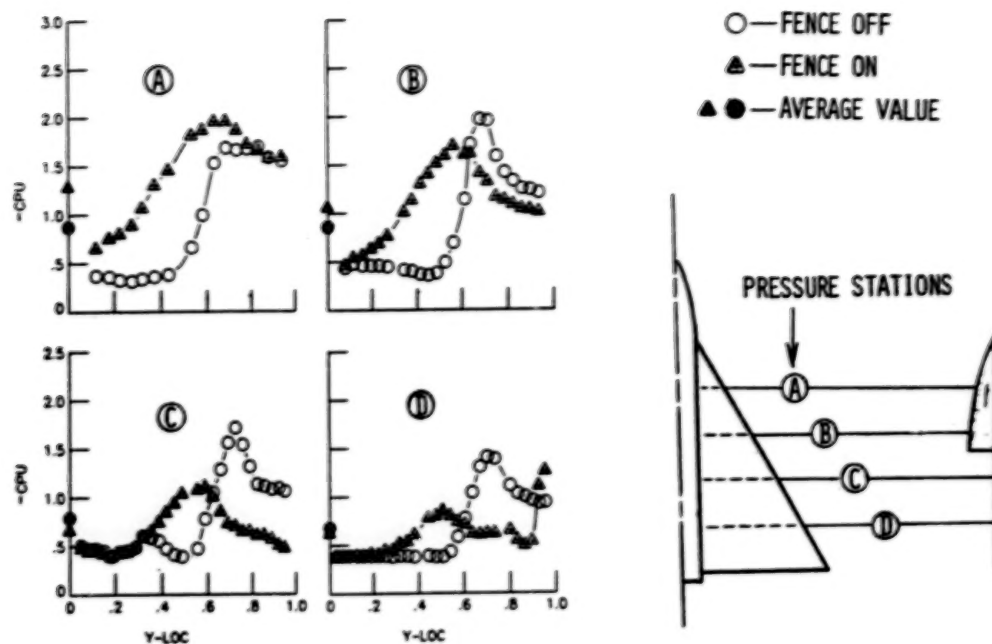


Fig. 5. Spanwise upper surface pressure distributions at 10 deg alpha with gothic fence.

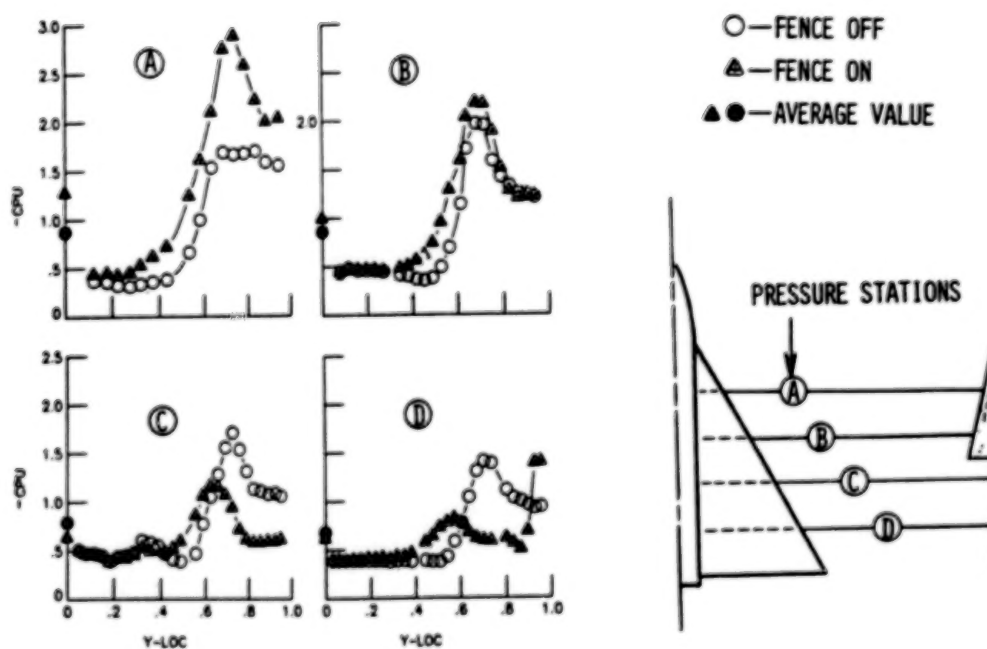


Fig. 6. Spanwise upper surface pressure distributions at 10 deg alpha with gothic fence.

ORIGINAL PAGE IS  
OF POOR QUALITY

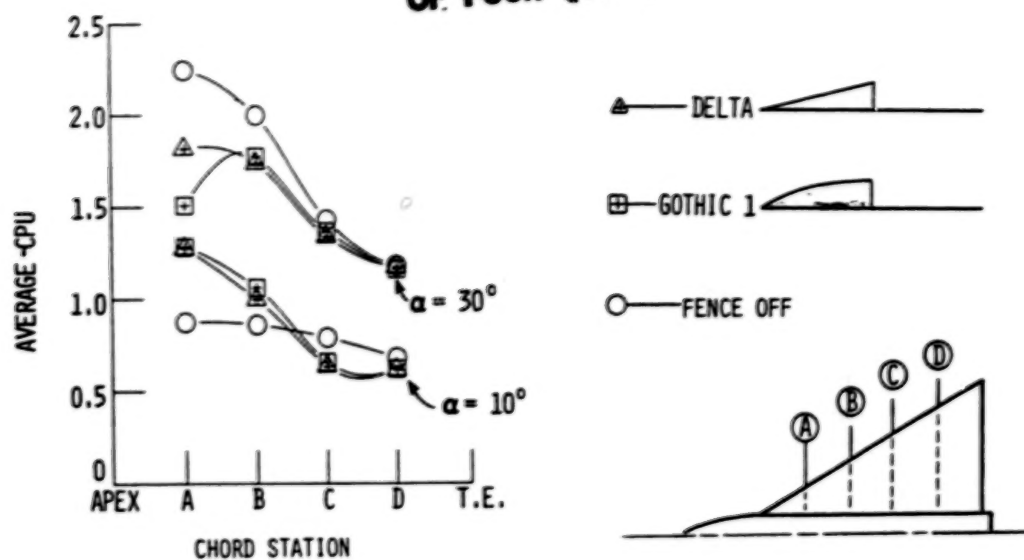


Fig. 7. Longitudinal distributions of span-averaged upper surface pressure coefficients.

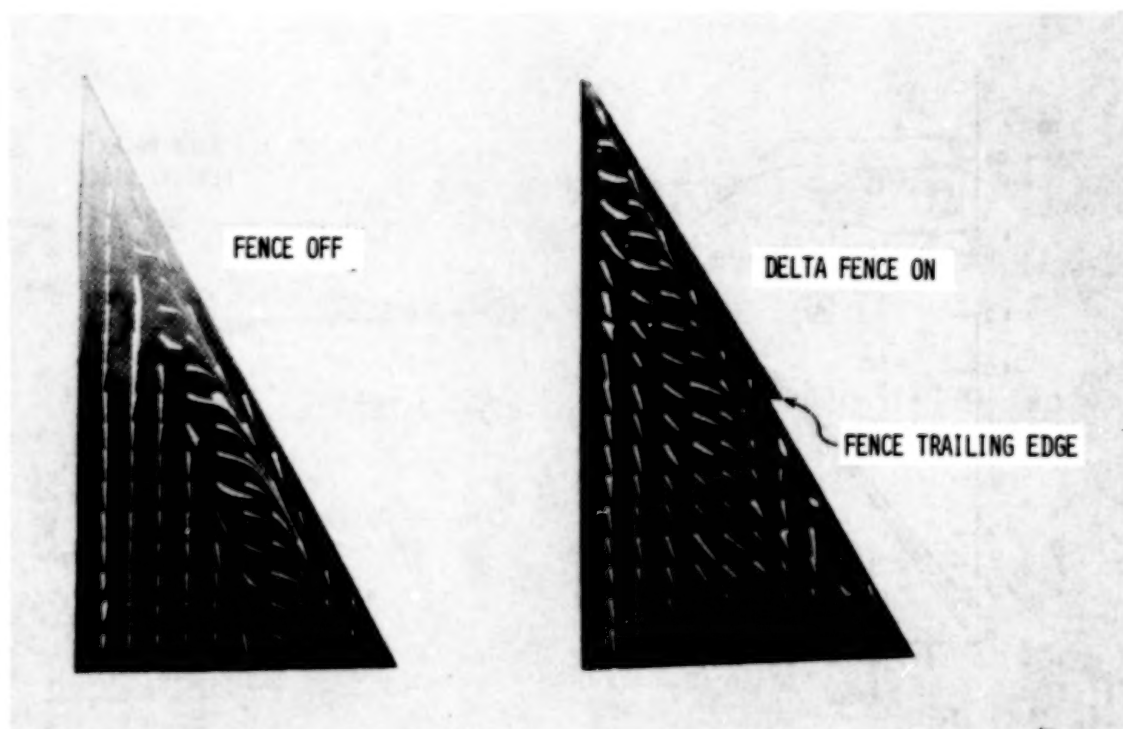


Fig. 8. Typical oil-flow patterns on force model, showing fence effect at  $95^\circ$  alpha.

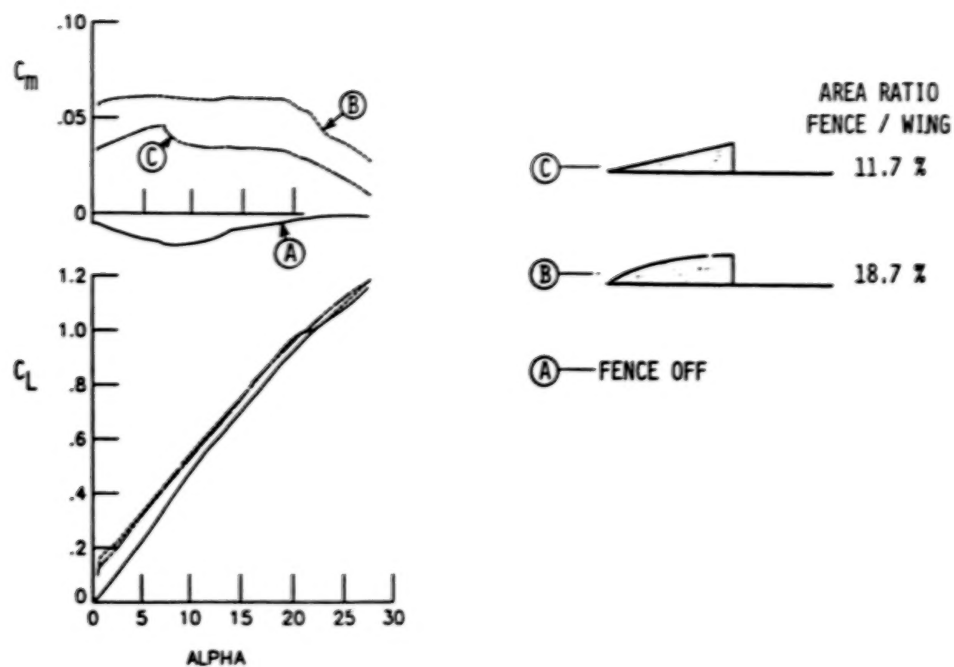


Fig. 9. Lift and pitching moment effects of longest delta and gothic fences.

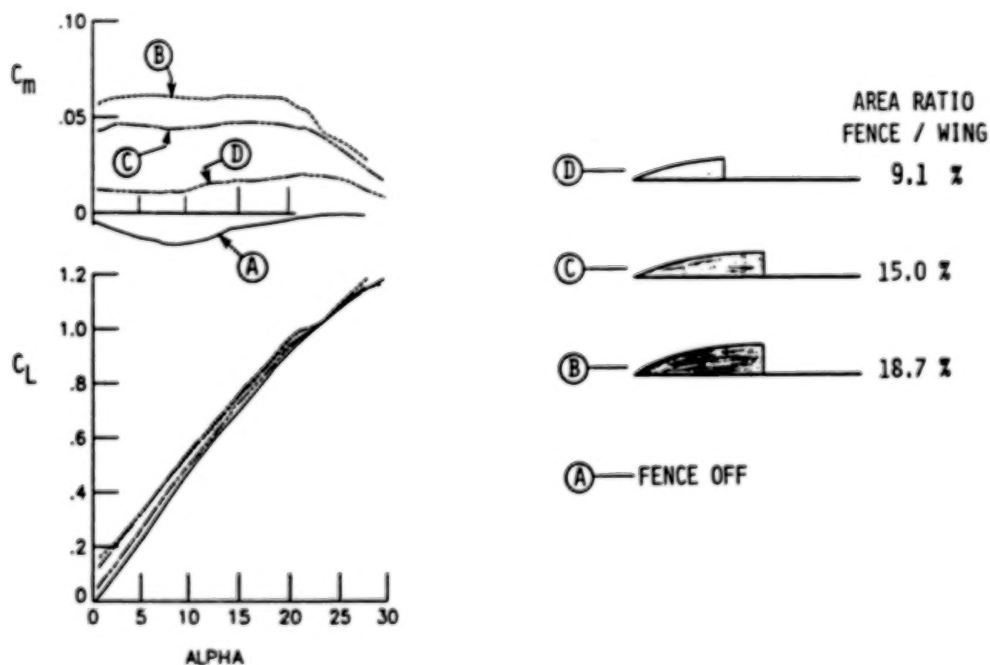


Fig. 10. Lift and pitching moment effects of gothic fence variations.



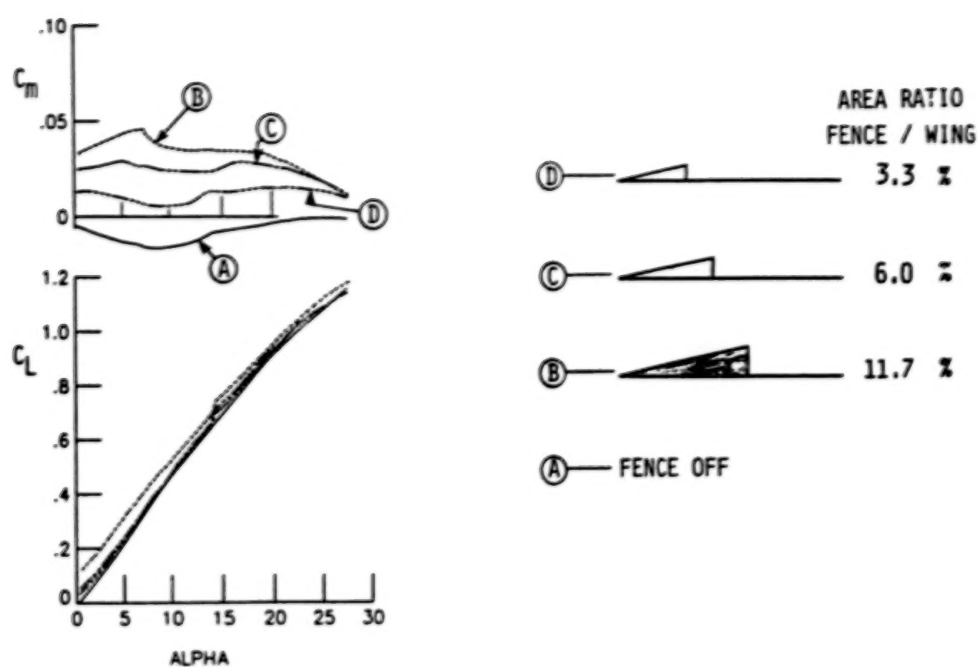


Fig. 11. Lift and pitching moment effects of delta fence variations.

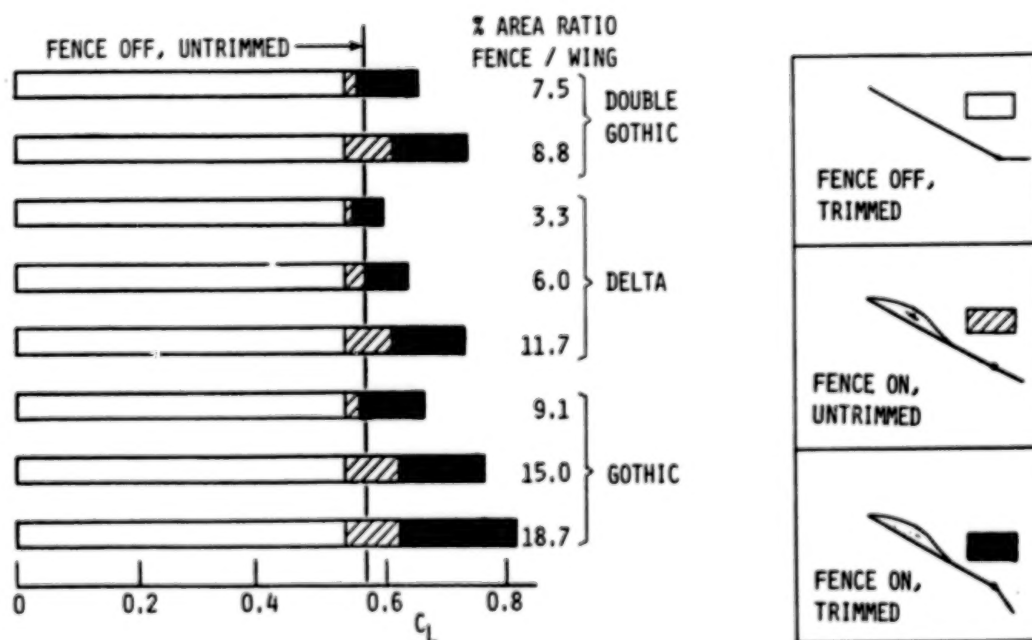


Fig. 12. Trimmed and untrimmed lift increments due to various fences at 12 deg alpha.

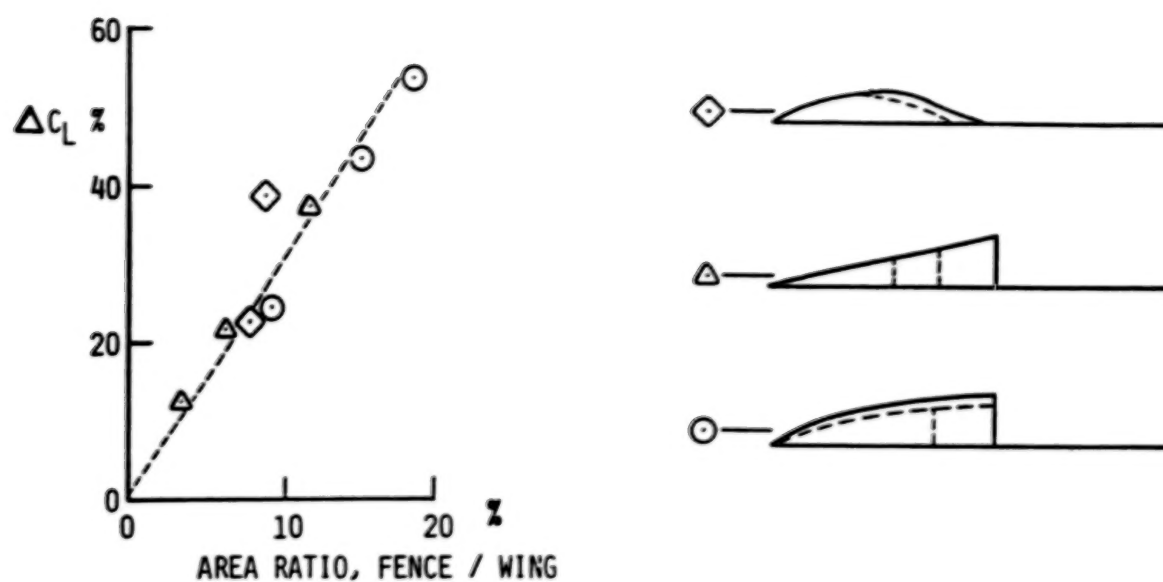


Fig. 13. Fence area effect on trimmed lift increment at 12 deg alpha.

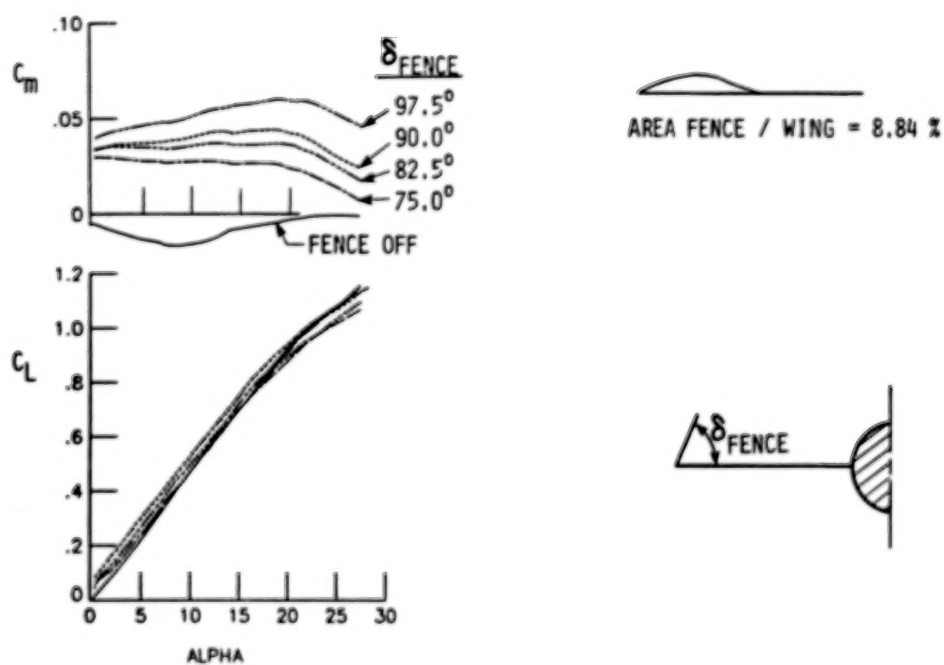


Fig. 14. Lift and pitching moment effects of fence deflection.

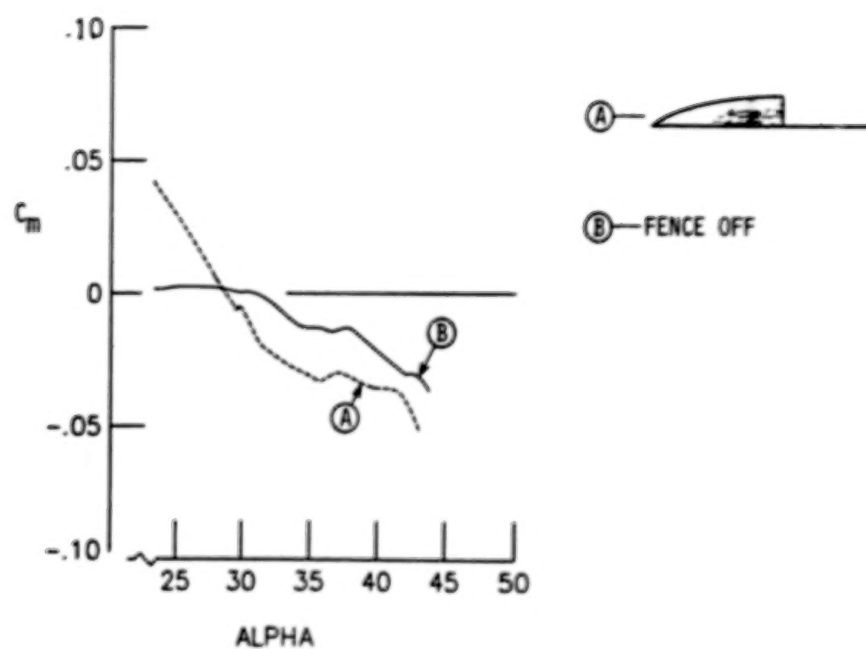


Fig. 15. Fence effect on pitching moment at high alphas.

**TOWARDS AN ADVANCED VORTEX FLAP SYSTEM - THE "CAVITY" FLAP**

Dhanvada M. Rao  
Vigyan Research Associates, Inc.  
Hampton, Virginia

**SUMMARY**

An extension of the vortex flap concept was explored with the aim of providing high-alpha flight control capability coupled with maneuver drag reduction for highly swept wing configurations. A retractable lower surface flap mounted on a translating hinge is proposed, allowing chordwise extension as well as deflection, the two movements being independently controlled. The frontal cavity formed by the partially extended and deflected flap captures a vortex above a certain angle of attack. The cavity vortex downwash alleviates the effective incidence of the wing leading edge, thus modulating vortex lift; at the same time, the induced suction in the cavity generates thrust. These postulated aerodynamic features of the cavity flap were validated through low-speed tunnel pressure and visualization tests on a 65 deg swept oblique wing model, which also provided initial trends of the leading edge vortex alleviation and cavity suction with respect to flap extension, deflection and angle of attack. Force tests on a 60 deg delta model further showed the cavity flap L/D performance to compare favorably with the conventional vortex flap. A two-segment flap arrangement with independently controlled segments was envisaged for exploiting the vortex modulation capability of the cavity flap for pitch, roll and yaw control, in addition to drag reduction at high angles of attack.

**INTRODUCTION**

The first wind tunnel demonstration of the vortex flap concept took place nearly seven years ago (ref. 1). The extensive experimental and theoretical research carried out since then (ref. 2) has concentrated on the application of vortex flap thrust recovery for drag reduction of highly swept wings at maneuver lift coefficients. Recent design studies related to advanced fighters have underlined the need to extend aerodynamic control effectiveness to increasingly high angles of attack. Accordingly there is considerable interest in evaluating vortex management ideas for improved high-alpha control.

Effective aerodynamic control of highly swept, slender vehicles at high angles of attack basically requires the ability to modify the onset, growth and shedding characteristics of large-scale vortices originating from forebody and wing leading-edge separation, and thereby to rapidly modulate the vortex lift and reposition its point of action relative to c.g. Although vortex lift modulation capability has been shown to be inherent to the vortex flap concept, its potential has not yet been explored in detail. This paper discusses an advanced vortex flap system, called the cavity flap, conceived for the purpose of obtaining high-alpha control as well as

**PRECEDING PAGE BLANK NOT FILMED**

drag reduction from the same set of aerodynamic surfaces. Some results are presented of low-speed wind tunnel experiments undertaken to verify the aerodynamic basis of the cavity flap and to compare its drag reduction performance with that of a conventional vortex flap.

### CAVITY VORTEX FLAP

The conventional (or leading-edge) vortex flap aims to contain the vortex and its peak suction over the flap (fig. 1). Drag reduction then is a combined result of thrust recovery on the forward-sloping flap and reduced suction on the aft-sloping wing surface.

With increasing alpha the flap frontal projected area decreases and its direct contribution to drag reduction tends to zero. A 30-deg deflected flap on a 60-deg delta wing, for example, becomes essentially aligned with free-stream at 14 deg angle of attack (or  $C_L = 0.65$ ), beyond which it is the re-attached flow on the wing rather than the flap vortex force that yields a drag reduction.

If the flap hinge were to be moved some distance aft of the leading edge under the wing and a vortex trapped in the resulting cavity, the frontal area under vortex suction can be largely recovered. The leading-edge overlap now covers a large part of the flap plan area and therefore reduces its own vortex lift contribution. This cavity flap arrangement promises a substantial vortex lift modulation capability by independently varying the flap projection and deflection at a given angle of attack. In the limit, an optimum cavity vortex leading to a fully attached flow on the wing will essentially eliminate vortex lift. Additional cavity flap advantages envisioned are its applicability to sharp or blunt leading edges, plus a structurally superior attachment to the wing in comparison with the leading-edge hinged flap.

Figure 2 suggests a practical implementation of the cavity flap. The retracted flap is fully conformal to the wing lower surface contour. The flap hinge slides on internal tracks, the extension and deflection angle being actuated independently. Pure extension of the flap projects a sharp edge which can be used to augment vortex lift on blunt leading-edge wings (ref. 3). Partial extension plus deflection yields the cavity flap configuration. At the forward limit of extension the flap functions essentially as a conventional vortex flap. At a large deflection angle with the hinge at its aft limit, a vortex will form behind the flap, making it an effective drag brake.

### OBLIQUE WING TESTS

The key hypothesis underlying the cavity flap concept, namely the capture of a stable cavity vortex and its use to modulate vortex lift on the wing, was tested on a highly swept oblique wing model (fig. 3). The variable-sweep oblique wing was chosen to facilitate future study of the sweep-angle effect on the cavity vortex stability. In the initial tests reported here, however, the wing was set at the maximum sweep of 65 deg.

The wing section perpendicular to leading edge was a 12-percent thick, conventional subsonic type airfoil with a flat undersurface. Two chordwise pressure



stations were incorporated in the wing, one on the fore panel and one on the aft panel. At each station, taps were provided on the upper surface and over the first 15 percent chord on the lower surface.

A constant chord, flat plate flap was tested on the forward wing panel. Three deflection angles (10, 20 and 30 deg), and three hinge positions at each angle including the leading-edge position, were investigated. The tests were carried out in the North Carolina State Subsonic Tunnel at a free-stream velocity of 100 fps.

The vortex characteristics of oblique wings are not well known. Therefore, the oblique wing model was first tested with flap off in order to establish its suitability for evaluating the cavity flap. Figure 4 shows typical oil-flow and pressure distribution results. The oil pattern at  $\alpha = 16$  deg reveals independent leading-edge vortices on the fore and the aft wing panels. The upper surface pressures at four angles of attack (10, 12, 14 and 16 deg) show the evolution of the vortex suction peak. Comparison of the fore and aft pressure stations with increasing angle of attack shows the forward wing vortex to develop continuously, whereas on the aft wing the suction peak is gradually smeared out due to the locally thickened boundary layer (resulting from a spanwise outflow as on a swept-back wing). These tests showed that the fore panel of the oblique wing generated a leading-edge vortex flow representative of swept wings, thus providing a proper aerodynamic environment for validation of the cavity flap concept.

Typical flap effects on the forward wing pressures at an angle of attack 16 deg will now be discussed. Figure 5 shows the effect of moving the flap hinge forward with the flap angle held constant at 20 deg. The sketches on the right interpret the corresponding vortex patterns.

At the aft hinge position, the flap hardly affects the upper surface suction characteristics; on the lower surface, however, an increased suction suggests that a cavity vortex is already formed. No change in vortex lift due to flap deployment can be expected in this case although some drag reduction should be obtained.

Moving the flap hinge to the mid-position is seen to produce a marked reduction in the vortex suction on the wing upper surface. At the same time, the cavity suction is almost doubled. This position of the flap appears to come close to the postulated cavity vortex flow with attached flow on the wing. Substantial lift reduction can therefore be anticipated in this case, together with enhanced drag-reduction.

At the leading-edge position of the flap the vortex appears to be partly spilled onto the wing. Due to the fully exposed flap area in this case, lift reduction on the wing is likely to be largely compensated by the vortex lift on the flap. The drag reduction capability will be degraded due to the negligible frontal area projected by the flap.

The pressure results in figure 6 show the effect of increasing flap angle at a constant hinge position. A progressive decrease in the vortex suction on the wing upper surface is noted. There is little change in the cavity suction level with increasing flap angle; however, since the associated frontal area is increasing, the drag reduction should improve.

By integrating the upper surface pressures a local normal force coefficient is obtained. This upper surface normal force directly reflects the changes in the

vortex suction characteristics and is therefore useful for presenting the trends with respect to flap angle and hinge line position. It is seen in figure 7 that, at all three flap angles, a forward extension of cavity flap results in progressive and marked reduction in the wing normal force at angles of attack above 8 deg.

Typical cavity suction characteristics are shown in figure 8 for the mid-position of the flap hinge. Also shown for reference is the pressure at the same lower surface tap with the flap off. It is evident that with increasing flap angle, the onset of cavity vortex is delayed. At higher angles of attack, however, all three flap angles approach the same cavity suction levels.

#### 60-DEG DELTA FORCE TEST

Force measurements to evaluate the cavity flap were conducted on a 60-deg delta model (fig. 9) during a brief investigation in the NASA Langley 12-Foot Low-Speed Tunnel. The object of these initial tests was to compare the drag reduction capabilities of leading-edge flap and cavity flap at constant flap angles of 20 deg and 40 deg.

The leading-edge thrust due to a flap is most sensitively indicated in the balance axial force component. Figure 10 plots the axial force versus normal force coefficients and includes the flap-off data for reference. The vertical gap between the flap-on and flap-off data (i.e. a negative  $\Delta C_A$ ) indicates the aerodynamic thrust attained. At 20 deg flap angle, the cavity flap is seen to generate more thrust than the leading-edge flap throughout the  $C_N$  range. At 40 deg deflection, the onset of cavity vortex is delayed to a higher angle of attack, and as a result the cavity flap begins to show an advantage only above  $C_N = 0.6$ .

Figure 11 presents the corresponding drag reductions. On the left is absolute  $\Delta C_D$  and on the right,  $\Delta C_D$  as a percentage of the basic drag (i.e. flap off). It is noted that the 40-deg cavity flap advantage appears at higher angles of attack when the percentage drag reduction has already peaked and is rapidly declining. It is reasonable to expect therefore that a more moderately deflected cavity flap (say at 30 deg) might be advantageous in the region of peak percentage drag reduction. Note also that the hinge line position remains to be optimized in combination with flap deflection, which should yield additional improvement in the cavity flap performance.

Since both the leading edge and cavity flaps produce reductions in lift as well as in drag, the final evaluation must be in terms of L/D ratio as a function of lift coefficient. Figure 12 shows the 20-deg cavity flap to be advantageous across  $(L/D)_{max}$ . The 40-deg cavity flap evidently is over-deflected, but catches up with the leading-edge flap at  $C_L = 0.7$  and thereafter yields the same L/D improvement. The L/D results again suggest that flap angles between 20 and 40 deg deserve investigation and that a coordinated study of hinge-line position should also be conducted.

#### CAVITY FLAP FOR HIGH ALPHA CONTROL

It is interesting to speculate on the ways of exploiting the vortex lift modula-

tion capability of the cavity flap for high-alpha control (fig. 13). A spanwise segmented cavity flap system is envisaged with two segments per leading edge, each flap segment being under independent control. For maximum drag reduction, all four flap segments will be deployed; the attendant loss in vortex lift is proposed to be compensated by the use of a trailing-edge flap. By deploying the inner segments only, the vortex lift forward of the c.g. will be reduced thus generating a nose-down moment for accelerated recovery from high alpha. When both segments are deployed on the right leading edge only, the excess of vortex lift prevailing on the left wing panel will produce a right roll. At the same time, a side force component towards the right will be generated by the flap thrust, favorable in a right turn. The inner left and outer right segments deployed at their maximum thrust setting will develop a nose-left yawing moment. Not included in this figure is the additional use of the cavity flap for aerodynamic braking at low angles of attack.

### CONCLUSIONS

A cavity vortex flap has been postulated in which the forward extension and deflection are independently controlled to allow vortex lift modulation while producing thrust.

The cavity vortex postulate was verified on a 65-deg oblique wing, demonstrating alleviation of the leading-edge vortex effect on the wing and generation of cavity suction through a range of flap extension, deflection and angle of attack.

Balance tests on a 60-deg delta wing indicated that the cavity flap was at least equal to the conventional leading-edge flap in L/D improvement and could be better with optimized combinations of extension and deflection. High-alpha pitch, roll and yaw control possibilities of the cavity flap concept, as well as its effectiveness as a drag brake, should be evaluated in future investigations.

### REFERENCES

1. Rao, Dhanvada M.: Leading Edge Vortex Flap Experiments on a 74 Deg Delta Wing. NASA CR-159161, Nov. 1979.
2. Campbell, James F. and Osborne, Russell F.: Leading-Edge Vortex Research: Some Nonplanar Concepts and Current Challenges. Vortex Flow Aerodynamics - Volume I, NASA CP-2416, paper no. 2, 1986.
3. Rao, Dhanvada M. and Johnson, T. D., Jr.: Investigation of Delta Wing Leading Edge Devices. J. Aircraft, Vol. 18, No. 3, pp. 161-167, March 1981.

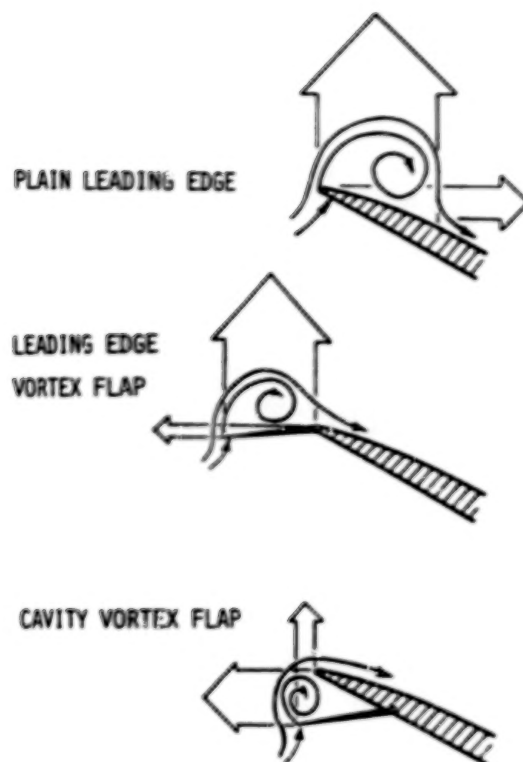


Figure 1 The cavity vortex flap concept.

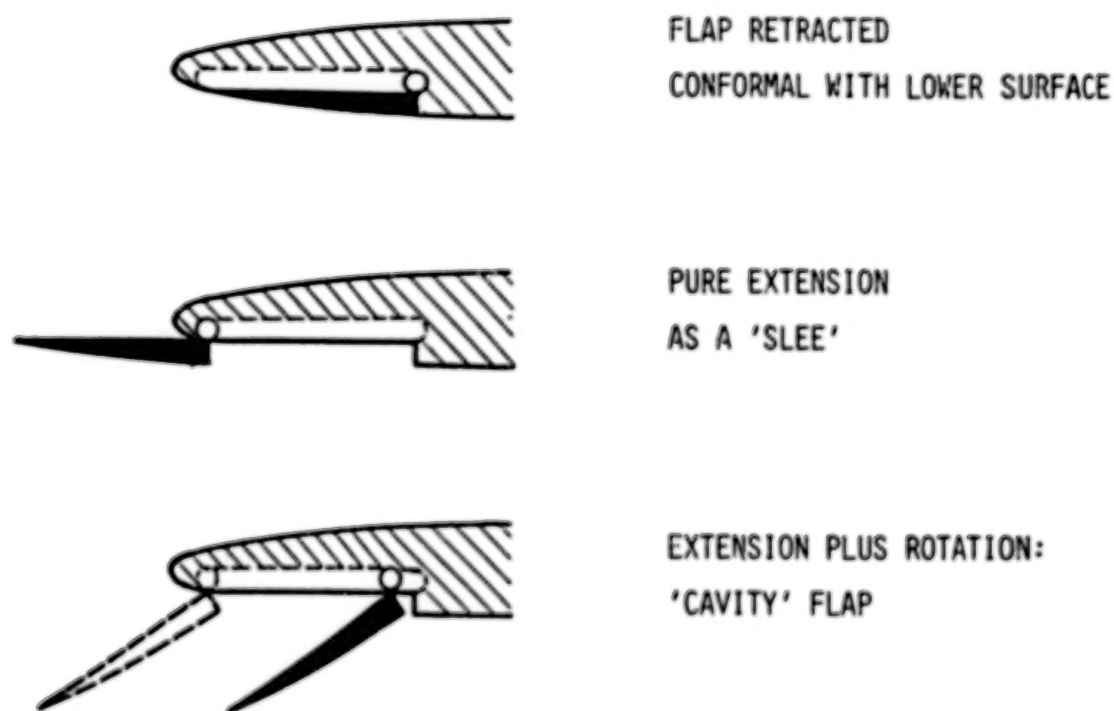


Figure 2 Cavity flap arrangement with independent extension and rotation.



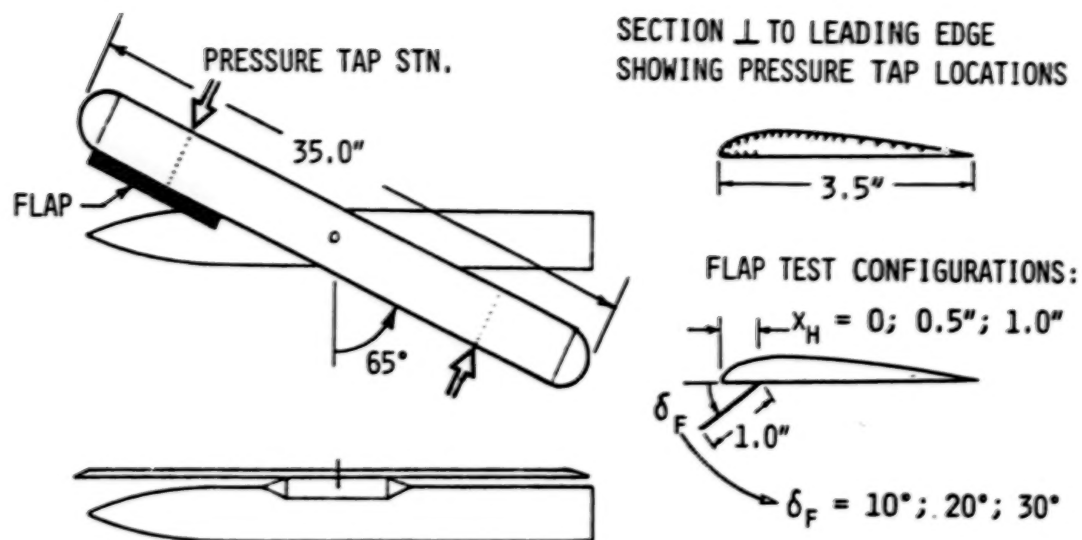


Figure 3 Oblique wing model tested in North Carolina State University Subsonic Wind Tunnel.

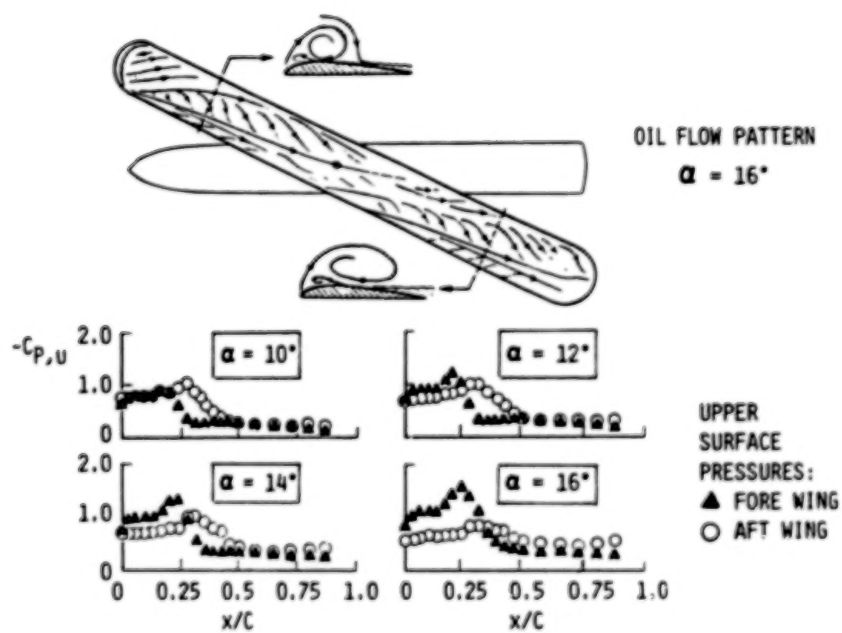


Figure 4 65-deg oblique wing flow and pressure characteristics with flap off.



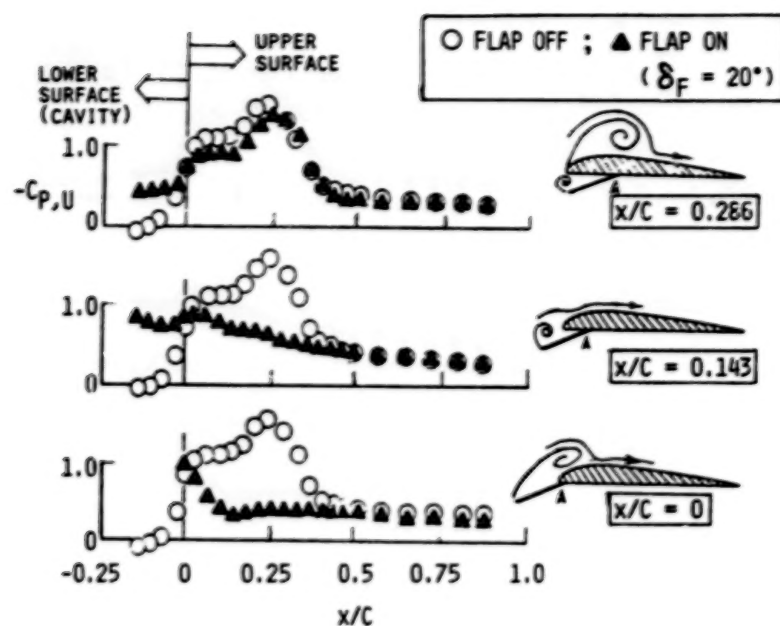


Figure 5 Pressure distributions showing effect of flap hinge position at 16-deg angle of attack.

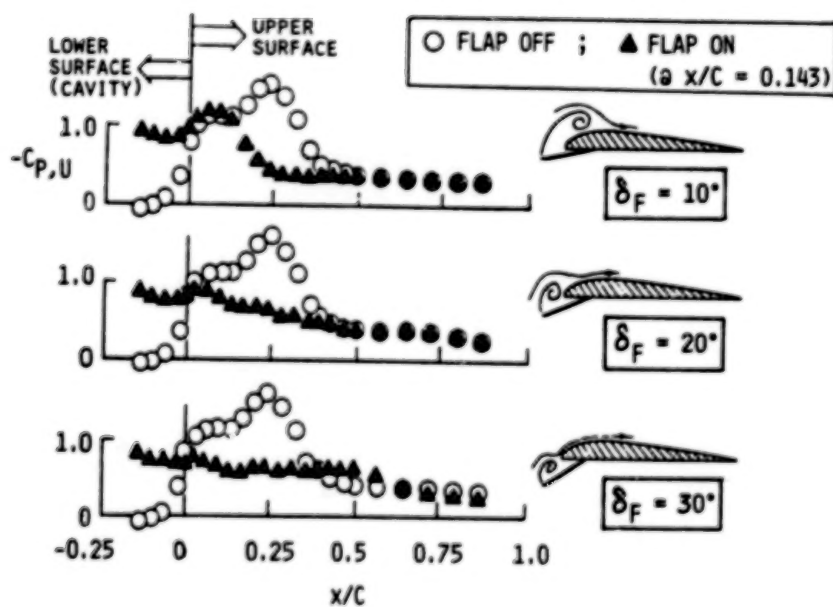


Figure 6 Pressure distributions showing effect of flap angle at 16-deg angle of attack.

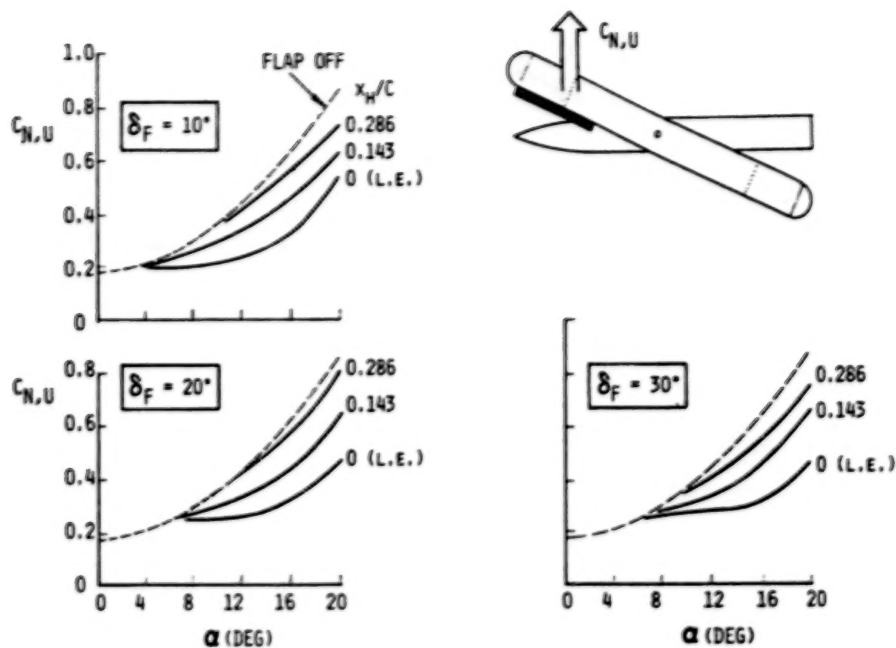


Figure 7 Pressure-integrated upper surface normal force characteristics.

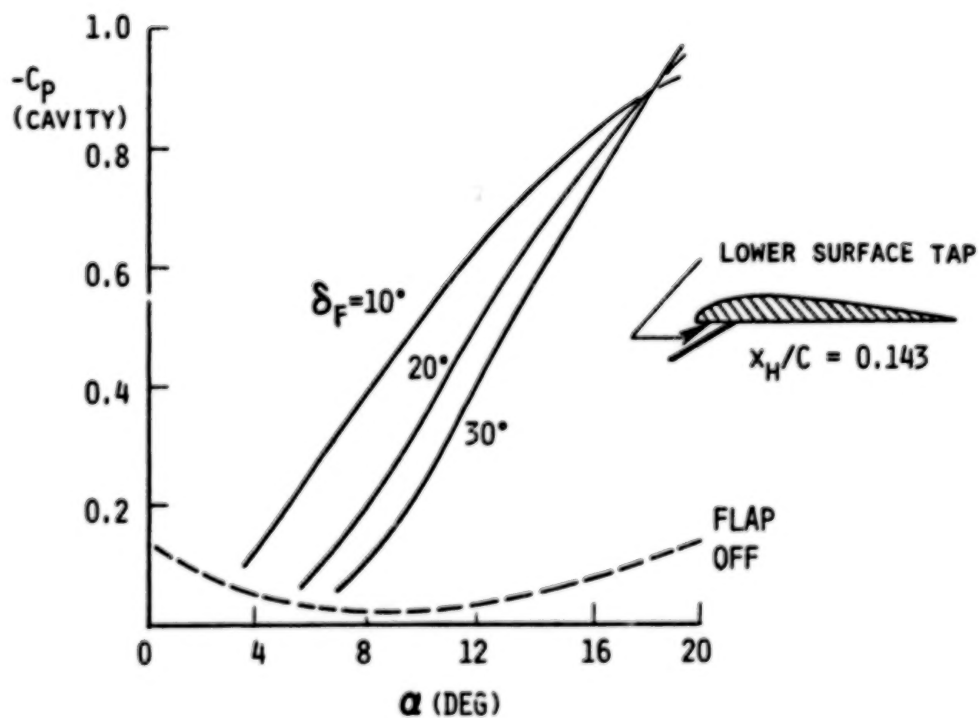


Figure 8 Cavity suction characteristics showing effect of flap angle.

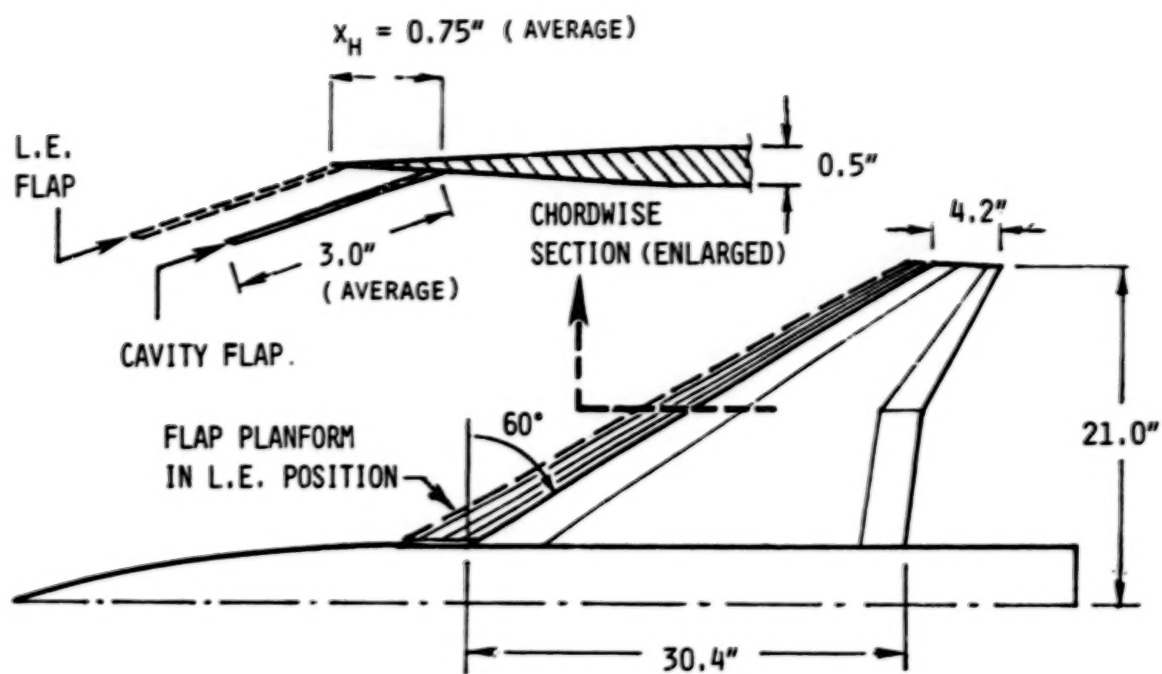


Figure 9 60-deg delta wing axial versus normal force characteristics.

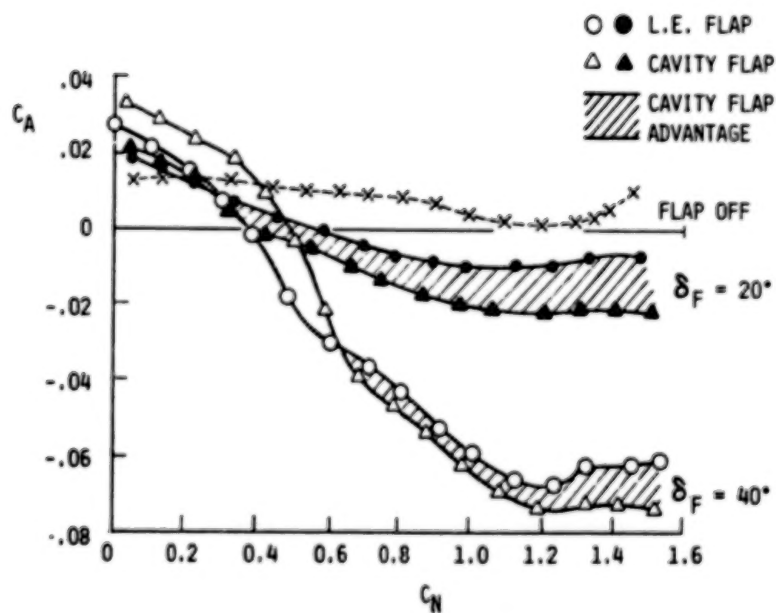


Figure 10 60-deg delta wing drag reduction with leading-edge and cavity flaps.

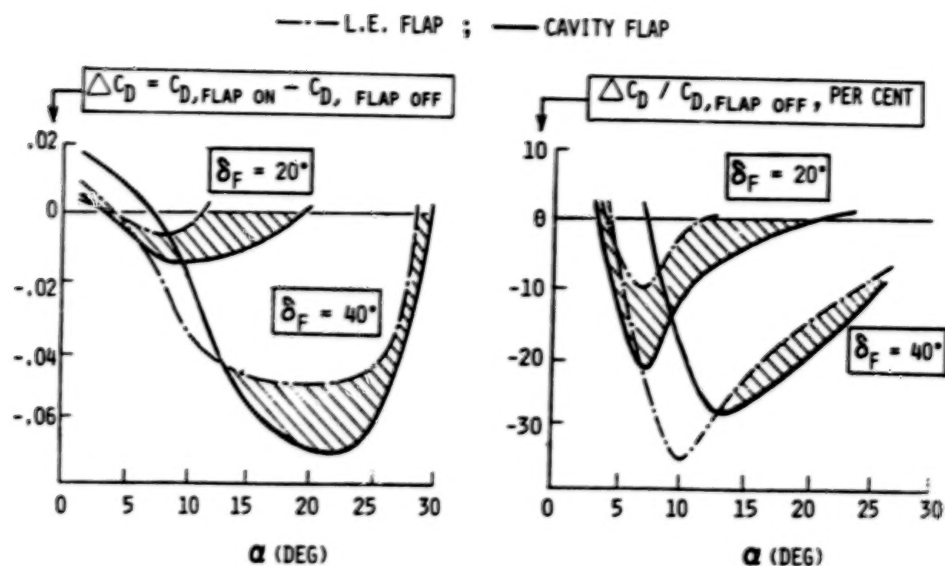


Figure 11 60-deg delta wing drag reduction with leading-edge and cavity flaps.

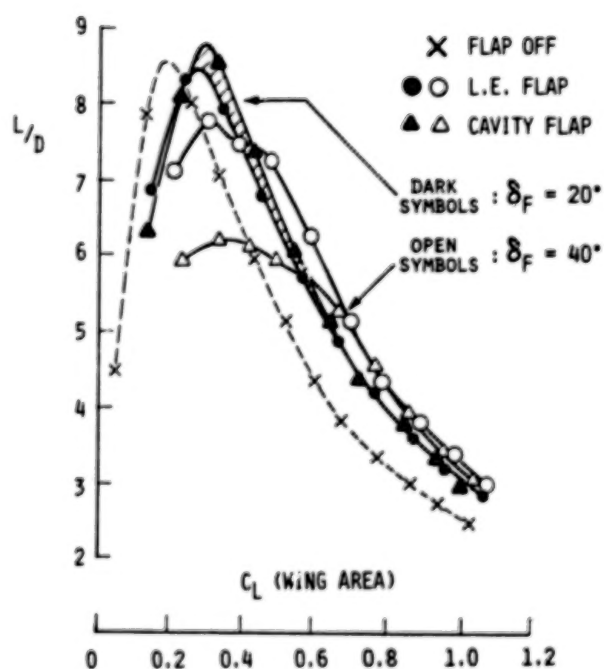


Figure 12 60-deg delta wing lift/drag ratio with leading-edge and cavity flaps.

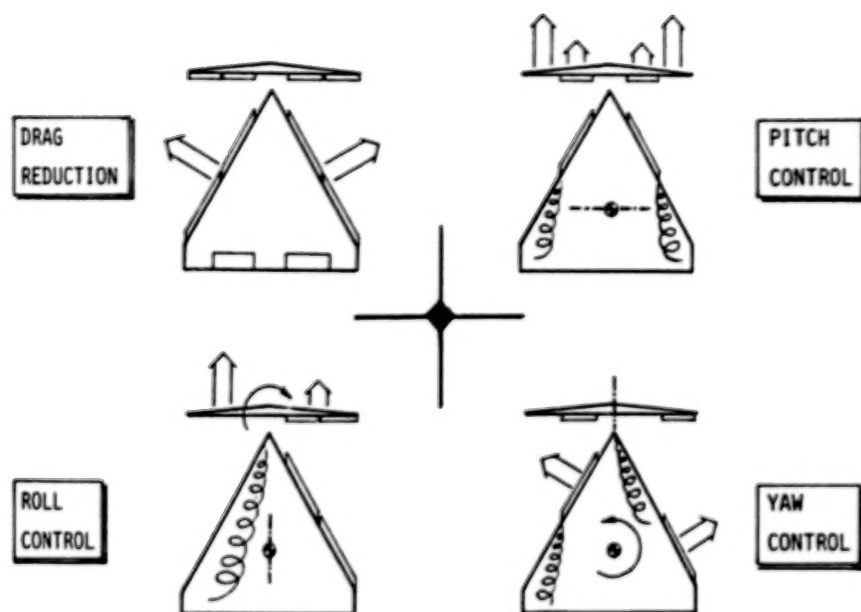


Figure 13 Cavity flap applications for control at high angles of attack utilizing thrust and lift modulation.



## VORTEX FLOW HYSTERESIS

Atlee M. Cunningham, Jr.  
General Dynamics  
Fort Worth Division  
Fort Worth, Texas

## SUMMARY

An experimental study was conducted to quantify the hysteresis associated with various vortex flow transition points and to determine the effect of planform geometry. The transition points observed consisted of the appearance (or disappearance) of trailing-edge vortex burst and the transition to (or from) flat plate or totally separated flows. Flow visualization with smoke injected into the vortices was used to identify the transitions on a series of semi-span models tested in a low-speed tunnel. The planforms tested included simple deltas (55 deg to 80 deg sweep), cranked wings with varying tip panel sweep and dihedral, and a straked wing. High-speed movies at 1000 frames per second were made of the vortex flow visualization in order to better understand the dynamics of vortex flow, burst and transition.

## INTRODUCTION

Recent interest in flying at very high angles of attack beyond the static stall conditions has been kindled by proposals to exploit this flow regime to improve fighter aircraft maneuverability (refs. 1 and 2). Herbst's concept to fly into the post-stall regime to achieve quicker turns (ref. 1) and the use of unsteady aerodynamics at high incidence discussed by Lang and Francis (ref. 2) open a Pandora's box of new aerodynamic problems. Because these ideas require flying at incidences as high as 90 deg or beyond, a single maneuver could cover vortex and burst vortex flows as well as totally separated flows. Also, because of the maneuver dynamics, pitch rate and time history effects could be very important. The understanding of these flow fields and the dynamic effects represents a quantum jump over current aerodynamic technology. Thus, as a first step toward this goal, a need exists to identify the various flow regimes and their characteristics as well as transition points from one type to another and the associated hysteresis effects.

The upper surface flow fields that exist over slender, highly swept or straked wings at high angles of attack may take on various forms. These forms may be broadly classified as three types summarized in Figure 1:

- (1) Vortex flows (stable leading edge or strake vortex)
- (2) Burst vortex flows (unsteady but still vortical)
- (3) Flat plate flows (unsteady, completely separated)

The normal force curve slope for type 1 flows is quite high compared to that of the attached flow region which generally exists below 5 deg. to 8 deg. incidence as illustrated in figure 1. The slope is reduced once vortex bursting begins to occur over the wing but normal force still increases with increasing incidence. Once the flow breaks down to the final stage of flat plate flow, normal force remains about constant, even up to 90 deg. incidence. The transition to flat plate flow is generally quite abrupt and may be accompanied by a loss in normal force or a destabilizing change in pitching moment with increasing incidence. Another very important property of these transitions is the hysteresis effect that results from transitions occurring at different incidences depending on whether the angle is increasing or decreasing. Quantification of this hysteresis and the determination of the effect of planform geometry on its characteristics are the objectives of this paper.

In order to accomplish these objectives, an experimental program was conducted in which a series of delta and cranked flat plate wings were tested. Flow visualization techniques were used to determine the transition points and the associated hysteresis. The tests were conducted in a small low speed tunnel at General Dynamics' Fort Worth Division using smoke for the flow visualization. The smoke generator was a special design that was evolved at General Dynamics for testing vortical flows at very high incidence. The models were semi-span models cut from flat aluminum plate with rounded leading edges. The planforms tested included simple deltas, cranked wings with varying tip panel sweep, a cranked wing with varying tip panel dihedral, and a straked wing. Data taken during the test for increasing and decreasing incidence included angles of the appearance of vortex burst at the wing trailing edge and transition to or from flat plate flow. High speed movies were made of the vortex flows to reveal the spiral nature of vortex burst and other unsteady phenomena.

#### TEST SETUP AND PROCEDURE

The small continuous low speed wind tunnel at General Dynamics' Fort Worth Division was used for this investigation. The tunnel has a  $0.356 \times 0.356\text{m}^2$  ( $14 \times 14\text{ in.}^2$ ) test section with a splitter plate installed on one wall and clear glass on the other three walls for viewing flow visualization experiments. Test velocities used were held approximately constant at 30m/sec (98 ft/sec) which previous experience has shown to yield reliable vortex flow characteristics and good flow visualization using smoke.

The semi-span models were cut from flat aluminum plate stock, 0.160 cm (0.063 in) thick, and mounted on a bracket attached to a shaft extending outside the tunnel as shown in figure 2. Angle of incidence was set by rotating the shaft which was attached to a calibrated plate with angle marks. The settings were made manually so that very slow and smooth approaches to flow transition points could be achieved. Angle readings were made visually and recorded by hand.

The smoke generator was also installed on the wing mounting bracket as shown in figure 2 to permit injection of smoke as close as possible to the nose so as to provide maximum visualization of the leading-edge vortex. The smoke generator consisted of 0.05 cm ID (0.02 in.) stainless-steel tubing through which kerosene was forced from a pressurized vessel as shown in figure 3. A 23 cm (9 in.) section of the tubing near the nozzle was heated with DC current at about 10 amps. The heated kerosene vaporized when it exited from the nozzle in a reasonably steady flow. Pulsation was minimized by adjusting current and kerosene flow.

The semi-span models tested are shown in figure 4 with specifications listed in table 1. The leading edges were rounded such that they were semi-circular with a diameter of the thickness of the plate, 0.160 cm (0.063 in.). This was done to avoid adding any leading-edge camber that would result from having a sharp edge with a flat upper surface and also to simplify model fabrication. The cranked wing planforms all had a common inboard leading-edge sweep of 70 deg with the crank placed at 70% span. Only the tip panel sweep was varied from 30 deg to 70 deg and the tip panel dihedral varied from -90 deg to +90 deg with a fixed tip sweep of 30 deg. The straked wing planform was tested to provide insight as to the character of strake flows as opposed to simple delta and cranked wings. All sweep and dihedral were measured and recorded after fabrication.

The test procedure was very simple once the optimum conditions for smoke visualization were established. The wings were attached to the mounting bracket, the tunnel started, then the smoke turned on. The test was conducted on a continuous basis for each wing. The determination of transition angles was made as an average of at least three observations for each point. For increasing incidence, the angle was always lowered far below the transition point and then slowly increased until the transition occurred. For decreasing incidence, the reverse procedure was followed. In all cases fully established flow was obtained just before transition.

Calibration of test set-up was accomplished by comparing measured transition points with existing data for planforms of similar geometries. The items checked were wall interference and gap between the splitter plate and model root chord. Wall interference was about 10% at an incidence of 45 deg for the cranked wings and the delta wings for an incidence less than 70 deg. To check this effect, the angle for trailing-edge burst was compared with data published in



reference 3. This comparison shown in figure 5 indicates that the correlation is quite good. Another check on interference was a qualitative assessment of vortex burst development downstream of the model. Progression of the burst point toward the wing was very uniform and controllable with wing incidence.

The idea of leaving a small gap between the splitter plate and wing root chord was to prevent contamination of the vortex development by the wall boundary layer. This problem is unique to semi-span testing. The gap was set at the estimated displacement thickness of the wall boundary layer, 0.16 cm (1/16 in.). Variation of this gap to zero was shown to have little effect on the trailing-edge (TE) vortex burst angle but a profound effect on the transition to flat plate (FP) flow. Data available from a large-scale full span low-speed test of a General Dynamics research model similar to the 70 deg/50 deg cranked wing indicated that the transition to FP flow should occur at about 43 deg - 47 deg incidence. With the gap set at 0.16 cm, this transition occurred at about 45 deg - 46 deg but with zero gap, it occurred at about 55 deg - 60 deg. Therefore the gap was maintained at the 0.16 cm value for all models tested.

## RESULTS AND DISCUSSION

The objective of this test was to quantify the hystereses associated with various vortex flow transition points and determine the effect of planform geometry on their characteristics. The transition points observed consisted of the appearance (or disappearance) of trailing-edge (TE) vortex burst and transition to (or from) flat plate (FP) flows. Flow visualization with smoke injected into the vortices was used to identify the transitions that occurred over a series of flat plate models that included a set of deltas, a cranked wing with varying tip panel sweep or dihedral, and a straked wing (see fig. 4). Finally, high-speed movies were made to reveal the spiral nature of vortex breakdown and other dynamic effects.

### Transition Points and Hysteresis

The results for TE vortex burst on the delta wings already discussed in the previous section are shown in figure 5. Shown also in the figure are data from other sources (reference 3) that indicate good agreement with the present data. Hysteresis could not be detected during the test for the TE vortex burst; in fact, when the angle was held steady at the TE vortex burst point, the burst would slowly move back and forth with a range of only about 5% of the wing root chord. TE vortex burst for the delta wings was highly stable.

Results for FP flow transition for the delta wings are shown in figure 6. The influence of sweep is similar to that for the TE vortex burst angle in figure 5; however, a definite hysteresis effect is present. Amplitude of the hysteresis is about constant at 3 to 4 deg for all sweeps with the exception of 70 deg which is only about 2 deg. These points were re-checked for several wings but results were still the same. A possible explanation is that it appears that vortex asymmetry develops in the incidence range of 45 deg for 70 deg delta wings (ref. 4). If this is the case, then the higher swept wings would also be in the asymmetric vortex range and semi-span testing which enforces symmetry of these models could be questionable. Although this subject requires further investigation with full span models, it is felt that the hysteresis trends as a function of wing sweep are reasonable because the variation over the test range is orderly and closely parallels that of TE vortex burst.

The influence of tip sweep angle on TE vortex burst for the cranked wing with 70 deg inboard sweep is shown in figure 7. The reduction of hysteresis with increasing tip sweep was expected. It is interesting that the maximum angle for increasing incidence was very close to that of the simple 70 deg delta wing at 29 deg and is essentially independent of tip sweep. A more interesting observation, however, is that when TE burst appeared, it would not occur at the trailing edge - instead it would develop with the usual orderly upstream progression on the wake vortex and upon reaching the trailing edge would immediately jump forward to a point just upstream of the axial location of the wing crank (approximately 79% of the root chord). When vortex burst reached the trailing edge with decreasing incidence, however, it did so in an orderly fashion as observed for the delta wings but then jumped from the trailing edge to a point further downstream as it passed the trailing edge.

The observed hysteresis of TE vortex burst on the cranked wings is attributed to flow conditions on the tip panel just prior to TE vortex burst. With increasing incidence, the tip panel flow fields are well behaved and dominated by the inboard panel leading-edge vortex; hence, forward progression of burst in the wake is fairly insensitive to the tip panel presence or geometry. When burst reaches the trailing edge, the tip upper surface flow field suddenly collapses with a resulting rise in pressure that forces burst to abruptly move forward of the wing crank axial location. With decreasing incidence, the opposite process takes place. In this case the lower sweep panel does not re-establish its flow as quickly because its starting point is burst vortex flow. Aft progression of the burst with decreasing incidence is similar to that of a lower swept wing. For example, TE vortex burst for decreasing incidence on the cranked wing with tip sweep of 30 deg occurs at about 21 deg as shown in figure 7. This compares favorably with the angle of TE vortex burst for a delta wing with a sweep of about 64 deg as shown



in figure 5. Upon reaching the trailing edge, however, the tip panel flow fields are then fully re-established and the burst must jump abruptly downstream to a point corresponding to that which would occur during the case of increasing incidence but at the lower angle of attack.

A second variation of tip panel geometry which affects TE vortex burst hysteresis is tip panel dihedral. Results for this investigation, shown in figure 8, indicate that changing the dihedral with a fixed tip sweep of 30 deg has a profound effect on the hysteresis. In general, positive dihedral reduces hysteresis from 8 deg at zero to 0.5 deg at 45 deg. At 60 deg dihedral, the hysteresis has disappeared and the TE vortex burst point angle has increased to 30 deg. A further increase to 90 deg dihedral results in a drop of TE vortex burst angle to 27.5 deg but has not introduced any hysteresis.

Negative dihedral for -30 deg to -90 deg shows a large reduction in hysteresis but it also shows a reduction in TE vortex burst angle to an average of about 26 deg for all dihedral angles. The reasons why tip dihedral has these effects on TE vortex burst are not clear; however, several possibilities will be discussed.

Changing of the tip panel dihedral does at least two things: (1) it changes the leading-edge sweep with angle of attack, and (2) it changes the orientation of the tip leading edge relative to the local upwash fields, i.e., positive dihedral leads to a more spanwise flow whereas negative dihedral leads to a more perpendicular or two dimensional flow. With positive dihedral, these two changes tend to improve the tip panel flow fields at higher angles of attack; hence, with increasing dihedral, the hysteresis disappears. In the case of 60 deg dihedral, the TE vortex burst angle was actually increased over that of the 70 deg delta. Going too far, however, to 90 deg results in adverse effects which lower the TE vortex burst angle but still do not introduce any hysteresis. At this high dihedral, the spanwise flow must make an abrupt turn when it encounters the vertical tip panel and hence a corner vortex forms that precipitates premature burst of the main wing vortex. With exception of the 90 deg dihedral, the main vortex structure and path seemed to be little affected by the dihedral.

Negative dihedral has the interesting effect of lowering the TE vortex burst angle but also reducing the hysteresis. In fact, this dihedral direction was more effective at reducing hysteresis than positive dihedral. It is suspected, however, that the reduction in hysteresis was bought at the price of premature separation of the tip panel due to both decreased sweep and higher upwash angles at the leading edge. Therefore, it appears that configuration designs based on cranked wings with large negative tip dihedrals would not be very efficient at high angles of attack.

The transition to and from FP flows for the cranked wings was found to be relatively unaffected by the wing tip geometry. Results shown in figure 9 indicate the influence of tip panel sweep on the FP flow transition. Hysteresis amplitudes and the angles show very little variation, in fact 30 deg and 70 deg have identical values. Data obtained for tip dihedral effects also exhibited the same characteristic and hence are not shown. The reasons attributed to this observation are based on the fact that the large inboard part of the cranked wing is the dominant geometric feature that governs the flow fields near FP flow transition. Thus, radical changes in the small tip have very little effect on this transition.

The straked wing shown in figure 4 represents a variation of cranked wing planforms where the outboard "tip" panel is dominant. This wing was tested because: (1) it is representative of the F-16 planform, and (2) a force and pressure model of this same geometry will be tested at a later date by General Dynamics. High-speed movies were also made of the vortex flow visualizations for this model which will be discussed in the next subsection. Test results for the straked wing were:

|                    |                                 |
|--------------------|---------------------------------|
| TE vortex burst    | = 18 deg increasing incidence   |
| FP flow transition | = 48 deg increasing incidence   |
| FP flow transition | = 43.5 deg decreasing incidence |
| TE vortex burst    | = 18 deg decreasing incidence   |

For a strake sweep of 76 deg, the delta wing TE vortex burst angle would be about 34 deg as shown in figure 5. In the presence of the large outboard 40 deg panel, this was reduced to 18 deg which illustrates the effect increasing the tip panel size for cranked wing geometries. In the case of the cranked wings discussed earlier, the observation that TE vortex burst angle for increasing incidence was little affected by tip sweep or positive dihedral was attributed to small tip panel size. In that case, the inboard panel vortex dominated the outboard panel flow fields prior to burst. For the straked wing, earlier breakdown of the large outboard panel due to lower sweep led to early breakdown of the strake vortex. The FP flow transition angle was likewise reduced to 43.5 - 48 deg from the range of about 52 - 55 deg shown in figure 6 for a 75 deg delta wing. The idea of straked wing designs, however, is not to achieve the high incidence characteristics of the strake but to extend the incidence range of lower swept higher aspect-ratio wings which have better efficiencies than highly swept delta wings (refs. 5 and 6).

The absence of hysteresis for TE vortex burst on the straked wing is puzzling but the 4.5 deg amplitude for FP flow transition is in line with those amplitudes shown in figure 6. The angle for TE vortex burst of 18 deg correlates quite well with the observed lift curve break at 18 deg for the YF-16 at low speeds (ref. 6); therefore, the basic flow field properties are probably correct. A possible explanation is that the outboard panel exhibits orderly growth of trailing-edge separation and since it dominates the strake, the

strake vortex likewise bursts in an orderly fashion. In this case the outboard panel dominates for both increasing and decreasing incidence and hence little or no hysteresis appears in the TE vortex burst point. For the case of the cranked wings discussed earlier, the hysteresis was a result of differing dominance with incidence direction; with increasing incidence, the inboard panel leading-edge vortex dominated the tip panel flow fields, and with decreasing incidence, the separated flow on the wing tip dominated itself.

### High-Speed Movie Results

High-speed movies at 1000 frames per second were made of the vortex flow visualization in order to better understand the dynamics of the unsteady separated flows. A schematic of the flow visualization is shown in figure 10 to orient the reader with the photos to be discussed. These discussions will be based on conclusions arrived at from viewing the movies, thus the writer will verbally add the dynamic effects to the individual frames taken from the movies.

The frames shown in figure 11 are taken from a high-speed movie made of a slow pitch sweep up to 55 deg incidence for the straked wing that was just discussed in the previous subsection. The only difference between the movie configuration and that above was the flat extension just aft of the wing as noted in figure 10. At about 15 deg (figure 11a) the strake vortex is about to burst as noted by a kink that developed just aft of the trailing edge. At about 20 deg (figure 11b) the vortex has burst and the movie is already showing the swirling pattern associated with spiral burst. Also, in the movie it is evident that significant spanwise flow outboard along the trailing edge is occurring which is attributed to trailing-edge separation as discussed previously for the straked wing. At about 28 deg (figure 11c) the burst has progressed to a point just aft of the wing/strake intersection. The spiral vortex breakdown as well as the spanwise trailing-edge flow are now more evident. At about 35 deg (figure 11d), the burst has moved forward and developed further but is similar in appearance to that at 28 deg. At about 45 deg (figure 11e), the outer wing panel has transitioned to FP flow as indicated by absence of smoke over that region. As shown in the movie, this transition was very abrupt. At about 55 deg (figure 11f), the flow picture has not changed much from that at 45 deg. In both figures 11e and 11f, the strake flow forward of the outboard panel leading edge is completely burst but still vortical.

Figure 12 shows a similar sequence of frames taken from a high-speed movie made of a slow pitch sweep up to about 60 deg for a cranked wing with 68.5 deg/21.5 deg leading-edge sweeps. The wing planform, also shown in figure 12, is similar to but slightly different than that discussed in the previous subsection of this paper. Nevertheless, the basic flow field characteristics are similar. At



about 20 deg (figure 12a) the vortex is well formed. Burst occurs at about 24-25 deg as shown in figure 12b which correlates well with the data in figure 5 for a 68.5 deg swept delta. The burst is located just forward of the wing crank right after its initial appearance. The high-speed movie shows a very rapid movement of the burst from the trailing edge to the point shown in figure 12b which is part of the hysteresis mechanism discussed previously. About 35 deg (figure 12c) the burst has further developed and is very close to the wing vertex. This frame very clearly shows the spiral vortex burst. At about 45 deg (figure 12d) the vortex is completely burst but the flow is still vortical just prior to FP flow transition. At about 55 deg (figure 12e) FP flow, or total separation, is shown for which the transition occurred very abruptly at about 46-47 deg. During the reverse pitch sweep back to zero incidence as shown in the movie, hysteresis for the FP flow transition is not as clear as that for TE vortex burst. The angle for the TE vortex burst with decreasing incidence is about 16-17 deg, thus the hysteresis amplitude of about 8-9 deg can be easily detected in the movie. Also, the different speed of vortex burst movement near the trailing edge for increasing and decreasing incidence is clearly evident.

The high-speed movies of vortex flow visualization have provided valuable insight to the dynamics of vortex flows, burst, and transitions. With a shutter speed of 1/3000 sec at 1000 frames per second and flow velocities of about 30 m/sec, the spiral motion of vortex burst was stopped. Vortex burst movement on the cranked wing during initial development was slowed down to show that even though the development was very rapid, it was orderly. Also spanwise trailing-edge flow during vortex burst on the straked wing was shown to be a possible explanation for the absence of TE vortex burst hysteresis for that wing. FP flow transitions were shown to be very rapid for all wings for either increasing or decreasing incidence.

#### CONCLUDING REMARKS

An experimental study was conducted to quantify the hysteresis associated with various vortex flow transition points and determine the effect of planform geometry on their characteristics. The transition points observed consisted of the appearance (or disappearance) of trailing-edge (TE) vortex burst and transition to (or from) flat plate (FP) flows. Flow visualization with smoke injected into the vortices was used to identify the transitions that occurred on a series of semi-span models tested in a low-speed wind tunnel at about 30m/sec. The planforms tested consisted of simple deltas (55 to 80 deg sweep), cranked wings with varying tip panel sweep and dihedral,

and a straked wing. High-speed movies at 1000 frames/sec were made of the vortex flow visualization in order to better understand the dynamics of vortex flow and burst as well as the transition from one flow type to another.

Results were obtained for the hysteresis characteristics of both TE vortex burst and FP flow. Delta wings were first tested for a series of leading-edge sweeps of 55, 60, 65, 70, 75 and 80 degrees. TE vortex burst angles were determined and good correlation with other published data verified the test setup and procedure; however, little or no hysteresis was observed. Particular attention was paid to the semi-span test techniques. FP flow transition angles were found to increase with leading-edge sweep in much the same way as TE vortex burst; however, a hysteresis was observed which was constant at about 3-4 deg. This transition consistently occurred at higher angles for increasing incidence than for decreasing incidence.

Test results for the cranked wings exhibited very interesting effects of tip panel geometry on the hysteresis characteristics. For a fixed inboard sweep of 70 deg, varying the outboard sweep from 30 to 70 deg showed a reduction of TE vortex burst hysteresis from 8 deg at 30 deg sweep to 0 deg at 60 deg and 70 deg sweeps. Varying tip panel dihedral from -90 to +90 deg for the 70 deg/30 deg cranked wing also showed a reduction of TE vortex burst hysteresis. For dihedral varying from 0 to 90 deg, the hysteresis was reduced from 8 deg at 0 deg dihedral to 0 deg at 60 deg dihedral where the angle for TE vortex burst was also slightly increased. At 90 deg dihedral, the hysteresis was zero; however, the TE vortex burst angle was lowered significantly. For negative dihedral, the hysteresis was again reduced, but the TE vortex burst angle was consistently lower for all values. The influence of tip panel geometry was found to be insignificant for the transition to FP flows. This characteristic was about the same as that for the 70 deg delta.

The straked wing tested with 76 deg/40 deg leading-edge sweep was similar to an idealized F-16 and represented a variation on cranked wings where the outboard panel was the dominant surface. The absence of TE vortex burst hysteresis was attributed to the orderly development of trailing-edge separation on the 40 deg panel as observed in the high-speed movies. Hysteresis was observed for FP flow transition and was associated with total separation of the 40 deg panel. This separation was observed in the high-speed movies to be very abrupt.

The high-speed movies provided valuable insight to the dynamics of vortex flows, burst and transition. The spiral motion of vortex burst was stopped and the very rapid initial movement of the burst point on the cranked wings was shown to have an orderly development. Spanwise flow along the trailing edge for vortex burst on the straked



wing was shown to be a possible explanation for the absence of TE vortex burst hysteresis for that wing. Finally, the transition to FP flow was found to be very abrupt, even at 1000 frames/secs for all wings for either increasing or decreasing incidence.

#### REFERENCES

1. Herbst, W. B.: Dynamics of Air Combat., J. Aircraft, vol. 20, No. 7, July 1983, pp. 594-598.
2. Lang, J. and Francis, M. S.: Unsteady Aerodynamics and Dynamic Aircraft Maneuverability. Presented at AGARD Symposium on Unsteady Aerodynamics - Fundamentals and Applications to Aircraft Dynamics, Gottingen, Germany, 6-9 May 1985, Paper No. 29.
3. Malcom, G. N.: Impact of High-Alpha Aerodynamics on Dynamic Stability Parameters of Aircraft and Missiles. AGARD-LS-114, 1981.
4. Ericsson, L. E.: Wing Rock Flow Phenomena. Presented at AFOSR/FJSRL/U. Colorado Workshop on Unsteady Separated Flows, USAF Academy, 10-11 August 1983.
5. Peake, D. J. and Tobak, M.: On Issues Concerning Flow Separation and Vortical Flows in Three Dimensions. AGARD-CP-342, 1983, Paper No. 1.
6. Smith, C. W., Ralston, J. N. and Mann, H. W.: Aerodynamic Characteristics of Forebody and Nose Strakes Based on F-16 Wind Tunnel Test Experience. NASA CR-3053, 1979.

TABLE 1 Model Specifications

| Root Chord, cm       | Leading Edge Sweep, Deg | Tip Panel Sweep, Deg | Tip Panel Dihedral, Deg | Location of Crank, % Span |
|----------------------|-------------------------|----------------------|-------------------------|---------------------------|
| <b>DELTA WINGS</b>   |                         |                      |                         |                           |
| 22.9 cm              | 55°                     | -                    | -                       | -                         |
| 25.4 cm              | 60°                     | -                    | -                       | -                         |
| 27.9 cm              | 65°                     | -                    | -                       | -                         |
| 30.5 cm              | 70°                     | -                    | -                       | -                         |
| ↓                    | 75°                     | -                    | -                       | -                         |
| ↓                    | 80°                     | -                    | -                       | -                         |
| <b>CRANKED WINGS</b> |                         |                      |                         |                           |
| 30.5 cm              | 70°                     | 30°                  | 0°                      | 70%                       |
| ↓                    | ↓                       | 40°                  | ↓                       | ↓                         |
| ↓                    | ↓                       | 50°                  | ↓                       | ↓                         |
| ↓                    | ↓                       | 60°                  | ↓                       | ↓                         |
| 30.5 cm              | 70°                     | 30°                  | -89°                    | 70%                       |
| ↓                    | ↓                       | ↓                    | -60°                    | ↓                         |
| ↓                    | ↓                       | ↓                    | -46.5°                  | ↓                         |
| ↓                    | ↓                       | ↓                    | -30°                    | ↓                         |
| ↓                    | ↓                       | ↓                    | 15°                     | ↓                         |
| ↓                    | ↓                       | ↓                    | 31°                     | ↓                         |
| ↓                    | ↓                       | ↓                    | 46°                     | ↓                         |
| ↓                    | ↓                       | ↓                    | 90°                     | ↓                         |
| <b>STRAKED WING</b>  |                         |                      |                         |                           |
| 26 cm                | 76°                     | 40°                  | 0°                      | 25%                       |

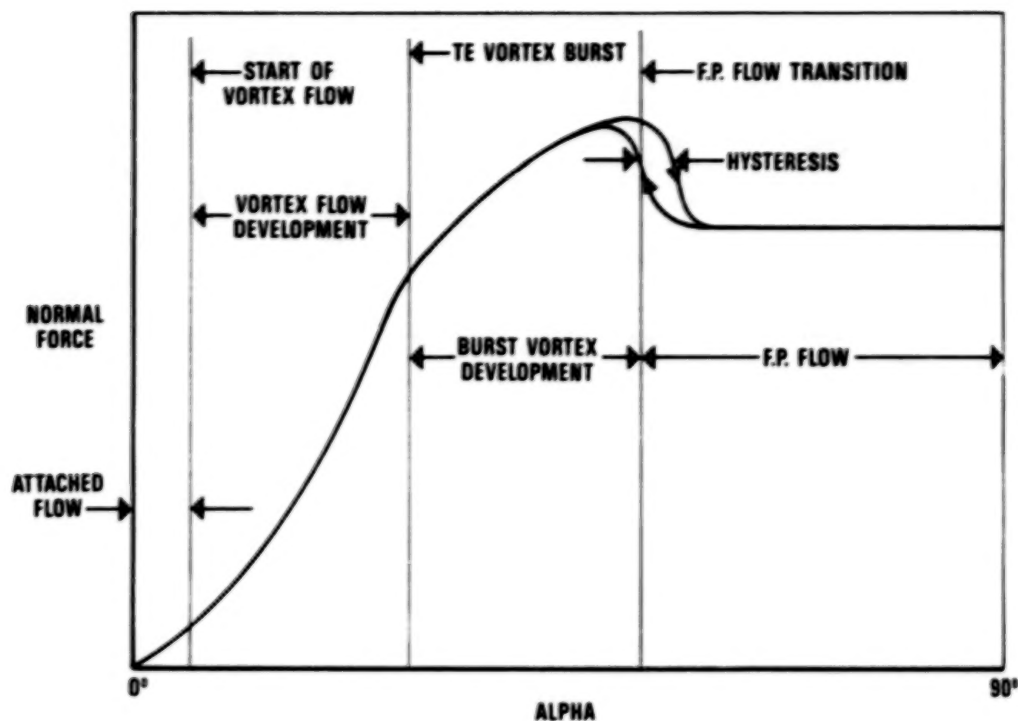


Figure 1 Regimes of Vortical Flow Development.

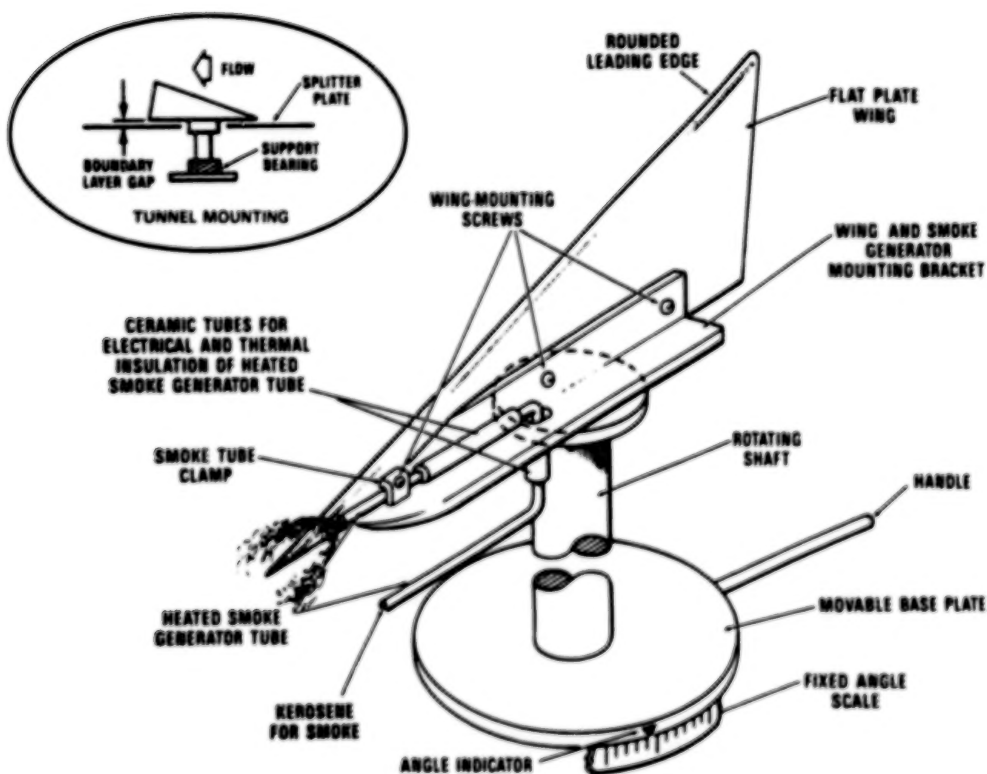


Figure 2 Schematic View of the Semi-Span Model Test Assembly.

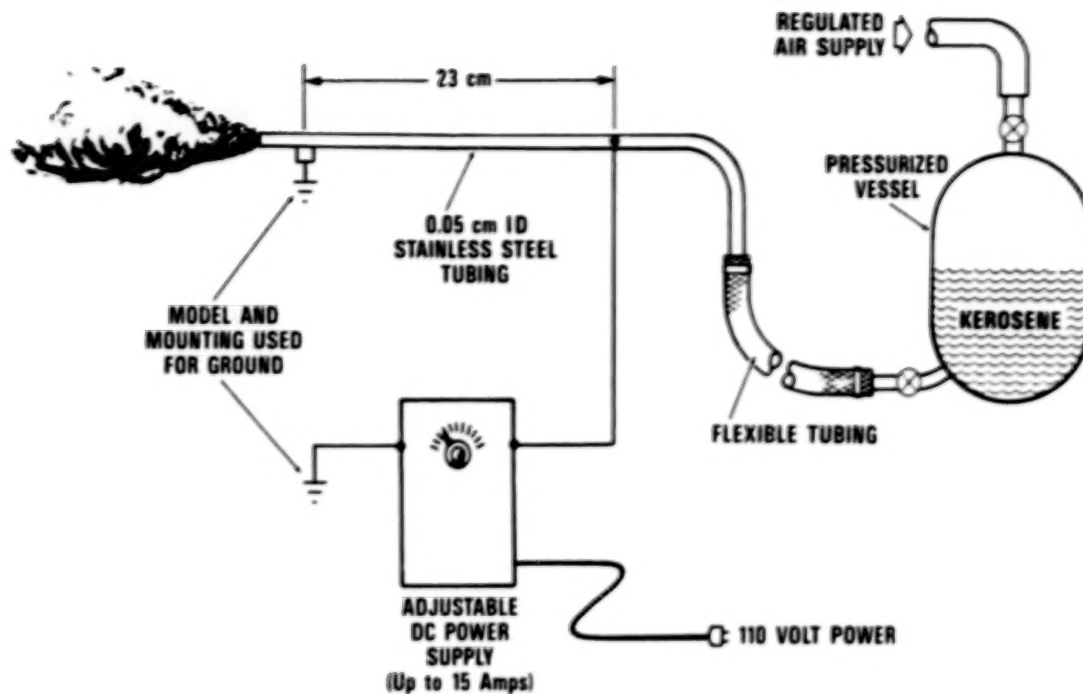


Figure 3 Schematic Diagram of the Smoke Generator.

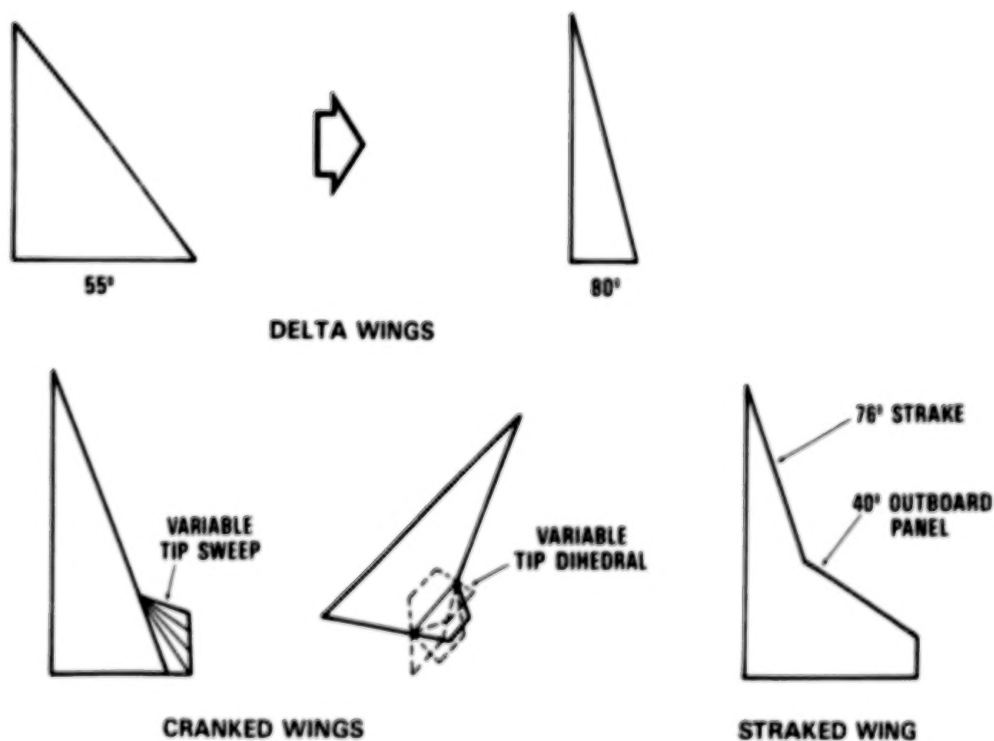
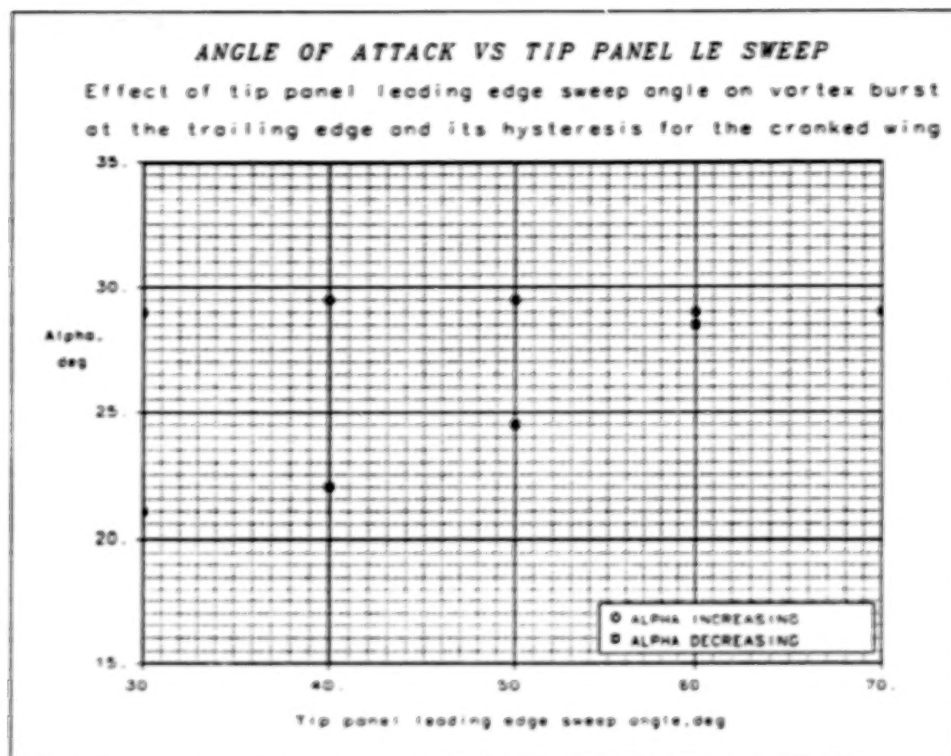


Figure 4 Semi-Span Planforms Tested.







**Figure 7 Effect of Tip Panel Sweep on TE Vortex Burst on Cranked Wings.**

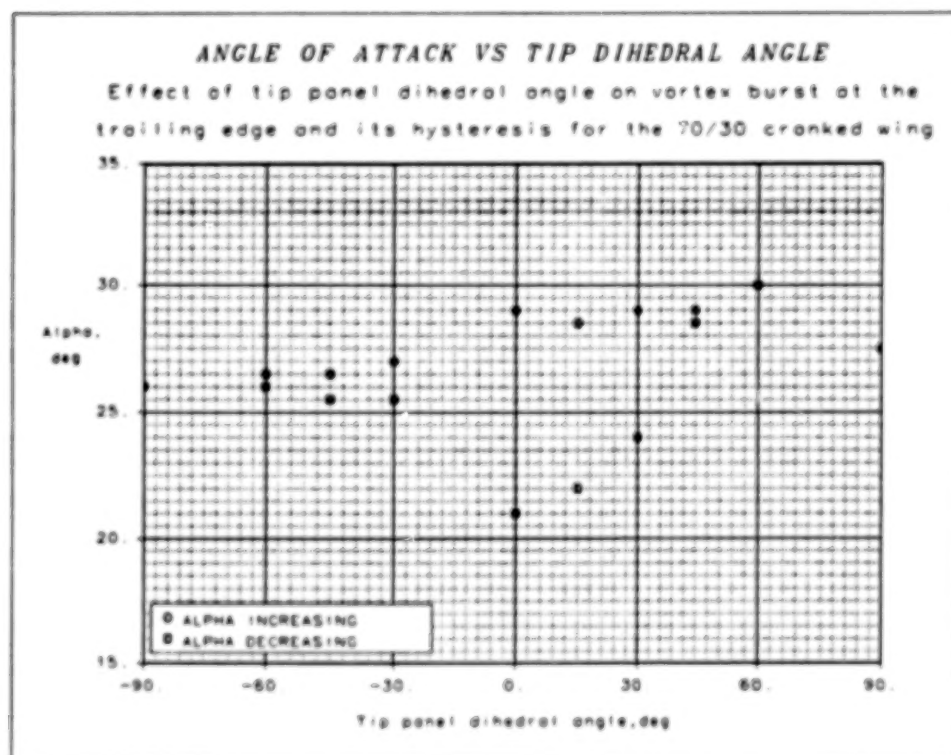


**Figure 8 Effect of Tip Panel Dihedral on TE Vortex Burst on a 70°/30° Cranked Wing.**

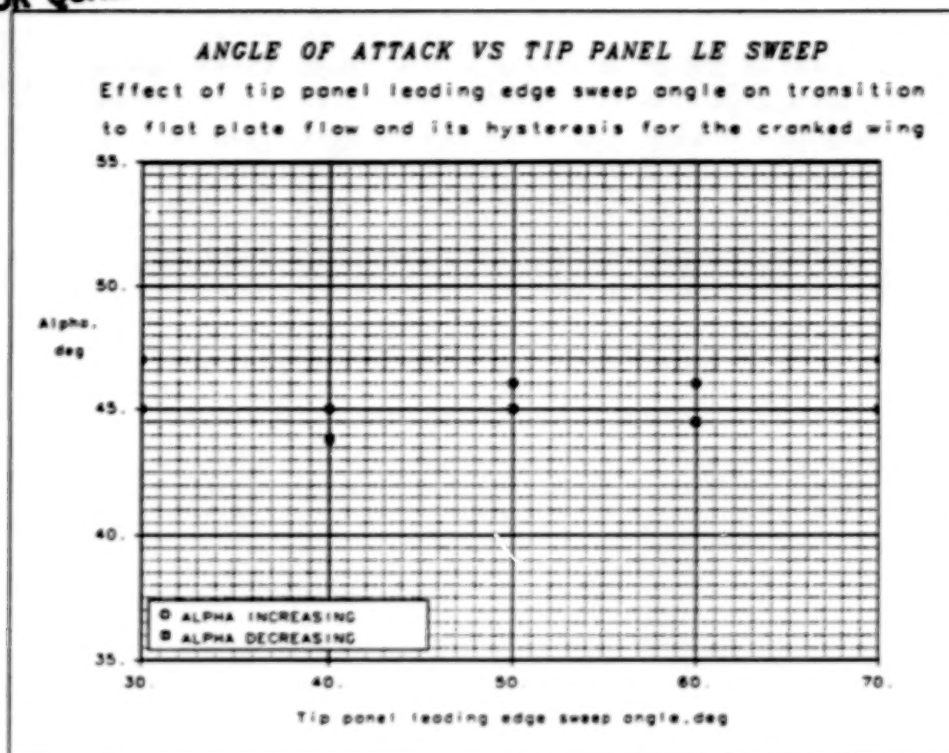


**Figure 9 Effect of Tip Panel Sweep on FP Flow Transition on Cranked Wings.**

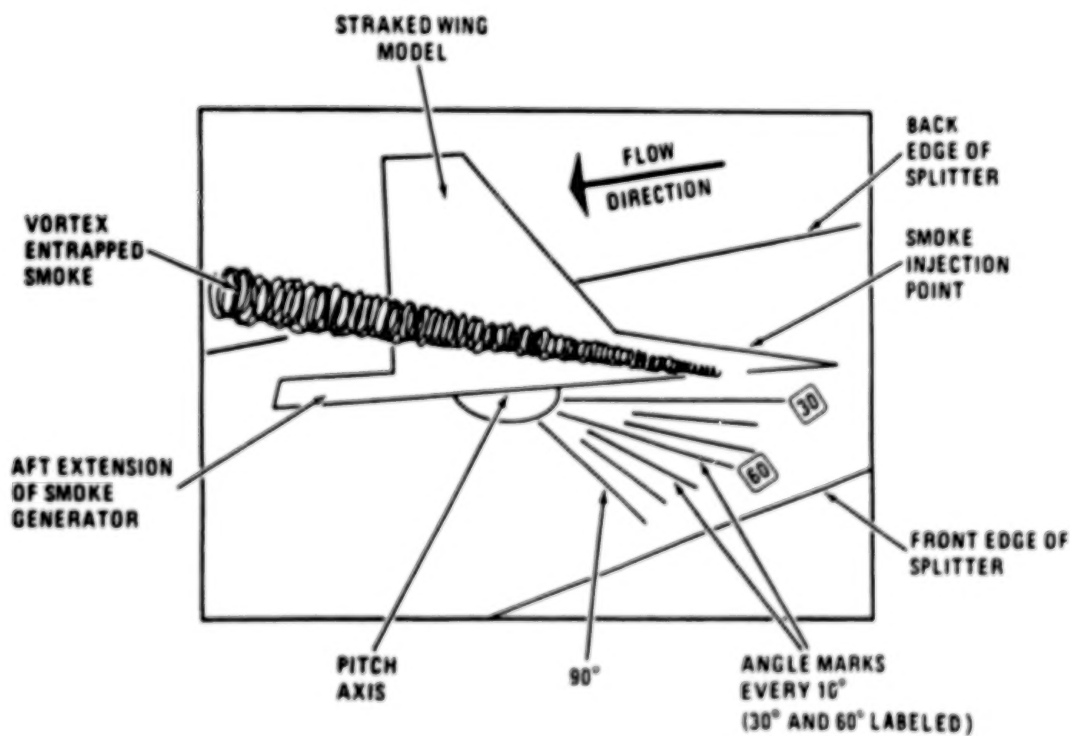


**Figure 10 Explanation of Flow Visualization Results.**

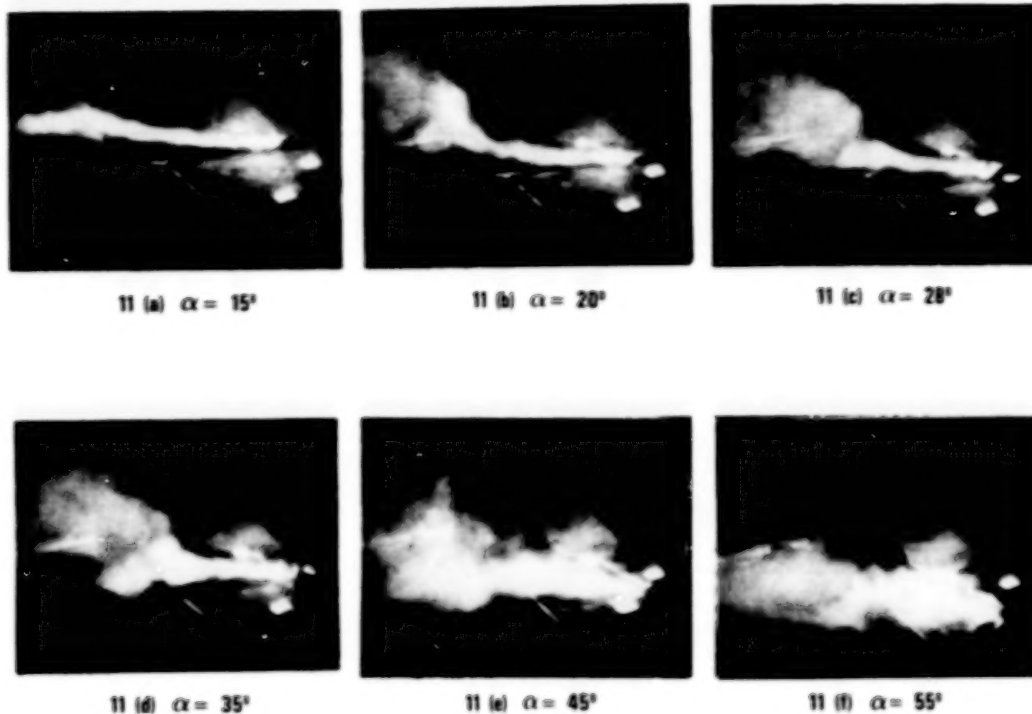


**Figure 11 Flow Visualization Results for the Straked Wing.**

**ORIGINAL PAGE IS  
OF POOR QUALITY**

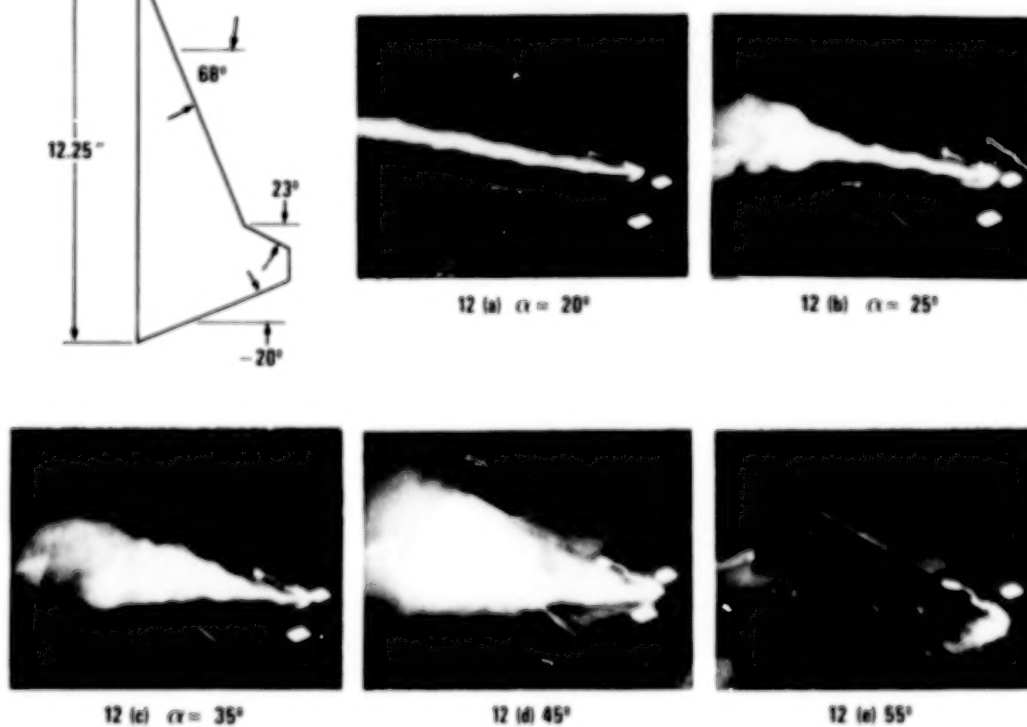
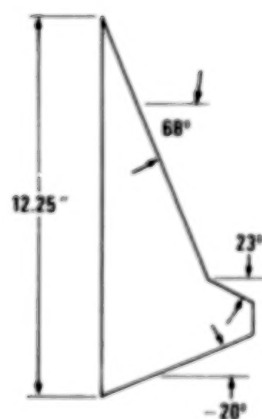


**Figure 12 Flow Visualization Results for a Cranked Wing.**

## VISCOUS VORTICAL FLOW CALCULATIONS OVER DELTA WINGS

G. Blom, J. C. Wai, and H. Yoshihara  
Boeing Military Airplane Company  
Seattle, Washington

## SUMMARY

Two approaches to calculate turbulent vortical flows over delta wing configurations are illustrated. The first is for a simple delta wing at low speeds using the boundary layer approximation to treat the effects of the secondary separation. The second is for the supersonic case of a generic fighter using the NASA Ames parabolized Navier/Stokes method. Test/theory comparisons are given in both cases.

## INTRODUCTION

The concept of controlled separations due to D. Küchemann (ref. 1) plays an important role in the high lift performance of advanced combat aircraft. Here the sharp leading edges of the highly swept wing required for supersonic performance are parlayed into producing stable lift-generating leading-edge separation vortices. Such vortices can further serve as the base for a potentially powerful fast-response control system.

In the following, two cases of turbulent vortical flows are calculated. In the first, the low-speed flow over a slender flat plate delta wing at a large angle of attack is considered. Here the flow separates along the sharp leading edges forming the familiar primary separation vortices. Their effect, to a good approximation, can be treated by an inviscid theory. The primary vortices in turn impress an adverse pressure gradient on the upper surface boundary layer causing it to separate when the angle of attack is sufficiently large. The consequence of these secondary separations is to suppress significantly the suction peaks generated by the primary vortices. Our objective is the calculation of the displacement effects of the secondary separation, coupling the 3D integral boundary layer method with the leading-edge vortex panel method. The problem that must be resolved is the proper formulation (and solution) of the boundary layer problem and its convergent coupling with the inviscid problem.

In the second case, the supersonic flow over a generic fighter (Model -350) at large angles of attack is considered. Here a significantly more complex system of separation vortices arises which is shed from the wing and fuselage nose. For this complex flow the boundary layer approach used in the first case is no longer expedient. The flow is treated globally using the parabolized Navier/Stokes (PNS) equations with a mixing length turbulence model.



## THE BOUNDARY LAYER LIMIT LOW-SPEED DELTA WING\*

The 3D integral boundary layer method used was developed by L. Wigton (ref. 3) and is essentially that of P. D. Smith (ref. 4). Here the planar Green's lag entrainment equations are embedded in the streamwise direction, and the transverse equations are derived assuming Mager's cross-flow velocity profile. The resulting system of equations is composed of four first-order partial differential equations containing six unknowns. It must be presumed that these equations become fully determinate when coupled to the equivalent inviscid flow problem. Since it is difficult to solve the problem in this global formulation, the solution is sought by an iterative procedure coupling the boundary layer and inviscid flows.

The resulting boundary layer problem is made determinate by assigning the values of two of the six unknowns. The choice of the two input functions must be such that the resulting boundary layer problem can be solved expeditiously for the separated case and that a convergent coupling with the inviscid flow can be achieved in a systematic fashion. We shall use the direct formulation of the boundary layer problem where the inviscid surface velocity components are used as inputs. By this choice there is a direct input/output compatibility between the boundary layer and inviscid flow problems. The resulting set of equations is fully hyperbolic permitting a finite-difference marching when the initial data lines are space-like. The limiting and inviscid surface streamlines form two of the four characteristics which define the domain of dependence.

For the problem of the secondary separation for the delta wing, we shall use the  $x = \text{constant}$  lines ( $x$  is in the streamwise direction) which are proper initial data lines. The initial data to be assigned are not known in advance and must be determined by a "march/step back" procedure assuming the flow in the wing apex region to be conical. Once the initial data are established, a streamwise finite-difference marching is carried out using a first-order explicit differencing, biasing the lateral derivatives to cover the characteristic domain of dependence.

For severely separated cases ( $\bar{H} \geq 2.5$ ) an ill-conditioning of one of Green's equations arises caused by the derivative of the form factor function  $A = A(\bar{A}_1)$  becoming very large (ref. 5). This ill-conditioning has been erroneously attributed to the appearance of separation with its envelope of limiting streamlines as well to the Goldstein singularity, but it is clearly due to the  $A = A(\bar{A}_1)$  modeling required for the closure. The ill-conditioning can be circumvented by recalling that severely separated boundary layers assume an equilibrium state whereby the form factor  $A$  is given directly in terms of the pressure gradient (ref. 6). The errant differential equation is then replaced by blending in the equilibrium flow as the ill-conditioning arises. Such large values of  $A$  occur for example in the shock-induced and aft separations arising in the transonic flow over swept wings, but they will not arise in the present case of the low-speed secondary separation.

(From Ref. 2)



For the low-speed case considered, the leading-edge vortex panel method is used for the equivalent inviscid flow. Here the leading-edge separation vortices are paneled as a potential vortex sheet, and their locations are determined by an iterative procedure. Since this panel method did not have provisions for viscous transpiration velocities, the upper surface viscous displacements were halved to approximate a wing camber change.

The first case considered was a flat plate delta wing of  $76^\circ$  sweep (aspect ratio = 1) at  $11^\circ$  angle of attack and a Reynolds number of  $35 \times 10^6$  based on the 7.3 meter root chord. Boundary layer measurements were obtained by East (ref. 7). For this case, only the boundary layer was calculated inputting the measured surface velocity and flow direction. In figure 1 the calculated boundary layer variables are compared with the measurements, while in figure 2 the limiting streamline slopes are shown together with a comparison of the calculated and measured secondary separation lines. Good agreement is seen in both figures.

To illustrate the inviscid/viscid flow coupling, we have next considered the low-speed flow over the same flat plate delta wing at  $20.5^\circ$  angle of attack and at a smaller Reynolds number of  $0.9 \times 10^6$  based on the 0.75-meter root chord. Wind tunnel tests were carried out for this case by Hummel (ref. 8). Four iterations between the panel method and the boundary layer solutions achieved a reasonable convergence. The resulting pressure distribution at two chordwise stations are shown in figure 3. Though the test/theory comparison is only fair, the theory appears to have yielded the general effects of the viscous displacement under the suction peak. The undesirable reexpansion near the leading edge is most probably due to the inadequate paneling of the free sheet adjacent to the leading edge. Here convergence of the vortex solution could not be achieved when a more refined paneling of the free sheet was used. The agreement of the pressures in the inboard region might be improved by incorporating the full transpiration velocity effects. With the relatively poor experience with the leading-edge vortex panel method, it would be desirable to repeat the calculations using the Euler equations with the proper viscous transpiration velocities.

In figure 4 the limiting streamline slopes are shown. Good test/theory agreement in the secondary separation line is found. Here also an oil-flow picture from reference 8 is shown. It should be noted that the Reynolds number was inadequate in the experiments to achieve natural turbulent flow. A radial boundary layer trip was required as shown in figure 4. The calculations were however carried out assuming the boundary layer to be fully turbulent.

#### PNS CALCULATIONS-SUPERSONIC MODEL - 350 FIGHTER

The calculations for the Model-350, shown in figure 5, were carried out under a NASA Ames/Boeing cooperative study. Other results from this effort were presented earlier by Dr. D. Chaussee (ref. 9). The Model-350 was selected since pressure distribution and boundary layer profile measurements were available (ref. 10).

The Ames PNS code was originally developed by L. Schiff and J. Steger (ref. 11). The PNS equations are the steady thin-layer Reynolds-averaged Navier/Stokes equations in which the pressure is assumed to be invariant across the subsonic portion of the boundary layer. The resulting equations can be marched in the streamwise direction when the inviscid flow is supersonic.

The bow shock from the fuselage nose is fitted, but all interior shocks arising farther downstream are captured as for example the Kutta shock from the trailing edge of the wing (fig. 6). A Kutta shock and an expansion fan are the dominant mechanisms by which the differing upper and lower surface flows adjust to form the wake. There is also a weaker "Kutta adjustment" through the subsonic sublayer embedding the trailing edge which is distorted by both the sublayer approximation in the boundary layer and the overlaying unphysically thickened shock (fig. 6). The consequence of this distortion is local and should not affect the overall lift.

The calculations were carried out for a Mach number of 2.2 and a Reynolds number of  $4.3 \times 10^6$  based on the 2.4 foot mean wing chord. Angles of attack of  $4^\circ$ ,  $10^\circ$ ,  $14^\circ$ , and  $18^\circ$  were calculated, but only the results for  $14^\circ$  are presented. In figure 7 is shown the mesh at a wing station generated by an elliptic method. There are 45 points in the radial direction and 91 points along the half circumference. In figure 8 the calculated pressure distributions at  $14^\circ$  angle of attack are compared with the measured distributions at several streamwise stations. Good agreement is seen here consistent with the comparisons found at the other angles of attack. In figure 9 we compare the corresponding pitot pressure profiles in the boundary layer at several locations in a streamwise cut. The agreement in the profiles is reasonably good except where an inadequately refined mesh was used as at Station A. The inadequacy of the mesh here becomes evident by noting the steepness of the measured velocity gradient in the sublayer relative to the mesh used. The calculations have further yielded details of the profile as the "wobble" at the fuselage side (Station C) and on the wing (Station G) caused by a streamwise vortex which was detected from total pressure and vorticity maps. Thus to improve the overall test/theory match of the pitot profiles, one must refine the mesh in the sublayer, perhaps inserting a wall function to moderate the resulting computer cost.

In figure 10 the streamwise vorticity and Mach number contours in a transverse plane at a wing station are shown, while in figure 11 the corresponding transverse velocity vector map is given. Here the fuselage and wing vortices are evident. It is further seen that the separation on the wing originates not along the leading edge but at farther downstream points.

#### CONCLUDING REMARKS

Two levels of computing the viscous vortical flows over delta wing configurations at large angles of attack were demonstrated. In the first, the boundary layer method was used to determine the viscous displacement effects of the secondary separation over a flat plate delta wing at low speeds. Here the equivalent inviscid flow containing the primary separation vortices was

calculated using the leading-edge vortex panel method with the separation line fixed along the leading edge. The results indicated that the formulation of the boundary layer problem in the direct mode and the solution procedure were sound for the secondary separation but the leading-edge vortex panel method for the equivalent inviscid flow was inadequate. Here the substitution of the Euler code with provisions for viscous transpiration velocities would be desirable. The direct mode inviscid/viscid flow coupling did not offer any difficulties.

In the more complicated case of the Model-350 fighter a more global approach with the PNS method was used. Reasonable test/theory match was obtained for the surface pressure distributions and for the boundary layer pitot pressure profiles when an adequately refined mesh was used. Remarkably the algebraic Baldwin/Lomax turbulence model (basically the two-layer Cebeci/Smith model) continues to be a viable framework to treat complex viscous flows as the present one. There clearly is no immediate need to turn to more fundamental, though not necessarily more accurate, transport equation models that greatly increase the computer time.

The more widely recognized advantage of the PNS method relative to the ARC 3D method is the greatly reduced computing time due to the reduction of an unsteady problem to a steady one. A less obvious though a more important advantage for complex configurations as the Model -350 with nacelles and aft stabilizing surfaces is the resultant simplification of the mesh generation from a 3D to a 2D problem.

These significant advantages must be weighed against the shortcomings of the PNS method which preclude reversed flows and distort the elliptic influence mechanism through the thin subsonic portion of the boundary layer. The consequences of the latter however should not be of significance except where abrupt streamwise configuration slope changes arise, as at the leading edge of the wing root section or along the wing trailing edge, where large streamwise pressure gradients as shock waves are produced. Here the upstream influence through the subsonic portion of the boundary layer will be localized for turbulent flows in the absence of separation.

The experience with the two levels of treating viscous vortical flows suggests generally that the global approach with the Navier/Stokes method is the simpler more straightforward method for the user. Computer costs, particularly with the ARC 3D code, will continue to be a significant issue for some time. The boundary layer method will thus have its role of treating the simpler separated flows as those considered herein.

Finally we would like to express our gratitude to Dr. L. Schiff and Dr. D. Chaussee of NASA/Ames for indoctrinating us on the PNS code.

#### REFERENCES

1. Küchemann, D.: On the Possibility of Designing Wings that Combine Vortex Flows with Classical Aerofoil Flows. RAE T. M. Aero 1363, Oct. 1971.



2. Wai, J. C.; Baille, J. C.; and Yoshihara, H.: Calculation of Turbulent Separated Flow Over Wings. 3rd Symposium on Numerical and Physical Aspects of Aerodynamic Flows, California State Univ.-Long Beach, Cal., Jan. 1985.
3. Wigton, L.; and Yoshihara, H.: Viscous-Inviscid Interactions with a Three-Dimensional Inverse Boundary Layer Code. 2nd Symposium on Numerical and Physical Aspects of Aerodynamic Flows, California State Univ.-Long Beach, Cal. Jan. 1984.
4. Smith, P. D.: An Integral Prediction Method for Three-Dimensional Compressible Turbulent Boundary Layers. ARC R&M 3739, 1972.
5. Yoshihara, H.: Separated Flow Calculations in the B. L. Limit. Boeing TN BMAC 85-02, 1985.
6. East, L.; Smith, P. D.; and Merryman, P.: Prediction of the Development of Separated Turbulent Boundary Layers by the Lag Entrainment Method. RAE TR 77046, 1977.
7. East, L.: Measurements of the 3D Incompressible Turbulent Boundary Layer Induced on the Surface of a Slender Delta Wing by the Leading Edge Vortex. ARC R&M 3768, 1975.
8. Hummel, D.: On the Vortex Formation over a Slender Wing at Large Angles of Attack. AGARD CP-247, 1979.
9. Chaussee, D.; Blom, G.; and Wai, J. C.: Numerical Simulation of Viscous Supersonic Flow over a Generic Fighter Configuration. Sixth GAMM Conference on Numerical Methods in Fluid Dynamics, Gottingen, Sept. 1985.
10. Capone, F.J.; Bare, E. A.; Hollenback, D.; and Hutchison, R.: Subsonic/Supersonic Characteristics for a Tactical Supercruiser. AIAA Paper No. 84-2192, 1984.
11. Schiff, L.; and Steger, J.: Numerical Simulation of Steady Supersonic Viscous Flow. NASA TP 1749, 1981.

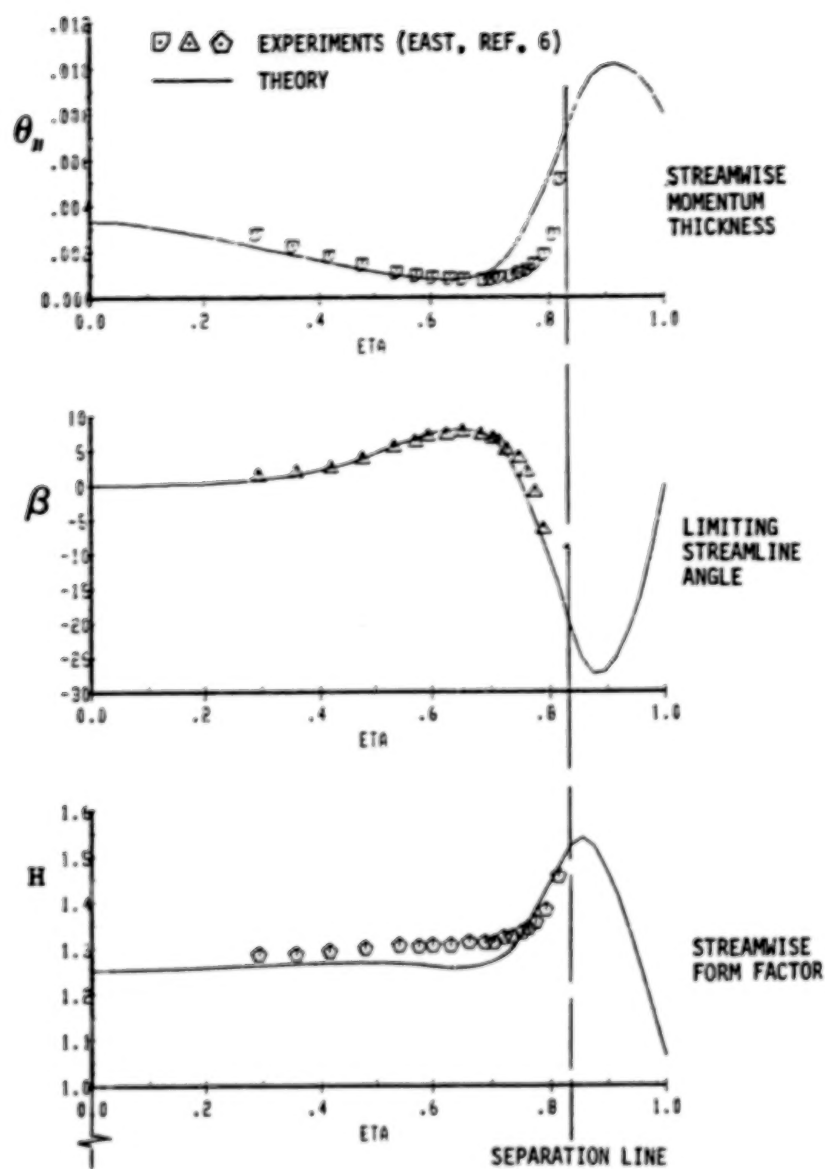


Figure 1. Test/Theory Comparison of Viscous Variables for East's Delta Wings



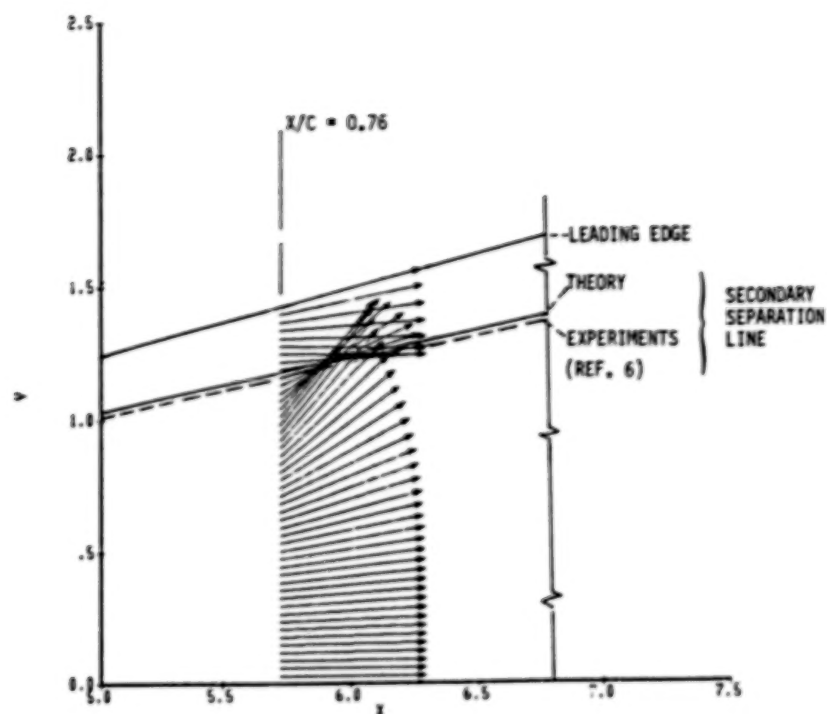


Figure 2. Limiting Streamline Vectors for East's Delta Wing.

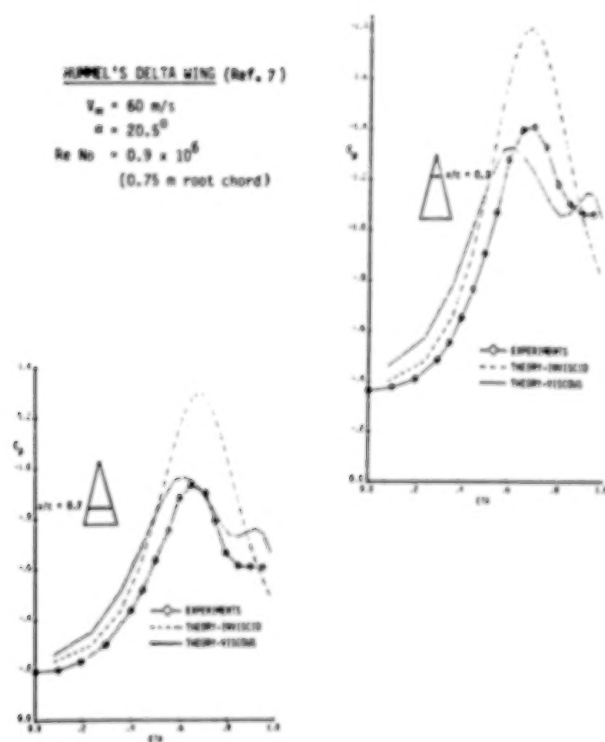


Figure 3. Test/Theory Comparison of Spanwise Pressure Distribution.

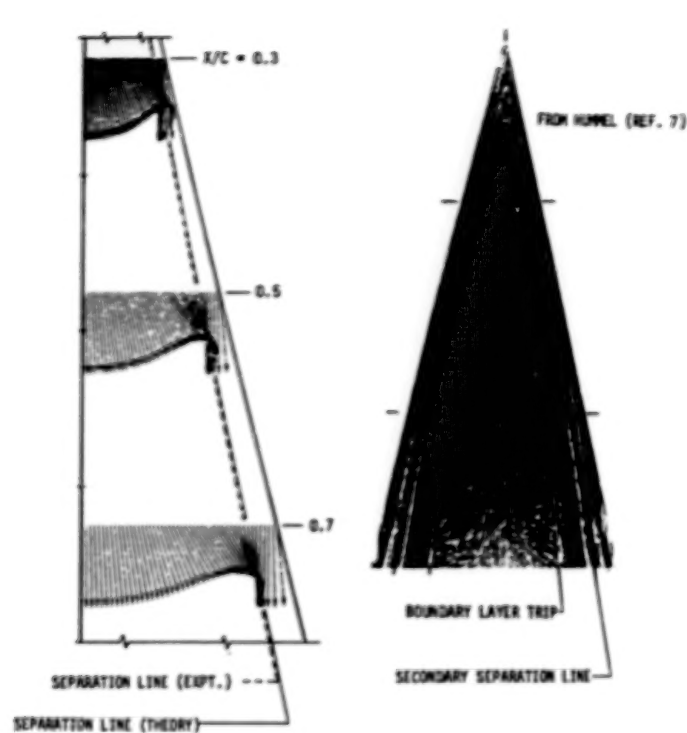


Figure 4. Limiting Streamlines and Separation Line of Hummel's Delta Wing.

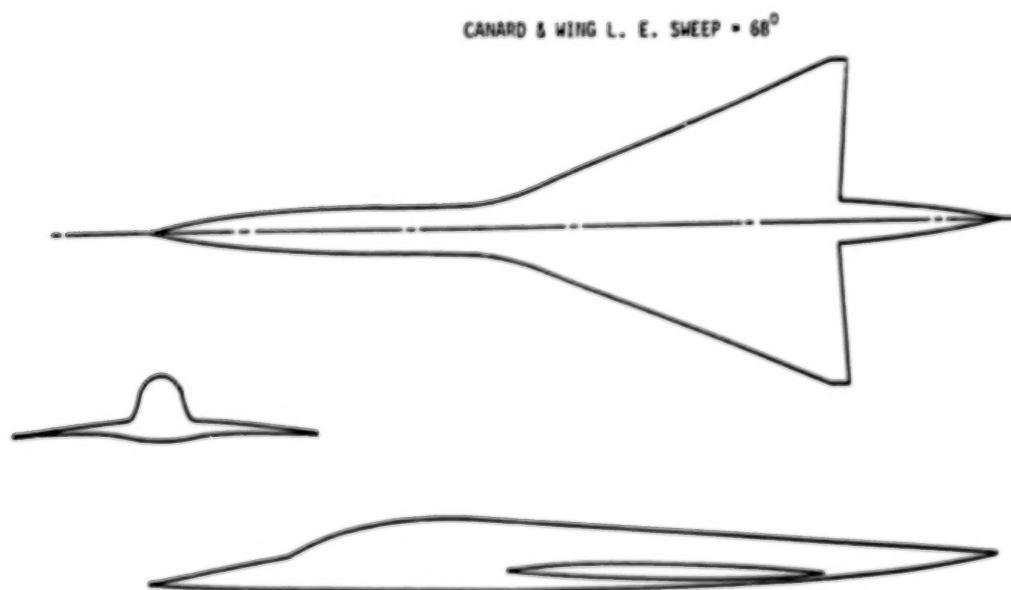


Figure 5. Model-350 Wing Fuselage.

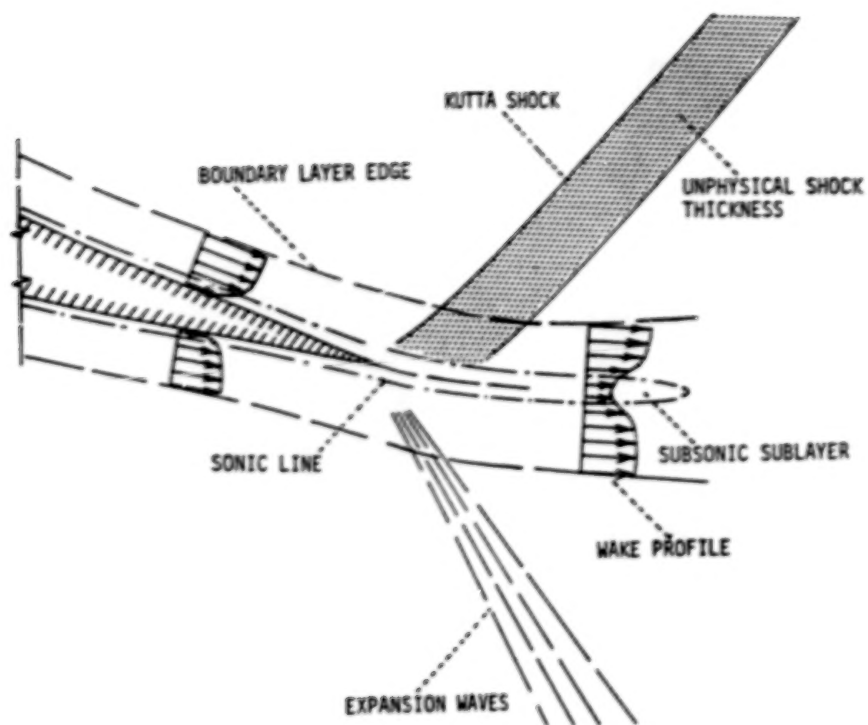


Figure 6. Schematic of Trailing-Edge Flow.

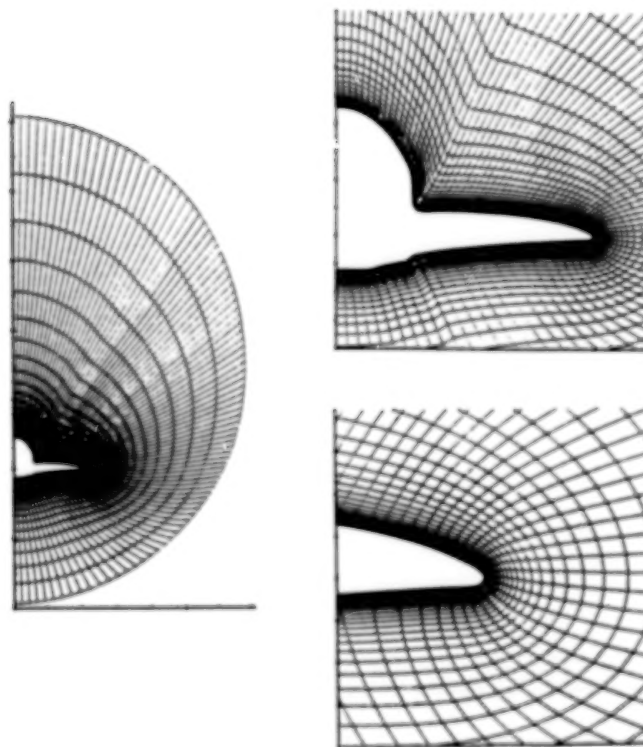


Figure 7. Elliptically Generated Wing Station Mesh.

ORIGINAL PAGE IS  
OF POOR QUALITY

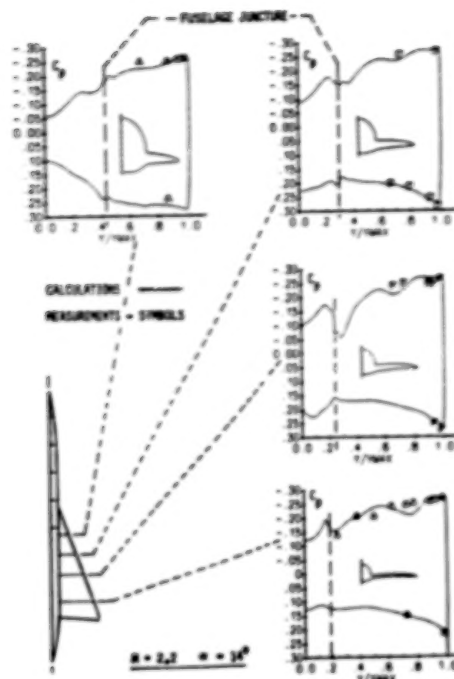


Figure 8. Test Theory Comparisons of Pressures.

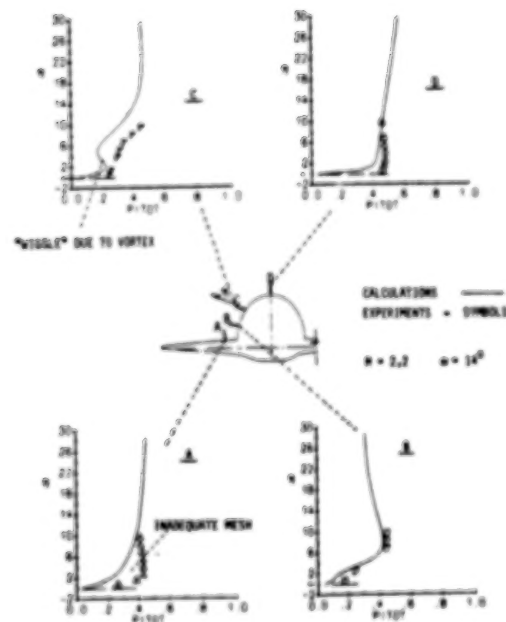


Figure 9. Test Theory Comparison of Pitot Pressure Profiles.

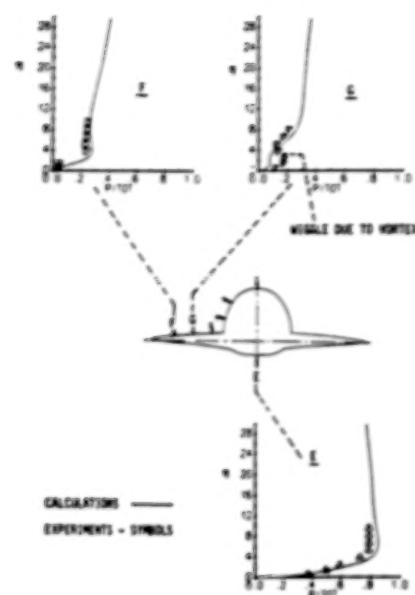


Figure 9. Concluded.

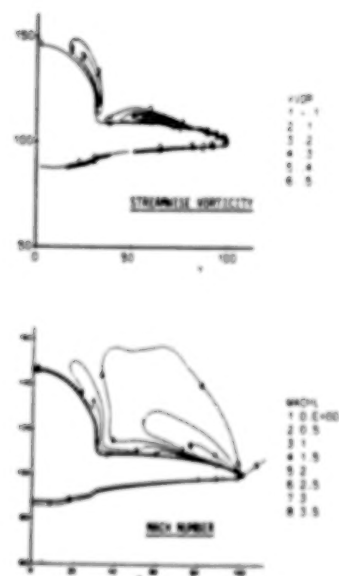


Figure 10. Streamwise Vorticity and Mach Number Contours.



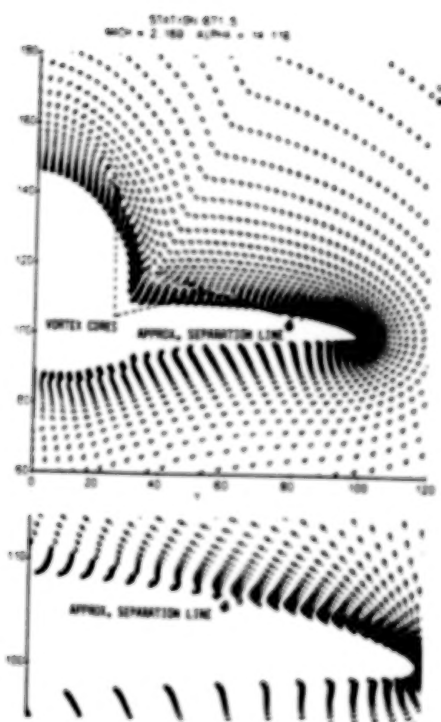


Figure 11. Transverse Velocity Vector Pattern.

## AN EULER AERODYNAMIC METHOD FOR LEADING-EDGE VORTEX FLOW SIMULATION

Pradeep Raj  
Lockheed - California Company  
Burbank, California

Lyle N. Long  
Lockheed - Advanced Aeronautics Company  
Valencia, California

## SUMMARY

This paper describes the current capabilities and the future plans for a three-dimensional Euler Aerodynamic Method. The basic solution algorithm is based on the finite-volume, Runge-Kutta pseudo-time-stepping scheme of FLO-57. Several modifications to improve accuracy and computational efficiency have been incorporated and others are being investigated. The computer code is used to analyze a cropped delta wing at 0.6 Mach number and an arrow wing at 0.85 Mach number. Computed aerodynamic parameters are compared with experimental data. In all cases, the configuration is impulsively started and no Kutta condition is applied at sharp edges. The results indicate that with additional development and validation, the present method will be a useful tool for engineering analysis of high-speed aircraft.

## INTRODUCTION

The simulation of three-dimensional vortices interacting with lifting surfaces is of considerable importance to aircraft designers. This problem is of special significance for supersonic-cruise aircraft which have highly swept slender wings. At moderate-to-high angles of attack, the flow invariably separates from the leading edges resulting in the formation of free vortices above the wing. Significant improvements in aerodynamic performance can be derived, as shown in Figure 1, by careful generation and control of these vortices. At the present time, a designer has to rely on extensive and costly wind-tunnel tests. The development of accurate, efficient, and reliable computational methods will provide a more economical means of designing aerospace vehicles.

Past research on leading-edge-separated-flow simulation has produced a variety of computational methods. At one end of the spectrum are the vortex-lattice (Refs. 1-4) and free-vortex-sheet methods (Refs. 5,6). Since they are based on a linearized potential-flow formulation, rotational vortex flow cannot be predicted as part of the solution. The leading-edge vortex has to be explicitly modeled either indirectly using the suction analogy of Polhamus (Ref. 7) or directly using singularity distributions (Refs. 4,5). At the other end of the spectrum are the finite-difference methods based on the Reynolds-averaged Navier-Stokes equations (Ref. 8) which provide an essentially complete fluid-dynamic model. Their use offers the major advantage that the leading-edge vortices result as a part of the solution. However, the available methods are not suitable for routine practical applications due to the exorbitant requirements of computational resources and the lack of a suitable universal turbulence model.

Recent advances in numerical algorithms to solve the Euler equations (Refs. 9,10) provide an attractive and cost-effective alternative to using Navier-Stokes codes. Their ability to automatically capture regions of rotational flows has been demonstrated by several investigations (Refs. 11-15). In this paper, the current

status and planned development of a three-dimensional Euler Aerodynamic Method (TEAM) and its application to model leading-edge separated flow about a cropped-delta wing and an arrow wing are presented.

TEAM represents a modular computational system being developed by the Lockheed-California Company for analyzing complete aircraft configurations. A schematic of the system is shown in Figure 2. This development is being partially funded by the U. S. Air Force Wright Aeronautical Laboratory (AFVAL)/Flight Dynamics Laboratory (FDL) under a three-year contract (F33615-84-C-3005). The basic features of the method are described in the next section.

### THREE-DIMENSIONAL EULER AERODYNAMIC METHOD

The explicit pseudo-time-stepping, finite-volume algorithm of Jameson et al. (Ref. 9), modified by Lockheed-California Company over the past three years, forms the core of the TEAM code. Jameson's original wing-alone code is widely known as FLO-57. The region surrounding a given configuration is subdivided into small cells. In each of the cells, the time-dependent Euler equations (in integral equation form), representing the mass, momentum, and energy conservation, are integrated in time using a multi-stage Runge-Kutta scheme. To accelerate convergence to the steady state, local rather than global time steps are used. Implicit residual smoothing (Ref. 16) further reduces the number of time steps required to reach the steady state. Appropriate non-reflecting boundary conditions based on Riemann invariants (Ref. 16) are used at the far-field boundaries and no-normal-flow conditions are used on the solid surface.

The finite-volume formulation essentially decouples the flow solver from the grid generator. The grids can be constructed in any convenient manner; only the Cartesian coordinates of the nodal points are required by the solver. This aspect of the basic algorithm has been exploited to build the TEAM system for analyzing complete aircraft configurations. An overview of the four major modules (Figure 2) constituting the system is presented in this section.

#### TEAM PREPROCESSOR MODULE

This module will provide a capability to process geometry-definition data supplied by a designer in order to construct an accurate geometrical model of a configuration and a suitable grid on its surface. The designer-supplied data typically contain a series of cross-sectional curves defining various components. In some instances, the configuration may be geometrically defined for some other aerodynamic analysis code. Constructing a model that accurately reflects the information contained in this form is the crucial first step. A surface grid on this model forms the key input for any grid-generation method. Appropriate interfaces are being developed to accomplish these tasks using the Configuration Data Management System (CDMS), which Lockheed - Georgia Company is developing for the U.S. Air Force under contract F33615-84-C-3001.

#### TEAM GRID GENERATOR MODULE

A variety of techniques, both algebraic and differential, are included in the grid-generator module, as shown in Figure 3. This is essential because, at the present time, there is no single method that can be used to generate suitable grids for all configurations. The current capabilities of the various methods are summarized in Figure 4. Their desirable features are also compared in the same figure. For instance, the algebraic Trans-Finite Interpolation (TFI) method is computationally

efficient and powerful but requires considerable user interaction to generate suitable grids as compared to the differential-equation methods, such as the Boundary Integral Grid (BIG) generation method (Ref. 17). This automation is achieved at the expense of computational efficiency. The Parabolic Conformal Mapping with Shearing (PACMAPS) technique (Ref. 18) is computationally efficient and easy to use; however, the grids must be of C-H topology. The C-H grid topology is illustrated in Figure 5.

Two diagnostic tools are crucial to the grid-generator module: Lockheed's PLOT3D program for interactively displaying grids and an analytical grid checking program. The grid checker can automatically locate regions where the grid lines either cross or are highly skewed. These regions are then further examined using PLOT3D and modified as necessary.

#### TEAM FLOW SOLVER MODULE

As mentioned above, the flow solver is based on the finite-volume, pseudo-time-marching algorithm of Jameson et al. (Ref. 9). Since the mathematical and numerical features of the basic scheme are adequately described in References 9 and 19, they will not be repeated here. Several modifications have been and are being incorporated by Lockheed to enhance the capabilities of the solver as summarized in Figure 6. These modifications are briefly described below.

**Flux Computation.** -- The cell-centered finite-volume scheme used for spatially discretizing the Euler equations expresses the time-rate of change of a flow quantity in a cell as the net flux through the surfaces of the cell. A variety of approximations can be used to numerically compute this flux. The current version of the code uses a strongly conservative formulation. It is compared with the original FLO-57 formulation in Figure 7. Quantitative improvement in accuracy is under investigation.

**Numerical Dissipation.** -- The present finite-volume scheme reduces to a central-difference scheme on a uniform grid. To suppress the well-known tendency for odd and even point decoupling of such schemes, and to limit the generation of wiggles and overshoots near shock waves, blended second and fourth differences have to be added. The coefficient of the second-order terms is proportional to the local pressure gradient. Therefore, these terms are turned on only where larger amounts of dissipation are needed, e.g., near shocks and stagnation points. Elsewhere, the fourth-difference terms keep the dissipation small.

The dissipation terms are approximated by central-difference formulas for all cells except those near the boundaries. In the original FLO-57 code, the contribution of  $\eta$ -direction terms (normal to the surface) was ignored for cells adjacent to the boundaries. This approach, designated Scheme 1 here, leads to an erroneous production of entropy. To eliminate this deficiency, alternative schemes have been incorporated.

All those cells that do not abut the solid surface (including the ones aft of the trailing edge) were treated like any other interior cell. For those adjacent to the solid boundary, four schemes are available. The order of approximation of the  $\eta$ -direction differences for these schemes is compared in Figure 8. An extensive evaluation is in progress in order to select one of these schemes for the solver. For the results shown in this paper, Scheme 2 is used.

**Surface Boundary Conditions.** -- On a solid surface, the no-normal-flow boundary condition is imposed by setting all convected flux quantities to zero. Only the pressure on the solid surface contributes to the momentum flux balance. Since



pressure is calculated at the cell center, one is forced to estimate its value at the actual surface. This is accomplished by computing the derivative of pressure normal to the surface using the momentum equation:

$$\rho \nabla \cdot (\mathbf{V} \cdot \mathbf{n}) = \mathbf{n} \cdot \nabla p$$

where:  $\mathbf{V}$ ,  $\mathbf{n}$ , and  $p$  are the fluid velocity, surface normal, and pressure, respectively. This derivative and the cell-centered values are then combined to determine the surface pressure. A precise implementation requires that all metric quantities and flow variables occurring in the equation above be evaluated right on the surface. In the original FLO-57 program, this was not done; the cell-center values were used instead. In the present version of the solver, three additional approaches may be used to obtain the desired flow variables on the actual surface: (1) A Taylor series expansion about the cell center, (2) Lagrange two-point extrapolation along the local normal direction, and (3) Averaging the cell-center values for cells next to the surface in the flow domain and ghost cells outside of the flow domain. An extensive evaluation of the different approaches is under way.

**Grid Topologies.** -- The present version of the solver can accommodate single global grids of various topologies. The original FLO-57 solver was limited to isolated wings having C-H grids, whereas the O-O and C-O types offer improved resolution (Ref. 20). If a C-H mesh is used, adequate resolution near the wing tip can be obtained only by increasing the number of cells in the spanwise direction. It must be noted that none of these topologies is as suitable as the H-H when detailed flow field about all sections of a wing-body or wing-body-tail configuration is desired. With these considerations, the solver was modified to accommodate O-O, C-O and H-H grids, in addition to the C-H.

**Patched Zonal Solver.** -- The development of a zonal solver is motivated by the need to analyze complex geometries and to improve computational efficiency. For complex geometries, e.g., a complete aircraft, it becomes extremely difficult to generate a single global grid. The difficulty is further aggravated by the necessity to cluster cells in regions of large flow gradients. These problems can be largely alleviated by dividing the flow domain into a number of zones and by constructing the grid in each zone independently.

A significant improvement in computational efficiency may be achieved by using refined meshes in zones where large gradients in flow variables are expected and using relatively coarse meshes elsewhere. Work is presently under way to develop a solver that can accommodate patched zonal grids. The feasibility of this approach has been demonstrated for two dimensions by Rai (Ref. 21).

#### TEAM POSTPROCESSOR MODULE

This module is composed of sub-modules to accurately determine forces and moments using the flow variables computed by the solver and to graphically display surface pressure distributions, flow-field velocity vectors, and iso-parametric contours.

The surface-pressure integration method for computing forces and moments is currently used in the code. This method is only accurate when a relatively fine grid is used. Small errors in surface pressures and geometry can lead to large errors in drag. Also, this approach cannot give an estimate of how the total drag is split into lift-induced and wave drag. Alternative approaches are being pursued.



For graphically displaying data, appropriate interfaces will be developed for linking the TEAM code with CDMS.

## RESULTS

A number of configurations have been analyzed using the TEAM code during its development to date. Results for a cropped delta wing and an arrow wing are presented here. For each case, the entire region is initialized to free-stream conditions. This is equivalent to impulsively starting the configuration. No Kutta condition is explicitly applied at the sharp edges.

### CROPPED DELTA WING

This wing has a leading-edge sweep of 63 degrees, a taper ratio of 0.1, and an aspect ratio of 1.64. Its cross section is a NACA 63A002 airfoil. It was analyzed using the TEAM code at a Mach number of 0.6 and angles of attack of 8, 16, and 24 degrees. Two grids were used, one having 24,576 (96x16x16) cells and the other having 98,304 (96x32x32) cells. Both were topologically C-H. The airfoil sections are defined by 30 cells on both the upper and lower surfaces (for both grids). In the spanwise direction the wing is described by 10 cells for the coarse grid and 20 cells for the finer grid. Between the wing and the far-field, there are 16 and 32 cells for the two grids respectively. The C-curves are clustered around the wing using a control curve (Ref. 18).

The computed aerodynamic forces and moments are compared with the experimental data (Ref. 22) in Figure 9. The overall agreement between the predictions and the measurements is good. The code is able to model the nonlinear nature of the flow. The differences between the predictions can be traced to the differences in flow resolution provided by the two grids. This is illustrated by cross-plane surface pressure distributions at  $x/c = 0.6$  and  $0.9$  (where  $c$  is the root chord) shown in Figure 10 and the corresponding velocity vectors in Figure 11 for the 16-degree angle-of-attack case. The presence of a leading-edge separated vortex is clearly shown in Figure 11.

One aspect of this particular configuration deserves special attention. The convergence history plot for the coarse mesh presented in Figure 12 shows that the average error (net mass-flux) is reduced by 4 orders of magnitude for all the cases. The fine mesh results also converge for the 8 and 16 degrees angle-of-attack cases, as shown in Figure 13.

However, the fine mesh results clearly do not converge at 24 degrees angle of attack. It is interesting to note that the experimental data (Figure 9) shows a definite break in the lift-curve slope above approximately 20 degrees angle of attack; and, as shown by the horizontal line in Figure 9, the predicted lift oscillates about the experimental data. In the absence of detailed experimental data on the flow field, one can only speculate on the flow phenomena involved here. The leading-edge vortex bursting and/or massive viscous separation could be responsible. The set of computed cross-plane pressure distributions and velocity-vector plots shown in Figure 14 indicate that the leading-edge vortex is essentially stable after 600 cycles at  $x/c=0.6$  cross-plane; but, as shown in Figure 15, its structure and location are changing continuously at  $x/c=0.9$  cross-plane. This latter fact is responsible for the lack of convergence seen in Figure 13. It would be most interesting to obtain more detailed experimental data and compare them to these numerical results in order

to validate the predictions of the code. Of course, the time histories shown here cannot be taken literally since pseudo-time marching was used and they are not time accurate.

It is quite obvious from the studies to date that a refined grid is essential to the simulation of leading-edge vortex flows even for relatively simple wings. Additional studies are needed to answer the obvious question: "How refined should a grid be?" Lockheed is conducting such studies under an on-going cooperative program with NASA Langley Research Center. Since the TEAM code is being developed to analyze entire aircraft configurations, studies such as these will help determine the number of cells required to adequately predict leading-edge vortex flows on complex configurations.

#### ARROW WING

The next set of results is for an arrow wing with a leading-edge sweep of 71.2 degrees, a taper ratio of 0.1, and an aspect ratio of 1.4. The wing was analyzed at 0.85 Mach number and -4, 8, and 16 degrees angle of attack using a C-H grid having 98,304 (96x32x32) cells.

The computed normal force and pitching moment coefficients are compared with experimental data (Ref. 23) in Figure 16. Cross-plane surface pressure distributions are compared to experimental data for four locations in Figure 17. Velocity vector plots for the same locations are shown in Figure 18. Measured velocity vectors are not available for this configuration. However, recent advances in Laser-Doppler Velocimetry (Ref. 24) now make it possible to compare measured and predicted velocity vectors for complicated three-dimensional flow fields.

Additional studies are under way to use even more refined grids to determine the source of discrepancy between the theory and measurements. Two possible sources are: (1) the experiments were conducted for a wing-body configuration whereas the computations are for an isolated wing, and (2) the present wing has a rounded leading edge and the point of separation may not be correctly located by the present code. These issues will be addressed in future studies.

#### CONCLUDING REMARKS

The current status and proposed development of a three-dimensional Euler Aerodynamic Method (TEAM) were presented in this paper. Correlations of computed aerodynamic parameters and surface pressure distributions with experimental data indicate its ability to capture leading-edge separated vortices. Unlike the procedures based on velocity potential, it is not required to explicitly model these vortices. In addition, the same code can be used for analysis throughout the subsonic, transonic, and supersonic flight regimes. The results presented in this paper point to a need for more extensive validation. A number of questions, especially related to the effect of grid density and numerical dissipation on the solution, remain to be answered. With continuing development and validation, it promises to provide an effective engineering tool for analyzing nonlinear flows containing both shock waves and leading-edge-separated vortices.

## REFERENCES

1. Lamar, J. E., "Extension of Leading-Edge-Suction Analogy to Wings with Separated Flow Around the Side Edges at Subsonic Speeds," NASA TR R-428, October 1974.
2. Lamar, J. E. and Gloss, B. B., "Subsonic Aerodynamic Characteristics of Interacting Lifting Surfaces with Separated Flow Around Sharp Edges Predicted by a Vortex-Lattice Method," NASA TN D-7921, September 1975.
3. Lan, C. E. and Chang, Jen-Fu, "Calculation of Vortex Lift Effect for Cambered Wings by Suction Analogy," NASA CR 3449, July 1981.
4. Mehrotra, S. C. and Lan, C. E., "A Theoretical Investigation of the Aerodynamics of Low-Aspect-Ratio Wings with Partial Leading-Edge Separation," NASA CR 145304, 1978.
5. Johnson, F. T., Lu, P., Tinoco, E. N., and Epton, M. A., "An Improved Panel Method for the Solution of Three-dimensional Leading-edge Vortex Flows," NASA CR 3279, July 1980.
6. Luckring, J. M., Schoonover, W. E., and Frink, N. T., "Recent Advances in Applying Free Vortex Sheet Theory for the Estimation of Vortex Flow Aerodynamics," AIAA 82-0095, 20th Aerospace Sciences Meeting, Orlando, Florida, January 11-14, 1982.
7. Polhamus, E. C., "A Concept of the Vortex Lift of Sharp Edge Delta Wings Based on a Leading-Edge-Suction Analogy," NASA TN D-3767, 1966.
8. Fujii, K. and Kutler, P., "Numerical Simulation of the Leading-Edge Separation Vortex for a Wing and Strake-Wing Configuration," AIAA Paper 83-1908-CP, 6th Computational Fluid Dynamics Conference, Danvers, Massachusetts, July 13-15, 1983.
9. Jameson, A., Schmidt, W., and Turkel, E., "Numerical Solutions of the Euler Equations by Finite Volume Methods Using Runge-Kutta Time-Stepping Schemes," AIAA Paper 81-1259, 14th Fluid and Plasma Dynamics Conference, Palo Alto, California, June 23-25, 1981.
10. Rizzi, A., "Damped Euler Equation Method to Compute Transonic Flow Around Wing-Body Combinations," AIAA Journal, Vol. 20, No. 10, October 1982, pp. 1321-1328.
11. Hitzel, S. M. and Schmidt, W., "Slender Wings with Leading-Edge Vortex Separation -- A Challenge for Panel Methods and Euler Codes," AIAA Paper 83-0562, 21st Aerospace Sciences Meeting, Reno, Nevada, January 10-13, 1983.
12. Raj, P. and Sikora, J. S., "Free-Vortex Flows: Recent Encounters with an Euler Code," AIAA Paper 84-0135, 22nd Aerospace Sciences Meeting, Reno, Nevada, January 9-12, 1984.
13. Rizzi, A., "Computer Simulation of Non-potential Flows Around Wings," Aeronautical Journal, June/July 1984, pp. 238-248.
14. Raj, P., "Computational Simulation of Free-Vortex Flows Using An Euler Code," ICAS-84-1.3.1, 14th Congress of the International Council of the Aeronautical Sciences, Toulouse, France, September 9-14, 1984.

15. Rizzi, A. and Eriksson, L.E., "Computation of Flow Around Wings Based on the Euler Equations," *Journal of Fluid Mechanics*, Vol. 148, November 1984, pp. 45-71.
16. Jameson, A. and Baker, T. J., "Solution of the Euler Equations for Complex Configurations," AIAA Paper 83-1929-CP, 6th Computational Fluid Dynamics Conference, Danvers, Massachusetts, July 13-15, 1983.
17. Sikora, J. S. and Miranda, L. R., "Boundary Integral Grid Generation Technique," AIAA Paper 85-4088, 3rd Applied Aerodynamics Conference, Colorado Springs, Colorado, October 14-16, 1985.
18. Raj, P., "PACMAPS: A Three-dimensional Grid Generation Method, Version 1.0," LR 30811, Lockheed-California Company, October 1984.
19. Agarwal, R. K. and Deese, J. E., "Transonic Wing-Body Calculations Using Euler Equations," AIAA Paper 83-0501, 21st Aerospace Sciences Meeting, Reno, Nevada, January 10-13, 1983.
20. Eriksson, L. E., "Generation of Boundary-Conforming Grids About Wing-Body Configurations Using Transfinite Interpolation," AIAA Journal, Vol. 20, No. 10, October 1982, pp. 1313-1320.
21. Rai, M. M., "A Conservative Treatment of Zonal Boundaries for Euler Equation Calculations," AIAA Paper 84-0164, 22nd Aerospace Sciences Meeting, Reno, Nevada, January 9-12, 1984.
22. Emerson, H. F., "Wind-Tunnel Investigation of the Effect of Clipping the Tips of Triangular Wings of Different Thickness, Camber, and Aspect Ratio - Transonic Bump Method," NACA TN 3671, June 1956.
23. Manro, M. E., Manning, K. J. R., Hallstaff, T. H., and Rogers, J. T., "Transonic Pressure Measurements and Comparison of Theory to Experiment for an Arrow-Wing Configuration," NASA CR-2610, August 1976.
24. Novak, C. J., Huie, C. R., and Cornelius, K. C.; "Laser Velocimetry in Highly Three-Dimensional and Vortical Flows," *Vortex Flow Aerodynamics - Volume I*, NASA CP-2416, paper no. 7, 1986.



- INCREASED MANEUVER LIFT
- INCREASED LANDING AND TAKEOFF LIFT
- LIGHT WEIGHT
- AERODYNAMIC CENTER CONTROL
- LITTLE INCREASE IN GUST RESPONSE
- REDUCED BUFFET INTENSITY

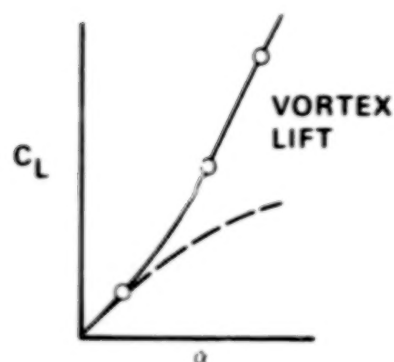
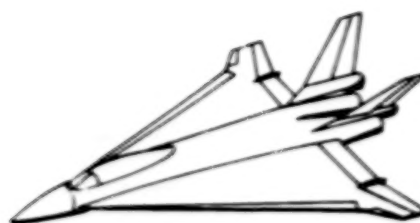


Figure 1. Benefits of vortex flow for high-speed aircraft.

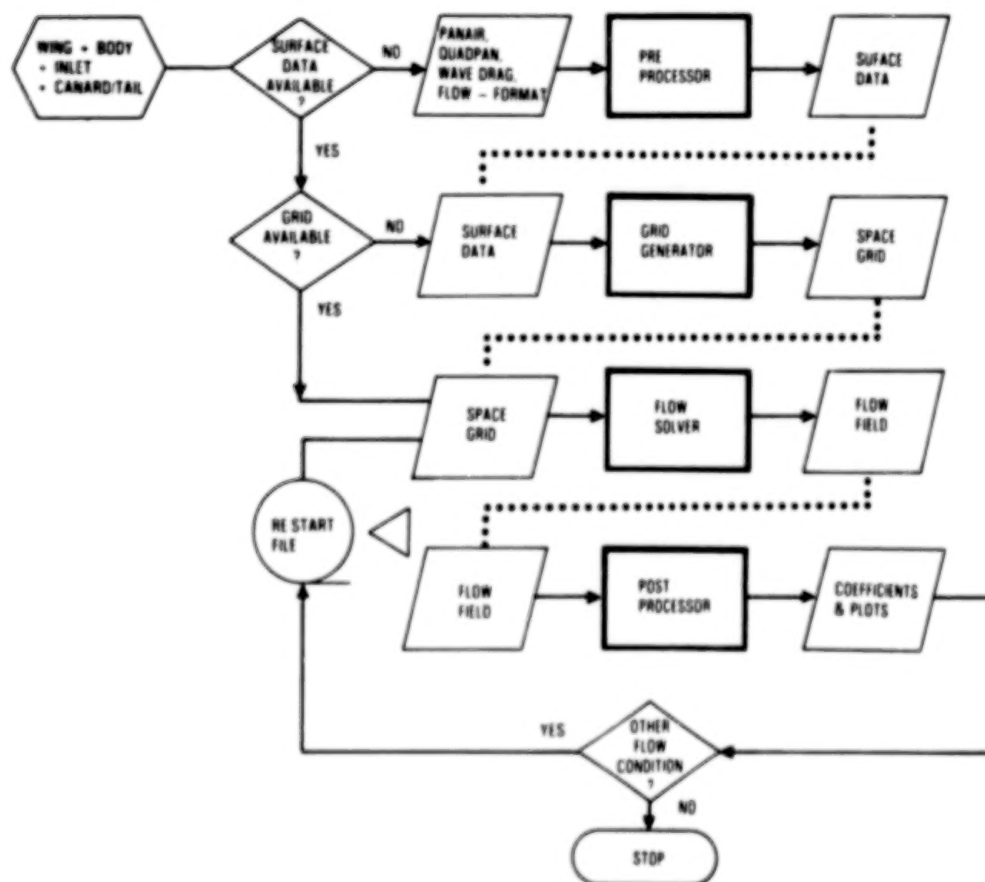


Figure 2. Lockheed-California Company's three-dimensional Euler aerodynamic method (TEAM).



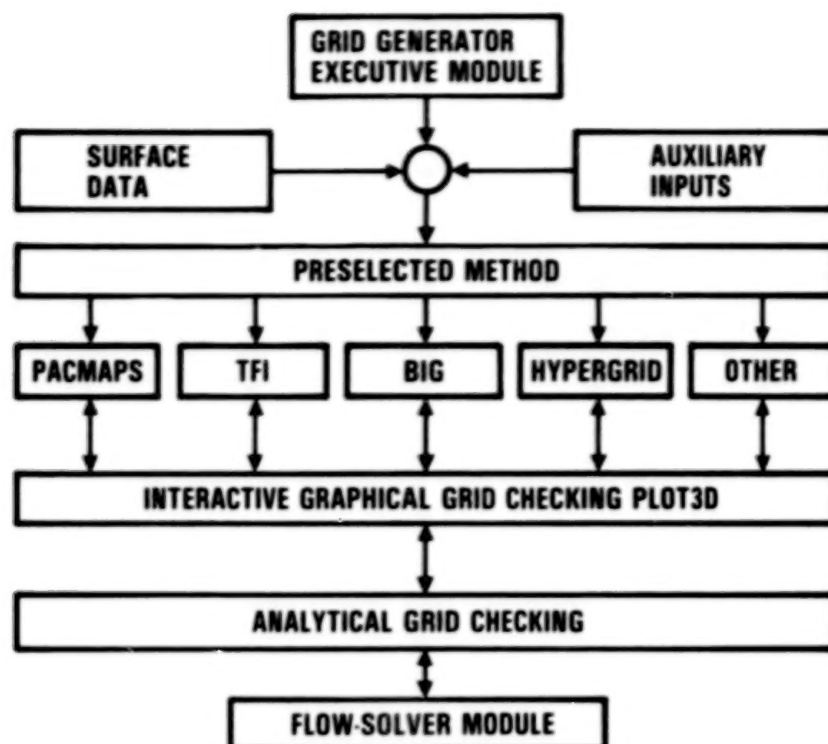


Figure 3. Schematic of TEAM's grid generator module.

| METHODS                              | GEOMETRY CAPABILITIES |           |                          |                           |                  | DESIRABLE FEATURES                |               |                              |                          |                           |
|--------------------------------------|-----------------------|-----------|--------------------------|---------------------------|------------------|-----------------------------------|---------------|------------------------------|--------------------------|---------------------------|
|                                      | WING                  | WING BODY | WING BODY<br>TAIL CANARD | WING BODY<br>TAIL NACELLE | GRID<br>TOPOLOGY | INTERACTIVE<br>GRID<br>GENERATION | USER FRIENDLY | COMPUTATIONALLY<br>EFFICIENT | SMALL AMOUNT<br>OF INPUT | SPECIFY OUTER<br>BOUNDARY |
| ALGEBRAIC:<br>PACMAPS                | ●                     | ●         | ○                        |                           | CH               | ●                                 | ●             | ●                            | ●                        |                           |
| TFI                                  | ●                     | ●         | ●                        | ●                         | CH, HH<br>CO, OO | ●                                 |               | ●                            |                          | ●                         |
| BOUNDARY INTEGRAL:<br>BIG            | ●                     | ●         | ●                        | ○                         | OO<br>CO         |                                   | ●             |                              | ●                        | ●                         |
| DIFFERENTIAL EQUATION:<br>HYPERBOLIC | ●                     | ●         | ○                        | ○                         | CO, OO<br>CH, HH |                                   | ●             | ●                            | ●                        |                           |
| ELLIPTIC                             | ○                     | ○         | ○                        | ○                         | CO, OO<br>CH, HH |                                   | ●             |                              |                          | ●                         |

● DEVELOPED

◐ DEVELOPING

○ PROPOSED

Figure 4. Lockheed-California Company's grid generation methods.

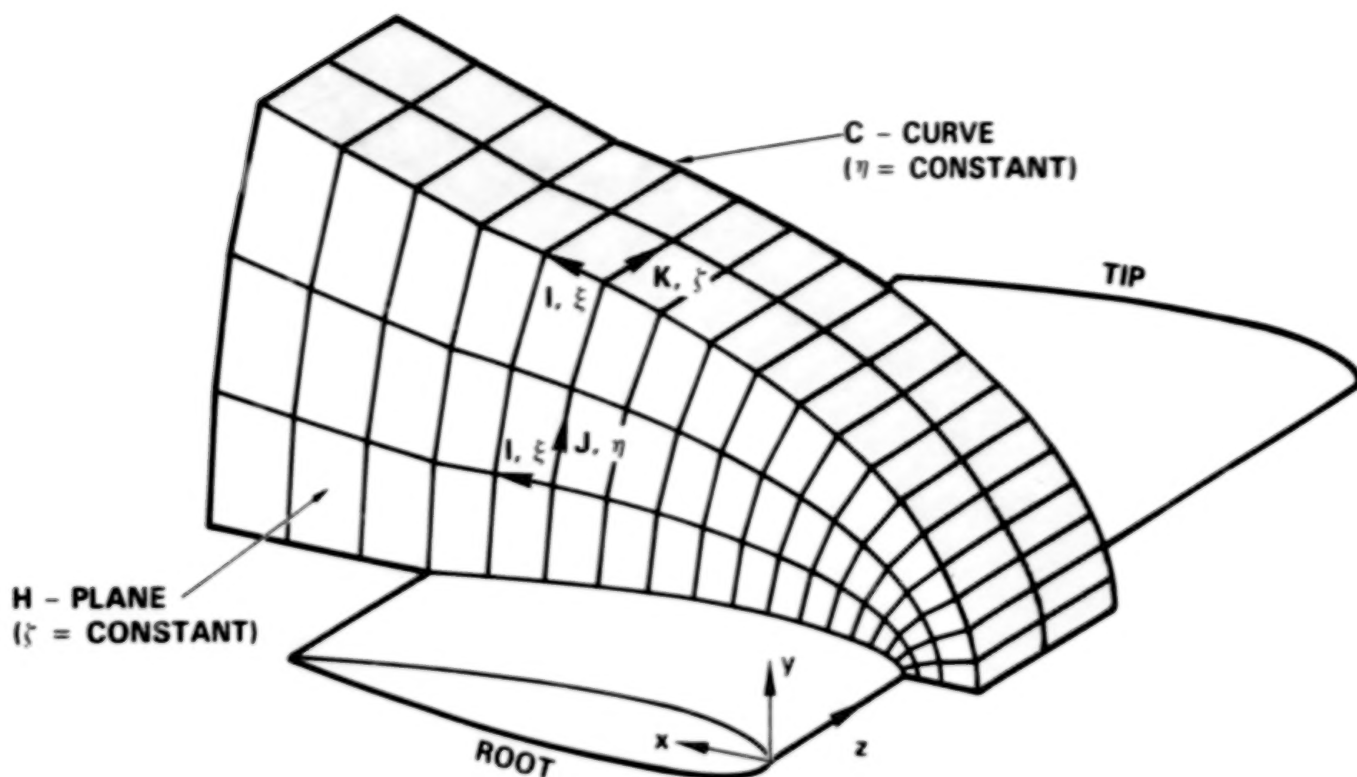


Figure 5. Example of a C-H grid.

| YEAR    | CAPABILITIES |     |     |     | GEOMETRY   |           |                | FLIGHT REGIME        |          | GRID STRUCTURE |            |               |   | ADDITIONAL FEATURES |   |               |                    |                    |
|---------|--------------|-----|-----|-----|------------|-----------|----------------|----------------------|----------|----------------|------------|---------------|---|---------------------|---|---------------|--------------------|--------------------|
|         |              |     |     |     | WING ALONE | WING BODY | WING BODY-TAIL | WING BODY-INLET-TAIL | SUBSONIC | TRANSONIC      | SUPERSONIC | SINGLE GLOBAL |   |                     |   | PATCHED ZONAL | INCREASED ACCURACY | FASTER CONVERGENCE |
|         | C-H          | C-O | O-O | H-H |            |           |                |                      |          |                |            |               |   |                     |   |               |                    |                    |
|         |              |     |     |     |            |           |                |                      |          |                |            |               |   |                     |   |               |                    |                    |
| 1982    | ●            |     |     |     | ●          | ●         |                | ●                    |          |                |            |               |   |                     |   |               |                    |                    |
| 1983    | ●            | ●   |     |     | ●          | ●         | ●              | ●                    | ●        |                |            |               |   |                     |   |               |                    |                    |
| 1984    | ●            | ●   | ●   |     | ●          | ●         | ●              | ●                    | ●        | ●              | ●          |               | ● | ●                   |   |               |                    |                    |
| 1985-86 | ●            | ●   | ●   | ○   | ●          | ●         | ●              | ●                    | ●        | ●              | ●          | ●             | ● | ●                   | ● | ○             | ●                  | ●                  |

● DEVELOPED

◐ DEVELOPING

○ PROPOSED

Figure 6. Capabilities of TEAM's flow solver module.

- **STRONGLY CONSERVATIVE FORMULATION IMPLEMENTED**

$$\frac{\partial}{\partial t} \iiint_{\Omega} \mathbf{Q} \, d\Omega + \iint_A \bar{\mathbf{F}} \cdot \hat{\mathbf{n}} \, dA = 0$$

$$\mathbf{Q} \equiv \begin{bmatrix} \rho \\ \rho u_i \\ \rho e \end{bmatrix} \quad \bar{\mathbf{F}} \cdot \hat{\mathbf{n}} = \begin{bmatrix} (\rho u_i) n_i \\ (\rho u_i u_j + p \delta_{ij}) n_j \\ (\rho u_i h) n_i \end{bmatrix}$$



- **ORIGINAL FORMULATION**

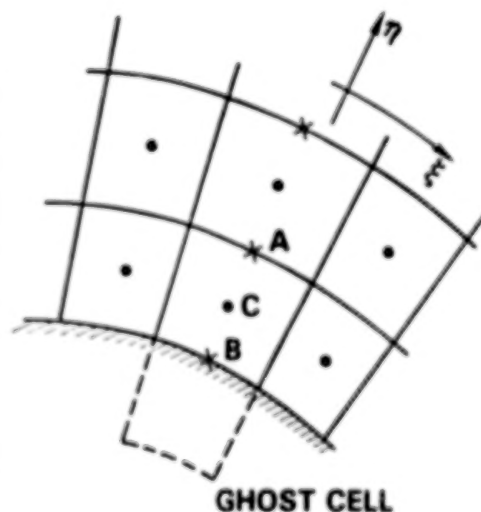
$$\bar{\mathbf{F}} \cdot \hat{\mathbf{n}} = \begin{bmatrix} \rho (u_i n_i) \\ (\rho u_i) (u_j n_j) \\ (\rho h) (u_i n_i) \end{bmatrix} + \begin{bmatrix} 0 \\ p n_i \delta_{ij} \\ 0 \end{bmatrix}$$

- **ACCURACY IMPROVEMENT UNDER INVESTIGATION**
- **APPROXIMATELY 30% MORE COMPUTATIONS**

Figure 7. Comparison of TEAM and FLO-57 convective flux computation.

## ORDER OF APPROXIMATION

| SCHEME \ CELL | 1           | 2         | $\geq 3$  |
|---------------|-------------|-----------|-----------|
| 1             | (ZERO FLUX) | 2ND       | 2ND + 4TH |
| 2             | 2ND         | 2ND + 3RD | 2ND + 4TH |
| 3*            | 1ST + 2ND   | 2ND + 3RD | 2ND + 4TH |
| 4†            | 2ND + 3RD   | 2ND + 4TH | 2ND + 4TH |



\*GLOBALLY CONSERVATIVE  
†GHOST CELLS

Figure 8. Four schemes for calculating dissipation terms near a solid surface.

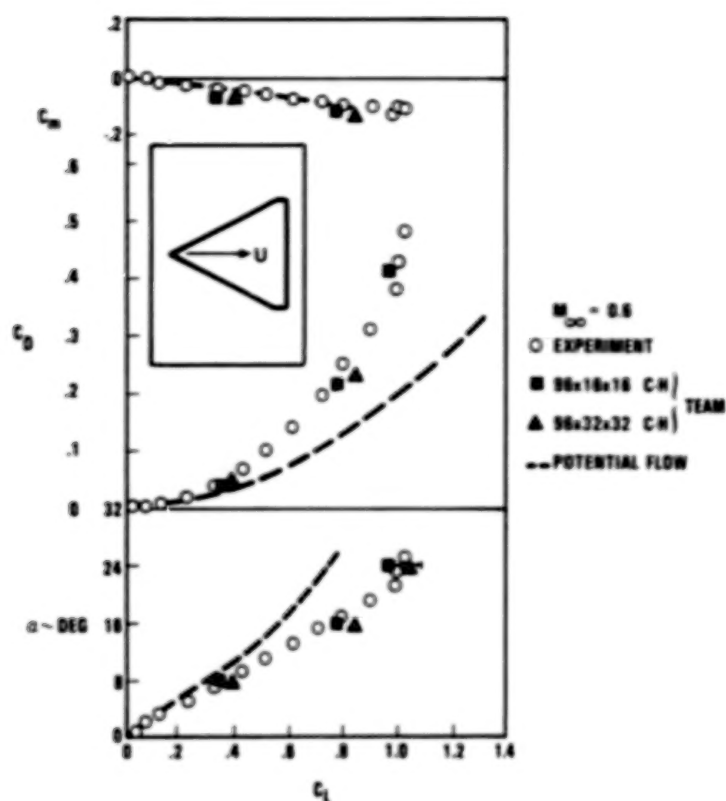


Figure 9. TEAM code results compared to experimental values for a cropped delta wing.

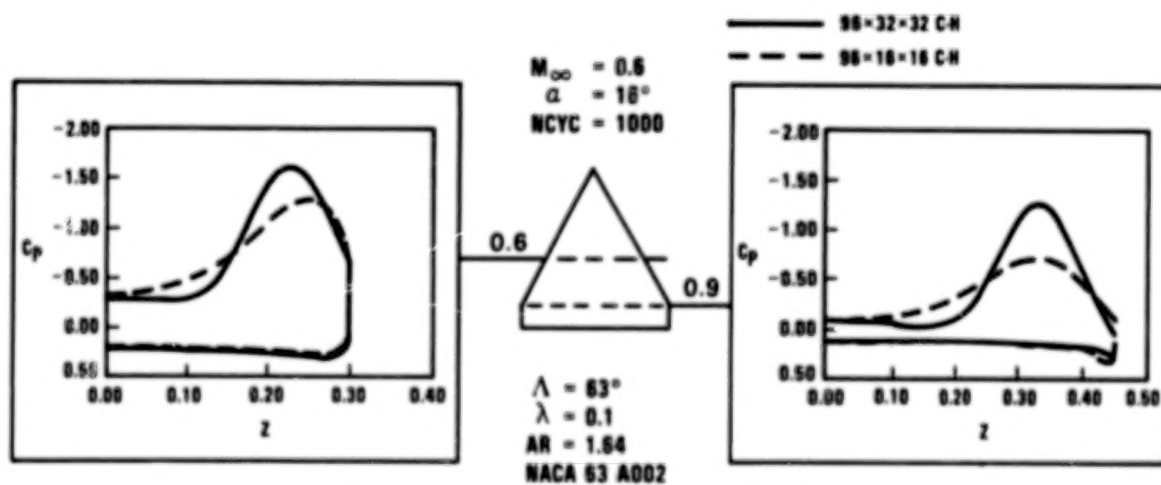


Figure 10. Predicted spanwise pressure distributions for two grids.

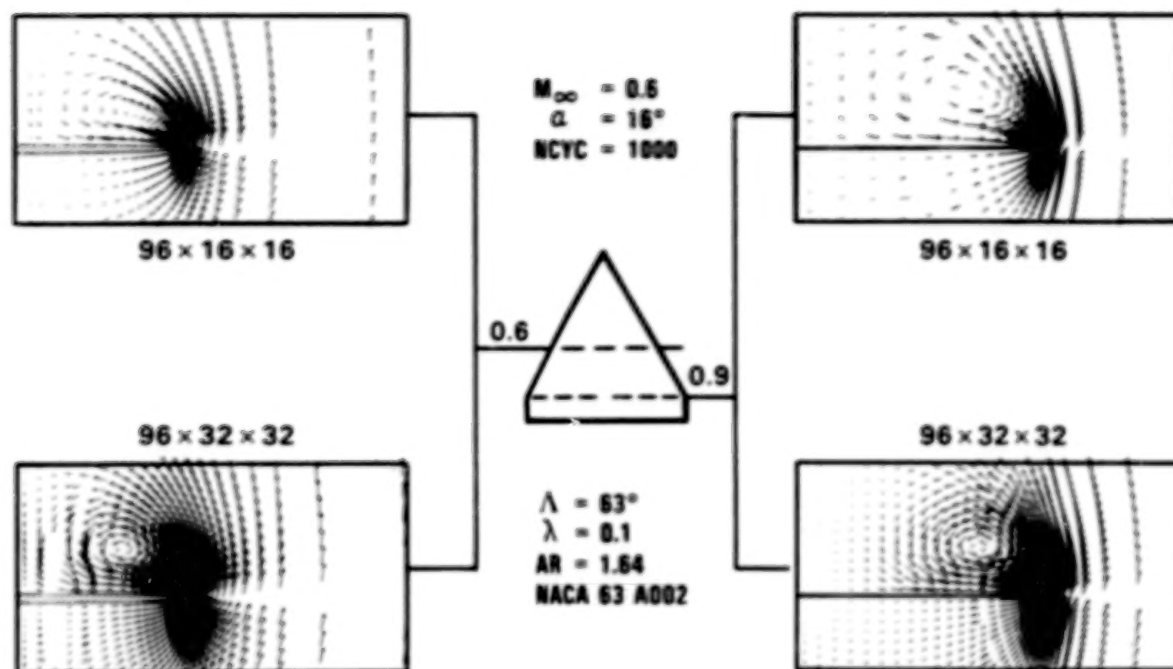


Figure 11. Cross-flow velocity vectors for two grids and two chordwise locations.

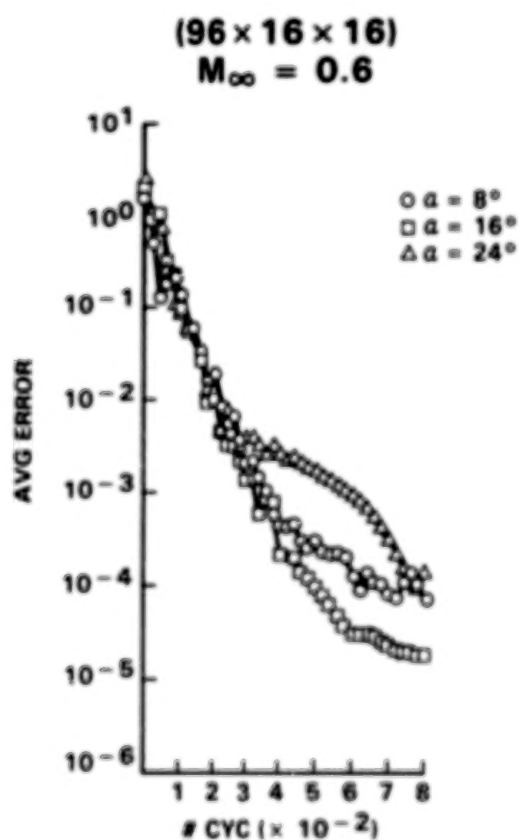


Figure 12. Convergence history for a coarse grid ( $96 \times 16 \times 16$ ) at three different angles of attack.



(96x32x32)  
 $M_\infty = 0.6$

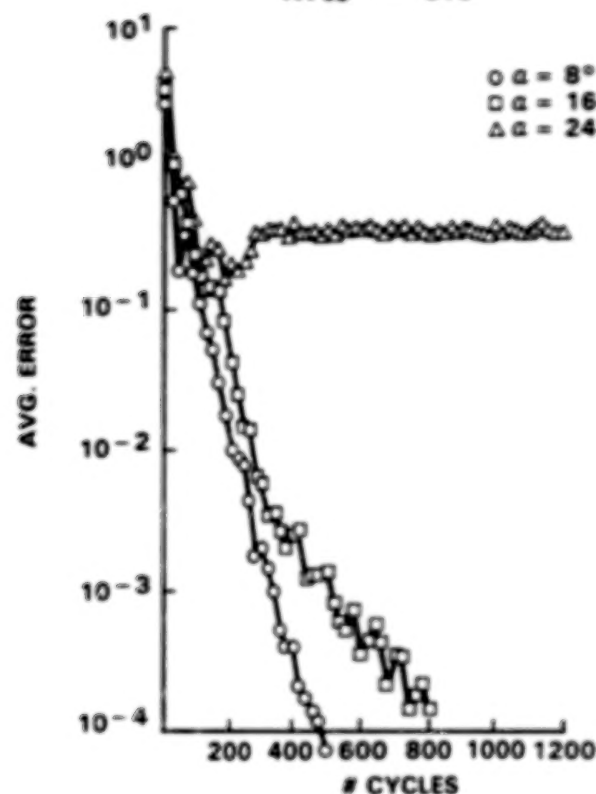


Figure 13. Convergence history for a fine grid (96 x 32 x 32) at three different angles of attack.

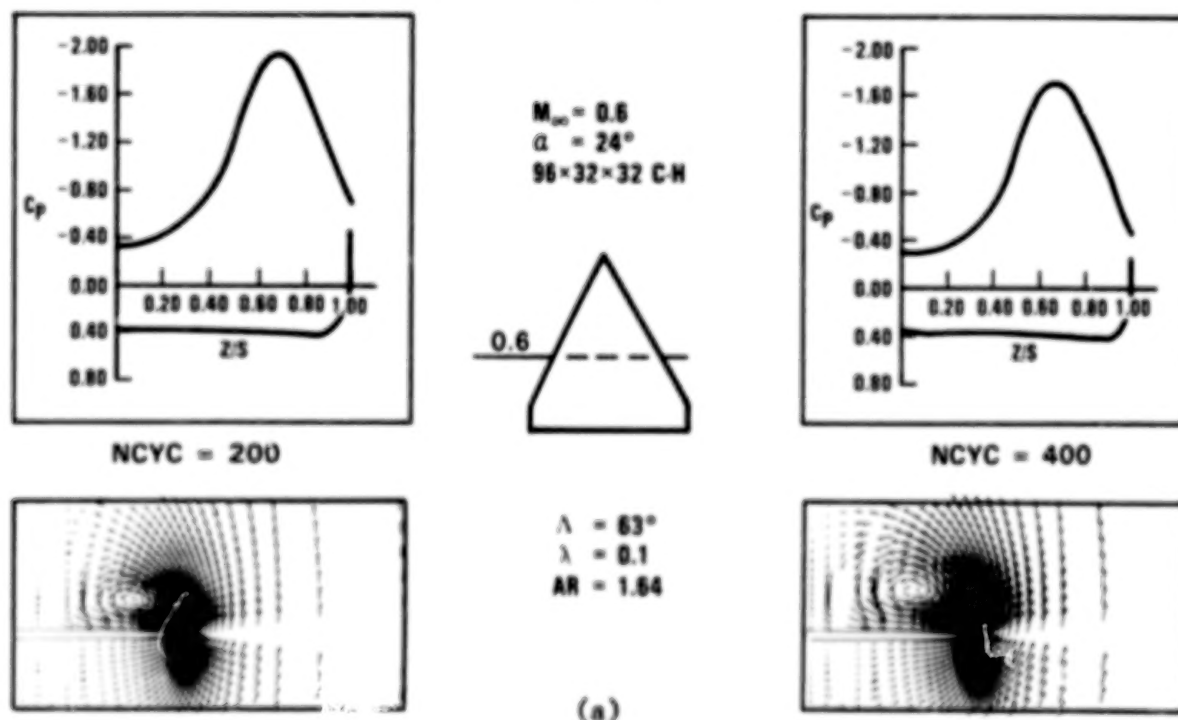


Figure 14. Spanwise pressure distributions and velocity vectors for six different times in integration process ( $x/c = .6$ ).

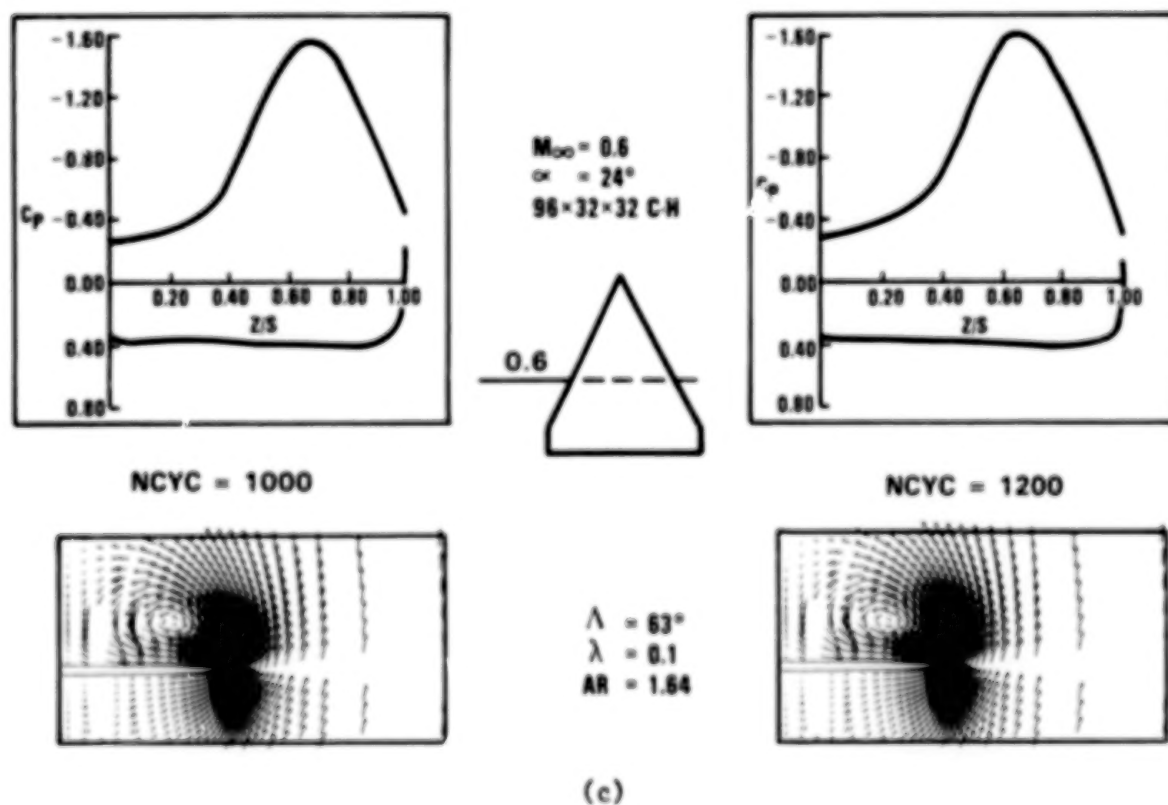
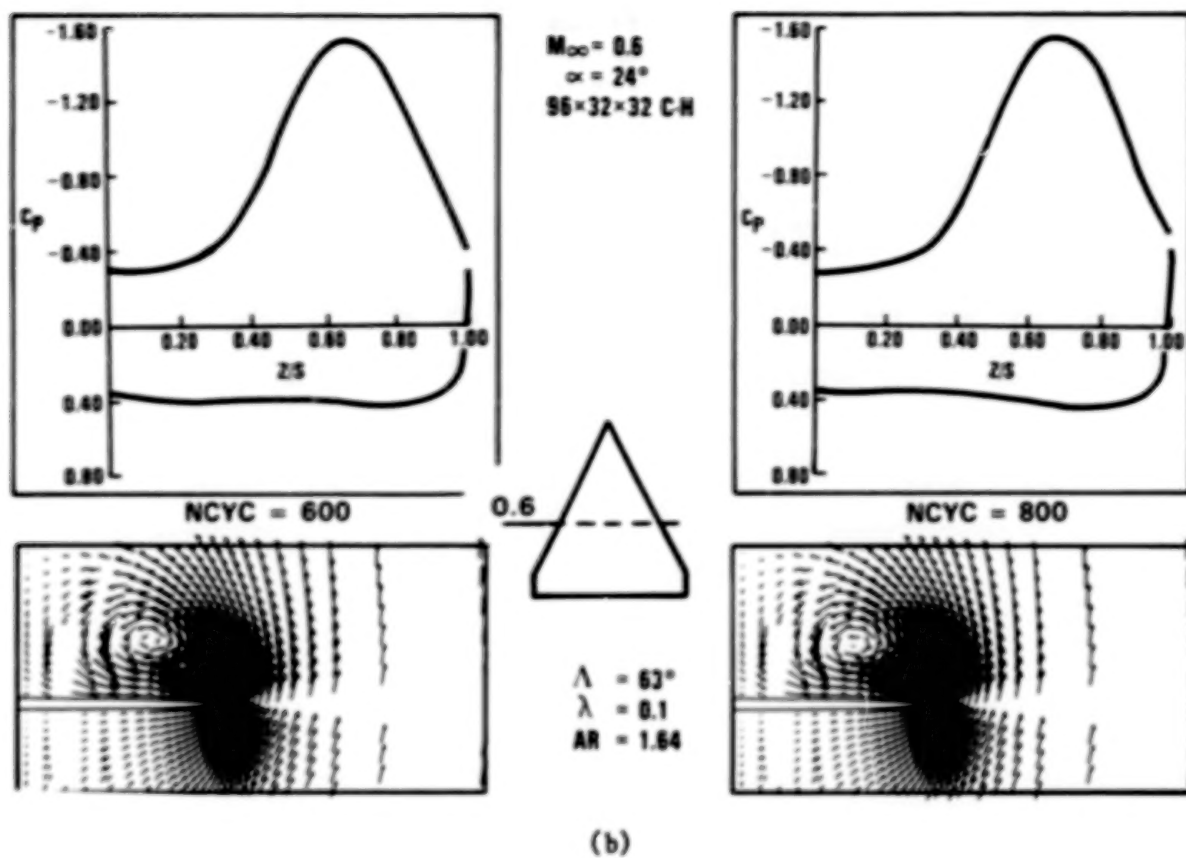


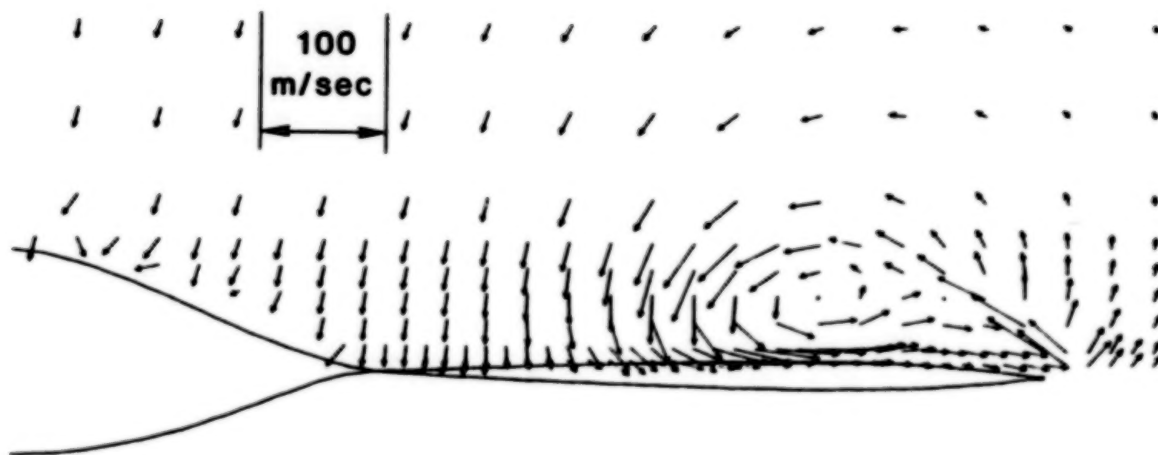
Figure 14. Concluded



# Mean Crossflow Velocity Vectors

$\alpha = 10^\circ$

$x/c = 1.000$



(f)

Figure 18 (Concluded)

## Vortex Track

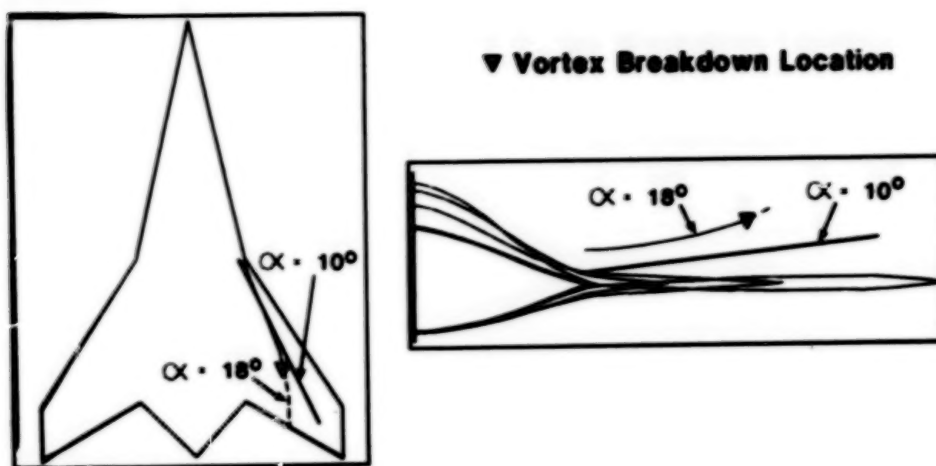


Figure 19

## Mean Axial Velocity

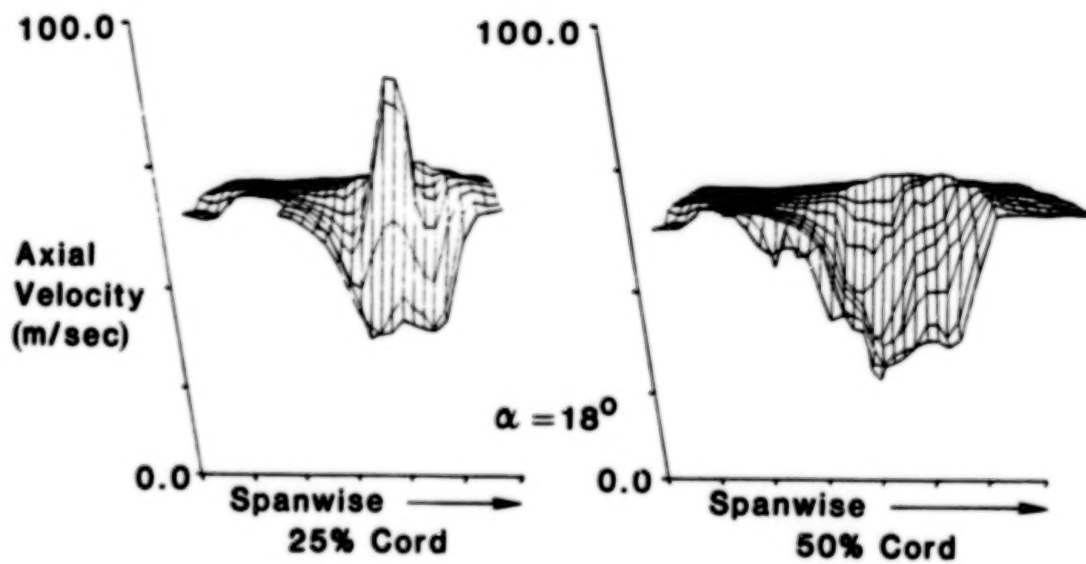


Figure 20



## IN-FLIGHT AND WIND TUNNEL LEADING-EDGE VORTEX STUDY ON THE F-106B AIRPLANE

John E. Lamar  
NASA Langley Research Center  
Hampton, Virginia

## SUMMARY

The vapor-screen technique has been successfully applied to an F-106B fighter aircraft during subsonic and transonic maneuvers. This system has allowed the viewing of multiple vortex systems on the wing upper surface at angles of attack less than  $19^\circ$ . In addition, similarities as well as differences were determined to exist between the vortex systems for a full-scale semispan model and the flight vehicle at  $20^\circ$  incidence. Furthermore, variations in Reynolds number and Mach number have been identified as to how they affect vortex system details at flight conditions.

## INTRODUCTION

The visualization of vortex systems which originate from aerodynamic surfaces is a common occurrence in wind tunnels, where techniques like tuft grids, schlieren, smoke wands, and vapor screens have been used (see refs. 1-6). Some of these seed the working fluid with smoke or sufficient water vapor (ref. 6) in order to highlight the core by either smoke entrainment or water condensation. This may occur along much of the length of the vortex, thereby yielding a visible record of the core path as can be seen in figure 1 for a wind tunnel model with upward deflected vortex flaps. Flight examples are not as readily available, but figure 2 shows the strake flow of an F-16 during a low-altitude maneuver. Both examples are the result of naturally occurring condensed water vapor (light areas) forming around and outlining the dark core regions.

In-flight use of smoke has been documented, in references 7 and 8, on delta wings to observe the leading-edge vortex breakdown progression (HP 115) and the outer panel flow (AVRO 707B) with increasing angle of attack, respectively. However, in order to obtain vortex system details, one needs to use a flight version of the vapor screen technique. Since the hardware to implement this was not available\* when interest was expressed in observing the Reynolds number effects on the vortex system for the F-106B, the equipment had to be developed.\*\* An illustration of what the vortex system looks like with such an implementation is shown schematically for the F-106B by the flight project logo in figure 3.

After the equipment was developed to seed the flow with vaporized propylene glycol in order that the observations be weather independent, illuminate the details with a light sheet, and record the events with a television system, applications were made

\*Reference 9 reports the Soviet use of a ruby laser sheet and atmospheric water vapor to observe the vortex system at subsonic speeds above an ogee wing up to high incidence.

\*\*Reference 10 used limited surface tufts near the middle of an F-106B wing during a flight test program and determined a reattachment line associated with a vortex system.

to both flight (see fig. 4) and wind tunnel vehicles. The particular information sought was to quantify the effect that the Reynolds number may have on the details of the leading-edge vortex system of full-scale vehicles at high angles of attack and subsonic speeds, including a 5-G transonic maneuver. This paper documents these results and offers a selected comparison of system details on a full-scale semispan F-106B model.

#### SYMBOLS

|           |  |
|-----------|--|
| G         | acceleration due to gravity, ft/sec <sup>2</sup>                                   |
| K         | thousand   |
| LE        | leading edge   |
| $\lambda$ | inboard distance to vortex core from leading edge, inches                          |
| M         | Mach number  |
| m         | inboard distance to inner edge of vortex system envelope from leading edge, inches |
| $R_n$     | Reynolds number  |
| TE        | trailing edge  |
| z         | vertical distance to vortex core above upper surface, inches                       |
| $\alpha$  | angle of attack, degree  |

#### TEST SETUP

The wind tunnel tests were performed on a half-airplane model of the F-106B mounted in the Langley Research Center 30- by 60-Foot Wind Tunnel. This model was made by cutting an airplane in half and mounting it wingtip upward from a reflection plane. It should be pointed out that the full-scale model differed primarily from the flight vehicle only in the leading-edge region. The former had all the camber, essentially conical, ahead of the local 90-percent semispan; whereas, the latter had its conic-like camber ahead of the 80-percent local semispan. They are called Case XIV and Case XXIX cambers, respectively, by the manufacturer.

The tests in the 30- by 60-Foot Wind Tunnel were for the purpose of establishing starting values for the flight project in the areas of seeding flow rate and probe position, light-sheet width and orientation, and TV camera parameters. One great uncertainty remained after the wind tunnel test, and it was whether sufficient seeding material could be produced to make the vortex system visible at flight speeds.

The range of test parameters for the wind tunnel and flight is given in figure 5. This range includes the vapor screen variables such as seeding flow rate and probe position, and light-sheet width and location, as well as the two different types of maneuvers flown. The wind tunnel conditions are standard ones with the dynamic pressure not exceeding 10 lb/ft<sup>2</sup>.

For both the 1-G constant altitude and the 5-G transonic maneuvers, six probe positions were tried in order to find the one that worked best overall. Five of these were underneath the leading edge and one was on top. These positions were numbered sequentially, and number 6 was found to be preferable. Its approximate location underneath the leading edge is shown on figure 6, along with the relative locations of the camera and light sheet.

The right side of this figure shows the view displayed on the monitor. Since the camera is looking down and aft onto the left wing panel, the wing trailing edge is at the top of the screen, the leading edge intersects the right side, and the fuselage cuts across the left corner. The light sheet is seen to lie in the middle of the screen and does not extend to the wing leading edge because of camber.

There were two light sheet locations used in the wind tunnel, one perpendicular to the fuselage centerline and the other perpendicular to the wing leading edge, as can be seen in figure 7. For the flight experiment, it was the intent to have the light also perpendicular to the leading edge. However, space constraints associated with attaching the light source to the fuselage limited the sheet to only reaching  $11^\circ$  ahead of perpendicular to the centerline as opposed to the  $30^\circ$  desired for this  $60^\circ$  swept wing. Hence, the light sheet location used in flight is closer to the more aft one used in the wind tunnel.

The slit width in the light sheet generator was varied from 0.003" to 0.041" for both wind tunnel and flight with most testing done at 0.041". In addition, most of the seeding was done with the pump operating at approximately 3 gallons per hour. For both of these systems, the intent was to use the smallest amount possible which would still seed and illuminate the vortex system sufficiently.

## RESULTS AND DISCUSSION

It should be remembered that the primary data taken, other than test conditions, during both the flight and wind tunnel tests are video-tape visual records of the vortex systems. Using these records, photographs of portions of particular flights were made from a monitor in order that a comparative study may be done and the pertinent test effects may be identified. (The photographs presented are from an orientation delineated on the right-hand side of figure 6.)

From flight, there are basically two kinds of effects to be presented corresponding to the two types of flights flown. The first type is one in which the altitude is held essentially constant, and the Mach number is adjusted to keep the aircraft at 1-G flight over an angle-of-attack range up to  $23^\circ$ . For each of these constant altitude flights, which ranged from 35,000 feet to 15,000 feet in 5,000-foot increments, the Mach number did not vary appreciably from 0.4; however, the Reynolds number increased by  $6 \times 10^6$  as the altitude decreased. The other type was for a transonic maneuver at 5-G and  $M \sim 0.8$ , accomplished during a spiral descent, at a fixed angle of attack,  $19^\circ$ , in which the Reynolds number varied significantly.

### Effect of Reynolds Number

The effect of Reynolds number can be seen in figures 8 to 13, using comparative photographs at angles of attack from  $17^\circ$  to  $23^\circ$ . These 1-G flights show that at  $17^\circ$ , leading-edge separation is well established at  $R_n = 26 \times 10^6$ , which corresponds to the highest altitude, but has not even begun at  $R_n = 32 \times 10^6$ . Between these extremes, progressively smaller amounts of leading-edge separation are noted with increasing Reynolds number. Much the same occurs at  $18^\circ$ , but at  $19^\circ$  there is a first indication of leading-edge separation at the highest Reynolds number. The delay in separation onset associated with increasing Reynolds number is not new for round-edged wings with camber, but that it would be observed in flight is remarkable.



It is also noteworthy to point out evidences of other vortical action inboard of the leading edge at  $\alpha = 19^\circ$  and  $R_n = 32 \times 10^6$ . The innermost may be associated with the juncture flow; however, the mid-semispan vortex may well be coming from the upper surface shear layer tearing and forming another system of the same rotational sense as at the leading edge. This may occur when the leading-edge vortex is not yet strong enough to dominate the entire outer panel flow. Figure 11 has been prepared to show the postulated positions of the various vortical systems at the 20,000-foot altitude. When this system is viewed from above, it has an appearance which resembles the discrete vortices in the feeding sheet, arranged roughly parallel to the leading edge, around the primary vortex found in water tunnel tests and reported in reference 11. One important difference is that, in flight, each vortex extends to the upper surface.

Figure 12 shows that, at  $20^\circ$ , only a single vortex system exists outboard and, as it gets bigger with decreasing Reynolds number, the innermost one grows smaller. The same is true at  $23^\circ$ , as seen in figure 13.

It is apparent from this series of comparative photographs that the leading-edge vortex is Reynolds number dependent. To help establish the quantitative dependence, figure 14 has been prepared in which the vortex system envelopes and "cores" have been determined for two different values of Reynolds number. They are displayed against the aft part of the left wing panel and are for values of angle of attack from  $18^\circ$  to  $23^\circ$ . The "cores" are not determined from finding the "black hole," since none was seen for these flights, but are established by an examination of where the smoke was the brightest and its rotation centered. The brightest smoke was chosen since it represented an increased density/reflectivity which one would expect to surround the very core itself. By superimposing the results shown in figure 14 onto a similarly recorded target board marked off in 6-inch squares, quantifiable information was established for the inner extent of the envelope and core location; this information is presented in figure 15.

From this figure it can be seen that, in general, the inner extent of the vortex system envelope and of the core locations is more inboard at the lower Reynolds number. Also, at the lower value, the envelope and core tend to be more monotonic in their growth with angle of attack. It is interesting to note that at  $20^\circ$  the results seem to coalesce, after which the measurements corresponding to the higher Reynolds number have a slower inboard growth. The core elevation seems insensitive to Reynolds number.

Figure 16 compares these results, taken from the Case XXIX flight wing, with those from the 30- by 60-Foot Wind Tunnel test of the Case XIV wing. Though the vortex flow was much unsteadier in the wind tunnel, as its lateral position oscillated between outboard and inboard, an interpolated aggregate position, shown by the filled diamond, does compare surprisingly well with the flight data. The interpolation is required since the light sheet locations used in the wind tunnel lie on either side of the flight position. Note that the height of the wind tunnel core is above the flight ones. No other conclusions can be drawn, since there was not enough time in the wind tunnel with the right probe position to get sufficient data.

#### Effect of Mach Number

Figure 17 provides details of the vortex systems for both 1-G and 5-G flights, which occurred at roughly 0.4 and 0.8 Mach number, respectively. These photographs were taken with two different light sheet widths, and the 5-G maneuvers were done both to

the left and right to rule out any centrifugal force effects on the results. Basically, with either light sheet width, the vortex appears similar under these test conditions. However, for the thinner light sheet and 5-G maneuver, one is able to see a core along with what appears to be a shear layer feeding into it.

To identify the effect of Mach number, the envelope and core are compared in figure 18 for these two different maneuvers. It is readily apparent that the doubling of Reynolds number has not delayed the leading-edge vortex formation to a higher angle of attack. This is in contrast to the effect of increasing Reynolds number discussed previously (see fig. 10). The more inboard extent of the envelope and of the core is therefore attributed to the Mach number doubling. This was an unexpected effect.

#### CONCLUDING REMARKS

In this paper, two basic topics have been covered: vapor screen technology implementation for manned flight vehicles, in particular, the F-106B, and the vortex system features revealed by using this technology in flight and in the wind tunnel. Regarding the first topic, it has been demonstrated that the vapor screen technique can be applied successfully to large-scale vehicles both in the wind tunnel and in flight under a variety of test conditions. These include the transonic maneuver, which future fighter aircraft will continue to need to perform.

Concerning the results obtained using this technique, significant differences have been noted in the size of the leading-edge vortex system and its core location at subsonic speeds with only relatively small changes in flight Reynolds number. The prime effect seems to be the well-known delay of separation on round-edged wings associated with increased Reynolds number. At 20° angle of attack, where flight and wind tunnel vortex system details could be directly compared, there was close overall agreement even with differences in wing camber and with the flight Reynolds number being greater by a factor of 2. This occurred in spite of the vortex system being more stable in flight than in the wind tunnel. In addition, during the transonic maneuver, the Mach number effect can overcome the trend of increasing Reynolds number to reduce the vortex system by producing a larger, more inboard, and well-defined vortex system relative to the constant altitude 1-G flight.

#### REFERENCES

1. Settles, G. S.: Flow Visualization Techniques for Practical Aerodynamic Testing. Presented at the Supersonic Tunnel Association Meeting, Williamsburg, Virginia, October 1983.
2. Peake, D. J.; and Tobak, M.: On Issues Concerning Flow Separation and Vortical Flows in Three Dimensions. Aerodynamics of Vortical Type Flows in Three Dimensions, AGARD CP-342, Paper No. 1, 1983.
3. Werlé, H.: Visualization des Ecoulements Tourbillonnaires Tridimensionnels. Aerodynamics of Vortical Type Flows in Three Dimensions, AGARD CP-342, Paper No. 8, 1983.
4. Wentz, W. H., Jr.; and Kohlman, D. L.: Wind-Tunnel Investigation of Vortex Breakdown on Slender Sharp-Edged Wings. NASA CR-98737, 1968.



5. Snow, W. L.; and Morris, O. A.: Investigation of Light Source and Scattering Medium Related to Vapor-Screen Flow Visualization in a Supersonic Wind Tunnel. NASA TM-86290, December 1984.
6. Jorgensen, L. H.: Prediction of Static Aerodynamic Characteristics for Slender Bodies Alone and with Lifting Surfaces to Very High Angles of Attack. NASA TR R-474, September 1977.
7. Fennell, L. J.: Vortex Breakdown - Some Observations in Flight on the HP 115 Aircraft. R&M No. 3805, British A. R. C., 1977.
8. Perry, D. H.; Port, W. G. A.; and Morrall, J. C.: Low Speed Flight Tests on a Tailless Delta Wing Aircraft (AVRO 707B). C.P. No. 1107, British A. R. C., 1970.
9. Burdin, I. Yu.; Zhirnov, A. V.; Kulesh, V. P.; Orlov, A. A.; Pesetskiy, V. A.; and Fonov, S. D.: Use of Laser Methods for the Study of Detached Flows in a Wind Tunnel and in Flight. Translated from "Scientific Notes of TsAGI-Central Institute of Aerohydrodynamics," USSR, 1981, pp. 1-19.
10. Chamberlin, R.: Flight Investigation of 24° Boattail Nozzle Drag at Varying Subsonic Flight Conditions. NASA TM X-2626, November 1972.
11. Gad-el-Hak, M.; and Blackwelder, R. F.: The Discrete Vortices from a Delta Wing. AIAA Journal, Vol. 23, No. 6, June 1985, pp. 961 and 962.

#### BIBLIOGRAPHY

Other useful papers dealing with in-flight flow visualization are listed below for completeness.

1. Roberts, S. C.; and Smith, M. R.: Flow-Visualization Techniques Used in Full-Scale Flight Tests. TRECOM Technical Report 64-39, U. S. Army Transportation Research Command, Ft. Eustis, VA., July 1964.
2. Curry, R.; Meyer, R. R., Jr.; and O'Connor, M.: The Use of Oil for In-Flight Flow Visualization. NASA TM-84915, August 1983.

ORIGINAL PAGE IS  
OF POOR QUALITY

Subsonic

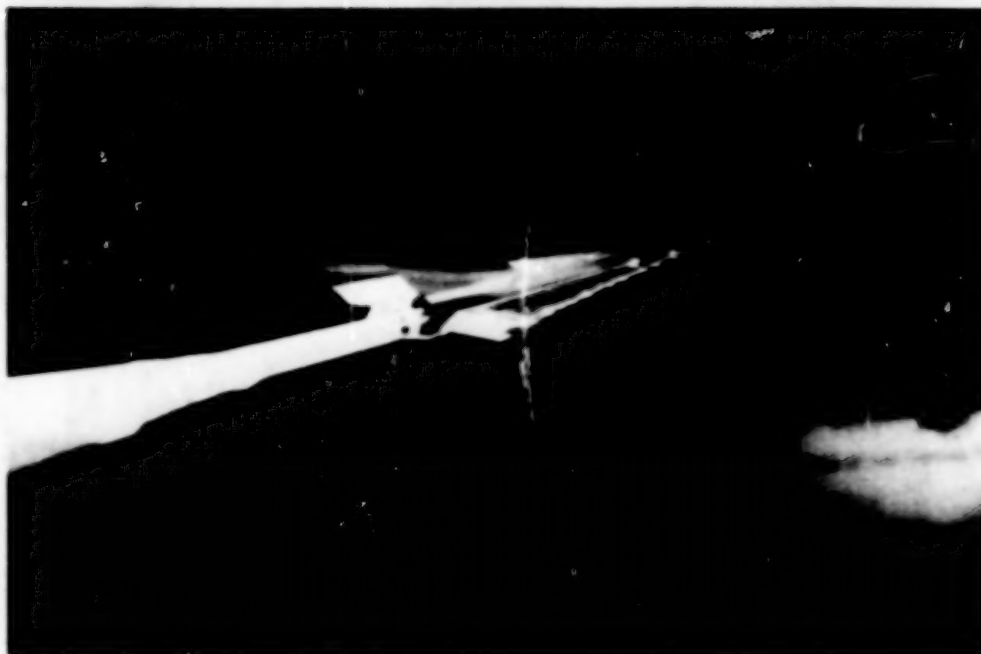


Figure 1. Leading-edge vortex core visualization on  $74^\circ$  delta with upward deflected vortex flap.



Figure 2. Strake vortex core visualization on F-16 during low-speed maneuver.

ORIGINAL PAGE IS  
OF POOR QUALITY



Figure 3. Flight project logo.

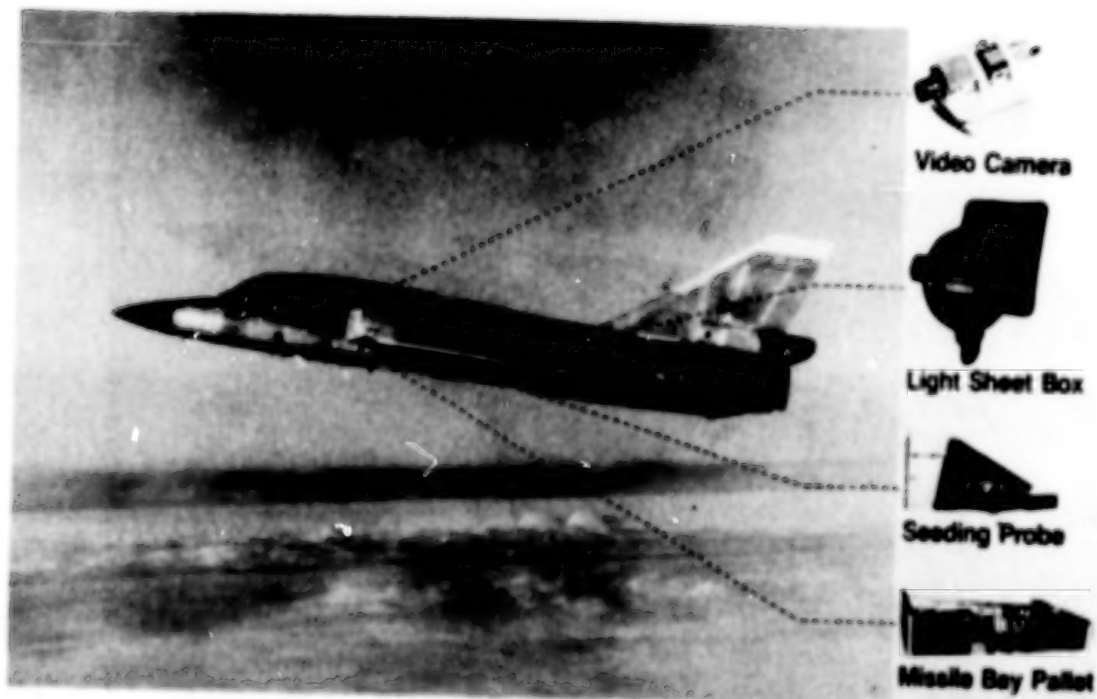


Figure 4. F-106 flow visualization elements.

- Vapor screen variables

- Seeding flow rate - (1.5  $\rightarrow$  3.6 gal/hr) 3.0 gal/hr
- Probe position - 6 tried in flight, # 6 preferred  
- many tried in wind tunnel, one preferred
- Light slit/sheet width - (.041", .012", .003") .041"
- Light sheet location - one in flight  
- two in wind tunnel

- Flight conditions

- Constant altitude 1-G decelerations - (35K, 30K, 25K, 20K, 15K, ft)  
 $M \sim .4$ ,  $\alpha \leq 23^\circ$
- Spiral descent  $\sim 5$  G, 40K, ft  $\rightarrow$  20K, ft (right and left)  
 $M \sim .8$ ,  $\alpha \sim 19^\circ$

- Wind tunnel conditions

- Mach number  $\leq .10$
- Angle of attack,  $12^\circ \rightarrow 20^\circ$
- Elevon deflection,  $15^\circ$  down  $\rightarrow 27^\circ$  up

Figure 5. Test parameters.

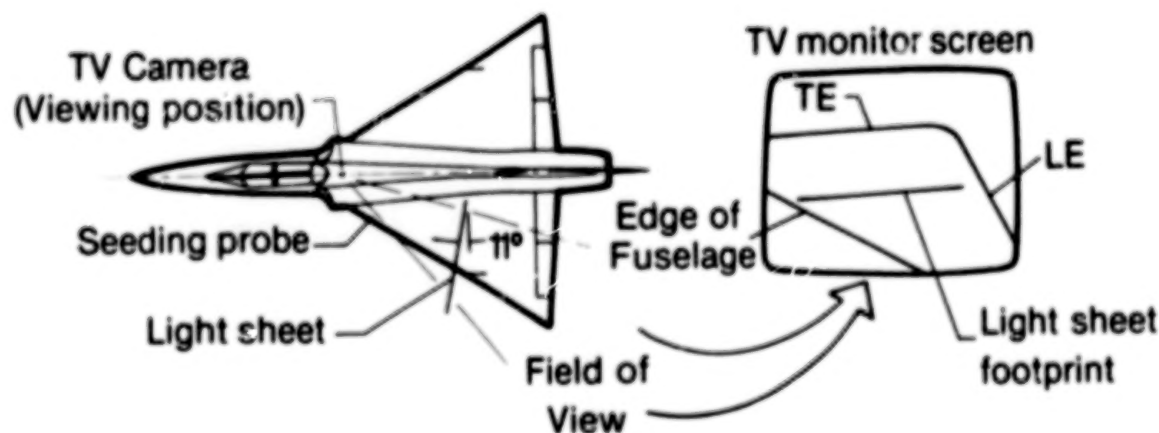


Figure 6. In-flight leading-edge vortex flow visualization on F-106B.

ORIGINAL PAGE IS  
OF POOR QUALITY

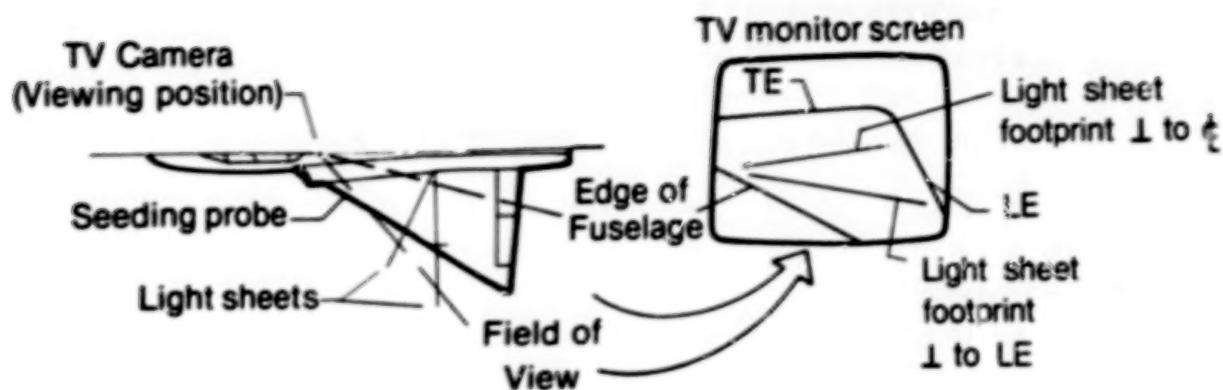


Figure 7 - Wind tunnel (30- by 60-ft) leading-edge vortex flow visualization on F-106B.

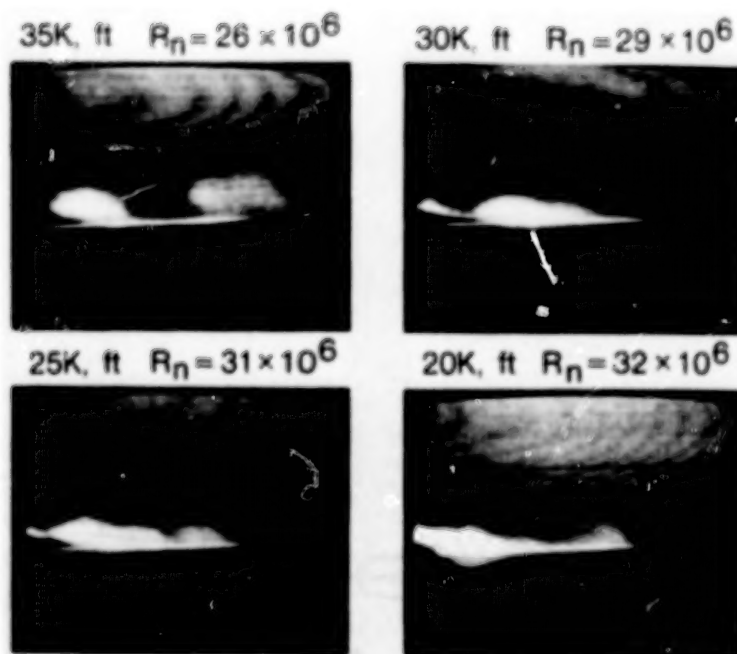


Figure 8. Effect of Reynolds number on vortex system,  $\sim 1G$ , probe #6, slit width = .041 in.,  $\alpha \sim 17^\circ$ .



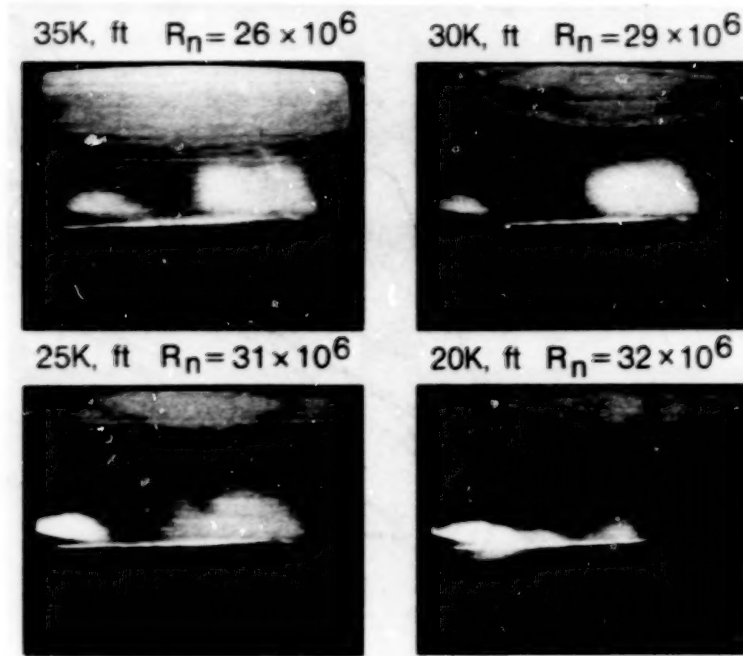


Figure 9. Effect of Reynolds number on vortex system,  $\sim 1G$ , probe #6, slit width = .041 in.,  $\alpha \sim 18^\circ$ .

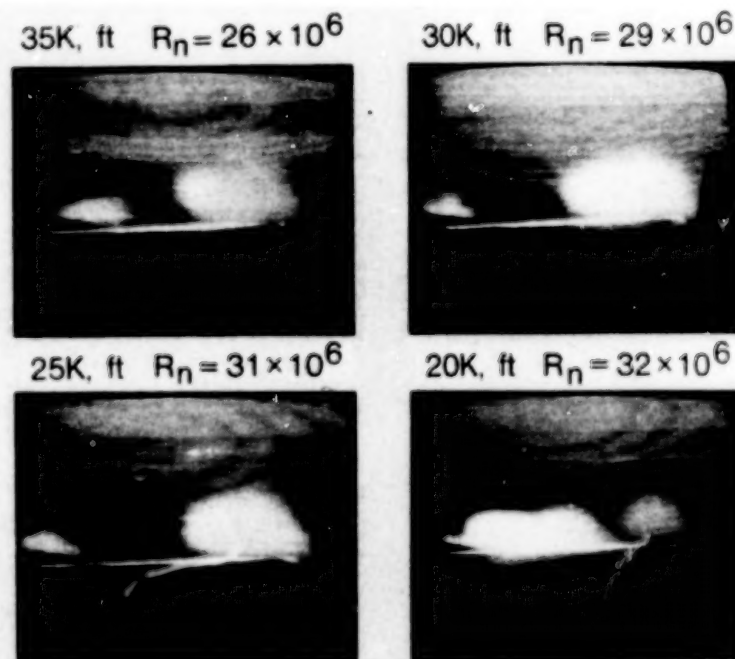


Figure 10. Effect of Reynolds number on vortex system,  $\sim 1G$ , probe #6, slit width = .041 in.,  $\alpha \sim 19^\circ$ .

ORIGINAL PAGE IS  
OF POOR QUALITY

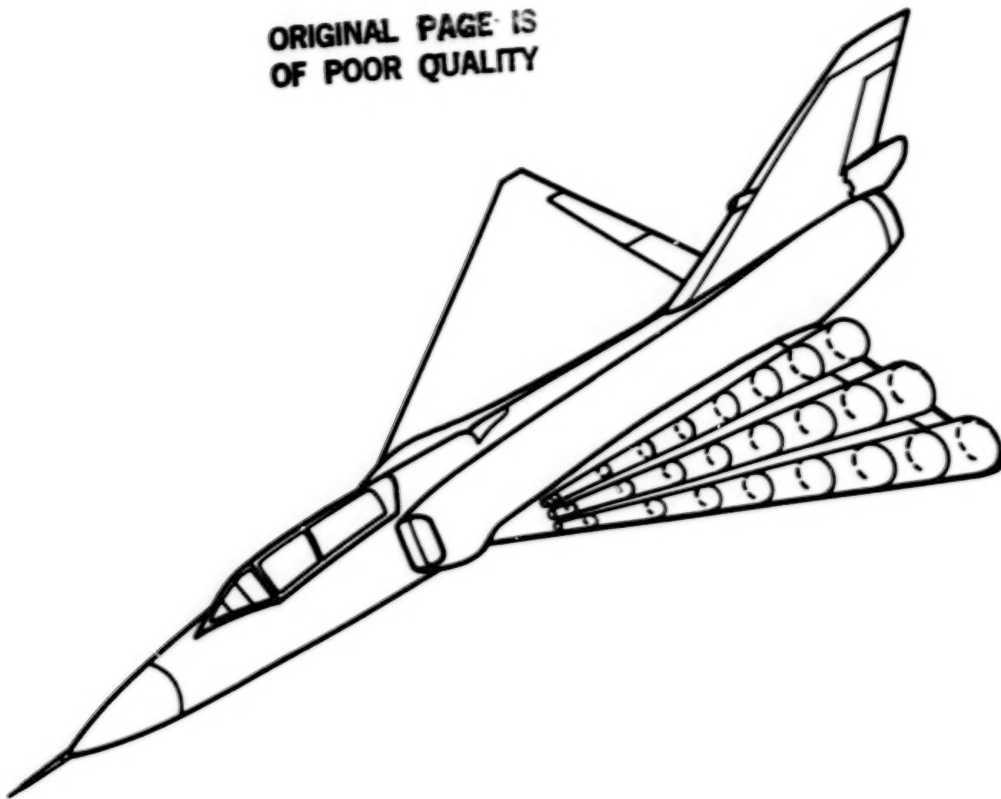


Figure 11. Multiple vortex systems on round-edged cambered delta,  
 $\alpha < 19^\circ$ , 1G.

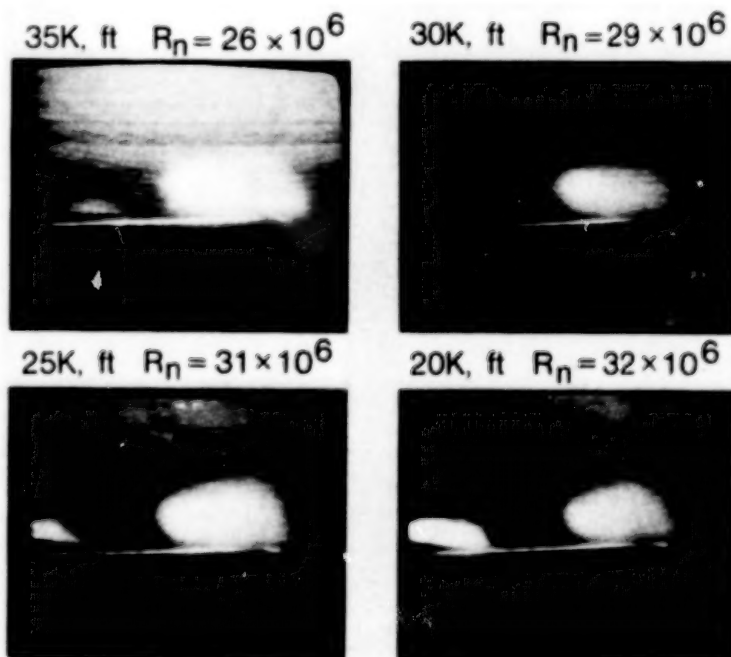


Figure 12. Effect of Reynolds number on vortex system,  $\sim 1G$ , probe #6,  
slit width = .041 in.,  $\alpha \sim 20^\circ$ .

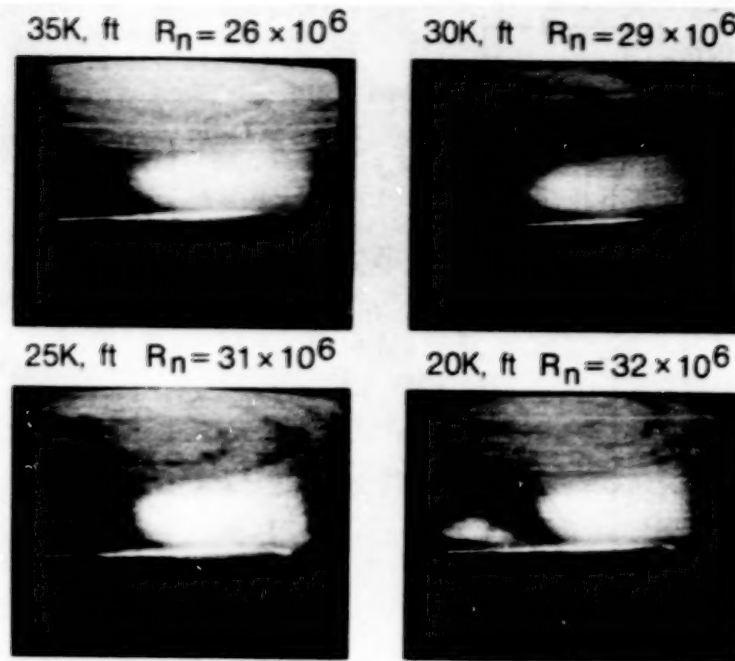


Figure 13. Effect of Reynolds number on vortex system, ~ 1G, probe #6, slit width = .041 in.,  $\alpha \sim 23^\circ$ .

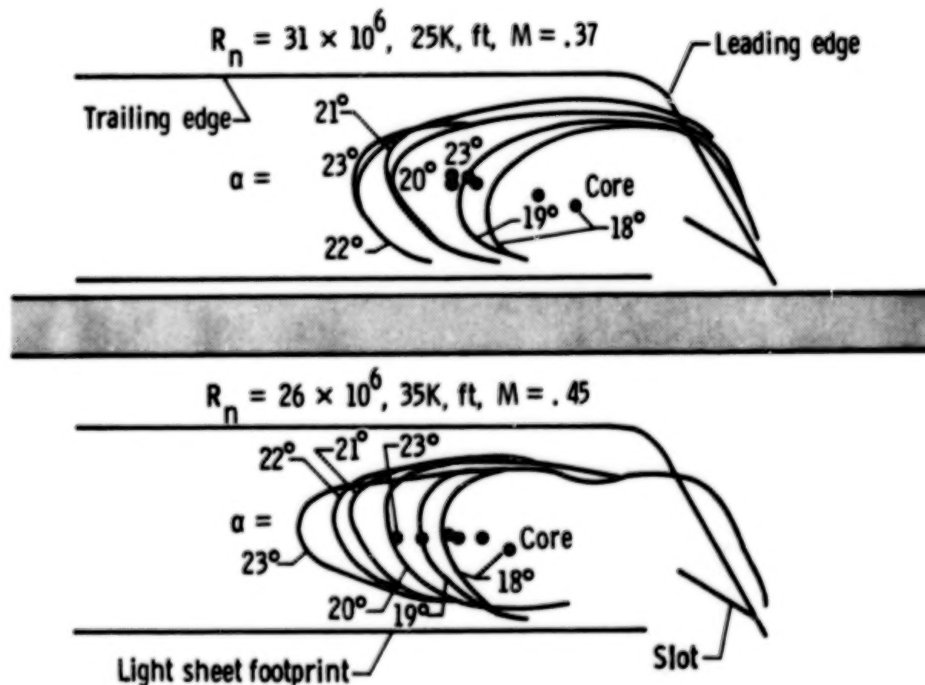


Figure 14. Effect of Reynolds number on vortex system, 1G, probe #6.

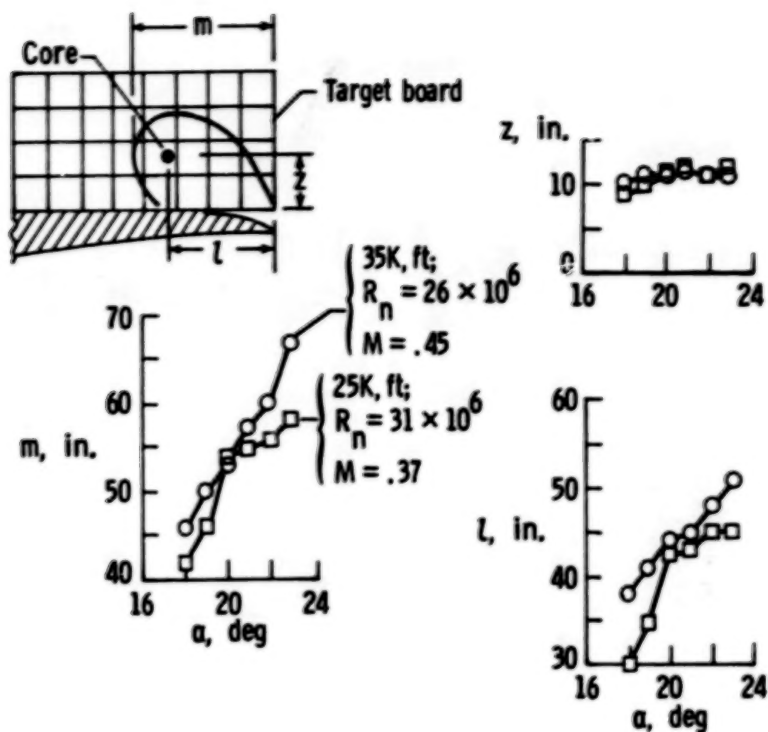


Figure 15. Measured vortex system details at two Reynolds numbers, 1G, probe #6.

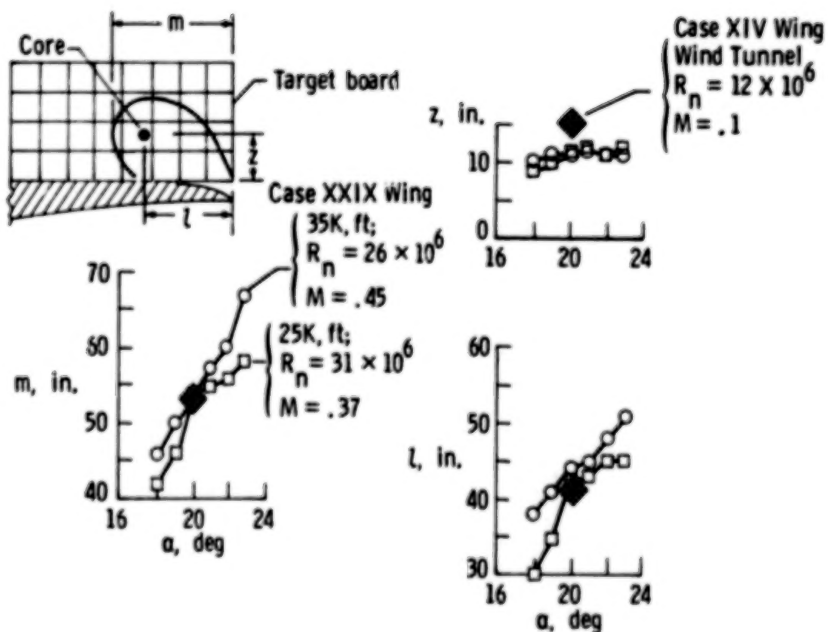


Figure 16. Measured vortex system details at three Reynolds numbers, 1G, probe #6.

ORIGINAL PAGE IS  
OF POOR QUALITY

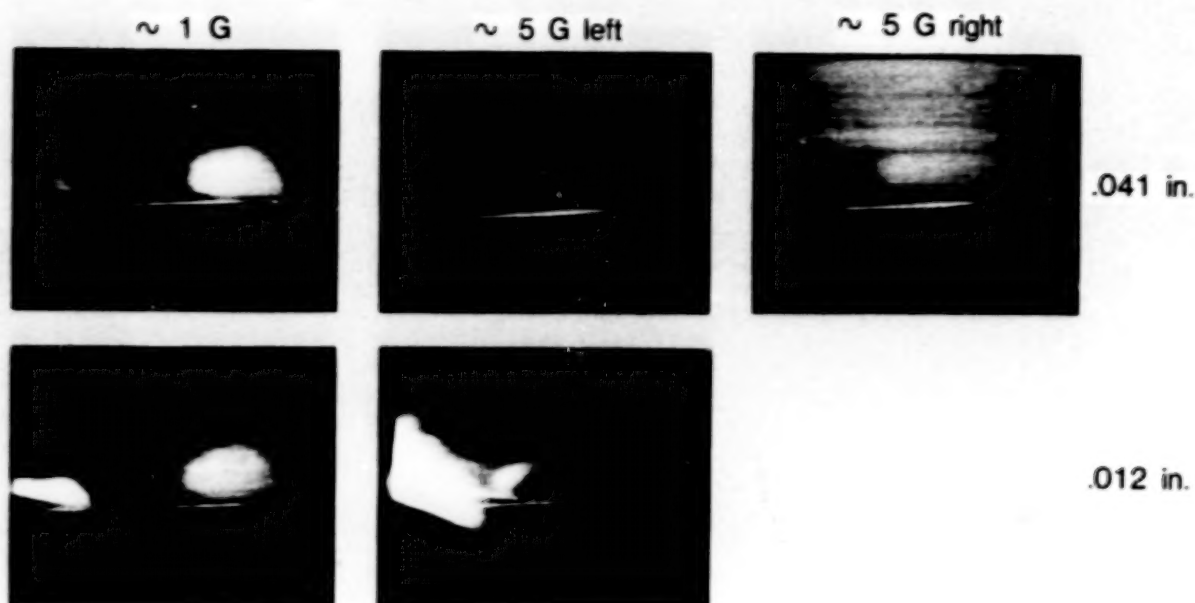


Figure 17. Vortex system details at two maneuvers and slit widths,  
 $\alpha \sim 19^\circ$ ,  $\sim 25K$  ft, probe #6.

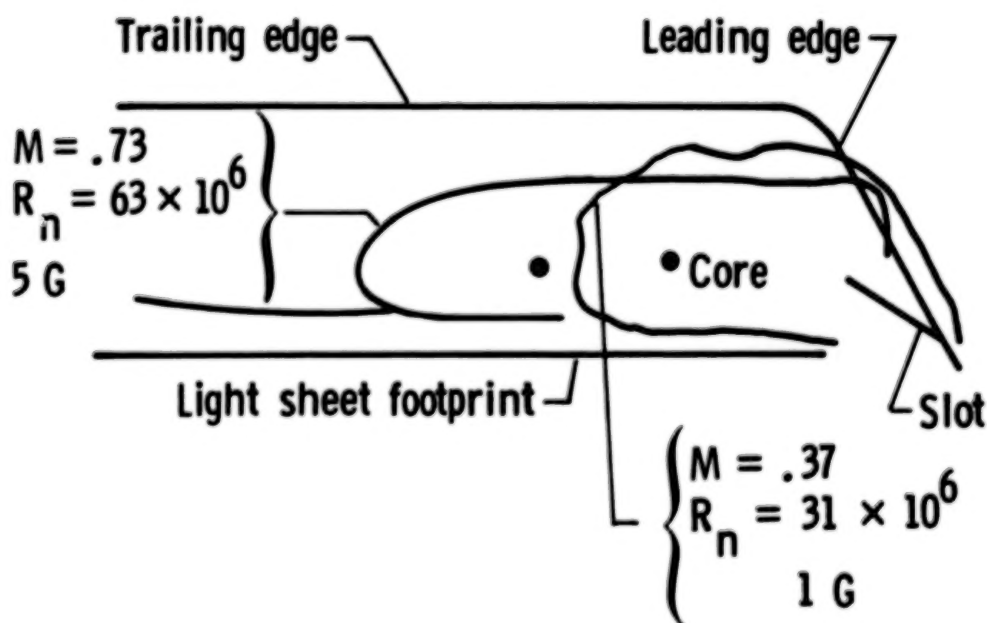


Figure 18. Effect of Mach number and load factor on vortex system,  
 $\alpha = 19^\circ$ ,  $25K$  ft.



BASIC STUDIES ON DELTA WING FLOW MODIFICATIONS

BY MEANS OF APEX FENCES

Keith D. Hoffler and Dhanvada M. Rao  
Vigyan Research Associates, Inc.  
Hampton, Virginia

Mark C. Frassinelli  
Air Force Wright Aeronautical Labs  
Wright-Patterson Air Force Base, Ohio

SUMMARY

The effectiveness of 'apex fences' on a 60-deg delta wing at low speeds has been experimentally investigated. Resembling highly swept spoilers in appearance, the fences are designed to fold out of the wing apex region upper surface near the leading edges, where they generate a powerful vortex pair. The intense suction of the fence vortices augments lift in the apex region, the resulting positive pitching moment being utilized to trim trailing-edge flaps for lift augmentation during approach and landing at relatively low angles of attack. The fences reduce the apex lift at high angles of attack, leading to a desirable nose-down moment.

The above projected functions of the apex fence device were validated and quantified through low-speed tunnel tests, comprising upper surface pressure surveys on a semi-span model and balance measurements on a geometrically similar full-span wing/body configuration. Fence parameters such as area, shape, hinge position and deflection angle were investigated. Typical results are presented indicating the apex fence potential in controlling the longitudinal characteristics of a tail-less delta.

SYMBOLS

|                  |   |
|------------------|---|
| AVERAGE CPU      | - Span-averaged CPU at local station                                    |
| CL               | - Lift coefficient, based on total wing area                            |
| CM               | - Pitching moment, based on total wing area and mean aerodynamic chord  |
| CPU              | - Upper surface pressure coefficient                                    |
| $C_R$            | - Root chord (inches)   |
| L/D              | - Lift-to-drag ratio  |
| X                | - Chordwise distance measured from apex (inches)                        |
| Y-LOC            | - Spanwise distance from root nondimensionalized by the local semi-span |
| $\alpha$ (ALPHA) | - Angle of attack (degrees)   |

- $\Delta CL\%$  -  $(CL, \text{ fence on} - CL, \text{ fence off}) / (CL, \text{ fence off}) \times 100$
- $\delta_{TE, \text{ELEVATOR}}$  - Trailing-edge flap deflection, inboard only (degrees)
- $\delta_F$  - Fence deflection (degrees)

## INTRODUCTION

The aerodynamics of pitch control and longitudinal trim of highly swept fighter configurations have received considerable attention in recent years. Close-coupled canards are currently popular because of their ability to generate powerful pitching moments and low trim drag. However, the canard downwash reduces wing efficiency, and at high angles of attack canards tend to lose pitch-down capability. The adverse interaction between canard and wing vortices in sideslip also leads to non-linearities and roll instability at high alpha (ref. 1). Unloading the canard above a critical angle of attack is made difficult by the strong upwash induced locally by the forebody and wing.

A different approach towards pitch control of highly swept wings, viz., to modulate vortex lift in the apex region, was explored in the apex flap concept (ref. 2). The appeal of this concept was the ability to undeflect the apex, for cruise flight conditions, and deflect downward for recovery from high alpha. Tests showed however that like the canard the up-deflected apex flap also generated strong downwash over the wing, and suffered a severe lift loss in the neighborhood of the transverse hinge-line. The wing-alone model tested in reference 2 also could not represent the fuselage interference which is likely to degrade apex flap effectiveness. These considerations led the second author to propose an alternate method of apex lift control, viz., the apex fence.

Resembling highly swept spoilers, the apex fences are hinged to the wing upper surface along the leading edges (fig. 1). When folded out vertically at low angles of attack, the fences generate an intense vortex pair whose suction augments lift in the apex region, resulting in a nose-up moment. Conversely, at high angles of attack the fence vortices are greatly weakened and also raised higher above the apex; the combined effect is to reduce apex lift in comparison with the basic wing, thus generating a desirable nose-down moment. The apex fences will not be subject to fuselage interference and they also avoid the adverse transverse corner of the apex flap hinge. A noteworthy advantage of apex fences is that they can be shaped and oriented for most efficient vortex-generation capability quite independently of the wing planform.

Exploratory small-scale wind tunnel investigations of the apex fence concept applied to a 74 and 65 deg delta wing have been reported in reference 3. Upper surface pressure surveys supplemented with oil flow and helium bubble visualization confirmed the existence of strong and stable vortices produced by apex fences. These promising early results encouraged a more comprehensive study of the concept applied to a 60-deg delta wing, this sweep angle being more in keeping with the current fighter design studies. This investigation was undertaken primarily to validate and quantify the hypothesized aerodynamics effects of apex fences in controlling the longitudinal characteristics of a tail-less delta through the angle-of-attack range.

## MODELS AND TEST DETAILS

### Pressure Model

Major dimensions of the generic semi-span 60 deg delta wing body model are shown in figure 2. This model incorporated four spanwise rows of pressure taps, the first row being well inside the apex region occupied by the fence. The model was mounted on a boundary layer bypass plate seven inches above the tunnel floor. Six fence shapes were tested on this model, only two shapes being presented herein (fig. 3). The test was conducted in the North Carolina State University Merrill Subsonic Wind Tunnel at a mean-aerodynamic-chord Reynold's number of 0.67 million, and angles of attack ranging from zero to 30 deg.

### Force Model

Major dimensions of the force model are shown in figure 4. This model was geometrically similar to the pressure model and was fitted with four trailing-edge flaps. Only the inboard flap segments were deflected during the present tests. A total of eleven fence shapes were investigated, some at different mounting positions on the wing and some in asymmetric arrangement. Eight of the fences, all in symmetric configuration and mounted along the leading edge, are discussed herein. The fence shapes and their respective areas are presented in the figures with the results. Unless otherwise noted the fence deflection is 90 deg (i.e., perpendicular to the wing plane). The test was conducted in the Air Force Institute of Technology 5-Foot subsonic wind tunnel at a mean-aerodynamic-chord Reynolds number of 1.11 million. The sting was mounted in two alternate positions, giving a low (-6 to 30 deg) and a high (20 to 45 deg) angle-of-attack range.

## RESULTS AND DISCUSSION

### Pressure Results

Typical spanwise distributions resulting from vertical apex fences placed at the leading edge of the delta wing will be examined at a constant angle of attack of 10 deg (representative of the 'low-alpha' range). The Gothic (18.7 percent area) fence (fig. 5) results in broadening of the vortex suction footprint at the first two pressure stations (A and B), and a significant increase of the span-averaged local -CPU above the basic wing value with the load center shifted inboard. At the downstream stations (C and D) the spanwise distribution is similarly altered but the average -CPU is somewhat reduced. The Delta (11.7 percent area) fence (fig. 6) produces more accentuated suction peaks while the vortex footprints in this case are not as broad as with the Gothic fence. Nevertheless, the resulting -CPU average is practically equal with both fence configurations. At the aft station, the pressure fields due to the Gothic and Delta fences are almost identical.

The longitudinal variation of -CPU AVERAGE presented in figure 7 clearly shows the augmented apex suction due to both fences at  $\alpha = 10$  deg. Just the opposite effect is evident at  $\alpha = 30$  deg (representing the high-alpha case), when the apex suction is reduced below the basic wing value. Accordingly, a nose-up moment increment at low alpha and a nose-down effect at high alpha are to be expected due



to fence deployment, as postulated. This trend was encountered in varying degrees with all the fence configurations tested.

### Oil-Flow Study

Typical oil-flow photographs of the basic wing and the wing with the delta fence on at  $\text{ALPHA} = 9.5$  deg on the force model are presented in Figure 8. In this comparison, the oil streaks in the apex region are longer and more highly curved in a spanwise direction, indicating a significantly stronger vortex with the fence on. An inboard shift of the fence vortex is evident downstream and a separate leading-edge vortex appears, as observed in the foregoing pressure results.

### Balance Results

The Gothic and Delta fences studied on the semi-span pressure model were initially tested on the balance model. The lift and pitching moment characteristics are compared with the basic model in figure 9. The lift increment due to fences in the low-alpha range is evident, as is the nose-up pitching moment anticipated from the foregoing pressure results. Between the two fence shapes compared, the Gothic generates higher pitching moment increments; however, since this fence was also nearly 60 percent larger in area than the Delta, it was decided to study the area effect in some detail on these two fence shapes.

The original Gothic fence area was reduced serially in two steps: the height was reduced at constant length, and then the length was shortened. The result of height reduction (fig. 10) shows virtually no change in lift characteristics and a relatively small reduction in moment; length reduction results in a visible drop in lift and a more pronounced reduction in the pitching moment.

The Delta fence was cut in length in two successive steps. The results (fig. 11) show a roughly proportional drop in lift as well as pitching moment in the low-alpha range, the moment increments narrowing towards higher angles of attack.

To obtain a broader picture of the effect of fence area, the lift increments with various fence configurations at a constant angle of attack of 12 deg, with and without trailing-edge flap deflection for trim, are compared with the basic model (or fence-off case) in figure 12. Included in this comparison is a Double-Gothic fence shape, in which the rear half was tapered down to zero width. Most of the fences increased the untrimmed lift, with the exception of the smallest fences in each shape family which showed a lift loss at this angle of attack. However, all fences irrespective of size and shape produced marked increases in the trimmed lift due to down-deflected trailing-edge flaps (as indicated by the blackened portion of the bars). Generally, reduction of fence area also reduced the trimmed lift increment.

In an attempt to separate out the fence shape and area effects on the trimmed lift capability, the incremental lift at  $\text{ALPHA} 12$  deg is plotted versus fence area ratio for the three shape families in figure 13. An almost linear increase of trimmed lift coefficient with fence area is evident, an outstanding exception being the large Double-Gothic fence. Note that the smaller Double-Gothic fence was not geometrically similar, having a convex aft taper in contrast to a concave taper of the larger Double Gothic. While the present data are quite inadequate to draw conclusions regarding the Double-Gothic fence, their potential as an area-efficient fence shape is worthy of further investigation.

As already mentioned, the vortex load on the apex fences produces a drag component. While drag increment in combination with lift augmentation is a desired feature during approach and landing, it is of interest to examine the aerodynamic efficiency of apex fences as a trimming device. This may be done by comparing the L/D at a constant lift coefficient with and without the fences (see Table 1). The corresponding trailing-edge flap deflections for trim and angle of attack are also given. Because the basic delta wing requires an up-deflected trailing-edge flap to trim with a positive static margin, the angle of attack must be increased to obtain the same lift coefficient. In contrast, fence deployment allows a down deflection of trailing-edge flap for trim and therefore the angle of attack can be reduced for the same approach speed. For example, the Gothic fence provided a nearly 6 deg reduction in angle of attack from  $\text{ALPHA} = 18$  deg of the basic delta. The consequent wing drag reduction compensates for the fence drag to a large extent, as indicated by the relatively small decrease in L/D.

The foregoing results pertained to vertically deployed apex fence, i.e.  $\delta f = 90$  deg; in practice, the hinged fences may be actuated to a smaller or a larger angle. The effect of varying fence deflection on either side of 90 deg is presented in figure 14 for the case of the large Double-Gothic fence. The results indicate that the fence angle controls the pitching moment in an almost linear fashion.

In some tests the high-alpha range was explored to observe the apex fence effect on pitching moment. A typical result is shown in figure 15 using Gothic fences, where a reversal of the longitudinal moment is evident at high angles of attack. Thus the apex fence can be viewed as a natural alpha-limiting device.

### CONCLUSIONS

Exploratory low-speed wind tunnel investigations were conducted to evaluate the effects of apex fences on a 60 deg delta wing/body configuration. An initial test program surveyed upper surface pressures on a semi-span model including the apex region between the fences, followed by balance measurements on a geometrically similar full-span model with trailing-edge flaps. The scope of the investigation covered varying fence shape, area and deflection angles.

The apex fences produced opposite effects over the wing apex region in the low-alpha and high-alpha regimes. At low angles of attack fence vortices augmented the suction level over the apex, whereas at high angles of attack the apex suction was reduced from the basic wing case. Balance data showed corresponding lift increase together with a nose-up pitching moment at low alpha, and lift loss with a nose-down moment at high alpha.

In combination with down-deflected trailing-edge flaps, fences in the low alpha range produced marked increases in the trimmed lift capability of the configuration. The trimmed lift increment was essentially proportional to fence/wing area ratio in case of Gothic and Delta fences. An exception was the Double-Gothic fence of 8.8 percent area, which indicated an area efficiency almost twice as high as the others.

Varying fence deflection angle (on either side of the nominal 90 deg position) was found to control the pitching moment in an almost-linear fashion, showing the apex fence to be a promising pitch moment control and trimming device. The effectiveness of asymmetric fence deployment in lateral and directional control is currently being evaluated.



## REFERENCES

1. Wedekind, G.: Tail Versus Canard Configuration, An Aerodynamic Comparison with Regard to the Suitability for Future Tactical Combat Aircraft. ICAS Proc. 1982, pp. 247-254.
2. Rao, D. M. and Buter, T. A.: Experimental and Computational Studies of a Delta Wing Apex Flap. AIAA Paper No. 83-1815, July 1983.
3. Wahls, R. A., Vess, R. J. and Moskovitz, C. A.: An Experimental Investigation of Apex Fence Flaps on Delta Wings. AIAA Paper No. 85-4055, October 1985.

## ACKNOWLEDGMENTS

This research was supported by the Air Force Flight Dynamics Laboratory, Wright-Patterson AFB, under contract No. FY1456-85-00032. Considerable assistance was received from Lt. Mike Stuart and Capt. Chris Smith, graduate students of the Air Force Institute of Technology (AFIT), which is greatly appreciated. The authors also extend their gratitude to AFIT for the use of a model, the 5-ft Tunnel Facility and associated personnel.

Table 1

TRIMMED  $C_L = 0.82$

| <u>FENCE TYPE</u> | <u>AREA RATIO<br/>FENCE / WING</u> | <u><math>\delta_{TE, ELEVATOR}</math></u> | <u>L/D</u> | <u>ALPHA</u> |
|-------------------|------------------------------------|---|------------|--------------|
| FENCE OFF         | ----                               | -2.1°                                     | 2.92       | 17.9°        |
| GOTHIC FENCE      | 18.7 %                             | 26.8°                                     | 2.21       | 12.0°        |
| DELTA FENCE       | 11.7 %                             | 14.7°                                     | 2.64       | 14.0°        |

APEX FLAP (RAO, BUTER, 1983)

APEX FENCE

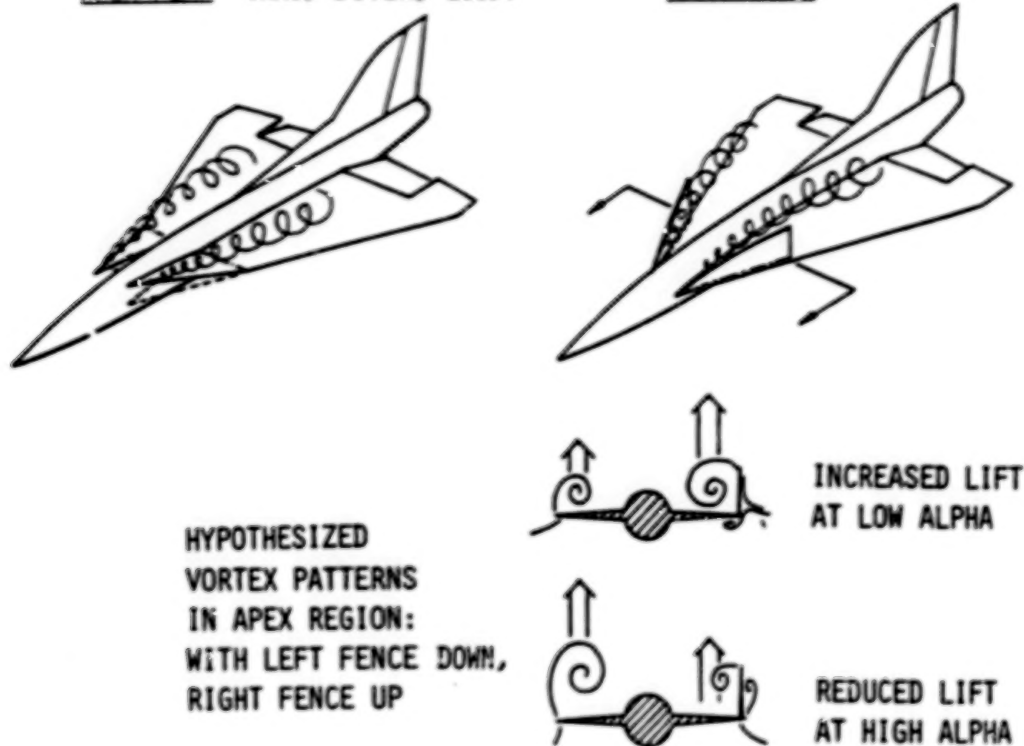


Fig. 1. Apex fence concept.

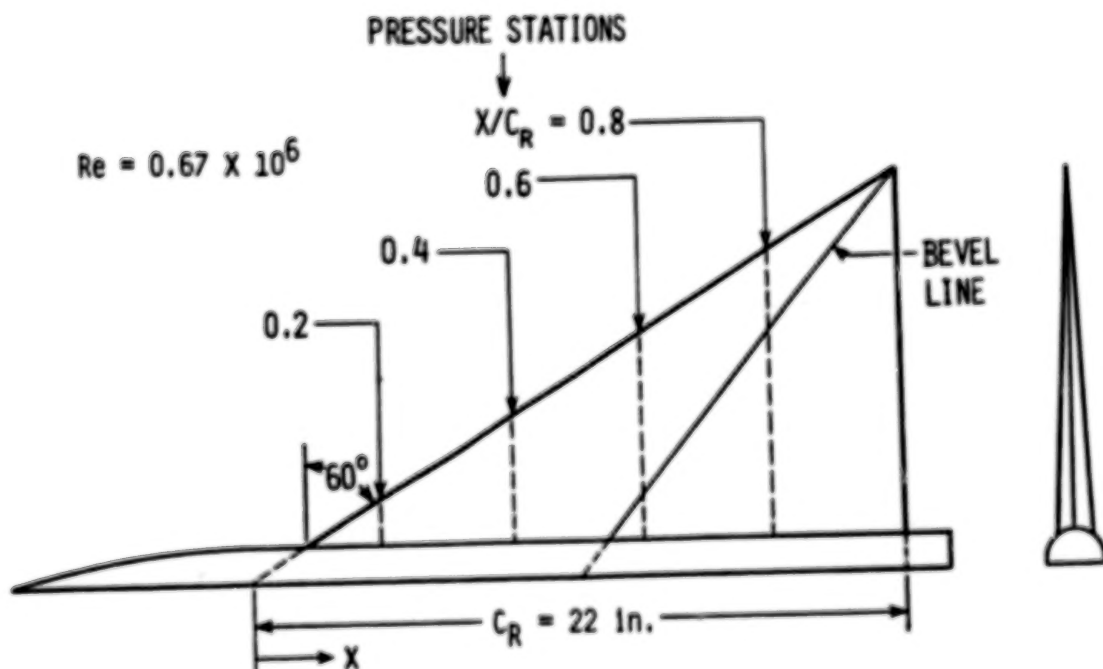


Fig. 2. 60-deg delta semi-span pressure model.

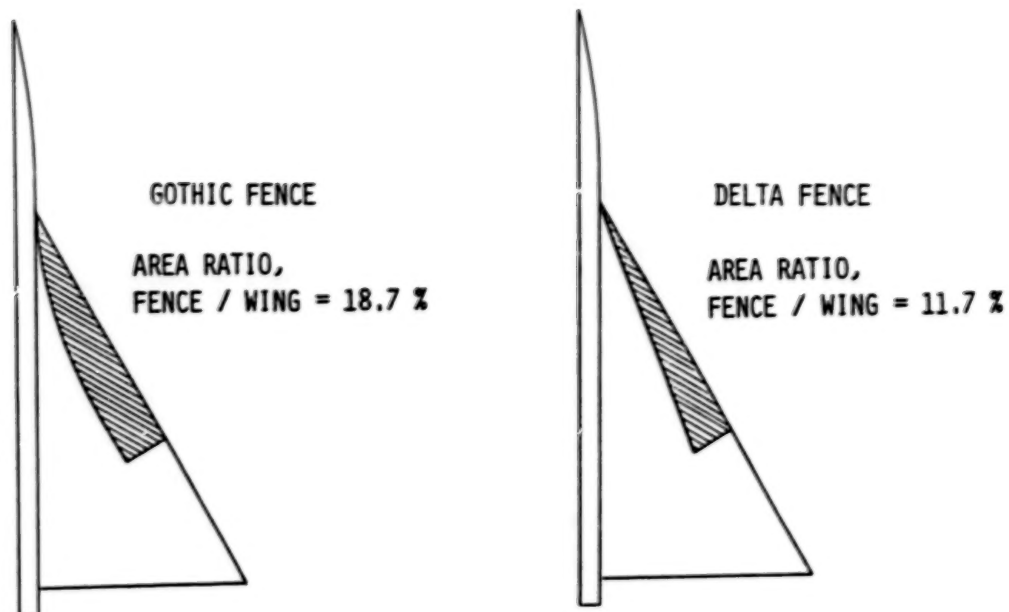


Fig. 3. Typical fence shapes tested on semi-span delta model.

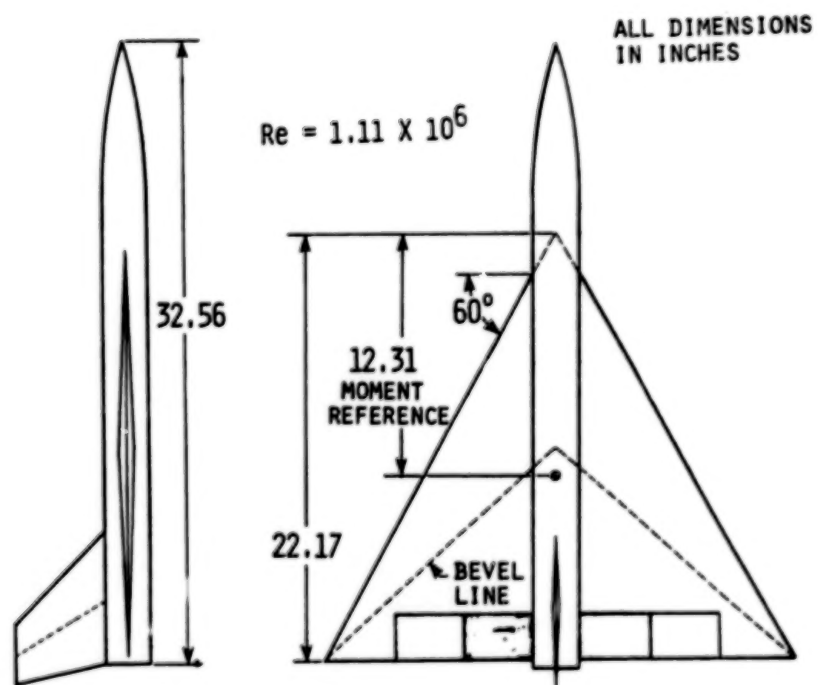


Fig. 4. 60-deg delta full-span force model.

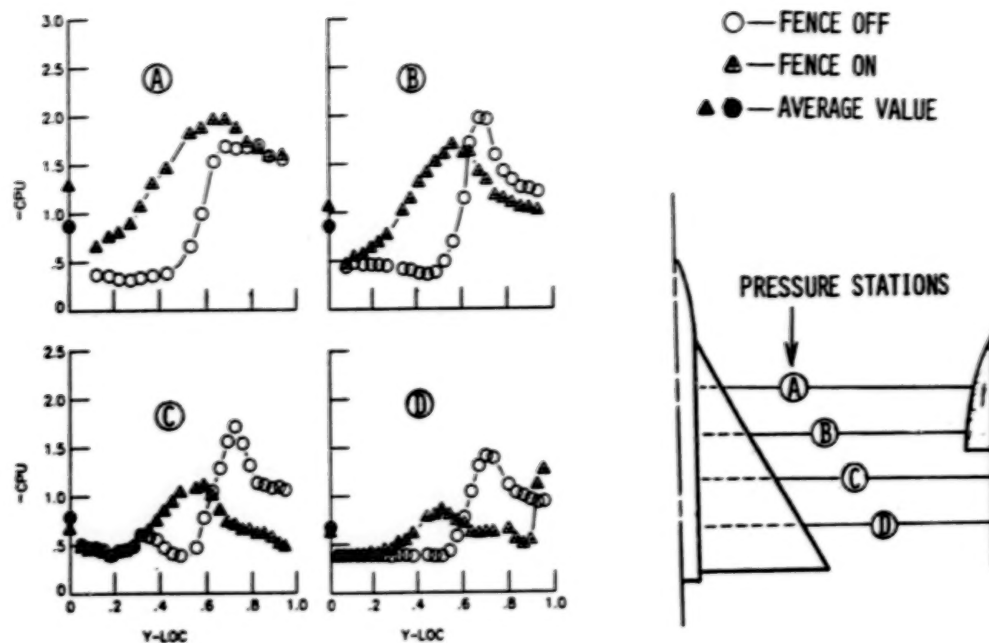


Fig. 5. Spanwise upper surface pressure distributions at 10 deg alpha with gothic fence.

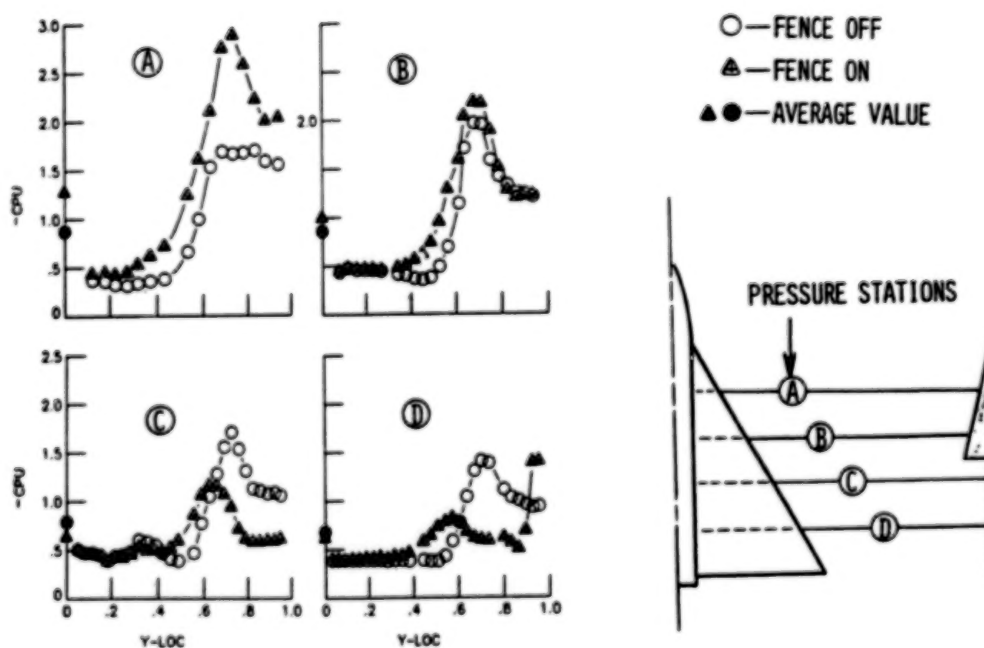


Fig. 6. Spanwise upper surface pressure distributions at 10 deg alpha with gothic fence.



ORIGINAL PAGE IS  
OF POOR QUALITY

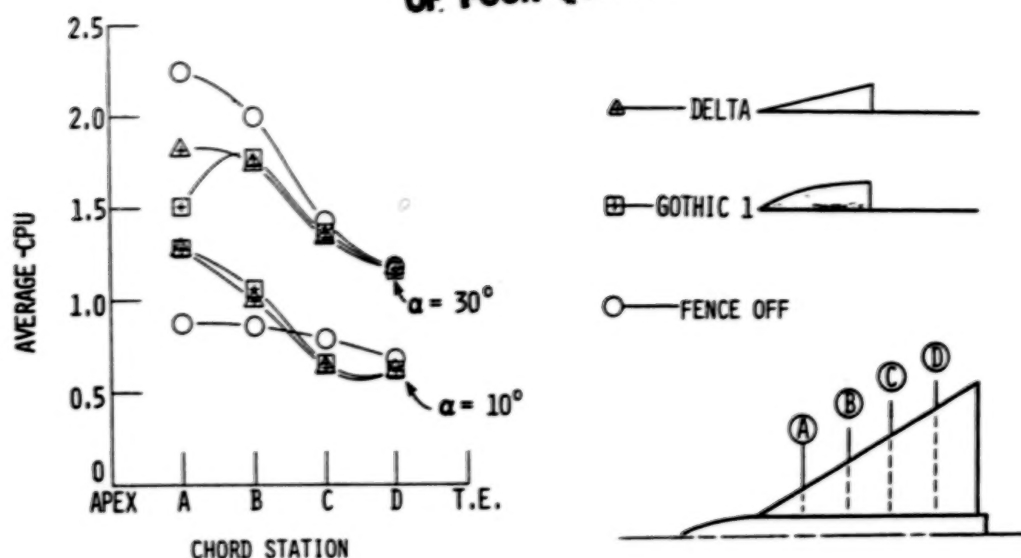


Fig. 7. Longitudinal distributions of span-averaged upper surface pressure coefficients.

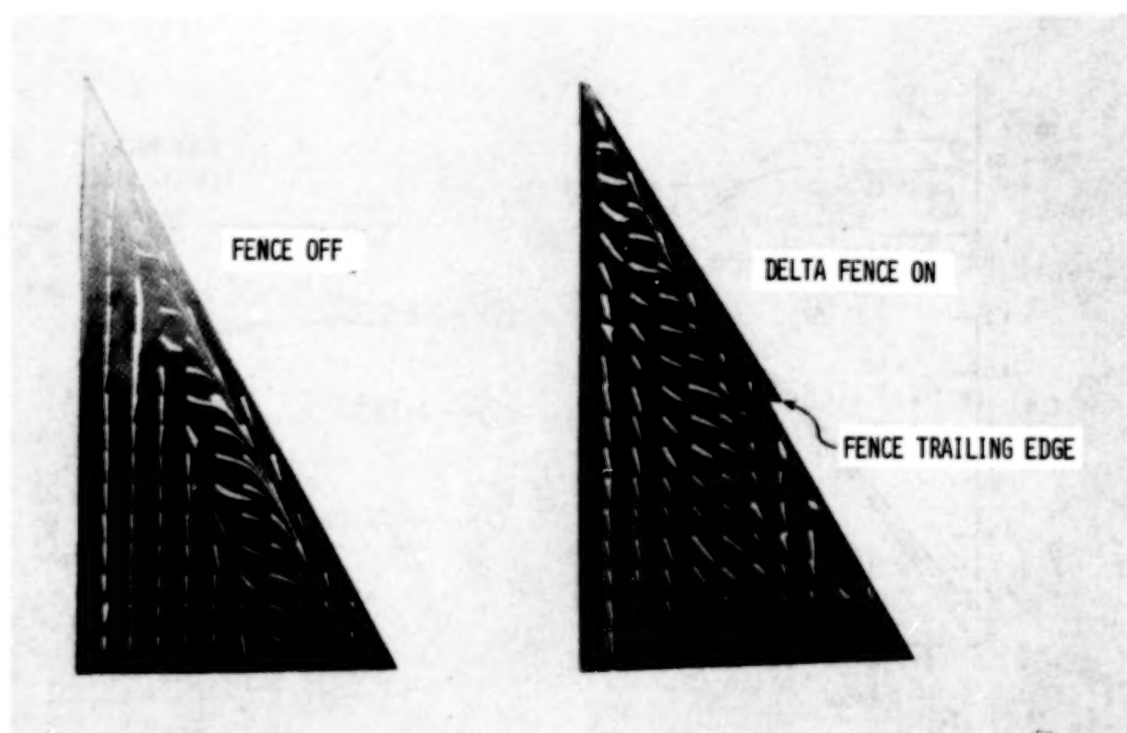


Fig. 8. Typical oil-flow patterns on force model, showing fence effect at 95 deg  $\alpha$ .

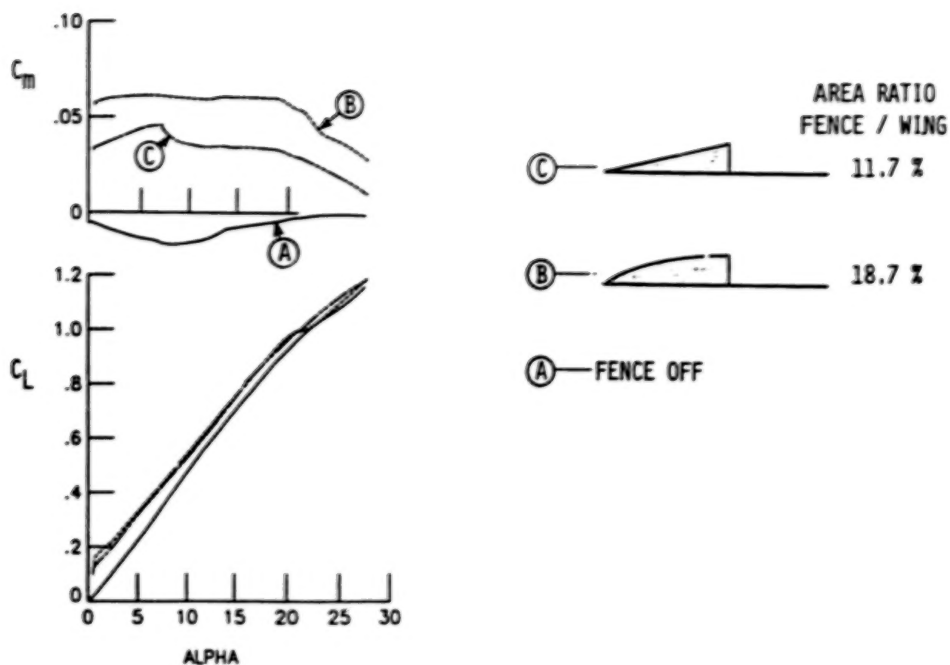


Fig. 9. Lift and pitching moment effects of longest delta and gothic fences.

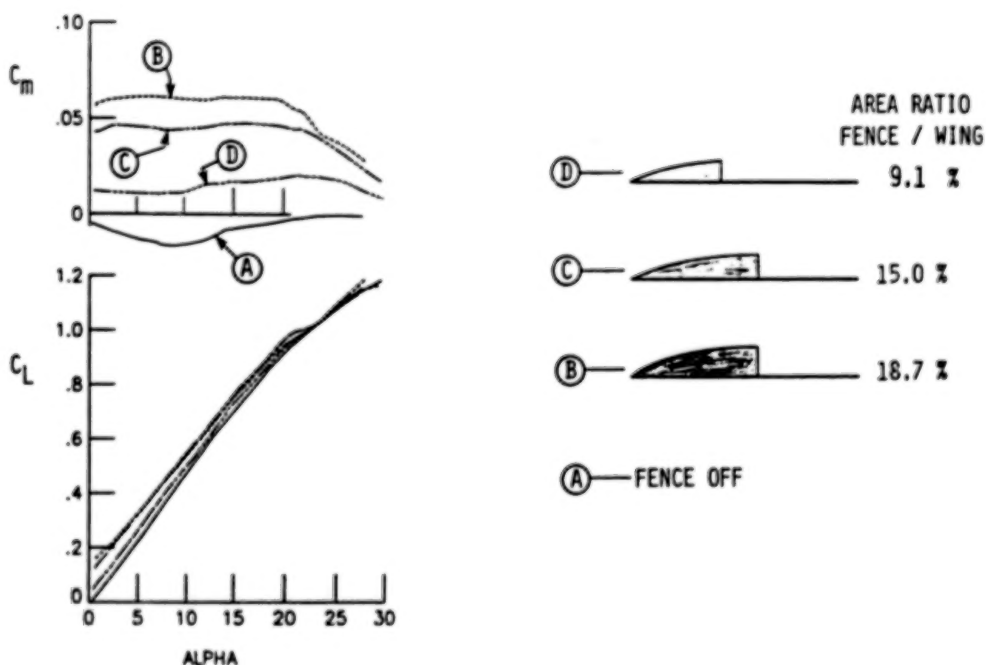


Fig. 10. Lift and pitching moment effects of gothic fence variations.

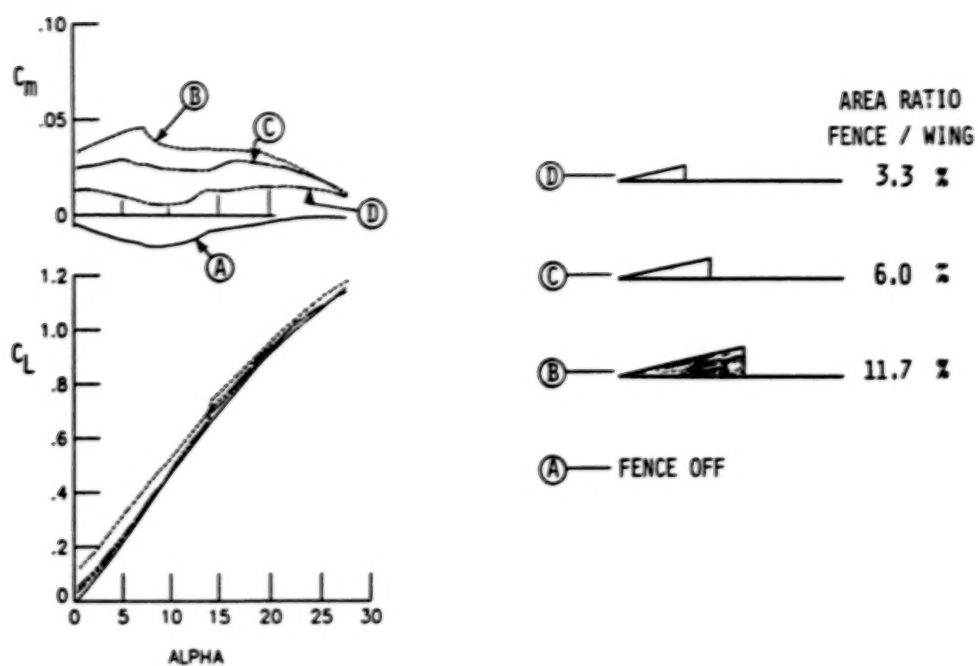


Fig. 11. Lift and pitching moment effects of delta fence variations.

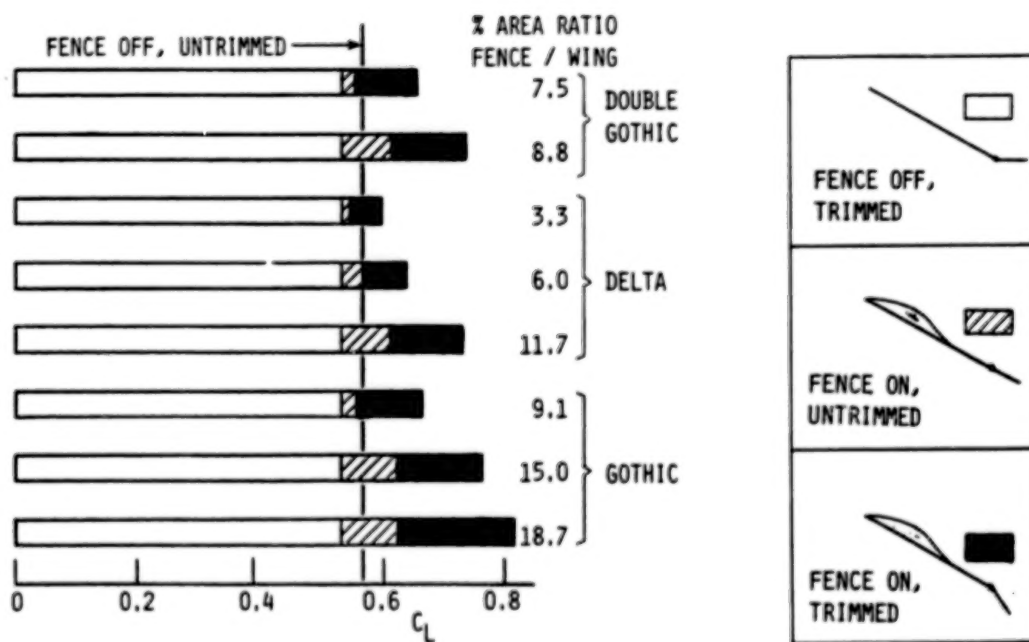


Fig. 12. Trimmed and untrimmed lift increments due to various fences at 12 deg alpha.

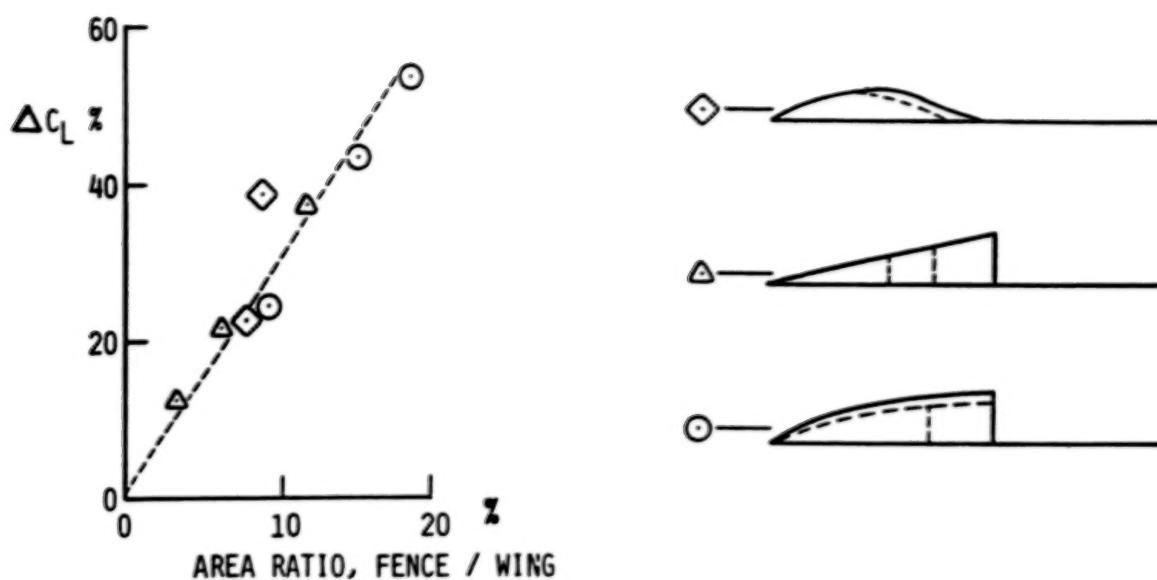


Fig. 13. Fence area effect on trimmed lift increment at 12 deg alpha.

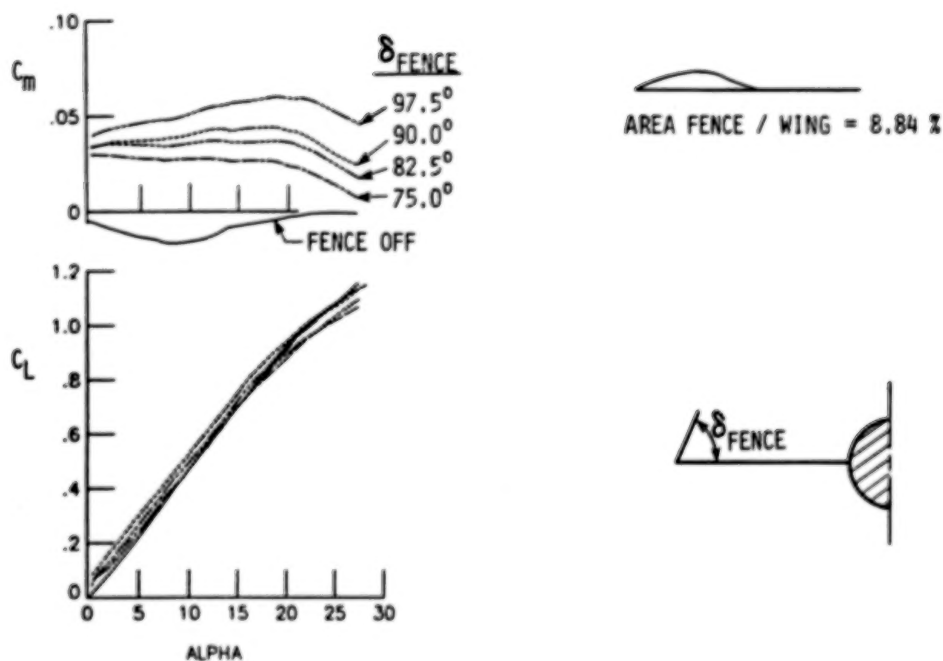


Fig. 14. Lift and pitching moment effects of fence deflection.

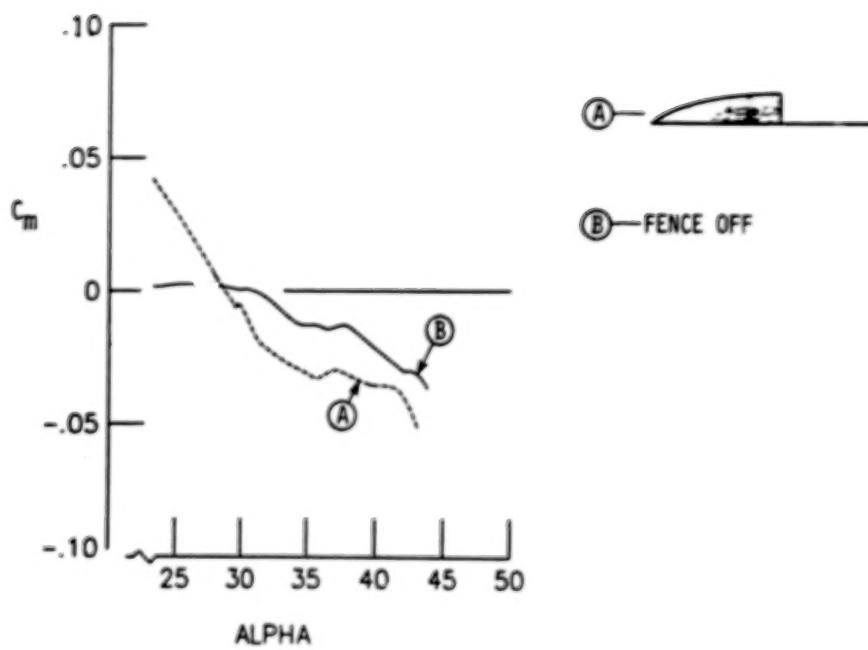


Fig. 15. Fence effect on pitching moment at high alphas.



**TOWARDS AN ADVANCED VORTEX FLAP SYSTEM - THE "CAVITY" FLAP**

Dhanvada M. Rao  
Vigyan Research Associates, Inc.  
Hampton, Virginia

**SUMMARY**

An extension of the vortex flap concept was explored with the aim of providing high-alpha flight control capability coupled with maneuver drag reduction for highly swept wing configurations. A retractable lower surface flap mounted on a translating hinge is proposed, allowing chordwise extension as well as deflection, the two movements being independently controlled. The frontal cavity formed by the partially extended and deflected flap captures a vortex above a certain angle of attack. The cavity vortex downwash alleviates the effective incidence of the wing leading edge, thus modulating vortex lift; at the same time, the induced suction in the cavity generates thrust. These postulated aerodynamic features of the cavity flap were validated through low-speed tunnel pressure and visualization tests on a 65 deg swept oblique wing model, which also provided initial trends of the leading edge vortex alleviation and cavity suction with respect to flap extension, deflection and angle of attack. Force tests on a 60 deg delta model further showed the cavity flap L/D performance to compare favorably with the conventional vortex flap. A two-segment flap arrangement with independently controlled segments was envisaged for exploiting the vortex modulation capability of the cavity flap for pitch, roll and yaw control, in addition to drag reduction at high angles of attack.

**INTRODUCTION**

The first wind tunnel demonstration of the vortex flap concept took place nearly seven years ago (ref. 1). The extensive experimental and theoretical research carried out since then (ref. 2) has concentrated on the application of vortex flap thrust recovery for drag reduction of highly swept wings at maneuver lift coefficients. Recent design studies related to advanced fighters have underlined the need to extend aerodynamic control effectiveness to increasingly high angles of attack. Accordingly there is considerable interest in evaluating vortex management ideas for improved high-alpha control.

Effective aerodynamic control of highly swept, slender vehicles at high angles of attack basically requires the ability to modify the onset, growth and shedding characteristics of large-scale vortices originating from forebody and wing leading-edge separation, and thereby to rapidly modulate the vortex lift and reposition its point of action relative to c.g. Although vortex lift modulation capability has been shown to be inherent to the vortex flap concept, its potential has not yet been explored in detail. This paper discusses an advanced vortex flap system, called the cavity flap, conceived for the purpose of obtaining high-alpha control as well as

**PRECEDING PAGE BLANK NOT FILMED**

00275 - 884

drag reduction from the same set of aerodynamic surfaces. Some results are presented of low-speed wind tunnel experiments undertaken to verify the aerodynamic basis of the cavity flap and to compare its drag reduction performance with that of a conventional vortex flap.

### CAVITY VORTEX FLAP

The conventional (or leading-edge) vortex flap aims to contain the vortex and its peak suction over the flap (fig. 1). Drag reduction then is a combined result of thrust recovery on the forward-sloping flap and reduced suction on the aft-sloping wing surface.

With increasing alpha the flap frontal projected area decreases and its direct contribution to drag reduction tends to zero. A 30-deg deflected flap on a 60-deg delta wing, for example, becomes essentially aligned with free-stream at 14 deg angle of attack (or  $C_L \approx 0.65$ ), beyond which it is the re-attached flow on the wing rather than the flap vortex force that yields a drag reduction.

If the flap hinge were to be moved some distance aft of the leading edge under the wing and a vortex trapped in the resulting cavity, the frontal area under vortex suction can be largely recovered. The leading-edge overlap now covers a large part of the flap plan area and therefore reduces its own vortex lift contribution. This cavity flap arrangement promises a substantial vortex lift modulation capability by independently varying the flap projection and deflection at a given angle of attack. In the limit, an optimum cavity vortex leading to a fully attached flow on the wing will essentially eliminate vortex lift. Additional cavity flap advantages envisioned are its applicability to sharp or blunt leading edges, plus a structurally superior attachment to the wing in comparison with the leading-edge hinged flap.

Figure 2 suggests a practical implementation of the cavity flap. The retracted flap is fully conformal to the wing lower surface contour. The flap hinge slides on internal tracks, the extension and deflection angle being actuated independently. Pure extension of the flap projects a sharp edge which can be used to augment vortex lift on blunt leading-edge wings (ref. 3). Partial extension plus deflection yields the cavity flap configuration. At the forward limit of extension the flap functions essentially as a conventional vortex flap. At a large deflection angle with the hinge at its aft limit, a vortex will form behind the flap, making it an effective drag brake.

### OBLIQUE WING TESTS

The key hypothesis underlying the cavity flap concept, namely the capture of a stable cavity vortex and its use to modulate vortex lift on the wing, was tested on a highly swept oblique wing model (fig. 3). The variable-sweep oblique wing was chosen to facilitate future study of the sweep-angle effect on the cavity vortex stability. In the initial tests reported here, however, the wing was set at the maximum sweep of 65 deg.

The wing section perpendicular to leading edge was a 12-percent thick, conventional subsonic type airfoil with a flat undersurface. Two chordwise pressure

stations were incorporated in the wing, one on the fore panel and one on the aft panel. At each station, taps were provided on the upper surface and over the first 15 percent chord on the lower surface.

A constant chord, flat plate flap was tested on the forward wing panel. Three deflection angles (10, 20 and 30 deg), and three hinge positions at each angle including the leading-edge position, were investigated. The tests were carried out in the North Carolina State Subsonic Tunnel at a free-stream velocity of 100 fps.

The vortex characteristics of oblique wings are not well known. Therefore, the oblique wing model was first tested with flap off in order to establish its suitability for evaluating the cavity flap. Figure 4 shows typical oil-flow and pressure distribution results. The oil pattern at  $\alpha = 16$  deg reveals independent leading-edge vortices on the fore and the aft wing panels. The upper surface pressures at four angles of attack (10, 12, 14 and 16 deg) show the evolution of the vortex suction peak. Comparison of the fore and aft pressure stations with increasing angle of attack shows the forward wing vortex to develop continuously, whereas on the aft wing the suction peak is gradually smeared out due to the locally thickened boundary layer (resulting from a spanwise outflow as on a swept-back wing). These tests showed that the fore panel of the oblique wing generated a leading-edge vortex flow representative of swept wings, thus providing a proper aerodynamic environment for validation of the cavity flap concept.

Typical flap effects on the forward wing pressures at an angle of attack 16 deg will now be discussed. Figure 5 shows the effect of moving the flap hinge forward with the flap angle held constant at 20 deg. The sketches on the right interpret the corresponding vortex patterns.

At the aft hinge position, the flap hardly affects the upper surface suction characteristics; on the lower surface, however, an increased suction suggests that a cavity vortex is already formed. No change in vortex lift due to flap deployment can be expected in this case although some drag reduction should be obtained.

Moving the flap hinge to the mid-position is seen to produce a marked reduction in the vortex suction on the wing upper surface. At the same time, the cavity suction is almost doubled. This position of the flap appears to come close to the postulated cavity vortex flow with attached flow on the wing. Substantial lift reduction can therefore be anticipated in this case, together with enhanced drag-reduction.

At the leading-edge position of the flap the vortex appears to be partly spilled onto the wing. Due to the fully exposed flap area in this case, lift reduction on the wing is likely to be largely compensated by the vortex lift on the flap. The drag reduction capability will be degraded due to the negligible frontal area projected by the flap.

The pressure results in figure 6 show the effect of increasing flap angle at a constant hinge position. A progressive decrease in the vortex suction on the wing upper surface is noted. There is little change in the cavity suction level with increasing flap angle; however, since the associated frontal area is increasing, the drag reduction should improve.

By integrating the upper surface pressures a local normal force coefficient is obtained. This upper surface normal force directly reflects the changes in the



vortex suction characteristics and is therefore useful for presenting the trends with respect to flap angle and hinge line position. It is seen in figure 7 that, at all three flap angles, a forward extension of cavity flap results in progressive and marked reduction in the wing normal force at angles of attack above 8 deg.

Typical cavity suction characteristics are shown in figure 8 for the mid-position of the flap hinge. Also shown for reference is the pressure at the same lower surface tap with the flap off. It is evident that with increasing flap angle, the onset of cavity vortex is delayed. At higher angles of attack, however, all three flap angles approach the same cavity suction levels.

#### 60-DEG DELTA FORCE TEST

Force measurements to evaluate the cavity flap were conducted on a 60-deg delta model (fig. 9) during a brief investigation in the NASA Langley 12-Foot Low-Speed Tunnel. The object of these initial tests was to compare the drag reduction capabilities of leading-edge flap and cavity flap at constant flap angles of 20 deg and 40 deg.

The leading-edge thrust due to a flap is most sensitively indicated in the balance axial force component. Figure 10 plots the axial force versus normal force coefficients and includes the flap-off data for reference. The vertical gap between the flap-on and flap-off data (i.e. a negative  $\Delta C_A$ ) indicates the aerodynamic thrust attained. At 20 deg flap angle, the cavity flap is seen to generate more thrust than the leading-edge flap throughout the  $C_N$  range. At 40 deg deflection, the onset of cavity vortex is delayed to a higher angle of attack, and as a result the cavity flap begins to show an advantage only above  $C_N = 0.6$ .

Figure 11 presents the corresponding drag reductions. On the left is absolute  $\Delta C_D$  and on the right,  $\Delta C_D$  as a percentage of the basic drag (i.e. flap off). It is noted that the 40-deg cavity flap advantage appears at higher angles of attack when the percentage drag reduction has already peaked and is rapidly declining. It is reasonable to expect therefore that a more moderately deflected cavity flap (say at 30 deg) might be advantageous in the region of peak percentage drag reduction. Note also that the hinge line position remains to be optimized in combination with flap deflection, which should yield additional improvement in the cavity flap performance.

Since both the leading edge and cavity flaps produce reductions in lift as well as in drag, the final evaluation must be in terms of L/D ratio as a function of lift coefficient. Figure 12 shows the 20-deg cavity flap to be advantageous across  $(L/D)_{max}$ . The 40-deg cavity flap evidently is over-deflected, but catches up with the leading-edge flap at  $C_L = 0.7$  and thereafter yields the same L/D improvement. The L/D results again suggest that flap angles between 20 and 40 deg deserve investigation and that a coordinated study of hinge-line position should also be conducted.

#### CAVITY FLAP FOR HIGH ALPHA CONTROL

It is interesting to speculate on the ways of exploiting the vortex lift modula-

tion capability of the cavity flap for high-alpha control (fig. 13). A spanwise segmented cavity flap system is envisaged with two segments per leading edge, each flap segment being under independent control. For maximum drag reduction, all four flap segments will be deployed; the attendant loss in vortex lift is proposed to be compensated by the use of a trailing-edge flap. By deploying the inner segments only, the vortex lift forward of the c.g. will be reduced thus generating a nose-down moment for accelerated recovery from high alpha. When both segments are deployed on the right leading edge only, the excess of vortex lift prevailing on the left wing panel will produce a right roll. At the same time, a side force component towards the right will be generated by the flap thrust, favorable in a right turn. The inner left and outer right segments deployed at their maximum thrust setting will develop a nose-left yawing moment. Not included in this figure is the additional use of the cavity flap for aerodynamic braking at low angles of attack.

### CONCLUSIONS

A cavity vortex flap has been postulated in which the forward extension and deflection are independently controlled to allow vortex lift modulation while producing thrust.

The cavity vortex postulate was verified on a 65-deg oblique wing, demonstrating alleviation of the leading-edge vortex effect on the wing and generation of cavity suction through a range of flap extension, deflection and angle of attack.

Balance tests on a 60-deg delta wing indicated that the cavity flap was at least equal to the conventional leading-edge flap in L/D improvement and could be better with optimized combinations of extension and deflection. High-alpha pitch, roll and yaw control possibilities of the cavity flap concept, as well as its effectiveness as a drag brake, should be evaluated in future investigations.

### REFERENCES

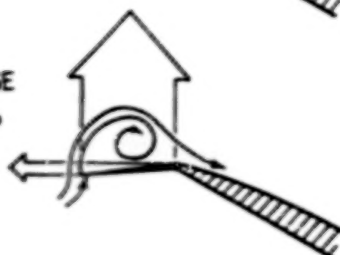
1. Rao, Dhanvada M.: Leading Edge Vortex Flap Experiments on a 74 Deg Delta Wing. NASA CR-159161, Nov. 1979.
2. Campbell, James F. and Osborne, Russell F.: Leading-Edge Vortex Research: Some Nonplanar Concepts and Current Challenges. Vortex Flow Aerodynamics - Volume I, NASA CP-2416, paper no. 2, 1986.
3. Rao, Dhanvada M. and Johnson, T. D., Jr.: Investigation of Delta Wing Leading Edge Devices. J. Aircraft, Vol. 18, No. 3, pp. 161-167, March 1981.



PLAIN LEADING EDGE



LEADING EDGE  
VORTEX FLAP



CAVITY VORTEX FLAP

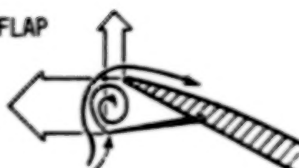
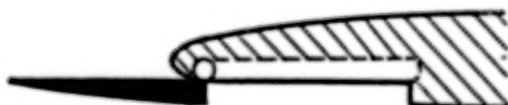


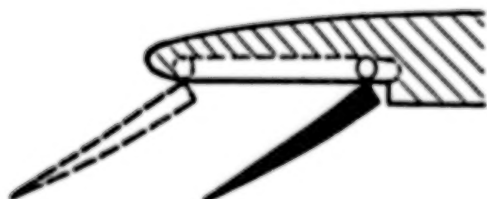
Figure 1 The cavity vortex flap concept.



FLAP RETRACTED  
CONFORMAL WITH LOWER SURFACE



PURE EXTENSION  
AS A 'SLEE'



EXTENSION PLUS ROTATION:  
'CAVITY' FLAP

Figure 2 Cavity flap arrangement with independent extension and rotation.

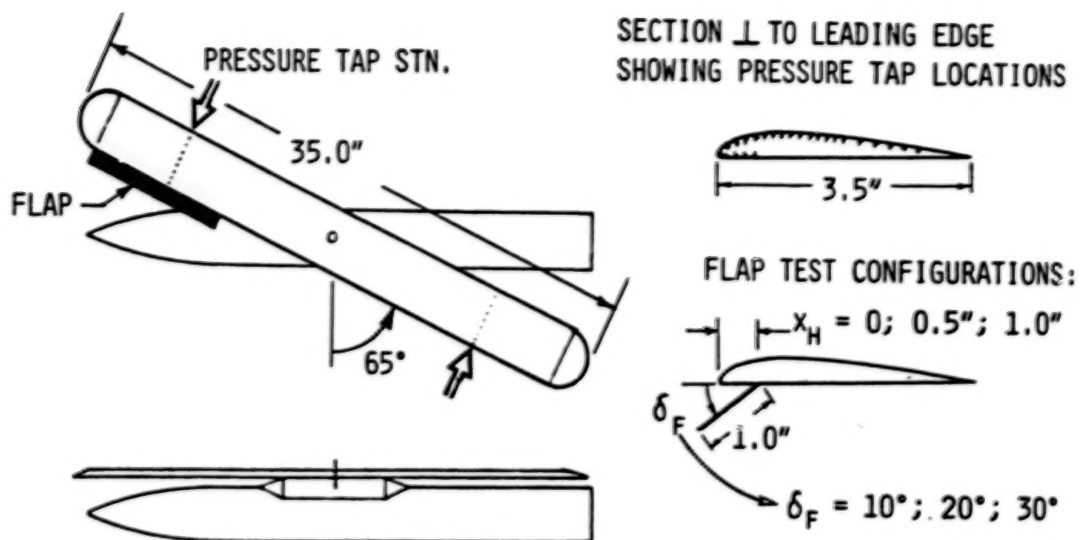


Figure 3 Oblique wing model tested in North Carolina State University Subsonic Wind Tunnel.

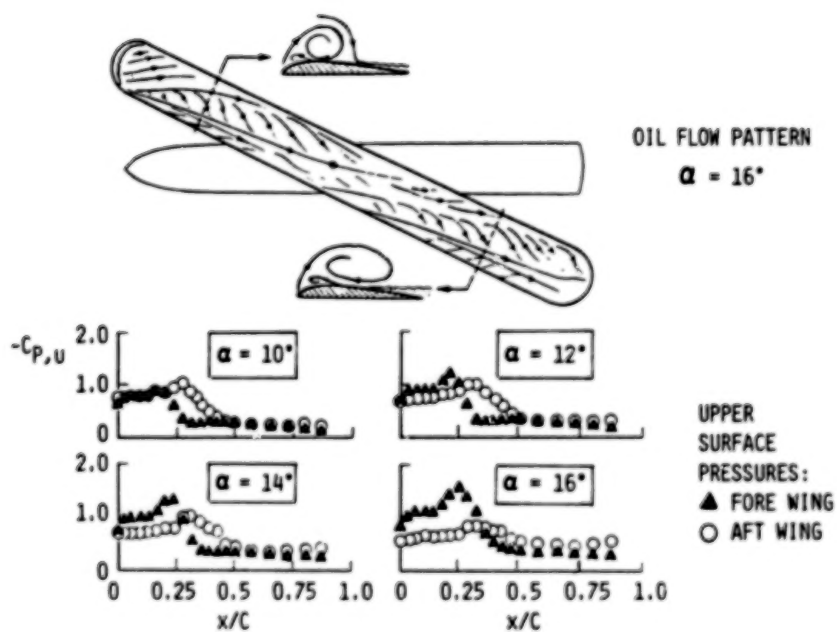


Figure 4 65-deg oblique wing flow and pressure characteristics with flap off.

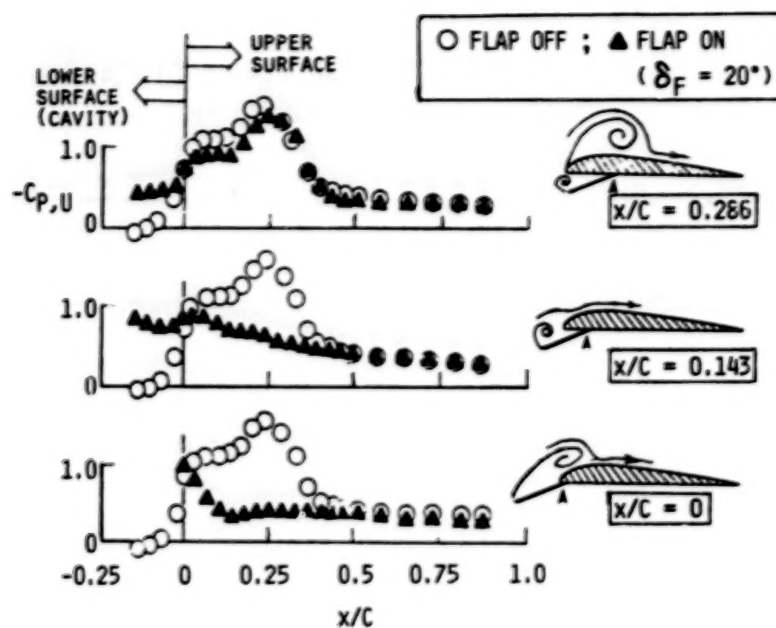


Figure 5 Pressure distributions showing effect of flap hinge position at 16-deg angle of attack.

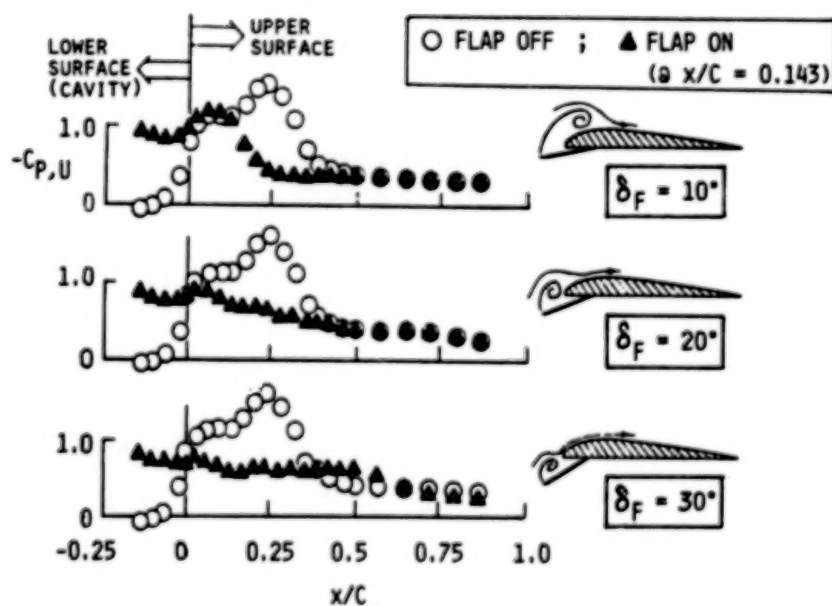


Figure 6 Pressure distributions showing effect of flap angle at 16-deg angle of attack.

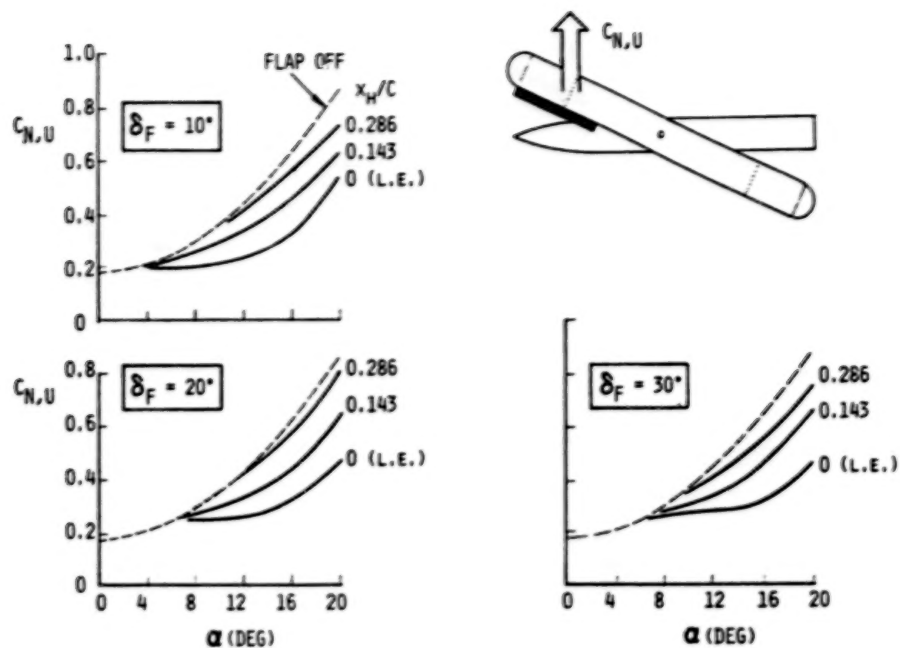


Figure 7 Pressure-integrated upper surface normal force characteristics.

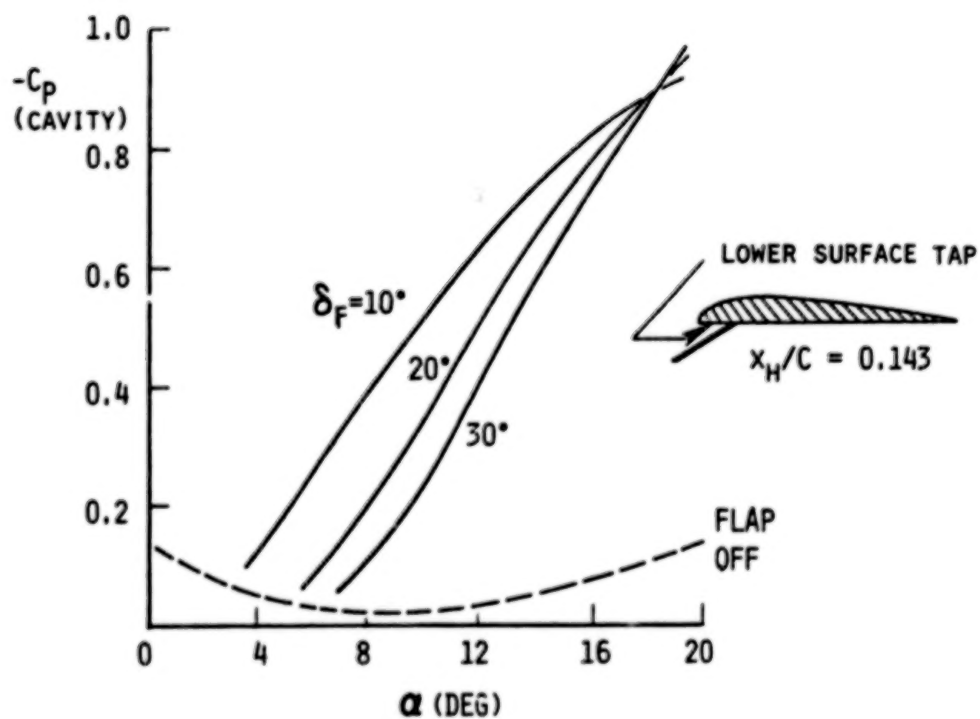


Figure 8 Cavity suction characteristics showing effect of flap angle.

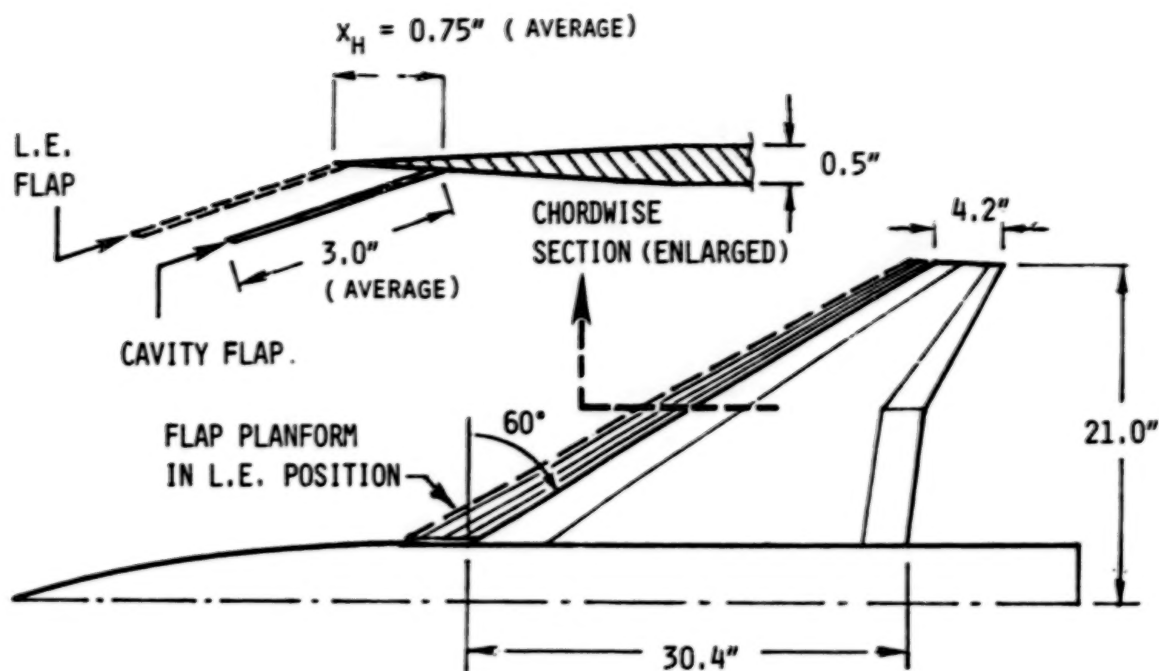


Figure 9 60-deg delta wing axial versus normal force characteristics.

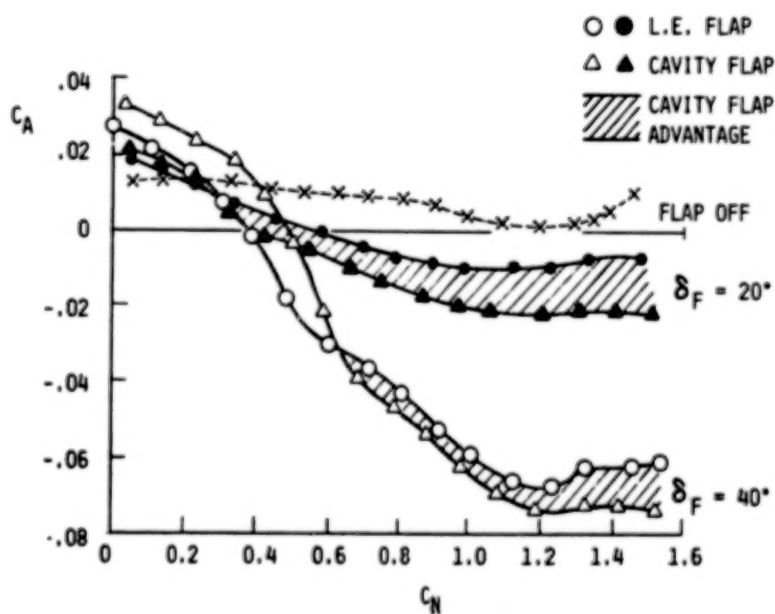


Figure 10 60-deg delta wing drag reduction with leading-edge and cavity flaps.



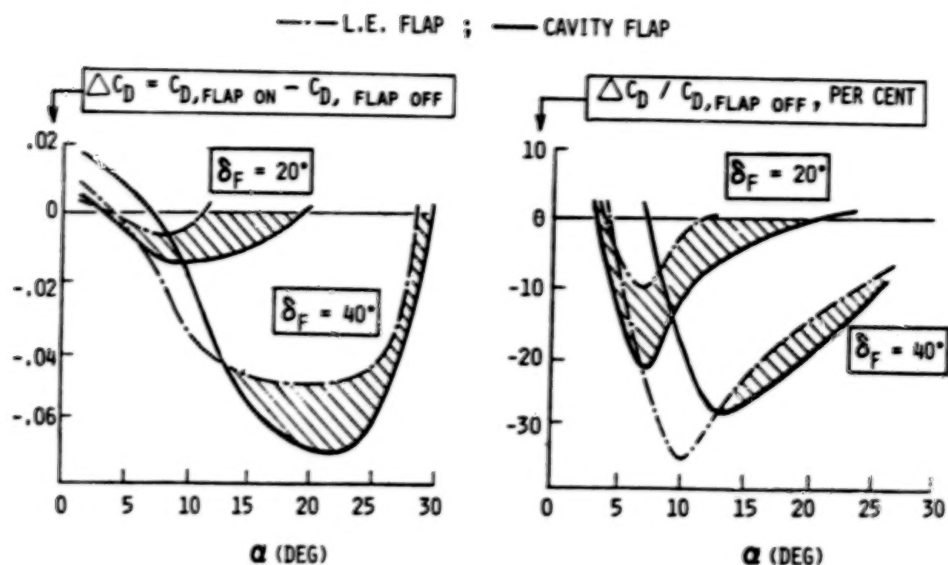


Figure 11 60-deg delta wing drag reduction with leading-edge and cavity flaps.

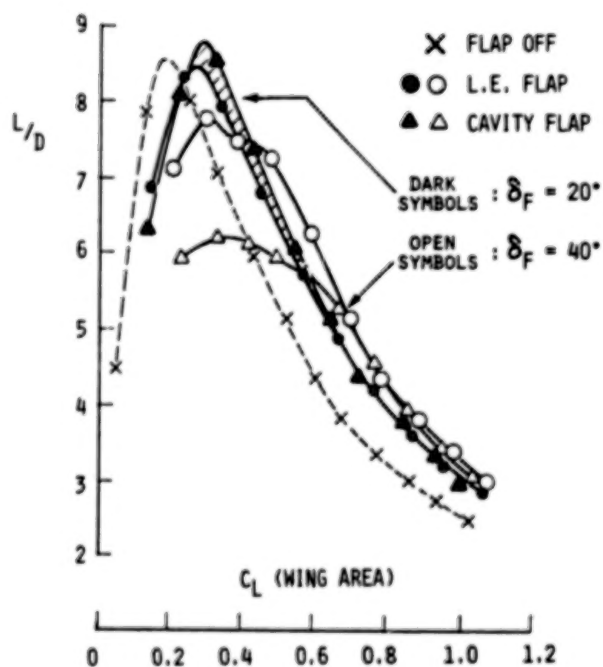


Figure 12 60-deg delta wing lift/drag ratio with leading-edge and cavity flaps.

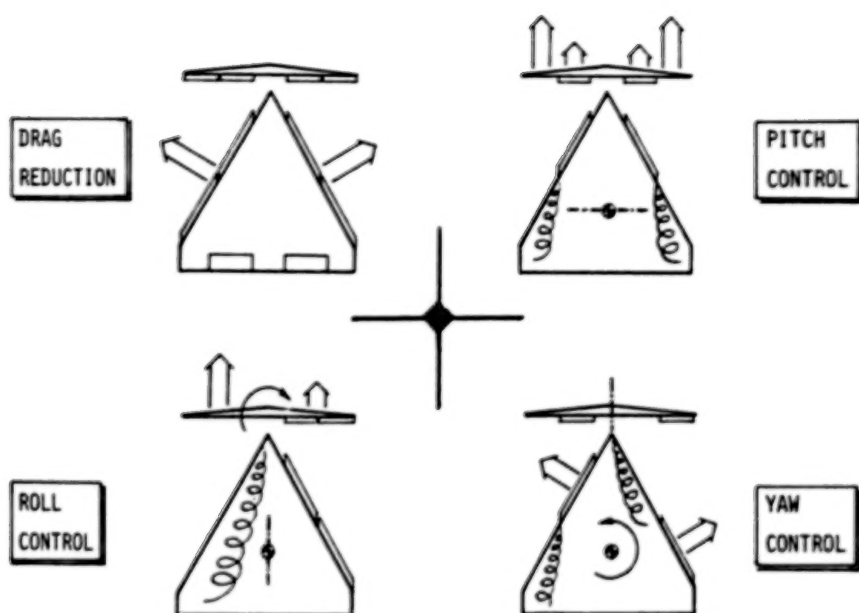


Figure 13 Cavity flap applications for control at high angles of attack utilizing thrust and lift modulation.

N86-27201

## VORTEX FLOW HYSTERESIS

Atlee M. Cunningham, Jr.  
General Dynamics  
Fort Worth Division  
Fort Worth, Texas

### SUMMARY

An experimental study was conducted to quantify the hysteresis associated with various vortex flow transition points and to determine the effect of planform geometry. The transition points observed consisted of the appearance (or disappearance) of trailing-edge vortex burst and the transition to (or from) flat plate or totally separated flows. Flow visualization with smoke injected into the vortices was used to identify the transitions on a series of semi-span models tested in a low-speed tunnel. The planforms tested included simple deltas (55 deg to 80 deg sweep), cranked wings with varying tip panel sweep and dihedral, and a straked wing. High-speed movies at 1000 frames per second were made of the vortex flow visualization in order to better understand the dynamics of vortex flow, burst and transition.

### INTRODUCTION

Recent interest in flying at very high angles of attack beyond the static stall conditions has been kindled by proposals to exploit this flow regime to improve fighter aircraft maneuverability (refs. 1 and 2). Herbst's concept to fly into the post-stall regime to achieve quicker turns (ref. 1) and the use of unsteady aerodynamics at high incidence discussed by Lang and Francis (ref. 2) open a Pandora's box of new aerodynamic problems. Because these ideas require flying at incidences as high as 90 deg or beyond, a single maneuver could cover vortex and burst vortex flows as well as totally separated flows. Also, because of the maneuver dynamics, pitch rate and time history effects could be very important. The understanding of these flow fields and the dynamic effects represents a quantum jump over current aerodynamic technology. Thus, as a first step toward this goal, a need exists to identify the various flow regimes and their characteristics as well as transition points from one type to another and the associated hysteresis effects.

The upper surface flow fields that exist over slender, highly swept or straked wings at high angles of attack may take on various forms. These forms may be broadly classified as three types summarized in Figure 1:

- (1) Vortex flows (stable leading edge or strake vortex)
- (2) Burst vortex flows (unsteady but still vortical)
- (3) Flat plate flows (unsteady, completely separated)

The normal force curve slope for type 1 flows is quite high compared to that of the attached flow region which generally exists below 5 deg. to 8 deg. incidence as illustrated in figure 1. The slope is reduced once vortex bursting begins to occur over the wing but normal force still increases with increasing incidence. Once the flow breaks down to the final stage of flat plate flow, normal force remains about constant, even up to 90 deg. incidence. The transition to flat plate flow is generally quite abrupt and may be accompanied by a loss in normal force or a destabilizing change in pitching moment with increasing incidence. Another very important property of these transitions is the hysteresis effect that results from transitions occurring at different incidences depending on whether the angle is increasing or decreasing. Quantification of this hysteresis and the determination of the effect of planform geometry on its characteristics are the objectives of this paper.

In order to accomplish these objectives, an experimental program was conducted in which a series of delta and cranked flat plate wings were tested. Flow visualization techniques were used to determine the transition points and the associated hysteresis. The tests were conducted in a small low speed tunnel at General Dynamics' Fort Worth Division using smoke for the flow visualization. The smoke generator was a special design that was evolved at General Dynamics for testing vortical flows at very high incidence. The models were semi-span models cut from flat aluminum plate with rounded leading edges. The planforms tested included simple deltas, cranked wings with varying tip panel sweep, a cranked wing with varying tip panel dihedral, and a straked wing. Data taken during the test for increasing and decreasing incidence included angles of the appearance of vortex burst at the wing trailing edge and transition to or from flat plate flow. High speed movies were made of the vortex flows to reveal the spiral nature of vortex burst and other unsteady phenomena.

#### TEST SETUP AND PROCEDURE

The small continuous low speed wind tunnel at General Dynamics' Fort Worth Division was used for this investigation. The tunnel has a  $0.356 \times 0.356\text{m}^2$  ( $14 \times 14 \text{ in.}^2$ ) test section with a splitter plate installed on one wall and clear glass on the other three walls for viewing flow visualization experiments. Test velocities used were held approximately constant at 30m/sec (98 ft/sec) which previous experience has shown to yield reliable vortex flow characteristics and good flow visualization using smoke.



The semi-span models were cut from flat aluminum plate stock, 0.160 cm (0.063 in) thick, and mounted on a bracket attached to a shaft extending outside the tunnel as shown in figure 2. Angle of incidence was set by rotating the shaft which was attached to a calibrated plate with angle marks. The settings were made manually so that very slow and smooth approaches to flow transition points could be achieved. Angle readings were made visually and recorded by hand.

The smoke generator was also installed on the wing mounting bracket as shown in figure 2 to permit injection of smoke as close as possible to the nose so as to provide maximum visualization of the leading-edge vortex. The smoke generator consisted of 0.05 cm ID (0.02 in.) stainless-steel tubing through which kerosene was forced from a pressurized vessel as shown in figure 3. A 23 cm (9 in.) section of the tubing near the nozzle was heated with DC current at about 10 amps. The heated kerosene vaporized when it exited from the nozzle in a reasonably steady flow. Pulsation was minimized by adjusting current and kerosene flow.

The semi-span models tested are shown in figure 4 with specifications listed in table 1. The leading edges were rounded such that they were semi-circular with a diameter of the thickness of the plate, 0.160 cm (0.063 in.). This was done to avoid adding any leading-edge camber that would result from having a sharp edge with a flat upper surface and also to simplify model fabrication. The cranked wing planforms all had a common inboard leading-edge sweep of 70 deg with the crank placed at 70% span. Only the tip panel sweep was varied from 30 deg to 70 deg and the tip panel dihedral varied from -90 deg to +90 deg with a fixed tip sweep of 30 deg. The straked wing planform was tested to provide insight as to the character of strake flows as opposed to simple delta and cranked wings. All sweep and dihedral were measured and recorded after fabrication.

The test procedure was very simple once the optimum conditions for smoke visualization were established. The wings were attached to the mounting bracket, the tunnel started, then the smoke turned on. The test was conducted on a continuous basis for each wing. The determination of transition angles was made as an average of at least three observations for each point. For increasing incidence, the angle was always lowered far below the transition point and then slowly increased until the transition occurred. For decreasing incidence, the reverse procedure was followed. In all cases fully established flow was obtained just before transition.

Calibration of test set-up was accomplished by comparing measured transition points with existing data for planforms of similar geometries. The items checked were wall interference and gap between the splitter plate and model root chord. Wall interference was about 10% at an incidence of 45 deg for the cranked wings and the delta wings for an incidence less than 70 deg. To check this effect, the angle for trailing-edge burst was compared with data published in



reference 3. This comparison shown in figure 5 indicates that the correlation is quite good. Another check on interference was a qualitative assessment of vortex burst development downstream of the model. Progression of the burst point toward the wing was very uniform and controllable with wing incidence.

The idea of leaving a small gap between the splitter plate and wing root chord was to prevent contamination of the vortex development by the wall boundary layer. This problem is unique to semi-span testing. The gap was set at the estimated displacement thickness of the wall boundary layer, 0.16 cm (1/16 in.). Variation of this gap to zero was shown to have little effect on the trailing-edge (TE) vortex burst angle but a profound effect on the transition to flat plate (FP) flow. Data available from a large-scale full span low-speed test of a General Dynamics research model similar to the 70 deg/50 deg cranked wing indicated that the transition to FP flow should occur at about 43 deg - 47 deg incidence. With the gap set at 0.16 cm, this transition occurred at about 45 deg - 46 deg but with zero gap, it occurred at about 55 deg - 60 deg. Therefore the gap was maintained at the 0.16 cm value for all models tested.

## RESULTS AND DISCUSSION

The objective of this test was to quantify the hystereses associated with various vortex flow transition points and determine the effect of planform geometry on their characteristics. The transition points observed consisted of the appearance (or disappearance) of trailing-edge (TE) vortex burst and transition to (or from) flat plate (FP) flows. Flow visualization with smoke injected into the vortices was used to identify the transitions that occurred over a series of flat plate models that included a set of deltas, a cranked wing with varying tip panel sweep or dihedral, and a straked wing (see fig. 4). Finally, high-speed movies were made to reveal the spiral nature of vortex breakdown and other dynamic effects.

### Transition Points and Hysteresis

The results for TE vortex burst on the delta wings already discussed in the previous section are shown in figure 5. Shown also in the figure are data from other sources (reference 3) that indicate good agreement with the present data. Hysteresis could not be detected during the test for the TE vortex burst; in fact, when the angle was held steady at the TE vortex burst point, the burst would slowly move back and forth with a range of only about 5% of the wing root chord. TE vortex burst for the delta wings was highly stable.

Results for FP flow transition for the delta wings are shown in figure 6. The influence of sweep is similar to that for the TE vortex burst angle in figure 5; however, a definite hysteresis effect is present. Amplitude of the hysteresis is about constant at 3 to 4 deg for all sweeps with the exception of 70 deg which is only about 2 deg. These points were re-checked for several wings but results were still the same. A possible explanation is that it appears that vortex asymmetry develops in the incidence range of 45 deg for 70 deg delta wings (ref. 4). If this is the case, then the higher swept wings would also be in the asymmetric vortex range and semi-span testing which enforces symmetry of these models could be questionable. Although this subject requires further investigation with full span models, it is felt that the hysteresis trends as a function of wing sweep are reasonable because the variation over the test range is orderly and closely parallels that of TE vortex burst.

The influence of tip sweep angle on TE vortex burst for the cranked wing with 70 deg inboard sweep is shown in figure 7. The reduction of hysteresis with increasing tip sweep was expected. It is interesting that the maximum angle for increasing incidence was very close to that of the simple 70 deg delta wing at 29 deg and is essentially independent of tip sweep. A more interesting observation, however, is that when TE burst appeared, it would not occur at the trailing edge - instead it would develop with the usual orderly upstream progression on the wake vortex and upon reaching the trailing edge would immediately jump forward to a point just upstream of the axial location of the wing crank (approximately 79% of the root chord). When vortex burst reached the trailing edge with decreasing incidence, however, it did so in an orderly fashion as observed for the delta wings but then jumped from the trailing edge to a point further downstream as it passed the trailing edge.

The observed hysteresis of TE vortex burst on the cranked wings is attributed to flow conditions on the tip panel just prior to TE vortex burst. With increasing incidence, the tip panel flow fields are well behaved and dominated by the inboard panel leading-edge vortex; hence, forward progression of burst in the wake is fairly insensitive to the tip panel presence or geometry. When burst reaches the trailing edge, the tip upper surface flow field suddenly collapses with a resulting rise in pressure that forces burst to abruptly move forward of the wing crank axial location. With decreasing incidence, the opposite process takes place. In this case the lower sweep panel does not re-establish its flow as quickly because its starting point is burst vortex flow. Aft progression of the burst with decreasing incidence is similar to that of a lower swept wing. For example, TE vortex burst for decreasing incidence on the cranked wing with tip sweep of 30 deg occurs at about 21 deg as shown in figure 7. This compares favorably with the angle of TE vortex burst for a delta wing with a sweep of about 64 deg as shown

in figure 5. Upon reaching the trailing edge, however, the tip panel flow fields are then fully re-established and the burst must jump abruptly downstream to a point corresponding to that which would occur during the case of increasing incidence but at the lower angle of attack.

A second variation of tip panel geometry which affects TE vortex burst hysteresis is tip panel dihedral. Results for this investigation, shown in figure 8, indicate that changing the dihedral with a fixed tip sweep of 30 deg has a profound effect on the hysteresis. In general, positive dihedral reduces hysteresis from 8 deg at zero to 0.5 deg at 45 deg. At 60 deg dihedral, the hysteresis has disappeared and the TE vortex burst point angle has increased to 30 deg. A further increase to 90 deg dihedral results in a drop of TE vortex burst angle to 27.5 deg but has not introduced any hysteresis.

Negative dihedral for -30 deg to -90 deg shows a large reduction in hysteresis but it also shows a reduction in TE vortex burst angle to an average of about 26 deg for all dihedral angles. The reasons why tip dihedral has these effects on TE vortex burst are not clear; however, several possibilities will be discussed.

Changing of the tip panel dihedral does at least two things: (1) it changes the leading-edge sweep with angle of attack, and (2) it changes the orientation of the tip leading edge relative to the local upwash fields, i.e., positive dihedral leads to a more spanwise flow whereas negative dihedral leads to a more perpendicular or two dimensional flow. With positive dihedral, these two changes tend to improve the tip panel flow fields at higher angles of attack; hence, with increasing dihedral, the hysteresis disappears. In the case of 60 deg dihedral, the TE vortex burst angle was actually increased over that of the 70 deg delta. Going too far, however, to 90 deg results in adverse effects which lower the TE vortex burst angle but still do not introduce any hysteresis. At this high dihedral, the spanwise flow must make an abrupt turn when it encounters the vertical tip panel and hence a corner vortex forms that precipitates premature burst of the main wing vortex. With exception of the 90 deg dihedral, the main vortex structure and path seemed to be little affected by the dihedral.

Negative dihedral has the interesting effect of lowering the TE vortex burst angle but also reducing the hysteresis. In fact, this dihedral direction was more effective at reducing hysteresis than positive dihedral. It is suspected, however, that the reduction in hysteresis was bought at the price of premature separation of the tip panel due to both decreased sweep and higher upwash angles at the leading edge. Therefore, it appears that configuration designs based on cranked wings with large negative tip dihedrals would not be very efficient at high angles of attack.



The transition to and from FP flows for the cranked wings was found to be relatively unaffected by the wing tip geometry. Results shown in figure 9 indicate the influence of tip panel sweep on the FP flow transition. Hysteresis amplitudes and the angles show very little variation, in fact 30 deg and 70 deg have identical values. Data obtained for tip dihedral effects also exhibited the same characteristic and hence are not shown. The reasons attributed to this observation are based on the fact that the large inboard part of the cranked wing is the dominant geometric feature that governs the flow fields near FP flow transition. Thus, radical changes in the small tip have very little effect on this transition.

The straked wing shown in figure 4 represents a variation of cranked wing planforms where the outboard "tip" panel is dominant. This wing was tested because: (1) it is representative of the F-16 planform, and (2) a force and pressure model of this same geometry will be tested at a later date by General Dynamics. High-speed movies were also made of the vortex flow visualizations for this model which will be discussed in the next subsection. Test results for the straked wing were:

|                    |                                 |
|--------------------|---------------------------------|
| TE vortex burst    | = 18 deg increasing incidence   |
| FP flow transition | = 48 deg increasing incidence   |
| FP flow transition | = 43.5 deg decreasing incidence |
| TE vortex burst    | = 18 deg decreasing incidence   |

For a strake sweep of 76 deg, the delta wing TE vortex burst angle would be about 34 deg as shown in figure 5. In the presence of the large outboard 40 deg panel, this was reduced to 18 deg which illustrates the effect increasing the tip panel size for cranked wing geometries. In the case of the cranked wings discussed earlier, the observation that TE vortex burst angle for increasing incidence was little affected by tip sweep or positive dihedral was attributed to small tip panel size. In that case, the inboard panel vortex dominated the outboard panel flow fields prior to burst. For the straked wing, earlier breakdown of the large outboard panel due to lower sweep led to early breakdown of the strake vortex. The FP flow transition angle was likewise reduced to 43.5 - 48 deg from the range of about 52 - 55 deg shown in figure 6 for a 75 deg delta wing. The idea of straked wing designs, however, is not to achieve the high incidence characteristics of the strake but to extend the incidence range of lower swept higher aspect-ratio wings which have better efficiencies than highly swept delta wings (refs. 5 and 6).

The absence of hysteresis for TE vortex burst on the straked wing is puzzling but the 4.5 deg amplitude for FP flow transition is in line with those amplitudes shown in figure 6. The angle for TE vortex burst of 18 deg correlates quite well with the observed lift curve break at 18 deg for the YF-16 at low speeds (ref. 6); therefore, the basic flow field properties are probably correct. A possible explanation is that the outboard panel exhibits orderly growth of trailing-edge separation and since it dominates the strake, the

strake vortex likewise bursts in an orderly fashion. In this case the outboard panel dominates for both increasing and decreasing incidence and hence little or no hysteresis appears in the TE vortex burst point. For the case of the cranked wings discussed earlier, the hysteresis was a result of differing dominance with incidence direction; with increasing incidence, the inboard panel leading-edge vortex dominated the tip panel flow fields, and with decreasing incidence, the separated flow on the wing tip dominated itself.

### High-Speed Movie Results

High-speed movies at 1000 frames per second were made of the vortex flow visualization in order to better understand the dynamics of the unsteady separated flows. A schematic of the flow visualization is shown in figure 10 to orient the reader with the photos to be discussed. These discussions will be based on conclusions arrived at from viewing the movies, thus the writer will verbally add the dynamic effects to the individual frames taken from the movies.

The frames shown in figure 11 are taken from a high-speed movie made of a slow pitch sweep up to 55 deg incidence for the straked wing that was just discussed in the previous subsection. The only difference between the movie configuration and that above was the flat extension just aft of the wing as noted in figure 10. At about 15 deg (figure 11a) the strake vortex is about to burst as noted by a kink that developed just aft of the trailing edge. At about 20 deg (figure 11b) the vortex has burst and the movie is already showing the swirling pattern associated with spiral burst. Also, in the movie it is evident that significant spanwise flow outboard along the trailing edge is occurring which is attributed to trailing-edge separation as discussed previously for the straked wing. At about 28 deg (figure 11c) the burst has progressed to a point just aft of the wing/strake intersection. The spiral vortex breakdown as well as the spanwise trailing-edge flow are now more evident. At about 35 deg (figure 11d), the burst has moved forward and developed further but is similar in appearance to that at 28 deg. At about 45 deg (figure 11e), the outer wing panel has transitioned to FP flow as indicated by absence of smoke over that region. As shown in the movie, this transition was very abrupt. At about 55 deg (figure 11f), the flow picture has not changed much from that at 45 deg. In both figures 11e and 11f, the strake flow forward of the outboard panel leading edge is completely burst but still vortical.

Figure 12 shows a similar sequence of frames taken from a high-speed movie made of a slow pitch sweep up to about 60 deg for a cranked wing with 68.5 deg/21.5 deg leading-edge sweeps. The wing planform, also shown in figure 12, is similar to but slightly different than that discussed in the previous subsection of this paper. Nevertheless, the basic flow field characteristics are similar. At



about 20 deg (figure 12a) the vortex is well formed. Burst occurs at about 24-25 deg as shown in figure 12b which correlates well with the data in figure 5 for a 68.5 deg swept delta. The burst is located just forward of the wing crank right after its initial appearance. The high-speed movie shows a very rapid movement of the burst from the trailing edge to the point shown in figure 12b which is part of the hysteresis mechanism discussed previously. About 35 deg (figure 12c) the burst has further developed and is very close to the wing vertex. This frame very clearly shows the spiral vortex burst. At about 45 deg (figure 12d) the vortex is completely burst but the flow is still vortical just prior to FP flow transition. At about 55 deg (figure 12e) FP flow, or total separation, is shown for which the transition occurred very abruptly at about 46-47 deg. During the reverse pitch sweep back to zero incidence as shown in the movie, hysteresis for the FP flow transition is not as clear as that for TE vortex burst. The angle for the TE vortex burst with decreasing incidence is about 16-17 deg, thus the hysteresis amplitude of about 8-9 deg can be easily detected in the movie. Also, the different speed of vortex burst movement near the trailing edge for increasing and decreasing incidence is clearly evident.

The high-speed movies of vortex flow visualization have provided valuable insight to the dynamics of vortex flows, burst, and transitions. With a shutter speed of 1/3000 sec at 1000 frames per second and flow velocities of about 30 m/sec, the spiral motion of vortex burst was stopped. Vortex burst movement on the cranked wing during initial development was slowed down to show that even though the development was very rapid, it was orderly. Also spanwise trailing-edge flow during vortex burst on the straked wing was shown to be a possible explanation for the absence of TE vortex burst hysteresis for that wing. FP flow transitions were shown to be very rapid for all wings for either increasing or decreasing incidence.

#### CONCLUDING REMARKS

An experimental study was conducted to quantify the hysteresis associated with various vortex flow transition points and determine the effect of planform geometry on their characteristics. The transition points observed consisted of the appearance (or disappearance) of trailing-edge (TE) vortex burst and transition to (or from) flat plate (FP) flows. Flow visualization with smoke injected into the vortices was used to identify the transitions that occurred on a series of semi-span models tested in a low-speed wind tunnel at about 30m/sec. The planforms tested consisted of simple deltas (55 to 80 deg sweep), cranked wings with varying tip panel sweep and dihedral,

and a straked wing. High-speed movies at 1000 frames/sec were made of the vortex flow visualization in order to better understand the dynamics of vortex flow and burst as well as the transition from one flow type to another.

Results were obtained for the hysteresis characteristics of both TE vortex burst and FP flow. Delta wings were first tested for a series of leading-edge sweeps of 55, 60, 65, 70, 75 and 80 degrees. TE vortex burst angles were determined and good correlation with other published data verified the test setup and procedure; however, little or no hysteresis was observed. Particular attention was paid to the semi-span test techniques. FP flow transition angles were found to increase with leading-edge sweep in much the same way as TE vortex burst; however, a hysteresis was observed which was constant at about 3-4 deg. This transition consistently occurred at higher angles for increasing incidence than for decreasing incidence.

Test results for the cranked wings exhibited very interesting effects of tip panel geometry on the hysteresis characteristics. For a fixed inboard sweep of 70 deg, varying the outboard sweep from 30 to 70 deg showed a reduction of TE vortex burst hysteresis from 8 deg at 30 deg sweep to 0 deg at 60 deg and 70 deg sweeps. Varying tip panel dihedral from -90 to +90 deg for the 70 deg/30 deg cranked wing also showed a reduction of TE vortex burst hysteresis. For dihedral varying from 0 to 90 deg, the hysteresis was reduced from 8 deg at 0 deg dihedral to 0 deg at 60 deg dihedral where the angle for TE vortex burst was also slightly increased. At 90 deg dihedral, the hysteresis was zero; however, the TE vortex burst angle was lowered significantly. For negative dihedral, the hysteresis was again reduced, but the TE vortex burst angle was consistently lower for all values. The influence of tip panel geometry was found to be insignificant for the transition to FP flows. This characteristic was about the same as that for the 70 deg delta.

The straked wing tested with 76 deg/40 deg leading-edge sweep was similar to an idealized F-16 and represented a variation on cranked wings where the outboard panel was the dominant surface. The absence of TE vortex burst hysteresis was attributed to the orderly development of trailing-edge separation on the 40 deg panel as observed in the high-speed movies. Hysteresis was observed for FP flow transition and was associated with total separation of the 40 deg panel. This separation was observed in the high-speed movies to be very abrupt.

The high-speed movies provided valuable insight to the dynamics of vortex flows, burst and transition. The spiral motion of vortex burst was stopped and the very rapid initial movement of the burst point on the cranked wings was shown to have an orderly development. Spanwise flow along the trailing edge for vortex burst on the straked

wing was shown to be a possible explanation for the absence of TE vortex burst hysteresis for that wing. Finally, the transition to FP flow was found to be very abrupt, even at 1000 frames/secs for all wings for either increasing or decreasing incidence.

#### REFERENCES

1. Herbst, W. B.: Dynamics of Air Combat., J. Aircraft, vol. 20, No. 7, July 1983, pp. 594-598.
2. Lang, J. and Francis, M. S.: Unsteady Aerodynamics and Dynamic Aircraft Maneuverability. Presented at AGARD Symposium on Unsteady Aerodynamics - Fundamentals and Applications to Aircraft Dynamics, Gottingen, Germany, 6-9 May 1985, Paper No. 29.
3. Malcom, G. N.: Impact of High-Alpha Aerodynamics on Dynamic Stability Parameters of Aircraft and Missiles. AGARD-LS-114, 1981.
4. Ericsson, L. E.: Wing Rock Flow Phenomena. Presented at AFOSR/FJSRL/U. Colorado Workshop on Unsteady Separated Flows, USAF Academy, 10-11 August 1983.
5. Peake, D. J. and Tobak, M.: On Issues Concerning Flow Separation and Vortical Flows in Three Dimensions. AGARD-CP-342, 1983, Paper No. 1.
6. Smith, C. W., Ralston, J. N. and Mann, H. W.: Aerodynamic Characteristics of Forebody and Nose Strakes Based on F-16 Wind Tunnel Test Experience. NASA CR-3053, 1979.

TABLE 1 Model Specifications

| Root<br>Chord, cm    | Leading Edge<br>Sweep, Deg | Tip Panel<br>Sweep, Deg | Tip Panel<br>Dihedral, Deg | Location of<br>Crank, % Span |
|----------------------|----------------------------|-------------------------|----------------------------|------------------------------|
| <b>DELTA WINGS</b>   |                            |                         |                            |                              |
| 22.9 cm              | 55°                        | -                       | -                          | -                            |
| 25.4 cm              | 60°                        | -                       | -                          | -                            |
| 27.9 cm              | 65°                        | -                       | -                          | -                            |
| 30.5 cm              | 70°                        | -                       | -                          | -                            |
| ↓                    | 75°                        | -                       | -                          | -                            |
|                      | 80°                        | -                       | -                          | -                            |
| <b>CRANKED WINGS</b> |                            |                         |                            |                              |
| 30.5 cm              | 70°                        | 30°                     | 0°                         | 70%                          |
| ↓                    | ↓                          | 40°                     | ↓                          | ↓                            |
|                      |                            | 50°                     |                            |                              |
|                      |                            | 60°                     |                            |                              |
| 30.5 cm              | 70°                        | 30°                     | -89°                       | 70%                          |
| ↓                    | ↓                          | ↓                       | -60°                       | ↓                            |
|                      |                            |                         | -46.5°                     |                              |
|                      |                            |                         | -30°                       |                              |
|                      |                            |                         | 15°                        |                              |
|                      |                            |                         | 31°                        |                              |
|                      |                            |                         | 46°                        |                              |
|                      |                            |                         | 90°                        |                              |
| <b>STRAXED WING</b>  |                            |                         |                            |                              |
| 26 cm                | 76°                        | 40°                     | 0°                         | 25%                          |

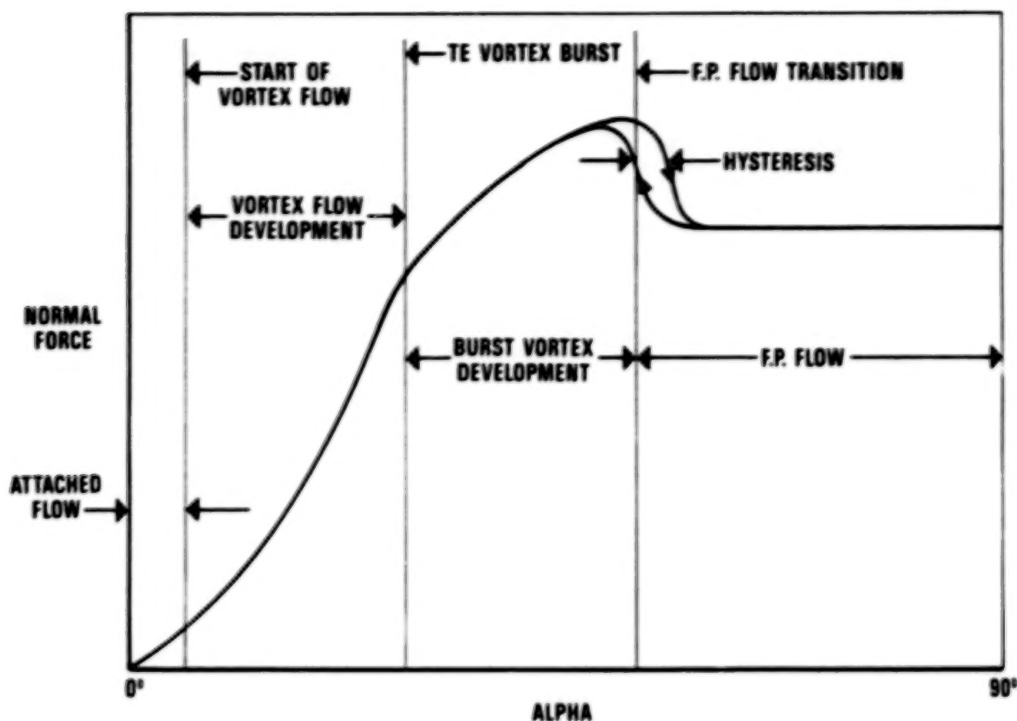


Figure 1 Regimes of Vortical Flow Development.

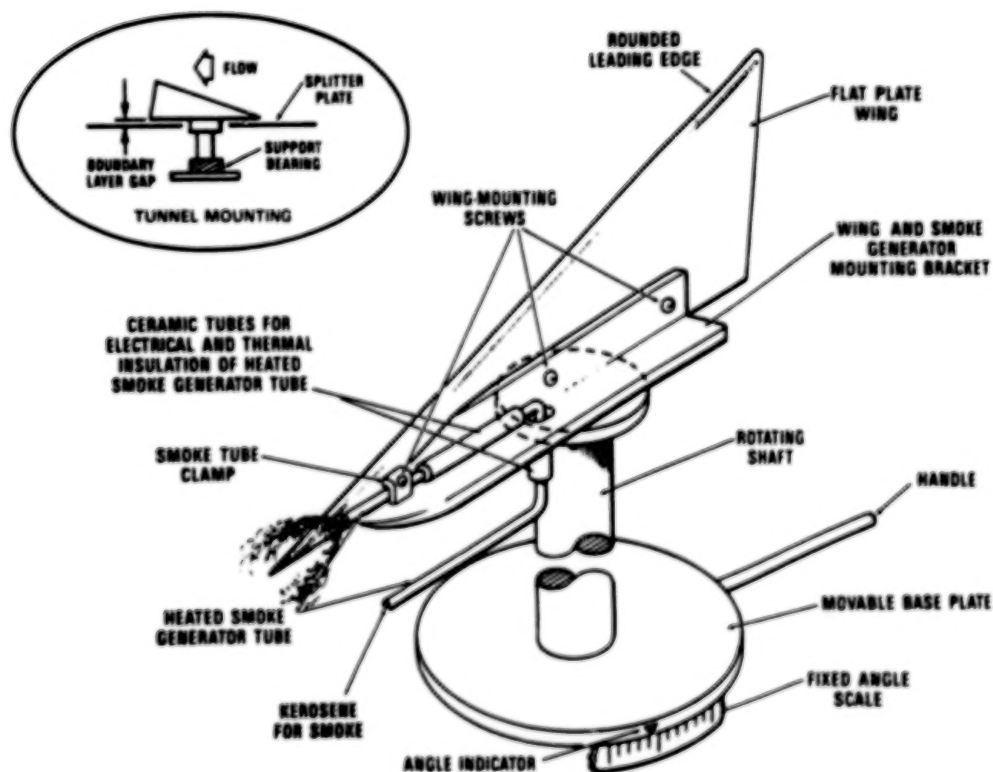


Figure 2 Schematic View of the Semi-Span Model Test Assembly.



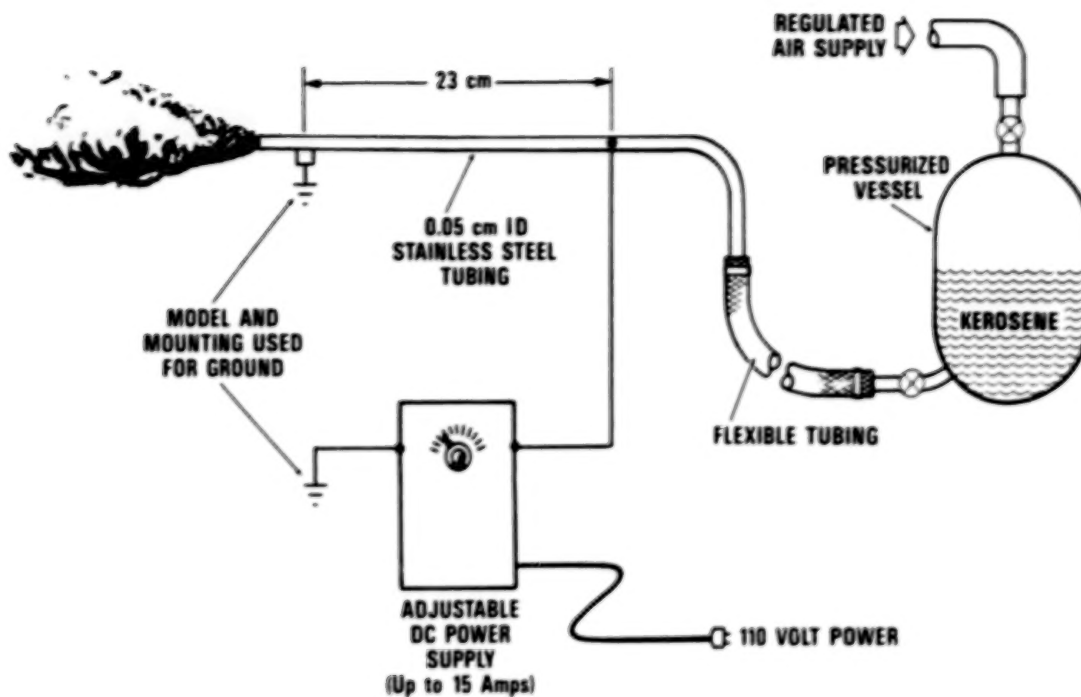


Figure 3 Schematic Diagram of the Smoke Generator.

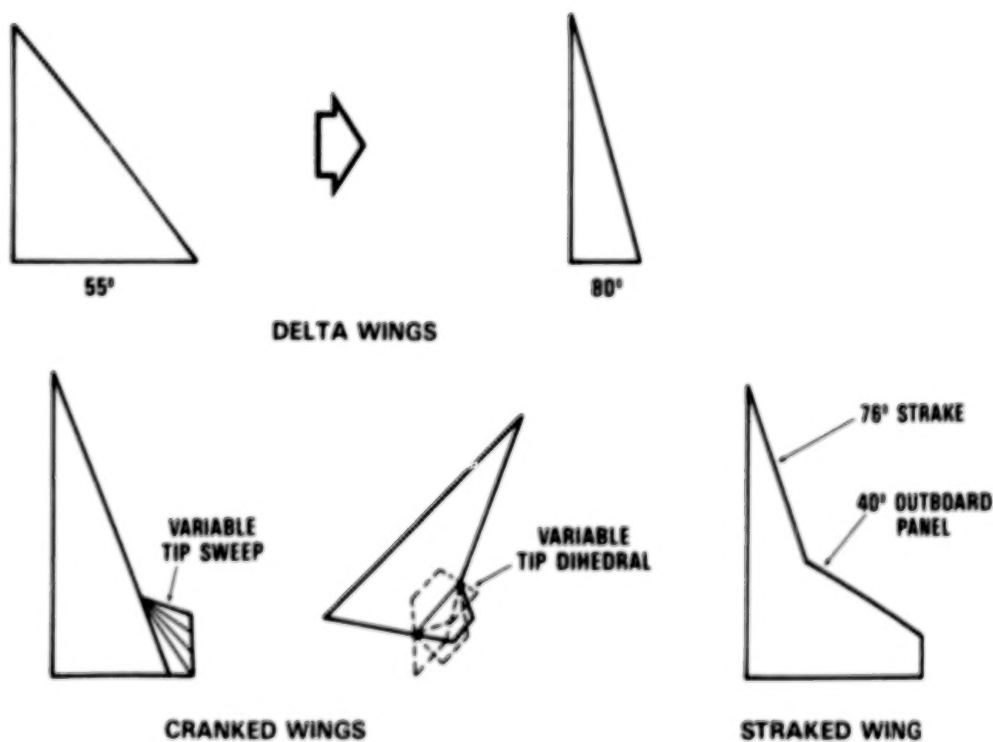
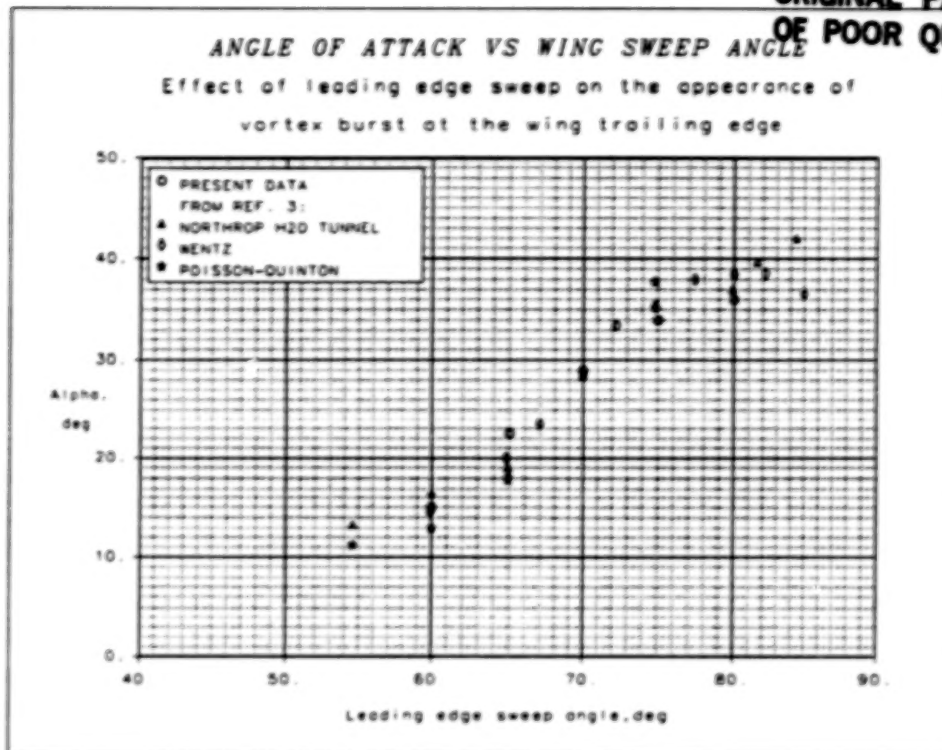
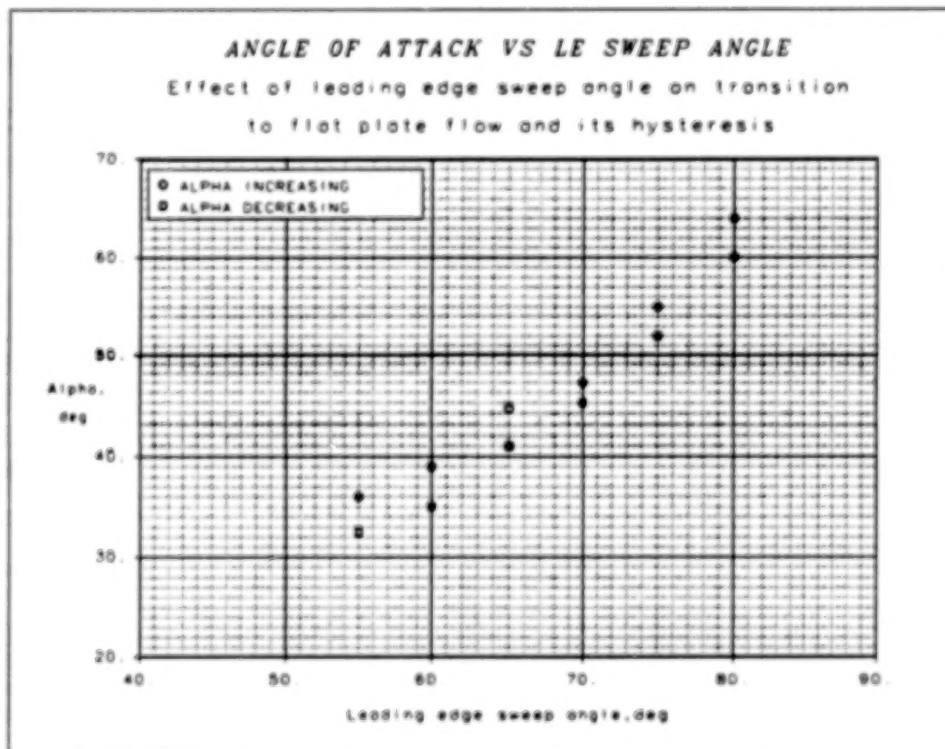


Figure 4 Semi-Span Planforms Tested.



**Figure 5 Effect of Wing Sweep on TE Vortex Burst.**



**Figure 6 Effect of Wing Sweep on FP Flow Transition.**

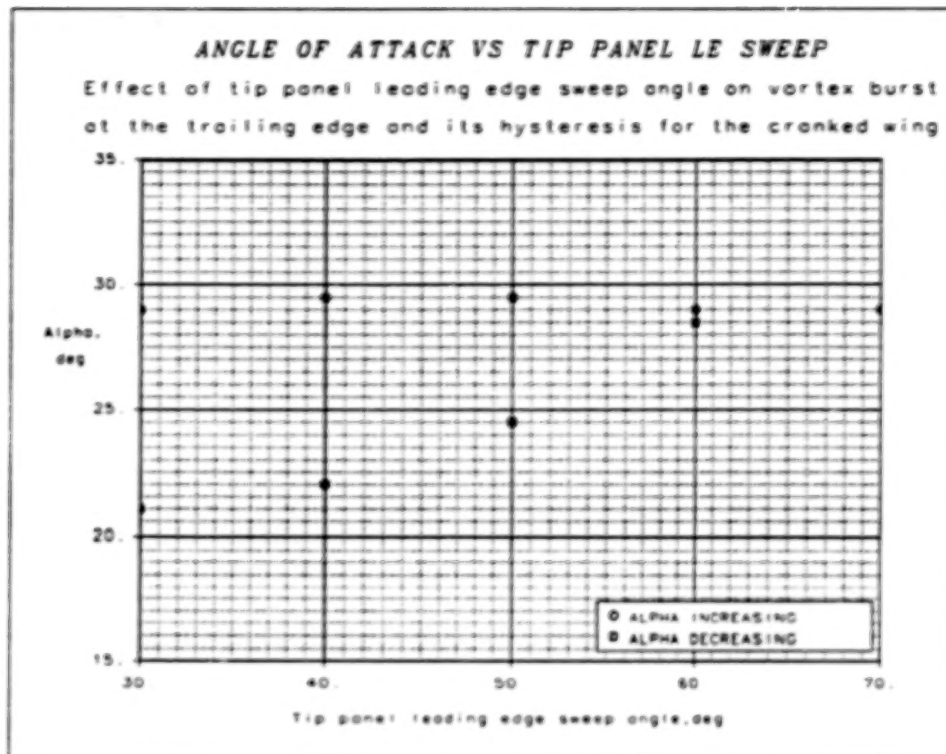


**Figure 7 Effect of Tip Panel Sweep on TE Vortex Burst on Cranked Wings.**

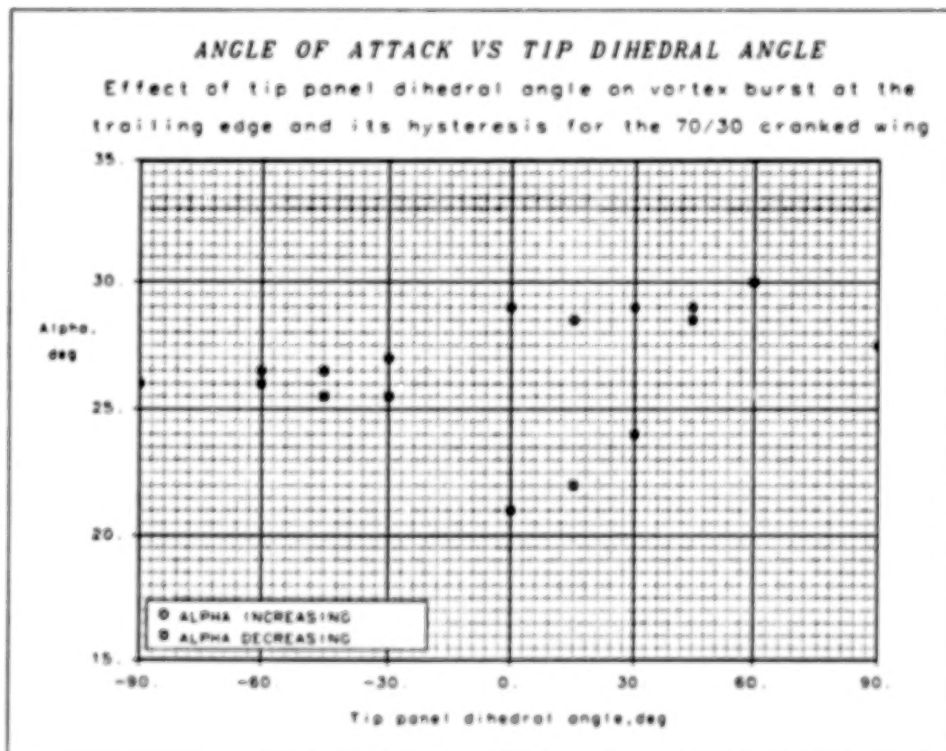


**Figure 8 Effect of Tip Panel Dihedral on TE Vortex Burst on a 70°/30° Cranked Wing.**

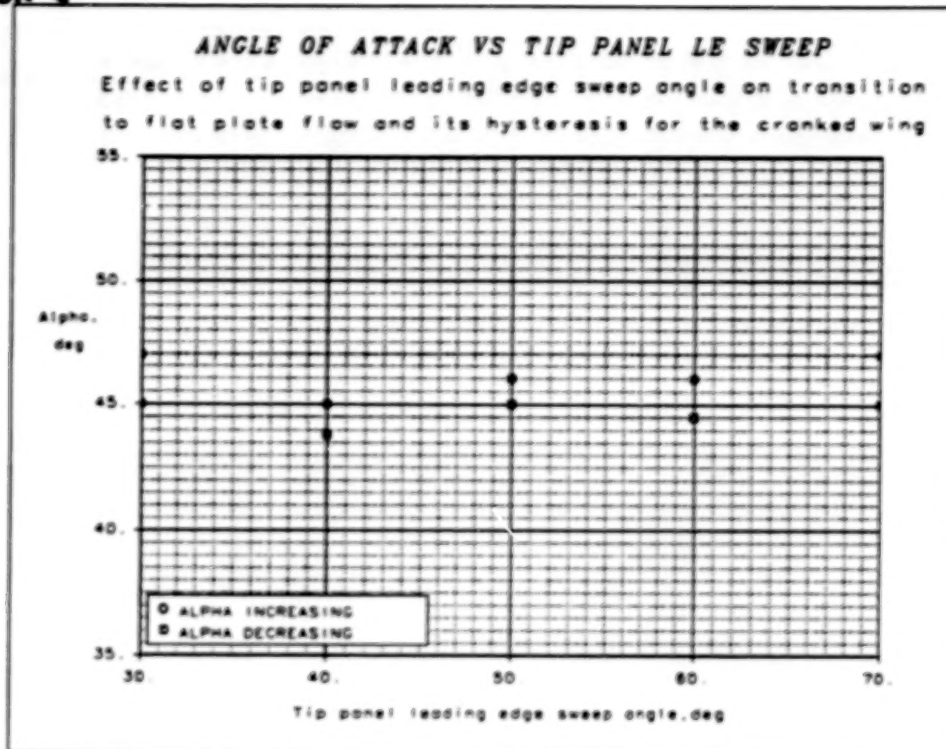


**Figure 9 Effect of Tip Panel Sweep on FP Flow Transition on Cranked Wings.**

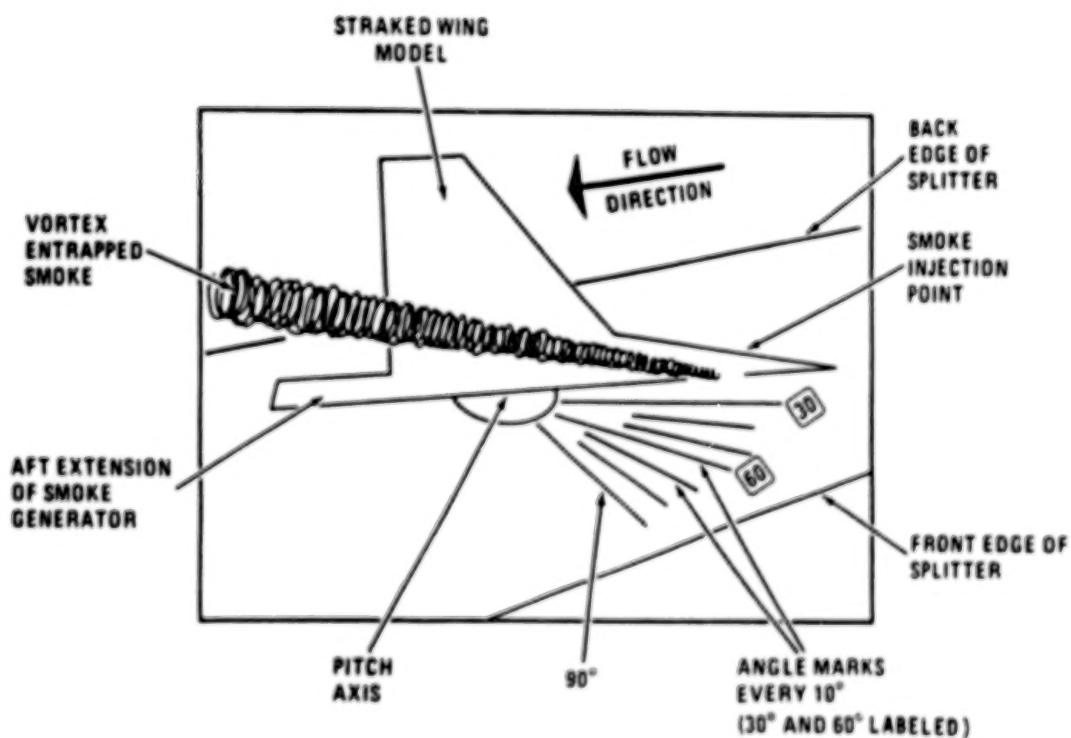


**Figure 10 Explanation of Flow Visualization Results.**

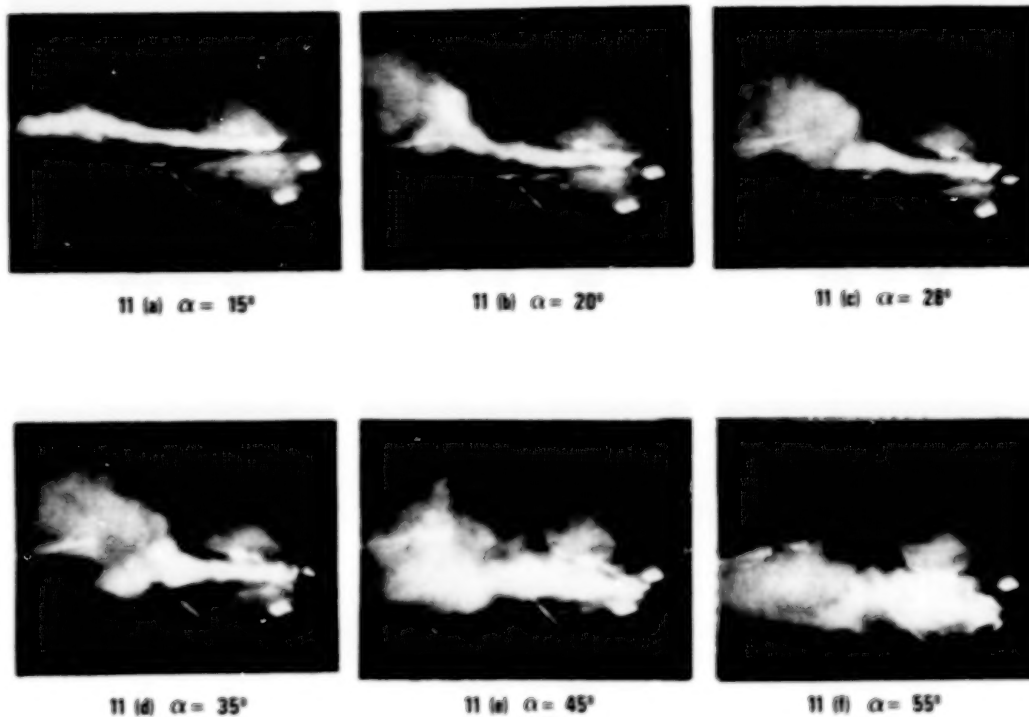


**Figure 11 Flow Visualization Results for the Straked Wing.**

**ORIGINAL PAGE IS  
OF POOR QUALITY**

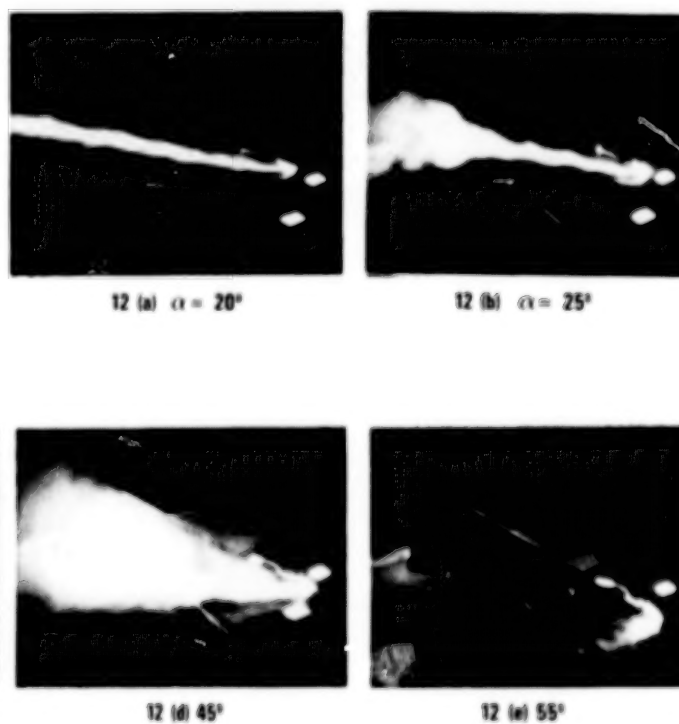
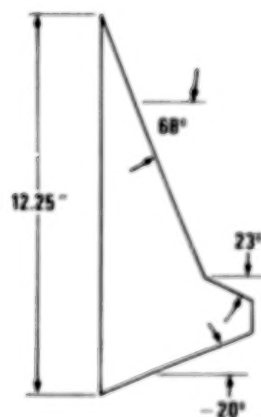


**Figure 12 Flow Visualization Results for a Cranked Wing.**



## VISCIOUS VORTICAL FLOW CALCULATIONS OVER DELTA WINGS

G. Blom, J. C. Wai, and H. Yoshihara  
Boeing Military Airplane Company  
Seattle, Washington

## SUMMARY

Two approaches to calculate turbulent vortical flows over delta wing configurations are illustrated. The first is for a simple delta wing at low speeds using the boundary layer approximation to treat the effects of the secondary separation. The second is for the supersonic case of a generic fighter using the NASA Ames parabolized Navier/Stokes method. Test/theory comparisons are given in both cases.

## INTRODUCTION

The concept of controlled separations due to D. Küchemann (ref. 1) plays an important role in the high lift performance of advanced combat aircraft. Here the sharp leading edges of the highly swept wing required for supersonic performance are parlayed into producing stable lift-generating leading-edge separation vortices. Such vortices can further serve as the base for a potentially powerful fast-response control system.

In the following, two cases of turbulent vortical flows are calculated. In the first, the low-speed flow over a slender flat plate delta wing at a large angle of attack is considered. Here the flow separates along the sharp leading edges forming the familiar primary separation vortices. Their effect, to a good approximation, can be treated by an inviscid theory. The primary vortices in turn impress an adverse pressure gradient on the upper surface boundary layer causing it to separate when the angle of attack is sufficiently large. The consequence of these secondary separations is to suppress significantly the suction peaks generated by the primary vortices. Our objective is the calculation of the displacement effects of the secondary separation, coupling the 3D integral boundary layer method with the leading-edge vortex panel method. The problem that must be resolved is the proper formulation (and solution) of the boundary layer problem and its convergent coupling with the inviscid problem.

In the second case, the supersonic flow over a generic fighter (Model -350) at large angles of attack is considered. Here a significantly more complex system of separation vortices arises which is shed from the wing and fuselage nose. For this complex flow the boundary layer approach used in the first case is no longer expedient. The flow is treated globally using the parabolized Navier/Stokes (PNS) equations with a mixing length turbulence model.

## THE BOUNDARY LAYER LIMIT LOW-SPEED DELTA WING\*

The 3D integral boundary layer method used was developed by L. Wigton (ref. 3) and is essentially that of P. D. Smith (ref. 4). Here the planar Green's lag entrainment equations are embedded in the streamwise direction, and the transverse equations are derived assuming Mager's cross-flow velocity profile. The resulting system of equations is composed of four first-order partial differential equations containing six unknowns. It must be presumed that these equations become fully determinate when coupled to the equivalent inviscid flow problem. Since it is difficult to solve the problem in this global formulation, the solution is sought by an iterative procedure coupling the boundary layer and inviscid flows.

The resulting boundary layer problem is made determinate by assigning the values of two of the six unknowns. The choice of the two input functions must be such that the resulting boundary layer problem can be solved expeditiously for the separated case and that a convergent coupling with the inviscid flow can be achieved in a systematic fashion. We shall use the direct formulation of the boundary layer problem where the inviscid surface velocity components are used as inputs. By this choice there is a direct input/output compatibility between the boundary layer and inviscid flow problems. The resulting set of equations is fully hyperbolic permitting a finite-difference marching when the initial data lines are space-like. The limiting and inviscid surface streamlines form two of the four characteristics which define the domain of dependence.

For the problem of the secondary separation for the delta wing, we shall use the  $x = \text{constant}$  lines ( $x$  is in the streamwise direction) which are proper initial data lines. The initial data to be assigned are not known in advance and must be determined by a "march/step back" procedure assuming the flow in the wing apex region to be conical. Once the initial data are established, a streamwise finite-difference marching is carried out using a first-order explicit differencing, biasing the lateral derivatives to cover the characteristic domain of dependence.

For severely separated cases ( $\bar{H} \geq 2.5$ ) an ill-conditioning of one of Green's equations arises caused by the derivative of the form factor function  $A = A(R_1)$  becoming very large (ref. 5). This ill-conditioning has been erroneously attributed to the appearance of separation with its envelope of limiting streamlines as well to the Goldstein singularity, but it is clearly due to the  $A = A(R_1)$  modeling required for the closure. The ill-conditioning can be circumvented by recalling that severely separated boundary layers assume an equilibrium state whereby the form factor  $A$  is given directly in terms of the pressure gradient (ref. 6). The errant differential equation is then replaced by blending in the equilibrium flow as the ill-conditioning arises. Such large values of  $A$  occur for example in the shock-induced and aft separations arising in the transonic flow over swept wings, but they will not arise in the present case of the low-speed secondary separation.

(From Ref. 2)

For the low-speed case considered, the leading-edge vortex panel method is used for the equivalent inviscid flow. Here the leading-edge separation vortices are paneled as a potential vortex sheet, and their locations are determined by an iterative procedure. Since this panel method did not have provisions for viscous transpiration velocities, the upper surface viscous displacements were halved to approximate a wing camber change.

The first case considered was a flat plate delta wing of  $76^\circ$  sweep (aspect ratio = 1) at  $11^\circ$  angle of attack and a Reynolds number of  $35 \times 10^6$  based on the 7.3 meter root chord. Boundary layer measurements were obtained by East (ref. 7). For this case, only the boundary layer was calculated inputting the measured surface velocity and flow direction. In figure 1 the calculated boundary layer variables are compared with the measurements, while in figure 2 the limiting streamline slopes are shown together with a comparison of the calculated and measured secondary separation lines. Good agreement is seen in both figures.

To illustrate the inviscid/viscid flow coupling, we have next considered the low-speed flow over the same flat plate delta wing at  $20.5^\circ$  angle of attack and at a smaller Reynolds number of  $0.9 \times 10^6$  based on the 0.75-meter root chord. Wind tunnel tests were carried out for this case by Hummel (ref. 8). Four iterations between the panel method and the boundary layer solutions achieved a reasonable convergence. The resulting pressure distribution at two chordwise stations are shown in figure 3. Though the test/theory comparison is only fair, the theory appears to have yielded the general effects of the viscous displacement under the suction peak. The undesirable reexpansion near the leading edge is most probably due to the inadequate paneling of the free sheet adjacent to the leading edge. Here convergence of the vortex solution could not be achieved when a more refined paneling of the free sheet was used. The agreement of the pressures in the inboard region might be improved by incorporating the full transpiration velocity effects. With the relatively poor experience with the leading-edge vortex panel method, it would be desirable to repeat the calculations using the Euler equations with the proper viscous transpiration velocities.

In figure 4 the limiting streamline slopes are shown. Good test/theory agreement in the secondary separation line is found. Here also an oil-flow picture from reference 8 is shown. It should be noted that the Reynolds number was inadequate in the experiments to achieve natural turbulent flow. A radial boundary layer trip was required as shown in figure 4. The calculations were however carried out assuming the boundary layer to be fully turbulent.

#### PNS CALCULATIONS-SUPERSONIC MODEL - 350 FIGHTER

The calculations for the Model-350, shown in figure 5, were carried out under a NASA Ames/Boeing cooperative study. Other results from this effort were presented earlier by Dr. D. Chaussee (ref. 9). The Model-350 was selected since pressure distribution and boundary layer profile measurements were available (ref. 10).



The Ames PNS code was originally developed by L. Schiff and J. Steger (ref. 11). The PNS equations are the steady thin-layer Reynolds-averaged Navier/Stokes equations in which the pressure is assumed to be invariant across the subsonic portion of the boundary layer. The resulting equations can be marched in the streamwise direction when the inviscid flow is supersonic.

The bow shock from the fuselage nose is fitted, but all interior shocks arising farther downstream are captured as for example the Kutta shock from the trailing edge of the wing (fig. 6). A Kutta shock and an expansion fan are the dominant mechanisms by which the differing upper and lower surface flows adjust to form the wake. There is also a weaker "Kutta adjustment" through the subsonic sublayer embedding the trailing edge which is distorted by both the sublayer approximation in the boundary layer and the overlaying unphysically thickened shock (fig. 6). The consequence of this distortion is local and should not affect the overall lift.

The calculations were carried out for a Mach number of 2.2 and a Reynolds number of  $4.3 \times 10^6$  based on the 2.4 foot mean wing chord. Angles of attack of  $4^\circ$ ,  $10^\circ$ ,  $14^\circ$ , and  $18^\circ$  were calculated, but only the results for  $14^\circ$  are presented. In figure 7 is shown the mesh at a wing station generated by an elliptic method. There are 45 points in the radial direction and 91 points along the half circumference. In figure 8 the calculated pressure distributions at  $14^\circ$  angle of attack are compared with the measured distributions at several streamwise stations. Good agreement is seen here consistent with the comparisons found at the other angles of attack. In figure 9 we compare the corresponding pitot pressure profiles in the boundary layer at several locations in a streamwise cut. The agreement in the profiles is reasonably good except where an inadequately refined mesh was used as at Station A. The inadequacy of the mesh here becomes evident by noting the steepness of the measured velocity gradient in the sublayer relative to the mesh used. The calculations have further yielded details of the profile as the "wiggle" at the fuselage side (Station C) and on the wing (Station G) caused by a streamwise vortex which was detected from total pressure and vorticity maps. Thus to improve the overall test/theory match of the pitot profiles, one must refine the mesh in the sublayer, perhaps inserting a wall function to moderate the resulting computer cost.

In figure 10 the streamwise vorticity and Mach number contours in a transverse plane at a wing station are shown, while in figure 11 the corresponding transverse velocity vector map is given. Here the fuselage and wing vortices are evident. It is further seen that the separation on the wing originates not along the leading edge but at farther downstream points.

#### CONCLUDING REMARKS

Two levels of computing the viscous vortical flows over delta wing configurations at large angles of attack were demonstrated. In the first, the boundary layer method was used to determine the viscous displacement effects of the secondary separation over a flat plate delta wing at low speeds. Here the equivalent inviscid flow containing the primary separation vortices was

calculated using the leading-edge vortex panel method with the separation line fixed along the leading edge. The results indicated that the formulation of the boundary layer problem in the direct mode and the solution procedure were sound for the secondary separation but the leading-edge vortex panel method for the equivalent inviscid flow was inadequate. Here the substitution of the Euler code with provisions for viscous transpiration velocities would be desirable. The direct mode inviscid/viscid flow coupling did not offer any difficulties.

In the more complicated case of the Model-350 fighter a more global approach with the PNS method was used. Reasonable test/theory match was obtained for the surface pressure distributions and for the boundary layer pitot pressure profiles when an adequately refined mesh was used. Remarkably the algebraic Baldwin/Lomax turbulence model (basically the two-layer Cebeci/Smith model) continues to be a viable framework to treat complex viscous flows as the present one. There clearly is no immediate need to turn to more fundamental, though not necessarily more accurate, transport equation models that greatly increase the computer time.

The more widely recognized advantage of the PNS method relative to the ARC 3D method is the greatly reduced computing time due to the reduction of an unsteady problem to a steady one. A less obvious though a more important advantage for complex configurations as the Model -350 with nacelles and aft stabilizing surfaces is the resultant simplification of the mesh generation from a 3D to a 2D problem.

These significant advantages must be weighed against the shortcomings of the PNS method which preclude reversed flows and distort the elliptic influence mechanism through the thin subsonic portion of the boundary layer. The consequences of the latter however should not be of significance except where abrupt streamwise configuration slope changes arise, as at the leading edge of the wing root section or along the wing trailing edge, where large streamwise pressure gradients as shock waves are produced. Here the upstream influence through the subsonic portion of the boundary layer will be localized for turbulent flows in the absence of separation.

The experience with the two levels of treating viscous vortical flows suggests generally that the global approach with the Navier/Stokes method is the simpler more straightforward method for the user. Computer costs, particularly with the ARC 3D code, will continue to be a significant issue for some time. The boundary layer method will thus have its role of treating the simpler separated flows as those considered herein.

Finally we would like to express our gratitude to Dr. L. Schiff and Dr. D. Chaussee of NASA/Ames for indoctrinating us on the PNS code.

#### REFERENCES

1. Küchemann, D.: On the Possibility of Designing Wings that Combine Vortex Flows with Classical Aerofoil Flows. RAE T. M. Aero 1363, Oct. 1971.



2. Wai, J. C.; Baille, J. C.; and Yoshihara, H.: Calculation of Turbulent Separated Flow Over Wings. 3rd Symposium on Numerical and Physical Aspects of Aerodynamic Flows, California State Univ.-Long Beach, Cal., Jan. 1985.
3. Wigton, L.; and Yoshihara, H.: Viscous-Inviscid Interactions with a Three-Dimensional Inverse Boundary Layer Code. 2nd Symposium on Numerical and Physical Aspects of Aerodynamic Flows, California State Univ.-Long Beach, Cal. Jan. 1984.
4. Smith, P. D.: An Integral Prediction Method for Three-Dimensional Compressible Turbulent Boundary Layers. ARC R&M 3739, 1972.
5. Yoshihara, H.: Separated Flow Calculations in the B. L. Limit. Boeing TN BMAC 85-02, 1985.
6. East, L.; Smith, P. D.; and Merryman, P.: Prediction of the Development of Separated Turbulent Boundary Layers by the Lag Entrainment Method. RAE TR 77046, 1977.
7. East, L.: Measurements of the 3D Incompressible Turbulent Boundary Layer Induced on the Surface of a Slender Delta Wing by the Leading Edge Vortex. ARC R&M 3768, 1975.
8. Hummel, D.: On the Vortex Formation over a Slender Wing at Large Angles of Attack. AGARD CP-247, 1979.
9. Chaussee, D.; Blom, G.; and Wai, J. C.: Numerical Simulation of Viscous Supersonic Flow over a Generic Fighter Configuration. Sixth GAMM Conference on Numerical Methods in Fluid Dynamics, Gottingen, Sept. 1985.
10. Capone, F.J.; Bare, E. A.; Hollenback, D.; and Hutchison, R.: Subsonic/Supersonic Characteristics for a Tactical Supercruiser. AIAA Paper No. 84-2192, 1984.
11. Schiff, L.; and Steger, J.: Numerical Simulation of Steady Supersonic Viscous Flow. NASA TP 1749, 1981.

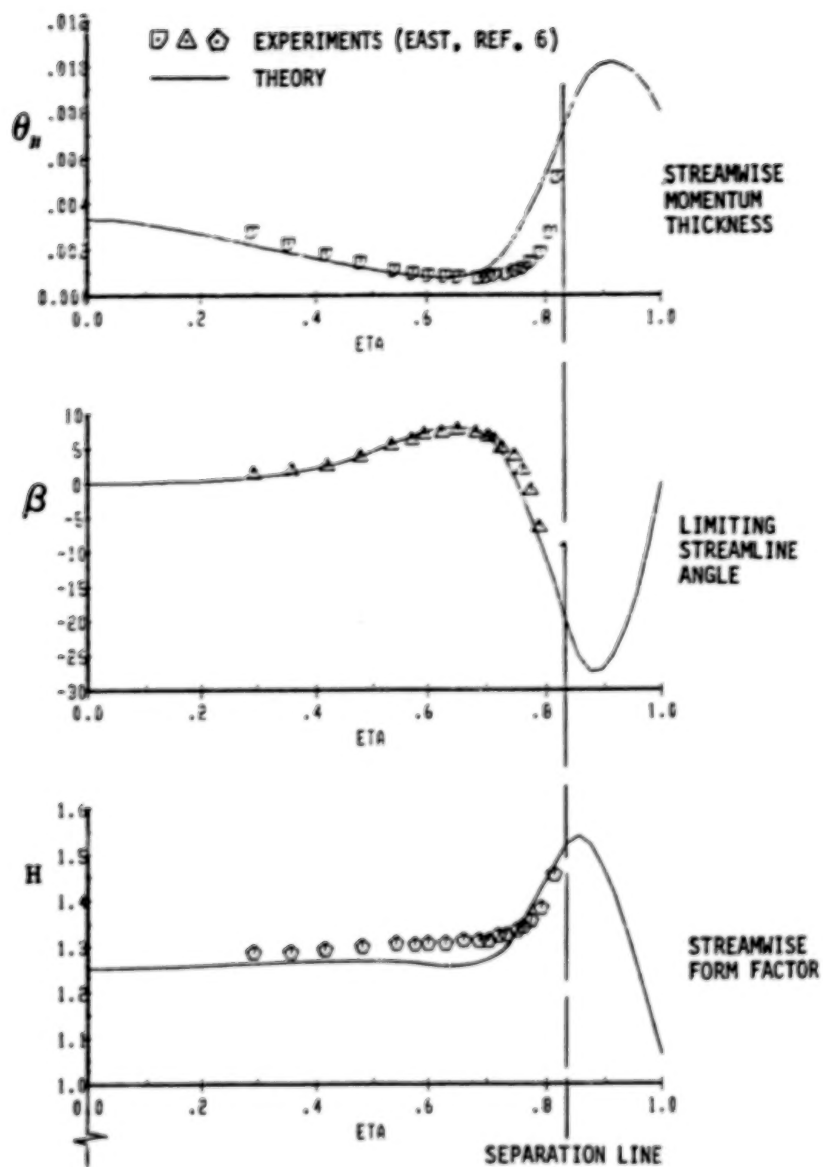


Figure 1. Test/Theory Comparison of Viscous Variables for East's Delta Wings

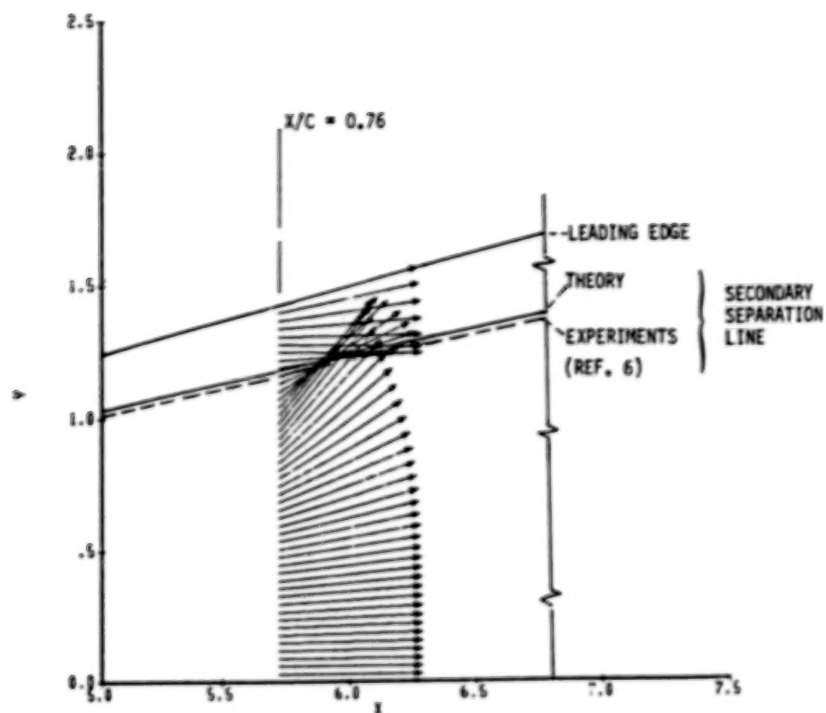


Figure 2. Limiting Streamline Vectors for East's Delta Wing.

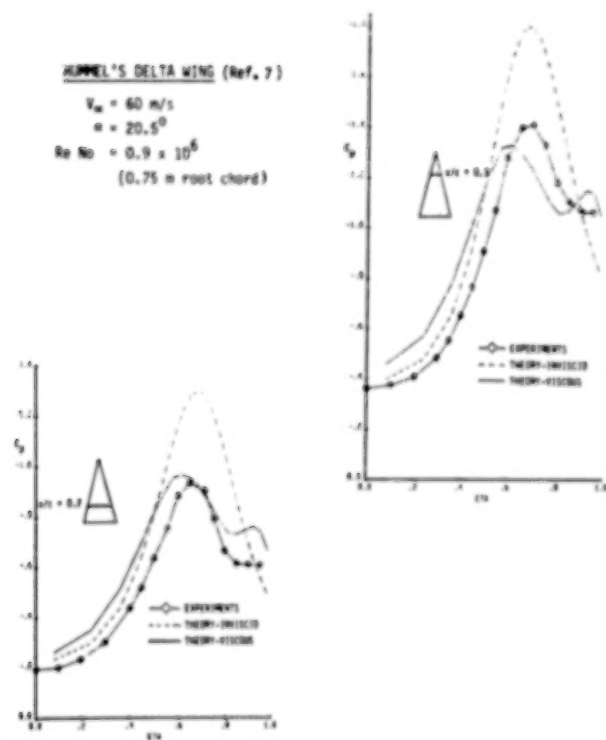


Figure 3. Test/Theory Comparison of Spanwise Pressure Distribution.

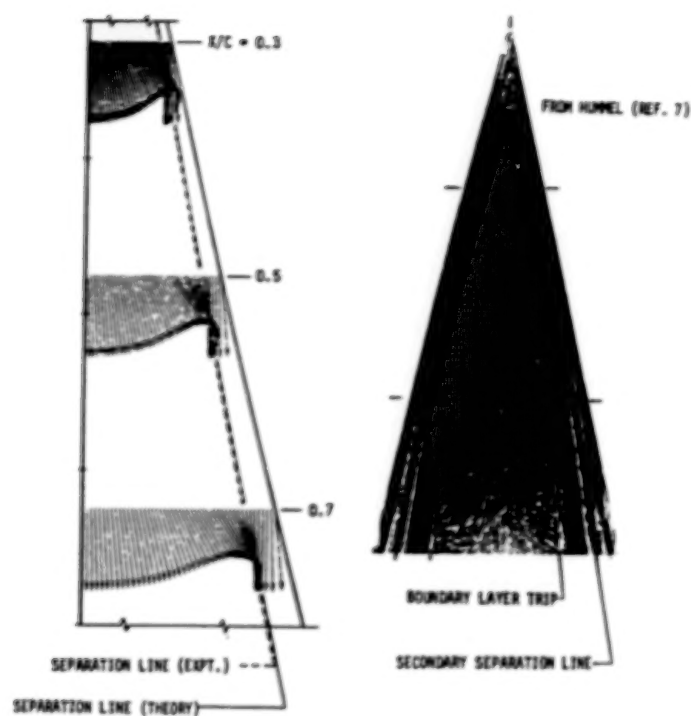


Figure 4. Limiting Streamlines and Separation Line of Hummel's Delta Wing.

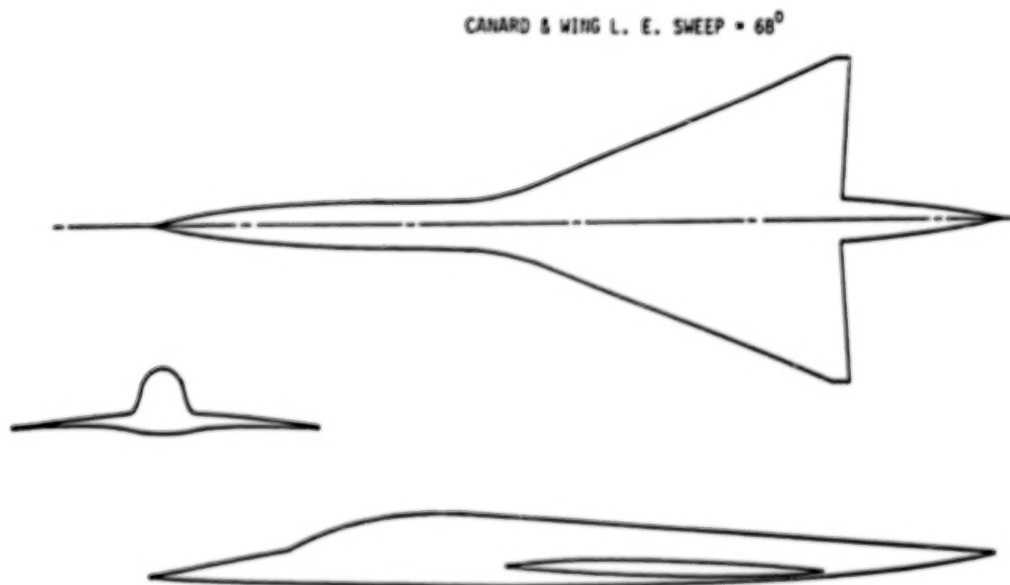


Figure 5. Model-350 Wing Fuselage.

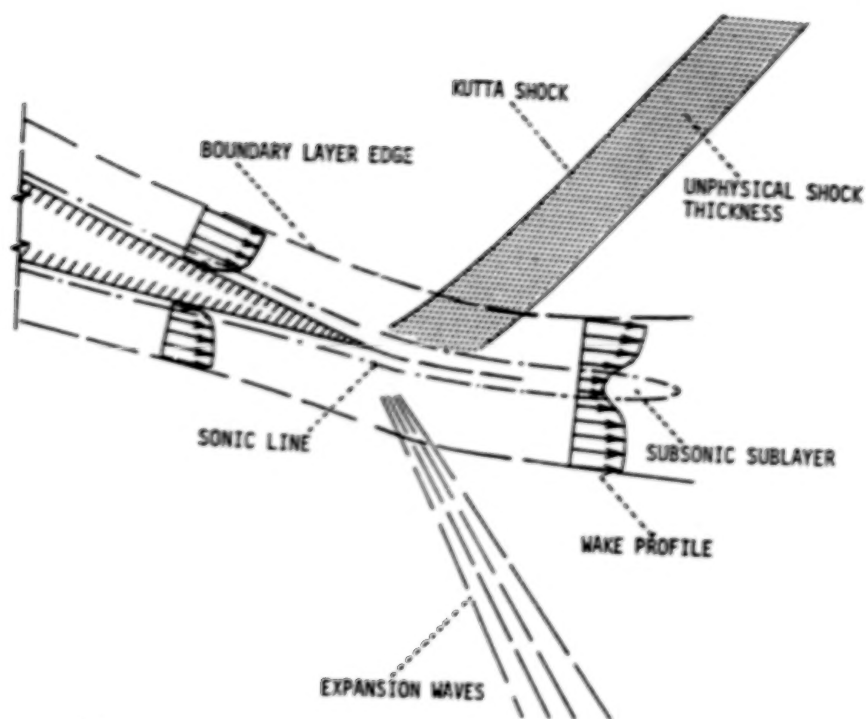


Figure 6. Schematic of Trailing-Edge Flow.

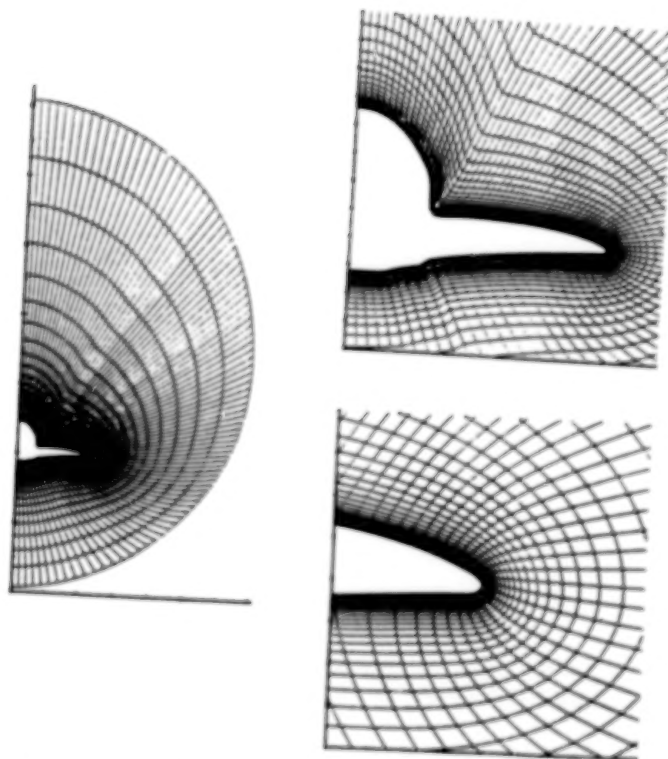


Figure 7. Elliptically Generated Wing Station Mesh.



ORIGINAL PAGE IS  
OF POOR QUALITY

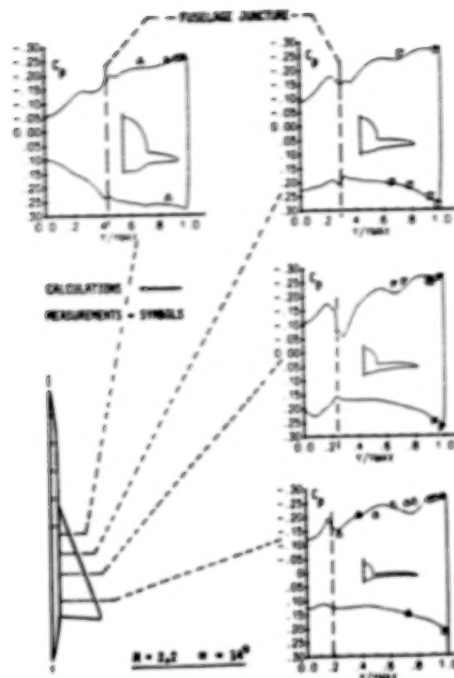


Figure 8. Test Theory Comparisons of Pressures.

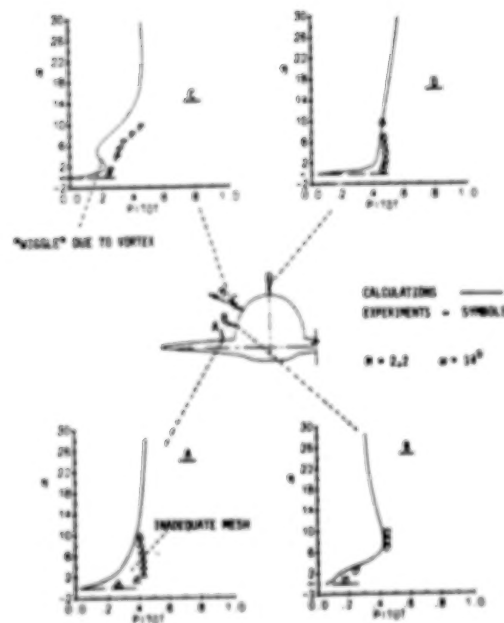


Figure 9. Test Theory Comparison of Pitot Pressure Profiles.

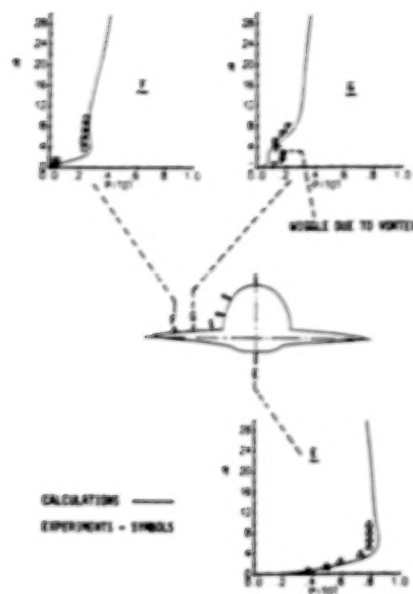


Figure 9. Concluded.

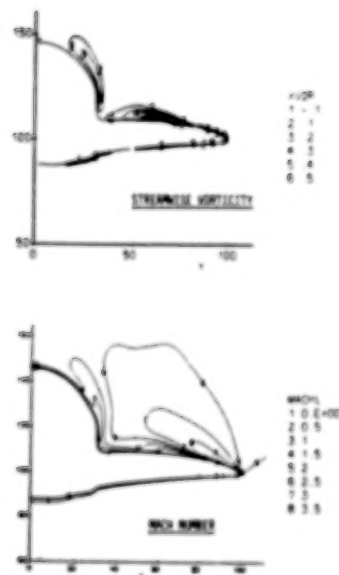


Figure 10. Streamwise Vorticity and Mach Number Contours.

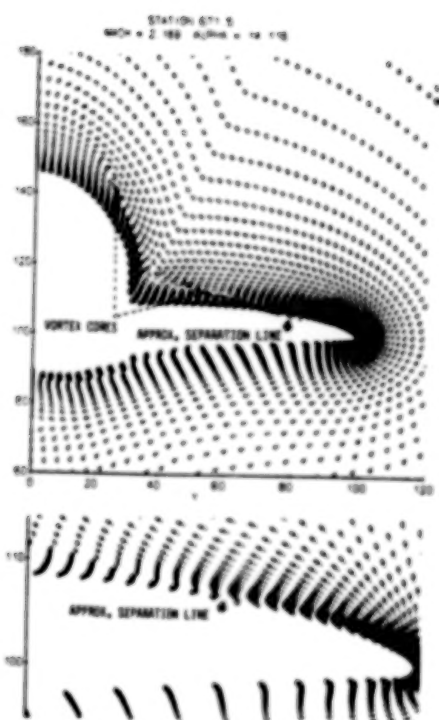


Figure 11. Transverse Velocity Vector Pattern.

## AN EULER AERODYNAMIC METHOD FOR LEADING-EDGE VORTEX FLOW SIMULATION

Pradeep Raj  
Lockheed - California Company  
Burbank, California

Lyle N. Long  
Lockheed - Advanced Aeronautics Company  
Valencia, California

## SUMMARY

This paper describes the current capabilities and the future plans for a three-dimensional Euler Aerodynamic Method. The basic solution algorithm is based on the finite-volume, Runge-Kutta pseudo-time-stepping scheme of FLO-57. Several modifications to improve accuracy and computational efficiency have been incorporated and others are being investigated. The computer code is used to analyze a cropped delta wing at 0.6 Mach number and an arrow wing at 0.85 Mach number. Computed aerodynamic parameters are compared with experimental data. In all cases, the configuration is impulsively started and no Kutta condition is applied at sharp edges. The results indicate that with additional development and validation, the present method will be a useful tool for engineering analysis of high-speed aircraft.

## INTRODUCTION

The simulation of three-dimensional vortices interacting with lifting surfaces is of considerable importance to aircraft designers. This problem is of special significance for supersonic-cruise aircraft which have highly swept slender wings. At moderate-to-high angles of attack, the flow invariably separates from the leading edges resulting in the formation of free vortices above the wing. Significant improvements in aerodynamic performance can be derived, as shown in Figure 1, by careful generation and control of these vortices. At the present time, a designer has to rely on extensive and costly wind-tunnel tests. The development of accurate, efficient, and reliable computational methods will provide a more economical means of designing aerospace vehicles.

Past research on leading-edge-separated-flow simulation has produced a variety of computational methods. At one end of the spectrum are the vortex-lattice (Refs. 1-4) and free-vortex-sheet methods (Refs. 5,6). Since they are based on a linearized potential-flow formulation, rotational vortex flow cannot be predicted as part of the solution. The leading-edge vortex has to be explicitly modeled either indirectly using the suction analogy of Polhamus (Ref. 7) or directly using singularity distributions (Refs. 4,5). At the other end of the spectrum are the finite-difference methods based on the Reynolds-averaged Navier-Stokes equations (Ref. 8) which provide an essentially complete fluid-dynamic model. Their use offers the major advantage that the leading-edge vortices result as a part of the solution. However, the available methods are not suitable for routine practical applications due to the exorbitant requirements of computational resources and the lack of a suitable universal turbulence model.

Recent advances in numerical algorithms to solve the Euler equations (Refs. 9,10) provide an attractive and cost-effective alternative to using Navier-Stokes codes. Their ability to automatically capture regions of rotational flows has been demonstrated by several investigations (Refs. 11-15). In this paper, the current

status and planned development of a three-dimensional Euler Aerodynamic Method (TEAM) and its application to model leading-edge separated flow about a cropped-delta wing and an arrow wing are presented.

TEAM represents a modular computational system being developed by the Lockheed-California Company for analyzing complete aircraft configurations. A schematic of the system is shown in Figure 2. This development is being partially funded by the U. S. Air Force Wright Aeronautical Laboratory (AFVAL)/Flight Dynamics Laboratory (FDL) under a three-year contract (F33615-84-C-3005). The basic features of the method are described in the next section.

### THREE-DIMENSIONAL EULER AERODYNAMIC METHOD

The explicit pseudo-time-stepping, finite-volume algorithm of Jameson et al. (Ref. 9), modified by Lockheed-California Company over the past three years, forms the core of the TEAM code. Jameson's original wing-alone code is widely known as FLO-57. The region surrounding a given configuration is subdivided into small cells. In each of the cells, the time-dependent Euler equations (in integral equation form), representing the mass, momentum, and energy conservation, are integrated in time using a multi-stage Runge-Kutta scheme. To accelerate convergence to the steady state, local rather than global time steps are used. Implicit residual smoothing (Ref. 16) further reduces the number of time steps required to reach the steady state. Appropriate non-reflecting boundary conditions based on Riemann invariants (Ref. 16) are used at the far-field boundaries and no-normal-flow conditions are used on the solid surface.

The finite-volume formulation essentially decouples the flow solver from the grid generator. The grids can be constructed in any convenient manner; only the Cartesian coordinates of the nodal points are required by the solver. This aspect of the basic algorithm has been exploited to build the TEAM system for analyzing complete aircraft configurations. An overview of the four major modules (Figure 2) constituting the system is presented in this section.

#### TEAM PREPROCESSOR MODULE

This module will provide a capability to process geometry-definition data supplied by a designer in order to construct an accurate geometrical model of a configuration and a suitable grid on its surface. The designer-supplied data typically contain a series of cross-sectional curves defining various components. In some instances, the configuration may be geometrically defined for some other aerodynamic analysis code. Constructing a model that accurately reflects the information contained in this form is the crucial first step. A surface grid on this model forms the key input for any grid-generation method. Appropriate interfaces are being developed to accomplish these tasks using the Configuration Data Management System (CDMS), which Lockheed - Georgia Company is developing for the U.S. Air Force under contract F33615-84-C-3001.

#### TEAM GRID GENERATOR MODULE

A variety of techniques, both algebraic and differential, are included in the grid-generator module, as shown in Figure 3. This is essential because, at the present time, there is no single method that can be used to generate suitable grids for all configurations. The current capabilities of the various methods are summarized in Figure 4. Their desirable features are also compared in the same figure. For instance, the algebraic Trans-Finite Interpolation (TFI) method is computationally



efficient and powerful but requires considerable user interaction to generate suitable grids as compared to the differential-equation methods, such as the Boundary Integral Grid (BIG) generation method (Ref. 17). This automation is achieved at the expense of computational efficiency. The Parabolic Conformal Mapping with Shearing (PACMAPS) technique (Ref. 18) is computationally efficient and easy to use; however, the grids must be of C-H topology. The C-H grid topology is illustrated in Figure 5.

Two diagnostic tools are crucial to the grid-generator module: Lockheed's PLOT3D program for interactively displaying grids and an analytical grid checking program. The grid checker can automatically locate regions where the grid lines either cross or are highly skewed. These regions are then further examined using PLOT3D and modified as necessary.

#### TEAM FLOW SOLVER MODULE

As mentioned above, the flow solver is based on the finite-volume, pseudo-time-marching algorithm of Jameson et al. (Ref. 9). Since the mathematical and numerical features of the basic scheme are adequately described in References 9 and 19, they will not be repeated here. Several modifications have been and are being incorporated by Lockheed to enhance the capabilities of the solver as summarized in Figure 6. These modifications are briefly described below.

**Flux Computation.** -- The cell-centered finite-volume scheme used for spatially discretizing the Euler equations expresses the time-rate of change of a flow quantity in a cell as the net flux through the surfaces of the cell. A variety of approximations can be used to numerically compute this flux. The current version of the code uses a strongly conservative formulation. It is compared with the original FLO-57 formulation in Figure 7. Quantitative improvement in accuracy is under investigation.

**Numerical Dissipation.** -- The present finite-volume scheme reduces to a central-difference scheme on a uniform grid. To suppress the well-known tendency for odd and even point decoupling of such schemes, and to limit the generation of wiggles and overshoots near shock waves, blended second and fourth differences have to be added. The coefficient of the second-order terms is proportional to the local pressure gradient. Therefore, these terms are turned on only where larger amounts of dissipation are needed, e.g., near shocks and stagnation points. Elsewhere, the fourth-difference terms keep the dissipation small.

The dissipation terms are approximated by central-difference formulas for all cells except those near the boundaries. In the original FLO-57 code, the contribution of  $\eta$ -direction terms (normal to the surface) was ignored for cells adjacent to the boundaries. This approach, designated Scheme 1 here, leads to an erroneous production of entropy. To eliminate this deficiency, alternative schemes have been incorporated.

All those cells that do not abut the solid surface (including the ones aft of the trailing edge) were treated like any other interior cell. For those adjacent to the solid boundary, four schemes are available. The order of approximation of the  $\eta$ -direction differences for these schemes is compared in Figure 8. An extensive evaluation is in progress in order to select one of these schemes for the solver. For the results shown in this paper, Scheme 2 is used.

**Surface Boundary Conditions.** -- On a solid surface, the no-normal-flow boundary condition is imposed by setting all convected flux quantities to zero. Only the pressure on the solid surface contributes to the momentum flux balance. Since

pressure is calculated at the cell center, one is forced to estimate its value at the actual surface. This is accomplished by computing the derivative of pressure normal to the surface using the momentum equation:

$$\rho \nabla \cdot (\mathbf{V} \cdot \mathbf{n}) = \mathbf{n} \cdot \nabla p$$

where:  $\mathbf{V}$ ,  $\mathbf{n}$ , and  $p$  are the fluid velocity, surface normal, and pressure, respectively. This derivative and the cell-centered values are then combined to determine the surface pressure. A precise implementation requires that all metric quantities and flow variables occurring in the equation above be evaluated right on the surface. In the original FLO-57 program, this was not done; the cell-center values were used instead. In the present version of the solver, three additional approaches may be used to obtain the desired flow variables on the actual surface: (1) A Taylor series expansion about the cell center, (2) Lagrange two-point extrapolation along the local normal direction, and (3) Averaging the cell-center values for cells next to the surface in the flow domain and ghost cells outside of the flow domain. An extensive evaluation of the different approaches is under way.

**Grid Topologies.** -- The present version of the solver can accommodate single global grids of various topologies. The original FLO-57 solver was limited to isolated wings having C-H grids, whereas the O-O and C-O types offer improved resolution (Ref. 20). If a C-H mesh is used, adequate resolution near the wing tip can be obtained only by increasing the number of cells in the spanwise direction. It must be noted that none of these topologies is as suitable as the H-H when detailed flow field about all sections of a wing-body or wing-body-tail configuration is desired. With these considerations, the solver was modified to accommodate O-O, C-O and H-H grids, in addition to the C-H.

**Patched Zonal Solver.** -- The development of a zonal solver is motivated by the need to analyze complex geometries and to improve computational efficiency. For complex geometries, e.g., a complete aircraft, it becomes extremely difficult to generate a single global grid. The difficulty is further aggravated by the necessity to cluster cells in regions of large flow gradients. These problems can be largely alleviated by dividing the flow domain into a number of zones and by constructing the grid in each zone independently.

A significant improvement in computational efficiency may be achieved by using refined meshes in zones where large gradients in flow variables are expected and using relatively coarse meshes elsewhere. Work is presently under way to develop a solver that can accommodate patched zonal grids. The feasibility of this approach has been demonstrated for two dimensions by Rai (Ref. 21).

#### TEAM POSTPROCESSOR MODULE

This module is composed of sub-modules to accurately determine forces and moments using the flow variables computed by the solver and to graphically display surface pressure distributions, flow-field velocity vectors, and iso-parametric contours.

The surface-pressure integration method for computing forces and moments is currently used in the code. This method is only accurate when a relatively fine grid is used. Small errors in surface pressures and geometry can lead to large errors in drag. Also, this approach cannot give an estimate of how the total drag is split into lift-induced and wave drag. Alternative approaches are being pursued.

For graphically displaying data, appropriate interfaces will be developed for linking the TEAM code with CDMS.

## RESULTS

A number of configurations have been analyzed using the TEAM code during its development to date. Results for a cropped delta wing and an arrow wing are presented here. For each case, the entire region is initialized to free-stream conditions. This is equivalent to impulsively starting the configuration. No Kutta condition is explicitly applied at the sharp edges.

### CROPPED DELTA WING

This wing has a leading-edge sweep of 63 degrees, a taper ratio of 0.1, and an aspect ratio of 1.64. Its cross section is a NACA 63A002 airfoil. It was analyzed using the TEAM code at a Mach number of 0.6 and angles of attack of 8, 16, and 24 degrees. Two grids were used, one having 24,576 ( $96 \times 16 \times 16$ ) cells and the other having 98,304 ( $96 \times 32 \times 32$ ) cells. Both were topologically C-H. The airfoil sections are defined by 30 cells on both the upper and lower surfaces (for both grids). In the spanwise direction the wing is described by 10 cells for the coarse grid and 20 cells for the finer grid. Between the wing and the far-field, there are 16 and 32 cells for the two grids respectively. The C-curves are clustered around the wing using a control curve (Ref. 18).

The computed aerodynamic forces and moments are compared with the experimental data (Ref. 22) in Figure 9. The overall agreement between the predictions and the measurements is good. The code is able to model the nonlinear nature of the flow. The differences between the predictions can be traced to the differences in flow resolution provided by the two grids. This is illustrated by cross-plane surface pressure distributions at  $x/c = 0.6$  and  $0.9$  (where  $c$  is the root chord) shown in Figure 10 and the corresponding velocity vectors in Figure 11 for the 16-degree angle-of-attack case. The presence of a leading-edge separated vortex is clearly shown in Figure 11.

One aspect of this particular configuration deserves special attention. The convergence history plot for the coarse mesh presented in Figure 12 shows that the average error (net mass-flux) is reduced by 4 orders of magnitude for all the cases. The fine mesh results also converge for the 8 and 16 degrees angle-of-attack cases, as shown in Figure 13.

However, the fine mesh results clearly do not converge at 24 degrees angle of attack. It is interesting to note that the experimental data (Figure 9) shows a definite break in the lift-curve slope above approximately 20 degrees angle of attack; and, as shown by the horizontal line in Figure 9, the predicted lift oscillates about the experimental data. In the absence of detailed experimental data on the flow field, one can only speculate on the flow phenomena involved here. The leading-edge vortex bursting and/or massive viscous separation could be responsible. The set of computed cross-plane pressure distributions and velocity-vector plots shown in Figure 14 indicate that the leading-edge vortex is essentially stable after 600 cycles at  $x/c=0.6$  cross-plane; but, as shown in Figure 15, its structure and location are changing continuously at  $x/c=0.9$  cross-plane. This latter fact is responsible for the lack of convergence seen in Figure 13. It would be most interesting to obtain more detailed experimental data and compare them to these numerical results in order



to validate the predictions of the code. Of course, the time histories shown here cannot be taken literally since pseudo-time marching was used and they are not time accurate.

It is quite obvious from the studies to date that a refined grid is essential to the simulation of leading-edge vortex flows even for relatively simple wings. Additional studies are needed to answer the obvious question: "How refined should a grid be?" Lockheed is conducting such studies under an on-going cooperative program with NASA Langley Research Center. Since the TEAM code is being developed to analyze entire aircraft configurations, studies such as these will help determine the number of cells required to adequately predict leading-edge vortex flows on complex configurations.

#### ARROW WING

The next set of results is for an arrow wing with a leading-edge sweep of 71.2 degrees, a taper ratio of 0.1, and an aspect ratio of 1.4. The wing was analyzed at 0.85 Mach number and -4, 8, and 16 degrees angle of attack using a C-H grid having 98,304 (96x32x32) cells.

The computed normal force and pitching moment coefficients are compared with experimental data (Ref. 23) in Figure 16. Cross-plane surface pressure distributions are compared to experimental data for four locations in Figure 17. Velocity vector plots for the same locations are shown in Figure 18. Measured velocity vectors are not available for this configuration. However, recent advances in Laser-Doppler Velocimetry (Ref. 24) now make it possible to compare measured and predicted velocity vectors for complicated three-dimensional flow fields.

Additional studies are under way to use even more refined grids to determine the source of discrepancy between the theory and measurements. Two possible sources are: (1) the experiments were conducted for a wing-body configuration whereas the computations are for an isolated wing, and (2) the present wing has a rounded leading edge and the point of separation may not be correctly located by the present code. These issues will be addressed in future studies.

#### CONCLUDING REMARKS

The current status and proposed development of a three-dimensional Euler Aerodynamic Method (TEAM) were presented in this paper. Correlations of computed aerodynamic parameters and surface pressure distributions with experimental data indicate its ability to capture leading-edge separated vortices. Unlike the procedures based on velocity potential, it is not required to explicitly model these vortices. In addition, the same code can be used for analysis throughout the subsonic, transonic, and supersonic flight regimes. The results presented in this paper point to a need for more extensive validation. A number of questions, especially related to the effect of grid density and numerical dissipation on the solution, remain to be answered. With continuing development and validation, it promises to provide an effective engineering tool for analyzing nonlinear flows containing both shock waves and leading-edge-separated vortices.

## REFERENCES

1. Lamar, J. E., "Extension of Leading-Edge-Suction Analogy to Wings with Separated Flow Around the Side Edges at Subsonic Speeds," NASA TR R-428, October 1974.
2. Lamar, J. E. and Gloss, B. B., "Subsonic Aerodynamic Characteristics of Interacting Lifting Surfaces with Separated Flow Around Sharp Edges Predicted by a Vortex-Lattice Method," NASA TN D-7921, September 1975.
3. Lan, C. E. and Chang, Jen-Fu, "Calculation of Vortex Lift Effect for Cambered Wings by Suction Analogy," NASA CR 3449, July 1981.
4. Mehrotra, S. C. and Lan, C. E., "A Theoretical Investigation of the Aerodynamics of Low-Aspect-Ratio Wings with Partial Leading-Edge Separation," NASA CR 145304, 1978.
5. Johnson, F. T., Lu, P., Tinoco, E. N., and Epton, M. A., "An Improved Panel Method for the Solution of Three-dimensional Leading-edge Vortex Flows," NASA CR 3279, July 1980.
6. Luckring, J. M., Schoonover, W. E., and Frink, N. T., "Recent Advances in Applying Free Vortex Sheet Theory for the Estimation of Vortex Flow Aerodynamics," AIAA 82-0095, 20th Aerospace Sciences Meeting, Orlando, Florida, January 11-14, 1982.
7. Polhamus, E. C., "A Concept of the Vortex Lift of Sharp Edge Delta Wings Based on a Leading-Edge-Suction Analogy," NASA TN D-3767, 1966.
8. Fujii, K. and Kutler, P., "Numerical Simulation of the Leading-Edge Separation Vortex for a Wing and Strake-Wing Configuration," AIAA Paper 83-1908-CP, 6th Computational Fluid Dynamics Conference, Danvers, Massachusetts, July 13-15, 1983.
9. Jameson, A., Schmidt, W., and Turkel, E., "Numerical Solutions of the Euler Equations by Finite Volume Methods Using Runge-Kutta Time-Stepping Schemes," AIAA Paper 81-1259, 14th Fluid and Plasma Dynamics Conference, Palo Alto, California, June 23-25, 1981.
10. Rizzi, A., "Damped Euler Equation Method to Compute Transonic Flow Around Wing-Body Combinations," AIAA Journal, Vol. 20, No. 10, October 1982, pp. 1321-1328.
11. Hitzel, S. M. and Schmidt, W., "Slender Wings with Leading-Edge Vortex Separation -- A Challenge for Panel Methods and Euler Codes," AIAA Paper 83-0562, 21st Aerospace Sciences Meeting, Reno, Nevada, January 10-13, 1983.
12. Raj, P. and Sikora, J. S., "Free-Vortex Flows: Recent Encounters with an Euler Code," AIAA Paper 84-0135, 22nd Aerospace Sciences Meeting, Reno, Nevada, January 9-12, 1984.
13. Rizzi, A., "Computer Simulation of Non-potential Flows Around Wings," Aeronautical Journal, June/July 1984, pp. 238-248.
14. Raj, P., "Computational Simulation of Free-Vortex Flows Using An Euler Code," ICAS-84-1.3.1, 14th Congress of the International Council of the Aeronautical Sciences, Toulouse, France, September 9-14, 1984.



15. Rizzi, A. and Eriksson, L.E., "Computation of Flow Around Wings Based on the Euler Equations," *Journal of Fluid Mechanics*, Vol. 148, November 1984, pp. 45-71.
16. Jameson, A. and Baker, T. J., "Solution of the Euler Equations for Complex Configurations," AIAA Paper 83-1929-CP, 6th Computational Fluid Dynamics Conference, Danvers, Massachusetts, July 13-15, 1983.
17. Sikora, J. S. and Miranda, L. R., "Boundary Integral Grid Generation Technique," AIAA Paper 85-4088, 3rd Applied Aerodynamics Conference, Colorado Springs, Colorado, October 14-16, 1985.
18. Raj, P., "PACMAPS: A Three-dimensional Grid Generation Method, Version 1.0," LR 30811, Lockheed-California Company, October 1984.
19. Agarwal, R. K. and Deese, J. E., "Transonic Wing-Body Calculations Using Euler Equations," AIAA Paper 83-0501, 21st Aerospace Sciences Meeting, Reno, Nevada, January 10-13, 1983.
20. Eriksson, L. E., "Generation of Boundary-Conforming Grids About Wing-Body Configurations Using Transfinite Interpolation," *AIAA Journal*, Vol. 20, No. 10, October 1982, pp. 1313-1320.
21. Rai, M. M., "A Conservative Treatment of Zonal Boundaries for Euler Equation Calculations," AIAA Paper 84-0164, 22nd Aerospace Sciences Meeting, Reno, Nevada, January 9-12, 1984.
22. Emerson, H. F., "Wind-Tunnel Investigation of the Effect of Clipping the Tips of Triangular Wings of Different Thickness, Camber, and Aspect Ratio - Transonic Bump Method," NACA TN 3671, June 1956.
23. Manro, M. E., Manning, K. J. R., Hallstaff, T. H., and Rogers, J. T., "Transonic Pressure Measurements and Comparison of Theory to Experiment for an Arrow-Wing Configuration," NASA CR-2610, August 1976.
24. Novak, C. J., Huie, C. R., and Cornelius, K. C.; "Laser Velocimetry in Highly Three-Dimensional and Vortical Flows," *Vortex Flow Aerodynamics - Volume I*, NASA CP-2416, paper no. 7, 1986.

- INCREASED MANEUVER LIFT
- INCREASED LANDING AND TAKEOFF LIFT
- LIGHT WEIGHT
- AERODYNAMIC CENTER CONTROL
- LITTLE INCREASE IN GUST RESPONSE
- REDUCED BUFFET INTENSITY

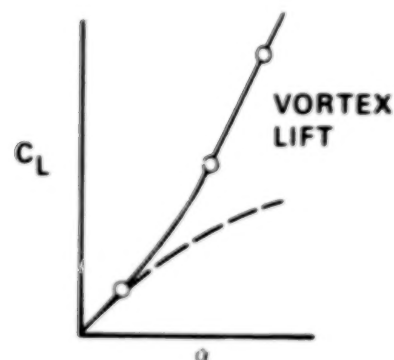
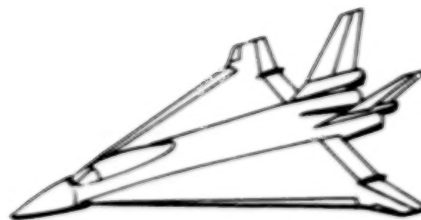


Figure 1. Benefits of vortex flow for high-speed aircraft.

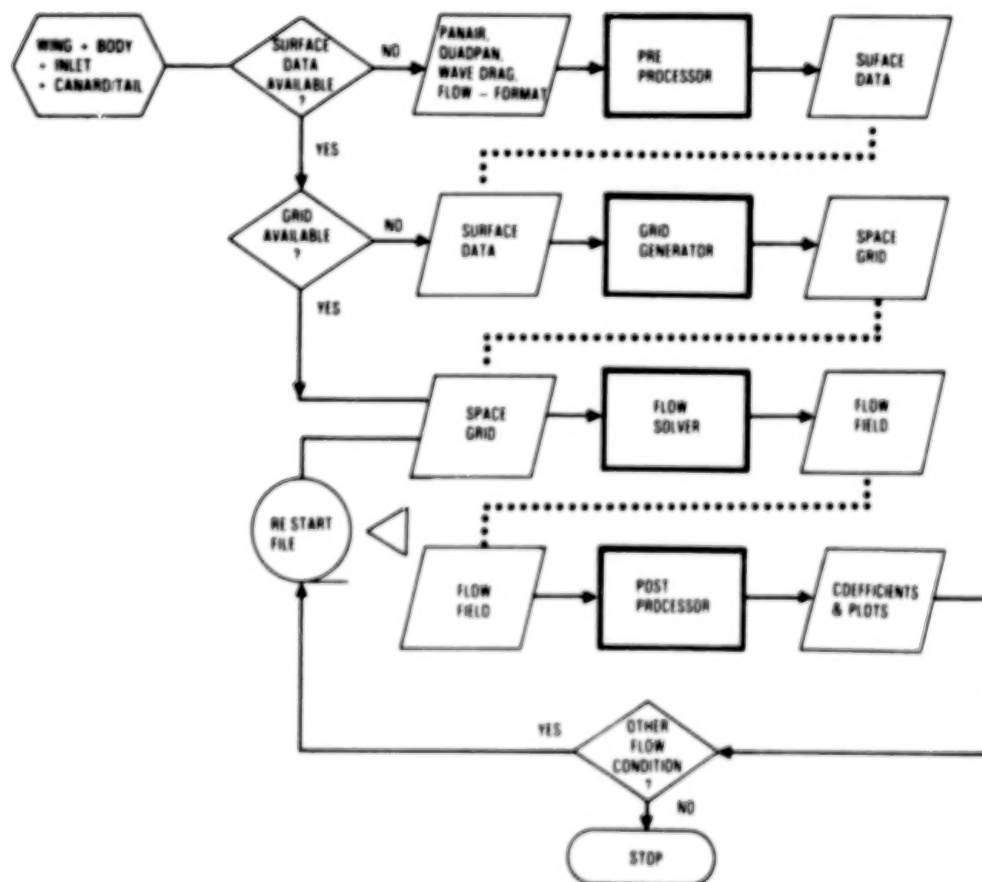


Figure 2. Lockheed-California Company's three-dimensional Euler aerodynamic method (TEAM).

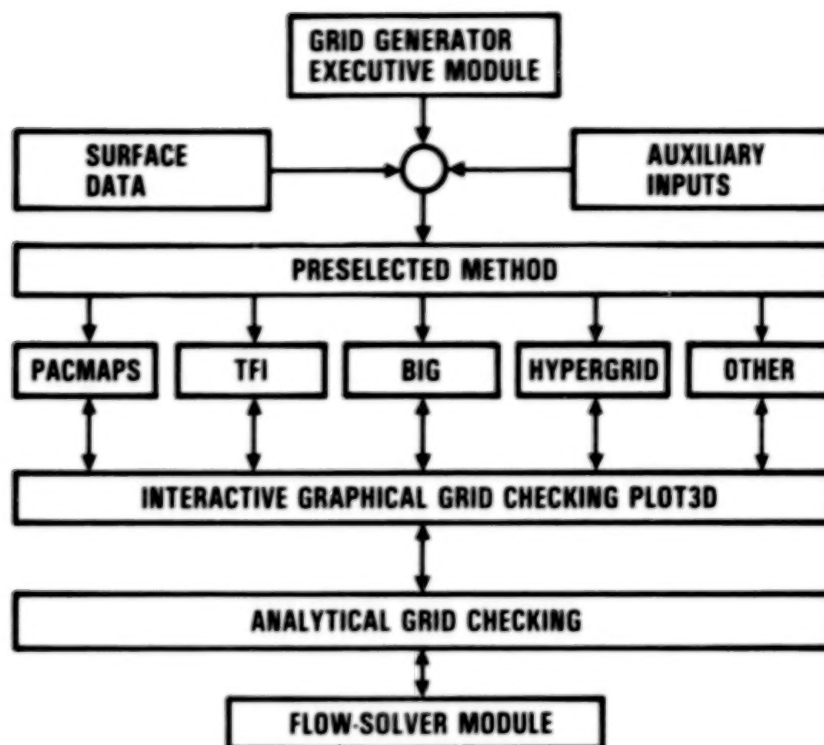


Figure 3. Schematic of TEAM's grid generator module.

| METHODS                              | GEOMETRY CAPABILITIES |           |                          |                           |                  | DESIRABLE FEATURES                |               |                              |                          |                           |
|--------------------------------------|-----------------------|-----------|--------------------------|---------------------------|------------------|-----------------------------------|---------------|------------------------------|--------------------------|---------------------------|
|                                      | WING                  | WING BODY | WING BODY<br>TAIL CANARD | WING BODY<br>TAIL NACELLE | GRID<br>TOPOLOGY | INTERACTIVE<br>GRID<br>GENERATION | USER FRIENDLY | COMPUTATIONALLY<br>EFFICIENT | SMALL AMOUNT<br>OF INPUT | SPECIFY OUTER<br>BOUNDARY |
| ALGEBRAIC:<br>PACMAPS                | ●                     | ●         | ○                        |                           | CH               | ●                                 | ●             | ●                            | ●                        |                           |
| TFI                                  | ●                     | ●         | ●                        | ●                         | CH, HH<br>CO, OO | ●                                 |               | ●                            |                          | ●                         |
| BOUNDARY INTEGRAL:<br>BIG            | ●                     | ●         | ●                        | ○                         | OO<br>CO         |                                   | ●             |                              | ●                        | ●                         |
| DIFFERENTIAL EQUATION:<br>HYPERBOLIC | ●                     | ●         | ○                        | ○                         | CO, OO<br>CH, HH |                                   | ●             | ●                            | ●                        |                           |
| ELLIPTIC                             | ○                     | ○         | ○                        | ○                         | CO, OO<br>CH, HH |                                   | ●             |                              |                          | ●                         |

● DEVELOPED    ◐ DEVELOPING    ○ PROPOSED

Figure 4. Lockheed-California Company's grid generation methods.

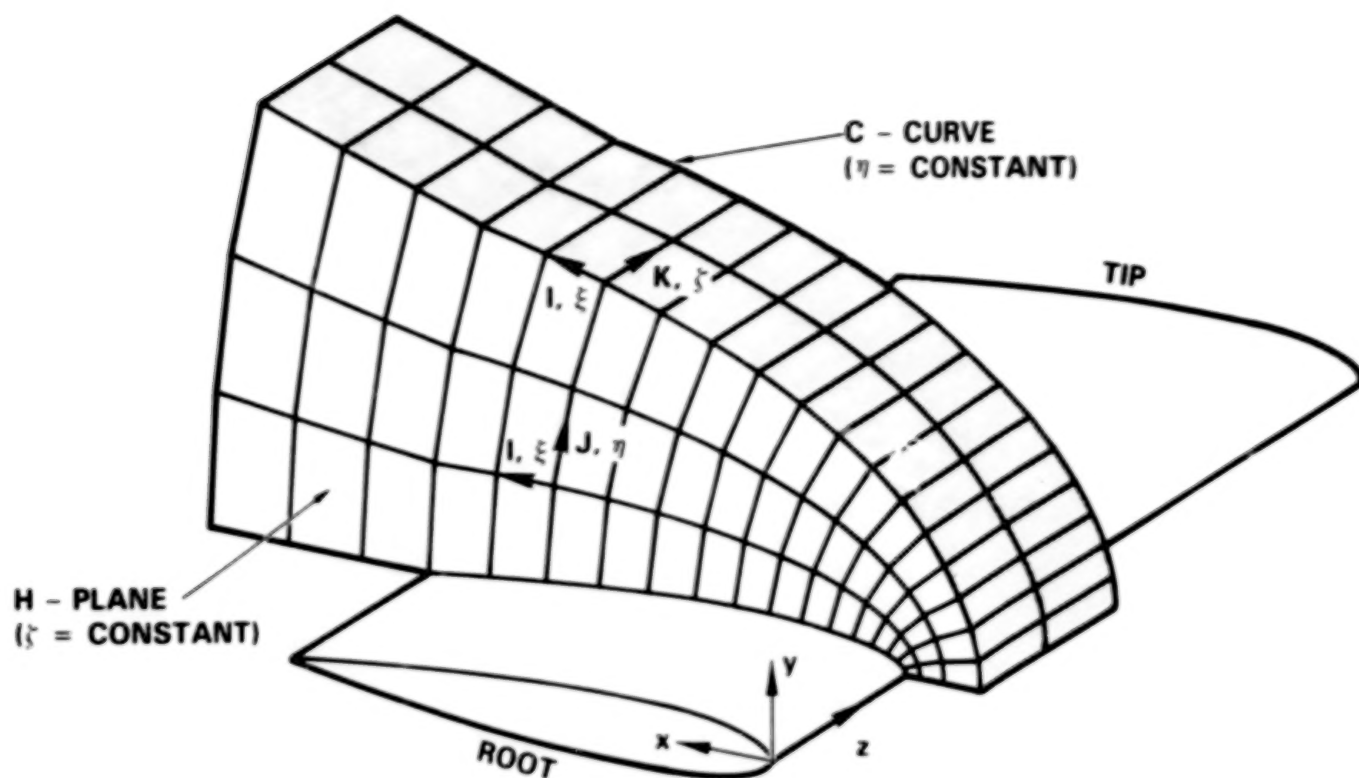


Figure 5. Example of a C-H grid.

| YEAR    | CAPABILITIES |           |                |                      | GEOMETRY |           |            |     | FLIGHT REGIME |     |     |               | GRID STRUCTURE |                    |                    |                             | ADDITIONAL FEATURES |  |  |  |
|---------|--------------|-----------|----------------|----------------------|----------|-----------|------------|-----|---------------|-----|-----|---------------|----------------|--------------------|--------------------|-----------------------------|---------------------|--|--|--|
|         | WING ALONE   | WING-BODY | WING-BODY-TAIL | WING-BODY-INLET-TAIL | SUBSONIC | TRANSONIC | SUPERSONIC | C-H | C-O           | O-O | H-H | SINGLE GLOBAL | PATCHED ZONAL  | INCREASED ACCURACY | FASTER CONVERGENCE | INVISCID/VISCID INTERACTION | ASYMMETRICAL FLIGHT |  |  |  |
|         |              |           |                |                      |          |           |            |     |               |     |     |               |                |                    |                    |                             |                     |  |  |  |
|         |              |           |                |                      |          |           |            |     |               |     |     |               |                |                    |                    |                             |                     |  |  |  |
| 1982    | ●            |           |                |                      | ●        | ●         | ●          |     |               |     |     |               |                |                    |                    |                             |                     |  |  |  |
| 1983    | ●            | ●         |                |                      | ●        | ●         | ●          | ●   | ●             |     |     |               |                |                    |                    |                             |                     |  |  |  |
| 1984    | ●            | ●         | ●              |                      | ●        | ●         | ●          | ●   | ●             | ●   | ●   |               | ●              | ●                  |                    |                             |                     |  |  |  |
| 1985-86 | ●            | ●         | ●              | ○                    | ●        | ●         | ●          | ●   | ●             | ●   | ●   | ●             | ●              | ●                  | ●                  | ○                           | ●                   |  |  |  |

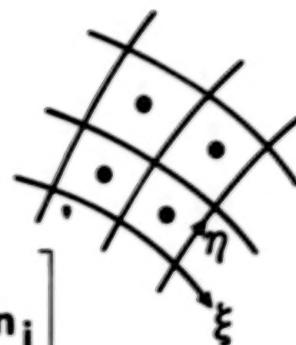
● DEVELOPED      ○ DEVELOPING      ○ PROPOSED

Figure 6. Capabilities of TEAM's flow solver module.

- **STRONGLY CONSERVATIVE FORMULATION IMPLEMENTED**

$$\frac{\partial}{\partial t} \iiint_{\Omega} \mathbf{Q} \, d\Omega + \iint_A \bar{\mathbf{F}} \cdot \hat{\mathbf{n}} \, dA = 0$$

$$\mathbf{Q} \equiv \begin{bmatrix} \rho \\ \rho u_i \\ \rho e \end{bmatrix} \quad \bar{\mathbf{F}} \cdot \hat{\mathbf{n}} = \begin{bmatrix} (\rho u_i) n_i \\ (\rho u_i u_j + p \delta_{ij}) n_j \\ (\rho u_i h) n_i \end{bmatrix}$$



- **ORIGINAL FORMULATION**

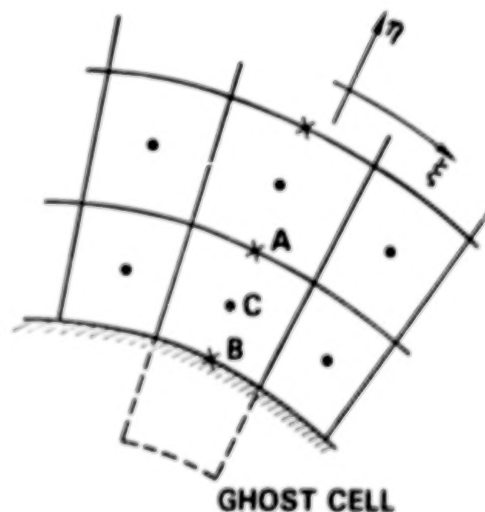
$$\bar{\mathbf{F}} \cdot \hat{\mathbf{n}} = \begin{bmatrix} \rho (u_i n_i) \\ (\rho u_i) (u_j n_j) \\ (\rho h) (u_i n_i) \end{bmatrix} + \begin{bmatrix} 0 \\ p n_i \delta_{ij} \\ 0 \end{bmatrix}$$

- **ACCURACY IMPROVEMENT UNDER INVESTIGATION**
- **APPROXIMATELY 30% MORE COMPUTATIONS**

Figure 7. Comparison of TEAM and FLO-57 convective flux computation.

## ORDER OF APPROXIMATION

| SCHEME \ CELL | 1           | 2         | $\geq 3$  |
|---------------|-------------|-----------|-----------|
| 1             | (ZERO FLUX) | 2ND       | 2ND + 4TH |
| 2             | 2ND         | 2ND + 3RD | 2ND + 4TH |
| 3*            | 1ST + 2ND   | 2ND + 3RD | 2ND + 4TH |
| 4†            | 2ND + 3RD   | 2ND + 4TH | 2ND + 4TH |



\*GLOBALLY CONSERVATIVE  
†GHOST CELLS

Figure 8. Four schemes for calculating dissipation terms near a solid surface.



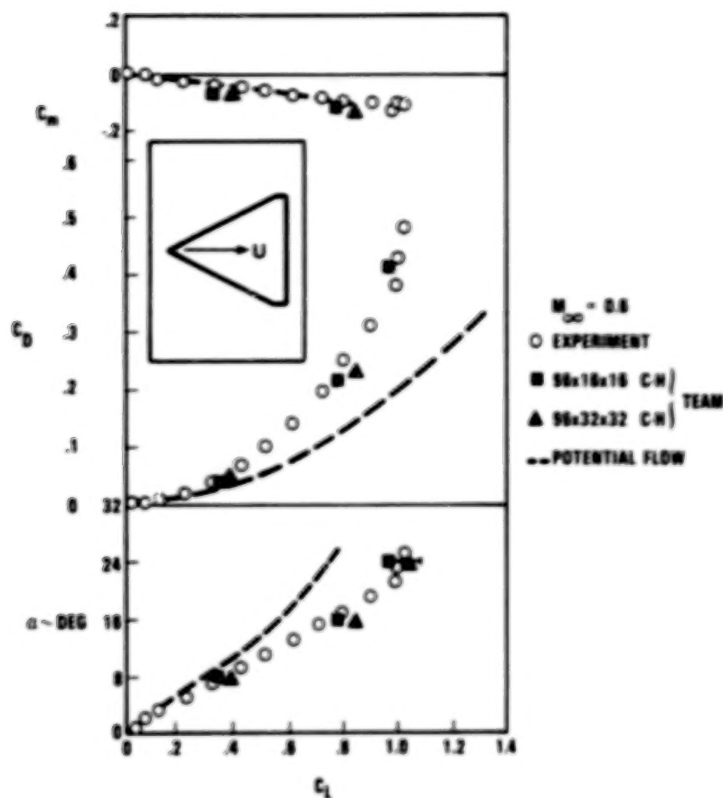


Figure 9. TEAM code results compared to experimental values for a cropped delta wing.

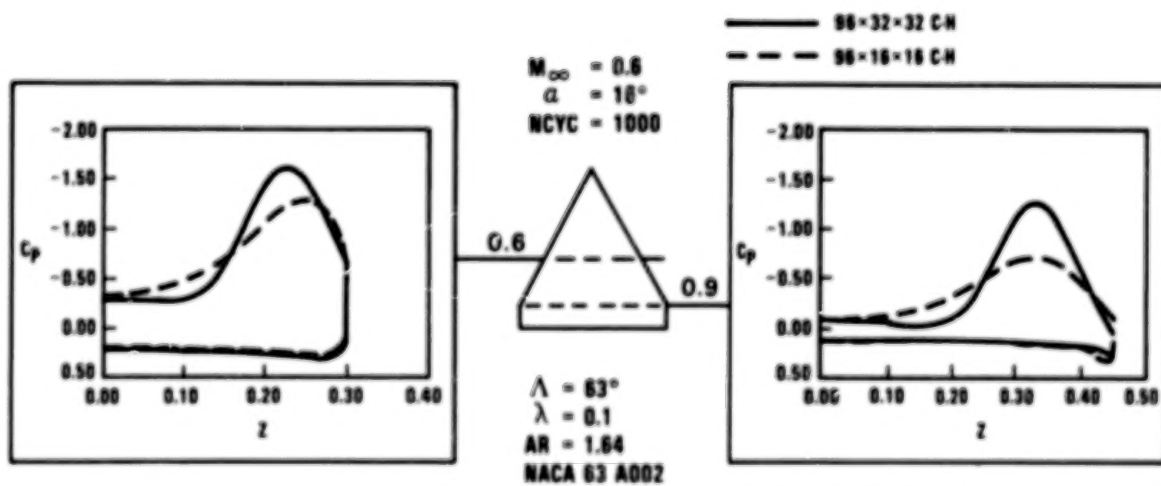


Figure 10. Predicted spanwise pressure distributions for two grids.

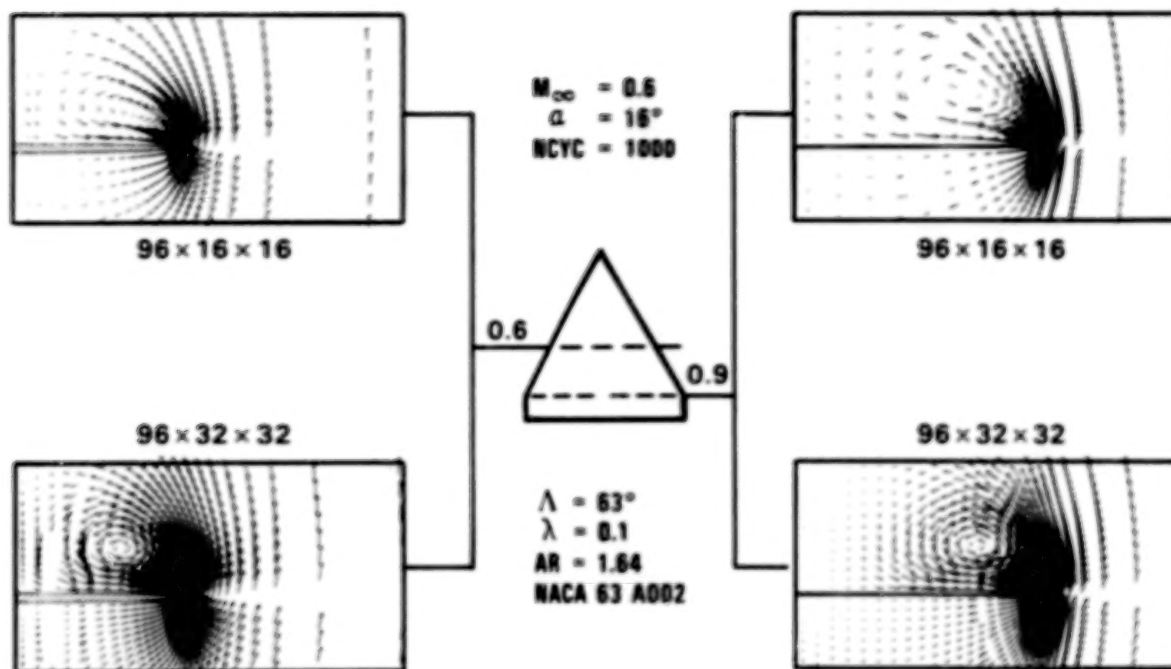


Figure 11. Cross-flow velocity vectors for two grids and two chordwise locations.

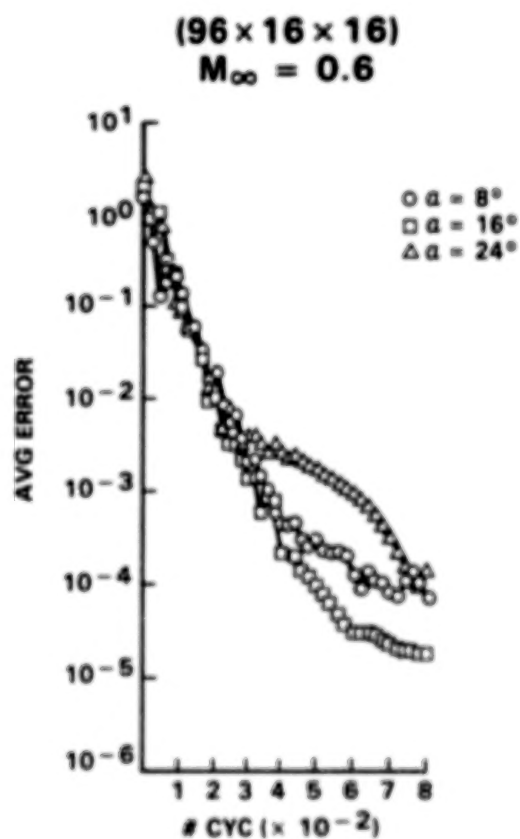


Figure 12. Convergence history for a coarse grid ( $96 \times 16 \times 16$ ) at three different angles of attack.

(96x32x32)  
 $M_\infty = 0.6$

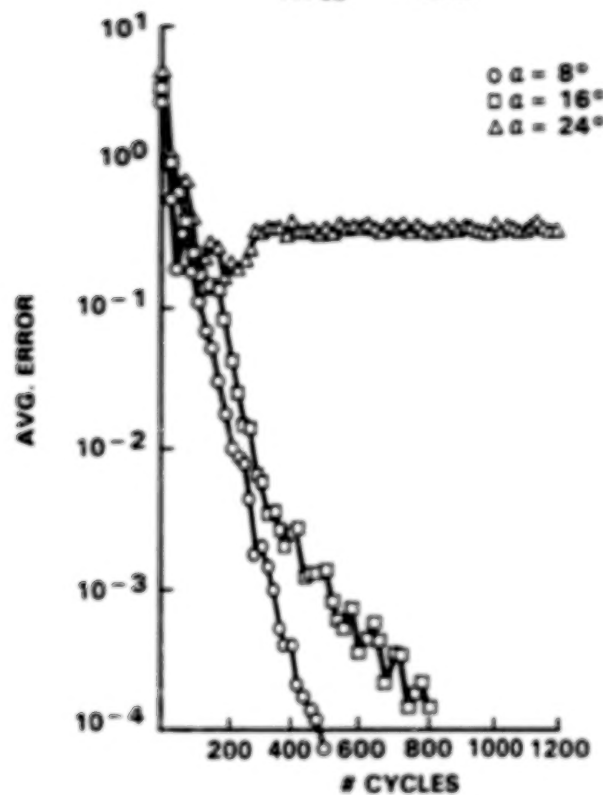


Figure 13. Convergence history for a fine grid (96 x 32 x 32) at three different angles of attack.

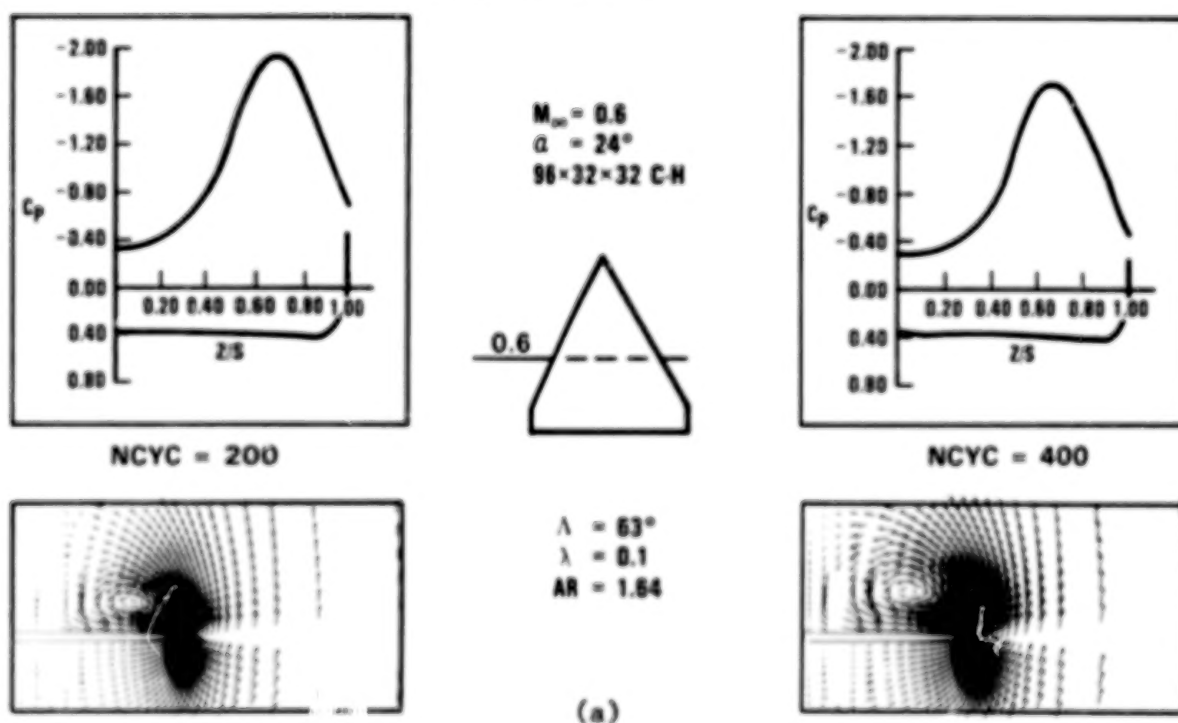
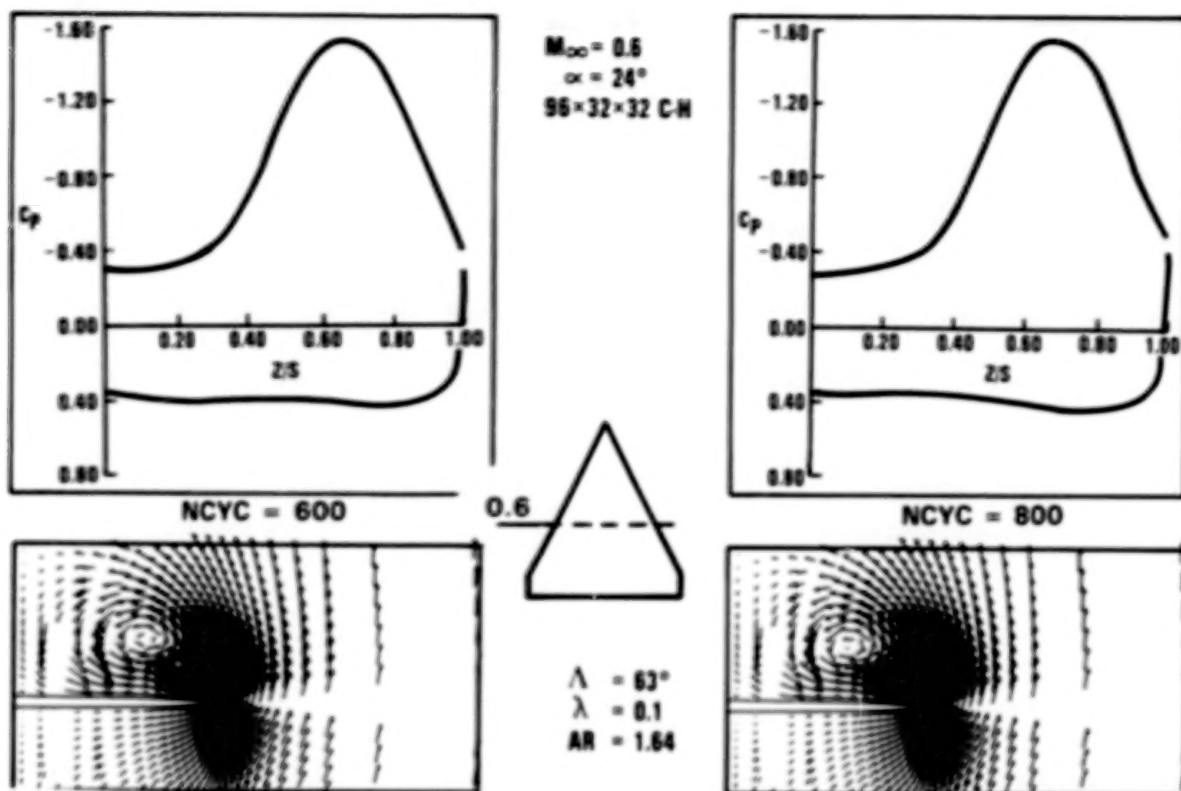
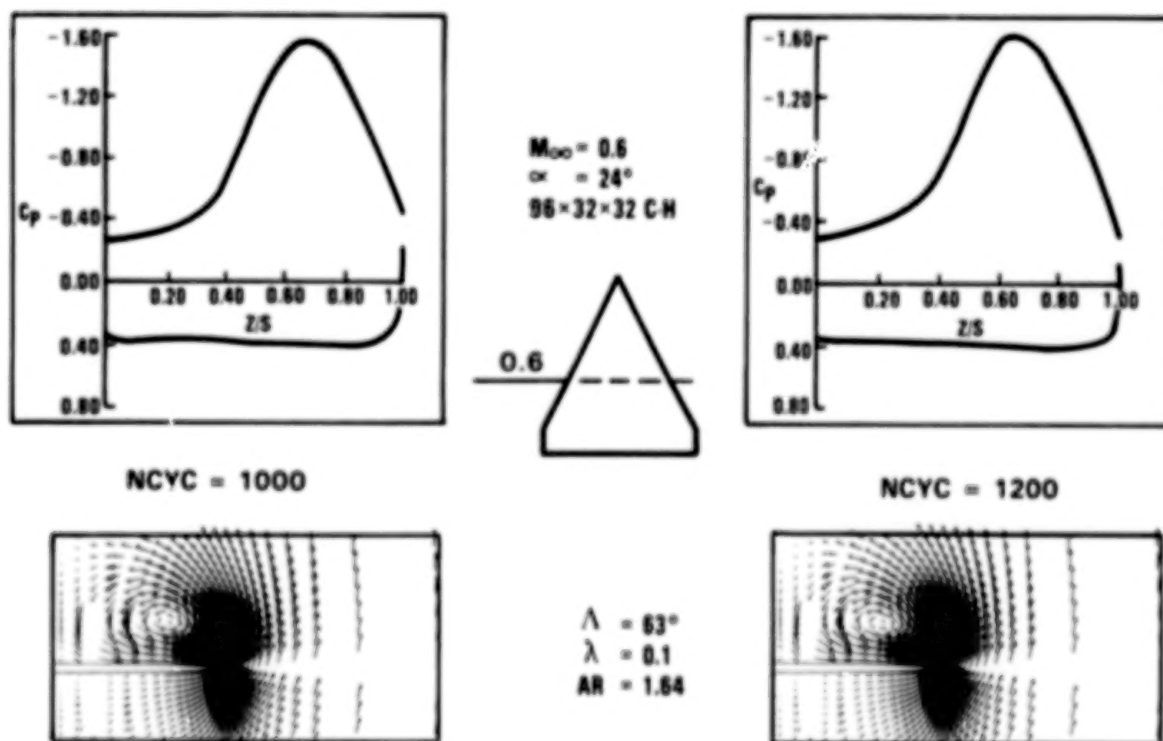


Figure 14. Spanwise pressure distributions and velocity vectors for six different times in integration process ( $x/c = .6$ ).



(b)



(c)

Figure 14. Concluded

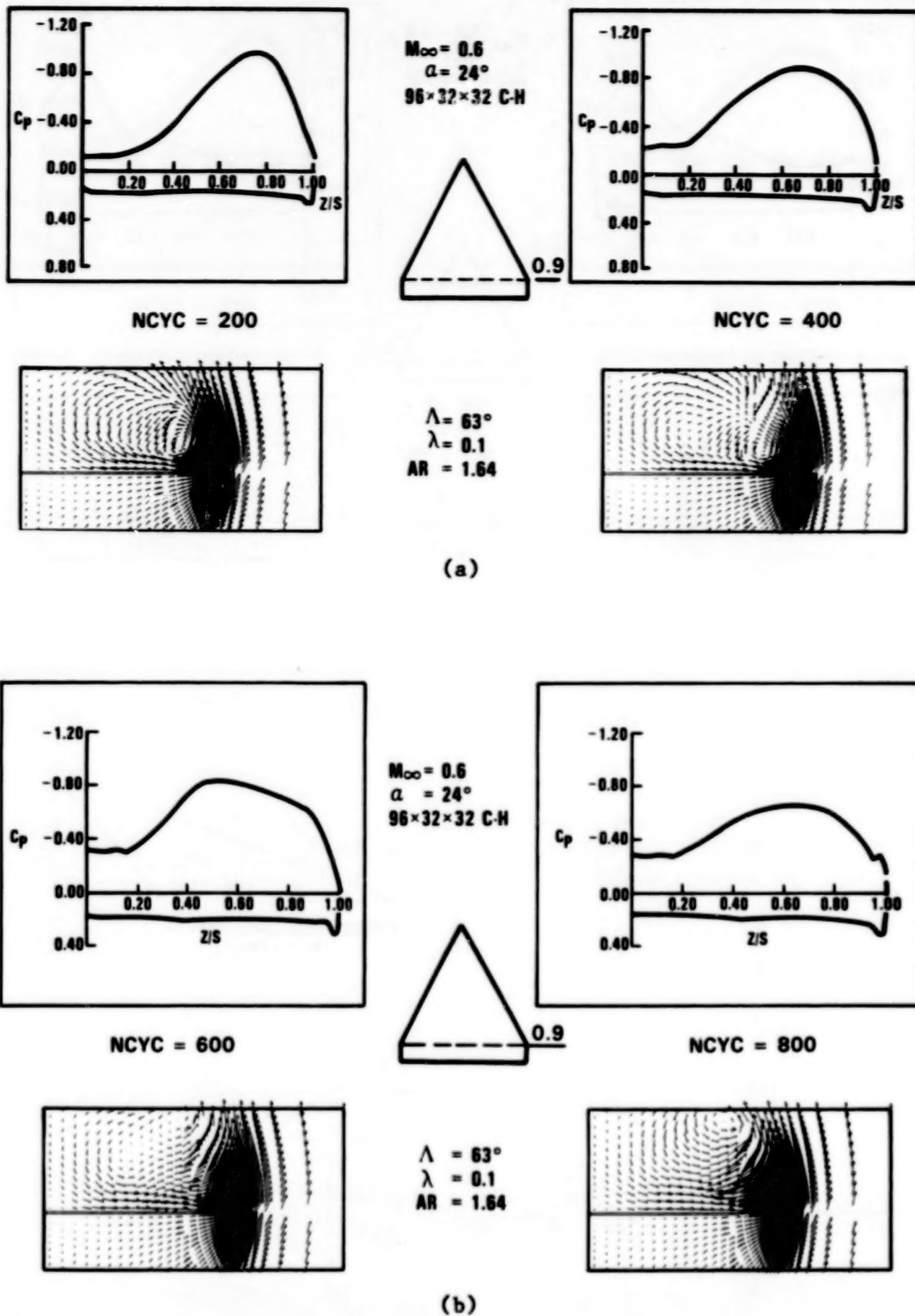


Figure 15. Spanwise pressure distributions and velocity vectors for six different times in integration process ( $x/c = .9$ ).

C-4



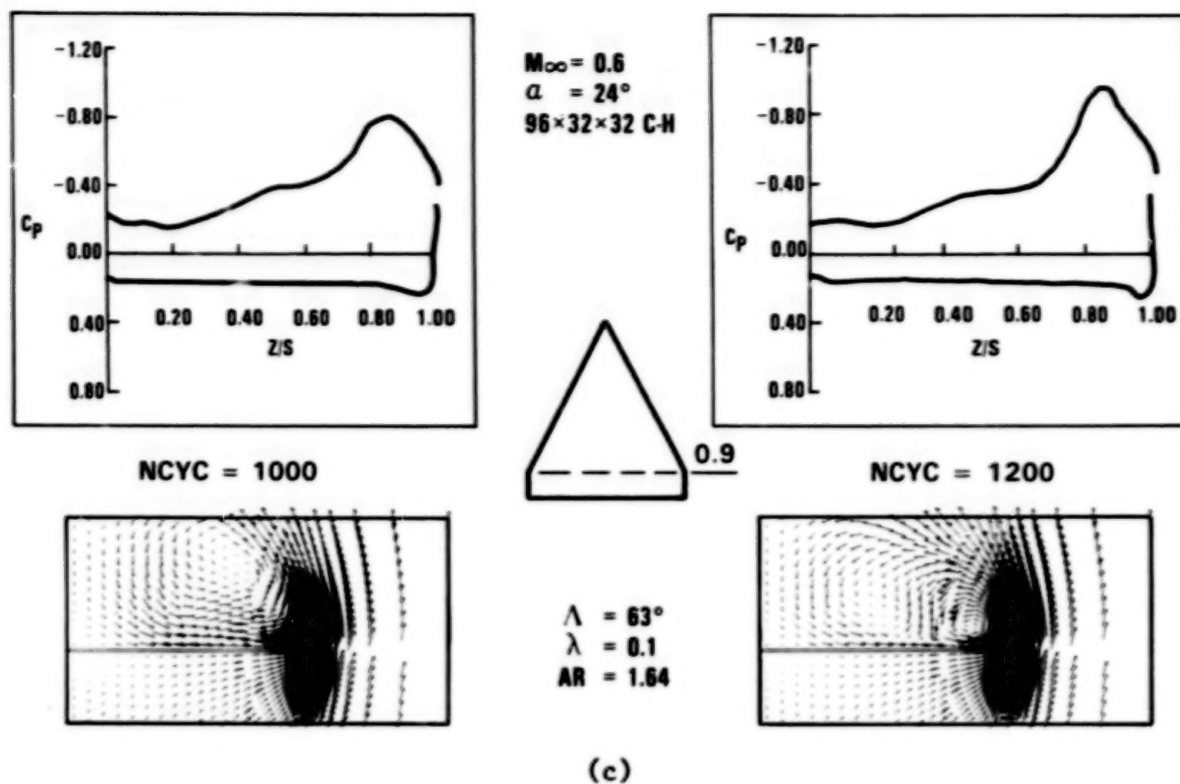


Figure 15. Concluded

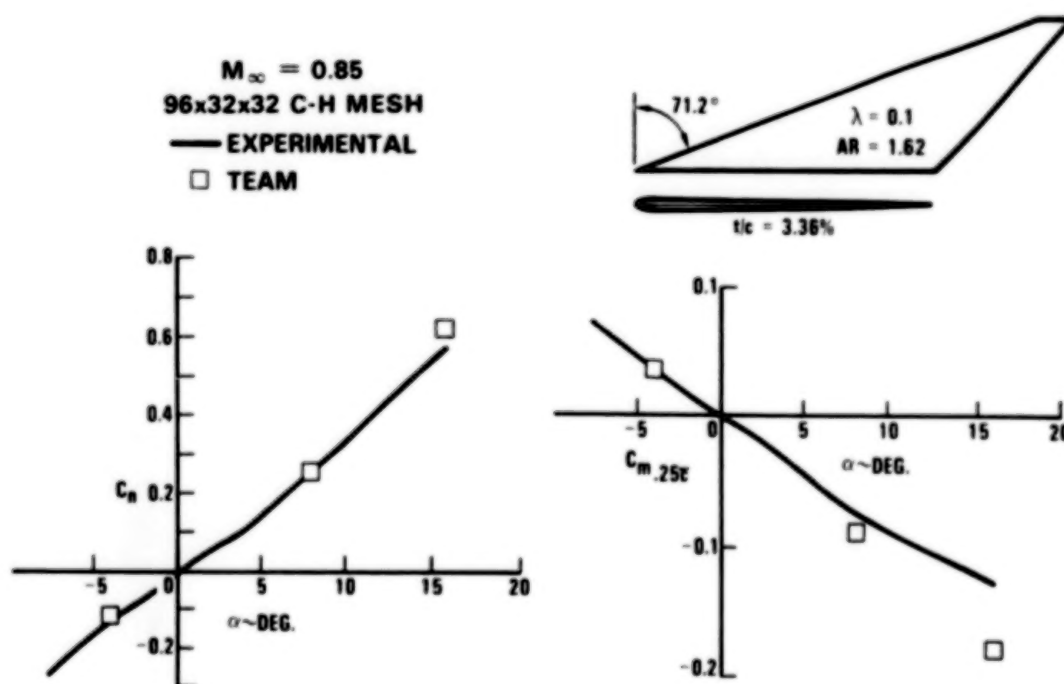


Figure 16. Computed and measured aerodynamic coefficients for an arrow wing.

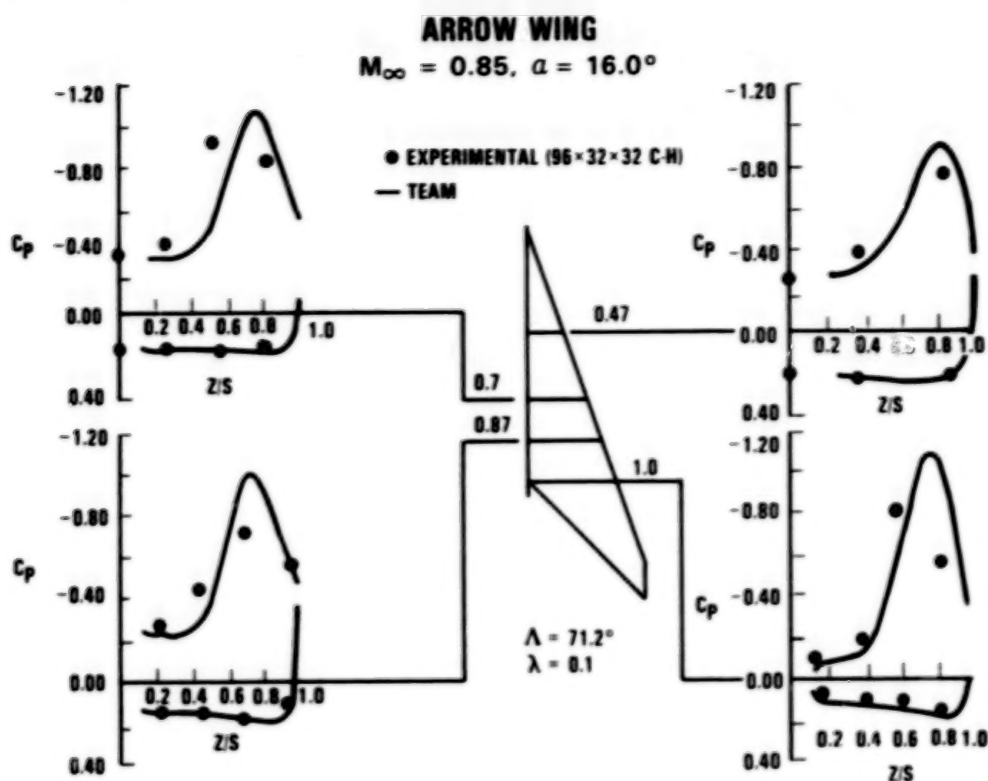


Figure 17. Computed and measured pressure distributions for four spanwise locations.

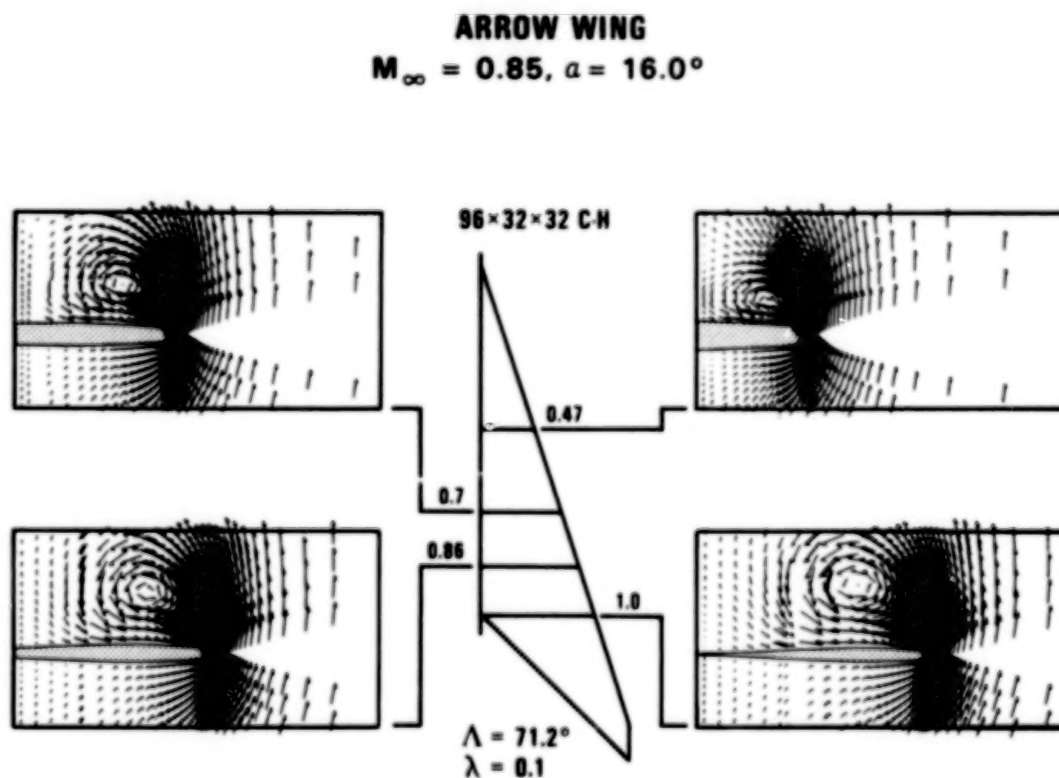


Figure 18. Computed velocity vectors for four spanwise locations.

## EULER ANALYSIS OF AN ELLIPTIC MISSILE BODY

## AT ANGLES OF ATTACK

James R. Sirbaugh  
Air Force Wright Aeronautical Laboratories  
Wright-Patterson Air Force Base, Ohio

## SUMMARY

The Euler code FL057 has been applied to a blunt nose smooth surface missile body shape. A range of angle of attacks was analyzed at Mach numbers of 0.55 and 2.0. A Mach number sweep from 0.55 to 2.0 was run for 12 degrees angle of attack. Experimental force and moment data were compared to Euler results at all Mach numbers and surface pressure data were compared at Mach 2.0. The Euler code agreed with the experimental data over the linear portion of the Mach 0.55 data and over the entire angle-of-attack range at Mach 2.0.

## INTRODUCTION

The capability to predict aerodynamic characteristics of smooth surfaced missile bodies is required by weapons designers. Missile body prediction techniques need to be able to analyze subsonic, transonic, supersonic flows, subsonic pockets in supersonic flow and vortex flow. At present there is no available numerical method to analyze these flow regimes within reasonable time and cost limits. The Navier-Stokes equations are the most logical choice to perform the analysis, but at present, computers and algorithms are too slow to make the analysis practical. The Euler equations have been successfully applied to the Mach range in question, but viscous effects are not accounted for and therefore vortex flow prediction may be inaccurate. Other techniques are available which have a more limited range of application, such as full-potential, parabolized Navier-Stokes and free vortex sheet theory.

This paper presents the results of applying the Euler code FL057 to an elliptical missile body for a Mach number range of 0.55 to 2.0. The motivation behind the work was to determine if FL057 could be used to predict the aerodynamic characteristics of simple missile shapes at low supersonic speeds, where subsonic pockets exist at blunt noses and vortex flow exists at moderate angles of attack. At present only hybrid methods are used to analyze these flow conditions in a reasonable time limit. In addition to investigating the use of FL057 for low supersonic Mach numbers, subsonic and transonic Mach numbers were also considered.

PRECEDING PAGE BLANK NOT FILMED

## SYMBOLS

|                  |  |
|------------------|--|
| A                | Missile body semi-major axis at a given body X-station |
| AL               | Angle of attack  |
| A <sub>max</sub> | Missile body base semi-major axis                      |
| B                | Missile body semi-minor axis at a given body X-station |
| B <sub>max</sub> | Missile body base semi-minor axis                      |
| C <sub>A</sub>   | Axial force coefficient                                |
| C <sub>M</sub>   | Pitching moment coefficient                            |
| C <sub>N</sub>   | Normal force coefficient                               |
| C <sub>P</sub>   | Coefficient of pressure                                |
| I, J, K          | Grid coordinates                                       |
| L                | Missile body length                                    |
| M <sub>∞</sub>   | Freestream Mach number                                 |
| X                | Missile body station measured relative to nose         |
| 3-D              | Three dimensional                                      |

## CONFIGURATION

The missile body is a simple shape built and tested for the purpose of developing and validating aerodynamic prediction methods. The missile body was one of three built with elliptical cross sections along the entire length of the model. The missile body used in this study had a 2.5 to 1.0 major to minor axis ratio (Figure 1). The two other missile bodies built had 2.0 to 1.0 and a 3.0 to 1.0 cross-section ratios. The semi-major axis varied along the body by the square root law

$$A = \frac{A_{\max}}{L^{1/2}} X^{1/2}$$

and the semi-minor axis varied along the body by the square root law

$$B = \frac{B_{\max}}{L^{1/2}} X^{1/2}$$

$A_{max}$  and  $B_{max}$  were the base semi-major and semi-minor axes and  $L$  was the missile body length. These missile bodies were tested in four stages. Stage one produced surface pressure data from eleven rows of spanwise pressure taps at Mach numbers from 1.5 to 5.0. During stage two, force and moments were taken for Mach numbers of 1.76 to 5.0. Stage three was a force and moment test for Mach numbers of 0.4 to 1.3. Stage four data were not available at the time of this analysis and were the Mach numbers 0.4 to 1.3 pressure tests. All testing was done at Arnold Engineering Development Center. References 1 and 2 contain detailed information of the test results.

#### EULER GRID AND FLOW SOLVER

The grid used for the Euler calculations was originally developed for predicting flow fields about delta wings and was modified for use on the test missile body shape. The grid topology is intended to provide adequate grid resolution at the missile nose while positioning the grid singularity on the plane of symmetry and out of regions of high flow gradients (Figure 2). The topology can best be thought of as a sheared O-H grid. Indicated in Figure 3 are the coordinate directions on the missile surface and a cut through the 3-D grid. The O portion of the O-H grid is formed by the I indexing grid lines that start on the lower plane of symmetry aft of the grid singularity and follow a path along the missile surface, around the leading edge and back to the upper plane of symmetry. The J indexing lines start at the missile surface and proceed outward to the far field. The K indexing lines start on the plane of symmetry forward of the grid singularity and follow paths along the missile going aft. Figure 4 is the downstream exit grid or maximum K grid layer. The base of the missile was extended downstream with solid surface boundary conditions being applied to the extension's outer surface. This extension does not resemble the wind tunnel model, but was required to perform the computations. The grid had 49 grid points in the I or wrap-around direction and 44 points in the K direction on the missile surface. There were 25 J layers of grid points extending outward from the surface to the far-field boundary.

The flow solver used was FL057 without any special treatment for vortex flows (Reference 3). FL057 has been applied previously to round and sharp leading-edge delta wing vortex flow problems for both subsonic and transonic Mach numbers. No attempt was made in generating the missile grid to align the 3-D grid with the bow shock shape. The bow shock is dependent on the configuration angle of attack (AL) and freestream Mach number. The Euler solution scheme uses centered difference approximation to the flux terms. Shock smearing will occur when the bow shock is unaligned with the grid, introducing an unknown amount of error in the solution. At the immediate nose of the configuration the shock should approximate the shape of the blunt nose and therefore align with the grid at moderate supersonic Mach numbers.



## FORCE AND MOMENT RESULTS

### $C_N$ Versus Alpha, $M_\infty = 0.55$

FL057 predicted lower  $C_N$ 's at Mach 0.55 (Figure 5) than were measured in the wind tunnel test in the nonlinear portion of the  $C_N$  versus the Alpha curve. At the low angle-of-attack range (0.0 - 6.0 degrees) the Euler and wind tunnel test results are in excellent agreement. It appears that the Euler method is not predicting vortex flow that is present in the wind tunnel data at the higher angles of attack.

### $C_A$ Versus Alpha, $M_\infty = 0.55$

The axial force coefficient was not measured directly in the wind tunnel test but was calculated by subtracting the measured base axial force from the balance measured total axial force. Two wind tunnel data points are plotted at each 2.0 and 4.0 degrees on Figure 6 corresponding to plus and minus angles of attack and indicate the degree of uncertainty of the wind tunnel axial force coefficients. The Euler results are inviscid and do not reflect skin friction axial force. To permit direct comparisons of the wind tunnel and Euler results the wind tunnel  $C_A$ 's have been shifted to match the Euler results at 0.0 degrees angle of attack. This shifting of wind tunnel is only useful if the axial force due to skin friction is constant at all angles of attack for a given Mach number. The wind tunnel  $C_A$  at 0.0 degrees angle of attack is due only to skin friction. The predicted Euler results are in general agreement with the experimental data.

### $C_M$ Versus $C_N$ , $M_\infty = 0.55$

The slopes of the  $C_M$  versus  $C_N$  curves (Figure 7) at  $C_N = 0.0$  for the Euler and wind tunnel data are in excellent agreement. Above a  $C_N$  value of 0.7 the two curves are in disagreement indicating the vortex contribution to  $C_M$  is not present in the Euler results.

### $C_N$ Versus Alpha, $M_\infty = 2.0$

The predicted Euler  $C_N$  values (Figure 8) are in excellent agreement with the wind tunnel data below 6.0 degrees angle of attack. Above 6.0 degrees the curve slopes of the two sets of data are in excellent agreement but appeared to be shifted by approximately 0.5 degrees angle of attack. There are several possible sources of the Euler angle-of-attack shift, although it is not clear as to which factor is most important. The Euler results are inviscid and therefore are missing the physics of boundary layer separation in the vortex region. The angle-of-attack shift is a delay in vortex formation which may be attributed to missing viscous effects. Another possible source of the angle-of-attack shift

is the smearing of the bow shock due to misalignment of the low shock and grid. Since FL057 is inviscid and little if any vortex lift was apparent in the Mach 0.55 results (Figure 5), the assumption must be made that the Mach 2.0 vortex formation is due largely to entropy production through the bow shock. Any smearing of the bow shock can effect the amount of entropy produced by the bow shock and thus shift the  $C_N$  versus curve.

#### $C_A$ Versus Alpha, $M_\infty = 2.0$

The wind tunnel test  $C_A$ 's have been shifted to match the Euler  $C_A$  value at 0.0 degree of angle of attack (Figure 9). The predicted values and trends of the Euler  $C$  values are in general agreement with the experimental data. The uncertainty of the experimental  $C_A$ 's was as great as 0.0056 at 4.0 degrees angle of attack.

#### $C_M$ Versus $C_N$ , $M_\infty = 2.0$

The Euler  $C_M$  versus  $C_N$  curve (Figure 10) is in good agreement with the wind tunnel data both in magnitude and in slope.

#### $C_N$ Versus Mach, Alpha = 12.0°

The Euler predicted  $C_N$  values were shown to disagree with the experimental data at subsonic and transonic Mach numbers by a large amount. The agreement improved as the Mach increased from 1.3 to 2.0 as shown in Figure 11.

#### $\Delta C_N$ Versus Mach, Alpha = 12.0°

A  $\Delta C_N$  parameter is plotted in Figure 12. The  $\Delta C_N$  is the vortex-induced increment or nonlinear addition to the  $C_N$  due to the vortex. The wind tunnel test ( $\partial C_N / \partial \alpha$ ) slope at zero angle of attack was multiplied by 12.0 degrees to compute a linear value of  $C_N$  at 12.0 degrees. The difference between the experimental value of  $C_N$  and computed linear  $C_N$  is  $\Delta C_N$ . The same extrapolation was used to compute  $\Delta C_N$  for the Euler results. Several interesting observations can be made by studying Figure 12. The experimental curve can be broken into two regions based on Mach number range. Region one is the subsonic and low supersonic Mach number range where the bow shock is weak. Region two starts about Mach 1.25 or 1.30, where the bow shock is strong enough to produce entropy. The two regions have different slopes and should be thought of as the viscous separation dominated region and bow shock entropy addition region.

The Euler results appear to have a more strongly Mach number dependent shape. At a purely subsonic Mach number of 0.55,  $\Delta C_N$  is very low and only increases a small amount by going to Mach 0.8 in comparison to the experimental data. At Mach numbers from 1.3 to 1.75 the Euler curve is considerably steeper than the experimental data. Mach 1.3 is the point where entropy levels begin to be strongly influenced by shock strength. It appears that the Euler  $\Delta C_N$  is

predominately a function of bow shock entropy production and not numerical or artificial viscosity. The Euler and experimental values of  $\Delta C_N$  at Mach numbers of 1.75 and 2.0 appear in reasonable agreement as was previously shown in Figure 8.

#### $C_M$ Versus Mach, Alpha = 12.0°

The Euler predicted value of  $C_M$  is relatively independent of Mach number. Only a slight decrease in  $C_M$  appears at transonic Mach numbers. The wind tunnel data indicated a strong dependency on Mach number in the Mach 0.8 to 1.1 range. Above Mach 1.3 the Euler and experimental values of  $C_M$  are in good agreement. A discrepancy in  $C_M$  between Euler and experiment appears at a Mach number of 2.0 in Figure 13, but is not as apparent in Figure 10.

#### SURFACE PRESSURE DATA

The Euler and wind tunnel  $C_p$  values are plotted against semi-span for four X-stations in Figures 14-25. The nose of the missile is X = 0.0 station and the missile base is X = 36.0 station. The computational grid points did not lie precisely on the required X-stations; therefore, all computational grid points within a prescribed distance to the required X-station were plotted. The method of selecting a computational grid was examined for accuracy and does not contribute any discrepancies that may be visible in the  $C_p$  comparison plots, Figures 14-25.

The 4.0 degree angle-of-attack results indicated an attached "potential like" flow over the entire length of the missile (Figures 14-17). The Euler results agree in shape with the wind tunnel data, but appear to be shifted in a more negative  $C_p$  direction than the wind tunnel results. At 8.0 degrees angle of attack the Euler results still indicate an attached "potential like" flow while the experimental data have signs of vortex separation starting at X-station 16.0 (Figures 18-21). The shift in  $C_p$  of the Euler results still appears and is roughly of the same magnitude. The  $C_p$  shift is constant even at 12.0 degrees angle of attack (Figures 22-25) on the lower surface. The reason for  $C_p$  shift is not obvious and may be due to not properly capturing the bow shock. A smeared bow shock can introduce angularity to the flow impinging on the missile body and create an apparent angle-of-attack shift. At 12.0 degrees angle of attack both the Euler and wind tunnel data indicate vortex separation (Figures 22-25). The wind tunnel data indicate a more forward separation point than does the Euler results. At X-stations 25.6 and 35.2 (Figures 24 and 25) the Euler and experimental  $C_p$ 's indicate that the secondary vortex may have a significant effect on the strength and position of the primary vortex. The Euler results have a single vortex that has a larger peak pressure and is more outboard than the experimental data. The secondary vortex is also visible in the experimental data. The effect of a secondary vortex is to move the primary vortex inboard and thus reduce the peak pressure of the primary vortex.

## VORTEX FLOW FIELD

Plotted in Figure 26 is the velocity flow field at the X-station 35.2 for Mach 2.0 and 12.0 degrees angle of attack. The vortex region can clearly be seen along with the high velocities occurring at the leading edge. To better visualize the flow region, a "constrained particle path" plot was made (Figure 27). At different locations in the X-station 35.2 vertical plane particles are released and allowed to trace paths as they are carried along by the cross flow velocities. The components of velocity aligned with the body axis are considered zero in this process, causing all "particles" to remain in the X-station vertical plane. The area of vortex flow is clearly visible. Figure 28 is a plot of local static pressure normalized by freestream and should provide information valuable to a designer.

## CONCLUDING REMARKS

The accuracy of the FLO57 Euler code is dependent on Mach number for the blunt nose smooth surface missile body used in this investigation. The formation and strength of the vortex appear dependent on the supersonic nose shock and not on surface viscous effects. The code is accurate and useful in the linear angle-of-attack range at both subsonic and supersonic Mach numbers. Sufficient entropy is produced by bow shocks at Mach numbers of 1.7 and above to confidently apply the code at higher angles of attacks for freestream Mach numbers above 1.7.

All Euler calculations presented in this paper were generated on the NASA Ames Cray XMP computer using approximately 0.9 million words in core and 1.0 million words out of core. All out-of-core memory resided on the 16 million word SSD using "buffer in" and "buffer out" statements to transfer data. A typical case required 500 iterations to converge from an initial guess of freestream conditions, which corresponds to approximately 600.0 seconds of CPU time and 10.0 seconds of IO time. Convergence criteria were an average residual of  $1.0 \times 10^{-5}$  plus  $C_N$  and  $C_A$  remaining constant for 20 iterations.

## REFERENCES

1. Amidon, P.F., "Supersonic Aerodynamic Characteristics of Elliptical Cross Section Bodies," AIAA Paper No. 85-1607, 1985.
2. Sellers, M.E., "Static Stability Test of Three Elliptic Missile Body Configurations," Arnold Engineering Development Center, Tenthoma, Tenn., AEDC-TSR-85-Pb, May 1985.
3. Jameson, A., and Baker, T.J., "Multigrid Solution of the Euler Equations for Aircraft Configurations," AIAA Paper No. 84-0093, 1984.



## 2.5: 1.0 ELLIPTIC MISSILE BODY

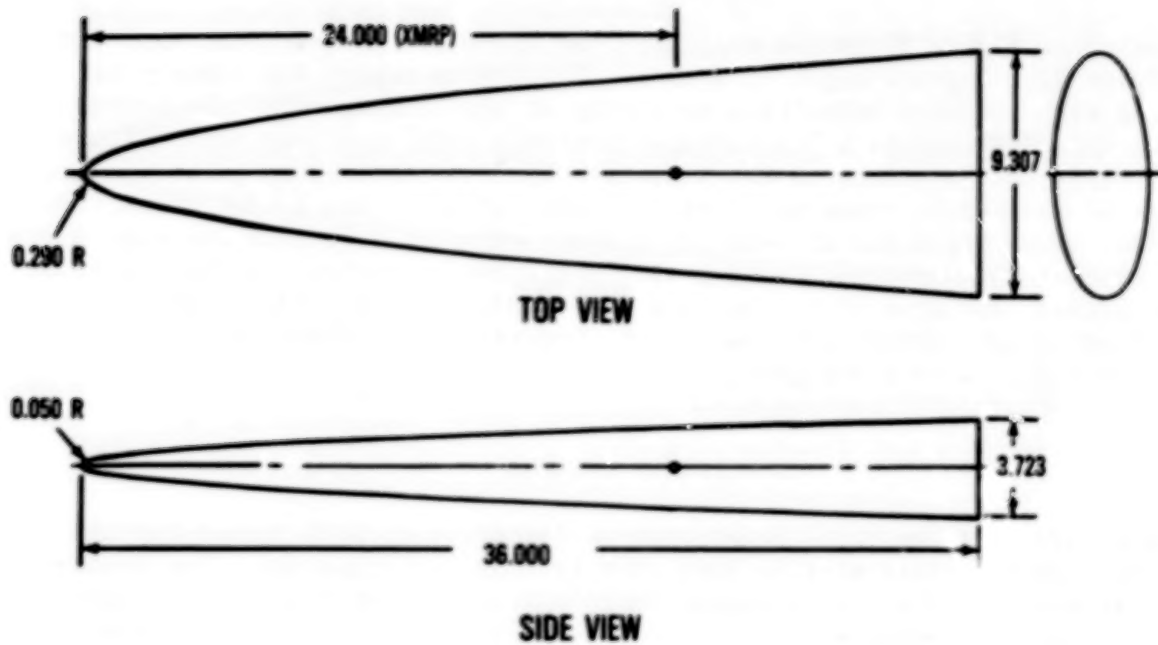


Figure 1.- Wind tunnel model (from ref. 2).

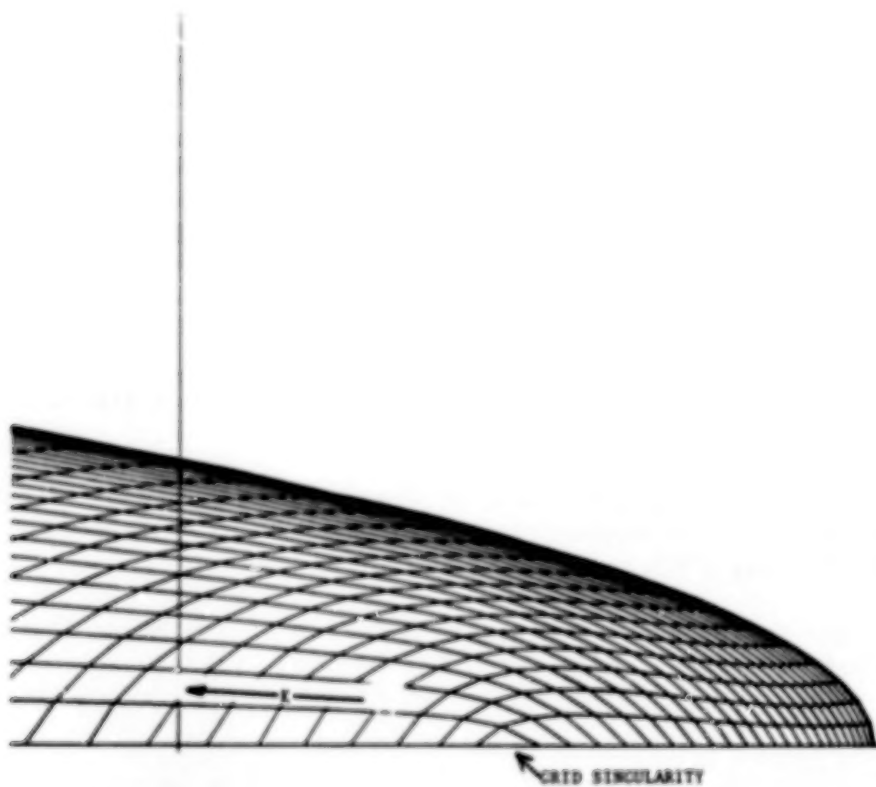


Figure 2.- Missile surface grid in nose region.



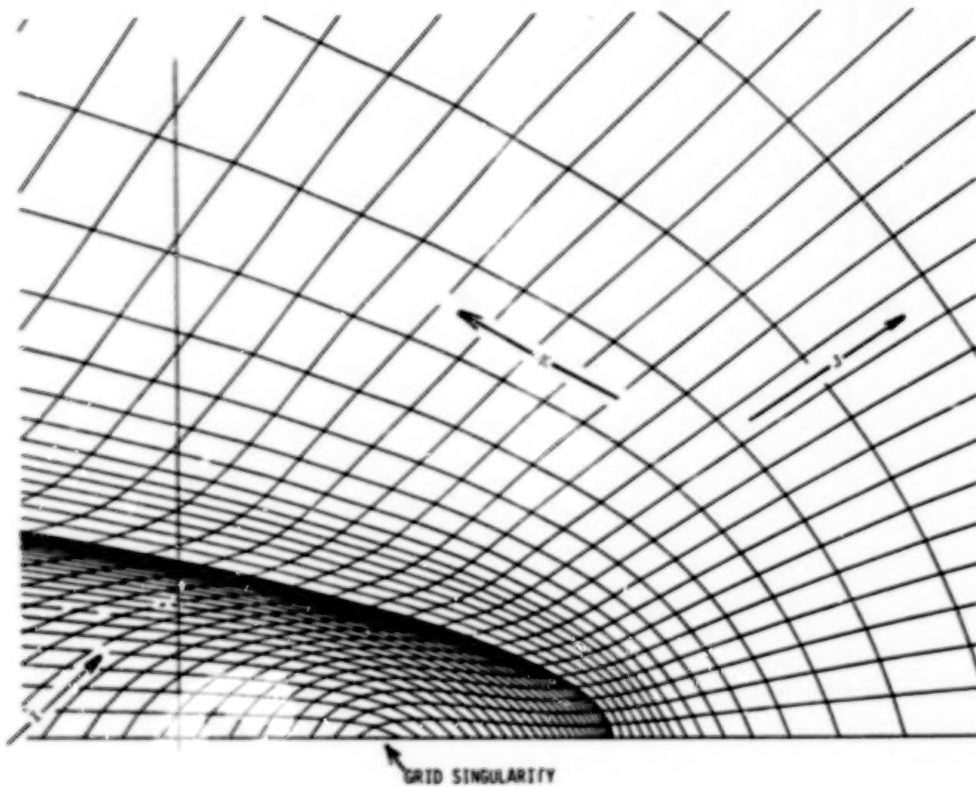


Figure 3.- Missile 3-D grid.

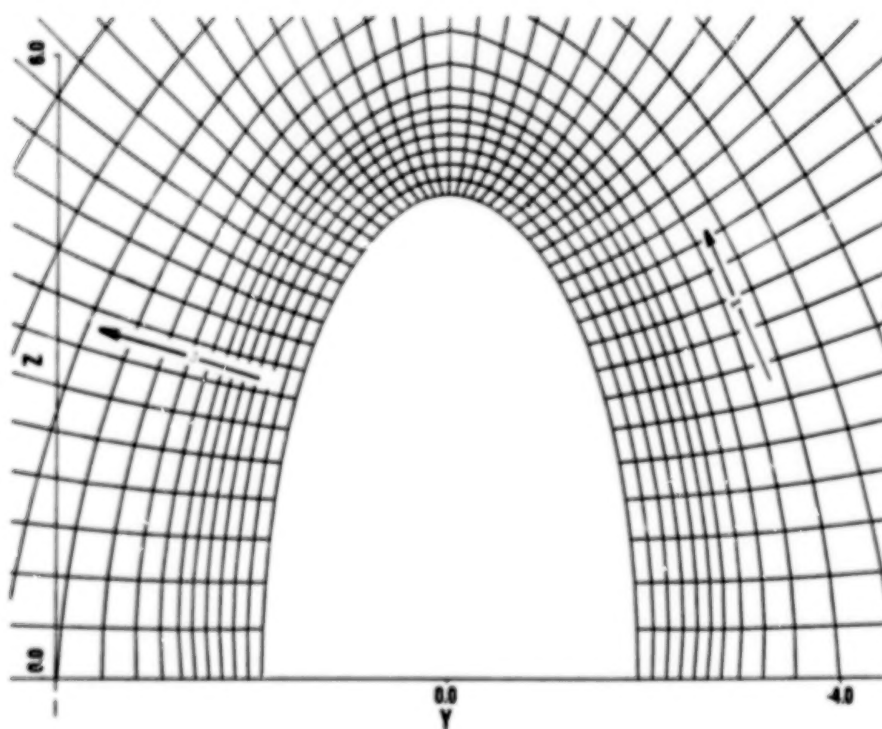


Figure 4.- Missile base grid.

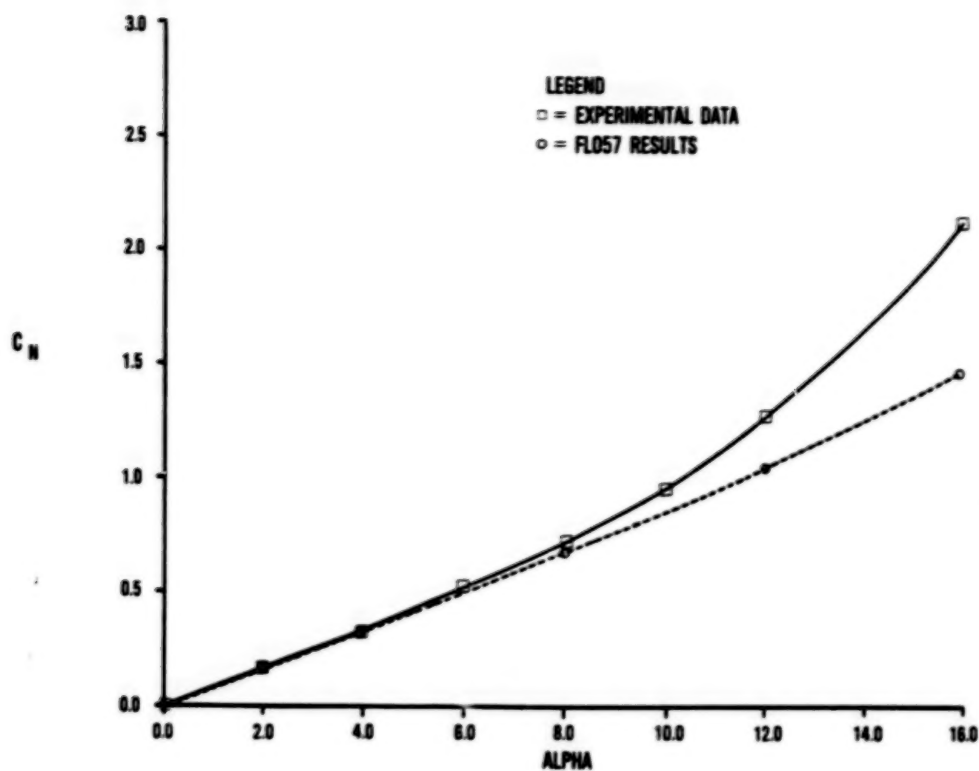


Figure 5.- Comparison of Euler and Ref. 1,  $C_N$  versus  $\alpha$ .

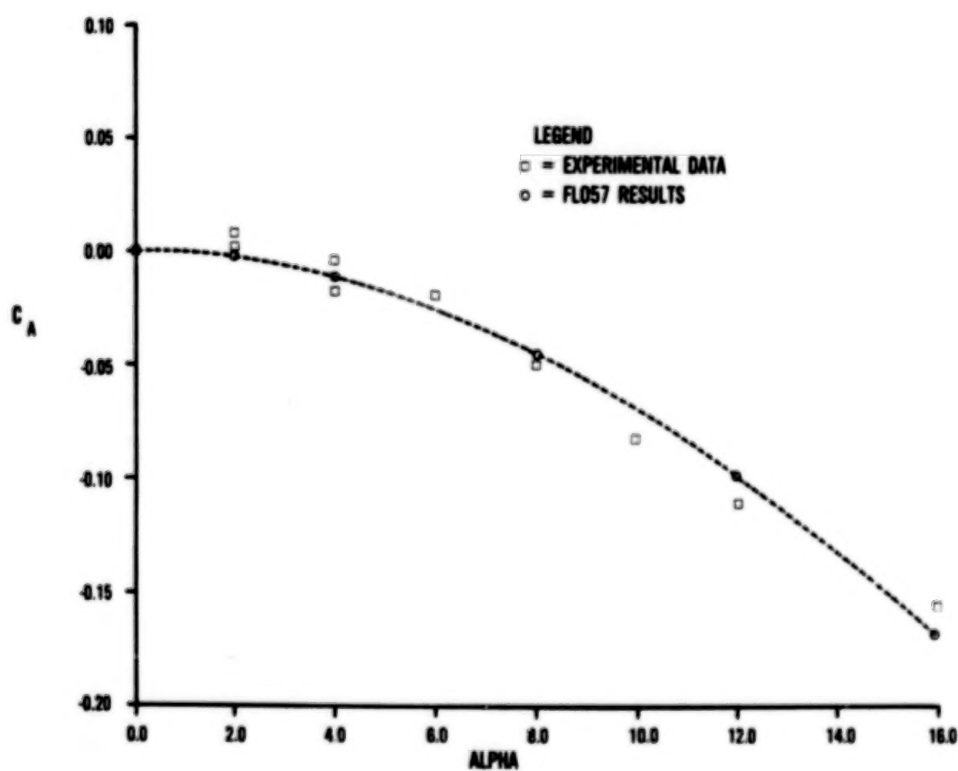


Figure 6.- Comparison of Euler and Ref. 1,  $C_A$  versus  $\alpha$ .

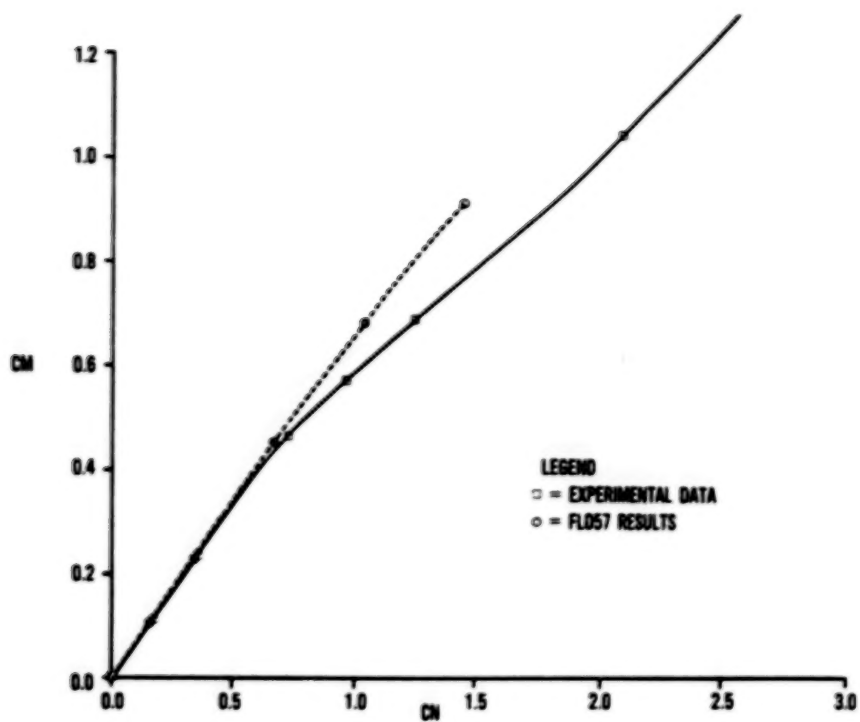


Figure 7.- Comparison of Euler and Ref. 1,  $C_M$  versus  $C_N$ .

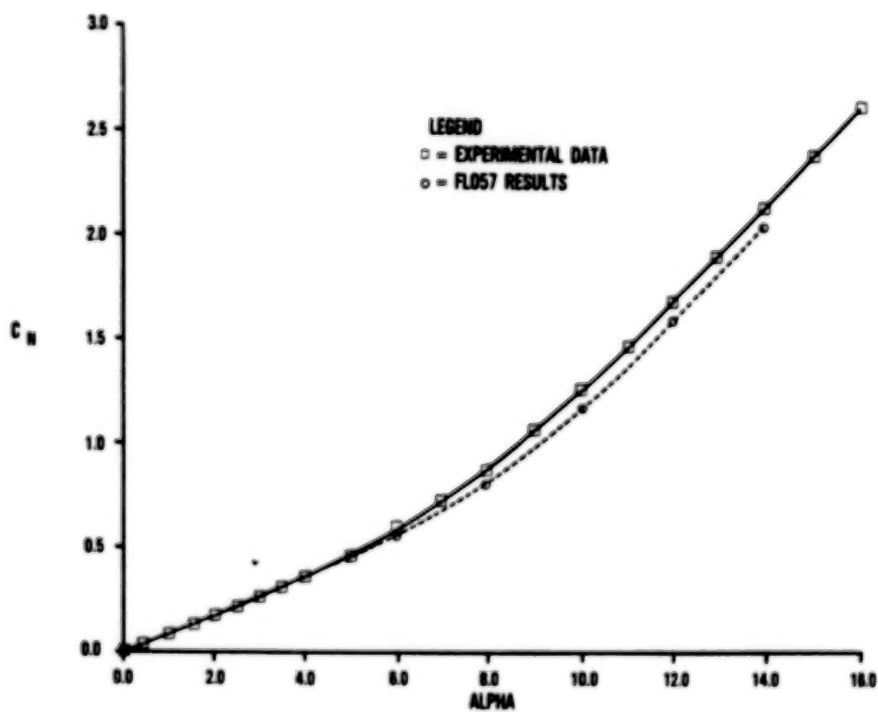


Figure 8.- Comparison of Euler and Ref. 1,  $C_N$  versus  $\alpha$ .

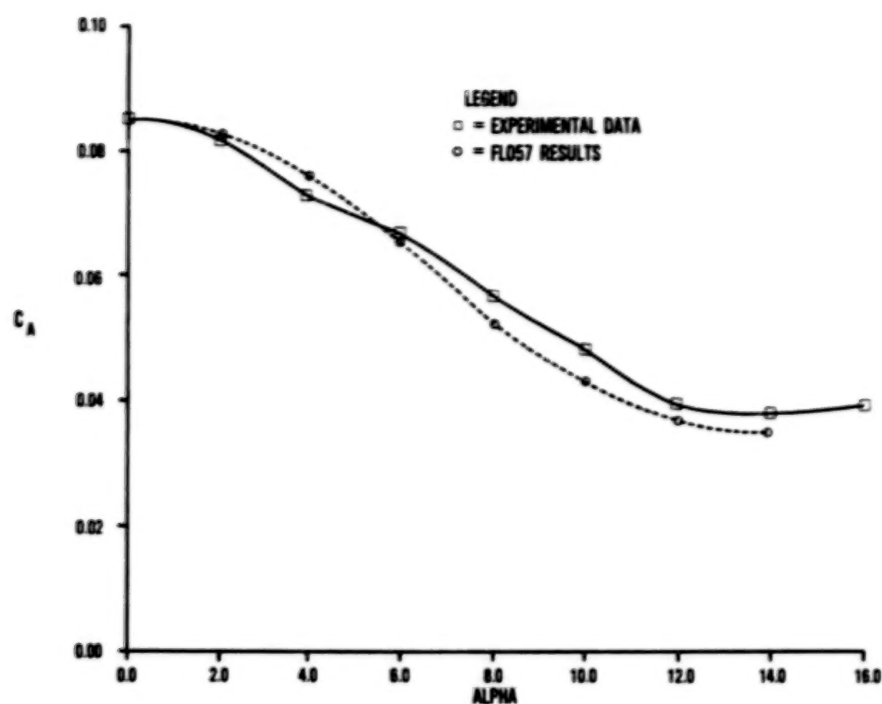


Figure 9.- Comparison of Euler and Ref. 1,  $C_A$  versus  $\alpha$ .

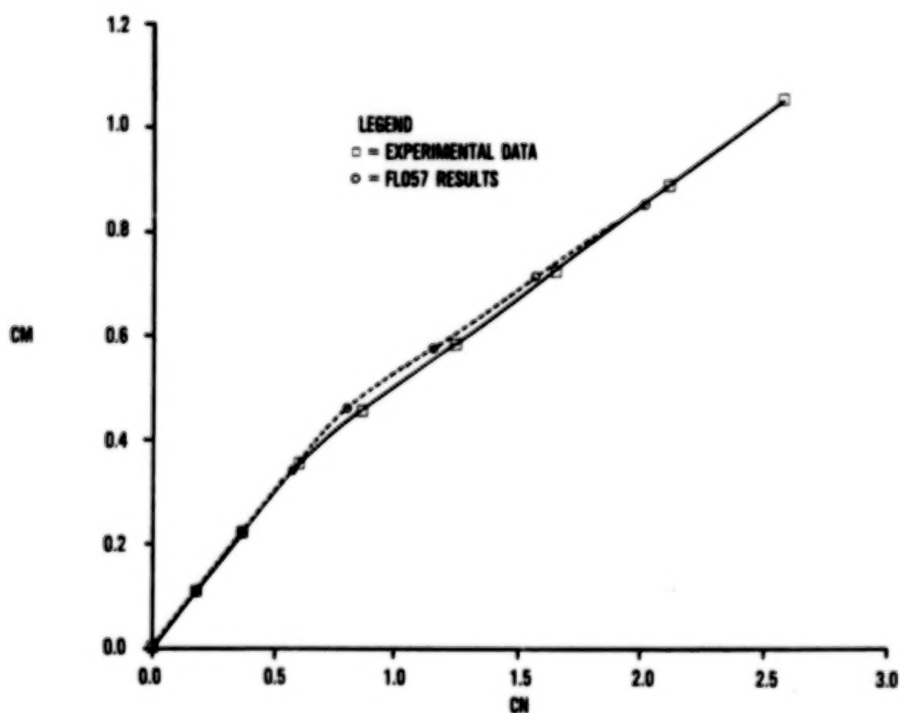


Figure 10.- Comparison of Euler and Ref. 1,  $C_n$  versus  $C_N$ .

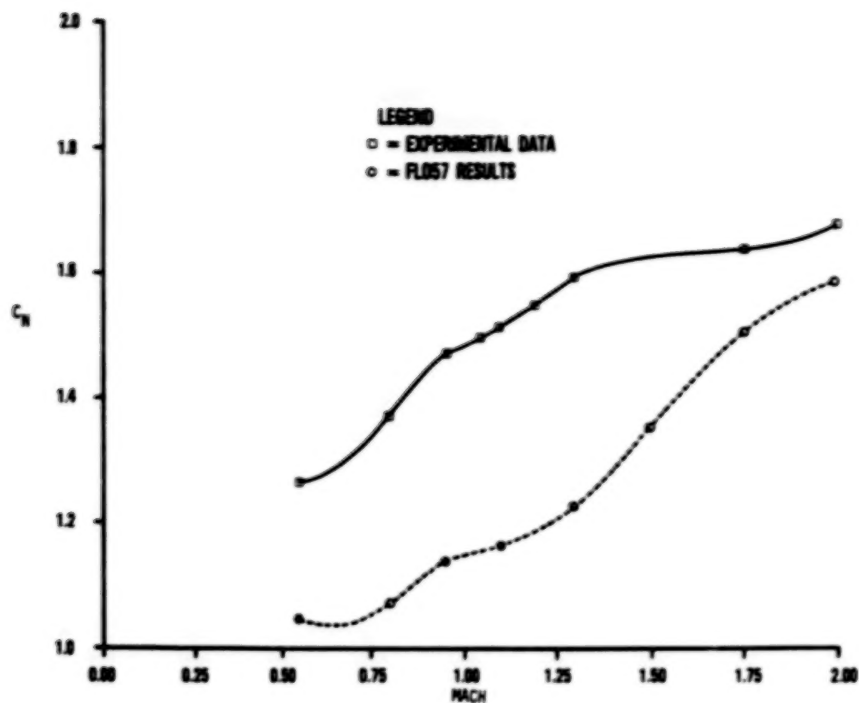


Figure 11.- Comparison of Euler and Ref. 1,  $C_N$  versus Mach,  $AL = 12.0$  degrees.

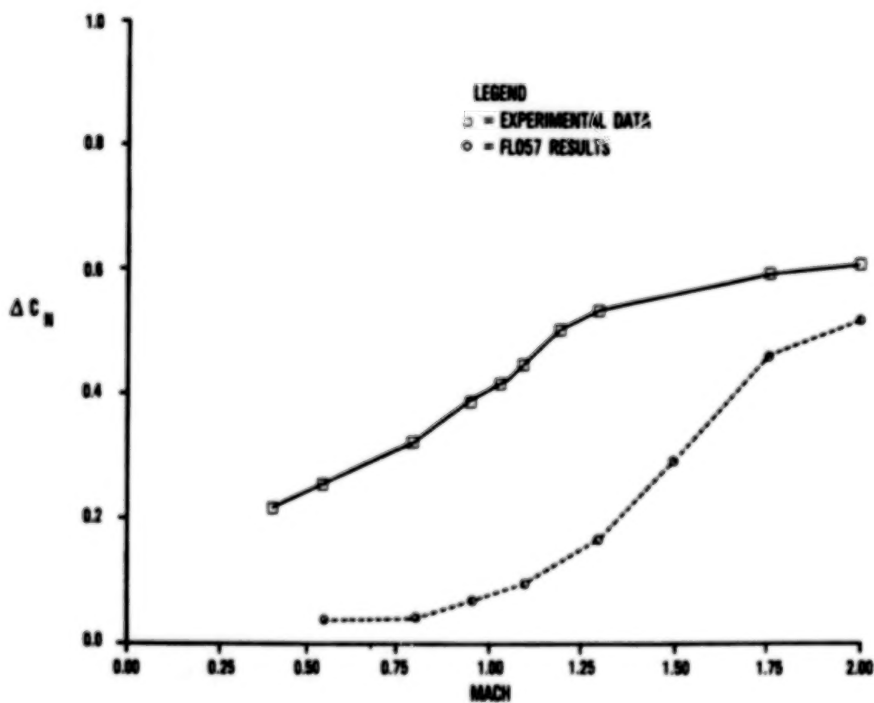


Figure 12.- Comparison of Euler and Ref. 1,  $\Delta C_N$  versus Mach,  $AL = 12.0$  degrees.



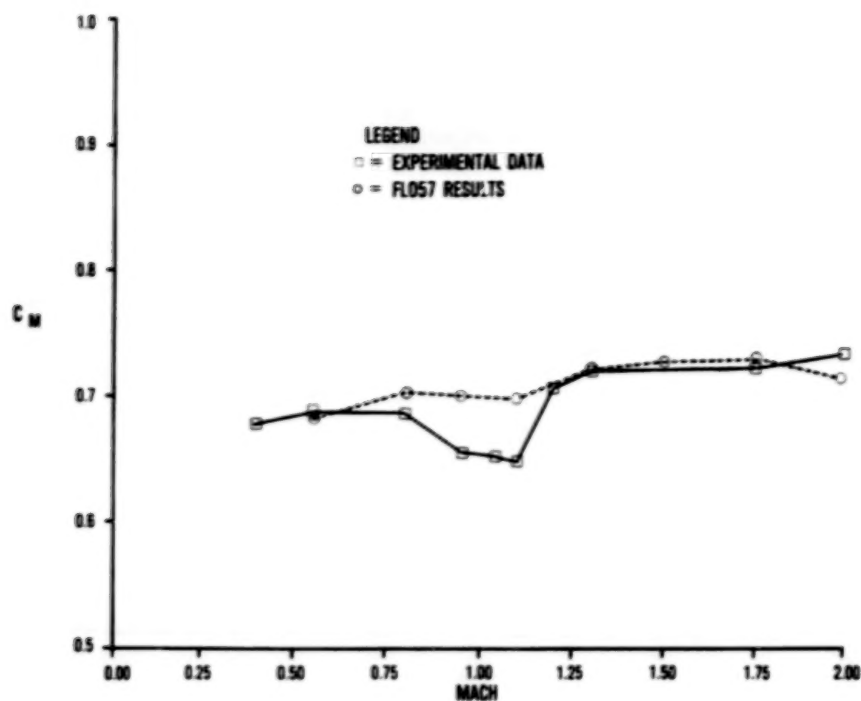


Figure 13.- Comparison of Euler and Ref. 1,  $C_M$  versus Mach,  $AL = 12.0$  degrees.

X STATION = 3.20

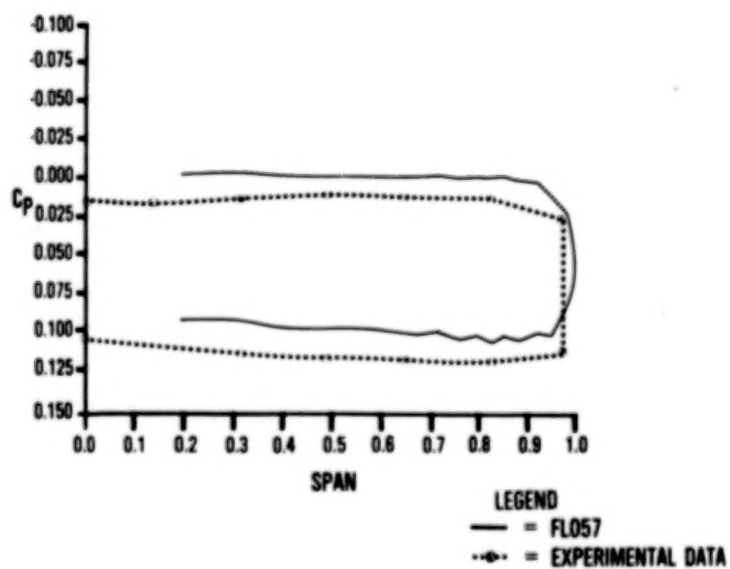


Figure 14.- Comparison of Euler and Ref. 1,  $C_p$  data,  $M_\infty = 2.0$ ,  $AL = 4.0$ ,  $X = 3.20$ .

X STATION = 16.0

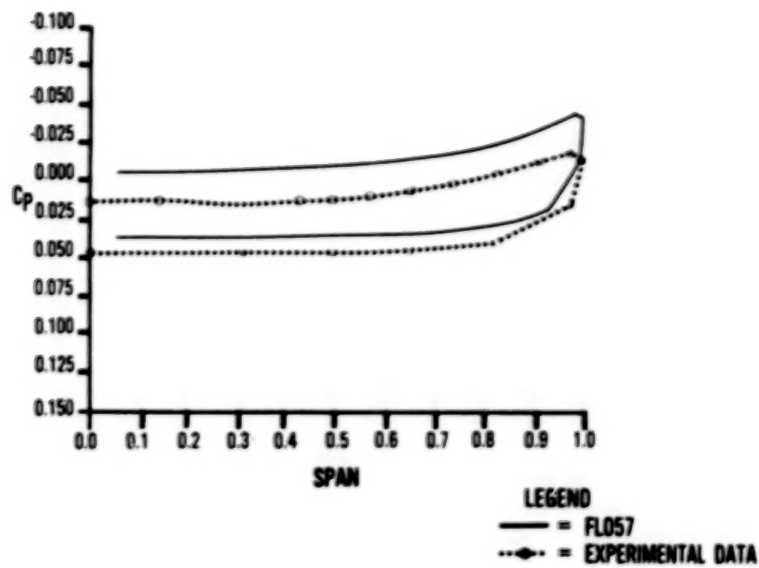


Figure 15.- Comparison of Euler and Ref. 1,  $C_p$  data,  
 $M_\infty = 2.0$ ,  $AL = 4.0$ ,  $X = 16.0$ .

X STATION = 25.6

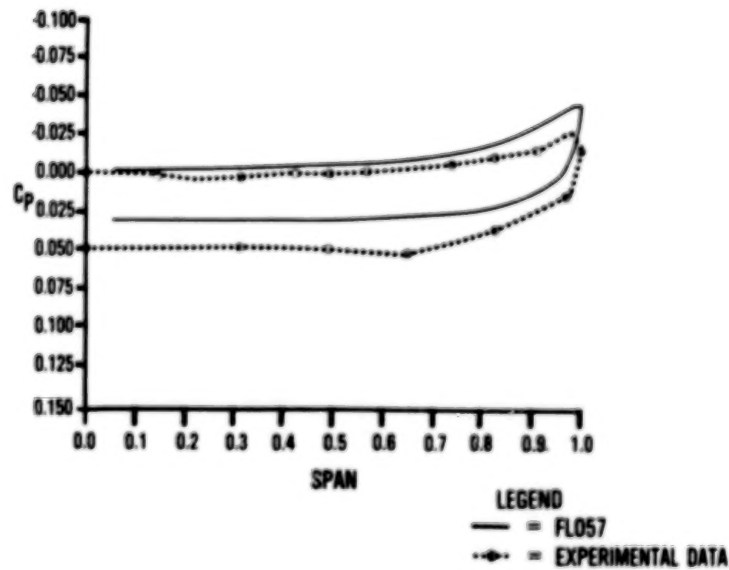


Figure 16.- Comparison of Euler and Ref. 1,  $C_p$  data,  
 $M_\infty = 2.0$ ,  $AL = 4.0$ ,  $X = 25.6$ .

X STATION = 35.2

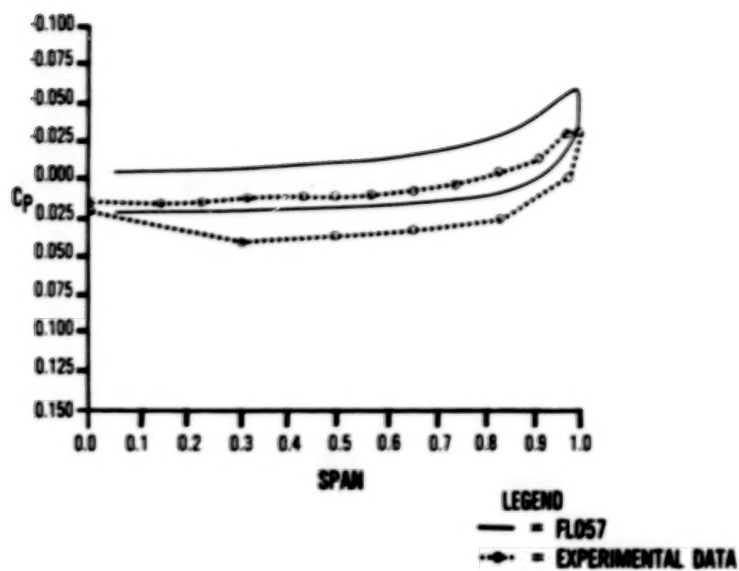


Figure 17.- Comparison of Euler and Ref. 1,  $C_p$  data,  $M_\infty = 2.0$ ,  $AL = 4.0$ ,  $X = 35.2$ .

X STATION = 3.20

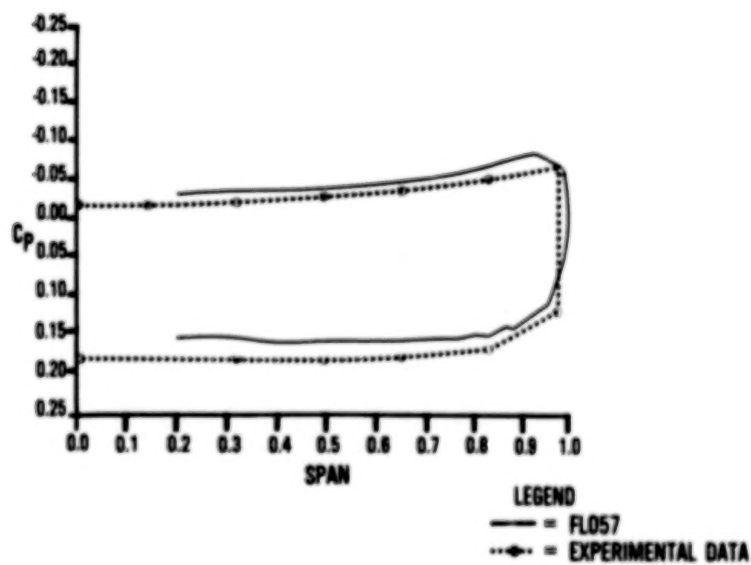


Figure 18.- Comparison of Euler and Ref. 1,  $C_p$  data,  $M_\infty = 2.0$ ,  $AL = 8.0$ ,  $X = 3.20$ .

X STATION = 16.0

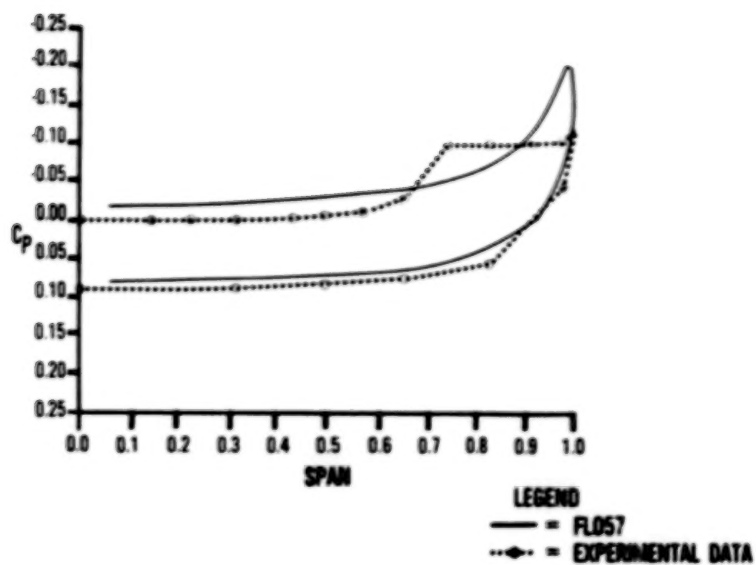


Figure 19.- Comparison of Euler and Ref. 1,  $C_p$  data,  
 $M_\infty = 2.0$ ,  $AL = 8.0$ ,  $X = 16.0$ .

X STATION = 25.6

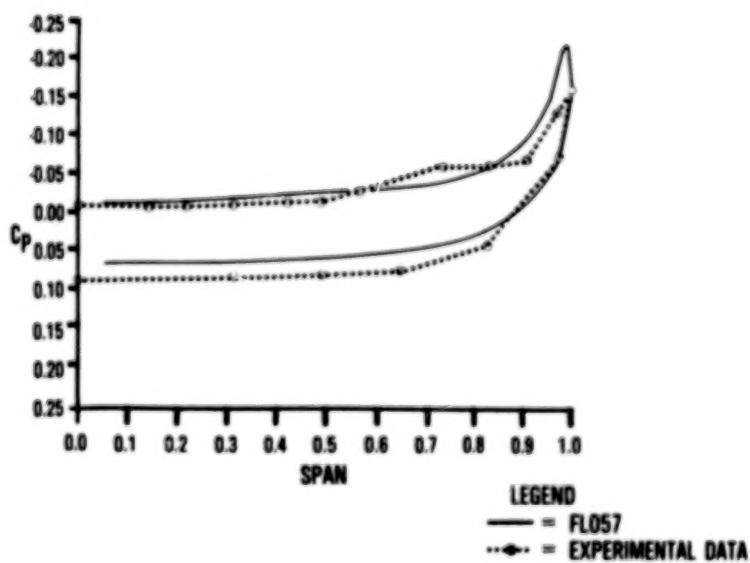


Figure 20.- Comparison of Euler and Ref. 1,  $C_p$  data,  
 $M_\infty = 2.0$ ,  $AL = 8.0$ ,  $X = 25.6$ .

X STATION = 35.2

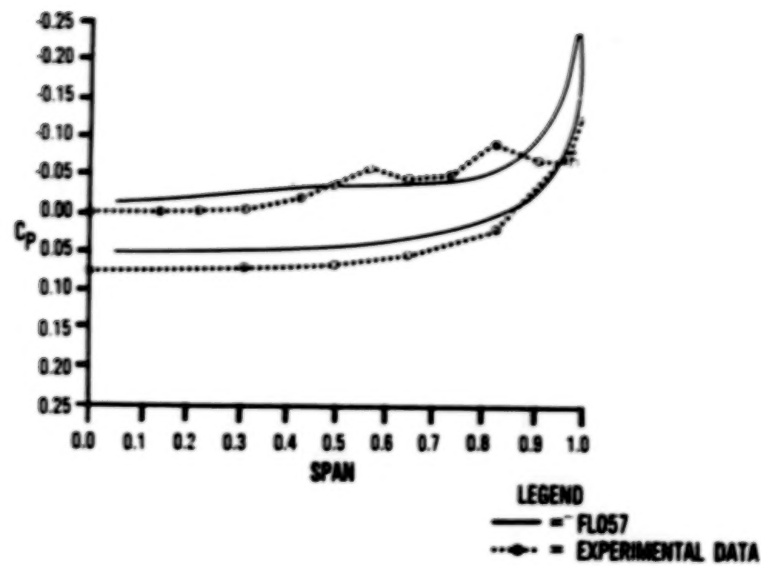


Figure 21.- Comparison of Euler and Ref. 1,  $C_p$  data,  $M_\infty = 2.0$ ,  $AL = 8.0$ ,  $X = 35.2$ .

X STATION = 3.20

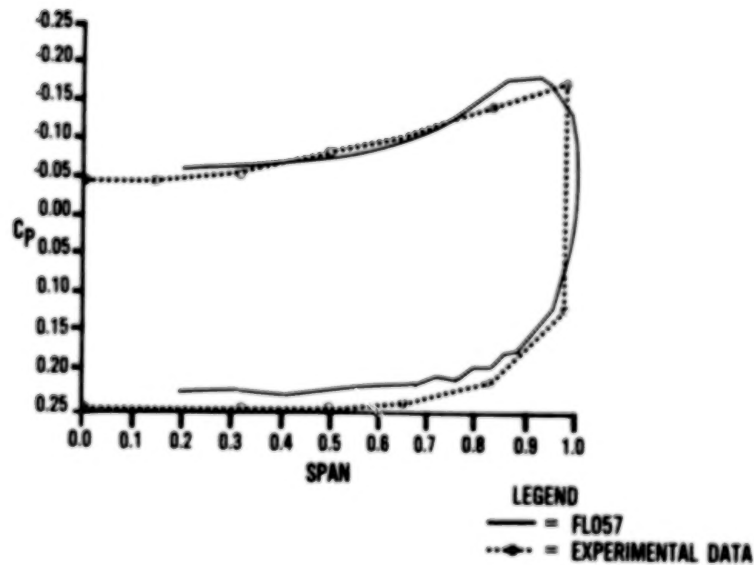


Figure 22.- Comparison of Euler and Ref. 1,  $C_p$  data,  $M_\infty = 2.0$ ,  $AL = 12.0$ ,  $X = 3.20$ .



X STATION = 16.0

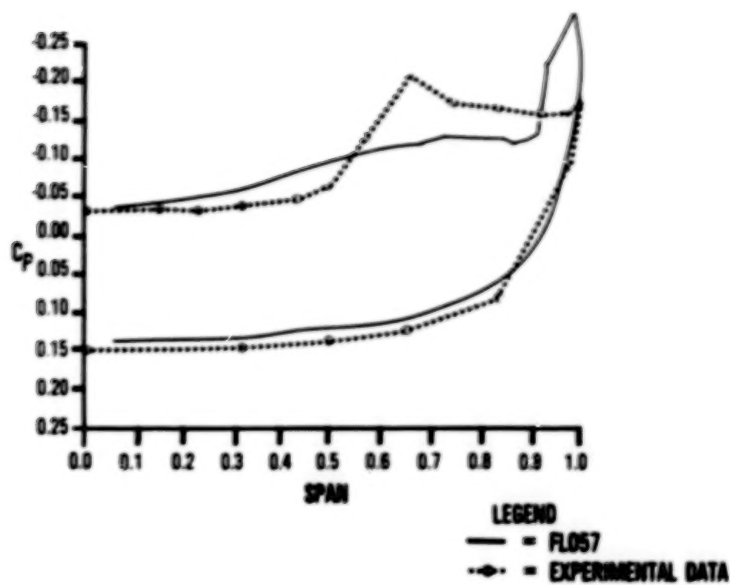


Figure 23.- Comparison of Euler and Ref. 1,  $C_p$  data,  $M_\infty = 2.0$ ,  $AL = 12.0$ ,  $X = 16.0$ .

X STATION = 25.6

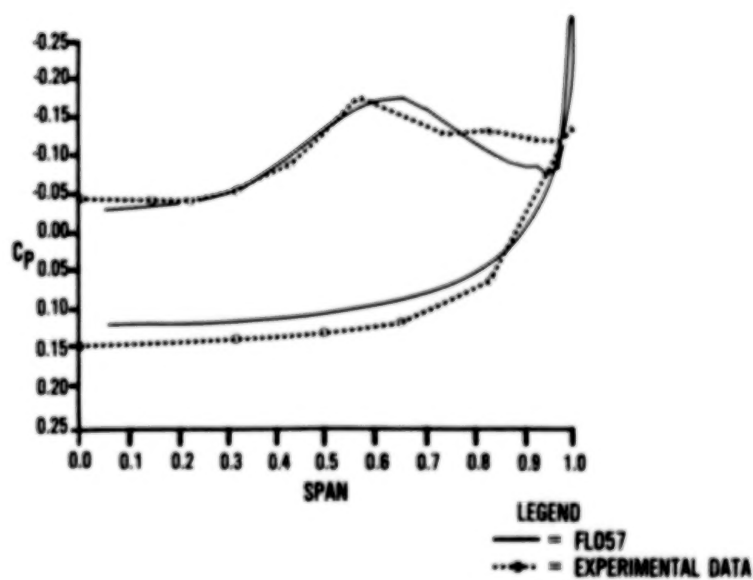


Figure 24.- Comparison of Euler and Ref. 1,  $C_p$  data,  $M_\infty = 2.0$ ,  $AL = 12.0$ ,  $X = 25.6$ .

X STATION = 35.2

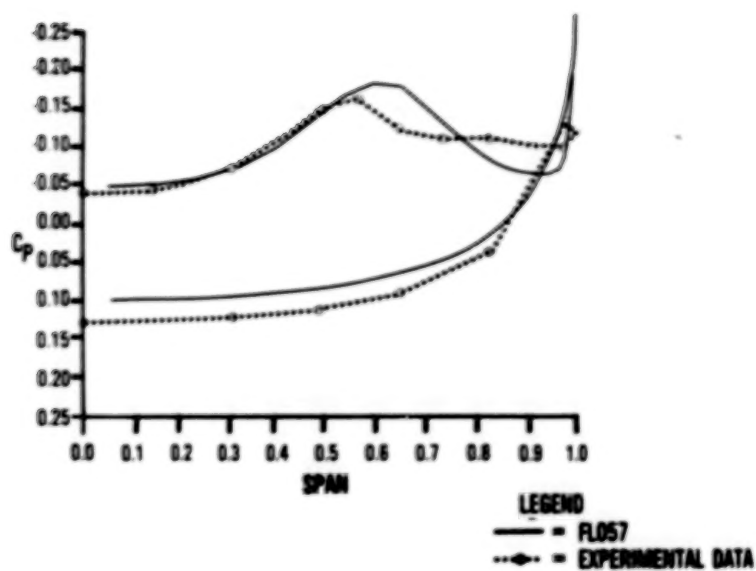


Figure 25.- Comparison of Euler and Ref. 1,  $C_p$  data,  
 $M_\infty = 2.0$ ,  $AL = 12.0$ ,  $X = 35.2$

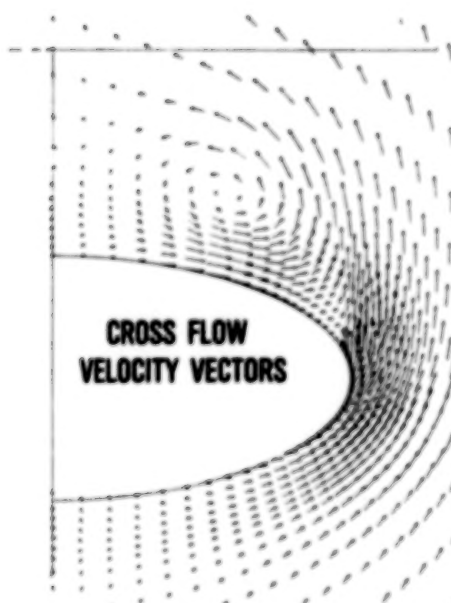


Figure 26.- Cross-flow velocities,  
 $M_\infty = 2.0$ ,  $AL = 12.0$ ,  $X = 35.2$ .

ORIGINAL PAGE IS  
OF POOR QUALITY

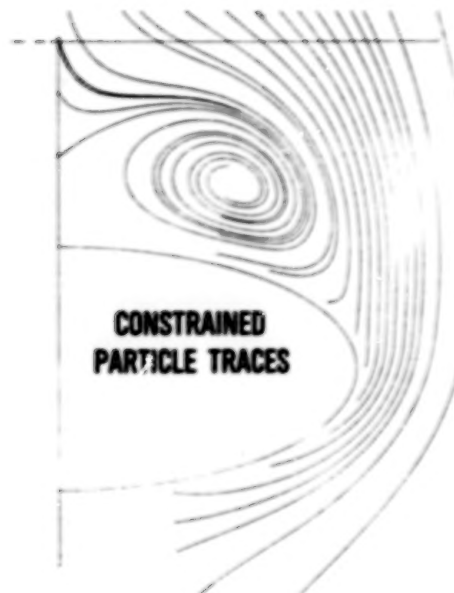


Figure 27.- Constrained particle paths,  
 $M_\infty = 2.0$ ,  $AL = 12.0$ ,  $X = 35.2$ .

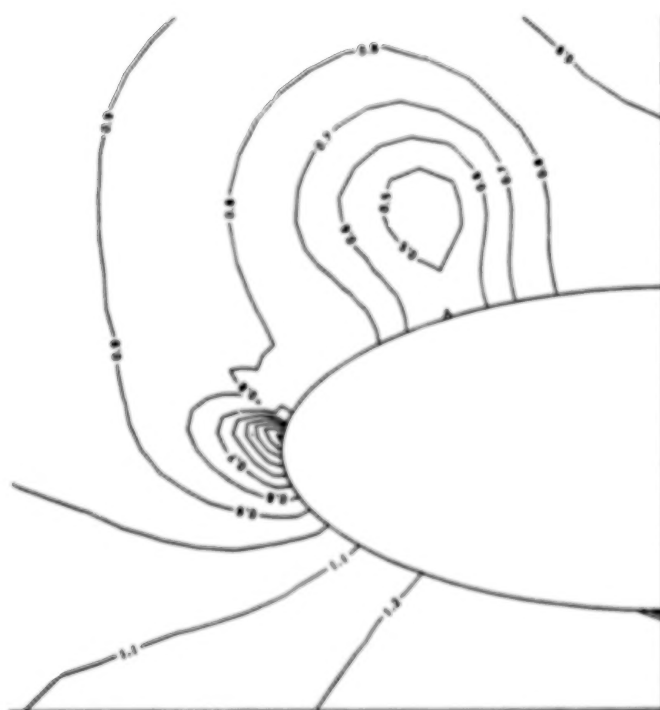


Figure 28.- Static pressure contour plot,  $M_\infty = 2.0$ ,  
 $AL = 12.0$ ,  $X = 35.2$ .

## COMPUTATION OF LEADING-EDGE VORTEX FLOWS

Richard W. Newsome  
Air Force Wright Aeronautical Laboratories  
AFSC Liaison Office, NASA Langley Research Center  
Hampton, Virginia

James L. Thomas  
NASA Langley Research Center  
Hampton, Virginia

## SUMMARY

The simulation of the leading-edge vortex flow about a series of conical delta wings through solution of the Navier-Stokes and Euler equations is studied. The occurrence, the validity, and the usefulness of separated flow solutions to the Euler equations are of particular interest. Central and upwind difference solutions to the governing equations are compared for a series of cross-sectional shapes, including both rounded and sharp tip geometries.

For the rounded leading edge and the flight condition considered, viscous solutions obtained with either central or upwind difference methods predict the classic structure of vortical flow over a highly swept delta wing. Predicted features include the primary vortex due to leading-edge separation and the secondary vortex due to crossflow separation. Central difference solutions to the Euler equations show a marked sensitivity to grid refinement. On a coarse grid, the flow separates due to numerical error and a primary vortex which resembles that of the viscous solution is predicted. In contrast, the upwind difference solutions to the Euler equations predict attached flow even for first-order solutions on coarse grids. On a sufficiently fine grid, both methods agree closely and correctly predict a shock-curvature-induced inviscid separation near the leeward plane of symmetry.

Upwind difference solutions to the Navier-Stokes and Euler equations are presented for two sharp leading-edge geometries. The viscous solutions are quite similar to the rounded leading-edge results with vortices of similar shape and size. The upwind Euler solutions predict attached flow with no separation for both geometries. However, with sufficient grid refinement near the tip or through the use of more accurate spatial differencing, leading-edge separation results. Once the leading-edge separation is established, the upwind solution agrees with recently published central difference solutions to the Euler equations.

## INTRODUCTION

The current interest in high angle-of-attack aerodynamics and vortical flows has focused considerable attention on the numerical simulation of the flow about a swept delta wing at moderate to high angles of attack. For subsonic leading edges which are sharp or of small radius of curvature, the flow separates at the tips and forms two counter-rotating vortices on opposite sides of the leeward wing surface. The presence of the vortices produces a pressure minimum on the upper surface and results in an additional lift component not predicted by linear theory.

Interest, here, is restricted to methods which "capture" the vortex rather than modeling it in an approximate manner. Thus, we consider only methods which solve the Euler and Navier-Stokes equations. The Navier-Stokes equations model all physical mechanisms and provide the most accurate results. Vigneron et al.<sup>1</sup> solved the conical and parabolic approximations to the Navier-Stokes equations for the vortical flow about a sharp-edged delta wing at supersonic speeds. Fujii and Kutler<sup>2,3</sup> solved the three-dimensional Navier-Stokes equations for the leading-edge separation about a delta wing with rounded edges at subsonic speeds. Rizzetta and Shang<sup>4</sup> presented three-dimensional Navier-Stokes solutions for a delta wing with sharp edges at supersonic and hypersonic speeds. The principal drawbacks of the Navier-Stokes equations are the higher computational costs necessary to resolve small-scale viscous effects and the need to model turbulence in an approximate manner. However, the Navier-Stokes solutions set the standard by which less exact solutions must be judged.

In the last several years, it has been suggested that Euler codes could be the method of choice in the simulation of leading-edge vortex flows.<sup>5</sup> In contrast to potential methods, the Euler equations provide the correct Rankine-Hugoniot shock jump conditions. They also admit rotational flow solutions. Indeed, numerous Euler solutions with leading-edge separation have been reported for both rounded and sharp leading edges using a variety of numerical schemes. A partial list includes the works of Rizzi et al.<sup>6-10</sup>, Raj and Sikora,<sup>11</sup> and Powell, Murman et al.<sup>12</sup> using a finite volume Runge-Kutta algorithm; Fujii and Obayashi<sup>13</sup> using a LU factored scheme whose right-hand side is identical to the Beam and Warming scheme; and Manie et al.<sup>14</sup> and Newsome<sup>15</sup> using a MacCormack scheme.

Since flow separation is usually associated with generation of vorticity through the no-slip boundary condition in a viscous flow, its occurrence in an inviscid solution is of both theoretical and practical importance. Necessary conditions for flow separation include the presence of vorticity in the flow as well as an adverse pressure gradient. While the Euler equations admit rotational solutions through the transport (and for three-dimensional flow, stretching) of vorticity, there is only one valid mechanism for vorticity generation in an inviscid flow. In accord with Crocco's theorem, the Euler equations allow for the generation of vorticity through non-constant shock strength (shock curvature, shock intersection, etc.). Salas<sup>16</sup> first demonstrated shock-induced inviscid separation for the transonic flow about a circular cylinder. Marconi<sup>17</sup> published similar results for the supersonic flow about circular cones and more recently elliptic cones.<sup>18</sup>

The Euler equations are singular at a sharp tip. This, however, causes no particular problem for a finite volume scheme in which cell centered quantities are computed. Salas and Daywitt<sup>19</sup>, in considering conical flow about sharp external axial corners, have shown that a limiting form of the inviscid equations valid at the singular corner point leads to a conical analog of the isentropic Prandtl-Meyer expansion. The maximum Prandtl-Meyer expansion angle corresponds to vacuum pressure. It is not clear whether theoretically valid attached flow Euler solutions exist for geometries in which the vacuum expansion limit is exceeded. For any finite radius of curvature, the flow field is resolvable and a valid Euler solution must approach the expansion limit as the radius of curvature approaches zero. In a viscous gas, the flow separates well before the inviscid expansion limit is reached. Once the



separation and the level of shed vorticity are established, the dynamics of the vortex motion, i.e. its interaction with neighboring surfaces, are essentially inviscid and thus adequately described by the Euler equations (excluding viscous features such as secondary vortices).

In practice, numerical solutions to the Euler equations for wings of small radius of curvature often result in inviscid separation. Any numerical algorithm, whether central or upwind differenced, must be dissipative for stability. As such, there is an effective Reynolds number inherent in the calculation which is dependent on the local mesh resolution and the order of the method. Upwind schemes are naturally dissipative. Central difference schemes are not naturally dissipative and dissipative terms are generally added to the discretized equations. The added dissipative terms are generally of two types: a third-order fourth-difference term to provide dissipation in smooth regions and an adaptive second difference term to control shock oscillations. The latter term reverts to first order at a shock but it also is significant in regions of rapid expansion. Finally, error can be introduced by the application of surface boundary conditions.

In reference 15, from which parts of this paper are taken, central difference solutions to the Euler and Navier-Stokes equations for the flow about a delta wing with a rounded leading edge (elliptic cone) were considered. The separation vortex predicted with the Euler equations, which is characteristic of the viscous solution, was found to be numerically induced. More recently, upwind difference Euler solutions<sup>20</sup> were shown to be much less susceptible to spurious inviscid separation. In the present paper, the upwind difference method is extended to the conical Navier-Stokes equations and a more detailed comparison of central and upwind difference solutions for both the Euler and Navier-Stokes equations is given for the round leading-edge wing. The upwind code is further extended to consider Navier-Stokes and Euler solutions for several sharp leading-edge wings.

#### SOLUTION METHOD

If interest is restricted to supersonic flow past conical bodies, then the governing equations may be simplified since the resulting flow will also be conical. A conical flow has the property that all flow quantities are invariant on rays which pass through the apex of the conical surface. All derivatives in the radial direction may then be neglected, reducing a three-dimensional problem into a much more tractable two-dimensional one. The conical assumption is exact for inviscid flow. For viscous flow, a length scale dependence is contained in the Reynolds number. The flow may be thought of as locally conical with the Reynolds number determining the location of the conical plane at which the solution is determined. The conical equations may be obtained by introduction of the conical variables

$$\xi = \xi(x) = x \quad Y = \frac{y}{x} \quad Z = \frac{z}{x}$$

$$\eta = \eta(x, y, z) = \eta(Y, Z)$$

$$\zeta = \zeta(x, y, z) = \zeta(Y, Z)$$

into the three-dimensional Navier-Stokes equations, written in terms of the non-dimensional Cartesian variables  $(x,y,z)$ . Upon simplifying for conical flow, the governing equations may be expressed in conservation form as

$$\frac{\partial}{\partial t}(\hat{Q}) + \frac{\partial}{\partial \eta}(\hat{G} - \hat{G}_v) + \frac{\partial}{\partial \zeta}(\hat{H} - \hat{H}_v) + (\hat{S} - \hat{S}_v) = 0 \quad (1)$$

The inviscid equations are obtained by dropping the terms  $(\hat{G}_v, \hat{H}_v, \hat{S}_v)$ .

The general three-dimensional, upwind, Euler/thin layer Navier-Stokes code developed by Thomas<sup>20,21</sup> was specialized for conical flow. In the finite volume formulation, a single array of crossflow plane volumes was constructed such that the inflow and outflow surfaces are scaled by the conical transformation, as above. While the code uses a finite volume approach, the equations may be written in generalized coordinates as

$$\frac{\partial}{\partial t}(\hat{Q}) + \frac{\partial}{\partial \xi}(\hat{F}) + \frac{\partial}{\partial \eta}(\hat{G}) + \frac{\partial}{\partial \zeta}(\hat{H} - \hat{H}_v) = 0 \quad (2)$$

At each iteration, the inflow conditions are updated with the results of the previous iteration so that, at convergence,  $\partial \hat{Q} / \partial \xi = 0$ , consistent with the conical flow approximation.

The inviscid and viscous flux vectors in equations (1) and (2) are defined as

$$\hat{Q} = \frac{\hat{Q}}{J} = \frac{1}{J} \begin{bmatrix} \rho \\ \rho u \\ \rho v \\ \rho w \\ \rho E \end{bmatrix} \quad \hat{F}, \hat{G}, \hat{H} = \frac{1}{J} \begin{bmatrix} \rho U_c \\ \rho U_c u + \alpha_x p \\ \rho U_c v + \alpha_y p \\ \rho U_c w + \alpha_z p \\ [\rho E + p] U_c \end{bmatrix} \quad (3)$$

$$\hat{S} = \frac{2}{J} \begin{bmatrix} \rho u \\ \rho u^2 + p \\ \rho uv \\ \rho uw \\ [\rho E + p] u \end{bmatrix} \quad E = e_I + \frac{1}{2}(u^2 + v^2 + w^2)$$

$$U_c = \alpha_x u + \alpha_y v + \alpha_z w$$

$$\hat{G}_v, \hat{H}_v = \frac{1}{J} \begin{bmatrix} 0 \\ \alpha_x \tau_{xx} + \alpha_y \tau_{xy} + \alpha_z \tau_{xz} \\ \alpha_x \tau_{xy} + \alpha_y \tau_{yy} + \alpha_z \tau_{yz} \\ \alpha_x \tau_{xz} + \alpha_y \tau_{yz} + \alpha_z \tau_{zz} \\ \alpha_x b_x + \alpha_y b_y + \alpha_z b_z \end{bmatrix} \quad \hat{S}_v = \frac{1}{J} \begin{bmatrix} 0 \\ \tau_{xx} \\ \tau_{xy} \\ \tau_{xz} \\ b_x \end{bmatrix}$$

Although the flux vectors can be written in a common form, they are in fact quite different as applied to equations (1) or (2). A general three-dimensional transformation between the Cartesian variables (x,y,z) and the computational variables is implied in equation (2), so that the flux terms can be defined as below:

$$\begin{aligned} \hat{F}: \quad \alpha &= \xi; \quad U_c = U = \xi_x u + \xi_y v + \xi_z w \\ \hat{G}: \quad \alpha &= \eta; \quad U_c = V = \eta_x u + \eta_y v + \eta_z w \\ \hat{H}, \hat{H}_v: \quad \alpha &= \zeta; \quad U_c = W = \zeta_x u + \zeta_y v + \zeta_z w \\ J &= \partial(\xi, \eta, \zeta) / \partial(x, y, z) \end{aligned} \quad (4)$$

In the finite volume formulation, expressions for the transformation derivatives and the Jacobian, J, are evaluated geometrically.

When working with the conical equations (1), it is convenient to work in terms of the conical variables, Y and Z. This allows a simpler form for the equations using the two-dimensional transformation:

$$\begin{bmatrix} \eta_Y & \zeta_Y \\ \eta_Z & \zeta_Z \end{bmatrix} = \begin{bmatrix} Y_\eta & Z_\eta \\ Y_\zeta & Z_\zeta \end{bmatrix}^{-1} \quad J = \begin{vmatrix} \eta_Y & \zeta_Y \\ \eta_Z & \zeta_Z \end{vmatrix}$$

Since

$$\begin{aligned} \eta_x &= -\frac{1}{x} [Y\eta_Y + Z\eta_Z] & \zeta_x &= -\frac{1}{x} [Y\zeta_Y + Z\zeta_Z] \\ \eta_y &= \frac{1}{x} [\eta_Y] & \zeta_y &= \frac{1}{x} [\zeta_Y] \\ \eta_z &= \frac{1}{x} [\eta_Z] & \zeta_z &= \frac{1}{x} [\zeta_Z] \end{aligned} \quad (5)$$

it is convenient to define the terms

$$\eta_x = -[Y\eta_Y + Z\eta_Z] \quad \zeta_x = -[Y\zeta_Y + Z\zeta_Z]$$

so that the flux terms in equation (3) can be defined as

$$\hat{G}, \hat{G}_V: \alpha = \eta; (\alpha_x, \alpha_y, \alpha_z) = (\eta_x, \eta_y, \eta_z) \quad U_c = V = \eta_x u + \eta_y v + \eta_z w \quad (6)$$

$$\hat{H}, \hat{H}_V: \alpha = \zeta; (\alpha_x, \alpha_y, \alpha_z) = (\zeta_x, \zeta_y, \zeta_z) \quad U_c = W = \zeta_x u + \zeta_y v + \zeta_z w$$

The term,  $\frac{1}{x}$ , is absorbed into equation (1) when the Reynolds number and the time scale are defined with respect to the length scale,  $L$ , where  $L$  is the length from the body apex to the crossflow solution plane.

Upon nondimensionalization in terms of the freestream density,  $\rho_\infty$  and sound speed,  $c_\infty$ , the shear stress and heat flux terms are defined in tensor notation (summation convention implied) as:

$$\tau_{x_\alpha x_\beta} = \frac{1}{Re_\infty} \left[ \mu \left( \frac{\partial u_\alpha}{\partial x_\beta} + \frac{\partial u_\beta}{\partial x_\alpha} \right) + \lambda \frac{\partial u_\gamma}{\partial x_\gamma} \delta_{\alpha\beta} \right] \quad (7)$$

$$\dot{q}_{x_\alpha} = - \left( \frac{M_\infty}{Re_\infty Pr(\gamma-1)} \right) \frac{\partial c^2}{\partial x_\alpha} \quad b_{x_\alpha} = u_\beta \tau_{x_\alpha x_\beta} - \dot{q}_{x_\alpha}$$

$$Re_\infty = \frac{\rho_\infty u_\infty L}{\mu_\infty}$$

The chain rule is used to evaluate derivatives with respect to  $(x, y, z)$  in terms of  $(\eta, \zeta)$ . When the thin layer assumption is made, only those derivatives in the direction normal to the wall ( $\zeta$ ) are retained in the stress and heat flux terms. Equations (1) and (2) are closed by the perfect gas equation of state and Sutherland's law for molecular viscosity. All calculations are for laminar flow only.

The conical flow equations (1) were solved with the MacCormack<sup>22</sup> unsplit, explicit finite-difference algorithm. Since the algorithm is well known, a detailed description is unnecessary. The method is second-order accurate in space and time and is conditionally stable. To control shock oscillations, MacCormack's<sup>23</sup> pressure damping was incorporated into the scheme. The damping term is  $O(\Delta x^3)$  except in regions of large pressure gradients where the pressure gradient switch forces the damping to  $O(\Delta x)$ . MacCormack's scheme is also naturally dissipative due to unsymmetric differencing in the predictor and corrector steps.

Upwind solutions were obtained with the flux vector splitting algorithm developed by Thomas.<sup>20</sup> The generalized fluxes  $\hat{F}, \hat{G}, \hat{H}$ , representing pressure and convection terms are split into forward and backward contributions according to the sign of the eigenvalues of the Jacobian matrices

$$\hat{\partial F}/\partial Q, \hat{\partial G}/\partial Q, \hat{\partial H}/\partial Q$$

and differenced accordingly. For example, the flux difference in the  $\xi$ -direction is

$$\delta_{\xi} \hat{F} = \delta_{\xi}^{-} \hat{F}^{+} + \delta_{\xi}^{+} \hat{F}^{-} \quad (8)$$

where  $\delta_{\xi}^{-}$  and  $\delta_{\xi}^{+}$  denote general backward and forward divided difference operators respectively, in the  $\xi$ -direction. In reference 20, van Leer's flux vector splitting was extended to three-dimensional generalized coordinates.

The flux,  $\hat{F}$ , as an example, is split according to the contravariant Mach number in the  $\xi$ -direction, defined as  $M_{\xi} = \bar{u}/c$ , where  $\bar{u} = U/|\text{grad}(\xi)|$ . For supersonic flow,  $|M_{\xi}| > 1$

$$\begin{aligned} \hat{F}^{+} &= \hat{F}, \hat{F}^{-} = 0 \quad M_{\xi} > +1 \\ \hat{F}^{-} &= \hat{F}, \hat{F}^{+} = 0 \quad M_{\xi} < -1 \end{aligned} \quad (9)$$

and for subsonic flow,  $|M_{\xi}| < 1$

$$\hat{F}^{\pm} = \frac{|\text{grad} \xi|}{J} \begin{bmatrix} f_{\text{mass}}^{\pm} \\ f_{\text{mass}}^{\pm} [\hat{k}_x (-\bar{u} \pm 2c)/\gamma + u] \\ f_{\text{mass}}^{\pm} [\hat{k}_y (-\bar{u} \pm 2c)/\gamma + v] \\ f_{\text{mass}}^{\pm} [\hat{k}_z (-\bar{u} \pm 2c)/\gamma + w] \\ f_{\text{energy}}^{\pm} \end{bmatrix} \quad (10)$$

where

$$f_{\text{mass}}^{\pm} = \pm \rho c (M_{\xi} \pm 1)^2 / 4$$

$$f_{\text{energy}}^{\pm} = f_{\text{mass}}^{\pm} [ \{ -(\gamma-1)\bar{u}^2 \pm 2(\gamma-1)\bar{u}c + 2c^2 \} / (\gamma^2-1) + \frac{1}{2}(u^2+v^2+w^2) ]$$

The surface area of the cell interface in the  $\xi$  direction is  $|\text{grad} \xi|/J$ , the cell volume is  $1/J$ , and

$$(\hat{k}_x, \hat{k}_y, \hat{k}_z) = (\xi_x, \xi_y, \xi_z) / |\text{grad} \xi| \quad (11)$$



are the direction cosines of the cell interfaces in the  $\xi$  direction. The split-flux differences are implemented as a flux balance across a cell as (for  $\Delta\xi = \Delta\eta = \Delta\zeta = 1$ )

$$\delta_{\xi}^{-} \hat{F}_1^{+} + \delta_{\xi}^{+} \hat{F}_1^{-} = [\hat{F}^{+}(Q^{-}) + \hat{F}^{-}(Q^{+})]_{i+1/2} - [\hat{F}^{+}(Q^{-}) + \hat{F}^{-}(Q^{+})]_{i-1/2} \quad (12)$$

The notation  $\hat{F}^{+}(Q^{-})_{i+1/2}$  denotes a forward flux evaluated using the metric terms at the cell interface  $(i+1/2)$ , with conserved variables obtained by an upwind biased interpolation

$$Q_{i+1/2}^{-} = Q_i + \frac{1}{4}\phi_{\xi} [(1-\kappa_{\xi})\nabla_{\xi} + (1+\kappa_{\xi})\Delta_{\xi}] Q_i \quad (13)$$

$$Q_{i+1/2}^{+} = Q_{i+1} - \frac{1}{4}\phi_{\xi} [(1+\kappa_{\xi})\nabla_{\xi} + (1-\kappa_{\xi})\Delta_{\xi}] Q_{i+1}$$

where

$$\Delta_{\xi} Q_i = Q_{i+1} - Q_i \quad \nabla_{\xi} Q_i = Q_i - Q_{i-1}$$

Only fully upwind first or second-order accurate differencing has been used in the results that follow:

$$\begin{aligned} \phi_{\xi} &= 0 & (\text{first-order upwind}) \\ \phi_{\xi} &= 1, \kappa_{\xi} = -1 & (\text{second-order upwind}) \end{aligned} \quad (14)$$

Differencing for the diffusion terms representing shear stress and heat transfer effects corresponds to second-order central differences in which second derivatives are treated as differences across cell interfaces of first derivative terms

$$\delta_{\zeta}^{\pm} \hat{H}_{v_k} = \hat{H}_{v_{k+1/2}} - \hat{H}_{v_{k-1/2}} \quad (15)$$

where, for example, the term,

$$\tau_{xy} = \frac{M_{\infty}}{Re_{\infty}} \left[ \mu \left( \frac{\partial u}{\partial y} + \frac{\partial v}{\partial x} \right) \right]$$

under the thin layer approximation, becomes,

$$\tau_{xy} = \left( \frac{M_{\infty}}{Re_{\infty}} \right) \mu \left( \zeta_y \frac{\partial u}{\partial \zeta} + \zeta_x \frac{\partial v}{\partial \zeta} \right) \quad (16)$$

and is differenced in  $\hat{H}_{v_{k\pm 1/2}}$  as

$$\frac{M_\infty}{Re_\infty} u_{k\pm 1/2} (\zeta_{y_{k\pm 1/2}} \delta_\zeta u_{k\pm 1/2} + \zeta_{x_{k\pm 1/2}} \delta_\zeta v_{k\pm 1/2}) \quad (17)$$

where

$$\delta_\zeta u_{k+1/2} = u_{k+1} - u_k$$

The linearized, backward time approximation in delta form for the three-dimensional equations is given as

$$\left[ \frac{I}{J\Delta t} + \delta_\xi \frac{\partial \hat{F}}{\partial Q} + \delta_\eta \frac{\partial \hat{G}}{\partial Q} + \delta_\zeta \left( \frac{\partial \hat{H}}{\partial Q} - \frac{\partial \hat{H}_v}{\partial Q} \right) \right] \Delta Q = R^N \quad (18)$$

As described in reference 20, equation (18) is solved by streamwise relaxation ( $\xi$ -direction) and approximate factorization in the crossflow plane as

$$[M + \delta_\eta \frac{\partial \hat{G}}{\partial Q}] [M]^{-1} [M + \delta_\zeta \left( \frac{\partial \hat{H}}{\partial Q} - \frac{\partial \hat{H}_v}{\partial Q} \right)] \Delta Q = R(Q^N, Q^{N+1}) \quad (19)$$

where

$$M = \left[ \frac{I}{J\Delta t} + \frac{\partial \hat{F}^+}{\partial Q} - \frac{\partial \hat{F}^-}{\partial Q} \right]$$

In general, the solution is obtained by alternate forward and backward sweeping through the crossflow planes with a nonlinear update of the residual  $R$  indicated on the right side of (19). For the degenerate conical flow case, this corresponds to reinitialization of the inflow plane and update of the crossflow plane until convergence is achieved. Since the spatial implicit discretizations may be taken as first order with no loss in steady-state accuracy, the solution of equation (19) involves the solution of two block tridiagonal equations.

Initial conditions for both central and upwind difference methods consisted of freestream conditions. Boundary conditions consisted of freestream conditions on the outer boundary, reflection conditions in the crossflow symmetry plane and slip or no slip conditions on the body surface depending upon whether the viscous or inviscid equations are considered.

## RESULTS

The flow about several different conical delta wings with a  $70^\circ$  wing sweep angle at a Mach number of 2 and 10 degrees angle of attack was chosen for study. A thin elliptic cone, Fig. 1, with half angles,  $\tan^{-1} (y_{LE}/x) =$

20°, and  $\tan^{-1}(z_{CL}/x) = 1.5^\circ$ , was used as a model for round leading edges with small curvature radius. For sharp tips, a thinner conical body was defined with a vertical half angle,  $\tan^{-1}(z_{CL}/x) = 0.75^\circ$  and a tip half angle given as  $\tan^{-1}(dz/dy)_{LE} = 10^\circ$ . As an extreme case, a zero thickness flat delta wing was also considered.

Central and upwind difference solutions to the Navier-Stokes and Euler equations are compared for the rounded leading-edge wing. Upwind difference Euler and Navier-Stokes results are then presented for the sharp tip geometries.

## ROUNDED LEADING EDGES

### Navier-Stokes Solutions

A comparison of central and upwind difference calculations was made at Reynolds numbers of  $Re_\infty = 0.1 \times 10^6$  and  $0.5 \times 10^6$ . The grid consisted of 151 points around and 65 points normal to the body with an equal minimum step size at the tip, in both directions,  $\Delta s/x = .0002$ . This minimum step size in the body normal direction was relaxed to a maximum value  $\Delta s/x = .0006$  away from the tip. The grid and an enlarged view of the tip are shown in Fig. 2. At a Reynolds number of  $Re_\infty = 0.1 \times 10^6$ , the windward symmetry plane boundary layer contained 14 points and the leading-edge boundary layer contained 7 points.

In general, central and upwind difference solutions, both second-order accurate, are in good agreement. A plot of the crossflow velocity for the central difference solution is shown in Fig. 3 (the upwind result is nearly identical). In this and the results to follow, the radial velocity component has been subtracted out of the Cartesian crossflow components. The flow separates at the leading edge with a large primary vortex and a smaller secondary vortex. At the higher Reynolds number,  $Re_\infty = 0.5 \times 10^6$ , the secondary vortex is smaller relative to the primary vortex. A comparison of pressure coefficients, Fig. 4, for both the central and upwind difference solutions, shows the suction peak to be stronger for the higher Reynolds number. At the higher Reynolds number, minor differences appear in the two solutions in the separation zone, particularly near the leading edge.

Squire<sup>24</sup> presented experimental data for the same elliptic cone with a small circular centerbody. To verify the viscous calculations, the upwind scheme was applied to the elliptic cone at conditions corresponding to the experimental data of Squire:  $M_\infty = 1.8$ ,  $Re_\infty = 2.1 \times 10^6$ . The pressure coefficient is shown in figure 5. The solution is in reasonable agreement with the experiment. Miller and Wood<sup>25</sup> delineated seven different flow classifications according to leading-edge normal Mach number and angle of attack. The present results, which indicate a primary and secondary vortex with no crossflow shock, are in agreement with Miller's classification.

Since some Reynolds number dependence was found in the previous cases, a wider range of Reynolds numbers were investigated with the thin-layer upwind Navier-Stokes code for laminar flow. Although the grid, Fig. 2, was not refined with increasing Reynolds number, the results are believed to be

generally valid. The pressure coefficient for the various Reynolds numbers is shown in Fig. 6. The leeward suction pressure appears to approach a limit with increasing Reynolds number. The flow fields are similar with the exception of the lowest Reynolds number in which the secondary vortex is not present. Consistent with the experimental results of reference 26, differences with respect to Reynolds number are confined to the size and position of the vortex as well as the peak suction pressure.

### Euler Solutions

The Euler solutions (for conical flow) are characterized by the presence of vortical singularities. The entire flow is weakly rotational inside the bow shock due to variable shock strength. Since streamlines terminate at one of the vortical singularities and each streamline crosses the shock at a different location, the flow at the singularities is multivalued. As a practical matter, for the present case, the bow shock is extremely weak and the entropy variation due to the bow shock is negligible.

Inviscid solutions for the central and upwind difference methods are compared on coarse and fine grids. While the two methods agree closely on fine grids, there are dramatic differences on the coarse grid.

### Coarse Grid Euler

Since a prime motivation in solving the Euler equations is the desire to avoid the grid fineness necessary for viscous resolution, a coarse grid (75 x 55) was first considered. The minimum step size,  $\Delta s/x = 0.005$ , gives poor resolution at the tip as can be seen in Fig. 7. The crossflow velocities for the central difference solution are shown in Fig. 8. Corresponding crossflow Mach number and entropy contours are given in Fig. 9. Entropy is defined as

$$\frac{\Delta s}{R} = \frac{s - s_\infty}{R} = \frac{1}{\gamma - 1} \ln \left( \frac{[p/p_\infty]}{[\rho/\rho_\infty]}^\gamma \right)$$

For constant total enthalpy, total pressure loss is given as

$$\frac{p_o}{p_{o_\infty}} = e^{-\left[\frac{\Delta s}{R}\right]}$$

A comparison of the crossflow velocities, Figs. 4 and 8, reveals a large primary vortex of similar shape and size. Notably absent is the secondary vortex since there is no vorticity generating mechanism on the upper wing surface. A comparison of the pressure coefficient, Fig. 10, for the central difference inviscid and viscous results, shows surprising agreement with the exception of the over expansion at the leading edge. From Fig. 9, it can be seen that entropy is generated at the tip and is convected through the vortex. The entropy and vorticity at the tip are spurious since there is no valid mechanism for their generation in the Euler equations. In the present case, the flow does not separate at the tip but at about 92% of chord on the leeward surface. The separation occurs downstream of a small shock at this point dividing supersonic flows of opposite directions. With less accurate



boundary conditions or large values of the damping coefficient, the point of separation moves closer to the leading edge. In reference 15, several different boundary conditions were tried. The damping coefficient was also varied over its usual range of stability. With minor exceptions in the location of the separation point, the result was always the same - a large primary separation vortex. It should be noted that a minimum value of the damping coefficient was necessary to maintain a stable solution. Computations by E. Murman (Massachusetts Institute of Technology, private communication) for this case, on a similarly coarse grid with a finite volume Runge-Kutta scheme, also resulted in a leading-edge separation vortex.

A better understanding of the separation can be gained by a look at the transient development of the vortex. From the initial condition, the flow quickly expanded about the leading edge to a supersonic crossflow. A crossflow shock also developed on the leeward surface with no separation evident. Concurrently, the leading-edge expansion produced large entropy/vorticity errors which were convected downstream to the developing crossflow shock. The interaction of the two produced a separated region at the base of the shock. The separation then expanded to form the primary vortex and the shock is either absent or confined to the vortex near the tip at the point of separation.

First- and second-order accurate upwind solutions were computed on the same coarse grid. The first-order scheme is the most dissipative scheme considered and does not accurately resolve the detailed flow structure. However, as can be seen in Fig. 11, the flow remains attached at the leading edge. The second-order solution is shown in Fig. 12, and the higher accuracy now correctly predicts the shock-induced vortex centered near the point  $y/x = 0.1$ . Crossflow Mach number and entropy plots for the second-order accurate solution are given in Fig. 13. The pressure coefficient for the first- and second-order accurate solutions is shown in Fig. 14. As would be expected, the leading-edge expansion and crossflow shock are better resolved with the more accurate differencing. Chakravarthy<sup>27</sup> has also solved the present case with an upwind Euler code on the same coarse grid and found no evidence of leading-edge separation.

#### Fine Grid Euler

The grid used in the viscous solutions, Fig. 2, was also used for the inviscid calculation. The intent was to reduce the effect of numerically induced errors through better spatial resolution of the tip region. Second-order accurate central and upwind difference solutions are virtually identical on this grid. As can be seen in Fig. 15, the central difference solution is now attached at the leading edge. In both solutions, as in the coarse grid upwind solution, a small vortex appears downstream from the crossflow shock. The vortex is due to shock generated vorticity and is a valid Euler solution. A plot of the crossflow Mach numbers, Fig. 16, shows both the crossflow shock and the shock induced wake. In Fig. 17, enlarged views of the crossflow Mach number and entropy contours are given for the central difference solution. Entropy is generated across the shock according to the local shock strength. It is the entropy variation normal to the streamline which produces the vorticity as required by Crocco's theorem and the subsequent vortex. On the fine grid, the leading-edge expansion is essentially isentropic. This can also be seen in Fig. 18 where the leading-



edge expansion is noticeably sharper than the upwind solution on the coarse grid. The small bump at  $y/y_{LE} = 0.3$  is due to the expansion under the vortex.

Since boundary condition error, truncation error, and added artificial dissipation all go to zero in the limit as the grid is refined, it is rather difficult to ascertain the precise cause of the central difference separation. However, when compared with the upwind results, certain possibilities can be eliminated. Both schemes enforce the surface boundary conditions with equivalent accuracy. Since the first-order upwind solution has the largest truncation error and yet remains attached on the coarse grid, the cause of the central difference separation is not just a matter of inadequate numerical resolution. The one distinguishing characteristic between the upwind and central difference methods is the added artificial dissipation model necessary for stability and to control shock oscillations. Although in regions of smooth flow, the added terms are of higher order than the truncation error, in regions of large gradients, the pressure switch built into the model causes the scheme to revert to first order. For this reason, it has been widely speculated, but not proven, that the artificial dissipation model is responsible for spurious inviscid separation. It is interesting to note, in comparing entropy generation at the tip between the central and upwind solutions on the coarse grid (Figs. 9 and 13), that although the upwind value is lower (0.3) than the central difference value (0.6), the terms are of the same order of magnitude.

## SHARP LEADING EDGES

### Navier-Stokes Solutions

A thin-layer Navier-Stokes solution was computed for the thin, sharp-edged wing at a Reynolds number,  $Re_\infty = 0.1 \times 10^6$ , using the second-order accurate scheme. The grid, Fig. 19, consisted of  $151 \times 65$  points with a minimum step size  $\Delta s/x = 0.0002$ . The crossflow velocities, Fig. 20, exhibit the same primary and secondary vortices at the same locations as the rounded leading edge. Crossflow Mach contours are given in Fig. 21.

### Euler Solutions

Since the upwind code was found to be much less susceptible to spurious inviscid separation for rounded leading edges, its behavior for sharp leading edges was investigated. The essential difference is that, unlike the rounded leading edge, the local behavior at the sharp edge is singular. Both first- and second-order solutions were computed on coarse and fine grids. Because of the very large gradients in the flow near the tip, it was found necessary to use first-order interpolation (equation 13) in the flux calculations for some 3-4 points away from and on either side of the tip in the second-order solutions. This type of flux limiting has been used (ref. 28) to ensure monotone shock profiles for strong shocks. The calculation remains fully conservative.

### Coarse Grid Euler

The coarse grid, Fig. 22, consisted of  $75 \times 55$  points. The local tip resolution is significantly less than that of the sharp tip viscous grid, Fig. 19. On this grid, both first- and second-order solutions are attached at the

leading edge. The second-order solution predicts a vortex downstream of the crossflow shock as can be seen in Fig. 23. Crossflow Mach number and entropy contours for the second-order solution are given in Fig. 24. Despite the presence of large entropy errors generated at the tip, leading-edge separation does not occur. The pressure coefficient, Fig. 25, is similar to the rounded edge result with a well-defined crossflow shock.

#### Zero-Thickness Wing

A zero thickness wing was considered in order to determine if attached flow solutions could be obtained in this extreme case. Powell et al.<sup>12</sup> recently presented leading-edge vortex solutions for similar geometries using a finite volume central difference scheme. The grid dimensions were the usual  $151 \times 65$  points. However, as seen in Fig. 26, the local resolution at the tip is relatively coarse. The first-order solution did not exhibit leading-edge separation. The crossflow velocities, Fig. 27, show a vortex downstream of the crossflow shock. Crossflow Mach number and entropy are given in Fig. 28. The second-order solution exhibits leading-edge separation, as is evident in Fig. 29. Both solutions are first-order accurate at the leading edge. Although the (pseudo) transient development of the two solutions was not observed, it is presumed that the interaction of the crossflow shock with the rotationality induced at the leading edge is unstable in the more accurate calculation. As a consequence, the flow separates at the base of the crossflow shock and the separation bubble grows to form the primary vortex. In Fig. 30, it can be seen that the crossflow shock has been displaced to a position above the vortex near its inboard boundary. The pressure coefficient for the two solutions is given in Fig. 31. The second-order solution has been compared with the results obtained by K. Powell and E. Murman (Massachusetts Institute of Technology, private communication). Although the comparison is not shown, the two computations are in close agreement, including the level of minimum pressure coefficient and the extent and shape of the separation vortex.

#### Fine Grid Euler

Upwind Euler solutions were computed for the thin, sharp-tipped wing using the finer viscous grid, Fig. 19. In contrast to the previous coarse grid calculations, both the first- and second-order solutions are separated at the leading edge. The first-order solution predicts a very shallow vortex extending from the leading edge to the centerline. The second-order solution predicts the more familiar separation vortex. The crossflow velocity plot, Fig. 32, reveals two smaller secondary vortices near the leading edge. Referencing the crossflow Mach number plot, Fig. 33, the secondary vortices are triggered by a small crossflow shock embedded in the vortex. These features were not found in the viscous calculation,  $Re_{\infty} = 0.1 \times 10^6$ , Fig. 20. The inviscid calculation also predicts a crossflow shock above the vortex near the inboard boundary which is not present in the viscous result. A thin layer (laminar) viscous calculation at a Reynolds number of  $Re_{\infty} = 50 \times 10^6$  also failed to exhibit the inviscid shock-induced secondary vortices. The pressure coefficient at the lower Reynolds number is compared with the viscous solution in Fig. 34.

## CONCLUSIONS

Central and upwind difference solutions to the Euler and Navier-Stokes equations have been presented for conical delta wings with several cross-sectional shapes. For the rounded leading edge, central and upwind difference Navier-Stokes solutions agree well. Although adequate resolution is necessary for accurate results, the Navier-Stokes equations describe all relevant physical mechanisms and provide a consistent flow description. On a coarse grid, the central difference Euler solution predicts a primary separation vortex which resembles the viscous result. This separation vortex, however, is due entirely to numerical error. With sufficient grid refinement, the vortex disappears. On both coarse and fine grids, the upwind solution does not produce leading-edge separation. Both methods correctly predict shock-induced inviscid separation on the fine grid. The separation in this case is a valid Euler solution. Upwind solutions to the Navier-Stokes and Euler equations were computed for sharp leading-edge geometries. The viscous solutions again represent a consistent physical model. Attached flow Euler solutions were found for very sharp leading edges and even for the infinitely thin zero thickness wing. However, with sufficient grid refinement or resort to higher order spatial accuracy, the upwind scheme also predicts leading-edge separation.

The behavior of central and upwind difference schemes in the solution of the Euler equations for flow about the leading edges of highly swept delta wings raises questions of theoretical and practical importance. In this paper, the emphasis has been on the latter question. As a model for the prediction of leading-edge separation vortices, the Euler equations lack the essential quality of consistency. Further, they are fundamentally incapable of predicting secondary flow features such as Reynolds numbers dependence or the presence of secondary vortices. On the same grid, the cost of evaluating the viscous terms in the thin layer Navier-Stokes equations relative to the inviscid Euler equations is less than a 2% increase in CPU time per iteration for the implicit upwind code. This figure reflects the fact that a majority of the CPU time is spent assembling and solving the linear systems arising from the the implicit time discretization. The penalty for an explicit method is significantly higher. In any event, the increase in accuracy and consistency in the resulting solutions would seem to justify the marginal increase in computational cost.

## REFERENCES

1. Vigneron, Y. C.; Rakich, J. V.; and Tannehill, J. C.: Calculation of Supersonic Viscous Flow Over Delta Wings With Sharp Subsonic Leading Edges. AIAA Paper 78-1137, July 1978.
2. Fujii, K.; and Kutler, P.: Numerical Simulation of the Leading Edge Separation Vortex for a Wing and Strake-Wing Configuration. AIAA Paper 83-1908, July 1983.
3. Fujii, K.; and Kutler, P.: Numerical Simulation of the Viscous Flow Over Three-Dimensional Complicated Geometries. AIAA Paper 84-1550, June 1984.



4. Rizzetta, D. P.; and Shang, J. S.: Numerical Simulation of Leading Edge Vortex Flows. AIAA Paper 84-1544, June 1984.
5. Hitzel, S. M.; and Schmidt, W.: Slender Wings With Leading-Edge Vortex Separation - A Challenge for Panel-Methods and Euler Codes. AIAA Paper 83-0562, Jan. 1983.
6. Rizzi, A.: Damped Euler-Equation Method to Compute Transonic Flow Around Wing-Body Combinations. AIAA Journal, vol. 20, no. 10, Oct. 1982, pp. 1321-1328.
7. Rizzi, A.; Eriksson, L. E.; Schmidt, W.; and Hitzel, S. M.: Simulating Vortex Flows Around Wings. Aerodynamics of Vortical Type Flows in Three Dimensions, AGARD Conference Preprint No. 342, 1983.
8. Rizzi, A.; and Erickson, L. E.: Computation of Flow Around Wings Based on the Euler Equations. Journal of Computational Physics, vol. 148, 1984, pp. 45-71.
9. Rizzi, A.: Euler Solutions of Transonic Vortex Flow Around the Dillner Wing - Compared and Analyzed. AIAA Paper 84-2142, Aug. 1984.
10. Rizzi, A.: Modelling Vortex Flow Fields by Supercomputers With Supersize Memory. Aeronautical Journal, April 1985, pp. 149-161.
11. Raj, P.; and Sikora, J.: Free Vortex Flows: Recent Encounters With an Euler Code. AIAA Paper 84-0135, Jan. 1984.
12. Powell, K.; Murman, E.; Perez, E.; and Baron, T.: Total Pressure Loss in Vortical Solutions of the Conical Euler Equations. AIAA Paper 85-1701, July 1985.
13. Fujii, K.; and Obayashi, S.: Evaluation of Euler and Navier-Stokes Solutions for Leading-Edge and Shock-Induced Separations. AIAA Paper 85-1563, July 1985.
14. Manie, F.; Neron, M.; and Schmitt, V.: Experimental and Computational Investigation of the Vortex Flow Over a Swept Wing. 14th Congress of the International Council of the Aeronautical Sciences, ICAS-84-2.8.1, Sept. 1984.
15. Newsome, R.: A Comparison of Euler and Navier-Stokes Equations for Supersonic Flow Over a Conical Delta Wing. AIAA Paper 85-0111, Jan. 1985.
16. Salas, M. D.: Recent Developments in Transonic Euler Flow Over a Circular Cylinder. Mathematics and Computers in Simulation, vol. 25, 1983, pp. 232-236.
17. Marconi, F.: The Spiral Singularity in the Supersonic Inviscid Flow Over a Cone. AIAA Paper 84-0135, Jan. 1984.
18. Marconi, F.: Shock Induced Vorticities on Elliptic Cones in Supersonic Flow. AIAA Paper 85-0433, Jan. 1985.

19. Salas, M. D.; and Daywitt, J.: Structure of the Conical Flow Field About External Axial Corners. AIAA Journal, vol. 17, no. 1, pp. 41-47, Jan. 1979.
20. Thomas, J. L.; van Leer, B.; and Walters, R. W.: Implicit Flux-Split Schemes for the Euler Equations. AIAA Paper 85-1680, July 1985.
21. Thomas, J. L.; and Walters, R. W.: Upwind Relaxation Algorithms for the Navier-Stokes Equations. AIAA Paper 85-1501 CP, July 1985.
22. MacCormack, R. W.: Numerical Solutions of the Interactions of a Shock Wave With a Laminar Boundary Layer. Lecture Notes in Physics, vol. 59, Springer Verlag, 1970, pp. 151-163.
23. MacCormack, R. W.; and Baldwin, B. S.: A Numerical Method for Solving the Navier-Stokes Equations With Application to Shock-Boundary Layer Interactions. AIAA Paper 75-1, Jan. 1975.
24. Squire, L. C.: Leading-Edge Separation and Crossflow Shocks on Delta Wings. AIAA Journal, vol. 23, no. 9, March 1985, pp. 321-325.
25. Miller, D. S.; and Wood, R. M.: An Investigation of Wing Leading-Edge Vortices at Supersonic Speeds. AIAA Paper 83-1816, July 1983.
26. Szodruch, J.: Reynolds Number Influence on Leaside Flow Fields, AIAA Journal, vol 16., no. 12, Dec. 1978, pp. 1306-1309.
27. Chakravarthy, S.; and Ota, D.: Numerical Issues in Computing Inviscid Supersonic Flow Over Conical Delta Wings. AIAA Paper 86-0440, January 1986.
28. Walters, R. W.; and Dwoyer, D. L.: An Efficient Strategy Based on Upwind/Relaxation Schemes for the Euler Equations. AIAA Paper 85-1529-CP, July 1985.



ORIGINAL PAGE IS  
OF POOR QUALITY

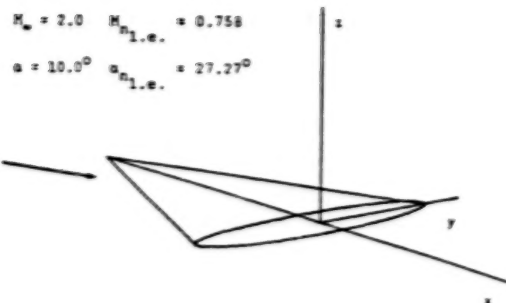


Fig. 1 Elliptic cone,  $y_{LE}/x = \tan(20^\circ)$ ,  
 $z_{CL}/x = \tan(1.5^\circ)$ .

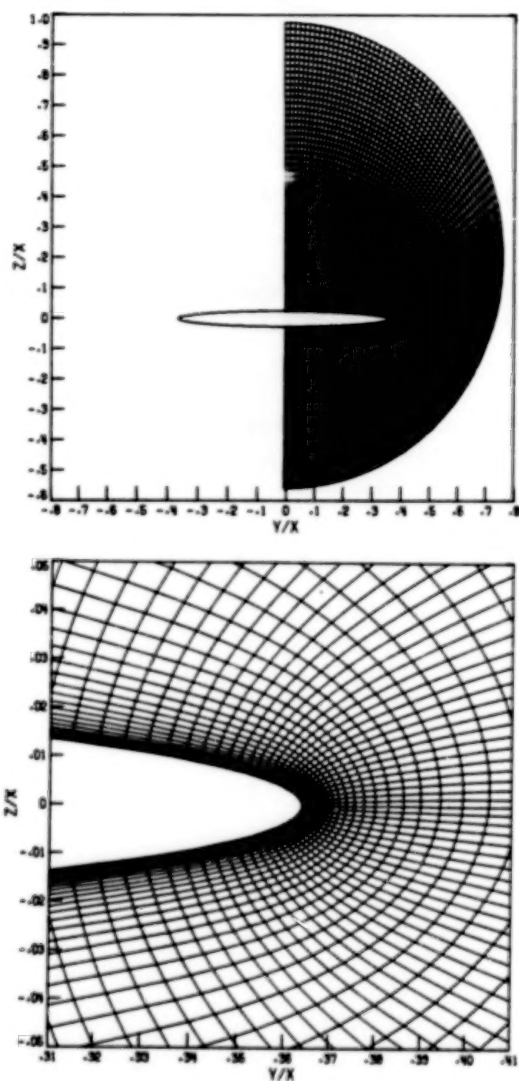


Fig. 2 Fine grid (151 x 65 points).

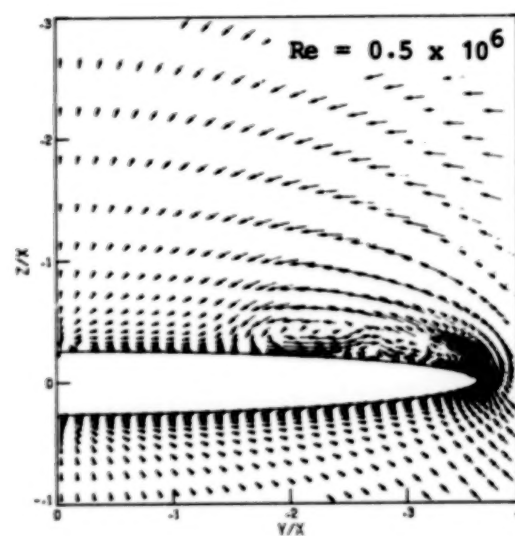
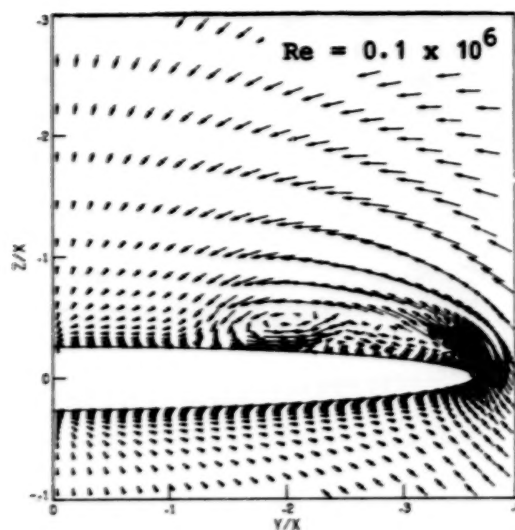


Fig. 3 Crossflow velocity vectors,  
central difference Navier-Stokes.

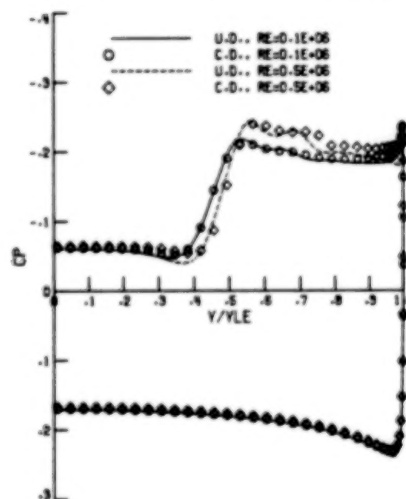


Fig. 4 Pressure coefficient, central  
and upwind difference Navier-  
Stokes.

ORIGINAL PAGE IS  
OF POOR QUALITY

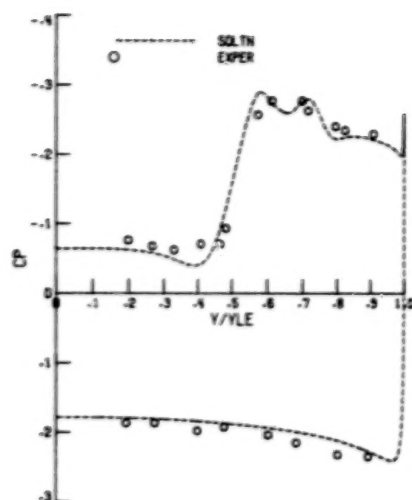


Fig. 5 Pressure coefficient, upwind difference Navier-Stokes versus data of Squire.

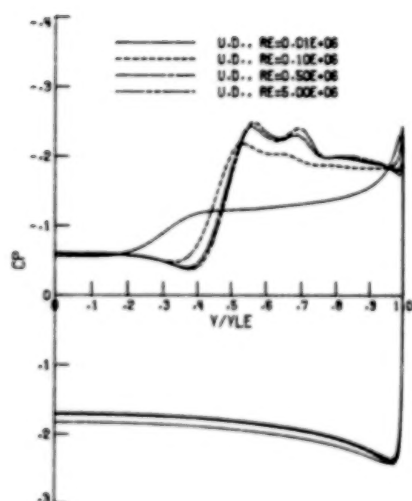


Fig. 6 Pressure coefficient, sensitivity to Reynolds number, upwind difference Navier-Stokes.

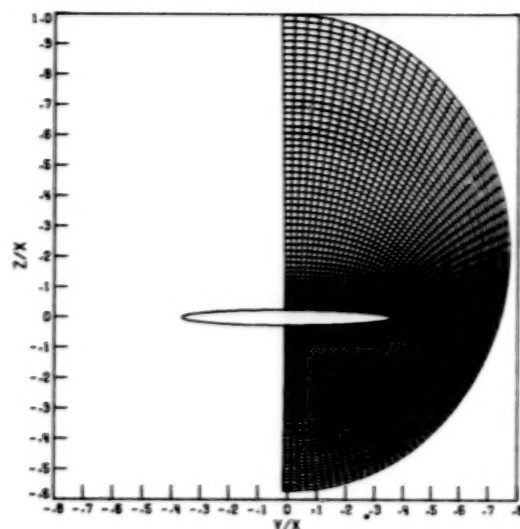


Fig. 7 Coarse grid (75 x 55 points).

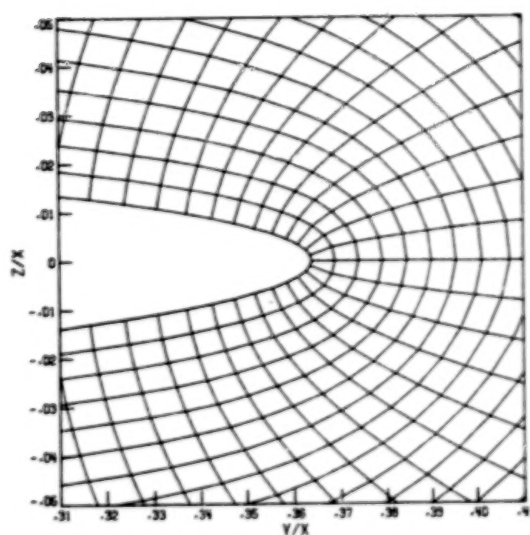


Fig. 8 Crossflow velocity vectors, central difference Euler, coarse grid.

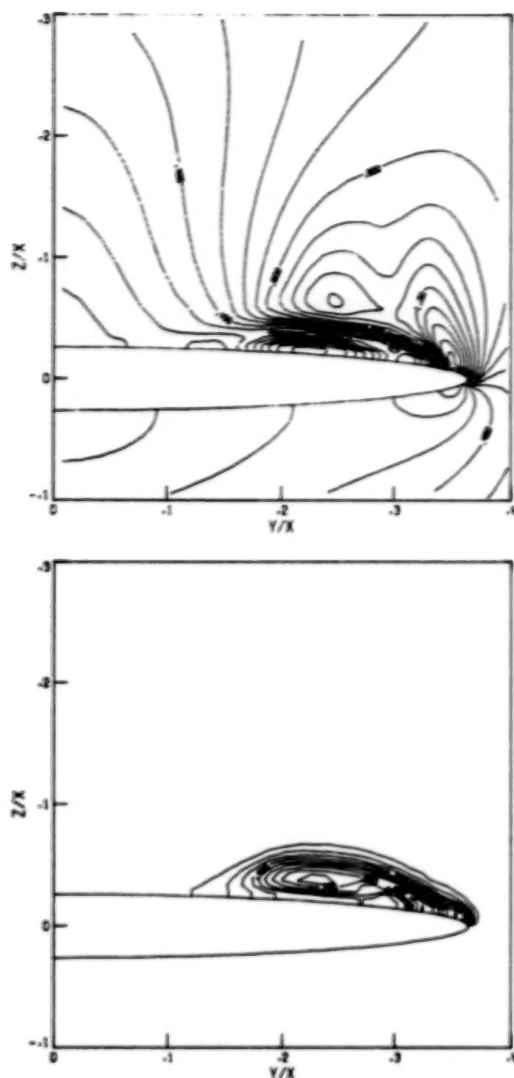


Fig. 9 Crossflow Mach number and entropy contours, coarse grid, central difference Euler.

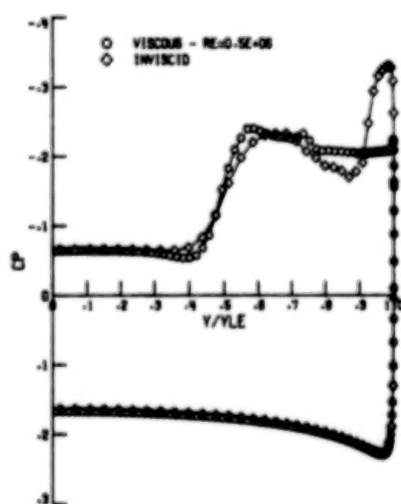


Fig. 10 Pressure coefficient, central difference coarse grid Euler versus fine grid Navier-Stokes.

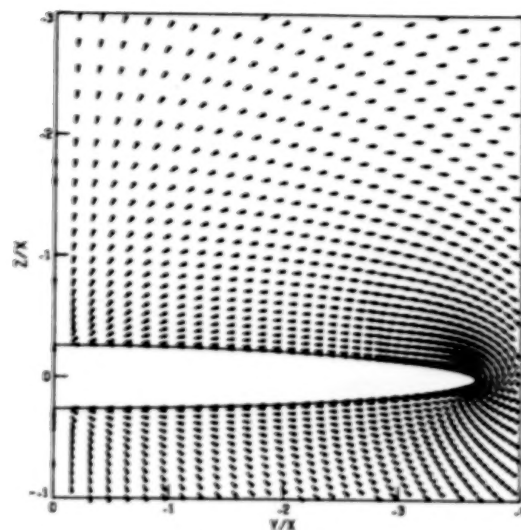


Fig. 11 Crossflow velocity vectors, coarse grid, 1st-order, upwind Euler.

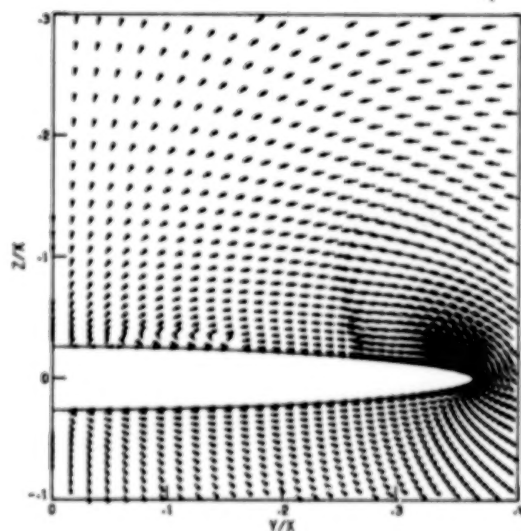


Fig. 12 Crossflow velocity vectors, coarse grid, 2nd-order upwind Euler.

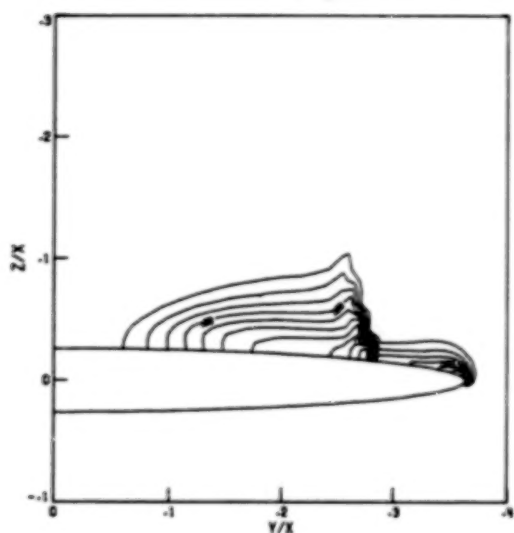
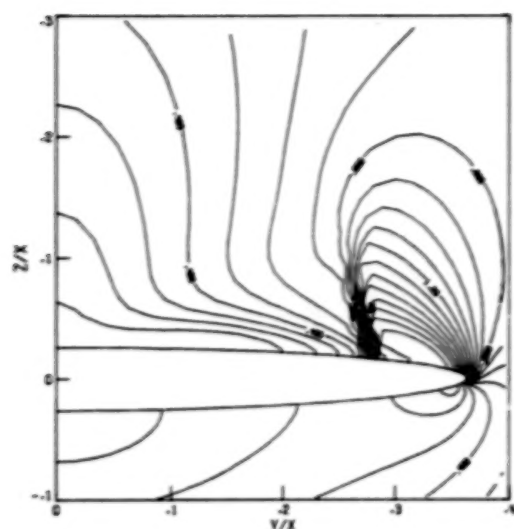


Fig. 13 Crossflow Mach number and entropy contours, coarse grid 2nd-order upwind Euler.

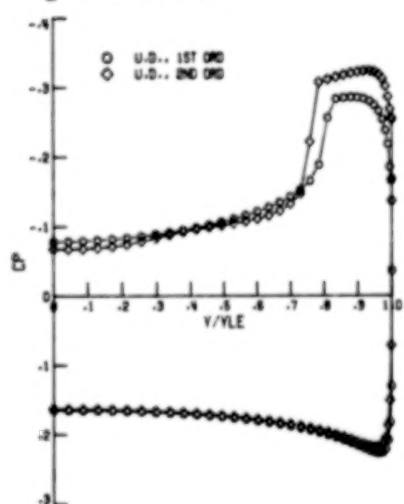


Fig. 14 Pressure coefficient, coarse grid, 1st- and 2nd-order upwind Euler.

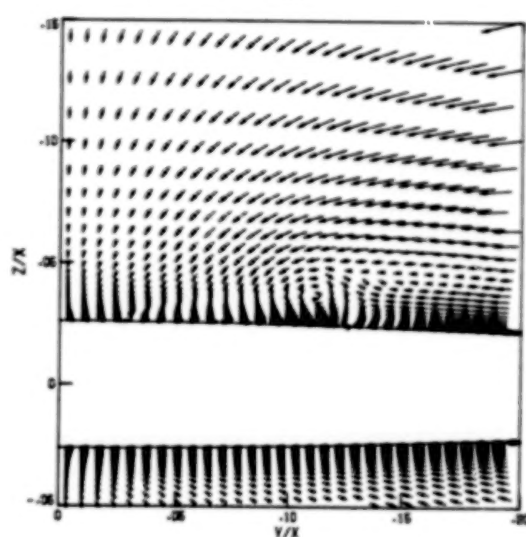
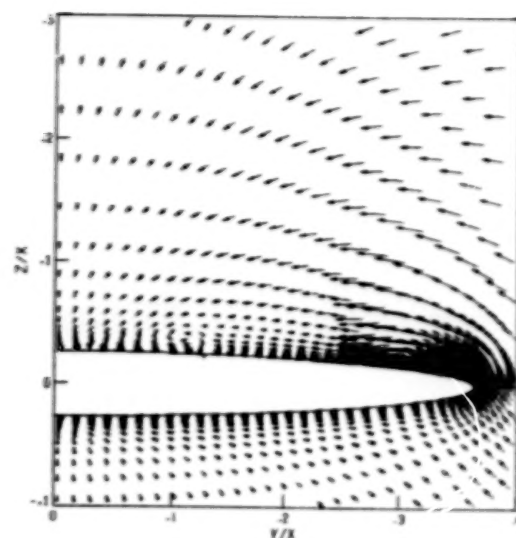


Fig. 15 Crossflow velocity vectors, fine grid central difference Euler.

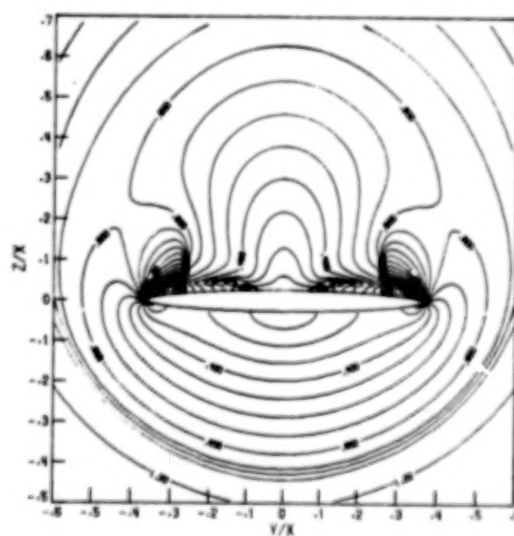


Fig. 16 Crossflow Mach number, fine grid, central difference Euler.

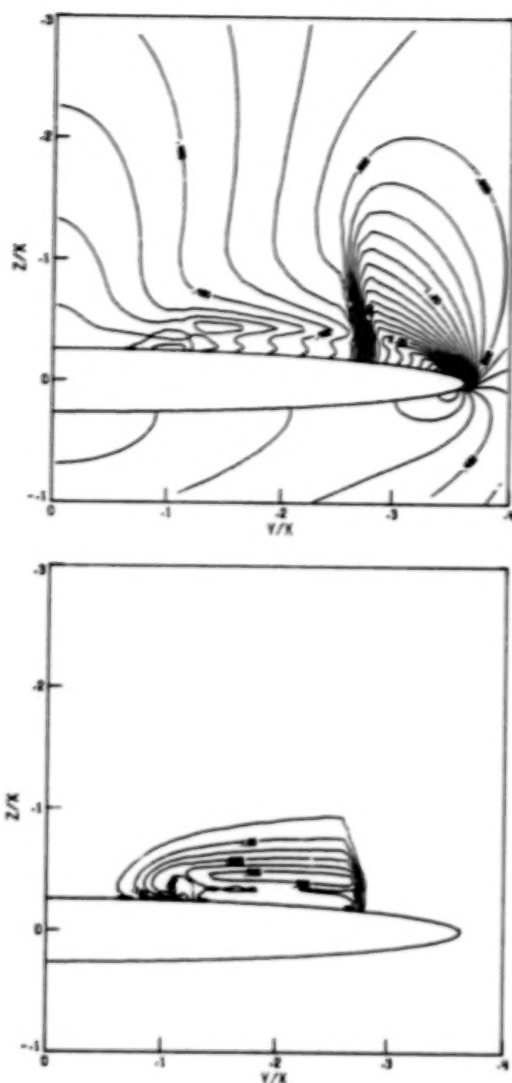


Fig. 17 Crossflow Mach number and entropy contours, fine grid central difference Euler.

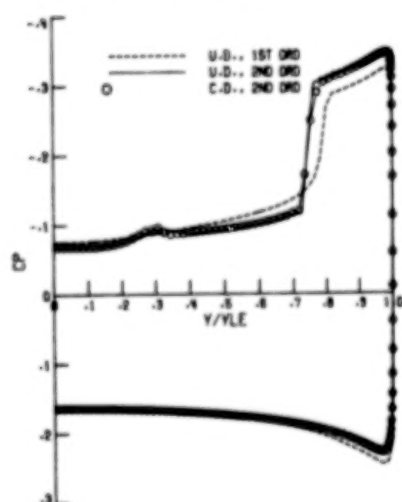


Fig. 18 Pressure coefficient, fine grid, central difference Euler versus upwind difference Euler.

ORIGINAL PAGE IS  
OF POOR QUALITY

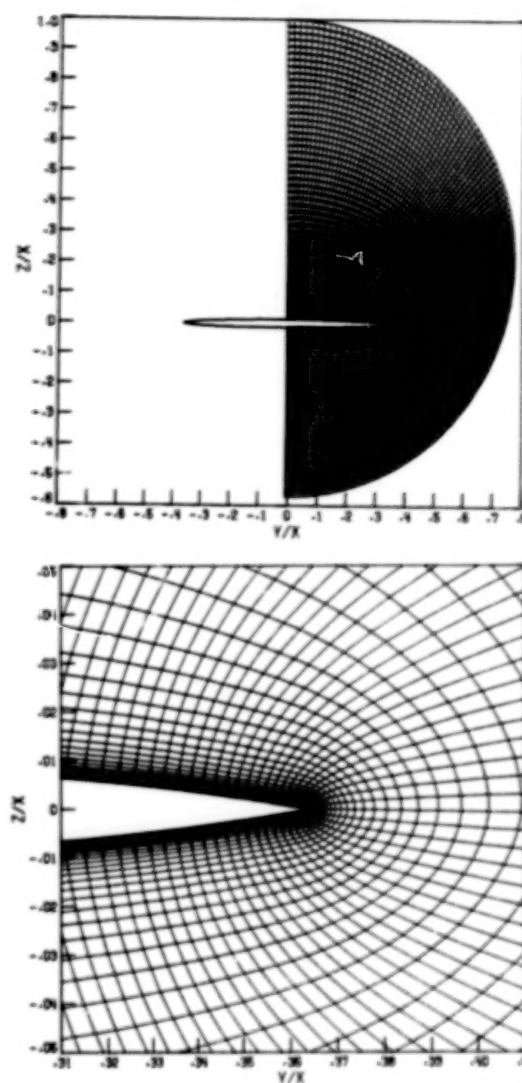


Fig. 19 Fine, sharp tip, grid (151 x 65) points.



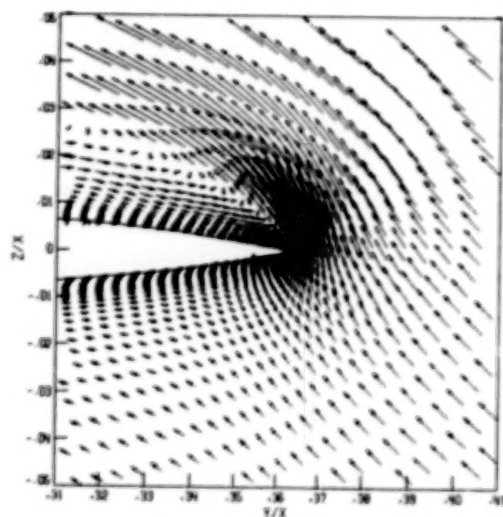
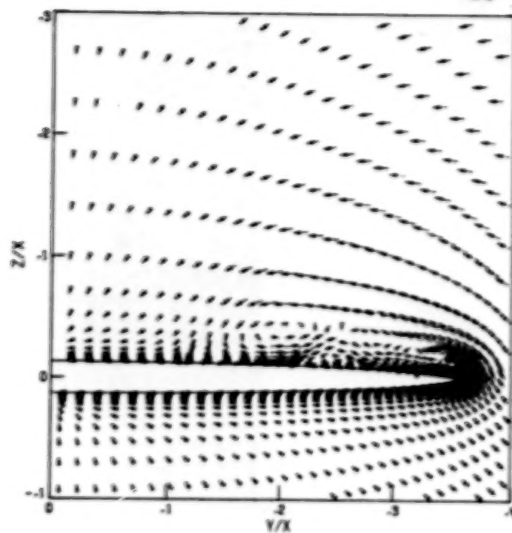


Fig. 20 Crossflow velocity vectors, fine grid, upwind difference Navier-Stokes,  $Re = 0.1 \times 10^6$ .

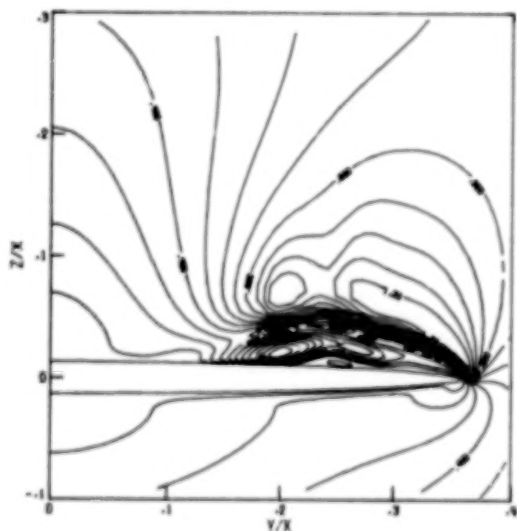


Fig. 21 Crossflow Mach number, fine grid, upwind difference Navier-Stokes,  $Re = 0.1 \times 10^6$ .

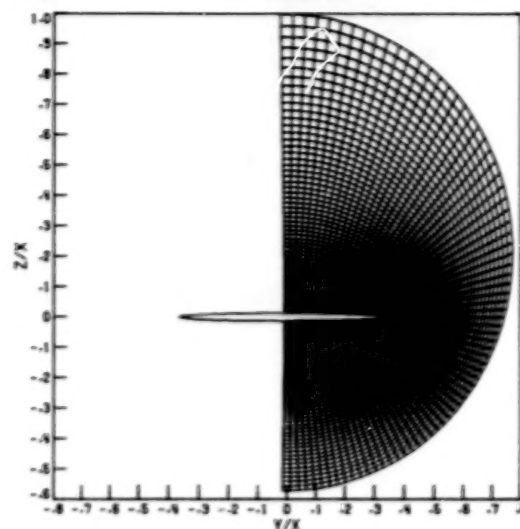


Fig. 22 Coarse, sharp tip, grid (75 x 55 points).

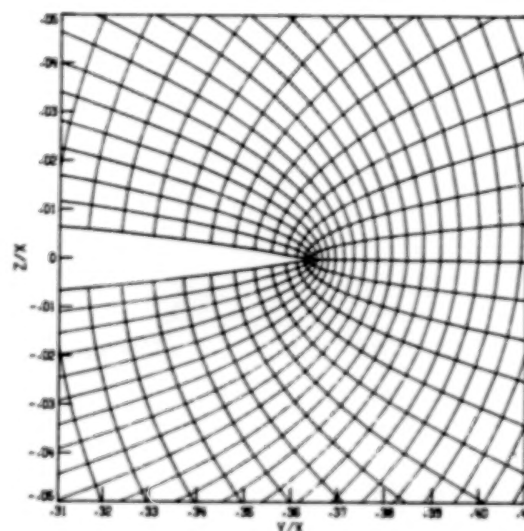


Fig. 23 Crossflow velocity vectors, coarse grid 2nd-order, upwind Euler.

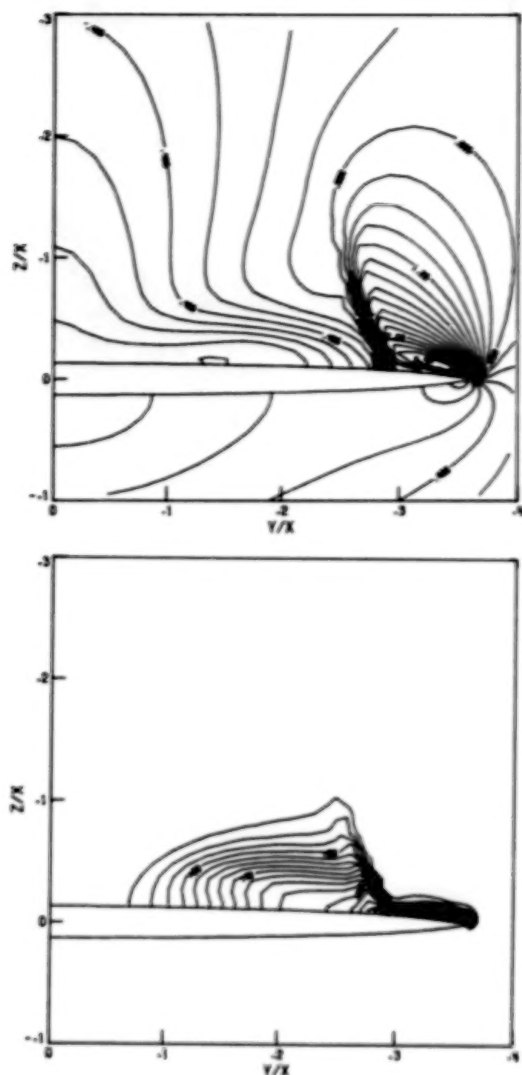


Fig. 24 Crossflow Mach number and entropy contours, coarse grid, 2nd-order, upwind Euler.

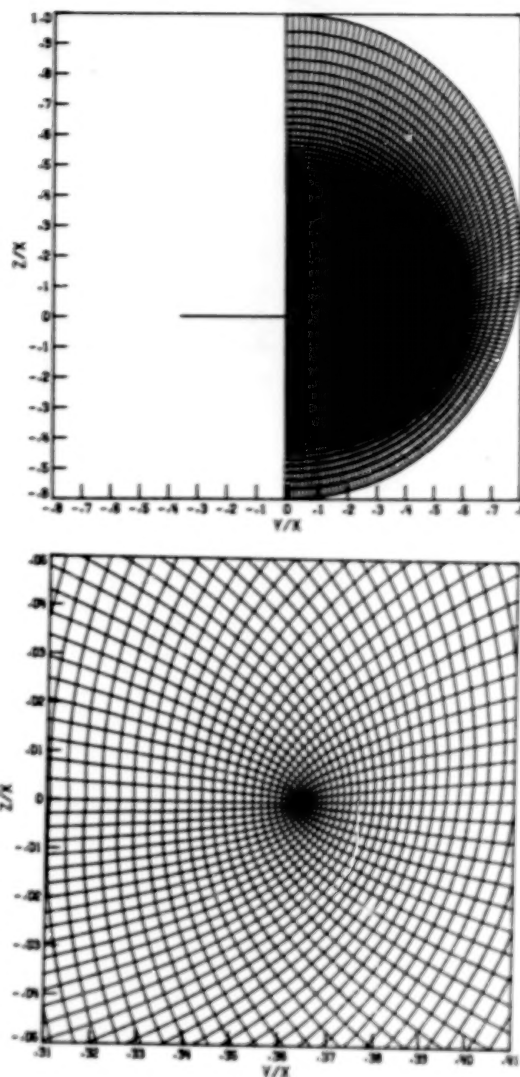


Fig. 26 Zero thickness wing grid (151 x 65 points).

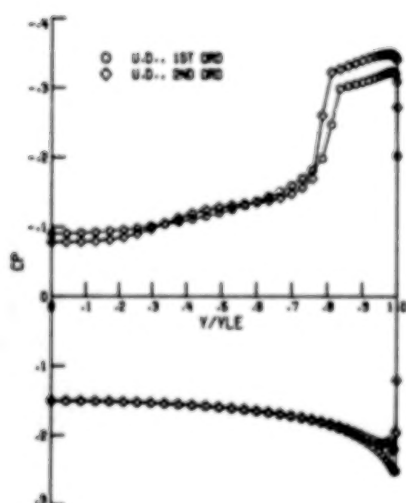


Fig. 25 Pressure coefficient, coarse grid 1st- and 2nd-order upwind Euler.

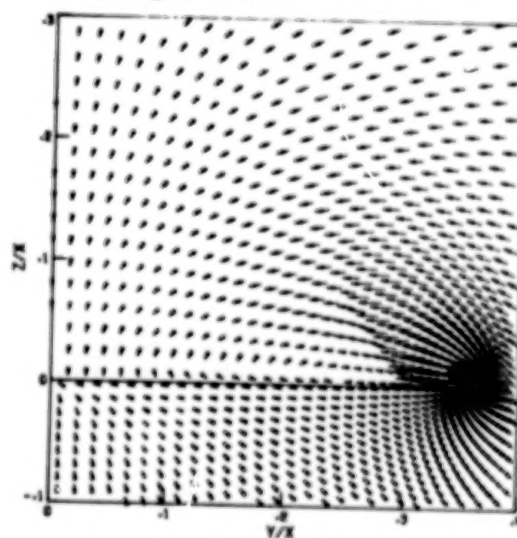


Fig. 27 Crossflow velocity vectors, zero thickness wing, 1st-order upwind Euler.

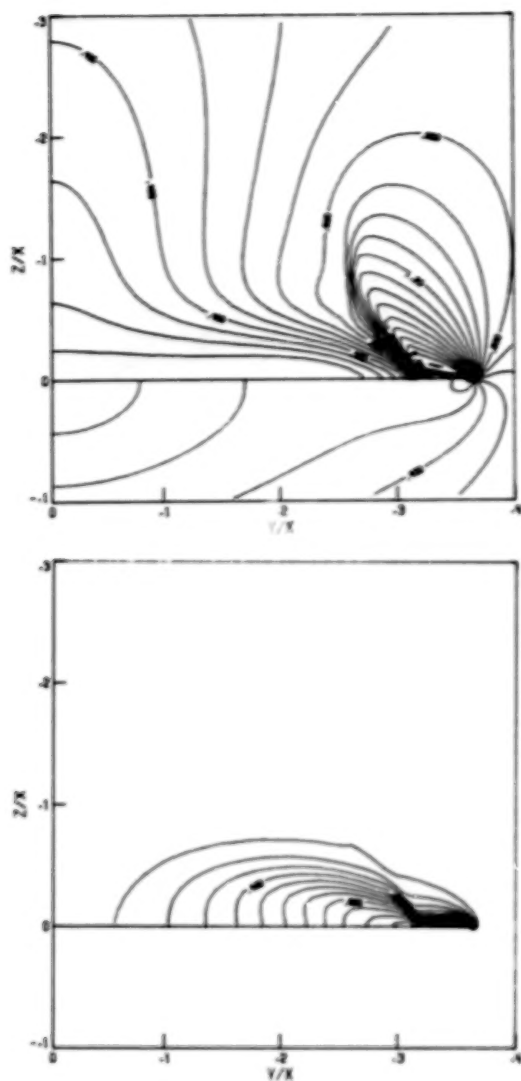


Fig. 28 Crossflow Mach number and entropy contours, zero thickness wing, 1st-order upwind Euler.

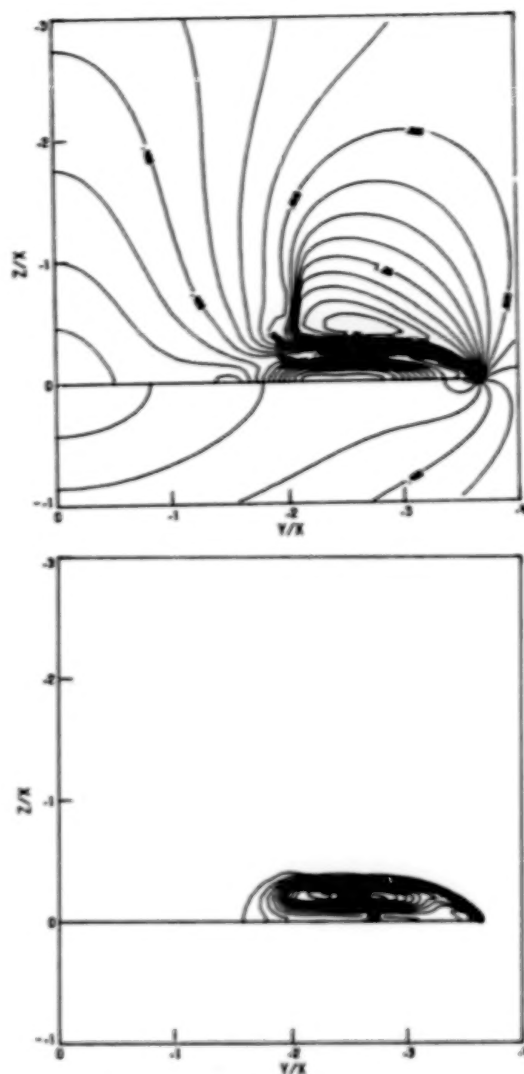


Fig. 30 Crossflow Mach number and entropy contours, zero thickness wing 2nd-order upwind Euler.

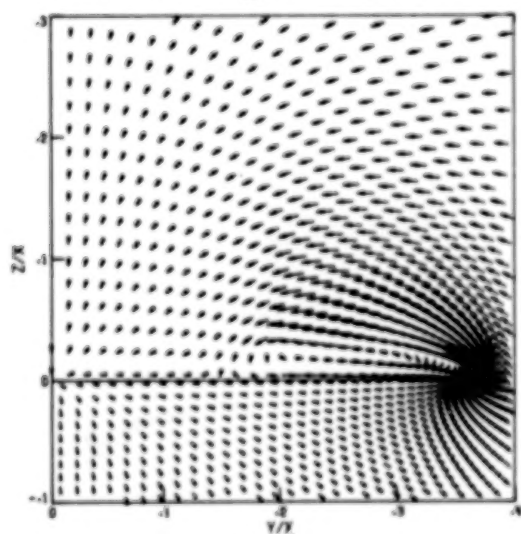


Fig. 29 Crossflow velocity vectors, zero thickness wing, 2nd-order upwind Euler.

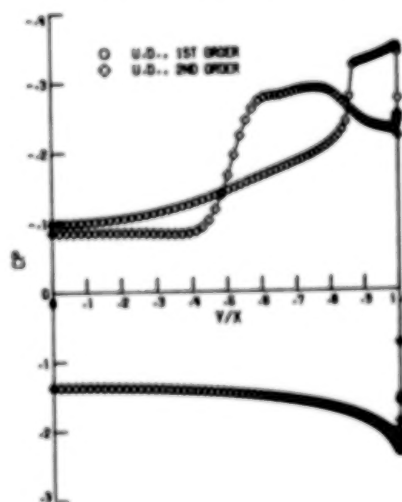


Fig. 31 Pressure coefficient, zero thickness wing, 1st- and 2nd-order upwind Euler.

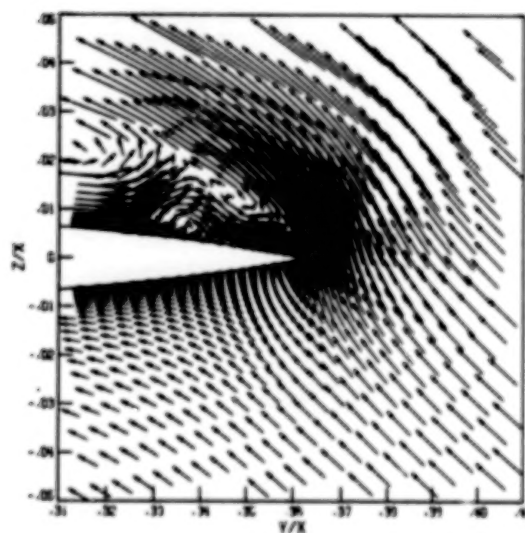
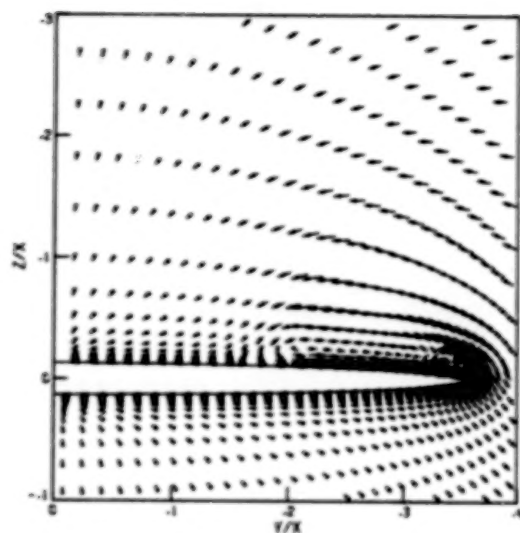


Fig. 32 Crossflow velocity vectors, fine grid, 2nd-order, upwind Euler.

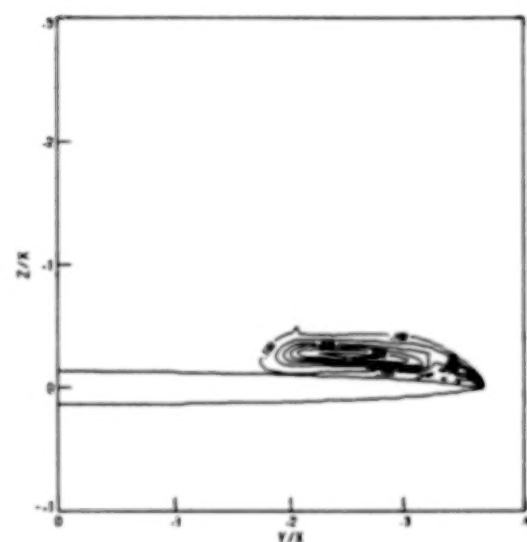
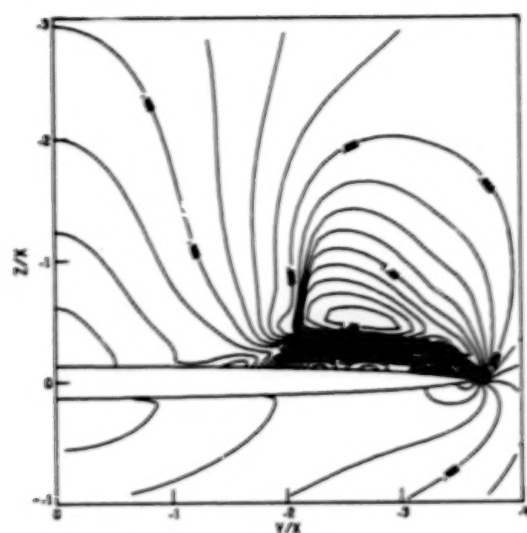


Fig. 33 Crossflow Mach number and entropy contours, fine grid, 2nd-order upwind Euler.

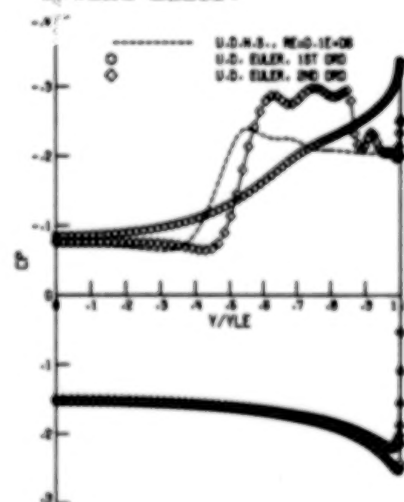


Fig. 34 Pressure coefficient, fine grid, 1st- and 2nd-order upwind Euler versus upwind Navier-Stokes  $Re = 0.1 \times 10^6$ .

Thomas A. Buter and Donald P. Rizzetta  
Air Force Wright Aeronautical Laboratories  
Wright-Patterson Air Force Base, Ohio

## ABSTRACT

Steady solutions about a slender sharp-edged delta wing in a supersonic freestream for moderate and high angles of attack are obtained numerically by time integration of the unsteady compressible three-dimensional laminar Navier-Stokes equations. The main features of the flow, including primary and secondary separation, and vortex position and strength, are adequately simulated in the numerical solutions. Improved resolution of the computational grid in the leading-edge region from a previous solution had considerable effect on the accuracy of the solutions. Good agreement between numerical solutions and experimental data was obtained for two cases. A local timestepping procedure is used to speed convergence by approximately a factor of two.

## NOMENCLATURE

|                 |   |
|-----------------|---|
| A               | attachment line   |
| c               | speed of sound $(\gamma RT)^{1/2}$  |
| $C_p$           | pressure coefficient, $2(P - P_\infty)/\rho U_\infty^2$                       |
| e               | internal specific energy  |
| E               | total specific energy   |
| F, G, H         | vector fluxes   |
| L               | model length, mm  |
| M               | freestream Mach number  |
| P               | pressure  |
| Pr              | Prandtl number, 0.73 for air  |
| $q_x, q_y, q_z$ | components of heat flux vector  |
| R               | gas constant  |
| Re              | Reynolds number, based on the root chord                                      |
| S               | separation line   |
| t               | time  |
| T               | temperature   |
| u, v, w         | Cartesian velocity components in x, y, z directions, respectively             |
| $u_{1,2,3}$     | u, v, w   |
| U               | vector of mass averaged variables   |
| x, y, z         | Cartesian coordinates in axial, normal, and spanwise directions, respectively |
| $\alpha$        | angle of attack   |
| $\beta$         | numerical damping coefficient   |
| $\gamma$        | ratio of specific heats   |
| $\Delta$        | finite difference step size   |



60872 - 2000  
 $\mu$  molecular viscosity coefficient  
 $\xi, \eta, \zeta$  transformed body fitted coordinates  
 $\rho$  density  
 $\tau_{xx}, \tau_{xy}, \tau_{xz},$   
 $\tau_{yy}, \tau_{yz}, \tau_{zz}$  components of viscous stress tensor

#### Subscripts

aw adiabatic wall value  
 LE evaluated at wing leading edge  
 max maximum value  
 min minimum value  
 loc local value  
 T pitot conditions  
 $\infty$  freestream value

#### INTRODUCTION

In recent years, with the advent of the supercomputer, computational aerodynamicists have devoted considerable effort to the solution of increasingly complex three-dimensional separated flows with a view toward the solution of airframe design problems. One of the most interesting and most practical of these is the separated flow field associated with a slender sharp-edged delta wing at angle of attack. Characterized by a pair of leeward spiraling vortices emanating from the separated leading-edge flow this inviscid-viscous flow problem has been computed using several techniques. Higher order panel methods (1-3) have enjoyed some measure of success by modeling the vortex roll-up as a sheet of quadratic doublets. However, this method requires the presence of a vortex and some awareness of its size and position. These restrictions are removed when a 3-D Euler approach is used (4,5). The physical meaning of such solutions is questionable, however, given the apparent dependency on grid resolution (6) and on the use of numerical viscosity. Using a conical flow approximation, Vigneron (7) et al. obtained a Navier-Stokes solution for a delta wing having a subsonic leading edge. With this approach, the location and basic structure of the primary vortex may be accurately computed. However, in cases where the adverse pressure gradient in the outboard region of the wing, induced by the leading-edge expansion, is of sufficient strength to produce a secondary separation, the conical approach becomes inadequate as evidenced by the results of Reference 7. Previous results presented by Rizzetta and Shang (8) illustrated that by using the full 3-D compressible laminar Navier-Stokes equations secondary effects may be accurately resolved numerically. The current investigation adopts this technique for an additional high angle-of-attack case and attempts to enhance the results of the previous study by improving the grid resolution and leading-edge definition. The present study investigates numerically the 75° sweep delta wing studied experimentally by Monnerie and Werle (9) depicted in Figure 1.

# GOVERNING EQUATIONS

The governing equations for this computation are taken to be the unsteady compressible three-dimensional Navier-Stokes equations in mass-averaged variables which may be expressed notationally in the following chain-rule conservative form:

$$\frac{\partial U}{\partial t} + \left( \frac{\partial \xi}{\partial x}, \frac{\partial \xi}{\partial y}, \frac{\partial \xi}{\partial z} \right) \begin{bmatrix} \frac{\partial F}{\partial \xi} \\ \frac{\partial G}{\partial \xi} \\ \frac{\partial H}{\partial \xi} \end{bmatrix} + \left( \frac{\partial \eta}{\partial x}, \frac{\partial \eta}{\partial y}, \frac{\partial \eta}{\partial z} \right) \begin{bmatrix} \frac{\partial F}{\partial \eta} \\ \frac{\partial G}{\partial \eta} \\ \frac{\partial H}{\partial \eta} \end{bmatrix} + \left( \frac{\partial \zeta}{\partial x}, \frac{\partial \zeta}{\partial y}, \frac{\partial \zeta}{\partial z} \right) \begin{bmatrix} \frac{\partial F}{\partial \zeta} \\ \frac{\partial G}{\partial \zeta} \\ \frac{\partial H}{\partial \zeta} \end{bmatrix} = 0 \quad (1)$$

Here  $x, y, z$  are Cartesian coordinates in the axial, normal and spanwise directions respectively and  $\xi, \eta, \zeta$  are the corresponding transformed coordinates in a body-oriented system and

$$U = \begin{bmatrix} \rho \\ \rho u \\ \rho v \\ \rho w \\ \rho E \end{bmatrix} \quad (2)$$

$$F = \begin{bmatrix} \rho u \\ \rho u^2 + \tau_{xx} \\ \rho uv + \tau_{xy} \\ \rho uw + \tau_{xz} \\ (\rho E + \tau_{xx})u + \tau_{xy}v + \tau_{xz}w - q_x \end{bmatrix} \quad (3)$$

$$G = \begin{bmatrix} \rho v \\ \rho v u + \tau_{xy} \\ \rho v^2 + \tau_{yy} \\ \rho v w + \tau_{yz} \\ (\rho E + \tau_{yy}) v + \tau_{yx} u + \tau_{yz} w - q_y \end{bmatrix} \quad (4)$$

$$H = \begin{bmatrix} \rho w \\ \rho w u + \tau_{wx} \\ \rho w v + \tau_{wy} \\ \rho w^2 + \tau_{ww} \\ (\rho E + \tau_{zz}) w + \tau_{zx} u + \tau_{zy} v - q_z \end{bmatrix} \quad (5)$$

$$\tau_{xy} = \tau_{yx} = -\mu \left( \frac{\partial u}{\partial y} + \frac{\partial v}{\partial x} \right) \quad (6)$$

$$\tau_{xz} = \tau_{zx} = -\mu \left( \frac{\partial u}{\partial z} + \frac{\partial w}{\partial x} \right) \quad (7)$$

$$\tau_{yz} = \tau_{zy} = -\mu \left( \frac{\partial v}{\partial z} + \frac{\partial w}{\partial y} \right) \quad (8)$$

$$q_x = \frac{\mu \gamma}{Pr} \left( \frac{\partial \theta}{\partial x} \right) \quad (9)$$

$$q_y = \frac{\mu \gamma}{Pr} \left( \frac{\partial \theta}{\partial y} \right) \quad (10)$$

$$q_z = \frac{\mu \gamma}{Pr} \left( \frac{\partial \theta}{\partial z} \right) \quad (11)$$

$$E = e + (u^2 + v^2 + w^2)/2 \quad (12)$$

The Cartesian velocity components are given by  $u$ ,  $v$  and  $w$ ,  $\rho$  is the density,  $E$  the total energy per unit mass, and  $e$  the specific internal energy. Completion of this system is provided by the perfect gas law:

$$P = \rho RT \quad (13)$$

and the Sutherland law for the molecular viscosity coefficient  $\mu$ . Freestream values are specified as boundary conditions for all dependent variables at the upstream, outboard, upper and lower computational boundaries, i.e.,  $U = U_\infty$ . At the wing midspan a plane of symmetry is imposed which results in:

$$\frac{\partial \rho}{\partial \zeta} = \frac{\partial \rho u}{\partial \zeta} = \frac{\partial \rho v}{\partial \zeta} = \frac{\partial \rho E}{\partial \zeta} = w = 0 \text{ along } \zeta = 0 \quad (14)$$

On the upper and lower wing surface

$$u = v = w = 0$$

$$T = T_w$$

$$\frac{\partial P}{\partial \hat{n}} = \frac{\partial w}{\partial \hat{n}}, \text{ where } \hat{n} \text{ is the unit normal to the surface} \quad (15)$$

Because only computations corresponding to supersonic freestream conditions were considered, no formal mathematical downstream boundary conditions were needed. However, due to the requirements of the numerical algorithm used, values of the dependent variables at the downstream computational boundary are obtained by second-order extrapolation from the interior domain.

## NUMERICAL PROCEDURE

The laminar computation performed in Reference 8 for  $M=1.95$  and  $\alpha=10^\circ$  was repeated in the present study. Since it was of interest to compute a high angle of attack, a  $20^\circ$  case was chosen for the same Mach number. This necessitated increasing the size of the computational domain due to the expansion of the physical region of interest. The grid size was increased from  $20 \times 64 \times 40$  to  $21 \times 70 \times 50$  in the  $\xi, \eta, \zeta$  directions and was algebraically generated in a fashion similar (Figure 2) with two notable exceptions. In the work of Reference 8 the plane of symmetry was straddled to obtain a second-order centered difference implementation of the symmetry condition. While this technique was successful, the grid in this region was rather coarse. For the present study points were exponentially clustered near the plane of symmetry (Figure 2) to improve resolution in that region. This becomes particularly critical for the  $20^\circ$  case because the gradients near the plane of symmetry are greater due to the growth of the primary vortex and its inboard migration. The second modification to the grid structure was made at the wing tip, where resolution was increased and hence it was expected that the expansion about the leading edge might be more accurately resolved. This improvement, however, was gained at the expense of decreasing the time step (Table 1) due to the decreased step size in the  $y$  direction. In order to alleviate some of this degradation of efficiency, the lower surface  $\eta$  lines were bent down and away from the surface near the tip, thereby increasing the size of  $\Delta y_{\min}$  (Figure 3).

For the purpose of improved vortex resolution the current grid system employs an additional 6  $\eta$ -grid lines (yielding a total of 46) on and above the wing surface and an additional 5  $\zeta$ -grid lines (total - 29) inboard of the wing leading edge. Further, 5  $\zeta$ -grid lines were added to the outboard field region to resolve the expansion about the leading edge. An additional  $\eta$ - $\zeta$  plane was added at  $\frac{x}{L} = 0.05$  to improve the resolution near the apex.

This grid, although sized for the  $\alpha=20^\circ$  case, was used for both the  $\alpha=10^\circ$  and  $20^\circ$  cases to determine if for the present  $\alpha=10^\circ$  case a higher degree of accuracy might be obtained than its predecessor and for the purpose of uniformity between the current solutions.

Steady-state solutions to Equation 1 were generated using the time-dependent explicit unsplit two-step predictor-corrector finite-difference algorithm due to MacCormack (10) which has evolved as a reliable technique for numerical solution of a wide variety of fluid dynamic problems. As part of this algorithm, a commonly employed fourth-order pressure damping term (11) was used to suppress numerical oscillations in regions with large gradients in the dependent variables. The form of this term is given as

$$\beta \Delta t \sum_{j=1}^3 (\Delta v_j)^3 \frac{\partial}{\partial v_j} \left[ \frac{\partial U}{\partial v_j} \left| \frac{\partial^2 P}{\partial v_j^2} \right| \frac{|u_j + c|}{P} \right] \text{ where } v_{1,2,3} = \xi, \eta, \zeta \quad (16)$$

which is then added to the new value of  $U$  at each time step. In the present study, as in the previous effort, a damping coefficient of  $\beta = 2.0$  was used.



Freestream values were used as the initial conditions save for the interior boundary where surface conditions were applied. In order to remove the initial transients, the numerical flow fields were allowed to evolve for 100 time steps in the time accurate mode with  $\Delta t$  chosen such that the maximum Courant Fredricks Lewy (CFL) number was 0.5. Subsequently, the CFL number was increased to 0.8 and the computation was allowed to progress to steady state in a local timestepping fashion, where each grid point advances at its own rate ( $\Delta t_{loc}$  corresponding to a CFL number of 0.8) for a given iteration. This procedure has the advantage of advancing the solution to a steady-state value much more expeditiously since the more coarse regions of the physical domain are able to advance more quickly than in a time accurate mode. This modification resulted in the appearance of the primary and secondary vortex structures in the numerical solution much earlier than in the work of reference 8.

The computations were made on a Cray 1-S computer using a vectorized solver (12) written specifically for the Cray 1 computer. The solver advances the solution from one time step to the next in  $\eta$ - $\zeta$  planes by marching in the  $\xi$ -direction, thus minimizing the data flow to and from central memory. Using the previously defined computational grid, approximately  $1.124 \times 10^6$  decimal words of storage were required. A data processing rate of  $6.9 \times 10^{-5}$  CPU seconds per time step per grid point was achieved where vectorization occurred in the  $\zeta$ -direction, with a vector length of 50.

## RESULTS

Numerical solutions were generated for the flow about the delta wing illustrated in Figure 1 at a Mach number of 1.95 (0.5 normal to the leading edge) for  $10^\circ$  and  $20^\circ$  angles of attack. The freestream conditions correspond to those of the experimental work of Monnerie and Werle<sup>9</sup>, the specifics of which are given in the table on Figure 1. A comparison of pitot pressure contours from reference 8 to the current  $\alpha = 10^\circ$  solution is given in Figure 4. Both solutions are a marked improvement over the results of reference 7 which employed a conical approximation and did not capture the secondary separation. However, while the shape and location of the primary and secondary vortices are roughly the same, the pitot pressure levels on the wing upper surface are not. The solution of reference 8 shows less evidence of pitot pressure loss in the primary vortex region as shown by the large disparity in the  $P_T/P_\infty = 0.7$  pressure levels. This may be attributed to the improved resolution in the leading-edge tip region which leads to a more accurate computation of the leading-edge expansion, hence the improved correlation with experiment as shown in Figure 5. The expanded grid size in the  $\eta$  and  $\zeta$ -directions may also account for some of this improvement as the outer boundaries are much farther from the wing. In addition, the increased resolution of the apex region by the addition of the  $\frac{X}{L} = 0.05$  station improves the modeling of the flow being entrained into the inviscid core.

The improved resolution in the  $\eta$  or  $y$  direction accounts for the increased clarity of the upper surface "oil flow" patterns shown in Figure 6. While the position of the primary and secondary lines of separation ( $S_1$  and  $S_2$  respectively) and reattachment ( $A_1$ ,  $A_2$ ) are nearly the same, their sharpness, particularly near the trailing edge, is improved. This improvement is attributed to a second-order treatment of the downstream boundary condition. However, in spite of these differences, the aerodynamic loading perceived on the wing is similar as shown in the  $C_p$  distributions given in Figure 7. Here the suction peaks associated with the primary and secondary vortices are clearly in evidence and are similarly located.

The development of the cross-plane velocity with  $X$  is illustrated in Figures 8 and 9 for  $10^\circ$  and  $20^\circ$  respectively. Here the growth of the primary and secondary vortices and their inboard migration with angle of attack are evident and the non-conical nature of the flow field near the apex is revealed. Interesting to note is the fact that the secondary vortex originates at approximately  $\frac{X}{L} = 0.3$  for both cases. These same features are also evident

in the upper surface "oil flow" pattern given in Figure 10. While the flow is non-conical in the apex region, analysis of Figures 7-10 indicates that for the majority of the planform the flow is fairly conical.

The effect of angle of attack on loading is emphasized in the comparison of pressure coefficient depicted in Figure 11. The expected increase in loading and the inboard shift of vortex-associated surface pressure loss with  $\alpha$  is evident. From analysis of the pitot pressure contours in Figure 12 one can observe the growth of the secondary vortex and its displacement effect on the primary. The increased circumferential velocity in the primary vortex with angle of attack induces the observed pressure loss in the vortex core. Comparison of the  $20^\circ$  solution to the experiment of Monnerie and Werle in Figure 13 illustrates the remarkable accuracy of the laminar Navier-Stokes computation in spite of the rather high Reynolds number of the experiment.

## CONCLUSIONS AND DISCUSSIONS

Steady laminar solutions of the full 3-dimensional Navier-Stokes equations have been generated for the supersonic ( $M = 1.95$ ) flow over a  $75^\circ$  sweep sharp-edged delta wing at  $10^\circ$  and  $20^\circ$  angles of attack. Comparison with experiment and with the Navier-Stokes solution of reference 8 shows the following:

1. For both cases, the flow field solution correlates well with experiment. The position and strength of the primary and secondary vortices are accurately predicted. This leads one to believe that a laminar Navier-Stokes solution to the leading-edge vortex problem is adequate for obtaining pitot pressure, particularly for configurations with a Reynolds number less than  $1 \times 10^6$  such as in the present study, at least until an adequate turbulence model is developed for vortical flows.

2. An accurate geometrical modeling of the leading edge and considerable resolution of the tip region appear critical to the accurate computation of the leading-edge expansion. The agreement obtained in the present study is attributed in part to these two modifications to the grid of reference 8. A more accurate treatment of the downstream boundary condition also accounts for the improved solution in the trailing-edge region. In addition, the expansion of the computational domain in the  $\eta$  and  $\zeta$  directions probably resulted in some improvement in the  $10^\circ$  solution.

3. Because secondary separation develops axially as well as radially, methods employing a conical assumption will not adequately resolve a large portion of the flow field. In addition, resolution of the apex region is critical due to its highly non-conical structure.

4. The use of a local timestepping procedure increased the convergence rate by roughly a factor of two. It is estimated that each solution of the laminar 3-dimensional compressible Navier-Stokes equations presented herein required approximately 2 hours of CPU time on a CRAY 1-S computer to reach steady state based on a four order of magnitude reduction in L2NORM for all dependent variables.

#### REFERENCES

1. Weber, J.A., Brune, G.W., Johnson, F.T., Lu, P., and Rubbert, P.E., "Three-Dimensional Solution of Flows over Wings with Leading-Edge Vortex Separation," AIAA Journal, Vol. 14, April 1976, pp 519-525.
2. Luckring, J.M., Schoonover, W.E., Jr., and Frink, N.T., "Recent Advances in Applying Free Vortex Sheet Theory for the Estimation of Vortex Flow Aerodynamics," AIAA Paper 82-0095, Jan. 1982.
3. Hoeijmakers, H.W.M., and Rizzi A., "Vortex Fitted Potential Solution Compared with Vortex-Captured Euler Solution for Delta Wing with Leading-Edge Vortex Separation," AIAA Paper 84-2144, 1984.
4. Erikson, L.E., and Rizzi, A., "Computation of Vortex Flow Around Wings Using the Euler Equations," Proceedings of the Fourth GAMM Conference on Numerical Methods in Fluid Mechanics, Notes on Numerical Fluid Mechanics, Vol. 5, 1981, pp 137-148.
5. Hitzel, S.M., and Schmidt, W., "Slender Wings with Leading-Edge Vortex Separation - A Challenge for Panel-Methods and Euler-Codes," AIAA Paper 83-0562, Jan. 1983.
6. Newsome, R.W., "A Comparison of Euler and Navier-Stokes Solutions For Supersonic Flow Over a Conical Delta Wing," AIAA Paper 85-0111, January 14-17, 1985.

7. Vigneron, Y.C., Rakich, J.V., and Tannehill, J.C., "Calculation of Supersonic Viscous Flow over Delta Wings with Sharp Subsonic Leading Edges," AIAA Paper 78-1137, July 1978.
8. Rizzetta, D.P., and Shang, J.S., "Numerical Simulation of Leading-Edge Vortex Flows," AIAA Paper No. 84-1544, July 1984.
9. Monnerie, B., and Werle, H., "Study of Supersonic and Hypersonic Flow About a Slender Wing at an Angle of Attack," AGARD CP-30, May 1968 (in French).
10. MacCormack, R.W., "The Effect of Viscosity in Hypervelocity Impact Cratering," AIAA Paper 69-354, Apr-May 1969.
11. MacCormack, R.W., and Baldwin, B.S., "A Numerical Method for Solving the Navier-Stokes Equations with Application to Shock-Boundary Layer Interactions," AIAA Paper 75-1, Jan. 1975.
12. Shang, J.S., Buning, P.G., Hankey, W.L., and Wirth, M.C., "Performance of a Vectorized Three-Dimensional Navier-Stokes Code on a CRAY-1 Computer," AIAA Journal, Vol. 18, Sep. 1980, pp 1073-1079.

TABLE I COMPUTATIONAL PARAMETERS

| M    | $\alpha$     | $\Delta$                | $y_{\min}/z_{LE}$ | $y_{\max}/z_{LE}$ | $z_{\max}/z_{LE}$ | Iteration |
|------|--------------|-------------------------|-------------------|-------------------|-------------------|-----------|
| 1.95 | $10^\circ$ * | $9.7971 \times 10^{-1}$ | -3.0              | 3.25              | 2.75              | 6000      |
| 1.95 | $10^\circ$   | $7.973 \times 10^{-1}$  | -3.7              | 4.6               | 3.5               | 2500      |
| 1.95 | $20^\circ$   | $7.973 \times 10^{-1}$  | -3.7              | 4.6               | 3.5               | 2500      |

\* Reference 8

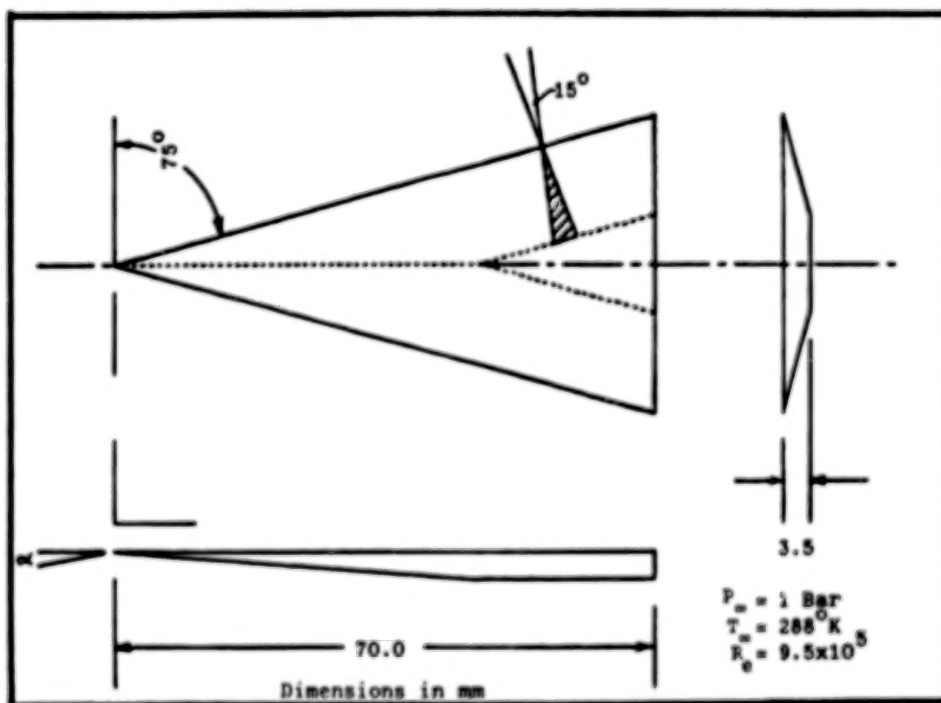


Figure 1. Delta wing geometry.



$$X/L=1.0$$

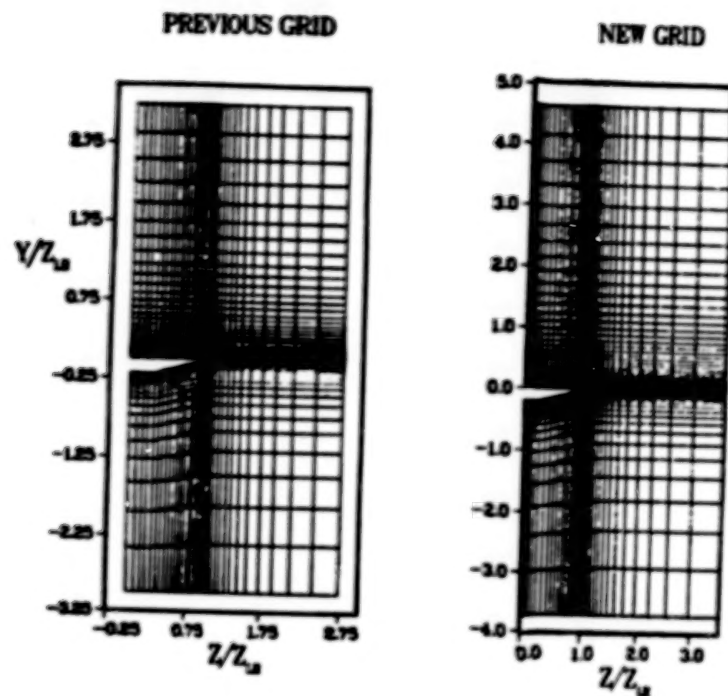


Figure 2. Comparison of Y-Z grid structure.

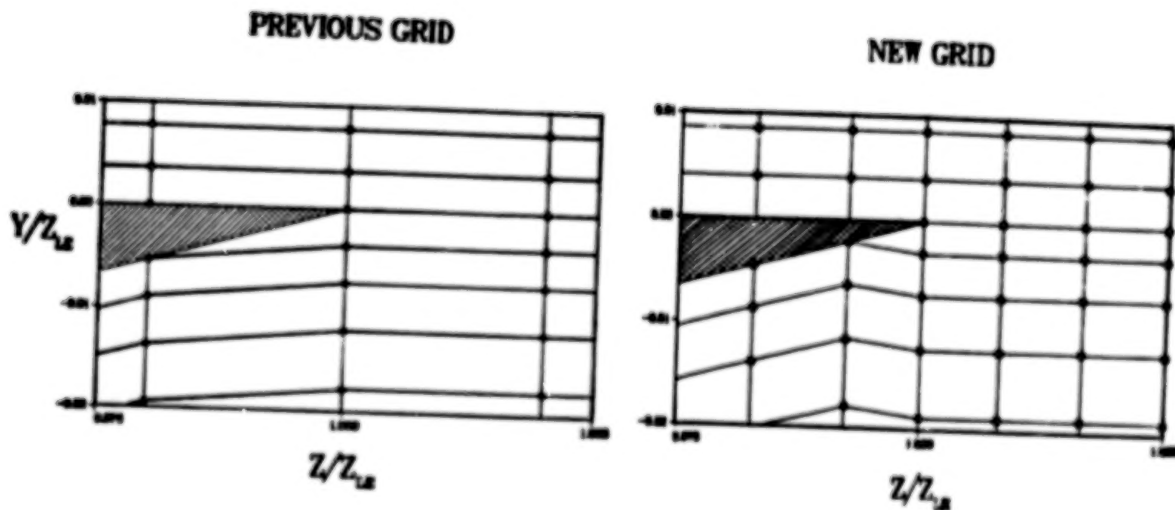


Figure 3. Comparison of Y-Z grid structure in tip region.

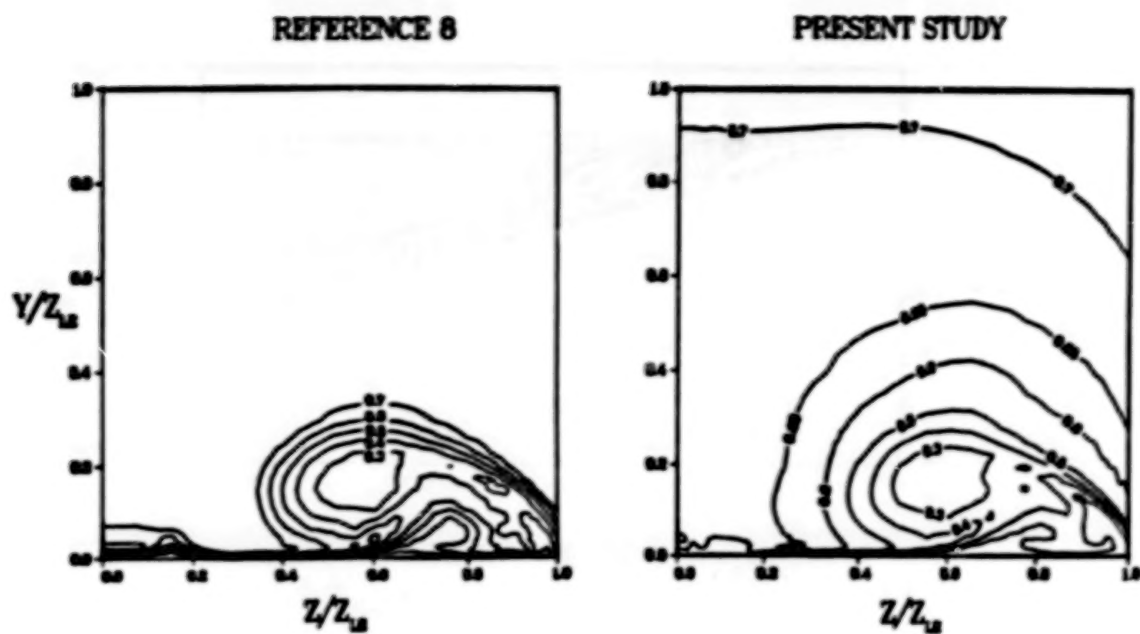


Figure 4. Comparison of Pitot pressure,  $X/L = 0.8$ .

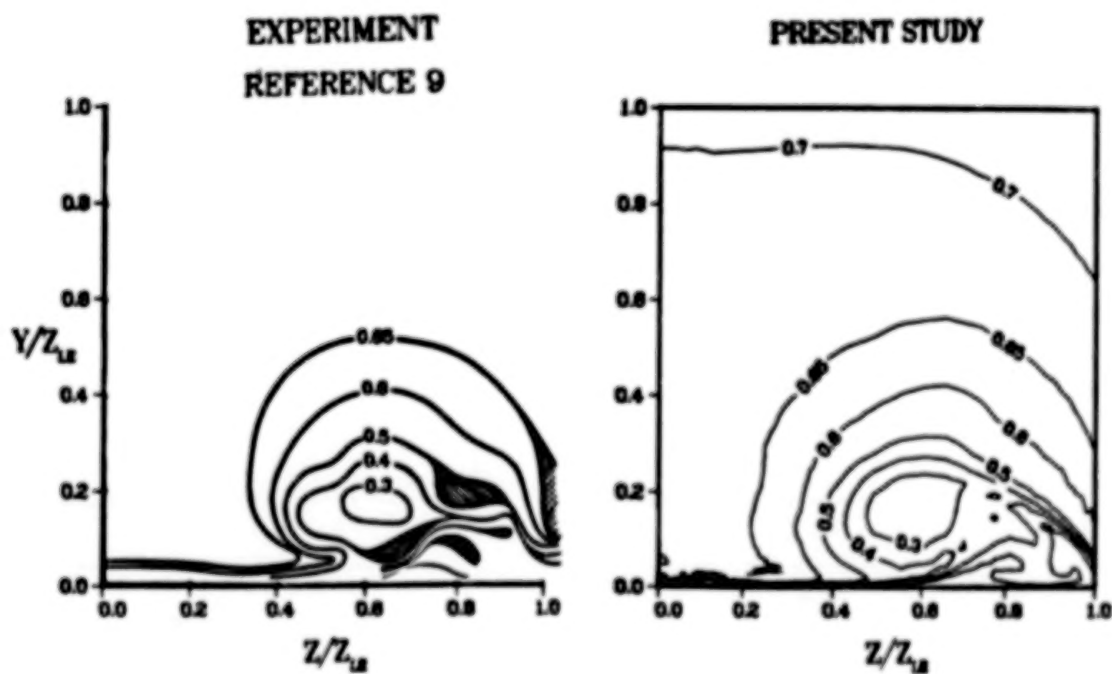


Figure 5. Comparison of Pitot pressure,  $X/L = 0.8$ .

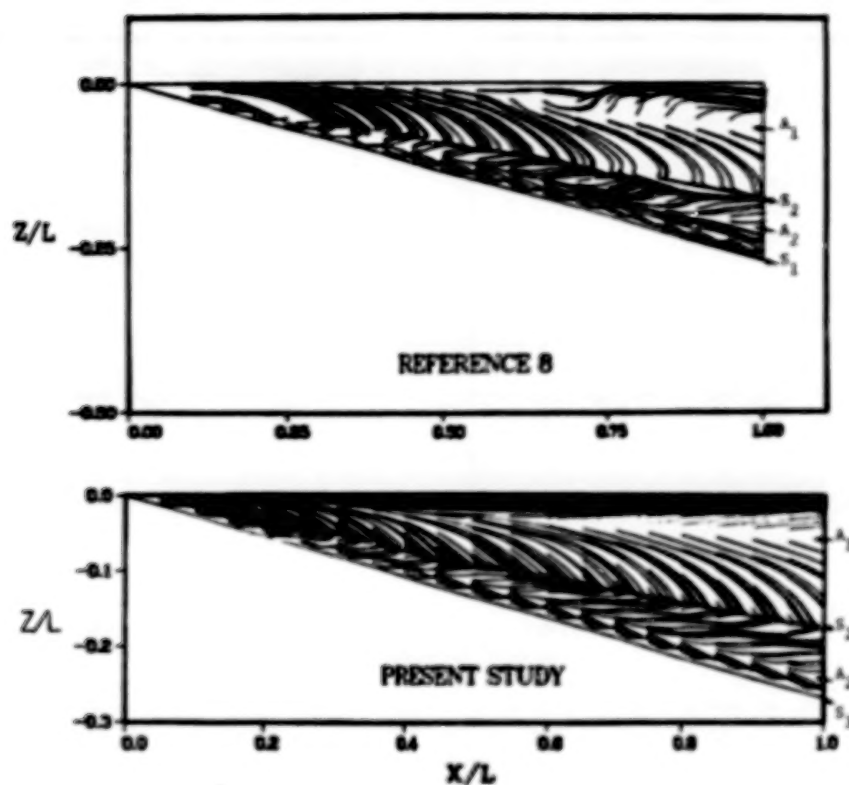


Figure 6. Upper surface oil flow pattern,  $\alpha = 10^\circ$ .

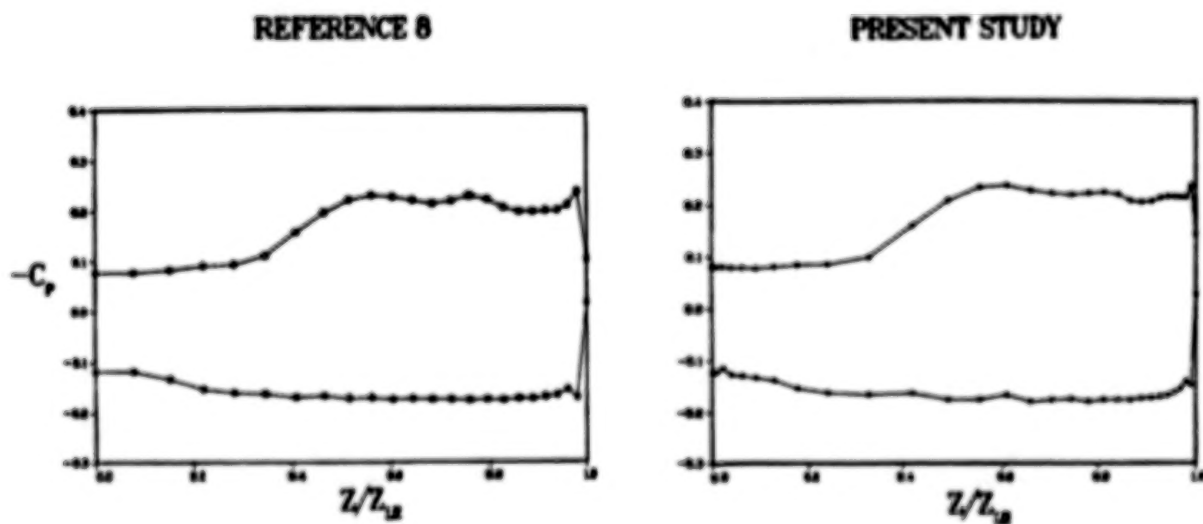


Figure 7. Spanwise pressure distribution,  $\alpha = 10^\circ$   $X/L = 0.8$ .

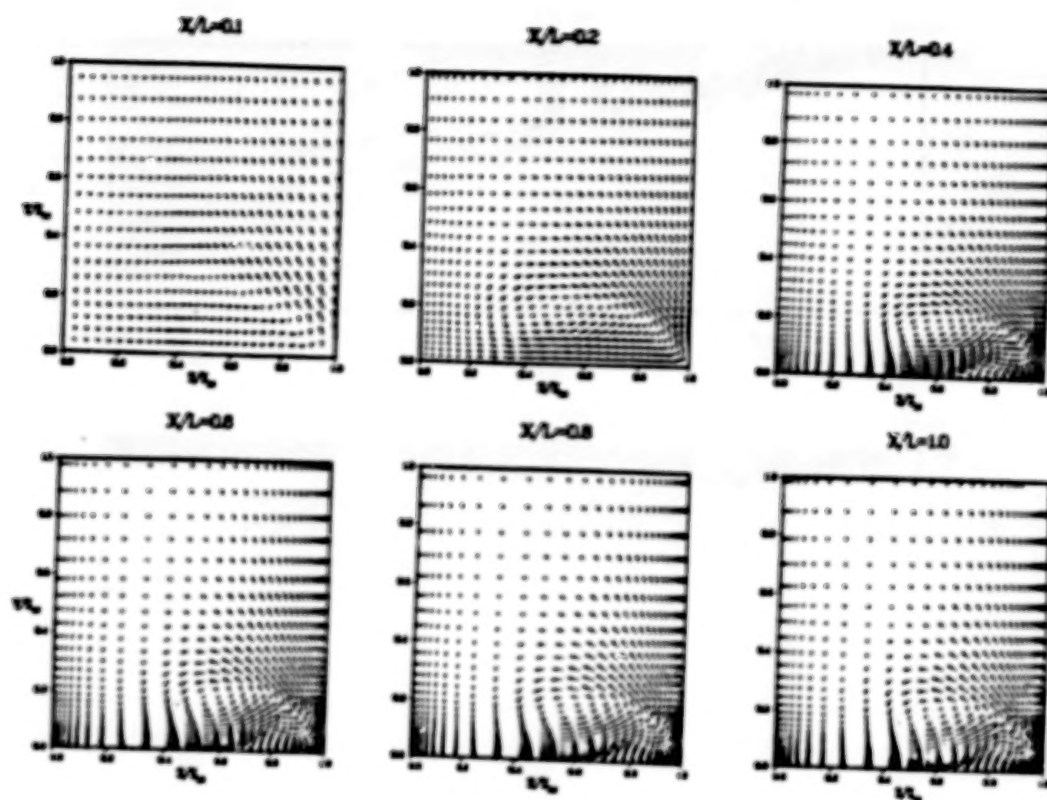


Figure 8. Development of cross-plane velocity,  $\alpha = 10^\circ$ .

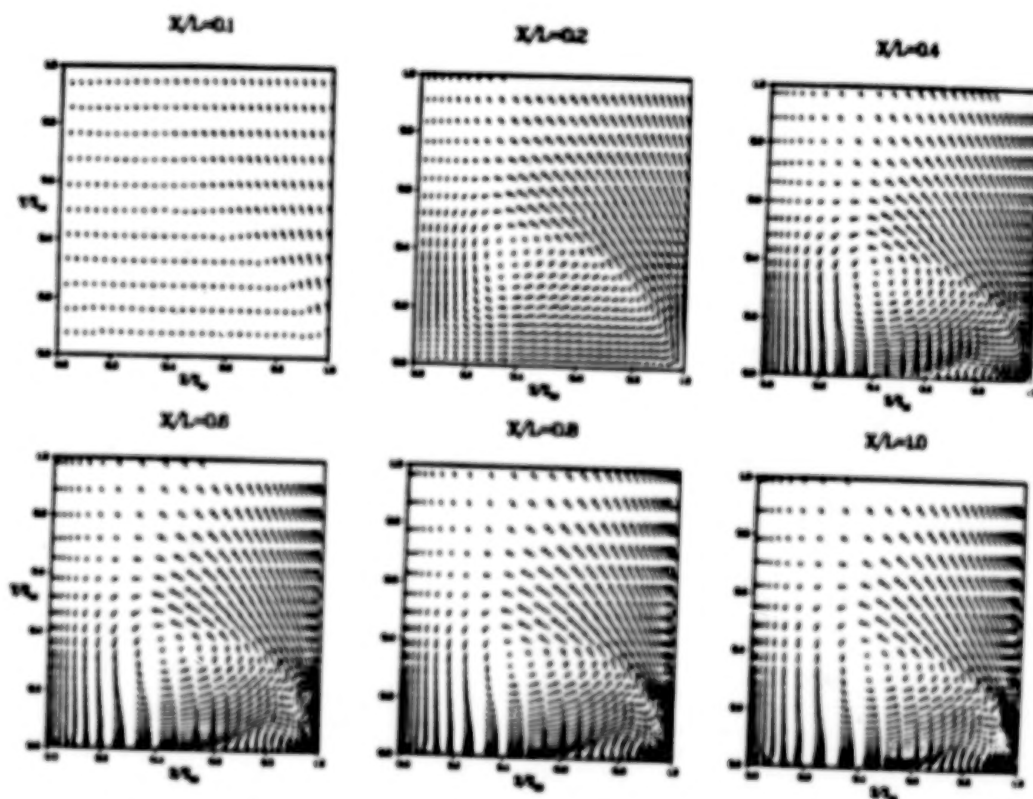


Figure 9. Development of cross-plane velocity,  $\alpha = 20^\circ$ .

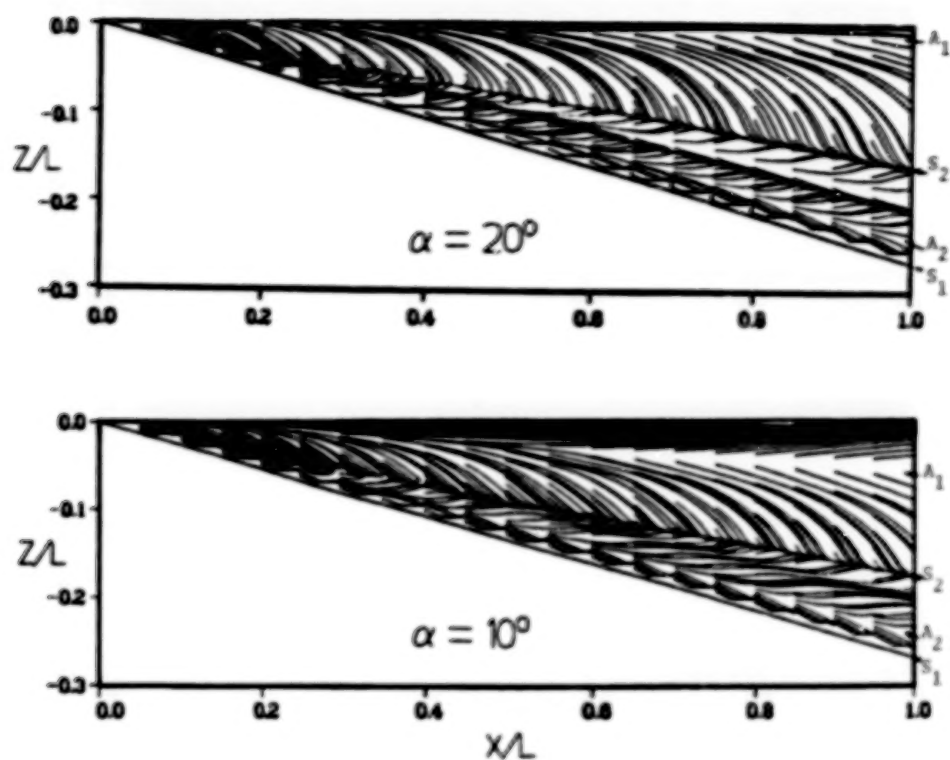


Figure 10. Upper surface oil flow pattern.

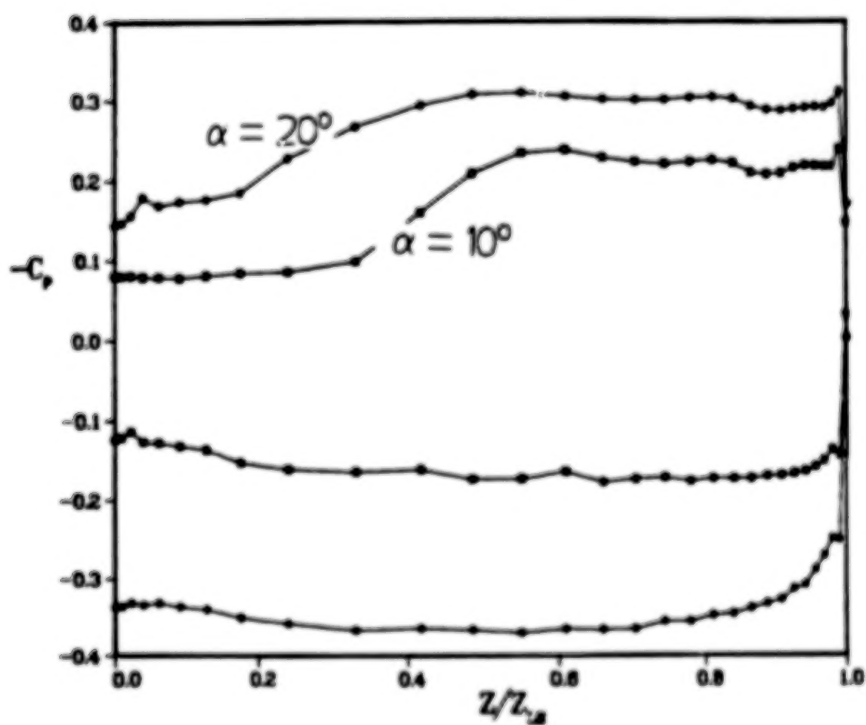


Figure 11. Effect of  $\alpha$  on pressure distribution,  $X/L = 0.8$ .



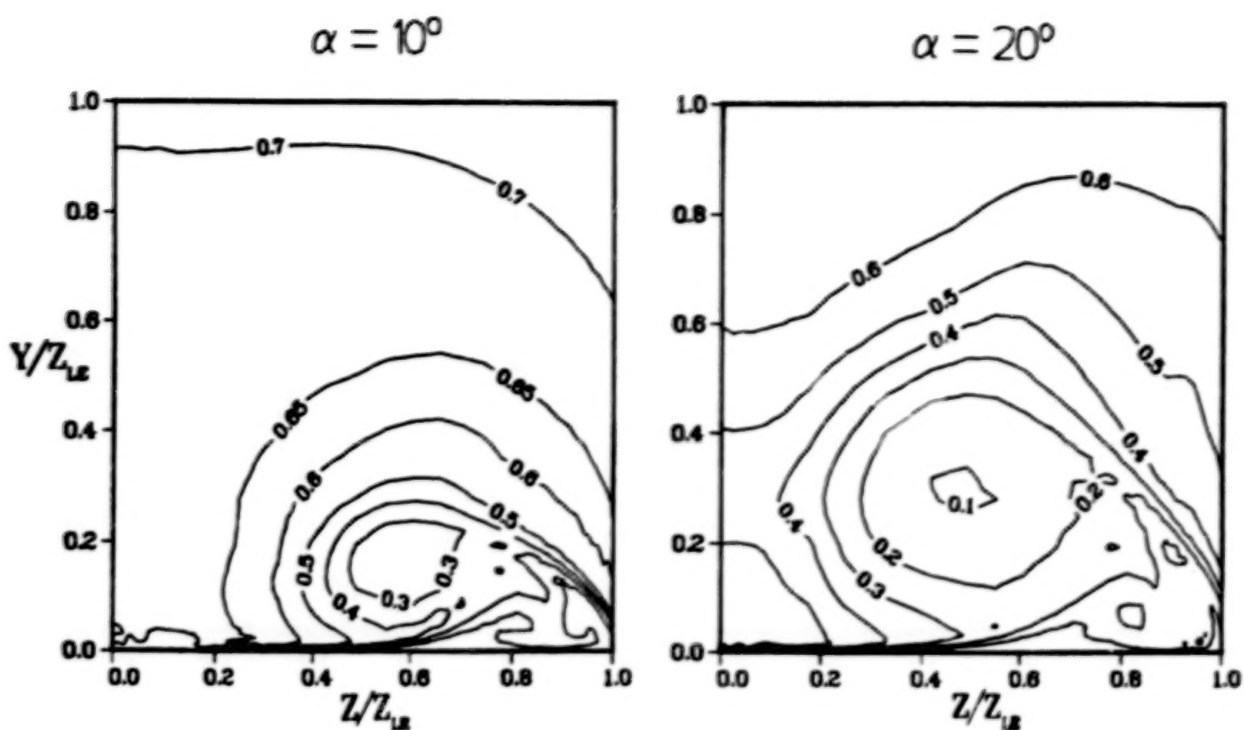


Figure 12. Effect of  $\alpha$  on Pitot pressure,  $X/L = 0.8$ .

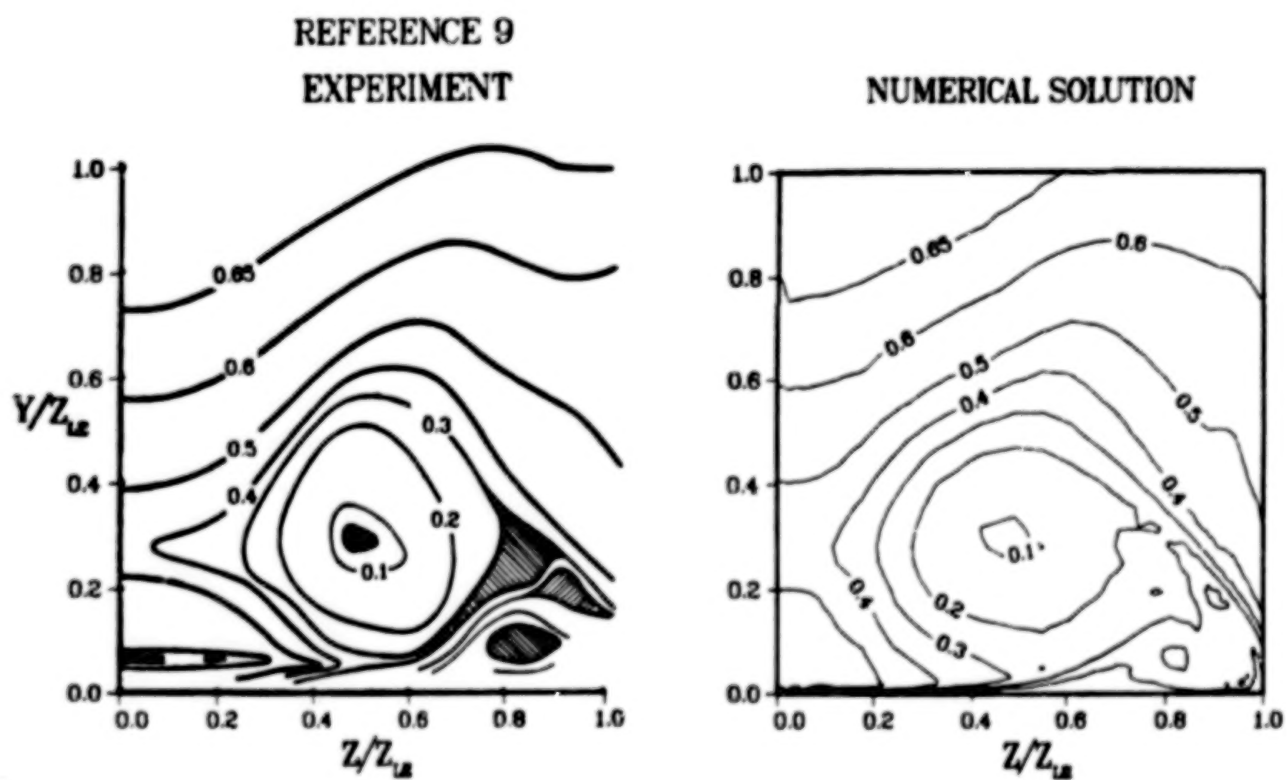


Figure 13. Comparison of Pitot pressure,  $\alpha = 20^\circ$ .

AN OVERVIEW OF THE FUNDAMENTAL AERODYNAMICS BRANCH'S RESEARCH ACTIVITIES  
IN WING LEADING-EDGE VORTEX FLOWS AT SUPERSONIC SPEEDS

David S. Miller, Richard M. Wood, and Peter F. Covell  
NASA Langley Research Center  
Hampton, Virginia

### SUMMARY

For the past 3 years, a research program pertaining to the study of wing leading-edge vortices at supersonic speeds has been conducted in the Fundamental Aerodynamics Branch of the High-Speed Aerodynamics Division at the Langley Research Center. The purpose of the research is to provide an understanding of the factors governing the formation and the control of wing leading-edge vortices and to evaluate the use of these vortices for improving supersonic aerodynamic performance. The studies include both experimental and theoretical investigations and focus primarily on planform, thickness and camber effects for delta wings. This paper will present an overview of this research activity.

### INTRODUCTION

During the last 20 years, aerodynamicists have attempted to design aircraft wings for efficient supersonic flight using attached-flow concepts. For cruise levels of lift, linearized-theory wing-design methods (refs. 1 and 2) have successfully produced optimum twisted and cambered wings. Because of the early success of these methods, the methods have been continuously modified and refined to include the effects of component-on-wing interference (ref. 3), real-flow constraints (ref. 4), and attainable leading-edge thrust (ref. 5). Example applications of this low level-of-lift wing-design technology can be found in references 6 through 8.

For maneuver levels of lift at supersonic speeds, basically two approaches are available for the design of wings. One approach is to provide an attached-flow, controlled expansion around the wing leading edge and on the upper surface (refs. 9 and 10). This attached-flow approach for producing efficient high lift depends on the ability to accelerate the flow around the leading edge to supercritical conditions on the upper surface and then decelerate the flow without causing separation or producing strong shocks. This concept has been experimentally verified, and a summary of the investigation is given in reference 11. The second approach for obtaining efficient high-lift wings uses a controlled, separated, leading-edge vortex flow which not only produces vortex lift, but when the vortex is properly located on a deflected leading-edge, also produces significant levels of effective leading-

edge thrust. Investigations at subsonic and transonic speeds (refs. 12 to 16) of the fundamental vortex behavior on the leeward surface of wings have led to the design of several unique and novel leading-edge devices (refs. 17 to 21) commonly referred to as "vortex flaps." Also, to aid in the design of vortex flaps, several computer codes (refs. 22 to 24) with varying degrees of complexity are being developed to predict vortex location, strength, and effect on the wing. As summarized in reference 25, the development of this new wing-design technology has been extensive but has been confined mainly to subsonic and transonic flows.

In 1982, a research effort was begun to explore the fundamental characteristics of wing leading-edge vortex flows at supersonic speeds. A review of the literature indicated that various aspects of the problem had been previously explored; however, there did not exist a complete and systematic set of experimental data from which one could determine the most basic effects such as Mach number, planform, thickness and camber. To provide this information, an experimental program was formulated first and closely followed by a complementary theoretical effort. This paper will present an overview of the experimental and theoretical programs. Following the overview, a discussion of aerodynamic performance is presented. In this discussion, a comparison is made between wings designed for optimum camber, wings with conventional leading-edge flaps, and wings with conical vortex flaps.

#### NOMENCLATURE

|              |  |
|--------------|--|
| $C_D$        | drag coefficient   |
| $\Delta C_D$ | incremental change in drag coefficient from the minimum drag of a flat wing                                      |
| $C_L$        | lift coefficient   |
| $C_{N_v}$    | vortex induced normal-force coefficient  |
| $C_p$        | pressure coefficient   |
| $C_{p_v}$    | vacuum pressure coefficient  |
| $L$          | model length   |
| $M$          | Mach number  |
| $M_N$        | component of Mach number normal to wing leading edge = $M \cos \Lambda (1 + \sin^2 \alpha \tan^2 \Lambda)^{1/2}$ |
| $X$          | longitudinal distance measured from model origin   |

|                  |  |
|------------------|--|
| Y                | spanwise distance measured from model centerline                                       |
| Y <sub>max</sub> | maximum spanwise model dimension   |
| $\alpha$         | angle of attack, deg   |
| $\alpha_N$       | angle of attack normal to wing leading edge = $\tan^{-1} (\tan \alpha / \cos \Lambda)$ |
| $\beta$          | $\sqrt{M^2 - 1}$ and angle of yaw, deg   |
| $\delta_f$       | leading-edge-flap deflection angle measured streamwise, deg                            |
| $\Lambda$        | wing leading-edge-sweep angle, deg   |
| n                | fraction of local wing semispan  |

### DISCUSSION

An experimental-theoretical research effort is under way to investigate the fundamental characteristics of wing leading-edge vortex flows at supersonic speeds. In order to present a complete overview of the program, both completed, ongoing and planned investigations will be included in the following discussion.

#### Experimental Program

The primary objective of the experimental program is to obtain a complete and consistent set of data necessary to determine the effects of wing planform, thickness and camber on the characteristics of wing leading-edge vortex flows. To obtain a consistent set of data for the entire program, an effort was made to keep the wing planforms, flow conditions and types of data consistent throughout. The specific ingredients for consistency were established in the planform investigation which was the first part of the experimental research program.

**Wing planform investigation.** - Shown in figure 1 are planform sketches of the 4 wind tunnel models selected for testing. The models had leading-edge-sweep values ranging from 52.5° to 75°. In this initial test, it was desirable to minimize the effect of airfoil shape and thickness; therefore, the leading edge was made sharp (10° angle normal to leading edge located on lower surface) and the upper surface was made flat. Each model had a span of 12 in. and a spanwise row of 19 evenly spaced pressure orifices located approximately 1 in. forward of the trailing edge.

Previous experimental tests employed only a single type of flow-visualization data with or without pressure data to explain the vortex phenomena. However, as shown in figure 2, these experimental pressure data were obtained along with three types of flow-visualization data. As shown at the



top of the figure, both tuft and oil-flow photographs were used to examine the flow characteristics on the model surface. These two techniques give slightly different types of information. Both methods are used to determine surface flow direction by the alignment of the tufts or the streaking of the oil; however, the tufts tend to reflect the velocity direction at the edge of the boundary layer, and the direction of oil streaking is influenced not only by the surface velocity but also by the pressure distribution.

Only the vapor-screen flow-visualization technique provides flow-field information on the size, shape, and location of the vortex as shown in the lower right side of figure 2. The dark areas in the photographs are regions having less vapor than the light areas and thus, the dark areas correspond to the highly rotational vortex-flow regions in which the vapor particles have been displaced. Examples and discussion of these various types of data and their relationship with leading-edge vortex behavior are given in reference 26. Each model was tested at Mach numbers of 1.7, 2.0, 2.4 and 2.8 for angles of attack ranging from  $0^\circ$  to  $20^\circ$ .

In a previous study, Stanbrook and Squire (ref. 27) suggested that the flow conditions normal to the leading edge, specifically normal angle of attack ( $\alpha_N$ ) and normal Mach number ( $M_N$ ), govern the type of flow which exists. Stanbrook and Squire initially reported that near  $M_N = 1$  a boundary existed dividing the flow into two distinct regions: for  $M_N < 1$  the flow was characterized by a leading edge, separated, rolled-up vortex-type flow and for  $M_N > 1$  the flow was characterized by an attached flow with possible shock-induced separation. The classification into just two types of flow provided by the Stanbrook-Squire boundary was revised by Ganzer, Hoder and Szodruch (ref. 28); however, this latter effort was based on a single leading-edge-sweep angle of  $73^\circ$  and flow conditions of  $M_N > 1$ . A complete review of this work was presented by Szodruch and Peake (ref. 29). In the present planform study, four leading-edge-sweep values were used to examine the type of flow for conditions which lie above and below the  $M_N = 1$  Stanbrook-Squire boundary.

Using primarily vapor-screen information, the types of flow observed in this test were divided into the seven categories as shown in figure 3. A detailed discussion of each of these flow types can be found in reference 26. In figure 4, all of the test data are summarized according to one of the seven flow types. The  $\alpha_N - M_N$  space is clearly divided into regions where the flow type is indicated by the vapor-screen sketch placed in each region. As an added feature to provide additional information, the open symbols identify flows with shocks; the closed symbols identify shockless flows; the circular symbols identify flows with primary and secondary vortices; the square symbols identify flows containing separation bubbles; the diamond symbols identify flows with shock induced separation; and the triangle symbols identify flows with no separation. As shown by the solid triangles in the figure, the only flow conditions which produced shockless attached flows were angles of attack of zero ( $\alpha_N = 0$ ); however, this occurs only because the next smallest angle of



attack in the test matrix was  $4^\circ$ . Because the two most effective types of separated flow being considered for aerodynamic performance enhancements are the shockless bubble and shockless vortex, it is interesting to note that these two types of flow occupy the majority of the region for  $M_N$  less than unity. Also above  $20^\circ$  normal angle of attack, the upper boundary of the region decreases towards  $M_N = 0$  with increasing  $\alpha_N$ .

**Wing thickness investigation.** - The experimental wing planform investigation was conducted with wind tunnel wing models designed to minimize the effects of airfoil shape and thickness; i.e., the leeward wing surface under investigation was made flat. However, calculated Euler code results, obtained by the method described in reference 30, are shown in figure 5 and indicate that the estimated effects of thickness can be significant. Mach number contours are shown for two delta wings each having  $70^\circ$  leading-edge-sweep angle but with different airfoil sections. One wing has a zero-thick airfoil section to represent a flat wing and the other wing has a 7-percent-thick circular-arc airfoil section. Although the calculations for both wings were made at exactly the same flow conditions of  $M = 2.5$  and  $\alpha = 18^\circ$ , the Mach number contours indicate that the types of flow were completely different. The flow over the leeside of the zero-thick wing is characterized by a well-developed leading-edge vortex with a shock located on top of the vortex; the zero-thick wing flow conditions correspond to  $M_N = 1.13$  and  $\alpha_N = 44^\circ$  and, as shown in the  $\alpha_N - M_N$  graphic, agree with the type of flow experimentally observed in the flat-wing planform study previously discussed. In contrast, flow over the leeside of the 7-percent circular-arc thick wing is characterized by a cross-flow shock with no signs of separation of any type. As indicated in figure 4, this type of flow would be expected to occur at a value of  $M_N$  greater than unity and a value of  $\alpha_N$  less than  $12^\circ$ . Because the wing leading-edge local angle of attack is continuously varying along the span due to the nonconical geometry, it is not clear how to calculate the  $\alpha_N$  and  $M_N$  values in order to apply the flow classification chart of figure 4. For this particular thick-wing example, reducing the wing angle of attack of  $18^\circ$  by  $8^\circ$  (which corresponds to one-half the value of the total thickness angle of the 7-percent parabolic arc at the leading edge) resulted in a  $\alpha_N = 27^\circ$  and a  $M_N = 0.95$  as shown for the thick wing location on the  $\alpha_N - M_N$  chart in figure 5. This location corresponds to the boundary of several regions which all should have some type of separated flow. Obviously additional information is needed to understand the effects of thickness on the leeside-flow characteristics.

To provide a set of thick-wing data to compare with the flat-wing data, a set of eight wind tunnel wing models has been constructed. The models have delta planforms identical to the flat wings with leading-edge sweep angles of  $52.5^\circ$ ,  $60^\circ$ ,  $67.5^\circ$  and  $75^\circ$ . One set of models has 7-percent-thick circular-arc airfoil section and the other set of models has 7-percent-thick diamond airfoil sections (see fig. 6). Although both wing sets have the same thickness-to-chord ratio of 7 percent, their leading-edge thickness angles are considerably different. The circular-arc airfoil has a leading-edge thickness

half angle of approximately  $8^\circ$  and the diamond airfoil has a leading-edge thickness half angle of  $4^\circ$ . The test plans include oil flow, tuft and vapor screen flow-visualization data which will be correlated with the flat-wing flow-visualization data to identify thickness effects.

**Wing-camber investigation.** - The purpose of the wing-camber study was to experimentally determine the effects of wing leading-edge camber on both the aerodynamic forces and moments as well as the wing's leeside flow characteristics. The camber was represented by a deflected leading-edge flap on an otherwise uncambered wing having a flat upper surface. Two sets of delta-wing models were constructed. One set had a leading-edge-sweep angle of  $67.5^\circ$ , and the other set had a leading-edge-sweep angle of  $75^\circ$ . Each set had a leading-edge flap with its hinge line located at 70 percent of the local span; the leading-edge flap could be deflected down  $0^\circ$ ,  $5^\circ$ ,  $10^\circ$  or  $15^\circ$ . The flap deflection angle is measured streamwise. As shown in the photograph of figure 7, the models have a minimum-body balance housing which is conical back to approximately two-thirds of the model length at which point the body balance housing becomes cylindrical. As a result of this design, all model configurations tested had conical leeside surface geometries forward of the cylindrical portion of the body balance housing. For each of the two sets of wings, a removable fuselage forebody was constructed so that data could be obtained with and without fuselage forebody effects. The fuselage forebodies extended approximately 5 in. beyond the wing apex and had a fineness-ratio 2.5 circular-arc nose and a 2.0-in.-diameter cylindrical circular aft section.

Testing of the  $\Lambda = 75^\circ$  wing with the fuselage forebody removed has been completed. Data were obtained for the same flow conditions as those of the planform study, i.e. Mach numbers from 1.5 to 2.8 and angles of attack from  $0^\circ$  to  $20^\circ$ . Figure 8 illustrates the behavior of the leeside flow characteristics at  $M = 1.7$ . Similar behavior was observed at the other Mach numbers. For the range of flap-deflection angles ( $\delta_f$ ) and angles of attack ( $\alpha$ ) tested, three distinctly different flow types were observed. The flow type is characterized by the existence, origin and location of the vortex and is denoted by the sketches on the figure. The sketch indicates the character of both the vortex and the associated surface pressure distribution. The shaded region corresponds to the situation in which the vortex originates at the wing leading edge and its primary influence is confined to the leading-edge flap; this is the ideal situation for the operation of a vortex flap. For angles of attack between  $0^\circ$  and  $10^\circ$ , the shaded region has both upper and lower boundaries. For a given angle of attack, the upper boundary denotes the flap-deflection angle above which the flow is attached on the flap but separates at the hinge line. For a given flap-deflection angle, the lower boundary denotes the angle of attack above which the vortex is no longer confined to the leading-edge flap but extends beyond the hinge line. There also exists a point where the upper and lower boundaries of the shaded region intersect. This point defines the maximum flap-deflection angle at which the leading-edge flap could be made to act as a vortex flap. It remains to be seen how the force and moment data

correlate with the leeside flow characteristics.

Because a definite interaction was observed between the hinge-line vortex and the leading-edge vortex, an experimental study of hinge-line separation is planned. As illustrated in figure 9, the hinge-line study will involve the testing of three hinge-line models mounted on a splitter plate. The models will have different leading-edge-sweep angles of 0°, 50°, and 70° and leading-edge flap deflection angles ranging from 0° to 40°. Each model will be instrumented so that pressure distributions can be measured both streamwise and normal to the hinge line. As indicated in the figure, flow field pressures will be measured using a flow survey pressure probe.

### Theoretical Program

The objective of the theoretical program was to explore the use of computational methods for predicting the leading-edge vortex characteristics of wings at supersonic speeds. Two methods were examined. A modified linearized-theory method was found to adequately predict the flow characteristics of flat wings but was not adequate for predicting the flow over cambered wings. An Euler solution technique was found to adequately predict the general characteristics of both flat and cambered wings. The following discussion will briefly describe each method and highlight results obtained with each method.

**Modified linearized-theory method.** - A supersonic linearized-theory aerodynamic prediction method has been modified to account for both nonlinear attached-flow effects (primarily a windward surface phenomena) and nonlinear separated-flow effects (primarily a leeward surface phenomena) (ref. 31). The leading-edge separated flow is represented by a technique which uses the Polhamus suction analogy (ref. 32) to determine the leading-edge vortex-induced force and then modifies the upper surface attached-flow pressures to distribute this additional force over the wing upper surface. The vortex-induced force is distributed about a "vortex action point" located downstream of the wing leading edge. The location of the vortex action point is determined from an empirical relationship that is a function of angle of attack only. The method also limits the leeward surface pressures to values greater than those corresponding to vacuum conditions.

The ability of this modified linearized-theory method to predict wing vortex characteristics was evaluated for the series of flat delta wings used in the previously discussed experimental planform investigation. A detailed discussion of this evaluation is given in reference 26, and typical results are presented in figure 10. The results shown in the figure are for an uncambered delta wing with 75° of leading-edge sweep; the Mach numbers and angle of attack correspond to conditions which lie within the classical vortex region depicted in the upper portion of the figure. The vortex-induced normal-force coefficient,  $C_{N_v}$ , represents the vortex strength and the spanwise surface pressure distribution indicates both vortex strength and location. As



shown across the bottom of the figure, the agreement between theoretical and experimental results is sufficient for preliminary design applications of the modified linearized-theory method.

The method was next evaluated for wings with deflected leading-edge flaps. At the time of this evaluation, the experimental data had not been obtained on the conical wing-flap models described in the "Wing Camber Investigation" section of this paper; however, data from references 33 and 34 were sufficient to evaluate the method. A comparison of theoretical and experimental forces and surface pressures can be made from the results shown in figure 11. Although the pressure results were obtained at slightly different conditions than the force data, the flow characteristics which produced the force data at  $C_L = 0.3$  closely correspond to the flow characteristics of the pressure distribution shown in the figure. Discrepancies between the experimental data and the computed results are found in both the drag polar and pressure distributions. The theoretical drag polars indicate that for values of lift-coefficient above 0.2 the wing with the  $16^\circ$  flap deflection produces less drag than the wing with zero flap deflection; however, the experimental data show that deflecting the leading-edge flap  $16^\circ$  resulted in a drag increase with respect to the wing with zero-flap deflection. An explanation for this discrepancy is clearly shown in the spanwise pressure distributions. The theoretical spanwise pressure distribution shows the presence of a small vortex its induced pressure acting on the leading-edge flap; theoretically this is the ideal situation for achieving performance benefits employing a vortex flap. However, the experimental pressures indicate both a small leading-edge vortex and a much larger hinge-line vortex. Because the hinge-line vortex induced pressures dominate and lie on the undeflected flat surface inboard of the hinge line, no drag reduction would be realized as a result of deflecting the leading-edge flap  $16^\circ$ .

From this discussion it is clear that the modified-linearized theory method is not capable of analyzing the flow over sharp leading-edge wings having deflected leading-edge flaps.

**Euler code method.** - Because the modified-linearized method failed to predict the leeward flow over delta wings with deflected leading-edge flaps, it was decided to explore the use of more complex codes such as Navier-Stokes and Euler codes. A number of researchers have applied Navier-Stokes codes and Euler codes to the calculation of wing leading-edge-vortex flows at supersonic speeds; and both methods have produced encouraging results for the flow over flat, uncambered wings (ref. 35). The Navier-Stokes equations model both the viscous and inviscid mechanisms and would be expected to provide the most accurate results. However, because Navier-Stokes methods have very high computational costs and because Euler methods have been shown to produce the general characteristics of vortex flows, it was decided to look first at the capabilities of Euler codes. In selecting a particular Euler code the choice ranged from large, complex 3-D, well-developed codes to a small, simple 2-D

conical code under development for the specific purpose of calculating wing leading-edge vortex flows. A code of the latter type, specifically the conical Euler code by Perez and Powell et al. (refs. 36 and 37), was selected because of the code developers' expressed interest in this particular problem.

A complete description of the code has been reported previously in reference 38 and only a brief description is presented herein. The basic solution technique employs a finite volume spatial discretization of the unsteady Euler equations in conservation form which is solved using a Runge-Kutta type method as discussed in reference 39. The bow shock is fitted, and both second and forth order damping are employed to capture internal shocks and yield smooth solutions. The grid is generated using a Joukowski transformation in which the zero-thick wing surface becomes a circle. For all calculations shown, the grid density consisted of 128 radial lines in the half plane and 128 points on each radial line. The wing is represented by zero-thick impermeable surface.

To compare with the Euler code solutions, eight cases were selected from the data obtained in the experimental program. The cases were selected to provide a large variety of wing leeside flow characteristics. In all eight cases, the geometry was a delta wing with  $75^\circ$  of leading-edge sweep. Four of the cases compare results for a flat wing, and four of the cases compare results for a wing with a deflected leading-edge flap.

The comparisons between experiment and theory include both flow-field and surface data. The calculated flow-field data consist of plots of the cross-flow velocity vectors and the measured flow-field data consist of vapor screen photographs. The flow-field data are presented in a plane perpendicular to the free-stream velocity vector. The calculated and measured surface data consist of spanwise pressure distributions.

Experimental and theoretical results for a flat wing at  $12^\circ$  angle of attack are shown in figures 12 and 13 for Mach numbers of 1.7 and 2.8, respectively. At both Mach numbers, the experimental and theoretical flow-field data show leading-edge separation which results in a well-developed primary vortex located above the leeside surface of the wing. The most notable difference between the theoretical and experimental results is the absence of the secondary vortex in the Euler results. This is found for all cases because the secondary vortex is a viscous phenomena which cannot be predicted by an inviscid Euler code. Otherwise, the agreement between the experimental and theoretical results is very good. Both results indicate the flattening and inboard movement of the primary vortex as Mach number is increased from 1.7 to 2.8. At Mach numbers of 1.7, the experimental and theoretical spanwise pressure distributions are in good agreement except for the influence of the secondary vortex. The experimental pressures show two pressure peaks, one near 60-percent span and another near 85-percent span; the theoretical pressure distributions show a single slightly higher pressure peak located at approximately the 70-percent span station. Although the higher Mach number



2.8 results of figure 12 still contain a secondary vortex, there is little or no influence of this secondary vortex on the surface pressure distribution. This observation seems to be typical, and it can be generally stated that effect of the secondary vortex on the wing upper surface pressures diminishes with increasing Mach number.

Results for a flat wing at  $12^\circ$  angle of attack and at  $8^\circ$  angle of yaw are shown in figures 14 and 15 for Mach numbers of 1.7 and 2.8, respectively. As seen in the figures, flow-field and surface-pressure data are shown for both the left side ( $y/y_{\max}$  negative) and the right side ( $y/y_{\max}$  positive) of the wing. For this yawed orientation, the left side of the wing has a windward leading edge and the right side has a leeward leading edge. Because vapor-screen photographs were not taken for the yawed wings, the only flow-field data shown are plots of the theoretically computed crossflow velocity vectors. In both figures 14 and 15, the asymmetry of the flow due to yaw is clearly shown in both the flow field and surface pressure data. For the low Mach number of 1.7, the cross-flow velocity contours show that leading-edge separation occurs on both the windward and leeward edges. The windward-edge separation develops into a separation bubble which lies close to the wing surface and the leeward-edge separation develops into a classical vortex. These two considerably different flow types result in different surface pressure distributions shown at the bottom of figure 14. The separation bubble results in a more negative pressure extending over a larger portion of the wing span as compared to the pressures resulting from the classical vortex. In figure 15, the higher Mach number 2.8 results indicate that the flow is attached on the windward edge and separated on the leeward edge. The attached flow produces a plateau-type pressure distribution over the outboard 75 percent of the left wing span; the pressure distribution on the right-wing span is typical of that produced by a classical vortex. For both Mach numbers, the Euler-code predicted pressures are in excellent agreement with the measured pressures.

Results from the experimental conical-wing-flap study indicated that four types of flow were observed to occur. The type of flow depends on the angle of attack and the wing leading-edge flap angle. To evaluate the ability of Euler code to predict the flow over the wings with deflected leading-edge flaps, four combinations of  $\alpha$  and  $\delta_f$  were selected to correspond to each of the four observed types of flow. These four  $\alpha$ - $\delta_f$  combinations are shown in figure 16 and are labeled as points A, B, C, and D. The flow-field results and surface pressure distributions corresponding to points A, B, C, and D are shown in figures 17 to 20 respectively.

In figure 17, results are shown for  $\alpha = 4^\circ$  and  $\delta_f = 5^\circ$ . According to the location of this condition on figure 16 (point A), the flow should be characterized by a classical leading-edge vortex. The experimental pressure distribution does indeed show a lower pressure region on the upper surface of the leading-edge flap, which could result from the presence of a weak vortex.

However, the experimental flow-field data do not show a vortex; this indicates that the vapor screen techniques may not be sensitive enough to detect weak vortex conditions or that condensation effects may have altered the flow conditions to delay vortex formation. Note also that neither the theoretical pressure distribution nor the theoretical flow-field data exhibit signs of a leading-edge vortex. These conflicting observations indicate that the characteristics of a weak vortex are very sensitive to the flow conditions.

In figure 18, results are shown for  $\alpha = 12^\circ$  and  $\delta_f = 5^\circ$ . These results correspond to point B in figure 16. The experimental and theoretical results clearly show a primary vortex which originates at the wing leading edge and extends well inboard of the flap hinge line. The experimental and theoretical pressures are in good agreement and both reflect the presence of the primary vortex. The theoretical flow-field data unexpectedly indicate the presence of a secondary separation region lying on the leading-edge flap; this secondary separation is produced as the outboard flow passing under the primary vortex encounters the hinge line and separates. Although not clearly shown in the experimental flow-field data, both the experimental and theoretical pressure distributions exhibit the signs of this secondary separation.

Results for  $\alpha = 4^\circ$  and  $\delta_f = 15^\circ$  are shown in figure 19; these results correspond to point C on figure 16. The theoretical flow-field data show that a large flap deflection and small angle of attack produce two primary vortices. One of these vortices originates from the leading edge and lies on the lower surface of the leading-edge flap; this lower surface vortex cannot be seen in the experimental flow-field data because the light source is blocked by the leading-edge flap. The other primary vortex is produced when the attached flow on the flap upper surface separates at the flap hinge-line; this vortex lies inboard of the flap hinge line and is clearly visible in both the experimental and theoretical flow-field data. Although the vortex-induced pressures on the leeward wing surface are theoretically predicted slightly lower than those experimentally measured, the general agreement between theory and experiment is very good. The theoretically predicted pressure distribution shows the strong influence of the windward primary vortex as a reduced pressure region on the windward (lower) wing-flap surface; unfortunately, lower surface pressures were not measured and a comparison between experimental and theoretical pressures could not be made.

The fourth and final set of cambered delta-wing results are shown in figure 20. These results correspond to  $\alpha = 12^\circ$  and  $\delta_f = 15^\circ$  which is point D on figure 16. Both the experimental and the theoretical results indicate similar leeside flow characteristics. Both show leading-edge separation and hinge-line separation which result in two regions of vortex-type flow. The leading-edge vortex results in the most outboard suction pressure peak and the hinge-line vortex results in the largest suction pressure peak located slightly inboard of the hinge line. The major difference between the experimental and theoretical results is the extent of the leading-edge vortex. The

experimental results show a separation-bubble type vortex flow which extends over the entire length of the flap and produces the plateau type pressure distributions shown in the figure. The theoretical results also show a separation-bubble type vortex flow which begins at the wing leading edge and reattaches on the flap at approximately half way between the leading edge and the hinge line; in the theoretical distribution this flow reattachment produces the compression region between the two suction pressure peaks.

### Aerodynamic Performance

In this section, the measured aerodynamic performance for a conical vortex-flap wing and the performance of a conventional attached-flow leading-edge flap wing are presented. These performance results are compared with each other and with a "practical performance goal" established from data measured on a series of optimum twisted and cambered wings.

Aerodynamic performance results for a vortex-flap wing are presented in figure 21. These results were obtained at  $M = 1.7$  on the  $\Lambda = 75^\circ$  delta wing with leading-edge flaps deflected  $0^\circ$ ,  $5^\circ$ ,  $10^\circ$  and  $15^\circ$ . Experimental values of drag-due-to-lift parameter are presented as a function of lift coefficient. For reference purposes, the linearized-theory 0-percent thrust and 100-percent thrust boundaries are also shown; these boundaries do not vary with lift coefficient. The data show that significant drag reductions can be achieved at supersonic speeds by the management of wing leading-edge vortices. Compared to the  $5^\circ$  flap-deflection data, which did not experience hinge-line separation, the data for the  $10^\circ$  and  $15^\circ$  leading-edge flap deflection show a loss in performance due to hinge-line separation. However, all flap deflections resulted in a drag reduction compared to the flat wing.

Aerodynamic performance results for a wing using a conventional attached-flow leading-edge flap were extracted from data obtained in the experimental study (ref. 40) depicted in figure 22. As indicated in the figure, the study involved testing four sets of flap planforms on a trapezoidal wing and two sets of flap planforms on a cranked wing. Both wings had aspect ratios of 1.75 and were mounted on a generic fuselage as shown in the photograph of figure 22. All leading-edge flap geometries were effective in reducing the flat-wing drag; however, the largest drag reductions were produced by the combination of flap A on the cranked wing. For this wing-flap combinations, experimental values of the drag-due-to-lift factor versus lift coefficient are shown in the lower left portion of the figure for flap deflection angles of  $0^\circ$ ,  $5^\circ$  and  $10^\circ$ . The linearized-theory 0-percent thrust and 100-percent thrust boundaries are also shown. These data indicate that the lowest drag-due-to-lift is produced by scheduling the flap deflection angle with lift coefficient. As shown in the figure, the proper schedule would be  $\delta_f = 0^\circ$  for lift coefficients below 0.1;  $\delta_f = 5^\circ$  for lift coefficients between 0.1 and 0.4; and  $\delta_f = 10^\circ$  for lift coefficients above 0.4. This flap schedule and the drag-due-to-lift data shown in figure 22 were used to develop the curve for



the performance summary representing conventional attached-flow leading-edge flaps.

A comparison of the aerodynamic performance of the vortex-flap wing and the attached-flow flap wing can be made from the data which are summarized in figure 23. In this figure, the aerodynamic performance is expressed as a percent of full, theoretical, leading-edge thrust and is presented as a function of lift coefficient.

For reference purposes, a practical-goal curve was established from experimental data measured on several twisted and cambered wings where each wing camber was optimized for a specific lift coefficient. For example, the data used to generate the portion of the practical-goal curve for lift coefficients from 0.0 to 0.2 were taken from the cruise cambered-wing designs reported in reference 41, and the data used to establish the performance level for the 0.4 value of lift coefficient were taken from the high-lift wing designs reported in references 42 and 43.

The information contained in figure 23 represents the state of the art in experimentally measured supersonic aerodynamic performance. At low levels of lift ( $C_L = 0.1$ ), the results indicate that the practical goal of near 100-percent thrust has been obtained with both traditional leading-edge flaps and vortex leading-edge flaps. However, at high-lift conditions ( $C_L = 0.4$ ), the practical goal, which is reduced to approximately 60 percent thrust, has not been obtained by either of the flap concepts. At this high-lift condition, the traditional leading-edge flap produces less than 25-percent thrust and the data of reference 40 indicate that this is probably the best that can be obtained using the attached-flow flap concept. However, the conical vortex flap produces approximately 40-percent thrust and it is anticipated that the use of other nonconical flap geometries along with eliminating the hinge-line separation would increase the performance considerably.

#### CONCLUDING REMARKS

This paper presents an overview of a research program directed at the study of wing leading-edge vortices at supersonic speeds. The studies include both experimental and theoretical investigations and focus primarily on determining planform, thickness and camber effects for delta wings. The effects of planform and leading-edge camber have been experimentally determined, and an experimental study to identify thickness effects has been initiated. Theoretical studies have shown that a modified linearized-theory method, which was capable of predicting the planform effects for flat wings, was not adequate for predicting leading-edge camber effects. Preliminary results obtained with an Euler code have been shown to contain the correct primary-vortex characteristics for delta wings of various planforms and with various amounts of leading-edge camber.

In a summary of measured aerodynamic performance for high-lift conditions, wings with leading-edge vortex flaps were shown to have a considerably higher level of performance (40-percent thrust) than wings employing conventional attached-flow leading-edge flaps (25-percent thrust). However, the performance levels achieved with vortex flaps were considerably less than the performance levels experimentally established as a practical goal (60 percent thrust).

#### ACKNOWLEDGMENT

The authors wish to thank Dr. Earl M. Murman and Mr. Kenneth G. Powell of the Massachusetts Institute of Technology for providing the Euler solution results presented in this paper.

#### REFERENCES

1. Carlson, H. W.; and Middleton, W. D.: A Numerical Method for the Design of Camber Surfaces of Supersonic Wings with Arbitrary Planforms. NASA TN D-2341, 1964.
2. Carlson, H. W.; and Miller, D. S.: Numerical Methods for the Design and Analysis of Wings at Supersonic Speeds. NASA TN D-7713, 1974.
3. Mack, R. J.: A Numerical Method for Evaluation and Utilization of Supersonic Nacelle-Wing Interference. NASA TN D-5057, 1969.
4. Kulfan, R. M.; and Sigallo, A.: Real Flow Limitations in Supersonic Airplane Design. AIAA-78-147, Jan. 1978.
5. Carlson, H. W.; and Miller, D. S.: The Influence of Leading-Edge Thrust on Twisted and Cambered Wing Design for Supersonic Cruise. AIAA-81-1656, Aug. 1981.
6. Carlson, H. W.: Aerodynamic Characteristics at Mach Number 2.05 of a Series of Highly-Swept Arrow Wings Employing Various Degrees of Twist and Camber. NASA TM X-332, 1960.
7. Morris, O. A.; and Fournier, R. H.: Aerodynamic Characteristics at Mach Numbers 2.30, 2.60, and 2.96 of a Supersonic Transport Model Having a Fixed, Warped Wing. NASA TM X-1115, 1965.
8. Miller, D. S.; and Schemensky, R. T.: Design Study Results of a Supersonic Cruise Fighter Wing. AIAA-79-0062, Jan. 1979.
9. Mason, W. H.; and Miller, D. S.: Controlled Supercritical Crossflow on Supersonic Wings - An Experimental Validation. AIAA-80-1421, July 1980.



10. Mason, W. H.; Miller, D. S.; Pittman, J. L.; and Siclari, M. J.: A Supersonic Wing Designed for Nonlinear Attached Flow. AIAA-83-0425, Jan. 1983.
11. Miller, D. S.; Pittman, J. L.; and Wood, R. M.: An Overview of Two Non-Linear Supersonic Wing-Design Studies. AIAA-83-0182, Jan. 1983.
12. Lambourne, N. C.; and Bryer, D. W.: Some Measurements in the Vortex Flow Generated by a Sharp Leading Edge Having 65 Degrees Sweep. C.P. No. 447, British A.R.C., 1960.
13. Squire, L. C.: Camber Effects on the Nonlinear Lift of Slender Wings with Sharp Leading Edges. C.P. No. 924, British A.R.C., 1967.
14. Matoi, T. K.: On the Development of a Unified Theory for Vortex-Flow Phenomena for Aeronautical Applications. Contract No. N00014-57-A-0204-0085, MIT, April 1975. (Available from DTIC as AD-A012-339.)
15. Kulfan, R. M.: Wing Airfoil Shape Effects on the Development of Leading-Edge Vortices. AIAA Paper 79-1675, 1979.
16. Manro, M. E.: Transonic Pressure Measurements and Comparison of Theory to Experiment for Three Arrow-Wing Configurations. Vol. I: Experimental Data Report-Basic Data and Effect of Wing Shape. NASA CR-165701, 1981.
17. Rao, D. M.: Leading-Edge Vortex Flap Experiments on a 74-Deg Delta Wing. NASA CR-159161, 1979.
18. Rao, D. M.: Leading-Edge Vortex Flaps for Enhanced Subsonic Aerodynamics of Slender Wings. ICAS 80-13.5, 1980.
19. Smith, C. W.; Campbell, J. F.; and Huffman, J. K.: Experimental Results of a Leading-Edge Vortex Flap on a Highly Swept Cranked Wing. Tactical Aircraft Research and Technology. NASA CP-2162, 1980.
20. Rao, D. M.; and Johnson, T. D.: Investigation of Delta Wing Leading-Edge Devices. J. Aircraft, vol. 18, no. 3, March 1981, pp. 161-167.
21. Rao, D. M.: Segmented Vortex Flaps. AIAA-83-0424, 1983.
22. Johnston, F. T.; Lu, P.; Tinoco, E. N.; and Epton, M. A.: An Improved Panel Method for the Solution of Three-Dimensional Leading-Edge Vortex Flows. Volume I. - Theory Document. NASA CR-3278, 1980.

23. Lan, C. E.; and Chang, J. F.: VORCAM - A Computer Program for Calculating Vortex Lift Effect of Cambered Wings by the Suction Analogy. NASA CR-165800, 1981.
24. Lamar, J. E.; and Herbert, H. E.: Production Version of the Extended NASA-Langley Vortex Lattice FORTRAN Computer Program - Volume I - User's Guide. NASA TM-83303, 1982.
25. Lamar, J. E.; and Campbell, J. F.: Recent Studies at NASA-Langley of Vortical Flows Interacting with Neighboring Surfaces. Aerodynamics of Vortical Type Flows in Three Dimensions, AGARD-CP-342, July 1983.
26. Miller, D. S.; and Wood, R. M.: Lee-Side Flow Over Delta Wings at Supersonic Speeds. NASA TP-2430, 1985.
27. Stanbrook A.; and Squire, L. C.: Possible Types of Flow at Swept Leading Edges. Aeron. Quarterly, vol. XV, Feb. 1964.
28. Ganzer, W.; Hoder, H.; and Szodruch, J.: On the Aerodynamics of Hypersonic Cruise Vehicles of Off-Design Conditions. Proceedings of the XI Congress of the ICAS, Lisbon, Portugal, vol. I., Sept. 10-16, 1978, p. 152-161.
29. Szodruch, J. G.; and Peake, D. J.: Leeward Flow Over Delta Wings at Supersonic Speeds. NASA TM-81187, 1980.
30. Rizzi, A.; Eriksson, L. E.; Schmidt, W.; and Hitzel, S. M.: Simulating Vortex Flows Around Wings. Aerodynamics of Vortical Type Flows in Three Dimensions, AGARD Conference Preprint N. 342, 1983.
31. Carlson, H. W.; and Mack, R. J.: Estimation of Wing Nonlinear Aerodynamic Characteristics at Supersonic Speeds. NASA TP-1718, 1980.
32. Polhamus, E. C.: A Concept of the Vortex Lift of Sharp-Edged Delta Wings Based on a Leading-Edge Suction Analogy. NASA TN D-3767, 1976.
33. Igglesden, M. S.: Wind Tunnel Measurements of the Lift-Dependent Drag of Thin Conically Cambered Slender Delta Wings at Mach Numbers 1.4 and 1.8. Tech. Note No. Aero. 2677, British A.R.C., 1960.
34. Michael, W. H., Jr.: Flow Studies on Drooped-Leading-Edge Delta Wings at Supersonic Speeds. NACA TN-3614, 1956.
35. Newsome, R. W.; and Thomas, J. L.: Computation of Leading-Edge Vortex Flows. Presented at the Vortex Flow Aerodynamics Conference, NASA Langley Research Center, October 8-10, 1985.

36. Perez, E.: Computation of Conical Flows with Leading Edge Vortices. S.M. Thesis, MIT, 1984.
37. Powell, K. G.; Perez, E. S.; Murman, E. M.; and Baron, J. R.: Total Pressure Loss in Vortical Solutions of the Conical Euler Equations. AIAA Paper 85-1701, July 1985.
38. Murman, E. M.; Rizzi, A.; and Powell, K.: High Resolution Solutions of the Euler Equations for Vortex Flows. Progress & Supercomputing in Computational Fluid Dynamics, Birkhauser-Boston, Inc., 1985.
39. Jameson, A.; Schmidt, W.; and Turkel, E.: Numerical Solution of the Euler Equations by Finite Volume Method Using Runge-Kutta Time-Stepping Schemes. AIAA-81-1259, June 1981.
40. Covell, P. F.; Miller, D. S.; and Wood, R. M.: An Evaluation of Leading-Edge Flap Performance on Delta and Double Delta Wings at Supersonic Speeds. AIAA-86-0315, 1986.
41. Wood, R. M.; Miller, D. S.; Raney, D. L.; and Roesch, M. T.: A Low-Lift Wing Camber Design Approach for Fighter Aircraft. NASA TP-2465, 1985.
42. Miller, D. S.; Landrum, E. J.; Townsend, J. C.; and Mason, W. H.: Pressure and Force Data for a Flat Wing and a Warped Conical Wing Having a Shockless Recompression at Mach 1.62. NASA TP-1759, 1981.
43. Pittman, J. L.; Miller, D. S.; and Mason, W. H.: Supersonic, Nonlinear Attached-Flow Wing Design for High Lift with Experimental Validation. NASA TP-2336, 1984.

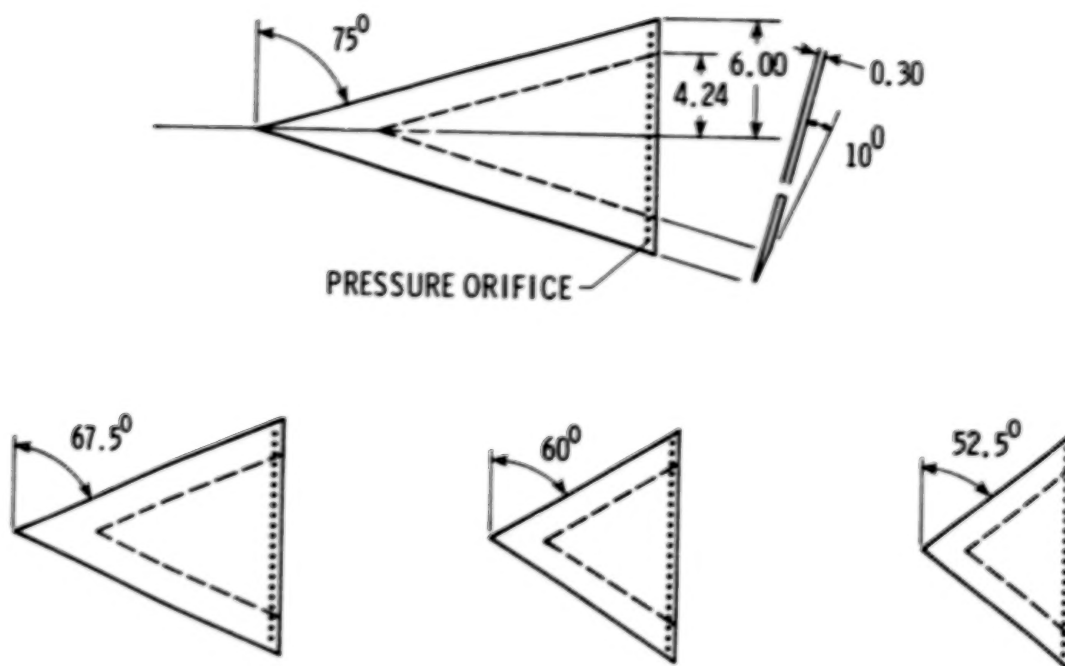


Figure 1. Planforms of flat delta-wing models.

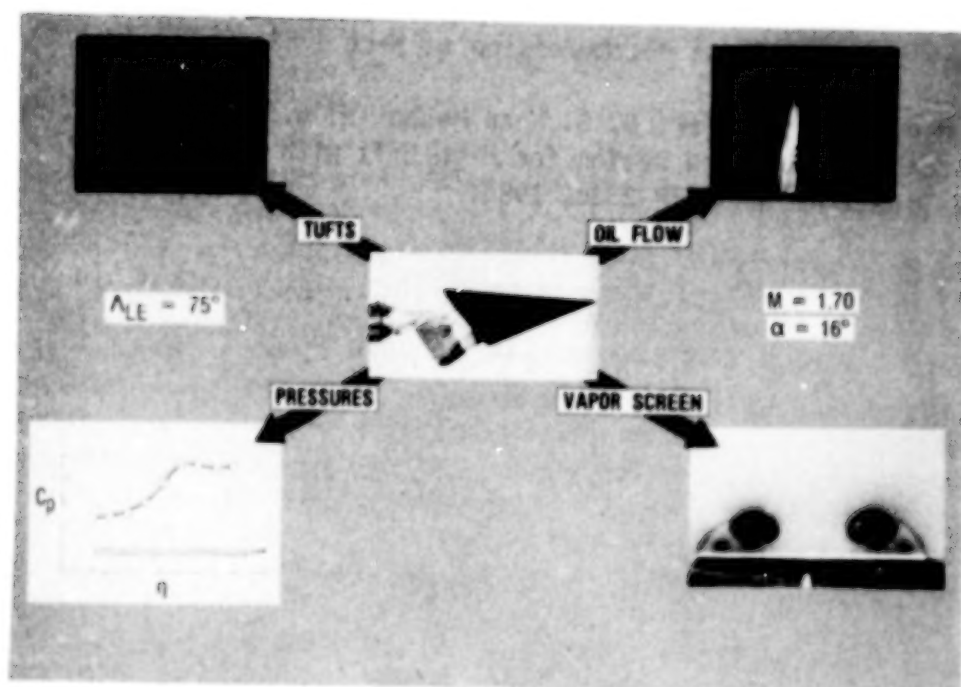


Figure 2. Types of experimental data.

ORIGINAL PAGE IS  
OF POOR QUALITY

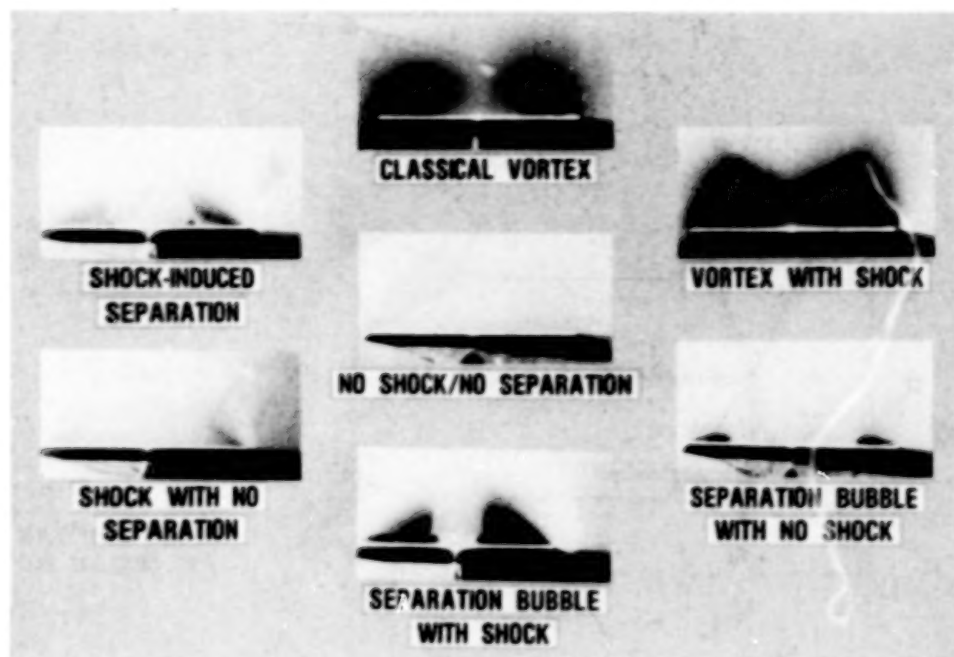


Figure 3. Flow classifications.

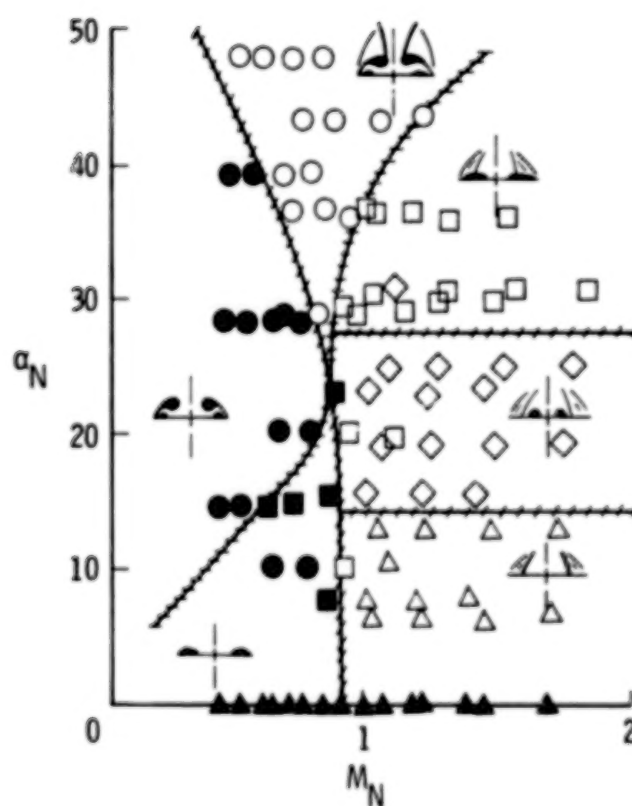


Figure 4. Classification of test data.



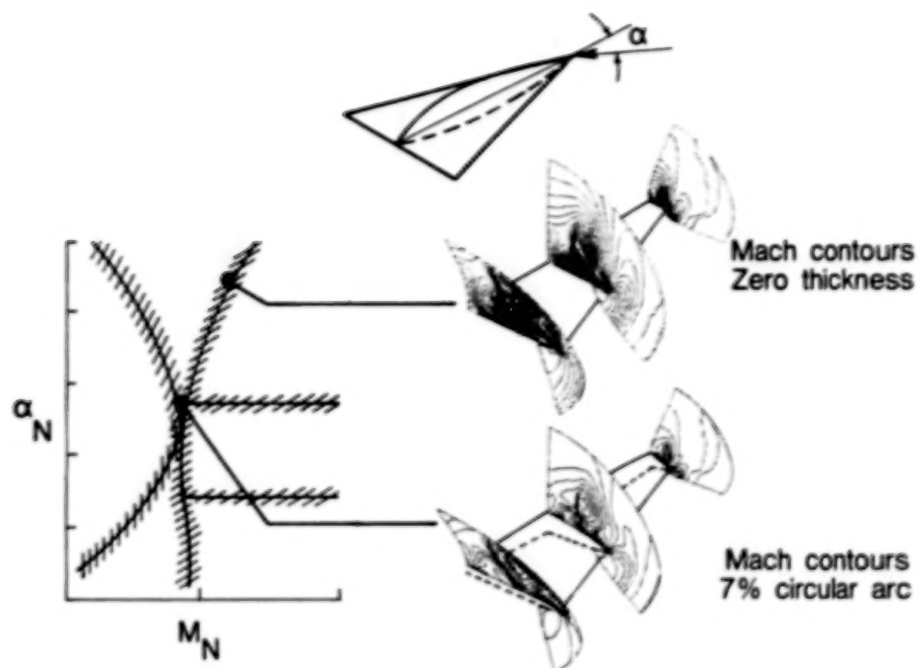


Figure 5. Estimated thickness effects.

Experimental flow visualization

$$\Lambda = 52.5^\circ - 75^\circ$$

$$M = 1.5 - 2.8$$

$$\alpha = 0^\circ - 20^\circ$$

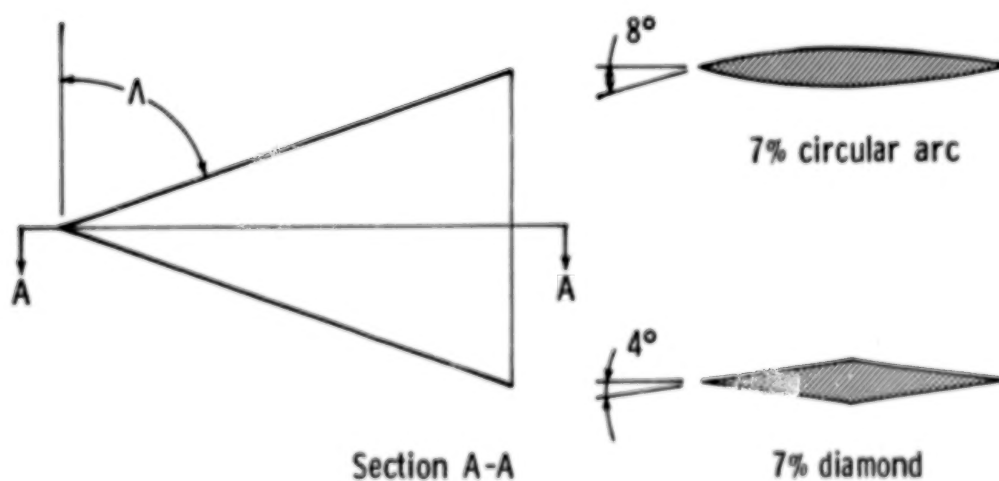


Figure 6. Elements of thickness effects study.

ORIGINAL PAGE IS  
OF POOR QUALITY

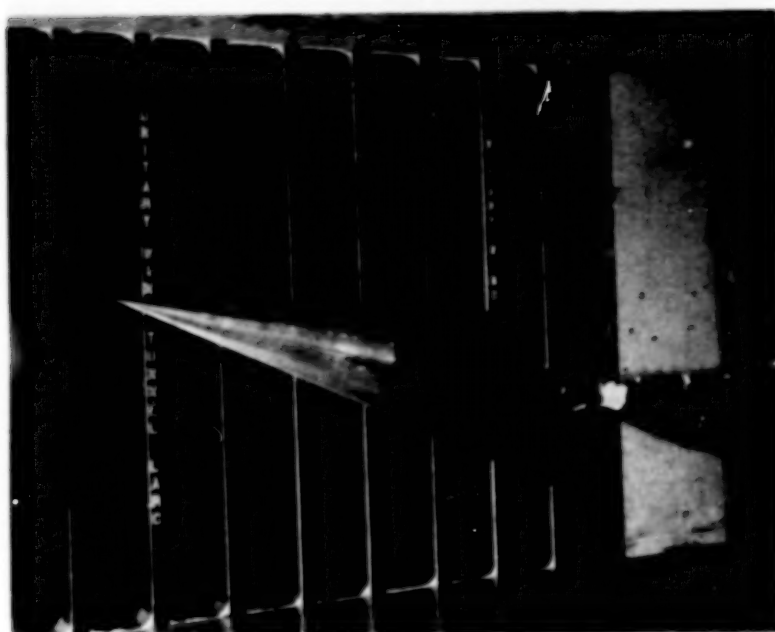


Figure 7. Photograph of  $\Lambda = 75^\circ$  conical wing-flap model.

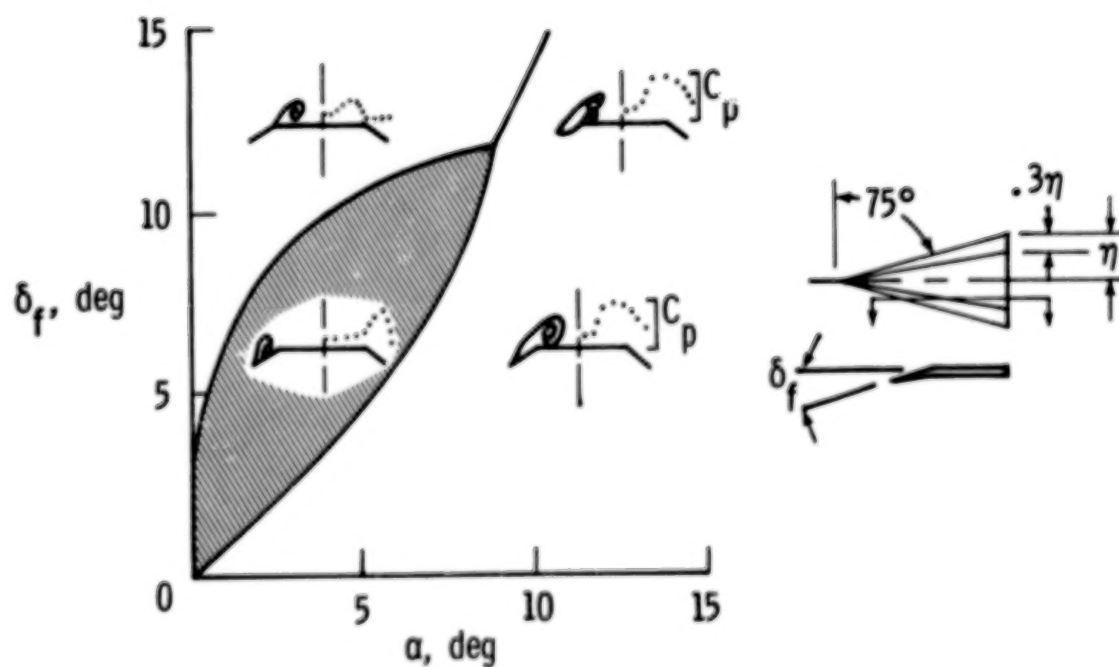


Figure 8. Typical wing-flap leeside flow characteristics.

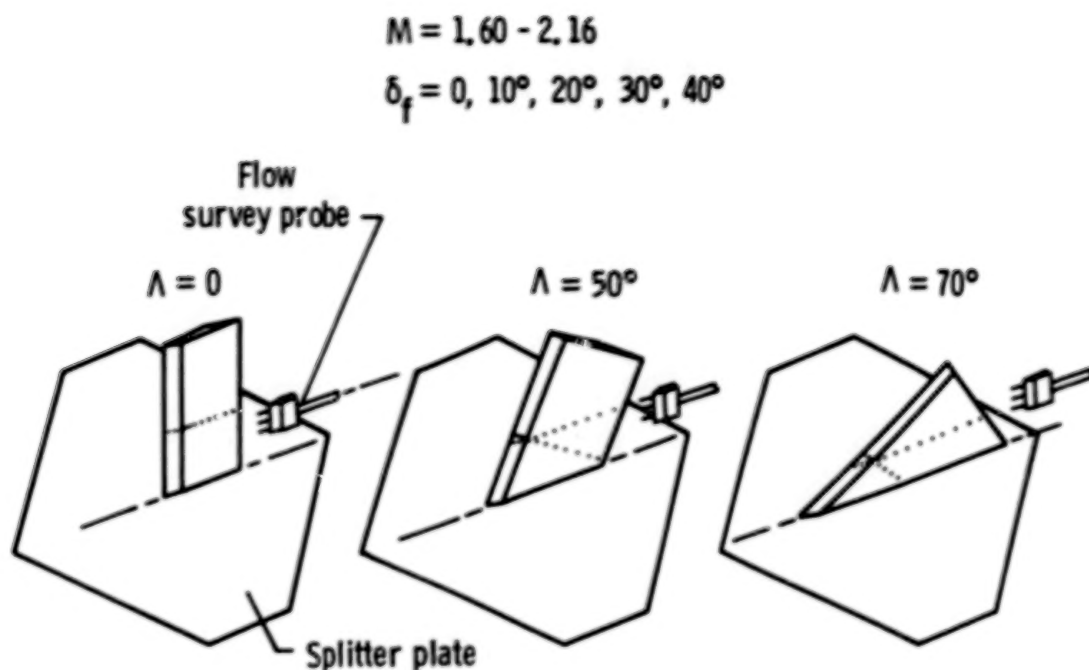


Figure 9. Elements of hinge-line study.

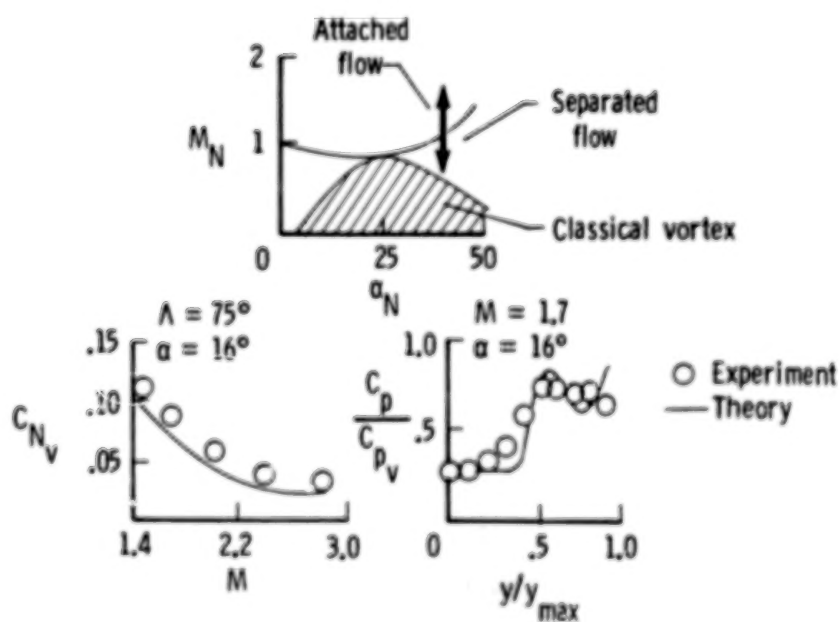


Figure 10. Modified linear-theory predictions for uncambered delta wing.

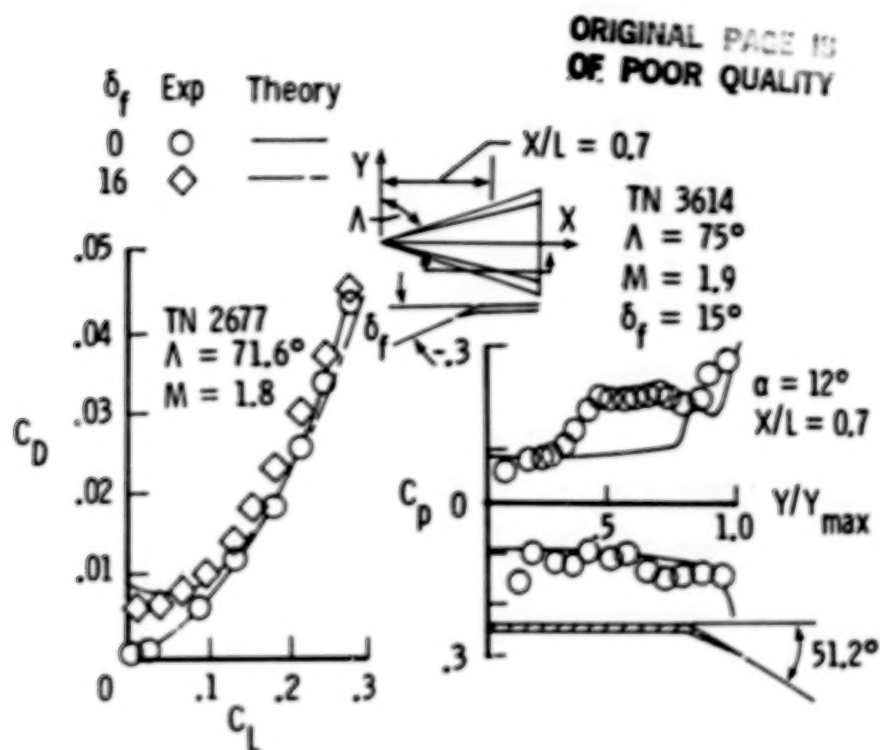


Figure 11. Modified linear-theory predictions for delta wing with leading-edge flap.

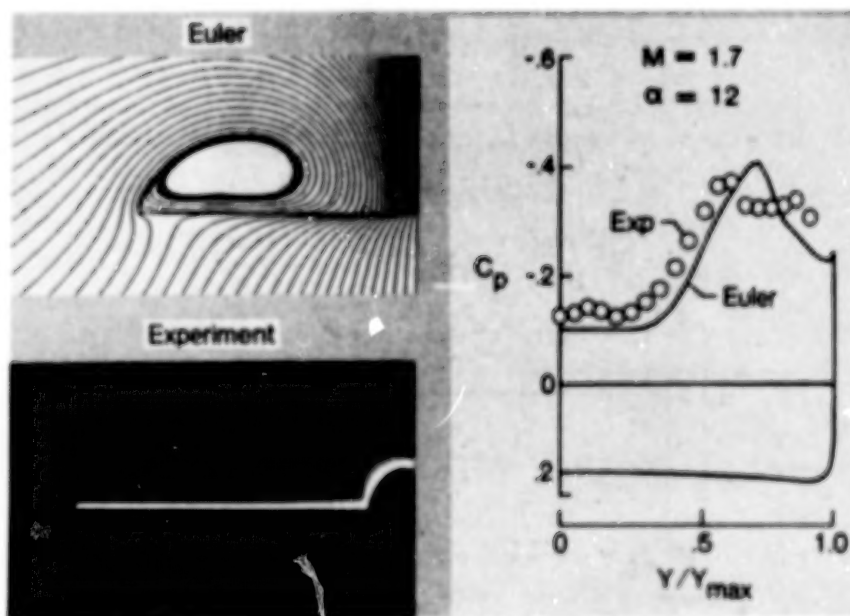


Figure 12. Experimental and Euler code results for flat delta wing at  $M = 1.7$ ,  $\alpha = 12^\circ$ ,  $\beta = 0^\circ$ .

ORIGINAL PAGE IS  
OF POOR QUALITY

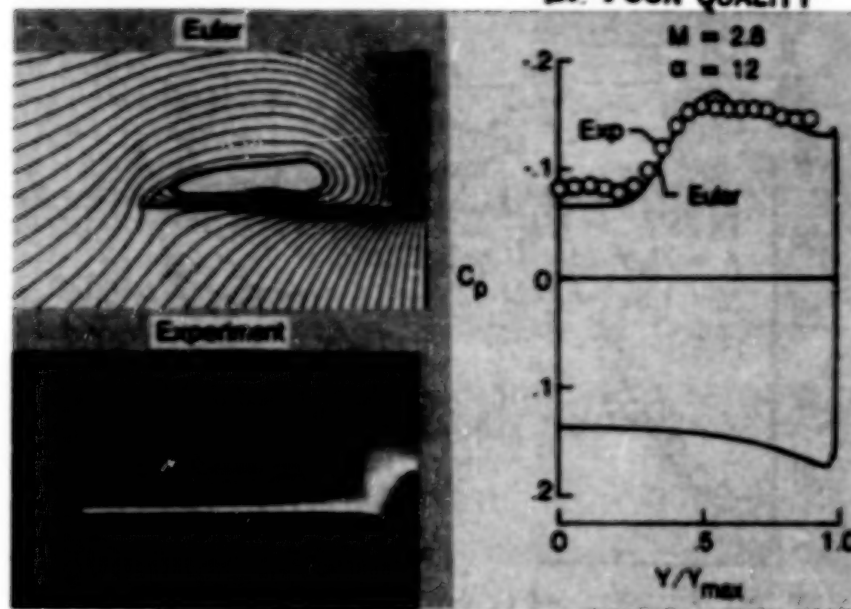


Figure 13. Experimental and Euler code results for flat delta wing at  $M = 2.8$ ,  $\alpha = 12^\circ$ ,  $\beta = 0^\circ$ .

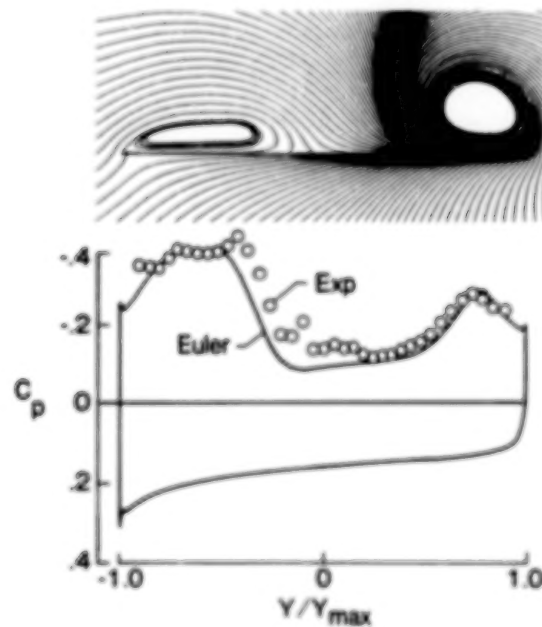


Figure 14. Experimental and Euler code results for flat delta wing at  $M = 1.7$ ,  $\alpha = 12^\circ$ ,  $\beta = 8^\circ$ .



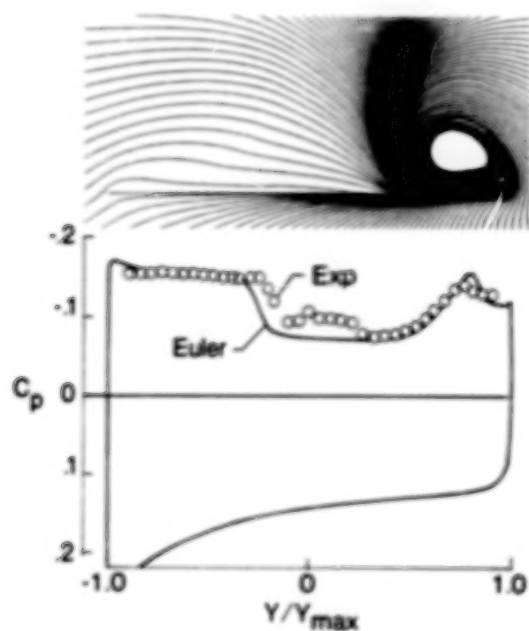


Figure 15. Experimental and Euler code results for flat delta wing at  $M = 2.8$ ,  $\alpha = 12^\circ$ ,  $\beta = 8^\circ$ .

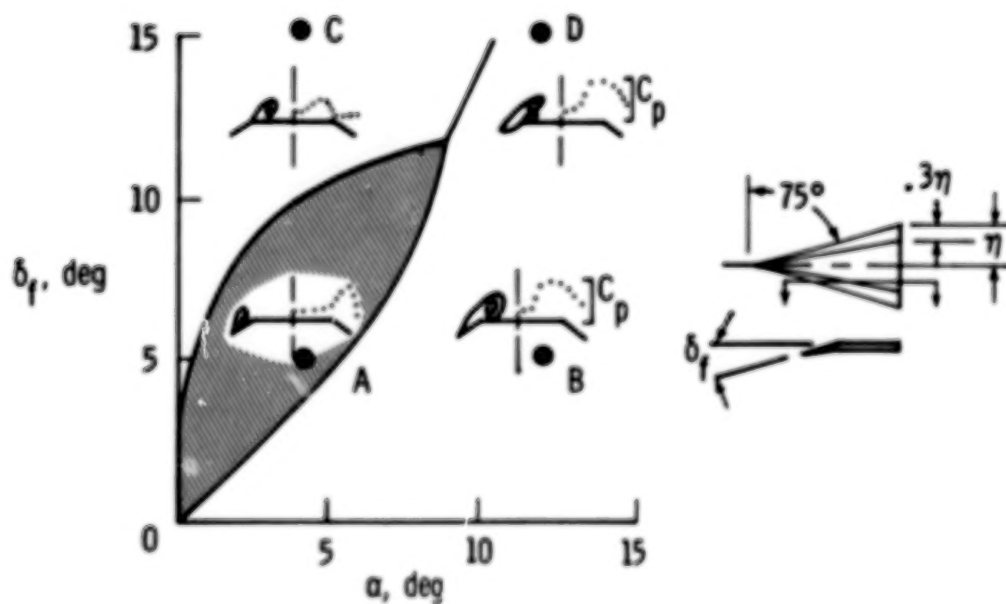


Figure 16. Illustration of the four wing flap conditions subjected to Euler code analysis.

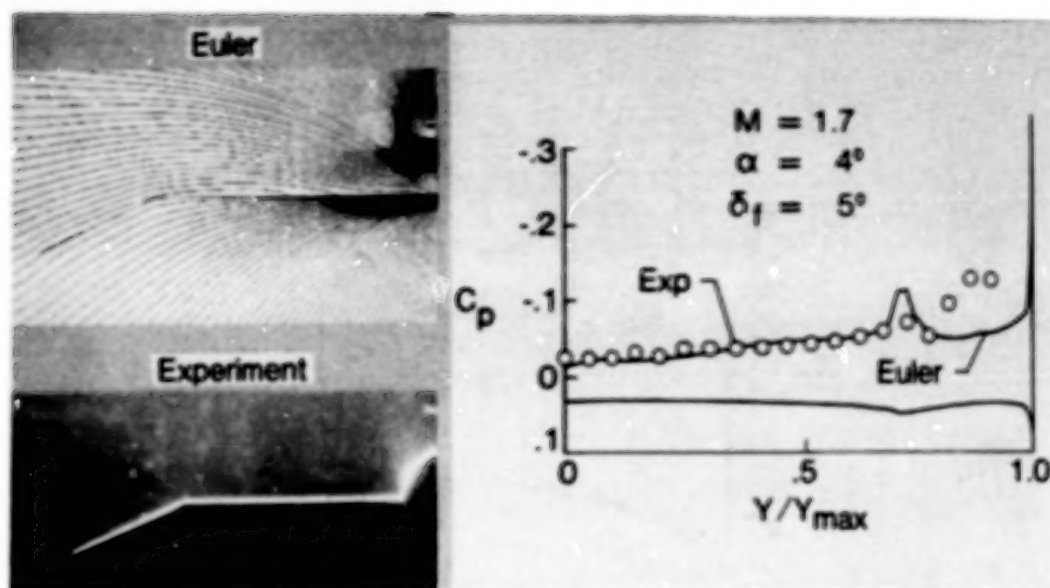


Figure 17. Experimental and Euler code results for wing flap at  $M = 1.7$ ,  $\alpha = 4^\circ$ ,  $\delta_f = 5^\circ$ .

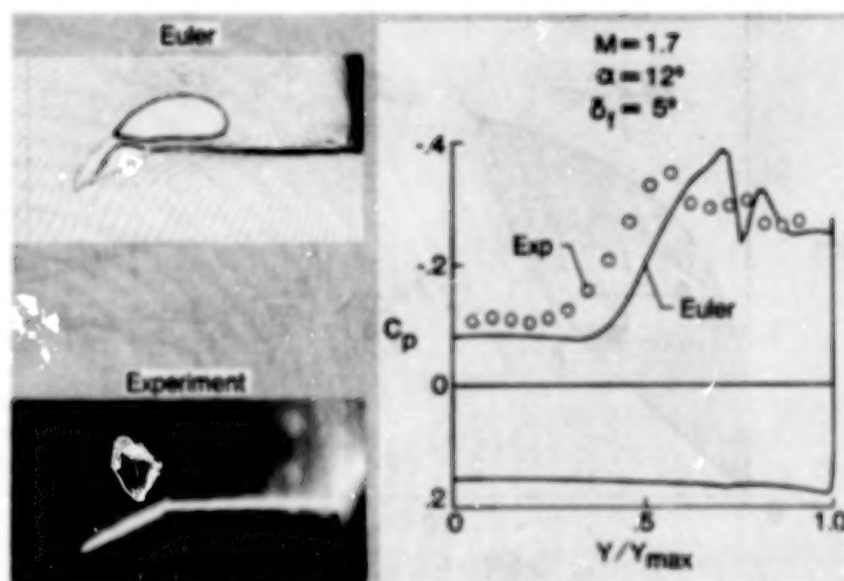


Figure 18. Experimental and Euler code results for wing flap at  $M = 1.7$ ,  $\alpha = 12^\circ$ ,  $\delta_f = 5^\circ$ .

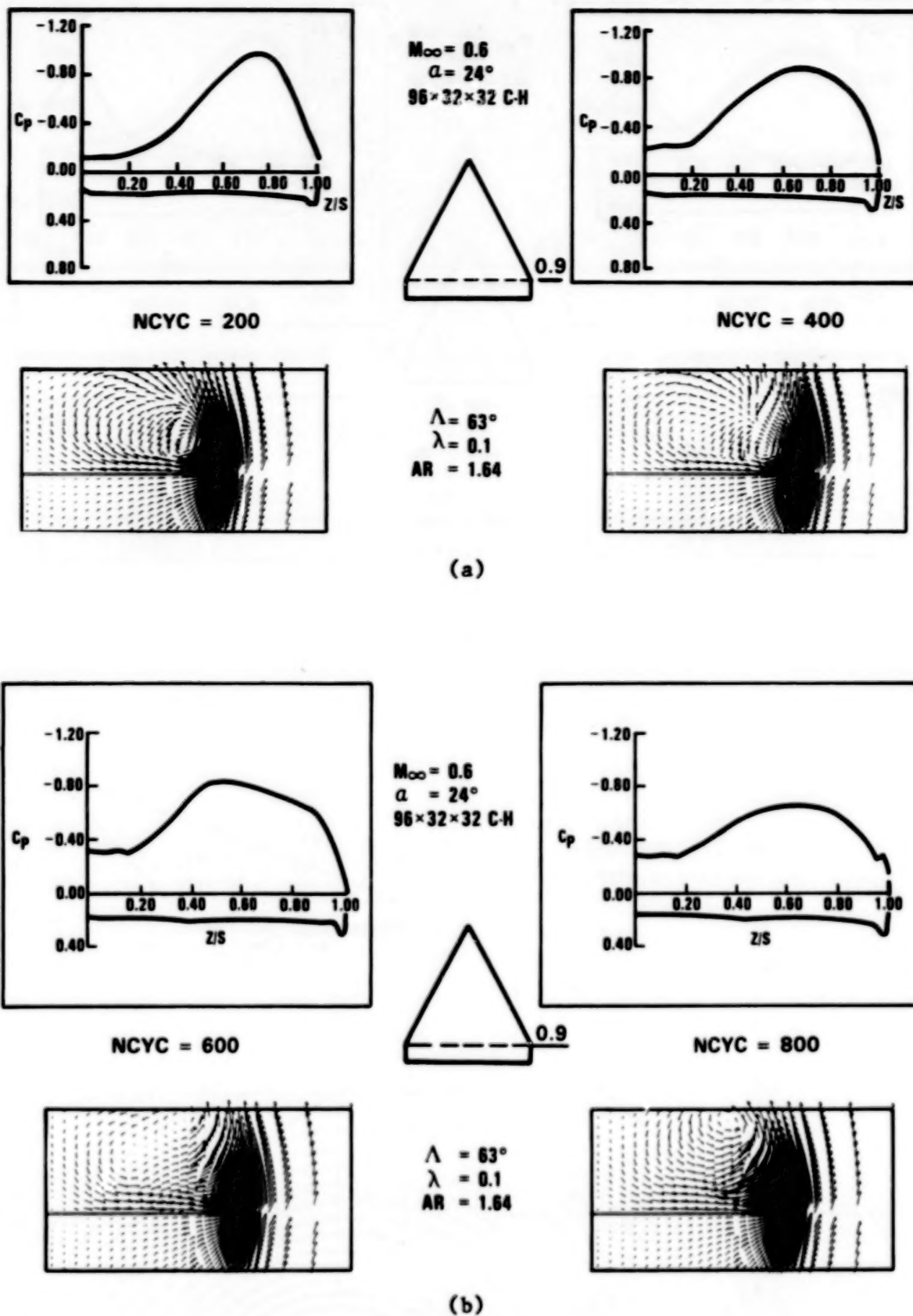


Figure 15. Spanwise pressure distributions and velocity vectors for six different times in integration process ( $x/c = .9$ ).

C-4

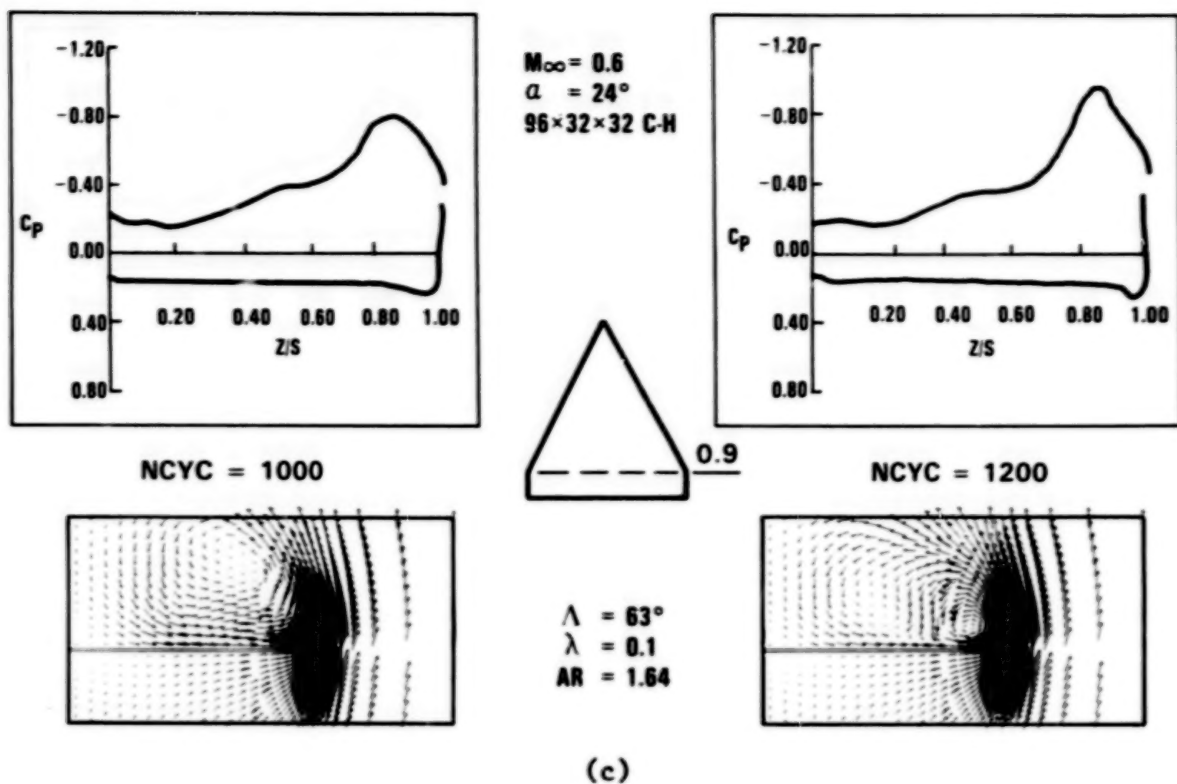


Figure 15. Concluded

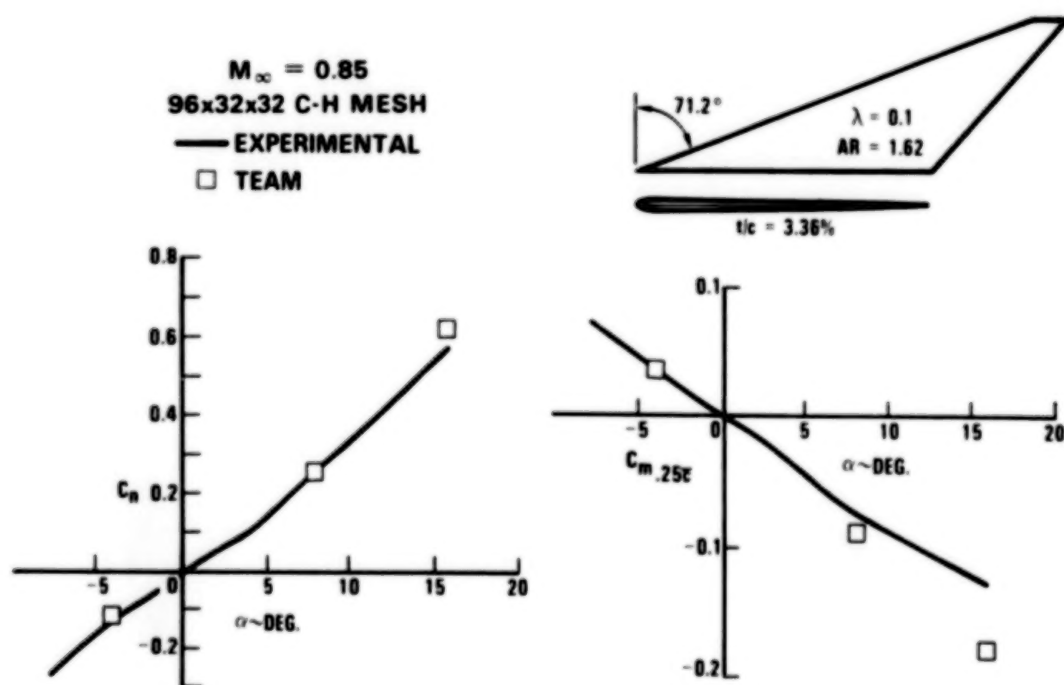


Figure 16. Computed and measured aerodynamic coefficients for an arrow wing.

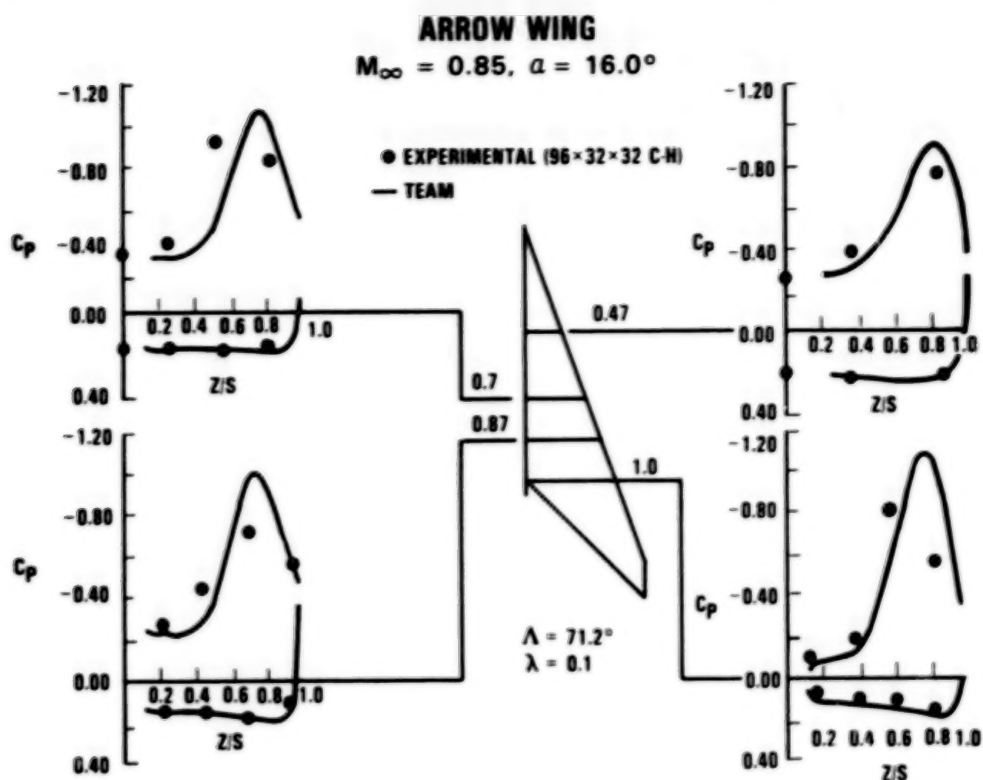


Figure 17. Computed and measured pressure distributions for four spanwise locations.

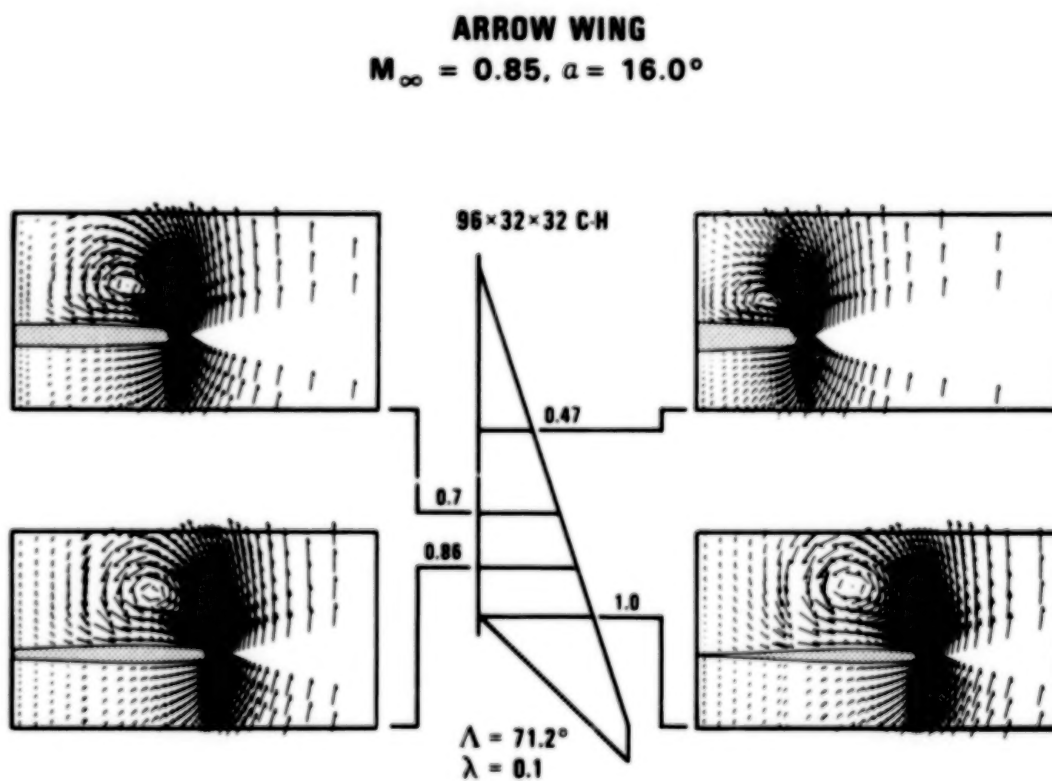


Figure 18. Computed velocity vectors for four spanwise locations.



EULER ANALYSIS OF AN ELLIPTIC MISSILE BODY  
AT ANGLES OF ATTACK

James R. Sirbaugh  
Air Force Wright Aeronautical Laboratories  
Wright-Patterson Air Force Base, Ohio

SUMMARY

The Euler code FL057 has been applied to a blunt nose smooth surface missile body shape. A range of angle of attacks was analyzed at Mach numbers of 0.55 and 2.0. A Mach number sweep from 0.55 to 2.0 was run for 12 degrees angle of attack. Experimental force and moment data were compared to Euler results at all Mach numbers and surface pressure data were compared at Mach 2.0. The Euler code agreed with the experimental data over the linear portion of the Mach 0.55 data and over the entire angle-of-attack range at Mach 2.0.

INTRODUCTION

The capability to predict aerodynamic characteristics of smooth surfaced missile bodies is required by weapons designers. Missile body prediction techniques need to be able to analyze subsonic, transonic, supersonic flows, subsonic pockets in supersonic flow and vortex flow. At present there is no available numerical method to analyze these flow regimes within reasonable time and cost limits. The Navier-Stokes equations are the most logical choice to perform the analysis, but at present, computers and algorithms are too slow to make the analysis practical. The Euler equations have been successfully applied to the Mach range in question, but viscous effects are not accounted for and therefore vortex flow prediction may be inaccurate. Other techniques are available which have a more limited range of application, such as full-potential, parabolized Navier-Stokes and free vortex sheet theory.

This paper presents the results of applying the Euler code FL057 to an elliptical missile body for a Mach number range of 0.55 to 2.0. The motivation behind the work was to determine if FL057 could be used to predict the aerodynamic characteristics of simple missile shapes at low supersonic speeds, where subsonic pockets exist at blunt noses and vortex flow exists at moderate angles of attack. At present only hybrid methods are used to analyze these flow conditions in a reasonable time limit. In addition to investigating the use of FL057 for low supersonic Mach numbers, subsonic and transonic Mach numbers were also considered.

PRECEDING PAGE BLANK NOT FILMED

## SYMBOLS

|              |  |
|--------------|--|
| A            | Missile body semi-major axis at a given body X-station |
| AL           | Angle of attack  |
| $A_{\max}$   | Missile body base semi-major axis                      |
| B            | Missile body semi-minor axis at a given body X-station |
| $B_{\max}$   | Missile body base semi-minor axis                      |
| $C_A$        | Axial force coefficient                                |
| $C_M$        | Pitching moment coefficient                            |
| $C_N$        | Normal force coefficient                               |
| $C_P$        | Coefficient of pressure                                |
| I, J, K      | Grid coordinates                                       |
| L            | Missile body length                                    |
| $M_{\infty}$ | Freestream Mach number                                 |
| X            | Missile body station measured relative to nose         |
| 3-D          | Three dimensional                                      |

## CONFIGURATION

The missile body is a simple shape built and tested for the purpose of developing and validating aerodynamic prediction methods. The missile body was one of three built with elliptical cross sections along the entire length of the model. The missile body used in this study had a 2.5 to 1.0 major to minor axis ratio (Figure 1). The two other missile bodies built had 2.0 to 1.0 and a 3.0 to 1.0 cross-section ratios. The semi-major axis varied along the body by the square root law

$$A = \frac{A_{\max}}{L^{1/2}} X^{1/2}$$

and the semi-minor axis varied along the body by the square root law

$$B = \frac{B_{\max}}{L^{1/2}} X^{1/2}$$

$A_{max}$  and  $B_{max}$  were the base semi-major and semi-minor axes and  $L$  was the missile body length. These missile bodies were tested in four stages. Stage one produced surface pressure data from eleven rows of spanwise pressure taps at Mach numbers from 1.5 to 5.0. During stage two, force and moments were taken for Mach numbers of 1.76 to 5.0. Stage three was a force and moment test for Mach numbers of 0.4 to 1.3. Stage four data were not available at the time of this analysis and were the Mach numbers 0.4 to 1.3 pressure tests. All testing was done at Arnold Engineering Development Center. References 1 and 2 contain detailed information of the test results.

#### EULER GRID AND FLOW SOLVER

The grid used for the Euler calculations was originally developed for predicting flow fields about delta wings and was modified for use on the test missile body shape. The grid topology is intended to provide adequate grid resolution at the missile nose while positioning the grid singularity on the plane of symmetry and out of regions of high flow gradients (Figure 2). The topology can best be thought of as a sheared O-H grid. Indicated in Figure 3 are the coordinate directions on the missile surface and a cut through the 3-D grid. The O portion of the O-H grid is formed by the I indexing grid lines that start on the lower plane of symmetry aft of the grid singularity and follow a path along the missile surface, around the leading edge and back to the upper plane of symmetry. The J indexing lines start at the missile surface and proceed outward to the far field. The K indexing lines start on the plane of symmetry forward of the grid singularity and follow paths along the missile going aft. Figure 4 is the downstream exit grid or maximum K grid layer. The base of the missile was extended downstream with solid surface boundary conditions being applied to the extension's outer surface. This extension does not resemble the wind tunnel model, but was required to perform the computations. The grid had 49 grid points in the I or wrap-around direction and 44 points in the K direction on the missile surface. There were 25 J layers of grid points extending outward from the surface to the far-field boundary.

The flow solver used was FLO57 without any special treatment for vortex flows (Reference 3). FLO57 has been applied previously to round and sharp leading-edge delta wing vortex flow problems for both subsonic and transonic Mach numbers. No attempt was made in generating the missile grid to align the 3-D grid with the bow shock shape. The bow shock is dependent on the configuration angle of attack (AL) and freestream Mach number. The Euler solution scheme uses centered difference approximation to the flux terms. Shock smearing will occur when the bow shock is unaligned with the grid, introducing an unknown amount of error in the solution. At the immediate nose of the configuration the shock should approximate the shape of the blunt nose and therefore align with the grid at moderate supersonic Mach numbers.

## FORCE AND MOMENT RESULTS

### $C_N$ Versus Alpha, $M_\infty = 0.55$

FL057 predicted lower  $C_N$ 's at Mach 0.55 (Figure 5) than were measured in the wind tunnel test in the nonlinear portion of the  $C_N$  versus the Alpha curve. At the low angle-of-attack range (0.0 - 6.0 degrees) the Euler and wind tunnel test results are in excellent agreement. It appears that the Euler method is not predicting vortex flow that is present in the wind tunnel data at the higher angles of attack.

### $C_A$ Versus Alpha, $M_\infty = 0.55$

The axial force coefficient was not measured directly in the wind tunnel test but was calculated by subtracting the measured base axial force from the balance measured total axial force. Two wind tunnel data points are plotted at each 2.0 and 4.0 degrees on Figure 6 corresponding to plus and minus angles of attack and indicate the degree of uncertainty of the wind tunnel axial force coefficients. The Euler results are inviscid and do not reflect skin friction axial force. To permit direct comparisons of the wind tunnel and Euler results the wind tunnel  $C_A$ 's have been shifted to match the Euler results at 0.0 degrees angle of attack. This shifting of wind tunnel is only useful if the axial force due to skin friction is constant at all angles of attack for a given Mach number. The wind tunnel  $C_A$  at 0.0 degrees angle of attack is due only to skin friction. The predicted Euler results are in general agreement with the experimental data.

### $C_M$ Versus $C_N$ , $M_\infty = 0.55$

The slopes of the  $C_M$  versus  $C_N$  curves (Figure 7) at  $C_N = 0.0$  for the Euler and wind tunnel data are in excellent agreement. Above a  $C_N$  value of 0.7 the two curves are in disagreement indicating the vortex contribution to  $C_M$  is not present in the Euler results.

### $C_N$ Versus Alpha, $M_\infty = 2.0$

The predicted Euler  $C_N$  values (Figure 8) are in excellent agreement with the wind tunnel data below 6.0 degrees angle of attack. Above 6.0 degrees the curve slopes of the two sets of data are in excellent agreement but appeared to be shifted by approximately 0.5 degrees angle of attack. There are several possible sources of the Euler angle-of-attack shift, although it is not clear as to which factor is most important. The Euler results are inviscid and therefore are missing the physics of boundary layer separation in the vortex region. The angle-of-attack shift is a delay in vortex formation which may be attributed to missing viscous effects. Another possible source of the angle-of-attack shift



is the smearing of the bow shock due to misalignment of the low shock and grid. Since FL057 is inviscid and little if any vortex lift was apparent in the Mach 0.55 results (Figure 5), the assumption must be made that the Mach 2.0 vortex formation is due largely to entropy production through the bow shock. Any smearing of the bow shock can effect the amount of entropy produced by the bow shock and thus shift the  $C_N$  versus curve.

#### $C_A$ Versus Alpha, $M_\infty = 2.0$

The wind tunnel test  $C_A$ 's have been shifted to match the Euler  $C_A$  value at 0.0 degree of angle of attack (Figure 9). The predicted values and trends of the Euler  $C$  values are in general agreement with the experimental data. The uncertainty of the experimental  $C_A$ 's was as great as 0.0056 at 4.0 degrees angle of attack.

#### $C_M$ Versus $C_N$ , $M_\infty = 2.0$

The Euler  $C_M$  versus  $C_N$  curve (Figure 10) is in good agreement with the wind tunnel data both in magnitude and in slope.

#### $C_N$ Versus Mach, Alpha = 12.0°

The Euler predicted  $C_N$  values were shown to disagree with the experimental data at subsonic and transonic Mach numbers by a large amount. The agreement improved as the Mach increased from 1.3 to 2.0 as shown in Figure 11.

#### $\Delta C_N$ Versus Mach, Alpha = 12.0°

A  $\Delta C_N$  parameter is plotted in Figure 12. The  $\Delta C_N$  is the vortex-induced increment or nonlinear addition to the  $C_N$  due to the vortex. The wind tunnel test ( $\partial C_N / \partial \alpha$ ) slope at zero angle of attack was multiplied by 12.0 degrees to compute a linear value of  $C_N$  at 12.0 degrees. The difference between the experimental value of  $C_N$  and computed linear  $C_N$  is  $\Delta C_N$ . The same extrapolation was used to compute  $\Delta C_N$  for the Euler results. Several interesting observations can be made by studying Figure 12. The experimental curve can be broken into two regions based on Mach number range. Region one is the subsonic and low supersonic Mach number range where the bow shock is weak. Region two starts about Mach 1.25 or 1.30, where the bow shock is strong enough to produce entropy. The two regions have different slopes and should be thought of as the viscous separation dominated region and bow shock entropy addition region.

The Euler results appear to have a more strongly Mach number dependent shape. At a purely subsonic Mach number of 0.55,  $\Delta C_N$  is very low and only increases a small amount by going to Mach 0.8 in comparison to the experimental data. At Mach numbers from 1.3 to 1.75 the Euler curve is considerably steeper than the experimental data. Mach 1.3 is the point where entropy levels begin to be strongly influenced by shock strength. It appears that the Euler  $\Delta C_N$  is



predominately a function of bow shock entropy production and not numerical or artificial viscosity. The Euler and experimental values of  $\Delta C_M$  at Mach numbers of 1.75 and 2.0 appear in reasonable agreement as was previously shown in Figure 8.

#### $C_M$ Versus Mach, Alpha = 12.0°

The Euler predicted value of  $C_M$  is relatively independent of Mach number. Only a slight decrease in  $C_M$  appears at transonic Mach numbers. The wind tunnel data indicated a strong dependency on Mach number in the Mach 0.8 to 1.1 range. Above Mach 1.3 the Euler and experimental values of  $C_M$  are in good agreement. A discrepancy in  $C_M$  between Euler and experiment appears at a Mach number of 2.0 in Figure 13, but is not as apparent in Figure 10.

#### SURFACE PRESSURE DATA

The Euler and wind tunnel  $C_p$  values are plotted against semi-span for four X-stations in Figures 14-25. The nose of the missile is X = 0.0 station and the missile base is X = 36.0 station. The computational grid points did not lie precisely on the required X-stations; therefore, all computational grid points within a prescribed distance to the required X-station were plotted. The method of selecting a computational grid was examined for accuracy and does not contribute any discrepancies that may be visible in the  $C_p$  comparison plots, Figures 14-25.

The 4.0 degree angle-of-attack results indicated an attached "potential like" flow over the entire length of the missile (Figures 14-17). The Euler results agree in shape with the wind tunnel data, but appear to be shifted in a more negative  $C_p$  direction than the wind tunnel results. At 8.0 degrees angle of attack the Euler results still indicate an attached "potential like" flow while the experimental data have signs of vortex separation starting at X-station 16.0 (Figures 18-21). The shift in  $C_p$  of the Euler results still appears and is roughly of the same magnitude. The  $C_p$  shift is constant even at 12.0 degrees angle of attack (Figures 22-25) on the lower surface. The reason for  $C_p$  shift is not obvious and may be due to not properly capturing the bow shock. A smeared bow shock can introduce angularity to the flow impinging on the missile body and create an apparent angle-of-attack shift. At 12.0 degrees angle of attack both the Euler and wind tunnel data indicate vortex separation (Figures 22-25). The wind tunnel data indicate a more forward separation point than does the Euler results. At X-stations 25.6 and 35.2 (Figures 24 and 25) the Euler and experimental  $C_p$ 's indicate that the secondary vortex may have a significant effect on the strength and position of the primary vortex. The Euler results have a single vortex that has a larger peak pressure and is more outboard than the experimental data. The secondary vortex is also visible in the experimental data. The effect of a secondary vortex is to move the primary vortex inboard and thus reduce the peak pressure of the primary vortex.

## VORTEX FLOW FIELD

Plotted in Figure 26 is the velocity flow field at the X-station 35.2 for Mach 2.0 and 12.0 degrees angle of attack. The vortex region can clearly be seen along with the high velocities occurring at the leading edge. To better visualize the flow region, a "constrained particle path" plot was made (Figure 27). At different locations in the X-station 35.2 vertical plane particles are released and allowed to trace paths as they are carried along by the cross flow velocities. The components of velocity aligned with the body axis are considered zero in this process, causing all "particles" to remain in the X-station vertical plane. The area of vortex flow is clearly visible. Figure 28 is a plot of local static pressure normalized by freestream and should provide information valuable to a designer.

## CONCLUDING REMARKS

The accuracy of the FLO57 Euler code is dependent on Mach number for the blunt nose smooth surface missile body used in this investigation. The formation and strength of the vortex appear dependent on the supersonic nose shock and not on surface viscous effects. The code is accurate and useful in the linear angle-of-attack range at both subsonic and supersonic Mach numbers. Sufficient entropy is produced by bow shocks at Mach numbers of 1.7 and above to confidently apply the code at higher angles of attacks for freestream Mach numbers above 1.7.

All Euler calculations presented in this paper were generated on the NASA Ames Cray XMP computer using approximately 0.9 million words in core and 1.0 million words out of core. All out-of-core memory resided on the 16 million word SSD using "buffer in" and "buffer out" statements to transfer data. A typical case required 500 iterations to converge from an initial guess of freestream conditions, which corresponds to approximately 600.0 seconds of CPU time and 10.0 seconds of IO time. Convergence criteria were an average residual of  $1.0 \times 10^{-5}$  plus  $C_N$  and  $C_A$  remaining constant for 20 iterations.

## REFERENCES

1. Amidon, P.F., "Supersonic Aerodynamic Characteristics of Elliptical Cross Section Bodies," AIAA Paper No. 85-1607, 1985.
2. Sellers, M.E., "Static Stability Test of Three Elliptic Missile Body Configurations," Arnold Engineering Development Center, Telehoma, Tenn., AEDC-TSR-85-P8, May 1985.
3. Jameson, A., and Baker, T.J., "Multigrid Solution of the Euler Equations for Aircraft Configurations," AIAA Paper No. 84-0093, 1984.

## 2.5: 1.0 ELLIPTIC MISSILE BODY

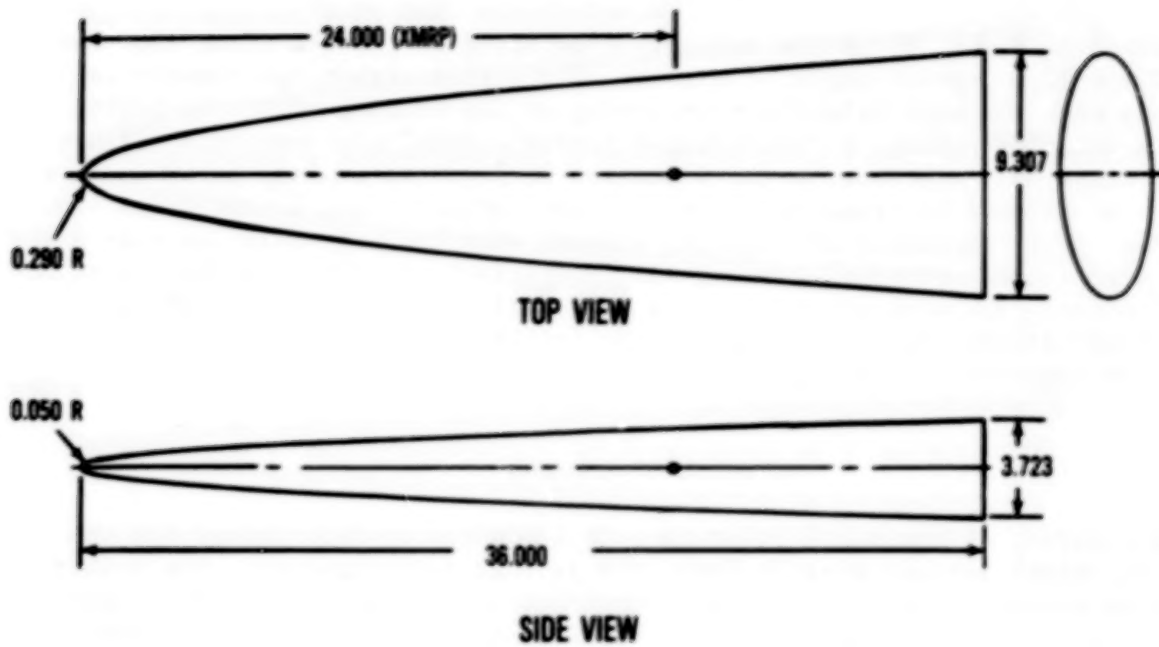


Figure 1.- Wind tunnel model (from ref. 2).

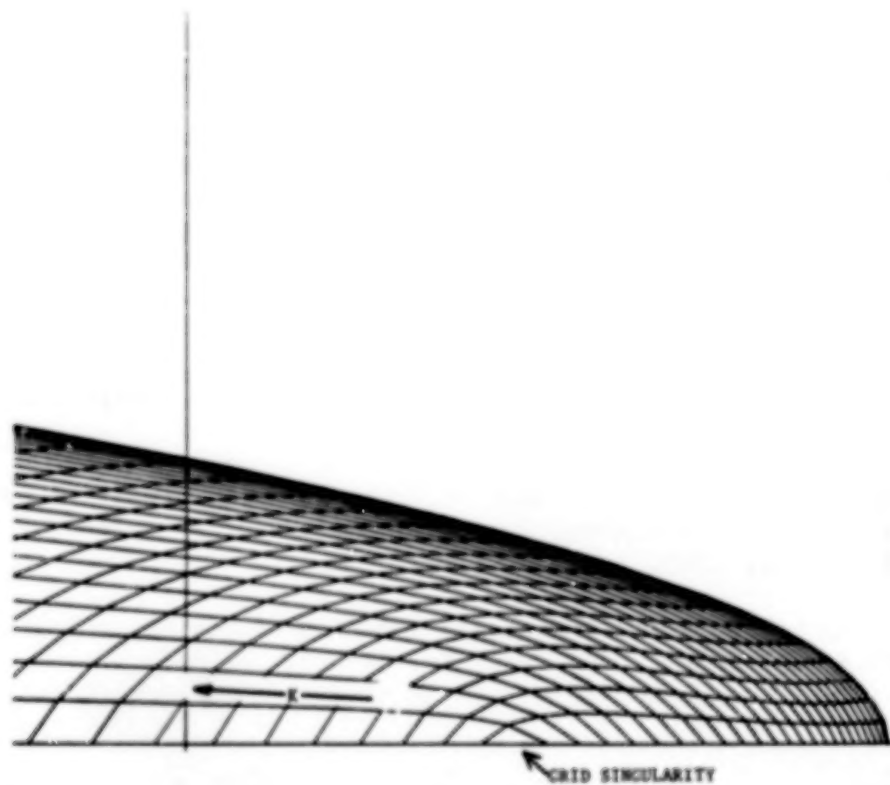


Figure 2.- Missile surface grid in nose region.

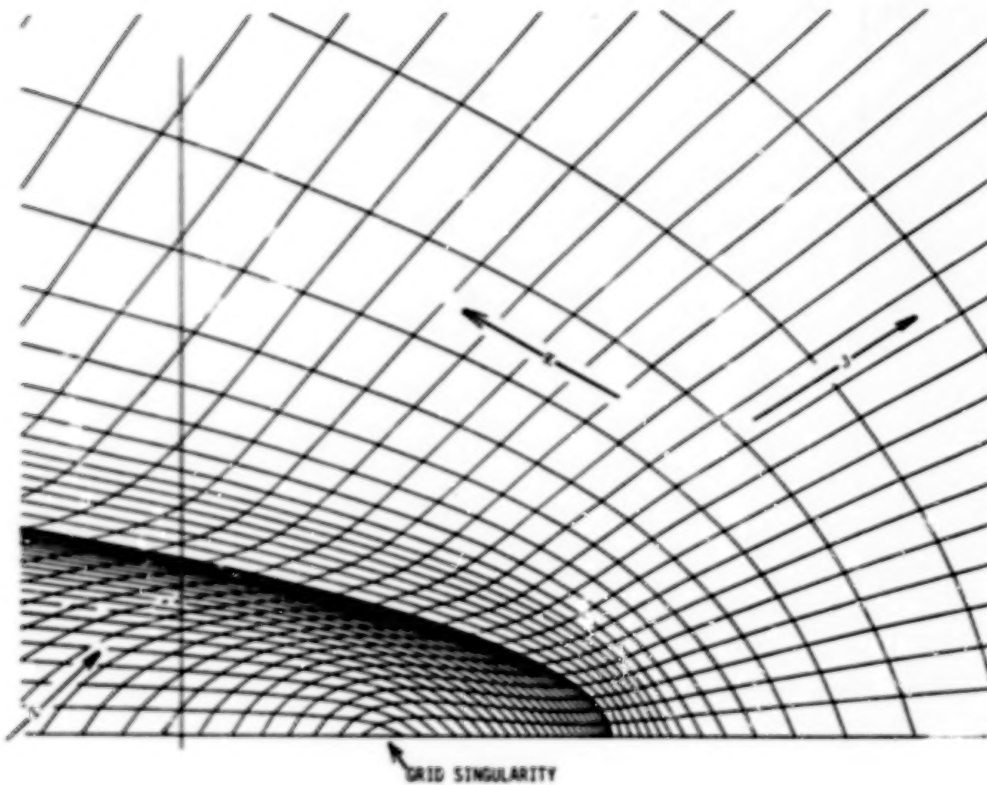


Figure 3.- Missile 3-D grid.

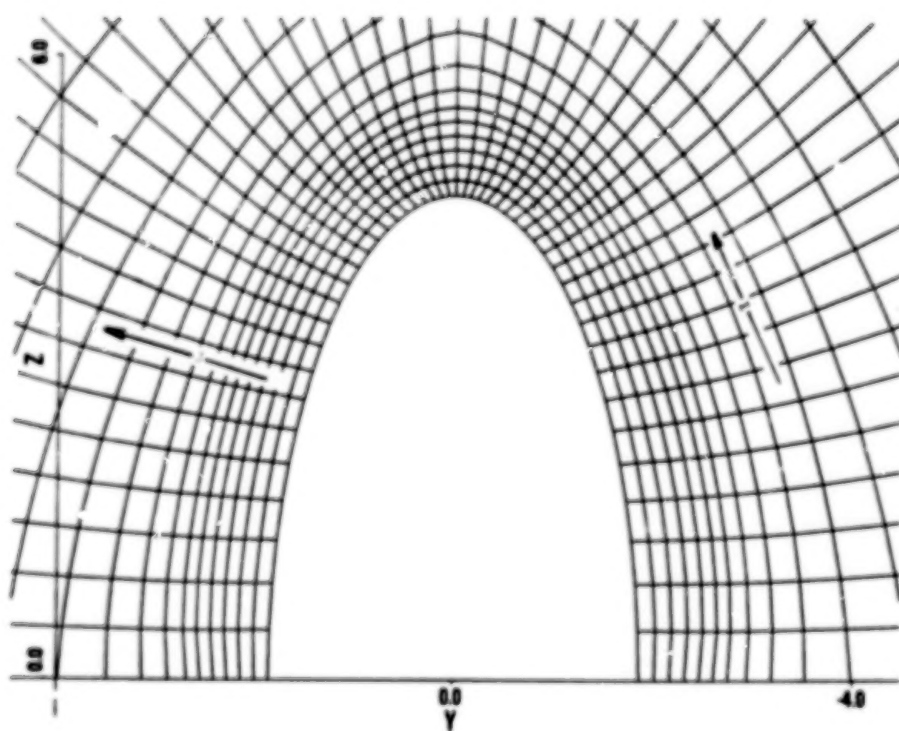


Figure 4.- Missile base grid.

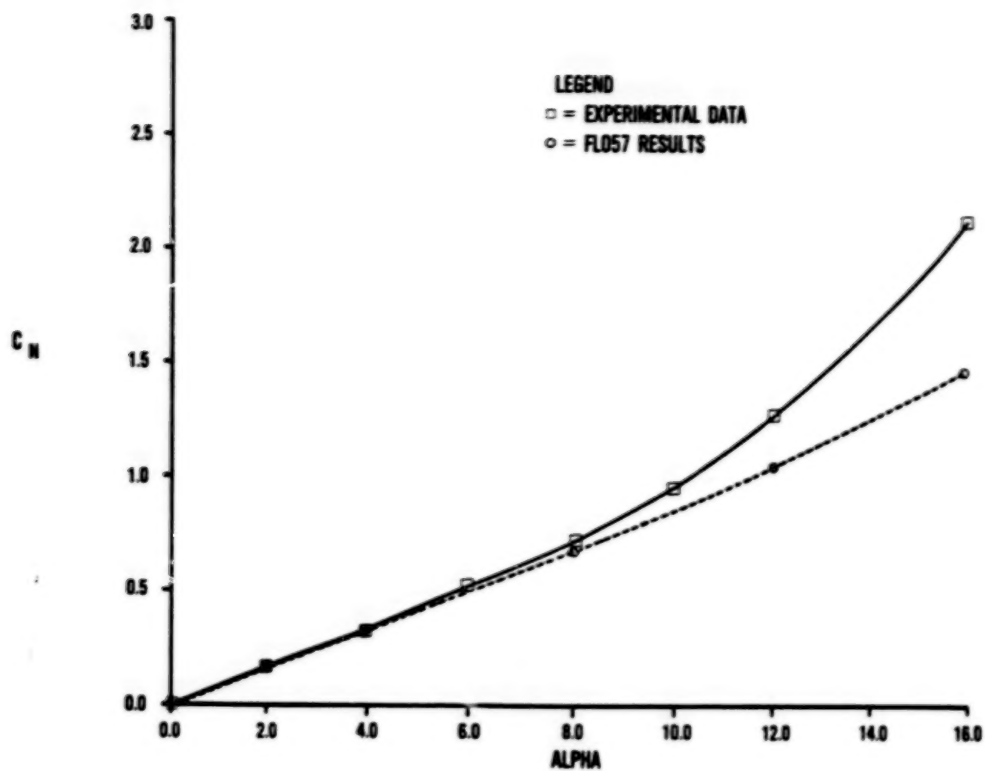


Figure 5.- Comparison of Euler and Ref. 1,  $C_N$  versus  $\alpha$ .

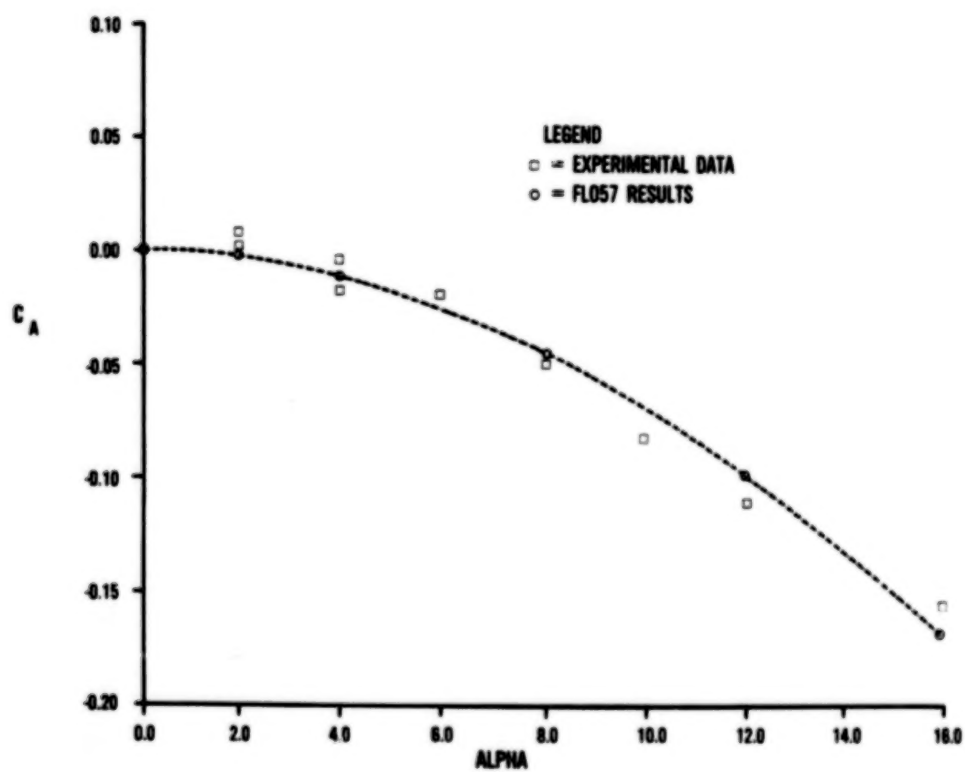


Figure 6.- Comparison of Euler and Ref. 1,  $C_A$  versus  $\alpha$ .



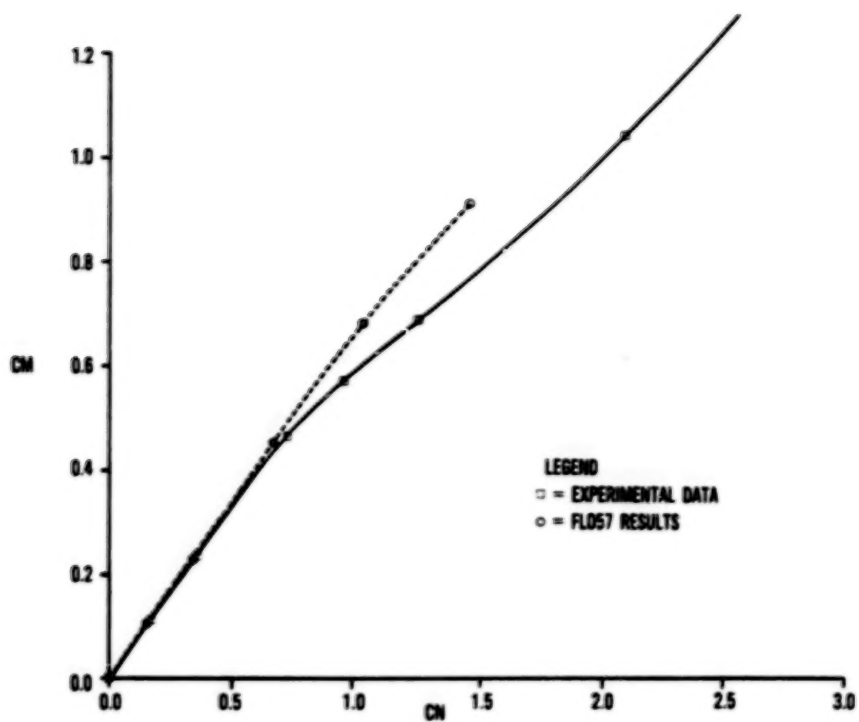


Figure 7.- Comparison of Euler and Ref. 1,  $C_M$  versus  $C_N$ .

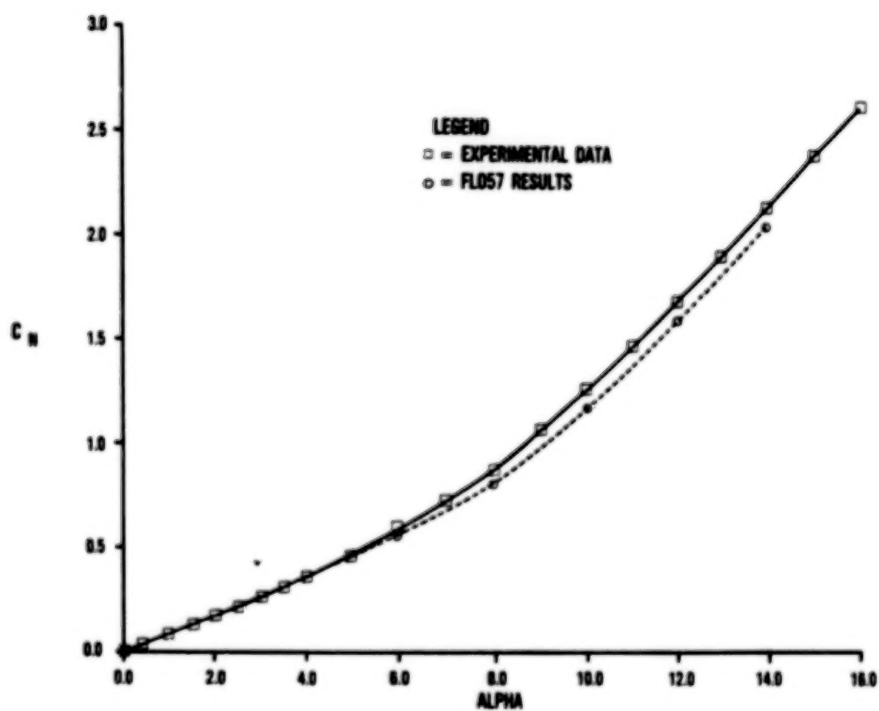


Figure 8.- Comparison of Euler and Ref. 1,  $C_N$  versus  $\alpha$ .

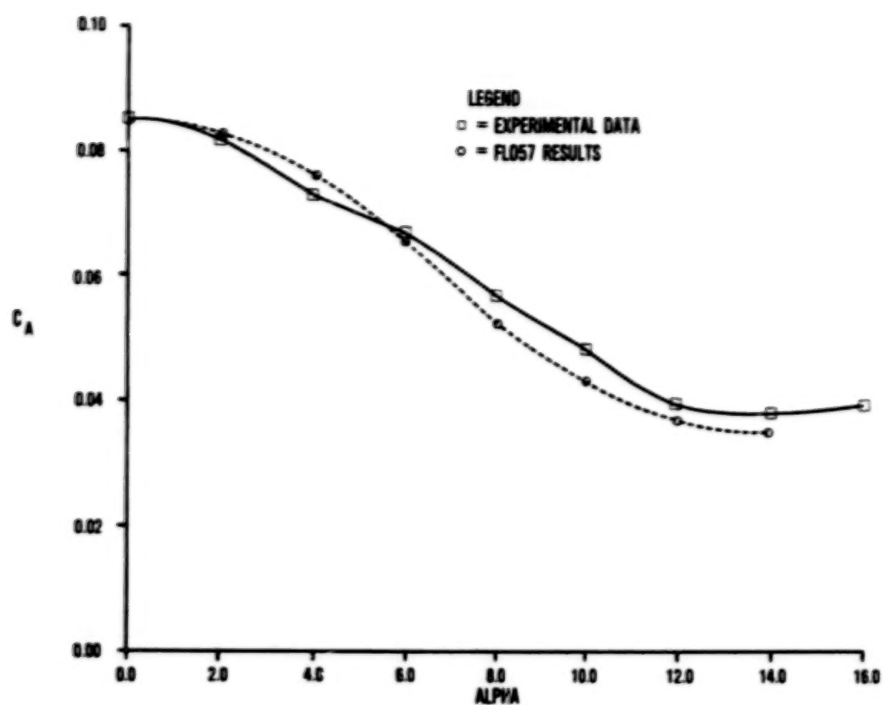


Figure 9.- Comparison of Euler and Ref. 1,  $C_A$  versus  $\alpha$ .

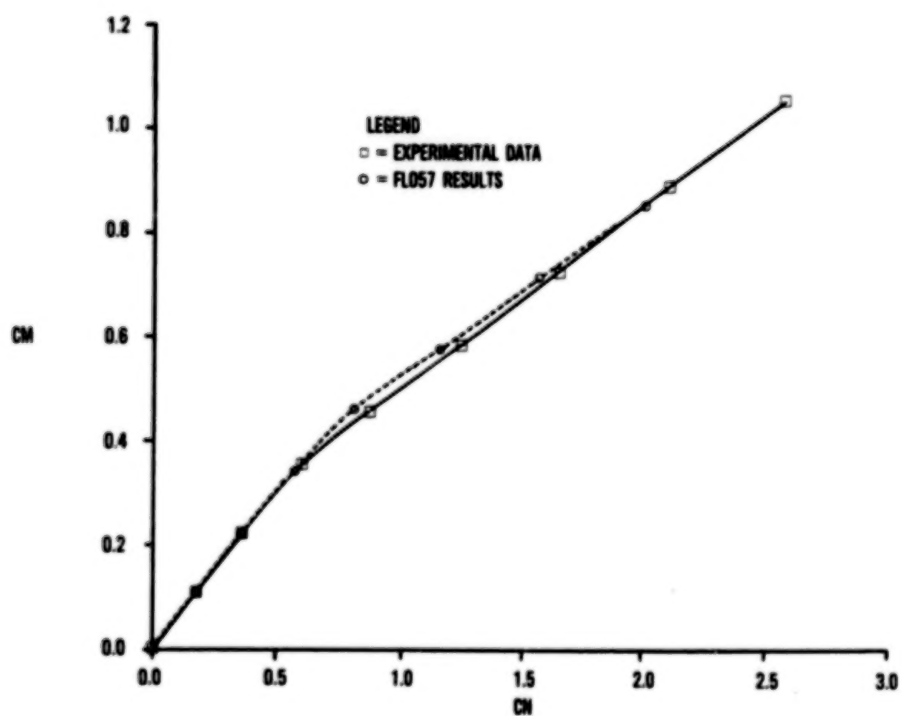


Figure 10.- Comparison of Euler and Ref. 1,  $C_n$  versus  $C_N$ .

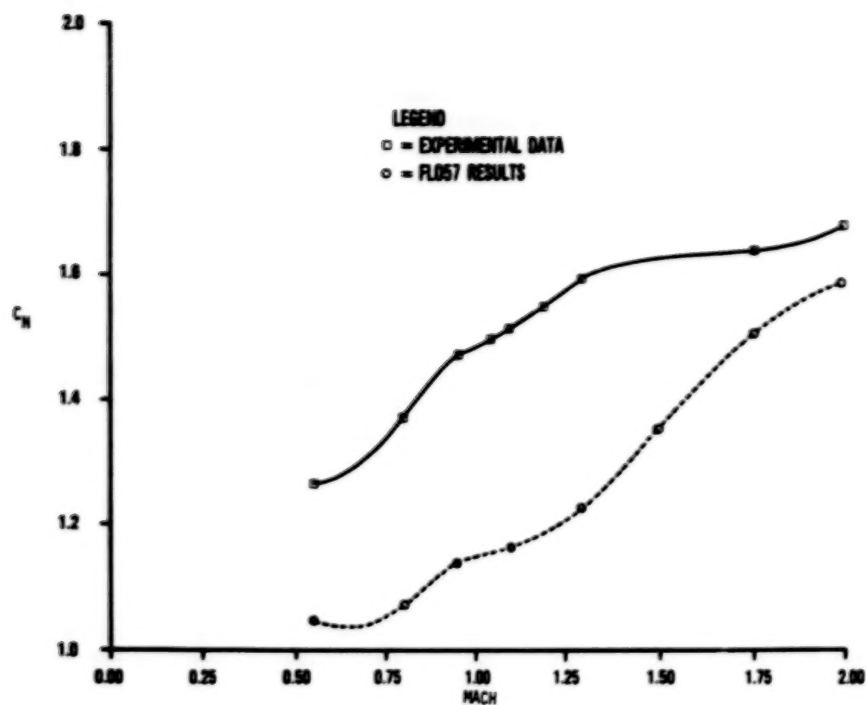


Figure 11.- Comparison of Euler and Ref. 1,  $C_N$  versus Mach,  $AL = 12.0$  degrees.

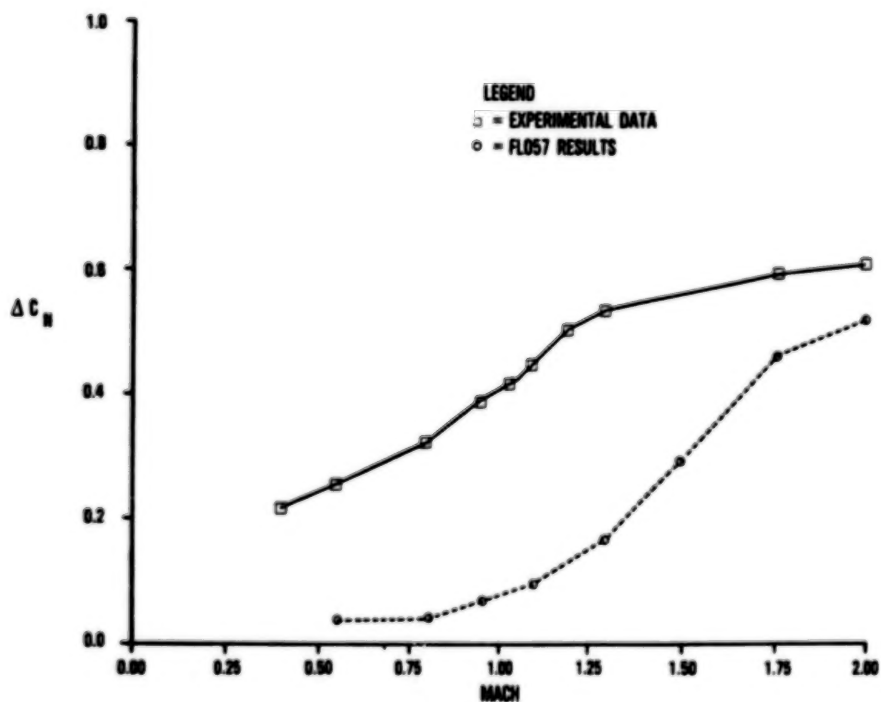


Figure 12.- Comparison of Euler and Ref. 1,  $\Delta C_N$  versus Mach,  $AL = 12.0$  degrees.

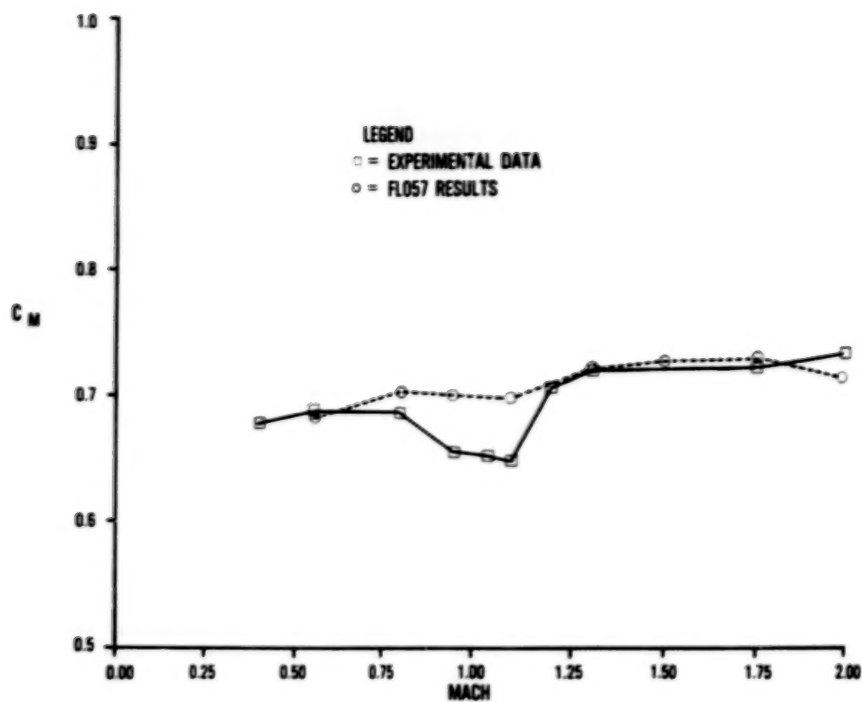


Figure 13.- Comparison of Euler and Ref. 1,  $C_M$  versus Mach,  $AL = 12.0$  degrees.

X STATION = 3.20

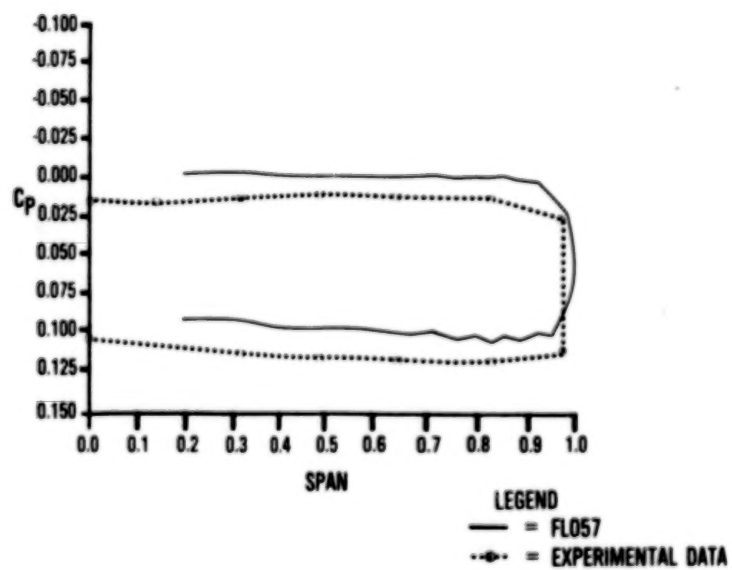


Figure 14.- Comparison of Euler and Ref. 1,  $C_p$  data,  $M_\infty = 2.0$ ,  $AL = 4.0$ ,  $X = 3.20$ .

X STATION = 16.0

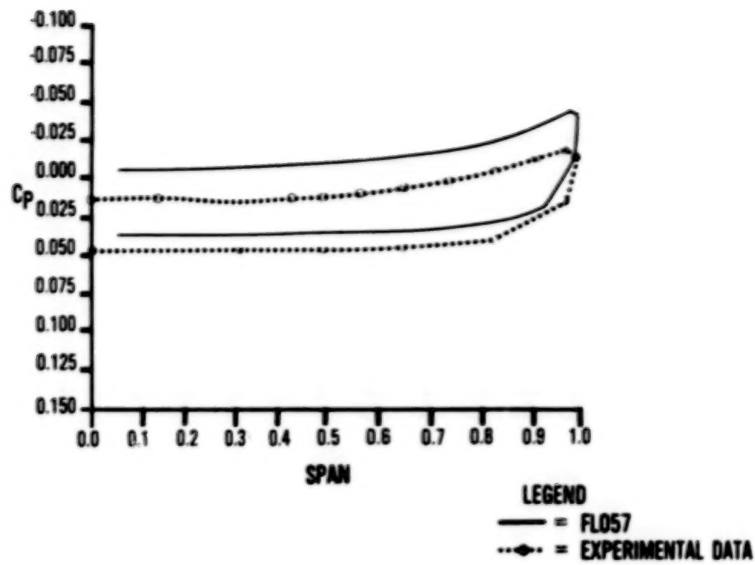


Figure 15.- Comparison of Euler and Ref. 1,  $C_p$  data,  
 $M_\infty = 2.0$ ,  $AL = 4.0$ ,  $X = 16.0$ .

X STATION = 25.6

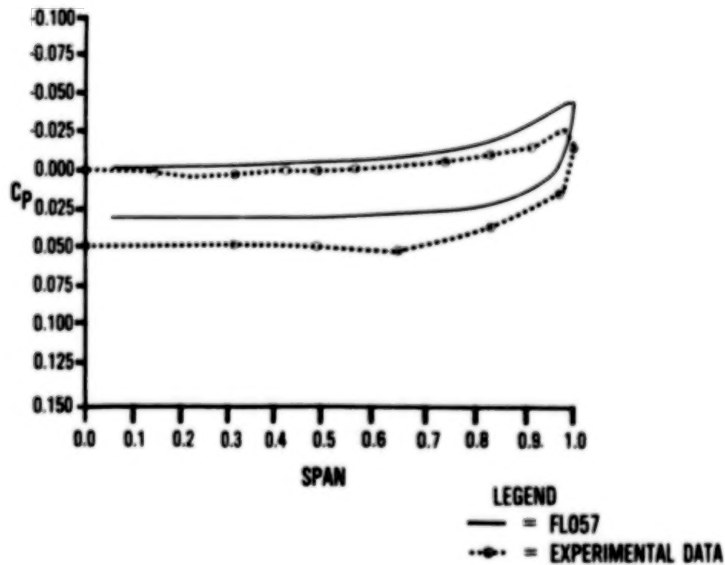


Figure 16.- Comparison of Euler and Ref. 1,  $C_p$  data,  
 $M_\infty = 2.0$ ,  $AL = 4.0$ ,  $X = 25.6$ .



X STATION = 35.2

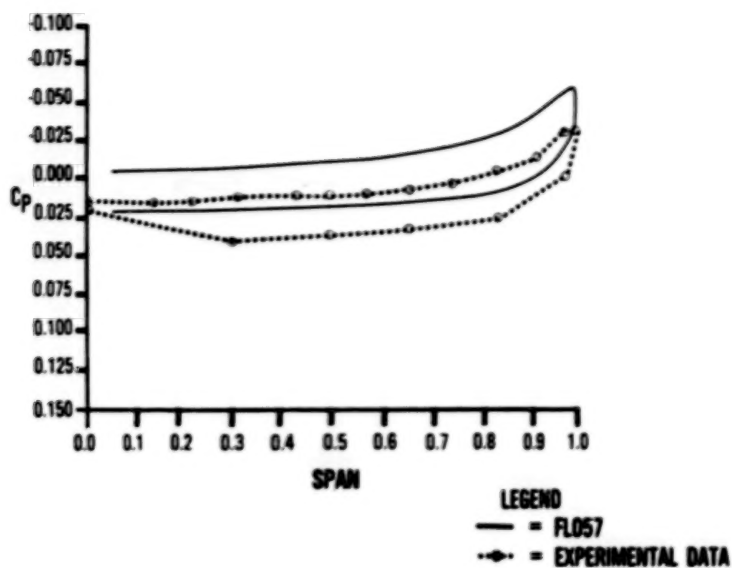


Figure 17.- Comparison of Euler and Ref. 1,  $C_p$  data,  
 $M_\infty = 2.0$ ,  $AL = 4.0$ ,  $X = 35.2$ .

X STATION = 3.20

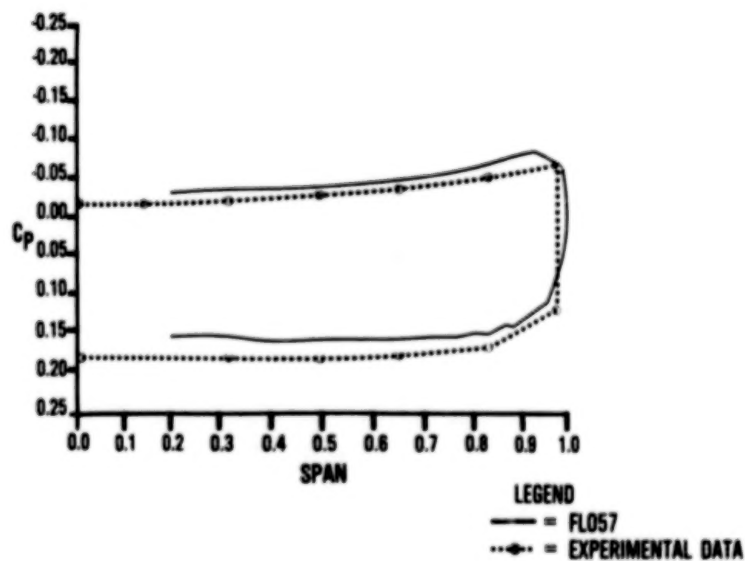


Figure 18.- Comparison of Euler and Ref. 1,  $C_p$  data,  
 $M_\infty = 2.0$ ,  $AL = 8.0$ ,  $X = 3.20$ .

X STATION = 16.0

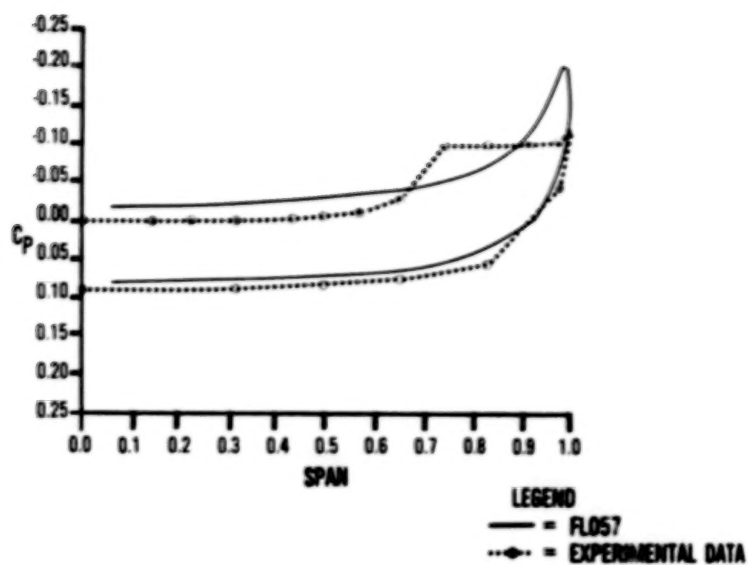


Figure 19.- Comparison of Euler and Ref. 1,  $C_p$  data,  
 $M_\infty = 2.0$ ,  $AL = 8.0$ ,  $X = 16.0$ .

X STATION = 25.6

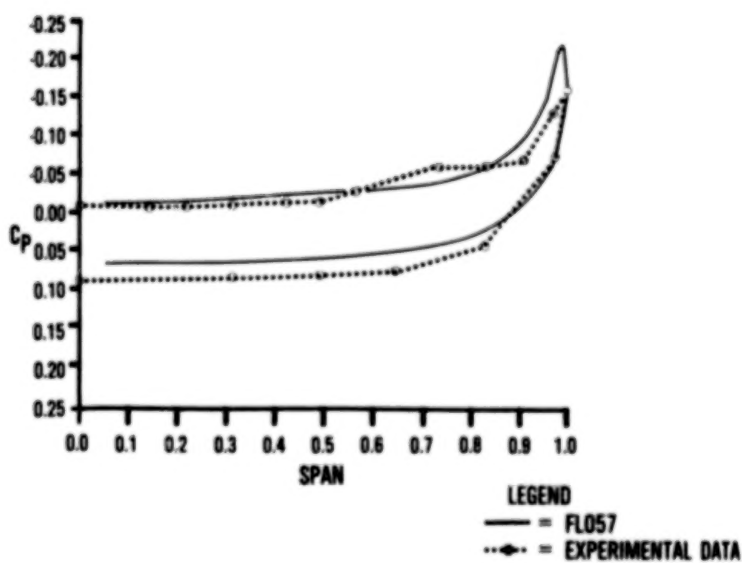


Figure 20.- Comparison of Euler and Ref. 1,  $C_p$  data,  
 $M_\infty = 2.0$ ,  $AL = 8.0$ ,  $X = 25.6$ .

X STATION = 35.2

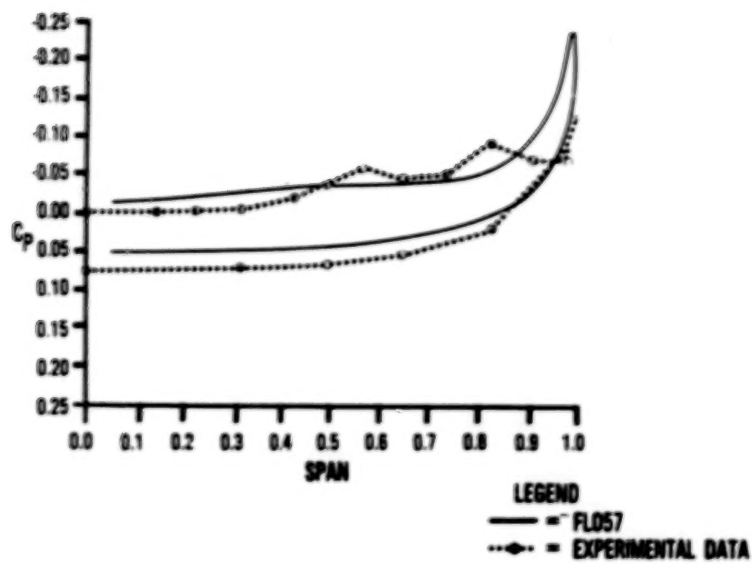


Figure 21.- Comparison of Euler and Ref. 1,  $C_p$  data,  $M_\infty = 2.0$ ,  $AL = 8.0$ ,  $X = 35.2$ .

X STATION = 3.20

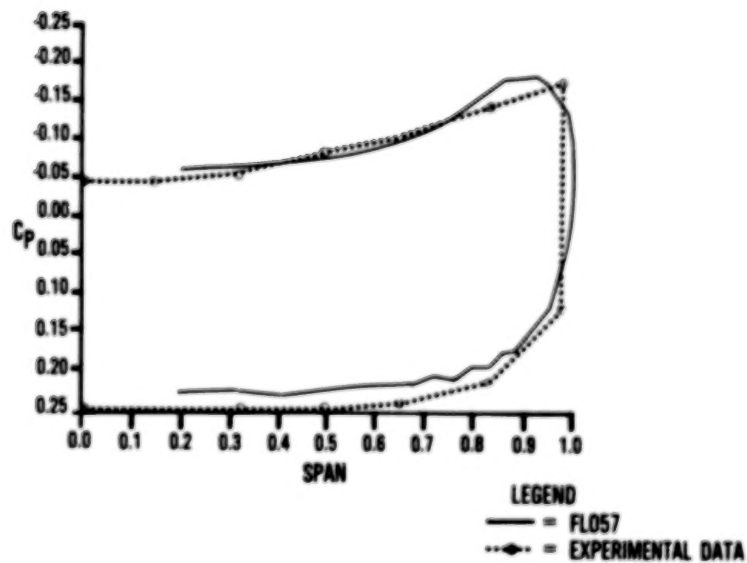


Figure 22.- Comparison of Euler and Ref. 1,  $C_p$  data,  $M_\infty = 2.0$ ,  $AL = 12.0$ ,  $X = 3.20$ .

X STATION = 16.0

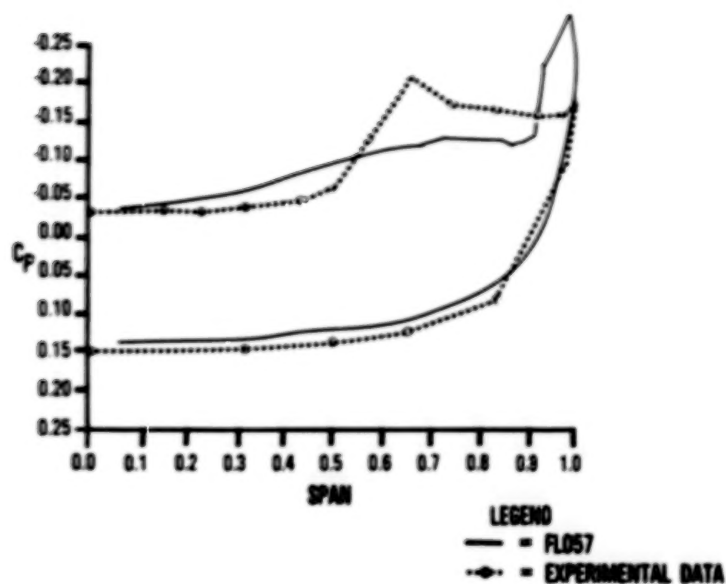


Figure 23.- Comparison of Euler and Ref. 1,  $C_p$  data,  
 $M_\infty = 2.0$ ,  $AL = 12.0$ ,  $X = 16.0$ .

X STATION = 25.6

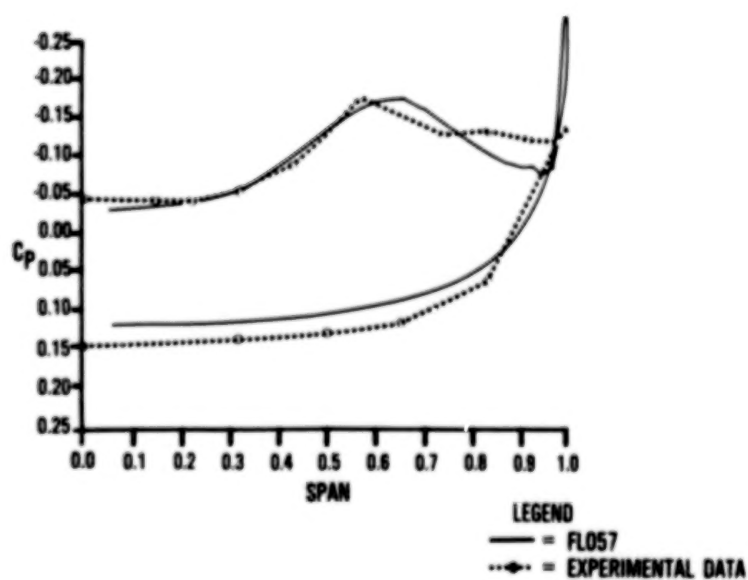


Figure 24.- Comparison of Euler and Ref. 1,  $C_p$  data,  
 $M_\infty = 2.0$ ,  $AL = 12.0$ ,  $X = 25.6$ .

X STATION = 35.2

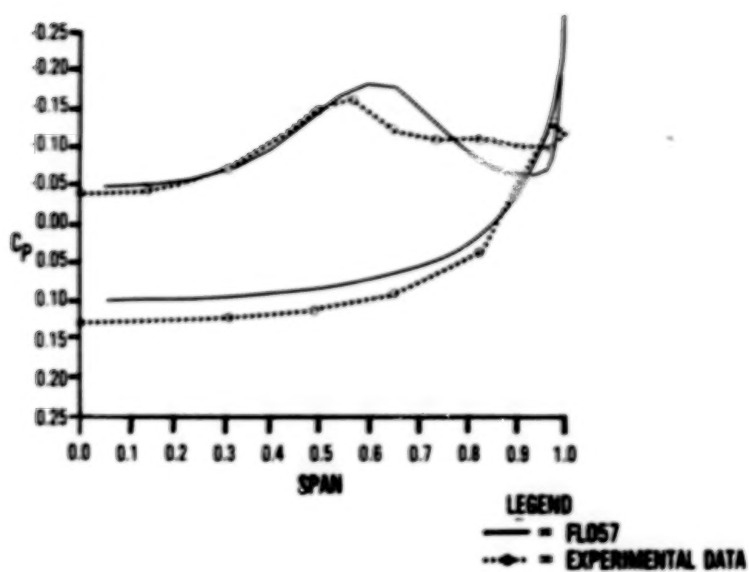


Figure 25.- Comparison of Euler and Ref. 1,  $C_p$  data,  
 $M_\infty = 2.0$ ,  $AL = 12.0$ ,  $X = 35.2$

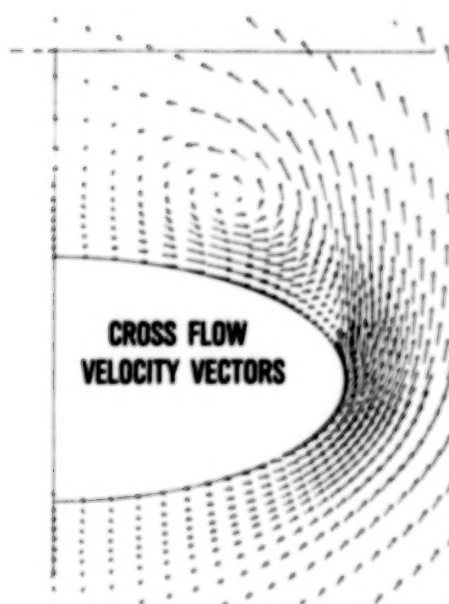


Figure 26.- Cross-flow velocities,  
 $M_\infty = 2.0$ ,  $AL = 12.0$ ,  $X = 35.2$ .



ORIGINAL PAGE IS  
OF POOR QUALITY

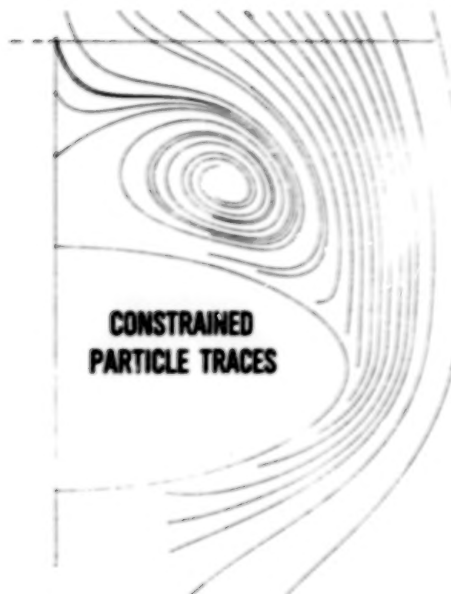


Figure 27.- Constrained particle paths,  
 $M_\infty = 2.0$ ,  $AL = 12.0$ ,  $X = 35.2$ .

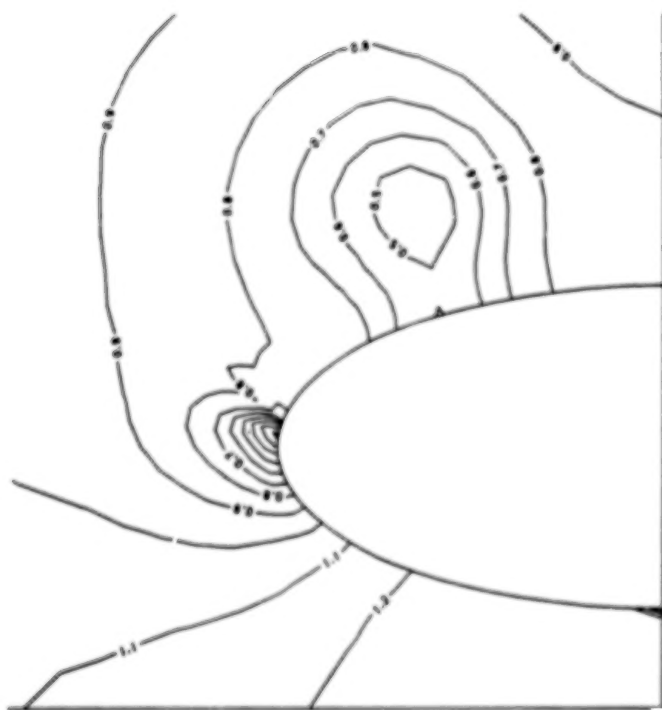


Figure 28.- Static pressure contour plot,  $M_\infty = 2.0$ ,  
 $AL = 12.0$ ,  $X = 35.2$ .

## COMPUTATION OF LEADING-EDGE VORTEX FLOWS

Richard W. Newsome  
Air Force Wright Aeronautical Laboratories  
APSC Liaison Office, NASA Langley Research Center  
Hampton, Virginia

James L. Thomas  
NASA Langley Research Center  
Hampton, Virginia

## SUMMARY

The simulation of the leading-edge vortex flow about a series of conical delta wings through solution of the Navier-Stokes and Euler equations is studied. The occurrence, the validity, and the usefulness of separated flow solutions to the Euler equations are of particular interest. Central and upwind difference solutions to the governing equations are compared for a series of cross-sectional shapes, including both rounded and sharp tip geometries.

For the rounded leading edge and the flight condition considered, viscous solutions obtained with either central or upwind difference methods predict the classic structure of vortical flow over a highly swept delta wing. Predicted features include the primary vortex due to leading-edge separation and the secondary vortex due to crossflow separation. Central difference solutions to the Euler equations show a marked sensitivity to grid refinement. On a coarse grid, the flow separates due to numerical error and a primary vortex which resembles that of the viscous solution is predicted. In contrast, the upwind difference solutions to the Euler equations predict attached flow even for first-order solutions on coarse grids. On a sufficiently fine grid, both methods agree closely and correctly predict a shock-curvature-induced inviscid separation near the leeward plane of symmetry.

Upwind difference solutions to the Navier-Stokes and Euler equations are presented for two sharp leading-edge geometries. The viscous solutions are quite similar to the rounded leading-edge results with vortices of similar shape and size. The upwind Euler solutions predict attached flow with no separation for both geometries. However, with sufficient grid refinement near the tip or through the use of more accurate spatial differencing, leading-edge separation results. Once the leading-edge separation is established, the upwind solution agrees with recently published central difference solutions to the Euler equations.

## INTRODUCTION

The current interest in high angle-of-attack aerodynamics and vortical flows has focused considerable attention on the numerical simulation of the flow about a swept delta wing at moderate to high angles of attack. For subsonic leading edges which are sharp or of small radius of curvature, the flow separates at the tips and forms two counter-rotating vortices on opposite sides of the leeward wing surface. The presence of the vortices produces a pressure minimum on the upper surface and results in an additional lift component not predicted by linear theory.

Interest, here, is restricted to methods which "capture" the vortex rather than modeling it in an approximate manner. Thus, we consider only methods which solve the Euler and Navier-Stokes equations. The Navier-Stokes equations model all physical mechanisms and provide the most accurate results. Vigneron et al.<sup>1</sup> solved the conical and parabolic approximations to the Navier-Stokes equations for the vortical flow about a sharp-edged delta wing at supersonic speeds. Fujii and Kutler<sup>2,3</sup> solved the three-dimensional Navier-Stokes equations for the leading-edge separation about a delta wing with rounded edges at subsonic speeds. Rizzetta and Shang<sup>4</sup> presented three-dimensional Navier-Stokes solutions for a delta wing with sharp edges at supersonic and hypersonic speeds. The principal drawbacks of the Navier-Stokes equations are the higher computational costs necessary to resolve small-scale viscous effects and the need to model turbulence in an approximate manner. However, the Navier-Stokes solutions set the standard by which less exact solutions must be judged.

In the last several years, it has been suggested that Euler codes could be the method of choice in the simulation of leading-edge vortex flows.<sup>5</sup> In contrast to potential methods, the Euler equations provide the correct Rankine-Hugoniot shock jump conditions. They also admit rotational flow solutions. Indeed, numerous Euler solutions with leading-edge separation have been reported for both rounded and sharp leading edges using a variety of numerical schemes. A partial list includes the works of Rizzi et al.<sup>6-10</sup>, Raj and Sikora,<sup>11</sup> and Powell, Murman et al.<sup>12</sup> using a finite volume Runge-Kutta algorithm; Fujii and Obayashi<sup>13</sup> using a LU factored scheme whose right-hand side is identical to the Beam and Warming scheme; and Manie et al.<sup>14</sup> and Newsome<sup>15</sup> using a MacCormack scheme.

Since flow separation is usually associated with generation of vorticity through the no-slip boundary condition in a viscous flow, its occurrence in an inviscid solution is of both theoretical and practical importance. Necessary conditions for flow separation include the presence of vorticity in the flow as well as an adverse pressure gradient. While the Euler equations admit rotational solutions through the transport (and for three-dimensional flow, stretching) of vorticity, there is only one valid mechanism for vorticity generation in an inviscid flow. In accord with Crocco's theorem, the Euler equations allow for the generation of vorticity through non-constant shock strength (shock curvature, shock intersection, etc.). Salas<sup>16</sup> first demonstrated shock-induced inviscid separation for the transonic flow about a circular cylinder. Marconi<sup>17</sup> published similar results for the supersonic flow about circular cones and more recently elliptic cones.<sup>18</sup>

The Euler equations are singular at a sharp tip. This, however, causes no particular problem for a finite volume scheme in which cell centered quantities are computed. Salas and Daywitt<sup>19</sup>, in considering conical flow about sharp external axial corners, have shown that a limiting form of the inviscid equations valid at the singular corner point leads to a conical analog of the isentropic Prandtl-Meyer expansion. The maximum Prandtl-Meyer expansion angle corresponds to vacuum pressure. It is not clear whether theoretically valid attached flow Euler solutions exist for geometries in which the vacuum expansion limit is exceeded. For any finite radius of curvature, the flow field is resolvable and a valid Euler solution must approach the expansion limit as the radius of curvature approaches zero. In a viscous gas, the flow separates well before the inviscid expansion limit is reached. Once the

separation and the level of shed vorticity are established, the dynamics of the vortex motion, i.e. its interaction with neighboring surfaces, are essentially inviscid and thus adequately described by the Euler equations (excluding viscous features such as secondary vortices).

In practice, numerical solutions to the Euler equations for wings of small radius of curvature often result in inviscid separation. Any numerical algorithm, whether central or upwind differenced, must be dissipative for stability. As such, there is an effective Reynolds number inherent in the calculation which is dependent on the local mesh resolution and the order of the method. Upwind schemes are naturally dissipative. Central difference schemes are not naturally dissipative and dissipative terms are generally added to the discretized equations. The added dissipative terms are generally of two types: a third-order fourth-difference term to provide dissipation in smooth regions and an adaptive second difference term to control shock oscillations. The latter term reverts to first order at a shock but it also is significant in regions of rapid expansion. Finally, error can be introduced by the application of surface boundary conditions.

In reference 15, from which parts of this paper are taken, central difference solutions to the Euler and Navier-Stokes equations for the flow about a delta wing with a rounded leading edge (elliptic cone) were considered. The separation vortex predicted with the Euler equations, which is characteristic of the viscous solution, was found to be numerically induced. More recently, upwind difference Euler solutions<sup>20</sup> were shown to be much less susceptible to spurious inviscid separation. In the present paper, the upwind difference method is extended to the conical Navier-Stokes equations and a more detailed comparison of central and upwind difference solutions for both the Euler and Navier-Stokes equations is given for the round leading-edge wing. The upwind code is further extended to consider Navier-Stokes and Euler solutions for several sharp leading-edge wings.

#### SOLUTION METHOD

If interest is restricted to supersonic flow past conical bodies, then the governing equations may be simplified since the resulting flow will also be conical. A conical flow has the property that all flow quantities are invariant on rays which pass through the apex of the conical surface. All derivatives in the radial direction may then be neglected, reducing a three-dimensional problem into a much more tractable two-dimensional one. The conical assumption is exact for inviscid flow. For viscous flow, a length scale dependence is contained in the Reynolds number. The flow may be thought of as locally conical with the Reynolds number determining the location of the conical plane at which the solution is determined. The conical equations may be obtained by introduction of the conical variables

$$\xi = \xi(x) = x \quad Y = \frac{y}{x} \quad Z = \frac{z}{x}$$

$$\eta = \eta(x, y, z) = \eta(Y, Z)$$

$$\zeta = \zeta(x, y, z) = \zeta(Y, Z)$$



into the three-dimensional Navier-Stokes equations, written in terms of the non-dimensional Cartesian variables  $(x,y,z)$ . Upon simplifying for conical flow, the governing equations may be expressed in conservation form as

$$\frac{\partial}{\partial t}(\hat{Q}) + \frac{\partial}{\partial \eta}(\hat{G} - \hat{G}_v) + \frac{\partial}{\partial \zeta}(\hat{H} - \hat{H}_v) + (\hat{S} - \hat{S}_v) = 0 \quad (1)$$

The inviscid equations are obtained by dropping the terms  $(\hat{G}_v, \hat{H}_v, \hat{S}_v)$ .

The general three-dimensional, upwind, Euler/thin layer Navier-Stokes code developed by Thomas<sup>20,21</sup> was specialized for conical flow. In the finite volume formulation, a single array of crossflow plane volumes was constructed such that the inflow and outflow surfaces are scaled by the conical transformation, as above. While the code uses a finite volume approach, the equations may be written in generalized coordinates as

$$\frac{\partial}{\partial t}(\hat{Q}) + \frac{\partial}{\partial \xi}(\hat{F}) + \frac{\partial}{\partial \eta}(\hat{G}) + \frac{\partial}{\partial \zeta}(\hat{H} - \hat{H}_v) = 0 \quad (2)$$

At each iteration, the inflow conditions are updated with the results of the previous iteration so that, at convergence,  $\partial \hat{Q} / \partial \xi = 0$ , consistent with the conical flow approximation.

The inviscid and viscous flux vectors in equations (1) and (2) are defined as

$$\hat{Q} = \frac{\hat{Q}}{J} = \frac{1}{J} \begin{bmatrix} \rho \\ \rho u \\ \rho v \\ \rho w \\ \rho E \end{bmatrix} \quad \hat{F}, \hat{G}, \hat{H} = \frac{1}{J} \begin{bmatrix} \rho U_c \\ \rho U_c u + \alpha_x p \\ \rho U_c v + \alpha_y p \\ \rho U_c w + \alpha_z p \\ [\rho E + p] U_c \end{bmatrix} \quad (3)$$

$$\hat{S} = \frac{2}{J} \begin{bmatrix} \rho u \\ \rho u^2 + p \\ \rho uv \\ \rho uw \\ [\rho E + p] u \end{bmatrix} \quad E = e_I + \frac{1}{2}(u^2 + v^2 + w^2)$$

$$U_c = \alpha_x u + \alpha_y v + \alpha_z w$$



$$\hat{G}_v, \hat{H}_v = \frac{1}{J} \begin{bmatrix} 0 \\ \alpha_x \tau_{xx} + \alpha_y \tau_{xy} + \alpha_z \tau_{xz} \\ \alpha_x \tau_{xy} + \alpha_y \tau_{yy} + \alpha_z \tau_{yz} \\ \alpha_x \tau_{xz} + \alpha_y \tau_{yz} + \alpha_z \tau_{zz} \\ \alpha_x b_x + \alpha_y b_y + \alpha_z b_z \end{bmatrix} \quad \hat{S}_v = \frac{1}{J} \begin{bmatrix} 0 \\ \tau_{xx} \\ \tau_{xy} \\ \tau_{xz} \\ b_x \end{bmatrix}$$

Although the flux vectors can be written in a common form, they are in fact quite different as applied to equations (1) or (2). A general three-dimensional transformation between the Cartesian variables (x,y,z) and the computational variables is implied in equation (2), so that the flux terms can be defined as below:

$$\begin{aligned} \hat{F}: \quad \alpha &= \xi; \quad U_c = U = \xi_x u + \xi_y v + \xi_z w \\ \hat{G}: \quad \alpha &= \eta; \quad U_c = V = \eta_x u + \eta_y v + \eta_z w \\ \hat{H}, \hat{H}_v: \quad \alpha &= \zeta; \quad U_c = W = \zeta_x u + \zeta_y v + \zeta_z w \\ J &= \partial(\xi, \eta, \zeta) / \partial(x, y, z) \end{aligned} \quad (4)$$

In the finite volume formulation, expressions for the transformation derivatives and the Jacobian, J, are evaluated geometrically.

When working with the conical equations (1), it is convenient to work in terms of the conical variables, Y and Z. This allows a simpler form for the equations using the two-dimensional transformation:

$$\begin{bmatrix} \eta_Y & \zeta_Y \\ \eta_Z & \zeta_Z \end{bmatrix} = \begin{bmatrix} Y_\eta & Z_\eta \\ Y_\zeta & Z_\zeta \end{bmatrix}^{-1} \quad J = \begin{vmatrix} \eta_Y & \zeta_Y \\ \eta_Z & \zeta_Z \end{vmatrix}$$

Since

$$\begin{aligned} \eta_x &= -\frac{1}{x} [Y\eta_Y + Z\eta_Z] & \zeta_x &= -\frac{1}{x} [Y\zeta_Y + Z\zeta_Z] \\ \eta_y &= \frac{1}{x} [\eta_Y] & \zeta_y &= \frac{1}{x} [\zeta_Y] \\ \eta_z &= \frac{1}{x} [\eta_Z] & \zeta_z &= \frac{1}{x} [\zeta_Z] \end{aligned} \quad (5)$$

it is convenient to define the terms

$$\eta_x = -[Y\eta_Y + Z\eta_Z] \quad \zeta_x = -[Y\zeta_Y + Z\zeta_Z]$$

so that the flux terms in equation (3) can be defined as

$$\hat{G}, \hat{G}_V: \alpha = \eta; (\alpha_x, \alpha_y, \alpha_z) = (\eta_x, \eta_y, \eta_z) \quad U_c = V = \eta_x u + \eta_y v + \eta_z w \quad (6)$$

$$\hat{H}, \hat{H}_V: \alpha = \zeta; (\alpha_x, \alpha_y, \alpha_z) = (\zeta_x, \zeta_y, \zeta_z) \quad U_c = W = \zeta_x u + \zeta_y v + \zeta_z w$$

The term,  $\frac{1}{x}$ , is absorbed into equation (1) when the Reynolds number and the time scale are defined with respect to the length scale,  $L$ , where  $L$  is the length from the body apex to the crossflow solution plane.

Upon nondimensionalization in terms of the freestream density,  $\rho_\infty$  and sound speed,  $c_\infty$ , the shear stress and heat flux terms are defined in tensor notation (summation convention implied) as:

$$\tau_{\alpha\beta} = \frac{1}{Re_\infty} \left[ \mu \left( \frac{\partial u_\alpha}{\partial x_\beta} + \frac{\partial u_\beta}{\partial x_\alpha} \right) + \lambda \frac{\partial u_\gamma}{\partial x_\gamma} \delta_{\alpha\beta} \right] \quad (7)$$

$$\dot{q}_{x_\alpha} = - \left( \frac{M_\infty}{Re_\infty Pr(\gamma-1)} \right) \frac{\partial c^2}{\partial x_\alpha} \quad b_{x_\alpha} = u_\beta \tau_{x_\alpha x_\beta} - \dot{q}_{x_\alpha}$$

$$Re_\infty = \frac{\rho_\infty u_\infty L}{\mu_\infty}$$

The chain rule is used to evaluate derivatives with respect to  $(x, y, z)$  in terms of  $(\eta, \zeta)$ . When the thin layer assumption is made, only those derivatives in the direction normal to the wall ( $\zeta$ ) are retained in the stress and heat flux terms. Equations (1) and (2) are closed by the perfect gas equation of state and Sutherland's law for molecular viscosity. All calculations are for laminar flow only.

The conical flow equations (1) were solved with the MacCormack<sup>22</sup> unsplit, explicit finite-difference algorithm. Since the algorithm is well known, a detailed description is unnecessary. The method is second-order accurate in space and time and is conditionally stable. To control shock oscillations, MacCormack's<sup>23</sup> pressure damping was incorporated into the scheme. The damping term is  $O(\Delta x^3)$  except in regions of large pressure gradients where the pressure gradient switch forces the damping to  $O(\Delta x)$ . MacCormack's scheme is also naturally dissipative due to unsymmetric differencing in the predictor and corrector steps.

Upwind solutions were obtained with the flux vector splitting algorithm developed by Thomas.<sup>20</sup> The generalized fluxes  $\hat{F}, \hat{G}, \hat{H}$ , representing pressure and convection terms are split into forward and backward contributions according to the sign of the eigenvalues of the Jacobian matrices

$$\hat{F}/\partial Q, \partial G/\partial Q, \partial H/\partial Q$$

and differenced accordingly. For example, the flux difference in the  $\xi$ -direction is

$$\delta_{\xi} \hat{F} = \delta_{\xi}^{-} \hat{F}^{+} + \delta_{\xi}^{+} \hat{F}^{-} \quad (8)$$

where  $\delta_{\xi}^{-}$  and  $\delta_{\xi}^{+}$  denote general backward and forward divided difference operators respectively, in the  $\xi$ -direction. In reference 20, van Leer's flux vector splitting was extended to three-dimensional generalized coordinates.

The flux,  $\hat{F}$ , as an example, is split according to the contravariant Mach number in the  $\xi$ -direction, defined as  $M_{\xi} = \bar{u}/c$ , where  $\bar{u} = U/|\text{grad}(\xi)|$ . For supersonic flow,  $|M_{\xi}| > 1$

$$\begin{aligned} \hat{F}^{+} &= \hat{F}, \hat{F}^{-} = 0 \quad M_{\xi} > +1 \\ \hat{F}^{-} &= \hat{F}, \hat{F}^{+} = 0 \quad M_{\xi} < -1 \end{aligned} \quad (9)$$

and for subsonic flow,  $|M_{\xi}| < 1$

$$\hat{F}^{\pm} = \frac{|\text{grad} \xi|}{J} \begin{bmatrix} f_{\text{mass}}^{\pm} \\ f_{\text{mass}}^{\pm} [k_x (-\bar{u} \pm 2c)/\gamma + u] \\ f_{\text{mass}}^{\pm} [k_y (-\bar{u} \pm 2c)/\gamma + v] \\ f_{\text{mass}}^{\pm} [k_z (-\bar{u} \pm 2c)/\gamma + w] \\ f_{\text{energy}}^{\pm} \end{bmatrix} \quad (10)$$

where

$$f_{\text{mass}}^{\pm} = \pm \rho c (M_{\xi} \pm 1)^2 / 4$$

$$f_{\text{energy}}^{\pm} = f_{\text{mass}}^{\pm} \left[ \{-(\gamma-1)\bar{u}^2 \pm 2(\gamma-1)\bar{u}c + 2c^2\}/(\gamma^2-1) + \frac{1}{2}(u^2+v^2+w^2) \right]$$

The surface area of the cell interface in the  $\xi$  direction is  $|\text{grad} \xi|/J$ , the cell volume is  $1/J$ , and

$$(\hat{k}_x, \hat{k}_y, \hat{k}_z) = (\xi_x, \xi_y, \xi_z)/|\text{grad} \xi| \quad (11)$$

are the direction cosines of the cell interfaces in the  $\xi$  direction. The split-flux differences are implemented as a flux balance across a cell as (for  $\Delta\xi = \Delta\eta = \Delta\zeta = 1$ )

$$\delta_{\xi}^{-} \hat{F}_1^{+} + \delta_{\xi}^{+} \hat{F}_1^{-} = [\hat{F}^{+}(Q^{-}) + \hat{F}^{-}(Q^{+})]_{i+1/2} - [\hat{F}^{+}(Q^{-}) + \hat{F}^{-}(Q^{+})]_{i-1/2} \quad (12)$$

The notation  $\hat{F}^{+}(Q^{-})_{i+1/2}$  denotes a forward flux evaluated using the metric terms at the cell interface  $(i+1/2)$ , with conserved variables obtained by an upwind biased interpolation

$$Q_{i+1/2}^{-} = Q_i + \frac{1}{4}\phi_{\xi} [(1-\kappa_{\xi})\nabla_{\xi} + (1+\kappa_{\xi})\Delta_{\xi}] Q_i \quad (13)$$

$$Q_{i+1/2}^{+} = Q_{i+1} - \frac{1}{4}\phi_{\xi} [(1+\kappa_{\xi})\nabla_{\xi} + (1-\kappa_{\xi})\Delta_{\xi}] Q_{i+1}$$

where

$$\Delta_{\xi} Q_i = Q_{i+1} - Q_i \quad \nabla_{\xi} Q_i = Q_i - Q_{i-1}$$

Only fully upwind first or second-order accurate differencing has been used in the results that follow:

$$\begin{aligned} \phi_{\xi} &= 0 & (\text{first-order upwind}) \\ \phi_{\xi} &= 1, \kappa_{\xi} = -1 & (\text{second-order upwind}) \end{aligned} \quad (14)$$

Differencing for the diffusion terms representing shear stress and heat transfer effects corresponds to second-order central differences in which second derivatives are treated as differences across cell interfaces of first derivative terms

$$\delta_{\zeta} \hat{H}_{v_k} = \hat{H}_{v_{k+1/2}} - \hat{H}_{v_{k-1/2}} \quad (15)$$

where, for example, the term,

$$\tau_{xy} = \frac{M_{\infty}}{Re_{\infty}} \left[ \mu \left( \frac{\partial u}{\partial y} + \frac{\partial v}{\partial x} \right) \right]$$

under the thin layer approximation, becomes,

$$\tau_{xy} = \left( \frac{M_{\infty}}{Re_{\infty}} \right) \mu \left( \zeta_y \frac{\partial u}{\partial \zeta} + \zeta_x \frac{\partial v}{\partial \zeta} \right) \quad (16)$$

and is differenced in  $\hat{H}_{v_{k\pm 1/2}}$  as

$$\frac{M_\infty}{Re_\infty} u_{k\pm 1/2} (\zeta_{y_{k\pm 1/2}} \delta_\zeta u_{k\pm 1/2} + \zeta_{x_{k\pm 1/2}} \delta_\zeta v_{k\pm 1/2}) \quad (17)$$

where

$$\delta_\zeta u_{k+1/2} = u_{k+1} - u_k$$

The linearized, backward time approximation in delta form for the three-dimensional equations is given as

$$\left[ \frac{I}{J\Delta t} + \delta_\xi \frac{\partial \hat{F}}{\partial Q} + \delta_\eta \frac{\partial \hat{G}}{\partial Q} + \delta_\zeta \left( \frac{\partial \hat{H}}{\partial Q} - \frac{\partial \hat{H}_v}{\partial Q} \right) \right] \Delta Q = R^N \quad (18)$$

As described in reference 20, equation (18) is solved by streamwise relaxation ( $\xi$ -direction) and approximate factorization in the crossflow plane as

$$[M + \delta_\eta \frac{\partial \hat{G}}{\partial Q}] [M]^{-1} [M + \delta_\zeta \left( \frac{\partial \hat{H}}{\partial Q} - \frac{\partial \hat{H}_v}{\partial Q} \right)] \Delta Q = R(Q^N, Q^{N+1}) \quad (19)$$

where

$$M = \left[ \frac{I}{J\Delta t} + \frac{\partial \hat{F}^+}{\partial Q} - \frac{\partial \hat{F}^-}{\partial Q} \right]$$

In general, the solution is obtained by alternate forward and backward sweeping through the crossflow planes with a nonlinear update of the residual  $R$  indicated on the right side of (19). For the degenerate conical flow case, this corresponds to reinitialization of the inflow plane and update of the crossflow plane until convergence is achieved. Since the spatial implicit discretizations may be taken as first order with no loss in steady-state accuracy, the solution of equation (19) involves the solution of two block tridiagonal equations.

Initial conditions for both central and upwind difference methods consisted of freestream conditions. Boundary conditions consisted of freestream conditions on the outer boundary, reflection conditions in the crossflow symmetry plane and slip or no slip conditions on the body surface depending upon whether the viscous or inviscid equations are considered.

## RESULTS

The flow about several different conical delta wings with a 70° wing sweep angle at a Mach number of 2 and 10 degrees angle of attack was chosen for study. A thin elliptic cone, Fig. 1, with half angles,  $\tan^{-1}(y_{LE}/x) =$



20°, and  $\tan^{-1} (z_{CL}/x) = 1.5^\circ$ , was used as a model for round leading edges with small curvature radius. For sharp tips, a thinner conical body was defined with a vertical half angle,  $\tan^{-1} (z_{CL}/x) = 0.75^\circ$  and a tip half angle angle given as  $\tan^{-1} (dz/dy)_{LE} = 10^\circ$ . As an extreme case, a zero thickness flat delta wing was also considered.

Central and upwind difference solutions to the Navier-Stokes and Euler equations are compared for the rounded leading-edge wing. Upwind difference Euler and Navier-Stokes results are then presented for the sharp tip geometries.

## ROUNDED LEADING EDGES

### Navier-Stokes Solutions

A comparison of central and upwind difference calculations was made at Reynolds numbers of  $Re_\infty = 0.1 \times 10^6$  and  $0.5 \times 10^6$ . The grid consisted of 151 points around and 65 points normal to the body with an equal minimum step size at the tip, in both directions,  $\Delta s/x = .0002$ . This minimum step size in the body normal direction was relaxed to a maximum value  $\Delta s/x = .0006$  away from the tip. The grid and an enlarged view of the tip are shown in Fig. 2. At a Reynolds number of  $Re_\infty = 0.1 \times 10^6$ , the windward symmetry plane boundary layer contained 14 points and the leading-edge boundary layer contained 7 points.

In general, central and upwind difference solutions, both second-order accurate, are in good agreement. A plot of the crossflow velocity for the central difference solution is shown in Fig. 3 (the upwind result is nearly identical). In this and the results to follow, the radial velocity component has been subtracted out of the Cartesian crossflow components. The flow separates at the leading edge with a large primary vortex and a smaller secondary vortex. At the higher Reynolds number,  $Re_\infty = 0.5 \times 10^6$ , the secondary vortex is smaller relative to the primary vortex. A comparison of pressure coefficients, Fig. 4, for both the central and upwind difference solutions, shows the suction peak to be stronger for the higher Reynolds number. At the higher Reynolds number, minor differences appear in the two solutions in the separation zone, particularly near the leading edge.

Squire<sup>24</sup> presented experimental data for the same elliptic cone with a small circular centerbody. To verify the viscous calculations, the upwind scheme was applied to the elliptic cone at conditions corresponding to the experimental data of Squire:  $M_\infty = 1.8$ ,  $Re_\infty = 2.1 \times 10^6$ . The pressure coefficient is shown in figure 5. The solution is in reasonable agreement with the experiment. Miller and Wood<sup>25</sup> delineated seven different flow classifications according to leading-edge normal Mach number and angle of attack. The present results, which indicate a primary and secondary vortex with no crossflow shock, are in agreement with Miller's classification.

Since some Reynolds number dependence was found in the previous cases, a wider range of Reynolds numbers were investigated with the thin-layer upwind Navier-Stokes code for laminar flow. Although the grid, Fig. 2, was not refined with increasing Reynolds number, the results are believed to be

generally valid. The pressure coefficient for the various Reynolds numbers is shown in Fig. 6. The leeward suction pressure appears to approach a limit with increasing Reynolds number. The flow fields are similar with the exception of the lowest Reynolds number in which the secondary vortex is not present. Consistent with the experimental results of reference 26, differences with respect to Reynolds number are confined to the size and position of the vortex as well as the peak suction pressure.

### Euler Solutions

The Euler solutions (for conical flow) are characterized by the presence of vortical singularities. The entire flow is weakly rotational inside the bow shock due to variable shock strength. Since streamlines terminate at one of the vortical singularities and each streamline crosses the shock at a different location, the flow at the singularities is multivalued. As a practical matter, for the present case, the bow shock is extremely weak and the entropy variation due to the bow shock is negligible.

Inviscid solutions for the central and upwind difference methods are compared on coarse and fine grids. While the two methods agree closely on fine grids, there are dramatic differences on the coarse grid.

### Coarse Grid Euler

Since a prime motivation in solving the Euler equations is the desire to avoid the grid fineness necessary for viscous resolution, a coarse grid (75 x 55) was first considered. The minimum step size,  $\Delta s/x = 0.005$ , gives poor resolution at the tip as can be seen in Fig. 7. The crossflow velocities for the central difference solution are shown in Fig. 8. Corresponding crossflow Mach number and entropy contours are given in Fig. 9. Entropy is defined as

$$\frac{\Delta s}{R} = \frac{s - s_\infty}{R} = \frac{1}{\gamma - 1} \ln \left( \frac{[p/p_\infty]}{[\rho/\rho_\infty]}^\gamma \right)$$

For constant total enthalpy, total pressure loss is given as

$$\frac{P_0}{P_{0_\infty}} = e^{-\left[\frac{\Delta s}{R}\right]}$$

A comparison of the crossflow velocities, Figs. 4 and 8, reveals a large primary vortex of similar shape and size. Notably absent is the secondary vortex since there is no vorticity generating mechanism on the upper wing surface. A comparison of the pressure coefficient, Fig. 10, for the central difference inviscid and viscous results, shows surprising agreement with the exception of the over expansion at the leading edge. From Fig. 9, it can be seen that entropy is generated at the tip and is convected through the vortex. The entropy and vorticity at the tip are spurious since there is no valid mechanism for their generation in the Euler equations. In the present case, the flow does not separate at the tip but at about 92% of chord on the leeward surface. The separation occurs downstream of a small shock at this point dividing supersonic flows of opposite directions. With less accurate

boundary conditions or large values of the damping coefficient, the point of separation moves closer to the leading edge. In reference 15, several different boundary conditions were tried. The damping coefficient was also varied over its usual range of stability. With minor exceptions in the location of the separation point, the result was always the same - a large primary separation vortex. It should be noted that a minimum value of the damping coefficient was necessary to maintain a stable solution. Computations by E. Murman (Massachusetts Institute of Technology, private communication) for this case, on a similarly coarse grid with a finite volume Runge-Kutta scheme, also resulted in a leading-edge separation vortex.

A better understanding of the separation can be gained by a look at the transient development of the vortex. From the initial condition, the flow quickly expanded about the leading edge to a supersonic crossflow. A crossflow shock also developed on the leeward surface with no separation evident. Concurrently, the leading-edge expansion produced large entropy/vorticity errors which were convected downstream to the developing crossflow shock. The interaction of the two produced a separated region at the base of the shock. The separation then expanded to form the primary vortex and the shock is either absent or confined to the vortex near the tip at the point of separation.

First- and second-order accurate upwind solutions were computed on the same coarse grid. The first-order scheme is the most dissipative scheme considered and does not accurately resolve the detailed flow structure. However, as can be seen in Fig. 11, the flow remains attached at the leading edge. The second-order solution is shown in Fig. 12, and the higher accuracy now correctly predicts the shock-induced vortex centered near the point  $y/x = 0.1$ . Crossflow Mach number and entropy plots for the second-order accurate solution are given in Fig. 13. The pressure coefficient for the first- and second-order accurate solutions is shown in Fig. 14. As would be expected, the leading-edge expansion and crossflow shock are better resolved with the more accurate differencing. Chakravarthy<sup>27</sup> has also solved the present case with an upwind Euler code on the same coarse grid and found no evidence of leading-edge separation.

#### Fine Grid Euler

The grid used in the viscous solutions, Fig. 2, was also used for the inviscid calculation. The intent was to reduce the effect of numerically induced errors through better spatial resolution of the tip region. Second-order accurate central and upwind difference solutions are virtually identical on this grid. As can be seen in Fig. 15, the central difference solution is now attached at the leading edge. In both solutions, as in the coarse grid upwind solution, a small vortex appears downstream from the crossflow shock. The vortex is due to shock generated vorticity and is a valid Euler solution. A plot of the crossflow Mach numbers, Fig. 16, shows both the crossflow shock and the shock induced wake. In Fig. 17, enlarged views of the crossflow Mach number and entropy contours are given for the central difference solution. Entropy is generated across the shock according to the local shock strength. It is the entropy variation normal to the streamline which produces the vorticity as required by Crocco's theorem and the subsequent vortex. On the fine grid, the leading-edge expansion is essentially isentropic. This can also be seen in Fig. 18 where the leading-



edge expansion is noticeably sharper than the upwind solution on the coarse grid. The small bump at  $y/y_{LE} = 0.3$  is due to the expansion under the vortex.

Since boundary condition error, truncation error, and added artificial dissipation all go to zero in the limit as the grid is refined, it is rather difficult to ascertain the precise cause of the central difference separation. However, when compared with the upwind results, certain possibilities can be eliminated. Both schemes enforce the surface boundary conditions with equivalent accuracy. Since the first-order upwind solution has the largest truncation error and yet remains attached on the coarse grid, the cause of the central difference separation is not just a matter of inadequate numerical resolution. The one distinguishing characteristic between the upwind and central difference methods is the added artificial dissipation model necessary for stability and to control shock oscillations. Although in regions of smooth flow, the added terms are of higher order than the truncation error, in regions of large gradients, the pressure switch built into the model causes the scheme to revert to first order. For this reason, it has been widely speculated, but not proven, that the artificial dissipation model is responsible for spurious inviscid separation. It is interesting to note, in comparing entropy generation at the tip between the central and upwind solutions on the coarse grid (Figs. 9 and 13), that although the upwind value is lower (0.3) than the central difference value (0.6), the terms are of the same order of magnitude.

## SHARP LEADING EDGES

### Navier-Stokes Solutions

A thin-layer Navier-Stokes solution was computed for the thin, sharp-edged wing at a Reynolds number,  $Re_{\infty} = 0.1 \times 10^6$ , using the second-order accurate scheme. The grid, Fig. 19, consisted of  $151 \times 65$  points with a minimum step size  $\Delta s/x = 0.0002$ . The crossflow velocities, Fig. 20, exhibit the same primary and secondary vortices at the same locations as the rounded leading edge. Crossflow Mach contours are given in Fig. 21.

### Euler Solutions

Since the upwind code was found to be much less susceptible to spurious inviscid separation for rounded leading edges, its behavior for sharp leading edges was investigated. The essential difference is that, unlike the rounded leading edge, the local behavior at the sharp edge is singular. Both first- and second-order solutions were computed on coarse and fine grids. Because of the very large gradients in the flow near the tip, it was found necessary to use first-order interpolation (equation 13) in the flux calculations for some 3-4 points away from and on either side of the tip in the second-order solutions. This type of flux limiting has been used (ref. 28) to ensure monotone shock profiles for strong shocks. The calculation remains fully conservative.

### Coarse Grid Euler

The coarse grid, Fig. 22, consisted of  $75 \times 55$  points. The local tip resolution is significantly less than that of the sharp tip viscous grid, Fig. 19. On this grid, both first- and second-order solutions are attached at the

leading edge. The second-order solution predicts a vortex downstream of the crossflow shock as can be seen in Fig. 23. Crossflow Mach number and entropy contours for the second-order solution are given in Fig. 24. Despite the presence of large entropy errors generated at the tip, leading-edge separation does not occur. The pressure coefficient, Fig. 25, is similar to the rounded edge result with a well-defined crossflow shock.

#### Zero-Thickness Wing

A zero thickness wing was considered in order to determine if attached flow solutions could be obtained in this extreme case. Powell et al.<sup>12</sup> recently presented leading-edge vortex solutions for similar geometries using a finite volume central difference scheme. The grid dimensions were the usual 151 x 65 points. However, as seen in Fig. 26, the local resolution at the tip is relatively coarse. The first-order solution did not exhibit leading-edge separation. The crossflow velocities, Fig. 27, show a vortex downstream of the crossflow shock. Crossflow Mach number and entropy are given in Fig. 28. The second-order solution exhibits leading-edge separation, as is evident in Fig. 29. Both solutions are first-order accurate at the leading edge. Although the (pseudo) transient development of the two solutions was not observed, it is presumed that the interaction of the crossflow shock with the rotationality induced at the leading edge is unstable in the more accurate calculation. As a consequence, the flow separates at the base of the crossflow shock and the separation bubble grows to form the primary vortex. In Fig. 30, it can be seen that the crossflow shock has been displaced to a position above the vortex near its inboard boundary. The pressure coefficient for the two solutions is given in Fig. 31. The second-order solution has been compared with the results obtained by K. Powell and E. Murman (Massachusetts Institute of Technology, private communication). Although the comparison is not shown, the two computations are in close agreement, including the level of minimum pressure coefficient and the extent and shape of the separation vortex.

#### Fine Grid Euler

Upwind Euler solutions were computed for the thin, sharp-tipped wing using the finer viscous grid, Fig. 19. In contrast to the previous coarse grid calculations, both the first- and second-order solutions are separated at the leading edge. The first-order solution predicts a very shallow vortex extending from the leading edge to the centerline. The second-order solution predicts the more familiar separation vortex. The crossflow velocity plot, Fig. 32, reveals two smaller secondary vortices near the leading edge. Referencing the crossflow Mach number plot, Fig. 33, the secondary vortices are triggered by a small crossflow shock embedded in the vortex. These features were not found in the viscous calculation,  $Re_{\infty} = 0.1 \times 10^6$ , Fig. 20. The inviscid calculation also predicts a crossflow shock above the vortex near the inboard boundary which is not present in the viscous result. A thin layer (laminar) viscous calculation at a Reynolds number of  $Re_{\infty} = 50 \times 10^6$  also failed to exhibit the inviscid shock-induced secondary vortices. The pressure coefficient at the lower Reynolds number is compared with the viscous solution in Fig. 34.



## CONCLUSIONS

Central and upwind difference solutions to the Euler and Navier-Stokes equations have been presented for conical delta wings with several cross-sectional shapes. For the rounded leading edge, central and upwind difference Navier-Stokes solutions agree well. Although adequate resolution is necessary for accurate results, the Navier-Stokes equations describe all relevant physical mechanisms and provide a consistent flow description. On a coarse grid, the central difference Euler solution predicts a primary separation vortex which resembles the viscous result. This separation vortex, however, is due entirely to numerical error. With sufficient grid refinement, the vortex disappears. On both coarse and fine grids, the upwind solution does not produce leading-edge separation. Both methods correctly predict shock-induced inviscid separation on the fine grid. The separation in this case is a valid Euler solution. Upwind solutions to the Navier-Stokes and Euler equations were computed for sharp leading-edge geometries. The viscous solutions again represent a consistent physical model. Attached flow Euler solutions were found for very sharp leading edges and even for the infinitely thin zero thickness wing. However, with sufficient grid refinement or resort to higher order spatial accuracy, the upwind scheme also predicts leading-edge separation.

The behavior of central and upwind difference schemes in the solution of the Euler equations for flow about the leading edges of highly swept delta wings raises questions of theoretical and practical importance. In this paper, the emphasis has been on the latter question. As a model for the prediction of leading-edge separation vortices, the Euler equations lack the essential quality of consistency. Further, they are fundamentally incapable of predicting secondary flow features such as Reynolds numbers dependence or the presence of secondary vortices. On the same grid, the cost of evaluating the viscous terms in the thin layer Navier-Stokes equations relative to the inviscid Euler equations is less than a 2% increase in CPU time per iteration for the implicit upwind code. This figure reflects the fact that a majority of the CPU time is spent assembling and solving the linear systems arising from the implicit time discretization. The penalty for an explicit method is significantly higher. In any event, the increase in accuracy and consistency in the resulting solutions would seem to justify the marginal increase in computational cost.

## REFERENCES

1. Vigneron, Y. C.; Rakich, J. V.; and Tannehill, J. C.: Calculation of Supersonic Viscous Flow Over Delta Wings With Sharp Subsonic Leading Edges. AIAA Paper 78-1137, July 1978.
2. Fujii, K.; and Kutler, P.: Numerical Simulation of the Leading Edge Separation Vortex for a Wing and Strake-Wing Configuration. AIAA Paper 83-1908, July 1983.
3. Fujii, K.; and Kutler, P.: Numerical Simulation of the Viscous Flow Over Three-Dimensional Complicated Geometries. AIAA Paper 84-1550, June 1984.

4. Rizzetta, D. P.; and Shang, J. S.: Numerical Simulation of Leading Edge Vortex Flows. AIAA Paper 84-1544, June 1984.
5. Hitzel, S. M.; and Schmidt, W.: Slender Wings With Leading-Edge Vortex Separation - A Challenge for Panel-Methods and Euler Codes. AIAA Paper 83-0562, Jan. 1983.
6. Rizzi, A.: Damped Euler-Equation Method to Compute Transonic Flow Around Wing-Body Combinations. AIAA Journal, vol. 20, no. 10, Oct. 1982, pp. 1321-1328.
7. Rizzi, A.; Eriksson, L. E.; Schmidt, W.; and Hitzel, S. M.: Simulating Vortex Flows Around Wings. Aerodynamics of Vortical Type Flows in Three Dimensions, AGARD Conference Preprint No. 342, 1983.
8. Rizzi, A.; and Erickson, L. E.: Computation of Flow Around Wings Based on the Euler Equations. Journal of Computational Physics, vol. 148, 1984, pp. 45-71.
9. Rizzi, A.: Euler Solutions of Transonic Vortex Flow Around the Dillner Wing - Compared and Analyzed. AIAA Paper 84-2142, Aug. 1984.
10. Rizzi, A.: Modelling Vortex Flow Fields by Supercomputers With Supersize Memory. Aeronautical Journal, April 1985, pp. 149-161.
11. Raj, P.; and Sikora, J.: Free Vortex Flows: Recent Encounters With an Euler Code. AIAA Paper 84-0135, Jan. 1984.
12. Powell, K.; Murman, E.; Perez, E.; and Baron, T.: Total Pressure Loss in Vortical Solutions of the Conical Euler Equations. AIAA Paper 85-1701, July 1985.
13. Fujii, K.; and Obayashi, S.: Evaluation of Euler and Navier-Stokes Solutions for Leading-Edge and Shock-Induced Separations. AIAA Paper 85-1563, July 1985.
14. Manie, F.; Neron, M.; and Schmitt, V.: Experimental and Computational Investigation of the Vortex Flow Over a Swept Wing. 14th Congress of the International Council of the Aeronautical Sciences, ICAS-84-2.8.1, Sept. 1984.
15. Newsome, R.: A Comparison of Euler and Navier-Stokes Equations for Supersonic Flow Over a Conical Delta Wing. AIAA Paper 85-0111, Jan. 1985.
16. Salas, M. D.: Recent Developments in Transonic Euler Flow Over a Circular Cylinder. Mathematics and Computers in Simulation, vol. 25, 1983, pp. 232-236.
17. Marconi, F.: The Spiral Singularity in the Supersonic Inviscid Flow Over a Cone. AIAA Paper 84-0135, Jan. 1984.
18. Marconi, F.: Shock Induced Vorticities on Elliptic Cones in Supersonic Flow. AIAA Paper 85-0433, Jan. 1985.

19. Salas, M. D.; and Daywitt, J.: Structure of the Conical Flow Field About External Axial Corners. AIAA Journal, vol. 17, no. 1, pp. 41-47, Jan. 1979.
20. Thomas, J. L.; van Leer, B.; and Walters, R. W.: Implicit Flux-Split Schemes for the Euler Equations. AIAA Paper 85-1680, July 1985.
21. Thomas, J. L.; and Walters, R. W.: Upwind Relaxation Algorithms for the Navier-Stokes Equations. AIAA Paper 85-1501 CP, July 1985.
22. MacCormack, R. W.: Numerical Solutions of the Interactions of a Shock Wave With a Laminar Boundary Layer. Lecture Notes in Physics, vol. 59, Springer Verlag, 1970, pp. 151-163.
23. MacCormack, R. W.; and Baldwin, B. S.: A Numerical Method for Solving the Navier-Stokes Equations With Application to Shock-Boundary Layer Interactions. AIAA Paper 75-1, Jan. 1975.
24. Squire, L. C.: Leading-Edge Separation and Crossflow Shocks on Delta Wings. AIAA Journal, vol. 23, no. 9, March 1985, pp. 321-325.
25. Miller, D. S.; and Wood, R. M.: An Investigation of Wing Leading-Edge Vortices at Supersonic Speeds. AIAA Paper 83-1816, July 1983.
26. Szodrach, J.: Reynolds Number Influence on Leaside Flow Fields, AIAA Journal, vol 16., no. 12, Dec. 1978, pp. 1306-1309.
27. Chakravarthy, S.; and Ota, D.: Numerical Issues in Computing Inviscid Supersonic Flow Over Conical Delta Wings. AIAA Paper 86-0440, January 1986.
28. Walters, R. W.; and Dwoyer, D. L.: An Efficient Strategy Based on Upwind/Relaxation Schemes for the Euler Equations. AIAA Paper 85-1529-CP, July 1985.

ORIGINAL PAGE IS  
OF POOR QUALITY

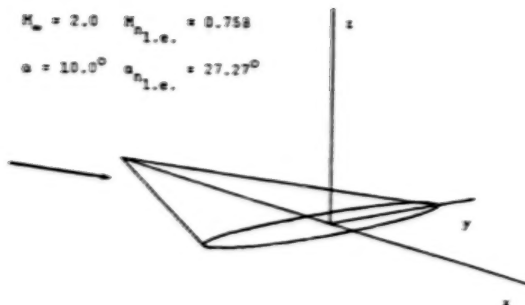


Fig. 1 Elliptic cone,  $y_{LE}/x = \tan(20^\circ)$ ,  
 $z_{CL}/x = \tan(1.5^\circ)$ .

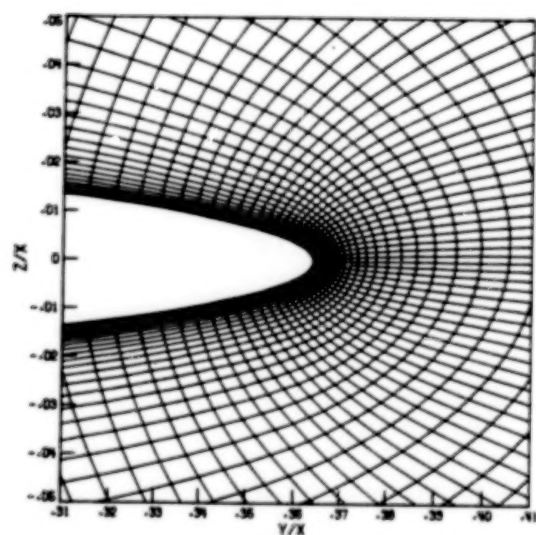
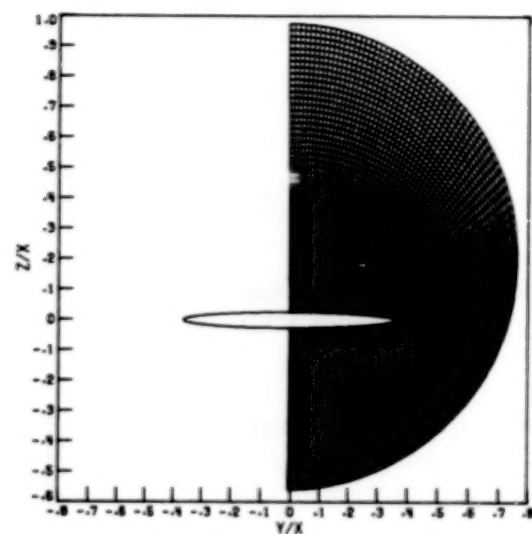


Fig. 2 Fine grid (151 × 65 points).

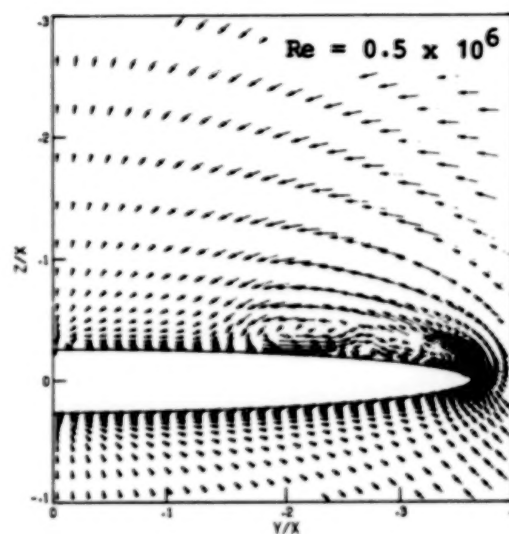
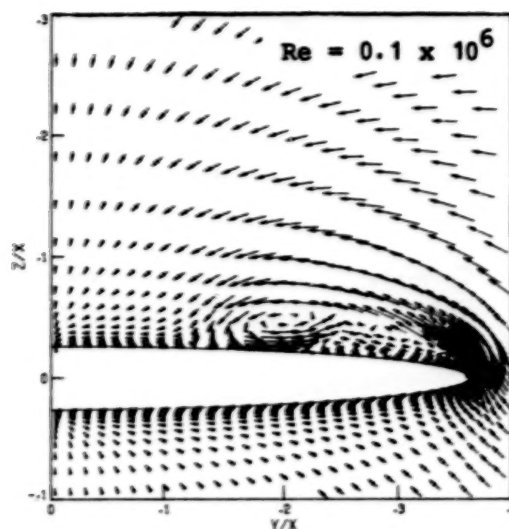


Fig. 3 Crossflow velocity vectors,  
central difference Navier-Stokes.

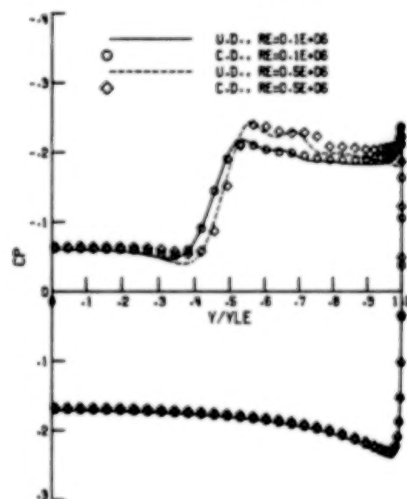


Fig. 4 Pressure coefficient, central  
and upwind difference Navier-  
Stokes.



ORIGINAL PAGE IS  
OF POOR QUALITY

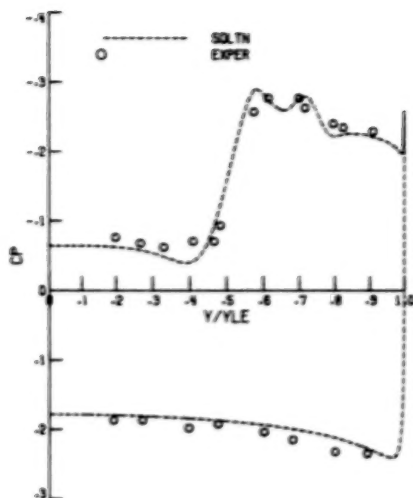


Fig. 5 Pressure coefficient, upwind difference Navier-Stokes versus data of Squire.

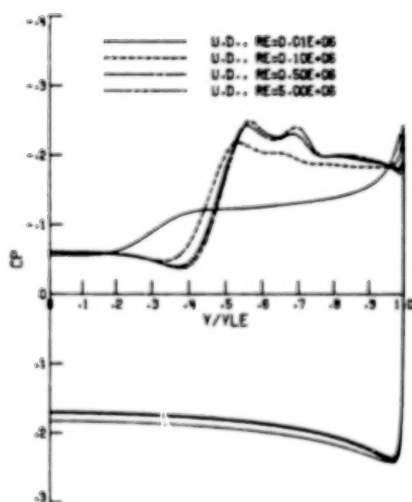


Fig. 6 Pressure coefficient, sensitivity to Reynolds number, upwind difference Navier-Stokes.

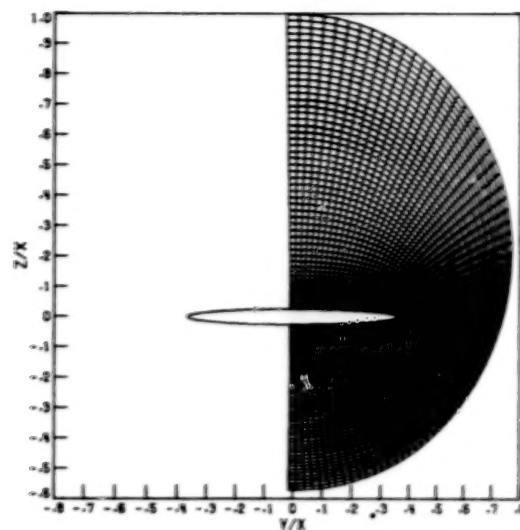


Fig. 7 Coarse grid (75 x 55 points).

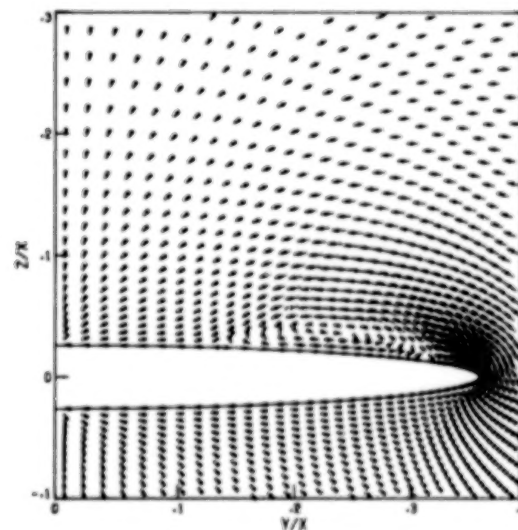


Fig. 8 Crossflow velocity vectors, central difference Euler, coarse grid.



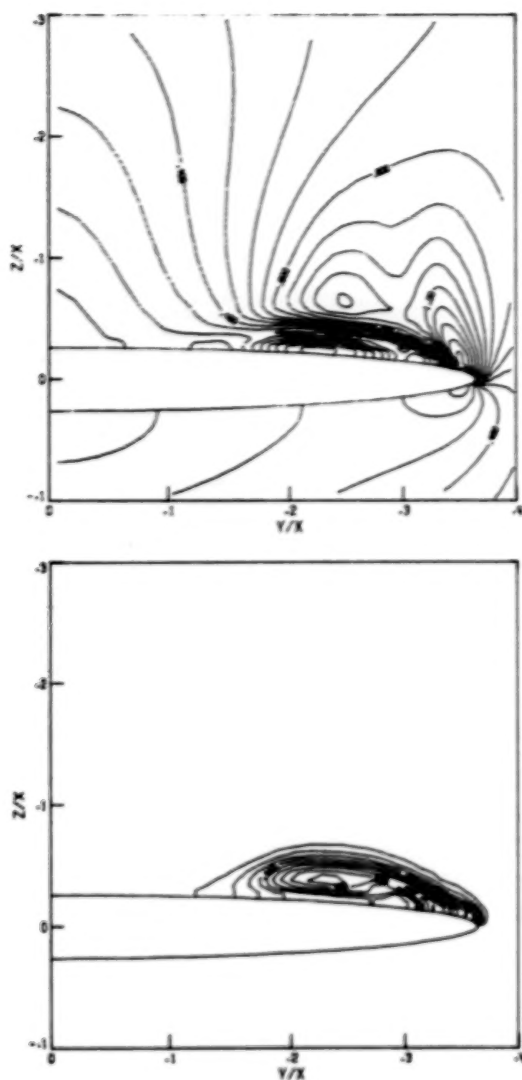


Fig. 9 Crossflow Mach number and entropy contours, coarse grid, central difference Euler.

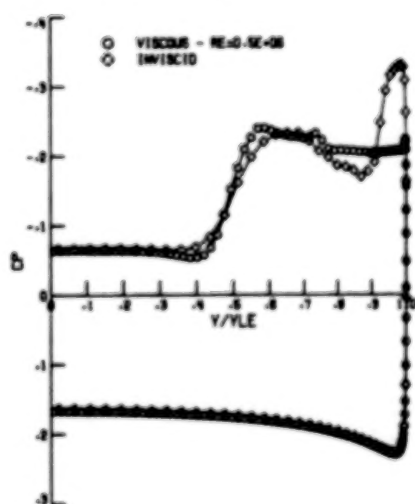


Fig. 10 Pressure coefficient, central difference coarse grid Euler versus fine grid Navier-Stokes.

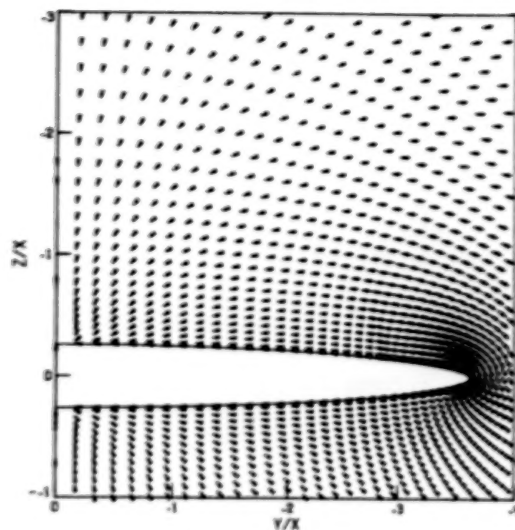


Fig. 11 Crossflow velocity vectors, coarse grid, 1st-order, upwind Euler.

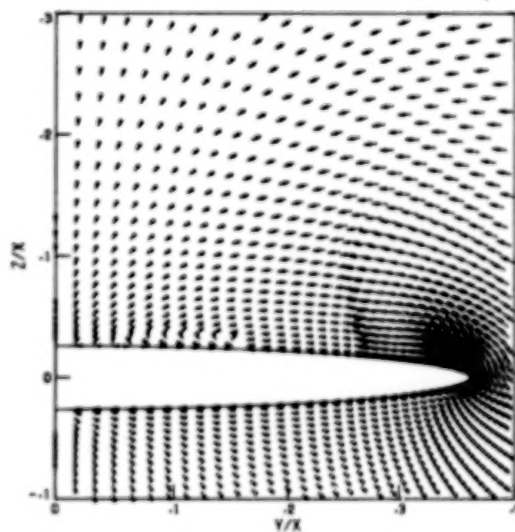


Fig. 12 Crossflow velocity vectors, coarse grid, 2nd-order upwind Euler.

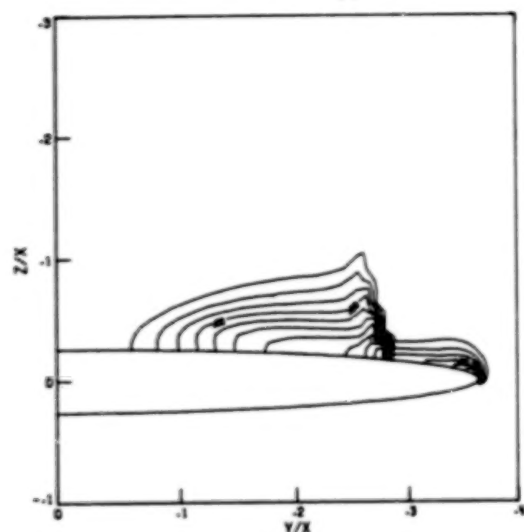
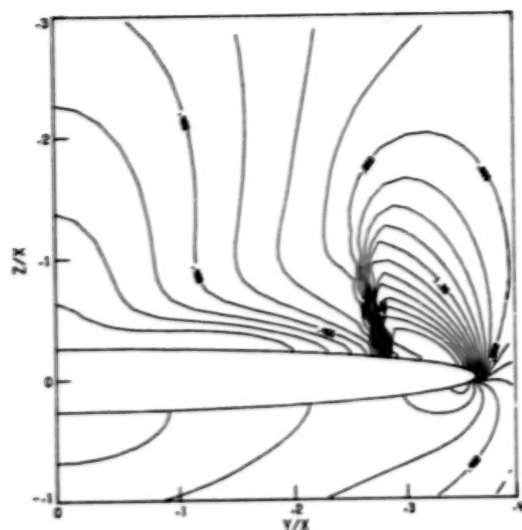


Fig. 13 Crossflow Mach number and entropy contours, coarse grid 2nd-order upwind Euler.

Fig. 15 Crossflow velocity vectors, fine grid central difference Euler.

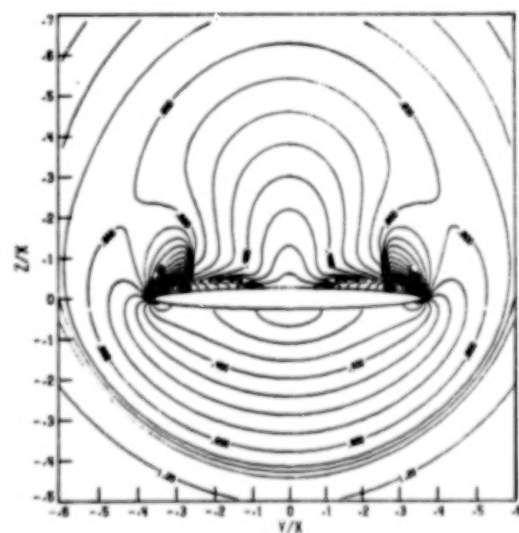
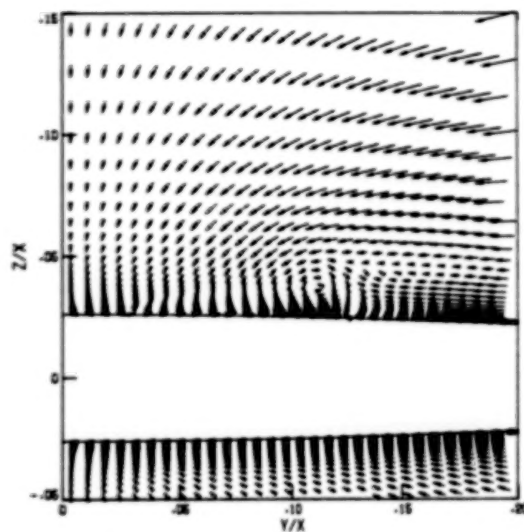
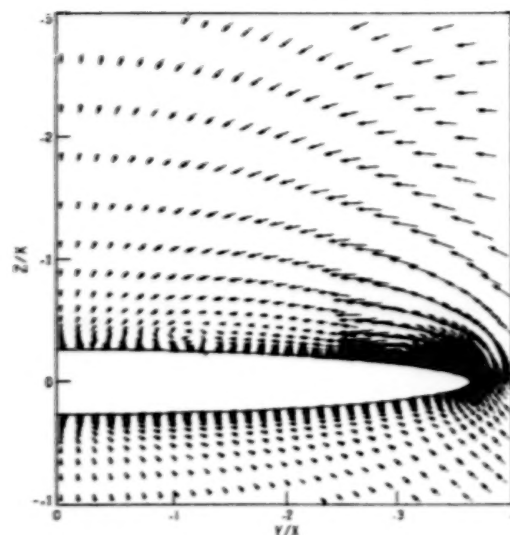


Fig. 14 Pressure coefficient, coarse grid 1st- and 2nd-order upwind Euler.

Fig. 16 Crossflow Mach number, fine grid, central difference Euler.

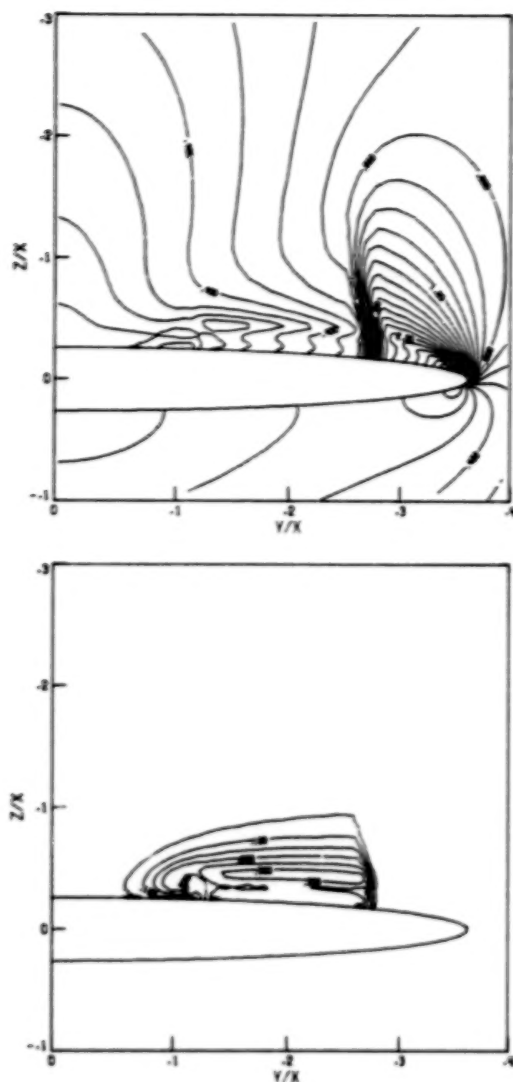


Fig. 17 Crossflow Mach number and entropy contours, fine grid central difference Euler.

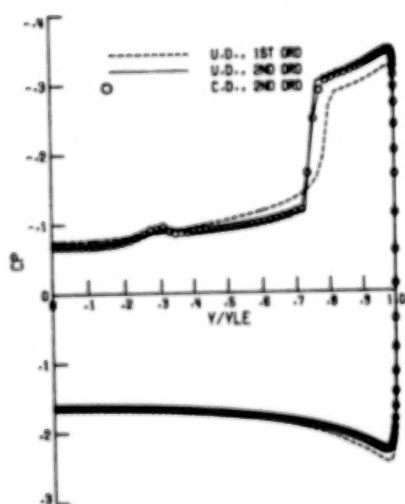


Fig. 18 Pressure coefficient, fine grid, central difference Euler versus upwind difference Euler.

ORIGINAL PAGE IS  
OF POOR QUALITY

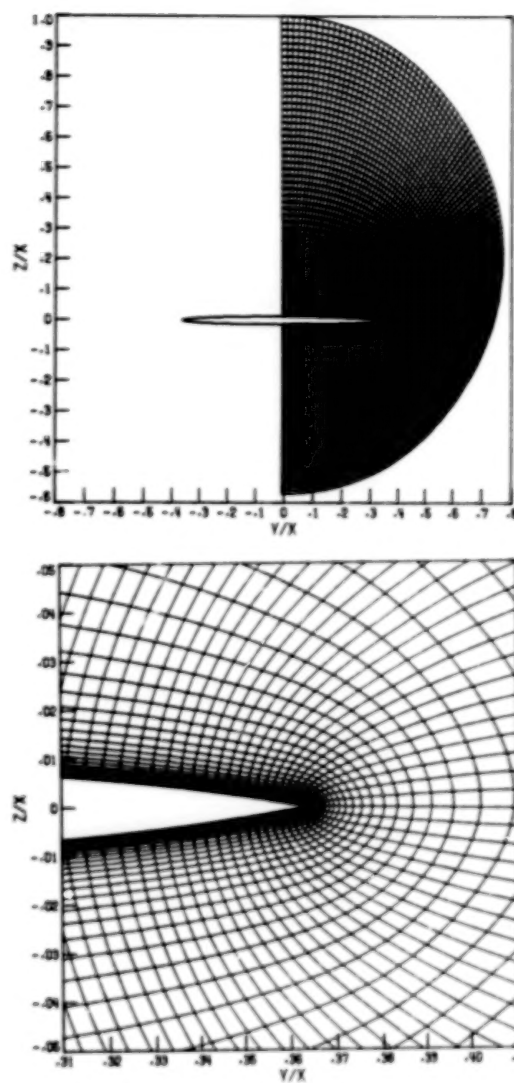


Fig. 19 Fine, sharp tip, grid (151 x 65) points.

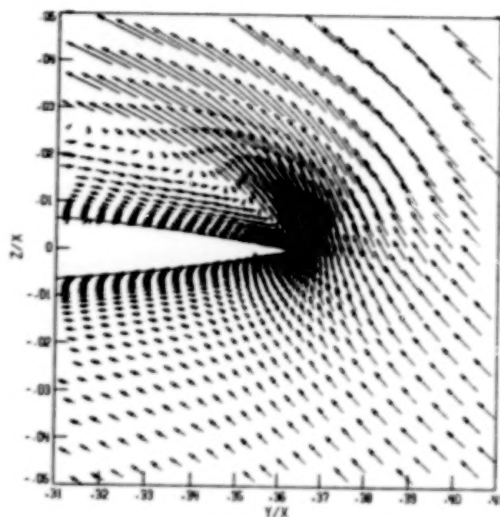
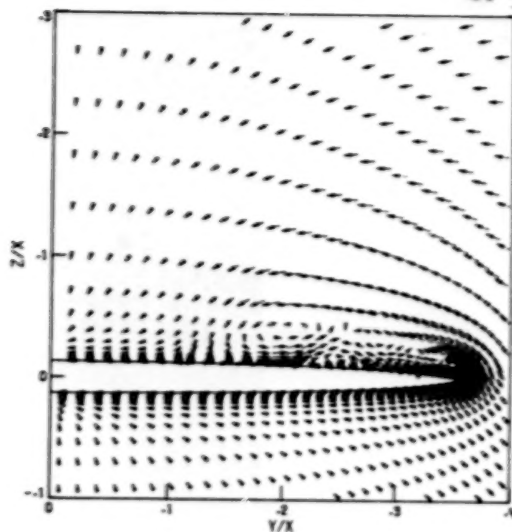


Fig. 20 Crossflow velocity vectors, fine grid, upwind difference Navier-Stokes,  $Re = 0.1 \times 10^6$ .

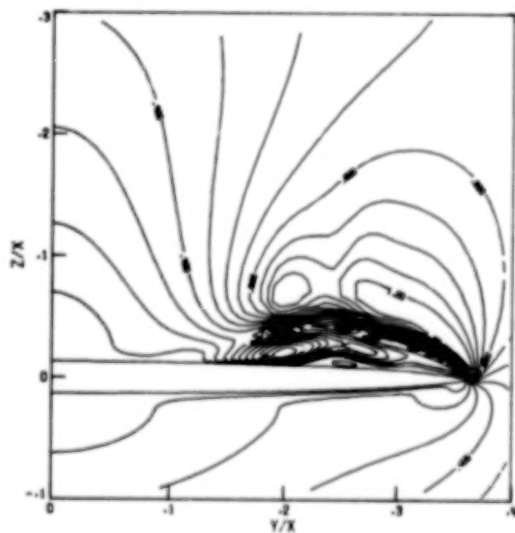


Fig. 21 Crossflow Mach number, fine grid, upwind difference Navier-Stokes,  $Re = 0.1 \times 10^6$ .

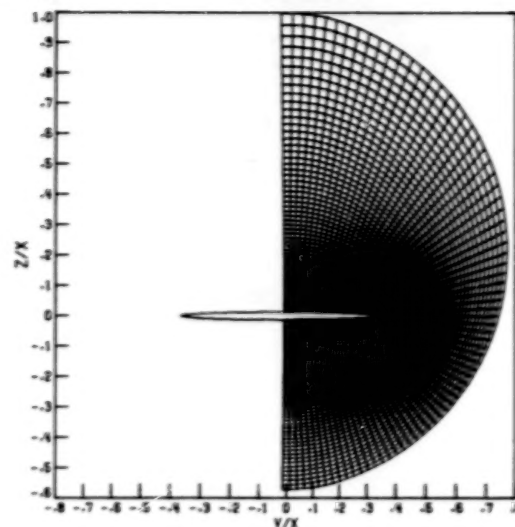


Fig. 22 Coarse, sharp tip, grid (75 x 55 points).

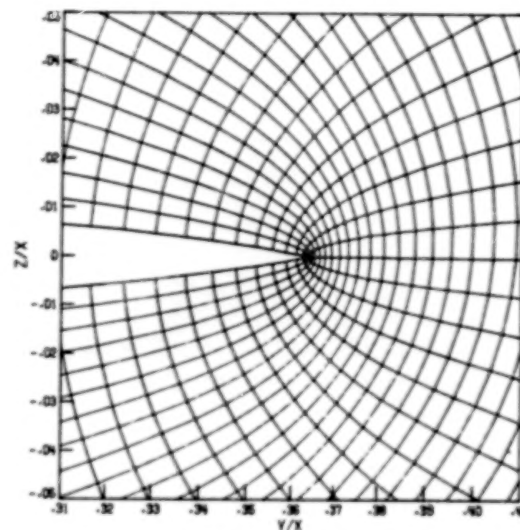


Fig. 23 Crossflow velocity vectors, coarse grid 2nd-order, upwind Euler.

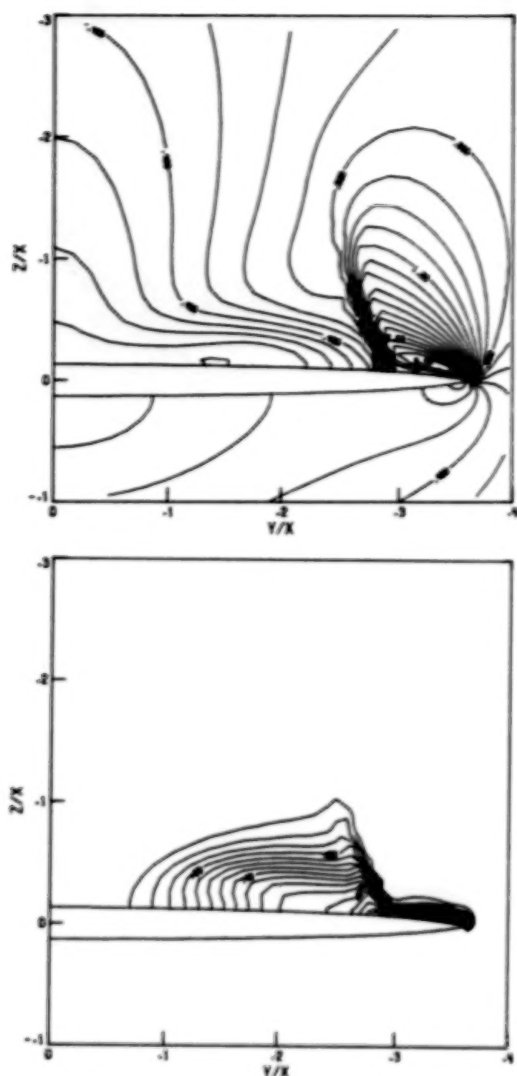


Fig. 24 Crossflow Mach number and entropy contours, coarse grid, 2nd-order, upwind Euler.

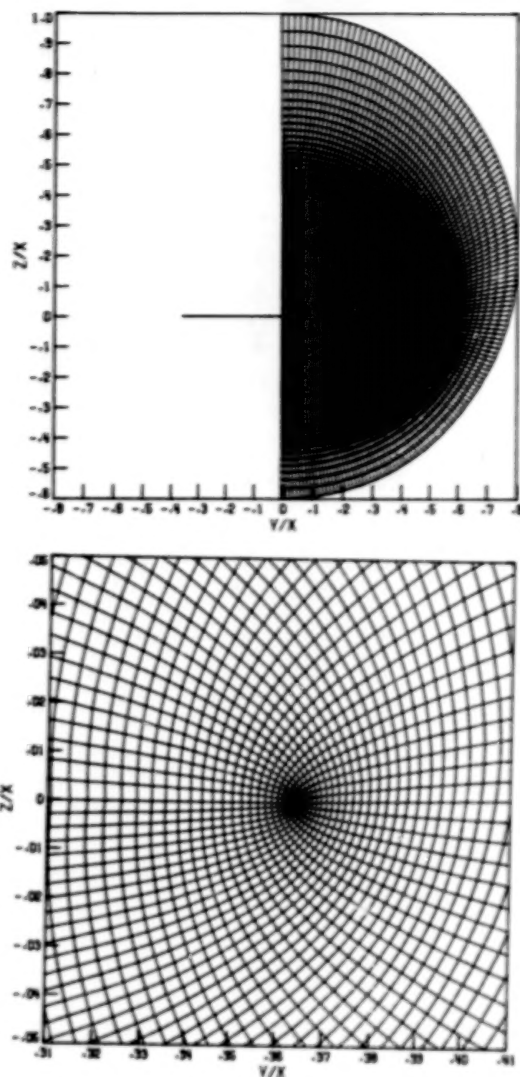


Fig. 26 Zero thickness wing grid (151 x 65 points).

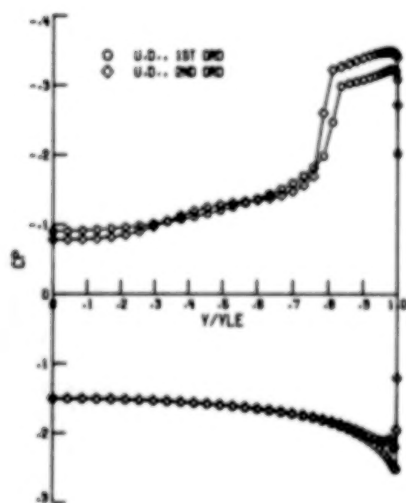


Fig. 25 Pressure coefficient, coarse grid 1st- and 2nd-order upwind Euler.

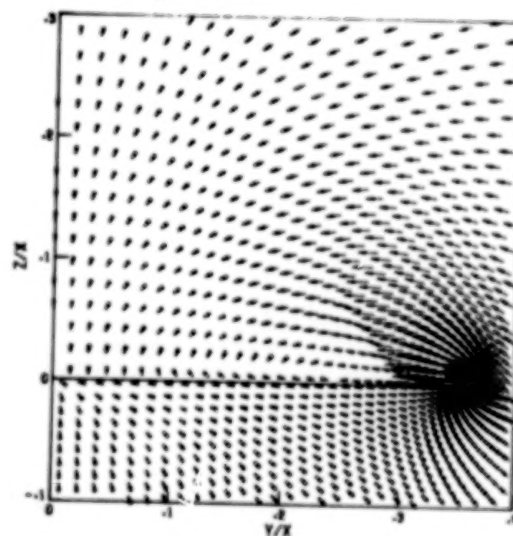


Fig. 27 Crossflow velocity vectors, zero thickness wing, 1st-order upwind Euler.



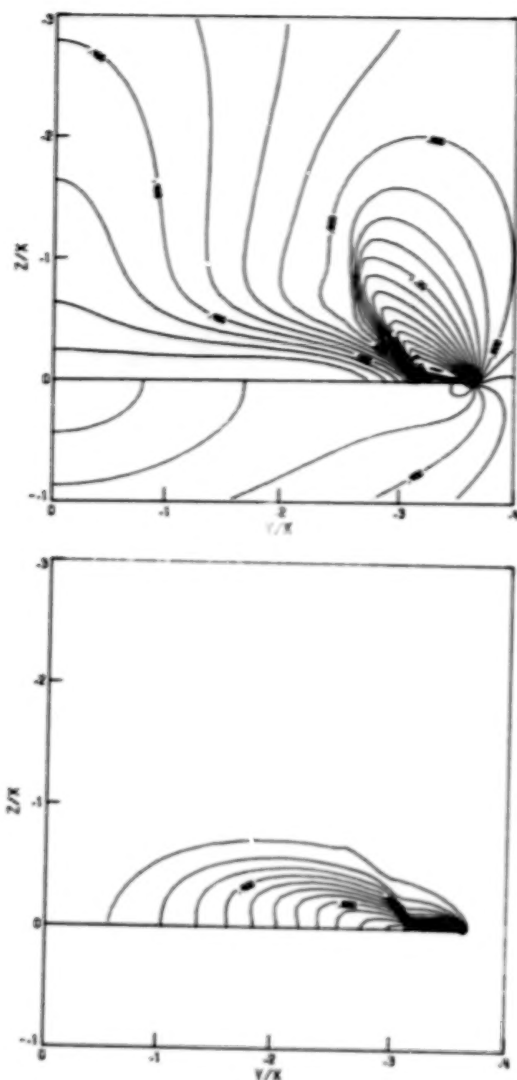


Fig. 28 Crossflow Mach number and entropy contours, zero thickness wing, 1st-order upwind Euler.

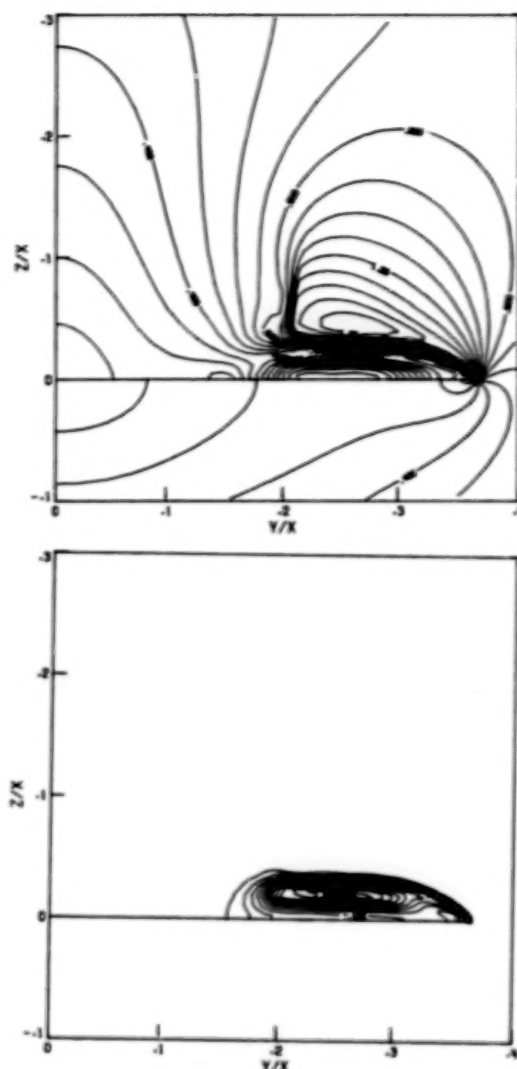


Fig. 30 Crossflow Mach number and entropy contours, zero thickness wing 2nd-order upwind Euler.

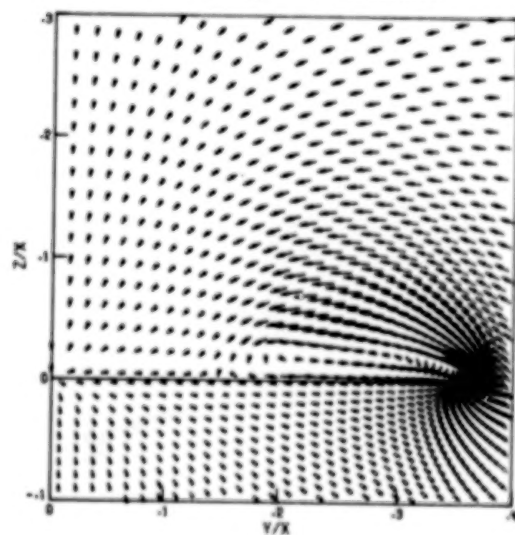


Fig. 29 Crossflow velocity vectors, zero thickness wing, 2nd-order upwind Euler.

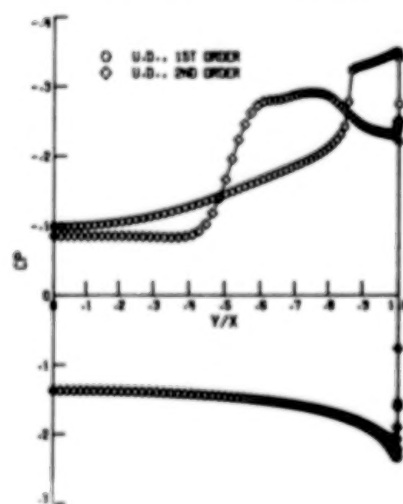


Fig. 31 Pressure coefficient, zero thickness wing, 1st- and 2nd-order upwind Euler.

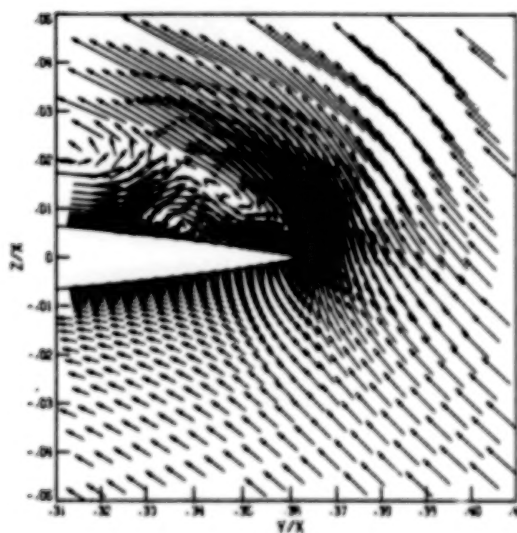
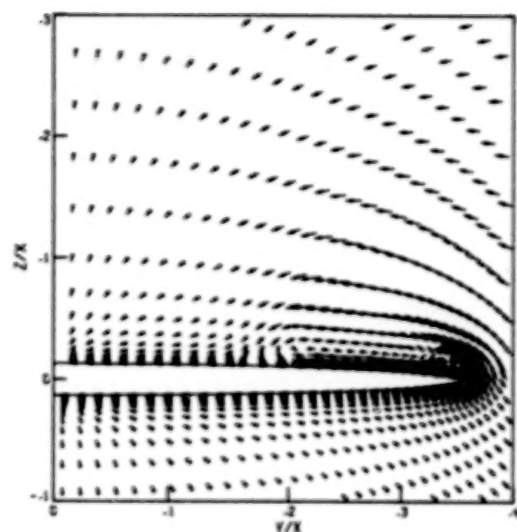


Fig. 32 Crossflow velocity vectors, fine grid, 2nd-order, upwind Euler.

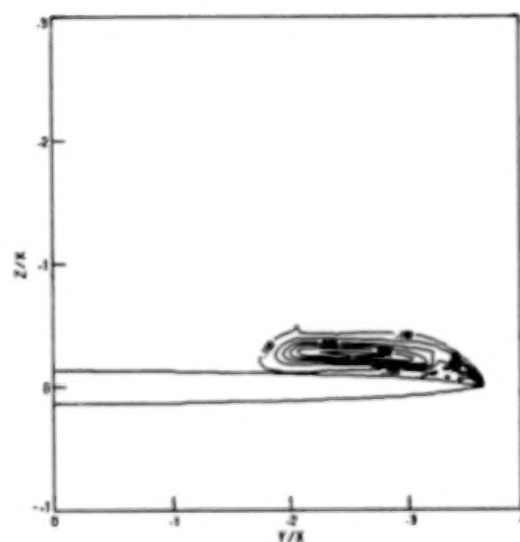
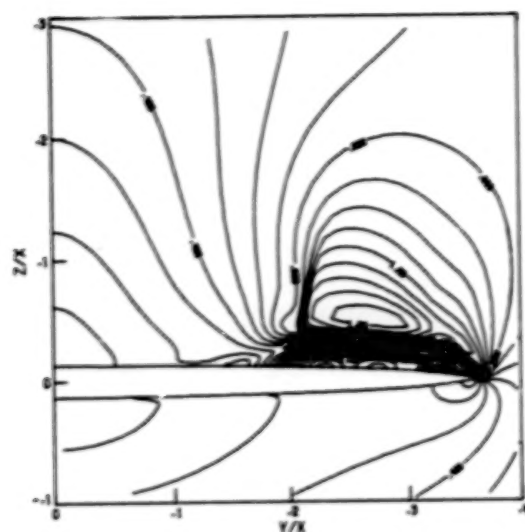


Fig. 33 Crossflow Mach number and entropy contours, fine grid, 2nd-order upwind Euler.

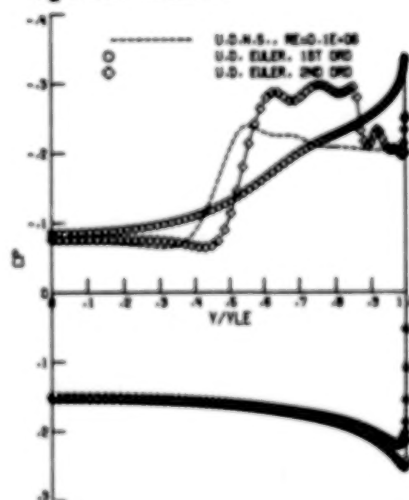


Fig. 34 Pressure coefficient. fine grid, 1st- and 2nd-order upwind Euler versus upwind Navier-Stokes  $Re = 0.1 \times 10^6$ .

Thomas A. Buter and Donald P. Rizzetta  
Air Force Wright Aeronautical Laboratories  
Wright-Patterson Air Force Base, Ohio

## ABSTRACT

Steady solutions about a slender sharp-edged delta wing in a supersonic freestream for moderate and high angles of attack are obtained numerically by time integration of the unsteady compressible three-dimensional laminar Navier-Stokes equations. The main features of the flow, including primary and secondary separation, and vortex position and strength, are adequately simulated in the numerical solutions. Improved resolution of the computational grid in the leading-edge region from a previous solution had considerable effect on the accuracy of the solutions. Good agreement between numerical solutions and experimental data was obtained for two cases. A local timestepping procedure is used to speed convergence by approximately a factor of two.

## NOMENCLATURE

|  |   |
|--|---|
| A  | attachment line   |
| c  | speed of sound ( $\gamma RT$ ) <sup>1/2</sup>                                 |
| C <sub>p</sub>                                   | pressure coefficient, $2(P - P_\infty) / \rho U_\infty^2$                     |
| e  | internal specific energy  |
| E  | total specific energy   |
| F, G, H  | vector fluxes   |
| L  | model length, mm  |
| M  | freestream Mach number  |
| P  | pressure  |
| Pr   | Prandtl number, 0.73 for air  |
| q <sub>x</sub> , q <sub>y</sub> , q <sub>z</sub> | components of heat flux vector  |
| R  | gas constant  |
| Re   | Reynolds number, based on the root chord                                      |
| S  | separation line   |
| t  | time  |
| T  | temperature   |
| u, v, w  | Cartesian velocity components in x, y, z directions, respectively             |
| u <sub>1,2,3</sub>                               | u, v, w   |
| U <sub>1,2,3</sub>                               | vector of mass averaged variables   |
| x, y, z  | Cartesian coordinates in axial, normal, and spanwise directions, respectively |
| $\alpha$   | angle of attack   |
| $\beta$  | numerical damping coefficient   |
| $\gamma$   | ratio of specific heats   |
| $\Delta$   | finite difference step size   |

00872-2

|   |                                     |
|---|-------------------------------------|
| $\mu$   | molecular viscosity coefficient     |
| $\xi, \eta, \zeta$  | transformed body fitted coordinates |
| $\rho$  | density                             |
| $\tau_{xx}, \tau_{xy}, \tau_{xz},$<br>$\tau_{yy}, \tau_{yz}, \tau_{zz}$ | components of viscous stress tensor |

#### Subscripts

|          |                                |
|----------|--------------------------------|
| aw       | adiabatic wall value           |
| LE       | evaluated at wing leading edge |
| max      | maximum value                  |
| min      | minimum value                  |
| loc      | local value                    |
| T        | pitot conditions               |
| $\infty$ | freestream value               |

#### INTRODUCTION

In recent years, with the advent of the supercomputer, computational aerodynamicists have devoted considerable effort to the solution of increasingly complex three-dimensional separated flows with a view toward the solution of airframe design problems. One of the most interesting and most practical of these is the separated flow field associated with a slender sharp-edged delta wing at angle of attack. Characterized by a pair of leeward spiraling vortices emanating from the separated leading-edge flow this inviscid-viscous flow problem has been computed using several techniques. Higher order panel methods (1-3) have enjoyed some measure of success by modeling the vortex roll-up as a sheet of quadratic doublets. However, this method requires the presence of a vortex and some awareness of its size and position. These restrictions are removed when a 3-D Euler approach is used (4,5). The physical meaning of such solutions is questionable, however, given the apparent dependency on grid resolution (6) and on the use of numerical viscosity. Using a conical flow approximation, Vigneron (7) et al. obtained a Navier-Stokes solution for a delta wing having a subsonic leading edge. With this approach, the location and basic structure of the primary vortex may be accurately computed. However, in cases where the adverse pressure gradient in the outboard region of the wing, induced by the leading-edge expansion, is of sufficient strength to produce a secondary separation, the conical approach becomes inadequate as evidenced by the results of Reference 7. Previous results presented by Rizzetta and Shang (8) illustrated that by using the full 3-D compressible laminar Navier-Stokes equations secondary effects may be accurately resolved numerically. The current investigation adopts this technique for an additional high angle-of-attack case and attempts to enhance the results of the previous study by improving the grid resolution and leading-edge definition. The present study investigates numerically the 75° sweep delta wing studied experimentally by Monnerie and Werle (9) depicted in Figure 1.

# GOVERNING EQUATIONS

The governing equations for this computation are taken to be the unsteady compressible three-dimensional Navier-Stokes equations in mass-averaged variables which may be expressed notationally in the following chain-rule conservative form:

$$\frac{\partial U}{\partial \xi} + \left( \frac{\partial \xi}{\partial x}, \frac{\partial \xi}{\partial y}, \frac{\partial \xi}{\partial z} \right) \begin{bmatrix} \frac{\partial F}{\partial \xi} \\ \frac{\partial G}{\partial \xi} \\ \frac{\partial H}{\partial \xi} \end{bmatrix} + \left( \frac{\partial \eta}{\partial x}, \frac{\partial \eta}{\partial y}, \frac{\partial \eta}{\partial z} \right) \begin{bmatrix} \frac{\partial F}{\partial \eta} \\ \frac{\partial G}{\partial \eta} \\ \frac{\partial H}{\partial \eta} \end{bmatrix} + \left( \frac{\partial \zeta}{\partial x}, \frac{\partial \zeta}{\partial y}, \frac{\partial \zeta}{\partial z} \right) \begin{bmatrix} \frac{\partial F}{\partial \zeta} \\ \frac{\partial G}{\partial \zeta} \\ \frac{\partial H}{\partial \zeta} \end{bmatrix} = 0 \quad (1)$$

Here  $x, y, z$  are Cartesian coordinates in the axial, normal and spanwise directions respectively and  $\xi, \eta, \zeta$  are the corresponding transformed coordinates in a body-oriented system and

$$U = \begin{bmatrix} \rho \\ \rho u \\ \rho v \\ \rho w \\ \rho E \end{bmatrix} \quad (2)$$

$$F = \begin{bmatrix} \rho u \\ \rho u^2 + \tau_{xx} \\ \rho uv + \tau_{xy} \\ \rho uw + \tau_{xz} \\ (\rho E + \tau_{xx}) u + \tau_{xy} v + \tau_{xz} w - q_x \end{bmatrix} \quad (3)$$



$$G = \begin{bmatrix} \rho v \\ \rho v u + \tau_{xy} \\ \rho v^2 + \tau_{yy} \\ \rho v w + \tau_{yz} \\ (\rho E + \tau_{yy}) v + \tau_{yx} u + \tau_{yz} w - q_y \end{bmatrix} \quad (4)$$

$$H = \begin{bmatrix} \rho w \\ \rho w u + \tau_{wx} \\ \rho w v + \tau_{wy} \\ \rho w^2 + \tau_{zz} \\ (\rho E + \tau_{zz}) w + \tau_{zx} u + \tau_{zy} v - q_z \end{bmatrix} \quad (5)$$

$$\tau_{xy} = \tau_{yx} = -\mu \left( \frac{\partial u}{\partial y} + \frac{\partial v}{\partial x} \right) \quad (6)$$

$$\tau_{xz} = \tau_{zx} = -\mu \left( \frac{\partial u}{\partial z} + \frac{\partial w}{\partial x} \right) \quad (7)$$

$$\tau_{yz} = \tau_{zy} = -\mu \left( \frac{\partial v}{\partial z} + \frac{\partial w}{\partial y} \right) \quad (8)$$

$$q_x = \frac{\mu \gamma}{Pr} \left( \frac{\partial \theta}{\partial x} \right) \quad (9)$$

$$q_y = \frac{\mu \gamma}{Pr} \left( \frac{\partial \theta}{\partial y} \right) \quad (10)$$

$$q_z = \frac{\mu \gamma}{Pr} \left( \frac{\partial \theta}{\partial z} \right) \quad (11)$$

$$E = e + (u^2 + v^2 + w^2)/2 \quad (12)$$

The Cartesian velocity components are given by  $u$ ,  $v$  and  $w$ ,  $\rho$  is the density,  $E$  the total energy per unit mass, and  $e$  the specific internal energy. Completion of this system is provided by the perfect gas law:

$$P = \rho RT \quad (13)$$

and the Sutherland law for the molecular viscosity coefficient  $\mu$ . Freestream values are specified as boundary conditions for all dependent variables at the upstream, outboard, upper and lower computational boundaries, i.e.,  $U = U_\infty$ . At the wing midspan a plane of symmetry is imposed which results in:

$$\frac{\partial \rho}{\partial \zeta} = \frac{\partial \rho u}{\partial \zeta} = \frac{\partial \rho v}{\partial \zeta} = \frac{\partial \rho E}{\partial \zeta} = w = 0 \text{ along } \zeta = 0 \quad (14)$$

On the upper and lower wing surface

$$u = v = w = 0$$

$$T = T_w$$

$$\frac{\partial P}{\partial \hat{n}} = \frac{g w}{\delta}, \text{ where } \hat{n} \text{ is the unit normal to the surface} \quad (15)$$

Because only computations corresponding to supersonic freestream conditions were considered, no formal mathematical downstream boundary conditions were needed. However, due to the requirements of the numerical algorithm used, values of the dependent variables at the downstream computational boundary are obtained by second-order extrapolation from the interior domain.

## NUMERICAL PROCEDURE

The laminar computation performed in Reference 8 for  $M=1.95$  and  $\alpha=10^\circ$  was repeated in the present study. Since it was of interest to compute a high angle of attack, a  $20^\circ$  case was chosen for the same Mach number. This necessitated increasing the size of the computational domain due to the expansion of the physical region of interest. The grid size was increased from  $20 \times 64 \times 40$  to  $21 \times 70 \times 50$  in the  $\xi, \eta, \zeta$  directions and was algebraically generated in a fashion similar (Figure 2) with two notable exceptions. In the work of Reference 8 the plane of symmetry was straddled to obtain a second-order centered difference implementation of the symmetry condition. While this technique was successful, the grid in this region was rather coarse. For the present study points were exponentially clustered near the plane of symmetry (Figure 2) to improve resolution in that region. This becomes particularly critical for the  $20^\circ$  case because the gradients near the plane of symmetry are greater due to the growth of the primary vortex and its inboard migration. The second modification to the grid structure was made at the wing tip, where resolution was increased and hence it was expected that the expansion about the leading edge might be more accurately resolved. This improvement, however, was gained at the expense of decreasing the time step (Table 1) due to the decreased step size in the  $y$  direction. In order to alleviate some of this degradation of efficiency, the lower surface  $\eta$  lines were bent down and away from the surface near the tip, thereby increasing the size of  $\Delta y_{\min}$  (Figure 3).

For the purpose of improved vortex resolution the current grid system employs an additional 6  $\eta$ -grid lines (yielding a total of 46) on and above the wing surface and an additional 5  $\zeta$ -grid lines (total - 29) inboard of the wing leading edge. Further, 5  $\zeta$ -grid lines were added to the outboard field region to resolve the expansion about the leading edge. An additional  $\eta$ - $\zeta$  plane was added at  $\frac{x}{L} = 0.05$  to improve the resolution near the apex.

This grid, although sized for the  $\alpha=20^\circ$  case, was used for both the  $\alpha=10^\circ$  and  $20^\circ$  cases to determine if for the present  $\alpha=10^\circ$  case a higher degree of accuracy might be obtained than its predecessor and for the purpose of uniformity between the current solutions.

Steady-state solutions to Equation 1 were generated using the time-dependent explicit unsplit two-step predictor-corrector finite-difference algorithm due to MacCormack (10) which has evolved as a reliable technique for numerical solution of a wide variety of fluid dynamic problems. As part of this algorithm, a commonly employed fourth-order pressure damping term (11) was used to suppress numerical oscillations in regions with large gradients in the dependent variables. The form of this term is given as

$$\beta \Delta t \sum_{j=1}^3 (\Delta v_j)^3 \frac{\partial}{\partial v_j} \left[ \frac{\partial U}{\partial v_j} \left| \frac{\partial^2 P}{\partial v_j^2} \right| \frac{|u_j + c|}{P} \right] \text{ where } v_{1,2,3} = \xi, \eta, \zeta \quad (16)$$

which is then added to the new value of  $U$  at each time step. In the present study, as in the previous effort, a damping coefficient of  $\beta = 2.0$  was used.

Freestream values were used as the initial conditions save for the interior boundary where surface conditions were applied. In order to remove the initial transients, the numerical flow fields were allowed to evolve for 100 time steps in the time accurate mode with  $\Delta t$  chosen such that the maximum Courant Fredicks Lewy (CFL) number was 0.5. Subsequently, the CFL number was increased to 0.8 and the computation was allowed to progress to steady state in a local timestepping fashion, where each grid point advances at its own rate ( $\Delta t_{loc}$  corresponding to a CFL number of 0.8) for a given iteration. This procedure has the advantage of advancing the solution to a steady-state value much more expeditiously since the more coarse regions of the physical domain are able to advance more quickly than in a time accurate mode. This modification resulted in the appearance of the primary and secondary vortex structures in the numerical solution much earlier than in the work of reference 8.

The computations were made on a Cray 1-S computer using a vectorized solver (12) written specifically for the Cray 1 computer. The solver advances the solution from one time step to the next in  $\eta$ - $\zeta$  planes by marching in the  $\zeta$ -direction, thus minimizing the data flow to and from central memory. Using the previously defined computational grid, approximately  $1.124 \times 10^6$  decimal words of storage were required. A data processing rate of  $6.9 \times 10^{-5}$  CPU seconds per time step per grid point was achieved where vectorization occurred in the  $\zeta$ -direction, with a vector length of 50.

## RESULTS

Numerical solutions were generated for the flow about the delta wing illustrated in Figure 1 at a Mach number of 1.95 (0.5 normal to the leading edge) for  $10^\circ$  and  $20^\circ$  angles of attack. The freestream conditions correspond to those of the experimental work of Monnerie and Werle<sup>9</sup>, the specifics of which are given in the table on Figure 1. A comparison of pitot pressure contours from reference 8 to the current  $\alpha = 10^\circ$  solution is given in Figure 4. Both solutions are a marked improvement over the results of reference 7 which employed a conical approximation and did not capture the secondary separation. However, while the shape and location of the primary and secondary vortices are roughly the same, the pitot pressure levels on the wing upper surface are not. The solution of reference 8 shows less evidence of pitot pressure loss in the primary vortex region as shown by the large disparity in the  $P_T/P_\infty = 0.7$  pressure levels. This may be attributed to the improved resolution in the leading-edge tip region which leads to a more accurate computation of the leading-edge expansion, hence the improved correlation with experiment as shown in Figure 5. The expanded grid size in the  $\eta$  and  $\zeta$ -directions may also account for some of this improvement as the outer boundaries are much farther from the wing. In addition, the increased resolution of the apex region by the addition of the  $\frac{X}{L} = 0.05$  station improves

the modeling of the flow being entrained into the inviscid core.



The improved resolution in the  $\eta$  or  $y$  direction accounts for the increased clarity of the upper surface "oil flow" patterns shown in Figure 6. While the position of the primary and secondary lines of separation ( $S_1$  and  $S_2$  respectively) and reattachment ( $A_1$ ,  $A_2$ ) are nearly the same, their sharpness, particularly near the trailing edge, is improved. This improvement is attributed to a second-order treatment of the downstream boundary condition. However, in spite of these differences, the aerodynamic loading perceived on the wing is similar as shown in the  $C_p$  distributions given in Figure 7. Here the suction peaks associated with the primary and secondary vortices are clearly in evidence and are similarly located.

The development of the cross-plane velocity with  $X$  is illustrated in Figures 8 and 9 for  $10^\circ$  and  $20^\circ$  respectively. Here the growth of the primary and secondary vortices and their inboard migration with angle of attack are evident and the non-conical nature of the flow field near the apex is revealed. Interesting to note is the fact that the secondary vortex originates at approximately  $\frac{X}{L} = 0.3$  for both cases. These same features are also evident

in the upper surface "oil flow" pattern given in Figure 10. While the flow is non-conical in the apex region, analysis of Figures 7-10 indicates that for the majority of the planform the flow is fairly conical.

The effect of angle of attack on loading is emphasized in the comparison of pressure coefficient depicted in Figure 11. The expected increase in loading and the inboard shift of vortex-associated surface pressure loss with  $\alpha$  is evident. From analysis of the pitot pressure contours in Figure 12 one can observe the growth of the secondary vortex and its displacement effect on the primary. The increased circumferential velocity in the primary vortex with angle of attack induces the observed pressure loss in the vortex core. Comparison of the  $20^\circ$  solution to the experiment of Monnerie and Werle in Figure 13 illustrates the remarkable accuracy of the laminar Navier-Stokes computation in spite of the rather high Reynolds number of the experiment.

## CONCLUSIONS AND DISCUSSIONS

Steady laminar solutions of the full 3-dimensional Navier-Stokes equations have been generated for the supersonic ( $M = 1.95$ ) flow over a  $75^\circ$  sweep sharp-edged delta wing at  $10^\circ$  and  $20^\circ$  angles of attack. Comparison with experiment and with the Navier-Stokes solution of reference 8 shows the following:

1. For both cases, the flow field solution correlates well with experiment. The position and strength of the primary and secondary vortices are accurately predicted. This leads one to believe that a laminar Navier-Stokes solution to the leading-edge vortex problem is adequate for obtaining pitot pressure, particularly for configurations with a Reynolds number less than  $1 \times 10^6$  such as in the present study, at least until an adequate turbulence model is developed for vortical flows.



2. An accurate geometrical modeling of the leading edge and considerable resolution of the tip region appear critical to the accurate computation of the leading-edge expansion. The agreement obtained in the present study is attributed in part to these two modifications to the grid of reference 8. A more accurate treatment of the downstream boundary condition also accounts for the improved solution in the trailing-edge region. In addition, the expansion of the computational domain in the  $\eta$  and  $\zeta$  directions probably resulted in some improvement in the  $10^\circ$  solution.

3. Because secondary separation develops axially as well as radially, methods employing a conical assumption will not adequately resolve a large portion of the flow field. In addition, resolution of the apex region is critical due to its highly non-conical structure.

4. The use of a local timestepping procedure increased the convergence rate by roughly a factor of two. It is estimated that each solution of the laminar 3-dimensional compressible Navier-Stokes equations presented herein required approximately 2 hours of CPU time on a CRAY 1-S computer to reach steady state based on a four order of magnitude reduction in L2NORM for all dependent variables.

#### REFERENCES

1. Weber, J.A., Brune, G.W., Johnson, F.T., Lu, P., and Rubbert, P.E., "Three-Dimensional Solution of Flows over Wings with Leading-Edge Vortex Separation," AIAA Journal, Vol. 14, April 1976, pp 519-525.
2. Luckring, J.M., Schoonover, W.E., Jr., and Frink, N.T., "Recent Advances in Applying Free Vortex Sheet Theory for the Estimation of Vortex Flow Aerodynamics," AIAA Paper 82-0095, Jan. 1982.
3. Hoeijmakers, H.W.M., and Rizzi A., "Vortex Fitted Potential Solution Compared with Vortex-Captured Euler Solution for Delta Wing with Leading-Edge Vortex Separation," AIAA Paper 84-2144, 1984.
4. Erikson, L.E., and Rizzi, A., "Computation of Vortex Flow Around Wings Using the Euler Equations," Proceedings of the Fourth GAMM Conference on Numerical Methods in Fluid Mechanics, Notes on Numerical Fluid Mechanics, Vol. 5, 1981, pp 137-148.
5. Hitzel, S.M., and Schmidt, W., "Slender Wings with Leading-Edge Vortex Separation - A Challenge for Panel-Methods and Euler-Codes," AIAA Paper 83-0562, Jan. 1983.
6. Newsome, R.W., "A Comparison of Euler and Navier-Stokes Solutions For Supersonic Flow Over a Conical Delta Wing," AIAA Paper 85-0111, January 14-17, 1985.

7. Vigneron, Y.C., Rakich, J.V., and Tannehill, J.C., "Calculation of Supersonic Viscous Flow over Delta Wings with Sharp Subsonic Leading Edges," AIAA Paper 78-1137, July 1978.
8. Rizzetta, D.P., and Shang, J.S., "Numerical Simulation of Leading-Edge Vortex Flows," AIAA Paper No. 84-1544, July 1984.
9. Monnerie, B., and Werle, H., "Study of Supersonic and Hypersonic Flow About a Slender Wing at an Angle of Attack," AGARD CP-30, May 1968 (in French).
10. MacCormack, R.W., "The Effect of Viscosity in Hypervelocity Impact Cratering," AIAA Paper 69-354, Apr-May 1969.
11. MacCormack, R.W., and Baldwin, B.S., "A Numerical Method for Solving the Navier-Stokes Equations with Application to Shock-Boundary Layer Interactions," AIAA Paper 75-1, Jan. 1975.
12. Shang, J.S., Buning, P.G., Hankey, W.L., and Wirth, M.C., "Performance of a Vectorized Three-Dimensional Navier-Stokes Code on a CRAY-1 Computer," AIAA Journal, Vol. 18, Sep. 1980, pp 1073-1079.

TABLE I COMPUTATIONAL PARAMETERS

| M    | $\alpha$ | $\Delta$                | $y_{\min}/z_{LE}$ | $y_{\max}/z_{LE}$ | $z_{\max}/z_{LE}$ | Iteration |
|------|----------|-------------------------|-------------------|-------------------|-------------------|-----------|
| 1.95 | 10°*     | $9.7971 \times 10^{-1}$ | -3.0              | 3.25              | 2.75              | 6000      |
| 1.95 | 10°      | $7.973 \times 10^{-1}$  | -3.7              | 4.6               | 3.5               | 2500      |
| 1.95 | 20°      | $7.973 \times 10^{-1}$  | -3.7              | 4.6               | 3.5               | 2500      |

\* Reference 8

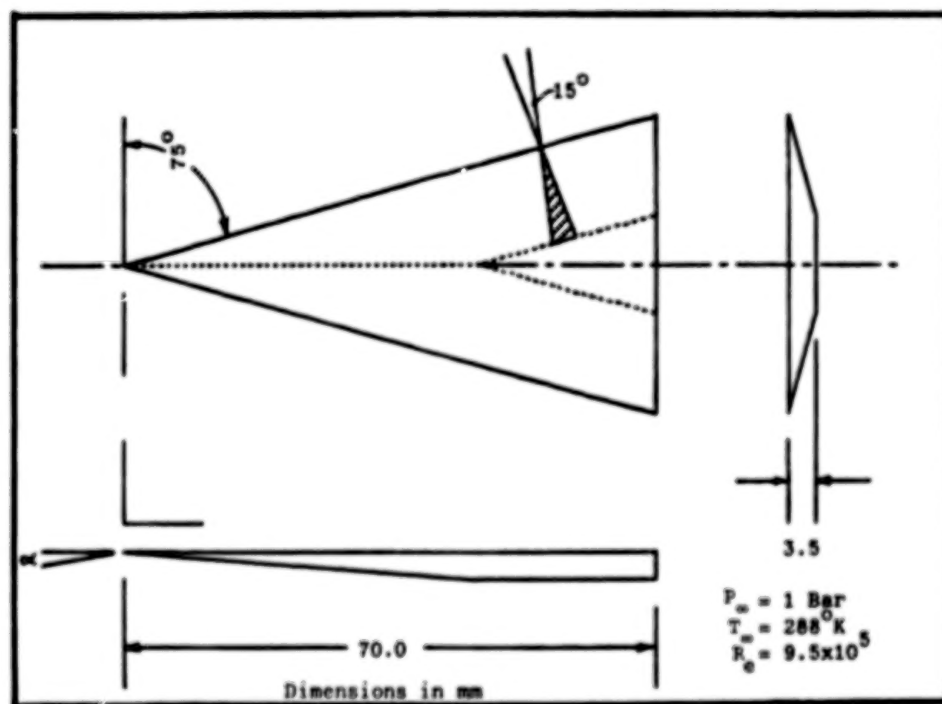


Figure 1. Delta wing geometry.

$$X/L=1.0$$

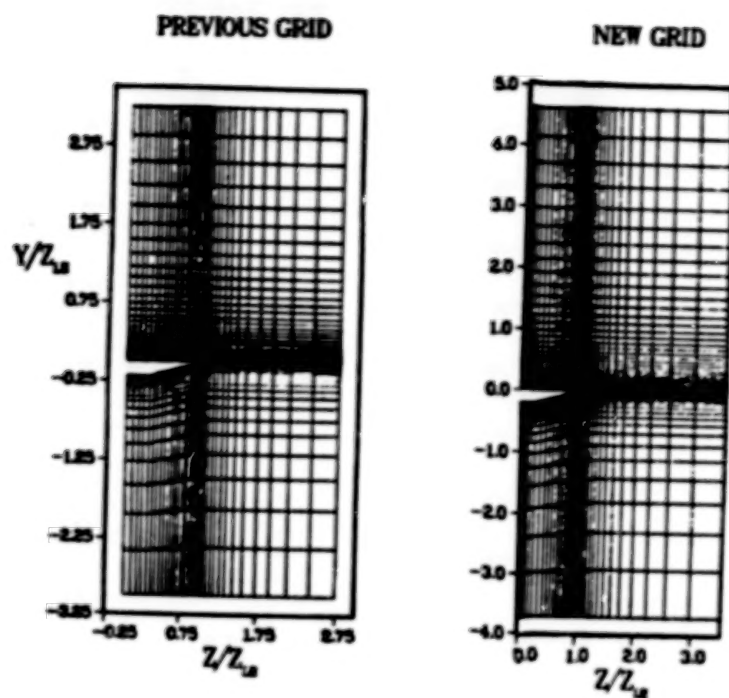


Figure 2. Comparison of Y-Z grid structure.

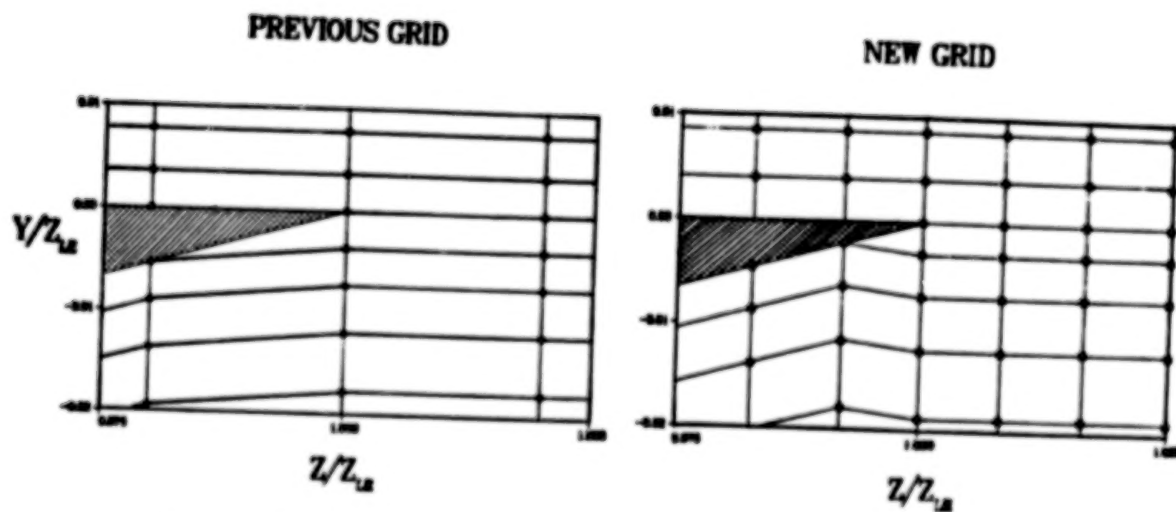


Figure 3. Comparison of Y-Z grid structure in tip region.

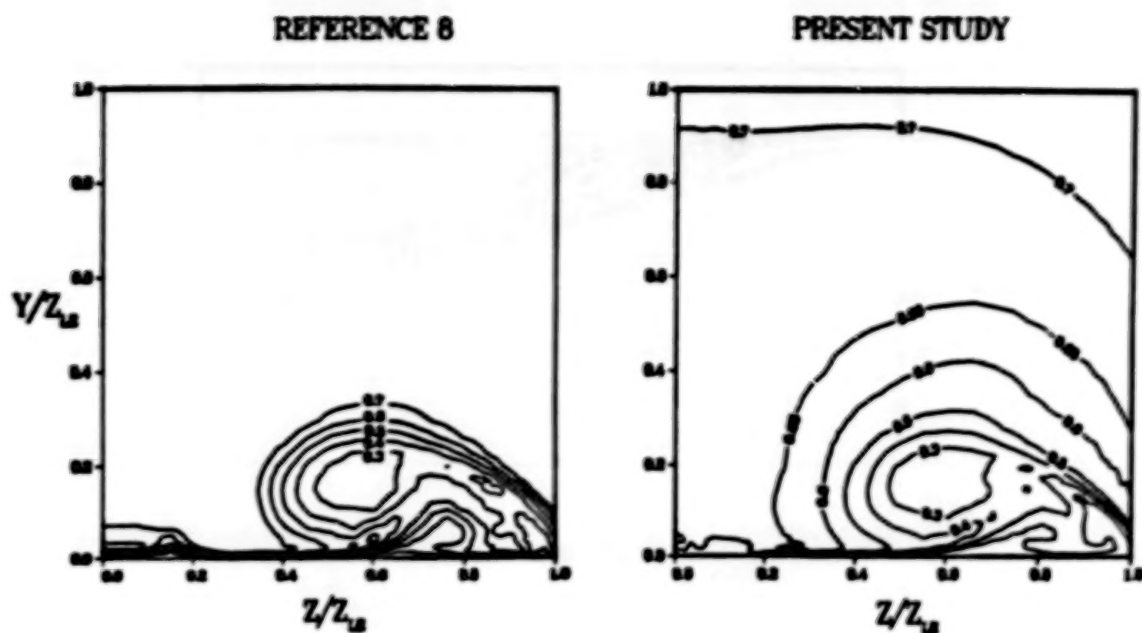


Figure 4. Comparison of Pitot pressure,  $X/L = 0.8$ .

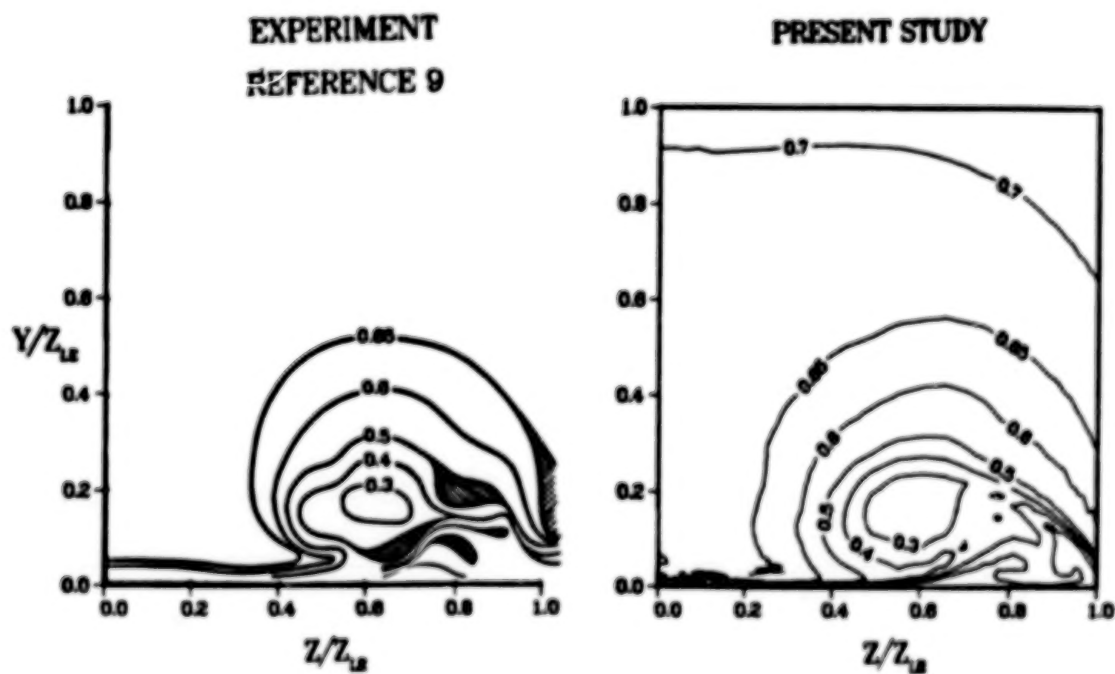


Figure 5. Comparison of Pitot pressure,  $X/L = 0.8$ .



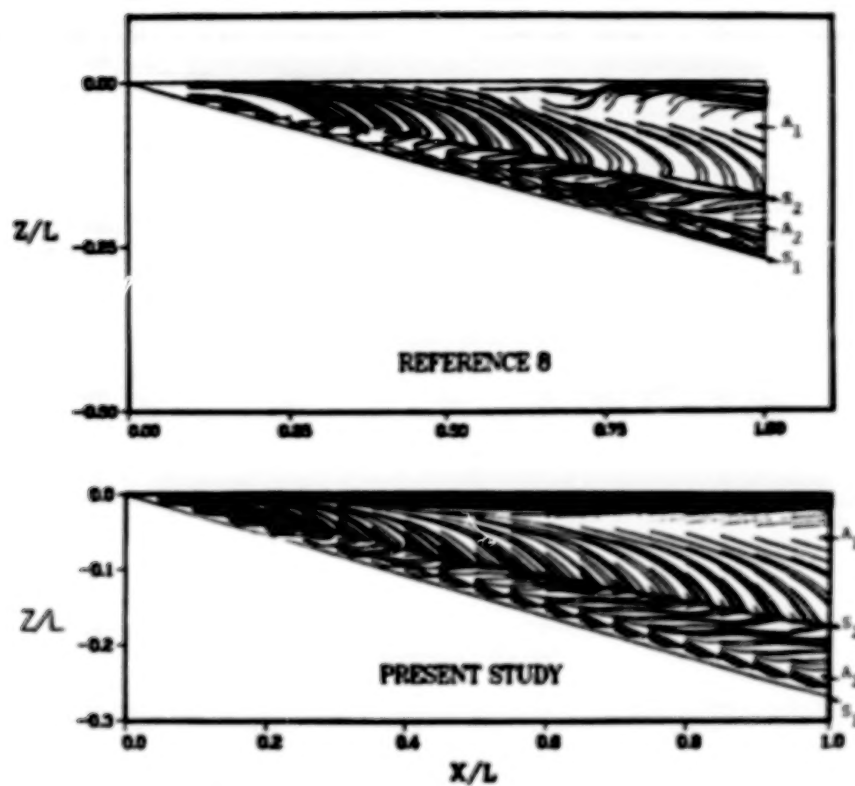


Figure 6. Upper surface oil flow pattern,  $\alpha = 10^\circ$ .

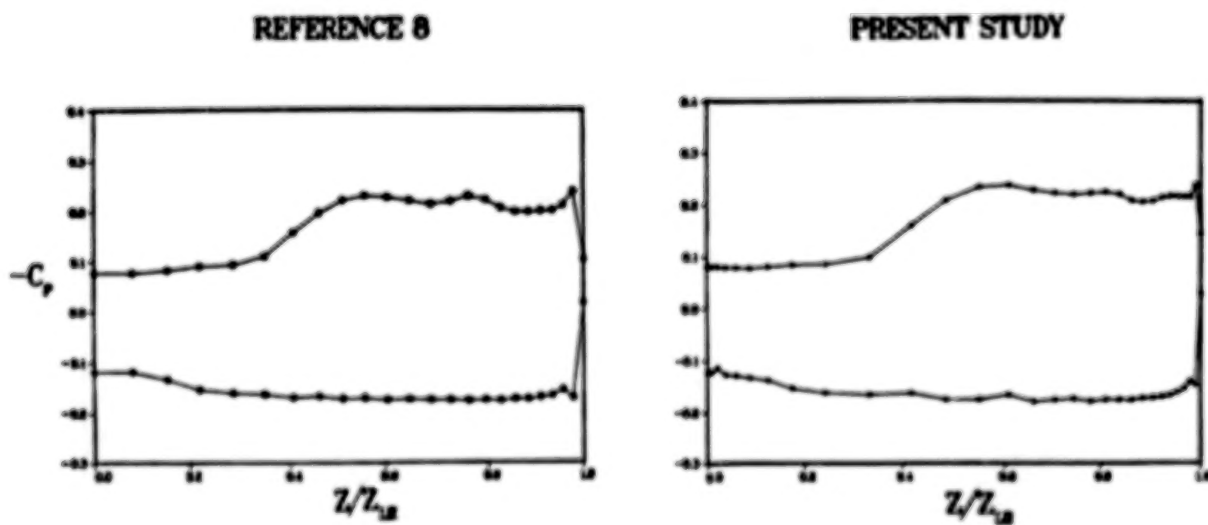


Figure 7. Spanwise pressure distribution,  $\alpha = 10^\circ$   $X/L = 0.8$ .

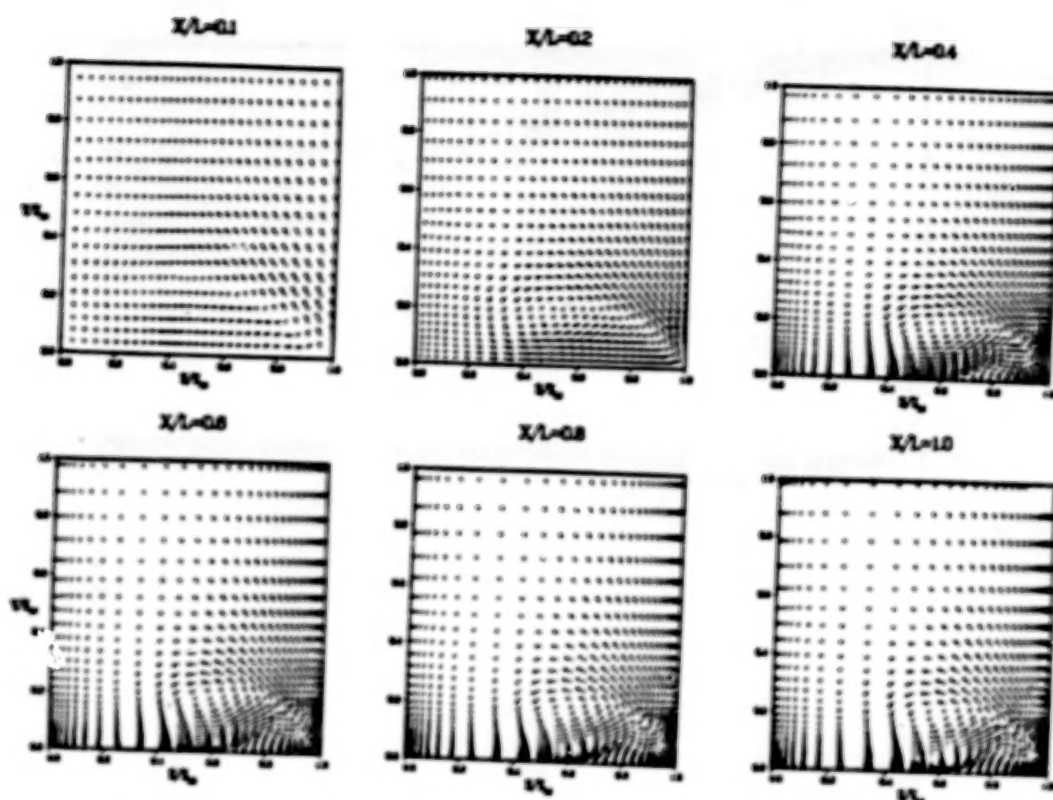


Figure 8. Development of cross-plane velocity,  $\alpha = 10^\circ$ .

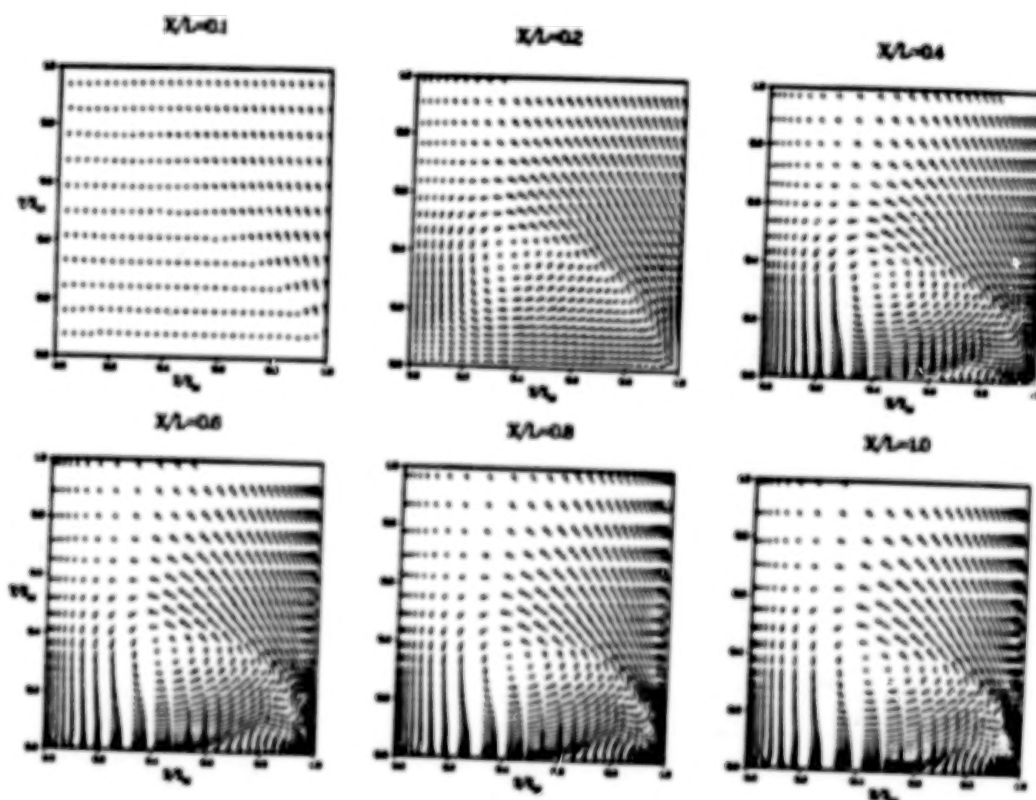


Figure 9. Development of cross-plane velocity,  $\alpha = 20^\circ$ .

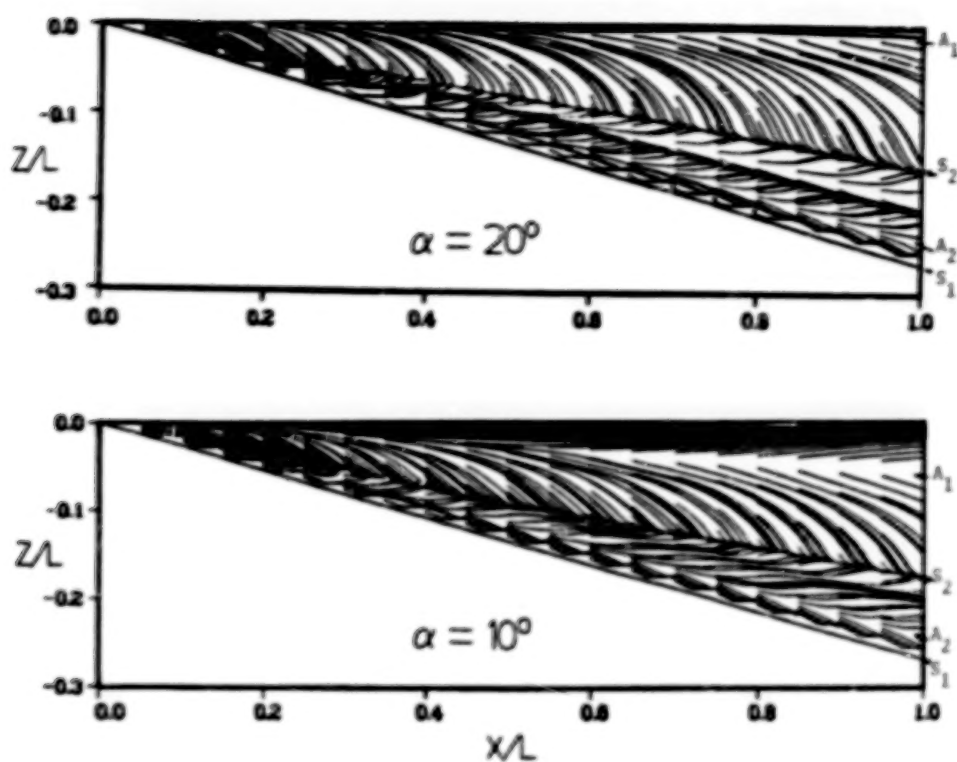


Figure 10. Upper surface oil flow pattern.

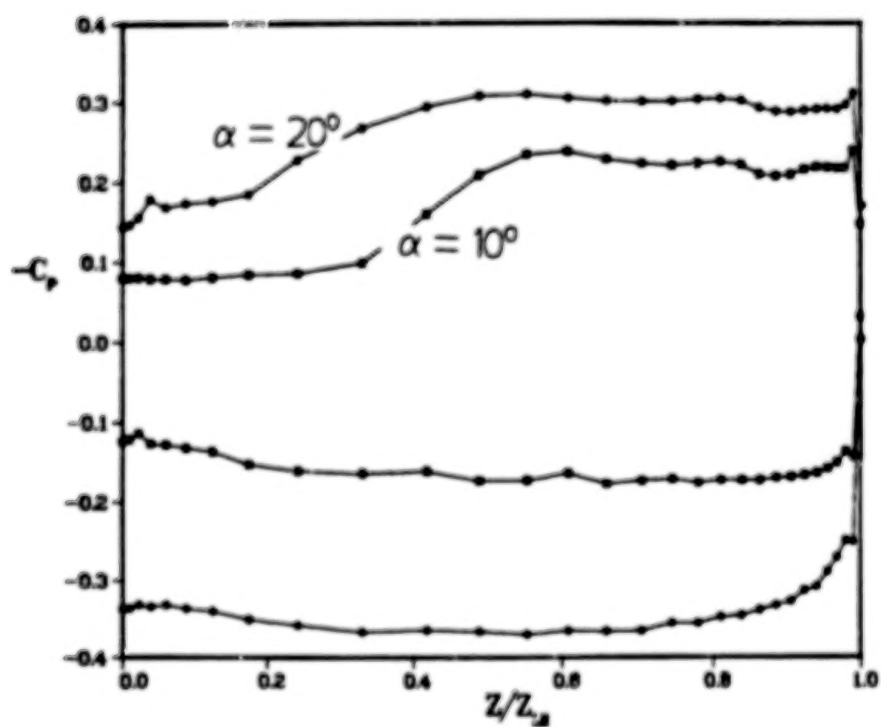


Figure 11. Effect of  $\alpha$  on pressure distribution,  $X/L = 0.8$ .

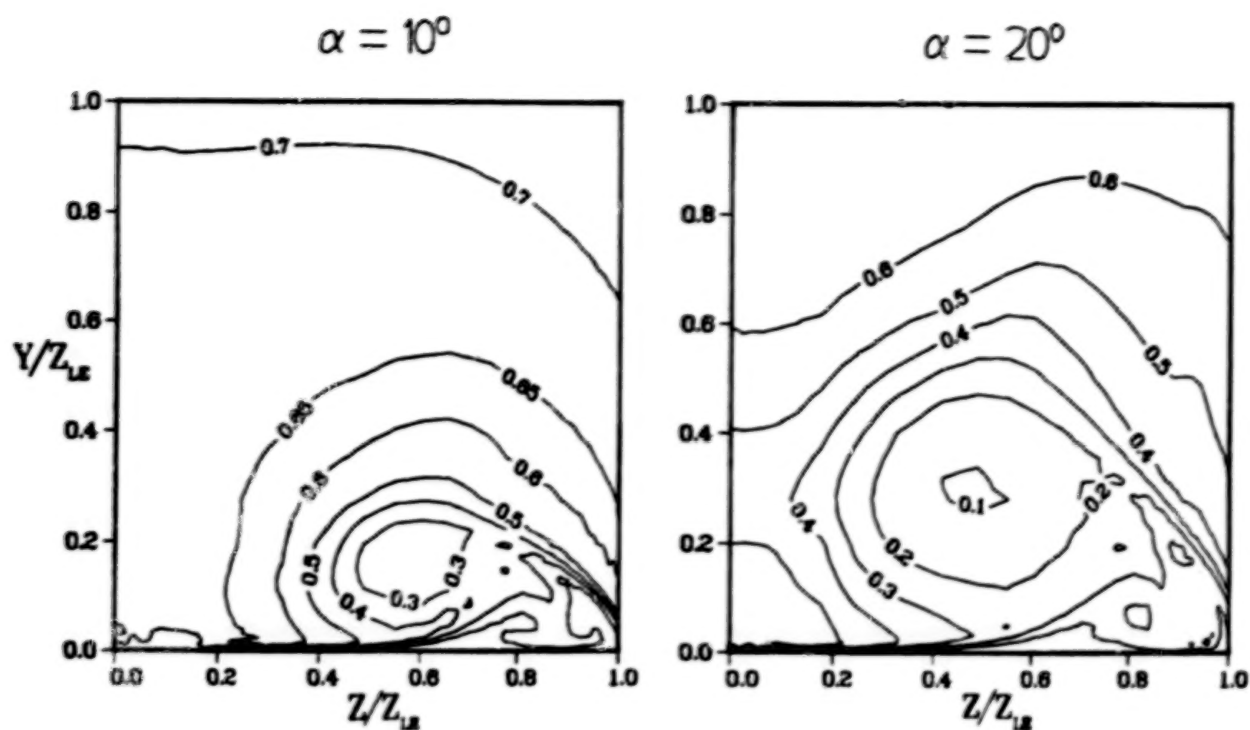


Figure 12. Effect of  $\alpha$  on Pitot pressure,  $X/L = 0.8$ .

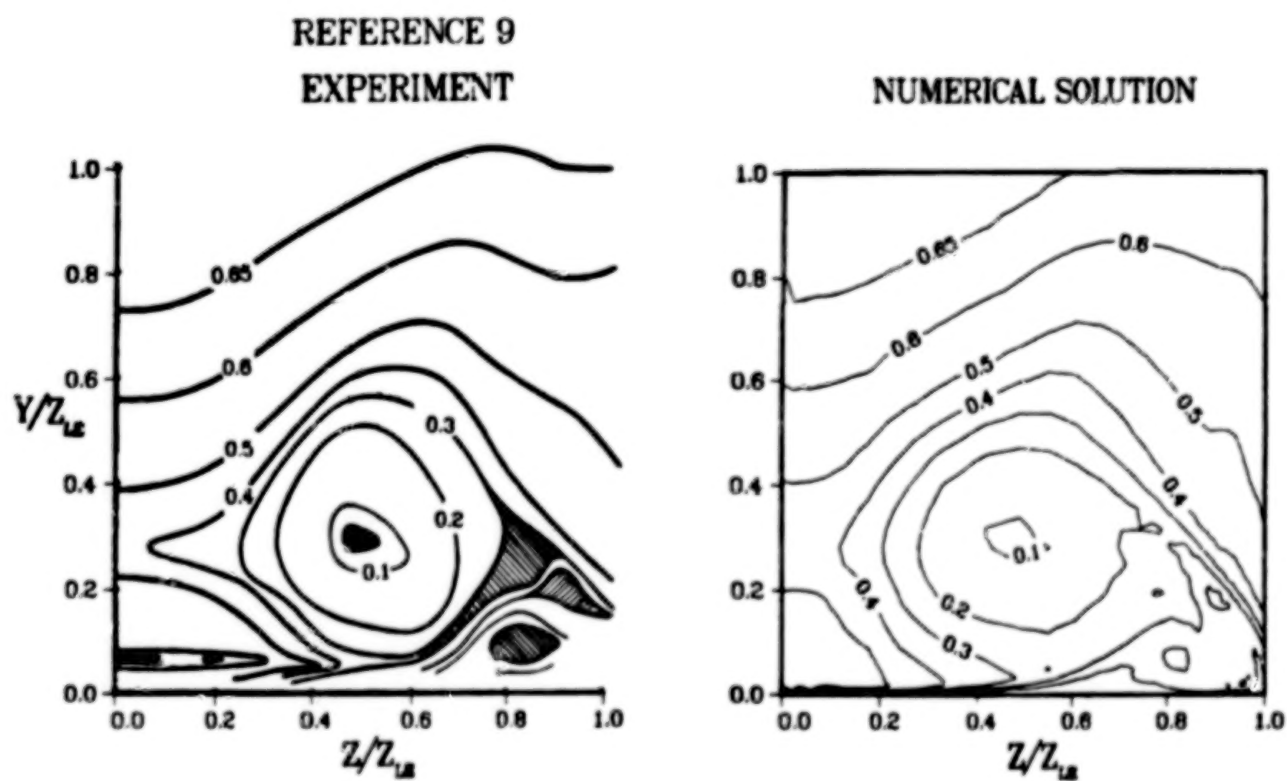


Figure 13. Comparison of Pitot pressure,  $\alpha = 20^\circ$ .

## AN OVERVIEW OF THE FUNDAMENTAL AERODYNAMICS BRANCH'S RESEARCH ACTIVITIES

## IN WING LEADING-EDGE VORTEX FLOWS AT SUPERSONIC SPEEDS

David S. Miller, Richard M. Wood, and Peter F. Covell  
NASA Langley Research Center  
Hampton, Virginia

## SUMMARY

For the past 3 years, a research program pertaining to the study of wing leading-edge vortices at supersonic speeds has been conducted in the Fundamental Aerodynamics Branch of the High-Speed Aerodynamics Division at the Langley Research Center. The purpose of the research is to provide an understanding of the factors governing the formation and the control of wing leading-edge vortices and to evaluate the use of these vortices for improving supersonic aerodynamic performance. The studies include both experimental and theoretical investigations and focus primarily on planform, thickness and camber effects for delta wings. This paper will present an overview of this research activity.

## INTRODUCTION

During the last 20 years, aerodynamicists have attempted to design aircraft wings for efficient supersonic flight using attached-flow concepts. For cruise levels of lift, linearized-theory wing-design methods (refs. 1 and 2) have successfully produced optimum twisted and cambered wings. Because of the early success of these methods, the methods have been continuously modified and refined to include the effects of component-on-wing interference (ref. 3), real-flow constraints (ref. 4), and attainable leading-edge thrust (ref. 5). Example applications of this low level-of-lift wing-design technology can be found in references 6 through 8.

For maneuver levels of lift at supersonic speeds, basically two approaches are available for the design of wings. One approach is to provide an attached-flow, controlled expansion around the wing leading edge and on the upper surface (refs. 9 and 10). This attached-flow approach for producing efficient high lift depends on the ability to accelerate the flow around the leading edge to supercritical conditions on the upper surface and then decelerate the flow without causing separation or producing strong shocks. This concept has been experimentally verified, and a summary of the investigation is given in reference 11. The second approach for obtaining efficient high-lift wings uses a controlled, separated, leading-edge vortex flow which not only produces vortex lift, but when the vortex is properly located on a deflected leading-edge, also produces significant levels of effective leading-



edge thrust. Investigations at subsonic and transonic speeds (refs. 12 to 16) of the fundamental vortex behavior on the leeward surface of wings have led to the design of several unique and novel leading-edge devices (refs. 17 to 21) commonly referred to as "vortex flaps." Also, to aid in the design of vortex flaps, several computer codes (refs. 22 to 24) with varying degrees of complexity are being developed to predict vortex location, strength, and effect on the wing. As summarized in reference 25, the development of this new wing-design technology has been extensive but has been confined mainly to subsonic and transonic flows.

In 1982, a research effort was begun to explore the fundamental characteristics of wing leading-edge vortex flows at supersonic speeds. A review of the literature indicated that various aspects of the problem had been previously explored; however, there did not exist a complete and systematic set of experimental data from which one could determine the most basic effects such as Mach number, planform, thickness and camber. To provide this information, an experimental program was formulated first and closely followed by a complementary theoretical effort. This paper will present an overview of the experimental and theoretical programs. Following the overview, a discussion of aerodynamic performance is presented. In this discussion, a comparison is made between wings designed for optimum camber, wings with conventional leading-edge flaps, and wings with conical vortex flaps.

#### NOMENCLATURE

|              |  |
|--------------|--|
| $C_D$        | drag coefficient   |
| $\Delta C_D$ | incremental change in drag coefficient from the minimum drag of a flat wing                                      |
| $C_L$        | lift coefficient   |
| $C_{N_V}$    | vortex induced normal-force coefficient  |
| $C_p$        | pressure coefficient   |
| $C_{p_v}$    | vacuum pressure coefficient  |
| $L$          | model length   |
| $M$          | Mach number  |
| $M_N$        | component of Mach number normal to wing leading edge = $M \cos \Lambda (1 + \sin^2 \alpha \tan^2 \Lambda)^{1/2}$ |
| $X$          | longitudinal distance measured from model origin   |

|            |  |
|------------|--|
| Y          | spanwise distance measured from model centerline                                       |
| $Y_{\max}$ | maximum spanwise model dimension   |
| $\alpha$   | angle of attack, deg   |
| $\alpha_N$ | angle of attack normal to wing leading edge = $\tan^{-1} (\tan \alpha / \cos \Lambda)$ |
| $\beta$    | $\sqrt{M^2 - 1}$ and angle of yaw, deg   |
| $\delta_f$ | leading-edge-flap deflection angle measured streamwise, deg                            |
| $\Lambda$  | wing leading-edge-sweep angle, deg   |
| n          | fraction of local wing semispan  |

### DISCUSSION

An experimental-theoretical research effort is under way to investigate the fundamental characteristics of wing leading-edge vortex flows at supersonic speeds. In order to present a complete overview of the program, both completed, ongoing and planned investigations will be included in the following discussion.

#### Experimental Program

The primary objective of the experimental program is to obtain a complete and consistent set of data necessary to determine the effects of wing planform, thickness and camber on the characteristics of wing leading-edge vortex flows. To obtain a consistent set of data for the entire program, an effort was made to keep the wing planforms, flow conditions and types of data consistent throughout. The specific ingredients for consistency were established in the planform investigation which was the first part of the experimental research program.

**Wing planform investigation.** - Shown in figure 1 are planform sketches of the 4 wind tunnel models selected for testing. The models had leading-edge-sweep values ranging from 52.5° to 75°. In this initial test, it was desirable to minimize the effect of airfoil shape and thickness; therefore, the leading edge was made sharp (10° angle normal to leading edge located on lower surface) and the upper surface was made flat. Each model had a span of 12 in. and a spanwise row of 19 evenly spaced pressure orifices located approximately 1 in. forward of the trailing edge.

Previous experimental tests employed only a single type of flow-visualization data with or without pressure data to explain the vortex phenomena. However, as shown in figure 2, these experimental pressure data were obtained along with three types of flow-visualization data. As shown at the

top of the figure, both tuft and oil-flow photographs were used to examine the flow characteristics on the model surface. These two techniques give slightly different types of information. Both methods are used to determine surface flow direction by the alignment of the tufts or the streaking of the oil; however, the tufts tend to reflect the velocity direction at the edge of the boundary layer, and the direction of oil streaking is influenced not only by the surface velocity but also by the pressure distribution.

Only the vapor-screen flow-visualization technique provides flow-field information on the size, shape, and location of the vortex as shown in the lower right side of figure 2. The dark areas in the photographs are regions having less vapor than the light areas and thus, the dark areas correspond to the highly rotational vortex-flow regions in which the vapor particles have been displaced. Examples and discussion of these various types of data and their relationship with leading-edge vortex behavior are given in reference 26. Each model was tested at Mach numbers of 1.7, 2.0, 2.4 and 2.8 for angles of attack ranging from  $0^\circ$  to  $20^\circ$ .

In a previous study, Stanbrook and Squire (ref. 27) suggested that the flow conditions normal to the leading edge, specifically normal angle of attack ( $\alpha_N$ ) and normal Mach number ( $M_N$ ), govern the type of flow which exists. Stanbrook and Squire initially reported that near  $M_N = 1$  a boundary existed dividing the flow into two distinct regions: for  $M_N < 1$  the flow was characterized by a leading edge, separated, rolled-up vortex-type flow and for  $M_N > 1$  the flow was characterized by an attached flow with possible shock-induced separation. The classification into just two types of flow provided by the Stanbrook-Squire boundary was revised by Ganzer, Hoder and Szodruch (ref. 28); however, this latter effort was based on a single leading-edge-sweep angle of  $73^\circ$  and flow conditions of  $M_N > 1$ . A complete review of this work was presented by Szodruch and Peake (ref. 29). In the present planform study, four leading-edge-sweep values were used to examine the type of flow for conditions which lie above and below the  $M_N = 1$  Stanbrook-Squire boundary.

Using primarily vapor-screen information, the types of flow observed in this test were divided into the seven categories as shown in figure 3. A detailed discussion of each of these flow types can be found in reference 26. In figure 4, all of the test data are summarized according to one of the seven flow types. The  $\alpha_N - M_N$  space is clearly divided into regions where the flow type is indicated by the vapor-screen sketch placed in each region. As an added feature to provide additional information, the open symbols identify flows with shocks; the closed symbols identify shockless flows; the circular symbols identify flows with primary and secondary vortices; the square symbols identify flows containing separation bubbles; the diamond symbols identify flows with shock induced separation; and the triangle symbols identify flows with no separation. As shown by the solid triangles in the figure, the only flow conditions which produced shockless attached flows were angles of attack of zero ( $\alpha_N = 0$ ); however, this occurs only because the next smallest angle of



attack in the test matrix was  $4^\circ$ . Because the two most effective types of separated flow being considered for aerodynamic performance enhancements are the shockless bubble and shockless vortex, it is interesting to note that these two types of flow occupy the majority of the region for  $M_N$  less than unity. Also above  $20^\circ$  normal angle of attack, the upper boundary of the region decreases towards  $M_N = 0$  with increasing  $\alpha_N$ .

**Wing thickness investigation.** - The experimental wing planform investigation was conducted with wind tunnel wing models designed to minimize the effects of airfoil shape and thickness; i.e., the leeward wing surface under investigation was made flat. However, calculated Euler code results, obtained by the method described in reference 30, are shown in figure 5 and indicate that the estimated effects of thickness can be significant. Mach number contours are shown for two delta wings each having  $70^\circ$  leading-edge-sweep angle but with different airfoil sections. One wing has a zero-thick airfoil section to represent a flat wing and the other wing has a 7-percent-thick circular-arc airfoil section. Although the calculations for both wings were made at exactly the same flow conditions of  $M = 2.5$  and  $\alpha = 18^\circ$ , the Mach number contours indicate that the types of flow were completely different. The flow over the leeside of the zero-thick wing is characterized by a well-developed leading-edge vortex with a shock located on top of the vortex; the zero-thick wing flow conditions correspond to  $M_N = 1.13$  and  $\alpha_N = 44^\circ$  and, as shown in the  $\alpha_N - M_N$  graphic, agree with the type of flow experimentally observed in the flat-wing planform study previously discussed. In contrast, flow over the leeside of the 7-percent circular-arc thick wing is characterized by a cross-flow shock with no signs of separation of any type. As indicated in figure 4, this type of flow would be expected to occur at a value of  $M_N$  greater than unity and a value of  $\alpha_N$  less than  $12^\circ$ . Because the wing leading-edge local angle of attack is continuously varying along the span due to the nonconical geometry, it is not clear how to calculate the  $\alpha_N$  and  $M_N$  values in order to apply the flow classification chart of figure 4. For this particular thick-wing example, reducing the wing angle of attack of  $18^\circ$  by  $8^\circ$  (which corresponds to one-half the value of the total thickness angle of the 7-percent parabolic arc at the leading edge) resulted in a  $\alpha_N = 27^\circ$  and a  $M_N = 0.95$  as shown for the thick wing location on the  $\alpha_N - M_N$  chart in figure 5. This location corresponds to the boundary of several regions which all should have some type of separated flow. Obviously additional information is needed to understand the effects of thickness on the leeside-flow characteristics.

To provide a set of thick-wing data to compare with the flat-wing data, a set of eight wind tunnel wing models has been constructed. The models have delta planforms identical to the flat wings with leading-edge sweep angles of  $52.5^\circ$ ,  $60^\circ$ ,  $67.5^\circ$  and  $75^\circ$ . One set of models has 7-percent-thick circular-arc airfoil section and the other set of models has 7-percent-thick diamond airfoil sections (see fig. 6). Although both wing sets have the same thickness-to-chord ratio of 7 percent, their leading-edge thickness angles are considerably different. The circular-arc airfoil has a leading-edge thickness

half angle of approximately  $8^\circ$  and the diamond airfoil has a leading-edge thickness half angle of  $4^\circ$ . The test plans include oil flow, tuft and vapor screen flow-visualization data which will be correlated with the flat-wing flow-visualization data to identify thickness effects.

**Wing-camber investigation.** - The purpose of the wing-camber study was to experimentally determine the effects of wing leading-edge camber on both the aerodynamic forces and moments as well as the wing's leeside flow characteristics. The camber was represented by a deflected leading-edge flap on an otherwise uncambered wing having a flat upper surface. Two sets of delta-wing models were constructed. One set had a leading-edge-sweep angle of  $67.5^\circ$ , and the other set had a leading-edge-sweep angle of  $75^\circ$ . Each set had a leading-edge flap with its hinge line located at 70 percent of the local span; the leading-edge flap could be deflected down  $0^\circ$ ,  $5^\circ$ ,  $10^\circ$  or  $15^\circ$ . The flap deflection angle is measured streamwise. As shown in the photograph of figure 7, the models have a minimum-body balance housing which is conical back to approximately two-thirds of the model length at which point the body balance housing becomes cylindrical. As a result of this design, all model configurations tested had conical leeside surface geometries forward of the cylindrical portion of the body balance housing. For each of the two sets of wings, a removable fuselage forebody was constructed so that data could be obtained with and without fuselage forebody effects. The fuselage forebodies extended approximately 5 in. beyond the wing apex and had a fineness-ratio 2.5 circular-arc nose and a 2.0-in.-diameter cylindrical circular aft section.

Testing of the  $\Lambda = 75^\circ$  wing with the fuselage forebody removed has been completed. Data were obtained for the same flow conditions as those of the planform study, i.e. Mach numbers from 1.5 to 2.8 and angles of attack from  $0^\circ$  to  $20^\circ$ . Figure 8 illustrates the behavior of the leeside flow characteristics at  $M = 1.7$ . Similar behavior was observed at the other Mach numbers. For the range of flap-deflection angles ( $\delta_f$ ) and angles of attack ( $\alpha$ ) tested, three distinctly different flow types were observed. The flow type is characterized by the existence, origin and location of the vortex and is denoted by the sketches on the figure. The sketch indicates the character of both the vortex and the associated surface pressure distribution. The shaded region corresponds to the situation in which the vortex originates at the wing leading edge and its primary influence is confined to the leading-edge flap; this is the ideal situation for the operation of a vortex flap. For angles of attack between  $0^\circ$  and  $10^\circ$ , the shaded region has both upper and lower boundaries. For a given angle of attack, the upper boundary denotes the flap-deflection angle above which the flow is attached on the flap but separates at the hinge line. For a given flap-deflection angle, the lower boundary denotes the angle of attack above which the vortex is no longer confined to the leading-edge flap but extends beyond the hinge line. There also exists a point where the upper and lower boundaries of the shaded region intersect. This point defines the maximum flap-deflection angle at which the leading-edge flap could be made to act as a vortex flap. It remains to be seen how the force and moment data



correlate with the leeside flow characteristics.

Because a definite interaction was observed between the hinge-line vortex and the leading-edge vortex, an experimental study of hinge-line separation is planned. As illustrated in figure 9, the hinge-line study will involve the testing of three hinge-line models mounted on a splitter plate. The models will have different leading-edge-sweep angles of  $0^\circ$ ,  $50^\circ$ , and  $70^\circ$  and leading-edge flap deflection angles ranging from  $0^\circ$  to  $40^\circ$ . Each model will be instrumented so that pressure distributions can be measured both streamwise and normal to the hinge line. As indicated in the figure, flow field pressures will be measured using a flow survey pressure probe.

### Theoretical Program

The objective of the theoretical program was to explore the use of computational methods for predicting the leading-edge vortex characteristics of wings at supersonic speeds. Two methods were examined. A modified linearized-theory method was found to adequately predict the flow characteristics of flat wings but was not adequate for predicting the flow over cambered wings. An Euler solution technique was found to adequately predict the general characteristics of both flat and cambered wings. The following discussion will briefly describe each method and highlight results obtained with each method.

**Modified linearized-theory method.** - A supersonic linearized-theory aerodynamic prediction method has been modified to account for both nonlinear attached-flow effects (primarily a windward surface phenomena) and nonlinear separated-flow effects (primarily a leeward surface phenomena) (ref. 31). The leading-edge separated flow is represented by a technique which uses the Polhamus suction analogy (ref. 32) to determine the leading-edge vortex-induced force and then modifies the upper surface attached-flow pressures to distribute this additional force over the wing upper surface. The vortex-induced force is distributed about a "vortex action point" located downstream of the wing leading edge. The location of the vortex action point is determined from an empirical relationship that is a function of angle of attack only. The method also limits the leeward surface pressures to values greater than those corresponding to vacuum conditions.

The ability of this modified linearized-theory method to predict wing vortex characteristics was evaluated for the series of flat delta wings used in the previously discussed experimental planform investigation. A detailed discussion of this evaluation is given in reference 26, and typical results are presented in figure 10. The results shown in the figure are for an uncambered delta wing with  $75^\circ$  of leading-edge sweep; the Mach numbers and angle of attack correspond to conditions which lie within the classical vortex region depicted in the upper portion of the figure. The vortex-induced normal-force coefficient,  $C_{N_v}$ , represents the vortex strength and the spanwise surface pressure distribution indicates both vortex strength and location. As

shown across the bottom of the figure, the agreement between theoretical and experimental results is sufficient for preliminary design applications of the modified linearized-theory method.

The method was next evaluated for wings with deflected leading-edge flaps. At the time of this evaluation, the experimental data had not been obtained on the conical wing-flap models described in the "Wing Camber Investigation" section of this paper; however, data from references 33 and 34 were sufficient to evaluate the method. A comparison of theoretical and experimental forces and surface pressures can be made from the results shown in figure 11. Although the pressure results were obtained at slightly different conditions than the force data, the flow characteristics which produced the force data at  $C_l = 0.3$  closely correspond to the flow characteristics of the pressure distribution shown in the figure. Discrepancies between the experimental data and the computed results are found in both the drag polar and pressure distributions. The theoretical drag polars indicate that for values of lift-coefficient above 0.2 the wing with the  $16^\circ$  flap deflection produces less drag than the wing with zero flap deflection; however, the experimental data show that deflecting the leading-edge flap  $16^\circ$  resulted in a drag increase with respect to the wing with zero-flap deflection. An explanation for this discrepancy is clearly shown in the spanwise pressure distributions. The theoretical spanwise pressure distribution shows the presence of a small vortex its induced pressure acting on the leading-edge flap; theoretically this is the ideal situation for achieving performance benefits employing a vortex flap. However, the experimental pressures indicate both a small leading-edge vortex and a much larger hinge-line vortex. Because the hinge-line vortex induced pressures dominate and lie on the undeflected flat surface inboard of the hinge line, no drag reduction would be realized as a result of deflecting the leading-edge flap  $16^\circ$ .

From this discussion it is clear that the modified-linearized theory method is not capable of analyzing the flow over sharp leading-edge wings having deflected leading-edge flaps.

**Euler code method.** - Because the modified-linearized method failed to predict the leeside flow over delta wings with deflected leading-edge flaps, it was decided to explore the use of more complex codes such as Navier-Stokes and Euler codes. A number of researchers have applied Navier-Stokes codes and Euler codes to the calculation of wing leading-edge-vortex flows at supersonic speeds; and both methods have produced encouraging results for the flow over flat, uncambered wings (ref. 35). The Navier-Stokes equations model both the viscous and inviscid mechanisms and would be expected to provide the most accurate results. However, because Navier-Stokes methods have very high computational costs and because Euler methods have been shown to produce the general characteristics of vortex flows, it was decided to look first at the capabilities of Euler codes. In selecting a particular Euler code the choice ranged from large, complex 3-D, well-developed codes to a small, simple 2-D

conical code under development for the specific purpose of calculating wing leading-edge vortex flows. A code of the latter type, specifically the conical Euler code by Perez and Powell et al. (refs. 36 and 37), was selected because of the code developers' expressed interest in this particular problem.

A complete description of the code has been reported previously in reference 38 and only a brief description is presented herein. The basic solution technique employs a finite volume spatial discretization of the unsteady Euler equations in conservation form which is solved using a Runge-Kutta type method as discussed in reference 39. The bow shock is fitted, and both second and forth order damping are employed to capture internal shocks and yield smooth solutions. The grid is generated using a Joukowski transformation in which the zero-thick wing surface becomes a circle. For all calculations shown, the grid density consisted of 128 radial lines in the half plane and 128 points on each radial line. The wing is represented by zero-thick impermeable surface.

To compare with the Euler code solutions, eight cases were selected from the data obtained in the experimental program. The cases were selected to provide a large variety of wing leeside flow characteristics. In all eight cases, the geometry was a delta wing with  $75^\circ$  of leading-edge sweep. Four of the cases compare results for a flat wing, and four of the cases compare results for a wing with a deflected leading-edge flap.

The comparisons between experiment and theory include both flow-field and surface data. The calculated flow-field data consist of plots of the cross-flow velocity vectors and the measured flow-field data consist of vapor screen photographs. The flow-field data are presented in a plane perpendicular to the free-stream velocity vector. The calculated and measured surface data consist of spanwise pressure distributions.

Experimental and theoretical results for a flat wing at  $12^\circ$  angle of attack are shown in figures 12 and 13 for Mach numbers of 1.7 and 2.8, respectively. At both Mach numbers, the experimental and theoretical flow-field data show leading-edge separation which results in a well-developed primary vortex located above the leeside surface of the wing. The most notable difference between the theoretical and experimental results is the absence of the secondary vortex in the Euler results. This is found for all cases because the secondary vortex is a viscous phenomena which cannot be predicted by an inviscid Euler code. Otherwise, the agreement between the experimental and theoretical results is very good. Both results indicate the flattening and inboard movement of the primary vortex as Mach number is increased from 1.7 to 2.8. At Mach numbers of 1.7, the experimental and theoretical spanwise pressure distributions are in good agreement except for the influence of the secondary vortex. The experimental pressures show two pressure peaks, one near 60-percent span and another near 85-percent span; the theoretical pressure distributions show a single slightly higher pressure peak located at approximately the 70-percent span station. Although the higher Mach number



2.8 results of figure 12 still contain a secondary vortex, there is little or no influence of this secondary vortex on the surface pressure distribution. This observation seems to be typical, and it can be generally stated that effect of the secondary vortex on the wing upper surface pressures diminishes with increasing Mach number.

Results for a flat wing at  $12^\circ$  angle of attack and at  $8^\circ$  angle of yaw are shown in figures 14 and 15 for Mach numbers of 1.7 and 2.8, respectively. As seen in the figures, flow-field and surface-pressure data are shown for both the left side ( $y/y_{\max}$  negative) and the right side ( $y/y_{\max}$  positive) of the wing. For this yawed orientation, the left side of the wing has a windward leading edge and the right side has a leeward leading edge. Because vapor-screen photographs were not taken for the yawed wings, the only flow-field data shown are plots of the theoretically computed crossflow velocity vectors. In both figures 14 and 15, the asymmetry of the flow due to yaw is clearly shown in both the flow field and surface pressure data. For the low Mach number of 1.7, the cross-flow velocity contours show that leading-edge separation occurs on both the windward and leeward edges. The windward-edge separation develops into a separation bubble which lies close to the wing surface and the leeward-edge separation develops into a classical vortex. These two considerably different flow types result in different surface pressure distributions shown at the bottom of figure 14. The separation bubble results in a more negative pressure extending over a larger portion of the wing span as compared to the pressures resulting from the classical vortex. In figure 15, the higher Mach number 2.8 results indicate that the flow is attached on the windward edge and separated on the leeward edge. The attached flow produces a plateau-type pressure distribution over the outboard 75 percent of the left wing span; the pressure distribution on the right-wing span is typical of that produced by a classical vortex. For both Mach numbers, the Euler-code predicted pressures are in excellent agreement with the measured pressures.

Results from the experimental conical-wing-flap study indicated that four types of flow were observed to occur. The type of flow depends on the angle of attack and the wing leading-edge flap angle. To evaluate the ability of Euler code to predict the flow over the wings with deflected leading-edge flaps, four combinations of  $\alpha$  and  $\delta_f$  were selected to correspond to each of the four observed types of flow. These four  $\alpha$ - $\delta_f$  combinations are shown in figure 16 and are labeled as points A, B, C, and D. The flow-field results and surface pressure distributions corresponding to points A, B, C, and D are shown in figures 17 to 20 respectively.

In figure 17, results are shown for  $\alpha = 4^\circ$  and  $\delta_f = 5^\circ$ . According to the location of this condition on figure 16 (point A), the flow should be characterized by a classical leading-edge vortex. The experimental pressure distribution does indeed show a lower pressure region on the upper surface of the leading-edge flap, which could result from the presence of a weak vortex.

However, the experimental flow-field data do not show a vortex; this indicates that the vapor screen techniques may not be sensitive enough to detect weak vortex conditions or that condensation effects may have altered the flow conditions to delay vortex formation. Note also that neither the theoretical pressure distribution nor the theoretical flow-field data exhibit signs of a leading-edge vortex. These conflicting observations indicate that the characteristics of a weak vortex are very sensitive to the flow conditions.

In figure 18, results are shown for  $\alpha = 12^\circ$  and  $\delta_f = 5^\circ$ . These results correspond to point B in figure 16. The experimental and theoretical results clearly show a primary vortex which originates at the wing leading edge and extends well inboard of the flap hinge line. The experimental and theoretical pressures are in good agreement and both reflect the presence of the primary vortex. The theoretical flow-field data unexpectedly indicate the presence of a secondary separation region lying on the leading-edge flap; this secondary separation is produced as the outboard flow passing under the primary vortex encounters the hinge line and separates. Although not clearly shown in the experimental flow-field data, both the experimental and theoretical pressure distributions exhibit the signs of this secondary separation.

Results for  $\alpha = 4^\circ$  and  $\delta_f = 15^\circ$  are shown in figure 19; these results correspond to point C on figure 16. The theoretical flow-field data show that a large flap deflection and small angle of attack produce two primary vortices. One of these vortices originates from the leading edge and lies on the lower surface of the leading-edge flap; this lower surface vortex cannot be seen in the experimental flow-field data because the light source is blocked by the leading-edge flap. The other primary vortex is produced when the attached flow on the flap upper surface separates at the flap hinge-line; this vortex lies inboard of the flap hinge line and is clearly visible in both the experimental and theoretical flow-field data. Although the vortex-induced pressures on the leeward wing surface are theoretically predicted slightly lower than those experimentally measured, the general agreement between theory and experiment is very good. The theoretically predicted pressure distribution shows the strong influence of the windward primary vortex as a reduced pressure region on the windward (lower) wing-flap surface; unfortunately, lower surface pressures were not measured and a comparison between experimental and theoretical pressures could not be made.

The fourth and final set of cambered delta-wing results are shown in figure 20. These results correspond to  $\alpha = 12^\circ$  and  $\delta_f = 15^\circ$  which is point D on figure 16. Both the experimental and the theoretical results indicate similar leeside flow characteristics. Both show leading-edge separation and hinge-line separation which result in two regions of vortex-type flow. The leading-edge vortex results in the most outboard suction pressure peak and the hinge-line vortex results in the largest suction pressure peak located slightly inboard of the hinge line. The major difference between the experimental and theoretical results is the extent of the leading-edge vortex. The



experimental results show a separation-bubble type vortex flow which extends over the entire length of the flap and produces the plateau type pressure distributions shown in the figure. The theoretical results also show a separation-bubble type vortex flow which begins at the wing leading edge and reattaches on the flap at approximately half way between the leading edge and the hinge line; in the theoretical distribution this flow reattachment produces the compression region between the two suction pressure peaks.

### Aerodynamic Performance

In this section, the measured aerodynamic performance for a conical vortex-flap wing and the performance of a conventional attached-flow leading-edge flap wing are presented. These performance results are compared with each other and with a "practical performance goal" established from data measured on a series of optimum twisted and cambered wings.

Aerodynamic performance results for a vortex-flap wing are presented in figure 21. These results were obtained at  $M = 1.7$  on the  $\Lambda = 75^\circ$  delta wing with leading-edge flaps deflected  $0^\circ$ ,  $5^\circ$ ,  $10^\circ$  and  $15^\circ$ . Experimental values of drag-due-to-lift parameter are presented as a function of lift coefficient. For reference purposes, the linearized-theory 0-percent thrust and 100-percent thrust boundaries are also shown; these boundaries do not vary with lift coefficient. The data show that significant drag reductions can be achieved at supersonic speeds by the management of wing leading-edge vortices. Compared to the  $5^\circ$  flap-deflection data, which did not experience hinge-line separation, the data for the  $10^\circ$  and  $15^\circ$  leading-edge flap deflection show a loss in performance due to hinge-line separation. However, all flap deflections resulted in a drag reduction compared to the flat wing.

Aerodynamic performance results for a wing using a conventional attached-flow leading-edge flap were extracted from data obtained in the experimental study (ref. 40) depicted in figure 22. As indicated in the figure, the study involved testing four sets of flap planforms on a trapezoidal wing and two sets of flap planforms on a cranked wing. Both wings had aspect ratios of 1.75 and were mounted on a generic fuselage as shown in the photograph of figure 22. All leading-edge flap geometries were effective in reducing the flat-wing drag; however, the largest drag reductions were produced by the combination of flap A on the cranked wing. For this wing-flap combinations, experimental values of the drag-due-to-lift factor versus lift coefficient are shown in the lower left portion of the figure for flap deflection angles of  $0^\circ$ ,  $5^\circ$  and  $10^\circ$ . The linearized-theory 0-percent thrust and 100-percent thrust boundaries are also shown. These data indicate that the lowest drag-due-to-lift is produced by scheduling the flap deflection angle with lift coefficient. As shown in the figure, the proper schedule would be  $\delta_f = 0^\circ$  for lift coefficients below 0.1;  $\delta_f = 5^\circ$  for lift coefficients between 0.1 and 0.4; and  $\delta_f = 10^\circ$  for lift coefficients above 0.4. This flap schedule and the drag-due-to-lift data shown in figure 22 were used to develop the curve for

the performance summary representing conventional attached-flow leading-edge flaps.

A comparison of the aerodynamic performance of the vortex-flap wing and the attached-flow flap wing can be made from the data which are summarized in figure 23. In this figure, the aerodynamic performance is expressed as a percent of full, theoretical, leading-edge thrust and is presented as a function of lift coefficient.

For reference purposes, a practical-goal curve was established from experimental data measured on several twisted and cambered wings where each wing camber was optimized for a specific lift coefficient. For example, the data used to generate the portion of the practical-goal curve for lift coefficients from 0.0 to 0.2 were taken from the cruise cambered-wing designs reported in reference 41, and the data used to establish the performance level for the 0.4 value of lift coefficient were taken from the high-lift wing designs reported in references 42 and 43.

The information contained in figure 23 represents the state of the art in experimentally measured supersonic aerodynamic performance. At low levels of lift ( $C_L = 0.1$ ), the results indicate that the practical goal of near 100-percent thrust has been obtained with both traditional leading-edge flaps and vortex leading-edge flaps. However, at high-lift conditions ( $C_L = 0.4$ ), the practical goal, which is reduced to approximately 60 percent thrust, has not been obtained by either of the flap concepts. At this high-lift condition, the traditional leading-edge flap produces less than 25-percent thrust and the data of reference 40 indicate that this is probably the best that can be obtained using the attached-flow flap concept. However, the conical vortex flap produces approximately 40-percent thrust and it is anticipated that the use of other nonconical flap geometries along with eliminating the hinge-line separation would increase the performance considerably.

#### CONCLUDING REMARKS

This paper presents an overview of a research program directed at the study of wing leading-edge vortices at supersonic speeds. The studies include both experimental and theoretical investigations and focus primarily on determining planform, thickness and camber effects for delta wings. The effects of planform and leading-edge camber have been experimentally determined, and an experimental study to identify thickness effects has been initiated. Theoretical studies have shown that a modified linearized-theory method, which was capable of predicting the planform effects for flat wings, was not adequate for predicting leading-edge camber effects. Preliminary results obtained with an Euler code have been shown to contain the correct primary-vortex characteristics for delta wings of various planforms and with various amounts of leading-edge camber.

In a summary of measured aerodynamic performance for high-lift conditions, wings with leading-edge vortex flaps were shown to have a considerably higher level of performance (40-percent thrust) than wings employing conventional attached-flow leading-edge flaps (25-percent thrust). However, the performance levels achieved with vortex flaps were considerably less than the performance levels experimentally established as a practical goal (60 percent thrust).

#### ACKNOWLEDGMENT

The authors wish to thank Dr. Earl M. Murman and Mr. Kenneth G. Powell of the Massachusetts Institute of Technology for providing the Euler solution results presented in this paper.

#### REFERENCES

1. Carlson, H. W.; and Middleton, W. D.: A Numerical Method for the Design of Camber Surfaces of Supersonic Wings with Arbitrary Planforms. NASA TN D-2341, 1964.
2. Carlson, H. W.; and Miller, D. S.: Numerical Methods for the Design and Analysis of Wings at Supersonic Speeds. NASA TN D-7713, 1974.
3. Mack, R. J.: A Numerical Method for Evaluation and Utilization of Supersonic Nacelle-Wing Interference. NASA TN D-5057, 1969.
4. Kulfan, R. M.; and Sigallo, A.: Real Flow Limitations in Supersonic Airplane Design. AIAA-78-147, Jan. 1978.
5. Carlson, H. W.; and Miller, D. S.: The Influence of Leading-Edge Thrust on Twisted and Cambered Wing Design for Supersonic Cruise. AIAA-81-1656, Aug. 1981.
6. Carlson, H. W.: Aerodynamic Characteristics at Mach Number 2.05 of a Series of Highly-Swept Arrow Wings Employing Various Degrees of Twist and Camber. NASA TM X-332, 1960.
7. Morris, O. A.; and Fournier, R. H.: Aerodynamic Characteristics at Mach Numbers 2.30, 2.60, and 2.96 of a Supersonic Transport Model Having a Fixed, Warped Wing. NASA TM X-1115, 1965.
8. Miller, D. S.; and Schemensky, R. T.: Design Study Results of a Supersonic Cruise Fighter Wing. AIAA-79-0062, Jan. 1979.
9. Mason, W. H.; and Miller, D. S.: Controlled Supercritical Crossflow on Supersonic Wings - An Experimental Validation. AIAA-80-1421, July 1980.

10. Mason, W. H.; Miller, D. S.; Pittman, J. L.; and Siclari, M. J.: A Supersonic Wing Designed for Nonlinear Attached Flow. AIAA-83-0425, Jan. 1983.
11. Miller, D. S.; Pittman, J. L.; and Wood, R. M.: An Overview of Two Non-Linear Supersonic Wing-Design Studies. AIAA-83-0182, Jan. 1983.
12. Lambourne, N. C.; and Bryer, D. W.: Some Measurements in the Vortex Flow Generated by a Sharp Leading Edge Having 65 Degrees Sweep. C.P. No. 447, British A.R.C., 1960.
13. Squire, L. C.: Camber Effects on the Nonlinear Lift of Slender Wings with Sharp Leading Edges. C.P. No. 924, British A.R.C., 1967.
14. Matoi, T. K.: On the Development of a Unified Theory for Vortex-Flow Phenomena for Aeronautical Applications. Contract No. N00014-57-A-0204-0085, MIT, April 1975. (Available from DTIC as AD-A012-339.)
15. Kulfan, R. M.: Wing Airfoil Shape Effects on the Development of Leading-Edge Vortices. AIAA Paper 79-1675, 1979.
16. Manro, M. E.: Transonic Pressure Measurements and Comparison of Theory to Experiment for Three Arrow-Wing Configurations. Vol. I: Experimental Data Report-Basic Data and Effect of Wing Shape. NASA CR-165701, 1981.
17. Rao, D. M.: Leading-Edge Vortex Flap Experiments on a 74-Deg Delta Wing. NASA CR-159161, 1979.
18. Rao, D. M.: Leading-Edge Vortex Flaps for Enhanced Subsonic Aerodynamics of Slender Wings. ICAS 80-13.5, 1980.
19. Smith, C. W.; Campbell, J. F.; and Huffman, J. K.: Experimental Results of a Leading-Edge Vortex Flap on a Highly Swept Cranked Wing. Tactical Aircraft Research and Technology. NASA CP-2162, 1980.
20. Rao, D. M.; and Johnson, T. D.: Investigation of Delta Wing Leading-Edge Devices. J. Aircraft, vol. 18, no. 3, March 1981, pp. 161-167.
21. Rao, D. M.: Segmented Vortex Flaps. AIAA-83-0424, 1983.
22. Johnston, F. T.; Lu, P.; Tinoco, E. N.; and Epton, M. A.: An Improved Panel Method for the Solution of Three-Dimensional Leading-Edge Vortex Flows. Volume I. - Theory Document. NASA CR-3278, 1980.



23. Lan, C. E.; and Chang, J. F.: VORCAM - A Computer Program for Calculating Vortex Lift Effect of Cambered Wings by the Suction Analogy. NASA CR-165800, 1981.
24. Lamar, J. E.; and Herbert, H. E.: Production Version of the Extended NASA-Langley Vortex Lattice FORTRAN Computer Program - Volume I - User's Guide. NASA TM-83303, 1982.
25. Lamar, J. E.; and Campbell, J. F.: Recent Studies at NASA-Langley of Vortical Flows Interacting with Neighboring Surfaces. Aerodynamics of Vortical Type Flows in Three Dimensions, AGARD-CP-342, July 1983.
26. Miller, D. S.; and Wood, R. M.: Lee-Side Flow Over Delta Wings at Supersonic Speeds. NASA TP-2430, 1985.
27. Stanbrook A.; and Squire, L. C.: Possible Types of Flow at Swept Leading Edges. Aeron. Quarterly, vol. XV, Feb. 1964.
28. Ganzer, W.; Hoder, H.; and Szodruch, J.: On the Aerodynamics of Hypersonic Cruise Vehicles of Off-Design Conditions. Proceedings of the XI Congress of the ICAS, Lisbon, Portugal, vol. I., Sept. 10-16, 1978, p. 152-161.
29. Szodruch, J. G.; and Peake, D. J.: Leeward Flow Over Delta Wings at Supersonic Speeds. NASA TM-81187, 1980.
30. Rizzi, A.; Eriksson, L. E.; Schmidt, W.; and Hitzel, S. M.: Simulating Vortex Flows Around Wings. Aerodynamics of Vortical Type Flows in Three Dimensions, AGARD Conference Preprint N. 342, 1983.
31. Carlson, H. W.; and Mack, R. J.: Estimation of Wing Nonlinear Aerodynamic Characteristics at Supersonic Speeds. NASA TP-1718, 1980.
32. Polhamus, E. C.: A Concept of the Vortex Lift of Sharp-Edged Delta Wings Based on a Leading-Edge Suction Analogy. NASA TN D-3767, 1976.
33. Iggesden, M. S.: Wind Tunnel Measurements of the Lift-Dependent Drag of Thin Conically Cambered Slender Delta Wings at Mach Numbers 1.4 and 1.8. Tech. Note No. Aero. 2677, British A.R.C., 1960.
34. Michael, W. H., Jr.: Flow Studies on Drooped-Leading-Edge Delta Wings at Supersonic Speeds. NACA TN-3614, 1956.
35. Newsome, R. W.; and Thomas, J. L.: Computation of Leading-Edge Vortex Flows. Presented at the Vortex Flow Aerodynamics Conference, NASA Langley Research Center, October 8-10, 1985.



36. Perez, E.: Computation of Conical Flows with Leading Edge Vortices. S.M. Thesis, MIT, 1984.
37. Powell, K. G.; Perez, E. S.; Murman, E. M.; and Baron, J. R.: Total Pressure Loss in Vortical Solutions of the Conical Euler Equations. AIAA Paper 85-1701, July 1985.
38. Murman, E. M.; Rizzi, A.; and Powell, K.: High Resolution Solutions of the Euler Equations for Vortex Flows. Progress & Supercomputing in Computational Fluid Dynamics, Birkhauser-Boston, Inc., 1985.
39. Jameson, A.; Schmidt, W.; and Turkel, E.: Numerical Solution of the Euler Equations by Finite Volume Method Using Runge-Kutta Time-Stepping Schemes. AIAA-81-1259, June 1981.
40. Covell, P. F.; Miller, D. S.; and Wood, R. M.: An Evaluation of Leading-Edge Flap Performance on Delta and Double Delta Wings at Supersonic Speeds. AIAA-86-0315, 1986.
41. Wood, R. M.; Miller, D. S.; Raney, D. L.; and Roesch, M. T.: A Low-Lift Wing Camber Design Approach for Fighter Aircraft. NASA TP-2465, 1985.
42. Miller, D. S.; Landrum, E. J.; Townsend, J. C.; and Mason, W. H.: Pressure and Force Data for a Flat Wing and a Warped Conical Wing Having a Shockless Recompression at Mach 1.62. NASA TP-1759, 1981.
43. Pittman, J. L.; Miller, D. S.; and Mason, W. H.: Supersonic, Nonlinear Attached-Flow Wing Design for High Lift with Experimental Validation. NASA TP-2336, 1984.

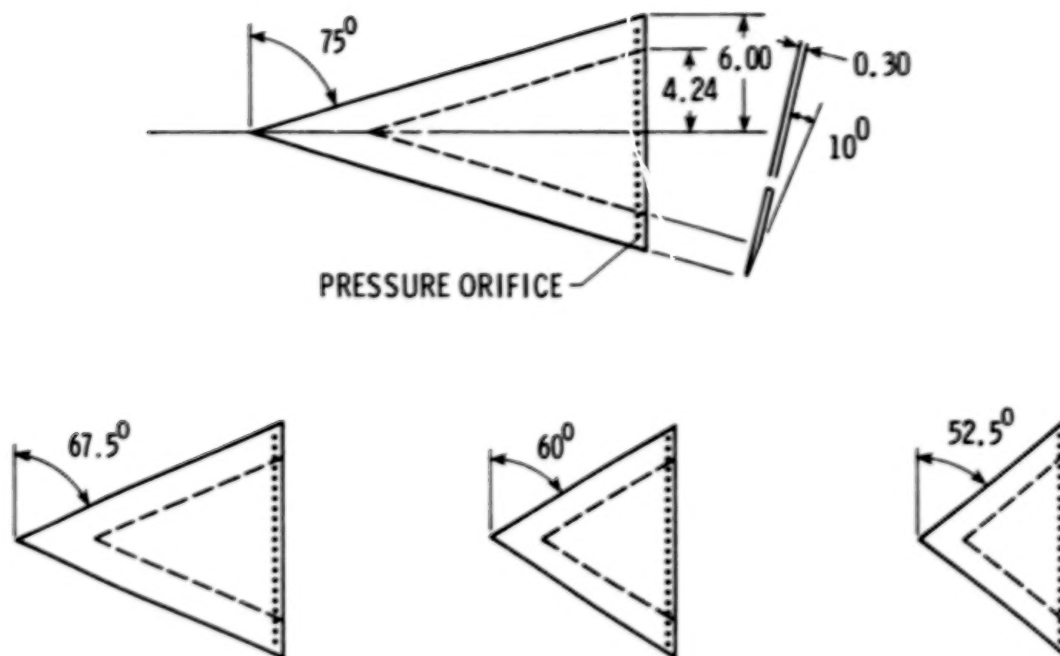


Figure 1. Planforms of flat delta-wing models.

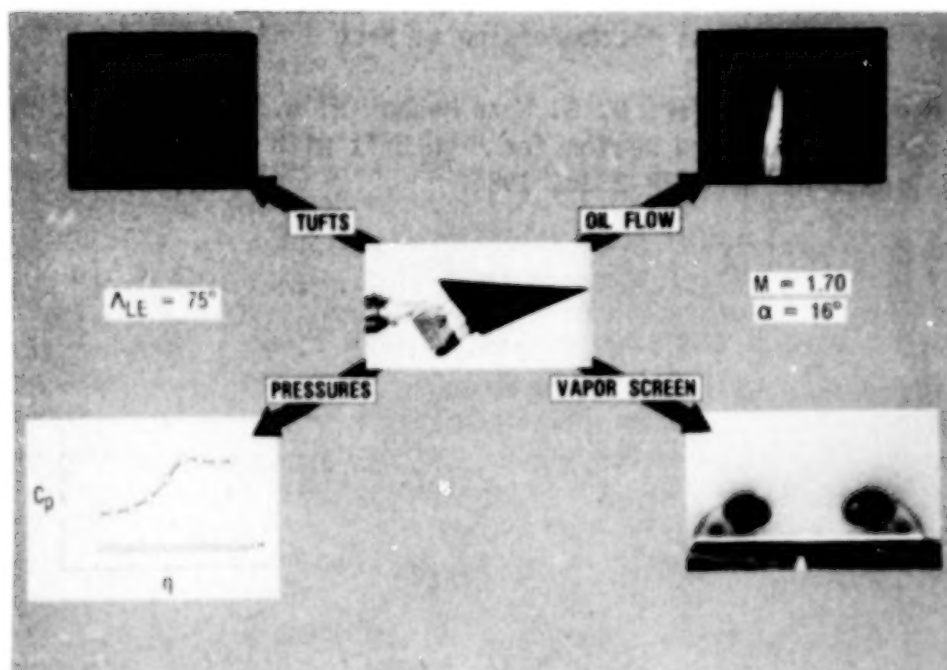


Figure 2. Types of experimental data.

ORIGINAL PAGE IS  
OF POOR QUALITY

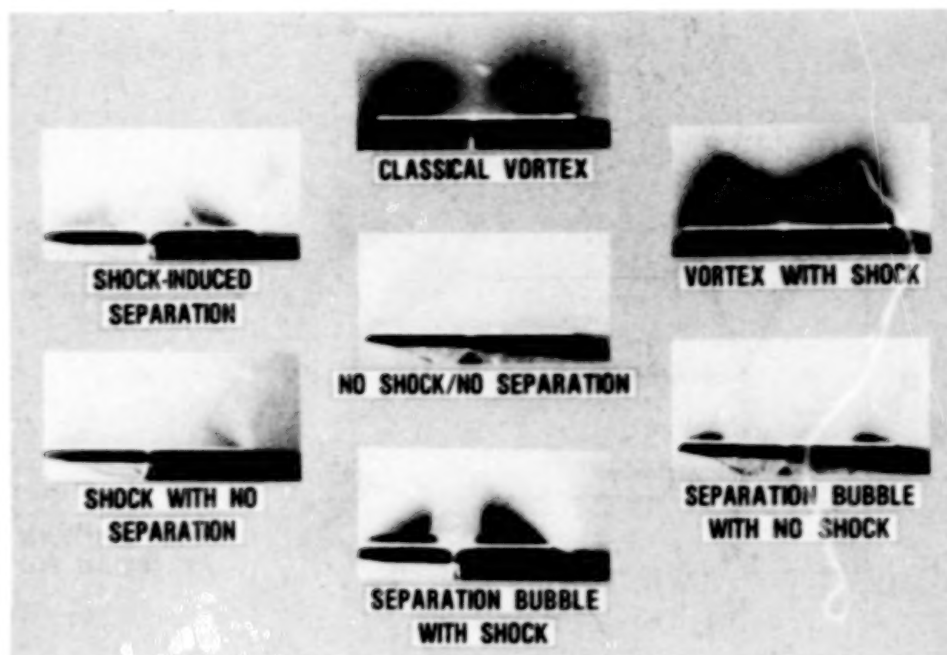


Figure 3. Flow classifications.

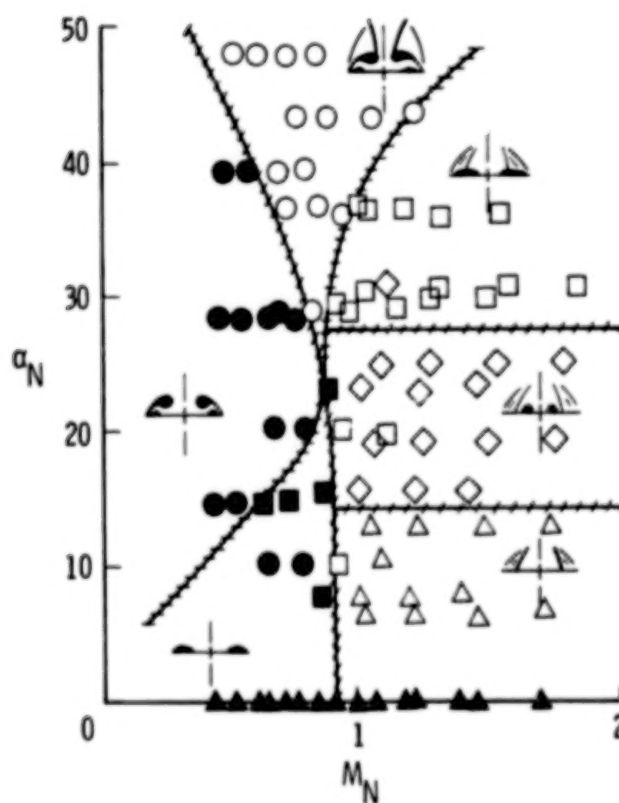


Figure 4. Classification of test data.

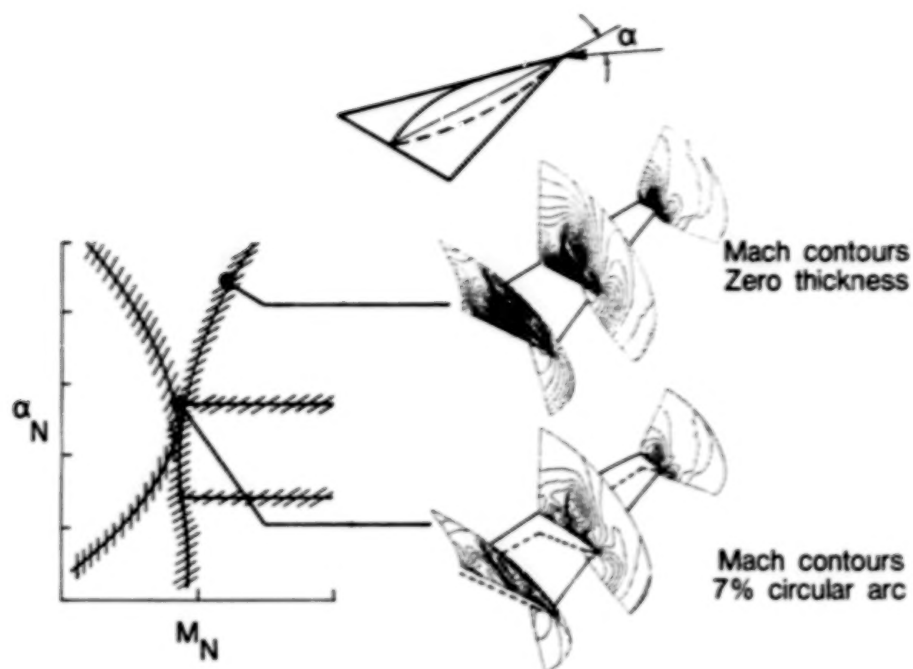


Figure 5. Estimated thickness effects.

Experimental flow visualization

$$\Lambda = 52.5^\circ - 75^\circ$$

$$M = 1.5 - 2.8$$

$$\alpha = 0^\circ - 20^\circ$$

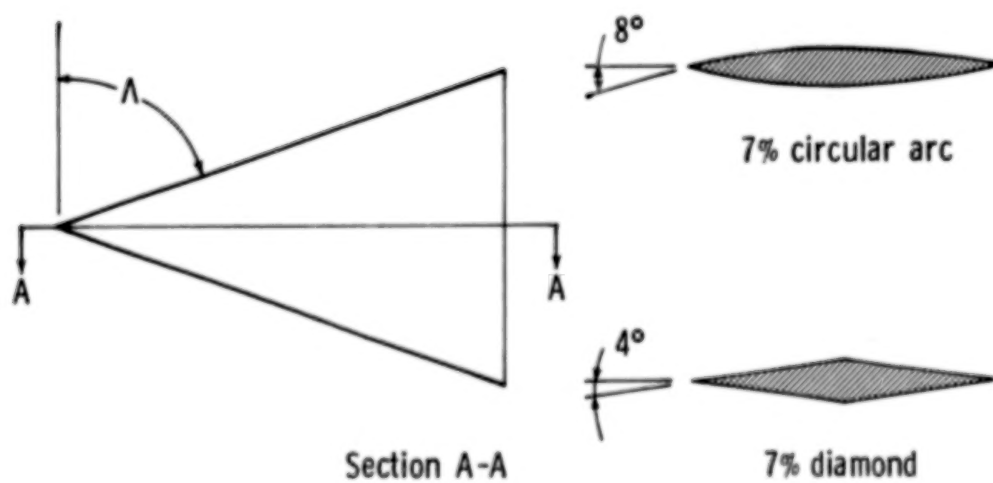


Figure 6. Elements of thickness effects study.

ORIGINAL PAGE IS  
OF POOR QUALITY

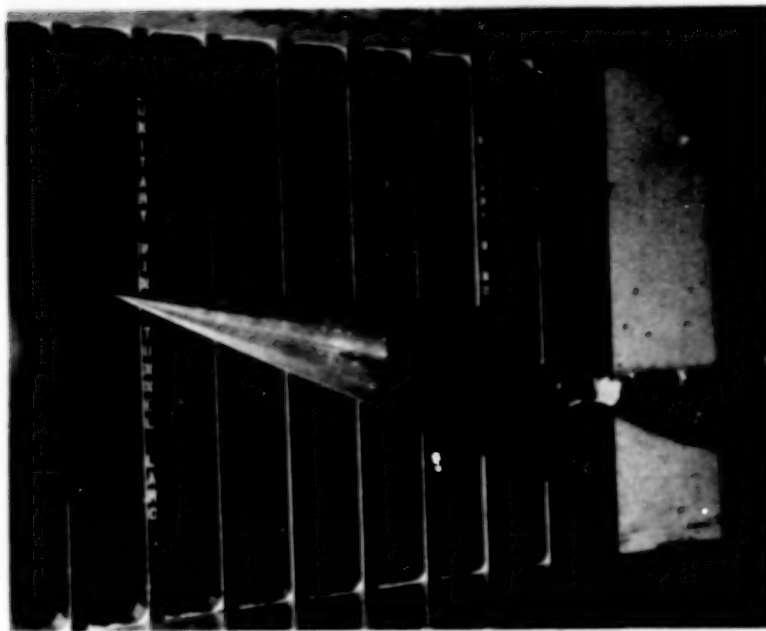


Figure 7. Photograph of  $\Lambda = 75^\circ$  conical wing-flap model.

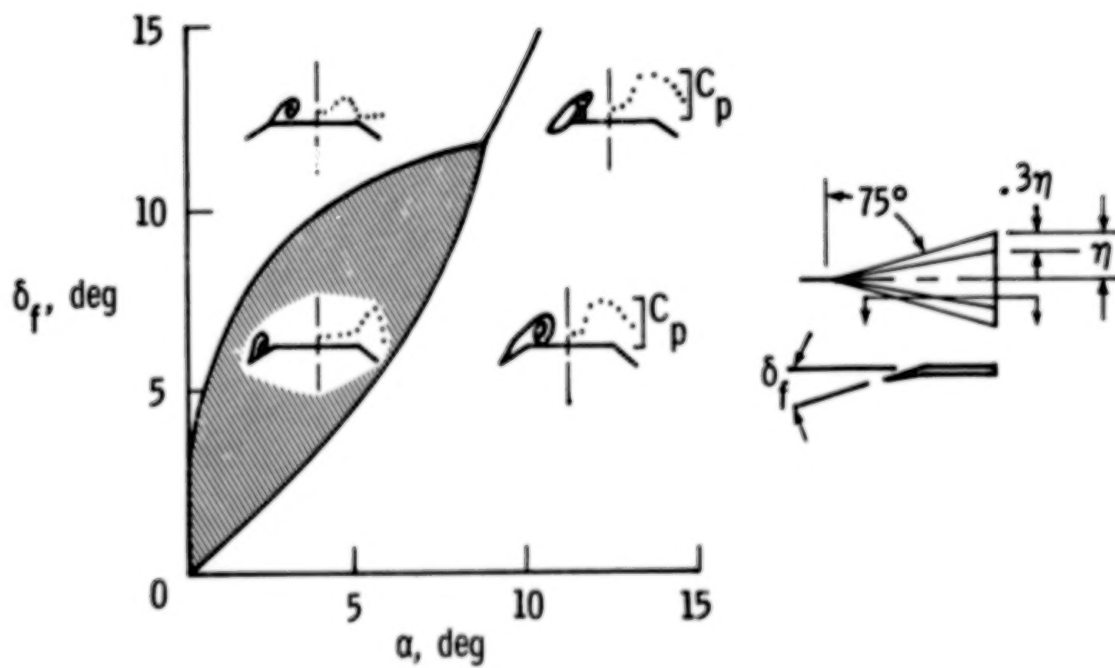


Figure 8. Typical wing-flap leeside flow characteristics.



$$M = 1.60 - 2.16$$

$$\delta_f = 0, 10^\circ, 20^\circ, 30^\circ, 40^\circ$$

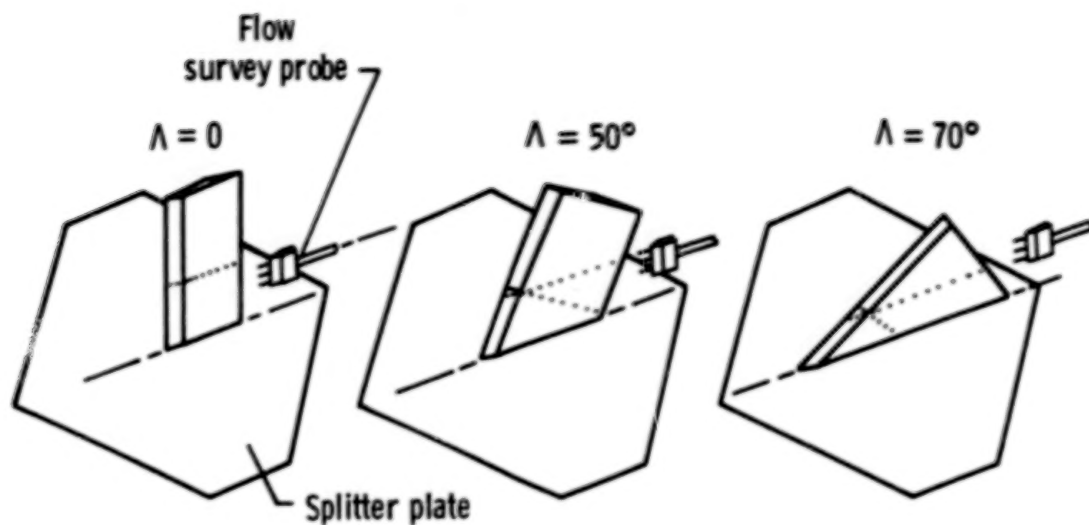


Figure 9. Elements of hinge-line study.

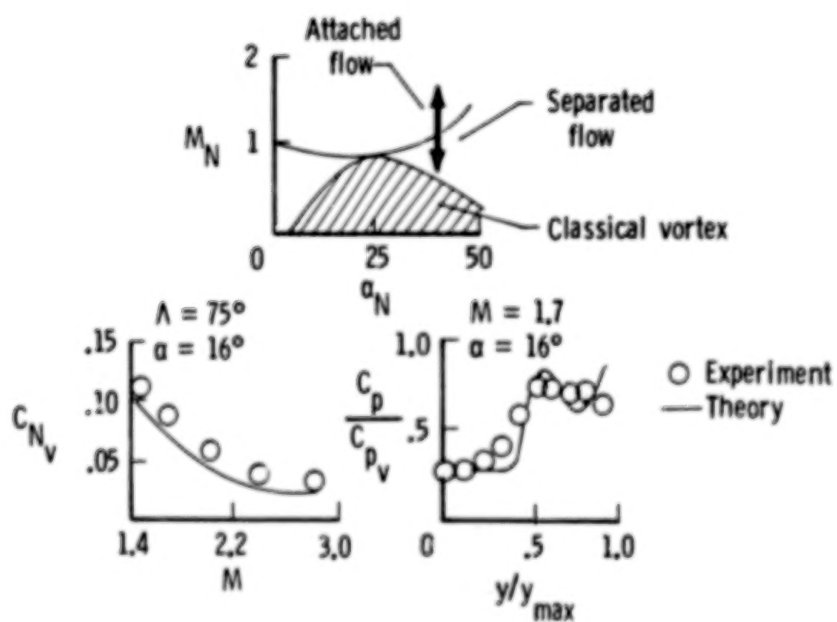


Figure 10. Modified linear-theory predictions for uncambered delta wing.

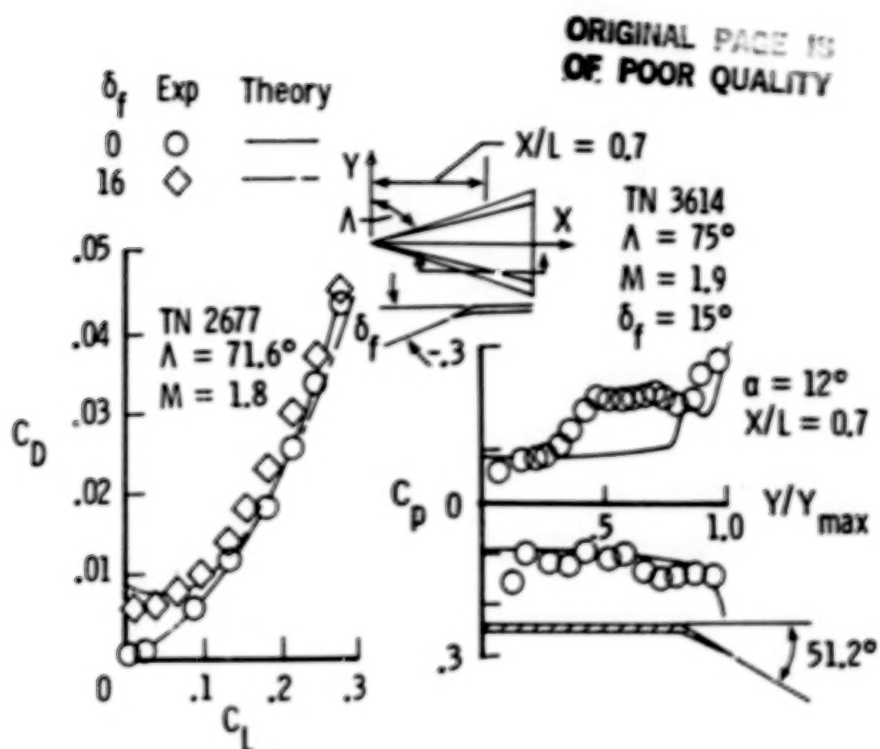


Figure 11. Modified linear-theory predictions for delta wing with leading-edge flap.

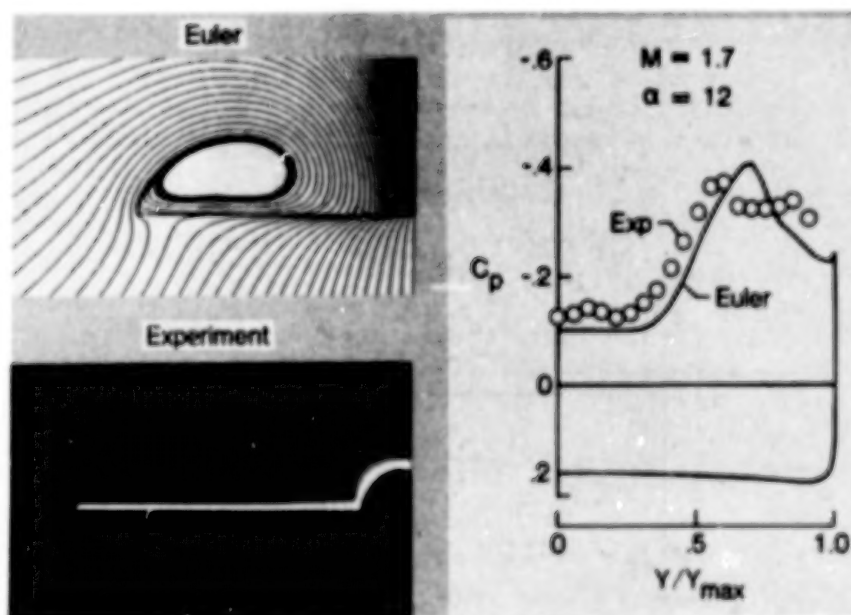


Figure 12. Experimental and Euler code results for flat delta wing at  $M = 1.7$ ,  $\alpha = 12^\circ$ ,  $\beta = 0^\circ$ .

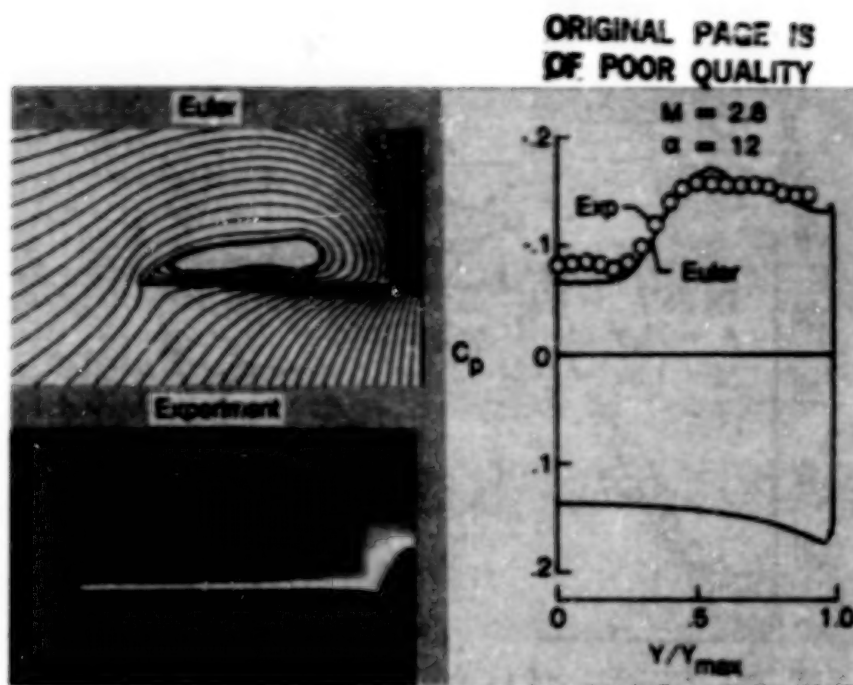


Figure 13. Experimental and Euler code results for flat delta wing at  $M = 2.8$ ,  $\alpha = 12^\circ$ ,  $\beta = 0^\circ$ .

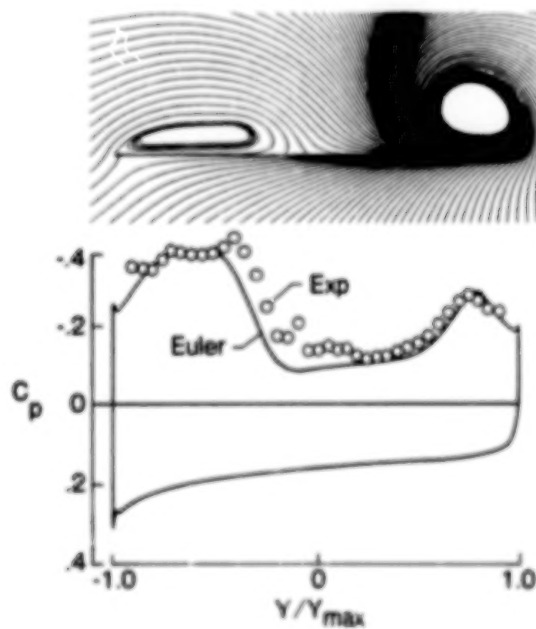


Figure 14. Experimental and Euler code results for flat delta wing at  $M = 1.7$ ,  $\alpha = 12^\circ$ ,  $\beta = 8^\circ$ .

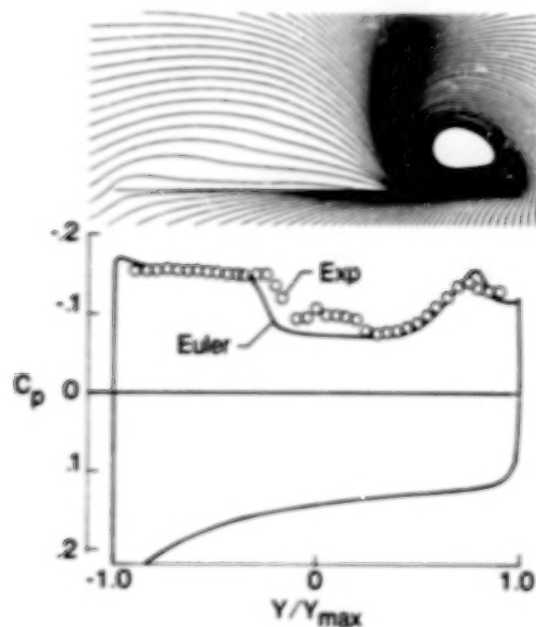


Figure 15. Experimental and Euler code results for flat delta wing at  $M = 2.8$ ,  $\alpha = 12^\circ$ ,  $\beta = 8^\circ$ .

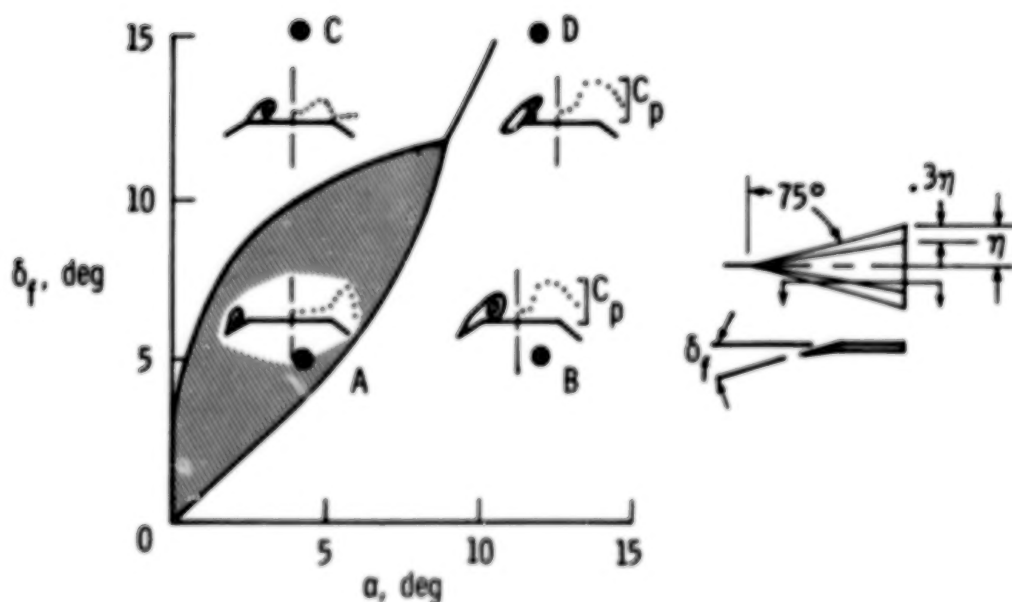


Figure 16. Illustration of the four wing flap conditions subjected to Euler code analysis.

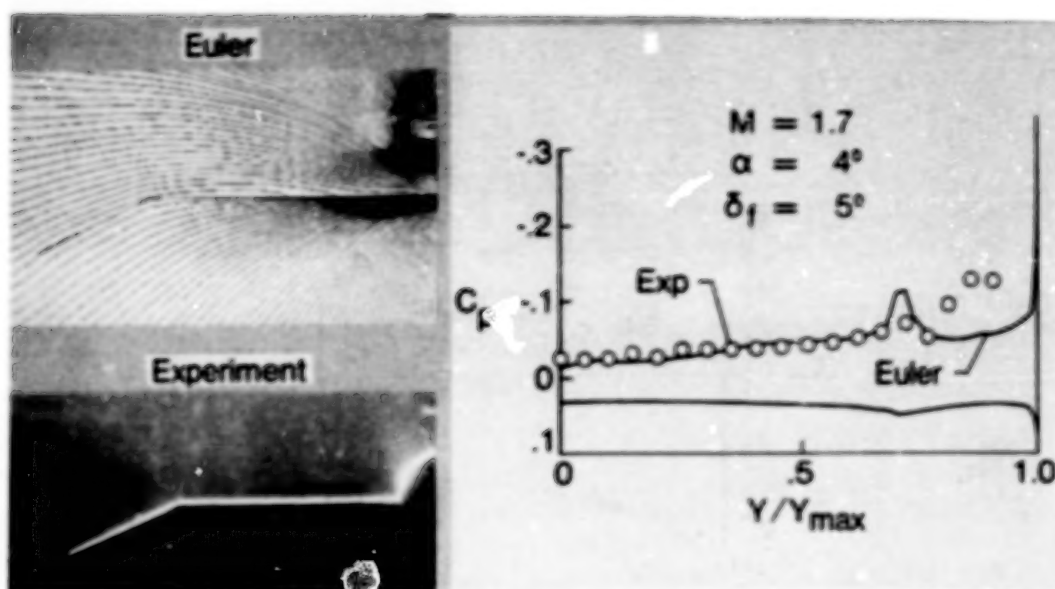


Figure 17. Experimental and Euler code results for wing flap at  $M = 1.7$ ,  $\alpha = 4^\circ$ ,  $\delta_f = 5^\circ$ .

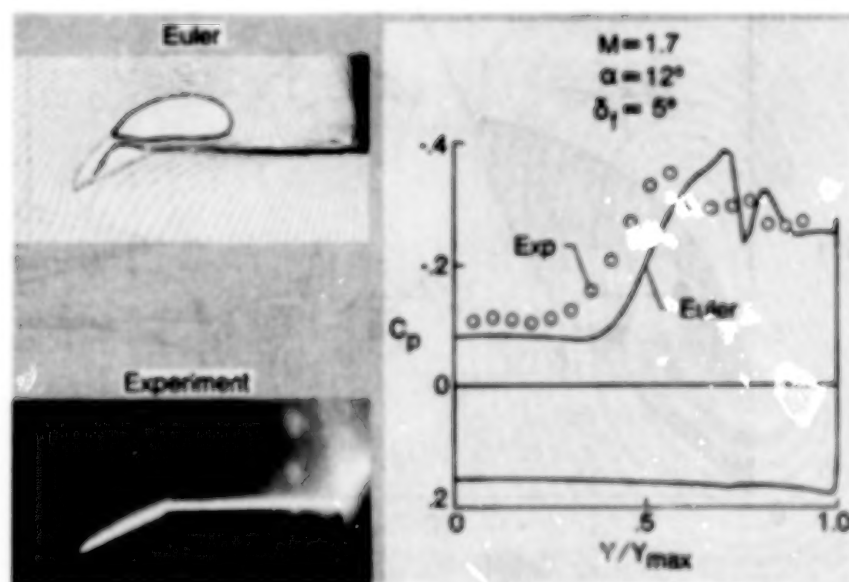


Figure 18. Experimental and Euler code results for wing flap at  $M = 1.7$ ,  $\alpha = 12^\circ$ ,  $\delta_f = 5^\circ$ .



ORIGINAL PAGE IS  
OF POOR QUALITY

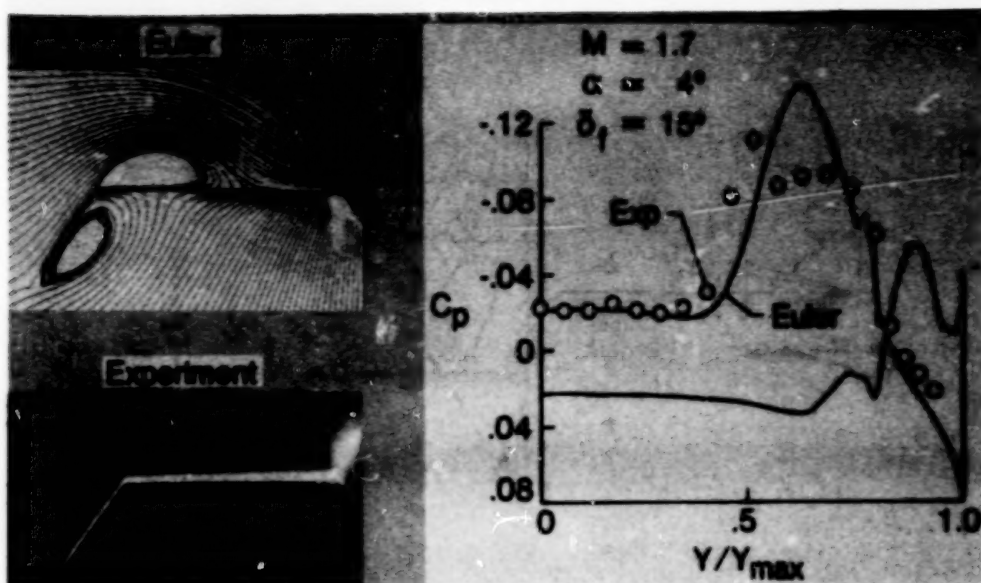


Figure 19. Experimental and Euler code results for wing flap at  $M = 1.7$ ,  $\alpha = 4^\circ$ ,  $\delta_f = 15^\circ$ .

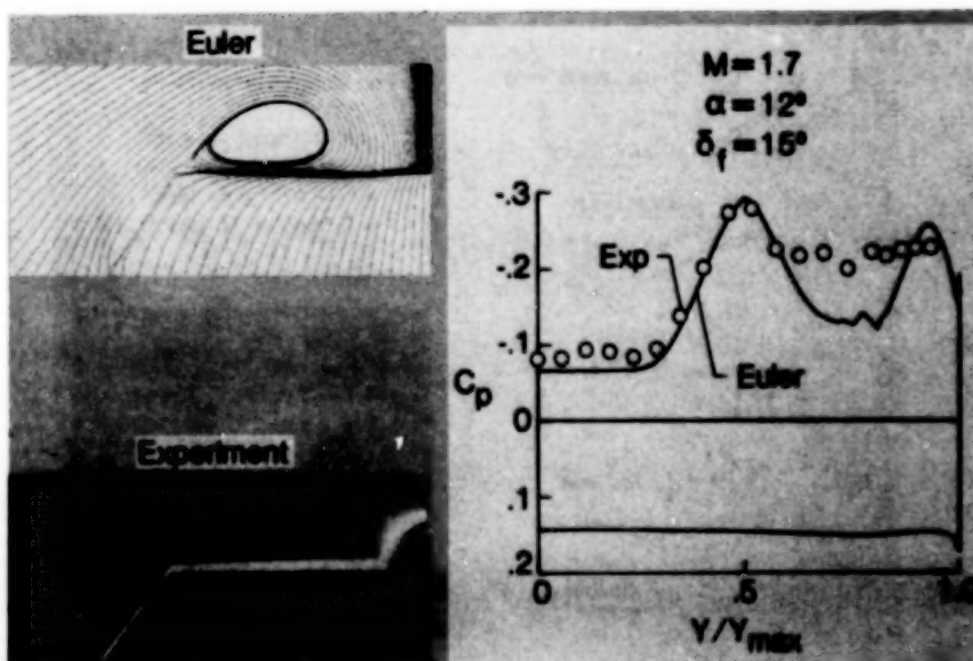


Figure 20. Experimental and Euler code results for wing flap at  $M = 1.7$ ,  $\alpha = 12^\circ$ ,  $\delta_f = 15^\circ$ .

C-5

ORIGINAL PAGE IS  
OF POOR QUALITY

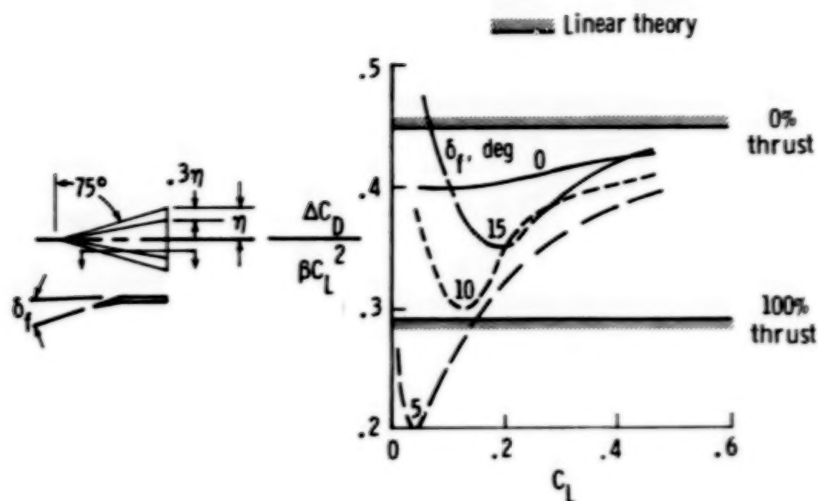


Figure 21. Experimental drag-due-to-lift factor for conical wing flap.

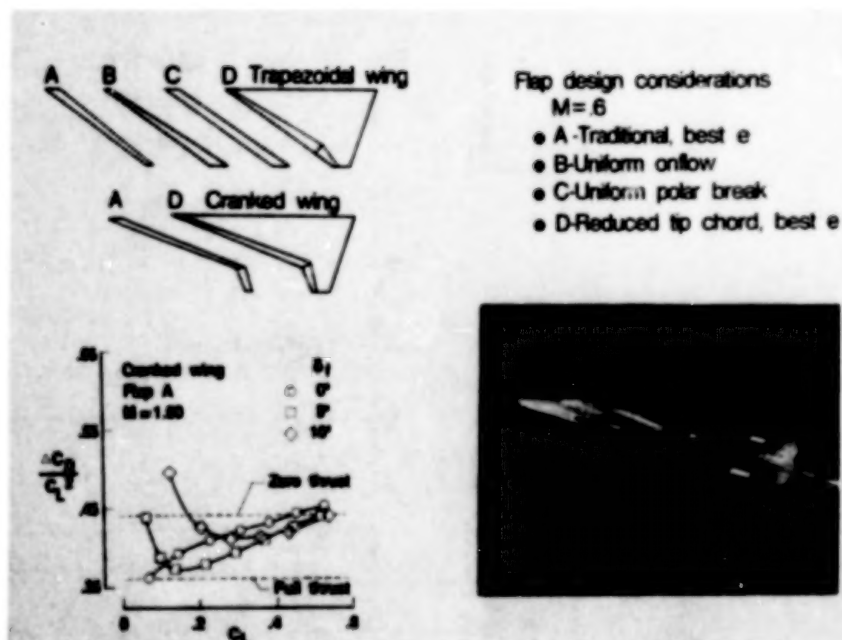


Figure 22. Elements of conventional leading-edge flap study.

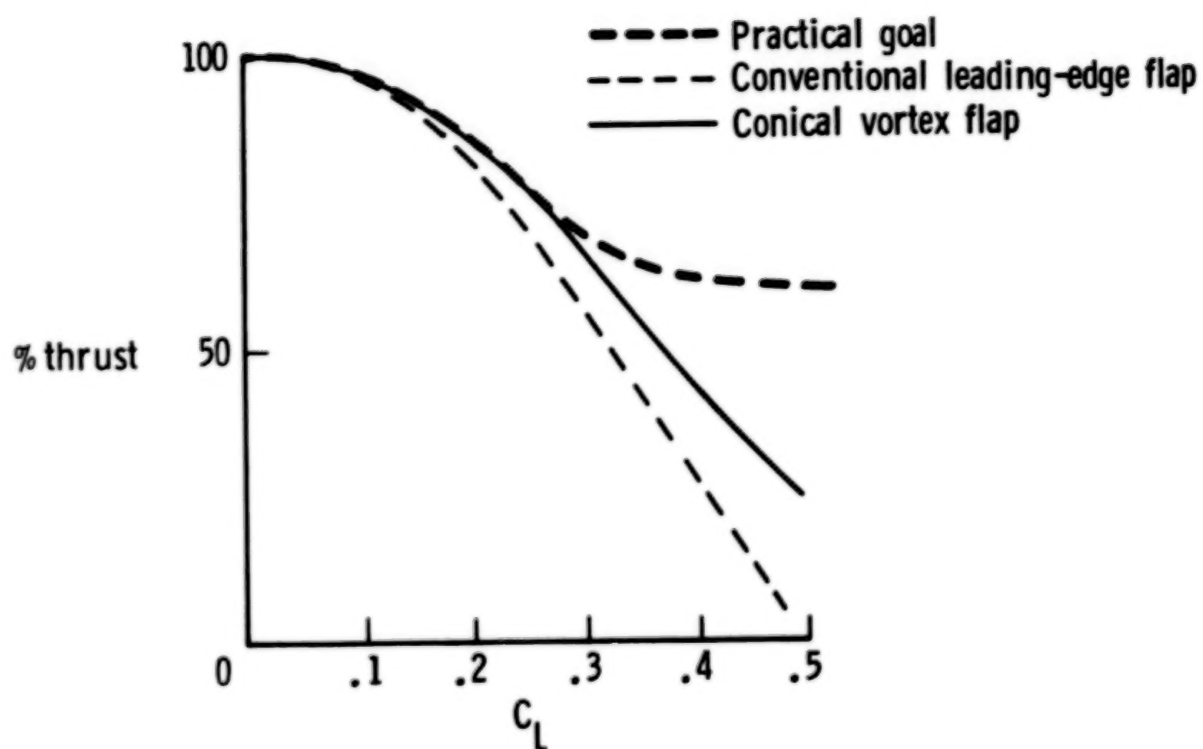


Figure 23. Supersonic performance summary.

WATER TUNNEL RESULTS OF LEADING-

EDGE VORTEX FLAP TESTS ON A

DELTA WING VEHICLE

N86-27208

John H. Del Frate  
NASA Ames Research Center  
Dryden Flight Research Facility  
Edwards, California

SUMMARY

A water tunnel flow visualization test on leading-edge vortex flaps was conducted at the flow visualization facility of the NASA Ames Research Center's Dryden Flight Research Facility. The purpose of the test was to visually examine the vortex structures caused by various leading-edge vortex flaps on the delta wing of an F-106 model. The vortex flaps tested were designed analytically and empirically at the NASA Langley Research Center. The three flap designs were designated as full-span gothic flap, full-span untapered flap, and part-span flap.

The test was conducted at a Reynolds number of 76,000/m (25,000/ft). This low Reynolds number was used because of the 0.076-m/s (0.25-ft/s) test section flow speed necessary for high-quality flow visualization. However, this low Reynolds number may have influenced the results.

Of the three vortex flaps tested, the part-span flap produced what appeared to be the strongest vortex structure over the flap area. The full-span gothic flap provided the next best performance.

INTRODUCTION

The vortex flap concept was conceived under the assumption that if the flap can be designed through planform shaping and/or twist to promote vortex flow reattachment along the hinge line at design lift, pressure distributions that reduce drag most efficiently per unit flap area will be established on the flap.<sup>1</sup> For a vortex flap to perform optimally, it should capture the entire leading-edge vortex on its upper surface and provide flow reattachment on the upper surface leading edge at or near the hinge line.<sup>2</sup>

To evaluate this concept, four vortex flaps were designed for the F-106 model. Three of these are bolt-on types and one is an integral type. The bolt-on flaps extend from the underside and ahead of the wing leading edge; integral flaps, when undeflected, are a part of the wing planform. The three bolt-on flaps, shown in figure 1,\* include an analytically designed full-span gothic flap, an untapered empirical variation of the full-span gothic flap, and an analytically designed

---

\*Color prints of figures 2, 5, 6, and 7 are available from the author.

part-span flap. The bolt-on flaps were designed for a Mach number of 0.3 and 30° downward deflection. The integral flap was designed for a Mach number of 0.8 and 40° downward deflection.

These flaps have been extensively tested in various wind tunnels on different scale models and at different Reynolds numbers. To better understand the vortex structure, Langley and Ames-Dryden jointly conducted a test on the three bolt-on flap configurations using an F-106A model. (An F-106A model was used instead of the F-106B model because of availability. Only slight geometric differences exist between the models, and these occur in locations that should not affect the flow field in the regions of interest.)

## EXPERIMENTAL METHODS

### Water Tunnel Facility

Except for a few modifications, the Ames-Dryden flow visualization facility (FVF) is based on the design of the Northrop Corporation closed-return water tunnel. Figure 2 shows a schematic of the FVF. The test section measures 0.41 m by 0.61 m (16 in. by 24 in.) and is 1.83 m (72 in.) long. The test section is oriented vertically and is made entirely of 5.08-cm (2-in.) thick plexiglass, which allows for 360° viewing of the tests. There is a door on the side of the test section for convenient access to the model and the support mechanism.

In general, the model angle of attack can be remotely varied  $\pm 45^\circ$ , and the sideslip angle can be varied  $\pm 15^\circ$  between runs. The velocity range of the FVF can be varied from 0.013 m/s (0.04 ft/s) to 0.335 m/s (1.1 ft/s). The flow velocity of the test section for this test was 0.076 m/s (0.25 ft/s), which is equivalent to a Reynolds number of 76,000/m (23,000/ft). This velocity is typically used because it allows excellent flow visualization.

The visualization technique used in this test is the colored dye technique. With this technique, colored dyes are pumped into the flow field through dye lines to provide a three-dimensional view of the flow.

### Model Description

The model tested was a modified 1/48-scale F-106A hobby model (figure 3). The modifications included the following:

1. The landing gear was placed in the retracted position
2. The inlets were made operational in order to simulate the proper mass flow ratio
3. The ailerons were repositioned to a zero deflection; the model originally came with the ailerons in the down position



4. Eight dye lines were installed externally underneath the wing with aluminum tape. The eight dye ports were located along the leading edge of the vortex flap (figure 2). Dye port locations were determined by trial and error.
5. Three different vortex flaps were installed on the model. Each vortex flap was tested with various deflection angles (see table 1). The flaps were formed from aluminum and bent to the proper deflection angle, and their leading edges were sharpened. These flaps were then attached to the underside of the wing with double-sided tape (figure 4).

#### Test Procedure

Each configuration was tested at sideslip  $\beta = 0^\circ$  and at  $8^\circ$ ,  $10^\circ$ ,  $12^\circ$ ,  $14^\circ$ ,  $16^\circ$ , and  $20^\circ$  angles of attack. Some configurations were also tested at a  $6^\circ$  angle of attack. In addition, most of the configurations were tested at  $\beta = +5^\circ$ .

The colored dye flow visualization technique was used because the primary purpose of this experiment was to provide localized three-dimensional views of any vortical activity on or near the vortex flaps. This technique allowed visualization of the vortex structure developed by the vortex flaps.

Data were recorded visually using both videotape and 35-mm slide film. Slides were taken of both the side view and the plan view of the model at sideslip  $\beta = 0^\circ$ . At  $\beta = +5^\circ$ , slides were taken of only the plan view. Videotape records were taken of only the plan view. Notes on peculiarities, trends, and onsets were recorded for each test run.

#### RESULTS AND DISCUSSION

This discussion is limited to a few selected cases. These cases illustrate general trends and are representative of the various configurations tested.

##### Performance Criteria

In a water tunnel flow visualization test, one is usually limited to a strictly qualitative set of data recorded at a very low Reynolds number. This was considered acceptable for the vortex flap test. As a result, performance criteria were limited to

1. strength of the leading-edge vortex that develops on the vortex flap (that is, vortex definition, rotation rate, length, and stability)
2. leading-edge vortex persistence (that is, the range of angle of attack through which the leading-edge vortex exists)

## General Introductory Comments for All Configurations

$\beta = 0^\circ$ . - In general, all flap configurations exhibit the same behavior at angles of attack  $\alpha$  in the range  $0^\circ < \alpha < 8^\circ$ . In this range, the flow on the upper surface of the flap and the wing is attached and laminar. As the angle of attack increases above a certain value ( $8^\circ < \alpha < 14^\circ$ , depending on the configuration) the flow on the upper surface of the flap begins to separate. As the flow separates, the leading-edge vortex begins to develop. As the angle of attack is increased, the leading-edge vortex continues to grow in strength.

With some configurations, as the leading-edge vortex develops there is a continuous shedding of this vortex at a consistent frequency. The leading-edge vortex is formed, then the whole vortex sheds itself from the flap and proceeds parallel (for the most part) to the flap over the upper wing surface. As this is taking place another leading-edge vortex has developed on the upper surface of the vortex flap. In addition, as the vortex gains strength, the portion of the leading-edge vortex towards the rear of the flap starts to lift off the flap surface, and separated stagnant backflow starts to creep forward along the surface of the vortex flap. The extent of this type of flow varies with each configuration.

$\beta = +5^\circ$ . - In general, the same trends noted for the  $\beta = 0^\circ$  case pertain to the  $\beta = +5^\circ$  case. The main difference is that the onset of any particular flow condition occurs at an angle of attack approximately  $2^\circ$  lower on the leeward flap and approximately  $2^\circ$  higher on the windward flap than in the  $\beta = 0^\circ$  case.

### Full-Span Gothic Vortex Flap

$\beta = 0^\circ$ . - With all configurations tested, the angle of attack at which the leading-edge vortex forms on the surface of the vortex flap is a function of the flap deflection angle. For the full-span gothic flap, approximate angles for the onset of vortex development are as follows:

| <u>Flap deflection <math>\delta</math>, deg</u> | <u>Angle of attack <math>\alpha</math> for vortex formation, deg</u> |
|---|--|
| 30  | 9  |
| 40  | 9  |
| 50  | 10   |
| 60  | 12   |

Results for  $30^\circ$  flap deflection, shown in figure 5, are discussed here. At  $\alpha = 9^\circ$ , a leading-edge vortex develops that is immediately shed. As the leading-edge vortex sheds from the vortex flap it travels past the hinge line to merge with two vortices on the wing surface. The forward section (approximately 30 to 40 percent of the leading-edge vortex) of the shed vortex merges with a vortex that originates at the forward wing/fuselage juncture (from this point on, this vortex will be referred to as the juncture vortex). The juncture vortex lies farther inboard and is approximately parallel to the fuselage. The remainder of the shed vortex travels just past the hinge line to merge with a vortex that lies approximately parallel to the hinge line (from this point on, this vortex will be referred to as the hinge line vortex). As the angle of attack increases ( $\alpha > 9^\circ$ ) the leading-edge vortices pro-

duced by the vortex flap increase in strength. As these vortices shed, they tend to increasingly feed the hinge line vortex, making it stronger, until it eventually overcomes and merges with the juncture vortex, becoming the only vortex structure seen on the surface of the wing. This occurs at  $\alpha \approx 18^\circ$ . At the upper angle-of-attack test limit of  $20^\circ$ , results remain approximately the same.

$\beta = +5^\circ$ . - The results noted previously in the general introductory comments also apply to the  $\beta = +5^\circ$  case.

Performance. - Based on the performance criteria, the full-span gothic flap produces a strong leading-edge vortex. The leading-edge vortex existed from  $\alpha \approx 9^\circ$  on up past  $20^\circ$  at what was judged to be the optimum flap deflection ( $\delta = 30^\circ$ ).

#### Full-Span Untapered Vortex Flap

$\beta = 0^\circ$ . - The results for the full-span untapered flap varied significantly from those of the other two flaps tested.

Again, the angle of attack at which the leading-edge vortex develops on the flaps varies with the deflection angle. For the full-span untapered flap, the approximate onset angles are as follows:

| <u>Flap deflection <math>\delta</math>, deg</u> | <u>Angle of attack <math>\alpha</math> for vortex formation, deg</u> |
|---|--|
| 30  | 8  |
| 40  | 10   |
| 40 <sup>a</sup>                                 | 12   |
| 50  | 12   |

<sup>a</sup>Hinge gap filled in with modeling clay.

Results for the  $50^\circ$  flap deflection, shown in figure 6, are discussed here. At  $\alpha = 12^\circ$ , a leading-edge vortex develops and is shed immediately (as described previously in the section concerning comments for all configurations). The vortex is different than those produced by the other flaps in that once the vortex is shed onto the wing upper surface it moves across and off the wing surface at the trailing edge of the wing.

The full-span untapered flap continues to develop leading-edge vortices at angles of attack up to  $20^\circ$  (and greater at some deflections); however, at  $\alpha = 20^\circ$  the strength of the juncture vortex overcomes everything else on the upper surface of the wing, and details are not well visualized.

It was thought that the discontinuity of the juncture between the flap surface and the wing leading edge might be the cause of the vortex shedding. Therefore, modeling clay was applied to smooth out the discontinuity. The modeling clay was applied such that the leading edge of the flap and the leading edge of the wing would form the edges of a smooth plane. After this modification, the leading-edge vortex continued to shed, and performance change, if any, was negative.

It was then hypothesized that the vortex shedding might be a Reynolds number effect instead of a configuration effect. At a Reynolds number this low, one might expect flow reattachment failure at the hinge line.<sup>3</sup> This in turn may be another

explanation as to why the leading-edge vortex is shed instead of remaining on the vortex flap.

$\beta = +5^\circ$ . - The results noted previously in the general introductory comments also apply to the  $\beta = +5^\circ$  case.

Performance. - The leading-edge vortex formed on the full-span untapered flap appears to have good definition. However, it is not as strong as that exhibited by the gothic flap. A flap deflection of  $50^\circ$  was judged to be the best for the full-span untapered vortex flap.

#### Part-Span Untapered Vortex Flap

$\beta = 0^\circ$ . - For the part-span untapered flap, the angles of attack at which the leading-edge vortex develops on the surface of the vortex flap are as follows:

| <u>Flap deflection <math>\delta</math>, deg</u> | <u>Angle of attack <math>\alpha</math> for vortex formation, deg</u> |
|---|--|
| 30  | 10   |
| 40  | 10   |
| 50  | 12   |
| 60  | 14   |

Results for the  $30^\circ$  flap deflection, shown in figure 7, are discussed here. At  $\alpha = 10^\circ$ , a leading-edge vortex develops on the flap surface and immediately sheds onto the upper surface of the wing. At  $\alpha \approx 12^\circ$ , the hinge line vortex (similar to the one observed on the Gothic flap) appears and merges with the shed leading-edge vortices. As the angle of attack increases to  $14^\circ$ , the forward 30 to 40 percent of the leading-edge vortex no longer sheds. It is stationary and very strong on the upper surface of the flap. At  $\alpha \approx 20^\circ$ , the rear section of the leading-edge vortex stops shedding, and it no longer develops on the flap surface but rather on the wing. The leading-edge vortex starts at the forward end of the flap and travels along approximately 30 to 40 percent of the flap where it turns streamwise until it goes off the trailing edge of the wing.

All the part-span flap configurations develop a leading-edge vortex beyond  $\alpha = 20^\circ$ .

Though not shown herein, the part-span flap at  $60^\circ$  deflection did not follow the general behavior of the other flap configurations; it never developed the hinge line vortex like the others did. This configuration allowed a strong juncture vortex to exist throughout all angles of attack tested. At  $\alpha > 14^\circ$  the flow coming over the flap surface separated, and the flap began producing leading-edge vortices that merged with the juncture vortex. This trend continued at  $\alpha > 20^\circ$ .

$\beta = +5^\circ$ . - The results noted previously in the general introductory comments also apply to the  $\beta = +5^\circ$  case.

Performance. - The part-span vortex flap performed very well (compared with the other flaps) with respect to its ability to hold a leading-edge vortex on the surface of the flap. Although this flap did not maintain a leading-edge vortex along



the full length of the flap, its performance was better than that of the other flaps. The strength and stability of the leading-edge vortex produced by the part-span vortex flap were judged to be the strongest of those observed. A part-span vortex flap deflection of 30° proved to be the best of the part-span flap configurations.

### CONCLUSIONS

Of the three sets of flap configurations tested, the part-span vortex flap at 30° deflection was judged to be the most effective leading-edge vortex flap based on the performance criteria used. The full-span gothic vortex flap at 30° deflection was the next most effective.

The low Reynolds number of 76,000/m (25,000/ft) may have been the cause for the flow failing to reattach after having traveled over the vortex structure on the flap. This in turn may have caused the periodic shedding of the leading-edge vortex.

Each of the three sets of vortex flap configurations changed the wing flow field significantly.

### REFERENCES

1. Frink, Neal T.: Concept for Designing Vortex Flap Geometries (U). NASA TP-2233, 1983.
2. Ghaffari, Farhad, and Lamar, John E.: An Attached Flow Design of a Non-interfering Leading Edge Extension to a Thick Delta Wing. AIAA Paper 85-0350, 1985.
3. Carmichael, B.H.: Low Reynolds Number Airfoil Survey, Vol. 1. NASA CR-165803, 1981.

TABLE 1. - LEADING-EDGE VORTEX FLAP TEST CONDITIONS<sup>a</sup>

| Full-span gothic flap |               | Full-span untapered flap |               | Part-span flap |               |
|-----------------------|---------------|--------------------------|---------------|----------------|---------------|
| $\delta$ , deg        | $\beta$ , deg | $\delta$ , deg           | $\beta$ , deg | $\delta$ , deg | $\beta$ , deg |
| 30                    | 0             | 30                       | 0             | 30             | 0             |
| 30                    | 5             | 40                       | 0             | 30             | 5             |
| 40                    | 0             | 40 <sup>b</sup>          | 0             | 40             | 0             |
| 40                    | 5             | 40                       | 5             | 40             | 5             |
| 50                    | 0             | 50                       | 0             | 50             | 0             |
| 50                    | 5             | 50                       | 5             | 50             | 5             |
| 60                    | 0             |                          |               | 60             | 0             |
| 60                    | 5             |                          |               | 60             | 5             |

<sup>a</sup>Angle-of-attack range varied from 6° to 20°.

<sup>b</sup>Hinge gap filled in with modeling clay.



ORIGINAL PAGE IS  
OF POOR QUALITY

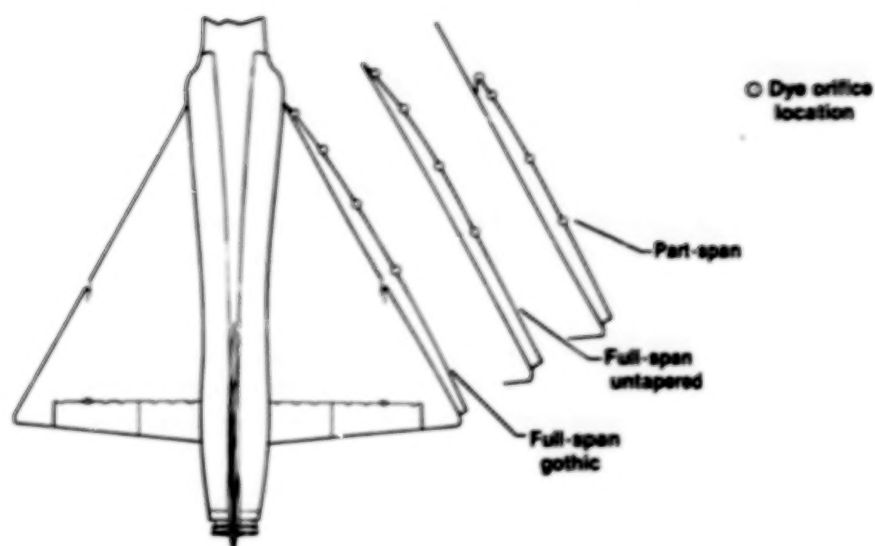


Figure 1. Schematic of flap planforms and dye orifice locations.

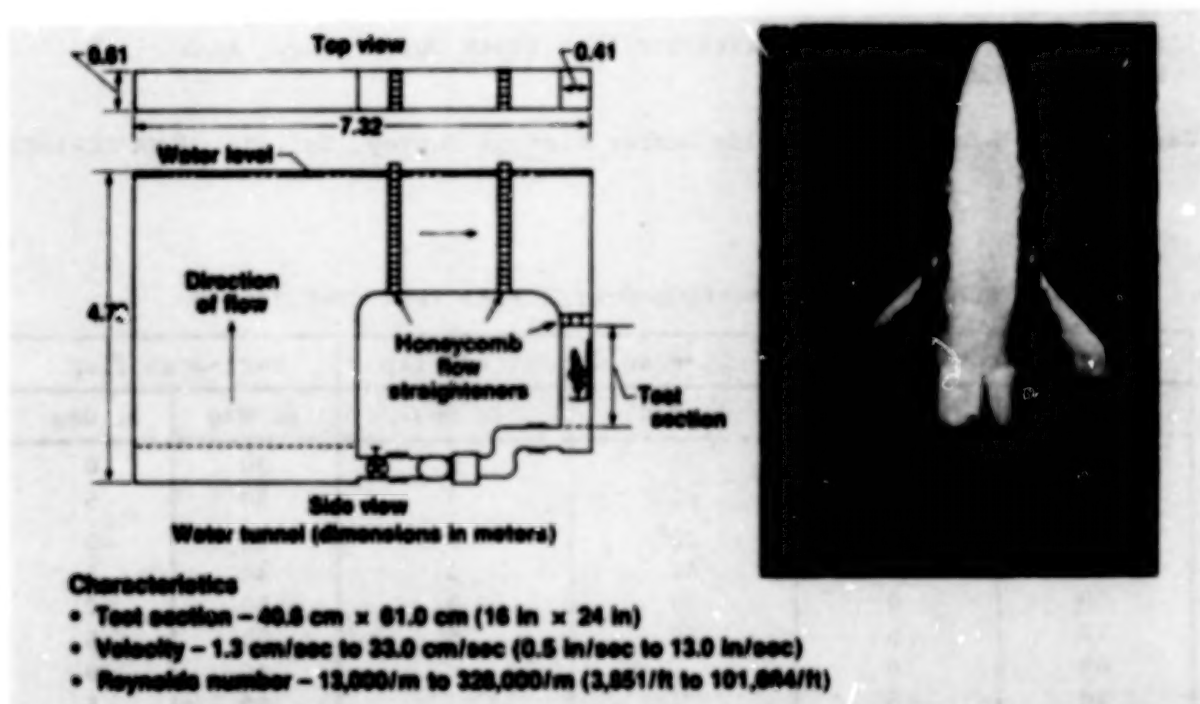


Figure 2. Flow visualization facility schematic and photograph of model in test section.



Figure 3. Three-view drawing of F-106A model with overall dimensions.

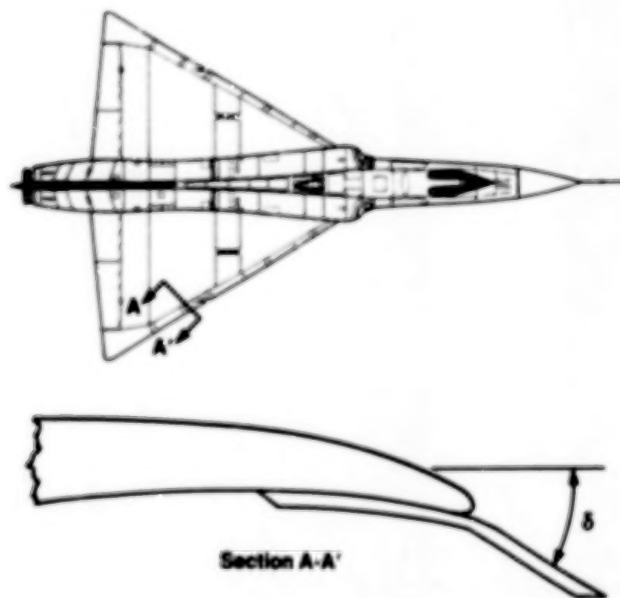


Figure 4. Typical cross-sectional view of an F-106 wing leading edge and a bolt-on flap.

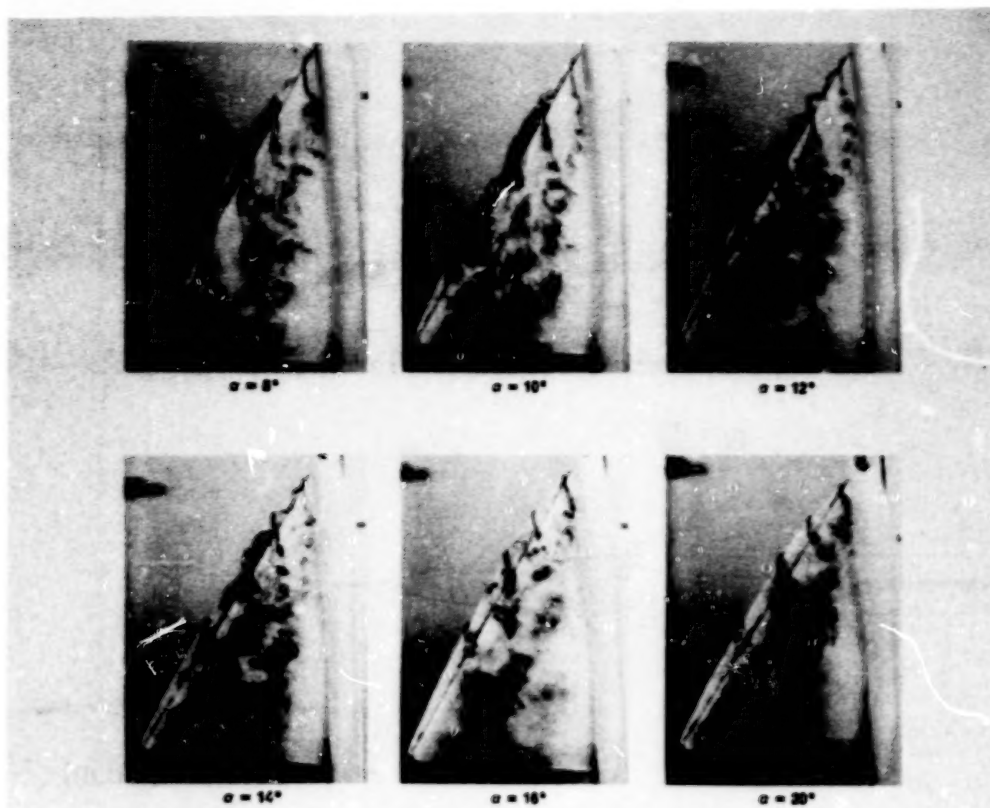


Figure 5. Results from the full-span gothic vortex flap test with flap deflected 30° (top view, left wing).

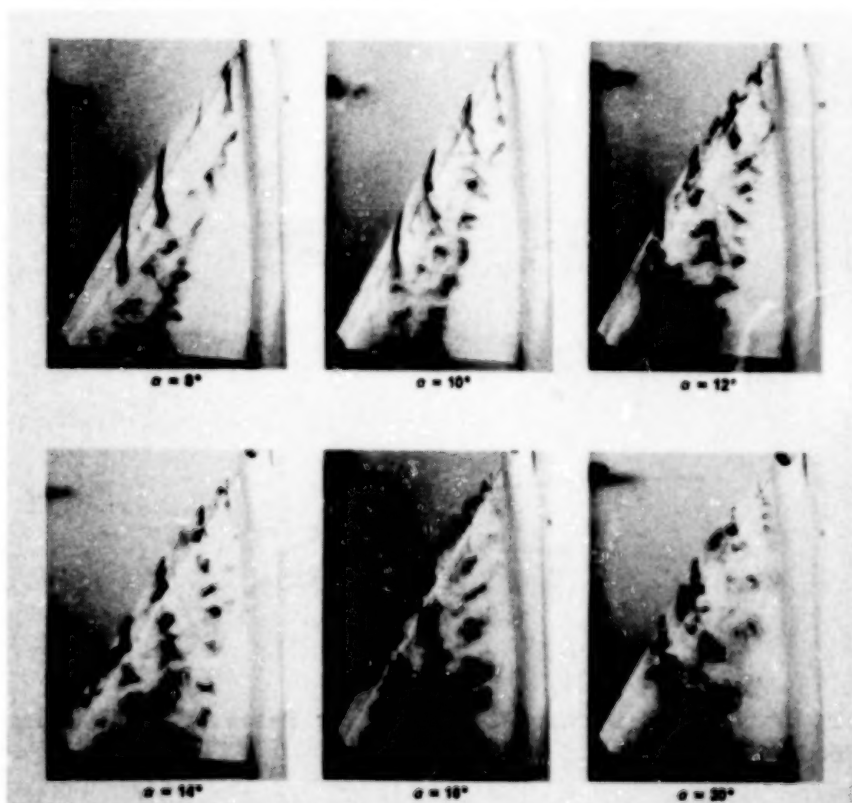


Figure 6. Results from the full-span untapered vortex flap test with flap deflected 50° (top view, left wing).

ORIGINAL PAGE IS  
OF POOR QUALITY

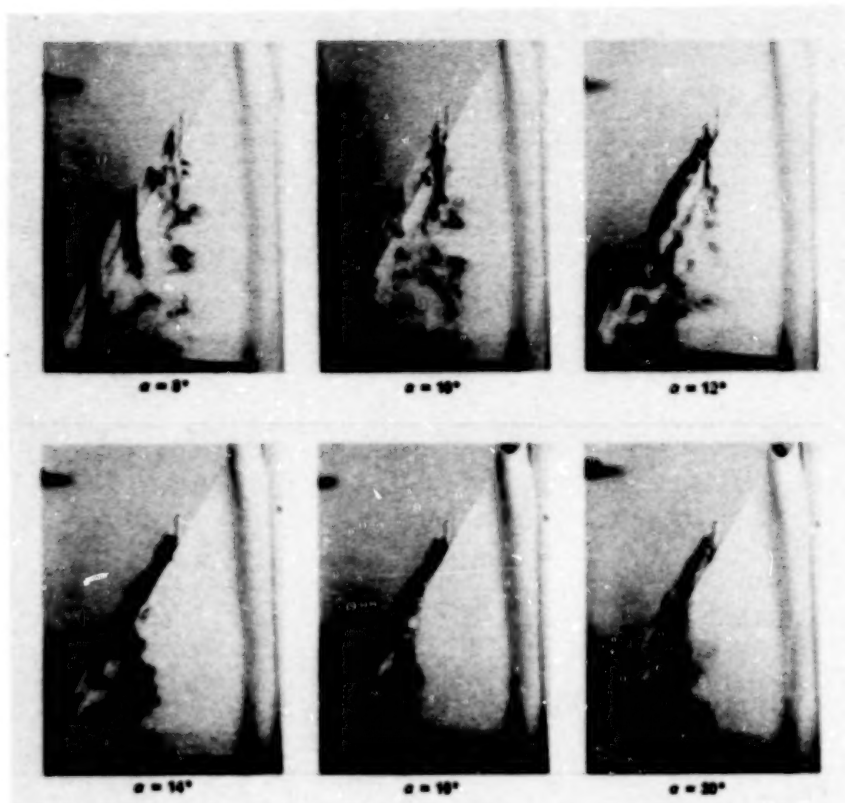


Figure 7. Results from the *pat*-span vortex flap test with flap deflected  $30^\circ$  (top view, left wing).

## ATTENDEES

### Non-Langley Attendees

Ballengee, Major James E.  
AFSC Liaison Office  
NASA Langley Research Center  
Langley Air Force Base, VA 23665-5000

Bevilaqua, Paul M.  
Lockheed Advanced Aeronautics Company  
25115 Avenue Stanford, Box 1  
Valencia, CA 93155

Blom, Gordon A.  
Boeing Military Airplane Company  
P. O. Box 3707  
Seattle, WA 98124

Buck, Melvin L.  
AFWAL/FIM  
Wright-Patterson Air Force Base  
Dayton, OH 45433-6553

Buter, Thomas A.  
AFWAL/FIMM  
Wright-Patterson Air Force Base  
Dayton, OH 45433-6553

Carlson, Harry W.  
PRC Kentron, Inc.  
NASA Langley Research Center  
Mail Stop 411  
Hampton, VA 23665-5225

Cathey, John R.  
ASD/XRHI,  
Wright-Patterson Air Force Base  
Dayton, OH 45433-6553

Cunningham, Atlee M, Jr.  
General Dynamics  
Mail Zone 2870  
P. O. Box 748  
Fort Worth, TX 76101

DeJarnette, Fred R.  
North Carolina State University  
Prof. Mechanical and Aerospace Eng.  
Box 7910  
Raleigh, NC 27695

Del Frate, John H.  
NASA Dryden Flight Research Facility  
P. O. Box 273  
Edwards, CA 93523

Dillner, Bertil  
Boeing Military Airplane Company  
P. O. Box 3707  
Seattle, WA 98124

Dixon, Charles J.  
Lockheed-Georgia Company  
86 S. Cobb Drive  
Dept. 72-74, Zone 403  
Marietta, GA 30063

Durham, Michael H.  
PRC Kentron, Inc.  
NASA Langley Research Center  
Mail Stop 340  
Hampton, VA 23665-5225

Erickson, Gary E.  
Northrop Corporation  
One Northrop Avenue, Dept. 3812/82  
Hawthorne, CA 90250

Ericsson, Lars E.  
Lockheed Missiles & Space Company, Inc.  
1111 Lockheed Way  
Orgn. 81-10, Bldg. 1575E  
Sunnyvale, CA 94088

Finley, Dennis B.  
General Dynamics  
Mail Zone 2882  
Fort Worth, TX 76101



Frassinelli, Mark C.  
AFWAL/FIMM  
Wright-Patterson Air Force Base  
Dayton, OH 45433-6553

Grantz, Arthur C.  
Northrop Corporation  
One Northrop Avenue, Dept. 3812/82  
Hawthorne, CA 90250

Hensch, Michael J.  
PRC Kentron, Inc.  
NASA Langley Research Center  
Mail Stop 294  
Hampton, VA 23665-5225

Herling, William W.  
Boeing Aerospace Company  
P. O. Box 3999  
Seattle, WA 98124

Hoffler, Keith D.  
Vigyan Research Associates, Inc.  
28 Research Drive  
Hampton, VA 23666

Huebner, Lawrence D.  
George Washington University  
NASA Langley Research Center  
Mail Stop 294  
Hampton, VA 23665-5225

Hunter, Daniel F.  
University of Notre Dame  
Aerospace Lab  
Notre Dame, IN 46556

Johnson, Thomas D., Jr.  
PRC Kentron, Inc.  
NASA Langley Research Center  
Mail Stop 294  
Hampton, VA 23665-5225

Joshi, Prakash B.  
Northrop Corporation  
One Northrop Avenue, Dept. 383/82  
Hawthorne, CA 90250

Kandil, Prof. Osama A.  
MEM Department  
Old Dominion University  
Norfolk, VA 23508

Klein, John R.  
McDonnell Douglas Corporation  
P. O. Box 516  
St. Louis, MO 63166

Lan, C. Edward  
The University of Kansas  
Department of Aerospace Engineering  
Lawrence, KS 66045

Long, Lyle N.  
Lockheed-California Company  
P. O. Box 551  
Burbank, CA 91520-7552

Malcolm, Gerald N.  
Eidetics, Int.  
3669 W. 240th Street  
Torrance, CA 90505

Marconi, Frank  
Grumman Aerospace Corporation  
Mail Stop A08-35  
Bethpage, NY 11714

Mason, William H.  
Grumman Aerospace Corporation  
Mail Stop C-31  
Bethpage, NY 11714

McMurray, Thomas J.  
ETA Systems, Inc.  
NCNB Plaza Suite 403  
Chapel Hill, NC 27514

Mehrotra, Sudhir C.  
Vigyan Research Associates, Inc.  
28 Research Drive  
Hampton, VA 23666

Meznarsic, Victor F.  
McDonnell Douglas Corporation  
P. O. Box 516  
St. Louis, MO 63166

Miranda, Luis R.  
Lockheed-California Company  
P. O. Box 551  
Burbank, CA 91520-7552

Muchmore, Bryam  
George Washington University  
NASA Langley Research Center  
Mail Stop 269  
Hampton, VA 23665-5225

Murman, Earl M.  
Massachusetts Institute of Technology  
Department of Aeronautics & Astronautics  
Room 33-217  
Cambridge, MA 02139

Nelson, Robert C.  
University of Notre Dame  
Department of Aerospace & Mechanical  
Engineering  
Notre Dame, IN 46556

Newsome, R. W.  
AFWAL  
NASA Langley Research Center  
Mail Stop 156  
Hampton, VA 23665-5225

Novak, Charlie J.  
Lockheed-Georgia Company  
86 S. Cobb Drive  
Dept. 72-74, Zone 403  
Marietta, GA 30063

Osborn, Russell F.  
AFWAL/FIMM  
Wright-Patterson Air Force Base  
Dayton, OH 45433-6553

Payne, Francis M.  
University of Notre Dame  
Department of Aerospace & Mechanical  
Engineering  
Notre Dame, IN 46556

Peake, David J.  
NASA Ames Research Center  
Mail Stop 227-2  
Moffett Field, CA 94035

Powell, Kenneth G.  
Massachusetts Institute of Technology  
Room 37-350  
Cambridge, MA 02139

Powers, Bruce G.  
NASA Dryden Flight Research Facility  
P. O. Box 273  
Edwards, CA 93523

Presley, Leroy L.  
NASA Ames Research Center  
Mail Stop 227-4  
Moffett Field, CA 94035

Rajkovic, Dario  
Grumman Aerospace Corporation  
Mail Stop C26-05  
Bethpage, NY 11714

Ram, Ram B.  
State University of New York  
NASA Langley Research Center  
Mail Stop 359  
Hampton, VA 23665-5225

Rao, Dhanvada M.  
Vigyan Research Associates, Inc.  
28 Research Drive  
Hampton, Va 23666

Reynolds, Gregory A.  
Lockheed-Georgia Company  
86 S. Cobb Drive  
Dept. 72-11, Zone 403  
Marietta, GA 30063

Rhodes, James A.  
MEM Department  
Old Dominion University  
Norfolk, VA 23508

Rogers, L. W.  
AFWAL/FIMM  
Wright-Patterson Air Force Base  
Dayton, OH 45433-6553

Shang, Joseph J. S.  
AFWAL/FIMM  
Wright-Patterson Air Force Base  
Dayton, OH 45433-6553

Siclari, Michael J.  
Grumman Aerospace Corporation  
Mail Stop A08-35  
Bethpage, New York 11714

Sirbaugh, J. R.  
AFWAL/FIMM  
Wright-Patterson Air Force Base  
Dayton, OH 45433-6553

Smith, Charles W.  
General Dynamics  
Mail Zone 2882  
P. O. Box 748  
Fort Worth, TX 76101

Snyder, James R.  
ASD/XRHI  
Wright-Patterson Air Force Base  
Dayton, OH 45433-6503

Snyder, Melvin H.  
NRC Research Associate  
NASA Langley Research Center  
Mail Stop 286  
Hampton, VA 23665-5225

Tai, Tsze C.  
David Taylor Naval Ship Research  
and Development Center  
Office of Naval Research  
Code 1132F  
800 N. Quincy Street  
Arlington, VA 22217

Vretakis, Nicholas G.  
AFSC Liaison Office  
NASA Langley Research Center  
Langley Air Force Base, VA 23665-5000

Walters, Marvin M.  
U. S. Naval Air Development Center  
Code 6053  
Warminster, PA 18974

Whitesides, John L.  
George Washington University  
NASA Langley Research Center  
Mail Stop 269  
Hampton, VA 23665-5225

Woan, Chung-Jin  
Rockwell International  
P. O. Box 92098  
Los Angeles, CA 90009

# NASA Langley Attendees

Allen, Jerry N.  
 Banks, Daniel W.  
 Barnwell, Richard W.  
 Bennett, Robert M.  
 Bland, Samuel R.  
 Bobbitt, Percy J.  
 Bower, Robert E.  
 Brandon, Jay  
 Campbell, Bryan A.  
 Campbell, James F.  
 Cathey, John R.  
 Cazier, Frank W., Jr.  
 Chambers, Joseph R.  
 Chu, Julio  
 Coe, Paul L., Jr.  
 Covell, Peter F.  
 Crabill, Norman L.  
 Croom, Mark A.  
 Dagenhart, John R.  
 Darden, Christine M.  
 Doggett, Robert V., Jr.  
 Dwoyer, Douglas L.  
 Edwards, John W.  
 Ferris, James D.  
 Foughner, Jerome T., Jr.  
 Fox, Charles H., Jr.  
 Frink, Neal T.  
 Gainer, Thomas G.  
 Gatlin, Gregory M.  
 Gifford, Robert V.  
 Gilbert, William P.  
 Gloss, Blair B.  
 Goodman, Wesley L.  
 Greene, George C.  
 Hall, Robert M.  
 Hallissy, James B.  
 Harris, Roy V., Jr.  
 Harvey, William D.  
 Hess, Robert W.  
 Hodges, William T.  
 Huffman, Jarrett K.  
 Johnson, Joseph L., Jr.  
 Kirkham, Frank S.  
 Kjølgaard, Scott O.  
 Lamar, John E.  
 Letchworth, Robert  
 Liu, Chen-Huei

Luckring, James M.  
 Mann, Michael J.  
 McGinley, Catherine B.  
 McKinney, L. Wayne  
 McMin, John D.  
 Miller, David S.  
 Molloy, John K.  
 Morris, Charles E. K., Jr.  
 Murri, Daniel G.  
 Newman, Perry A.  
 Nguyen, Luat T.  
 Patteson, James C., Jr.  
 Paulson, John W., Jr.  
 Polhamus, Edward C.  
 Pride, Joseph D.  
 Riebe, Gregory D.  
 Ruhl, Charles L.  
 Rush, Homer F., Jr.  
 Salas, Manuel D.  
 Sawyer, Wallace C.  
 Schoonover, Ward E., Jr.  
 Sellers, William L., III.  
 Shrout, Barrett L.  
 Small, William J.  
 Smith, Ronald H.  
 South, Jerry C., Jr.  
 Stack, Sharon H.  
 Stickle, Joseph W.  
 Taylor, John G.  
 Thomas, James L.  
 Vandever, Doris B.  
 Wahls, Richard A.  
 Whitlow, Woodrow  
 Williams, Louis J.  
 Wood, Richard M.  
 Worth, Catherine B.  
 Yates, E. Carson  
 Yeaton, Robert B.  
 Yip, Long P.

|   |  |                             |   |   |  |
|---|--|-----------------------------|---|---|--|
| 1. Report No.<br>NASA CP-2416   |  | 2. Government Accession No. |   | 3. Recipient's Catalog No.                                      |  |
| 4. Title and Subtitle<br><br>Vortex Flow Aerodynamics - Volume I  |  |                             |   | 5. Report Date<br>July 1986                                     |  |
|   |  |                             |   | 6. Performing Organization Code<br>505-60-21-02                 |  |
| 7. Author(s)<br>James F. Campbell, Russell F. Osborn, and<br>Jerome T. Foughner, Jr., Editors   |  |                             |   | 8. Performing Organization Report No.<br>L-16117                |  |
|   |  |                             |   | 10. Work Unit No.   |  |
| 9. Performing Organization Name and Address<br><br>NASA Langley Research Center<br>Hampton, VA 23665-5225   |  |                             |   | 11. Contract or Grant No.                                       |  |
|   |  |                             |   | 13. Type of Report and Period Covered<br>Conference Publication |  |
| 12. Sponsoring Agency Name and Address<br><br>National Aeronautics and Space Administration<br>Washington, DC 20546-0001<br><br>and<br><br>Air Force Wright Aeronautical Laboratories<br>Wright Patterson Air Force Base, OH 45433-6553   |  |                             |   | 14. Sponsoring Agency Code                                      |  |
|   |  |                             |   |   |  |
| 15. Supplementary Notes<br>James F. Campbell and Jerome T. Foughner, Jr.: Langley Research Center, Hampton, Virginia.<br>Russell F. Osborn: Air Force Wright Aeronautical Laboratories, Wright-Patterson Air Force Base, Ohio.  |  |                             |   |   |  |
| 16. Abstract<br><br>The objectives of the joint NASA/Air Force Vortex Flow Aerodynamics conference held at NASA Langley Research Center October 8-10, 1985, were to discuss (1) vortex modeling techniques, (2) experimental studies of research configurations utilizing vortex flows, (3) vortex flap investigations using generic and airplane research models, and (4) vortex flap theoretical analysis and design studies.<br><br>The proceedings are published in three volumes because of the range of classifications: Volume I, Unclassified (NASA CP-2416); Volume II, Unclassified, ITAR restricted (NASA CP-2417); and Volume III, Confidential (NASA CP-2418). |  |                             |   |   |  |
| 17. Key Words (Suggested by Author(s))<br>Aerodynamics<br>Leading-edge vortex flows<br>Vortex flaps<br>Aircraft   |  |                             | 18. Distribution Statement<br>Unclassified - Unlimited<br><br><br>Subject Category 02 |   |  |
| 19. Security Classif. (of this report)<br>Unclassified  | 20. Security Classif. (of this page)<br>Unclassified | 21. No. of Pages<br>402     | 22. Price<br>A18  |   |  |